SACLANTCEN CONFERENCE PROCEEDINGS SERIES CP-45

High Frequency Acoustics in Shallow Water

Proceedings of a conference held in
Lerici, Italy, 30 June to 4 July, 1997,
organized and sponsored by the
NATO SACLANT Undersea Research Centre

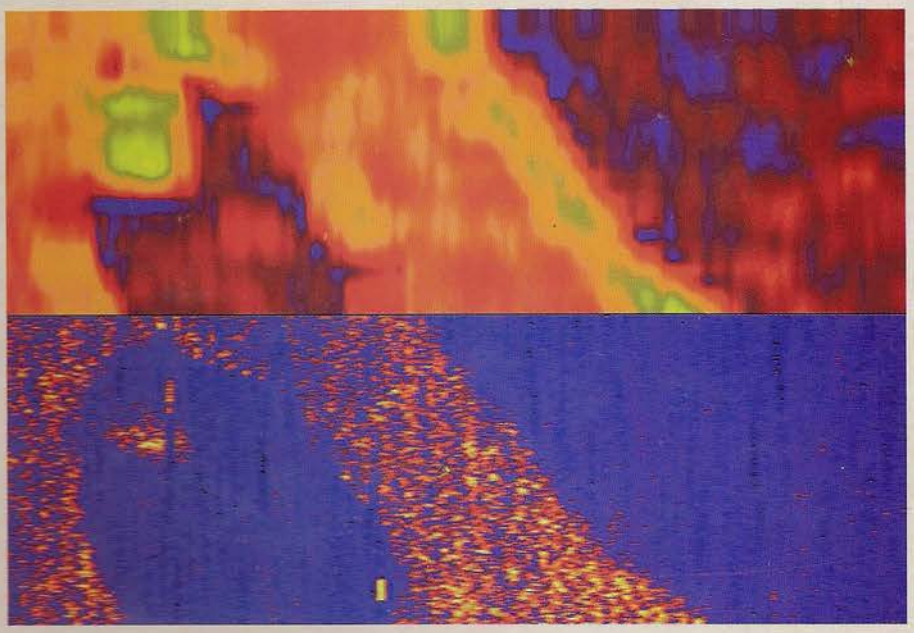

Pace N.G.
Pouliquen E.
Bergem O.and
Lyons A.P.
editors

NATO SACLANT Undersea Research Centre

High Frequency Acoustics in Shallow Water

SACLANTCEN Conference Proceedings CP-45

High Frequency Acoustics in Shallow Water

edited by

Nicholas G. Pace

Eric Pouliquen

Oddbjørn Bergem

and

Anthony P. Lyons

NATO SACLANT Undersea Research Centre,
La Spezia, Italy

NATO SACLANT Undersea Research Centre
La Spezia, Italy

Proceedings of the conference on high frequency acoustics in shallow water, Lerici, Italy, 30 June to 4 July, 1997, organized by:

NATO SACLANT Undersea Research Centre, La Spezia, Italy.

Published by: NATO SACLANT Undersea Research Centre,
Viale San Bartolomeo 400,
19138 LA SPEZIA, Italy.

email: library@saclantc.nato.int
Fax: +39 187 524 600

Distribution:

Requests for copies in the United Kingdom of Great Britain and Northern Ireland should be forwarded to:

Office of Naval Research, European Office, Code 400
Edison House,
223-231 Old Marylebone Road, London, NW1 5TH

Requests for copies in the United States of America should be forwarded to:

Office of Naval Research
United States National Liaison Officer (USNLO) to the SACLANTCEN
800 North Quincy Street
Arlington VA 22217-5660
USA

British Library Cataloguing in Publication Data

A catalogue record for this book is available from the British Library.

Cataloguing in publication data:

High frequency acoustics in shallow water
edited by Nicholas Gaze Pace 1945 - , Eric Pouliquen, Oddbjørn Bergem, and Anthony Patrick Lyons
p.612 24.5 cm.
Proceedings of a conference held in Lerici, (SP) Italy, 30 June to 4 July, 1997.
(SACLANTCEN Conference Proceedings Series CP-45)
ISBN 88-900194-1-7

Preface

In recent years there has been an increased awareness of the importance of processes in shallow water in the context of underwater acoustics. This heightened interest by national, environmental and other bodies has given impetus to new approaches in high frequency acoustics for sensing parameters of the water column, the seabed and sea surface together with applications in the civil and defence field.

The response to the Call for Papers for this conference was such that many high quality submissions could not be accommodated. The authors of the papers in this volume, published to coincide with the conference, are thanked for their efforts in responding with enthusiasm to the request for electronic only submission. There were problems with this, probably more than anticipated. However, thanks to the hard work of E. Pouliquen, O. Bergem and A. Lyons, publication was on schedule.

N.G. Pace
La Spezia, May 1997

High Frequency Acoustics in Shallow Water

Editors

N.G. Pace
E. Pouliquen
O. Bergem
A.P. Lyons

Conference Address

NATO SACLANT Undersea Research Centre
Viale San Bartolomeo 400
19138 La Spezia

Tel: +39 187 540 238
Fax: +39 187 540 331
email pace@saclantc.nato.int

Contents by First Author

Contents by Subject

Seabed classification

Seabed properties

Bubbles

Seabed scatter

Propagation and the environment

Shallow water channels

Seabed mapping

Scattering from objects

High Frequency Acoustic Propagation in Coastal Waters

Tuncay Akal, Anthony P. Lyons, Daniela Di Iorio, Piero Guerrini

SACLANT Undersea Research Centre
Viale San Bartolomeo, 400
19138 La Spezia, ITALY
Email: akal@saclantc.nato.int

Abstract

High Frequency Acoustic Propagation experiments were performed with bottom-mounted sources and receivers at different coastal sites. A measurement technique has been developed and propagation loss data have been taken using sources covering the 29-326 kHz frequency range out to 400 m distance. High-resolution monitoring of relevant environmental parameters took place at the time of the acoustic measurements. In the present paper the new measurement technique is described and examples of acoustic/environmental data are presented. Predictions from SACLANTCEN propagation models developed for lower frequency applications are used for comparison with the measurements.

1. Introduction

The ability to predict propagation loss in coastal environments (10-100 m depth) at high frequencies (30-330 kHz) depends upon understanding the mechanisms of propagation and attenuation of acoustic waves. Acoustic propagation in the ocean is influenced by many factors: the physical and chemical properties of the water column cause attenuation and refraction, while variations in seafloor properties and boundary roughness complicate reflection. Thus, any attempt to predict propagation in shallow water at high frequencies requires an accurate knowledge of the propagation medium, especially the fine scale structure of the sea surface, water column and bottom properties. As part of SACLANTCEN's high frequency research program, high resolution acoustic data covering a broad frequency range were collected in order to adequately describe acoustic propagation, including penetration into the seabed, along with water column environmental characteristics. We obtained measurements of propagation loss at selected experimental sites that had different seafloor properties. These sites, which had previously been used for detailed seafloor studies, provided knowledge on sediment characteristics. Comparisons are made between experimental data and predictions from existing propagation models in order to assess their validity at the frequencies and depths studied.

2. Experimental Technique

The frequency range of acoustic measurements roughly covers from 30 to 330 kHz, corresponding to acoustic wavelengths of a few centimeters to a few millimeters in scale. Acoustic energy propagating at these frequencies in coastal water (10-100 m depth) is subject to high volume attenuation, so that useful ranges are limited to a few hundred meters. Thus, the fine scale structure of the water column (in range and time) and the boundaries (sea surface and sea-floor sediment properties) become essential factors when considering experimental procedures. For acoustic measurements, the receiving ship would first launch a vertical hydrophone string and a thermistor chain attached to a sled on the seafloor which was connected to the ship by electro-mechanical cable. The vertical hydrophone string consisted of three RESON omnidirectional hydrohones spaced in a way as to cover most of the water column. The ship would then lay the cable on to the bottom for the maximum range and anchor approximately 500 meters from the hydrophone and thermistor chain deployment position. After anchoring, the ship would deploy a tower containing seven transducers at 29, 50, 80, 105, 120, 190, 326 kHz attached to a pan and tilt unit. During the experiment, CW pulses of various length were transmitted and the signals that were being received by the hydrophones were transmitted via conducting cable to the ship and acquired. This data was then processed in order to estimate transmission loss.

In order to understand the range and time dependence of high frequency acoustic propagation in shallow

coastal waters simultaneous environmental measurements were obtained. These measurements consisted mainly of time series measurements of conductivity, temperature and depth (CTD) profiles together with CTD time series at a specific depths, acoustic doppler current profiler (ADCP) and current meter measurements. Sea surface roughness and meteorological information were also obtained during the experiments. The equipment set-up used for the propagation experiments is shown in Figure 1.

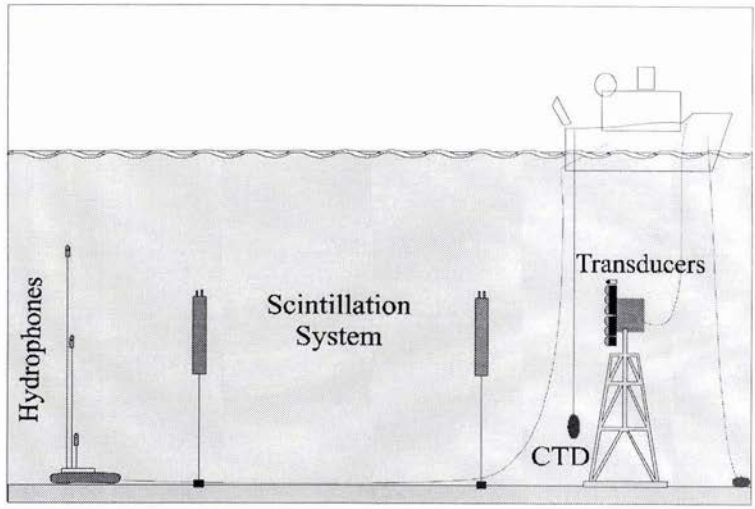

Figure 1: The experimental set-up.

The signals were transmitted one at a time, via different transducers. The positions of the transmitters were controlled by a pan and tilt unit upon which they are mounted. Received signals were preamplified near the hydrophones and transmitted to the ship via electromechanical cable. Onboard they are amplified, base-band filtered, digitized and acquired on a PC. Figure 2 shows the block diagram of the transmitting and receiving chain.

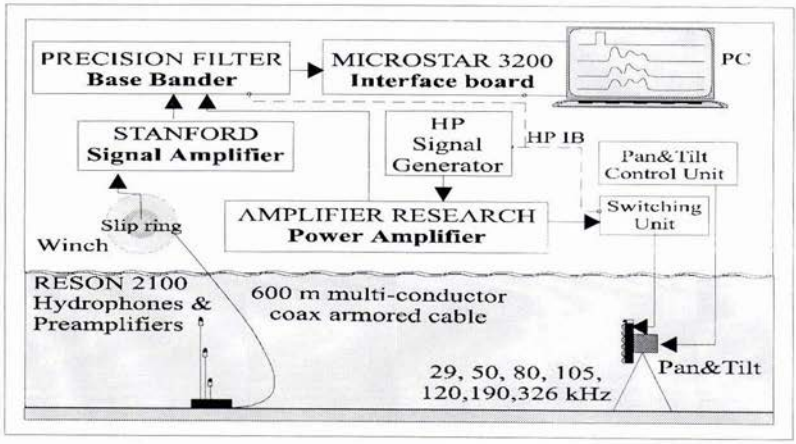

Figure 2: Block diagram of the measurement system

3. Watermass Characteristics Affecting High Frequency Acoustic Propagation

The coastal environment is often characterized by wind driven flow, and/or current flow interacting with topography, river runoff and increased variability in water properties as a result of enhanced mixing. The use of

high frequency acoustics in this kind of environment is sensitive to the random variations in temperature, current, sea surface and bottom roughness. In fact high frequency acoustic propagation measurements through random media have the potential for serving as a sensitive probe of coastal processes which differ markedly from those prevalent in less active waters of the deep ocean.

In order to better understand high frequency acoustic variability in coastal waters simultaneous environmental measurements should be obtained along with the acoustic measurements. These measurements may consist of time series of conductivity, temperature and depth (CTD) profiles together with CTD time series at a specific depth. In addition to sampling the temperature environment an acoustic doppler current profiler (ADCP) and current meters can be used to obtain measurement of current and circulation. For wind driven flow and sea surface roughness measurements, meteorological and wave rider buoys would be ideal for obtaining wind velocity and surface wave characteristics. The complete suite of environmental measurements taken can then be used as a guide to the causes of acoustic variability.

A high frequency (307.2 kHz) acoustic propagation system was deployed in one of the test sites near La Spezia, in 15 m water depth in March 1996 so as to observe acoustic amplitude variability over a continuous 8 hour period. Current and sound speed measurements were obtained simultaneously. The acoustic instrument consists of a transmitter and receiver unit each self contained and battery operated. The transmitter unit sends acoustic pulses of width 30 cycles at a transmission rate of 16 Hz. Pulses can be sent for a maximum 28 days before the batteries die. The receiving unit takes the incoming signals and complex demodulates them to obtain both amplitude and phase measurements for the direct path only. Path separation is possible because of the short pulse width, and the direct path can be tracked because of the large sampling rate. Since there is mooring motion the phase cannot be used to detect the effects of medium changes. The resulting acoustic variability is recorded within the receiver unit on flash EPROM recorder cards. The internal memory of the receiver unit limits the duration of data collection to 4.5 days at the 16 Hz sampling rate.

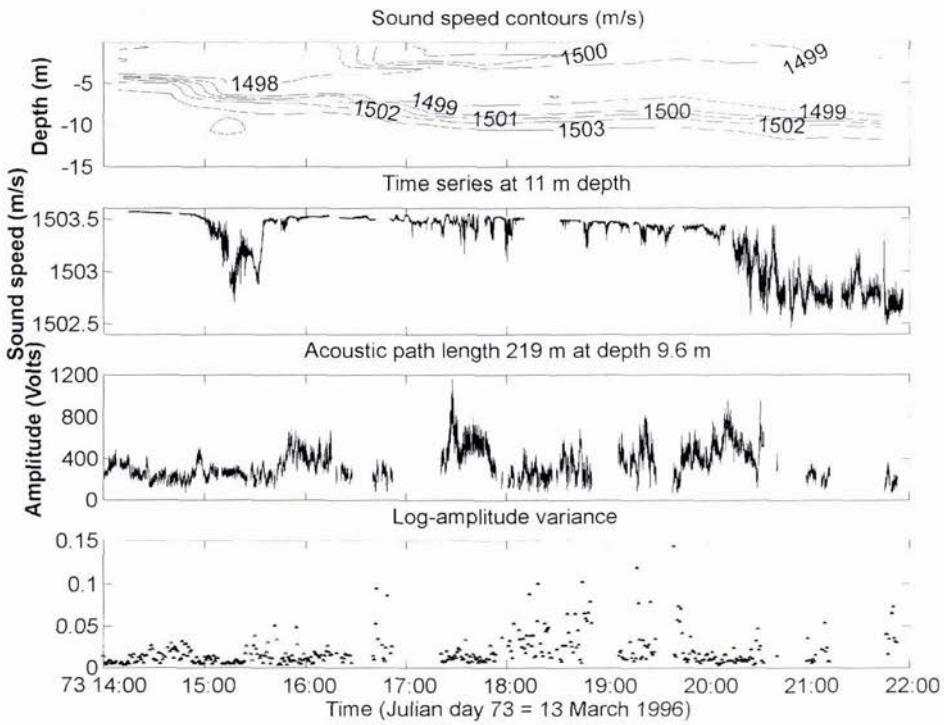

Figure 4: Comparison between environmental and acoustic measurements.

A comparison between environmental measurements and acoustic measurements is shown in Figure 4. A waterfall plot of the N-S and E-W current components from a bottom mounted ADCP (Figure 5) shows that there was a significant Northerly surface current for the first 4 hours (maximum current 10 cm/s). Contours of sound speed over the 8 hour measurement period show a strong thermocline that deepens with time and also show the onset of warm surface water caused by current advection. Between profiles the CTD was placed at 11 meters

depth to sample the temperature and salinity variability at a rate of 8 Hz. In the first 6 hours the CTD was below the thermocline. When the thermocline increased in depth to 11 m much temporal variability is seen.

The acoustic amplitude throughout the 8 hour measurement period shows significant temporal variability. The acoustic propagation measurements accumulate information along the 219 meter path at the depth 9m, thus the comparison to in situ measurements will show significant differences. The maximum variability corresponds to a 15 dB change over a period of 1 hour. In addition to mean amplitude, changes in the log-amplitude (ln(A/<A>) variance (calculated over 30 seconds) shows significant variability corresponding to fluctuations in the medium parameters. Since the temperature time series were taken at 11 m and the amplitude at 9 m, no direct correlation between the two measurements can be seen.

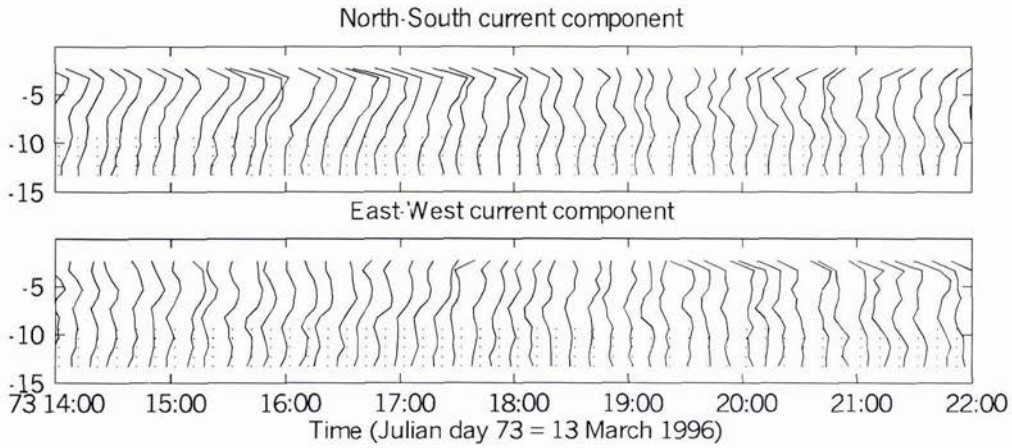

Figure 5: ADCP current estimates

4. Propagation Loss data

Acoustic transmission data were collected for each frequency at various distances of separation between the source and receiver along a track. This was accomplished by pulling the sled which held the receivers toward the transmitting tower. In this way a complete transmission loss data set as a function of range and frequency was formed. Data collected from the closest hydrophone to the source and at the closest experimental range was used as a reference in estimating the total outgoing energy at 1 m from the hydrophone. Noise was estimated for and removed from each received pulse (including the reference signals) by using the 20 ms of recorded data immediately preceding the arrival of the transmitted pulse. The transmission loss in dB is simply the energy in the received signal in dB (with noise removed) minus the energy in the reference signal in dB (with noise removed and spreading and attenuation losses added back in order to estimate the total outgoing energy at 1 m from the souce.) To evaluate the propagation loss at a particular frequency, the loss curves representing the total loss, without corrections for geometrical spreading are presented. It should also be noted that the loss values observed at each range position on a transmission loss curve are to be considered average values over 50 transmissions. In effect they also represent the average energy lost along a propagation path where, direct, surface, bottom and successive multi-path arrivals are all taken into account.

4.1 Examples from different areas

SACLANTCEN has carried out several sound propagation trials with the above described system in various test sites close to La Spezia and the Island of Elba. Analysis of propagation loss for the frequencies mentioned above was carried out and examples from three different tracks with different bottom conditions are presented in Figure 6 for the mid-depth receivers. Since transmission loss is a function of both range and frequency, in Figure 7 we present the isoloss contours in a Frequency/Range plane for three receiver depths. The information shown in Figure 7 corresponds to the Mud case presented in Figure 6.

Various models [1-3] were used and compared with the experimental propagation measurements to see if these models which were developed for lower frequency applications could accurately predict high frequency

transmission loss. Here we present a few examples from the OASES model [1] where model results are compared with measured data. Figure 8 shows the acoustic field at 29 kHz as a function of range and depth where it is possible to observe the general characteristics of propagation; at close ranges, the direct path is within the beam-width of the transmitter and after a certain range the effects of refraction and boundary reflections create interference patterns. Using measured environmental parameters, calculations using OASES were made and as an example the results for three frequencies are shown in figure 9. In general there is good agreement with the measured acoustic data.

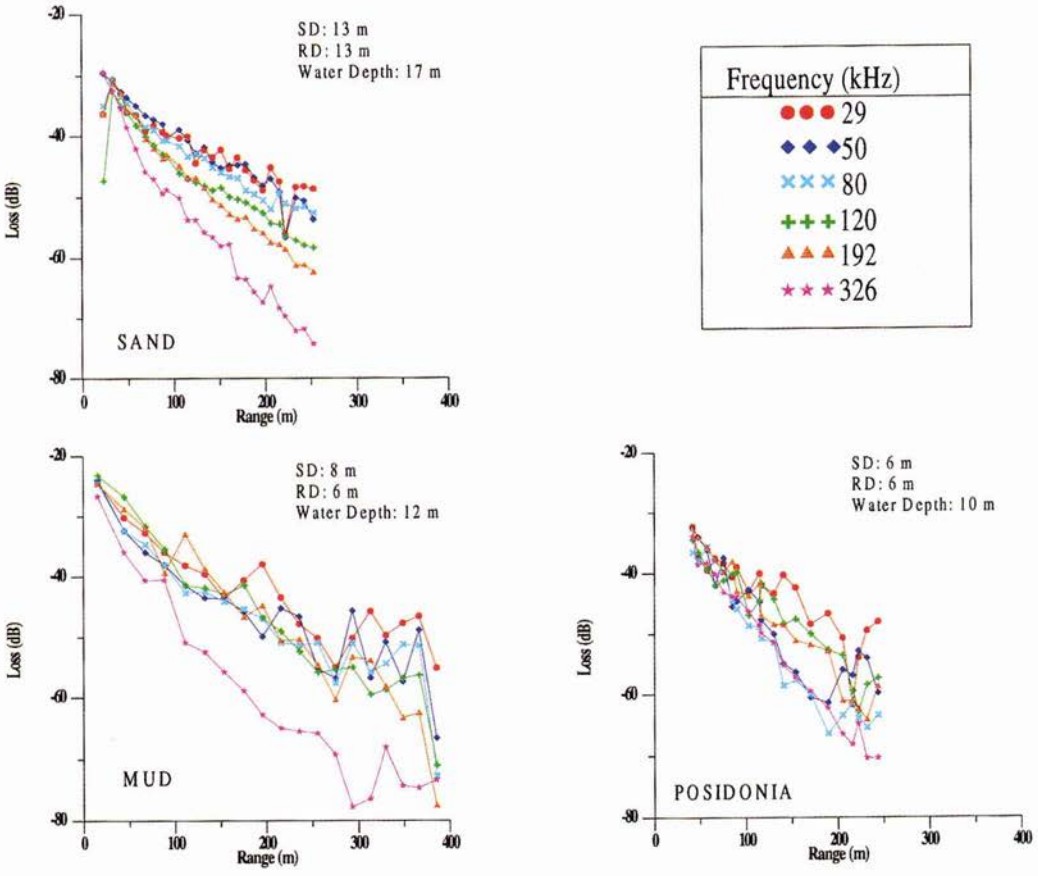

Figure 6: Examples of propagation losses measured over three different tracks with different environmental conditions.

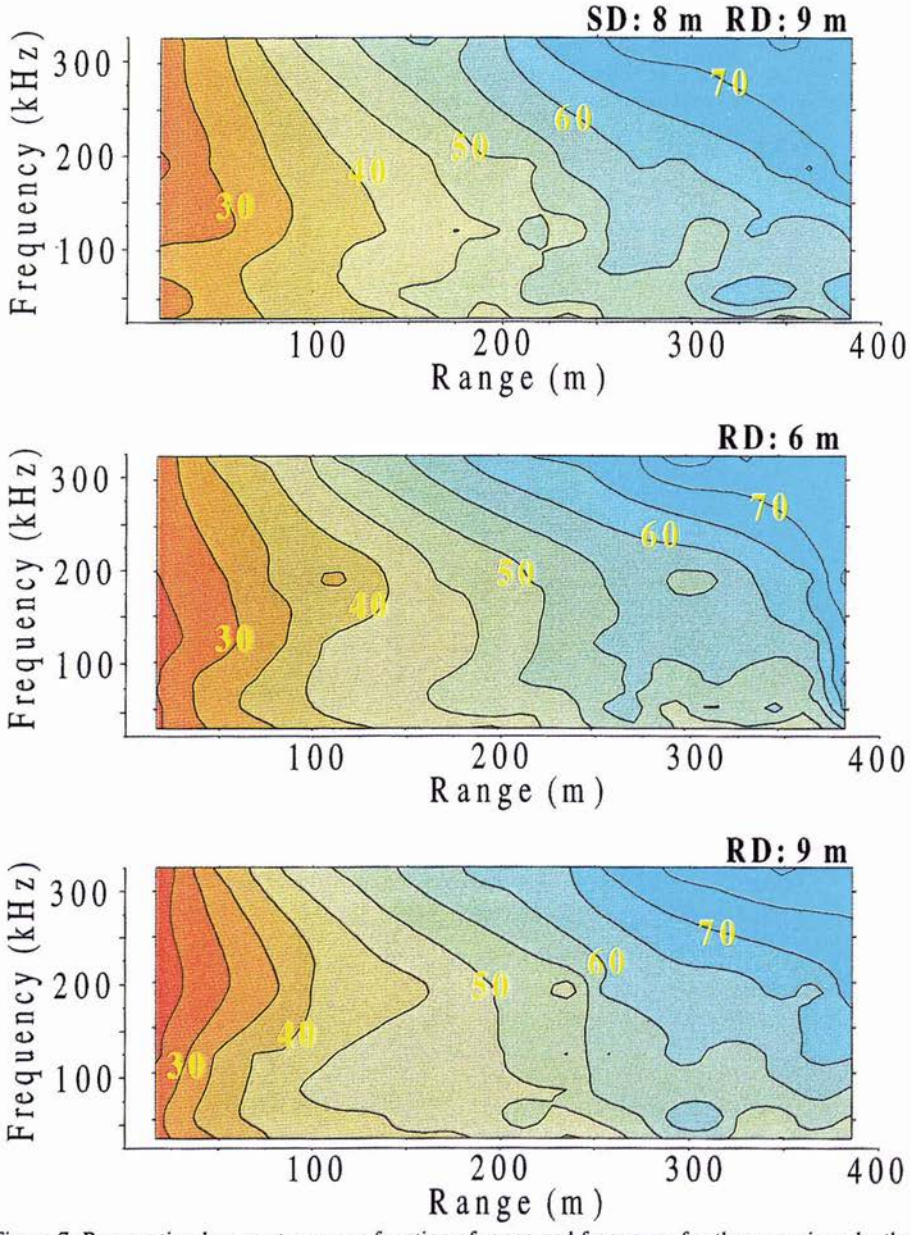

Figure 7: Propagation loss contours as a function of range and frequency for three receiver depths.

5. Conclusions

The significant purpose of this paper was to describe the measurement/analysis techniques that were developed to obtain reliable high frequency (30-320 kHz) propagation loss and related high-resolution environmental data and to also demonstrate the possibility of using acoustic propagation models developed and used widely for lower frequency applications at higher frequencies.

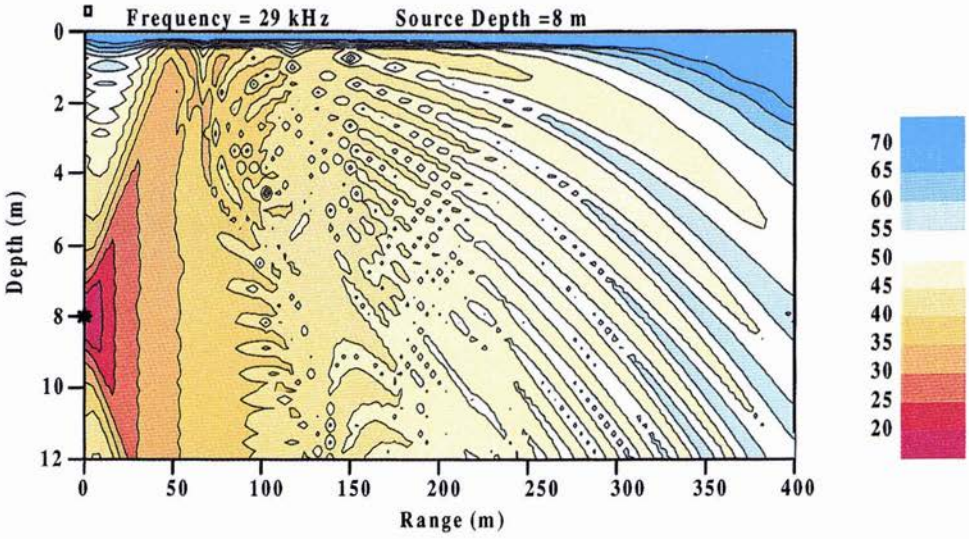

Figure 8: Acoustic field calculated with OASIS model.

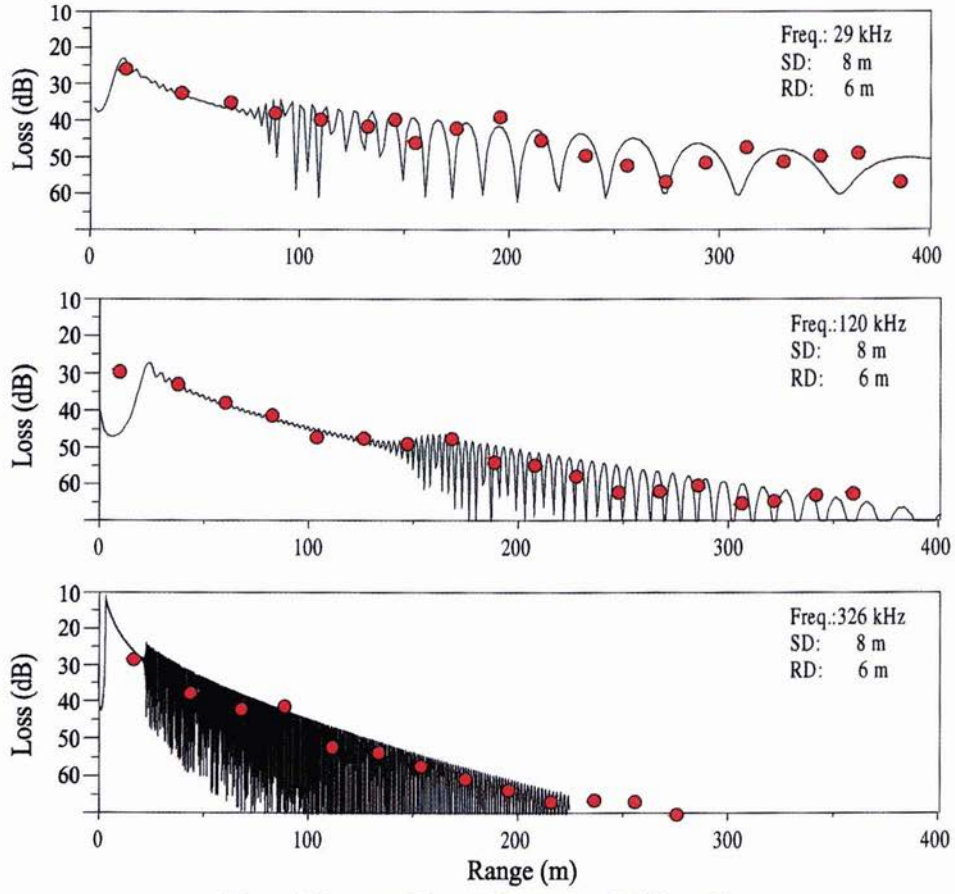

Figure 9: Data-model comparison using OASIS model.

6. Acknowledgments

The authors would like to express their appreciation to the captain and the crew of the T/B Manning for their efforts in collecting the data and also to Dr. F.B. Jensen and Dr. P. Nielsen for their inputs regarding the modeling component of this paper.

References

[1] H. Schmidt. OASES, version 1.6, application and upgrade notes. Cambridge, MA, Department of Ocean Engineering, Massachusetts Institute of Technology, 1993.

[2] M.C. Ferla, M.B. Porter, F.B. Jensen. C-SNAP: coupled SACLANTCEN normal mode propagation loss model, SACLANTCEN SM-274. La Spezia, Italy, NATO SACLANT Undersea Research Centre, 1993.

[3] H. Schmidt. SAFARI, seismo-acoustic fast field algorithm for range-independent environments, user's guide, SACLANTCEN SR-113. La Spezia, Italy, NATO SACLANT Undersea Research Centre, 1988.

Shallow-water coherence of broadband signals

M. Badiey[1], J. Simmen[2] and X. Tang[1]

[1]Ocean Acoustics Laboratory
Graduate College of Marine Studies
University of Delaware
Newark, DE 19716-3501, U.S.A

[2]Ocean Acoustics Program
Office of Naval Research, ONR 321 OA
Arlington, VA 22217–5660, U.S.A

Abstract

The frequency-dependent spatial and temporal variabilities of sound propagation in coastal regions is investigated by experiment and numerical simulations. Experimental observations show that temporal coherence of the propagated broadband signal changes significantly with pulse center-frequency, as well as varying with geographic location and time(i.e., different environments). Numerical simulations of such sound transmissions are carried out by using the full-wave broadband PE model and reasonable agreement with the experimental data is found.

1. Introduction

Sound propagation in shallow-water regions is complicated by multiple interactions of the acoustic waves with the sea bottom and sea surface, in addition to the usual interaction with the water column. The degree to which these different interactions cause degradation in the coherence of the pressure field at some distance is not well understood and depends on the scales of the variability in the water column, sea surface and sea bottom, as well as the frequency of the acoustic signal. Numerical modeling has indicated the importance and interplay of sea surface and bottom roughness alone [1] or of volume fluctuations.

Ocean environment monitoring techniques such as acoustical tomography [2] that exploit the use of acoustics have been practiced in deep water but may work equally as well in shallow water. The success of acoustical tomographic methods in shallow-water environments will be limited by our ability to separate out acoustic fluctuations due to the ocean volume from those due to the sea surface and sea bottom/subbottom. The optimal choice of a signal frequency or waveform to probe shallow-water environments is not obvious and will depend on the goals of the tomographic effort. To address this latter issue, we have initiated a study of the dependence of acoustic fluctuations on signal center-frequency for pulses propagated in shallow water [3]. Our immediate objective is to determine the dependence of coherence for a propagated broadband signal on center-frequency, bandwidth, ray path, and ocean environment. In this paper we present the results from a recent acoustic experiment and, for comparison, from corresponding numerical simulations intended to capture the primary features of the experiment.

2. Experimental Observation

In order to investigate the frequency dependence of broadband signals, several underwater acoustic experiments have been conducted in the last few years at locations where previous oceanographic studies have been conducted. These experiments have been performed primarly at two sites: one is the Atlantic Generating Station (AGS) site off shore New Jersey [4] in waters having a mean depth of approximately 14 m; the other is the Delaware Bay site [3] having a mean water depth of approximately 15 m. Figure 1 presents a general schematic layout of these experiments. To purposely avoid a contribution of instrument motion in the acoustic fluctuations, the source and receiver were mounted on tripods placed on the seafloor. The source-receiver ranges for these experiments varied from approximately 200 to 800 m. Series of M-sequences were transmitted at different center-frequencies

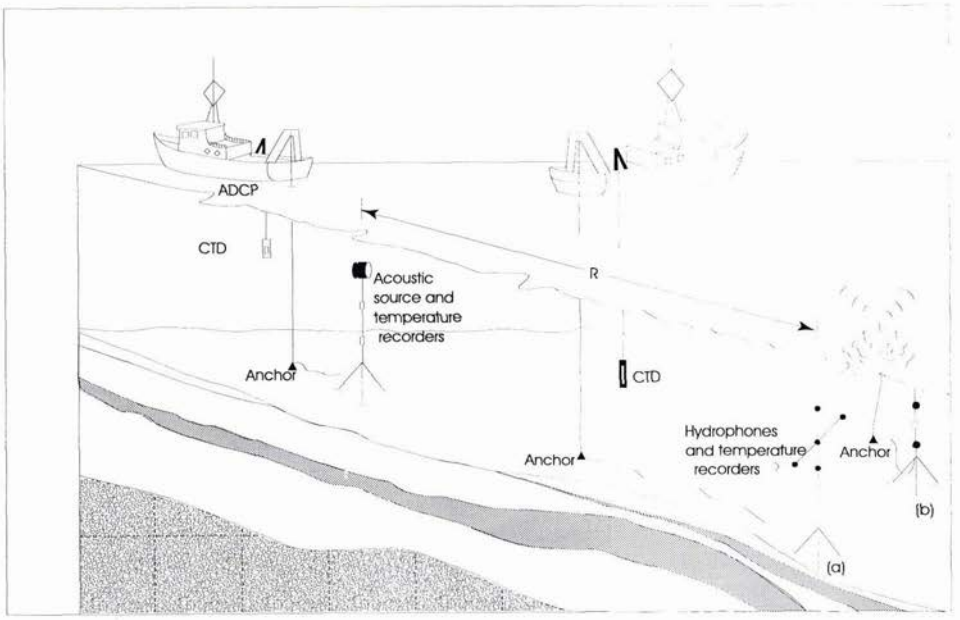

Figure 1: Experimental configuration: (a) Atlantic Generating Station site (range, R= 214 m) and (b) Delaware Bay site (R≈ 760 m).

to allow an easy examination of pulse propagation behavior as a function of frequency. Oceanographic parameters of temperature and salinity were measured by thermistors and CTD's.

In this paper we focus on the analysis for the second experiment which was conducted in the Delaware Bay. For the Delaware Bay site experiments, broadband pulses with variable bandwidths of 0-4 kHz, 0-8 kHz, 5-13 kHz, and 9-25 kHz were used. These bands were chosen to cover the entire low-to-mid frequency spectrum with overlapping coverage. The broadband pulses were filtered to divide the original 4 bands into Gaussian-shaped sub-bands with a fixed bandwidth and center-frequencies ranging from 1-22 kHz. The bandwidths of the lowest frequencies were narrower than those of the higher frequencies to insure that behaviors such as bottom interaction would not be averaged across too wide a band. For example, for 1-2 kHz center frequency the bandwidth was 1 kHz, for 3-6 kHz it was 2 kHz, for 7-11 kHz it was 3 kHz, and for 12-22 kHz the bandwidth was 4 kHz.

The receiver array in the Delaware Bay experiment was tethered to a surface buoy located approximately 760 meters from the source (Fig. 1), and the received acoustic signals were transmitted from the surface buoy to the source ship via VHF radio telemetry. The acoustic source was a F56 transducer with a maximum power of 160 dB re 1 μPa @ 1m (and the average signal to noise ratio for this experiment was 25 dB). This source was tethered to the ship (R/V Cape Henlopen).

Figure 2 shows, for a center-frequency of 2 kHz and geotimes from T_g= 0 to 12 hours, the received signal amplitude versus time. The solid curves in the figure show the predicted times for the first several groups of arrivals as a function of geotime, based primarily on the changing geometry of ray paths due to tide and secondarily on the advection of sound due to the ocean current. The first peak (i.e., 1) is actually comprised of three interfering arrivals, and subsequent peaks (i.e., 2,3,...) are comprised of pairs of interfering arrivals, corresponding to ray paths having multiple surface and bottom interactions. The three ray paths that comprise the first interfering group, include the direct path, single surface bounce, and surface-bottom bounce. Note how closely as a function of geotime the calculated arrival time tracks the measured arrival time for the first several arriving peaks. The strongest arriving peaks (i.e., 2 - 5) are those immediately following the first peak, followed by peaks (i.e., 6, 7, ...) with noticably reduced amplitudes, presumably due to the extended interaction with, and attenuation, from the sea surface and bottom.

Figure 3 illustrates the frequency dependence of the received signals. In this figure the received signal amplitude versus arrival time is presented as function of center-frequency for a fixed geotime (i.e., $T_g \approx$ 5 hrs). The monotonic

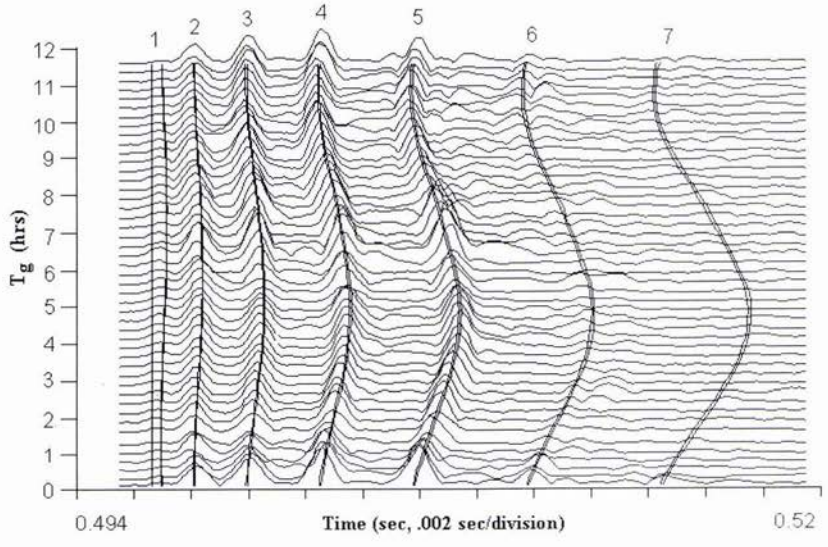

Figure 2: Measured signal amplitude versus time, after correction for source-receiver separation ($f_c = 2$ kHz). The solid lines are predicted arrival times versus geotime, T_g for the first several ray paths.

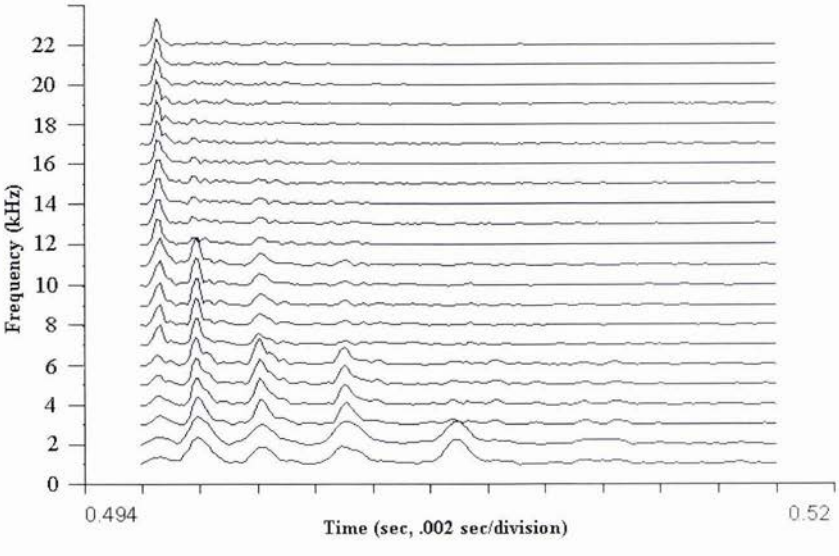

Figure 3: Time series of received signal amplitude as a function of frequency for $T_g \approx 5$ hrs.

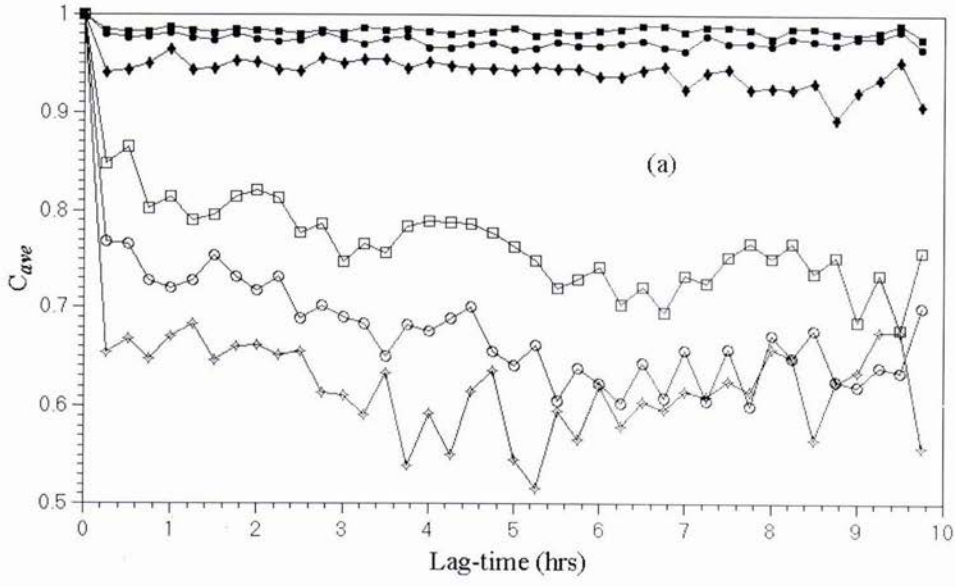

Figure 4: Average correlation for second peak (e.g., number 2 in Fig. 2) versus lag time for f_c =2, 4, 9, 12, 15 and 20 kHz.

growth of the first peak with frequency is a consequence of the fact that a different variable bandwidth filtering and normalization was applied to each frequency. Concealed by this frequency-dependent normalization, the amplitude of all arrivals at high frequencies is much reduced due to attenuation. Figure 3 suggests an inverse law: the number of relatively strong arrivals is approximately inversely proportional to the center-frequency.

In figure 4 the average correlation of the measured signal versus lag time for several center-frequencies and a fixed peak is presented. It clearly shows a rapid decorrelation at higher frequencies, especially those above 9 kHz. For lower center-frequencies there is hardly any decorrelation in signal over several hours, while for signals with the highest center-frequencies there was substantial decorrelation over times as short as 10 to 20 minutes. Generaly, the data analysis shows a trend of increasing signal decorrelation (between consecutive pulses) with increasing center-frequency, and increasing signal decorrelation for paths with increasing number of interface interactions. For those paths that multiply interact with the seafloor and sea surface there is an immediate decorrelation for center-frequencies of several kHz and higher. Futhermore, the data shows that at the higher frequencies, the strength of later arrivals seems to be a function of tidal cycle [3].

3. Numerical Simulations

Although the deterministic character of the measured acoustic data can simply be interpreted using the ray diagrams and experimental geometry, to accurately capture the effect of rough surface and rough bottom scattering, full-wave modeling is warranted. At high frequencies rough-surface scattering effects are strong enough that the consequences of these effects on pulse response functions in the time domain are not at all intuitive, and certainly ray-based approaches will fail to capture these frequency-dependent effects. Our modeling approach is to perform numerical simulations using the 2-D, full-wave broadband PE model, based on the efficient split-step Fourier algorithm.

The pulse signal is modeled via the frequency domain by Fourier synthesis of CW results within the frequency band of interest. This gives

$$\tilde{p}(z,r,t) = \int_{f_c - f_B/2}^{f_c + f_B/2} S(f) p(z,r,f) e^{-i2\pi f t}\, df, \tag{1}$$

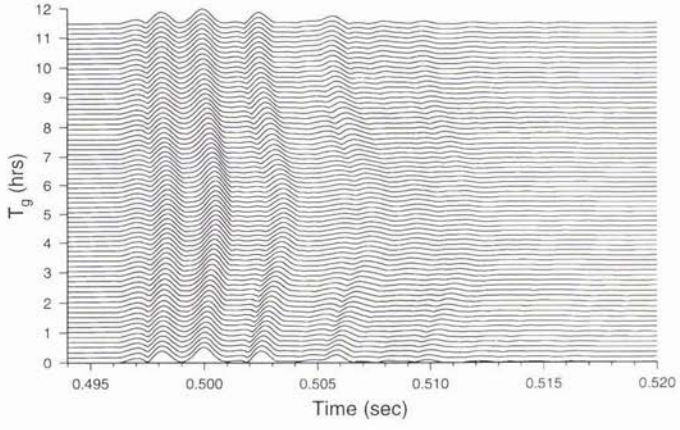

Figure 5: PE-predicted signal amplitude versus time for a rough surface and rough bottom at $f_c = 2$ kHz.

where f_c is the center frequency, f_B is the bandwidth of the signal, and $S(f)$ is the source spectrum. A Hann window filter in frequency domain is applied in order to minimize the artificial sidelobes which show up in the time domain. As in the experimental data, the carrier frequency f_c is eventually removed from the final Fourier synthesis to make for an easy comparison of pulse shapes across frequency. The seafloor was modeled as a fluid with a constant attenuation of 0.2 dB per wavelength. The soundspeed profiles calculated from the measured CTD data are used as input to the model. However, the surface and bottom roughness were not measured during the experiments, so we use numerically generated random boundaries instead. For the sea surface we choose a modified Toba spectrum [5] from which we realize surface roughness, while for the seafloor we choose the Goff-Jorda n spectrum [6] to realize the bottom roughness. The validity of these spectra in shallow water is certainly questionable, however, at least they provide a starting point for characterizing interface roughness.

For our experimental geometry, pulse transmissions are numerically simulated with interface roughness added according to these spectra models. In Figure 5, the simulated results of pulse arrivals for the case of a 2 kHz center-frequency are plotted for comparison to Fig. 2. There is a good agreement in the relative amplitudes of peak arrivals between the prediction (Fig. 5) and the actual data (Fig. 2). The numerical calculation confirms that the later peaks (i.e., 6,7,...) are noticeably weaker in amplitude than the earlier ones because of energy loss due to multiple bottom interactions at higher grazing angle and that the changing tide significantly influences the strength of the later arriving peaks. In Figure 5 the effects of interface roughness are seen most notably in the later arrivals, where the peaks are less coherent. At higher center-frequencies the simulation shows that the amplitudes of the later arrivals are much weaker and much less coherent due to the enhanced rough surface and bottom scattering and attenuation effects.

4. Summary

In very shallow water regions the temporal coherence for acoustic signals transmitted over several hundred meters is strongly frequency dependent. Above center-frequencies of only a few kHz, we have found significant decorrelation of the signal within a fraction of an hour. There is also a strong dependence of temporal coherence on the ray path or peak arrival. Modeling efforts have begun to account for the stochastic behavior of the ocean, in particular bottom and surface roughness, but before an accurate comparison of the modeled and measured acoustic receptions can be made, measurements of actual interface roughness will be necessary.

5. Acknowledgments

We are thankful to Steve Forsythe for his contributions to several aspects of this investigation. We also wish to thank the efforts of Art Sundberg and the crew of the R/V Cape Henlopen during the experiment.

References

[1] Rouseff, D., and Ewart, T., "Effect of random sea surface and bottom roughness on propagation in shallow water,"J. Acoust. Soc. Am., Vol. 98, No. 6, 3397-3404, 1995.

[2] Munk, W., Worcester, P., and Wunsch, C.,"*Ocean Acoustic Tomography*," Cambridge University Press, N.Y., 1995.

[3] Badiey, M., Simmen, J., and Forsythe, S. "Frequency dependence of broadband propagation in coastal regions," J. Acoust. Soc. Am. 1997 (in press).

[4] Badiey, M., Jaya, I., and Cheng, A. H-D. "Shallow water acoustic/geoacoustic experiments at the New Jersey Atlantic Generating Station Site," J. Acoust. Soc. Am. **96**(6), 3593–3604, 1994.

[5] Y. Toba, "Stochastic form of the growth of wind waves in a single-parameter representation with physical implications," Am. Met. Soc. **8**, 494-507 (1978).

[6] J. A. Goff and T. H. Jordan, "Stochastic modeling of seafloor morphology: Inversion of Sea Beam data fro second-order statistics," J. Geophys. Res. **93**, 13589-13609 (1988).

The Effect of Water Column Stability on Acoustic Backscatter from the Ocean Bubble Layer

Kathy K. Bekker, Kenneth E. Gilbert, and Ralph R. Goodman

Applied Research Laboratory and the Graduate Program in Acoustics
The Pennsylvania State University
P.O. Box 30, State College, PA 16804
E-mail: keg5@psu.edu

Abstract

This paper investigates the effect of near-surface water column stability on both low-frequency ($f < 5$ kHz) and high-frequency ($f = 248$ kHz) acoustic backscatter from the ocean bubble layer. It is shown that, with the same windspeed but different stability conditions, backscatter strengths can differ by more than an order of magnitude. It is concluded that water column stability is important not only for accurate predictions of total backscatter, but also for understanding the relative contributions of different surface and near-surface scattering mechanisms.

1. Introduction

The initial motivation for the present investigation came from the observation [1] that a good deal of low-frequency backscatter data show levels much lower than estimated by the empirical data fits proposed by Chapman/Harris [2] and Ogden/Erskin [3]. To explain the discrepancies, we have hypothesized that, in addition to wind speed, water column stability plays an important role in determining bubble cloud structure and hence backscatter strengths. Support for the validity of the hypothesis is given by the low-frequency backscatter data of a number of authors [2-6] and by calculations from a theoretical model for low-frequency backscatter [7]. In addition, the upward-looking 248 kHz sonar measurements of Thorpe [8] show directly the effect of water column stability on bubble cloud structure and on high-frequency backscatter. Thorpe's high-frequency backscatter data are used to infer the inputs needed for the low-frequency backscatter calculations which predict a strong dependence on water column stability.

2. Water Column Stability and Low-Frequency Backscatter

The backscattering of low-frequency sound from rough, wind driven sea surfaces has been the subject of many studies over the last half century [2-6,9]. The obvious relationship between windspeed and backscattering strength has been consistently observed and has led to the development of useful *empirical* algorithms relating the two quantities, [2,3]. It has been widely noted [1,3,4,10], however, that under similar windspeed conditions, there can be significant differences in backscatter strengths. The differences are large enough and common enough to lead one to conclude that windspeed alone is insufficient as a predictive parameter. In seeking an explanation for the discrepancies, we have found a significant correlation between low-frequency backscatter strength and the air-sea heat flux.

In the present discussion of low-frequency backscatter, we take as a working hypothesis that, at a given windspeed, air-sea heat flux controls the gravitational stability of the near-surface region of the water column (0-10 m), and that water column stability is an important parameter affecting surface backscatter. The hypothesis implicitly assumes that much of the low grazing angle backscatter is due to tenuous microbubble clouds (as opposed to the rough surface or dense near-surface plumes), and that the gravitational stability of the upper water column can strongly affect the distribution of wave-generated microbubbles near the surface, thereby affecting the backscatter.

Although the data available from reported backscatter experiments are insufficient to accurately determine the water column stability that existed during the acoustic measurements, there are some cases in which the environmental conditions allow limited comparisons to be made. We can compare, for example, the gross differences in scattering strength under conditions, which for purposes of discussion, we broadly categorize as "winter" or "summer" conditions. For "winter" conditions we mean specifically that the near-surface water is very well mixed, and the air above it is colder. For "summer" conditions the air is warmer than the sea, and there is sufficient heating to cause a strong temperature gradient .

Winter conditions, as we have defined them, were undoubtedly present during the measurements of Chapman-Harris

[2] and Chapman-Scott [4], as well as during Critical Sea Tests 2, 4, and 6, reported by Ogden and Erskin [3]. On the other hand, summer conditions probably prevailed in the early measurements taken during the FASOR tests [5] in summer in the Western Pacific, in the measurements made during CST 1, 3, and 5 [3], and probably in those of Richter [6] near Nassau in February. The experimental reverberation results, especially above 500 Hz, show markedly different scattering strengths, roughly 10 dB at angles 10° to 20°, with backscatter generally higher in winter conditions than the summer conditions. (See, for example, data reported by Ogden and Erskin [3], Figures 16 and 17, Runs 33A, 28B, 33M)

Although the correlation of low-frequency backscatter with winter/summer conditions is significant, there are cases where it is not evident. One obvious reason for the imperfect correlation is that, in addition to seasonal heat flux, other factors affect stability of the upper water column (e.g., diurnal convective heating and cooling, evaporation, cloud cover, etc.). As a result, the degree of near-surface stability spans a continuum in both winter and summer conditions, so that without measurements of the crucial environmental parameters, we can make only a partial correlation with backscatter. In order to obtain a better understanding of the relation between backscatter and water column stability, we have sought more definitive evidence for the effect. Such evidence can be found by considering high-frequency scattering from the bubble layer, which we discuss next.

3. High-Frequency Backscatter Measurements from an Upward-Looking Sonar

Upward-looking high-frequency sonars provide a useful visualization of the structure of the bubble layer as well as a quantitative measure of the high-frequency backscatter [8,11]. Thorpe, for example, in a comprehensive study of bubble clouds, has used sonagraphs from an upward-looking 248 kHz sonar to show clearly the different bubble cloud structures and bubble transport processes that occur in unstable and stable conditions [8]. He has also processed the data to obtain the scattering cross section per unit volume.

Figures 1 and 2 show results from Thorpe's measurements for unstable and stable conditions [8]. In the figures, note that while the average wind speed (bottom panel) is essentially the same for both cases, the bubble cloud structures shown in the sonagraph displays (top panels) are distinctly different. To describe the differences in the bubble cloud structure, Thorpe has coined the terms "columnar clouds" for the structure in the unstable case in Fig. 1 and "billow clouds" in the stable case in Fig. 2. In the unstable situation, heat is flowing from the ocean to the atmosphere so that there is a negative temperature gradient (temperature increases downward) and a positive density gradient (density increases upward). As a result of having denser water over less dense water in the upper water column, downward moving turbulent currents generated by breaking waves continue to move downward producing columnar bubble clouds. Conversely, in stable conditions, the reverse situation exists, with the less dense water over denser water in the upper water column. Because of buoyancy, turbulent currents created by breaking waves do not continue downward but, instead, decay rapidly and form billow clouds, which collectively make a thinner, more homogeneous bubble layer than in unstable conditions.

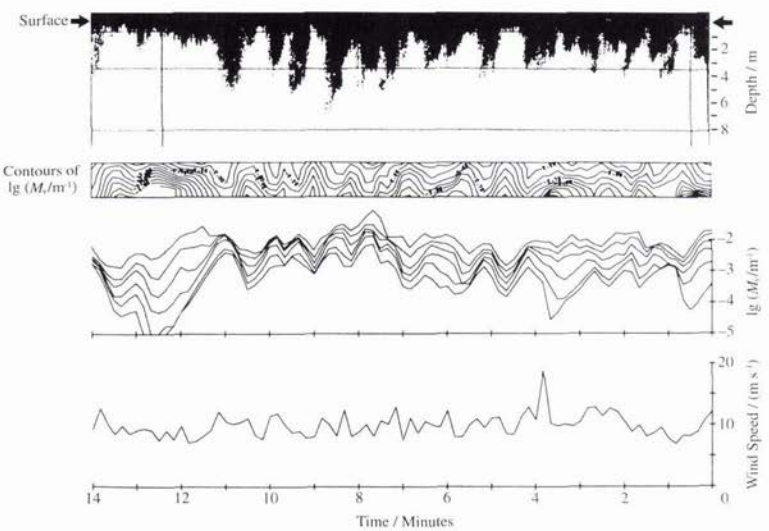

Fig. 1. Backscatter measurements from a 248 kHz upward-looking sonar for unstable conditions (air-sea temperature difference is -1.2 K). First panel: sonagraph records, time increasing to the left. Second panel: contours of $\log_{10}(M_v)$ vs depth and time (contour interval is 0.25). Third panel: values of $\log_{10}(M_v)$ vs time at six equally spaced depths (see description in text). Fourth panel: windspeed vs time. (From S.A. Thorpe [8].)

In Figs. 1 and 2, the second and third panels show the values of scattering strength per unit volume, M_v, measured by the upward-looking sonar. The second panel shows contours of $\log_{10}(M_v)$ vs time while the third panel gives the actual values of $\log_{10}(M_v)$ vs time at six depths equally spaced between the top two horizontal lines shown in the figure. The top line, which is not visible in the stable case, is approximately .5 m below the surface (indicated by an arrow). The second horizontal line marks the lower limit of the backscatter sampling region and is located at depths of approximately 3.5 m and 5.5 m, respectively, in the unstable and stable cases. The sampling depth indicated by the third horizontal line, at approximately 8 m, was normally well below the bubble clouds and was used to establish the noise level of the system.

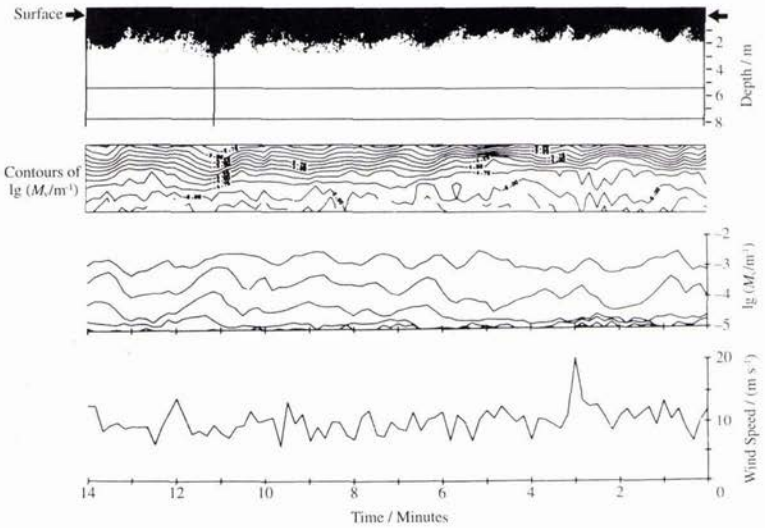

Fig. 2. Same as Fig. 1 except for stable conditions (air-sea temperature difference is +1.3 K). Note that the average windspeed is essentially the same as in Fig. 1, but the bubble-cloud structure is significantly different. (From S.A. Thorpe [8].)

Even a casual inspection of $\log_{10}(M_v)$ vs time in the third panel shows a drastic difference in backscatter in stable conditions compared to unstable conditions. To obtain a quantitative measure of the differences in M_v for unstable and stable conditions, we have digitized the $\log_{10}(M_v)$ vs time curves in the third panel and computed the time average of M_v and its standard deviation vs depth. We find, as did Thorpe in Ref.[8], that the depth dependence of the time average of M_v is well fit by an exponential of the form:

$$\langle M_V(z)\rangle = \langle M_V(0)\rangle e^{-z/\langle L\rangle}, \tag{1}$$

where $\langle M_v(0)\rangle$ is the value at z = 0 (extrapolated exponentially from .5 m), and $\langle L\rangle$ is the e-folding distance. The values we obtained for $\langle M_v(0)\rangle$ for unstable and stable conditions are 2.49×10^{-2} m^{-1} and 4.54×10^{-3} m^{-1}, respectively, a reduction in backscatter of almost a factor of ten in the stable case. The corresponding e-folding distances $\langle L\rangle$ are, respectively, 1.1 m and .7 m. The values we obtained for the exponential parameterization of $\langle M_v(z)\rangle$ are similar to the values reported by Thorpe and show that high-frequency backscatter in stable conditions can differ dramatically from that in unstable conditions.

In addition to computing the mean value, we have used the time series for M_v to compute the standard deviation in M_v vs depth and found it also to be well represented by an exponential:

$$\sigma_{Mv}(z) = \sigma_{Mv}(0)e^{-z/L}, \tag{2}$$

where for unstable and stable conditions, respectively, we obtained 1.96×10^{-2} m^{-1} and 6.65×10^{-3} m^{-1} for $\sigma_{Mv}(0)$, and 1.4 m and .5 m for the e-folding distance, L. Thus, in stable conditions, the standard deviation, like the mean, is greatly reduced.

The above results for $\langle M_v(z)\rangle$ and $\sigma_{Mv}(z)$ make it clear that both the mean and variance in high-frequency backscatter can be significantly less in stable conditions than in unstable conditions. The difference in the mean backscatter in the two situations implies not just a difference in bubble cloud structure (columnar clouds versus billow clouds) but, in addition, a much smaller density of bubbles in the billow bubble clouds that form in stable conditions. Thorpe [8] has hypothesized that in stable conditions there are fewer bubbles because wave breaking is reduced due to the gravitationally stable atmosphere that is coincident with the gravitationally stable ocean in summer conditions. It seems unlikely, however,

that wave breaking would be decreased by a factor of ten in even in very stable conditions. Consequently, the greatly reduced bubble density in stable conditions must be regarded at present as an unexplained phenomenon. Regardless of the physical mechanisms responsible for reducing the bubble density, it appears that in stable conditions, high-frequency backscatter can be systematically lower than in unstable conditions by as much as 10 dB.

4. Theoretical Analysis For Low-Frequency Backscatter

In this section we return to the issue of low-frequency backscatter. We seek to estimate the differences in low-frequency scattering strength one might expect at a fixed windspeed for unstable conditions (columnar clouds) and stable conditions (billow clouds). To do so, we use a low-frequency scattering model that depends on the statistics of the sound speed fluctuations in the bubble layer. Measurements of the sound speed fluctuations, which result from the stochastic distribution of bubbles in the bubble layer, are not presently available at a fixed windspeed for unstable and stable conditions. Consequently, it is necessary to infer the inputs needed for the low-frequency calculations from the high-frequency upward-looking sonar measurements in the previous section.

4.1 Backscatter Model

The theoretical model that we use for backscatter is a coherent backscatter model applicable to low-frequency (non-resonant), low grazing angle backscatter [7]. The essential input needed for the model is the variance (or standard deviation) in sound speed as a function of depth in the bubble layer. The theoretical model assumes that the standard deviation in sound speed versus depth can be fitted with an exponential of the form:

$$\sigma_c(z) = \sigma_c(0)e^{-z/L}, \tag{3}$$

where $\sigma_c(0)$ is the near-surface standard deviation, and L is the e-folding distance. We show below that $\sigma_c(z)$ is proportional to $\sigma_{Mv}(z)$, which itself decays exponentially with depth. Hence, at this point, the assumed exponential form is at least plausible. The exponential decay with depth has, in fact, been observed in in-situ measurements [11,12,13] and is a physically realistic representation of actual sound speed fluctuations.

With the coherent backscatter model of Ref. [7], the scattering cross section per unit area, Σ_{scat}, is given by

$$\Sigma_{scat} = [3/(4\pi c_o^2)][\sigma_c^2(0)L][k_o^4 S(-2k_h)]\left[\frac{4k_v^4L^4}{(1+4k_v^2L^2)(1+k_v^2L^2)}\right], \tag{4}$$

where c_o is the sound speed in bubble-free water, $k_o = \omega/c_o$ is the corresponding wavenumber, $k_h = k_o\cos\theta$ is the horizontal wavenumber, and $k_v = k_o\sin\theta$ is the vertical wavenumber. The normalized wavenumber spectrum for sound speed fluctuations, S(q), is taken to be Von Karman's interpolation formula for inertial subrange (Kolmogorov) turbulence [14],

$$S(q) = 0.35\,\frac{8\pi^{3/2}}{K_o^3}(1+q^2/K_o^2)^{-11/6}. \tag{5}$$

The parameter K_o is $2\pi/L_o$, where L_o is the outer scale of turbulence and is taken to be the mixed layer depth. For the sake of simplicity, the inner scale of turbulence is taken to be zero.

For wavelengths significantly smaller than the bubble layer thickness L, we have $\lambda/L << 1$, and $k_vL >> 1$, so that the fourth bracket in (4) is nearly unity. Hence, in the short wavelength limit, the ratio of the scattering cross sections for unstable and stable conditions is

$$\frac{\Sigma_{scat}(\text{unstable})}{\Sigma_{scat}(\text{stable})} \xrightarrow{\lambda/L \to 0} \frac{[\sigma_c^2(0)L]_{unstable}}{[\sigma_c^2(0)L]_{stable}}. \tag{6}$$

Thus, for non-resonant scattering, the crucial scaling parameter is $\sigma_c^2(0)L$, which can be thought of as the depth-integrated variance in sound speed. As described below, we can use Thorpe's high-frequency upward-looking sonar data to estimate the variance in sound speed as a function of depth.

4.2 Estimates for $\sigma_c(z)$

To get values for $\sigma_c(0)$ and L, and hence $\sigma_c(z)$, we make use of the time series measured by Thorpe for the high-frequency scattering per unit volume, M_v, at various depths in the bubble layer. To use M_v for this purpose, we first need to establish

the connection between M_v and the sound speed reduction in the bubble layer. We can then show that the standard deviation in sound speed is proportional to the standard deviation in M_v.

For low frequencies and low void fractions in tenuous microbubble clouds, the fractional sound speed reduction due to the presence of bubbles can be written as [15]

$$\Delta c(\mathbf{r},t)/c_0 = 8{,}200\ \phi(\mathbf{r},t)\ , \tag{7}$$

where $\phi(\mathbf{r},t)$ is the void fraction and c_0 is the speed of sound in bubble-free sea water. To proceed further, we need at this point to obtain a relation between $\phi(\mathbf{r},t)$ and $M_v(\mathbf{r},t)$.

Under the assumption of dominance by single scattering, we can write $M_v(\mathbf{r},t)$ as

$$M_V(\mathbf{r},t) = \int_0^\infty \Sigma_{bub}(\omega,a) N(\mathbf{r},a,t)\,da\ , \tag{8}$$

where $\Sigma_{bub}(\omega,a)$ is the scattering cross section at angular frequency ω for a single bubble of radius a. The quantity $N(\mathbf{r},a,t)da$ gives the number of bubbles per unit volume with radii between a and a + da as a function of space and time. With the assumption that the statistics of the bubble distribution scale with the number density but are otherwise stationary, we can approximate the bubble distribution as

$$N(\mathbf{r},a,t) \equiv N_0(\mathbf{r},t)\eta(a)\ , \tag{9}$$

where $N_0(\mathbf{r},t)$ is the space-time distribution for the total number of bubbles per unit volume, and $\eta(a)$ is the size distribution. We define the integral of $\eta(a)$ to be unity. The approximation in (9) is reasonable at depths far enough below the wave breaking region that the bubble cloud has had sufficient time to lose the larger bubbles and only the smaller bubbles ($a < 200\ \mu$) remain. Hence we can evaluate the integral in (8) as

$$M_V(\mathbf{r},t) = N_0(\mathbf{r},t)\int_0^\infty \Sigma_{bub}(\omega,a)\eta(a)\,da\ , \tag{10}$$

For a fixed frequency, the integral in (10) is a constant. Thus is clear that if (9) holds, then $M_V(\mathbf{r},t)$ is proportional to the total number of bubbles per unit volume:

$$M_V(\mathbf{r},t) = N_0(\mathbf{r},t)\langle\Sigma_{bub}(\omega)\rangle\ , \tag{11}$$

where $\langle\Sigma_{bub}(\omega)\rangle$ is the bubble-size averaged cross section resulting from the integral in (10).

The void fraction can be written in terms of the number of bubbles per unit volume and the average bubble volume:

$$\phi(\mathbf{r},t) = N_0(\mathbf{r},t)\langle v\rangle\ , \tag{12}$$

where the average bubble volume $\langle v\rangle$ is given by

$$\langle v\rangle = \frac{4}{3}\pi\int_0^\infty a^3\eta(a)\,da\ . \tag{13}$$

Hence the void fraction $\phi(\mathbf{r},t)$ is proportional to the scattering cross section per unit volume $M_v(\mathbf{r},t)$,

$$\phi(\mathbf{r},t) = \left[\frac{\langle v\rangle}{\langle\Sigma_{bub}(\omega)\rangle}\right] M_V(\mathbf{r},t)\ . \tag{14}$$

Since the reduction in sound speed Δc is proportional to M_v, the sound speed itself can be written as

$$c(\mathbf{r},t) = c_0 - \gamma M_V(\mathbf{r},t)\ , \tag{15}$$

where the constant of proportionality γ is given by

$$\gamma = 8{,}200\left[\frac{\langle v\rangle c_0}{\langle\Sigma_{bub}(\omega)\rangle}\right]\ . \tag{16}$$

The standard deviation in sound speed is hence proportional to the standard deviation in M_v:

$$\sigma_c(z) = \gamma\,\sigma_{M_V}(z)\ . \tag{17}$$

To determine the constant of proportionality, γ, we could assume some bubble distribution model and calculate the quantities in (16). However, since we are mainly interested in comparing backscatter in unstable and stable conditions, we simply adjust γ to obtain agreement with measured low-frequency backscatter for unstable conditions. Then, having the proportionality constant, we can make predictions for the stable situation. For typical backscatter in unstable conditions and a windspeed of 25 kts, the constant of proportionality was found to be $\gamma = 9.13 \times 10^{3}$. To give some idea of the values of sound speed reduction Δc that are associated with variations in M_V in unstable and stable conditions, in Fig. 3 we show both quantities versus time and at $z = 0$ (extrapolated exponentially from .5 m). The values obtained for $\sigma_c(z = 0)$ are 179 m/s and 61 m/s, respectively, for unstable and stable conditions. The associated e-folding distances are, of course, the same as obtained earlier for $\sigma_{M_V}(z)$, i.e., L = 1.4 m in unstable conditions and L = .5 m in stable conditions.

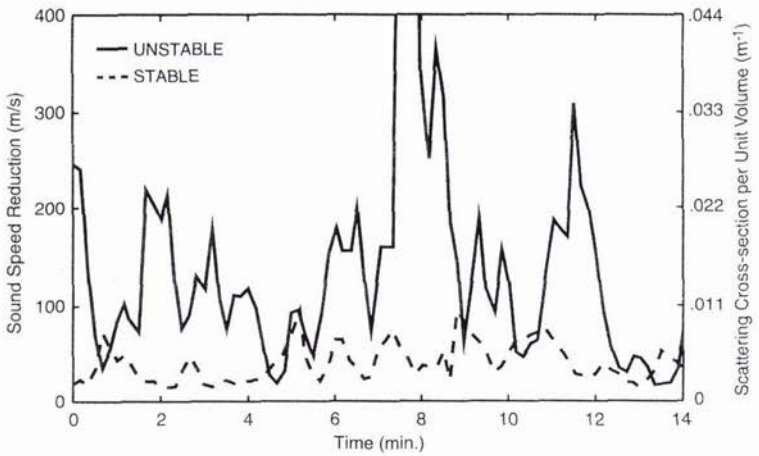

Fig. 3. Sound speed reduction and scattering strength per unit volume vs time for unstable conditions (solid line) and stable conditions (dashed line). The curves shown are values extrapolated exponentially to zero depth from the first sampling bin at approximately .5 m depth.

4.3 Predictions for Low-Frequency Backscatter

The above estimates for $\sigma_c(z)$, together with Σ_{scat} in (4), were used to make predictions for low-frequency backscatter from the ocean bubble layer in unstable and stable conditions. In the predictions shown in Figs. 4 and 5, scattering strength is defined as $10\log_{10}(\Sigma_{scat})$, and the outer scale L_O is taken to be 106 m, a value that is realistic in high sea states [16].

Figure 4 shows the predicted scattering strength vs grazing angle at several frequencies for unstable and stable conditions. The dashed lines are the backscatter for bubble layer scattering only. The lower curve (marked with x's) is for stable conditions and is essentially just a downward displaced (20 to 30 dB) version of the upper curve (marked with o's), which is for unstable conditions. As they stand, the unstable/stable curves for bubble layer scattering bear little resemblance to the winter/summer measurements of Ogden and Erskin, which generally differ by no more than 5 to 10 dB between winter and summer conditions and are not simply displaced versions of each other. The probable reason for the discrepancy is that other scattering mechanisms, such as rough surface scattering, are present. When scattering from the bubble layer drops below a certain level, other scattering mechanisms dominate the backscatter so that the backscatter level does not drop precipitously and, in addition, can have a different grazing angle dependence. To account approximately for rough surface scattering, and hence better represent the backscatter levels actually measured in stable conditions, we have added incoherently the rough surface scattering contribution from the perturbation model of Thorsos [17]. The backscatter results for the bubble layer plus rough surface scatter are the solid lines, with the o's and x's indicating unstable and stable conditions, respectively. The addition of a rough surface scattering contribution has little effect for unstable conditions but noticeably raises the backscatter levels in stable conditions. The net result is to capture the trends found in the data of Ogden and Erskin for winter and summer conditions (e.g., runs 28B and 33A). For example, in both the data and the predictions, the difference between unstable and stable conditions is larger at higher frequencies than at lower frequencies. Also, both data and predictions show that the effect of water column stability is larger at smaller grazing angles than at larger grazing angles. The predicted difference between winter/summer conditions (i.e., unstable/stable conditions) is 10 to 20 dB and hence is about twice the measured values. Nevertheless, the predicted trends with frequency and grazing angle are consistent with the data. Hence the theoretical predictions, together with the backscatter data, support the water column stability hypothesis. In addition, in the analysis of data, the theory helps to identify the relative contributions of scattering

from the microbubble layer and from other scattering mechanisms such as the rough surface and dense, near-surface plumes.

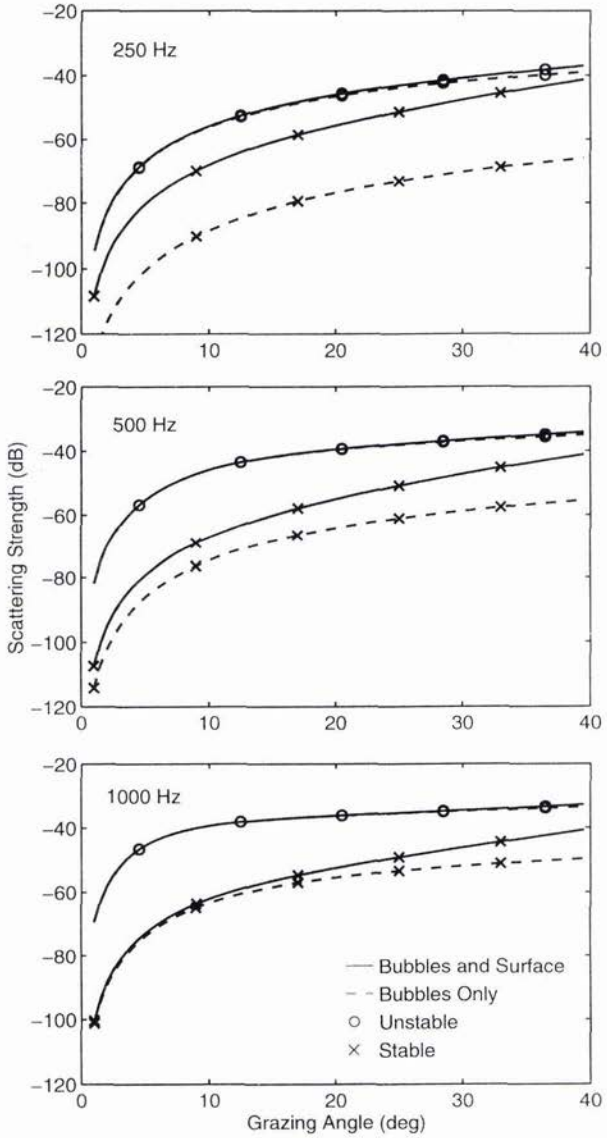

Fig. 4. Scattering strength vs grazing angle at several fixed frequencies. The circles and triangles are for unstable and stable conditions, respectively. The dashed lines denote backscatter just from the bubble layer. The solid line denotes the incoherent sum of bubble layer scattering and rough surface scattering.

Figure 5 shows scattering strength vs frequency at several fixed grazing angles. Although, in principle, Fig. 5 contains the same information as Fig. 4, the display of backscatter vs frequency shows more clearly the differences between backscatter in unstable and stable conditions. In Fig. 5, as in Fig. 4, without rough surface scatter the curves for stable conditions have the same shape as for unstable conditions but are displaced by 20 to 30 dB. With the inclusion of a rough surface contribution, however, the backscatter in stable conditions never drops below the rough surface scattering "floor" which has its own characteristic frequency dependence. As a result, the frequency dependence below 500 Hz is quite different in stable conditions from that in unstable conditions. The obvious difference in the frequency dependence should provide a useful way to sort out the different physical mechanisms that contribute to the observed total backscatter.

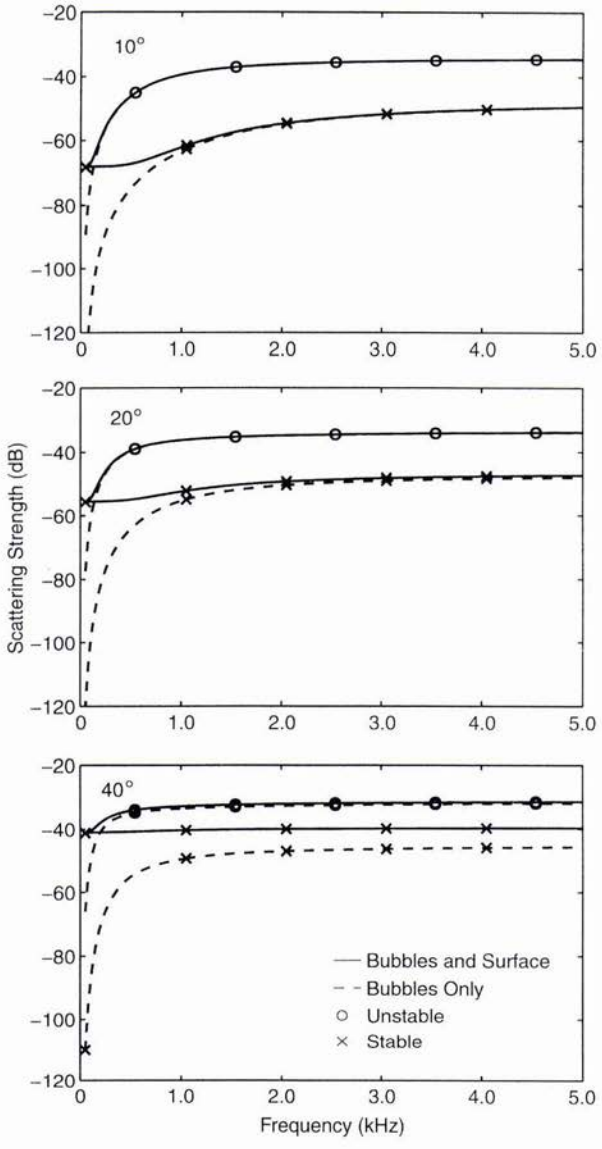

Fig. 5. Same as Fig. 4, except that the grazing angles are fixed and the frequency is varied.

5. Summary and Conclusions

We have presented experimental and theoretical evidence that the stability of the near-surface water column significantly affects both low-frequency and high-frequency backscatter from the ocean bubble layer. At low frequencies, the evidence was essentially circumstantial. However, at 248 kHz, the evidence from the upward-looking sonar measurements of Thorpe was direct and clear-cut. There seems to be little question that bubble cloud structure and high-frequency backscatter can vary dramatically with water column stability.

From the calculations of low-frequency backscatter, it was shown that analysis of backscatter in unstable and stable conditions can help to identify the relative contributions of different scattering mechanisms. In particular, if future low-frequency backscatter data show a marked dependence of backscatter on water column stability, it will point to microbubble clouds (as opposed to the rough sea surface or dense, near-surface plumes) as the primary low-frequency scattering mechanism.

Finally we point out that existing empirical expressions for low-frequency backscatter [2,3] apply to unstable conditions. Consequently, if stable conditions are found to occur frequently, it will be important to incorporate water column stability as a parameter in predictive operational models for low-frequency backscatter. Similarly, for reliable predictions in both unstable and stable conditions, high-frequency operational models should also include the effects of near-surface water column stability.

Acknowledgments

The authors are grateful for support from the Office of Naval Research. The first author (KKB) was supported under the Augmentation Awards for Science and Engineering Research Training (AASERT) program. The other authors (KEG and RRG) received partial support from the Ocean Acoustics Program (Code 321OA).

References

[1] R. R. Goodman, "A critique on the relationship between backscattering and environmental measurements," 123rd meeting of the Acoustical Society of America, Salt Lake City, May 11-15, 1992.

[2] R.P. Chapman and J.H. Harris, "Surface backscattering strengths measured with explosive sources," J. Acoust. Soc. Am., vol. 34, pp. 1592-1597, 1962.

[3] P.M. Ogden and F.T. Erskin, "Surface scattering measurements using broadband explosive charges in the Critical Sea Test experiments," J. Acoust. Soc. Am., vol. 95, pp. 746-761, 1993.

[4] R.P. Chapman and H.D. Scott, "Surface backscattering strengths measured over an extended range of frequencies and grazing angles," J. Acoust. Soc. Am., vol. 36, pp. 1735-1737, 1964.

[5] J.L. Percy, "Surface backscattering strengths from several FASOR II deep-water stations," Naval Undersea Research and Development Center Technical Publication NUC TP 185, 1970.

[6] R.M. Richter, "Measurements of backscattering from the sea surface," J. Acoust. Soc. Am., vol. 36, pp. 864-869, 1964.

[7] K.E. Gilbert, "A stochastic model for scattering from the near-surface oceanic bubble layer," J. Acoust. Soc. Am., vol. 94, pp. 3325-3334, 1993.

[8] S.A. Thorpe, "On the clouds of bubbles formed by breaking windwaves in deep water, and their role in air-sea gas transfer," Philos. Trans. R. Soc. London, Ser. A, vol. 304, pp. 155-210, 1982.

[9] J.R. Brown, J.A. Scrimger, and R.G. Turner, "Reverberation from the ocean surface," Pacific Naval Laboratory, Esquimalt, B.C., Canada, Technical Memorandum 66-8, 1966.

[10] S.T. McDaniel, "Sea surface reverberation: A review," J. Acoust. Soc. Am., vol. 94, pp. 1905-1922, 1993.

[11] D.M. Farmer and S. Vagle, "Waveguide propagation of ambient sound in the ocean surface bubble layer," J. Acoust. Soc. Am., vol. 86, pp. 1897-1908, 1989.

[12] E. Lamarre and W.K. Melville, "Sound-speed measurements near the ocean surface," J. Acoust. Soc. Am., vol. 96, pp. 3605-3616, 1994.

[13] M.Y. Su, personal communication, 1992.

[14] S.F. Clifford, "The Classical Theory of Wave Propagation in a Turbulent Medium," in *Laser Beam Propagation in the Atmosphere*, edited by J.W. Strohbehn (Springer-Verlag, New York, 1978).

[15] R.J. Urick, *Principles of Underwater Sound*, (McGraw-Hill, New York, 1975), 2nd ed., p. 224.

[16] D.M. Farmer, Cruise Report, CSS John P. Tully, 17 February to 6 March 1992, Institute of Ocean Sciences, Sidney, B.C., Canada.

[17] E.I. Thorsos, "Acoustic scattering from a 'Pierson-Moskowitz' sea surface," J. Acoust. Soc. Am., vol. 88, pp. 335-349, 1990.

The effect of source movements on shallow water bottom backscatter

O. Bergem, E. Pouliquen, N.G. Pace

SACLANT Undersea Research Centre
Viale San Bartolomeo, 400
19138 La Spezia, ITALY
E-mail: bergem@saclantc.nato.int

Abstract

The time-evolution model BORIS is used to study the effects of source movements on bottom backscatter. Changes in the backscattered time domain signals as functions of source depth, position and incident angles are simulated for broad band pulses both with narrow and wide beams. The results show that a change in the distance between a rough bottom and the source modifies the coherent and the non-coherent part of the pulse. A small change in horizontal position produces significant changes in the backscattered signal for both beams, while a small change to the incident angle produces significant changes in the narrow beam only.

1. Introduction

A stochastic model has been developed which enables the study of backscattered time domain signals as functions of source movements [1] [2]. In [2], examples show how the beam width and the seabed roughness affect the time-series return from the seafloor surface and from the volume. This paper continues the study of the model, and shows how the movement of the source in all three dimensions affects the time-series. When working with acoustic data from a moving source in shallow water, significant variations might be seen from one ping to another. If the causes of these variations can be understood, changes from one ping to another might be actively used in the work of characterizing the seafloor instead of being treated as "noise" in the data [3]. The ping to ping variations caused by changes in the propagation in the water columns is not included in this study.

The paper is divided into 5 sections. Section 2 gives a brief introduction to the model used, section 3 treats the effects of the source height above the bottom. In section 4 the horizontal movement of the source is treated, and the effects of roll is treated in section 5.

2. Description of the BORIS model

The model is designated BORIS which is an abbreviation for "BOttom Response from Inhomogeneities and Surface". A detailed specification of the implementation of BORIS is given in [4].

The following integral [1] forms the basis of the model:

$$\begin{aligned} p(\mathbf{P},t) &= p_s(\mathbf{P},t) + p_v(\mathbf{P},t) \\ &= \int_S dp_s(\mathbf{P},t) + \int_V dp_v(\mathbf{P},t) \end{aligned} \tag{1}$$

This integral expresses that the pressure field received at the source $\mathbf{P}$ from the seafloor is the sum of the elementary pressure fields over the seafloor surface (S) and the seafloor volume (V). For a monostatic source and receiver with directivity pattern D_i and D_r, the seafloor surface contribution is given by

$$dp_s(\mathbf{P},t) = \frac{\cos(\gamma(\mathbf{R}))}{2\pi\bar{c}_0 R_0^2} p_0$$

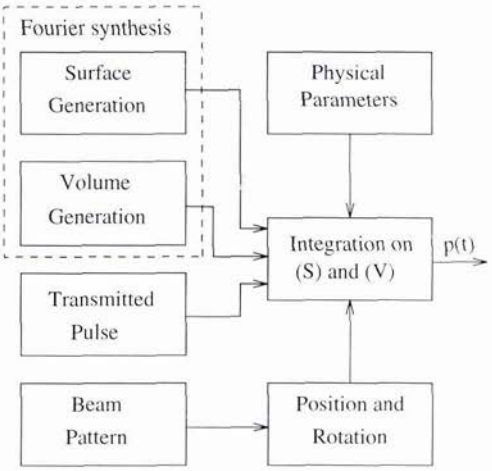

Figure 1: Simplified box diagram of the model.

$$\times \left(D_i D_r(\mathbf{R})\right) \Re_{01}(\mathbf{R}) e^{'}(t - \frac{2R_0}{\overline{c_0}}) d\mathbf{S_R} \tag{2}$$

Here, $\Re_{01}$ is the local water-sediment plane wave reflection coefficient at the point $\mathbf{R}$, $\overline{c_0}$ is the average sound speed in water, $\gamma(\mathbf{R})$ is the angle between the incident direction and the vector $\mathbf{n}$ normal to the surface at $(\mathbf{R})$ and p_0 is the source level. $e^{'}(t)$ is the time derivative of the transmitted pulse $e(t)$.

The volume contribution is given by

$$\begin{aligned} dp_v(\mathbf{P},t) &= \frac{-n_1^2(\mathbf{R}^{'})}{2\pi R_0^2 \overline{c_0}^2} \mu(\mathbf{R}^{'}) p_0 \\ &\times \quad D_i(\mathbf{R}) D_r(\mathbf{R}) \Im_{01}(\mathbf{R}) \Im_{10}(\mathbf{R}) \\ &\times \quad \left(\frac{1}{\pi} \frac{\frac{\alpha R_1}{2\pi}}{(\frac{\alpha R_1}{2\pi})^2 + t^2} * e^{"}(t - 2(\frac{\overline{n_1} R_1 + R_0}{\overline{c_0}})) \right) \\ &\times \quad d\mathbf{V_R} \end{aligned} \tag{3}$$

In this expression, $\overline{n_1}$ is the average refractive index in the first few metres of the bottom, n_1 is the local refractive index at location $\mathbf{R}^{'}$ and R_1 is the distance of penetration into the sediment. α is the attenuation coefficient, $\Im_{01}(\mathbf{R})$ and $\Im_{10}(\mathbf{R})$ are the plane wave transmission coefficients. The double time derivative of the transmitted pulse $e(t)$ is denoted by $e^{"}(t)$.

These equations give the sound pressure level for a given time t at position $\mathbf{P}$ by integration over the surface (S) and the volume (V). The local incident angle $\gamma(\mathbf{R})$, the local reflection coefficient $\Re_{01}(\mathbf{R})$ and the local degree of inhomogeneities in the volume $\mu(\mathbf{R}^{'})$ are assumed to be known. Instead of using average quantities for these parameters, a different approach has been taken. Before the calculations are carried out for the integral over S, one realization of the seafloor surface and volume is calculated based on a statistical set of parameters. The calculations are based on the Fourier synthesis method. For the surface, a filtered power law spectrum is used to calculate the height field, while for the volume part an exponential correlation function has been used to generate the inhomogeneity field. The model includes 3D rotation and position matrices for the source and receiver which allows for variations of position, heave, pitch and roll.

It is important to notice that the model has a stochastic nature, and that the result from one run to another will be different even with the same input parameters. This is because there is an infinite number of realizations of the seafloor for a fixed set of statistical parameters. However, the same realization might be used in several runs by controlling the random generator used in the model. A simplified block diagram of the model is shown in Fig. 1

3. Effect of the source height above the bottom

With a directive beam and a rough bottom, the shape of the returned signal is expected to change as a function of depth due either to the change in the size of the insonified surface or change in the surface aspect ratio. As demonstrated in [2], even for a perfectly flat surface, the shape of the signal depends on the insonified area if the beam is directive. For a rough surface, a larger insonified area will include more surface scatter with the effect of prolonging the tail of the surface contribution signal. To illustrate these effects, the BORIS model was run at varying depths over a soft, rough surface. The transmitted pulse was a Ricker pulse centered at 8 kHz. For the transducer, two different Gaussian beam patterns of amplitude *versus* angles were used at 3° and 15° respectively for the half beam width measured at -3 dB. The receiving beam pattern was omni directional. The other parameters used in the model are shown in Table 1. The surface and volume were unchanged for all runs in order to compare directly the results, i.e. the same realization of the surface and volume have been used.

Table 1: Model parameter settings.

Parameters	Values
Surface increment dp_s (m)	0.03
Volume increment dp_v (m)	0.03
Depth H (m)	10.0 (5-20)
Sound speed, c_1 (m/s)	1550
Density ρ_1 (g/cm^3)	1.4
Surf. rms rough. σ_h (m)	0.02 (0.01)
Surf. pow. e-p. ν	2.0
LP cutoff K_{lp} (rad/m)	30
HP cutoff K_{hp} (rad/m)	1
Volume inhomog. μ	0.03
Volume Hor. Cor. l_h (m)	0.3
Volume Ver. Cor. l_v (m)	0.02
Attenuation α (dB/m/kHz)	0.5

Figure 3 shows the time-domain signal returned from the surface as a function of depth and time. Plots a) and b) shows the results from the runs using narrow and wider beams respectively. No volume contribution is included in this figure, and the delays due to the water column have been removed in order to aligned the pulses in time. At 5 m, the narrow beam is insonifying a disc with diameter 0.52 m, the wider beam is insonifying an area with diameter 2.67 m. For the narrow beams, little energy is seen in the tail, and the first part of the return has a shape which tends towards the derivative of the transmitted pulse [2]. For the wider beam, scattering from the surface is evident in the tail. As the depth is increasing for the narrow beam, little energy is seen in the tail, and the first reflection resembles the transmitted pulse. It is interesting to observe the effect of roughness on the time domain signal. For the deeper runs, the surface features appear closer to the first part of the reflection. This can be explained by the simple geometric fact that the difference in time between the center of the beam and a distinct feature will decrease with depth increased (Fig. 2).

Figure 4 shows both volume and surface contribution. The volume contribution can now be seen for the narrow beam, while for the wider beam the scattering from the volume becomes mixed with the scattering from the surface. The contribution from the volume *versus* the contribution from the surface scatter will depend mainly on the volume and surface description parameters.

4. Effect of horizontal movements of the source

For a rough bottom, a horizontal translation of the source will change the insonified area of the bottom, and the time domain signal is expected to be affected. The change will depend on bottom parameters, beam pattern and transmitted pulse. Typically, a rougher bottom gives more changes than a smoother bottom. To study this effect, the BORIS model was run at a height of 10 m above the bottom, and the source was translated horizontally in steps of 0.1 m. The statistical realization of the bottom was unchanged during the runs. Figure 5 shows the time domain signals of the total scattering from a bottom with rms roughness 1 cm. The other parameters are unchanged (Tab. 1). A small change in the position changes the time-domain signal for the narrow and the wider beam. For the narrow beam, little energy is seen in the tail, and only small changes are seen in the first part of the signal. For the wider beam, the variations are greater, and the tails of the signals undergo a significant change. Figure 6 shows the same simulations with rms roughness of the bottom increased to 2 cm. Due to the limited insonified area, the scattering from the surface is still low for the narrow beam, but the changes seen in the first

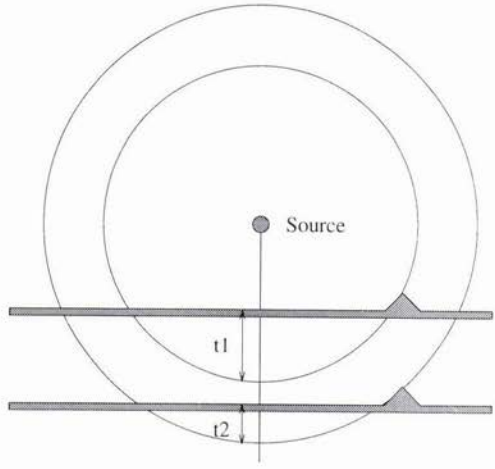

Figure 2: A distinct feature at the bottom will appear closer to the normal incident reflection if the depth is increasing.

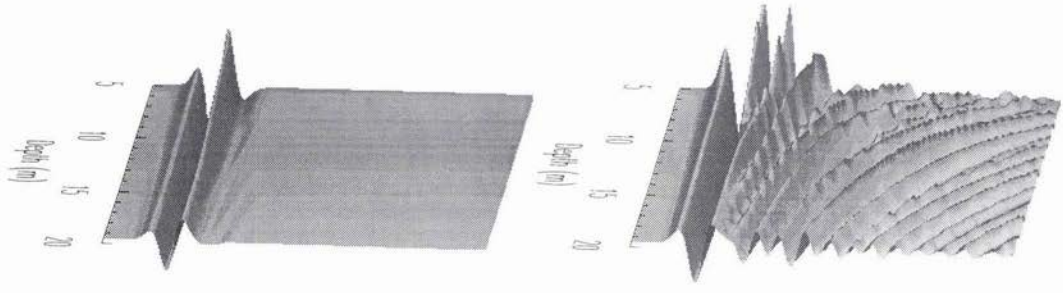

Figure 3: The pulse as function of depth and time including the surface return only. a) narrow beam, b) wide beam.

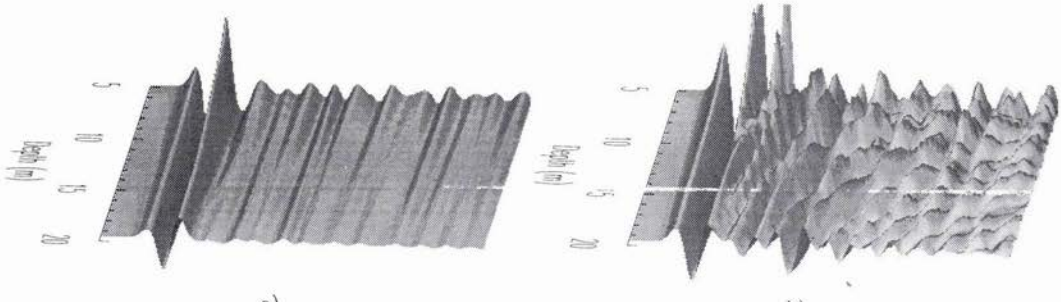

Figure 4: The pulse as function of depth and time including both the surface and volume return. a) narrow beam, b) wide beam.

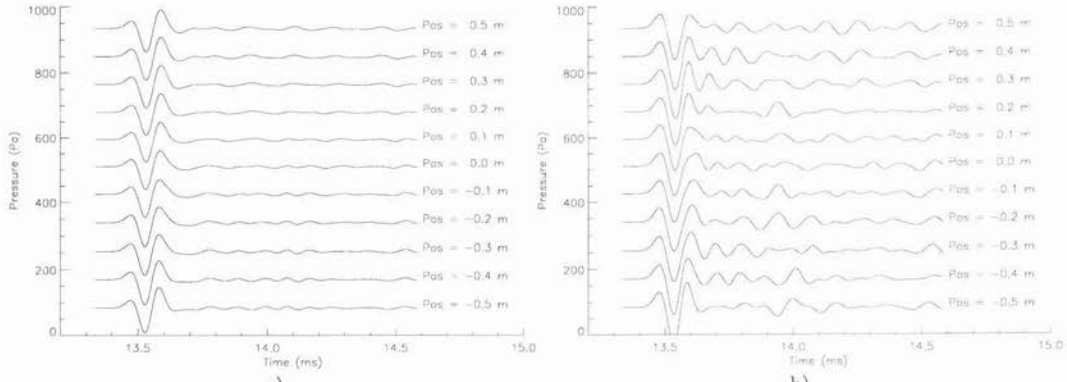

Figure 5: The return as function of position. The rms roughness is 1 cm. a) narrow beam, b) wide beam.

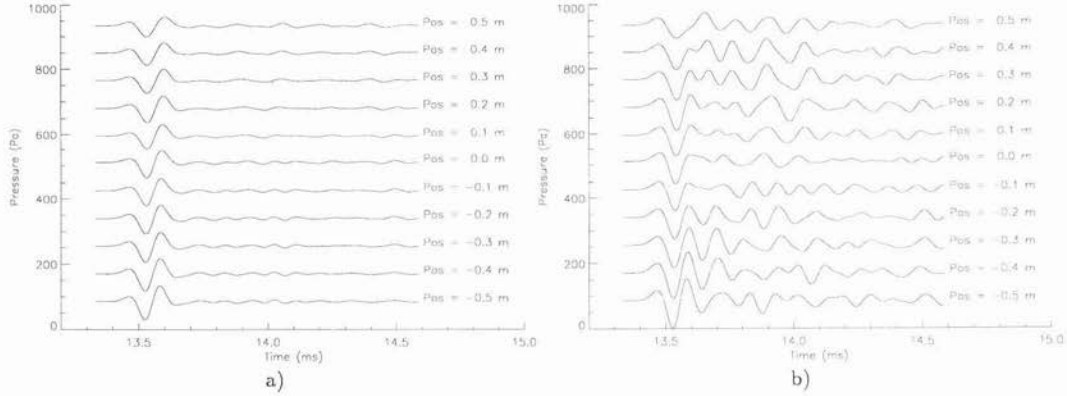

Figure 6: The return as function of position. The rms roughness is 2 cm. a) narrow beam, b) wide beam.

part of the signals are stronger than for the bottom with rms roughness equal to 1 cm. For the wider beam, the energy in the tail is generally increased due to the increased surface scatter with respect to the rms roughness of 1 cm and the variations from one position to the next are more significant.

From these simulations, the narrow beam appears to be less influenced by small changes in the position than the wider beam. Consequently, if the variations from one position to the other are used to extract seafloor roughness parameters, a wider beam might be a better choice. For impedance estimation, the narrow beam seems to be the better choice as in this case, the variations from one position to another are less dependent on the roughness. As the surface contribution is almost negligible in the tail, the narrow beams may be easier to use for volume contribution studies.

5. Effect of small changes in roll/pitch

For a typical situation with a hull mounted or a towed sonar, the source will be exposed to variations in pitch and roll. An interesting simulation can be performed looking at the time domain signal as function of variation in the incident angle. As the source used in the simulations has a symmetric beam pattern around the mean direction, only the effect in one dimension (roll) is studied. In Fig. 7 the roll of the source is simulated for angles between $-5°$ and $5°$. The rms roughness is 2 cm, the depth is 10 m, and the other parameters are unchanged. The source is at position 0, so that the results with Roll = $0°$ equal the result for Pos = 0 m in Fig. 6. For the narrow beams the roll has a significant influence on the time domain signal. The shape of the first reflection changes and for an increase in the roll, the level decreases strongly because the source is not at normal incidence. As expected, the

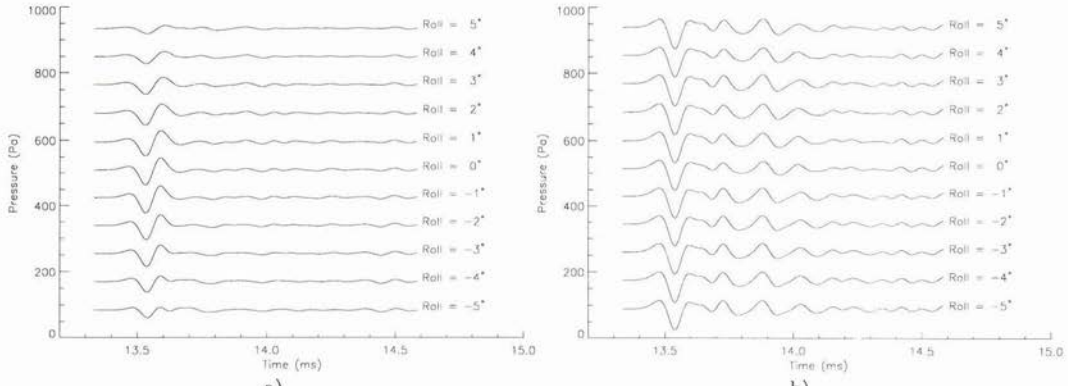

Figure 7: The return as function of roll (incident angle). a) narrow beam, b) wide beam.

change is much less marked for the wider beam, and the signal is almost constant from $-5°$ to $5°$.

6. Summary

The effects of source movements on backscattered time domain signals have been studied using model simulations. The simulations were carried out using a broad band Ricker pulse and two different beams of 3° and 15° respectively. The source height above the bottom varied from 5 to 20 m. The results showed that the signal changes notably over the depth range studied for both the narrow and the wider beam. Further simulations were conducted by moving the source horizontally over a rough bottom. Even for small variations in the position, the time-domain signal changed significantly, and the changes appeared to be higher for the wider beam. A simulation to study the effect of varying the incident angles showed that the narrow beam was more affected by the change than the wider beam. The continuation of this work will be focused on verifying the results with recorded data.

References

[1] E. Pouliquen, O. Bergem, N. G. Pace, "Time-evolution modelling of seafloor scatter, Part1: Theory", in *SACLANTCEN SM-328*. La Spezia, Italy, SACLANT Undersea Research Centre, (1997).

[2] O. Bergem, , E. Pouliquen, G. Canepa, N. G. Pace, "Time-evolution modelling of seafloor scatter, Part2: Experimental verification", in *SACLANTCEN SM-327*. La Spezia, Italy, SACLANT Undersea Research Centre, (1997).

[3] O. Bergem, E. Pouliquen, A. Lyons, N.G. Pace, "Normal incidence seafloor classification", in *Proc. Oceans96*, Fort Lauderdale, (1996).

[4] G. Canepa, O. Bergem, E. Pouliquen, "The implementation of BORIS-3D: BOttom Response from Inhomogeneities and Surface, Version 1.0", in *SACLANTCEN M-125*. La Spezia, Italy, SACLANT Undersea Research Centre, (1997).

Time-Frequency Representation Of Model Based High Frequency Broad Band Scattering From A Rough Interface

Garner C. Bishop and Judy Smith

Naval Undersea Warfare Center Division Newport
Newport, RI 02841

Abstract

A formalism for scattering a broad band high frequency pulse from a randomly rough surface of a penetrable oceanic sediment is developed and used to investigate the ability of local cosine transform (LCT) time-frequency (TF) representations to distinguish between randomly rough surfaces with different statistics.

1. Introduction

It is of interest to classify surface texture or roughness remotely using broad band acoustic scattering. In this paper, the interest is in classification of roughness on the surface of penetrable oceanic sediments. Previously[1,2], a T-matrix formalism was used to calculate broad band LFM scattering from an elastic sediment with periodic surface roughness. An adaptive windowed local cosine transform (LCT) was used to construct time-frequency (TF) representations of the time series and it was shown that this type of TF representation could distinguish between two different types of periodic roughness. In this paper, high frequency broad band scattering from penetrable sediments with random surface roughness is calculated and the ability of local cosine based TF representations of the scattered field time series to distinguish between rough surfaces with different statistics is explored.

It is assumed that a stationary source array is located in a homogeneous, isotropic, and non-viscous fluid half space bounded below by a semi-infinite penetrable sediment half space with a randomly rough surface. The surface roughness profile $\xi(x',y')$ is assumed to be a realization of a zero mean Gaussian random process with an RMS height h and correlation lengths l_x and l_y along the x- and y-axes. The fluid half space is denoted medium (1) and the sediment half space is denoted medium (2). In the fluid half space, the compressional Lame parameter is $\lambda^{(1)}$, the mass density is $\rho^{(1)}$, the p-wave speed is $c^{(1)\,2}=\lambda^{(1)}/\rho^{(1)}$, and the p-wave vector is $\hat{k}^{(1)}$ with $k^{(1)\,2}=\omega^2/c^{(1)\,2}$. Although scattering from sound hard, viscous fluid, viscoelastic solid, and fluid saturated poroelastic solid sediments was modeled, in this paper, numerical results are shown for a viscoelastic solid only. In the viscoelastic solid sediment, the Lame parameters are $\lambda^{(2)}$ and $\mu^{(2)}$, the mass density is $\rho^{(2)}$, the p and s wave speeds are, respectively, $c_p^{(2)\,2}=(\lambda^{(2)}+2\mu^{(2)})/\rho^{(2)}$ and $c_s^{(2)\,2}$ and $c_s^{(2)\,2}=\mu^{(2)}/\rho^{(2)}$, and the p and s wave vectors are, respectively, $\hat{k}_p^{(2)}$ with $k_p^{(2)\,2}=\omega^2/c_p^{(2)\,2}$ and $\hat{k}_s^{(2)}$ with $k_s^{(2)\,2}=\omega^2/c_s^{(2)\,2}$.

It is assumed that the source is a planar array and to orient and locate the array, two coordinate systems are considered: A reference coordinate system is located in the mean plane of the rough interface and is designated $x_i\ y_i\ z_i$ with origin O_i and a second coordinate system is located in the plane of the array and is designated, $x_s\ y_s\ z_s$ with origin O_s. The x_s and y_s axes are in the plane of the array and are parallel, respectively, to the width and length of the array and the z_s axis is normal to the $x_s\ y_s$ plane and in the direction of the main lobe of the beam. Initially both coordinate systems are coincident and colinear. First, the source is displaced from the origin O_i and then it is oriented so that the z_s-axis is along a radius vector $\hat{r}_s$ from O_s to O_i. The rotation of the z_s-axis is accomplished by performing a counterclockwise rotation by an angle ϕ_s about the z_s-axis followed by a second counterclockwise rotation by an angle $\pi+\theta_s$ about the y_s-

axis. In this analysis, the source is located on the negative x_s -axis so that $\phi_s = \pi$.

It is assumed that in the far field the source pressure field can be expressed in the following manner:

$$p^{(i)}(\dot{r},\dot{r}_s;t) = \frac{1}{2\pi}\int_{-\infty}^{\infty} d\omega\, T^{(i)}(\omega)\; p^{(i)}(\dot{r},\dot{r}_s;\omega)\; e^{-i\omega t} \tag{1a}$$

with

$$p^{(i)}(\dot{r},\dot{r}_s;\omega) = P_o\, D_s(\dot{r},\omega)\; e^{ik^{(1)}|\dot{r}-\dot{r}_s|}\,/4\pi|\dot{r}-\dot{r}_s| \tag{1b}$$

The quantity $D_s(\dot{r},\omega)$ is the source beam pattern and in this paper, a Gaussian beam is considered . When $D_s(\dot{r},\omega)$ is projected onto the mean plane of the interface it is given by

$$D_s^{(i)}(\dot{r}';\omega) = \exp[-(x'/X)^2]\exp[-(y'/Y)^2]. \tag{2a}$$

with

$$X = r_s\,\chi/\cos\theta_s\,, \tag{2b}$$

$$Y = r_s\,\phi\,, \tag{2c}$$

$$\chi = k_{min}\,\chi_{max}/k \tag{2d}$$

and

$$\phi = k_{min}\,\phi_{max}/k \tag{2e}$$

The angles χ and ϕ are, respectively, the beam widths measured from the z_s -axis in the z_s -x_s and z_s -y_s planes and the angles, χ_{max} and ϕ_{max} are the maximum values of these angles and occur when $k=k_{min}$. The beam pattern $D_s(\dot{r},\omega)$ is obtaind from $D_s^{(i)}(\dot{r}';\omega)$ by setting $\cos\theta_s = 1$.

The quantity $T^{(i)}(\omega)$ is the Fourier transform of the incident pulse $T^{(i)}(t)$ and in this paper, scattering of a linear frequency modulated (LFM) pulse is considered so that

$$T^{(i)}(t) = \begin{cases} e^{-i\omega(t)t} & 0 \le t \le \tau \\ 0 & t > \tau\,; t < 0 \end{cases} \tag{3}$$

with $\omega(t)=2\pi(f_{min}+t\Delta f/\tau)$. The parameter τ is the pulse width, f_{min} is the lowest frequency in the pulse, and Δf is the bandwidth.

The scattered field is synthesized from its spectrum using an inverse Fourier transform so that

$$p^{(s)}(\dot{r},\dot{r}_s;t) = \frac{1}{2\pi}\int_{-\infty}^{\infty} d\omega\, T^{(i)}(\omega)\, p^{(s)}(\dot{r},\dot{r}_s;\omega)\; e^{-i\omega t} \tag{4}$$

The quantity $p^{(s)}(\dot{r},\dot{r}_s;\omega)$ is the Fourier spectrum of the scattered pressure field and is calculated using a Kirchhoff scattering formalism.

2. Kirchhoff Scattering for a Randomly Rough Interface

2.1 Scattering Theory: CW Scattering

Since scattering from a randomly rough surface in the Kirchhoff approximation has been treated by many authors [3-5], the details of the formalism used in this paper are briefly reviewed. The pressure field scattered from the rough interface is given by the Helmholtz-Kirchhoff integral:

$$p^{(s)}(\dot{r},\dot{r}_s;\omega) = \int ds'\,[p^{(+)}(\dot{r}',\omega)\,\hat{n}(\dot{r}')\cdot\nabla' g(\dot{r}',\dot{r};\dot{k}^{(1)}) - g(\dot{r}',\dot{r};\dot{k}^{(1)})\,\hat{n}(\dot{r}')\cdot\nabla' p^{(+)}(\dot{r}',\omega)]. \tag{5}$$

The quantity $p^{(+)}(\dot{r}',\omega)$ is the total field evaluated in the limit in which the interface is approached from the fluid half

space and $g(\vec{r}', \vec{r}; \vec{k}^{(1)})$ is the free space scalar Green function. The vectors $\vec{r}$ and $\vec{r}'$ are, respectively, vectors to a feld point and to a point on the surface. The unit vector $\hat{n}(\vec{r}')$ is normal to the interface and is given by

$$\hat{n}(\vec{r}') = [\hat{z} - \partial_{x'}\xi(x',y')\hat{x} - \partial_{y'}\xi(x',y')\hat{y}]\{1+[\partial_{x'}\xi(x',y')]^2+[\partial_{y'}\xi(x',y')]^2\}^{-\frac{1}{2}} \tag{6}$$

and $ds' = dx'dy'\{1+[\partial_{x'}\xi(x',y')]^2+[\partial_{y'}\xi(x',y')]^2\}^{\frac{1}{2}}$ and is an infinitesimal area element on the interface.

The far-field approximation for the Green function and incident field evaluated on the rough surface are constructed in the Fraunhoffer approximation and are given by

$$p^{(i)}(\vec{r}', \vec{r}_s; \omega) = P_o D_s^{(i)}(\vec{r}'; \omega) e^{i(\vec{k}^{(1)} \cdot \vec{r}_s + \vec{k}^{(i)} \cdot \vec{r}')}/4\pi r_s \tag{7a}$$

and

$$g(\vec{r}', \vec{r}; \vec{k}^{(1)}) = e^{i(\vec{k}^{(1)} \cdot \vec{r} - \vec{k}^{(s)} \cdot \vec{r}')}/4\pi r. \tag{7a}$$

The wave vectors $\vec{k}^{(i)}$ and $\vec{k}^{(s)}$ are , respectively, the wave vectors for the incoming and outgoing waves.

Since scattering from a rough interface in the Fraunhoffer approximation is valid only when the source insonifies a relatively small area on the interface, the interface is located in the far field of the source array with $r_s > A_s/\lambda$ for all frequencies of interest (A_s is the planar area of the source array.), $r'/r_s << 1$, and $r'/r << 1$ for all r'. To be able to maintain the validity of the Fraunhoffer approximation and to obtain a computationally tractable numerical solution, the formalism is limited to narrow beam source arrays.

In the Kirchhoff approximation, it is assumed that the surface field and its normal derivative are given by

$$p^{(+)}(\vec{r}', \omega) = [1+R(\hat{r}', \hat{k}^{(i)})]\, p^{(i)}(\vec{r}', \vec{r}_s; \omega) \tag{8a}$$

and

$$\hat{n}(\vec{r}') \cdot \nabla' p^{(+)}(\vec{r}', \omega) = iP_o [1-R(\hat{r}', \hat{k}^{(i)})]\, \vec{k}^{(i)} \cdot \hat{n}(\vec{r}')\, D_s^{(i)}(\vec{r}'; \omega)\, e^{i(\vec{k}^{(1)} \cdot \vec{r}_s + \vec{k}^{(i)} \cdot \vec{r}')}/4\pi r_s . \tag{8b}$$

In Eqs. (8a) and (8b), $R(\hat{r}', \hat{k}^{(i)})$ is the plane wave amplitude reflection coefficient for a planar interface. In this paper, scattering from a viscoelastic solid sediment is calculated so that

$$R(\hat{r}', \hat{k}^{(i)}) = (A-B)/(A+B)$$

with (9a)

$$A = \rho_2 k_z^{(1)} [4k_{pz}^{(2)} k_{sz}^{(2)} k_{px}^{(2)2} + (k_{sz}^{(2)2} - k_{px}^{(2)2})^2]. \tag{9b}$$

$$B = \rho_1 k_{pz}^{(2)} \kappa_s^{(2)4}. \tag{9c}$$

$$k_{pz}^{(2)} = \sqrt{\kappa_p^{(2)2} - k_{px}^{(2)2}}. \tag{9d}$$

$$k_{sz}^{(2)} = \sqrt{\kappa_s^{(2)2} - k_{sx}^{(2)2}}. \tag{9e}$$

$$k_{px}^{(2)} = k_{sx}^{(2)} = k_x^{(1)}, \tag{9f}$$

$$\kappa_p^{(2)} = k_p^{(2)} + i\omega\alpha_p/8683, \tag{9g}$$

and

$$\kappa_s^{(2)} = k_s^{(2)} + i\omega\alpha_s/8683. \tag{9h}$$

The quantities $k_p^{(2)}$ and $k_s^{(2)}$ are, respectively, the wave numbers for the pressure and shear waves in the sediment and α_p and α_s are the corresponding log decrement attenuations. It is important to note that since the reflection coefficient depends on the local angle of incidence, it depends on the surface derivative as well as the plane wave angle of incidence. Therefore, when Eqs. (6)-(8) are used in the Helmholtz-Kirchhoff integral, the numerical evaluation of the resulting integral is complicated by the fact that the integrand depends on the surface derivatives. To simplify the evaluation of this

integral, it is assumed that for narrow beams and small surface slopes $R(\hat{r}', \hat{k}^{(i)})$ is approximately constant on the insonified portion of interface and may be evaluated by using the mean angle of incidence at the interface. For isotropic surface roughness, the mean slope angle of the interface is $\gamma = \tan^{-1}(\sqrt{2}\, h/l)$, where l is the correlation length [5]. Then the surface derivatives are eliminated by performing an integration by parts and the resulting expression for the scattered pressure field is

$$p^{(s)}(\dot{r}, \dot{r}_s; \omega) = -ik^{(1)} P_o \frac{e^{ik^{(1)} r_s}}{4\pi r_s} \frac{e^{ik^{(1)} r}}{4\pi r} \int dx'dy' \exp\left\{ ik^{(1)} [Ax'+By'+C\xi(x',y')] \right\} D_s^{(i)}(\dot{r}';\omega) \left[\frac{aA}{C} + \frac{bB}{C} + c\right]. \quad (10a)$$

with

$$a = \left\{ [1+R(\hat{r}', \hat{k}^{(i)})]\, \hat{k}^{(s)} + [1-R(\hat{r}', \hat{k}^{(i)})]\, \hat{k}^{(i)} \right\}_x , \quad (10b)$$

$$b = \left\{ [1+R(\hat{r}', \hat{k}^{(i)})]\, \hat{k}^{(s)} + [1-R(\hat{r}', \hat{k}^{(i)})]\, \hat{k}^{(i)} \right\}_y , \quad (10c)$$

$$c = \left\{ [1+R(\hat{r}', \hat{k}^{(i)})]\, \hat{k}^{(s)} + [1-R(\hat{r}', \hat{k}^{(i)})]\, \hat{k}^{(i)} \right\}_z , \quad (10d)$$

$$A = (\hat{k}^{(i)} - \hat{k}^{(s)})_x , \quad (10e)$$

$$B = (\hat{k}^{(i)} - \hat{k}^{(s)})_y , \quad (10f)$$

and

$$C = (\hat{k}^{(i)} - \hat{k}^{(s)})_z . \quad (10g)$$

In Eq. (10a), terms involving derivatives of the projected beam pattern have been omitted. For a Gaussian beam, these terms can be omitted when $2k^{(1)} AX >> 1$ and $2k^{(1)} AY >> 1$.

2.2 Rough Surface Realizations

A two dimensional generalization of the technique used by Thorsos[5] was used to construct two dimensional realizations of a rough surface with Gaussian statistics. The surface height is given by

$$\xi(x',y') = \frac{1}{L_x L_y} \sum_{m=-N/2}^{N/2-1} \sum_{n=-N/2}^{N/2-1} F(K_{xm}, K_{yn}) \exp[i(K_{xm} x' + K_{yn} y')] \quad (11a)$$

where the spectral amplitude $F(K_{xm}, K_{yn})$ is given by

$$F(K_{xm}, K_{yn}) = 2\pi \sqrt{L_x L_y W(K_{xm}, K_{yn})} \begin{cases} \cos\phi & \begin{matrix} m=0;N/2 \\ n=0;N/2 \end{matrix} \\ [\cos\phi + i\sin\phi] & \begin{matrix} m\neq 0;N/2 \\ n\neq 0;N/2 \end{matrix} \end{cases} \quad (11b)$$

with $\cos\phi = N_1(0,1)$, $\sin\phi = N_2(0,1)$, $K_{xm} = 2\pi m/L_x$, and $K_{yn} = 2\pi n/L_y$. When $m<0$ or $n<0$, $F(K_{x-m}, K_{y-n}) = F^*(K_{xm}, K_{yn})$ so that $\xi(x',y')$ is real. The lengths L_x and L_y are, respectively, the lengths along the x- and y-axes of the insonified area on the mean plane of the interface, c is the correlation coefficient, and $N_1(0,1)$ and $N_2(0,1)$ are independent samples from a zero mean unit variance Gaussian distribution. The quantity $W(K_{xm}, K_{yn})$ is the two dimensional Gaussian roughness spectrum is given by

$$W(K_{xm}, K_{yn}) = \frac{l_x l_y h^2}{4\pi\sqrt{1-c^2}} \exp\{ -[(l_x x')^2 + (l_y y')^2 - 2c l_x l_y x'y']/4\sqrt{1-c^2} \} \quad (12)$$

and is normalized such that $\int_{-\infty}^{\infty} d\acute{K}\, W(\acute{K}) = h^2$.

3. Adaptive Windowed Local Cosine Transform

An adaptive windowed local cosine transform[7] is used to construct TF representations of the scattered field time series. The time series are segmented or windowed in time so that the resolution in the TF plane is limited by the uncertainty principle which is expressed by the fact that the time-bandwidth product is constant i.e., $\Delta t \Delta f \geq 1$. The time-bandwidth product describes a Heisenberg cell and the ensemble of Heisenberg cells provides a tiling of the TF plane. The TF representation of a signal is displayed graphically in a TF plane in which the Heisenberg cells are shaded in proportion to the TF spectral amplitude:

In this paper, the segmentation or windowing process is used adaptively to construct a near optimal segmentation which is equivalent to a near-optimal localization in time and frequency. An optimal segmentation minimizes the number of large amplitude Heisenberg cells and the shaded area in the graphical display of the T-F representation. To obtain an optimal segmentation in time, the time series is segmented following a dyadic tree structure. The optimal distribution of windows is obtained by comparing the TF representation of the time series using two adjacent intervals with that produced by their union. The optimal window is the one that for a fixed number of largest coefficients maximizes energy or minimizes entropy. An optimal segmentation consists of a distribution of windows obtained from different levels of the dyadic tree and its graphical display is characterized by Heisenberg cells with different aspect ratios. A best level representation is obtained by using an optimal uniform segmentation, i.e., a single level within the dyadic tree structure, and its graphical display is characterized by Heisenberg cells with a constant aspect ratio.

The novel feature of the adaptive windowed LCT used in this paper is the bell shaped window $w_j(t)$ introduced by Coifman and Meyer [8]. On the interval $I_j = [a_j, a_{j+1}]$ with length l_j, $w_j(t)$ satisfies the following conditions:

$$0 \leq w_j(t) \leq 1, \tag{13a}$$

$$w_j(t) = 1 \quad t \in [a_j + \varepsilon_j, a_{j+1} - \varepsilon_{j+1}],$$

$$0 \quad t \notin [a_j - \varepsilon_j, a_{j+1} + \varepsilon_{j+1}], \tag{13b}$$

$$w_j(t) = w_{j-1}(2a_{j+1} - t), \tag{13c}$$

and

$$w_j^2(t) + w_{j-1}^2(t) = 1 \quad |t - a_j| \leq \varepsilon_j . \tag{13d}$$

The windows that satisfy the conditions in (13) extend beyond the interval I_j and provide a smooth and symmetrical overlap with adjacent windows.

The LCT basis functions introduced in [4] are given by

$$u_{j,k}(t) = \sqrt{2/l_j}\ \ w_j(t)\ \cos[\pi(k+1/2)(t-a_j)/l_j]. \tag{14}$$

The basis functions $u_{j,k}(t)$ are orthonormal not only within the interval I_j, but throughout the TF plane. It can be shown that if a function $f(t) \in L^2(R)$, then it can be represented in the following manner:

$$f(t) = \sum_{j=1}^{\infty} \sum_{k=0}^{\infty} c_{j,k}\, u_{j,k}(t) \tag{15a}$$

with

$$c_{j,k} = \int_{a_j - \varepsilon_j}^{a_{j+1} + \varepsilon_{j+1}} dt\ f(t) u_{j,k}(t) = \int_{a_j}^{a_{j+1}} dt s_j(t) \sqrt{2/l_j}\ \cos[\pi(k+1/2)(t-a_j)/l_j] \tag{15b}$$

and

$$s_j(t) = f(t) w_j(t) - f(2a_j - t) w(2a_j - t) + f(2a_{j+1} - t) w_j(2a_{j+1} - t) . \tag{15c}$$

The effect of the window $w_j(t)$ is evident in (15) where it is shown that the energy in the overlap region is folded back into the interval I_j and the function $s_j(t)$ is projected out from f(t) and onto the basis functions. Using the representation given in (15a), a signal can be represented by an optimal TF spectrum that can be used to reconstruct the signal. In addition, the Heisenberg cells are disjoint, there is no energy leakage between adjacent cells, and the uncertainty principle is obeyed.

4. Numerical Considerations and Parameters

When Eqs. (11) and (12) are used to generate a surface realization, l_x , l_y , c, and h are input parameters however, the lengths of the insonified surface area, L_x and L_y , need to be determined. These lengths are given by the values of $x'=L_x/2$ and $y'=L_y/2$ for which the Gaussian beam in the x and y-direction decreases by exp(-3), i.e., when $\exp[-(L_x/2X)^2] = \exp[-(L_y/2Y)^2] = \exp(-3)$ so that $L_x = 2\sqrt{3}\ r_s\ \chi/\cos\theta_s$ and $L_y = 2\sqrt{3}\ r_s\ \phi$. It is important to note that when θ_s or r_s change, the surface realization changes as well. However, in this analysis the same surface realization was used for all calculations and the lengths L_x and L_y were fixed at their values for $\theta_s = 30^\circ$ and $r_s = 20$ m. An FFT was used to calculate a surface realization on a 1024x1024 grid with spatial increments $\Delta x = L_x/1024 < \lambda/5$ and $\Delta y = L_y/1024 < \lambda/5$ [5]. To insure that the minimum spatial sampling $\lambda/5$ was obtained, the number of points $N_x = L_x/(\lambda/5)$ was calculated and if $N_x > 1024$, the calculation was not performed. The same spatial sampling was used to evaluate the integral over the interface.

Although a closed form expression for the Fourier transform of an LFM pulse can be obtained, it was found that the FFT evaluation of $T^{(i)}(\omega)$ was numerically more convenient. The number of time samples is $N = 2^n$ where the integer n is determined by dividing the time window by .he sample frequency. The time window is T and the sample frequency is the reciprocal of twice the highest frequency, i.e., the Nyquist frequency, so that $n = \ln[2(f_{min} + \Delta f)T]/\ln 2 + 1$ and for $= 10\tau$ and the parameters considered in this paper n=17.

Time series were calculated by evaluating the inverse Fourier transform of the product of the incident pulse and interface scattered field spectra. Since the calculation required a large number of spectral samples, the spectrum of the interface scattered field was calculated on 16 nodes of a Cray T3D. It is important to note that the spectrum of the incident pulse is confined to the range of positive frequencies ~22-28 kHz for which the Kirchhoff approximation is valid. So that it is not necessary to calculate interface spectral components for frequencies for which the Kirchhoff approximation is not valid.

A set of parameters was chosen for the source, the fluid half space, the rough surface, and the sediment. These parameters are summarized in Tables 1 and 2. In the following, these parameters remain fixed unless noted otherwise. The parameters for the viscoelastic sediment are for a a sandy sediment for which the p-wave speed is greater than that in the fluid.

5. Results and Conclusions

Time series and local cosine based TF representations were calculated for back scattering with $\theta_s = \theta_r = 30^\circ$ from surfaces with h=0.01 m and h=0.1 m with $l_x = l_y = 0.1$ m, 0.5 m, and 1.0 m. Figure 1 shows TF representations for scattering from surfaces with h=0.01 m and (a1) l=0.01m, (a2) l=0.5 m, and (a3) l=1.0. Figures (b1)-(b3) show similar results for surfaces between randomly rough surfaces with different statistics, i.e., rms surface heights and correlation lengths. In general, differences in the TF representations of the scatter from statistically different surfaces are not dramatic, however, differences are most apparent in the high frequency portion of the TF plane. This suggests that classification of randomly rough surfaces may be facilitated by broad band pulses whose spectrum includes frequencies higher than those considered here.

It may be concluded that LCT based TF representations of broad band time series scattered from randomly rough surfaces affect a data compression of the time series and that in the TF plane, scattering from randomly rough surfaces with different statistics can be distinguished. Although no attempt has been made to develop an algorithm to classify surface roughness, the results shown here indicate that it may be useful to consider local cosine based TF representations as a basis for an algorithm to classify surface roughness.

References

[1] G. C. Bishop and Q. Huynh,"Time-Frequency Analysis of Model Based Pulse Scattering from a Fluid-Elastic Interface with Periodic Roughness," in Proceedings of Oceans '94, 13-16 Sept. 1994, Brest, France, Vol. II, 521-526.

[2] G. C. Bishop and J. Smith, "A T-matrix for scattering from a doubly infinite doubly periodic fluid-solid interface with periodic surface roughness," J. Acoust. Soc. Am. **94**, 1560-1583 (1993).

[3] P. Beckmann and A. Spizzichino, *The Scattering of Electromagnetic Waves from Rough Surfaces*, (The Macmillan Company, New, York, 1963), Ch. 3.

[4] J. Ogilvy, *Theory of Wave Scattering from Random Rough Surfaces*, (Adam Hilger, New York, NY, 1991), Ch. 4.

[5] E. Thorsos, "The validity of the Kirchhoff approximation for rough surface scattering using a Gaussian roughness spectrum," J. Acoust. Soc. Am., **83**, 78-92, (1987).

[6] G. C. Bishop and J. Smith, "High frequency scattering from a target in proximity to a randomly rough interface," unpublished.

[7] R. R. Coifman, Y. Meyer, and M. V. Wickerhauser, "Wavelet analysis and signal processing," in *Wavelets and their Applications*, M. Ruskal et al., (eds.), (Jones and Bartlett, Boston, Ma, 1992), pp. 153-178.

[8] R. R. Coifman and Y. Meyer, "Remarques sur l'analyse de Fourier a fenetre," C. R. Acad. Sci., Ser. 1, 312, 259-261, (1991).

[9] G. Frisk, *Ocean And Seabed Acoustics*, (PTR Prentice Hall, Englewood Cliffs, NJ, 1994), p. 50.

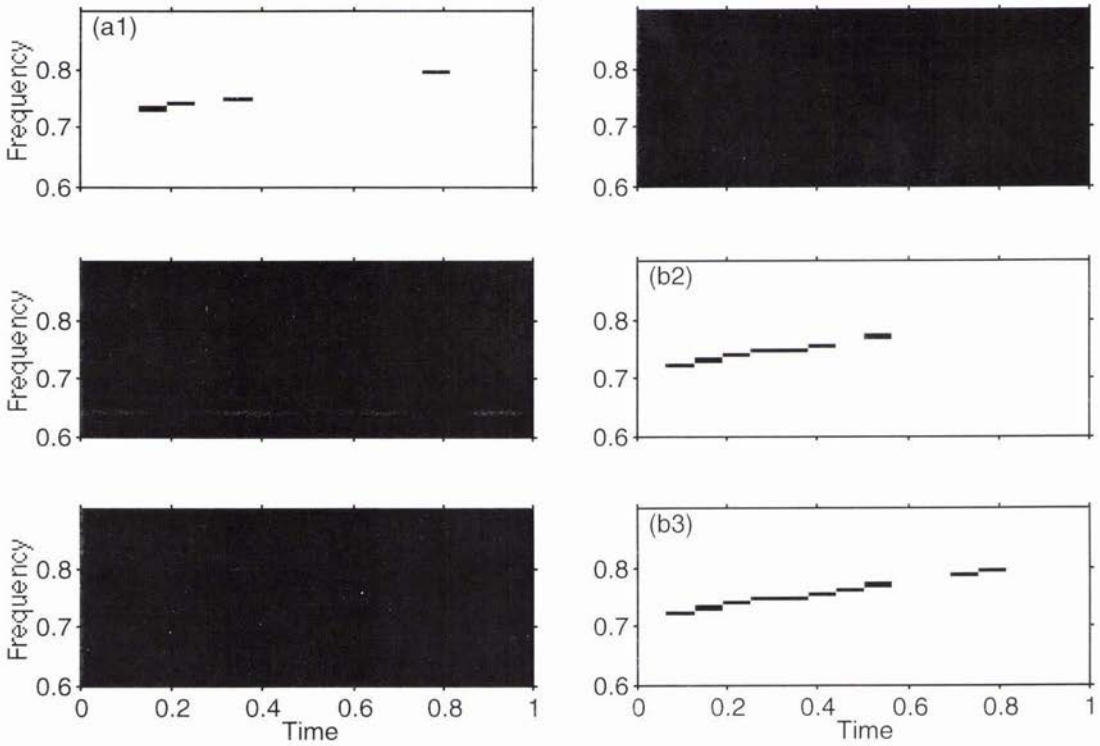

Fig. 1. Local cosine transform time-frequency representations of LFM scattering from randomly rough surfaces with h=0.01 m and (a1) l=0.1 m, (a2) l=0.5 m, and (a3) l=1.0 m and with h=0.1 m and (b1) l=0.1 m, (b2) l=0.5 m, and (b3) l=1.0 m.

Table 1. Source and receive parameters.

	symbol	parameter	value
source			
	P_o	incident amplitude	4π
	r_s	distance	20 m
	θ_s	polar angle	30^o
	ϕ_s	azimuthal angle	180^o
	χ_{max} , ϕ_{max}	beam widths	4^o
	D_s	beam pattern	Gaussian
	t	pulse width	0.2 s
	f_{min}	min frequency	23.75 kHz
	Δf	band width	2.5 kHz
receive			
	r_r	distance	20 m
	θ_r	polar angle	30^o
	θ_r	azimuthal angle	180^o

Table 2. Fluid, sediment, and roughness parameters.

	symbol	parameter	value
sfluid			
	$c_p^{(1)}$	sound speed	1500 m/s
	$\rho_f^{(1)}$	fluid density	1000 kg/m^3
sediment[9]			
	$c_p^{(2)}$	p-wave speed	1478.0 m/s
	$\alpha_p^{(2)}$	p-wave attenuation	0.07 dB/m/kHz
	$c_s^{(2)}$	s-wave speed	121.83 m/s
	$\alpha_s^{(2)}$	s-wave attenuation	4.474 dB/m/kHz
	$\rho^{(2)}$	density	1800.0 kg/m^3
roughness			
	h	mean height	0.01 m
	$l_x = l_y = l$	correlation length	0.5 m
	c	correlation coefficient	0

Multipath Field Representation for Seabed Parameter Extraction Using Backscatter Data from Shadow Zones

Judith Bishop

Naval Undersea Warfare Center
Division Newport, Code 3111
Newport, Rhode Island 02841-1708 USA
Email: bishop@a1.vsdec.nl.nuwc.navy.mil

Sven Ivansson

Swedish National Defence Research Establishment
Underwater Wave Propagation and Active Sonar Div.
17290 Stockholm, Sweden
Email: sveni@sto.foa.se

Abstract

Inversion strategies for bottom parameter estimation in shallow water impose stringent requirements on accuracy and speed of acoustic models. We highlight the importance of second order effects as first order determinants of the field using examples based on experimental data, employ high accuracy adaptive wavenumber integration techniques to evaluate the terms of the multipath expansion without approximation, and provide a basis for more accurate, efficient prediction of variable shallow water fields.

1. Introduction

Modeling environmental processes explicitly (with loss and scatter from surface, volume, bottom) rather than implicitly (from e.g. bottom layer descriptions) is common in many acoustic applications. However, explicit modeling approaches require decomposition of the incoming and outgoing fields in order to isolate propagation angles. One type of field decomposition in a range independent environment is multipath expansion (MPE). It is theoretically exact and can be interpreted using ray theory at sufficiently high frequencies, allowing efficient treatment of wavenumber and travel time integrals. The technique has proved valuable for modeling reverberation data in deep water and Raymode as well as the Generic Sonar Model (GSM) are based upon it [1],[2]. Both these models tabulate reverberation with sufficient speed to make rapid inversion applications in shallow water feasible (e.g. real time determination of bottom properties from sonar reverberation data [3]). Unfortunately, inversion schemes of this type have encountered limited success for long ranges in bottom limited conditions. Wavenumber integration methods in general struggle with the highly oscillatory nature of the Bessel function at long ranges and encounter practical difficulties in approximating the infinite upper limit of integration. As we shall see, the low amplitude fields in shadow zones are actually obtained from strong coherent reduction of high amplitude mathematical components of the integration. Thus, small errors in constructing the integrand or in treating the limits of integration can produce significant (60 dB and greater) errors in the calculated field.

Motivated by these considerations, the basis of MPE is revisited. RPRESS, a high accuracy propagation code based on compound matrix propagation [4] and adaptive wavenumber integration [5] has been employed to evaluate the terms of the multipath expansion without any approximations like WKBJ. We illustrate the physics that is absent in WKBJ-based treatments of the expanded Green's function. Specifically: (i) Accurate levels for evanescent energy contributions to the full wave field are determined and discussed relative to approximations which extend ray interpretations to diffracted energy (e.g. analytic continuation). (ii) Multipath coupling, driven by refraction in the water column, becomes increasingly more important as frequency decreases, causing redistribution of the directional components of the field and a modification in effective level at long ranges.

Our goal is to refine the numerical integrations performed in rapid implementations of MPE, using a well matched high accuracy benchmark, in order to achieve the performance needed for broadband inversion in real time. We begin with problems identified in inverting bottom parameters from US Navy sonar data using GSM, analyze the performance of its multipath integration (GSM-MPE) [2], and provide a context for interpreting the multipath field components obtained from general (non WKBJ) numerical methods. We subsequently approach the issue of modeling reverberation when shadow zones are involved, emphasizing the role played by hybrid events which scatter energy between classical and imaginary (diffraction-approximate) propagation paths.

2. Simple caustics and the shallow water propagation field

Downward refracting sound velocity profiles, common in shallow water, are caustic-forming. The importance of the associated diffraction effects will depend strongly on bottom type, and model errors will become apparent only when classical arrivals are weak. In particular, we link the unreliable performance of GSM-MPE in shallow water directly to this 'imaginary eigenray' problem. (By an 'imaginary eigenray', we mean a 'ray' that is horizontally displaced, much like a head wave, from a caustic and continued into a shadow zone. According to asymptotic ray theory [6], this construct can be used to represent diffraction in terms of ray equivalents.). We examine the approximations in common use for wavenumber integration codes, and isolate the numerical mechanisms responsible for the problems with the GSM code.

2.1 Inversion results and general modeling considerations

Our first example involves 3 kHz transmission loss (TL) data collected in shallow water (80 m) along the Korean Shelf in the Sea of Japan in the summer of 1994. Downward refraction combined with a low impedance contrast at the bottom (mud sediment) produced uniformly high TL measurements independent of receiver depth (z_r =7.6, 18.3, 45.7, 80 m). Attempts to invert bottom properties from these data failed. Specifically, inversion algorithms based upon GSM-MPE produced vanishing reflection coefficients, and curiously high residual field levels beyond the caustic. IFDPE [7], SAFARI [8] and RPRESS predict levels well below GSM-MPE using the GSM inverted bottom (Fig. 1b), while all but GSM produce reasonable model-data comparisons using typical mud sediment parameters (Fig 1a).

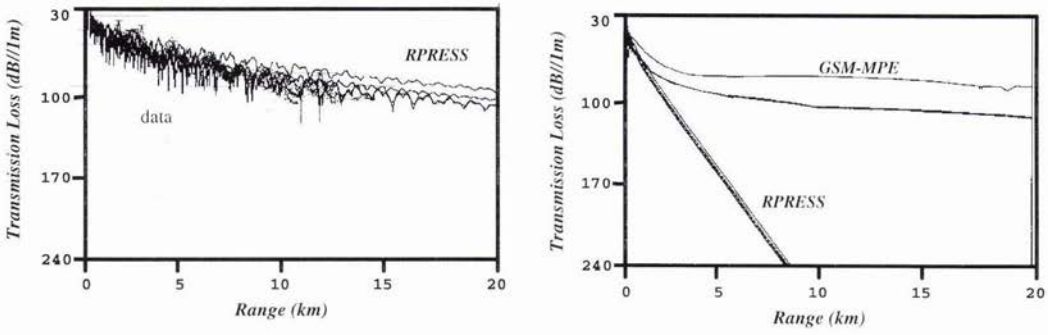

Fig 1. a) Reasonable sediment parameters for mud produce good agreement between data (obtained out to the range r = 15 km) and RPRESS. **b)** Comparison of GSM and RPRESS TL predictions using GSM derived Bottom Loss values.

The progressive failure of GSM to predict accurate TL levels is illustrated in Fig. 2. As the bottom impedance contrast is reduced, propagating energy escapes from the water column, leaving a residual field that consists entirely of diffracted energy beyond the caustic range. The GSM levels exhibit 60 dB errors at long ranges when compared to more accurate models, and are visible well above the noise for many measurement applications.

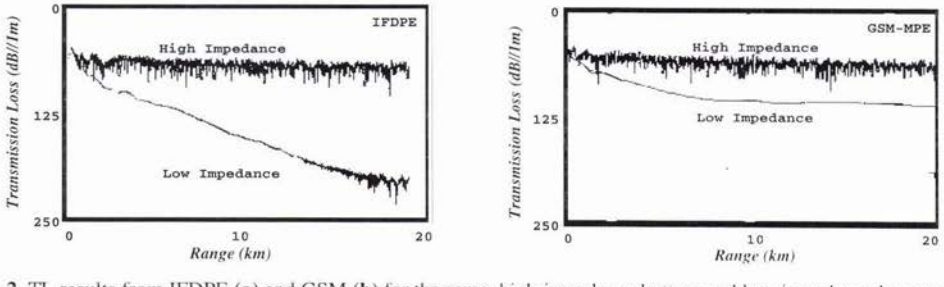

Fig. 2. TL results from IFDPE **(a)** and GSM **(b)** for the same high-impedance bottom and low-impedance bottom.

To provide better diagnostics, the profile was simplified to a $1/c^2$ linear velocity profile, decreasing from 1.5 km/s at the surface to 1.48 km/s at the bottom (z=80 m), so that a simple caustic at range r =1.3 km for source depth z_s =10 m and receiver depth z_r =80 m could be investigated (attenuation is neglected). Although GSM-MPE works reasonably well close to the caustic (Fig. 3b), its imaginary eigenray construction works poorly for longer ranges (Fig. 3a) where its levels hover near 100 dB, independent of frequency. Physically, TL in the shadow zone should increase with frequency, a result properly predicted by more accurate models. Thus the performance of GSM-MPE is here actually poorest at high frequencies.

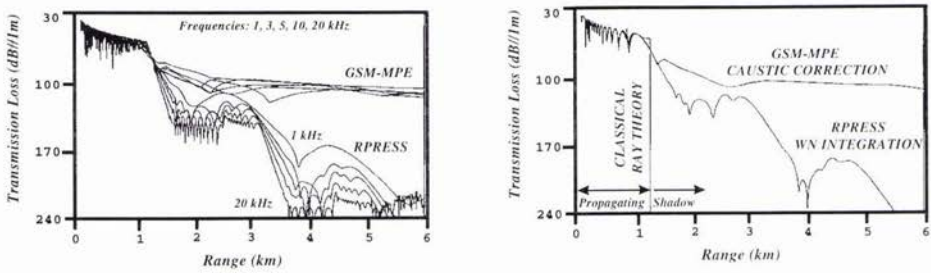

Fig. 3. a) Frequency dependence of RPRESS and GSM-MPE TL curves for a low-impedance bottom. **b)** The 3 kHz case is displayed with classical ray theory revealing the caustic at $r = 1.3$ km for $z_s = 10$ m and $z_r = 80$ m.

2.2 Numerical approximations

GSM-MPE involves approximations to the Green's function and Bessel function kernels in the integral representation of the field as well as truncations of the integration interval itself. To discuss these approximations we start from

$$P(r,z,z_s;\omega) = \int_0^\infty G(z,z_s;k,\omega) J_0(kr)\, k\, dk \tag{1}$$

which synthetizes the field from its wavenumber components [9]. By applying the well-known relation

$$J_0(kr) = 1/2\ H_0^{(1)}(kr) + 1/2\ H_0^{(2)}(kr)\,, \tag{2}$$

each wavenumber component of the field can be represented by an outgoing part and an ingoing part, cf. [10]. (This physical interpretation is poor for small kr, however). Note that the integral of the outgoing components should not be considered as the outgoing field since (1) is already an outgoing field according to the radiation condition from the source.

For the 3 kHz case of Fig. 3b, we will use RPRESS to investigate the effects in the shadow zone of approximations in setting up the field. The low-impedance bottom is modeled as a homogeneous half-space with density 1.0 kg/dm^3 and velocity 1.48 km/s to achieve continuity at z=80 m. We examine right endpoint wavenumber truncations which eliminate the evanescent field, ingoing components of the field , and left endpoint truncations which eliminate high angle contributions.

2.2.1 Evanescent energy

For our case, the separation between the evanescent and propagating regimes of wavenumbers would appear at a horizontal slowness $p_0 = k_0/\omega = 0.6678$ s/km, corresponding to the inverse of the maximum medium velocity between source and receiver (1.4975 km/s at z=10 m). The evanescent energy alone would appear by restricting the integral in (1) to the interval k_0 to infinity. As illustrated in Fig. 4, the total evanescent field can be ignored at short ranges, but it is a critical component beyond the caustic. The reason is that shadow zone levels will be controlled by horizontal wavenumber components close to the caustic wavenumber, which in this case lies very close to the truncation point k_0. The evanescent-field integrals of the outgoing and ingoing components are also shown separately in Fig. 4. The first integral is dominant, but wherever the two are similar in magnitude, a beating pattern emerges in the total evanescent field.

Even for an isovelocity channel governed by ray propagation, the evanescent field is important when wavenumber integration is used. Our earliest examinations of the shadow zone performance of GSM-MPE uncovered errors for isovelocity profiles which could be traced directly to wavenumber interval truncation. At long ranges, points of stationary phase fall close to the truncation point, causing field levels to dip below the geometric spreading loss expected for isovelocity propagation. These errors could be reproduced in RPRESS by using the same truncation point as in the GSM-MPE code.

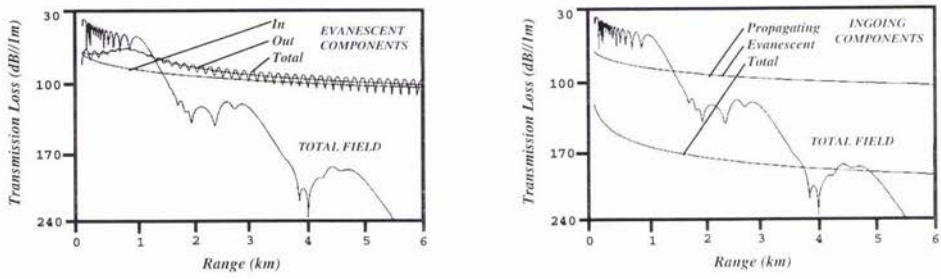

Fig. 4. The evanescent energy can be ignored in the propagating region but not in the shadow zone.
Fig. 5. The total integral of incoming components contributes far out in the shadow zone.

2.2.2 The integral of the ingoing field components

The integral of the ingoing field components is depicted in Fig. 5. Omission of this part is common in sound propagation codes. When the propagation is governed by rays or modes, this can be motivated mathematically: stationary phase points of rays will preferably appear in conjunction with $\exp(ikr)$ of $H_0^{(1)}(kr)$ rather than $\exp(-ikr)$ of $H_0^{(2)}(kr)$, a modal wavenumber (pole) slightly above the positive real axis will cause retarded phase variation in conjunction with $\exp(ikr)$ of $H_0^{(1)}(kr)$ but accelerated phase variation (and hence cancellation) in conjunction with $\exp(-ikr)$ of $H_0^{(2)}(kr)$. The integral of the ingoing components becomes of greater relative importance when a description in terms of rays or modes is lost, as it is far out in the shadow zone (cf. Fig. 5) and at low enough frequencies (cf. [10]). In Fig. 5, we may also note a significant destructive interference between propagating and evanescent parts to produce a very low-amplitude total result.

2.2.3 High-angle contributions

Another common approximation is to remove high-angle energy from (1), i.e. to truncate the integral at a left end-point $k_l = \omega p_l$. As an example, we depict in Fig. 6 the residual high-angle field for $p_l = 0.0617$ s/km, along with its decomposition into integrals of outgoing and ingoing components. Values smaller than p_l correspond to grazing angles at the source greater than 84.70 degrees. Apparently, this high-angle field cannot be neglected far out in the shadow zone where levels are low enough to make weak energy important. As in Fig. 4, truncation introduces a disturbance that does not drop off very fast as r is increased. Significant oscillations are caused by beating between the integrals of the out- and in-going components.

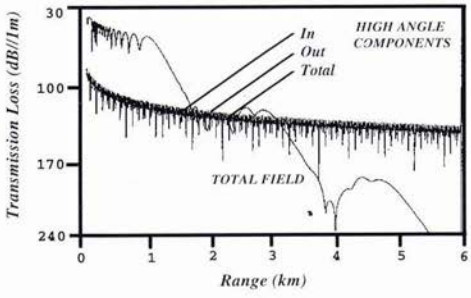

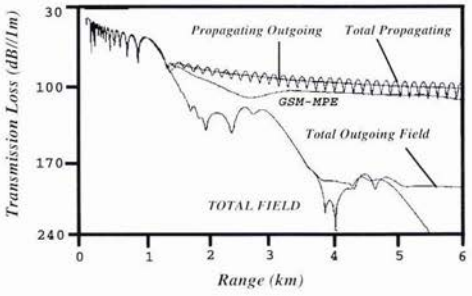

Fig. 6. High-angle contributions, isolated by integral truncation, become important far out in the shadow zone.
Fig. 7. The total RPRESS field along with some truncated fields. Note, in particular, the qualitative similarity between the GSM-MPE field and the propagating-field integral of the outgoing components.

2.2.4 Overall effects of truncating the field in a shadow-zone

We conclude from sections 2.2.1-2.2.3 that it is dangerous to remove parts of the field or to truncate the wavenumber integrals for ranges in a shadow zone. Consider Fig. 7, as a summary. The integral of the outgoing components is adequate except in the deep shadow zone. The propagating field is adequate at close ranges, but not at all in the shadow zone, where it exhibits significant beating between the integrals of ingoing and outgoing components. Note that the GSM-MPE field is quite similar to the propagating-field integral of the outgoing components, suggesting that the problem here, as in the isovelocity case for this model, is associated with wavenumber truncation in the evanescent regime. Classical and caustic-corrected asymptotic ray theory will, of course, predict a zero field and a low-level field, respectively.

Some of the truncation effects can also be understood by looking at the Green's function directly for horizontal slownesses p beyond $p_0 = 0.6678$ s/km, where the evanescent regime starts and an exponential decay should appear. It turns out that the RPRESS Green's function has not yet been reduced very much in magnitude at p_0.

3. Multipath decomposition of the field in an inhomogeneous medium

According to [2],[11], MPE is effected by an expansion of the Green's-function kernel $G(z,z_s;k,\omega)$ in (1):

$$G(z,z_s;k,\omega) = \sum_i \sum_j G_{ij}(z,z_s;k,\omega) \tag{3}$$

where i=1,2,3,4 denotes fundamental path type and j=0,..,∞ denotes ray cycle. The physical interpretation of this expansion in terms of a ray structure (Fig. 8) is valid asymptotically (high frequency) for a propagating wave. G_{ij} itself represents the z component of the propagation, while the r component is handled by the Bessel- (or Hankel-) function from (1)-(2).

In [2], the decomposition is effected by two particular solutions $F_-(z;k,\omega)$ and $F_+(z;k,\omega)$ of the depth-dependent wave equation. The WKBJ approximation allows unique association of F_- with an upgoing wave and F_+ with a downgoing wave, and the initial directional structure is preserved (for a propagating wave that does not turn between source and receiver). With 'exact' non-WKBJ computations, multiple internal reflections ('multi-path coupling') will complicate the picture, causing initially upgoing F_- to acquire downgoing components and initially downgoing F_+ to acquire upgoing components.

In fact, there does not appear to be any canonical way of choosing F_- and F_+. Each choice will produce a different decomposition of the field acccording to (3) and (1), and the multipath expansion is not unique. However, when the field is dominated by ray propagation with rays that do not turn between source and receiver, this nonuniqueness may not be essential and this may be the reason why this issue is not discussed in [2]. The arbitrariness of subdividing a field in an inhomogeneous medium into directional components is addressed in [12]. A particular scheme is the Bremmer series [13].

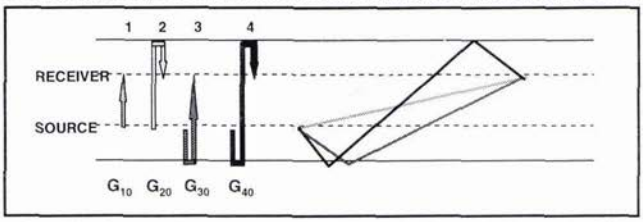

Fig. 8. The four fundamental multipath types for cycle number j=0. A positive j indicates j additional cycles (two-way paths between surface and bottom).

For a numerically careful benchmark implementation of (3), and the corresponding wavenumber integrals (1) of the separate multipath components, we introduce two specification depths: an upper one z_- for F_- and a lower one z_+ for F_+. At z_-, F_- is specified to be purely upgoing in some appropriately defined sense, whereas F_+ is specified to be purely downgoing at z_+. Since up- and down-going components can be defined unambiguously in a homogeneous layer, an obvious choice is to consider the medium to be locally homogeneous at z_- while defining F_- there, and locally homogeneous at z_+ while defining F_+ there. Another choice is to consider the medium to be $1/c^2$ linear above z_- or below z_+ and use Airy functions to define $F_-(z_-)$ or $F_+(z_+)$, respectively, in order to get a purely outgoing wave far out in the implied half-space. With a turning point in such a $1/c^2$ linear half-space above z_-, for example, F_- would contain a 'reflected' downgoing component at z_- in addition to an upgoing component there (see [14, Box 9.1] for the behavior of the WKBJ solution across a turning point) . Due to the arbitrariness that is involved, one should choose specification depths and types guided by the nature of the problem at hand.

In order for each G_{ij} integral to converge, it is in general necessary to choose the specification depths z_- and z_+ such that

$$z_- \le \min(z_s, z_r) \le \max(z_s, z_r) \le z_+ . \tag{4}$$

If $z_r < z_-$, for example, in the evanescent regime (large k) some velocity profiles would produce multiple 'reflections' causing an exponential increase of F_- in the upward direction towards z_r. In fact, $F_-(z_r;k,\omega)$ could increase exponentially with k, without sufficient control by the excitation factor from the source, and the individual multipath integrals would diverge.

Guided by these considerations, we have developed a version of RPRESS for accurate computation of the multipath components of the field. Using the example from Section 2 (Fig. 3b etc.), we choose $z_- = z_s = 10$ m and let $F_-(z_-)$ be defined by regarding the medium at z_- to be locally homogeneous. We choose $z_+ = z_r = 80$ m, but let $F_+(z_+)$ be defined from Airy functions as if the $1/c^2$ linear profile were continued in a lower half-space. For the multipath type 1 (i=1) and type 2 (i=2) fields, respectively, there is a 'bump' moving out in range with increasing cycle number j=0,1,2,... This bump represents energy coming from residual interaction with the boundaries (residual relative to the possible interaction prescribed by F_- and F_+ there). For a downward refracting profile, an effective 'skip distance' will appear. The i=1,j=0 field agrees exactly with the field in the modified medium obtained by continuing our medium (without contrast) above z=0 m to a homogeneous half-space and below z=80 m according to the $1/c^2$ linear profile above. Fig. 9a shows the (coherent) sum of the i=1,2 fields for the separate cycle numbers j = 0, 1, 2. For short ranges, direct and surface-'reflected' fields will interfere irregularly causing an oscillating sum. Beyond the caustic at r = 1.3 km, the j=0 field sum will decrease rapidly, being the total field for the modified medium obtained by replacing the homogeneous subbottom half-space with a $1/c^2$ linear continuation below z=80 m. Beyond about 2 km, the j=1 field sum will become important, explaining the plateau there in the total RPRESS field from Fig. 3b. The sum of the j=0 and j=1 field sums of Fig. 9a explains the total field out to about 3 km, where the total field again drops significantly, because of interaction with the type 3 and type 4 fields (not shown).

In Fig. 9 b) and c), the gradual acquisition by each multipath component of energy from multiple internal reflections is illustrated by the departure of F_- and F_+ from the up- and down-going WKBJ solutions. The straight lines alone, at 0 dB, represent what one would expect for the isovelocity case, where WKBJ is exact with F_- and F_+ void of down- and up-going components, respectively. For our $1/c^2$ linear example, F_- acquires downgoing components (Fig. 9b) and F_+ acquires upgoing components (Fig. 9c). The horizontal wavenumber considered was for a wave turning at the surface. Our choice

of upper specification initializes the downgoing part of F_- to zero at $z_-=10$ m, and it falls about 36 dB below the upgoing part at most other depths. Because of the Airy-function specification of F_+ at $z_+=80$ m, the upgoing part of F_+ will not vanish there. It falls about 62 dB below the downgoing part, and it becomes increasingly more important at lower depths.

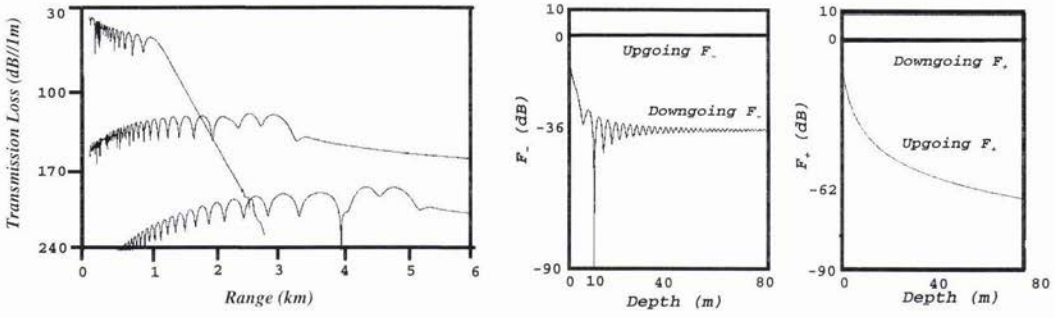

Fig. 9. a) The 3 kHz RPRESS field from Fig. 3b is decomposed into different multipath components. We show the sum of the i=1,2 fields for the cycle numbers j=0, 1, 2. **b)** The up- and down-going parts of F_-, as defined by the up- and down-going WKBJ solutions, for a particular horizontal wavenumber k. **c)** As b) but for F_+.

Similar figures for other horizontal wavenumbers show, as expected, that simple WKBJ-like F_- and F_+ solutions appear for small k, whereas the mixture of WKBJ up- and down-going pieces is enhanced for large k. Across a turning point, the change of character is of course dramatic [14, Box 9.1]. Furthermore, our rigorous implementation of multipath expansion allows rather precise quantitative bounds on the low frequency validity of the WKBJ approximation.

4. Simple caustics and the shallow water reverberation field

As we have seen, the propagation field in shallow water may move from regions of strong classical character to regions where diffracted energy dominates accompanied by a subtle palette of second order effects. This tendency is even more pronounced in the broadband reverberation case for two reasons: redistribution of path structure in the measured signal according to time of arrival, and redistribution of highlights produced by beamforming.

To illustrate the subtlety and importance of these effects, we provide an example based upon bottom backscatter data collected using a midwater depth source in shallow water under downward refracting conditions. Beamforming may strongly enhance the appearance of well resolved first, second, etc. bottom bounce (BB) peaks in the data (Fig. 10a). Based upon angle, the sonar beam pattern discriminates against the hybrid mixture of scattered paths which would otherwise smooth the region between the peaks due to their intermediate arrival times. Because the principal paths are strong vertexing paths, there will also be an extensive population of imaginary eigenrays which are strongly favored by the beam pattern. They are produced by about the same source angles which favor the principal paths but have a different geometric character and (typically) earlier arrival times. Including the possibility of different transmit and receive paths, a hybrid mixture of classical and imaginary paths is produced (Fig. 10b). The apparent times of arrival will shift away from the principal BB peaks and the hybrid events will form (in this example) the leading edge of each peak in the reverberation. Errors in modeling the level of these arrivals will produce mismatch (or, in general, convergence failure) for reverberation based inverse problems.

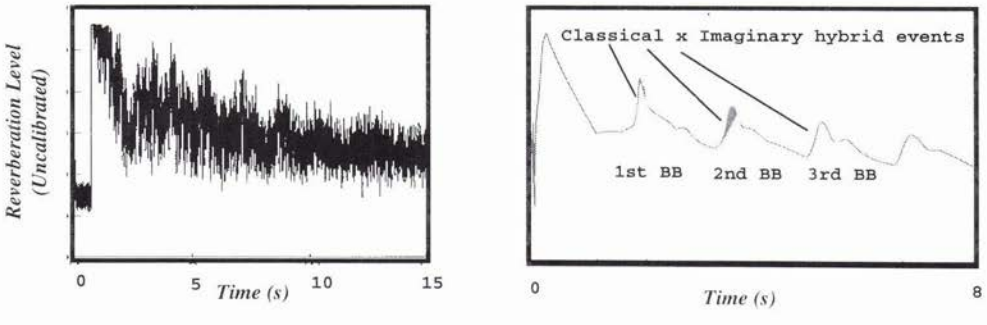

Fig 10. a) Reverberation data that exhibit BB peaks. **b)** GSM predicts leading edges dominated by diffracted energy.

The effect described can be illustrated by a pulse computation for our example case, using Fourier synthesis of monofrequency results. Fig. 11a shows time traces for a sinc-like pulse centered at about 1 kHz, and phase identification can be done conveniently by RPRESS pulse computations for the individual multipath components. The earlier and later (pair of) arrivals correspond essentially to cycle numbers j=0 and 1, respectively. The fundamental types i=1 and 2 contribute in each case. The time separation between these two types can be seen at the shorter ranges, but further out they merge into one apparent arrival. For j=0, the (surface-produced) caustic is reached at r =1.3 km. Beyond that distance the pulse becomes distorted (a low-pass filtering effect caused by a frequency-dependent distance to the caustic in terms of wavelengths), and the amplitude drops off significantly (Fig. 11b). As predicted by caustic-corrected ray theory (e.g. [15]), the pulse moves out in range and time as if it were shed by the caustic in the sense of an imaginary eigenray. In particular, an effective grazing angle can be associated at the bottom. The amplitude drop-off starts in fact well ahead of r =1.3 km (cf. Fig. 3b and Fig. 9a).

Turning to the later j=1 arrival(s), cf. Fig. 9a, the surface-produced caustic appears at r =3.25 km, beyond the ranges considered here. Hence, the corresponding amplitudes of Fig. 11b do not yet drop off significantly, and the propagation can be thought of in terms of classical rays (albeit with a tiny reflection from the bottom caused by a discontinuity in gradient only). The amplitude patterns in Fig. 11b agree with those of Fig. 9a for j=0 and 1. The variations in level before the caustic are averaged out in a broadband pulse calculation, however.

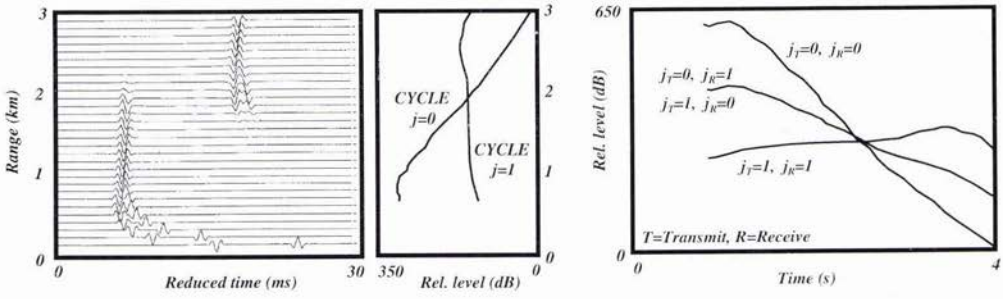

Fig. 11. a) RPRESS pulse computations for our example case, with z_s =10 m and z_r =80 m (the bottom). Thirty traces are given, one for every 100 m out to 3.0 km. The time axis shows reduced traveltime (t-r/1.5) according to the sound velocity 1.5 km/s at the surface. Each trace is scaled so that all traces are plotted with a common maximum amplitude. **b)** Relative amplitudes in dB for the two prominent arrival pairs, j=0 and 1, out to 3 km.
Fig. 12. Relative monostatic reverberation levels obtained by combining the two main paths of Fig. 11 for the outgoing and backscattered energy to give four combinations, among which the two hybrid ones are equivalent.

Neglecting effects such as scattering strength, integration over azimuth and the pulse length, a schematic computation of monostatic reverberation is attempted in Fig. 12. Each range bin will contribute to the reverberation trace with four arrivals at times t_0+t_0, t_0+t_1, t_1+t_0, t_1+t_1 , where t_0 and t_1 are arrival times for j=0 and 1, respectively. The two 'classical-to-imaginary' coupled paths appear at the same time, reinforcing each other. The amplitude-versus-time curves of Fig. 12 have been obtained by a positioning in time according to Fig. 11a for the reverberation contributions from different ranges according to Fig. 11b. The reverberation should be obtained as the sum of its contributing arrivals (with a mixed angle composition) at each time bin. In this case, imaginary-to-imaginary and classical-to-imaginary coupling of the outgoing and backscattered paths will obviously increase the level significantly at times between 1.0 and 2.5 s. Because of an extremely weak bottom 'reflection', caused by a discontinuous velocity gradient only, energy with high j is effectively stripped off and weak imaginary eigenray contributions become important, as compared to classical energy for cycle 1, far out in the shadow zone.

In reality, the imaginary eigenray energy would of course not be important too far from the caustic. It would be masked there by physical noise and by stronger j=1,2.. energy caused by a nonvanishing impedance contrast at the bottom. Hence, its region (time) of influence would be diminished but nevertheless present. With beamforming as a stripping mechanism for intermediate energy, we would approach the case shown in Fig. 10.

5. Summary and conclusions

The approximation techniques used to implement multipath expansion in shallow water require careful application. Traditional numerical approximations which work well in tabulating propagating fields can be very poor approximations in shadow zones, during cross layer propagation, or when source and receiver are close in depth. As a result, the difficulty in determining the correct Green's function in the evanescent regime has turned

out to be a critical shortcoming of the Generic Sonar Model in predicting accurate field levels at long ranges. Furthermore, the inherent nonunique character of multipath expansion needs to be taken into consideration when 'exact' non-WKBJ based computations are attempted.

The shallow water reverberation field is also significantly affected by inaccuracies of this type. Hybrid scattering events, beamforming and arrival time distribution functions act together to produce diffracted energy highlights in the reverberation time series. Errors in evaluating imaginary eigenray levels will affect the convergence and results of inverse algorithms.

Since GSM-MPE is a much and increasingly used tool for reverberation studies, it is important to improve its inaccurate shadow-zone field computations while maintaining its desirable high-speed performance. Our plans for future work include:

(i) Modification of the code. Different strategies are possible, with different preferences for caustic-corrected asymptotic ray theory and wavenumber integration [16].

(ii) Incorporation of an option to do full RPRESS bench-mark computations for the total field and its multipath components. Such computations would be too time-consuming for routine applications, however.

(iii) Reverberation studies with a modified GSM-MPE code, including an option for time-domain pulse computations. In particular, we would like to investigate the phenomenon of classical-to-imaginary eigenray coupling more closely.

(iv) The rapid inversion work has so far been confined to monostatic studies of reverberation. There is also a need for bistatic broadband treatments capable of near real-time performance.

Acknowledgments

We are especially grateful to George Botseas for support in our numerical studies, to Roy Deavenport for many useful discussions, to Lynne Dillman for providing access to SHAREM data, and to Henry Weinberg for discussions about his propagation code. One of us (J. Bishop) would like to thank the Office of Naval Research for support under the auspices of the Combatant Data Collection program. The work was completed as part of the Data Exchange Agreement (DEA) between the US Navy and Sweden.

References

[1] D.A. DiNapoli and R.L. Deavenport, "Numerical models of underwater acoustic propagation", in *Topics in Current Physics*. New York, Springer, pp. 79-157, 1979.

[2] H. Weinberg, "Application of ray theory to acoustic propagation in horizontally stratified oceans", *J. Acoust. Soc. Am.*, vol. 58, pp. 97-109, July 1975.

[3] J.L. Bishop, M.T. Sundvik and D.W. Grande, "Inverting sea bed acoustic parameters from reverberation", in *Full Field Inversion Methods in Ocean and Seismo-Acoustics*. New York, Kluwer, pp. 401-406, 1995.

[4] S. Ivansson, "The compound-matrix method for multi-point boundary-value problems", *Z. angew. Math. Mech.*, in press.

[5] S. Ivansson and I. Karasalo, "A high-order adaptive integration method for wave propagation in range-independent fluid-solid media", *J. Acoust. Soc. Am.*, vol. 92, pp. 1569-1577, 1992.

[6] D.W. White and M.A. Pedersen, "Evaluation of shadow-zone fields by uniform asymptotics and complex rays", *J. Acoust. Soc. Am.*, vol. 69, pp. 1029-1059, April 1981.

[7] D. Lee and G. Botseas, "An implicit finite-difference computer model for solving the parabolic equation", NUSC Technical Report 6659, May 1982.

[8] H. Schmidt, "SAFARI, Seismo-acoustic fast field algorithm for range-independent environments", SACLANTCEN Report SR-113, 1988.

[9] F. Jensen, W.Kuperman, M.Porter and H. Schmidt, Computational Ocean Acoustics. New York, AIP Press, 1993.

[10] Y.L. Li and M.J. White, "A note on using the fast field program", *J. Acoust. Soc. Am.*, vol. 95, pp. 3100-3102, June 1994.

[11] G.A. Leibiger and D. Lee, "Application of normal mode theory to convergence zone propagation", Vitro Lab. Res. Memo VL-8512-12-0, 1968.

[12] F.W. Sluijter, "Arbitrariness of dividing the total field in an optically inhomogeneous medium into direct and reversed waves", *J. Optical Soc. Am.*, vol. 60, pp. 8-10, Jan. 1970.

[13] F.W. Sluijter, "Generalizations of the Bremmer series based on physical concepts", *J. Math. Anal. Applic.*, vol. 27, pp. 282-302, 1969.

[14] K. Aki and P. Richards, Quantitative Seismology. San Francisco, Freeman, 1980.

[15] E.K. Westwood and C.T. Tindle, "Shallow water time-series simulation using ray theory", *J. Acoust. Soc. Am.*, vol. 81, pp. 1752-1761, June 1987.

[16] H. Weinberg, "Effective range derivative for acoustic propagation loss in a horizontally stratified ocean", *J. Acoust. Soc. Am.*, vol. 70, pp. 1736-1742, Dec. 1981.

Analysis of Broad-Band Echosounder Data Over a Gassy Seabed

F. A. Boyle*, N. P. Chotiros*, N. G. Pace**, O. Bergem**, E. Pouliquen**

*Applied Research Laboratories
The Unversity of Texas at Austin
P. O. Box 8029, Austin TX 78713-8029
Email: boyle@arlut.utexas.edu

**SACLANT Undersea Research Centre
Viale San Bartolomeo, 400
19138 La Spezia, ITALY

Abstract

Calibrated echosoundings from a well-characterized gassy seabed were examined. Acoustic reflection was significantly higher than expected. It is hypothesized that gas bubbles are responsible. Anomalously high levels of reflection appear at the edge of the spectral peak, possibly associated with nonlinear conversion of acoustic energy. An acoustic colormapping method was applied to the data, clearly showing its spectral character. The spectral features appear to carry relevant information about sediment interface roughness and gas content.

1. Introduction

Over the past several decades there has been considerable interest in the physics of sound penetration into the seabed. Much of this work has been driven by a need for reliable mine detection capability.

In 1993, Chotiros et.al. [1] compared the results of normal incidence echosoundings with expectations, based in current acoustic theories. It was found that sandy sediments generally had reflection coefficients that were most consistent with poroelastic modeling. These findings were consistent with previous acoustic penetration experiments [2], in which anomalous acoustic penetration was observed that is explainable via poroelastic theory. The reflection coefficient, in general, was found to have sensitive dependence on the sediment type, suggesting that it might be useful for determining seabed acoustic mechanisms.

A significant problem in seabed acoustics is the question of trapped gas bubbles. Gas bubbles are known to possess strong resonances; in water a bubble in resonance typically has an acoustic scattering cross section 1000 times its geometric cross section [3]. If bubbles are present, even in very small quantities, they can produce strong echoes that are indistinguishable from echoes from rigid objects like rocks. In order to understand the physics of acoustic interaction with the seabed, and the relevance of reflection coefficient measurements, calibrated acoustic data over well-characterized sediments is needed. Unfortunately at present, the database is quite sparse. The subject of this paper is the analysis of one such set of data, collected over a gassy sediment site near Viareggio, Italy in March 1996.

Section 2 contains a description of the data acquisition system. In section 3, the computation of reflection coefficients from the data is explained. Section 4 is a consideration of the ping to ping variability of the bottom echo. In section 5, possible evidence for nonlinear behavior is discussed. Section 6 describes a method of imaging the data to reveal spectral features by mapping the acoustic spectrum into colors. Conclusions are discussed in section 7.

2. Data Description

Acoustic data was collected as illustrated in Fig. 1. Broad band echosoundings were collected by an EG&G UNIBOOM echosounding system, which features an impulsive source, operating over a nominal band between 1

and 15 kHz, with a source level of 208 dB. The source was floated in the water column, with its beam directed downward at normal incidence toward the seabed. A hydrophone was suspended in the water column at a depth of 8 m directly underneath. Each ping recording included a direct acoustic signal from the projector, followed by its reflection from the seabed. Care was taken not to clip the signals, so that the direct arrival could be used for calibration.

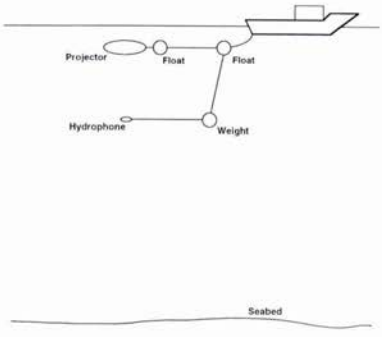

Figure 1: UNIBOOM echosounder configuration

2854 pings of data were collected over a 15 km track, depicted in Fig. 2. The water's depth was 23 m. The track passed over a previously charted front of trapped gas. The seabed consisted of soft sediment, with a mean grain size, determined from sediment grab samples, ranging from 3.8 to 5.3 ϕ, where ϕ is a logarithmic measure of grain size defined as follows:

$$2^{-\phi} = \text{grain diameter in mm}$$

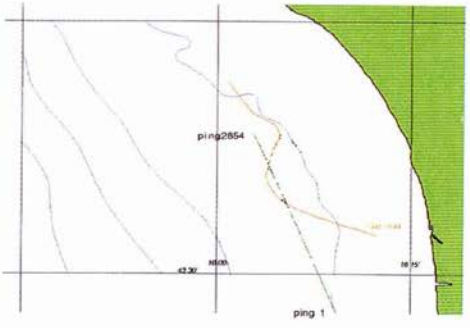

Figure 2: Track over experiment site

Fig. 3 is a waterfall recording of the whole set of pings. The first return, at 6 ms, is the direct arrival of the acoustic signal from the projector to the hydrophone. This is followed, at 30 ms by the bottom bounce. In general, the reflection consists of a bright interface return, followed by features from the sub-bottom that are horizontally stratified. In several locations there are vertical features, believed to be associated with gas bubbles percolating upward through the sediment column. Toward the end of the run is a very dominant example of such a feature, likely associated with the gas front.

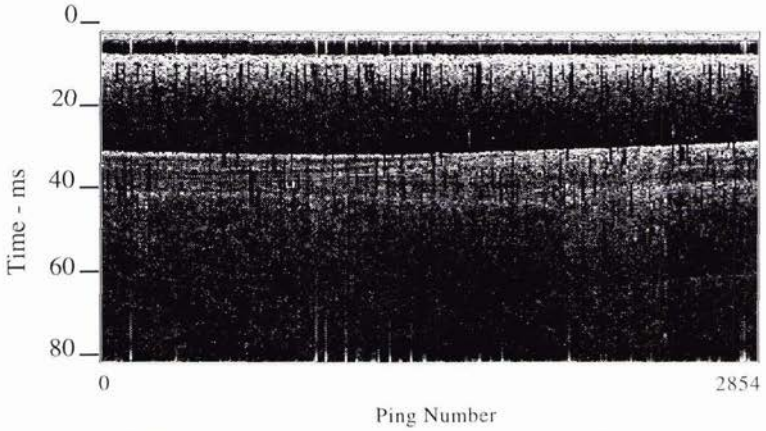

Figure 3: Waterfall plot of recorded data over track

3. Computation of Reflection Coefficient

By comparing the direct arrival with the initial portion of the bottom bounced signal, not including sub-bottom returns, a determination is made of the seabed's reflection coefficient. This calculation is summarized in Figure 4, for a single representative ping. Fig. 4a is an example of the raw time series. In Figure 4b, a linear time varying gain is applied to the signal to compensate for spherical spreading. This method of compensating for spreading insures that the correct spreading loss factor is used for each ping, even when the depth and source-to-receiver distance vary between pings. Apparent in Fig. 4b are the direct signal at 6 ms, followed by the bottom echo at 30 ms, and at 38 ms by a bottom-surface echo. Higher order bottom-surface interactions are obscured by noise. In Figures 4c and 4d, narrow windows are applied to the signal about each arrival, direct and bottom-reflected. This isolates the bottom echo from features within the sub-bottom. The windows applied in Figs. 4c and 4d were tapered, had a length of 2 ms, and were centered about the amplitude peak of each arrival. The window length was designed to encompassed most of the energy in the direct arrival.

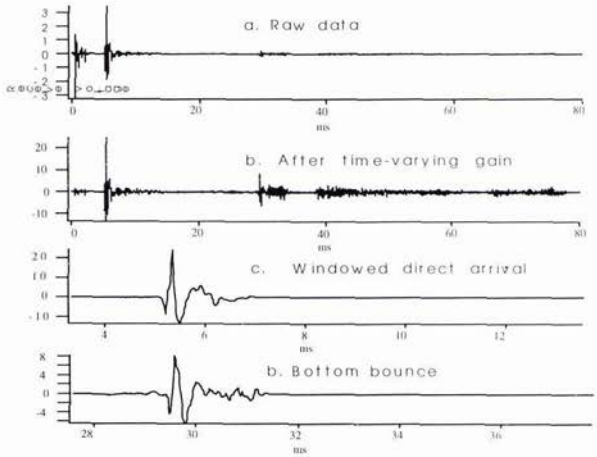

Figure 4: Processing of a single ping to compute reflection coefficient (ping1500)

In general, a bottom echo has two components; a coherent reflection and an incoherent scattered return. The bottom echo depicted in Fig. 4d is very similar in shape to the incident signal of Fig. 4c. This apparent preservation of waveform shape was generally observed in all the pings over the track, and implies that the bottom is acting primarily as a coherent reflector of sound. Acoustic modeling of the site [4], based on the available information about grain size and interface roughness, is consistent; reflection from the bottom is expected to dominate roughness backscatter for frequencies lower than 5 kHz, where most of the acoustic energy is concentrated. It is therefore assumed that the windowed signal in Fig. 4d is predominantly a coherent bottom reflection. This assumption enables an estimate of the reflection coefficient from Figs. 4c and 4d.

The squares of the signals of figs. 4c and 4d are proportional to the energies carried by each wavefront. Since spherical spreading has already been compensated for via the time-varying gain in Fig. 4b, and since absorption in the water column is negligible, the reflection coefficient R can be expressed as a ratio of the energies carried by each of the windowed returns,

$$R = 10log\left(\frac{\int (s_2)^2\, dt}{\int (s_1)^2\, dt}\right),$$

where s_1 and s_2 are windowed direct and bottom-reflected time-series signals depicted in Figs. 4c and 4d. The reflection coefficient is plotted for all pings in Figure 5.

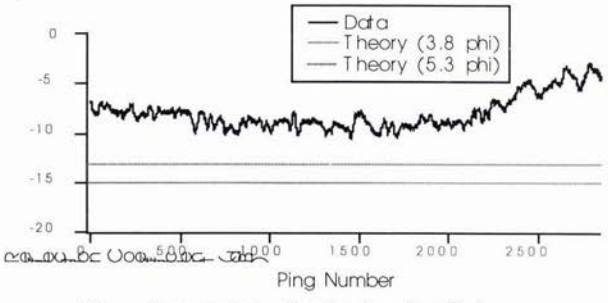

Figure 5: computed reflection loss for all pings

For comparison, theoretical predictions of the reflection coefficient, based on poroelastic modeling of sediments with mean grain sizes of 3.8 and 5.3 phi, are plotted alongside. The theoretical predictions are based on water-saturated sediments with no trapped gas. It is hypothesized that trapped gas bubbles are responsible for the difference between these predictions and the measurement. The measured reflection amplitude is highest toward the end of the track where, visually from the waterfall plot, trapped gas appears to be most prevalent.

The power spectra of the direct and bottom-bounce arrivals can be computed from the Fourier transforms of the windowed signals depicted in Figs. 4c and 4d. They are depicted in Fig. 6, along with their difference in dB, which is the frequency-dependent reflection coefficient.

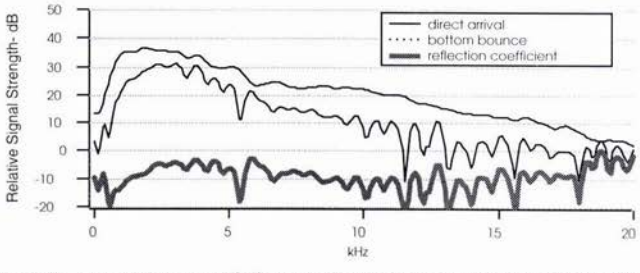

Figure 6: Power Spectra of direct and bottom-bounced arrivals for ping 1500

4. Ping to Ping Variability

There is considerable variability in the reflection coefficient from ping to ping, as is illustrated in Fig. 7, where the reflection coefficient spectra for 20 successive pings are overlaid. At frequencies above 10 kHz, where very little energy is transmitted, the variability is greatest. An explanation for this variability [5], involves interface roughness. A randomly rough bottom can be regarded as a collection of facets, some of which return sound to the sonar while others scatter sound away. Each bottom echo is a coherent sum of contributions from facets that are appropriately aligned. When the position of the sonar platform changes between pings, a different random set of facets will contribute, causing variability in the amplitude of the return.

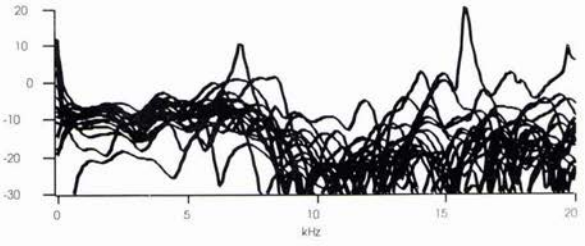

Figure 7: Reflection spectra of 20 successive pings

5. Evidence of Possible Nonlinear Behavior

The evolution of the reflection coefficient spectrum over the whole track is shown in Fig. 8. Although the ping to ping variability across the track is significant, there are clear trends in the reflection spectra. Consistent with Fig. 5, the spectral amplitude is highest near the end of the track where sediment gas is most prevalent. In this region the greatest reflection amplitude occurs between 5 and 10 kHz; frequencies significantly higher than the spectral peak of the incident wave. At these frequencies the reflection coefficients appear to be anomalously high and sometimes approach 0 dB.

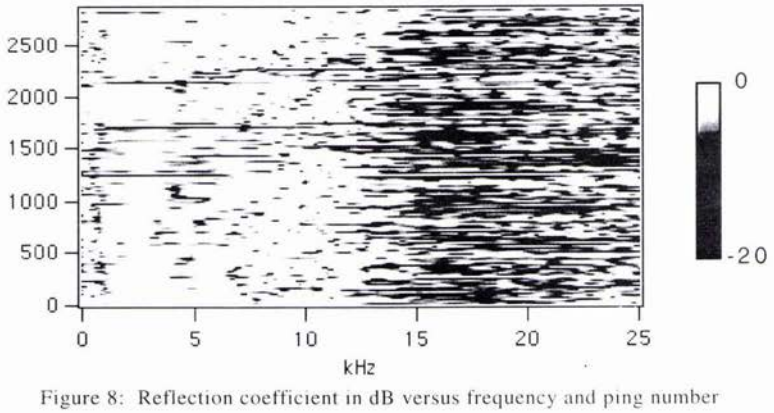

Figure 8: Reflection coefficient in dB versus frequency and ping number

Fig.9 is a comparison of power spectra over two different portions of the track. In each case an average of 50 sequential pings is considered, to offset the effects of ping to ping variability. Fig. 9a involves data taken from the middle of the track, while Fig. 9b is taken from the latter portion of the run, where trapped gas is more likely to prevail. In the former case, the reflection coefficient varies between -19 and -6 dB across the band, while in the latter, the reflection coefficient is as high as +1 dB between about 4 and 7 kHz.

At first glance this appears to suggest that, at some frequencies, more energy is returning than was incident upon the bottom. One hypothesis for this apparent amplification of sound at some frequencies is that the bottom is interacting nonlinearly with the incident sound. Sound that is incident at frequencies between 2 and 3 kHz, for example, may be scattered at second harmonic frequencies, between 4 and 6 kHz. The net effect of this would

be an upshift of acoustic energy toward higher frequencies, elevating the apparent reflection coefficient at higher frequencies at the expense of the lower frequencies. It is well known that bubbly media are highly nonlinear. Nonlinear conversion of acoustic energy by a gassy marine sediment was observed by Karpov, et.al.[6].

It is relevant that the frequency range of the anomaly is higher than the spectral peak for the incident signal. Most of the incident sound from the UNIBOOM is between 1.5 and 4 kHz. Second harmonic frequencies would range between 3 and 8 kHz, which is consistent with the band of the anomalously high reflection levels.

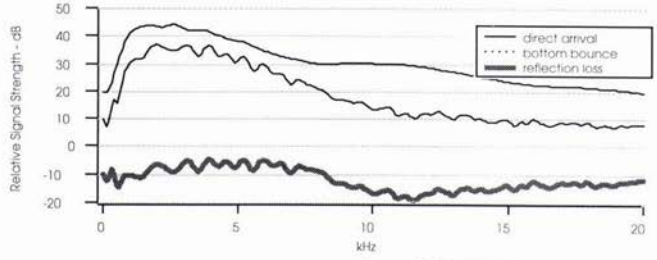

a. average over pings 1500-1550

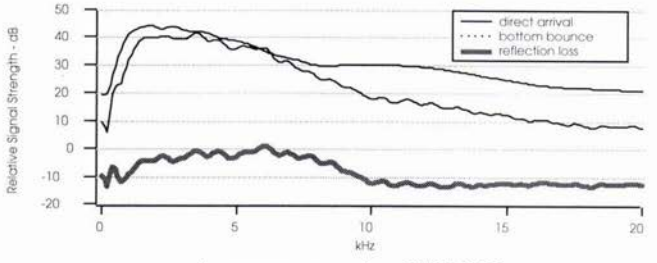

b. average over pings 2750-2800

Figure 9: 50 ping average reflection spectra from middle and final portions of track

6. Colormapping

An acoustic colormapping technique [7] was applied to the data. The method is illustrated in Fig. 10. It is biologically inspired and mimics the eye's treatment of optical signals. The acoustic data is passed, in parallel, through 3 different band-pass filters and the resulting signals displayed via the red, green, and blue pixel elements on a monitor.

In the colormapped display of the Viareggio data, clear spectral features emerge. These include a light gray echo from the water-sediment interface, followed by strata from the sub-bottom with various shades of color. These features appear to convey information about the structure of the seabed.

The light gray leading echo may give an indication about the interface roughness. As was previously stated, the initial echo from the bottom will possess two components; a coherent component and an incoherent one. The coherent component is the portion of sound that is reflected from the water-sediment boundary, while the incoherent component is the part that is scattered by the interface roughness. When the wavelength of the incident signal is large in comparison with the RMS roughness of the ensonified patch, the coherent part will dominate, whereas when the wavelength is relatively small, the incoherent part will dominate. If the band of the incident wave is wide enough to include wavelengths much greater and much less than the RMS interface roughness, the longer (reflected) wavelengths will return with stronger amplitude than the shorter (scattered) ones. In this case, the colormapped leading edge of the bottom return will appear red-enhanced.

The fact that the interface return in the Viareggio data has the same hue as the direct signal may indicate that the RMS roughness is not comparable to wavelengths contained in the incident signal. The colormapping in Fig. 10 was applied between 1500 and 8000 Hz , from 1/2 maximum of the lowest colormapping filter to 1/2 maximum of the highest. This corresponds to wavelengths between 100 cm and 18.75 cm. A bottom that is smooth to within 1/4 of the smallest wavelength, or 4.7 cm, will produce a reflected signal across the band,

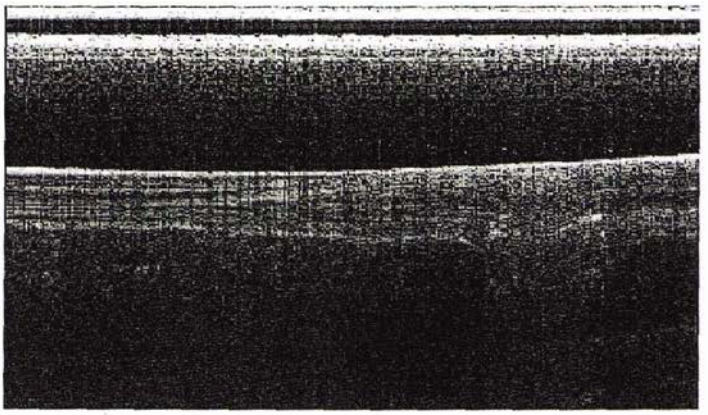

greyscale image of Uniboom data

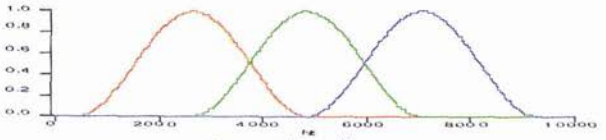

colormapping filters

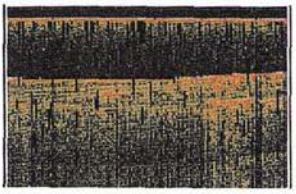

red filtered image

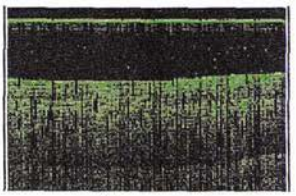

green filtered image

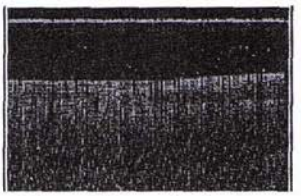

blue filtered image

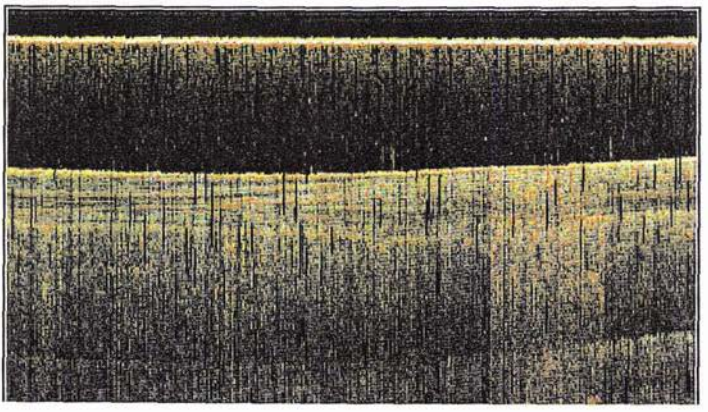

colormapped image

Figure 10: Colormapping of Viareggio data

without significant scattering. The fact that bottom interaction in the Viareggio data does not appear to influence the spectrum may therefore imply that the bottom is smooth to within 4.7 cm. This agrees qualitatively with photographs that were taken of the site. This is also consistent the assumption in section (3) that most of the sound from the interface was reflected rather than scattered.

One possible explanation for the colored strata from the sub-bottom is that they involve layers of trapped gas bubbles with varying size distributions. The colors may indicate the bubbles' resonance frequencies, which depend on their sizes [3]. The color red in the colormap of Fig.10 corresponds to bubbles with resonance frequencies between 1500 and 3500 kHz. For bubbles surrounded by water at sea level, this would correspond to diameters between 4.3 and 1.9 mm. Similarly, "green" bubbles range between 1.9 and 1.2 mm while "blue" bubbles range between 1.2 and 0.9 mm in diameter. The vertical features in the data, where upward migration of sediment gas is apparent, appear to be red-enhanced. This is consistent with the presence of larger bubbles, resonating at lower frequencies, percolating upward through the sediment column. At present this hypothesis is consistent with the data, but not positively conclusive. Other possible interpretations for the colormapped structures might involve coherent effects between boundaries. Further experimentation and analysis is needed.

7. Conclusions

Acoustic data from a gassy site strongly suggests that acoustic bubble interactions account for a significant portion of the sound returned. Anomalously high levels of acoustic reflection appear to be explainable via gas bubble interactions. The spectral content of the return suggests the existence of nonlinearities, possibly caused by gas bubbles.

A colormapping technique yields features that are consistent with scattering from interface roughness and from trapped bubbles. It is possible that the method might be used to obtain quantitative estimates of both. Further research is required.

References

[1] N. P. Chotiros, "Inversion and sandy ocean sediments," *in Modern Approaches in Geophysics*, Vol. XII, Kluwer, Dordrecht, 1995

[2] N. P. Chotiros, "Biot model of sound propagation in water-saturated sand," JASA 97(1), 199-214 (1994)

[3] H. Medwin, "Counting bubbles acoustically, a review," Ultrasonics 15(1) 7-13 (1977)

[4] F. A. Boyle and N. P. Chotiros, "Bottom Grain Gas and Roughness Version 3.0 Bottom Backscatter Model User's Guide," Applied Research Laboratories Technical Report No. 96-10 (1996)

[5] N. P. Chotiros, "Reflection and reverberation in normal-incidence echosounding," JASA 96(5), 2921-2929 (1994)

[6] S. V. Karpov, Z. Klusek, A. L. Matveev, A. I. Popatov, and A. M. Sutin, "Nonlinear Interaction of Acoustic Waves in Gas- saturated Marine Sediments," Acoustical Physics, 42 (4) 464-470 (1996)

[7] F. A. Boyle and N. P. Chotiros, "Mapping acoustic echosounder data to human color vision," JASA 99(4), Pt. 2, 2553 (1996)

A High Frequency Approach for Seabed Vegetation Characterization

Roberto Bozzano, Antonio Siccardi

Consiglio Nazionale delle Ricerche, CNR
Istituto per l'Automazione Navale, IAN
Via de' Marini, 6
16149 Genova, ITALY
Email: boz@ian.ge.cnr.it

Abstract

This paper focuses on the characterization of seabed vegetation, an interesting problem in a lot of Mediterranean sea coastal sites since water quality and pollution degree can be efficaciously solved by investigating the sea flora extents. The acquisition of the data about marine vegetation is accomplished by using a high frequency imaging sonar scanning the seabed. The proposed approach is based on a statistical feature-based description of the raw sonar data. A simple classifier attempts to characterize the acquired samples.

1. Introduction

1.1 The Shallow Water Surveying

The characterization of the sea bottom from acoustic data is an important problem with many applications in geophysics, biology, oceanography, geology and seismology. Acoustic characterization is made possible since the sea bottom material composition (either in or out of the bottom itself, e.g. sediments and vegetation) supports the excitation and propagation of acoustic waves [1].

Acoustic waves (or pings) energy impinges the sea floor (or whatever material lying between the transmitting device and the sea floor) and it is scattered in all directions by all the interfaces between two mediums: in general, echoes from the interface between the water and the sea bottom, from the volume of the sea bottom and from the volume lying close to the bottom can be detected in the scattered signal [2][3]. Reflections due to particular interfaces can be in some way emphasized, despite of other interface contributions, by using particular range of frequencies. For example, in order to investigate the subbottom geological composition, low frequencies must be used (i.e., 100 Hz - 10 KHz), while high frequencies must be employed (i.e., 70 KHz - 2 MHz) in order to detect fish-bank.

Then, the returned echo pulses carry the information about the seabed characteristics from which the pulses have been reflected: for this reason, by analyzing the scattered intensity, it is feasible to develop appropriate techniques in order to extract measures from the echo signals and to detect and classify different areas responsible of scattering.

1.2 Posidonia Oceanica

The survey of the seabed is coming more and more important in several coastal sites since marine vegetation makes up a natural and specially meaningful sea state of health gauge [4]. Several species of plants and algae, each with different biological and morphological characteristics, populate the seabed. In this work, attention is focused on the endemic Phanerogam Posidonia Oceanica which extents along the French and Ligurian coasts and in several other Mediterranean sea continental shelf sites, playing a leading role in the global Mediterranean coastal ecosystem. This marine plant forms underwater meadows in littoral areas creating an irreplaceable environment for several fish species, marine mammals and other species of plants and algae [5]. Moreover, Posidonia Oceanica leaves contributes to limit the energy of the sea swells and current, and create natural barriers, thus strongly reducing the coastal erosion, Furthermore, through the photosynthesis process, its meadows produce big amounts of oxygen, being really a green lung for the submersed world. Unfortunately, Posidonia Oceanica is very sensitive to both natural (temperature rise, turbid water, strong competition with

algae [6], etc.) and man-made changes (dikes, excavation, discharge of sewage and industrial waste, trawling): these factors often give rise to regression or quite disappearance of Posidonia beds. Nowadays, the survival of this plant depends not only on the pollution agents (chemical, biological, and physical) but also on the competitive growth of other species such as the tropical green alga Caulerpa Taxifolia. Therefore, the analysis of marine vegetation, and especially of this plant, assumes a scientific interest and also a practical importance to preserve the coastal water delicate ecosystems.

Posidonia Oceanica typically shows a great extent within a deep gradient from 1 to about 40 meters. It is organized in roots, a stem termed rhizome, and leaves (Fig. 1). The rhizomes can develop horizontally and vertically and act as anchors for the plant to the substrates by means of the roots in the lower part. The bright green leaves grow from the vertical rhizomes and are ribbon-like with rounded apices. They have a mean width of 1 centimeter and can be up to 1.5 meter long. Plants are arranged in six or seven number groups, organized in a fan-like structure. Older plant leaves, of greater length, are on the outside of the plant, whereas the smaller, younger leaves are on the inside of the sheaf-like arrangement. Posidonia leaves grow extremely slowly, up to 10 centimeters per year at the most, hence existing Posidonia meadows maintenance is essential.

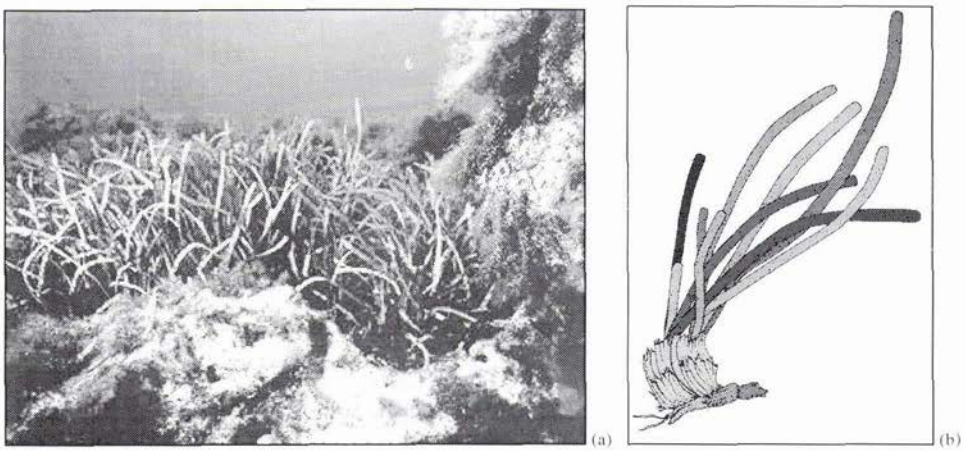

Figure 1: (a) Dense Posidonia Oceanica meadow; (b) drawing of the plant.

1.3 The Acoustic Survey

The only means to carefully analyse such small targets as represented by plant leaves consists in a high resolution acquisition of measures near to the seabed, and this operation can be performed by a high frequency acoustic device able to detect the response of low strength plant reflections and to perform a dense and accurate sampling of the sea bottom where the plants live.

Sector-scanning sonars carried by autonomous [7] or remotely operated vehicles are usually considered as one of the most efficient methods for object detection, identification and recognition in marine environment, where optical visibility is often limited and underwater cameras cannot be employed even at low ranges [8][9]. They generally provide noisy 2D range-vs.-bearing images of the insonified 3D scenes. The signals received by the sonar transducer are related to the insonified objects surfaces presented to the sonar head: hence, sonar acquisitions supply a distorted representation on a 2D space of the volume under inspection. Moreover, troublesome effects, such as clutter between the seabed and the surface, noise, reverberation and multipath, are generally present in sonar images, making them difficult to interpret [10].

If the purpose of our research had simply been the detection of vegetation presence, a side-scan sonar could have been sufficient [11]. In side-scan sonar images, vegetation is often recognizable by large dark areas, and meadows upper and lower limits are easily detectable. But, by using this type of sensors, only the detection and sometimes a macro-characterization is possible since spatial resolution is generally very poor [12]. Instead, our target is somehow more complex and ambitious, being to detect marine plants and trying to characterize them by supplying both quantitative and qualitative characteristics. Hence a high resolution survey is necessary. It is accomplished by a mechanically scanned, 2 MHz narrow pencil beam monostatic sonar, scanning a vertical sector towards the sea bottom: this sensor is used for insonifying the seabed, acquiring the backscattered signals and for the imaging process. The high frequency acoustic device assures a suitable resolution capability and a high sensitivity to low strength targets present upon the sea bottom.

2. The Technical Approach

2.1 Methodology

An autonomous or a remotely operated vehicle carrying the sonar head navigates at a very low speed with an almost constant distance from the sea bottom: while traveling, the head rotates around its axis of a variable sector, thus acquiring data about a strip-like area of the seabed. Hence, data referring to a strip-like area can be acquired and stored on the vehicle on-board digital memory or on a remote computer connected to the sonar by a standard serial link. The received echoes can be considered either as a sequence of raw scanline signals and processed in a one-dimensional space, or as correlated series of scanlines. In this second instance, a kind of image can be generated by placing side by side the sequence of scanlines.

The vegetation analysis is considered as a problem of pattern recognition [13] by using a statistical classifier. The basic concept at the basis of every classification sonar-based system is that the backscattered signals are in some way highly correlated with the characteristics of the area or the volume which return the signals. Therefore, the received echoes can be processed in order to extract significant features [14][15] and to identify different seabed areas in terms of vegetation presence and characteristics. The high frequency employed in our survey does not let penetration of the sonar signal in the subbottom, while allowing the backscattered echoes to be essentially referred to the low-strength vegetation leaves and to the water-bottom interface. This consideration shows the effectiveness of the chosen acoustic sensor.

2.2 Data Acquisition

A Tritech ST2000 2 MHz narrow pencil beam sonar, scanning a vertical sector towards the sea bottom was employed for the data collection. The sonar measurements result from the combination of a sequence of individual measurements made while it sweeps its nominal sensor axis through a defined sector spanning an area of interest. The sensor can generate scans containing 800 individual measurements at equally spaced intervals of 0.45° over a full 360° panorama. The sonar operates by transmitting an outgoing pulse (i.e., ping) of duration depending on the range of the target to be insonified, by listening the received signal up to the time corresponding to the selected range, and finally, by reorienting the transducer for the next ping cycle.

In order to better visualize the acquired data, the image of the observed underwater scene is build by placing side by side, in a vertical arrangement, each received scanline without any kind of pre-processing or compensation operation. The raw sonar signal can be mapped into a 8-bit image with standard range 0÷255 corresponding to the head dynamic range 0÷80 dB.

Figure 2 shows a sonar image acquired in a laboratory acoustical tank at 1 meter distance from the bottom. All the images presented in this paper were acquired in a tank where both real Posidonia Oceanica and flat plant leaves were fixed over a synthetic lawn, while the sonar scans variable sectors always at the best angular (0.45°) and spatial (1 sample every 6.4 μs in time, 4.8 mm in range) resolution. Low contrast and a preferred vertical direction are relevant factors that must be taken into account for the selection of suitable processing algorithms.

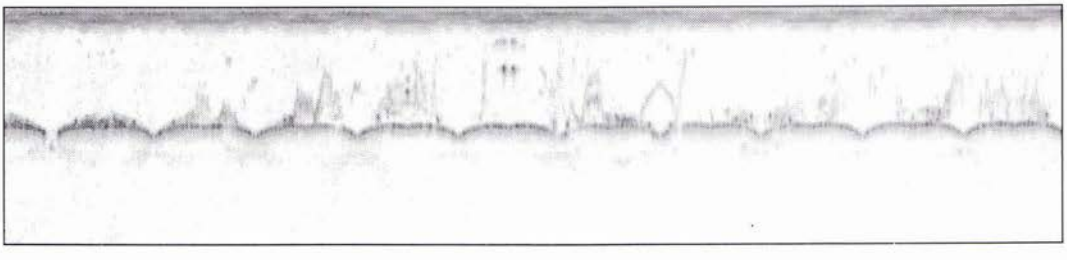

Figure 2: Sonar image of real plant leaves on a nearly flat bottom.

Vertical and horizontal resolutions are not a-priori fixed and this kind of image representation is effective only when a sufficiently high spatial resolution on the sea bottom really exists. The vertical resolution is influenced by the transmitted pulse length and the ratio between the selected range and the number of acquired samples: by sampling the backscattered echoes at the highest possible rate, a nominal range resolution of 4.8 mm is assured. However, the AD converter inside the sonar head can handle only 1500 samples per each scanline at the most and this characteristic involve a limitation about the maximum available range in order to maintain the best resolution. This limit is fixed at about 7 meters from the targets. But, the highest is the number of acquired samples and the vertical resolution, the longer is the time spent to acquire the scanline data and the worst is the horizontal resolution on the bottom, since while the head keeps silent to transfer the backscattered echoes to the processing unit, the vehicle moves forward along its path. The result is an image in which each columns is poorly related to its adjacent ones. Therefore, a balance between the desired vertical resolution and

the sampling interval on the seabed has to be reached, otherwise only a 1D analysis can be carried out.

2.3 Data Preprocessing

Before analyzing the acquired signals to extract features and to attempt the seabed classification, a preprocessing phase is applied in the 2D domain by using essentially image processing algorithms. They aim at filtering the received noisy signals and at focusing the attention on significant parts of each scanline, that correspond at isolating interesting areas within the corresponding image. This second objective is particularly important since most of the feature extraction algorithms to be successively applied, are time consuming and great improvement in computational burden can be drawn by considering a small portion of the signal instead of its wholeness.

The first operation applied to the raw scanline signals is a compensation for the local bottom slope: the information about the distance between the acoustic receiver and the bottom is supposed as a known variable, being either directly measurable from the raw data (if the acoustic pulse is not absorbed by the overhanging plant leaves) or provided by an external sensor such as an ecosounder.

Image processing techniques basically consist in a combination of non-linear [16] and morphological filters [17]. Figure 3 shows an acquired sonar image and the result obtained at the end of the preprocessing phase. The bottom lower limit and the upper bound of targets are clearly observable.

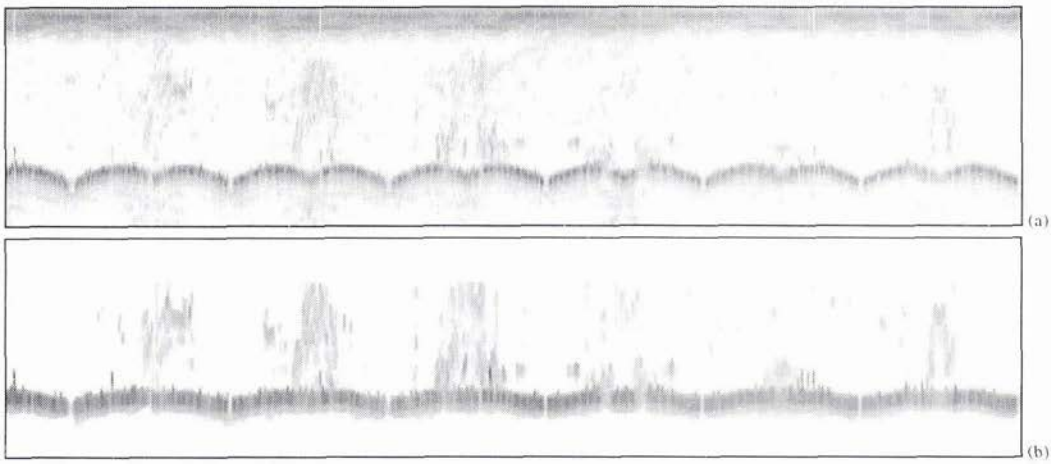

Figure 3: (a) An original sonar image and (b) the focused sonar image as it appears after the image preprocessing.

2.4 Feature Extraction

The first step of the proposed statistical classification consists in the extraction of feature vectors from the acquired and preprocessed data. This is a fundamental operation since only by considering features suitable for separation of different vegetation types, the successive classification phase can guarantee satisfying performances. In fact, the classifier's capability to discriminate between different information classes relies on how well the different classes are separated in the feature space [13].

We have directly access to the sampled backscattered data, hence methods examining echoes shape and strength appears suitable. Thus, several features based on backscattered strength, texture content and scanline shape analysis are extracted on the basis of the mentioned 2D representation. Each feature is extracted from the selected part of the original scanline signal: this corresponds to compute the feature value only within the portion of the signal that was preserved during the image preprocessing. This technique allows to reduce the required operations by saving time.

The following features were extracted from the focused data: mean value, standard deviation, mean deviation, skewness, kurtosis, distance between the bottom and the upper bound of the plants, number of maxima and minima of the signal, and several quantiles (from 0.1 up to 0.9) [14].

Most of the above mentioned features are related to the distribution of a random variable. Especially the quantiles can be useful to describe a distribution, being the pth quantile of a set of values defined as the mean value Q_p of the subset $\{x_i\}$ of values satisfying the following condition $P(x_i < Q_p) \leq p$ and $P(x_i \geq Q_p) \leq 1\text{-}p$.

Moreover, also the texture content was quantified in terms of energy, entropy, contrast and homogeneity, by supposing that variations in acoustic reflectivity may correspond to different structures (i.e., plant types) present

over the seabed. Texture features were calculated by defining the gray-level spatial co-occurrence matrix (GLCM) for small strip-like subsets of the whole image composed by 10, 15, and 20 successive pings (corresponding to angular sectors 4.5°, 6.75°, and 9.0° wide). The GLCM is a symmetric matrix of relative frequencies P_{ij} with which two neighboring pixels separated by a fixed distance d along a fixed direction θ occur in the image, one with gray level i and the other with gray level j. Within the defined area, several tests of the distance parameter value d were performed for all the four principal direction θ (0°, 45°, 90°, 135°).

Figure 4 shows four different normalized training features (standard deviation, skewness, lower and upper quartiles) derived from the images above corresponding to the three classes to be identified: seabed without any plant (left), and bottom with dense (center) and sparse (right) vegetation meadows.

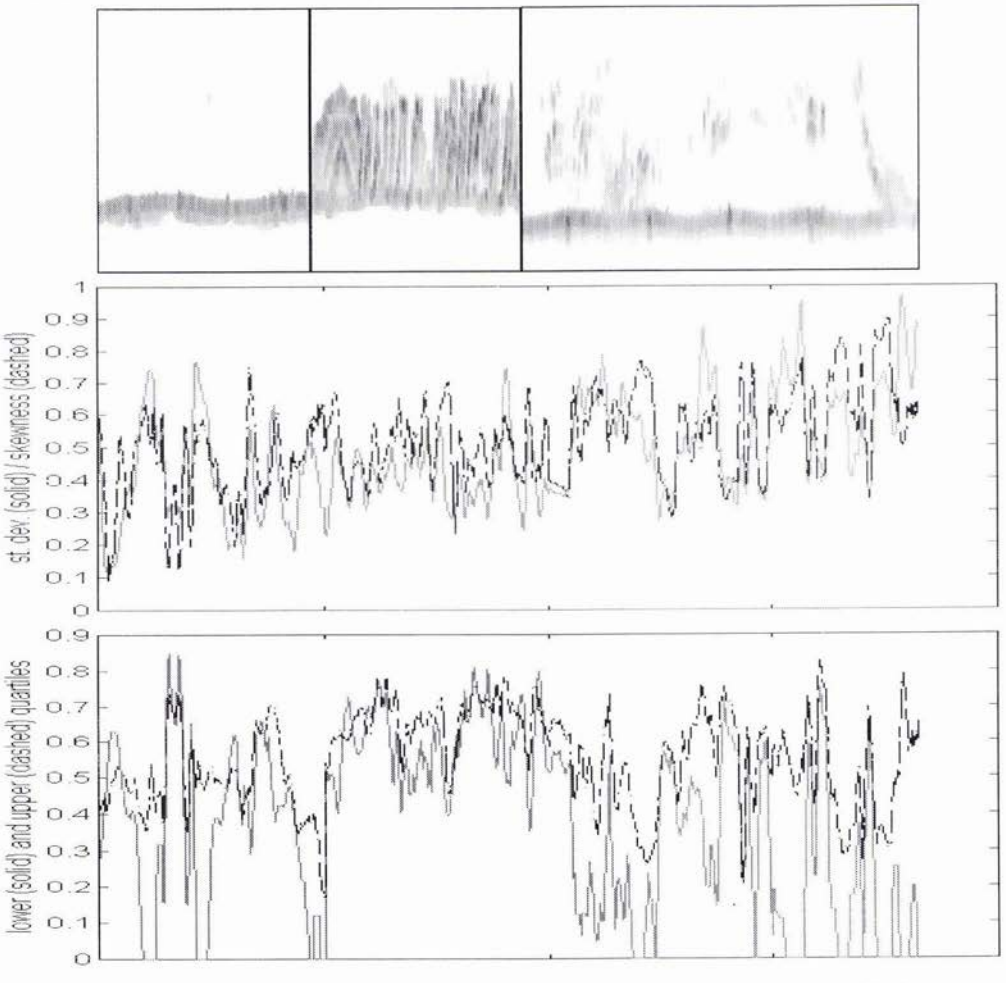

Figure 4: Some normalized feature values related to the corresponding scanlines from which they were extracted.

By carefully analyzing the plots contained in figure 4, it is evident how not even the most significant features are able to powerfully discriminate between different plant types since a lower differentiation is already present for dense and sparse plant arrangements.

About 78 features were extracted from the training data set (X) organized into a MxN matrix, being $M=78$ the dimensionality of the feature space and $N=20000$ the number of training scanlines, quite equally divided into the three classes: bottom, sparse Posidonia leaves and dense flat plant leaves. The feature space dimension is surely too large to be envisaged, giving rise to insurmountable computational and visualization difficulties. Furthermore, only a finite amount of information is contained in the data, hence, many features are likely to contribute no useful information, being noise sensitive, redundant or intrinsically not significant.

These are the main reasons to perform a feature space reduction consisting in mapping the full feature vector to a reduced feature vector with a very small dimension. This operation is performed by a principal component analysis (PCA) [18]. The statistics of the data are analyzed to determine a set of orthogonal axes in feature space along which the data varies at the most. Data principal components (PCs) are obtained by an eigen analysis of the data covariance matrix: the obtained eigenvectors provide the directions in which the data arrangement in the feature space is stretched most. Projections of data on the eigenvectors e_i (i=1, 2, ..., M) are the PCs. The corresponding eigenvalues λ_i give an indication of the amount of information the respective PCs represent: PCs corresponding to large eigenvalues represent much information in the data set and must be preserved, while other PCs may be discarded carrying much less information.

Table 1 shows the eigenvalues, the amount of variance associated to each eigenvalue and the cumulative variance: the corresponding first 7 (P=7<M) eigenvectors account for about 89.3 % of the total variance from the data set with 78 features. Hence, by reducing the original data set from 78 features down to only 7 vectors, there has only been a loss of 10.7 % of the total variance.

i	1	2	3	4	5	6	7	8	9	10	11	12	13	14	15-78
λ_i	0.953	0.415	0.184	0.117	0.069	0.056	0.044	0.022	0.019	0.017	0.015	0.014	0.012	0.011	-
Var. σ_i^2	46.24	20.14	8.94	5.70	3.36	2.76	2.18	1.09	0.94	0.86	0.73	0.71	0.59	0.55	-
Cum. Var.	46.24	66.38	75.32	81.02	84.38	87.14	89.32	90.41	91.35	92.21	92.94	93.65	94.24	94.79	100.0

Table 1: Eigenvalues amount of variance.

PCA provides with a set of reduced feature vectors containing most of the covariance energy. Since the covariance within the same class is expected to be less than the covariance between different classes, the reduced feature vectors should be clustered around location corresponding to a class in the reduced feature space.

The clustering method is a k-means algorithm based on the minimization of a performance index which is defined as the sum of the squared distance from all the points in a cluster domain to the cluster center [13]. This method is extremely simple but it is not a refined technique, since it is necessary to specify the desired number of clusters and it is sensitive to the choice of initial cluster centers and to the order of the training samples.

Figure 5 shows two views of the three clusters as obtained after several tests with different initial cluster centers by considering only the first three eigenvalues (corresponding to the 75.32 % of the total variance): a really good separation between the classes cannot be observed.

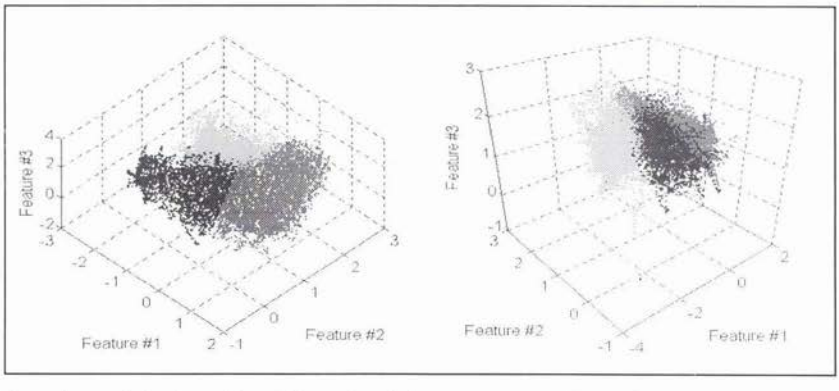

Figure 5: Two views of the clustering of the reduced feature vectors with the first three principal components.

2.5 Classification

In the presented application, classification consists in labeling each new ping (i.e., each column in the image domain) in view of its characteristics as individuated through its feature values to a pre-defined class, being the employed method a supervised classifier.

Three classification stages, with increasing order of complexity, can be defined: the first consists in the decision about the presence or the absence of vegetation on the seabed; the second concerns the identification of dense or sparse plants on different bottom substrates, and the third, according to the descriptive power of the

acquired data, relates to a more precise ,e.g., by distinguishing between Posidonia Oceanica and Caulerpa Taxifolia plants. Currently available results refer to the first two classification stages.

Moreover, two different levels of information can be associated to these three classification stages: the first and the second steps may supply with a quantitative information while the last classification result may provide a qualitative description of the surveyed area.

The employed classifier is the k-Nearest Neighbor (k-NN) classifier: it is a traditional non-parametric algorithm related to the Bayes decision rule: the most frequently represented class label among the k nearest training samples to the current samples x under examination is assigned to x. The vote is based on the Euclidean distance between the samples.

It is really impossible to provide precise performances for the classification algorithm on a ping-by-ping basis. Nevertheless, is it feasible to visually compare each acquired series of scanlines with the corresponding labels, by superimposing the labels on the scanlines image (Fig. 6).

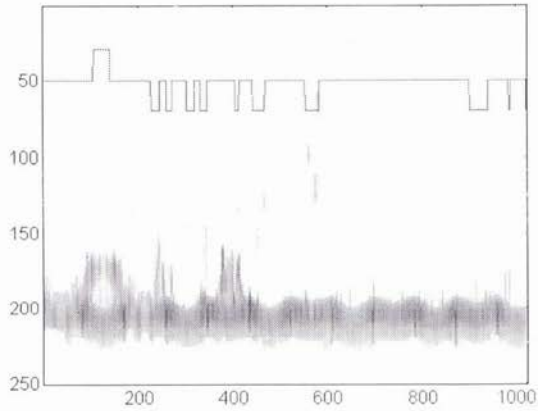

Upper level: dense plant arrangements

Middle level: sea bottom without any plant.

Lower level: sparse plant arrangements.

Figure 6: Classification results limited to the discrimination about sparse or dense settlements for a test sequence.

3. Conclusions and Future Perspectives

In this paper we investigated a system aiming at characterizing marine vegetation on the seabed by means of a high frequency imaging sonar. The problem is considered as a pattern recognition application, hence, aquatic plants are characterized by extracting meaningful features based on signal shape, intensity and texture content from the acquired echoes.

Data about real Posidonia and common flat plant leaves were collected in a controlled environment and then used as training input to the developed system. Acquired data were organized as images and image processing techniques were employed for the first analysis phase consisting in the detection of plants upon the simulated sea bottom. The characterization process performed only on the meaningful portions of the acquired data series was detailed together with the feature selection methodology. A simple k-NN classifier was tested.

Preliminary results shown in the paper demonstrate the effectiveness of the selected approach for what concern the possibility of investigating marine vegetation with a high frequency sonar. Both the resolution of the analysis and the performances of the preliminary characterization final stage are in accordance with the desired and expected results. Good performances may be obtained if only a quantitative description of the data is requested: plant detection behaves satisfactory in almost all the acquired samples without being heavily influenced by changes of the acquisition parameters and discrimination about sparse and dense plant settlements is equally satisfactory.

However, system performances make worse with respect to the increasing desired qualitative description degree: different plant types classification strongly depend on several factors especially due to the random plant arrangement and to the poor information contained in the backscattered data. Hence, for a more accurate and robust characterization in terms of distinction of different plant species, further research is required. Some changes in the sonar head characteristics parameters (i.e., transmission pulse duration, and head sensitivity) are necessary in order to increase the spatial resolution within each scanline, thus by detecting morphological differences between different plant types. Moreover, an intensive experimental activity at sea is going to be carried out along the Ligurian coast to collect more data about Posidonia Oceanica meadows.

4. Acknowledgments

This work was partially funded by the MAST-III programme of the Commission of the European Communities under contract MAS3-CT95-0036 "MAUVE".

References

[1] J. Bjorno, J.S. Papadakis, P.J. Papadakis, J. Sageloli, J.P. Sessarego, S. Sun, and M.I. Taroudakis, "Identification of seabed data from acoustic reflections: theory and experiment," *Acta Acustica*, vol. 2, pp. 359-374, October 1994.

[2] D.R. Jackson, and K.B. Briggs, "High-frequency bottom backscattering: roughness versus sediment volume scattering," *Journal of the Acoustical Society of America*, vol. 92 (2), pp. 962-977, 1992.

[3] P.D. Mourad, and D.R. Jackson, "High frequency sonar equation models for bottom backscatter and forward loss," in *IEEE Proceedings of OCEANS '89*, pp. 1168-1175, 1989.

[4] J.C. Stevenson, "Comparative ecology of submersed grass beds in freshwater, estuarine, and marine environments," *Limnology and Oceanography*, vol. 33, pp. 867-893, 1988.

[5] M.C. Buia, and L. Mazzella, "Reproductive phenology of the Mediterranean seagrasses Posidonia Oceanica (l.), Cymodocea nodosa (Ucria) Aschers and Zostera noltii Hornem," *Aquatic Botany*, vol. 40, pp. 343-362, 1991.

[6] A. Meinesz, J. de Vaugelas, B. Hesse, and X. Mari, "Spreading of the introduced tropical green alga Caulerpa Taxifolia in northern Mediterranean waters," *Journal of Applied Phycology*, vol. 5, pp. 141-147, 1993.

[7] A. Carof, "MAUVE: Miniaturized and reconfigurable instrumentation for multipurpose survey with a mini autonomous underwater vehicle," in *IEEE Proceedings. of OCEANS '96*, pp. 955-960, September 1996.

[8] M.J. Chantler, D.M. Lane, D. Dai, and N. Williams, "Detection and tracking of returns in sector-scan sonar image sequences," *IEE Proceedings Radar, Sonar and Navigation*, vol. 143 (3,) June 1996.

[9] J.L. Sutton, "Underwater acoustic imaging," in *IEEE Proceedings*, vol. 67 (4), April 1979.

[10]N. Williams, D.M. Lane, M.J. Chantler, and D. Dai, "Classification of sector-scanning sonar image sequences," in *IEE Proceedings of 5th International Conference on Image Processing and its Applications, IPA'95*, pp. 261-265, Edinburgh, July 4-6, 1995.

[11]P. Colantoni, and P. Zucchini, "Underwater mapping of the Posidonia Oceanica prairies around the Ischia island (Naples)," *Rapp. Comm. Int Mer. Medit.*, vol. 25/26 (6), pp. 89-90, 1979.

[12]D.R. Carmichael, L.M. Linnet, S.J. Clarke, and B.R. Calder, "Seabed classification through multifractal analysis of sidescan sonar imagery," *IEE Proceedings Radar, Sonar and Navigation*, vol. 143 (3), pp.140-148, June 1996.

[13]J.T. Tou, R.C. Gonzales, Pattern Recognition Principles, Addison-Wesley, 1974.

[14]O. Milvang, R.B. Huseby, K. Weisteen, and A. Solberg, "Feature extraction from backscatter sonar data," in *Proceedings of the Institute of Acoustics*, vol. 15, Part 2, pp. 157-163, 1993.

[15]W.K. Stewart, M. Marra, and M. Jiang, "A hierarchical approach to seafloor classification using neural networks," in *IEEE Proceedings of OCEANS '92*, pp. 109-113, 1992.

[16]W.K. Pratt, Digital Image Processing, John Wiley & Sons, New York, 1978.

[17]R.M. Haralik, L.G. Shapiro, Computer and Robot Vision, Addison-Wesley Pub., vol. 1, 1992.

[18]I.T. Jolliffe, Principal Component Analysis, Springer Verlag, 1986.

Vertical Porosity and Velocity Fluctuations in Shallow-Water Surficial Sediments and Their Use in Modeling Volume Scattering

Kevin B. Briggs

Naval Research Laboratory
Code 7431
Stennis Space Center, MS 39529-5004
USA
Email: kbriggs@zephyr.nrlssc.navy.mil

Donald B. Percival

Applied Physics Laboratory
College of Ocean and Fishery Sciences
University of Washington
Seattle, WA 98105 USA
Email: dbp@apl.washington.edu

Abstract

Variability in sediment porosity and velocity creates volume scattering which is a parameter used in high-frequency scattering models. High-resolution vertical profiles of sediment porosity and compressional wave velocity collected from 17 diverse sites on continental shelves are used to calculate vertical autocorrelation functions. Porosity and velocity fluctuations in the upper 20-35 cm of sediment exhibit correlation lengths which are highly variable. The variance of the porosity fluctuations varies with sediment type. Data comparisons indicate that fluctuations in sediment porosity are due to biological and sedimentological processes and fluctuations in sediment velocity are due to hydrodynamic processes.

1. Introduction

Recent field work in the field of high-frequency acoustics has focused attention on the potential contribution of sediment volume scattering to bottom backscattering from a sea floor lacking significant interface roughness [1]-[5]. Failure of acoustic models to accurately predict high measured levels of backscattering at small grazing angles has been attributed to lack of consideration of sediment volume scattering [1], [4], [6]. Scattering from the sediment volume is created by fluctuations in sediment density or sound velocity, and Hines [7] and Jackson *et al.* [8] have derived models for predicting acoustic backscatter from the sediment volume. In each approach, characterizing the fluctuations in sediment porosity within the sediment fabric and assessing the variance of these fluctuations are essential for accurate model predictions. The variance of porosity fluctuations is used to address scattering magnitude and the correlation lengths of these fluctuations are used to determine the frequency and grazing angle dependence of the backscatter. The model of Jackson *et al.* [8] employs the correlation length derived from the sediment sound velocity and density fluctuations as model parameters.

The correlation length associated with sediment density and sound velocity fluctuations has been invoked as a physical parameter for volume scattering models by a number of authors [7], [9]-[12]. In each case, lack of sufficient physical property data forced the authors to extrapolate meager existing data and make assumptions in order to arrive at a value for correlation length. In the absence of actual physical measurements, Nolle *et al.* [9] and Hines [7] assume correlation lengths are related to mean grain size (in relation to the ensonifying wavelength). Moreover, Hines allows the porosity variance to be a free parameter in his model so as to fit the model to the data. Lyons *et al.* [4] uses input parameters estimated from core data, but relies on only one core as ground truth for each sediment type.

Fortunately, a large body of data on sediment porosity and compressional wave velocity does exist for a variety of sediment types as a result of the Naval Research Laboratory (NRL) shallow-water high-frequency and coastal benthic

boundary layer programs. Since 1982, NRL scientists have collected physical and geoacoustic property data to support high-frequency field experiments in sandy and muddy sediments. Sediment porosity and compressional wave velocity as well as sediment grain size have been measured vertically at regular, closely spaced intervals from numerous diver-collected cores and boxcores in order to ascertain sediment variability. Geoacoustic data collected by NRL can be used to calculate parameters integral to the volume scattering models of Hines and/or Jackson: correlation functions of sediment porosity and velocity fluctuations, and variances of sediment porosity and velocity fluctuations.

2. Methodology

Collection of cores was accomplished with the goal of ascertaining the variability of surficial geoacoustic properties over a wide area selected as an experiment site. The locations of core collection were chosen randomly within the site to ascertain spatial variability of the parameters in the vertical dimension, yet be representative of the horizontal spatial variability throughout the site.

Cores on which geoacoustic and physical property measurements were made were collected with 6.1-cm diameter polycarbonate plastic cylindrical core liners. Each core was bevelled at one end to facilitate the careful manual penetration into the sediment. Cores were capped at both ends immediately upon collection to retain the water overlying the sediment and kept in an upright position during transport to the laboratory for analysis. Collection, measurement, and handling procedures were designed to minimize sampling disturbance and to maintain an intact sediment-water interface within the core samples. Of the 17 experimental sites, five sites were sampled from boxcores (Montauk Point, Quinault Range, Arafura Sea, Straits of Juan de Fuca, and Russian River), one was sampled by probes in diver-collected box cores (Long Island Sound), and the rest were sampled directly by divers [13]-[16].

Measurement of compressional wave velocity was made within 24 hours of collection, once the samples had equilibrated with laboratory temperature. Sediment compressional wave velocity was measured at 1-cm intervals using a pulse technique [15]. The probes used to measure sound velocity in box cores were piezoceramic transducer/receivers operated at a frequency of 70 kHz.

Samples were extruded from sediment cores upon completion of acoustic measurements and sectioned at 2-cm intervals (1-cm intervals in cores from L.I. Sound) to determine sediment porosity and grain size distribution. Porosity was determined from weight loss of sediment dried at 105°C for 24 hours. Sediment grain size was determined from disaggregated samples by dry sieving for sand-sized particles and by use of a Micromeritics Sedigraph for silt- and clay-sized particles when samples were collected from muddy environments.

The length of the sediment within the cores varied between 9 and 48 cm, depending on the sediment type. The acoustic frequencies at which the models are employed dictate that the length of the cores need only extend to the acoustic penetration depth and the number of measurements made from the cores result in increments corresponding to at most half a wavelength in order to accurately and usefully derive the correlation length. However, only the uppermost 20 to 30 cm of most shallow-water sediments are penetrated and allow reradiation back to the receiver at these high-frequencies (20-180 kHz). The one- and two-cm increments over which the measurements were made are sufficient to resolve fluctuations capable of scattering sound energy over most of the range of relevant acoustic wavelengths (1.5-7.5 cm). To avoid the problems involved in calculating the correlation function for essentially a truncated series of data, the first-order autoregressive model of Diggle [17] for analysis of a large number of relatively short series of data is used. Because of the short spatial series, the autocorrelation coefficent is estimated by Burg's algorithm [18]. Correlation length of a data sequence was calculated after Yaglom [19] by

$$l = \left(\frac{1}{2} + \frac{\phi_1}{1 - \phi_1} \right) \Delta z, \qquad (1)$$

where l is the correlation length, ϕ_1 is the autocorrelation coefficient and Δz is the sampling interval for the porosity and velocity fluctuations.

Although the NRL data were measured at 1- or 2-cm intervals, the assumption that the fluctuations have a correlation length of 1 cm or less was tested by the following procedure. All core data were separated into groups corresponding to location and sediment type. A linear regression was performed on each core to remove any trend due to depth gradients of sediment porosity or sound velocity. The residuals from each core were analyzed to determine if the residuals could be considered to be uncorrelated "white noise" as opposed to the alternative hypothesis, namely, that the residuals were generated by a first-order autoregressive process. If the residuals can be characterized as white noise, then the correlation length is equal to or less than the measurement interval. The Durbin-Watson test at the $\alpha < 0.05$ level of significance was used to choose between the two hypotheses. For sample sizes less than 15, a Monte-Carlo method (explained on p.304-305 by Conover [20]) was used to determine the percentage points for the Durbin-Watson statistic.

3. Results and Discussion

All environmental data were collected from diverse experiment sites located on or proximal to the continental shelf. The environments vary from a very fine sand off a beach near La Spezia, Italy at 6 m water depth to a clayey silt in the Juan de Fuca Canyon at 280 m water depth. Some sites exhibit more than one type of sediment and these sites are subdivided as to sediment texture in Table 1. Variances of the sediment porosity and sound velocity at each experimental site and sediment type reported in Table 1 are expressed as the mean of the individual variances from each core rather than a collective variance because the vertical variations of sediment velocity and porosity at any one point are of interest. From the sediment porosity and sound velocity data, correlation functions, and correlation lengths can be derived.

Experimental Site	Sediment Type	n	s_V^2	s_β^2
Long Island Sound	silty clay	3	51.72	0.0008
	clayey silt	3	137.54	0.0020
Mission Bay, CA	fine sand	10	247.63	—
	coarse sand	7	789.60	—
Montauk Point, NY	fine sand	2	198.20	0.00004
Quinault Range, WA	fine sand	7	233.73	0.0003
Charleston, SC	medium sand	10	169.48	0.0003
La Spezia, ITALY	silty clay	2	14.94	0.0023
	very fine sand	1	443.04	0.0007
Arafura Sea, AUSTRALIA	clayey sand	8	31.87	0.0016
Panama City, FL (I)	fine sand	13	226.77	0.0002
Panama City, FL (II)	coarse sand	4	192.89	0.0004
Panama City, FL (III)	coarse sand	18	428.49	0.0003
	fine sand	6	127.69	0.0002
	medium sand	2	153.64	0.0002
Jacksonville, FL (I)	medium sand	9	249.19	0.0001
Jacksonville, FL (II)	shelly sand	13	1180.57	0.0010
St. Andrew Bay, FL	clay	2	0.58	0.00003
	fine sand	2	19.29	0.00005
Straits of Juan de Fuca, WA	silty fine sand	4	144.12	0.0007
	medium sand	4	475.59	0.0004
	silty sand	8	1229.16	0.0026
	silty clay	4	5.33	0.0008
	clayey silt	4	8.24	0.0007
Russian River, CA	clayey silt	12	61.71	0.0015
Eckernförde Bay, FRG	silty clay	20	28.52	0.0002
Key West, FL	sand-silt-clay	11	100.49	0.0020
	sand-silt clay	4	130.10	0.0027
	coarse sand	2	606.00	0.0003

Table 1: Sediment type, number of sediment cores collected (n) and variances of compressional wave velocity (s_V^2) and porosity (s_β^2) at the 17 experimental sites. (velocity variance is expressed as $(m/s)^2$; porosity variance is expressed as the square of the fractional porosity).

3.1. Correlation Functions

Frequency and grazing angle dependence in the volume scattering are determined by the correlation function of acoustic impedance fluctuations in the sediment [7]. Because impedance is the product of sediment density and sound velocity, measurements of both of these parameters can be used to calculate a correlation function. Porosity is used in the

calculations instead of density because of the direct linear relation between density and porosity [15]. The data presented here are estimates that assume isotropy in the vertical and horizontal distribution of inhomogeneities.

Estimates of autocorrelation functions are made for sediment porosity and sound velocity fluctuations and examples are presented in Figs. 1-3. Due to the model chosen, autocorrelation functions derived from the sediment porosity and velocity data exhibit an exponential decay. Correlation functions having autocorrelation coefficients which did not pass the Durbin-Watson test for white noise residuals are not plotted. Most data series prove to be positively correlated. The majority of data series with uncorrelated, white noise for the least-square residuals are porosity measurements made at 2-cm intervals. Thus, many of the fluctuations of porosity may have correlation lengths less than 2 cm. The exponential autocorrelation function $R(\tau)$ is calculated as

$$R(\tau) = \phi_1^{\tau}, \tag{2}$$

where τ is the lag value in cm. The first-order autocorrelation coefficient ϕ_1 is evident in the figures as the value of the autocorrelation function at lag 1 cm.

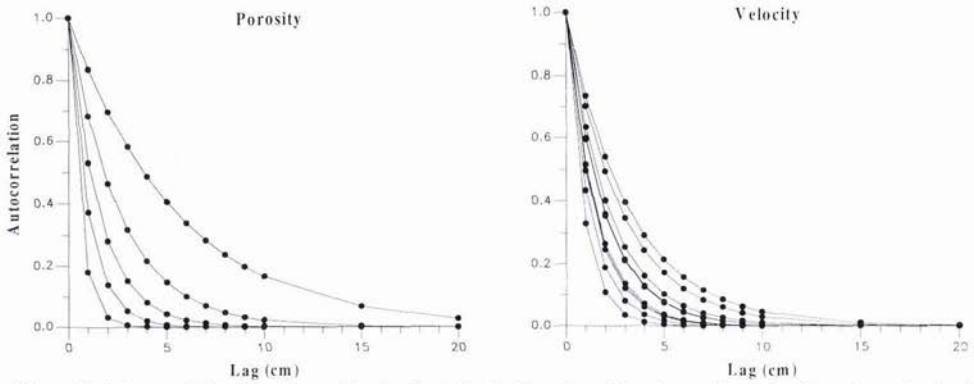

Figure 1: Autocorrelation functions estimated from fluctuations in sediment porosity and sediment sound velocity for cores collected in the Arafura Sea.

Figure 1 shows the autocorrelation functions for the sediment porosity and sound velocity data collected from the Arafura Sea. Autocorrelation functions calculated for velocity fluctuations exhibit steeper decay than those calculated for porosity fluctuations. The difference in the decay of the functions is probably due to the bimodal grain size distribution of the sediments. Sediments at the site are essentially sand- and gravel-sized particles (averaging 55% of sample weight) embedded in a silty clay matrix. Variation in mean grain size within the site is due to differences in proportions of coarser components. The coarse material consists of sand- and gravel-sized mollusk shells, shell fragments, and carbonate rocks. Sediment sound velocity exhibits little variability, whereas porosity and mean grain size exhibit much greater variability [3]. The relative constancy of the velocity data is indicative of the homogeneous silty clay matrix supporting the carbonate inhomogeneities. In contrast, the inhomogeneities which are embedded in the matrix create the variability in porosity and grain size. Hence, the autocorrelation functions derived from porosity fluctuations exhibit a wider spread of decay rates and associated correlation lengths than those derived from velocity fluctuations.

Autocorrelation functions calculated for measurements of Eckernförde Bay sediment are displayed in Fig. 2. The nature of the sediment porosity fluctuations yield autocorrelation functions which decay rapidly and are clustered together, indicating small correlation lengths. Eckernförde Bay sediment is a silty clay with high porosity and high concentrations of organic matter. Fluctuations in porosity, however, are confined to the uppermost 1-2 cm of sediment where the deposit-feeding animals flourish in a thin zone restricted by oxygen availability [21]. Below this oxygenated layer, the sediments exhibit strong chemically reducing conditions which inhibit the activities of most animals that cause porosity fluctuations. Sediment sound velocity fluctuations yield autocorrelation functions with divergent decay rates. The bay is open to the Baltic Sea to the east and the shallow depth allows the sediments to be subject to storm-induced sediment transport events. The sediment structure is characterized by coarser laminae deposited by storms [22]. Fluctuations in sediment sound velocity reflect the presence of these laminae and the autocorrelation functions diverge into three groups corresponding to fluctuations with correlation lengths of approximately 1, 2.5 and 10 cm.

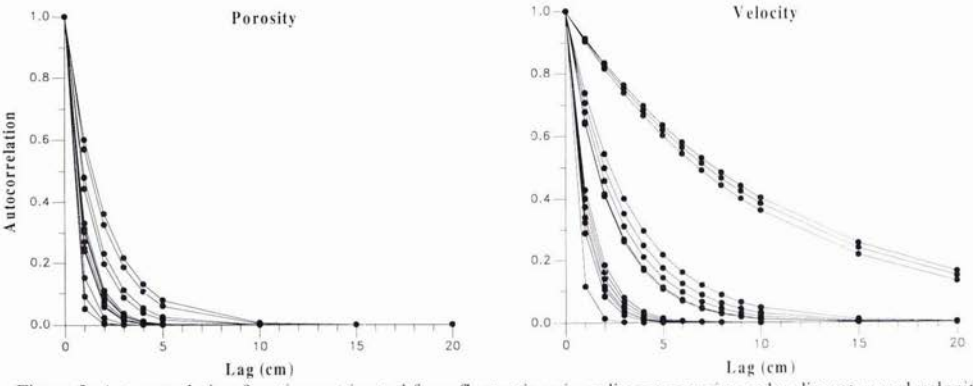

Figure 2: Autocorrelation functions estimated from fluctuations in sediment porosity and sediment sound velocity for cores collected in Eckernförde Bay.

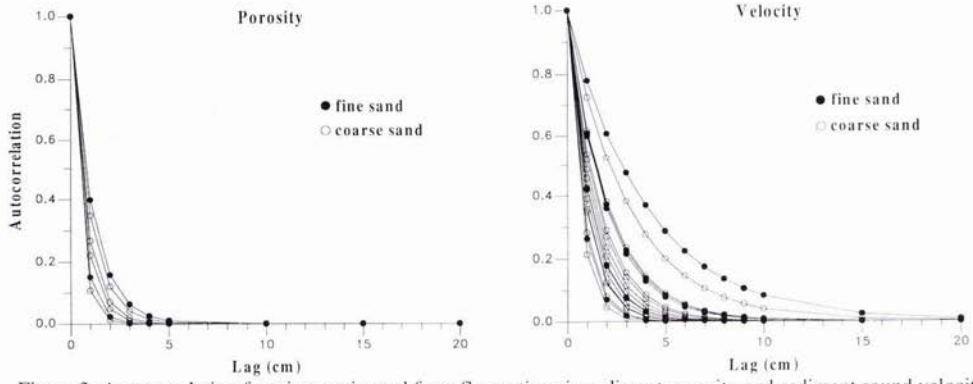

Figure 3: Autocorrelation functions estimated from fluctuations in sediment porosity and sediment sound velocity for cores collected at the Panama City (III) site.

A range of sediment grain sizes from the Panama City (III) site are represented in the autocorrelation functions displayed in Fig. 3. Porosity fluctuations in coarse and fine sands yield autocorrelation functions that decay rapidly without exception (porosity data from medium sand did not survive the Durbin-Watson test). There is no discrimination in terms of decay rate between the two sediment types. Generally, sands produce porosity autocorrelation functions with rapid decay rates and resultant short correlation lengths. Sediment sound velocity fluctuations in fine, medium and coarse sands from the Panama City (III) site yield autocorrelation functions with various decay rates, but no divergence into separate decay rates according to grain size.

The correlation lengths corresponding to each autocorrelation curve are plotted as a function of mean grain size of the sediment from each experiment site in Fig. 4. The data in Fig. 4 reveal the greatest amount of variation in the correlation lengths occurs in porosity measurements made in muds consisting of mixtures of sand, silt and clay (5 to 7 ϕ). This is not an unexpected result but indicates that stable predictions of density fluctuations in these type of sediments may be difficult to achieve with reasonable confidence. Porosity measurements made in coarser grained sediments (< 5 ϕ) exhibit the least variation in correlation length. There is no discernible trend related to grain size in the correlation lengths for velocity measurements plotted in Fig. 4, but values of correlation lengths are smaller than calculated for porosity measurements. Values of velocity correlation lengths are smaller than porosity correlation lengths due chiefly to the smaller increment over which velocity is measured. A higher level of correlation in velocity measurements may be explained by the ability of the autocorrelation function to resolve repeating patterns at correlation lengths less than 2 cm when the increment is only 1 cm.

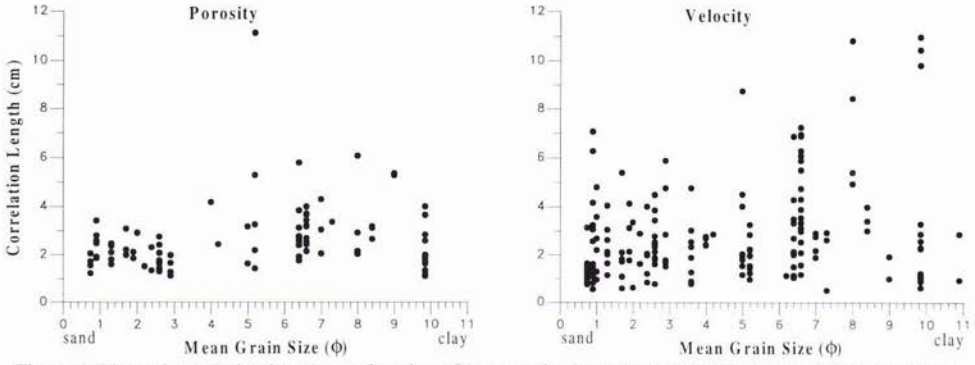

Figure 4: Plots of correlation length as a function of mean grain size (ϕ) calculated from porosity fluctuations and sound velocity fluctuations.

3.2. Parameter Variance and Sediment Type

The variances of sediment porosity and sound velocity define the nature of the impedance fluctuations in the sediment and these impedance fluctuations are responsible for the scattering of the sound from the sediment volume. Values for sediment sound velocity and porosity variances are somewhat interdependent and are indicative of particular sediment types. Values given in Table 1 are plotted in two-dimensional variance space in Fig. 5. Some experimental sites exhibit high values for porosity variance, but low values for velocity variance. Other sites exhibit low values for porosity variance, but high values for velocity variance. Generally, the former sites are muds and the latter sites are sands. The dashed lines demarcating the four regions in Fig. 5 are arbitrarily located, but effectively illustrate the pattern created by the distributions of the two variances. The parabolic relationship between sediment compressional wave velocity and porosity depicted in Richardson and Briggs [13] explains some of the pattern of high variance from one parameter paired with low variance from the other parameter: low porosity variance and high velocity variance is typical of the nearly vertical segment of the parabola, high porosity variance and low velocity variance is typical of the flattened segment of the parabola.

Those sediments having low variances in both velocity and porosity are unlikely to exhibit significant volume scattering. The three sites exhibiting low values for variance in sound velocity and sediment porosity are from St. Andrew Bay in Panama City, Florida and Eckernförde Bay, Germany. One sediment is a well sorted, fine sand which is relatively homogeneous and loosely packed since it is under the influence of strong oscillatory tidal currents. The other two sediments are muds with low rigidity and high organic content from protected embayments. The sediments from the protected embayments lack heterogeneities due to the hydrodynamically quiescent environment and the resultant anoxic conditions which reduce biological disturbances of the sediment fabric. Backscattering strengths from Eckernförde Bay are in fact anomalously high for muds due to the scattering from a methane-gas-bubble layer 1 m below the sediment surface [23]. The variance data presented here, however, are indicative of the upper 35 cm of sediment which is devoid of methane gas bubbles and relatively homogeneous.

Sediments having high variances in both parameters, however, are very likely to exhibit volume scattering. Sites located in the upper right corner of Fig. 5 are either sands with shell hash mixed in the sediment matrix or mixtures of silt and sand or silt and clay. Backscattering levels measured from three of the sites in this corner of Fig. 5 are quite high [2], [24].

Those sites exhibiting high variance in sediment porosity but low variance in sediment sound velocity are muds with inhomogeneities such as shell hash or animal burrows [3]. Backscattering levels measured from the Arafura Sea, the California coast off the Russian River, and approaches to the Strait of Juan de Fuca are all anomalously high for muds [3], [24]. The sands in the upper left corner of Fig. 5 are mixed with larger fragments of shells or other carbonate debris. Some of the elevation in variance values in these sediments are due to measurement error caused by scattering of the high-frequency sound by shell fragments (Richardson and Briggs, 1993). Nevertheless, scattering of sound from the sediment volume is characteristic of sediments in this region of the plot.

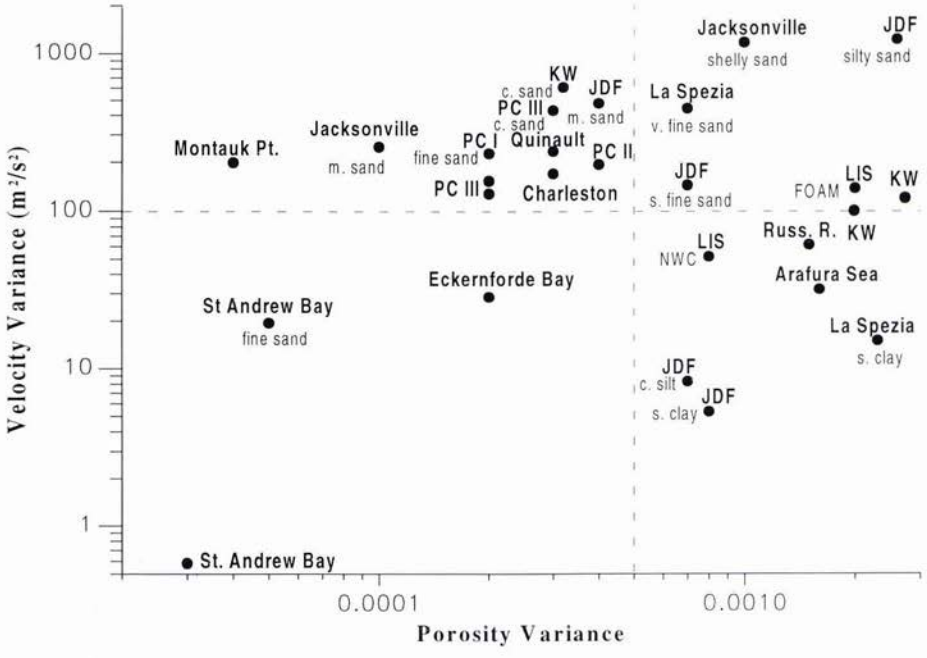

Figure 5: Plot of sediment sound velocity variance *vs.* sediment porosity variance for various experiment sites investigated.

Processes active on the continental shelf which tend to increase the variance of of the sediment porosity are primarily biological and sedimentological. Burrowing organisms such as polychaete worms and thalassinoid shrimp increase sediment porosity by building and maintaining irrigated tunnels within the sediment fabric. Sea cucumbers and heart urchins create a high-porosity, open sediment fabric by their ingestion and defecation of sediment as they burrow [25]. The presence of coarse shell hash layers within the sediment fabric decreases sediment porosity. Incorporation of mollusk shells in sediment fabric occurs during burial of coarse lag deposits by sedimentary events. Burial may occur through gradual or catastrophic settling of suspended material or migration of sand ripples over accumulations of coarser shells or shell fragments. The presence of burrows, reworked sediments and shells within the sediment fabric increases variance in porosity.

Variance of sediment sound velocity increases primarily as a result of hydrodynamic processes. Increasing fluid stress on the bottom caused by either oscillatory or unidirectional currents winnows the finer sediments and leaves coarser sediment behind. The episodic nature of hydrodynamic stress events, varying from regular tidal periods to occasional storms, creates layers of coarser sediments with higher values of sound velocity. Sites associated with higher values of velocity variance near the top of Fig. 5 are characteristic of higher stress regimes than sites associated with lower values of velocity variance. Hydrodynamic conditions vary from a quiescent lagoon in St. Andrew Bay at the lower left quadrant of the figure to continental shelf sediments subjected to winter storms at the Russian River, Charleston, Quinault, and Jacksonville sites at the upper portion of the figure.

4. Summary

Measurement of physical properties such as sediment porosity and density at small intervals downcore identifies inhomogeneities potentially creating sediment volume scattering. Fluctuations in sediment compressional wave velocity and sediment density are the most effective indicators of sediment fabric inhomogeneity because fluctuations in these two properties define sediment impedance differences.

Correlation functions derived from vertical gradients of sediment porosity and sound velocity are parameters determining the frequency and grazing angle dependence of sediment volume scattering in some models [4], [7]. The variance of sediment porosity and sediment sound velocity is a parameter determining volume scattering. Correlation length

and variance of physical parameters depend on sediment type and the processes (deposition, transport, bioturbation) in effect at the particular location. Sediments with uniform sediment size tend to exhibit stable estimates for correlation length of sediment property fluctuations. Conversely, sediments with a wider range of grain sizes or bimodal grain-size distributions exhibit higher variance of the sediment sound velocity and diverse estimates for correlation length.

Although values for sediment sound velocity and porosity variances are somewhat interdependent, their relationship to each other provides information about sediment type and processes acting upon the sediments. Sediments having low variances in both velocity and porosity are unlikely to exhibit significant volume scattering. Sediments having high variances in both parameters are very likely to exhibit volume scattering. Sediments exhibiting contrasting magnitudes in variances of porosity and sound velocity are sediments containing inhomogeneities or exhibiting bimodal grain-size distributions. Although biological, sedimentological and hydrodynamic processes do not act exclusively, certain generalizations are apparent in the continental shelf data: biological and sedimentological processes increase the porosity variance, whereas hydrodynamic processes increase the sound velocity variance.

5. Acknowledgments

This work was supported by the Coastal Benthic Boundary Layer program, funded by the Office of Naval Research (Dr. Fred E. Saalfeld, technical director) and Naval Research Laboratory program element N0601153N (Dr. H. Eppert, progam manager). We are indebted to the researchers who collected and measured the many samples involved in this study, and especially M. D. Richardson, D. K. Young, R. I. Ray, and S. Stanic. Thanks to R. H. Bennett for providing grain size data for the Russian River site. The NRL conrtibution number is NRL/PP/7431--97-0006.

6. References

[1] S. Stanic, K.B. Briggs, P. Fleischer, R.I. Ray and W.B. Sawyer, "Shallow-water high-frequency bottom scattering off Panama City, Florida," *Journal of the Acoustical Society of America*, vol. 83, pp. 2134-2144, 1988.

[2] S. Stanic, K.B. Briggs, P. Fleischer, W.B. Sawyer and R.I. Ray, "High-frequency acoustic backscattering from a coarse shell ocean bottom," *Journal of the Acoustical Society of America*, vol. 85, pp. 125-136, 1989.

[3] D.R. Jackson and K.B. Briggs, "High-frequency bottom backscattering: roughness vs. sediment volume scattering," *Journal of the Acoustical Society of America*, vol. 92, pp. 962-977, 1992.

[4] A.P. Lyons, A.L. Anderson, and F.S. Dwan, "Acoustic scattering from the seafloor: Modeling and data comparison," *Journal of the Acoustical Society of America*, vol. 95, pp. 2441-2451, 1994.

[5] T. Yamamoto, "Acoustic scattering in the ocean from velocity and density fluctuations in the sediments," *Journal of the Acoustical Society of America*, vol. 99, pp. 866-879, 1996.

[6] D.R. Jackson, D.P. Winebrenner and A. Ishimaru, "Application of the composite roughness model to high-frequency bottom backscattering," *Journal of the Acoustical Society of America*, vol. 79, pp. 1410-1422, 1986.

[7] P.C. Hines, "Theoretical model of acoustic backscatter from a smooth seabed," *Journal of the Acoustical Society of America*, vol. 88, pp. 324-334, 1990.

[8] D.R. Jackson, K.B. Briggs, K.L. Williams and M.D. Richardson, "Tests of models for high-frequency sea-floor backscatter," *IEEE Journal of Oceanic Engineering*, vol. 21, pp. 458-470, 1996.

[9] A.W. Nolle, W.A. Hoyer, J.F. Mifsud, W.R. Runyan and M.B. Ward, "Acoustic properties of water-filled sands," *Journal of the Acoustical Society of America*, vol. 35, pp. 1394-1408, 1963.

[10] A.V. Bunchuk and Yu.Yu. Zhitkovskii, "Sound scattering by the ocean bottom in shallow-water regions (review)," *Soviet Physical Acoustics*, vol. 26, pp. 363-370, 1980.

[11] A.N. Ivakin and Yu.P. Lysanov, "Underwater sound scattering by volume inhomogeneities of a bottom medium bounded by a rough surface," *Soviet Physical Acoustics.*, vol. 27, pp. 212-215, 1981.

[12] P.A. Crowther, "Some statistics of the sea-bed and scattering therefrom," in Acoustics and the Sea-Bed, edited by N.G. Pace, Bath, Bath Univ. Press, pp. 147-155, 1983.

[13] M.D. Richardson and K.B. Briggs, "On the use of acoustic impedance values to determine sediment properties," in *Proceedings of the Institute of Acoustics*, vol. 15, pt. 2, Acoustic Classification and Mapping of the Seabed, Bath, Bath Univ. Press, pp. 15-24, 1993.

[14] M.D. Richardson and K.B. Briggs, "In situ and laboratory geoacoustic measurements in soft mud and hard-packed sand sediments: Implications for high-frequency acoustic propagation and scattering," *Geo-Marine Letters*, vol. 16, pp. 196-203, 1996.

[15] K.B. Briggs, "High-frequency acoustic scattering from sediment interface roughness and volume inhomogeneities," Ph.D. dissertation, University of Miami, Coral Gables, FL, 1994.

[16] K.B. Briggs, D.L. Lavoie, K.P. Stephens, M.D. Richardson, and Y. Furukawa, "Physical and geoacoustic properties of sediments collected for the Key West Campaign, February 1995: A data report," NRL/MR/7431--96-8002, Naval Research Laboratory, Stennis Space Center, MS, 1996.

[17] P.J. Diggle, Times Series, A Biostatistical Introduction, Oxford, Clarendon Press, 1990.

[18] D.B. Percival and A.T. Walden, Spectral Analysis for Physical Applications, New York, Cambridge University Press, 1993.

[19] A.M. Yaglom, Correlation Theory of Stationary and Related Random Functions, Volume I: Basic Results, New York, Springer-Verlag Press, 1987.

[20] W.J. Conover, Practical Nonparametric Statistics, New York, Wiley & Sons, 1971.

[21] A.F. D'Andrea, N.I. Craig and G.R. Lopez, "Benthic macrofauna and depth of bioturbation in Eckernförde Bay, southwestern Baltic Sea," *Geo-Marine Letters*., vol. 16, pp. 155-159, 1996.

[22] T.H. Orsi, F. Werner, D. Milkert, A.L. Anderson and W.R. Bryant, "Environmental overview of Eckernförde Bay, northern Germany," *Geo-Marine Letters*, vol. 16, pp. 140-147, 1996.

[23] D. Tang, G. Jin, D.R. Jackson and K.L. Williams, "Analyses of high-frequency bottom and subbottom backscattering for two distinct shallow water environments," *Journal of the Acoustic Society of America*, vol. 96, pp. 2930-2936, 1994.

[24] D.R. Jackson, unpublished.

[25] D.C. Rhoads, "Organism-sediment relations on the muddy sea floor," *Oceanography and Marine Biology Annual Review*, vol. 12, pp. 263-300, 1974.

Sound Absorption by Suspended Particulate Matter

N.R. Brown[1], T.G. Leighton[1], S.D. Richards[2] and A.D. Heathershaw[2]

[1]Institute of Sound and Vibration Research
University of Southampton
Southampton, SO17 1BJ, UNITED KINGDOM
Email: nrb@isvr.soton.ac.uk

[2]Defence Evaluation & Research Agency
DERA Winfrith, Winfrith Technology Centre
Dorset, DT2 8XJ, UNITED KINGDOM

Abstract

A series of experiments has been performed to study the viscous absorption of sound by particulate suspensions typical of those found in coastal waters. The effect due to the particles in the frequency range of 50 - 150 kHz has been determined by taking the difference in reverberation times of a volume of water with and without particles. Measured attenuation agrees reasonably well with that predicted by theory for concentrations above 0.5 g/ℓ.

1. Introduction

The acoustic absorption properties of suspended particulate matter in natural bodies of water are not well characterised, though there are a number of applications (e.g., naval mine-hunting sonars, acoustic Doppler current profilers) where such knowledge would be important, particularly in shallow water in the frequency range 50 - 300 kHz. Typical suspensions contain particles in the size range 1 - 100 μm where a variety of shapes and concentrations from 0.1 kgm^{-3} up to 4 kgm^{-3} are possible. They are liable to produce significant absorption losses [1]. There may also be the potential for flocculation and turbulence. The acoustic absorption of such systems is not known and, if models or inversion procedures are to be successfully carried out, must be quantified [2]. Similar comments apply to the inversion processes associated with the acoustic characterisation of suspended particulate matter, where currently untested assumptions must be made regarding the absorptive properties of the suspension [3].

Most of the work concerning suspensions has focused on scattering. Other absorptive processes are, also, better understood. Within the water column, temperature, salinity, pressure, and the concentrations of absorbed gas may vary, affecting the overall acoustic absorption. If bubbles are present, they may contribute significantly to the loss of acoustic energy through thermal and viscous effects, and also through acoustic re-radiation. In addition to being entrained at the water surface through wind, wave, and rain action and carried to around 10 m by Langmuir circulation and turbulence etc., bubbles might also be generated at depth through biological processes, decomposition, or seepage. It is possible to incorporate such factors individually into a description of the acoustic absorption. For deployments in the environment in question, however, not only must the contribution from the suspended particulate matter be quantifiable, but also the possibility of synergy between these factors should be explored. There is, for example, an association between suspended particulate matter and the stabilisation of gas pockets [4].

This paper presents results from an experimental study which aims to quantify the viscous absorption associated with suspended particulate matter. Parallel with this study, theoretical descriptions of the phenomenon are being developed by Richards *et al.* [1, 5], such that theory and experiment can be compared. In this way the viscous absorption effects of the suspensions, once determined, can be incorporated into acoustic propagation models.

2. Experimental Method

2.1 The acoustic tests

A series of investigative tests have been performed in order to evaluate the experimental system and to begin characterising suspensions. The tests performed to date use the reverberation behaviour of a volume of liquid to characterise the attenuation of the fluid. Differences in decay rates may be equated to variations in the absorptive properties of the fluid and the boundaries of the volume. It is important, therefore, that the absorption of the water and container is well known so that the relative contribution due to the addition of particles can be determined. Preliminary tests were performed in a large, thick-walled plastic tank containing approximately 0.6 m^3 of water. Decay traces from this apparatus were compared to traces taken from a smaller system comprising a suspended polythene bag containing 16 ℓ of water. Although the ratio of surface area to volume was increased in the smaller system, the reverberation time increased, emphasising the importance of reducing the losses at the boundaries in order to maximise the relative losses in the fluid.

The system used is shown in schematic form in Figure 1. The signal generation, data acquisition and signal processing are controlled by a personal computer running LabVIEW software. The output signal is sent to a power amplifier and then to a Brüel & Kjær 8103 hydrophone. Signals are received by a second 8103 hydrophone and are monitored by a LeCroy digital storage oscilloscope, after suitable amplification, and are finally transferred for storage and analysis to the computer via a GPIB interface. The 16 ℓ of water is contained in a suspended, thin-walled polythene bag. This provides an approximation to a pressure release surface around the whole volume, thus minimising boundary losses. A mechanical stirrer is used to lift the particulate into suspension and is removed whilst data are being recorded. The dynamic concentration of the solution can be monitored using a light scattering sensor (LSS). This monitors the settling out from suspension of the particulate. The acoustic and LSS measurements are performed separately as the presence of the LSS in the solution has an adverse effect on the reverberation.

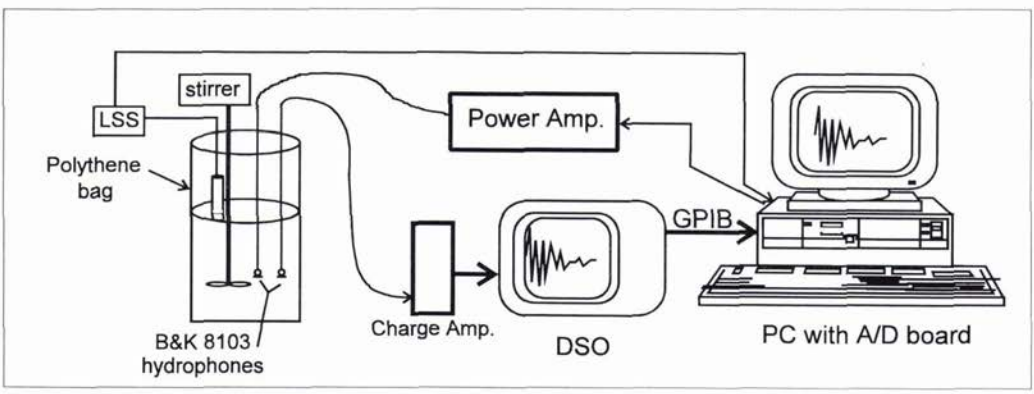

Figure 1: Experimental apparatus.

To measure the reverberation time of the volume it is necessary to record the decay of a sound field as a function of time. Ideally, the reverberation time is determined from the decay of a diffuse sound field. A diffuse sound field is one where the average energy density is the same throughout the volume considered and all directions of propagation are equally probable [6]. The onset of a diffuse sound field in an enclosure can be described by the Schroeder cut-off frequency. This gives an indication of the lowest frequency at which the modal density, i.e., the number of modes per bandwidth, is sufficient to constitute a diffuse field. The Schroeder cut-off frequency, f_{Sch}, can be expressed as [7]

$$f_{Sch} = \left(\frac{c^3}{4 \ln 10}\right)^{1/2} \left(\frac{T}{V}\right)^{1/2} \tag{1}$$

where T is the reverberation time of an impulsive noise source (i.e., the time for the sound pressure level to fall by 60 dB), c is the speed of sound in the fluid, and V is the volume of the enclosure. Typical values of f_{Sch} for the system used were between 50 and 75 kHz. This is near the lower limit of the frequency range under consideration in this project. This could be reduced to a value less than 50 kHz by slightly increasing the volume to 20 ℓ, although this is near the strength limit of the bag.

Two techniques have been used so far to generate a sound field: an impulse and a burst of uniform white

noise. Both these techniques produce a broadband sound field. The advantages of a long burst are that the sound field is given time to build up to a constant level before being cut. This improves the signal-to-noise ratio. Also, because there is a more uniform sound field, the decaying sound field is less prone to large perturbations due to direct reflections and particular modes of the volume.

A typical test sequence consists of the solution being stirred until it appears that the particulate is homogeneously spread throughout. The time for this to occur can be verified by the LSS and is of the order of a few seconds. Care must be taken to ensure that particulate does not collect in the eddies generated in the corners of the bag adjacent to the bottom seam during the stirring. Ten noise bursts are sent to the emitting hydrophone and their responses are recorded by the computer. The test sequence takes approximately 35 s. This is about the time limit before significant amounts of particulate have begun to settle out of solution.

The decay rates were determined by applying the method of integrated impulse response (IIR) [8] to the sound field from the time that the driving signal was cut-off. This method was used, even for signals derived from non-impulsional sources, as it gave a smooth estimate of the decay rate. The value of the integrated impulse response represents the ensemble average of the squared noise responses at time t after the onset of decay which is equal to the squared tone-burst response integrated from time t to "infinity." The practical implementation of this method is as follows. The response of the volume to the burst of random noise (which contains the frequency range of interest) is squared then backwards integrated from an upper time limit (some time before the response is exceeded by the background noise) to the lower time limit when the sound burst was cut off. This produces the IIR curves shown in the results section. The slope of this curve is determined from a linear regression over the initial, linear part of the curve. Typically, the lower time limit for the linear regression was 10 ms after the sound was cut off (the burst lasted 20 ms) and the upper limit was variable, the choice depending on the rapidity of the decay.

Post-processing of the results also involved performing the IIR analysis at each of the desired frequency bands. The raw data was filtered after acquisition using a Butterworth bandpass filter in 10 kHz bands over the frequency range of 50 - 150 kHz. Above this frequency, the response becomes increasingly non-linear making it difficult to obtain an estimate for the linear decay of the sound field. The data were also reduced into time bins which represent the RMS of the signal for a used-defined number of samples. This was typically 100 samples. The sampling frequency of the oscilloscope was 500 kHz.

Measurements were made on particulate-free water and then on water containing varying concentrations of glass beads. This type of particle has a high sphericity, as can be seen in Figure 1, and is, thus, representative of the particles used in the theoretical modelling. The difference in reverberation of the two systems determines the contribution of the particles to the total absorption according to the following analysis.

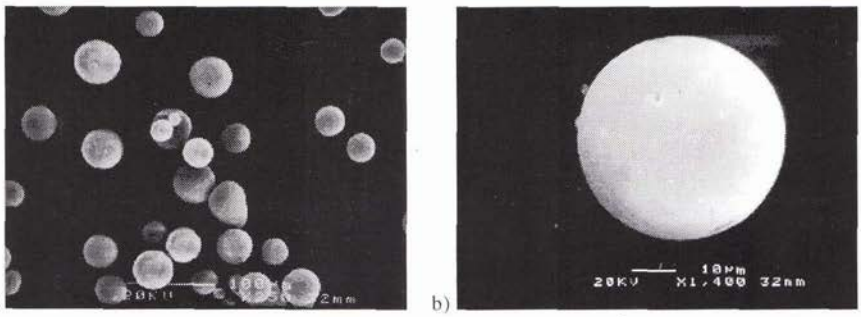

Figure 1: Scanning electron micrographs of the glass beads at a) 250 times magnification and b) 1400 times magnification.

2.2 Determination of absorption from reverberation times

The decay of a diffuse sound field where absorption occurs at the boundary and within the propagating medium is characterised by the reverberation time, T, given by [9]

$$T = \frac{55.3V}{c(A + 8\alpha V)} \tag{2}$$

where V is the volume (m^3), c is the speed of sound of the fluid (m/s), A is the total sound absorption at the boundaries of the volume, and α is the attenuation coefficient of the fluid (Np/m). The quantity $A = S\bar{a}$ is expressed in units of metric sabin, m^2, where S is the surface area of the volume (m^2) and $\bar{a}$ is the average Sabine absorptivity (dimensionless). The first term in the brackets represents the sound absorption at the

boundaries and the second term is the absorption in the medium. If T_w and T_s are the reverberation times of the particulate-free water and the water containing the particulate, respectively, then the difference in the attenuation coefficients of the fluids, $\Delta\alpha$, in dBm^{-1} is given by

$$\Delta\alpha = \left(10\log e^2\right)\frac{55.3}{8c}\left(\frac{1}{T_s}-\frac{1}{T_w}\right). \tag{3}$$

This represents the attenuation due to the addition of the particulate. This equation makes three important assumptions:

i) that the speed of sound of the solution stays constant as particles are added,

ii) that the volume remains constant, and

iii) that the addition of the particles does not affect the absorptivity of the boundaries.

The sound speed in suspensions can be calculated by using the formulation developed by Ahuja [10]. Assuming a rigid particle (i.e., the particle "viscosity" is much greater than the fluid viscosity), then the change in sound speed for the solutions considered in this work is less than 0.01%. The volume fraction of a 1 g/ℓ solution of glass beads having a density of 2400 kg/m^3 is only 0.042%, so the assumption of constant volume is reasonable. Finally, if changes in acoustic impedance are principally responsible for changes in behaviour at the boundary, then the product of the change in density and change in sound speed represents an error of less than 0.1%. This is reasonable to assume as the bag itself acts like a pressure release surface. Thus, the properties of the bag can be assumed to have almost no contribution to the absorptivity at the boundary. Any change in behaviour at the boundary will be due to changes in the properties of the fluid. This does not take into account the viscous losses due to fluid movement parallel to the bag. If the boundary can be taken to behave as a perfect air-water interface, then the absorption will be due to sound transmission to the surrounding air. For a normally incident plane wave, the absorption coefficient, α_b, is given by the expression [11]

$$\alpha_b = \frac{4\rho_w c_w \rho_a c_a}{\left(\rho_w c_w + \rho_a c_a\right)^2} \approx 0.001 \tag{4}$$

where $\rho_a c_a$ and $\rho_w c_w$ are the specific acoustic impedances of air and water, respectively, and typical values have been taken. The validity of assuming an ideal air-water interface are discussed in section 3.2.

3. Results

3.1 Particle concentration and size distribution measurements

An important aspect of the experimental method is the measurement of the particulate concentration and the particle size distribution. This is because the theory predicts the particulate attenuation is directly proportional to the concentration (for the concentrations under consideration here), a feature which is examined later, and is also a function of the particle size [12]. An infra-red LSS has been used to monitor the concentration of particles in suspension. The particulate is put into solution by means of a mechanical stirrer. Figure 2 shows the variation of concentration with time for a 1.0 g/ℓ solution of glass beads. The time that the stirrer was turned on is obvious from the plot and it is clear that the solution becomes quickly homogenised. The stirrer was stopped at 20 s and the particulate was allowed to settle. The measured concentration shows a gradual, though non-linear, reduction as the particles settle out. The pathlength of the LSS is approximately 0.05 m. It was placed 0.1 m below the surface of a 0.37 m deep volume of water. The large dip in concentration between 65 and 90 s is probably due to large scale circulation of the water producing a particulate-rich eddy, located away from the LSS, which rotates with time. This could make the concentration non-homogeneous throughout the volume even though the average concentration follows the expected exponential decay with time. It should be noted that the initial concentration of 0.1 g/ℓ does not represent a fully settled solution but the suspension concentration before the stirrer was activated.

The particle size distribution was measured following the test by taking a sample of the solution and analysing it in a laser diffraction analyser. This determines the volume distribution of particles over the size range, 0.4 μm - 1000 μm. This means. however, that the dynamic variation of the particle size distribution cannot readily be obtained as a relatively substantial volume of water must be taken from the solution. This would obviously affect the reverberation characteristics of the volume. Figure 3 shows the particle size distribution for the glass beads used in this study.

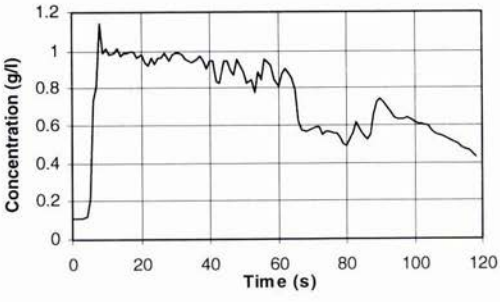

Figure 2: Variation of suspended particulate concentration with time of a 1.0 g/ℓ solution.

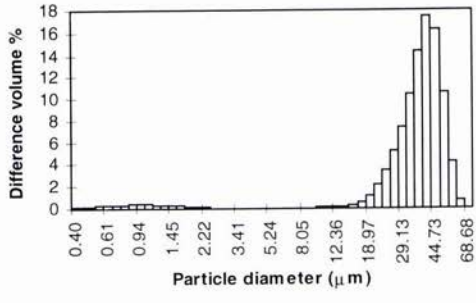

Figure 3: Particle size distribution for glass beads.

3.2 Glass bead solutions

A series of tests were performed on glass bead solutions with concentrations from 0.0 - 1.0 g/ℓ. The water used was passed through a reverse osmosis system and then filtered to remove any remaining particulate matter. As can be seen from Figure 3, there are very low concentrations of particles in the micron range. The glass beads were added in 3.2 g steps, i.e., 0.2 g/ℓ increments. The water was degassed prior to testing. The dissolved oxygen content varied from 41 - 60 % over the course of the measurements.

Figure 4 shows typical binned time traces and their corresponding IIR curve at 100 kHz for pure water and a 1.0 g/ℓ solution of glass beads. The IIR curve clearly represents the decay rate of the sound energy in the volume. The y-axis scale is the sound pressure level (SPL) in dB re 1 μPa. This only relates to the measured time trace. The reverberation times calculated for these traces were 0.233 s for the pure water and 0.132 s for the glass bead solution. At this frequency there is almost a 60 dB dynamic range. The output burst lasted 20 ms and the increase in the sound pressure over this time is clearly seen in the figures. The effect of the particulate is clearly seen.

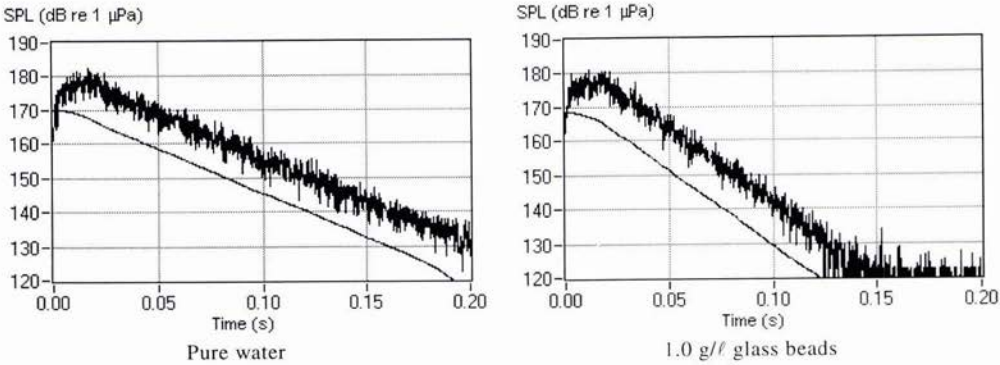

Pure water

1.0 g/ℓ glass beads

Figure 4: Typical binned time traces at 100 kHz for reverberation time calculation (upper trace) with their corresponding integrated impulse response curve (lower trace).

Figures 5 and 6 show, respectively, the reverberation time and the attenuation due to the addition of particles, $\Delta\alpha$, as functions of frequency. It should be noted that the reverberation times have been corrected for temperature and atmospheric pressure [13], which both affect the speed of sound of water. Because the temperature of the water changed over the course of the experiment from 16.0 - 15.1 °C, the reverberation times have been normalised to the conditions present for the particulate-free water measurements, i.e., 16.0 °C. Figure 5 shows that the reverberation time for the pure water decreases with increasing frequency, as is expected as the attenuation increases with increasing frequency. As particles are added, the reverberation time similarly decreases and, in general, as more particulate is added the reverberation decreases. This leads to a general increase in attenuation with increasing frequency, as expected. If the attenuation is normalised with respect to concentration, Figure 7, then it is clear that the curves do not reduce to a single value. The reasons for this are not yet clear. The variations at low frequencies for the more dilute solutions may be because the measurements

are made close to, or below, the Schroeder frequency. As the concentration increases and, thus, the reverberation time reduces, the Schroeder frequency reduces to around 50 kHz. The more dilute solutions show the greatest variation from the expected values. Considering the small variations in attenuation for these solutions, this is not altogether unexpected. The bold line in Figure 7 is the predicted normalised attenuation for a glass bead solution of the given particle size distribution. The measured attenuation agrees reasonably well with the prediction, particularly for the higher concentration solutions. The reasons for the discrepancies, especially for low concentrations, are discussed below.

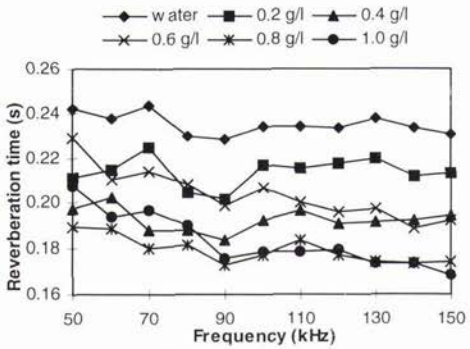

Figure 5: Reverberation time for various concentrations of glass beads.

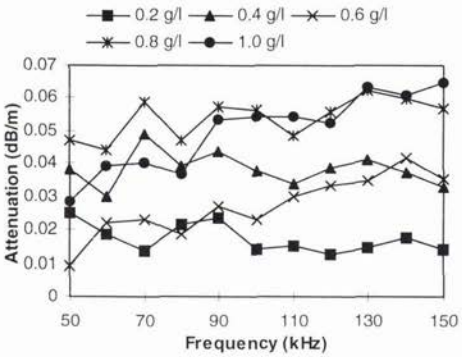

Figure 6: Particulate attenuation for various concentrations of glass beads.

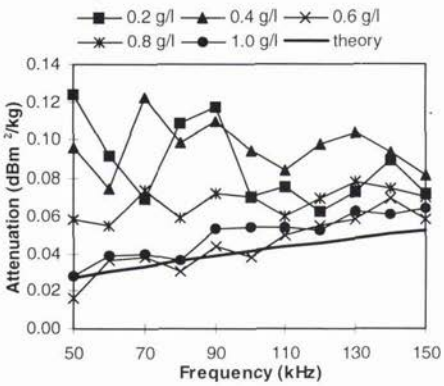

Figure 7: Normalised particulate attenuation for various concentrations.

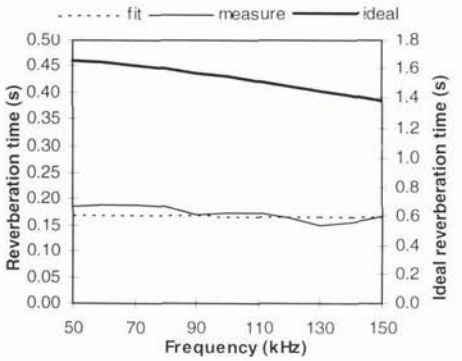

Figure 8: Reverberation times for distilled water. N.B. Ideal curve relates to right hand scale.

Consider the predicted reverberation time for particulate-free water calculated using an empirical formula for the attenuation of distilled water [14]. If it is assumed for the moment that all the boundaries behave as a perfect air-water interface for normally-incident rays, then it is evident that the measured reverberation time (and, hence, the attenuation) for pure water is considerably less than predicted (Figure 8). This is not unexpected; in a diffuse sound field many wall reflections will be at oblique incidence. In order to achieve a good fit to the measured data, the absorptivity at the boundary, i.e., the acoustic intensity transmission coefficient, must be increased from 0.001, for an ideal air-water interface at normal incidence, to 0.015 for the air-water interface and 0.0093 for the bag-water interface. These values were determined by taking reverberation measurements with different volumes of water and, thus, different proportions of surface area of the bag and the free surface. The absorption coefficients of the two types of boundary were varied in order to minimise the variation of the total absorption over the different water volumes and the frequency range of interest. Using these values of absorption and assuming ideal water, the fit to the measured reverberation is quite good. The calculation of the attenuation due to the addition of the particles is unaffected by the exact values of the boundary losses (provided they are small) because, first, this is not a function of the boundary properties, as shown in (3); and, second, because the difference in reverberation time is used, the attenuation of the water is eliminated. If, however, the absolute attenuation of the pure water or the water containing particles is to be found, a better understanding of

the losses at the boundaries must be obtained. This should also improve the measurement of dilute solutions where the variation from pure water attenuation is slight.

As mentioned previously, each result represents the average of ten measurements taken over 35 s. Figure 10 shows the reverberation times for particulate-free water and two concentrations with error bars equal to one standard deviation of the ten measurements at each of the frequency steps. Although there is some overlap, particularly at low frequencies, the amount of variation suggests that the observed trend is fairly consistent. If the variation of reverberation time with time is plotted for one solution (1.0 g/ℓ in this case) at a number of frequencies (Figure 11), then it is clear that there is a general increase in reverberation time as the test progresses. This is consistent with some of the particulate settling out of the solution and reducing the attenuation. There may also be a contribution from the variation in fluid movement as the solution calms after the stirring.

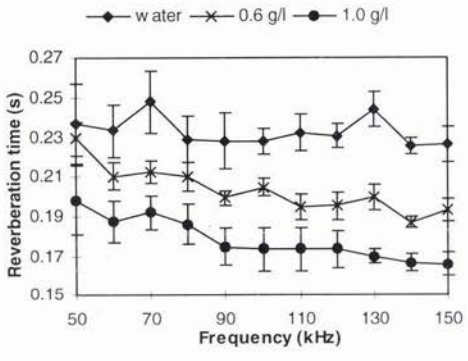

Figure 10: Reverberation times for water and selected solutions with 1 standard deviation error bars.

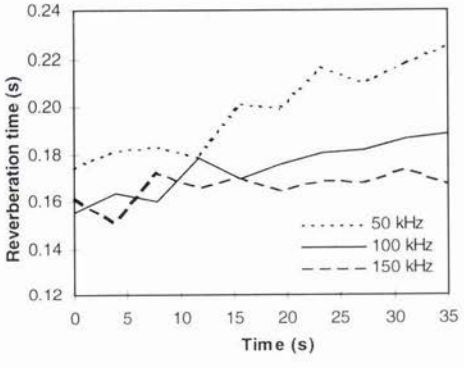

Figure 11: Variation of reverberation time with time for a 1.0 g/ℓ solution at three frequencies.

4. Conclusion

A series of reverberation tests performed on particulate-free water and water containing various concentrations of spherical glass beads have shown that the attenuation due to the particles is a readily measurable parameter using this technique. The attenuation measured agrees well with that predicted by theory for solutions with a concentration greater than 0.5 g/ℓ. Testing is continuing in order to obtain a better understanding of the loss mechanisms in the experimental system. In particular, the losses at the boundaries are being investigated. This may also resolve the variation from the predicted attenuation for the more dilute solutions. One aspect requiring investigation is the effect dissolved oxygen has on the measurements. As mentioned in section 3.2, in the tests performed to date the dissolved oxygen level showed a gradual increase over time. The contribution this makes to the reverberation behaviour requires further investigation. The dynamic concentration has been measured and this shows a gradual reduction with time which may, in part, explain the variation of reverberation time over the course of the test. The particle size distribution may also vary with time but, as yet, there is no method for monitoring this. It is evident that the contribution to attenuation of suspended particles due to viscous attenuation is small but, nevertheless, significant and should be taken into account in propagation models for turbid waters.

5. Acknowledgements

This work is funded by the DRA Winfrith (contract no. SSDW3/0001) and their support is gratefully acknowledged.

6. References

[1] S.D. Richards, A.D. Heathershaw and P.D. Thorne, "The effect of suspended particulate matter on sound attenuation in seawater," *Journal of the Acoustical Society of America*, vol. 100(3), pp.1447-50, 1996.

[2] A.D. Heathershaw and P.D. Thorne, "Impact of suspended particulate matter on acoustic propagation in turbid coastal waters," in *Proceedings of the. International Maritime Defence Exhibition and Conference*, vol. 2, Greenwich, London, pp.111-21, March 1995.

[3] S. Sun, P. Thorne, I. Bjørnø and T. Mazoyer, "Observations of acoustic backscatter by elastic cubes," in *Proceedings of the Third European Conference on Underwater Acoustics*, Heraklion, Crete, pp.51-6, June 1996.

[4] T.G. Leighton, The Acoustic Bubble, Academic Press, London, pp.78-83, 1994.

[5] S.D. Richards, A.D. Heathershaw, N.R. Brown and T.G. Leighton, "The effect of suspended particulate matter on the performance of high frequency sonars in turbid coastal waters," in these proceedings.

[6] L.E Kinsler, A.R. Frey, A.B. Coppens and J.V. Sanders, Fundamentals of Acoustics, 3rd ed., John Wiley & Sons, New York, p.313, 1982.

[7] A.D. Pierce, Acoustics: an introduction to its physical principles and applications, McGraw Hill, New York, p. 294, 1981.

[8] M.R. Schroeder, "New method of measuring reverberation time," *Journal of the Acoustical Society of America*, vol. 37(3), pp. 409-12, 1965.

[9] L.E. Kinsler *et al.*, *op. cit.*, p.319.

[10]A.S. Ahuja, "Formulation of wave equation for calculating velocity of sound in suspensions," *Journal of the Acoustical Society of America*, vol. 51(3), pp. 916-19, 1972.

[11]L.E. Kinsler *et al.*, *op. cit.*, p.126.

[12]R.J. Urick, "The absorption of sound in suspensions of irregular particles," *Journal of the Acoustical Society of America*, vol. 20(3), pp. 283-9, 1948.

[13]L.E. Kinsler *et al.*, *op. cit.*, p.107.

[14]F.H. Fisher and V.P. Simmons, "Sound absorption in sea water," *Journal of the Acoustical Society of America*, vol. 62(3), pp.558-64, 1977.

Seabed Characterization by Inversion of Parametric Sonar Data: Selection of the Cost Function

A. Caiti
DSEA - Dept. Electr. Sys. Autom.
Univ. of Pisa - via Diotisalvi 2
56100 Pisa, ITALY
andrea.caiti@ing.unipi.it

O. Bergem, E. Pouliquen
SACLANT Undersea Res. Ctr.
Viale San Bartolomeo, 400
19138 La Spezia, ITALY
bergem,pouliq@saclantc.nato.int

A. Biancheri, S. Scaricaciottoli
DIST- Dept. Comm. Comp. Sys. Sci.
Univ. of Genova, via Opera Pia 13
16145 Genova, ITALY
drago@dist.unige.it

Abstract

A class of possible cost functions to be used in model-based estimation of bottom parameters from high-frequency backscatter signals is introduced. The cost is based on the properties of the signal in the wavelet-transformed domain. It is shown, through a simulative study, that the cost can be selectively tuned to be sensitive only to subsets of the parameters to be estimated. This in turn suggests that a "divide-and-conquer" inversion strategy can be applied at least in the case of normal incidence bottom returns from parametric sonar data.

1. Introduction

Model-based inversion of acoustic data has been proved an efficient and valuable approach to the estimation of geophysical properties of the ocean and/or of seafloor sediments when working with deterministic acoustic propagation [1]. This situation usually arises when the acoustic signals propagating in the ocean environment are of low frequency nature (up to 1 KHz). When dealing with higher frequency acoustic, the stochastic nature of the interaction between the propagating signals and the medium inhomogeneities cannot be neglected. This makes the application of model based inversion techniques much more difficult (or even questionable) at the high frequency regime with respect to their low frequency counterparts. This work focuses on the problem of quantitatively estimate the upper seafloor sediment properties (sound speed, density, compressional wave attenuation, seabed rms height, etc.) from bottom backscatter data. The received signals can be modeled as the output of a stochastic process, whose parameters are to be estimated. This makes it meaningless to compare directly the measured data with model-predicted time series. On the other hand, some possible approaches based, for instance, on the computation (from the data) of the backscattering strength vs. grazing angle function may not exploit all the information present in the data.

In this work we discuss some possible choices of cost function, to be minimized in the inversion process, that attempt to exploit as much information as possible from the received data while at the same time avoiding or reducing the effect of the randomness implicit in the physical process. In particular, it is shown how multi-resolution wavelet based data analysis can be used in order to perform the inversion in the wavelet-transformed domain. Moreover, it is possible to tune the cost function in order to make it selectively sensitive only to a subset of the parameter at a time. This in turn suggests that a wavelet-based processing can be well suited for a divide-and-conquer inversion strategy, in which all the parameters of interest are recovered in sequence. Examples are shown from at-sea data collected with the "Topas" parametric sonar system, and with simulated data generated with the "Boris" backscattering stochastic model.

The paper is organized as follows: in the next section some preliminaries on the forward model and on wavelet processing are given. In section 3 it is shown, by means of examples on field data, how wavelet-based processing can effectively be employed to discriminate between different bottom types, at least in a qualitative way. In section 4, a systematic approach to the construction of a class of wavelet-based cost functions is proposed, and it is shown by simulative examples how to select, within the same class, cost functions sensitive to a subset of the sought-for parameters. Finally, some discussion of the current results, open problems, and future work is given.

2. Preliminaries

2.1 Choice of the forward model

A preliminary issue that has to be addressed before even discussing the inverse problem is the selection of the forward model. While the status of ocean acoustic models up to few kHz is relatively mature and well understood [2], the same does not apply to acoustic propagation at high frequency. It is common to have at hand models able to predict some average properties of the measured time signals [3]. Less common is the case in which a prediction of the measured time series is provided. The time series prediction has to be intended, in this context, as a *specific realization* of a stochastic process. It has to be underlined that, even in the case of perfect correspondence between model parameters and physical parameters, model predictions and measured data will in general be different, corresponding to different realizations of the same process. While this situation prevents from a direct time series comparison in any inverse scheme, the availability of a model that does predict data realizations gives, to the designer of a model-based estimation strategy, the greatest flexibility in terms of processing steps. A forward model for bottom backscattering with these capabilities is Boris. A complete description of Boris can be found in [4]-[7]. Boris is able to generate a time series realization given as input the parameters related to: the environment (sound speed in the water column, sound speed, density and attenuation in the sediment, bottom surface roughness as rms elevation, volume inhomogeneity as rms per cent variation of sound speed and density); the geometry (water depth, source-receiver position, grazing angle, tilt); the system (pulse shape transmitted, beam pattern, source level). The output of the model is produced by generating a specific realization of the bottom surface and volume with the specified average properties, and then by computing the specific (deterministic) acoustic return due to the generated surface and volume. The seafloor interface scattering is modeled using the Kirchhoff approximation, and the volume contribution with the small perturbation theory.

2.2 Wavelet processing

Wavelet processing and wavelet transform have received much attention in recent years, essentially due to their ability of producing a time-frequency analysis of a given signal with variable resolution. A general reference text on the subject is [8], while a tutorial paper with specific application of wavelet processing to high frequency backscatter data is [9]. Wavelet processing is based on the choice of a set of basis functions $\phi(t;\tau,\alpha)$ generated in the following form. Let $\phi(t;0,1)=f(t)$; then $\phi(t;\tau,\alpha)=f((t-\tau)/\alpha)$, where τ is a time shift and α is a scale factor. The function $f(t)$ is sometime called the "mother" wavelet, since it generates all the remaining wavelet basis by means of time shifts and scaling operations. It must be remarked that the mother wavelet cannot be any arbitrary function, but has to satisfy several conditions to guarantee orthonormality and completeness of the basis. Note also that if the shift and scale parameters are allowed to be continuous, we talk of wavelet transform; if they are allowed to take a numerable set of values we talk of wavelet series, in analogy with the case of Fourier basis functions. Given an admissible wavelet basis, a generic signal $x(t)$ has the following representation in the τ-α domain:

$$X(\tau,\alpha) = \int_{-\infty}^{+\infty} x(t)\phi(t;\tau,\alpha)dt \qquad (1)$$

There are some formal conditions that the basis and the signals have to satisfy to guarantee that the integral in (1) is convergent. In general, these conditions are respected if both the signal and the wavelets have finite energy, as it will be the case in the discussion in the following of the paper. Essentially $X(\tau,\alpha)$ is built as a bidimensional matrix by computing the correlation of the signal $x(t)$ with scaled versions of the mother wavelet $f(t)$. The scale factor α plays a role similar to that of the frequency in the more traditional time-frequency analysis. The similarity becomes a formal equivalence if $f(t)$ is taken as a windowed sine function. In this case, (1) becomes the common expression for the Short Time Fourier Transform. With respect to time-frequency analysis, wavelet processing offer in general more flexibility and variable resolution. However, depending on the specific wavelet basis chosen, it is not always clear what is the physical interpretation of the transform $X(\tau,\alpha)$.

In the following of the paper, we will make use of the wavelet transform with the mother wavelet described by Deaubechies [10], and reported in Figure 1. The reason for this specific choice is mainly because this is the mother wavelet whose shape is closest (at least, among those mother wavelets we are aware of) to that of the Ricker pulse transmitted by the parametric sonar system through which the field data have been obtained. This has some importance in understanding the physical meaning of the specific wavelet transform chosen. In particular, if the mother wavelet is chosen (as in our case) as equal to the transmitted pulse (or close to it as it can be), in the completely deterministic case (no roughness, no inhomogeneities) one would obtain a matrix composed by the deconvolved signal in one row, and zero in the other rows. The effect of the stochastic parameters is to blur the deconvolution results, and the wavelet transform is able to trace the blurring both in the time and scale domain.

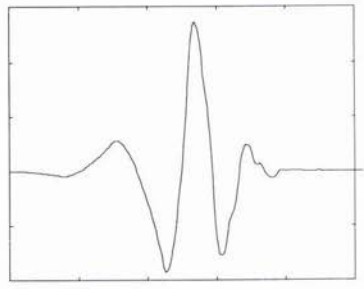

Fig. 1: Deaubechies wavelet used for the transform (1). Time and amplitude axes are not reported, since the function can be arbitrarily scaled and amplified

3. Field Data Analysis with the Wavelet Transform

In this section it is our intention to show how field data taken on different bottom types show systematic and quantifiable differences when processed with the wavelet transform introduced previously. This is a key point in order to attempt a definition of a meaningful cost function for a model-based inversion scheme.

The data to be shown have been collected at the Saclantcen test sites in the gulf of La Spezia, Italy, and have already been partially reported in [7]. The experiment configuration was as follows: the "Topas" 040 parametric sonar from SIMRAD was used in monostatic configuration; the system was transmitting a calibrated Ricker pulse with a center frequency of 8 kHz, and a bandwidth of approximately 8 kHz, steered at normal incidence toward the bottom. Data were acquired at a sampling rate of 100 kHz. The system has been used at three sites, in the following labeled as 'Tellaro', 'Portovenere' and 'Monasteroli', having water depths varying between 12 and 17 meters. At these three sites, the bottom is described as compact sand, silty clay and gravel on sand respectively.

Each signal in the data set has been transformed according to (1), with the following choices: 125 samples (corresponding to 1.25 ms of data) have been selected for each signal; the signals have been aligned, so to avoid any effect due to the different bottom depths; the scale parameter α has been let moving from 1 to 50. The following notational convention is used: $X_{i,j}(\tau,\alpha)$ is the wavelet-transformed signal, with $i=T,P,M$ identifying the location of the original signal, and $j=1,2,...$ identifying the specific signal among those of the location i. The wavelet transform of the different signals are now compared by means of the following difference matrix $\Delta(i,j,k,h)$ defined in the following way:

$$\Delta(i,j,k,h) = \left| \left| X_{i,j}(\tau,\alpha) \right| - \left| X_{k,h}(\tau,\alpha) \right| \right| \tag{2}$$

Note that Δ is a matrix whose elements are indexed by τ and α; each element in Δ is the modulus of the difference of the moduli of the corresponding elements in the matrices $X_{i,j}$ and $X_{k,h}$. By looking at the difference matrices, it appears systematically that the difference matrix of two signals taken in the same area has elements of about one order of magnitude smaller than the difference matrix of signals taken at different areas. This is shown for instance in fig. 2, where, with the same scale on the z-axis, the difference matrix of two signals from Portovenere and Tellaro is compared with the difference matrix of two signals from Portovenere.

Another example of the same kind is shown in fig. 3. This behaviour of the difference matrix is systematic, at least in the three data sets that we had available. This suggests that the comparison in the wavelet-transformed domain is able to capture the differences between different bottom types. This may be used, for instance, in a qualitative bottom classification scheme, in which the seafloor is characterized as "sand"-"silt"-"clay" types. The purpose of the next section is to explore if more quantitative information can be extracted by comparing the data with model realizations in the wavelet-transformed domain.

4. Cost function selection and parameter sensitivity

In this section we propose a systematic procedure for the definition of a cost function to be used in model-based inversion schemes, relying on the wavelet transform (1). Furthermore, we proceed with a sensitivity analysis of the cost function with respect to the bottom parameters to be estimated. A large use of the Boris model is made in this section, however the procedure in itself is independent of the particular choice of forward model.

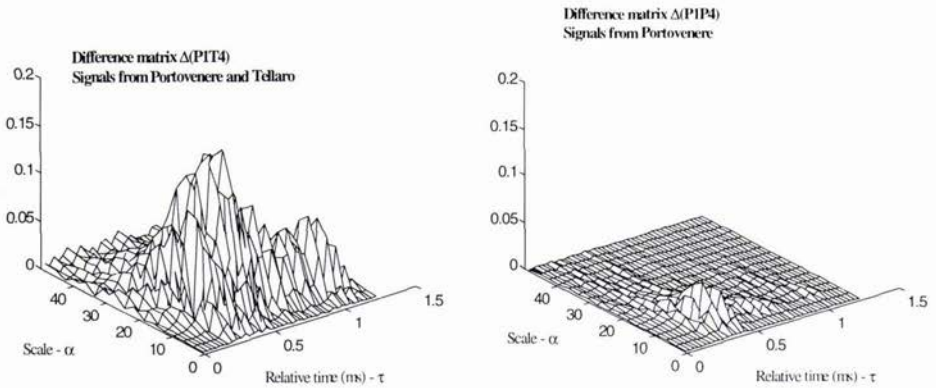

Fig. 2: Difference matrix between signals from Portovenere and Tellaro (left) and difference matrix between two signals from Portovenere (right). Note the difference in magnitude when the signals are coming from different areas.

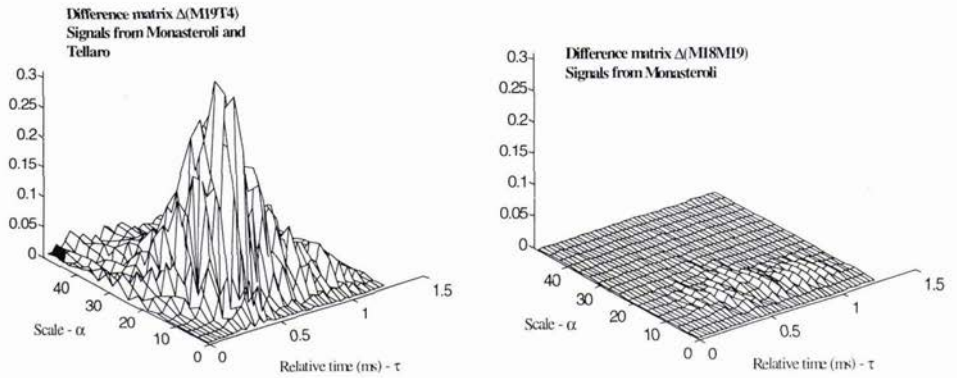

Fig. 3: Difference matrix between signals from Monasteroli and Tellaro (left) and difference matrix between two signals from Monasteroli (right). Note again the difference in magnitude when the signals are coming from different areas.

Let $X_d(\tau,\alpha)$ be the wavelet transform of the data time series $d(t)$. Let $\mathbf{m}$ be the vector of bottom parameters to be estimated. In particular, in the following we will consider $\mathbf{m}=[\sigma, c_p, \nu, \alpha_p]$, where σ is the surface roughness rms in meters, c_p is the sediment sound speed in m/s, ν is the rms sound speed and density volume inhomogeneity, in percent variation w.r. to c_p and ρ, α_p is the compressional wave attenuation in the sediment in db/m. The case of signals at vertical incidence is considered; it is well known that in this case sediment sound speed and sediment density ρ cannot be recovered independently, but only the acoustic impedance $z=\rho c_p$ can be estimated. In the simulation study presented in this section we keep the density linearly related with the sound speed, and we refer to sound speed estimation. However, it has to be clear that what is actually estimated is the acoustic impedance. The assumption of no layering in the sediment is also made. The case of multiple layers is briefly discussed in the next section. The knowledge of the other relevant environmental, geometric and system parameters is assumed.

For a given choice of the bottom parameters $\mathbf{m}$, N realizations of the data $r(t;\mathbf{m},i)$, $i=1,\ldots,N$, are generated through Boris or through any equivalent model. At each realization is associated its wavelet transform matrix $X_{ri}(\tau,\alpha;\mathbf{m})$. The ensemble average of the wavelet transform is then computed:

$$X_r(\tau,\alpha;\mathbf{m}) = \frac{1}{N}\sum_{i=1}^{N} X_{ri}(\tau,\alpha;\mathbf{m}) \tag{3}$$

At this point we are ready to define the following class of cost functions:

$$J(\mathbf{m}) = \left\| \left(\left| X_d(\tau,\alpha) - X_r(\tau,\alpha;\mathbf{m}) \right| \right) \exp\left(-\beta / \left(\left| X_d(\tau,\alpha) \right| + \left| X_r(\tau,\alpha;\mathbf{m}) \right| \right) \right) \right\| \tag{4}$$

where the absolute value operations are done element by element, *i.e.*, for each (τ,α) index; $\|\cdot\|$ stands for the usual euclidean matrix norm and the parameter β is a positive real constant selected by the user. The usefulness of the parameter β lies in the fact that, by appropriate tuning, it can be used to increase the sensitivity of the cost function J to some of the parameters in $\mathbf{m}$, and to decrease the sensitivity to some other parameters. The sensitivity of J to a generic element m_i of the vector $\mathbf{m}$ is defined in the usual way as:

$$S(m_i) = \frac{\partial J(\mathbf{m})}{\partial m_i} \tag{5}$$

Roughly speaking, a "large" value of β gives more weighting to the part of the signal with more energy, which is in general due to the sediment surface return contribution; on the contrary, a "low" value of β tends to preserve the energy content of the original time series (note that $\beta=0$ is a possible choice, which corresponds to no weighting applied to the signal in the wavelet-transformed domain). Note that here "large" and "low" strongly depend on the quantities $\left|X_d(\tau,\alpha)\right|$ and $\left|X_r(\tau,\alpha)\right|$: in our case, the sum of the two reaches peak values of the order of magnitude of 10^1. This means that, with the choice of β=20 (discussed in the following), the peak values will be weighted by a factor of about 0.1, and the weighting will rapidly decrease moving away from the peak. The idea of the parameter β comes from traditional seismic signal processing, where it is customary to use time-varying adaptive gain on the recorded time series. Here, however, the adaptation gain strategy is performed in the wavelet transformed domain. In particular, we will show, with simulated data generated with Boris, using the calibrated Topas beam pattern, pulse shape and source level, that, by taking β of the order of 10^1, the cost function (4) is such that the sensitivity (5) to the volume parameters v and α_p is negligible. This, in turn, suggests the following inversion strategy: a cost function (4) is defined with $\beta \geq 10$; the cost is minimized with respect to the parameters σ and c_p. With these estimated values, a new cost function is defined with $\beta=0$, and it is minimized with respect to the remaining parameters v and α_p.

The (simulated) reference data $d(t)$ have been generated by assuming an environment with the following parameters: σ=0.04 m; c_p=1720 m/s; v=5%; α_p=0.9 dB/m; ρ=1.9 g/cm^3. The time signals have been generated as in the field data test case, with a sampling of 100 kHz, and only 125 samples have been considered in the wavelet analysis. A value of β=20 has been chosen. The number N of different realizations to be used in computing the cost (4) has been fixed to 10. In fig. 4 we present the cost plotted as a function of σ and v. This has been obtained by computing J with values of σ ranging from 0.03 to 0.05 m at steps of 0.0015 m, and v ranging from 0.5% to 11% at steps of 0.75%. The other parameters were kept constant at their reference value.

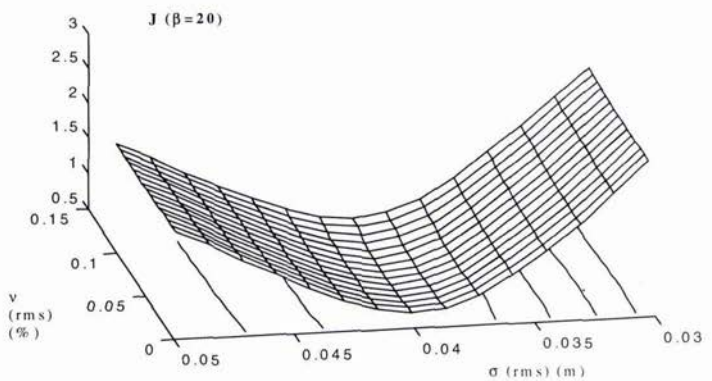

Fig. 4: Low sensitivity of the cost function J with β=20 to the volume inhomogeneity parameter (v).

It can be seen from the figure that the sensitivity of the cost function to the volume inhomogeneity parameter is negligible (the sensitivity (5) can be evaluated from the figures by looking at the variation of the cost in the direction parallel to that of the axis of the parameter whose sensitivity is investigated; if the contour lines are parallel to some of the axis, the cost is not sensitive to that parameter). Negligible sensitivity is also experienced with the sediment compressional wave attenuation, as it appears in figure 5. Here the cost function has been generated by varying the surface roughness as before, by varying the compressional wave attenuation between 0.3 and 1 dB/m at steps of 0.05 dB/m, and by keeping the remaining parameters fixed.

The cost function is sensitive to both the surface roughness and the sediment sound speed. In fig. 6 the cost as a

function of these two parameters is plotted. Note that not only the cost has been generated with different realization of the time series, but also, in this case, the insensitive parameters ν and α_p have been chosen at random for each realization, in order to further verify their passive influence on the cost. In this test the surface roughness has been sampled with the same range and step as before, while the sediment sound speed has been sampled from 1540 m/s to 1960 m/s with a step of 30 m/s. As stated before, the sediment sound speed is *not* independent from the density, since we are treating the normal incidence case. We have fictitiously imposed a dependence of the density from the sound speed of the form $\rho = 1.2*10^{-3}*c_p - 0.1640$. So the sound speed estimation has actually to be intended as an estimate of the acoustic impedance. From fig. 6 it can be seen that there is a unique well defined minimum in the cost function, corresponding to the correct reference data parameters. It is interesting to note that the cost function is very smooth, with a unique minimum.

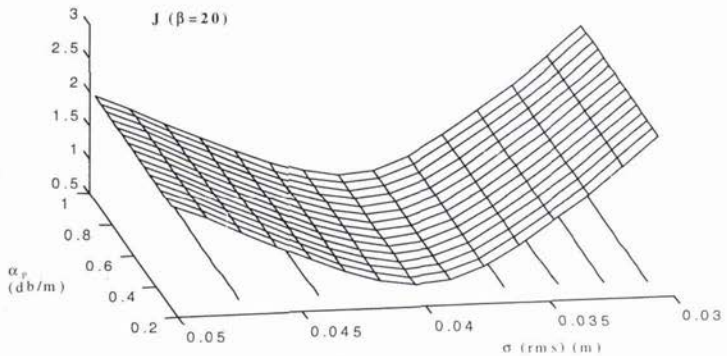

Fig.5: Low sensitivity of the cost function J with β=20 to the sediment compressional wave attenuation (α_p).

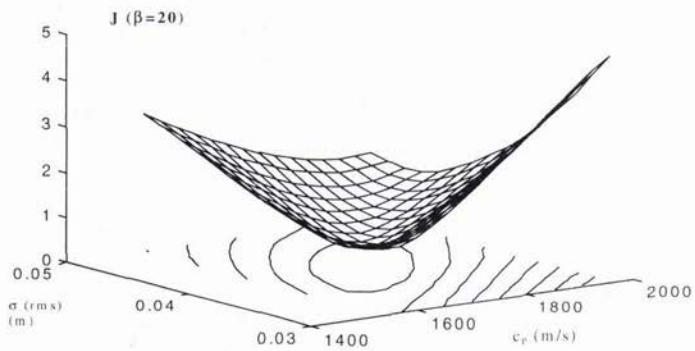

Fig. 6: Cost function J with β=20 w.r. to sediment sound speed and surface roughness

We remark that, although the simulations presented refer to a specific case, they have been run for a number of cases, and these results, at least qualitatively, are systematic. At this point, by selecting a proper value of the parameter β, it is assumed that a correct estimate of the surface roughness has been obtained. Having fixed the surface roughness, a new cost function belonging to the class (4) is defined, this time by choosing β=0. In fig. 7 the cost function is shown with respect to sediment sound speed and volume inhomogeneity. Also in this case, there is a unique minimum at the expected position, although the cost function is less smooth.

In this case, in which the volume gives significant contributions to the cost function, the compressional wave attenuation is also expected to play a significant role. However, in the example reported in fig. 7, the bidimensional cost has been obtained by fixing the attenuation to a constant value of 0.5 dB/m, different from that of the reference data. It can be seen that this has no influence on the correct determination of the other two parameters. This is confirmed if we plot the cost as a function of volume inhomogeneity and compressional wave attenuation, with surface roughness and sediment sound speed fixed to their correct (reference) values. As it can be seen in fig 8, the cost function has low sensitivity to the attenuation parameter; however, it has to be

remarked that the sensitivity to the compressional wave attenuation is not entirely negligible, as it was in the previous cases discussed. In any case, it is not sufficient to correctly identify the attenuation parameter. Note that the volume inhomogeneity parameter is correctly recovered.

It is not clear to us at the moment why the cost function is not sensitive to the sound speed attenuation; it may be due that, by taking only 1.25 ms of data, the travel time within the bottom is not sufficient to consistently show the effect of the attenuation; or, it may be that the wavelet-based cost function itself masks the attenuation.

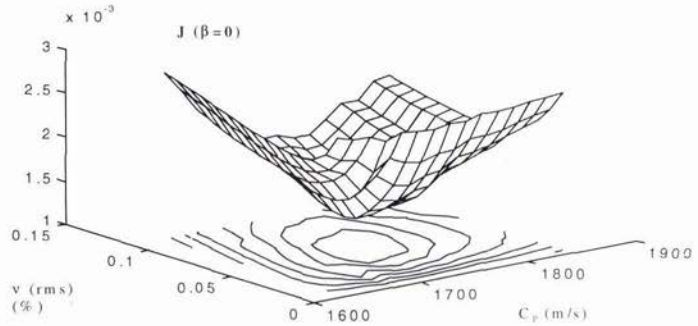

Fig.7: Cost function J with β=0 w.r. to sediment sound speed and volume inhomogeneity

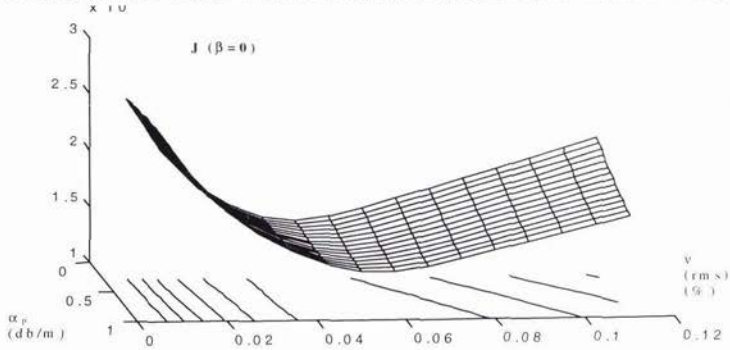

Fig 8: Low, although not entirely negligible, sensitivity of the cost function J with β=0 to the sediment compressional wave attenuation α_p

5. Discussion and Conclusions

Wavelet processing of normal incidence backscatter signals from parametric sonar seems to have the potential for a proper classification and model based inversion of both deterministic and stochastic sea bottom parameters. Many questions, however, remain open. One is the physical explanation of why should wavelet basis show this property. We are currently exploring other approaches to time-frequency and time-scale analysis (in particular, with the Wigner-Ville distribution) in an attempt to clarify this aspect.

An implementation of a "divide and conquer" inversion strategy, relying on the class of cost functions defined in (4), is currently under development. It is expected, however, that even better results, in terms of selectively reducing the sensitivity to some of the parameters, may be obtained by using backscatter signals at different frequencies. In particular, using a parametric sonar, the primary frequency may be used for the surface roughness and acoustic impedance determination, without recurring to the tuning of the parameter β. Note that, in the case of the Topas system, the primary frequency is at about 40 kHz, while the difference frequency signals taken as reference in this work have center frequency at 8 kHz.

The case of multiple layers can be treated with the same approach underlined here, by inverting the parameters of one layer at a time (a technique known as "layer stripping" in the seismic community). It has to be said, however, that all the inversion methods of the divide-and-conquer type, including layer stripping, may suffer of

severe inaccuracies from early errors: any inaccurate result is in fact carried over in the subsequent steps of the inversion procedure. This implies that an accurate analysis of the robustness of the proposed scheme will also be necessary in the near future.

Acknowledgements

This work has been partially supported by EU, under the MAST-III initiative, project "ISACS", contract no. MAS3-CT95-0046.

References

[1] O. Diachok, A. Caiti, P. Gerstoft, H. Schmidt (eds.), Full-Field Inversion Methods in Ocean and Seismo-Acoustics. Dordrecht, NL, Kluwer Acad. Publ., 1995.

[2] F. Jensen, W.A. Kuperman, M.B. Porter, H. Schmidt, Computational Ocean Acoustics. New York, American Institute of Physics, 1994.

[3] D.Jackson, D. Winebrenner, A. Ishimaru, "Application of the Composite Roughness Model to High-Frequency Bottom Backscattering", *Journal of the Acoustical Soc. Am.* , vol. 79, n. 5, pp., May 1986.

[4] G. Canepa, O. Bergem, E. Pouliquen, "The implementation of Boris-3D: BOttom Response from Inhomogeneities and Surface", *SACLANTCEN M-125*, La Spezia, Italy, 1997.

[5] E. Pouliquen, O. Bergem, N.G. Pace, "Time-evolution Modeling of Seafloor Scatter, Part 1: Theory", *SACLANTCEN SM-328*, La Spezia, Italy, 1997.

[6] O. Bergem, E. Pouliquen, G. Canepa, N.G. Pace, "Time-evolution Modeling of Seafloor Scatter, Part 2: Experimental Validation", *SACLANTCEN SM-327*, La Spezia, Italy, 1997.

[7] O. Bergem, E. Pouliquen, A. Lyons, N.G. Pace, "Normal Incidence Seafloor Classification Using a Parametric Sonar Array", in *Proceedings of the IEEE Conf. OCEANS'96*, Ft. Lauderdale, FL, 1996.

[8] G. Strang, T. Nguyen, Wavelets and Filter Banks, Wellesley, MA, Wellesley-Cambridge Press, 1996.

[9] G.C. Gaunard, H.C. Strifors, "Signal Analysis by Means of Time-Frequency (Wigner-Type) Distributions - Applications to Sonar and Radar Echoes", *Proceedings of the IEEE*, vol. 84, n. 9, pp. 1231-1248, 1996.

[10]Y. Deaubechies, Ten Lectures on Wavelets, SIAM, 1992.

Bayesian Inference and Sidescan Restoration

B R Calder L M Linnett

Department of Computing and Electrical Engineering
Heriot-Watt University
Riccarton
Edinburgh EH14 4AS
E-mail: (brc, lml)@cee.hw.ac.uk

Abstract

We consider a Bayesian approach to the problem of inferring parameters of the SONAR environment given only the gathered sidescan image. A simplified model of the process is developed along with suitable prior distributions on the parameters, and a sampling technique is utilised to estimate the parameters most likely given the data. As an example, we apply this technique to estimation of a step-gain TVG curve and use the results in restoration of legacy sidescan data.

1. Introduction

We attempt to draw a distinction between *processing* and *analysis* of SONAR data. Techniques for extracting information based on power spectra [1], fractals [2] and other statistical techniques [3] consider the surface statistics of the observed image, essentially treating the image as any other array of numbers with little regard to the creation process. Recently, attempts have been made by Beattie and Elder [4] and Dugelay *et al.* [5] to extract more data, although in Beattie's case the approach is motivated by visual arguments, and in Dugelay's examples, the effects are applied to very large scale processes where significant averaging has taken place.

We are more interested here in inferring parameters of the SONAR environment when the image considered was recorded, in an attempt to extract useful detail with which to further our understanding of the data. These parameters do not have to be recorded: anything which has a significant effect on the imaging process is implicit in the image created; all we have to do is devise a method with which to estimate the effect and hence infer the parameter value. Essentially, we are attempting to invert the SONAR imaging process, but given the complexity, a number of simplifications and assumptions have to be made. However, the assumptions are shown to be reasonable under normal operating conditions for typical surveys, and in particular for the dataset which we use for the example.

The process of inferring data in this manner is quite general; we choose a straightforward problem of estimating the step gains and durations of a staircase style TVG process in legacy data given no other information as an example in this case.

2. Data Description

The dataset considered consists of output from a high frequency sidescan operating in shallow coastal waters off the south coast of the UK. The electronics pack was an early model, and consequently used a simple staircase TVG, with consequent vertical striping of the record (figure 1). As well as being annoying on visual inspection, this process renders the data significantly non-stationary and complicates further analysis.

Unfortunately, this legacy data contains no record of the SONAR parameters, and even the first return time has been removed in an attempt to de-jitter the data and improve on storage. Thus, the task we consider is to estimate the relevant parameters, including the TVG step durations and gains with the intention of eventually removing the gain curve and replacing it with something more appropriate to avoid the observed artifacts.

The gains steps are observed to be of regular period. Figure 2(a) shows estimates of column means in the image of figure 1 using a sliding windows of width five columns. The periodic spikes are more easily seen in the FFT

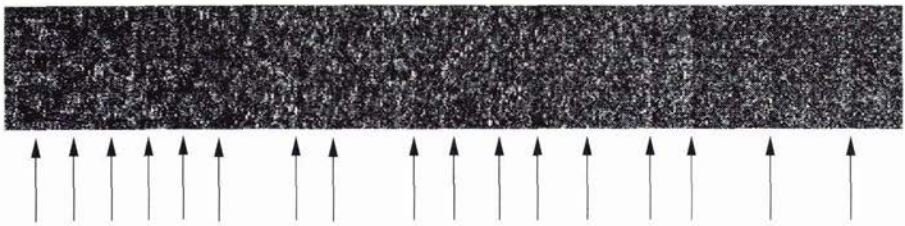

Figure 1: Example of staircase TVG on SONAR data.

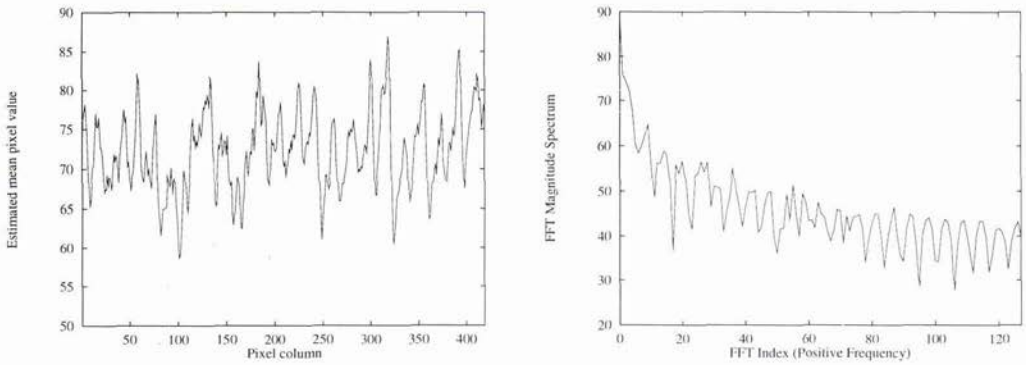

(a) Column mean estimates; sample mean estimates with five pixel sliding window

(b) FFT of column mean estimates; 512 sample radix-2 DIT algorithm

Figure 2: Observed periodic gain structure in SONAR image.

of the signal. This shows significant periodicity about the 14 sample period, equivalent to about 1.4 ms with the 10 kHz sampling rate used during digitisation. Such periodicity makes the effect unlikely to be natural, confirming that the observed artifacts are caused by the TVG.

The sections of data used in the analysis are 420 samples by 100 pings in size, and are extracted from a larger dataset essentially at random, under the constraint of satisfying the assumptions made in the next section.

3. Modelling Methodology

The technique used to extract information from SONAR images revolves around a simple model of the energy return expected from the seabed and a sampler technique to allow consistent estimates to be generated. In order to build a model which can be easily manipulated, a number of simplifying assumptions have to be made.

We assume firstly that the geometry of the system is simple. The towfish is maintained at the same height about the seabed, and is assumed to be sufficiently stable not to affect the images created; if fish motion is suspected, there are a number of techniques to improve the situation [6, 7]. To avoid complications with beam-pattern effects, we assume that the beam is sufficiently wide and narrow to avoid spotlighting and spreading in the assumed swathe width. The towfish for the dataset considered satisfies these conditions.

To further simplify the geometry, we assume that the towfish is of suffiently high frequency to allow a ray based solution to the propagation equations, and also that the speed of sound is constant so that the rays propagate in straight lines. We justify these latter two assumptions by noting that typical surveying with sidescan does not normally entail propagating through deep columns, and hence there is little chance of a thermocline being introduced, and that even if one is present, there is little chance of there being sufficient distance in propagation to allow the effects to become significant. Using a simple ray tracing model and temperature data from an instrumented range in a river estuary, typical rays even through strongly varying profiles show a maximum distance error of just over 1% for the longest ray examined. Consequently, the effect is insignificant compared to the other approximations made in the model.

The model includes spreading and absorbtion losses by assuming that the sound spreads spherically and that absorbtion is exponential, based on the propagation path length. The choice of spreading model is motivated purely by mathematical convenience, although the absorbtion is based on more accurate measurements [8].

Modelling of the seabed interaction is again motivated by mathematical convenience. We choose to simplify matters by using empirical justification of Lambert's Law (more correctly a "rule of thumb") [9] as a model, assuming that the seabed is a diffuse reflector, and considering only the monostatic scattering case for energy returned along the incident ray. More complex models such as those developed by Jackson *et al.* [10] could in theory be incorporated, but the manipulations would be much more difficult; in this pilot study, we opt to accept innacuracy in modelling as necessary to feasible implementation. A consequence of these modelling assumptions is that the point statistics of the observed image should be Rayleigh distributed [11], which can be shown by standard χ^2 testing on maximum likelihood fits of a Rayleigh distribution to estimated histograms from the dataset.

The TVG observed in the previous section is modelled by a base gain and a time varying component as illustrated in figure 3. We choose to parameterise in terms of step durations and additive gain for mathematical convenience in developing the sampler code. The step-like function $\lambda_\alpha(x)$ is used to allow differentiation to take place, but as $\alpha \to \infty$, this curve converges to the unit step (since $\lim_{\alpha\to\infty} d\lambda_\alpha(x)/dx|_{x\neq 0} \to 0$, and if $H(x)$ is the Hilbert step function, $\lim_{\alpha\to\infty} \int_{-\infty}^{\infty} |H(x) - \lambda_\alpha(x)|dx = 0$).

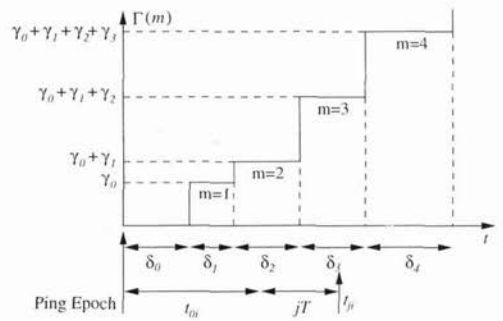

$$g_{ji} = \sum_{k=0}^{S} \gamma_{ki}\lambda_\alpha \left(t_{ji} - \sum_{m=0}^{k} \delta_{mi} \right) \quad (1)$$

$$\lambda_\alpha(x) = \frac{e^{\alpha x}}{1 + e^{\alpha x}} \quad (2)$$

Figure 3: Staircase TVG curve used in modelling.

We build the simplified model by concatenating all of these assumptions, modelling the expected return per pixel as μ_{ji} for the $(i,j)^{\text{th}}$ pixel. The return is a product of gain, absorbtion loss, spreading loss, and reflectivity at the seabed:

$$\mu_{ji} = \rho g_{ji} \cdot a(t_{ji}) \cdot s(t_{ji}) \cdot r(t_{ji}) \quad (3)$$

$$= \rho g_{ji} \cdot e^{vt_{ji}} \cdot \frac{1}{v^2 t_{ji}^2} \cdot \frac{t_{0i}^2}{t_{ji}^2} \quad (4)$$

$$= \frac{\rho e^{vt_{ji}} g_{ji} t_{0i}^2}{v^2 t_{ji}^4} \quad (5)$$

where $t_{ji} = t_{0i} + jT$ for samples of period T, and we allow that the first return time per ping may be variable. Some of the effects expected in the data cannot be distinguished from this model. For example, it is impossible to determine the reflectivity coefficient distinctly from the overall gain, or an increase in towfish height from a change in bottom depth. We assume, however, that these effects are not normally significant, and modelling potentially composite parameters is sufficient to gain further insight into the data.

4. Bayesian Posterior Analysis and Model Development

4.1. Sampler-based Approaches to Bayesian Analysis

Attempting to fit this model directly would be extremely difficult due to the interactions between the parameters, the non-linearity of the description and the possibility of multiple solutions. In an attempt to resolve these difficulties, we utilise the Bayesian approach to data analysis in order to incorporate prior knowledge of likely parameter values (and thus constrain possible parameter combinations), and use a sampler based scheme to deal with the complexities that this process generates.

In this application, the model developed forms the likelihood function, and we implement prior distributions on the parameters to complete the model. However, it would be almost certainly impossible to manipulate the posterior distribution analytically to determine the properties, and difficult even to implement a numerical attack on the integrations required for determination of the marginal distributions required. The alternative is to develop a Monte Carlo [12] scheme to estimate properties based on samples from the posterior.

However, due to the complexity of the model, it is impossible to draw samples from the (very highly dimensional) posterior distribution. Therefore, we utilise the ideas of Monte Carlo Markov chain (MCMC) analysis [13] to develop a Markov chain which has, as its limiting distribution, the posterior distribution. This allows the samples to be generated by simple simulation of the chain, essentially swapping one large sampling task for a number of simple samplers. After an initial settling period, samples generated from the Markov chain can be considered to be correlated samples from the distribution and thus can be used to estimate any required property of the posterior.

4.2. Sampler Implementation

We use the Gibbs sampler algorithm [14] to implement the MCMC analysis required. The MCMC technique originated in statistical physics [15] where many different sampler algorithms are used, but is now used extensively in both image reconstruction (e.g., [16]) and more mainstream statistical analysis (e.g., [17]), where variants of the Metropolis-Hastings algorithm are used. The Gibbs sampler is one such variant where the Markov chain is induced by sampling from the conditional distributions of the variables, i.e., $f(x_i|x_j \forall j \neq i)$.

However, determining the conditional distributions under general conditions is quite difficult. Here, we follow a simplification after Spiegelhalter *et al.* [18] where a graphical model is used to represent the relationship between the variables, and assumptions of marginal independence of the variables are made to allow development of the conditional distributions.

The graph representing the current model is shown in figure 4, where solid directed lines indicate statistical dependence of parameters in the indicated direction, and broken adirectional lines indicate a deterministic relationship. The relationships and distributions are summarised beside the graph, where $\mathcal{N}(\mu, \sigma^2)$ is a normal distribution, and $\mathcal{R}(\beta)$ is a Rayleigh distribution.

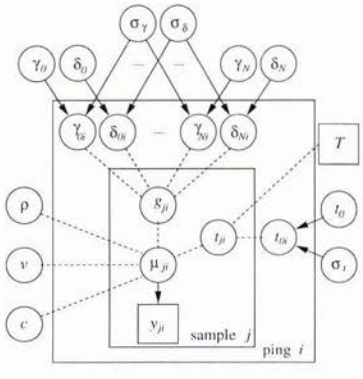

$$y_{ji} \sim \mathcal{R}(\mu_{ji})$$

$$\mu_{ji} = \frac{\rho c^{vt_{ji}} t_{0i}^2 g_{ji}}{v^2 t_{ji}^4}$$

$$t_{ji} = t_{0i} + jT$$

$$t_{0i} \sim \mathcal{N}(t_0, \sigma_t^2)$$

$$g_{ji} = \sum_{k=0}^{S} \gamma_{ki} \lambda_\alpha \left(t_{ji} - \sum_{m=0}^{k} \delta_{ki} \right)$$

$$\delta_{ki} \sim \mathcal{N}(\delta_k, \sigma_\delta^2)$$

$$\gamma_{ki} \sim \mathcal{N}(\gamma_k, \sigma_\gamma^2)$$

Figure 4: TVG estimation model and defining equations for stochastic and deterministic relationships

Use of rectangles in the graph indicates independence, and hence the graph here indicates that each ping is initially assumed to be marginally independent of all others (although, since they share a common ancestor in the t_0 and gain parameters, they are not necessarily marginally independent in the posterior distributions), as are the samples within each ping. This is required for consistency with the previous assumptions. The rectangles also represent a general variable, indicating that all of the pings have the same structure (so that, for example, the t_{0i} are marginally independent, but all depend on t_0 in the same manner).

The structures about t_{0i} are typical of models of this type (and are the same about the gain step durations, δ_{ki} and γ_{ki}). The structure indicates that some variation is expected, but the degree of variation is unknown. Therefore the variance of the parameter is included as another parameter of the sampler, and is also estimated as part of the fitting process. In this example, the value of σ_t could be expected to be reasonable, indicating small variation in the fish height or bottom bathymetry; the values for σ_γ and σ_δ might be expected to be smaller since they depend mainly on the stability of the electronics pack on the towfish, which should be good. They are, however, included for symmetry and so that this point can be determined by posterior marginal analysis.

Variable	Prior	Parameters		Support[i]
ρ^{ii}	$\mathcal{R}$	$\beta = 1.3 \times 10^6$		$[0, 3.95 \times 10^6]$
v^{iii}	$\mathcal{N}$	$\mu = 1500\,\text{ms}^{-1}$	$\sigma^2 = 600\,\text{m}^2\text{s}^{-2}$	$[1426, 1574]\,\text{ms}^{-1}$
$1 - c^{\text{iv}}$	$\mathcal{G}^{\text{v}}$	$\alpha = 11$	$\beta = 7 \times 10^{-4}$	$[0.98, 1.00]$
t_0	$\mathcal{R}$	$\beta = 10^{-2}\,\text{s}$		$[0, 30]$ ms
γ_k	$\mathcal{R}$	$\beta = 100$		$[0, 300]$
δ_k	$\mathcal{R}$	$\beta = 1.4\,\text{ms}$		$[0, 4.25]$ ms
$\sigma_t^{-2\,\text{vi}}$	$\mathcal{G}$	$\alpha = 0.01$	$\beta = 100$	N/A[vii]
σ_γ^{-2}	$\mathcal{G}$	$\alpha = 0.01$	$\beta = 10^{-6}$	N/A
σ_δ^{-2}	$\mathcal{G}$	$\alpha = 0.01$	$\beta = 100$	N/A

i Support ranges are for limits such that $\int_a^b p(x)dx = 0.99$.
ii Maximum gain is over 130 dB, based on deterministic estimates.
iii Medwin's formula [19] at $T = 4°\text{C}$, $S = 20\,\text{ppt}$ and $z = 40\text{m}$; variation of each parameter gives typical limits of $1420 - 1540\,\text{ms}^{-1}$.
iv Absorbtivity at 100 kHz at 4°C is 30 dB /km [8] ($c = 0.993$).
v i.e., a Gamma distribution, $\mathcal{G}(x; \alpha, \beta) = (\beta\Gamma(\alpha))^{-1}(x/\beta)^{\alpha-1}\exp(-x/\beta)$.
vi Inverse variance ("precision") is modelled to simplify the maths; the gamma distribution is conjugate to the Gaussian linking densities, giving a closed form conditional distribution.
vii Prior is intentionally vague since no information is available.

Table 1: Summary of prior distributions and parameters for TVG model.

The prior distributions used in the model are summarised in table 1, and while the parameters of the distributions are determined by physical constraints, the shape of the distributions are determined mainly for mathematical convenience. In most cases, the priors are fairly vague since only general constraints on the parameters are required; the purpose is to keep the sampler in a physically likely area of the parameter space, but to let it explore that region fairly freely.

The full conditional distributions required for sampling can be determined as follows. Let V be the set of all nodes in the graph (i.e., parameters), let c_v be the set of all *children* of node v (i.e., all those which depend on it, collapsing deterministic links as required), and let p_v be the set of parents of a node (i.e., those on which v depends). Then, Spiegelhalter *et al.* [20] show that the conditional is:

$$f(v|\cdot) = f(v|\mathsf{p}_v) \prod_{c \in \mathsf{c}_v} f(c|\mathsf{p}_c) \tag{6}$$

where $f(v|\cdot) = f(v|\mathsf{V} \setminus \{v\})$; nodes without parents use the prior for $f(v|\mathsf{p}_v)$. Thus, for example, the full conditional of t_{0i} can be read from the graph as:

$$f(t_{0i}|\cdot) = f(t_{0i}|t_0, \sigma_t) \prod_j f(y_{ji}|\cdot) \tag{7}$$

$$\propto \exp\left(-\frac{(t_{0i} - t_0)^2}{2\sigma_t^2}\right) \prod_j \frac{y_{ji}}{\mu_{ji}^2} \exp\left(-\frac{y_{ji}^2}{2\mu_{ji}^2}\right) \tag{8}$$

This level of complexity in full conditional distributions is common. In some cases the function may be a particular distribution (with conjugate priors), but this is not usual. In the case of log-concave distributions, the ARS algorithm [21] may be used, which automatically constructs an accept-reject envelope [22] for the variable using a numerical technique. However, many of the full conditionals in this model are not log-concave (or, at least, cannot be *proved* to be unconditionally log-concave), and the more general ARMS algorithm is used [23]. Although conceptually simple, implementing ARMS is an exacting task; the authors are indebted to W. R. Gilks (contact: `wally.gilks@mrc-bsu.cam.ac.uk`) for providing the code to implement this.

5. Experimental Analysis

Analysis with the sampler is a process of setting a suitable initialisation scheme, and then running the Gibbs sampler algorithm sufficiently long to ensure that the induced Markov chain has settled to its final distribution. In this example, the data set shown in figure 1 is processed.

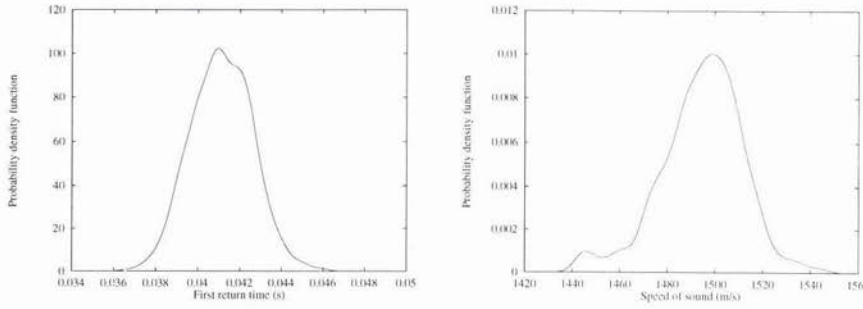

(a) First return time density estimates

(b) Speed of sound density estimate

Figure 5: Kernel density estimates of first return time and speed of sound. Estimates from last 1000 samples of 3000 in run.

The initialisation scheme is not critical; in theory, any parameter set should be sufficient under very weak conditions on the sampler. Experience with sampler algorithms suggests that starting the chain about the marginal posterior modes of the variables is as good an initialisation strategy as any, although it does not guarantee any better convergence rate for the sampler. The derived parameters (i.e., t_{0i}, γ_{ki} and δ_{ki}) are sampled initially according to their defining equations, ensuring that the values generated are physically possible (this is guaranteed on later samples by the construction method for the ARMS algorithm envelope).

The question of how many samples to allow for settling of the sampler (the "burn-in" time) and how many samples from the sequence to use is still uncertain except in special cases. Our (very conservative) scheme is to simulate 3000 samples from the chain and use only the very end of the run for estimation of properties. Judging from experience of other researchers (particularly [24]) and from traces of the parameter behaviour during development, convergence appears rapid and the estimates generated are stable. The only difficulty in this experiment is in the gain parameters for the last few stages of the TVG; the step parameters tend to settle sequentially from the first return side of the image, and longer runs are required to ensure sufficient time for all of the parameters to settle.

However, kernel estimates of the first return time and speed of sound, figure 5, show stable monomodal densities within the correct parameter range. Confirmation that the sampler is not simply sampling from the prior distributions is found in the fact that the first return time is significantly higher than first expected, and indeed is distinctly in the upper tail of the prior distribution. In addition, the posterior variances are much smaller than the prior variances, indicating that the vague priors used do not affect the sampler significantly. The mean values of the two parameters give $t_0 = 41.1\,\text{ms}$ and $v = 1491.2\,\text{ms}^{-1}$, leading to a towfish height of 30.6 m, typical of 100 kHz surveys.

Analysis of the sampling variances indicates that there is sufficient evidence in the t_{0i} to conclude that the first return time varies on a ping by ping basis, but that there is no significant variation between the gain duration and amplitudes. In subsequent runs, the model could be simplified accordingly.

The major test of this model, however, is in restoring the data set test image. The output from the last 1000 samples of the chain were averaged to give posterior estimates of the required variables, and these were used to remove the step gains and replace them with the TVG assumed in the model. The results, figure 6, show signifcant improvement from the original data, which is confirmed by the column mean estimates shown for original and processed images.

6. Discussion and Extentions

The results in figure 5–6 show that the system proposed can detect features of the SONAR environment from the images, and (since the values generated restore the image correctly) that the model developed has to be reasonably accurate for the data considered. The aim of this experiment, and similar techniques, is not necessarily to give a perfectly accurate physical model, merely one which is sufficiently close to approximate the data but also sufficiently flexible in support by its sampler to allow the imperfections to be compensated in fitting.

Close examination of figure 6 shows that much significant detail is obscured in the original data, particularly the gentle bathymetry in the middle of the swathe, which is very obvious in the restored image. Comparison of the before and after images shows that the detail is present in the original, but is obscured by the step-gain effects.

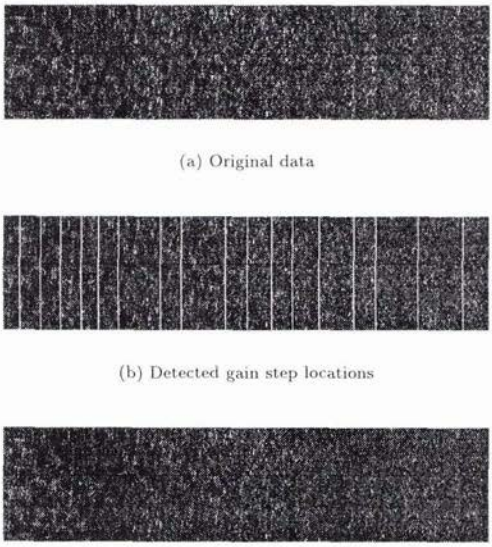

(a) Original data

(b) Detected gain step locations

(c) Restored data

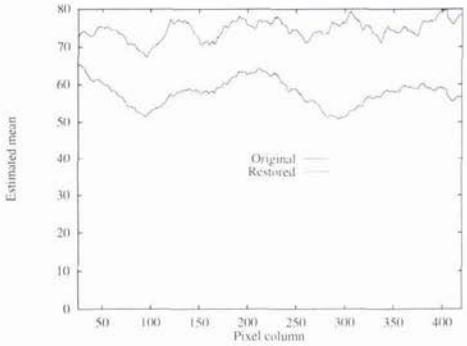

(d) Original and restored data column mean estimates

Figure 6: Original and restored data, with column means. Column means, estimated with a window width of five samples show significantly less periodicity after restoration, corresponding to the smoother appearance of the restored image.

This technique has a number of advantages over other analysis systems, not least that it can easily attack problems which would be difficult by other methods. The MCMC process makes it a simple task to specify the relationships between variables and then estimate their properties given the data, even when the variables were never measured. Although implementation may be computationally demanding, this has to measured against the observation that there often is no alternative estimation technique.

The process is also intuitively satisfying. Many other techniques attempt to infer properties of the seabed simply from the surface statistics, treating the data as simply another image. Here, we have the ability to infer probability densities of the SONAR environment parameters, and the understanding of the dataset which is implicit in this process is very powerful. Although fairly limited through the assumptions made in developing the pilot model, this technique is a first step towards infering real knowledge from the images.

Work on these techniques is continuing. We envision that the major improvements required initially are inclusion of more general seabed surfaces, both in terms of bathymetry and multiple sediment types. Extention to self-shadowing of surfaces, discrete objects and targets, and better models of the physical processes are also being considered in order to infer properties useful for further analysis.

7. Conclusions

A method has been proposed for structuring the problem of inference of parameters in SONAR. We construct a simple model of SONAR physics, use the Bayesian method to incorporate prior information on the parameters (to improve the stability of the system), and utilise a MCMC technique to numerically estimate features of the (high dimensionality) Bayesian posterior distribution. These parameters are useful in their own right, infering information on the SONAR environment when the image was gathered, and may also be used to manipulate the image whence they were generated.

In this particular example, a simple TVG restoration problem has been posed, and an example of the dataset has been processed. The sampler outputs can be summarised to present probability density functions for variables of interest, or can be used to remove and replace the step TVG curve with a more appropriate smooth function which reduces the artifacts. The consequence of this is much better visual appearance, and better visibility of significant effects in the SONAR trace.

It is possible to include a great deal of structuring information into a difficult problem, and hence to include complex statistical models without very complex analysis techniques. The specification of the model is simple, and although computationally demanding, implementation of the sampler system is quite straightforward. As well as adopting a more rigorous "investigative data analysis" approach to the problem, the system also builds inference on parameters that are otherwise difficult to obtain and leads to much better understanding of the process of image gathering.

The model is being actively developed. Planned improvements include a better model of image formation including self-shadowing and irregular seafloors, and the inclusion of multiple sediment types. The ultimate goal is to develop a sampler which will infer relative reflectivities of each sediment, taking into account shadowing effects, and hence give sediment rather than texture maps of the surveyed area.

References

[1] N. G. Pace and H. Gao. Swathe Seabed Classification. *IEEE Oceanic Eng.*, 13(2), 1988.

[2] D. R. Carmichael, L. M. Linnett, S. J. Clarke, and B. R. Calder. Seabed Classification Through Multifractal Analysis of Sidescan Sonar Imagery. *Proc. IEE*, 143(3), 1996.

[3] L. M. Linnett, D. R. Carmichael, and S. J. Clarke. Texture Classification using a Spatial Point Process Model. *IEE Proc. Vis. Image Signal Proc.*, 142(1), 1995.

[4] R. S. Beattie and S. C. Elder. Sidescan SONAR Image Restoration using Simulated Annealing and Iterative Conditional Modes. In *Sonar Signal Processing*, volume 17 of *Proc. Inst. Acoustics*, December 1995.

[5] S. Dugelay, X. Lurton, and J. M. Augustin. A New Method for Seafloor Characterisation with Multibeam Echosounders: Image Segmentation using Angular Backscattering. In *Proc. 3rd European Conference on Underwater Acoustics*, June 1996.

[6] D. T. Cobra, A. V. Oppenheim, and J. S. Jaffe. Geometric Distortions in Sidescan Sonar Images: A Procedure for Their Estimation and Correction. *IEEE J. Ocean. Eng.*, 17(4), 1992.

[7] R. S. Beattie and S. C. Elder. MAP Sidescan SONAR Motion Distortion Correction using Iterative Conditional Modes and Simulated Annealing. In *Sonar Signal Processing*, volume 17 of *Proc. Inst. Acoustics*, December 1995.

[8] F. H. Fisher and V. P. Simmons. Sound Absorption in Sea Water. *J. Accoust. Soc. Am.*, 62(3), 1977.

[9] S. Stanic, K. B. Briggs, P. Fleischer, R. I. Ray, and W. B. Sawyer. Shallow water high frequency bottom scattering off Panama City, Florida. *J. Accoust. Soc. Am.*, 83(6), 1988.

[10] D. R. Jackson, D. P. Winebrenner, and A. Ishimaru. Application of the composite roughness model to high frequency bottom backscattering. *J. Accoust. Soc. Am.*, 79(5), 1986.

[11] J. A. Ogilvy. *Theory of Wave Scattering from Random Rough Surfaces.* Adam Hilger, Bristol, 1991.

[12] J. M. Hammersley and D. C. Handscomb. *Monte Carlo Methods.* Methuen, 1964.

[13] W. R. Gilks, S. Richardson, and D. J. Spiegelhalter, editors. *Markov Chain Monte Carlo in Practice.* Chapman and Hall, 1996.

[14] A. E. Gelfand and A. F. M. Smith. Sampling-Based Approaches to Calculating Marginal Densities. *J. Am. Stat. Assoc.*, 85(410), 1990.

[15] K. Binder, editor. *The Monte Carlo method in Condensed Matter Pyhsics*, volume 71 of *Topics in Applied Physics.* Springer-Verlag, 1992.

[16] D. Geman and C. Yang. Nonlinear Image Recovery with Half-Quadratic Regularization. *IEEE Trans. Image Proc.*, 4(7), 1995.

[17] B. P. Carlin, A. E. Gelfand, and A. F. M. Smith. Hierarchical Bayesian Analysis of Changepoint Problems. *Appl. Stat.*, 41(2), 1992.

[18] D. J. Spiegelhalter, N. G. Best, W. R. Gilks, and H. Inskip. Hepatitis B: a case study in MCMC methods. In Gilks et al. [13].

[19] H. Medwin. Speed of sound in water: A simple equation for realisitic parameters. *J. Accoust. Soc. Am.*, 58(6), 1975.

[20] D. J. Spiegelhalter, A. P. Dawid, S. L. Lauritzen, and R. G. Cowell. Bayesian analysis in expert systems. *Stat. Sci.*, 8, 1993.

[21] W. R. Gilks and P. Wild. Adaptive Rejection Sampling for Gibbs Sampling. *Appl. Stat.*, 41, 1992.

[22] A. M. Law and W. D. Kelton. *Simulation Modeling and Analysis.* McGraw-Hill, 1991.

[23] W. R. Gilks, N. G. Best, and K. K. C. Tan. Adaptive Rejection Metropolis Sampling within Gibbs Sampling. *Applied Statistics*, 44(4), 1995.

[24] A. E. Rafferty and S. M. Lewis. How many iterations of the Gibbs sampler? In J. M. Bernardo, J. Berger, A. P. Dawid, and A. F. M. Smith, editors, *Bayesian Statistics 4.* Oxford University Press, Oxford, 1992.

Shallow Water Reverberation Modeling Using An Autoregressive Range-Scattering Function Approach

R. N. Carpenter

Naval Undersea Warfare Center Division
1176 Howell St.
Newport, RI 02841-1708, USA
E-mail: carpenterrn@tech.npt.nuwc.navy.mil

Abstract

The primary limitation on system performance for active sonars is reverberation — the reradiation of acoustic energy back to the receiver from inhomogeneities in the physical properties of the medium and its boundaries. A new technique for modeling reverberation using an autoregressive power spectral density function to describe the range-scattering function of the reverberation channel is presented. The method is used to estimate the range-scattering function from sampled reverberation time-series.

1. Introduction

Reverberation — the reradiation of acoustic energy back to the receiver from inhomogeneities in the physical properties of the medium and its boundaries can be particularly bothersome in shallow water when contributions from surface, volume, and bottom reverberation are present. Many techniques for modeling reverberation have been proposed, developed, and tested. These efforts have been motivated primarily by either the need to simulate reverberation time-series data to test existing processing techniques ([1], [2]) or the desire to formulate new detector-processing structures [3]. A new technique for modeling reverberation that can be used to address either of these two issues is presented below.

2. Linear Systems Theory Approach To Reverberation Modeling

Small amplitude acoustic signals are governed by the linear wave equation [4]; therefore, reverberation can be analyzed using a linear, time-varying filter. The input/output relationship of such a filter is

$$y(t) = \int_{-\infty}^{\infty} s(t-\tau)h(t;\tau)d\tau, \tag{1}$$

where $s(t)$ is the input signal, $y(t)$ is the output signal and $h(t;\tau)$ describes the output of the filter at time t due to a unit impulse applied τ seconds earlier. It is assumed that s, and therefore, y have negligible energy outside a band centered at some carrier frequency and can be designated as band-pass signals [3]. Analysis then continues with the equivalent lowpass complex representation of these signals and the impulse response h. To simplify notation, it is now assumed that s, h, and y refer to their complex lowpass representations.

Equation (1) will be equated to the system shown in Figure 1. Specifically, the deterministic signal $s(t)$ is the transmit waveform and $y(t)$ is the resultant reverberation time-series. The time-varying filter $h(t;\tau)$ models the effects of system parameters, propagation effects, and scattering effects and will be referred to as the "impulse response" of the reverberation channel. From this model it can be seen that τ is a variable representing time delay.

A simple approach to modeling the reverberation channel that has found widespread use assumes a first-order, uncorrelated scattering model [5]. It is assumed that the scattering regions are uncorrelated with each other no matter how closely spaced in the time-delay variable τ, and, at each time delay, the impulse response is a sample function of a stationary, zero-mean, complex Gaussian random process. These assumptions are typically

referred to as the "wide-sense stationary, uncorrelated scattering (WSSUS) assumptions." Because of the zero-mean, Gaussian assumption, the reverberation channel is completely characterized by the second-order statistics of $h(t;\tau)$. As a result of the WSSUS assumptions, the correlation function of $h(t;\tau)$ has the unique structure

$$E[h(t_1;\tau_1)h^*(t_2;\tau_2)] = R_h(t_1 - t_2;\tau_1)\delta(\tau_1 - \tau_2). \tag{2}$$

That is, in the variable t, the correlation function is only a function of the time difference $\Delta t = t_1 - t_2$, and in the variable τ, the correlation function has the structure of a nonstationary, white-noise process.

The time variations of the reverberation channel are caused by the motion of the medium inhomogeneities and the motion of the transmit/receive array relative to the medium. As measured by the variable Δt above, this motion manifests itself as a Doppler spread of the transmitted waveform. Under certain conditions [6] that are assumed to hold in this development, the channel can be assumed to be time invariant so that (1) reduces to a simple convolution integral

$$y(t) = \int_{-\infty}^{\infty} s(t-\tau)h(\tau)d\tau, \tag{3}$$

and the correlation function in (2) reduces to

$$\begin{aligned} E[h(\tau_1)h^*(\tau_2)] &= E[|h(\tau_1)|^2]\delta(\tau_1 - \tau_2) \\ &= r_h(\tau_1)\delta(\tau_1 - \tau_2). \end{aligned} \tag{4}$$

Now the impulse response of the reverberation channel is just a realization of a nonstationary, complex Gaussian, white-noise process where the average intensity function $r_h(\tau)$ is referred to as the "range-scattering function" [3]. Although $r_h(\tau)$ is a causal function of time delay and, in theory, is of infinite extent, for all practical purposes, there is a range of values of τ over which $r_h(\tau)$ is essentially nonzero. This limit will be denoted as τ_h. It is often referred to as the "multipath spread of the channel" [7].

The continuous-time Fourier Transform (CTFT) of $h(\tau)$ is also a stochastic process with correlation function,

$$\begin{aligned} R_H(f_1, f_2) &= E[H(f_1)H^*(f_2)] \\ &= E\left[\int_{-\infty}^{\infty} h(\tau_1)\exp(-j2\pi f_1\tau_1)d\tau_1 \int_{-\infty}^{\infty} h^*(\tau_2)\exp(j2\pi f_2\tau_2)d\tau_2\right] \\ &= \int_{-\infty}^{\infty} r_h(\tau)e^{j2\pi\tau(f_2-f_1)}d\tau \end{aligned} \tag{5}$$

that is only a function of the frequency difference $\Delta f = f_2 - f_1$ and therefore can be written as

$$R_H(\Delta f) = \int_{-\infty}^{\infty} r_h(\tau)e^{j2\pi\Delta f\tau}d\tau. \tag{6}$$

Therefore $H(f)$, the random transfer function of the reverberation channel, is a wide-sense stationary (WSS), zero-mean, complex Gaussian process. Also note that, from the Wiener-Khinchen theorem ,

$$r_h(\tau) = \int_{-\infty}^{\infty} R_H(\Delta f)e^{-j2\pi\Delta f\tau}d\Delta f. \tag{7}$$

That is, the range-scattering function is the CTFT of the correlation function $R_H(\Delta f)$. $R_H(\Delta f)$ is referred to as the "two-frequency correlation function" [3]. Since $R_H(\Delta f)$ is an autocorrelation function in the frequency variable Δf, it yields a measure of the frequency coherence of the channel. If f_h denotes a measure of the coherence bandwidth, then $f_h \approx \frac{1}{\tau_h}$. Two sinusoids with frequency separation greater than f_h are affected differently by the channel. It can also be shown that the time-varying intensity of the reverberation is

$$R_y(t,t) = E\left[|s(t-\tau)|^2 r_h(\tau)d\tau\right] = \int_{-\infty}^{\infty} |s(t-\tau)|^2 r_h(\tau)d\tau. \tag{8}$$

In summary, a range spread reverberation channel has been modeled as a random, time-invariant, linear system with a WSS, zero-mean complex Gaussian transfer function $H(f)$. The correlation function of the transfer function is the two-frequency correlation function in (6) and its power spectral density (PSD) function is the range-scattering function in (7). Knowledge of either of these second-order statistics completely characterizes the reverberation.

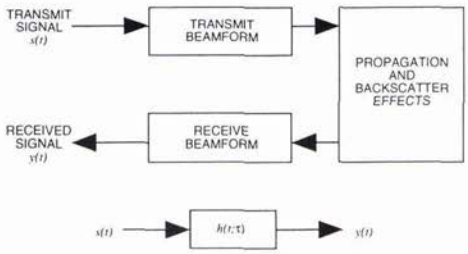

Figure 1: Linear System Model for Reverberation

3. Discrete Processes

The ultimate goal is to estimate the range-scattering function $r_h(\tau)$ from reverberation time-series data, and to this end the transfer function $H(f)$ is now sampled at equally spaced intervals δf along the frequency axis. The motivation being that (6) and (7) are equivalent to a PSD estimation problem in the time delay (τ) and frequency (Δf) domains. For the present time, it is assumed that access to the samples is available. Later it will be shown how to extract this information from the reverberation time-series data. The discrete-time process

$$H[n] = H(f = n\delta f),\ n = \cdots, -1, 0, 1, \cdots \tag{9}$$

is formed. $H[n]$ is a discrete-time, zero-mean, complex Gaussian WSS process with autocorrelation function $R[m] = R_H(\Delta f = m\delta f)$. As such, the z-transform of $R[m]$ can be defined as

$$r(z) = \sum_{m=-\infty}^{\infty} R[m] z^{-m}. \tag{10}$$

When z is limited to the unit circle, $r(z)$ is the discrete time Fourier transform (DTFT) of $R[m]$. In addition, if z is expressed as a continuous function of τ with δf held fixed, then on the unit circle, $z(\tau) = e^{j2\pi\tau\delta f}$ and

$$r(\tau) = r(z(\tau)) = r(e^{j2\pi\tau\delta f}) = \sum_{m=-\infty}^{\infty} R[m] e^{-j2\pi m\tau\delta f}, \tag{11}$$

and it is seen that $r(\tau)$, the DTFT of $R[m]$, is the PSD of the WSS process $H[n]$. Note that $r(\tau)$ is periodic in τ with period $= 1/\delta f$.

Since $R[m]$ was derived by sampling the continuous function $R_H(\Delta f)$ at equally spaced samples δf along the frequency axis, the sampling theorem yields,

$$r(\tau) = \frac{1}{\delta f} \sum_{k=-\infty}^{\infty} r_h(\tau - \frac{k}{\delta f}); \tag{12}$$

that is, the PSD of the WSS process $H[n]$ is equal to a periodic function of τ that is a scaled, infinite sum of displaced replicas of the scattering function $r_h(\tau)$. As long as the sampling interval in the frequency domain satisfies

$$\delta f \leq \frac{1}{\tau_h}, \tag{13}$$

aliasing in the time-delay domain is kept to a minimum and $r(\tau)$ is a good approximation (to within a scale factor) of $r_h(\tau)$. Note that in order to minimize aliasing, the frequency samples must be spaced less than the coherence bandwidth of the channel ($\delta f \leq f_h$).

3.1. Autoregressive Processes

It is now assumed that only a finite number of samples ($H[n]$, $n = 0, 1, \ldots, N-1$) are available and that $r(\tau)$, which was previously shown to be a good approximation to the scattering function $r_h(\tau)$, is desired. The problem now falls into the category of PSD estimation - determining the spectral content of a random process based on a finite set of observations from that process. Typically, the set of observations is made in the time domain and the

PSD estimate generated in the frequency domain, so *it is important to remember that in the current problem, the observations are made in the frequency domain, and the spectral estimates are generated in the time-delay domain.*

The approach taken in this effort assumes that $H[n]$, $n = 0, 1, \ldots, N-1$ are samples of a zero-mean, complex Gaussian, autoregressive process of known order p (referred to as an "AR(p) process") [8]

$$H[k] = -\sum_{n=1}^{p} a[n]H[k-n] + u[k]. \tag{14}$$

Here p is the order of the autoregressive process, $\mathbf{a} = [a[1]\, a[2] \cdots a[p]]^T$ is a vector whose elements are the complex AR coefficients, and $u[k]$ is a complex Gaussian, white-noise process with variance σ^2. The PSD of $H[k]$ is

$$r(\tau') = \frac{\sigma^2}{\left|1 + \sum_{m=1}^{p} a[m] \exp(-j2\pi m\tau')\right|^2} \tag{15}$$

where τ' represents a normalized time delay

$$\tau' = \frac{\tau}{\tau_h}. \tag{16}$$

This result is consistent with the requirement for minimizing aliasing in the time-delay domain, and the fundamental period of τ' is chosen to be $0 \leq \tau' \leq 1$.

4. Maximum Likelihood Estimation Of The Range-Scattering Function

In this section maximum likelihood estimates (MLEs) of $\mathbf{a}$ and σ^2 denoted as $\hat{\mathbf{a}}$ and $\hat{\sigma}^2$ are developed [9]. When these estimates are substituted into (15), a maximum likelihood estimate of the PSD (range-scattering function) is produced:

$$\hat{r}(\tau') = \frac{\hat{\sigma}^2}{\left|1 + \sum_{m=1}^{p} \hat{a}[m] \exp(-j2\pi m\tau')\right|^2}. \tag{17}$$

Recall that the MLEs are based on the data set $H[n]$, $n = 0, 1, \ldots, N-1$, which is denoted in vector form as $\mathbf{H}$. The approximate (actually conditional) probability density function (PDF) of $\mathbf{H}$ is:

$$p(\mathbf{H}; \boldsymbol{\Theta}) = \frac{1}{(\pi\sigma^2)^{N'}} \exp\left(-\frac{1}{\sigma^2} \sum_{n=p}^{N-1} \left|\sum_{k=0}^{p} a[k]H[n-k]\right|^2\right), \tag{18}$$

where the vector of unknown parameters $\boldsymbol{\Theta} = [\mathbf{a}^T \sigma^2]^T$, $N' = N - p$ and $a[0] = 1$. Maximizing this function with respect to σ^2 yields

$$\sigma^2 = \frac{1}{N'} J(\mathbf{a}) = \frac{1}{N'} \sum_{n=p}^{N-1} \left|\sum_{k=0}^{p} a[k]H[n-k]\right|^2. \tag{19}$$

When $\mathbf{a}$ is replaced by its MLE, σ^2 becomes $\hat{\sigma}^2$.

The MLE of $\mathbf{a}$ is found by minimizing $J(\mathbf{a})$ in (19). Note that $J(\mathbf{a})$ is a quadratic with respect to the $a[k]$'s and can be written as

$$J(\mathbf{a}) = \|\mathbf{H}_p + \mathbf{G}\mathbf{a}\|^2, \tag{20}$$

where

$$\mathbf{H}_p = [H[p]\, H[p+1] \cdots H[N-1]]^T, \tag{21}$$

and

$$\mathbf{G} = \begin{bmatrix} H[p-1] & H[p-2] & \ldots & H[0] \\ H[p] & H[p-1] & \ldots & H[1] \\ \vdots & \vdots & \ddots & \vdots \\ H[N-2] & H[N-3] & \ldots & H[N-1-p] \end{bmatrix}. \tag{22}$$

Minimizing $J(\mathbf{a})$ with respect to $\mathbf{a}$ yields

$$\hat{\mathbf{a}} = -\left(\mathbf{G}^H\mathbf{G}\right)^{-1}\mathbf{G}^H\mathbf{H}_p, \tag{23}$$

and substituting (23) into (19) yields

$$\hat{\sigma}^2 = \frac{1}{N'}\mathbf{H}_p^H\mathbf{P}_G^{\perp}\mathbf{H}_p, \tag{24}$$

where $\mathbf{P}_G^{\perp}$ is the projection matrix

$$\mathbf{P}_G^{\perp} = \mathbf{I} - \mathbf{G}\left(\mathbf{G}^H\mathbf{G}\right)^{-1}\mathbf{G}^H. \tag{25}$$

5. Processing Reverberation Time-Series

The previous development assumed that samples from the random process $H[n]$ were readily available. In reality, a finite set of samples must be derived from the time-series $y(t)$. These can be obtained as follows. Recall that $s(t)$ is a complex lowpass signal and $y(t)$, $h(t)$ are complex lowpass random processes. Assume that the energy of $s(t)$ is negligible outside the band $-B/2 \le f \le B/2$. Also assume that the bandwidth of the signal is greater than the coherence bandwidth of the channel, $B > f_h \approx 1/\tau_h$. Sample $y(t)$ with sample period $\Delta t = \frac{1}{B}$, and form the discrete-time version of (3)

$$y[n] = \sum_{k=0}^{N_h-1} h[k]s[n-k] \; n = 0, 1, \ldots, N_T - 2, \tag{26}$$

where $s[n] = s(t = n\Delta t)$, $h[n] = h(t = n\Delta t)$, $y[n] = y(t = n\Delta t)$, $N_T = N_h + N_s$, $N_h = \frac{\tau_h}{\Delta t}$, $N_s = \frac{T_s}{\Delta t}$ and T_s is the duration of the transmit waveform. The discrete-time system replaces the continuous-time system with negligible loss of information. Equation (26) represents a tapped delay line model of the reverberation channel [3].

Now assume that $\tau_h \gg T_s$ so that $N_h \gg N_s$ and assume that $N \approx N_T \approx N_h$ samples of $y[n]$ are collected. Performing an N point discrete Fourier transform (DFT) on $y[n]$, the linear convolution in (26) can be approximated with a circular convolution and can be written in the frequency domain as

$$\tilde{Y}[k] = \tilde{H}[k]\tilde{S}[k], \; k = 0, 1, \ldots, N-1, \tag{27}$$

where the DFT of $y[n]$ is defined to be $\tilde{Y}[k] = \sum_{n=0}^{N-1} y[n]\exp(-j2\pi nk/N)$, $k = 0, 1, \ldots, N-1$.
Now $\tilde{H}[k]$ is derived from $\tilde{Y}[k]$ by division under the assumption that $\tilde{S}[k] \neq 0$, $k = 0, 1, \ldots, N-1$.

Given the sample period above, the DFT approximates the CTFT reasonably well, that is, $\tilde{Y}[k]$ can be replaced with $Y[k]$, $\tilde{S}[k]$ with $S[k]$, and $\tilde{H}[k]$ with $Y[k]$. Also note that the discrete frequency index k corresponds to frequencies $\frac{k}{N\Delta t} \approx \frac{k}{\tau_h + T_s}$ so the sample period of the DFT output is $\frac{1}{\tau_h + T_s} < \frac{1}{\tau_h}$, which satisfies the requirement to minimize aliasing of the scattering function in (13). Note also that the $h[n]$ are samples from an independent, complex Gaussian random process, that is $h[n] \sim \mathcal{CN}(0, r[n])$, where

$$r[n] = r_h(\tau = n\Delta t). \tag{28}$$

The tap weights of the tapped delay line model are independent, zero-mean, complex Gaussian random variables, where the variance of $h[n]$ is $r[n]$. Finally, from (12), (15), (16), and (28), it can be seen that

$$\begin{aligned} r[n] &= r_h(\tau = n\Delta t) = r(\tau = n\Delta t) \\ &= r(\tau' = \frac{n\Delta t}{\tau_h}) = r(\tau' = \frac{n}{N_h}) \approx r(\tau' = \frac{n}{N}), \\ &\quad n = 0, 1, \ldots, N-1. \end{aligned} \tag{29}$$

The $r[n]$ are referred to as the "sampled range-scattering function" and are the quantities that are estimated with the MLE technique described in the previous section. In order to illustrate the efficacy of this approach and point out some of the processing details, several examples using actual in-water data are presented in the next section.

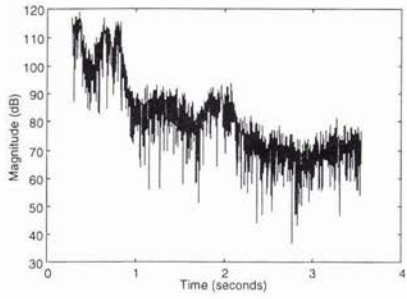

Figure 2: Time-series: Ping 1

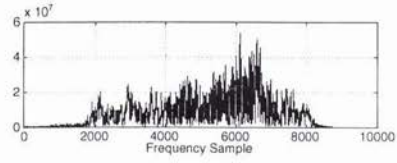

Figure 3: Spectral Content of Ping 1

6. IN-WATER RESULTS

The data were collected in approximately 100 meters of water. The sonar array transmitted a large time-bandwidth waveform ($T_s \approx 0.3$ seconds, $B \approx 2000$ Hz) and received the reverberation return while operating at a depth of approximately 30 meters. The element level data of the sonar array were processed to produce a digital version of the complex lowpass representation of the reverberation returns and the sum beam time-series was generated from the element level outputs. This is the time-series referred to as "$y[n]$" in (26). Figure 2 is the reverberation return time-series from the data set designated "Ping 1."

Figure 3 shows the spectral content of the time-series data of Ping 1 obtained by performing a DFT on the data. Note that this time-series possesses good spectral support over a wide frequency range (i. e. , $S[k] \neq 0$ over a wide range of frequencies). Since the AR modeling approach requires the estimation of only a small number of parameters ($p+1$, and in the examples shown in this section, $p = 13$ was chosen), not all of the data in Figure 3 must be processed. Frequency samples $5000 - 6000$ were chosen for this example and the deconvolution operation was performed.

When these data are inserted into (17), the MLEs of the AR coefficients produce an MLE of the sampled range-scattering function shown in Figure 4. When this scattering function estimate is convolved with the squared magnitude of the transmit signal (essentially a boxcar function of duration T_s seconds), an estimate of the intensity of the received time-series is produced (see (8) for the continuous-time version of this relationship). Figure 5 shows the intensity estimate for Ping 1. Note that there are transient effects contained in the results, but when these effects are removed and the intensity estimate is plotted along with the original time-series data, as in Figure 6, the intensity estimate follows the complex structure of the reverberation time-series very closely.

The scattering function estimate (Figure 4) was then used to generate a realization of the random impulse response via the use of a random number generator. This impulse response was used to simulate a reverberation time-series via (26). Figure 7 shows a plot of the original time-series in the top trace and the simulated time-series in the bottom trace. The similarity between the two time-series appears to be rather close, indicating that AR modeling of the range-scattering function shows promise. Note that additional simulated realizations of the time-series can be obtained by simply generating new realizations of the impulse response using the estimate of the sampled range-scattering function and the random number generator.

Another data set was examined to test the robustness of the AR approach. Data set designated "Ping 2" was processed in the same manner as Ping 1. This includes using the same model order $p = 13$. Since the sonar was moving through the water, these data were taken in slightly different water mass from Ping 92. Figure 8 shows the intensity function estimate and the in-water time-series for Ping 2. Comparing Figures 6 and 8, it is readily seen that each of the time-series is quite different, but the AR approach is able to capture the complex structure of each.

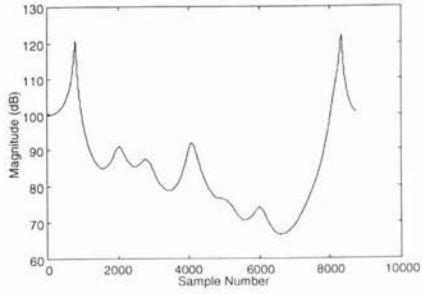

Figure 4: Scattering Function Estimate: Ping 1

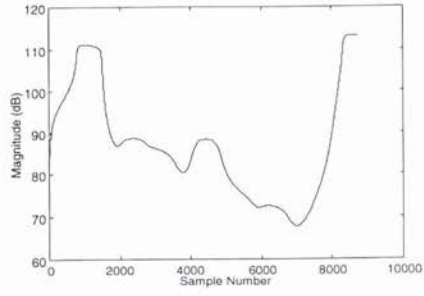

Figure 5: Intensity Function Estimate: Ping 1

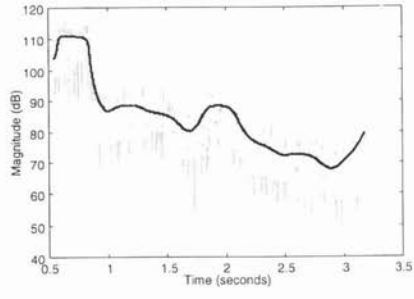

Figure 6: Intensity Function Estimate and Time-series: Ping 1

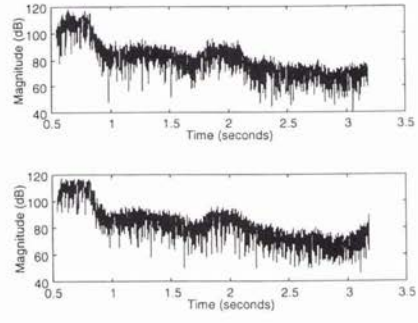

Figure 7: Actual and Simulated Time-series: Ping 1

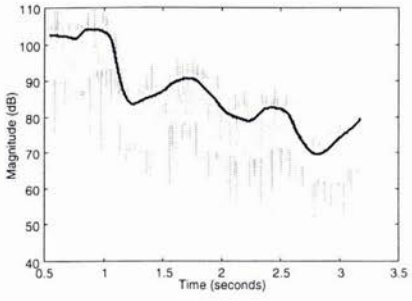

Figure 8: Intensity Function Estimate and Time-series: Ping 2

References

[1] J. C. Luby, "Autoregressive Modeling of Nonstationary Multibeam Sonar Reverberation," *IEEE Journal of Oceanic Engineering*, vol. OE-12, January 1987, pp. 116-129.

[2] W. S. Hodgkiss, "An Oceanic Reverberation Model," *IEEE Journal of Oceanic Engineering*, vol. OE-9, April 1984, pp. 63-72.

[3] H.L. VanTrees, *Detection, Estimation, and Modulation Theory, Part III.* J.Wiley, New York, NY, 1971.

[4] L.J. Ziomek, *Fundamentals of Acoustic Field Theory and Space-Time Signal Processing*, CRC Press, Boca Raton, FL, 1995.

[5] D. Middleton, "A Statistical Theory of Reverberation and Similar First-Order Scattered Fields," *IEEE Trans. Inform. Theory*, vol. IT-13, no. 3, July 1967, pp. 372-414.

[6] R.S. Kennedy *Fading Dispersive Communication Channels.* J.Wiley, New York, NY, 1969.

[7] J.G. Proakis, *Digital Communications.* McGraw-Hill, New York, NY, 1983.

[8] S. Kay, *Modern Spectral Estimation.* Prentice-Hall, Englewood Cliffs, NJ, 1988.

[9] S. Kay and V. Nagesha, "Maximum Likelihood Estimation of Signals in Autoregressive Noise," *IEEE Trans. Signal Process.*, pp. 88-101, January 1994.

Measurement and Interpretation of Angular Spreading from Multiple Boundary Interactions in a Shallow Water Channel

Peter H. Dahl and Warren L. J. Fox[1]

Applied Physics Laboratory
College of Ocean and Fishery Sciences
University of Washington
Seattle, WA 98195 USA
E-mail: dahl@apl.washington.edu; warren@saclantc.nato.int

Abstract

The problem of angular spreading of sound that has undergone multiple boundary scattering (both sea surface and sea bed) in a shallow water channel is discussed. Measurements made of the horizontal spatial coherence along a line array are related directly to the horizontal angular spread. The data are interpreted within the framework of a probability density function (PDF) for angular spread. The multiple-bounce situation is interpreted by convolving PDF's associated with each single bounce, wherein each single-bounce PDF is computed as if the other boundary interaction were replaced by a perfect mirror reflection.

1. Introduction

In shallow, littoral regions the acoustic transmission channel is typically governed by the process of multiple forward scattering from both the sea surface and the sea bed. With each boundary interaction, the signal may be further spread in time, frequency, and angle. In this paper we present results of an experimental study of the spatial coherence (or, equivalently, angular spreading) of high-frequency sound that has undergone multiple boundary interactions and therefore has been dispersed in angle. Measurements of the horizontal coherence along a line array oriented transverse to the direction of propagation are related directly to the net horizontal angular dispersion.

Both passive and active undersea acoustic detection and localization systems utilize horizontal arrays of receivers. Beamforming algorithms can then give increased signal-to-noise ratios for detection and high degrees of spatial resolution in the horizontal plane for localization. Such beamforming algorithms usually assume perfectly coherent plane-wave propagation for predicting performance. However, as presented in this paper, forward scattering of propagating signals from the sea surface and bottom can significantly degrade the performance of beamforming algorithms owing to loss of horizontal coherence. A thorough understanding of these processes is therefore necessary for determining the performance bounds of such systems.

2. Experimental Description

The experiment was conducted near the Dry Tortugus collection of islands (24°36.7′N 82°50.7′W) off south Florida. The water depth was 25.6 m, and the bottom consisted of calcium shell deposits and soft mud. The experimental layout for the forward-scattering measurements is shown in Figure 1. Signals were transmitted from one of two ITC-1032 omnidirectional transducers suspended from a spar buoy at depths of 7.7 and 17.2 m. The spar buoy was tethered to the research vessel *Seaward Explorer* (placed in a four-point moor) at ranges between 70 and 100 m and tended by a small boat for final positioning. The natural period of the spar buoy was 12 s, well away from the period of the dominant surface waves.

[1]Current address: SACLANT Undersea Research Centre, Viale S. Bartolomeo 400, 19138 La Spezia, Italy

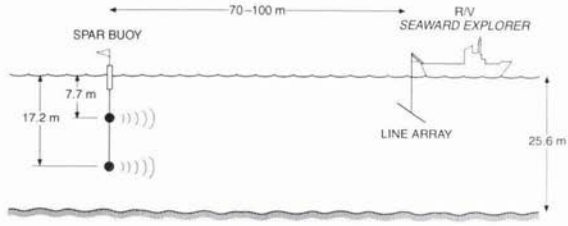

Figure 1: Experimental layout for the forward scattering measurements.

An experimental run consisted of 20 pulses transmitted at 5-s intervals. The pulses were cw transmissions of length 1 ms and frequency 30 kHz. At this frequency, the roughness parameter defined as $2kH \sin\theta_g$, where k is acoustic wavenumber, H is rms waveheight, and θ_g is grazing angle associated with the nominal specular point, ranged between 3 and 10. The signals were received on a horizontal line array suspended off the stern of the research vessel at a depth between 7 and 10 m. A bracing structure (not shown) was used to restrict other than controlled array rotation, and a damping mechanism was used to reduce array heave motion.

We simultaneously recorded signals from the eight-element array, on which the minimum and maximum element separations were 1.59 and 57.15 cm, respectively. (Note that during the experiment elements 7 and 8 became inoperable, which reduced the maximum separation to 31.75 cm and the element-spacing combinations from 28 to 15.) Details on data acquisition, data reduction, and the procedure for estimating spatial coherence are given by Dahl [1], who discusses similar measurements made in a deep water environment. Note that this procedure also includes a phase correction for any slight array rotation which invariably occurs during the 100-s averaging interval. We assume the received signal (of relative bandwidth 3%) is composed of only one frequency component, and thus the results given below are expressed in terms of the receiver separation normalized by the acoustic wavelength equivalent to 30 kHz.

Figure 2a illustrates the dominant ray paths that compose the arrival structure for a typical experimental run. With a 1-ms pulse, the first few paths can be resolved (Fig. 2b), and their spatial coherence studied separately. In particular, the horizontal spatial coherence for the surface-bounce, bottom-bounce, and surface–bottom bounce paths is derived from the time-windowed segments as shown in Figure 2b. Notice that the two bottom-interacting paths suffer an energy loss of approximately 25 dB, as bottom grazing angles exceed the critical angle (approximately 10°). The surface-bounce paths, on the other hand, experience essentially 0 dB energy loss for this run, during which the wind speed was 3.8 m/s.

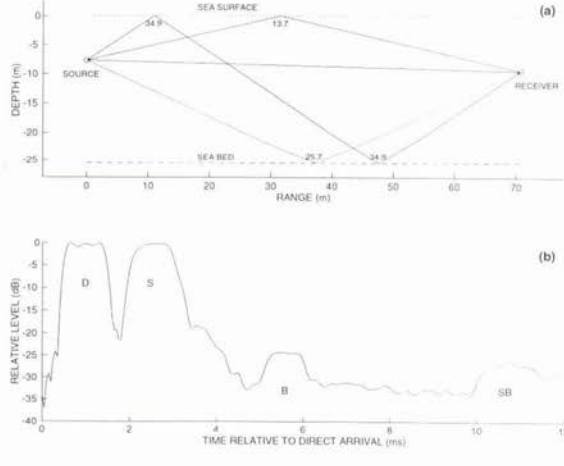

Figure 2: (a) Dominant ray paths contributing to a typical arrival structure. The nominal grazing angle (in degrees) for each boundary interaction is noted. (b) Ensemble average of forward-scattered signals showing the primary arrivals: direct (D), surface bounce (S), bottom bounce (B), and surface–bottom bounce (SB).

Thus, for this combination of $O(100)$ m range and mid-water source and receiver depths, this particular acoustic channel is dominated by the direct and single-surface-bounce paths. The acoustic measurements were accompanied by measurements of wind speed and direction and surface waveheight spectra. Wind-speed measurements were made at a height of 6.9 m above the sea surface and off the stern of the *Seaward Explorer* (this location resulting in minimal interference from vessel structures). Surface-wave displacement spectra, including directional information, were measured using a directional wave buoy moored approximately 200 m from the *Seaward Explorer*, and data were radio transmitted back to the vessel every hour. Conductivity, temperature, pressure (CTD) measurements were made approximately every 3 hours. The conditions were such that the sound speed profile was nearly isovelocity, with a sound speed of 1520 m/s. Bottom properties for this site are discussed in greater detail in a related paper [2] on the same experiment.

3. Interpretation of Spatial Coherence Associated with Single Boundary Interaction

Figure 3 shows the horizontal coherence for single-boundary-bounce paths as measured in three experimental runs. The three solid lines represent data from surface-bounce measurements, and the dashed line represents data from a bottom-bounce measurement (we postpone its discussion for now). Referring now to the surface measurements, the two runs symbolized by open circles and triangles were taken back to back but with different geometries (in this case, different source depths); otherwise the sea surface environment, as characterized by a wind speed of 3.8 m/s and an rms waveheight of 16 cm, was the same for each run. The third run (symbolized by asterisks) was taken with yet another geometry but also under different environmental conditions, characterized by a wind speed of ~ 1 m/s and an rms waveheight of 7.5 cm.

The solid lines are, in fact, from a model [1] for the horizontal spatial coherence resulting from forward scattering from the sea surface. The model is based on the high-frequency limit of the Kirchhoff approximation for computing the bistatic cross section (applicable only to forward scattering in the near-specular region). This quantity is related to the horizontal coherence by first forming a probability density function (PDF) for the arrival angle. In this case, the relevant PDF is the marginal PDF corresponding to the horizontal arrival angle, and it converts to horizontal coherence via a Fourier transform. This approach highlights the interrelations between the bistatic cross section, the horizontal angular density function, and the horizontal coherence. The solid lines can also be represented well by Gaussian parametric curves of the form $|\Gamma| = \exp(-(kd\sigma_{\theta_h})^2/2)$, where d is the element separation and the parameter σ_{θ_h} is the rms horizontal arrival angle. Estimates of σ_{θ_h} for the three solid lines, in order of decreasing coherence, are 0.57°, 0.86°, and 1.70°.

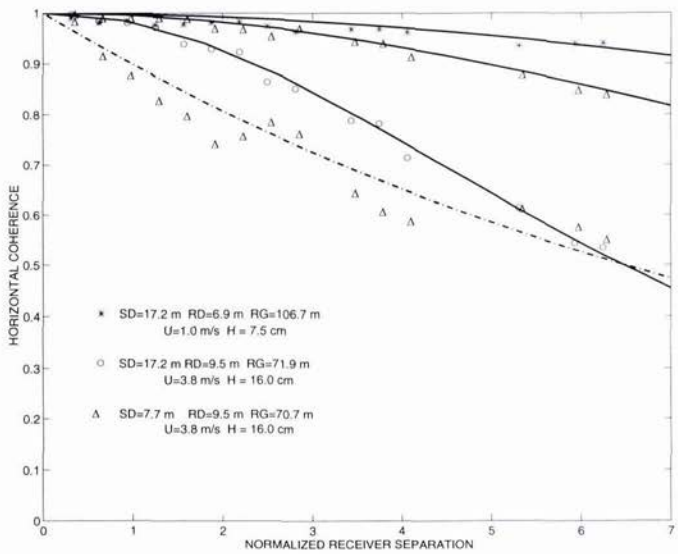

Figure 3: Horizontal coherence for single-boundary-bounce paths as measured in three experimental runs. The key geometric variables of source depth (SD), receiver depth (RD), and range (RG) are given along with the key sea-surface environmental variables of wind speed (U) and rms waveheight (H).

The case where only the geometry has changed is readily understood by the relation discussed in [1],

$$\sigma_{\theta_h} \propto \frac{s_L \sin\theta_g}{1 + RD/SD}, \tag{1}$$

where s_L is the rms large-scale sea-surface slope and RD and SD are the source and receiver depths, respectively. In both runs, $RD = 9.5$ m, but in the second run SD has changed from 17.2 m to 7.7 m, and θ_g has changed from 20.4° to 13.7°. Using these values, (1) predicts that the deeper source should result in about twice the horizontal angular spread, which is consistent with the estimates of σ_{θ_h}. This not only demonstrates the dramatic effect that array acquisition geometry has on spatial coherence, but also shows how coherence estimates obtained in one geometry can be translated to another geometry.

Understanding the effect of changing wind speed and surface conditions on the spatial coherence requires examination of the frequency spectra for surface waveheight taken at the same time as the acoustic measurements (Fig. 4). The maximum resolvable frequency for the wave-buoy measurements is 0.58 Hz, and thus beyond this point (about four times the peak frequency) we have appended an f^{-5} tail in order to compute the rms (large-scale) slope s_L as required by the coherence model. The large-scale slope is estimated using

$$s_L^2 = \frac{(2\pi)^4}{g^2} \int_0^{f_c} f^4 S(f) df \ , \tag{2}$$

where the cut-off frequency f_c is related to the cut-off wavenumber K_c via $(2\pi f_c)^2 = gK_c$ (g = gravitational constant) and defines what we mean by large scale (also cf. Ref. [1]). Numerical simulations [3] suggest setting $K_c = 0.25k$ which gives $s_L = 0.044$ for the lower wind speed case and $s_L = 0.100$ for the higher wind speed case. The actual s_L values used to produce the solid-line model fits in Fig. 3 were 0.055 and 0.105, which are remarkably close to the estimates based on (2) and the measured surface wave spectra. It is important to note that the precise form of the spectral decay is not a settled issue. Our use of f^{-5} follows that of Banner [4] (see also [5]), although others [6] suggest a less rapid decay. Furthermore, the directional information gathered by the wave buoy has been collapsed, or averaged out, in the omnidirectional spectra shown in Fig. 4. We are presently constructing full 2-D surface wave spectra and will revisit these measurements in a future work.

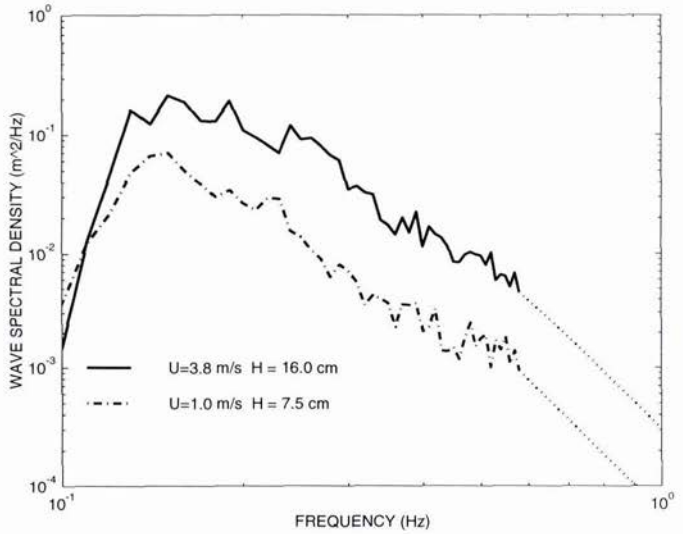

Figure 4: Frequency spectra for surface waveheight measurements taken at same time as the acoustic measurements shown in Fig. 3.

Finally, an estimate of the single-bottom-bounce coherence is also shown in Fig. 3 (open triangles, with dashed line representation). The line is an exponential curve of the form $|\Gamma| = \exp(-kd\beta)$, where the parameter β is equivalent to $\sigma_{\theta_h}/1.67$. These data are from the third arrival shown in Fig. 2b (shortly before 6 ms). For comparative reference, estimates of σ_{θ_h} for the first three arrivals in Fig. 2b, i.e., the direct path, surface-bounce path, and bottom-bounce path, are $< 0.5°$, 0.86°, and 1.63°. The bottom-bounce data in Fig. 3 also show slight oscillatory behavior, perhaps associated with bottom roughness in a manner described by Gulin and Malyshev [7]. At this stage we shall not interpret the oscillations and proceed with the smooth exponential curve representation.

4. Estimates of Spatial Coherence Associated with Multiple Boundary Interactions and Their Interpretation via Convolution of Angular PDFs

In this section we show that the measured spatial coherence functions for multiple boundary interactions are reasonably approximated by multiplying the spatial coherence functions associated with a single surface and a single bottom interaction. The interpretive framework here is that of convolving individual PDFs to arrive at the PDF for the sum of random variables. In this case, spatial coherence represents the characteristic function for the PDF of the horizontal arrival angle, and thus multiplication applies.

Tuteur and McDonald [8] developed a rigorous formalism for the time spreads associated with multiple-bounce acoustic channels, assuming certain spatial statistics apply to both surfaces. We postulate, in an analogy to the time spread model in [8], that the total horizontal angular spread is the sum of the angular spreads from individual bounces, wherein the spread from each bounce is computed as if the other boundary interaction were replaced by a perfect mirror reflection. Figure 5 illustrates this process for the surface–bottom path shown in Fig. 2a. A virtual source is used for the bottom-bounce segment (replacing the initial surface bounce), with SD equal to 33.3 m and RD equal to 16.1 m as measured from the sea bed. A virtual receiver is used for the surface-bounce segment (replacing the bottom bounce), with SD remaining at 7.7 m and RD now going to 41.7 m as measured from the sea surface.

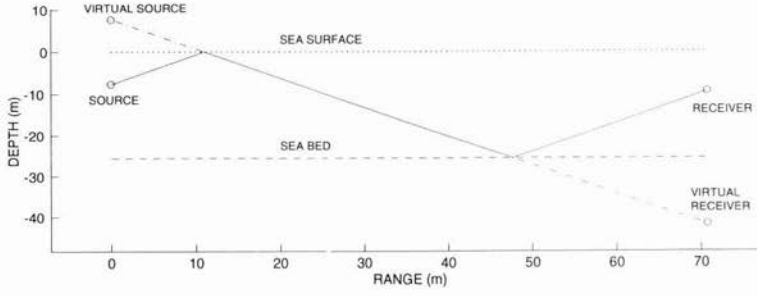

Figure 5: Illustration of process used to calculate total horizontal angular spread for the surface–bottom path shown in Fig. 2a.

Figure 6 shows estimates of the horizontal coherence for the surface–bottom bounce path that arrives shortly after 10 ms (Fig. 2b). The dashed line labeled SURFACE BOUNCE is derived from the aforementioned model [1] for surface coherence, using $s_L = 0.105$ and the new geometry illustrated in Fig. 5 for the surface bounce-to-virtual receiver path. The dashed line labeled BOTTOM BOUNCE is the result of transforming β as per (2), using the new geometry illustrated in Fig. 5 for the virtual source-to-bottom bounce path. Their multiplication, equivalent to convolving the angular PDFs for horizontal arrival angle, is shown by the solid line, with agreement to the measurements being quite satisfactory for coherence estimates that exceed about 0.45.

Two other examples of this method are shown in Figs 7a and 7b, in this case representing the surface–bottom (7a) and the bottom–surface (7b) bounce paths for the experimental run that immediately preceded the run discussed in Fig. 2. Thus $s_L = 0.105$ is again used for the surface coherence model, but the associated single-bounce geometries shown in Fig. 5 differ. Though agreement with the data is clearly better in Fig. 7a, in both examples the characteristic shape of the data is reproduced by the method.

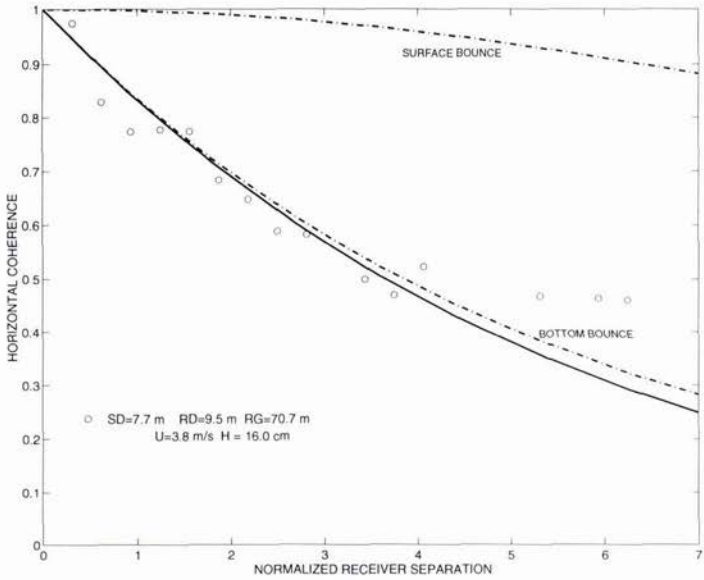

Figure 6: Horizontal coherence for surface–bottom bounce path shown in Fig. 2b, which arrives arrives shortly after 10 ms. The key geometric variables of source depth (SD), receiver depth (RD), and range (RG) are given along with the key sea-surface environmental variables of wind speed (U) and rms waveheight (H).

5. Summary

In this paper we have presented measurements of the horizontal spatial coherence of high-frequency sound that has been forward scattered from the sea surface, the sea bed, and their combination. The measurements were made at 30 kHz in a shallow-water channel of depth 25.6 m.

The single-bounce surface coherence estimates have been interpreted using a model based on bistatic scattering from the sea surface, applicable to the near-specular region, with model–data agreement being quite satisfactory. This model requires an estimate of rms large-scale slope, which was in turn derived from estimates of sea surface wave spectra taken at the same time as the acoustic measurements.

The multiple-bounce coherence estimates have been interpreted in terms of the convolution of PDFs for horizontal arrival angle, or equivalently, multiplication of horizontal coherence functions. The coherence functions in this case are associated with boundary interactions involving the surface and bottom separately and are computed as if the other boundary interaction were replaced by a perfect mirror reflection. The method described here can be readily generalized to two or more interactions with a surface or bottom scattering interface, as would apply to longer-range propagation in shallow water.

6. Acknowledgments

This work was supported by the Office of Naval Research, Code 321 OA.

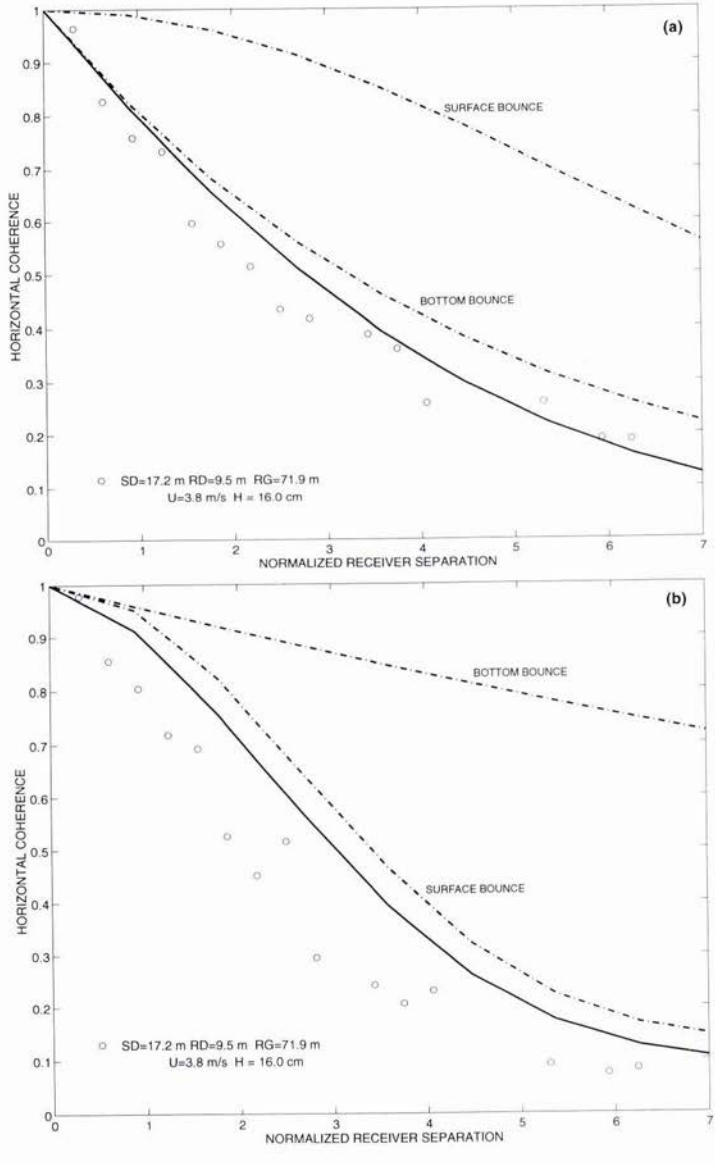

Figure 7: Same as Fig. 6 but for the experimental run immediately preceding the one in Fig. 2. (a) surface–bottom coherence; (b) bottom–surface coherence.

References

[1] P. H. Dahl, "On the spatial coherence and angular spreading of sound forward scattered from the sea surface: Measurements and interpretive model," *J. Acoust. Soc. Am.*, vol. 100, pp. 748–758, 1996.

[2] K. L. Williams and D. R. Jackson, "Bottom bistatic scattering: Experimental results and model comparison for a carbonate sediment," this issue, 1997.

[3] S. T. McDaniel and D. F. McCammon, "Composite-roughness theory applied to scattering from fetch-limited seas," *J. Acoust. Soc. Am.*, vol. 82, pp. 1712–1719, 1987.

[4] M. L. Banner, "Equilibrium spectra of wind waves," *J. Phys. Oceanogr.*, vol. 20, pp. 966–984, 1990.

[5] J. R. Apel, "An improved model of the ocean surface wave vector spectrum and its effects on radar backscatter," *J. Geophys. Res.*, vol. 99, pp. 16269–16291, 1994.

[6] R. E. Glazman, "Surface gravity waves at equilibrium with a steady wind," *J. Geophys. Res.*, vol. 99, pp. 5249–5262, 1994.

[7] E. P. Gulin and K. I. Malyshev, "Experiments in the spatial correlation of the amplitude and phase fluctuations of acoustic signals reflected from a rough ocean surface," *Soviet Physics-Acoustics*, vol. 10, pp. 365–368, 1965.

[8] F. B. Tuteur and J. F. McDonald, "Scattering function for multiple-bounce underwater acoustic channels," *J. Acoust. Soc. Am.*, vol. 64, pp. 614–621, 1978.

Seabed Sediment Characteristics Assessed Geophysically: Results of Experiments in the Clyde Sea, Scotland

Angela Davis, Ronald Haynes & Dei Huws

School of Ocean Sciences
University of Wales, Bangor
Menai Bridge
Anglesey
Wales, UK

Abstract

Within a research programme aimed at developing in situ sediment classification methodologies, it has been demonstrated that with only limited ground truth information, sub-bottom profiler data can be inverted to produce quantitative information on the spatial distribution of surficial sediment physical properties. Further, it has also been shown that using an integrated approach to the analysis of seismic shear wave velocity data and reflection responses can help discriminate subtle variations in the seabed sediment properties.

1. Introduction

In the past few years, there has been increasing interest in geophysical remote sensing of sea floor sediment properties, in particular, in research related to developing *in situ* sediment classification methodologies capable of providing input data for geo-acoustic and mine burial models. At the University of Wales, Bangor (UWB), research in this field has progressed along two fronts:

(i) research into extracting physical/geotechnical information from the seismic reflection response, and

(ii) studies of sediment seismic shear wave propagation characteristics, including development of methodologies for underway measurement.

This paper presents results of a series of integrated experiments (seismic reflection and shear wave) carried out in Irvine Bay, Scotland, an area of the eastern Clyde Sea near Glasgow, in 1995. The aims of the experiments were:

(i) to acquire high quality, high resolution digital sub-bottom profiler data in a suitable format for processing and analysis of the sea floor reflection response,

(ii) these data to be acquired in an area offering appropriate ground truth information to enable calibration of the sea floor reflection response and ultimately, to allow validation of the seismo-acoustic physical property predictions,

(iii) to process the acquired seismic data to provide maps of the physical property distribution in the area using geotechnical processing algorithms developed at UWB (on the basis of published empirical acoustic-physical property relationships), and

(iv) to acquire complementary shear wave velocity data to help interpret any anomalous areas observed on the `seismo-acoustic property` maps.

2. Background

2.1 High resolution seismic reflection studies

It has been known for several decades that the sea floor reflection coefficient (or acoustic impedance) can be used for the broad classification of sea floor sediment type e.g., [1]. During recent studies carried out in other areas [2], "in press" [3], the Marine Geophysics Group at UWB has demonstrated the potential for using the seismic reflection response recorded during surveying with a conventional boomer sub-bottom profiler system to provide semi-quantitative information on sea floor sediment properties. In the absence of precise quantitative control, the previously reported studies concentrated on attempting inferences on sediment property variability on the basis of spatial change in the relative reflection strength and bottom reflectivity variance. However, within the current study reported herein, interpretation of the seismic reflection response has been taken a stage further, with laboratory-derived control data (in the form of measured physical properties) used to calibrate the reflection response, thereby enabling a more 'absolute' acoustic measure of the *in situ* sediment properties.

2.2 Shear wave studies

As reported previously [4], there is clear correspondence between the surface sediment seismic shear wave velocity, sediment grade and bathymetry within the study area. In general, deeper water is characterised by the presence of muds of low shear wave velocity (c. 30 m/s); the areas of shallower water are predominantly sands and muddy sands displaying higher shear wave velocities (60-90 m/s) suggesting a bathymetric control on sediment properties. For the purpose of the current study (1995 experiment), the shear wave survey concentrated on a neighbouring sector of Irvine Bay, with the primary objective being the provision of information to help interpret any anomalies arising from the seismic reflection interpretation.

3. Data acquisition

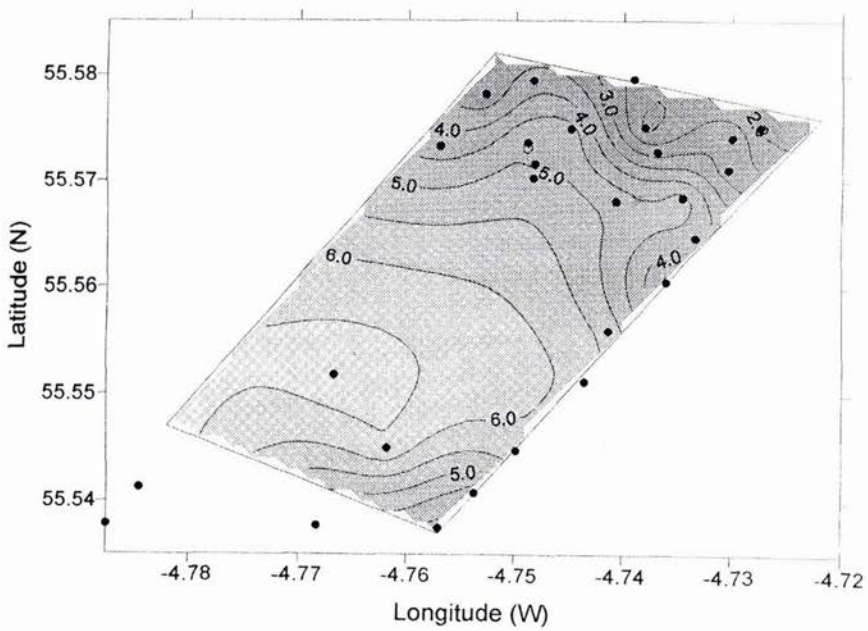

Figure 1: Grab sampled mean grain size

3.1 Seismic reflection response

High resolution digital seismic reflection data were acquired using a Uniboom surface towed source and a separately-towed hydrophone. Data were recorded digitally on an Elics-Delph 2 marine digital acquisition system. Sub-bottom profiles were initially interpreted to provide information on subsurface structure and seismic character of the various sedimentary units, en route to constructing a seismic stratigraphy for the area. The second stage interpretation was directed towards the extraction of physical/geotechnical information from the digital seismic reflection response.

3.2 Shear wave velocity

The UWB bottom-towed geophysical sledge [5] was used to acquire shear wave velocity data for the surficial sediment cover in a pseudo-underway fashion. For the shear wave measurements, the sledge-mounted horizontally-polarised shear wave source was fired at discrete locations along the survey track, with signals detected by an integral bottom-towed multi-element geophone array. Recorded travel-time data were inverted to provide information on the spatial variability of shear wave velocity in the upper 2-3 metres of the sediment cover. For the purpose of this study, the interpretation concentrated on arrivals at near source detectors in order to provide a velocity measure for the immediate surface layer.

3.3 Grab and core sampling

Thirty grab samples and three gravity cores were collected to provide a range of ground truth information. Core samples were both X-rayed and logged for compressional wave velocity prior to extrusion from the core barrel. In the laboratory the core material was analysed for grain size characteristics, moisture content, specific gravity of the grains, bulk density, porosity and shear strength. Grab samples were analysed for grain size distribution, with the data from all the samples used to produce grain distribution maps for the survey area (Figure 1).

4. Properties from the reflection response

4.1 Processing the seismo-acoustic data

In the first instance, the raw boomer data were compiled and processed to enable maps of the relative bottom reflectivity strength and shot-to-shot reflectivity variance to be produced. The bottom reflectivity variance i.e. the shot-to-shot variance of the relative bottom reflectivity strength, was calculated over a window of 40 shots. Ground truth data from the laboratory core analyses were then used to calibrate the relative reflectivity strength at the fixed core locations, this then allowing conversion of the relative bottom reflectivity strengths to absolute measures of the bottom reflection coefficient. The bottom reflection coefficient (or acoustic impedance) values could then be inverted to produce geophysically-determined maps of the bulk density, porosity and mean grain size of the sea floor sediments.

4.1.1 Calibration and inversion

The calibration of the seismo-acoustic data was carried out using the porosity and density information from the three gravity cores. Using the empirical equations of Richardson and Briggs [6], it was possible to determine an empirically-derived reflection coefficient for each of the cores for both density and porosity data. A linear regression technique was then used to determine the linear relationships between reflection coefficient and bottom reflectivity strength, making it possible to produce a reflection coefficient map for the entire area (Figure 2). Thenceforth, the same empirical relationships [6] were used to invert the seismo-acoustic data for the physical properties (bulk density, porosity and grain size) of the surficial sediment cover (using the UWB developed geotechnical processing algorithms).

4.2 Sediment type and grain size

The acoustically-derived sea floor sediment types, defined in terms of mean grain size, indicate that the south-western two-thirds of the area surveyed comprises sandy mud (Figure 3). This is in agreement with the published BGS map for the area [7]. As mentioned previously, there is a high degree of correlation between the grain size of the surficial sediments and the bathymetry. An examination of the seismo-acoustic data also shows a close relationship between bathymetry and the seabed reflection coefficients. For example, two topographic ridges in the area are associated with

areas of elevated reflection coefficients, providing an independent test of the strong inter-relationship between sea floor sediment type and bathymetry.

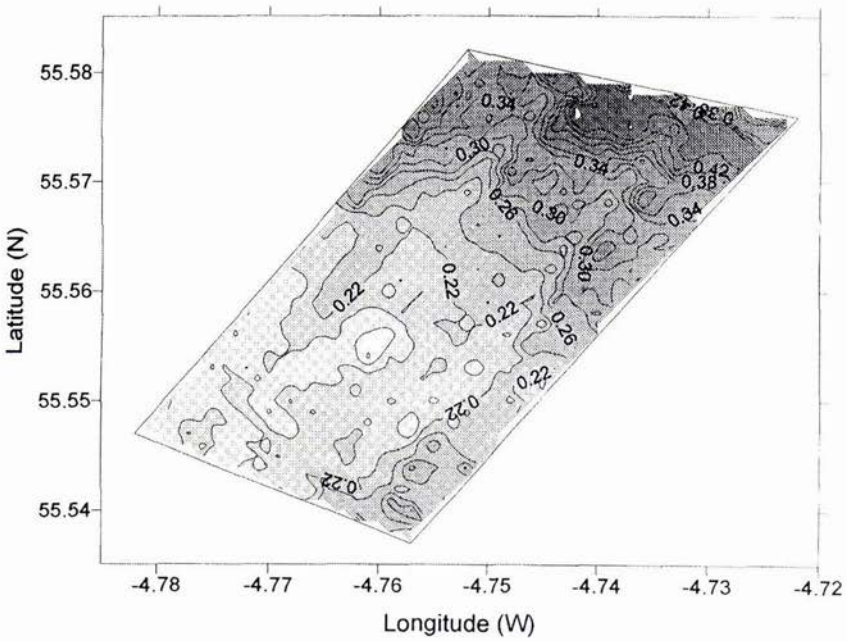

Figure 2: Sea floor reflection coefficient

Throughout the area there is good visual correlation between high reflection coefficients and low phi values (coarser grained sediments), the latter obtained from the analysis of grab samples. Similarly, there is a high degree of correlation between the acoustically-derived modified Folk sediment classification (based on the reflection coefficients) and the same obtained from grab samples. Further, examining the spatial distribution of surficial sediment across the survey area for both acoustically-derived and grab sample data, the contour boundaries between different sediment types appear markedly similar in position and form.

4.3 Bulk physical properties (bulk density and porosity)

Maps of acoustically-derived bulk density and porosity display similar trends to those seen for mean grain size distribution. Again, there seems to be a close inter-dependence between bathymetry and acoustically-derived properties, not unexpected on the strength of the earlier discussion.

4.4 Reflectivity variance as a sediment classification aid

Bottom reflectivity variance (Figure 4) can be used in a semi-quantitative manner to broadly discriminate between different types of sea floor as the parameter varies as a function of the sea floor sediment roughness. For the Irvine Bay survey, there was a high degree of visual correlation between the bottom reflection ceofficient and the shot-to-shot variance, the areas of high bottom reflection coefficients generally having correspondingly high values of shot-to-shot variability. This is to be expected as it is more probable that coarser grained sediments are both more highly reflective and more highly scattering; the latter is both as a consequence of the larger particle size and because these coarser sediments are more likely to exhibit bedforms (e.g. ripples).
Probably most importantly, shot-to-shot variance as a sediment discriminator allows areas where bottom surface scattering may be a problem (in acoustic sediment property inversion terms) to be recognised. With regard to the Irvine Bay data, areas of outcropping bedrock or glacial till could be identified by a combination of very high sea floor reflection coefficients (i.e. values that are above those of upper limits for normal marine sediments), and/or high shot-

to-shot bottom reflectivity variance. Clearly knowledge of bottom surface scattering is important if the results of acoustic surveys are to be used with confidence in sea floor sediment property prediction.

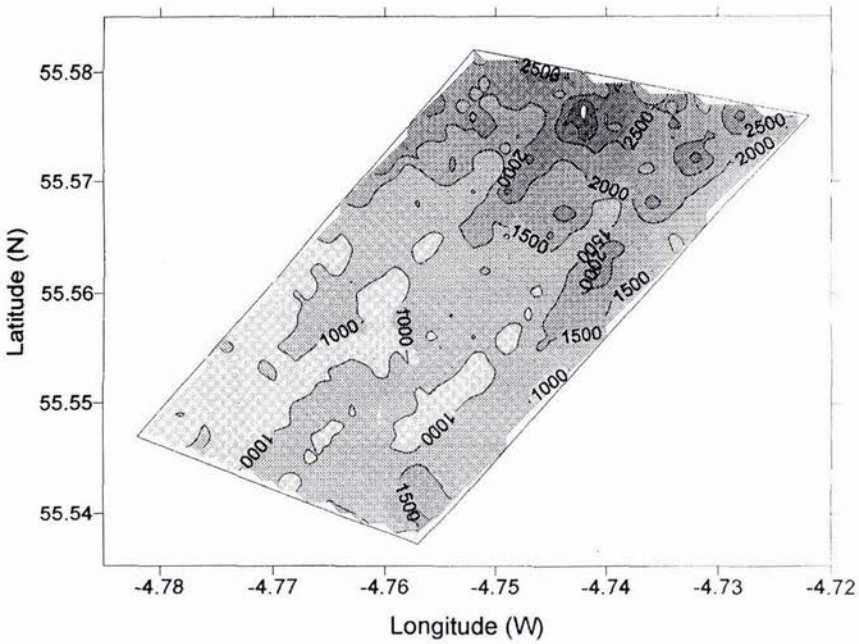

Figure 3: Sea floor reflectivity variance

4.5 Independent validation of the acoustic interpretation

To test the validity of the acoustic interpretation, a subset of the acoustically-derived physical property data was compared with a published data set produced from an independent laboratory study of the physical properties of the Irvine Bay sediments. The referenced data were gamma-density core logs acquired by the Admiralty Research Establishment in 1989 [8]. The ARE logs comprised a series of discrete density measurements at 10 cm intervals down the length of each core. Comparison of acoustically-derived densities with the gamma-density data yielded excellent agreement, lending support to the acoustic physical property classification methodology.

The second independent approach to method validation presented itself in terms of the comparisons between acoustic mean grain size predictions and grain size distributions produced from the analysis of grab samples. As with the independent density test and as discussed above (4.2), there appears to be close agreement between the acoustically-predicted and physically-derived properties.

5. Shear wave velocity data

5.1 Shear wave velocity as a sediment property indicator

The seismic shear wave velocity is widely recognised as an indicator of the structural strength of a sediment. Essentially the shear vibrations are translated through the skeletal frame of the sediment hence the relation to structural properties (of the sediment particle framework) and the significance for seabed classification/characterisation studies. Further comment on shear wave propagation in marine sediments and

velocity/physical property relations is beyond the scope of this paper but can be found in the expanding literature on the topic.

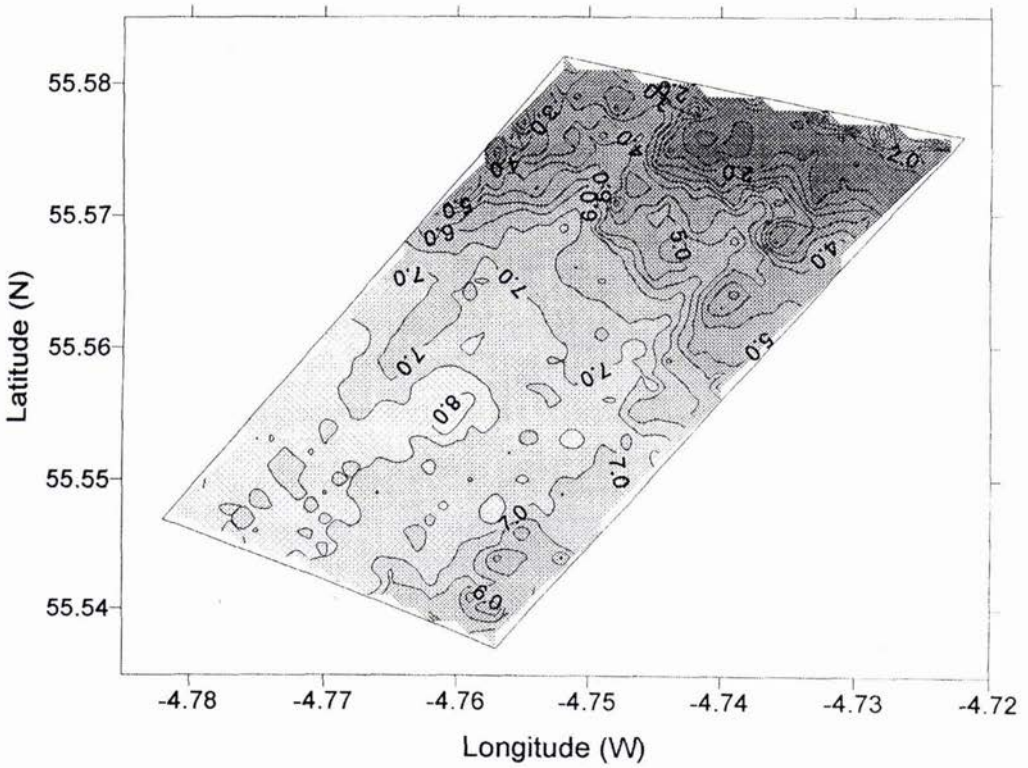

Figure 4: Acoustically derived sea floor mean grain size (phi)

5.2 Irvine Bay 1995 study

The velocity transect presented here as Figures 5. cross zones of the survey area (specifically the southernmost sector) which yielded subtle changes in sediment physical properties on the basis of the seismo-acoustic prediction. In the main part, these zones of subtle change occur in areas of predominantly finer grained sediment. On the basis of the seismo-acoustic prediction using boomer data, the south eastern margin of the area surveyed showed a decreased porosity, increased bulk density and increased grain size. For the same area, shear wave data show much scatter down this zone, but show subtly higher velocities at the start and end of the line with a mean value of c. 40-45 m/s. Those highs correspond with anomalies in the boomer property predictions, as do general trends in shear wave velocity along the southern margin of the area (in an east - west direction). Interestingly, a simultaneous survey with a USP Roxann system did not discern these anomalous zones.

5.3 Significance of the shear wave data

As well as providing inherently useful information in themselves, the shear wave data in this case have been shown to be capable of discerning very subtle changes in sediment properties. Indeed they have also revealed that the apparent increased sensitivity of the processed (inverted) boomer reflection response over the Roxann data may well be real and not artificial.

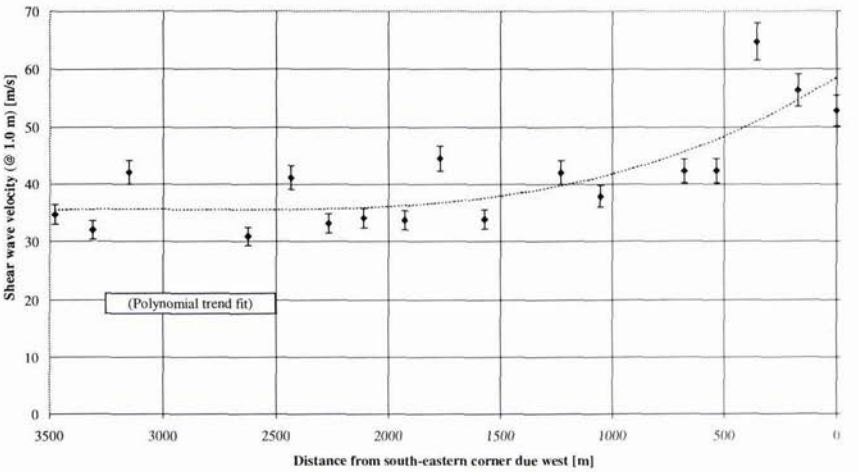

Figure 5: Variation of shear wave velocity along southern transect

6. Discussion and conclusions

Because of the highly variable nature of marine sediments and the problems associated with physically sampling sea floor materials, geophysical remote sensing methodologies probably hold the greatest potential for sea floor sediment classification/characterisation for a range of environmental and engineering applications. Further, it has become clear in recent years that engineering estimates and geo-acoustic models rely upon reliable *in situ* parameter estimates to provide a representative description of the sediment body.

Within this study it has been demonstrated that, with only limited ground truth information, it is possible to invert seismic reflection responses from sub-bottom profiler data to produce maps of the surficial distribution of sediment porosity, bulk density and mean grain size. Further, it has been shown that the seismic shear wave velocity is a sensitive indicator of sea floor sediment properties, and that the combined analysis of the sediment shear wave caharcter and seismic reflection response can be used to discriminate subtle variations in sea floor sediment properties.

Acknowledgements

The authors express their thanks to the captain and crew of the RV Prince Madog for their help with data acquisition at sea and to theDefence Research Agency for providing funding for the experiments.

References

[1] E.L. Hamilton, "Compressional wave attenuation in marine sediments," *Geophysics,* vol. 37, pp.620-646, 1972.
[2] R. Haynes, A.M. Davis, "Using seismic reflection attributes to resolve subsurface sediment characteristics," in *Proceedings of Modelling Methane-Rich Sediments at Eckernforde Bay,* Wever T.F. (Ed), FWG, Germany, pp. 44-49, June 1995.
[3] R .Haynes, D.G. Huws, A.M. Davis and J.D.Bennell, "Geophysical seafloor sensing in a carbonate sediment regime," *Geo-Marine Letters,* in press.
[4] D.G. Huws, A.M. Davis and J.D. Bennell, "Mapping of the seabed via in situ shear wave (SH) velocities," in *Shear Waves in Marine Sediments,* Hovem J.M. et al. (Eds.), Dordrecht. Kluwer Academic Publishers, pp.337-343, 1991.

[5] A.M. Davis, D.G. Huws, J.D. Bennell and D Thomas, "Development of a sea floor geophysical sledge," *Marine Geotechnology*, Vol. 8, pp.99-109, 1989.
[6] M.D. Richardson and K.B. Briggs, "On the use of acoustic impedance values to determine sediment properties," in *Proceedings of the Institute of Acoustics*, Vol. 15 (2), pp.15-24, 1993.
[7] British Geological Survey, Seabed Sediments and Quaternary Geology. Clyde Sheet 55 N - 06 W, 1:250 000 Series, 1985.
[8] UTH Tech Memo 23/89(C), "Analysis of cores from ARE (UTH2) Sea-bed Survey, October 1988," Sediment Analysis Services, 1989.

Critical Angle and Seabed Scattering Issues for Active-Sonar Performance Predictions in Shallow Water

Donald R. Del Balzo, James H. Leclere and Mona J. Collins

U.S. Naval Research Lab (7183)
Stennis Space Center, MS 39529-5004, USA
delbalzo@nrlssc.navy.mil

Abstract

Active sonar performance predictions (0.75 to 3 kHz) are examined in summer shallow-water environments to quantify the impact of variable seabed and watermass properties on detection. Scattering is computed with an environmentally sensitive modified Lambert's Law. The results show a) unmodified Lambert's Law yields optimistic performance by a factor of up to 30 in coarse sand, and b) with environmentally-sensitive scattering, performance is poor for sands (high reverberation) and clays (high TL) and optimum for silty areas.

1. Introduction

Naval operations in the post cold-war era are moving away from traditional, deep-water, fairly stable environments and into littoral regions where the water is shallow, complex and dynamic. The littoral environment presents significant new challenges in both (a) direct functions like sensor performance and tactics, and (b) supporting functions like environmental and sensor predictions, and environmental data surveys. Two mission areas of undersea warfare which are heavily influenced by local environmental conditions are Anti-Submarine Warfare (ASW) and Mine Counter-Measures (MCM). Most of the capability to perform ASW and MCM is with acoustic sensors (sonar) and associated systems at frequencies below 10 kHz for ASW and above 30 kHz for minehunting. For the analysis here, environmental influences on acoustic signals at ASW frequencies are considered in two categories; first, water-mass, as defined by water depth and sound-speed profiles, and second, the seabed sediment, as defined primarily by grain size and density. Future work will be directed toward the higher frequencies associated with minehunting.

In deep water, the effects of oceanography (e.g. internal waves, thermal fronts and eddies) on acoustic propagation and coherence can be significant but the physical processes and their impact on sonar performance are well understood and mostly predictable. However, in shallow water other processes, like tidal currents, fresh-water river outflows, solitons and surf waves may have significant influence on acoustic systems, by altering 4-D sound-speed structures. The space-time character of these water-mass processes is not well understood, nor easily predictable.

In deep water the sea bottom may not be a dominant factor in determining acoustic signal properties because upward refraction in the water column can reduce acoustic interaction with the bottom. However, in shallow-water areas most ASW operations involve significant acoustic interactions with the seabed which can have significant impact on sensor performance. Some mechanisms affecting performance at the seabed are transmission and reflection at the boundary (often described by bottom reflection loss), refraction and attenuation in the sediment, shear wave conversion in the bottom, creation of interface waves, and scattering (both forward and backward) at the interface and in the sediment. These phenomena are understood to varying degrees and their impact on acoustic signal properties are now being incorporated into advanced (research) models.

This analysis is focused on the ASW problem for tactical active sonars in shallow water. A fundamental question is addressed concerning the need to model low grazing angle energy with an adequate scattering kernel and the impact on reverberation over various sediment types as compared to using the environmentally insensitive Lambert's Law approach.

2. Scenario

This paper reports a simulation assessment of environmental impacts on active sonar performance in shallow-water, characterized by conditions found in the Strait of Sicily during the summer, when thermal conditions cause downward refraction and significant bottom interaction. Although the work is based on archival environmental information from a specific region, the data span a large set of bottom and water conditions which could apply at many other areas. The assessment is based on the predicted impact of variable environmental conditions on system performance, in terms of detection area.

The analysis has implication on actual tactical ASW operations because the sensor descriptions and scenarios are realistic (although generic). Specifically, the scenario involves notional sonars at 0.75 and 3 kHz operating at 50 m depth in 100 m water-depths against a zero-Doppler submarine with target strengths of 0 to 10 dB operating at 50 m depth. The source is modeled as a Hann-weighted 5-element vertical array, horizontally steered, with an intensity of 230 dB re µPa and a vertical beamwidth of 28 deg. The Hann weighting significantly reduces vertical sidelobes and undesirable reverberation. The receiver is modeled as a horizontal towed array with a broadside beamwidth of 10 deg which yields a 3-D directivity against omnidirectional noise of 13.6 dB. The sonar signal is a 100 ms CW pulse and the processor assumes incoherent integration over 3 pulses. The signal processing assumes a signal differential of 1.8 dB against noise and 9.5 dB against reverberation and a probability of false alarm of 10^{-4}.

2.1 Bottom Sediment Properties

Figure 1 shows the distribution of sediment types for the Strait of Sicily [1]. There is significant spatial variability, as seen by the localized regions with coarser grains (sands, silts without clay, gravel, pebbles, shells, and rock fragments) and larger regions with finer-grain material (sands and silts with clay in the northwest and around Sicily and fine silty-clays in the southeast).

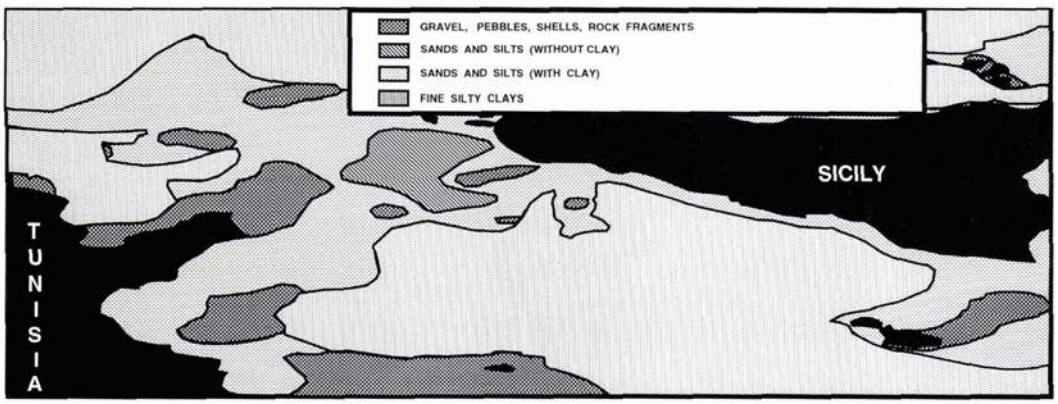

Fig. 1 Bottom properties in the Strait of Sicily.

A set of geophysical and geoacoustic descriptions, based on the sediment types shown in Fig. 1 and consistent with Hamilton's analyses [2], were constructed for this study. The sediments, which are considered to be thick (50 m) and upward refracting, are referred to by their phi-values (inversely related to their grain sizes, δ, as $\delta = [1/2]^{\phi}$). The six sediment types used here are coarse sand (ϕ=1), fine sand (ϕ=3), silty sand (ϕ=4.5), sand-silt-clay (ϕ=6), clayey silt (ϕ=7), and silty clay (ϕ=8.5). Standard geoacoustic properties (sound speed, density and attenuation profiles) were determined. There is a discontinuity in sound speed at the water-sediment interface which determines critical angles for bottom reflection. These discontinuities (in per cent) are 20, 13, 9, 3, 0.6, and -1 for coarse sand through silty clay, respectively, which give rise to critical angles (in deg) of 33.9, 27.9, 23.0, 13.6 and 6.3. Since the sound speed for silty clay is less than the water sound speed at the bottom, there is no critical angle, i.e.; there is penetration at all angles and there exists an angle of intromission at 9 deg where extremely high loss occurs. The sediment properties are listed in Table 1.

Sediment	Grain Size (mm)	Phi	Interface Discontinuity	Critical Angle (deg)
Coarse sand	0.500	1	20.5	33.9
Fine sand	0.125	3	13.2	27.9
Silty sand	0.044	4.5	8.6	23.0
Sand-silt-clay	0.016	6	2.9	13.6
Clayey silt	0.008	7	0.6	6.3
Silty clay	0.003	8.5	-1.1	----

Table 1. Sediment properties used in the analysis.

2.2 Water Sound Speed and Geoacoustic Profiles

Archival water sound speed profiles (SSPs) were extracted from the Master Oceanographic Observation Data Set (MOODS) during the summer season from the area shown in Fig. 1. Three profiles were constructed and smoothed for use in the simulations. One represents the mean water conditions and the other two represent extremes corresponding to +/- 2-standard deviations from the mean.

The 3 water SSPs are shown in Fig. 2, along with the geoacoustic profiles for each sediment type. All 3 water SSPs are downward refracting for a source at 50-m depth. The warmest condition (SSP max) produces the greatest amount of downward refraction and therefore the most bottom interaction.

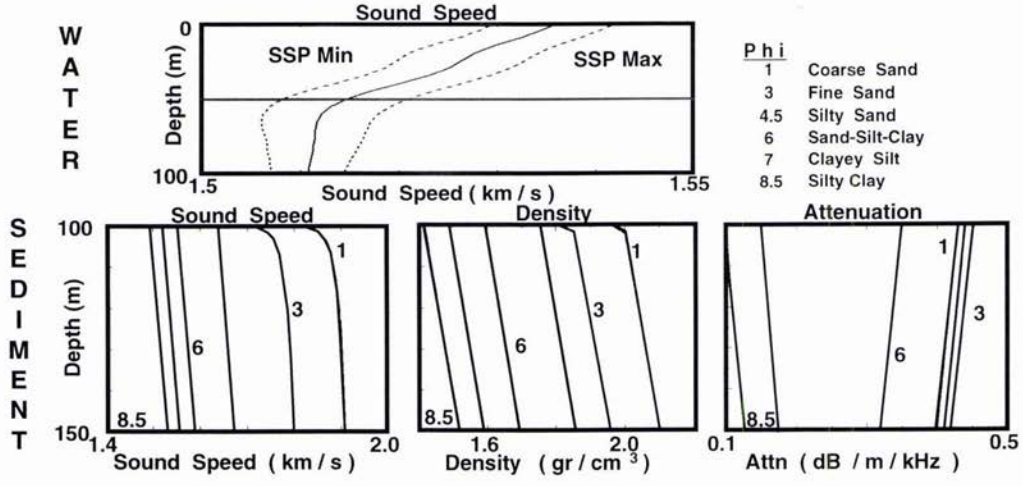

Fig. 2 Profiles of water sound speed (min, mean and max) for summer in the St. of Sicily and representative sediment geoacoustic properties from coarse-sand to silty-clay.

2.3 Bottom Reflection Loss

For each of the six bottom types, the corresponding geophysical / geoacoustic descriptions were converted into curves of bottom reflection loss (BRL) as a function of grazing angle. These are shown in Fig. 3 for the mean water SSP at 3 kHz. The water-sediment SSP discontinuity was assumed to be the same for each of the three water conditions; therefore the sediment geoacoustic profiles shown in Fig. 2 were adjusted slightly for each water condition to maintain the discontinuity. This gave rise to 18 BRL curves for each of the two frequencies, one for each combination of water condition and bottom type. The frequency dependence in BRL results from the frequency dependence of sediment attenuation.

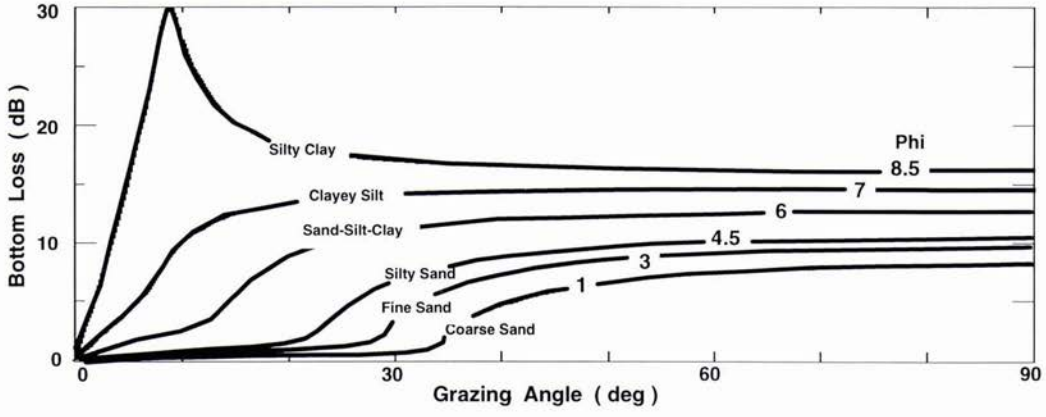

Fig. 3 Bottom reflection loss curves computed from geoacoustic properties.

2.4 Backscattering Strength and Reverberation

As acoustic energy propagates in shallow water, there are at least three scattering components (sea surface, volume and bottom) which redistribute energy in all directions. The first order effect of scattering on sonar system performance is backscattering and reverse propagation to the receiver. This produces reverberation, against which targets are to be detected. The analysis reported here includes calculations of backscattered reverberant energy from all three mechanisms. The total reverberation level is calculated and used in determining detection performance. In all cases considered the bottom component dominates.

2.4.1 Sea Surface Scattering

The amount of scattering at the pressure-release sea surface depends on the acoustic wavelength, the incident angle and on interface roughness, which is often characterized by sea state and waveheight. In low-wind conditions, the surface is nearly flat and the backscattered energy is usually negligible. For this study, surface reverberation is calculated using the Chapman-Harris empirical model [3]; however, the wind speed is assumed to be only 1 kt so that surface reverberation is small.

2.4.2 Volume scattering

The amount of scattering from volume inhomogeneities (primarily fish and fish schools) depends on frequency and the biologic distribution and density. These are so dependent on location, time of day, and season that a simple generic model which assumes a sparse marine-life population, is used.

2.4.3 Bottom scattering

The amount of scattering from the seabed depends primarily on the grazing angle and the type of material and secondarily on the frequency. The frequency dependence is not well understood, is probably insignificant in the band of interest (0.75 to 3 kHz) and is therefore not considered in this analysis. For many years, a simple sine squared (Lambert's Law) approach to diffuse scattering at the bottom has been adopted, with the normal incidence coefficient empirically determined to be -27 dB by Mackenzie [4] for deep-water sites. The formulation is simply

$$\mathrm{BBSS} = 10 \log (\mu \sin^2 \theta), \tag{1}$$

where BBSS is bottom backscattering strength in dB, θ is the grazing angle of the acoustic energy at the bottom and 10 log μ is the Mackenzie coefficient. To simplify terminology this approach will be labeled LM, for Lambert-Mackenzie. One deficiency with this simple LM formulation is that BBSS is independent of the bottom characteristics.

Another problem with the simple LM approach is that BBSS approaches negative infinity as the grazing angle approaches zero. Recent experimental evidence (e.g. from the Critical Sea Test (CST) Program [5] from 300 to 1500 Hz) is that BBSS does not become vanishingly small at low grazing angles. On the contrary, there exists a scattering-strength plateau caused by scattering inside the sediment rather than from the water-sediment interface which depends on the type of bottom material. This plateau and its dependence on the type of sediment has been analyzed [6]. One approach to deal with the low grazing angle scattering issue is to assume an "omnidirectional" scattering kernel proportional to the sine of the grazing angle and to adjust μ. This often provides a better "fit" to data from 10 to 30 deg, but it fails to describe the plateau at very low angles. To be consistent with CST and other data a new model for BBSS is proposed and used in this analysis. It is formulated as

$$\mathrm{BBSS} = 10 \log [\alpha(\phi) + \mu(\phi) \sin^2 \theta], \tag{2}$$

where α is the low grazing angle plateau and where both α and μ are functions of the environment through the grain-size parameter, ϕ. This modified Lambert's Law will be labeled ALM to indicate the α plateau at low angles.

A graphical representation of the proposed ALM approach for BBSS is shown in Fig. 4 for all 6 environments along with the standard Lambert's Law with a -27 dB coefficient. For coarse sand and fine sand Lambert's Law underestimates scattering (reverberation levels) at all angles. For the other environments Lambert's Law overestimates scattering above 15 deg and underestimates scattering below about 5 deg. From 5 to 15 deg (where one could expect the most interaction) the comparison depends on the exact sediment type.

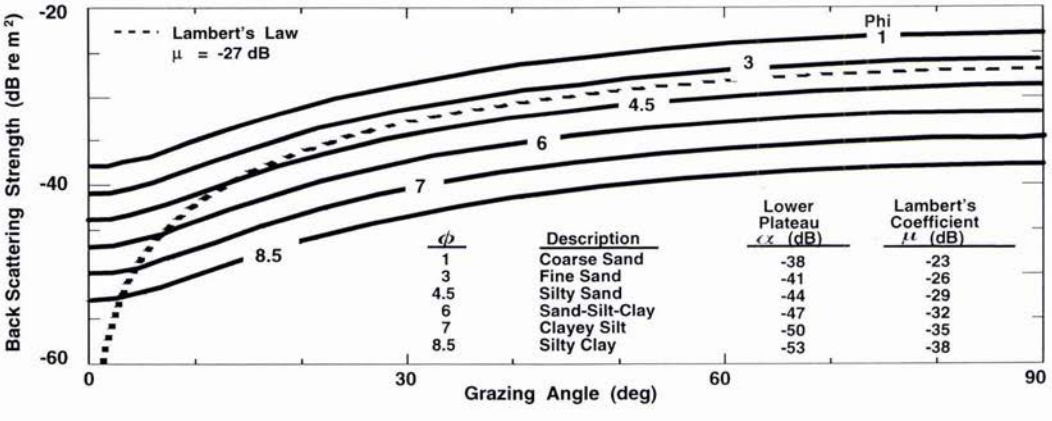

Fig. 4 Proposed ALM bottom backscattering strength curves (solid) with standard LM curve (dotted).

3. Transmission Loss and Reverberation

Transmission loss (TL) was calculated for all combinations of range-independent environments and frequencies. An example for a soft, ϕ=7, clayey-silt environment is shown in Fig. 5 as acoustic intensity vs. depth and range in the summer for a 50-m source in 100-m water using the Extended Finite Element Parabolic Equation approach [7]. The left and right columns correspond to the minimum (-2σ) and maximum (+2σ) SSPs for the area and the upper and lower rows are for 750 and 3000 Hz, respectively. In this case, the water conditions appear to have a major effect on propagation at both frequencies. In the maximum (max) SSP condition, the increased downward refraction causes significant penetration and attenuation in the sediment, compared to the minimum (min) SSP condition. The effect of warm water and sediment attenuation on transmission loss is much larger than the effect of changing the frequency.

In order to assess the relative importance of water conditions to sediment type, curves of TL vs range at a 50-m receiver depth for min and max SSPs were overlaid in Fig. 6 for ϕ = 1, 6, 7, and 8.5. The softer sediments (ϕ=7 and 8.5) on the top row show a large transmission loss and a significant difference between min and max SSP conditions, compared to the harder sediments (ϕ = 1 and 6) in the bottom row. The TL is so large for the softer sediments that sonar performance may be expected to be poor. The TL is much lower in the harder sediments so that one may anticipate good sonar performance, however hard interfaces (especially ϕ = 1 to 3) have high scattering strengths which increase reverberation and decrease detection range. The relative amounts of TL and reverberation must be considered in order to understand sonar performance.

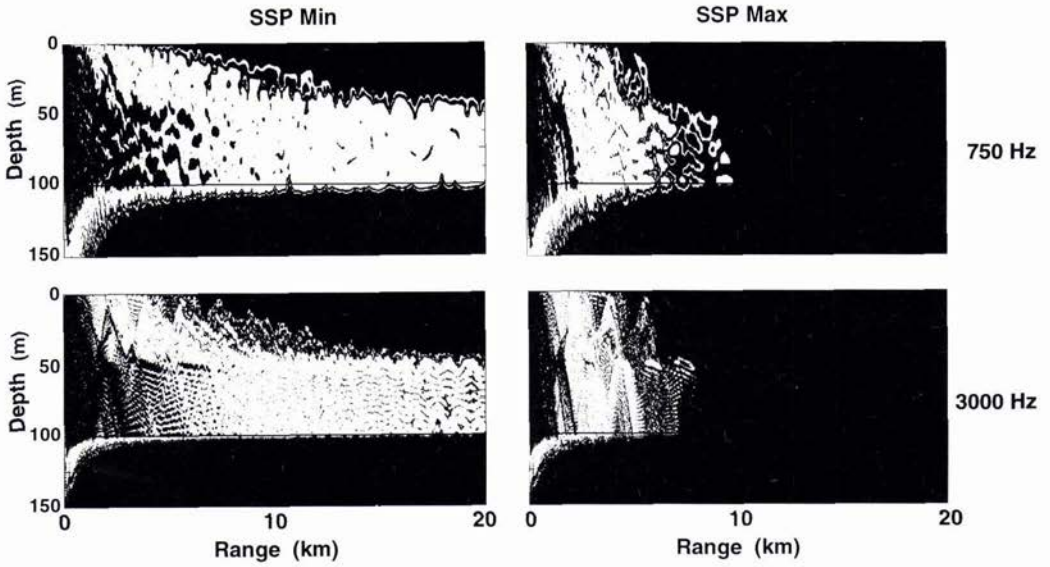

Fig. 5 Range-depth transmission loss contours for extreme water SSPs in the summer (min left and max right) for 750 Hz (upper) and 3000 Hz (lower). TL is computed with EFEPE using source depth = 50 m, water depth = 100 m and a soft, clayey-silt bottom sediment. Scale is defined by dark red at 53 dB and deep blue at 110 dB.

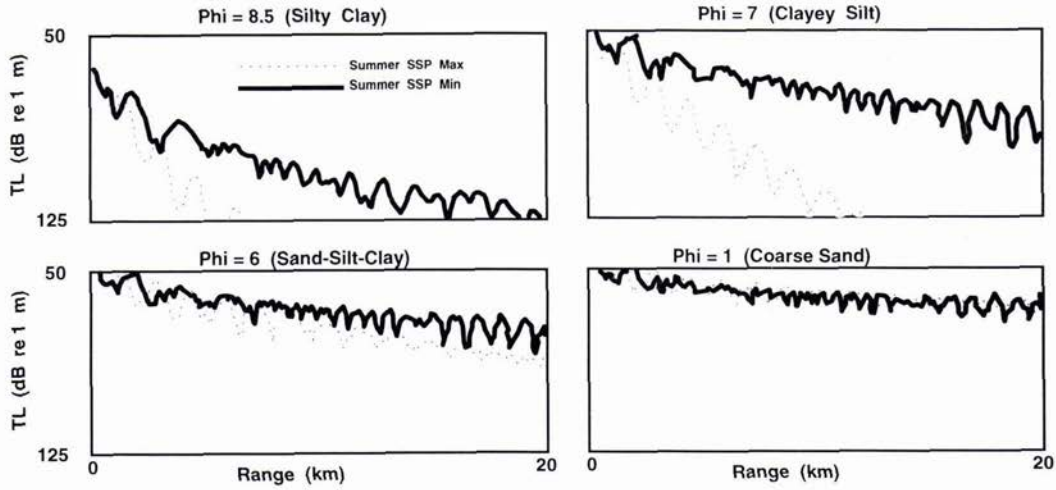

Fig. 6 TL at 3000 Hz for min and max water SSPs over 4 bottom sediment types. TL computed with EFEPE using source depth = 50 m, water depth = 100 m and receiver depth = 50 m.

Another observation from Fig. 6 is that in hard sediments (especially ϕ == 1 and 3) varying water conditions do not have a significant effect on TL. This is because hard sediments have high critical angles and little acoustic penetration. On the other hand, soft sediments have low critical angles and greater penetration. In this case the additional downward "ray bending" by the max SSP increases the acoustic angles at the sediment and this allows more penetration and attenuation and higher TL. Clearly, changes in either the water or bottom conditions can cause significant variation in TL, depending on the situation.

Reverberation levels also depend on water SSPs and sediment conditions through the scattering-strength curves shown in Fig. 4. The detailed results are not shown here because they have already been summarized; i.e. hard (soft) sediments produce high (low) reverberation. The important result is the balance between TL and reverberation through the sonar equation and the resulting detection performance in various environments, which is discussed in the next section.

4. Detection Performance

The ASW sonar scenario described in Section 2 is addressed here using a ray approach to computing TL and reverberation. Parallel EFEPE computations were performed to determine the efficacy of the ray-trace results. In some environments there were differences (e.g. the ray-based TLs were too high in soft sediments at 750 Hz) but the average differences were insignificant (less than 2 dB) out to maximum detection ranges. Most detections were against bottom reverberation even though realistic noise levels (from heavy shipping and low wind) were used. In a few cases corresponding to $\phi = 7$ and 8.5 the detections were noise limited at the maximum ranges. All calculations are for range-independent environments to simplify analysis and to allow generalization.

Some representative results of performance are given in Fig. 7 for the mean water SSP in all bottom sediments for a 750 Hz (top) and 3 kHz (bottom) notional sonar against a 0 dB (left) 10 dB (right) target strength. The circles result from assuming LM scattering and the triangles correspond to using the proposed ALM set of environmentally sensitive BBSS curves. The overall results for 0 dB target strength are about an order of magnitude worse than for the 10 dB target strength. The detailed results for LM and ALM are about the same for the 2 softest sediments; i.e. either scattering kernel is adequate because TL (not reverberation) dominates detection in these sediments. From $\phi = 6$ to 1 there is a monotonic increase in the difference between the 2 results because bottom scattering (not TL) dominates. The greatest differences in detection area occur in the hardest sediments. In all 3 sand areas the LM approach underestimates reverberation and predicts normalized detection areas from 3 to 30 times higher than the ALM approach. Separate calculations were made to isolate the impact of the low grazing angle plateau compared to the rest of the scattering. It was determined that in almost all cases the α plateau rather than the μ coefficient was the dominant parameter. This is consistent with the understanding that only low grazing angle energy propagates to long ranges since the steeper energy is absorbed by the sediment.

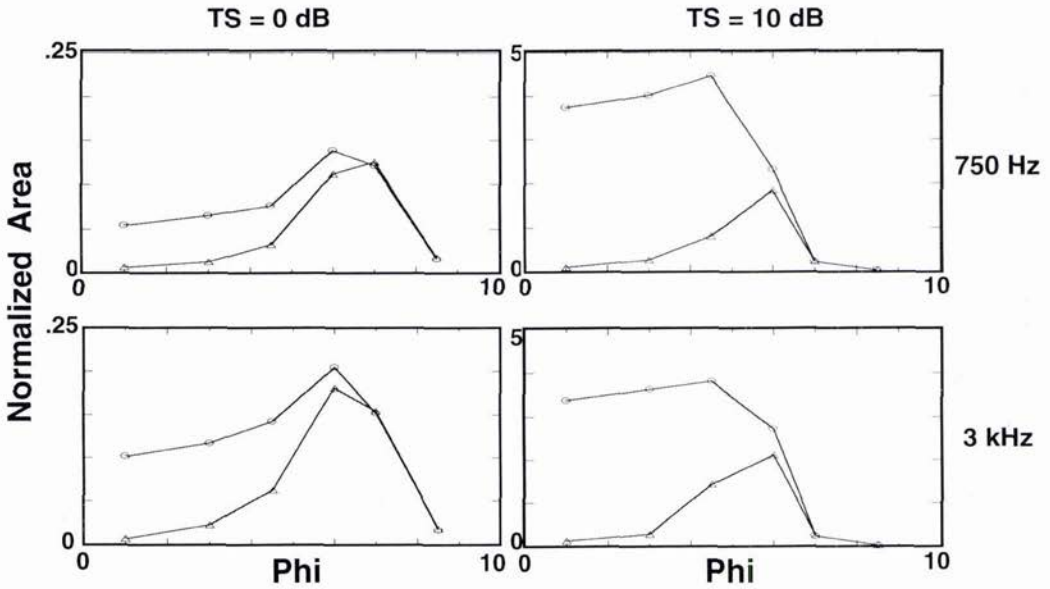

Fig. 7 Normalized detection area for 750 Hz (upper) and 3 kHz (lower) against a 0 dB (left) and 10 dB target in average water SSP conditions in all 6 bottom sediment types. The circles result from standard Lambert's Law / Mackenzie's Coefficient scattering and the triangles result from the proposed environmentally sensitive scattering kernel.

In all cases, the ALM detection performance is poor in the silty clay soft sediment (ϕ = 8.5) because TL is high and also poor in the coarse to fine sand hard sediments (ϕ = 1 to 3) because predicted reverberation from low grazing angles is large when the α plateau is applied. The proposed ALM approach shows a natural peak for optimum performance centered at the sand-silt-clay sediment.

Clearly, correct modeling of bottom scattering and bottom loss is essential to obtain accurate performance predictions. In addition, the water-mass properties must be carefully considered since they affect interface critical angles and ray trajectory angles, which has a significant impact on TL (see Figs. 5 and 6). An analysis was performed with these environmental-acoustic data to assess the relative impact of incorrect descriptions of water mass compared to bottom type in the regime of conditions considered in the St. of Sicily. Using detection area as a measure of effectiveness, it was found that correct bottom descriptions were about 5 times more important than correct water SSPs in this summer, downward refracting, shallow water situation. This result should be considered strategic rather than tactical. The implication is that for planning active acoustic ASW operations using archival environmental data, correct bottom descriptions are essential, whereas correct water SSPs are less important. However, during a tactical on-scene mission, the local details of the water mass can be extremely important due to dynamic changes in mixing layers and ducts which can affect choices to optimize sonar performance, like best source and receiver depth.

5. Summary

Based on a set of shallow-water geoacoustic descriptions and archival water sound speed information from the St. of Sicily, active sonar performance calculations were made for 750 Hz and 3 kHz in separate range-independent environments with water depth = 100 m. Performance against 0 to 10 dB targets at 50 m depth were compared in various possible environmental conditions using 2 approaches to modeling the scattering kernel; a) the standard Lambert's Law / Mackenzie Coefficient approach and b) Lambert's Law with the addition of environmentally sensitive Mackenzie's coefficient for moderate to high grazing angles and a low angle plateau. It was found that high transmission loss in soft sediments (with significant amounts of clay) caused poor detection performance. Further, high levels of bottom backscattering from hard sandy sediments limited detection areas when using the environmentally sensitive scattering function. Performance results were overly optimistic (by a factor of 3 to 30) when using the standard Lambert's Law / Mackenzie Coefficient. For intermediate sediments (grain sizes between sand and clay) detection performance was enhanced and optimized by a combination of only moderate TL and reverberation when the low angle plateau was employed.

6. Acknowledgements

This work was performed in support of the Warfare Effectiveness exploratory development project sponsored by the Office of Naval Research (ONR) and managed cooperatively by the Naval Research Lab and ONR.

References

[1] P. Fleischer, W. B. Sawyer and F. A. Bowles, "Development of a geological-geophysical database for the Strait of Sicily: southwestern offshore Italy," in *Geological development of the Sicilian-Tunisian Platform*, Ed. M. D. Max and P. Colantoni, UNESCO report, vol. 58, pp. 11-18, November 1992.

[2] E. L. Hamilton, "Geoacoustic modeling of the sea floor," *J. Acoust. Soc. Am.*, vol. 68, pp. 1313-1340, November 1980.

[3] R. P Chapman and J. H. Harris, "Surface backscattering strengths measured with explosive sound sources," *J. Acoust. Soc. Am.*, vol. 34, pp. 1592-1597, October 1962.

[4] K. V. Mackenzie, "Bottom reverberation for 530 and 1030 cps sound in deep water," *J. Acoust. Soc. Am.*, vol. 33, pp. 1498-1504, November 1961.

[5] Critical Sea Test Final Report, Space and Naval Warfare Systems Command, Washington DC, 1996.

[6] D. F. McCammon, Applied Research Lab, Penn State University, private communication.

[7] M. D. Collins, "A split-step Pade' solution for the parabolic equation method," *J. Acoust. Soc. Am.*, vol. 93, pp. 1736-1742, April 1993.

High frequency acoustic observations of Mediterranean flow into the Black Sea

Daniela Di Iorio

SACLANT Undersea Research Centre
Viale San Bartolomeo, 400
19138 La Spezia, ITALY
E-mail: daniela@saclantc.nato.int

Abstract

The physical behavior of Mediterranean flow entering the Black Sea through the Strait of Istanbul is described using a variety of high frequency acoustic systems. Because of the density difference between salty Mediterranean and fresh Black Sea water, a two layer exchange is formed which is confined within a canyon in the Black Sea exit region of the strait. A 120 kHz high resolution echo sounder is used to visualize the two layer dynamics which has a strong acoustic scattering strength. A 600 kHz broad band acoustic Doppler current profiler shows that the Mediterranean flow exhibits temporal variability associated with blockage. But during a time of maximum flow a balance of friction, Coriolis and pressure gradient forces give rise to Ekman current spirals and thus strong turbulence levels. A 307 kHz acoustical scintillation system over a 300 m path describes the turbulent boundary layer characteristics of the Mediterranean flow. The dominant component of the observed acoustic scintillation is from turbulent velocity rather than temperature variability. An assumption of isotropic and homogeneous turbulence leads to estimates of the turbulent kinetic energy dissipation rate, shear stress and bottom drag coefficient.

1. Introduction

The Strait of Istanbul separates two relatively large inland seas of differing hydrological characteristics (see Figure 1). Flow through the strait is a classic example of turbulent exchange flow. A high velocity surface current with relatively fresh Black sea water overlies a current running in the opposite direction, which transports the more saline water of the Mediterranean and Marmara Sea to the Black Sea. The higher salinity water, though warmer than the Black Sea surface layer, is more dense, and it flows through an underwater canyon which is an extension of the Bosporus canyon until it spreads on the shelf at some 80 m water depth (see Figure 1) and finally reaches the shelf break and sinks to the depth at which it finds a common density. This exchange through the strait entirely determines the hydrological properties of the Black Sea and is the only source of ventilation at depth. The surplus of fresh water from rivers and precipitation against evaporation keeps the surface layer in the Black Sea relatively fresh and leads to higher outflow through the Bosporus than the average amount of saline Mediterranean water that advances into the Black Sea (see Unluata *et.al.* [6]).

This paper describes oceanographic and acoustic measurements taken during a November/December 1995 sea trial to the Black Sea exit region. Collaboration with the Turkish Navy Department of Navigation, Hydrography and Oceanography (TN DNHO) made it possible to obtain a variety of data necessary to understand the physical oceanographic characteristics of this area during this time.

2. Experimental Results

A detailed hydrographic survey with SWATH mapping was obtained in order to determine the path of the Mediterranean inflow into the Black Sea as available bathymetry was not sufficient. The results in Figure 1 show that there is a narrow canyon extending from the Strait of Istanbul. At first the canyon is parallel with the strait and then turns to the North-West where it eventually merges with the continental shelf. Mediterranean water is confined and retained within this canyon over a distance of several kilometers until it spreads out on the shelf. In

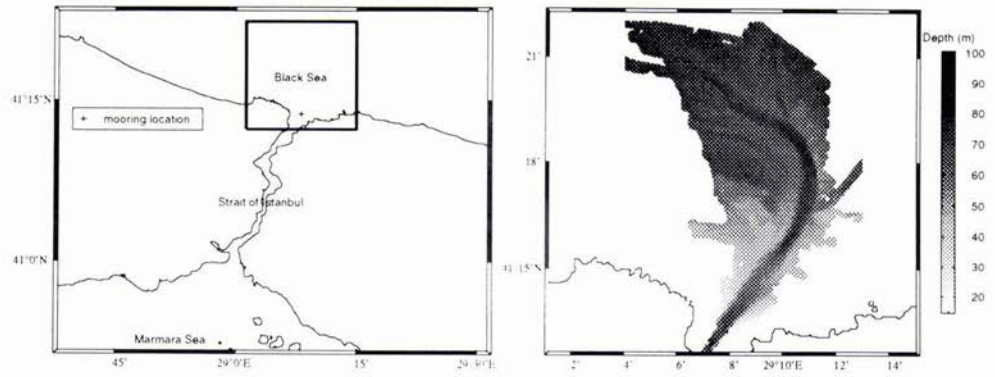

Figure 1: (left) The Strait of Istanbul separates the Black Sea and Marmara Sea basins. The enclosed area in the Black Sea exit region corresponds to the experimental site where acoustic scintillation and ADCP moorings were deployed. (right) Detailed bottom bathymetry obtained from SWATH multibeam soundings.

order to obtain accurate depth measurements simultaneous CTD profiles, from which sound speed is calculated, were obtained along the path of the underwater canyon.

The Mediterranean flow is observed within the canyon using a high resolution, high frequency (120 kHz) echo sounder (on loan from the Institute of Ocean Sciences, Sidney, B.C. CANADA) towed side NRV ALLIANCE. Figure 2 shows a cross section of the canyon from West to East taken in the location of the moored instrumentation together with a temperature and salinity profile. A section along the canyon from South to North identifies a 60 m sill (located at 3 km in the echo sounding image) that controls the flow of Mediterranean Sea water into the Black Sea. The interface between Black Sea and Mediterranean Sea water is an area of intense turbulence associated with mixing of the two different waters and thus has strong acoustic back scatter characteristics. Measurements show that the echo level from the interface is 40% that of the bottom reflection. Much structure is visible at the interface which suggests strong spatial variations associated with turbulent mixing both across and along the canyon.

A high frequency (307.2 kHz) acoustic scintillation system (also on loan from IOS) was deployed within the canyon containing Mediterranean sea water (see Figure 2). This instrument is self contained and battery operated. The transmitter array was deployed on the western side (at approximately 700 m range) and the receiver array on the eastern side (at approximately 980 m range) at a depth of 62.5 m. Each array consists of two transducers separated by 0.2 m. In order to keep the transducer array aligned in the direction of flow, a vane and swivel were attached to the mooring. This allows measurement of current flow perpendicular to the acoustic axis and measurement of turbulent structures as they are advected past the acoustic path. Each transducer is horizontal omni-directional with a 10 degree vertical beam width. Short pulses (30 cycles) are transmitted with a high repetition rate (16 Hz) and with a delay of 20 ms between the two spatially separated transducers. The receiver unit complex demodulates the signals, digitizes and calculates the acoustic amplitude, phase and travel time for the direct path using quadratic interpolation of the received enveloped. The data are then recorded on flash EPROM recorder cards. Table 1 summarizes the experimental parameters.

Two deployments were made: 4.5 days of continuous data were collected on the first and 8 days of sub-sampled data (20 minutes of data every hour) on the second. The data covered a variety of oceanographic phenomena but some of the scintillation data could not be analyzed. Figure 3 shows ADCP current vectors (together with density contours when available) which cover the two deployment periods. Deployment 1 was during a time when the Mediterranean under current was strong. Contours of density over 36 hours show salt entrainment into the Black Sea layer and salt depletion in the Mediterranean layer. Deployment 2 was during a time when there was blockage of Mediterranean water so that the interface passed through the acoustic path. The blockage by the 60 m sill is a result of increased barotropic pressure and strong North-Easterly winds which cause an increase in sea level difference between the Black Sea and Marmara Sea basins.

The acoustic log-amplitude, $\chi = \ln(A/ < A >)$ (where A is the acoustic amplitude and $<>$ denotes a time average), for the two parallel paths (T1/R1 and T2/R2) are shown in Figure 4 during a time when the Mediterranean current was strong. Much variability exists because of the turbulent nature of the Mediterranean

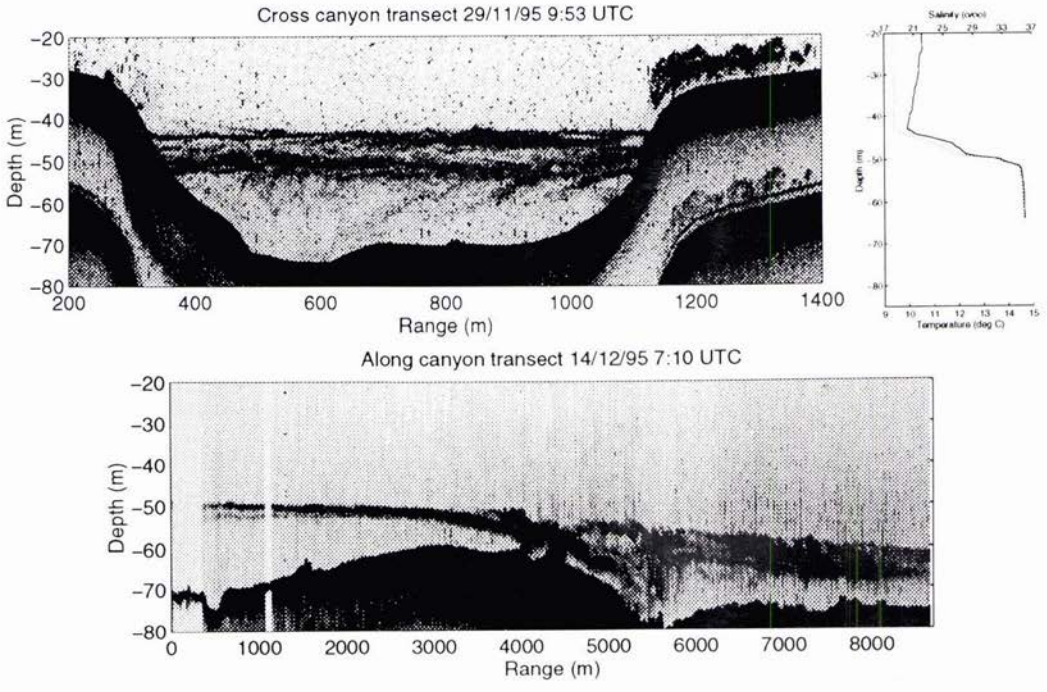

Figure 2: (top) A cross section of the canyon from West to East together with the temperature and salinity profile. (bottom) A section along the canyon from South to North.

Parameter	quantity
Deployment 1	27/11/95 1100 to 01/12/95 1700 UTC
Deployment 2	05/12/95 1000 to 13/12/95 1130 UTC
Transmission rate	16 Hz
– deployment 1	continuous
– deployment 2	20 minutes continuous every hour
Frequency	307.2 kHz
Pulse width	0.1 ms
Pulse delay	20 ms
Digitization rate	153600 Hz (1 sample/2 cycles)
Path length	282 m
Propagation direction	124 deg T
Transducer separation	0.2 m
Depth	62.5 m

Table 1: Acoustic scintillation instrument parameters.

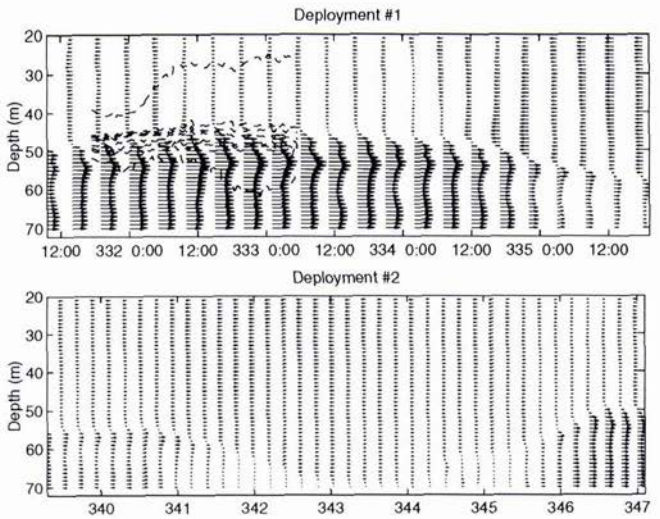

Figure 3: The ADCP current vectors as a function of Julian day, together with density contours ([1014, 1015, 1017, 1019, 1021, 1023, 1025, 1026.75] $kg \cdot m^{-3}$) when available, for each deployment.

flow. Also shown is the travel time difference between the two parallel paths. The periodic nature of this time series is a result of mooring oscillation. Since the transmission rate was high (16 Hz) and the oscillations small the direct path signal was tracked. The mooring motion does not affect amplitude variations but the phase and travel time could not be used as a measurement of medium properties.

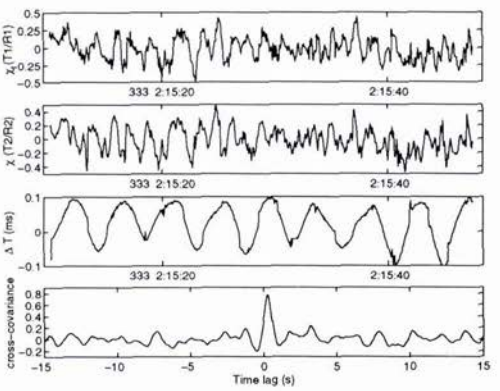

Figure 4: Acoustic scintillation during a time of strong current.

The statistics for the log-amplitude allow measurement of oceanographic parameters as discussed by Di Iorio and Farmer [1]. For example, Figure 4 shows the time-lagged log-amplitude cross-covariance function. This function shows the translation of turbulent structures perpendicular to the two acoustic paths separated by 0.2m. By measuring the time lag, the current speed is calculated and shown in Figure 5 for each deployment together with the ADCP measurement for comparison. Discrepancies between the scintillation technique and the ADCP can arise for a number of reasons. For example, the scintillation measurement is a path average whereas the ADCP measurement is essentially a volume measurement at a point location. Also because of mooring motion, there can

be changes in the acoustic path separation of 0.2 m.

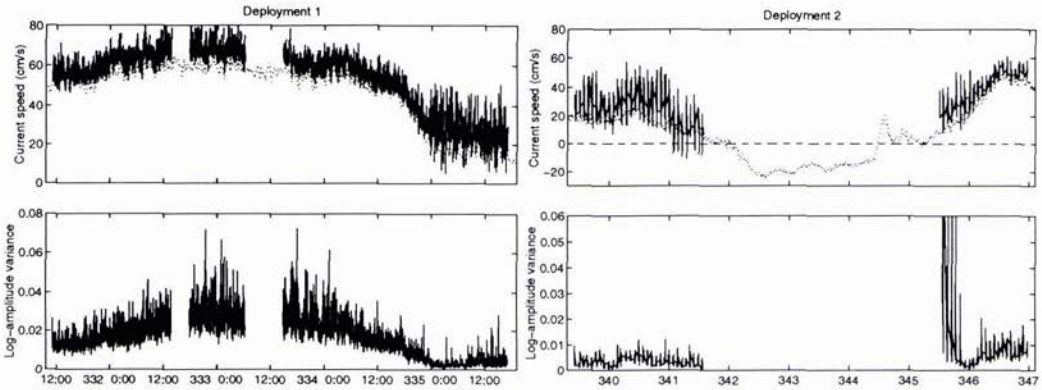

Figure 5: Current speed measured using acoustic scintillation and ADCP together with the log-amplitude variance for (left) deployment 1 and (right) deployment 2.

The log-amplitude variance shows increased variability associated with the increasing current. The large variance observed in deployment 2 may be the result of turbulent mixing between two very different water masses as the Mediterranean flow becomes unblocked. During blockage of the Mediterranean inflow the acoustic data for deployment 2 was not very good. This could be due to a number of reasons: misalignment of the transmitter/receiver arrays because of rotation, inability to track the direct path since the travel time of the acoustic signal changes by upto 3.9 ms and finally there may have been interference from multipaths so that path separation was not possible. Mediterranean water below the acoustic propagation axis creates strong upward refraction masking the effects of the bottom.

The level of the effective refractive index fluctuations defined by,

$$C^2_{n_{eff}} = C^2_{n_s} + \frac{11}{6} C^2_{n_v}, \tag{1}$$

(see Di Iorio and Farmer [2]) is expressed in terms of the refractive index fluctuations arising from temperature and salinity variability (scalars) and those arising from the current variability (vectors). The log-amplitude variance, σ^2_χ allows measurement of $C^2_{n_{eff}}$ through the equation,

$$\sigma^2_\chi = 0.124 C^2_{n_{eff}} k^{7/6} L^{11/6}, \tag{2}$$

where k is the acoustic wavenumber and L is the acoustic path length. Note that the acoustic amplitude variability cannot distinguish between fine scale variability from scalars and that from current. The dominant scale size which contributes to the log-amplitude variance as discussed by Tatarskii [5] is the Fresnel radius $\sqrt{\lambda L} = 1.2m$.

Independent measurements of the temperature and salinity structure was obtained by TRV CUBUKLU by lowering a conductivity, temperature and depth meter (CTD) to 62 m and collecting 10 minute time series at an 8 Hz sampling rate. This sampling rate can resolve scales sizes within 0.1 m to a few meters in size for a current 0.8 m/s. Thus the acoustics and CTD measurements probe the same scale sizes. Assuming isotropic and homogeneous turbulence the one-dimensional frequency spectrum for the refractive index fluctuations from temperature and salinity (see Di Iorio and Farmer [1] is defined as,

$$F_{\eta_s}(f) = 0.124 C_{\eta_s} (\frac{U}{2\pi})^{2/3} f^{-5/3}, \tag{3}$$

where U is the mean current speed resolved along the canyon which advects the small scale turbulence. Figure 6 shows a sample sound speed time series together with the one dimensional frequency spectrum for the refractive index fluctuations ($\eta_s = -c'/c_o$ where c_o and c' are the mean and fluctuating parts of the sound speed). A -5/3 slope is plotted to show that the variability can be modelled as described by (3) over the scales of most sensitivity. The level of the spectrum gives the structure parameter C_{η_s} which is compared to the acoustic forward scatter results.

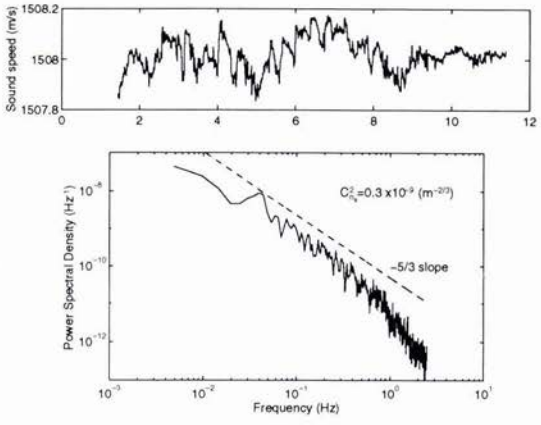

Figure 6: A sample sound speed time series together with the frequency spectrum for the refractive index fluctuations.

Figure 7 shows that the dominant acoustic scattering is from current velocity variability since $C_{n_v}^2$ is at most 10% of $C_{n_{eff}}^2$. Current velocity fluctuations arise because of hydrodynamic instability within the Mediterranean layer and also because flow over the bottom generates a turbulent boundary layer. The turbulence can be parameterized by the Reynolds number,

$$\mathrm{Re} = \frac{UL}{\nu}, \tag{4}$$

and the instability parameterized by the gradient Richardson number,

$$\begin{aligned} \mathrm{Ri} &= N^2 \left[\left(\frac{dU}{dz} \right)^2 + \left(\frac{dV}{dz} \right)^2 \right]^{-1}, \\ N^2 &= \frac{g}{\rho_o} \frac{d\rho_o}{dz}. \end{aligned} \tag{5}$$

The mean flow resolved along the canyon is U, the Mediterranean thickness is L and ν is the kinematic viscosity. The Brunt-Vaisala frequency is $N/(2\pi)$, ρ_o is the mean density as a function of depth, g is gravity, and V is the cross canyon flow component.

If the stratification is unstable, $\mathrm{Ri} < 0$ then density variations enhance the turbulence. If the gradient Richardson number becomes large then turbulence is suppressed since the density gradient stabilizes the variations caused by the current shear. More specifically stratified shear flow is hydrodynamically stable if $\mathrm{Ri} > 1/4$; if $\mathrm{Ri} < 1/4$ then turbulence is generated because of hydrodynamic instability (see Pond and Pickard [3]). Figure 8 shows an averaged profile of the Brunt-Vaisala frequency together with the current components U and V. From our time series measurements we find that throughout the Mediterranean layer the Richardson number was consistently $0 \leq \mathrm{Ri} < 1/4$ and the Reynolds number of order 2×10^7.

Since Mediterranean flow is confined between two boundaries (the bottom boundary below and Black Sea water above), a balance of friction, Coriolis and pressure gradient forces will result in a cross stream shear over the full thickness of the Mediterranean layer as seen by the profiles of U and V. Figure 8 also shows the current vectors as a function of depth. As the bottom boundary and interface are approached the current swings to the left.

Since velocity fluctuations dominate the acoustic scattering, the turbulent kinetic energy dissipation rate is determined via,

$$\epsilon^{2/3} = \frac{C_{n_v}^2 c_o^2}{1.97}, \tag{6}$$

where c_o is the mean sound speed at the depth of the acoustic path. Acoustic measurements of ϵ range from 1×10^{-6} to $5 \times 10^{-5} W/kg$. This parameter is useful since it gives the production of turbulent energy caused by shear stresses. Production of energy from buoyancy forces are assumed negligible since the Mediterranean layer is very well mixed. Following Monin and Ozmidov [4] the balance of production and dissipation of energy is then,

$$\frac{\tau_{xz}}{\rho_o} \frac{dU}{dz} + \frac{\tau_{yz}}{\rho_o} \frac{dV}{dz} = \epsilon, \tag{7}$$

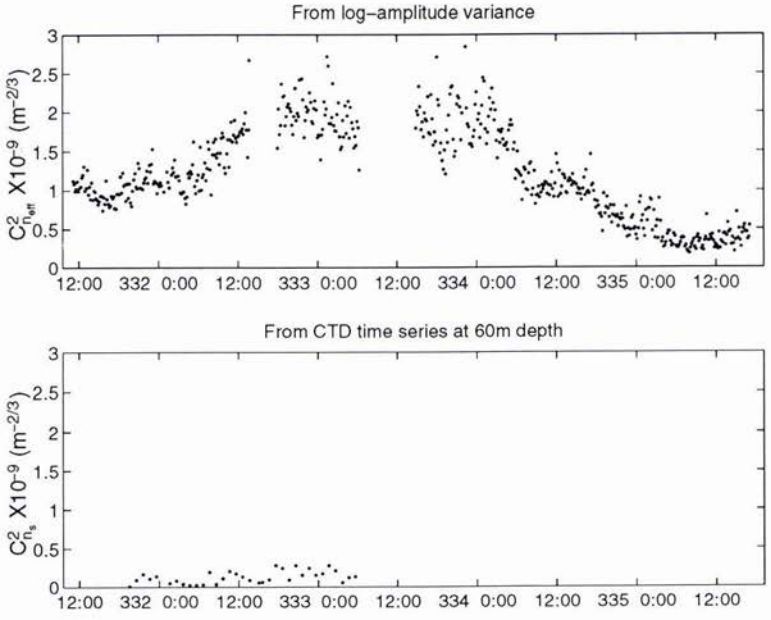

Figure 7: The level of effective refractive index fluctuations compared with the level of the scalar contribution to the refractive index fluctuations.

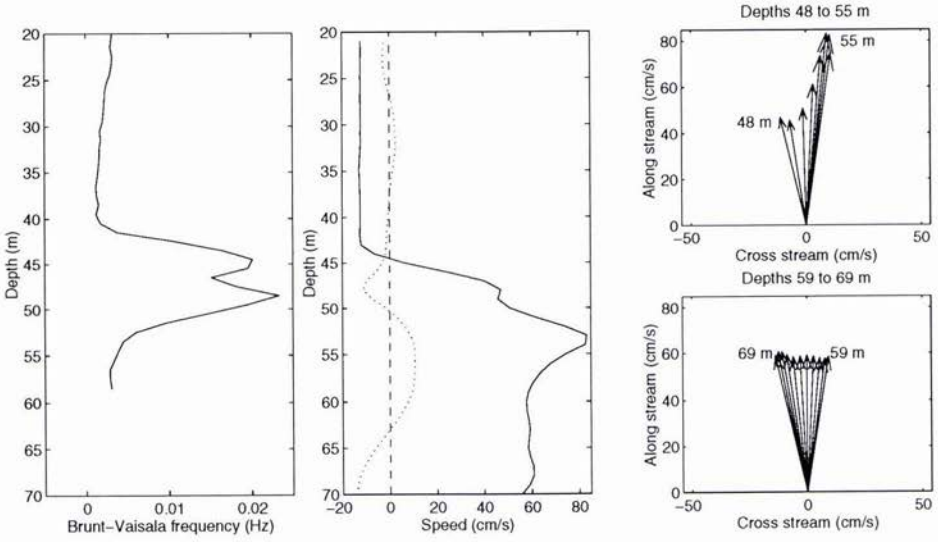

Figure 8: Averaged profiles for the Brunt-Vaisala frequency, U (solid) and V (dotted) current components together with the current vectors.

where the shear stresses are given by $\tau_{xz} =< u'w' >$ and $\tau_{yz} =< v'w' >$. To make estimates of the bottom drag coefficient the flow close to the boundary is modelled as a log-layer since $dV/dz \approx 0$. Therefore $\tau_{xz}/\rho_o \sim C_D U^2$. For a maximum dissipation rate of $5 \times 10^{-5} W/kg$ during the maximum outflow an estimated bottom drag coefficient is $C_D = 3.5 \times 10^{-3}$ which is consistent for a mixed sand and shell bottom.

3. Future Measurements

Future measurements in the Strait of Istanbul will be carried out in collaboration with IOS and the TN DNHO. At present a $50kHz$ reciprocal acoustic scintillation system is under development. This system is capable of transmitting pseudo random noise (PRN) m-sequences in both directions at a maximum rate of 5 Hz or at a rate of 20 Hz in one direction. The incoming signals are complex demodulated and all multipaths will be recorded. The use of PRN codes allows path separation within $180\mu s$.

The use of reciprocal transmission allows measurement of the temperature and current variability along the acoustic path as described by Di Iorio and Farmer [2]. The scintillation technique gives measurement of the advection of turbulent structures perpendicular to the acoustic path so that combining the two techniques one can determine the current velocity field (see [2]). In the Strait of Istanbul where a two layer flow exists the acoustic system will be deployed at two depths so as to measure turbulent temperature and velocity characteristics in each layer. Also since all multipaths are stored there is an opportunity to study the effects of bubbles from ship wakes on the surface reflected signals. Bottom reflected signals can also be studied to see if the Mediterranean undercurrent causes sediment transport.

In addition to the reciprocal acoustic scintillation system, a bottom mounted upward looking ADCP and echo sounder will be placed in the center of the strait so as to obtain temporal measurements of the interface structure.

It is hoped that these systems will remain in the strait for one year so that temporal variations associated with seasonal changes can be documented.

4. Conclusions

The use of high frequency acoustics is a valuable tool for obtaining fine structure characteristics of turbulent flow. In this paper, three acoustic systems were used to study Mediterranean flow into the Black Sea. High resolution echo sounding gave two dimensional imaging of the interface where mixing between two different water masses takes place. A scintillation system deployed within the Mediterranean layer was used to obtain turbulent boundary layer characteristics. It was shown that velocity variability dominated the acoustic scattering which leads to estimates of the turbulent kinetic energy dissipation rate and bottom drag coefficient.

5. Acknowledgements

Many thanks are given to P. Guerrini for his support with the scintillation and echo sounding systems. Also, thanks go to Capt. Yuce of DNHO for his support throughout the experiment. The scintillation analysis could not have been complete without the crew of TRV CUBUKLU of the Turkish Navy taking CTD time series measurements at our mooring location.

References

[1] D. Di Iorio and D.M. Farmer, "Path averaged turbulent dissipation measurements using high frequency acoustical scintillation analysis", *J.Acoust.Soc.Am.*, vol. 96, pp.1056-1069, August 1994.

[2] D. Di Iorio and D.M. Farmer, "Separation of current and sound speed in the effective refractive index for a turbulent environment using reciprocal acoustic transmission", *J.Acoust.Soc.Am.*, *J.Acoust.Soc.Am.* accepted for publication.

[3] S. Pond and G.L. Pickard, *Introductory Dynamical Oceanography* Oxford, Butterworth-Heinemann Ltd., 1983.

[4] A.S. Monin and R.V. Ozmidov, *Turbulence in the Ocean* Dordrecht, D. Reidel Publishing Company, 1985.

[5] V.I. Tatarskii, *The Effects of the Turbulent Atmosphere on Wave Propagation*, (translated from Russian by Israel Program for Scientific Translations, Jerusalem, 1971).

[6] U. Unluata, T. Oguz, M.A. Latif and E. Ozsoy, "On the physical oceanography of the Turkish Straits", *The Physical Oceanography of Sea Straits*, L.J. Pratt (ed), Netherlands, Kluwer Academic Pub, pp.25-60, 1990.

An Experimental Study of Sediment Discrimination using 1st and 2nd echoes

*C. Dyer, **K.Murphy, **G.Heald, * N. Pace

* University of Bath, School of Physics, Claverton Down, Bath, England

** Defence Research Agency, Newton Road, Weymouth, Dorset, England

Abstract

Analysis of Roxann seabed classification data, at 24 kHz and 200 kHz, using co-located echosounders is presented. Timeseries backscater data gathered at the same time as the Roxann data has also been analysed using variations on the integration schemes used. Variation due to both the frequency difference, depth dependancy and processing scheme are discussed

1. Introduction

During February 1995 a major international data gathering exercise was conducted off the Florida Keys in the region called Dry Tortugas. The overall experiment included contributions from 6 nations who all provided data gathering systems or ground truthing of the area where the acoustic experiments were being conducted. The Defence Research Agency provided two Roxann seabed classification systems and a Datasonics sub-bottom profiler. The Roxann systems were modified so that the band-shifted time-series data could be recorded and later used for a detailed analysis of how the first and second backscatter from the sea bed relates to sediment type. A description of the theory related to Roxann processing is given in [1]. In order to investigate the effect of penetration into the sea-bed each Roxann system was used to gather data at different frequencies. The time-series data has been analysed using schemes that are representative of the Roxann processing and additional analysis techniques have been applied in order to investigate their effect on sediment discrimination. A 24 kHz and 200 kHz echo sounder was used. The analysis described here is still in progress so conclusions are not drawn.

2. Data Gathering

2.1 The trials area

The output from the Roxann was available for this project both as binary coded files (containing navigation, E1 and E2 information, water depth, and time) and as time series data. A plot of the Roxann E1 and E2 output across the trial area is shown in figure 1. The area covered by the Roxann during the Key West survey includes the Dry Tortugas area which is a region of geological interest due to the presence of an ancient coral reef. The tracks surveyed in this area are shown in Figure 2. Also shown are the points where some ground truth data is available.

The ground truth data (collected by several organisations) is in the form of sediment core analysis, grain size histograms and percentage sand, silt, clay, etc. which show predominantly sand. Sidescan sonar, diver observations and sub-bottom profiles show the presence of a reef of highly reflective material across the south east corner of this area. This is clearly shown on the Roxann outputs given in figure 1.

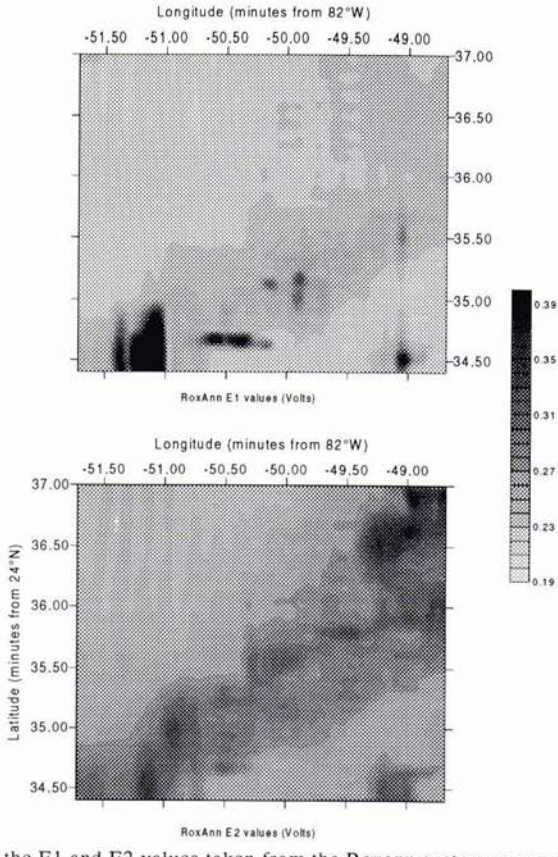

Figure 1. Plot of the E1 and E2 values taken from the Roxann system across the survey area

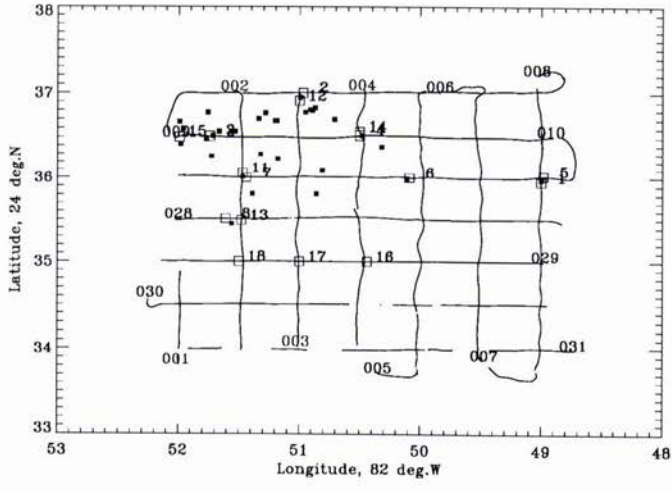

Figure 2. Tracks in the Tortugas area where the Roxann was deployed.
Solid squares show points where ground truth samples were taken.
Unfilled squares show track portions where the time series signals were digitised.

2.2 Digitisation and analysis of time series signals.

The signals from the 200kHz and 24kHz sonars were taken from the head amplifier of the Roxann, bandshifted to 15kHz and recorded onto VHS tapes, together with the transmit trigger pulse and the navigation. The output from this was in analogue form and was redigitised using a standard 12-bit A/D board installed in a PC computer. The board was controlled by a 'C' program to give 100kHz sampling, the samples being streamed to disk.

The large amount of data available from the survey was reduced on the basis of the known ground truth data. Twenty positions on the ship's track, where sediment core results were available, were chosen for initial analysis, mostly in the Tortugas area. Signal sample lengths of one or two minutes were digitised. This was further reduced by discarding signals beyond the second echo. It was then digitally filtered about 15kHz and rectified using a Hilbert transform. Typical filtered envelopes for the first echoes at both frequencies are shown in Figure 3, plotted against time(sec.).

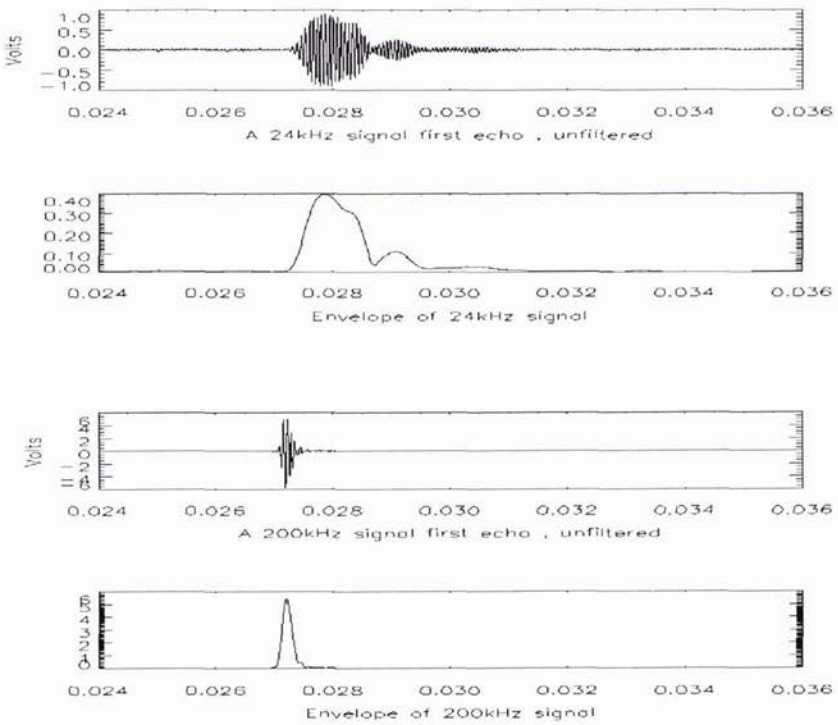

Figure 3. Digitised first echoes before and after being filtered and rectified .

The data was further reduced by broadly windowing the envelopes, starting at the bottom detection point for the first echo and twice this arrival time for the second echo. The envelopes were averaged over several pings using a sliding boxcar approach. The start and finish of each echo was estimated using a background noise criterion. These points were then used in the definition of integrals to calculate the parameters E1 and E2 by the four methods described below. The integrals were normalised by the energy under the first echo.

Integral 1: The first echo envelope from the peak to the end point(E1-1).

Integral 2: The first echo envelope from the -3dB point past the peak to the end point(E1-2), i.e. the 'tail'.

Integral 3: The whole of the first echo envelope(E1-3).

Integral 4: The whole of the second echo envelope(E2).

Integral 2 is thought to be most like the Roxann integral for E1; it is believed that the first return is saturated therefore the peak point cannot be determined.

3. Results.

The E1 and E2 integrals from two different survey areas are shown in Figures 4-7 for high and low frequency systems, for the Roxann output and that obtained from the above methods. The portions of output shown correspond to exactly the same seabed for both frequencies in each area. The 200kHz and 24kHz systems transmitted about 80 and 120 times per minute respectively. The values of method 2 may be compared with Roxann output. The Roxann method contains some threshold smoothing which has not been incorporated in this analysis as the details are not known. The threshold smoothing is applied to remove transmissions where the transducer is grossly off normal incidence due to boat motion. This technique is applied automatically using peak level of the backscatter and needs to be applied to the time-series before a direct comparison can be made.

4. Conclusions

The difference between the 24 kHz and 200 kHz requires further investigation to establish if the variation is due to sea-bed penetration or the difference in beamwidth (22° at 24 KHz and 7°at 200kHz). A comparison of the data with the output from the sub-bottom profiler is not yet done and should give an indication of the variation in the sub-surface layers.

It is clear from figure 1 that the Roxann system indicates the different backscatter from the coral reef and the sandy region of the trial site. The effect of sand wave region, where most of the ground truth data was gathered, can be seen in figures 1, 6 and 7. This variation may, of course, be due to the change in depth although there is evidence that the sediment at the peaks of the sand waves differs from the sediment in the troughs. A normalization for changes due to depth and ensonified area should be conducted. It is unfortunate that the experiment site did not contain a wider range of sediment types so that their effect could be observed.

References

[1] G.J.Heald and N.G.Pace, "*An analysis of 1st and 2nd backscatter for seabed classification*," Proceedings of III European Conference onUnderwater Acoustics, Crete. June 1996

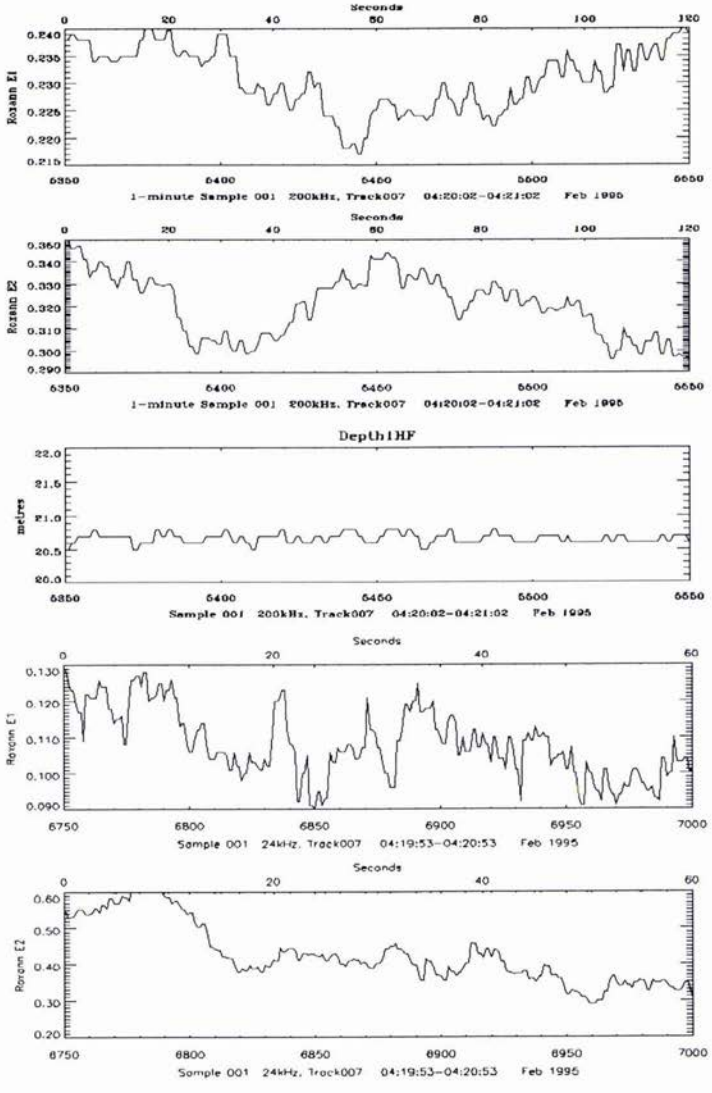

Figure 4. An example of high and low frequency Roxann output from a flat sandy area in the Tortugas region, digitised sample 1, track 7.

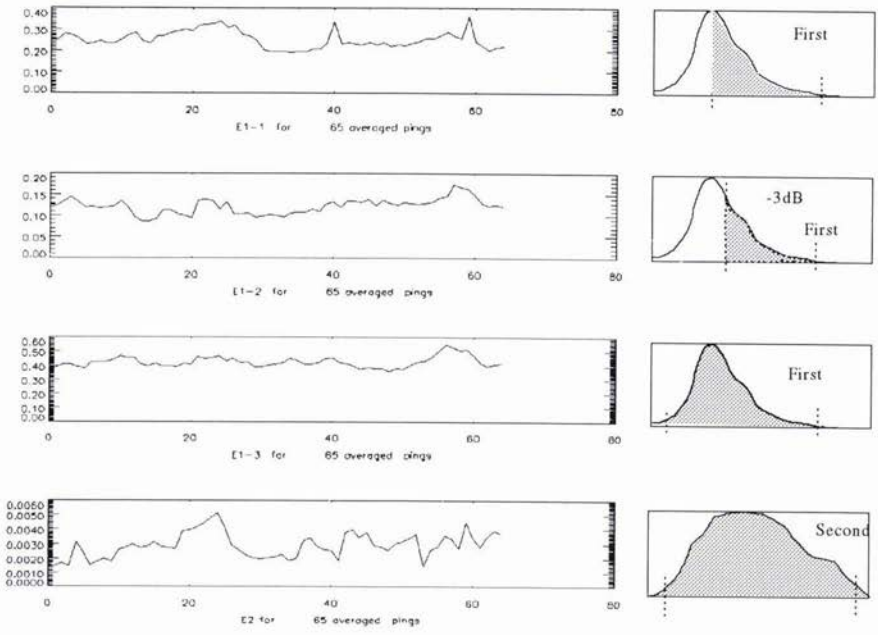

Figure 5a: E1 and E2 calculated from the integrals indicated, high frequency, at sample 1, track 7.

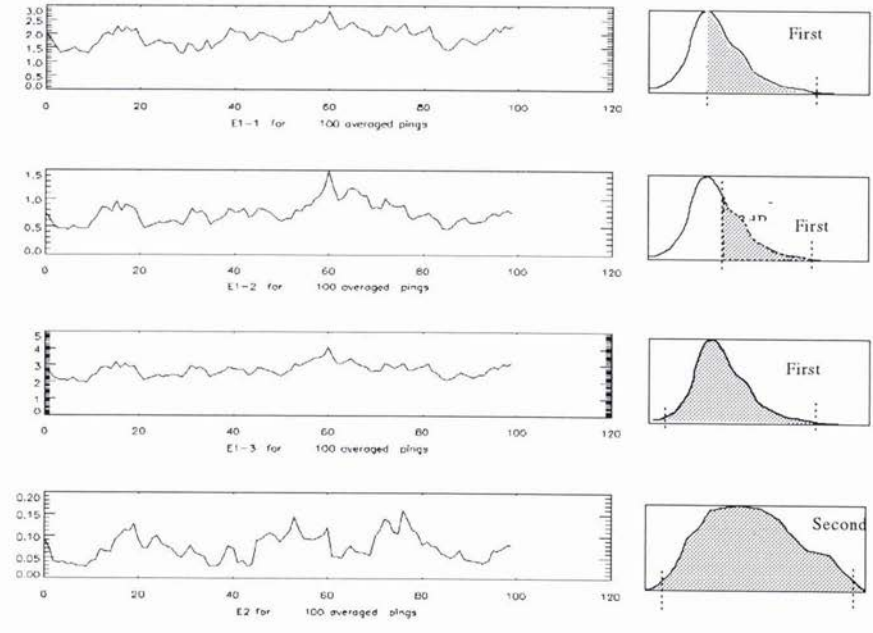

Figure 5b. E1 and E2 calculated from the integrals indicated, low frequency, at sample 1, track 7.

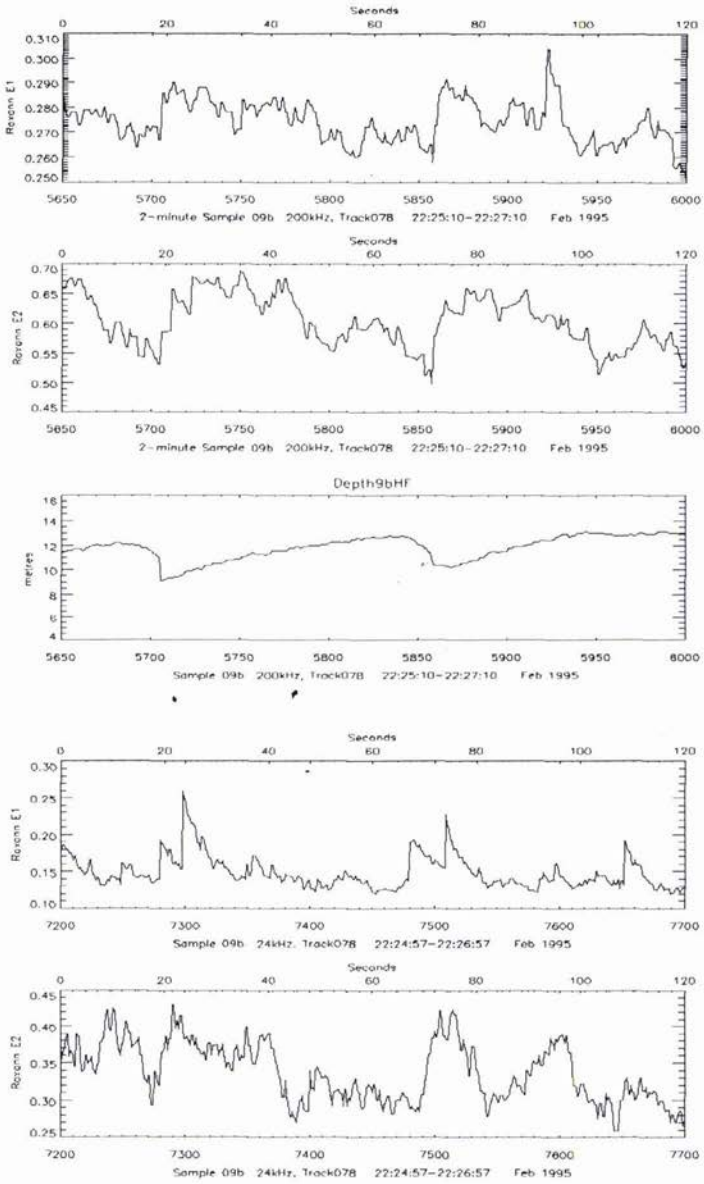

Figure 6. An example of high and low frequency Roxann output from a sandwave region, sample 9b, track 78, to the east of the Tortugas region .

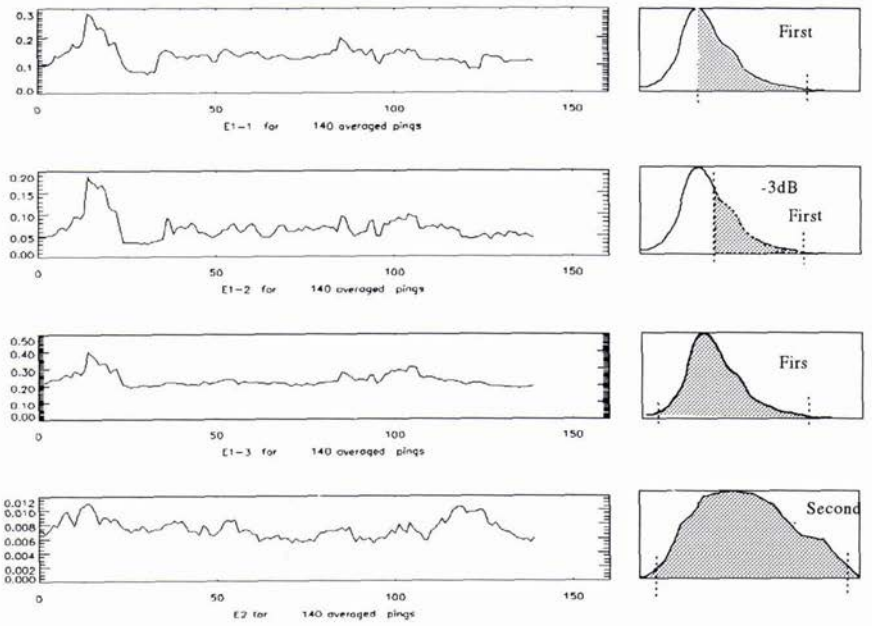

Figure 7a. E1 and E2 calculated from the integrals indicated, high frequency sample 9b, sandwave region, to the east of the Tortugas area.

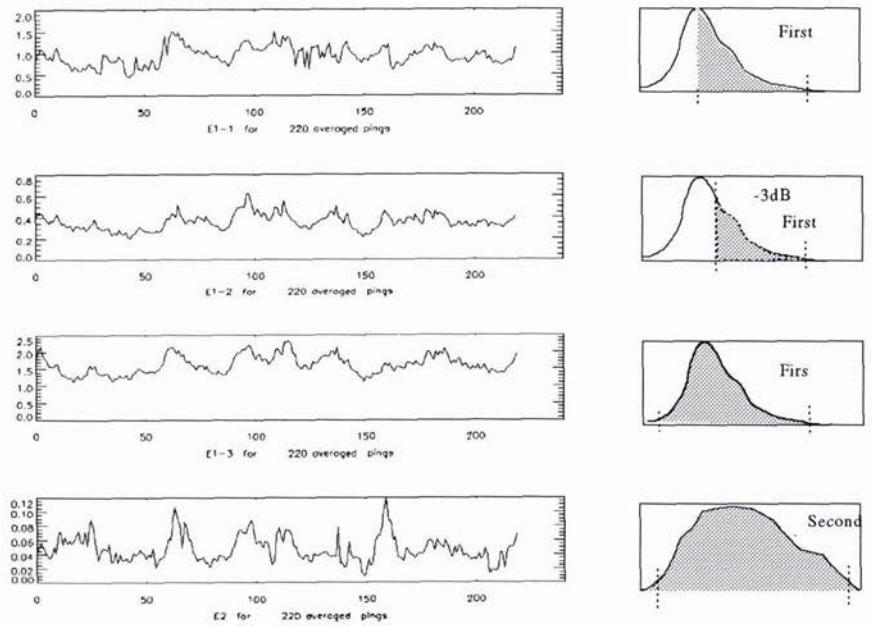

Figure 7b. E1 and E2 calculated from the integrals indicated, low frequency, sandwave region.

Scattering from an elastic cylinder buried beneath a rough water/sediment interface

John A. Fawcett

SACLANT Undersea Research Centre
Viale San Bartolomeo, 400
19138 La Spezia, ITALY
E-mail: fawcett@saclantc.nato.int

Abstract

In this paper a plane-wave decomposition method is used to compute the two-dimensional backscattering from a buried elastic cylinder as a function of frequency. The cases of a flat water/sediment interface and deterministically rough interfaces are considered. For rough interfaces, first-order perturbation theory is utilized to compute the interface reflection and transmission scattering matrices. In particular, the situation where the grazing angle in the water column is sub-critical is considered. In this case, at sufficiently high frequencies, the energy scattered into the bottom by the rough interface is dominant. The amplitude and spectral characteristics of the energy backscattered by the interface itself are also computed. Finally, the accuracy of using a simpler, single-scatter approximation is examined.

1. INTRODUCTION

In this paper, the backscattering from an elastic-shelled cylinder buried in sediment is considered. In particular, the grazing angle of the incident beam is taken to be subcritical. In this case, most of the energy transmitted into the bottom is evanescent and for sufficiently high frequencies it would be expected that very little of this energy would interact with the buried cylinder. However, some experiments [1],[2] have indicated that an anomalously large amount of energy does, in fact, penetrate into the bottom. Two possible explanations for this high level of energy are: (1) the existence of a Biot slow wave in the bottom [2,3], (2) a rough water/sediment interface which causes energy to be scattered into the bottom [4]. In this paper, the latter concept is investigated numerically. However, instead of simply considering the amount of energy which propagates in the bottom, the amplitude of the field backscattered from a buried steel-shelled cylinder is examined. The amplitude of this backscattered signal relative to the noise generated by the rough interface itself is also considered.

The plane-wave decomposition method for object and bathymetric scattering (see, for example [5],[6]) is used as the computational tool. We investigate burial below both flat and rough interfaces. For the case of a rough interface, first-order perturbation theory is used to compute the plane-wave scattering matrices for the interface. First-order perturbation theory has been shown by other authors [7] to be surprisingly accurate for the computation of the transmitted field. There has also been related work [8] for the case of an elastic sphere buried below a rough elastic interface.

2. THEORY

We consider a plane-wave incident upon an infinite elastic cylinder with an angle of incidence of θ_{in}. The cylinder is taken to be surrounded by a fluid with sound speed c_{se} and density ρ_{se}. The compressional potential scattered by the cylinder has the form

$$\phi_p^{sc} = \sum_{n=-\infty}^{\infty} \alpha_n H_n^1(k_{se} r) e^{in(\theta - \theta_{in})} \tag{1}$$

where α_n are coefficients determined from the solution of a system of equations. This system of equations is derived by assuming Fourier-Bessel series for compressional and shear potentials within the layers of the cylinder and then satisfying the appropriate continuity conditions across interfaces.

The individual azimuthal terms of (1) have a plane-wave decomposition given by:

$$H_n^1(kr)e^{in\theta} = \frac{e^{-in\pi/2}}{\pi}\int_C \frac{e^{i(k_x x+\gamma_{se}(k_x)z)}e^{in\beta(k_x)}}{\gamma_{se}(k_x)}dk_x \tag{2}$$

where "C" is an appropriate contour in the complex-k_x plane, $\beta(k_x)$ is the angle associated with the horizontal wavenumber k_x, and γ_a is defined in general as

$$\gamma_a = \sqrt{\frac{\omega^2}{c_a^2} - k_x^2}. \tag{3}$$

Using (2) with (1) it is thus possible to express the scattered field in terms of plane-waves. We will discretize the integral of (2). In this case, the effect of the cylinder on incident plane-waves is characterized by a finite matrix.

For a buried cylinder, the water/sediment interface modifies the incident field and also rescatters the scattered field from the cylinder. By characterizing the interface and cylinder in terms of plane-wave scattering matrices (or for a continuous spectrum, operators) we can express the vector of plane-wave components, $\vec{P}^u$ for the scattered field in the water column as,

$$\vec{P}^u = T_{UU}[I - \tilde{C}\tilde{R}_{UD}]^{-1}\tilde{C}\Phi_D T_{DD}\vec{P}^{in} \tag{4}$$

where $\vec{P}^{in}$ is the vector of incident plane-wave components. In (4) T_{UU} and T_{DD} denote transmission matrices for downgoing and upgoing plane-waves across the interface. For a flat interface, these matrices are diagonal. For a non-flat interface, a single plane-wave will scatter into a continuum of other plane-waves and these matrices will be full. The matrix Φ_D is diagonal and advances the vertical phases of the downgoing waves between the interface and the cylinder centre. For propagating waves these phase factors have unity norm; for evanescent waves these factors are decaying exponentials. Finally, $\tilde{C} \equiv \Phi_U C$ and $\tilde{R}_{UD} \equiv \Phi_D R_{UD}$ where C is the scattering matrix for the cylinder (for the scattering of downward incident plane-waves into upgoing plane-waves) ,R_{UD} is the interface reflection matrix for upgoing waves in the basement and Φ_U advances the phases of upgoing plane-waves. A schematic diagram of the scattering geometry with some of the operators indicated is shown in Fig. 1

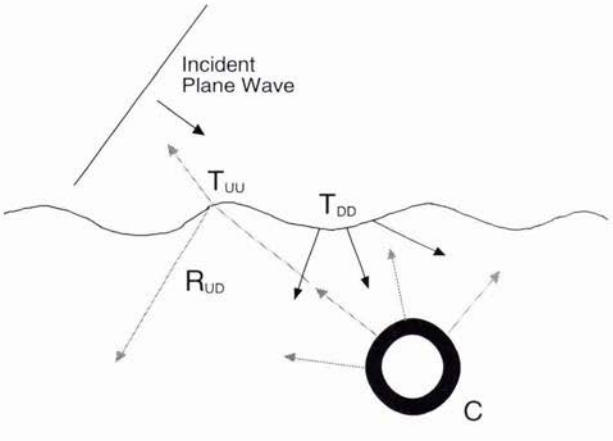

Figure 1: *A schematic of the scattering geometry*

In the case of a non-flat interface, it is non-trivial to compute the elements of T_{DD},T_{UU} and R_{UD} for general interfaces. We will assume that the interface is of the form

$$z = z_0 + h(x) \tag{5}$$

where $h(x)$ is much smaller in amplitude than a wavelength and that first-order perturbation theory will suffice to compute the scattering coefficients. In order to derive the perturbation theory the compressional potential in

the water, ϕ_w is taken to have the form

$$\phi_w = e^{i(k_0 x - \gamma_0 z)} + R_0 e^{i(k_0 x + \gamma_w z)} + \int_{-\infty}^{\infty} a(\lambda) e^{i(\lambda x + \gamma_w(\lambda) z)} d\lambda \tag{6}$$

and in the sediment the compressional potential ϕ_{se} has the form

$$\phi_{se} = T_0 e^{i(k_0 x + \gamma_{se} z)} + \int_{-\infty}^{\infty} b(\lambda) e^{i(\lambda x - \gamma_{se}(\lambda) z)} d\lambda, \tag{7}$$

where γ_w and γ_{se} are the vertical wavenumbers in the water and sediment respectively. The coefficients R_0 and T_0 are the plane-wave reflection and transmission coefficients for the unperturbed flat interface. The continuity equations which need to be satisfied at the water sediment interface are

$$\rho_w \phi_w = \rho_{se} \phi_{se} \tag{8}$$

and

$$-h'(x)\frac{\partial \phi_w}{\partial x} + \frac{\partial \phi_w}{\partial z} = -h'(x)\frac{\partial \phi_{se}}{\partial x} + \frac{\partial \phi_{se}}{\partial z}. \tag{9}$$

Substituting (6) and (7) into (8) and (9) and expanding for $h(x)$ and $h'(x)$ small, the leading order expression for $a(\lambda)$ and $b(\lambda)$ are obtained. We will not carry out the straightforward details here. It is important to note, however, that the coefficients $a(\lambda)$ for the backscattered direction (negative values of the wavenumber k_x) depend upon $\tilde{h}(|k_0|+|k_x|)$ whereas the coefficients for the scattered field in the forward direction depend upon $\tilde{h}(|k_0|-|k_x|)$, where $\tilde{h}$ denotes the Fourier Transform of h.

We now consider a particular set of rough interfaces. These interfaces have the form

$$h(x) = \epsilon e^{-x^2/(2\sigma^2)} cos(k_0 x). \tag{10}$$

The parameter k_0 allows us to control the wavelength of the perturbation and σ its effective lateral extent. The amplitude of the perturbation is controlled by ϵ. The Fourier Transform of the surface as defined in (10) is

$$\tilde{h}(k) = \frac{\epsilon\sigma}{4\sqrt{\pi/2}}(e^{-\sigma^2(k-k_0)^2/2} + e^{-\sigma^2(k+k_0)^2/2}). \tag{11}$$

In the numerical computations the amplitude ϵ will be decreased linearly as a function of frequency, in order that the height of the perturbation remain a fixed ratio of a wavelength.

We can make a simple prediction of the frequency dependence of these spectral curves. Recall that the amplitude of the forward scattered field is approximately proportional to $\tilde{h}(k - k_{in})$ or

$$T(k) \propto e^{-\sigma^2(k-k_{in}-k_0)^2/2} + e^{-\sigma^2(k-k_{in}+k_0)^2/2}. \tag{12}$$

We also recall that for $k > k_c = 2\pi f/c_{se}$ the energy in the bottom is evanescent. We first consider the situation where the acoustic wavelength is smaller than the wavelength of the interface roughness. Considering the second exponential in (12) and writing $k = k_c q$, $k_{in} = 2\pi f \cos(\theta_g)/c_w$ and $k_0 = \alpha\pi$, where θ_g denotes grazing angle, we derive the relation

$$q = \frac{c_{se}}{c_w}\cos(\theta_g) - \frac{\alpha c_{se}}{2f} \tag{13}$$

in order that the exponential's argument be zero. The maximum possible of q is unity before the dominantly scattered energy in the bottom is evanescent (recall that $k = k_c q$) and the value of the frequency for which this occurs is given by

$$f_{max} = \frac{\alpha c_{se}}{2[c_{se}/c_w \cos(\theta_g) - 1]}. \tag{14}$$

We do not expect significant energy to propagate in the bottom for acoustic frequencies much greater than this value.

On the other hand, if k_0 is very large then there will not be significant scattering in the bottom for frequencies which are too small. Following a similar analysis as before, it can be estimated that there will only be significant enhanced propagation in the sediment for

$$\frac{\alpha c_{se}}{2[c_{se}/c_w \cos(\theta_g) + 1]} \leq f \leq \frac{\alpha c_{se}}{2[c_{se}/c_w \cos(\theta_g) - 1]}. \tag{15}$$

For small values of frequency, the evanescent energy which is present in the sediment, regardless of the interface roughness, may dominate.

Another feature which can be derived from (12) is that for a frequency lying in the bounds of (15), the direction of the dominant energy in the sediment is in the $-k_x$ direction for the lower value of the frequency, increases to normal incidence with increasing frequency and then finally at the maximum frequency is nearly horizontal in the $+k_x$ direction.

3. NUMERICAL EXAMPLES

We consider an air-filled steel-shelled cylinder (c_p = 5950 m/s, c_{shear} = 3240 m/s and $\rho = 7.7g/cm^3$) of 15 mm thickness and outer radius 0.25 m. We consider an incident field with a plane-wave spectrum of the form

$$w(k_x) = exp(-(k_x - k_x^0)^2/{\sigma_b}^2) \tag{16}$$

where $k_x^0 = \omega\cos(20°)/c_w$ and $\sigma_b = 0.025\omega/c_w$ will be used in the computations. Thus a beam centred about the grazing angle of $\theta_g = 20°$ is produced, directed towards the centre of the cylinder. For angles approximately $\pm 3.85°$ on either side of 20°, the beam has e^{-1} of its maximum amplitude. In Fig. 2 we show the spectrum of the backscattered field at a receiver located at x=-2.747 m and z=1 m relative to the cylinder centre when the surrounding fluid has parameters c_p = 1700 m/s and ρ = 1500 kg/m^3. This receiver location corresponds to a direction of $-20°$ with respect to the cylinder centre (measured from the horizontal axis); thus we are considering a monostatic scattering geometry. We have computed the scattered field in two ways: (1) we used the plane-wave decomposition method (solid line) (2) we solved the scattering problem explicitly in terms of the Fourier-Bessel series for different incident plane-wave directions and then summed the results to produce the beam response (dashed line). As can be seen the two methods give essentially identical results

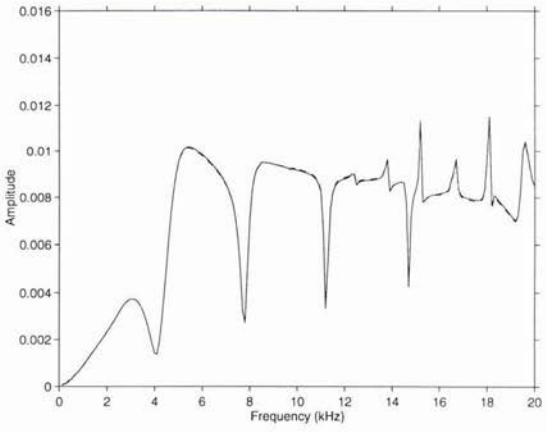

Figure 2: *Spectrum of backscattered field for surrounding fluid* $c_p = 1700m/s, \rho = 1500kg/m^3$ *as computed for an incident beam, using the plane-wave decomposition method(solid line) and a Fourier-Bessel series approach(dashed line)*

We now consider the incident beam to be in the water column ($c_p = 1500m/s, \rho = 1000kg/m^3$) and the cylinder in the sediment ($c_p = 1700m/s$, $\rho = 1500kg/m^3$) buried 0.5 m (2 radii) below the interface. For this sediment the critical grazing angle in the water column is equal to 28.1° and therefore the centre angle of the incident beam is 8° below critical. In Fig. 3a we show the field that is transmitted into the sediment for a frequency of 20 kHz. As can be seen, very little energy is transmitted into the sediment in this case. The fields that are scattered (the incident field is not shown) by a cylinder buried in the same sediment, but for a rough interface ($k_0 = 4\pi$), are shown in Figs. 3b and 3c for frequencies of 10 kHz and 20 kHz are shown. As can be seen, there is now significantly more energy in the bottom than in Fig. 3a. The scattered field is in fact strongest behind the cylinder where the total field would be a shadow zone. It can also be observed that directionality of the field is different for the two frequencies. This is in accordance with the predictions from (12). It can also be seen that the most energy is, in fact, backscattered at angles close to 90° back into the water column and that the amount of energy which reaches the receiver position is relatively small. In these and following computations, the value of ϵ is varied with frequency so as to be $\lambda/20$ ($\lambda \equiv$ wavelength) and σ in (10) is equal to 2. The roughness patch has its largest amplitude directly above the cylinder centre.

In Fig. 4 we show a plot of the backscattered spectral amplitudes for various rough interfaces. It can be seen that the Gaussian and flat bathymetries produce almost the same spectral response. The sinusoidal bathymetry with $k_0 = 4\pi$ produces a spectral curve which is significantly higher than the no-roughness curve for $f \geq 8kHz$. The spectral curve for the sinusoidal bathymetry with $k_0 = 0.75\pi$ is initially higher than the no-roughness curve but approaches it for increasing frequency, which is consistent with the behaviour as predicted by (15). The level of backscatter for the $k_0 = 4\pi$ curve is approximately equal to 2% of the level for the freespace curve of Fig. 2.

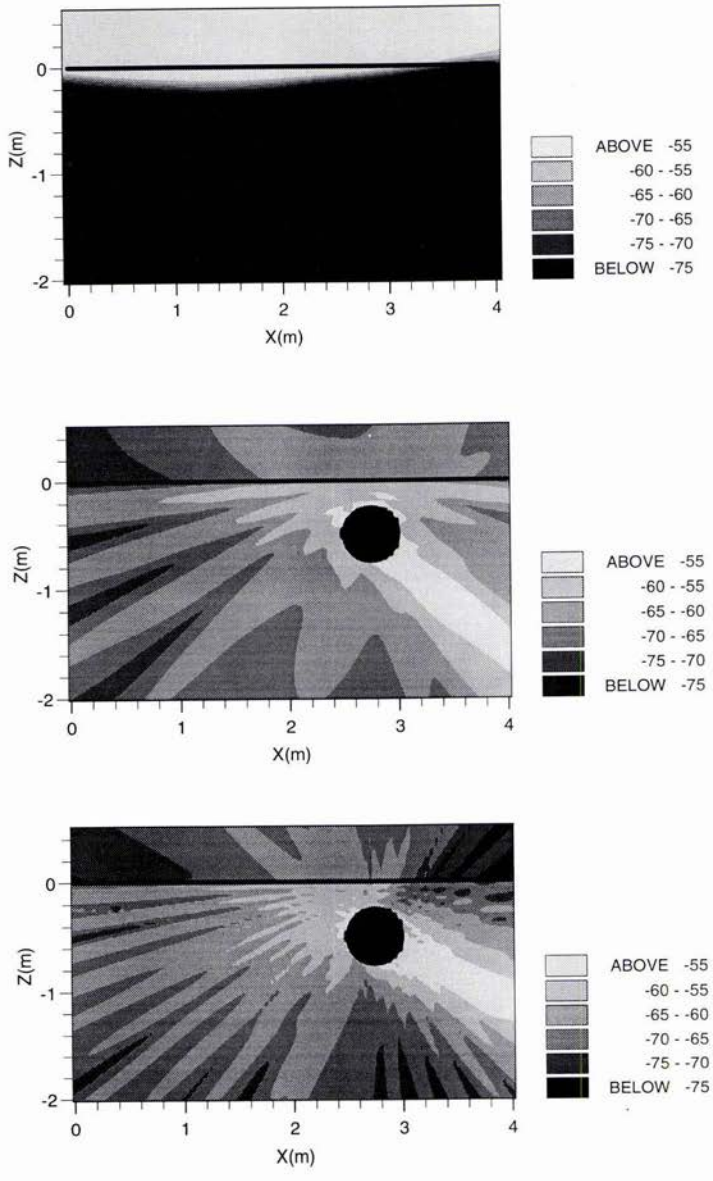

Figure 3: *Top figure is incident pressure field at 20 kHz; second figure is the pressure field scattered by the cylinder at 10 kHz for a rough interface ($k_0 = 4\pi$); third figure is the scattered pressure field at 20 kHz for the rough interface*

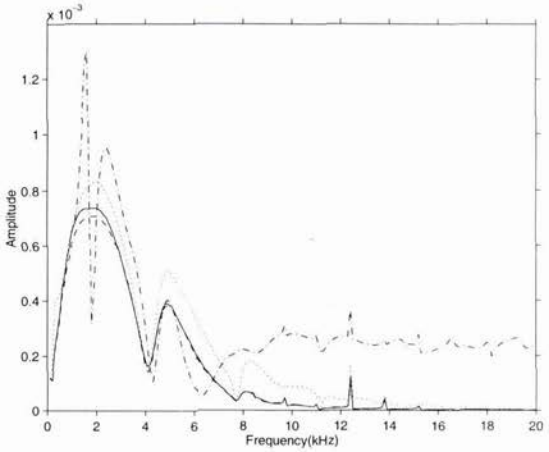

Figure 4: *Backscattered energy spectra for different types of surface roughnesses: no roughness (solid line), Gaussian profile (dashed), sinusoidal ($k_0 = 4\pi$) (dash-dotted) and sinusoidal ($k_0 = 0.75\pi$) (dotted)*

We now consider a flat interface and an interface with $k_0 = 4\pi$, in the case that the sediment has an attenuation of $0.5dB/\lambda$. The spectral curves for this case are shown in Fig. 5. As would be expected, the levels are less in this case and decrease with frequency. Also, note that most of the resonance structure of the curves has disappeared.

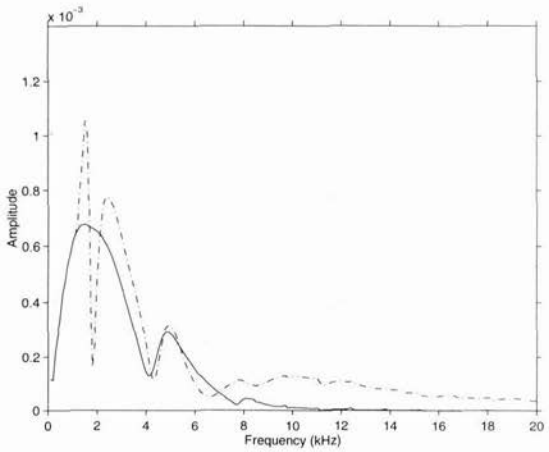

Figure 5: *Backscattered energy spectra for no roughness (solid line) and sinusoidal ($k_0 = 4\pi$) (dash-dotted) interfaces in the case that there is an attenuation of 0.5 dB/λ in the sediment*

We have seen that the presence of a rough interface increases the amount of energy in the sediment and leads to an increased amount of backscatter from the cylinder. However, there will also be increased backscatter from the interface itself and this will interfere with the backscattered energy from the cylinder. In Fig. 6 below we show the computed backscattered energy from the interface (ignoring the flat interface specular component) as a function of frequency (solid line) as well as the backscattered energy from the cylinder. As can be seen the energy backscattered from the interface dominates until f=10 kHz. Of course, in the time domain it maybe possible to separate the two types of energy, even when the reverberant energy dominates, by using appropriate filtering techniques.

Finally, we consider the modelling issue of when a single scatter approximation may be used. That is, instead of computing all the multiple interactions between the cylinder and the water/sediment interface above it, we may

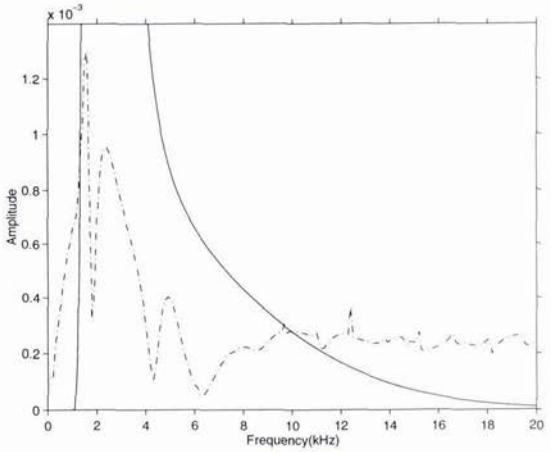

Figure 6: *Backscattered field from the interface (solid line), and backscattered signal from buried cylinder (dash-dotted) for sinusoidal ($k_0 = 4\pi$) interface*

approximate the scattering process as an incident field upon the cylinder, accounting for transmission through the rough interface, a single, free-space scattering (using the parameters of the surrounding sediment), and then transmission back into the water column. For the retransmission back into the water column from the sediment we consider two subcases; (1) we use the transmission coefficient for the flat interface (2) we account for the roughness for this second transmission process. There are computational advantages if the single scatter approximation is accurate; a variety of propagation codes can be used to propagate the incident field up to the scatterer and to propagate the scattered field away from the object. The scattering from the object can be computed using a free-space code. This type of approach has been used previously by other authors for waveguide scattering problems (see, for example, [9],[10]). In Fig. 7 we show the backscattered spectral curves using the exact solution (solid line), using the single scatter approximation with the flat interface transmission coefficients for transmission back into the water (dashed line), and the single scatter approximation with the rough interface transmission coefficients for transmission back into the water. As can be seen all three curves are very close, except near the strong peaks at

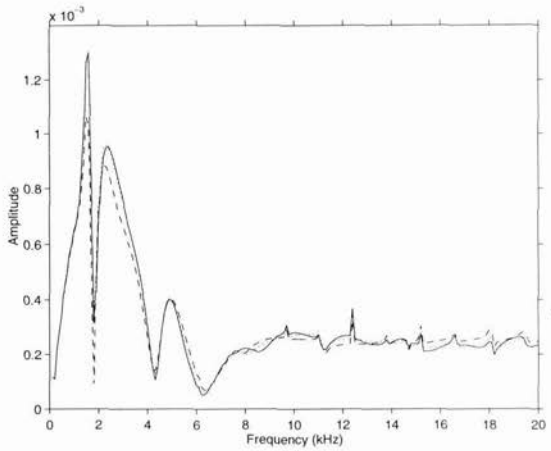

Figure 7: *Backscattered field from the cylinder for the rough interface ($k_0 = 4\pi$) using the exact solution (solid line), the single scatter approximation with simple retransmission back into water (dashed line), and the single scatter approximation with rough interface retransmission back into the water (dotted line).*

approximately 2kHz where using the correct rough interface transmission coefficients for retransmission into the water has a noticeable effect.

4. SUMMARY

It has been showed that the plane-wave decomposition method can be combined in a straightforward fashion with perturbation theory to compute scattering from objects buried below a rough interface. It was found that, for the case where the energy would normally be evanescent in the bottom, a rough interface can significantly increase the amount of object backscattered energy observed at a receiver in the water column. In fact, at sufficiently high frequencies this energy is higher than the energy backscattered from the interface itself (ignoring the specular component from the flat interface). The amount of energy and the directionality of the energy in the bottom depends upon the wavelength of the interface roughness. Finally, we have shown that a simpler (and computationally faster) single-scatter approximation can probably be used in many computations.

References

[1] J.L. Lopes, "Observations of anomalous acoustic penetration into sediment at shallow grazing angles", J. Acoust. Soc. Am., **99**, p. 2473, 1996.

[2] N.P. Chotiros, "Acoustic penetration of ocean sediments in the context of Biot's theory", J. Acoust. Soc. Am., **99**, p. 2474, 1996.

[3] N.P. Chotiros, "Biot model of sound propagation in water-saturated sand", J. Acoust. Soc. Am., **97**, pp.199–214, 1995.

[4] D.R. Jackson, J.E. Moe, E.I. Thorsos, and K.L. Williams, "Subcritical penetration of sandy sediments due to interface roughness", J. Acoust. Soc. Am., **99**, p.2474, 1996.

[5] B.L.N. Kennett, "Reflection operator methods for elastic waves I–Irregular interfaces and regions", Wave Motion, **6**, pp.407–418, 1984.

[6] J.A. Fawcett, "A plane-wave decomposition method for modeling scattering from objects and bathymetry in a waveguide", J. Acoust. Soc. Am., **100**, pp.183–192, 1996.

[7] E.I. Thorsos, "The accuracy of perturbation theory for acoustic penetration of sediment due to interface roughness", J. Acoust. Soc. Am., **99**, p.2475, 1996.

[8] G.C. Bishop and J. Smith, "Scattering from an elastic shell and a rough fluid-elastic interface: Theory", J. Acoust. Soc. Am., **101**, pp.767–788, 1997.

[9] F. Ingenito, "Scattering from an object in a stratified medium", J. Acoust. Soc. Am., **82**, pp.2051–2059, 1987.

[10] M.D. Collins and M.F. Werby, "A parabolic equation model for scattering in the ocean", J. Acoust. Soc. Am., **85**, pp.1895–1902, 1989.

Estimation of shear wave properties in the upper sea-bed using seismo-acoustical interface waves

S. A. Frivik, R. Allnor and J. M. Hovem

Norwegian university of science and technology, NTNU,
Department of telecommunications / Acoustics group
O. S. Bragstads plass 2b
N-7034 Trondheim, NORWAY
E-mail: [frivik, allnor, hovem]@tele.ntnu.no

Abstract

Acoustic interface waves have been recorded with a bottom deployed acoustic array at several locations. High resolution array processing technique (Prony) is used to estimate velocity versus frequency for the interface waves. An inversion scheme based general linearization is used to obtain estimates of shear velocity as function of depth. The data collection with subsequent processing and interpretation is intended for operational use in conjunction with normal refraction surveying using the same equipment. This paper discusses survey design in terms of measurable shear velocities, depth of investigation and resolution as function of frequency and array configuration. Examples of processing and interpretation of field data are presented.

1. Introduction

Marine refraction seismic surveys are usually done with a linear array of hydrophones and an "explosives" type source for generation of the refracted waves in the sea floor. The refracted arrivals are then picked as the first break, and estimation of compressional wave velocity(v_p) and thickness together with dip is determined for the different layers within the sediment [1].

The refraction technique gives however no information of the shear wave velocity structure in the bottom and for many applications shear information is very useful. The shear modulus of the bottom is very important for underwater acoustic propagation. For geotechnical use it is important that acoustic shear modulus of the bottom material is related to the strength, although the direct relation is generally not known. Another attractive feature is that shear wave velocity is often a better sediment identifier than the compressional wave velocity. Several different sediment types may have quite similar compressional wave velocity (e.g. clay/silt/sand) but very different values for the shear velocity.

A well known technique for measuring the shear wave velocity structure of the sea floor is based on the measurement and analysis of the seismo-acoustic interface waves. In the current project we have modified the data gathering and analysis of the refraction surveys to allow for the recording and analysis of acoustic interface waves without interference with the refraction survey. The main modification is extending the recording time, which allows recording of the late arrivals with in wave field. Modification of gain and filter settings avoids saturation and provides the recording of the interface waves. In this paper the design of the array and the processing to establish shear wave parameters are described together with results from three field surveys.

2. Theoretical aspects

The seismo-acoustical interface waves belong to a class of slowly propagating waves at the interface between two media, they are therefore often called boundary waves or just interface waves. The Scholte wave belongs to this class and propagates at the boundary between a solid and liquid (e.g. water and sediments). The properties of the Scholte wave can be summarized as ([2],[3] and [4]):

- It has a rotational particle movement in the sagital plane
- If the shear wave velocity is varying with depth, the Scholte wave becomes dispersive
- It is generated by a source close to, or at the sea floor
- The radiated pressure can be recorded by hydrophones close to or at the sea floor
- The velocity of the Scholte wave is approximately 0.9 times the shear velocity

The frequency dependent velocity (dispersion) can be estimated from the recorded time signals, and there exists algorithms for inverting the dispersion curves to shear wave velocity (v_s) as function of depth [5] and hence converting this to dynamic shear modulus (μ) also as function of depth. Figure 1 shows the flow chart of the working process to establish such estimates in addition to ordinary refraction analysis.

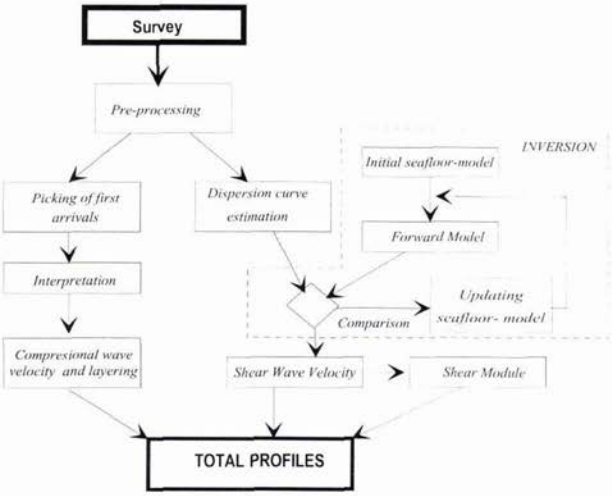

Figure 1: Flowchart of the processing refraction seismic data with extended recording time.

2.1. Survey design

The recorded wave field can either be processed using single- or multi sensor processing techniques for estimation of the dispersion curves. In the research community the multiple filter analysis [6] has been used extensively. The method gives an estimate of group velocity as a function of frequency. Since the method is a single sensor technique it suffers from problems like lack of resolution (velocity versus frequency) and it produces an average velocity estimate between source and receiver. This problems can be avoided by the use of the multi-sensor, high resolution estimators like the Prony method. The Prony method is based on wave number estimation from the signal recorded within the array, and represent therefor local estimate of the dispersion beneath the array. There are no problem with lack of resolution in velocity estimates. However, to use such a method, the array must be design to ensure a proper sampling of the wave field.

In general the receiver spacing (Δx) determines the lower limit of shear wave velocity which can be estimated. Since this parameter also are the target of the investigations a minimum velocity ($v_{s,min}$) has to be predicted/assumed. From this assumption one can derive the receiver spacing which must be equal or less then half a wavelength at the highest frequency of investigation (f_{max}):

$$\Delta x \leq \frac{\lambda}{2} = \frac{v_{s,min}}{2 \cdot f_{max}} \tag{1}$$

Assuming that $v_{s,min}$ is equal to 100 m/s, and that $f_{max} = 20$ Hz, the receiver spacing $\Delta x \leq 2.5$ meters. The distance from the source to the last receiver (R) is depending upon the attenuation of the waves in the sediments.

Here, it is assumed that the signal must be detected before the transmission loss (TL) is less than 20 dB, and using the absorption factor $\alpha_s = 0.002$ dB/m per. Hz [7]. The distance is determined by:

$$R = \frac{TL}{\alpha_s \cdot f_{max}} = \frac{10000}{f} \tag{2}$$

At $f_{max} = 20$ Hz, $R = 500$ meters.

In many cases a certain distance between the source and the array is required, to separate the waterborne and interface arrivals to avoid aliasing in the ($\omega - \kappa$-domain). Aliasing causes mis interpretation and occur when the surrounding environment is hard. The array length is given by $L = (M-1) \cdot \Delta x$, and it follows from eq. 2 and 1 that the source datum distance (SRD) is:

$$SRD \leq R - (M-1)\Delta x = \frac{1}{2 \cdot f_{max}} \left(2\frac{TL}{\alpha_s} - (M-1) \cdot v_{s,min} \right) \tag{3}$$

Using $M = 48$ receivers and the other parameters as described earlier: $SRD \leq 382$ meters. By use of the earlier assumptions, the minimum recording time becomes:

$$t_{rec} \geq \frac{R}{0.9 \cdot v_{s,min}} \tag{4}$$

Hence, $t_{rec} \geq 5.5$ seconds. In general we have used 8 seconds in our experiments.

2.2. Estimation of dispersion curves and inversion

The Prony method is a so called multi-sensor technique, that is a technique that makes use of an array of receivers to estimate the phase velocity as function of frequency. If N time samples has been recorded with M different receivers (receiver spacing Δx), the Prony method estimates the wave numbers κ. These can further be converted to phase velocity as function of frequency. The Prony method is deterministic, and the signal model for a certain frequency is [8]:

$$S_m = \sum_{p=1}^{P} h_p \cdot e^{\imath \cdot \kappa_p (m\Delta x + x_0)} \tag{5}$$

Here, h_p contains the magnitude and phase for the mode p, while κ_p is the wave number carrying the velocity information for the same mode. The recorded signal $s(t,x)$ in time and space, may be seen as a two dimensional Fourier transform, where $A(\omega,\kappa)$ is the response of the formation. Mathematically this is expressed as:

$$s(t,x) = \int_{-\infty}^{\infty} \int_{-\infty}^{\infty} A(\omega,\kappa) e^{\imath\omega t - \imath\kappa x} d\omega d\kappa \tag{6}$$

Eq.6 is continuous both in frequency and wave number. In most cases, only a limited number of modes are of interest. In addition, the frequency domain is band limited. Therefore eq. 6 can be rewritten as:

$$\hat{s}(x,t) = \int_0^{\omega_0} \Sigma_{p=1}^{D} A(\omega,\kappa_p) e^{\imath\omega t - \imath\kappa_p x} d\omega \tag{7}$$

Here, D represents the discrete and dominating modes. The bandwidth of inspection is set to ω_0. The algorithm for determining the velocity starts with a Fourier transform of each time series corresponding to the M recorded channels. The auto-covariance matrix ($\tilde{B}$), are calculated for each of the frequency-space vectors. After establishing the auto-covariance matrix we have a set of linear equations:

$$\tilde{B} \cdot \hat{g} = \delta \tag{8}$$

where δ is the model error. The solution $\hat{g}$ is further processed to $\hat{\kappa}$ [8]. The phase velocity as function of frequency (e.g. the dispersion curve) is then:

$$v_{dispersion} = \frac{2\pi f}{\hat{\kappa}} \tag{9}$$

The inversion process, as described in figure 1, is a typical minimization problem, where the object function is the the difference between the measured and a computed dispersion curves. The algorithm used for the inversion is the one presented by Caiti et. al [5]. The shear wave velocity and the shear modulus is related through:

$$\mu(z) = \rho(z) \cdot v_s^2(z) \tag{10}$$

Here, $\rho(z)$ is the density profile. This is not always known, but we have usually some knowledge about the sediments to make an assumption. From the Ranheim experiment the density profile is known from the geotechnical investigations.

Experiment	Nick name	Charge size [g]	Receivers	Δx [m]	SRD [m]	f_s [kHz]
Orkanger	Ork5	200	24	2.5	145	2
Ranheim	Ran7	300	24	2.5	323	2
	Ran16	200	24	2.5	165	2
Sandvik	p437	100	48	2.5	160	2

Table 1: Recording parameters of the different experiments.

3. Result from three field surveys

During the last three years we have performed three field surveys. Two have been carried out in the Trondheim fjord, at Orkanger in August 1994 and at Ranheim in December 1994 [9]. The third experiment was performed at Sandvik on the island Øland in Sweden in October 1996. All the experiments were done in shallow water and close to land. In the Trondheim fjord, one array of 24 receivers was used, while the Sandvik experiment was conducted with an array of 48 receivers. The receiver spacing was 2.5 meters, and "explosive" charges of size 25-300 grams have been used as sources. The parameters of each of the presented shots are given in table 1, and a side view of a typical recording is shown in figure 2.

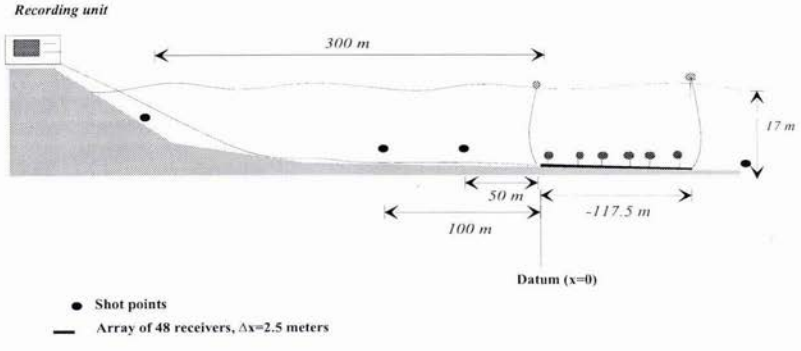

Figure 2: Side view of a typical recording (from the Sandvik experiment 1996).

3.1. The Orkanger experiment

The survey was performed in a natural river delta at Råbygda. Geotechnical investigations made close to the actual site uncovered sediments containing sand and gravel. Deposits of silt and fine sands was found both on top of and as thin layers buried within the sea bed [9]. Figure 3(a) shows the dispersion curve obtained with the Prony method using $p = 6$. The first two modes are interpreted ($d = 1$ and $d = 2$). The fundamental mode ($d = 1$) has been used for the inversion. The result of the inversion is shown in figure 3(b), as shear wave velocity as function of depth (left) and as shear modulus (right). The shear modulus is obtained using a iso-density profile of $1800kg/m^3$. The shear profile shows a $3-4$ meter thick loose layer on top of harder sediments. This is consistent with a layer of silt above sand and gravel.

3.2. The Ranheim experiment

From the Ranheim experiment, results from two shots are shown (Ran 7 and Ran 16). The dispersion curve from shot Ran 7 is shown in figure 4(a). Two modes has been interpreted, only the fundamental mode (d=1) have been used in the inversion. (The same has been done for shot Ran 16). The obtained shear modulus profiles are shown in figure 4(b), together with the geotechnical measured shear modulus (G_{max}) derived using the relations by Hardin and Black (o) and Hardin (x) [9]. The agreement between the two independent measurement techniques are quite good for Ran 7, while it has a deviating fit below 6 meters in case of Ran 16. Ran 16 is performed across the direction of deposition. The shot was made with an angle between the shot point and the array. Even after compensation for this angle, it is not possible to correct for the fact that the hard sediments are shallower around

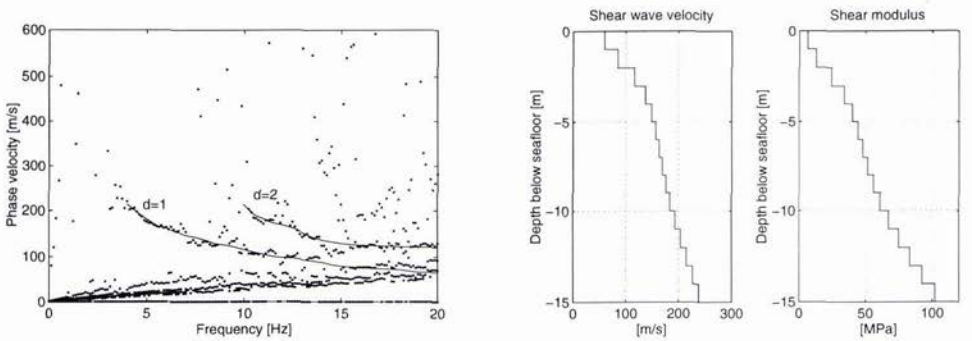

(a) (b)

Figure 3: a) Interpreted dispersion curve using Prony. b) Left: Inverted shear wave velocity profile. Right: Shear modulus profile

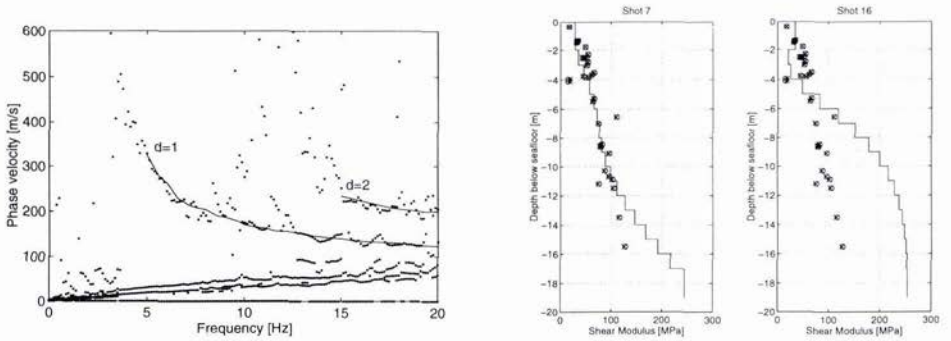

(a) (b)

Figure 4: Result form the Ranheim experiment;a) Interpreted dispersion curve using Prony on Ran7. b) Inverted-shear modulus profiles compared with geotechnical data Left: Ran 7, Right: Ran 16

the shot point than it is around the deployed array. This explains the disagreement between the modulus of Ran 7 and Ran 16, and hence the difference between Ran 16 and the G_{max} measurements.

3.3. The Sandvik experiment

The Sandvik experiment was conducted to record both compressional and interface waves. Figure 5(a) shows a typical time recording after filtering with a 30 Hz FIR (low pass) filter. The interface waves are found between $0.4 - 1.5$ seconds. The corresponding dispersion curve is shown in figure 5(b). The dispersion curve has been inverted from $10 - 20$ Hz, and the resulting shear wave velocity and shear modulus profile is found in figure 6. The shear modulus profile is generated using a iso-density profile of $2000 kg/m^3$. The dispersion below 10 Hz was not taken into account since this part might be influenced by aliasing due to interaction between waterborne and interface waves. The result from the standard refraction seismic analysis is plotted in figure 6. The comparison between shear wave and the compressional wave velocity shows that there is better resolution in the shear wave

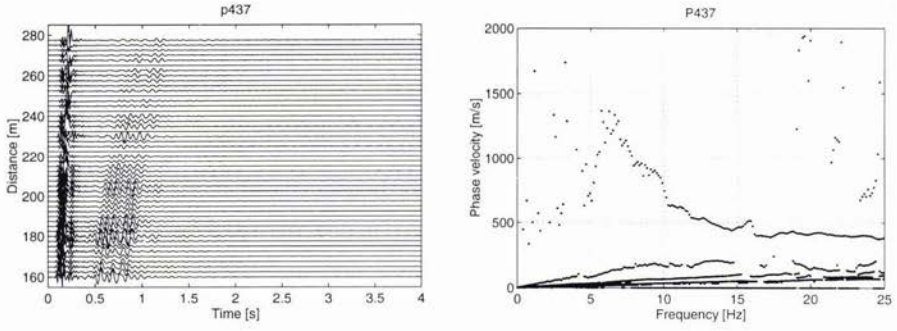

Figure 5: Result form the Sandvik experiment; a) Time series of profile p437. b) Dispersion curve using Prony.

velocity in the upper sediments.

To increase the information about the area data acquired with a bottom penetrating parametric sonar [10], *Topas*, (Simrad Norge) was available. The data were recorded using a Rickert wavelet as source pulse with a center frequency of 5 kHz. The data were taken several hundred meters south-west of profile p437, but close to the other three profiles. A stacked, amplified and processed signal from this system is shown in figure 7(a). Several reflectors have been interpreted, shown in 7(b). The reflector B defines the sea bottom. The water depth is estimated to be in the range of $12.9 - 11.8$ meters (using $v_p = 1450$ m/s). The bottom is quite hard in this area and only small amounts of energy has penetrated into the sediments. The reflector $R1$ determines the depth of the first layer , the depth is less than a meter using $v_p = 1700$ m/s, while $R2$ is the lower boundary of layer two, using $v_p = 2200$ m/s, this layer is 3 meter thick. There are just small variations in layer thickness for both these layers. The MB reflector is just a multiple reflection of the sea bottom. The *Topas* has here been used as a bottom profiler, the result gains no further knowledge about the area than already achieved by the refraction measurements. If the *Topas* had been used in a sweep modus, covering the area with angle dependent reflections/backscatter, such data could have been used for estimation of compressional wave velocity and layer thickness, but in this experiment this could be difficult due to the hard environment.

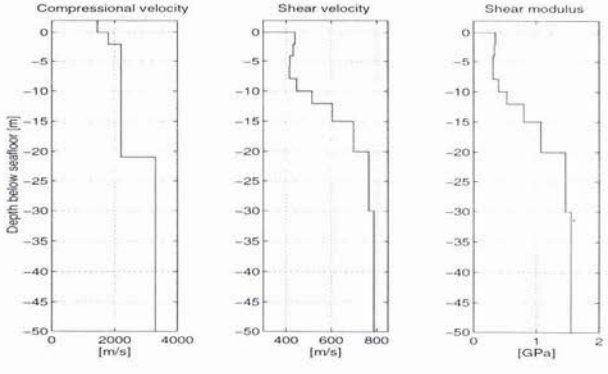

Figure 6: Result from the Sandvik experiment. Left: Shear wave velocity. Center: Shear modulus Right: Compressional wave velocity. All as function of depth.

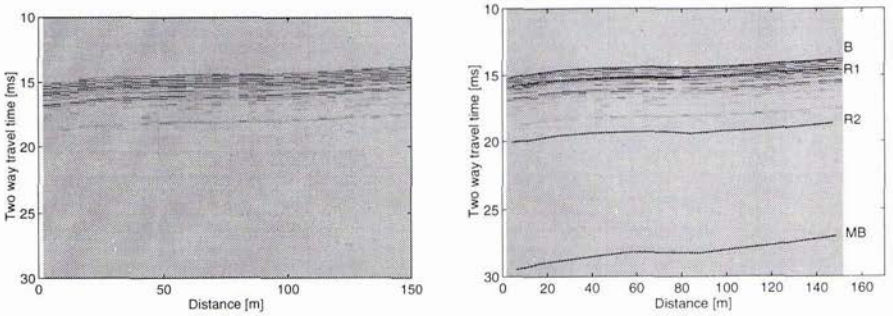

(a) (b)

Figure 7: Processed Topas data. a) un-interpreted b) interpreted (in color on PC-screen).

4. Discussion

The high resolution spectral estimators like the Prony method reduces the problem of averaging velocity estimates between source and receiver. The of resolution is increased, but with the result of increased computational cost. If one uses statistical methods the energy content can be estimated for the different modes, and the attenuation factors can be estimated as function of frequency. With an inversion technique for this parameter one could gain further knowledge about the upper sediments.

In the Ranheim experiment we have shown that the described technique fits quite well with geotechnical data. The shot must be set off in the in-line direction of the array. Further more, if the environment is laterally changing the size of the array must be small compared to these changes, since the forward model is based on plane layering. Therefor, if the environment is not piece-wise lateral plane layered, erroneous estimates will appear as results. To ensure good quality information the method should be combined with coring, but the number of cores can be reduced. The result will be a continuous profile of shear wave velocity and compressional wave velocity that can be correlated with the coring, resulting in a high quality identification of the different sediment layers.

As seen from the Sandvik experiment the method gives higher resolution in the upper sediments than what could have been achieved with only ordinary refraction seismic methods. Therefor this method can be used for better classification of the sea floor content in the top 10-20 meters. If the sediments are hard (like at Sandvik) the distance between the source and the array must be increased to separate the different arrivals in time to avoid aliasing effects. However, this problem have only appeared in the Sandvik experiment, it is no problems in the loose areas in the Trondheim fjord. The problem has trigged the idea of building an equipment with adjustable receiver spacing and source-array spacing. Such an array could be optimized to the actual environment, and combined with a source who generates less waterborne arrivals, like a vibrator. The source energy will then be coupled into the sediments and reduce the waterborne part of the wave field.

The Prony method is also able to reveal more than the fundamental interface wave mode. In figure 3 (a) and 4 (a) two modes are interpreted. Attempts to include such modes in the inversion [11], shows that the estimates for the deeper sediments becomes more reliable. The resolution of the upper sediments depends on the highest frequency in the analysis and thereby the receiver spacing (eq.1). By designing a tool with the appropriate settings, a new flexible equipment would provide velocity estimates lower than $100m/s$ (eq.1).

In future we will continue the work on development of processing techniques for analysis of hydrophone data as well as data recorded on three component geophones. A study of how the method functions in laterally changing environment is also necessary. This can be done with scaled models in laboratory or by numerical modeling. We have also started work which will investigated the the performance of the method in transversally anisotropic materials.

The method is well suited for investigations of cables and pipe-line routes as well as for evaluation of areas for placing sub-sea installations.

5. Conclusions

In this paper we have presented results from three field surveys. The data has been gathered with a linear hydrophone array deployed on the sea floor and with "explosives" as source. The recording time has been increased compared with standard refraction seismic survey to capture seismo-acoustical interface waves.

The data has been analyzed using standard refraction seismic methods, as well as we have applied more advanced processing algorithm to extract dispersion curves from the interface waves. The dispersion curves has been used as input to general linearization inversion.

The results of the inversion shows that there are more variations in shear wave velocity as function of depth, than it is for compressional waves. This result is important and shear wave velocity should be taken into account in sea floor classification and characterization. In the case of the Ranheim experiment the results has been compared with data from standard geotechnical investigations. The agreement between the different measurement techniques is good. We believe that there are potential in this technique to improve the classification and the characterization of the upper sea floor.

Acknowledgment

The field survey at Orkanger and Ranheim has been performed by O. K. Fjeld at GEOTEAM A/S. GEOTEAM A/S shot the seismic at the two site on their own expense and provided the geotechnical data from Ranheim. The geotechnical data was prepared by S. Kirkebø, Sintef Geotechnical Engineering, and this project was co-sponsored by the Norwegian Research Council under the TEFT-program.

The Sandvik experiment was a joint project between Statoil Gum T & T Kart, Geomap a.s and NTNU. The refraction seismic surveying and interpretation was done by A. Olsen and O. C. Pedersen (Geomap a.s). P. Morèn (FOA) helped us with the survey and J. Dybedal (Simrad Norge) provided the Topas data.

References

[1] J. G. Hagedoorn, "The plus-minus method of interpreting seismic refraction section", *Geophys. prosp.* , Vol. 7, pp.158-182, 1959.

[2] L. Cagniard *Reflection and Refraction of Progressive Waves* New York, McGraw-Hill, 2nd edition 1962.

[3] K. Aki and P. G. Richards *Quantitative Seismology, Theory and Methods (Vol. 1)* San Francisco, Freeman, 1982.

[4] D. Rauch, "Experimental and theoretical studies of seismic interface waves in coastal waters" in *Bottom Interaction, Ocean Acoustics*, edited by Kuperman and Jensen, Plenum Press , pp 307-327 , 1980.

[5] A. Caiti, R. D. Stoll and T. Akal, "Estimation of shear wave velocity in shallow marine sediments", *IEEE J. Oceanic Eng.* , Vol. 19, pp. 58-72, Oct. 1994.

[6] A. S. Dziewonski, S. Bloch and M. A. Landisman, "A technique for the analysis of transient seismic signals", *Bull. Seism. Soc.* , Vol. 59, pp.427-444, 1969.

[7] E. L. Hamilton, "Acoustic properties of sediments," in *Proceedings of the FASE Conference*,Acoustics and Ocean Bottom, Madrid pp. 3-58, 1987

[8] S. M. Kay and S. L. Marple, "Spectrum Analysis - A Modern Perspective", *Proceedings of the IEEE* , Vol. 69, No. 11 pp.1380-1419, November 1981.

[9] S. A. Frivik, G Svanø et al, "Use of interface waves for determination of shear stiffness in the upper sea floor" in *Proceedings of the IXV International conference on Soil Mechanics and Foundation Engineering*, Hamburg 6th-12th September, 1997, in press.

[10] P. Pettersen, J. M. Hovem, A. Løvik and T. Knudsen, "A new Sub-Bottom Profiling Sonar using Non-Linear Sound Source", *The radio and electric engineer*, Vol. 47, Nr. 3, pp 105-111, March 1977.

[11] R. Allnor, S. A.Frivik, A. Caiti, J. M. Hovem and Å. Sjøen Pedersen, "Inversion of Seismic Surface Waves containing multiple modes." in *Proceedings of the 3rd European Conference in Underwater Acoustics*, Heraklion, Crete pp. 637-642, 1996.

Sedimentological acoustics : an attempt to reduce the gap between acoustical modeling and sedimentological survey

Thierry Garlan, and Xavier Demoulin

EPSHOM 13, rue du Chatellier
292275 Brest Cedex, France
Email: garlan@shom.fr , demoulin@shom.fr

Abstract

A major task in shallow water acoustics is to provide pertinent geoacoustical data. The purpose of the work is to evaluate the state of the art in this field, connecting in situ sedimentological measurement and acoustical modeling aspects. According to sonar systems frequency ranges and to the kind of needs, the measurement in terms of sedimentological data is different. Parametrisation requirements are investigated for both propagation and reverberation models. We propose to translate differently the survey knowledge, of a calibrate zone, versus frequency to provide different parameter bottom sets to the users. We discuss the lack of availability of some of this parameters.

1. Introduction

We focus in that present work on the sea bed environment aspects and on the sonar acoustics aspects. For numerous maritime activities like fishing, resource development, mine burial and security of navigation, sedimentology is more specifically approached in terms of sea floor mapping; subbottom profiling is used for cables and pipeline laying, marine engineering, security research, ... So, most of the sedimentary applications have dual utility - military and civilian. Geoacoustical modelling, for ASW operation, takes into account most of the previous input. It also contributes to understand acoustics in sediments to the analysis of geophysical systems and concerns all the sea bed characterisation or classification systems.

Sedimentology and acoustic are closely linked, the acoustical data obtained during surveys is transformed in sedimentological parameters, then the process is inverted to give products suited to the beam angle and frequency of all kinds of sonar. Between all of the geological parameters: scaling of horizontal and vertical variability, heterogeneousness of sediments, sea bed roughness, influence of gas or bioclastes, wide range of rocks, which are the most important for acoustical modelling? What effect do they have on images or seismic systems data? And which roughness of sea bed interfaces is needed?.

First chapter concerns mostly sedimentological survey, measurement techniques and storage from large to very small regional scales. Sonar equation involves transmission loss and reverberation level. That terms contents reflection, scattering mechanisms, which are themselves strongly dependent of the bottom characteristics. We will develop that acoustical part in part two. Third part is devoted to an application. A recent calibrated area has been surveyed in Bay of Biscay. We propose to translate differently the survey knowledge versus frequency to provide different parameter bottom sets to the users and investigate their impact on sonar prediction.

2. Sedimentology

Sedimentological surveys are done with acoustical (imagery and seismic) and graded systems (samples, photographs). Since the sixties shallow water side scan sonar images are used in hydrography for seeking wrecks and dangerous obstructions. For sedimentological purposes, these data enable to differentiate rocky areas, limits of coarse and fine sediment, and sediment features. Many numerical processing were studied, they give nearly good results for textural characterisation (roughness) but not for grain size classification due to its unadapted high frequency (100 kHz or higher). With 10 to 20 kHz frequency, deep water multibeam echo sounder data are well done for sea bed characterisation [1]. In shallow water these multibeam systems have 100 kHz or more frequency, so they probably present the same limits as side scan sonar images with a less precision. All of these systems give morpho-sediments charts, but on the continental shelf, at 100 kHz or higher, side scan sonar received are modified by turbidity layers above the sea bottom, organic activities,

bioclastic proportion, sea bed roughness and sorting of sediments of surface. Multispectral satellite images and photogrammetric plotting carried out rapid assessment of clear water coastal field. In French Polynesia, radiometric data show variability up to 20 meters. On European continental shelf, these remote sensing systems provide sea bed information just from the beach to the slightly immerged zone (3 - 5 meter depth).

For subbottom knowledge, numerous systems could be used from some hertz for intra-crustal studies to some kHz for accurate description of the first tenth of meters. Numerical processing of the 3.5 kHz received signal, obtained with DELPH system on the hydrographic French vessels, could be used to calculate sediment type and geoacoustical parameters. The development of these studies complete the sediment thickness measure usually done with subbottom profiler. Questions on the necessary depth in sediment and accuracy needed are asked, so does the 3.5 kHz subbottom profiler give parameters needed for acoustical modelling?

Accurate topographic representation of sea floor contributes to the understanding of sediment distribution. The echo sounder used for bathymetric surveys could also be a source of data when the backscattering signal is processed. This signal processing, with systems like RoxAnn, characterise the sea bed and give parameters such as hardness and roughness (RoxAnn) or classified the sediment type, ... These methods offer several advantages : the real time results could be rapidly used for a broad spectrum of needs, the frequency could be chosen in accordance with the application. With a 33 kHz echo-sounder data are not modified by superficial turbidity, but it has the disadvantage of furnishing, in muddy and silty sediments, parameters which are the mean of the first decimetres of sediments.

All of the acoustic, photographic and radiometric data must be calibrated with samples. This bottom truth gives the name of the sediment. The quantification of various fractions, by dry sifting or laser diffraction particle sizing, enables the processing of sedimentological parameters as median, mean grain size, sorting and skewness. Carbonate determination completes these analysis. Spot samplings on cores are necessary to calibrate seismic profiles, the same parameters are obtained to construct a log of subbottom structures. These unequivocally reflect the deposition processes which laid down the sediment.

Density and celerity could be in-situ measured to have sedimentary and physical accurate data. In general, when cores aren't disturbed these parameters are measured in laboratory; in the other cases and for grab samples they are calculated with Hamilton and Bachman formulas. The comparison between these results proved that experiments and comparison must be done to improve the calculation method. The mean grain size don't give the real representation of the collection of particles which compose a sediment. The using of more sedimentological parameters (mean + sorting + skewness) depth and chemical parameters (carbonate and gas contents) would be better to improve density and celerity values. For roughness classification, RoxAnn, side scan sonar or echo sounder data must be calibrated with underwater video or photography.

Some of these sedimentary systems could not be used for every surveys. The aim of video and in-situ acquiring of acoustic parameters is to study the sedimentary-acoustic relationship and to obtain more accurate formulas.

2.1 From region to sediment

With the tectonic subsidence (when the sediment causes isostatic depression of the crust) sedimentary basins with some kilometres thick sedimentary sequences were built. The lack of subsidence since the Palaeogene, or earlier in some parts, have transformed the Channel and Bay of Biscay sedimentary basins in platform with soft sediment overlying different kinds of rocks. So, in view of the question set down, these zones are interesting to test acoustical modelling. Various kinds of sediments covered this continental shelf of the west of France, these bioclastic material mostly Holocene in age progressively contaminates ante Holocene lithoclastic relict deposits . The coarse lithoclastic material mainly result from frost shattering and solifluction during the Quaternary regressive stages. The distribution of the material is controlled by tidal currents in the open sea and swell close to the coast. From high energy areas to the minimum energy level - the wave base is from 6 m in the east Channel to 70 m in Celtic sea and in the Bay of Biscay - a sedimentary succession of decreasing grain size are thus observed. So as Larsonneur demonstrated [2] a sedimentary model which describe equilibrium between sediment distribution and hydrodynamic conditions can be mapped on a basin scale.

At sea, observations are different, they show higher precision offered by acoustic systems. Seaweeds, wrecks or local rock outcrops change environmental conditions, sand ribbons and other sand structures could be created downstream. In some muddy zones, sixty meters large pock marks, shown on side scan sonar sonographs, coming from gas. Thickness varying locally with sand structures and palaeo-rivers where 50 m of alluvium formations could be observed. With photographs or video images we see that roughness coming from small sand ridges, boulders and biological activity, is too small for side scan sonar and too large for samplings. The finer accurate data base obtained represent the primary source of information needed to support all of the different applications. The data processing of acoustic and samples are used to realise, with each kind of systems, maps at the scale of the survey (mosaics, isopach map, ...). The third product is a 3D sedimentary representation that we will develop during the next few years.

During the last 30 years, more than 20 000 samples were taken on the west of France continental platform. The whole granulometric range is represented from boulders and shingles to colloidal muddy particles. Well sorted sediments are the less represented. The mixing of ante-Holocene material, redistributed during the last transgression, with organogenic material give all kind of very poorly sorted. The sedimentary model is less accurate than surveyed data, but it could be sufficient for acoustical modelling, in the other case acquisition and data banking must be increased.

3. Acoustics

In this chapter, we suggest to split main mechanisms involved in four steps. Each step is a filter including modelisation, our misknowledge, and is designed to be compatible with the others filters.

1. Sedimentological survey. This point has been treated yet in the previous chapter. Sonar involve usually lower frequencies and lower grazing angles than sedimentological survey. So, a good knowledge of the whole problem is actually necessary to deal with seabed characterization and to design new instruments devoted to purely acoustical problems if necessary.
2. Parameters. Which geoacoustical parameters are necessary to describe the bottom and how calculate their values. Special attention is required to estimate thickness and accuracy of geoacoustical parameters given sonar constraints.
3. Local models. These models describe the physical interaction of acoustical waves with the bottom. They are the main part of the transfer function because they fix the parameters needing and limit the future acoustical impact study.
4. Global models. They are propagation and reverberation models. They are used to predict sonar performances. They have to manage with all kinds of constraints like water speed profile, sea surface state...In that context, shallow water and bottom's effect in shallow water are one of the numerous constraints to handle with and it is therefore usually necessary to simplify that problem. Such a simplification adds limitations to impact studies.

3.1 Parametrisation

Geoacoustic parameters depend on the local modelisation that will be used for the global modelisation. Usually we distinguish between reflection and scattering parameters. Reflection mainly depends on impedance. Impedance depends on speed, attenuation, and density of the medium. A reflection medium parametrisation is then oftenly given by 5 parameters : Compressional speed Cp, Shear speed Cs, Compressional attenuation Atp, Shear attenuation Cs and density ρ. Because it is hard to measure these parameters in laboratory (core needed, real in-situ conditions...), they are often calculated by empirical geoacoustical Hamilton relations. Actually, we often miss in situ calibration to be sure of our values. These values depend strongly on the in situ configuration as compaction for shear waves velocity for example. Parameters calculation depend on the frequency as well, dependence which is often discussed. Finally, as we will see later, substratum values are very important to estimate the reflection at low frequency (100Hz) and we seldom get in situ information about this. Reflection parameters usually used are:

	silt	sand	limestone	granite
Cp (m/s)	1550	1750	3000	5200
Cs (m/s)	80	130	1500	2500
Atp (dB/λ)	1	0.6	0.2	0.1
Ats (dB/λ)	1.5	2.25	0.4	0.2
ρ (Kg/m^3)	1.7	1.95	2.4	2.6

Scattering parameters depends as well on the local modelisation [3]. They generally split the problem on an interfacial rugosity and subfacial inhomogeneities but neglect the sediment stratification.They need parameters like micro-scale slopes or correlation length of inhomogeneities which are highly variables. They are related with frequency, and grazing angles and so very hard to estimate. In situ lack of data is a problem not only for sonar prediction but to calibrate sedimentological instruments as well. We present below an example of that kind of parameters [4]. To avoid such a complexity, scattering is sometimes described by the Lambert law characterized by one parameter only: $R(\theta,\theta') = \mu.\sin(\theta).\sin(\theta')$ where θ and θ' are respectively incident and reflected grazing angles and μ the bottom's scattering parameter.

	silt	sand	rock
μ (dB)	37	31	18
δ (degrees)	4	6	11
h_0 (cm)	3	7	50
μ_0 (%)	5	3	<1

Scattering parameters for 3 sediment classes first line concerns Lambert's law others come from Pouliquen [4]. δ is the rms sediment slope. h_0 the rms height of the rugosity and μ_0 the volume inhomogeneities parameter.

3.2 Local models

Local models treat of physical mechanisms of interaction between bottom and acoustical wave. Because they imply different mechanisms, it is easier to distinguish between reflection and scattering models.

Reflection coefficient

It is the ratio of the bottom reflected intensity by the incident intensity. Sea bed is modelised by a homogeneously stratified medium. $R(\theta)$ is then calculated applying the boundary conditions between different mediums.When the bottom is an infinite medium, it is characterized by a critical angle proportional to the ratio of the both mediums compressional speed

Cp2/Cp1 below which R =1. Actually, shear speed and attenuation generate reflection loss even below critical angle. When the modelisation of the stratification is more complicated, new phenomena appear such as frequency dependence, surface waves or shear waves resonance. It is important to notice that we focus on the low grazing angles. Those concern the propagation at long ranges because others are too attenuated. As we can see on the below figures, behavior at low and high grazing angle are very different .

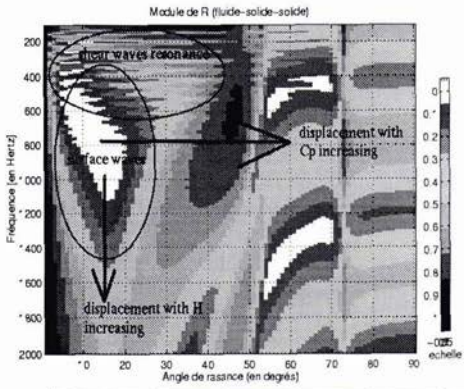

Reflexion coefficient versus frequency and grazing angle. The configuration is H =1m of solid silt over a granit substrat. An important loss at low grazing angle is due to shear resonance and to surface waves. Cp is sediment compressional speed.

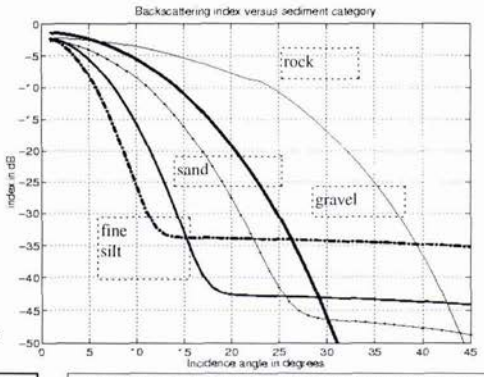

Reverberation index calculated with Brekhovskikh method. Parameters values are from Pouliquen [4]. We see that rugosity scatering is predominant for rock and near normal incidence. Inhomogeneities effect is stronger at high incidence angles.

Scattering

The scattering coefficient is defined by $R(\theta,\theta')$ like the reflection coefficient but involving non specular reflections. Various theories are possible to calculate $R(\theta,\theta')$. Because of the high number of parameters needed, they often suffer from a lack of in situ validation and calibration. It is the reason why we won't say a lot about it on the forward application.

Helmoltz Kirchhoff or Rayleigh Fourier theories applies for « smooth » roughness. Both of them are generally used for deterministic or measured interfaces. Unfortunately, it is seldom the case in practice. Some recent developments [5] modify Lambert`s law near specular direction. That kind of scattering lobes calculation is used in transmission loss global models. Modelling mixing interfacial rugosity and inhomogeneities are often found in literature [3]. They are useful for multibeam echosounder measurements for example.

3.3 Global models

Transmission problems

Shallow water bottom propagation problem is involved with reflection, scattering and bathymetric aspects. But it main characteristic is that it is a low grazing angles problem. So, local models must be especially accurate at this angles. Most of waves models can handle with reflection phenomena but not with scattering ones. This is mainly due to the complicated boundary condition that scattering generates. An other point to focus on is that few of them can handle with a varying medium. Unfortunately, it is often the ground truth. It is what we will partially answer in the next chapter investigating a varying calibrated zone.

Reverberation problems

It involves same constraints as for propagation modeling but it is now imperative to add the bistatic scattering effect. To simplify our explanation, we follow a geometrical approach as usually done. We proceed as for a classical ray models and each bottom reflected ray is directly backscattered to the receptor and time ray path stored. Reverberation level at a given time is the contribution of all simultaneously receptor arriving backscattered rays. The scattering law used in the below figure is a Lambert's law.

Bottom parameters involved in some propagation models

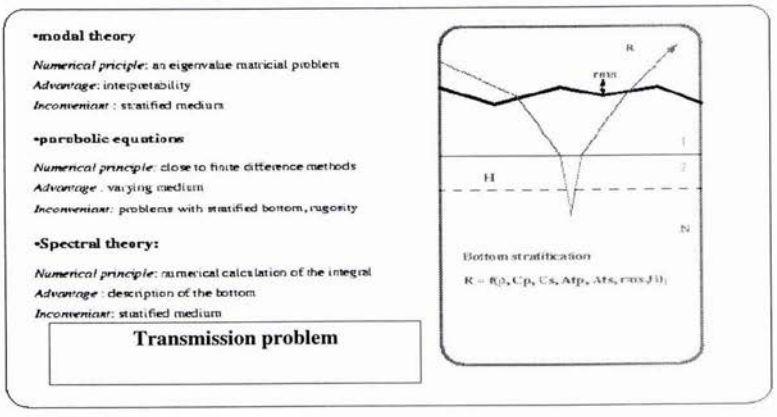

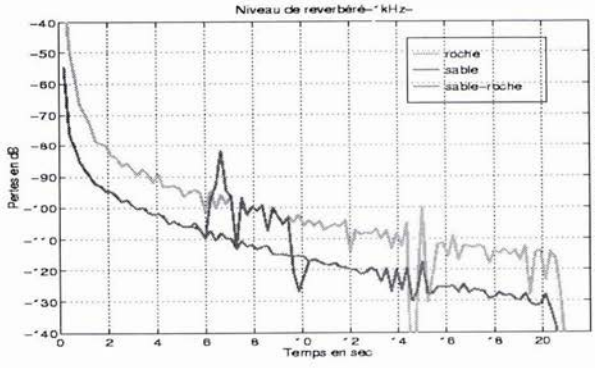

Reverberation problem

Reverberation level versus time. Calculated by rays theory with an isovelocity water of 100m.F = 5kHz. Zr=Zs = 50m. Lambert values for rock and sand are respectively 18dB and 31dB. Specular reflexion coefficients are respectively those of limestone and sand. We see the strong effect of 2kms of surficial rock on a sandy sea bed radiale.

4. Application

A calibrated zone was determined for testing acoustical modelling on real sedimentological data. So, we chose a deep near homogeneous flat zone on the sedimentological map of the Bay of Biscay. The depth of the 60 km long and 15 km wide area surveyed are from 130 to 144 meters. Sedimentological mapping at scale 1/40 000 was done with all of the systems previously described.

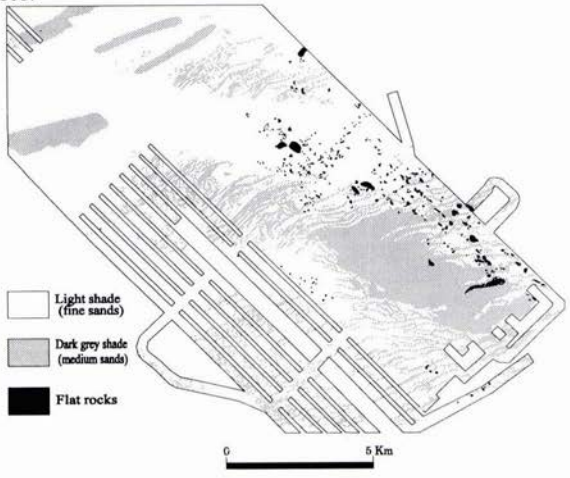

The side scan sonar morpho-sediment map reveal: - flat rock spots of several hectometres, we see on the bottom of one core that it is an eroded shelly limestone, - patchy light shade (fine sediment) covering the bottom horizon, - the main part of the zone is covered by dark grey shade, the cores show that it is bio-lithoclastic medium sands.
With the subbottom profiler different strata were define and an isopach map was done. The substratum is undoubtedly rock in the southern part of the zone; but in the north without any bottom truth the deeper reflector could be a coarse sediment or rock.
A synthetic 48 km long cross section was done with all data as shown in the following figure. It reveals a regressive succession - a coastal unit, probably beach bars of shelly gravel, were progressively covered by medium sand when the shoreline moved, with the increasing depth finer sand were deposited. The thin top layer of fine sand patches could be affected by storm waves.
Each point of the radial is described by a complete stratification including thickness of each sediment class. We make an impact study of such a variability on acoustical propagation. We follow the same methodology as in the precedent chapter. We focus on the different approximations to do versus frequency. We chose 3 frequencies 100Hz, 1kHz and 10kHz which scan the whole sonar ranging.

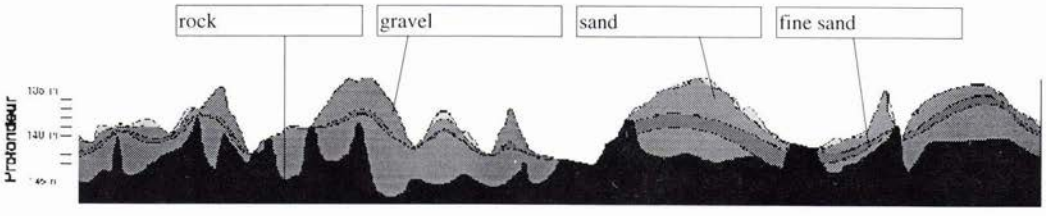

4.1 Parameters

The fifteen cores analysed contain different sediments, from bioclastic gravel to silty muddy sands. The following results of mean values are calculate for acoustical application:

	Fine sand	Sand	Gravel + sand	Shelly gravel	limestone
Density	2.01	2.21	2.28	2.37	2.4
Cp(m/s)	1773	1937	2002	2093	3000
Cs(m/s)	0	0	0	0	1500
Atp(dB/λ)	0.7	0.6	0.5	0.4	0.2
Ats(dB/λ)	0	0	0	0	0.4
μ(dB)	21.5	21	20	19	18

Density was measured in laboratory, compressional celerity was estimated with Hamilton formulas which take into account density (measures must be done during the next months with a core logger). Attenuation has been estimated from tab1 and shear sediment waves been ignored because we don't have any information on their actual values and because they are of few interest for that present study. We remark a quite high value of Cp for sediment classes. Because we don't have any measured scattering parameters, we choose to simplify them using a Lambert law fitting with values found in literature for such sediment at 10kHz only.

Backscattering index for 4 sediment classes at 10kHz. As we don't have any in situ indication on the scattering parameter class, we choose to fit a lambert law with that data. We then find μ = 21.5,21,20 and 19 dB. Angular dependency doen't follow a lambert law but we impose the fit in the 20-40° grazing angles. We will make the reverberation impact study with this values.

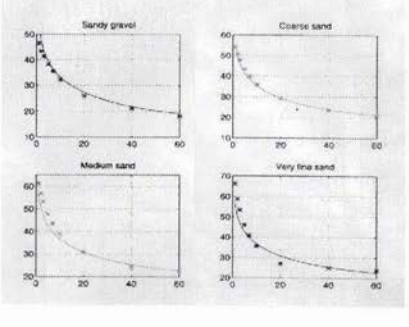

4.2 Local modelisation

Reflection

With such a radial, we calculate every reflection coefficient with SAFARI [6]. As expected, we observe a strong rock impact for the 3 frequencies.

- At 100Hz, the variability is quite important. R(θ) is rather sensible with sediment thickness but few with it Cp value. The main phenomenon is surface waves conditioned by sediment thickness and Cs substratum value. We modeled the stratification at 100Hz as a sand of thickness H over a limestone substratum. Calculations gave exactly the same result as for the complete original stratification. We focus on the lack of information we have about Cs substratum value. It could vary between 1500 and 1700 m/s and even probably more. This is a very important point to check in order to predict transmission loss .
- At 1kHz, variability is less important. R(θ) is few sensitive to the substratum except when sediment thickness is very little. Then, a similar phenomenon as before, generates a reflection loss. R(θ) is involved with the whole sediment stratification. Here, it is mainly dealt with the critical angle due to the superficial sediment because of the quite low contrasted sediment stratification. It is better to modelise the stratification by a simple superficial sediment than by a depth-averaged one.

At 100kHz, penetration at such low grazing angles is very few, and it appeared very convenient to modelise stratification by an infinite sediment corresponding to the superficial one as shown in the following figure.

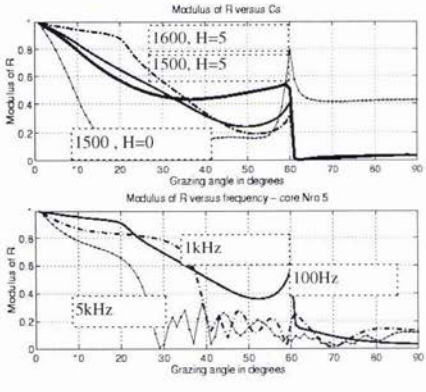

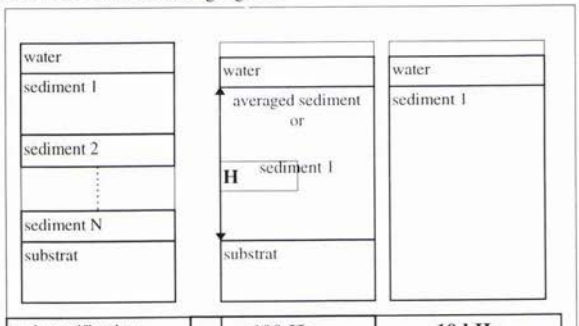

Diferent simplification of the stratification versus the used frequency. 100Hz mainly depends on the sediment thickness over a well defined substrat. 10kHz only depends on the surficial sediment

above left :reflexion loss variations with sediment thickness of 0 and 5 meters, Cs shear speed of limestone at 1500 m/s or 1600 m/s. below left:reflexion loss for core Nro5's stratification. 100Hz's one is drived by substrat shear speed (1600m/s). 1khz's one by sand's critical angle and 10kHz's one by the very thin silt superficial sediment.

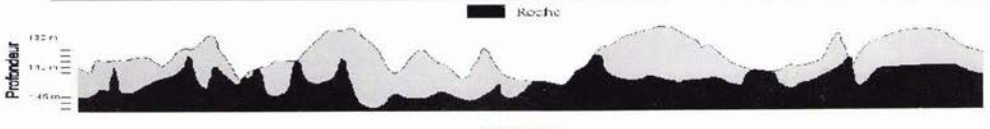

100 Hz

Final representation of the stratification for 100Hz and 10kHz. Because of their local reflexion loss properties, they are quite different and will be used for writing the input environemental data file for global propagation loss.

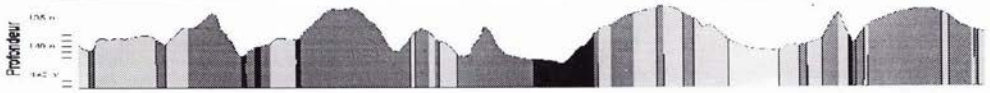

10 KHz

4.3 Global impact

It is then possible to give an input environmental data file to deal with propagation models.Few of usual wave propagation models allows us to handle with such a variable stratified bottom.We made simulations at respectively 100Hz and 1kHz.

- At 1kHz, We made simulations with FEPE [7], parabolic equations, with the 10kHz environmental data file, except the under laying rock which is changed by a superficial limestone. It is then possible to avoid stratification problems due to parabolic equation modeling. We made 3 simulations. One with the whole data set, one with the bottom's data set but with a flat bottom, and one with a homogeneously stratified flat

bottom. For the last one, geoacoustic parameters are those of an averaged sediment over all the radial.

At 100Hz, we can't deal with parabolic equations because of the stratified bottom's constraint. So, we must reduce the complexity and focus on what is the most important, according to us. As we said before, a very important variation of reflection loss is due to Cs, shear speed of the limestone. So we make two simulations, one with an homogeneous flat bottom with an averaged thickness of sand (3m) overlaying a substratum with Cs=1500m/s, and 1700m/s. We calculated transmission loss with the normal modes code KRAKENC [8].

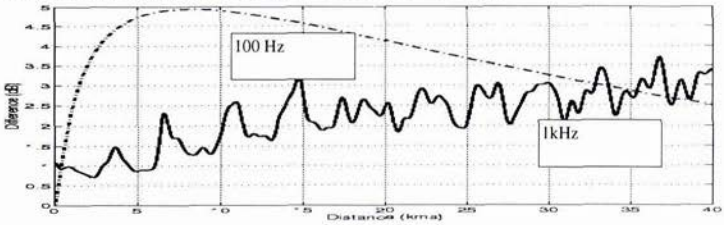

- At 1kHz, we make coherent loss calculations. We use a low filter to diminish interference effects and show difference in dB between the real and the simplified medium. There is no difference between a flat bottom and the true bathymetry. The difference increases slowly versus distance. Nevertheless, it is quite a low difference considering all ours environmental misknowledge.
- At 100Hz, the difference is stronger even at quite small distance. It tends to prove that sediment thickness and substratum shear speed can't be neglected even at small regional scales. It is necessary to map more accurately this parameters in order to improve passive sonar prediction.

5. Summary

Mixing sedimentological survey and acoustical modelling is a necessity to provide a performant acoustical survey and to predict sonar performances. Working on such a calibrated area is very useful to show the complexity of that problem and to enlight some important points. In all cases, multicriteria approach with imagery, seismic systems, in situ measurement, must be coupled with data bases to characterize the bottom truth and discussed the validity of geoacoustical relations.

Survey major problem is the lack of in-situ measurements to get a ground truth. Rugosity is then a recurrent problem which could be diminished by photography. Parameters quantification is mainly done by Hamilton's relations. But some of them remain still badly known (shear speed or attenuation) and others totally unknown like substratum shear speed. Some attempts to classify rugosity sediment parameters remain incertain according to us. Complexity of local scattering modeling add further to the difficulty of calculating scattering lobes. Wave propagation models show their limitations when they have to handle with a complex varying ground truth. Nevertheless, it seems that usual approximations as considering a homogeneous bottom on such a small regional scale and homogeneous medium may be quite enough accurate (at medium frequency). It's not the same at lower frequencies where strong bottom interactions can occurs.

References

[1] S Dugelay «Caracterisation des fonds marins a partir de donnees sondeur EM12» Thesis U. Orsay, 256 p, 1997.

[2] C Larsonneur, D Vaslet and JP Auffret «The surficial sediments of the english Channel», BRGM Ed., 1978.

[3] P.D. Mourad, D.R. Jackson, « High frequency sonar equation models for backscatter and forward loss », Proc. Oceans 89, 1168-1174, 1989.

[4] E. Pouliquen, « Identification des fonds marins superficiels à l'aide de signaux d'echosondeurs », thèse,1992.

[5] J.W. Caruthers, and J.C. Novarini, »Modeling bistatic bottom scattering strength including a forward scatter lobe », IEEE 18 (2), April 1993.

[6] H. Schmidth, « SAFARI, Users guide », SACLANT report, La Spezia, 1988.

[7] M.D. Collins, « A split step pade solution for the parabolic equation method », J. Acoust. Soc. Am 93, 1736-1742, 1993.

[8] M. Porter, « The KRAKEN normal mode program », SACLANT report, La Spezia, 1991.

Physics of bottom scattering and some applications

Marc Gensane

Thomson Marconi Sonar
6 rue Nieuport
78143 Vélizy-Villacoublay. FRANCE
Email: luc.leviandier@thomson-csf.fr

Abstract

The main bottom scattering theories are described in their bistatic formulation: composite-roughness, and volume scattering. Several applications are proposed. One of the main concerns is to check the mono- and bi-static Lambert rule: it is shown to which extent the models can bring some improvement. Another concern is the use of the expressions of the complex scattered pressure for statistical simulation and analysis purposes.

1. Introduction

Empirical models go on being used currently in underwater acoustics to calculate the reverberation. The classical Mackenzie (or Lambert) formula still holds, and propagation softwares have included it, combined with a correction for high grazing angles that is derived from the specular reflection theory [1]. Concurrently to the empirical approach, the theoretical one has given rise to some formulations that are now well-known; they have been applied since some years for comparison to experimental backscattering strengths measurements. The two most known of them will retain our attention: the composite-roughness theory for bottom topography scattering, and the first order scattering theory to treat the effect of the upper sediment volume. They are presented here, in their general bistatic form. The expressions of the scattered complex pressure, and then the scattering strength are given. The definition of their validity domains is important but is only summarised here. Some various applications are proposed. As a test, fittings with backscattering measurements are shown. Some aspects of the bistatic behaviour are studied to check the Lambert rule. Finally some simulations of temporal scattered signals show that not only the scattering strength, but also the complex pressure itself, can be an interesting.

2. Theory

Let an acoustic harmonic plane wave impinge on the sea floor, with frequency f, grazing angle θ_1, and azimut φ. The water has a density ρ_1 and a sound speed c_1, the sediment is supposed fluid, with mean density ρ_2, mean sound speed c_2, and mean attenuation α. Let $\rho = \rho_2/\rho_1$, $n_0 = c_1/c_2$, and $n = n_0 + i\beta$ (complex refraction index). The attenuation α is usually given in dB per wave length, and one has: $\beta = \alpha \ ln\ 10 / 40\pi$.

This wave splits in two parts. One part is reflected by the sea-bottom interface, the other is transmitted into the sediment. If the interface is perfectly plane and the sub-bottom perfectly homogeneous, reflected and transmitted waves are plane waves; their reflection and transmission coefficients are respectively:

$$V(\theta_1) = W(\theta_1) - 1 \quad ; \quad W(\theta) = \frac{2\rho \sin\theta}{\rho \sin\theta + \sqrt{n^2 - \cos^2\theta}} \tag{1}$$

If the interface exhibits some roughness or ondulations, scattering appears, which affect the reflected wave. If the sediment floor is not homogeneous, the transmitted wave scatters and part of it is returned into water. The first scattering will be named " interface scattering ", the second, " (sediment) - volume scattering ".

The geometry of the problem (figure 1) involves the following notations:

Incident and scattered unit vectors: $\vec{n}_1$ and $\vec{n}_2$; incident wave vector: $\vec{k}$, its horizontal component $\xi_1 = k\cos\theta_1$.

Bistatic wave vector: $\vec{K} = k(\vec{n}_1 - \vec{n}_2)$; its horizontal and vertical component: $\vec{\kappa}$ and $\vec{\gamma}$; bistatic angle ψ.

Hereafter, expressions of the complex scattered pressure p_s are derived for the interface and volume effects, and expressions of the scattering coefficient m_s therefrom. The near-vertical grazing angles are not considered here. The frequency domain of validity should be about 1 to 100 kHz.

The scattering coefficient m_s is defined per bottom unit surface, even for the volume effect, and the classical bottom scattering strength is: BSS = 10 log(m_s).

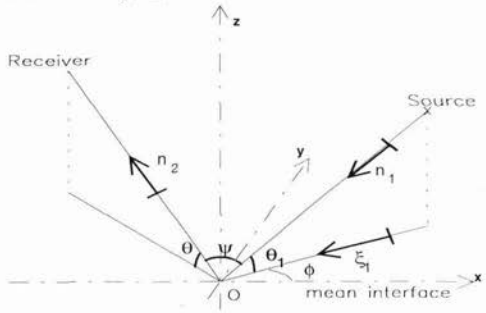

Figure 1. Geometry

2.1 Interface scattering.

2.1.1 Scattered pressure

The small-perturbation method is applied. Instead of using Kuo's developments [2], it is more straightforward to follow those of Brekhovskikh-Lysanov [3]. They have solved the problem for the sea-surface scattering, but the method is extensible to the bottom scattering, by taking in account the boundary condition of pressure and sound speed continuity at the interface:

$$p_1 = p_2 \quad ; \quad \frac{1}{\rho_1}\frac{\partial p_1}{\partial N} = \frac{1}{\rho_2}\frac{\partial p_2}{\partial N} \tag{2}$$

The pressures and their normal derivatives are developed up to the first order of the surface height ζ and its spatial derivatives. It is assumed that the total pressure is: $p_j = p_{0,j} + p_{s,j}$, where j = 1 in water, 2 in sediment. $p_{0,j}$ is the plane wave pressure obtained with the mean plane interface; $p_{s,j}$ is the scattered wave pressure. Equations (2) become:

$$p_{s1} + \zeta\frac{\partial p_{s1}}{\partial z} = p_{s2} + \zeta\frac{\partial p_{s2}}{\partial z} \quad ; \quad \rho\left(\frac{\partial p_{s1}}{\partial z} + \zeta\frac{\partial^2 p_{01}}{\partial z^2} - \vec{\nabla}_r p_{01}.\vec{\nabla}_r\zeta\right) = \frac{\partial p_{s2}}{\partial z} + \zeta\frac{\partial^2 p_{02}}{\partial z^2} - \vec{\nabla}_r p_{02}.\vec{\nabla}_r\zeta \tag{3}$$

where $\vec{\nabla}_r$ is the horizontal gradient. Let $z = \zeta(\vec{r})$ be the interface topography equation, and $A(\kappa)$ it's spatial Fourier transform:

$$\zeta(\vec{r}) = \iint A(\vec{\kappa})\, exp(i\,\vec{\kappa}.\vec{r})\, d\vec{\kappa}$$

The scattered pressures in the water is sought as a plane waves integral:

$$p_{s,j}(R) = \iint A(\vec{\kappa})\, F_j(\vec{\kappa})\, exp\left[i(\vec{\xi}_0 + \vec{\kappa}).\vec{r} + ic_j z\right] d\vec{\kappa} \quad , \quad j = 1, 2 \tag{4}$$

with: $$c_1 = \sqrt{k^2 - \left|\vec{\xi}_1 + \vec{\kappa}\right|^2} \quad ; \quad c_2 = -\sqrt{n^2k^2 - \left|\vec{\xi}_1 + \vec{\kappa}\right|^2}$$

Reporting (4) in (3) yields for j=1 [3]:

$$F_1 = \frac{1}{c_2 - \rho c_1}\left[W\left(\rho\gamma_1^2 - \gamma_2^2 + (1-\rho)\vec{\xi}_1.\vec{\kappa} - c_2\gamma_2\right) - (V-1)c_2\gamma_1\right] \tag{5}$$

with: $$\gamma_1 = k\,\sin\theta_1 \quad ; \quad \gamma_2 = nk\,\sin\theta_2$$

2.1.2 Scattering strength

To obtain the scattering coefficient, a random topography is supposed, whose spatial spectrum G is defined by:

$$\delta(\vec{\kappa}-\vec{\kappa}')\,G(\vec{\kappa})=\left\langle A(\vec{\kappa})\,A^{*}(\vec{\kappa}')\right\rangle$$

Following again Brekhovskikh-Lysanov method, the scattering coefficient is found to be:

$$m_s = k^2 \sin^2\theta\, f_1(\kappa)\, f_1^{*}(\kappa)\, G(\kappa) \tag{6}$$

(*: complex conjugate).

As particular cases, (6) leads easily to the sea-surface bistatic scattering strength [5]:

$$m_s = 4k^4 \sin^2\theta \sin^2\theta_1\, G(\vec{\kappa})$$

or the sea-bottom back-scattering strength [2] [6] which is (6) with $\theta = \theta_1$ and $\kappa = 2k\cos\theta$ and:

$$F_1 = 2\sin\theta\,\frac{(\rho-1)^2\cos^2\theta+\rho^2-n^2}{\rho\sin\theta+\sqrt{n^2-\cos^2\theta}} \tag{7}$$

2.2 **Volume scattering**

The volume inhomogeneities are spatial variations $\Delta\rho$ and Δc of the mean density ρ_2 and sound speed c_2.

$$\rho=\rho_2\left(1+\frac{\Delta\rho}{\rho_2}\right)\quad;\quad c=c_2\left(1+\frac{\Delta c}{c_2}\right)$$

2.2.1 Scattered pressure

With a plane incident wave, the total pressure obeys the equation [7]:

$$\Delta p + k^2 p = 2k^2\frac{\Delta c}{c_2}\,p+\vec{\nabla}\frac{\Delta\rho}{\rho_2}.\vec{\nabla}p \tag{8}$$

Provided that $\Delta\rho \ll \rho_2$ and $\Delta c \ll c_2$, the simple scattering or Born approximation holds, and one may replace p by the incident pressure p_i in (8). Since one expect that volume scattering should be important only for grazing angles greater than the critical angle of the sediment, the evanescent wave [8] may not be taken in account.

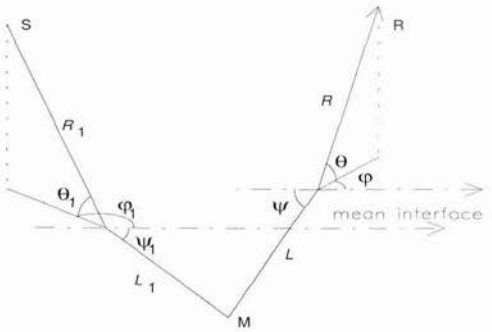

Figure 2. Geometry for volume scattering.

The scattered pressure is therefore:

$$p(f,R)=\iiint\left(2k^2\frac{\Delta c}{c_2}\,p_1+\frac{1}{\rho_2}\vec{\nabla}(\Delta\rho).\vec{\nabla}(p_i)\right)\Gamma(M,R)\,dM \tag{9}$$

where

$$\Gamma(M,R)=\frac{W(\theta)\exp(i\Phi)}{4\pi(R+L)}$$

is the Green function between the current scattering point M and the receiver R (figure 2). Φ/k is the complex travel between M and R. Here it is assumed that the interface is in the farfield of the scattering point M; this may be somewhat coarse, but useful to carry on easy calculations. It is supposed moreover that the volume may be splitted into volumes of dimensions bigger than the wavelength but smaller that the attenuation length (which

is a little bit coarse too).

$$p(f)=\frac{k\,W(\theta_1)W(\theta)\,exp(i\Phi_0-\delta z)}{2\pi\,R_1 R}\left[\frac{k}{c_2}G_c+\frac{i}{2\rho_2}\left(cos\theta'\,cos\phi\,G_{\rho x}+cos\theta'\,sin\phi\,G_{\rho y}+sin\theta'\,G_{\rho z}\right)\right] \tag{10}$$

$$G_c=\iiint \Delta c(x,y,z)\,exp\left[ik(ax+by+cz)\right]dxdydz \tag{11}$$

$$G_{\rho x}=\iiint \frac{\partial\Delta\rho(x,y,z)}{\partial x}\,exp\left[ik(ax+by+cz)\right]dxdydz \tag{12}$$

and so on for $G_{\rho y}$ and $G_{\rho z}$. The coefficients are:

$$\begin{aligned} a&=cos\theta_1\,cos\phi_1+cos\theta\,cos\phi \\ b&=cos\theta_1\,sin\phi_1+cos\theta\,sin\phi \end{aligned}\quad ;\quad c+i\delta\approx\frac{cos\theta_1}{tan\psi_1}+\frac{cos\theta}{tan\psi}-n\left(\frac{1}{sin\psi_1}-\frac{1}{sin\psi}\right)\quad ;\quad \Phi_0=k(R+R_1+n(L+L_1)) \tag{13}$$

This expression is interesting for simulation, because G_c and G_ρ are the Fourier transforms of the volume fluctuations, so one may simulate samples of volume fluctuations and calculate the FFT to obtain directly the complex pressure. More straightforward, if one knows the mean spatial power spectrum, the sampling may be made directly on the Fourier transform values, avoiding the FFT, and so the simulation is made with an analytical formula.

2.2.2 Scattering strength

From (9) one finds the bottom scattering coefficient [4] (per unit of surface):

$$m_s=\left|W(\theta_1)W(\theta)\right|^2\frac{1}{2\beta}\frac{sin\theta_1\,sin\theta}{sin\theta_1+sin\theta}\,m_v \tag{14}$$

where m_v is the sediment volumic scattering coefficient (that is, per unit of volume):

$$m_v=2\pi k^4\,\mu^2\,G(\vec{K}) \tag{15}$$

μ is the volume fluctuation:

$$\mu=\frac{\sigma_c}{c_2}+\frac{\sigma_\rho}{\rho_2}sin\frac{\psi}{2} \tag{16}$$

and it will be supposed that $\sigma_\rho = 3\sigma_c$ [9]. Here, G is a normalised spectrum.

2.3 Highlight points.

In (9), some deterministic functions may be used. The following:

$$\Delta c(x,y,z)=\sum_{i=1}^{N}\sigma_{ci}\,exp\left(-\frac{(x-x_i)^2}{x_{0i}^2}-\frac{(y-y_i)^2}{y_{0i}^2}-\frac{(z-z_i)^2}{z_{0i}^2}\right) \tag{17}$$

may simulate an ensemble of N highlight points centered at (x_i, y_i, z_i) if the characteristic dimensions x_{0i}, y_{0i} and z_{0i} are small compared with the signal duration. It lead to a relatively simple analytical expression of the complex scattered pressure (for one point):

$$p=\frac{\sqrt{\pi}}{2R_1R}W(\theta_1)\,W(\theta)\,x_0y_0z_0\,exp(i\Phi_0-\delta z)\left[\frac{\sigma_c}{c_2}+\frac{\sigma_\rho}{\rho_2}\left(a\,cos\psi_1\,cos\phi_1+b\,cos\psi_1\,sin\phi_1+c\,sin\psi_1\right)\right]Q(f) \tag{18}$$

with:

$$Q(f)=k^2\,exp\left[-\frac{k^2}{4}\left(x_0^2a^2+y_0^2b^2+z_0^2c^2\right)\right]$$

and a, b, c, δ given in (13).

2.4 Spatial spectra

The following formula is proposed:

$$G(\vec{\kappa})=\frac{A}{\left(K_0^2+\kappa^2\right)^{h/2}} \tag{19}$$

containing a " characteristic " wavelength $\Lambda_0=2\pi/K_0$, and a " spectral slope " h. This formula is often reduced to: $G(\kappa)=A\kappa^{-h}$. The volume inhomogeneity spectrum is $G(\vec{K})=G_H(\vec{\kappa})G_V(\vec{\gamma})$, where G_H and G_V

are the horizontal and vertical components, having the same expression as (17), so, with a horizontal and a vertical characteristic wavelength (resp. Λ_0 and Z_0), and a horizontal and a vertical spectral slope (resp. h and v). As an example, the experimental vertical spectrum of the figure 1 in [9] is best fitted with Z_0 = 15 cm.

3. Applications

3.1 Fitting to experiments

We intended to show some comparisons between the above scattering strength formulae and a panel of published experimental results, but the data basis is not yet available; only very few are digitized, and only from deep sea bottoms (but one may hope that the physics of the phenomena do not depend on the water depth). However, some trials may be attempted and are interesting to comment. A particularly drastic example is given in figure 3, extracted from Hines and Barry [10], frequencies 2 and 2.3 kHz; it exhibits a strong peak at a grazing angle of about 15 degrees. Such peaks appear sometimes [11] [12], but not so hard. The Lambert rule fits these data with a standard deviation of about 6 dB. Use of (6) or (14) should be much better. Anyway, this kind of peak is the signature of an interface effect. The sound speed and density are fixed in the model to 1600 m/s and 1.64, as proposed by the authors. The best fit is obtained by the interface effect, with h = 4 and Λ_0 = 0.4 m (which leads to a RMS roughness of 0.14 cm); for θ < 15 degrees, the composite-roughness model is used, and the best fit is obtained with a RMS long-wave slope of 5 degrees. The deviation between the model and the data is 1.2 dB. The attenuation has been fixed to 0.3 dB per wavelength; fitting would have been still better with lower values.

These measurements have been done at 5 frequencies. Retaining four of them (0.9, 1.2, 2, 2.3 kHz) leads to the following fit: no characteristic wavelength, h = 5 (slight decrease with frequency), deviation 2.2 dB.

In the same paper, there is another case which now could be characteristic of a dominating volume effect. In figure 4, the particular behaviour around the critical angle is correctly fitted by a volume scattering with spectral slopes h = 3 and v = 2, a wavelength Z_0 = 1.5 m, and a mean fluctuation σ_c = 16 m/s; mean velocity and density are fixed to 1700 m/s and 1.9, as suggested by the authors; the deviation is 1.3 dB. Obviously, the best fit of the interface effect do not follow at all the behaviour of the experimental values, and its deviation is 3.8 dB, worse than the Lambert rule fit (2.6 dB). A better interface fit can be obtained, with a deviation of 1.8 dB, but with a mean velocity of near 1900 m/s, which is too far from the announced value to be retained. Curiously, in this case, the volume effect seems to dominate 1) even at subcritical angles, 2) even without taking the evanescent wave in account, and 3) even with a plane wave formula which is quite approximative for near- and sub-critical angles (see [8]). So one must not be too affirmative about the interpretation of this case.

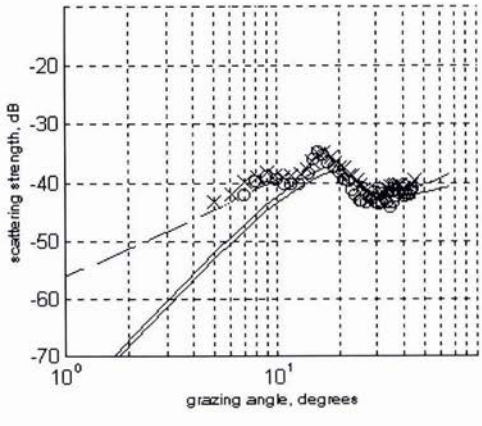

Figure 3. Points: experimental values [10 A]. Solid line: best fit of (8) on angles > 11 deg.. Dashed: best fit of composite-roughness on angles < 15 deg.

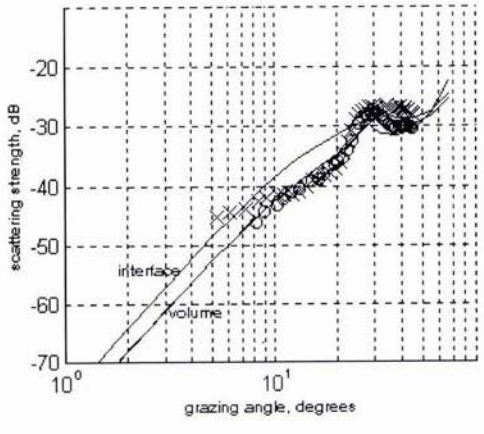

Figure 4. Points: experimental values [10 B]. Solid lines: best fits of (8) and (14) on angles > 10 deg.

3.2 Bistatic behavior: Does Lambert rule work well?

Since one is far from being ready to feed the theoretical models with the good parameters values in every

world's sea, empirical rules such as Lambert's one, even well-corrected near the vertical [1], may stay useful for a while. The bistatic Lambert rule is:

$$BSS = \mu_0 + 10\log(\sin\theta_1 \sin\theta) \qquad (20)$$

We have just seen some cases, and especially in figure 3, which are far from a $\sin^2\theta_1$ behaviour; these are rather uncommon, and on other hand, many authors have pointed out the relative validity of this rule (less authors tend towards the " Lommel-Zeeliger " rule).

It is easy to compare the rule to the above models, by dividing (6) or (14) by the product $\sin\theta_1 \sin\theta$, leading directly to the value of the " Lambert parameter " μ_0. Since (20) imply no azimut variation, it is interesting to look for example at a grazing-azimut representation. Figures 5 and 6 show the Lambert parameter for the following typical case: θ_1 = 40 degrees; α = 1 dB/wavelength; ρ = 1.8; A of (19) = 0.004; f = 1 kHz. For figure 5 (interface effect): h = 3.5. For figure 6 (volume effect): Z_0 = 0.3 wavelength, Λ_0 = 10 Z_0; mean Δc = 30 m/s; h = 3, v = 2. These cases have a rather strong critical angle effect. Nevertheless, there exists large angular domains where the parameter does not diverge too much from a constant; it does diverge, particularly in very forward scattering, or at very low grazing angles. But note that at low grazing angles, generally an integration of either (6) or (14) with respect to the local slopes distribution has for effect to increase the scattering coefficient and bring it near a Lambert one (as in figure 3).

The mean Lambert parameter and its standard deviation have been computed for azimuts between 90 and 180 degree (whole " backward direction "), and grazing angles between 5 and 60 degrees (apart from the very low angles, and the specular effect). They are reported in Table 1 for some various cases. The interface spectral slope is 4, its amplitude 0.004. The volume parameters are the same as above.

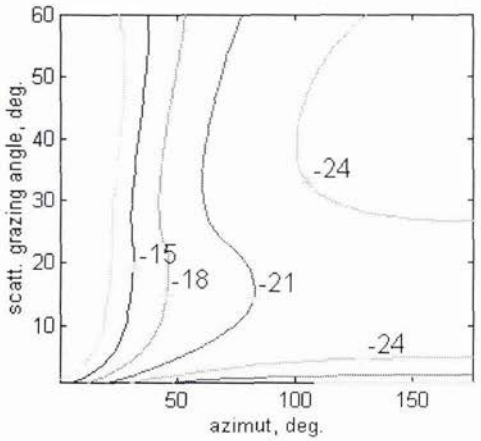

Figure 5. Contour lines of Lambert param. for (6)

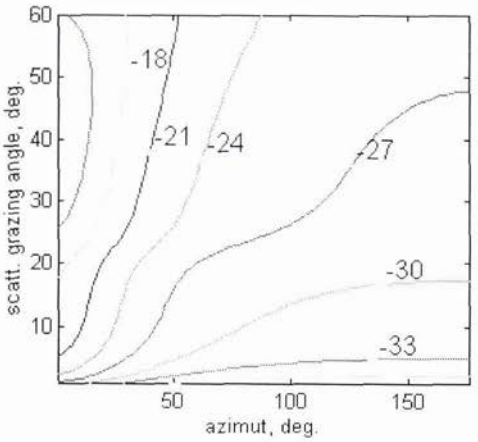

Figure 6. Id, for (14)

case	mean μ_0 (dB)	deviation (dB)
ρ = 1.5; θ = 40 deg; [θ, φ] graph; interface effect	-30.5	0.61
ρ = 1.8; id.	-23.6	1.18
ρ = 1.5; θ = 10 deg; [θ, φ] graph; interface effect	-29.2	0.75
ρ = 1.8; id.	-20.8	1.56
ρ = 1.8; φ = 180 deg; [θ_1, θ] graph; interface effect	-22.8	1.93
φ = 90 deg; id.	-21.4	1.26
ρ = 1.5; θ_1 = 40 deg; [θ, φ] graph; volume effect	-26.3	0.77
ρ = 1.8; id.	-27.8	1.87
ρ = 1.5; φ = 180 deg; [θ_1, θ] graph; volume effect	-26.7	0.58
ρ = 1.8; id.	-28.7	1.82

Table 1. Lambert parameter fit for typical cases. $90 < \varphi < 180$ deg. $5 < \theta$ and $\theta_1 < 60$ deg.

It appears that the deviation is never strong for most practical cases. It is clear that for soft sediments (no or very small critical angle) the Lambert rule works better than for sediments exhibiting a critical angle behaviour, and this, for both interface and volume effects.

As a conclusion for §§ 3.1 and 3.2, Lambert rule has some validity for soft sediments, preferably with no critical angle - which is not so uncommon. On the contrary, one should be cautious in using it on hard sediments, and prefer to apply the theoretical formulae, even with common typical values fo the parameters if the real ones are not known.

3.3 Simulation of temporal signals

The expressions of the scattered complex pressure (4) and (10) or (18) can be used to simulate temporal signals, by sampling the formulae in a given bandwidth, and inverse Fourier transform. To show this capability, an example is presented. Signals can be simulated with various statistical distributions. Some volume backscattered signals are computed in a typical high-frequency case [13]: linear modulated frequency 10-25 kHz, pulse duration 1 ms; range 11 m; insonified area 3 m long; refraction index 1; since we have not still analysed the density derivative statistics, only the velocity spectrum G_c is sampled in (10), with the hypothesis of gaussian or exponential correlation. Due to computer memory limitations, the volume is divided in sub-volumes of 128^3 points.

Adding some highlight points to this volume, one expects to obtain for example a log-normal signal distribution.These points are simulated with (18) using $x_0 = y_0 = z_0 = 1.5$ cm, Δc with a gaussian distribution, ratio σ_c of (18) to σ_c of (12) = rc, filling rate $rf = \sum_{i=1}^{N} x_{0i} y_{0i} z_{0i} / V$ (V: insonified sediment volume). The capability of simulation with only a combination of highlight points is also tested, by varying the filling rate, the statistical distribution of the points dimensions (z_0), and the distribution of Δc. Table 1 shows some statistical results. The temporal signals are matched-filtered, square-detected and integrated with constant 1/15 ms. Some statistical tests (Kolmogorov-Smirnov and χ^2) are performed to check exponential and log-normal distributions, as in [13]. The value of the best-fitted log-normal parameter is indicated. The tests are applied to series of 8 recurrences of 4 ms, that is, about 480 independant samples.

Gaussian or exponential volumes do not really lead to gaussian signals (exponential after integration), but the difference between exponential and log-normal fits are not so strong as it seems, since the χ^2 test is very severe. As expected, one can simulate really log-normal behaviours by adding some highlight points. This behaviour increases by diminishing the filling rate (the number of echoes), or by increasing the mean echo level (rc). By this way one can obtain signals which looks like real ones [13], and moreover, with good values of the parameter (δ comprised between 0.8 and 0.9).

But another interesting conclusion is that one can obtain about the same results only with highlight points, without simulating the whole volume: the table shows one example where the highlight points lead to a signal gaussian even for the χ^2 test, and another example following a log-normal distribution with a correct value of δ (and, alas, a poor probability of the χ^2 test - but sometimes real signals are not best). And this is interesting for by this way there is no need of huge computer memory.

volume simulation process	Exponential distribution		Log-normal distribution		
	Kolmo. prob.	chi-2 prob	Kolmo prob.	chi-2 prob.	param. δ
Gaussian correlation volume	0.28	0.000	0.74	0.13	0.9
Exponential correl. Volume	0.21	0.000	0.59	0.06	0.94
Gaussian corr. volume + highlight points: rf=.0004, rc=1.4, z_0=1.5 cm, Δc gaussian	0.000	0.000	0.9	0.006	0.81
Gaussian volume + highlight points: rf=.0002, rc=1, z_0=1.5 cm, Δc gaussian	0.01	0.000	0.87	0.000	0.84
Gaussian volume + highlight points: rf=.001, rc=1, z_0=1.5 cm, Δc gaussian	0.26	0.000	0.71	0.66	0.88
Highlight pts only, rf=0.2, z0=2 cm, and Δc=10 m/s (constants)	0.16	0.012	0.43	0.013	1.03
id., rf=0.2, z0 =χ^2(1.5 cm), Δc= lognor(mean 10 m/s, dev. 20 m/s)	0.00	0.00	0.81	0.000	0.82

Table 2. Statistical tests for some temporal signals simulations.

Acknowledgements

These works have been done with the aid of the Direction Générale pour l'Armement (Contracts DRET 91.306.32, and CTSN 92 48 690), and the European Community (Contract MAST 3 n° 9: DEO).

References

[1] D.D. Ellis and D.R. Haller. A scattering function for bistatic reverberation calculations. J. Acoust. Soc. Am. 82 (S), p 124, 1987.

[2] E.Y.T. Kuo. Wave scattering and transmission at irregular surfaces. J. Acoust. Soc. Am. 36, pp 2135-2142, 1964.

[3] L.M. Brekhovskikh and Yu.P. Lysanov. Fundamentals of ocean acoustics, 2nd edition, chap. 9. Springer-Verlag. 1990.

[4] M. Gensane. Low frequency bistatic reverberation. Thomson-Sintra ASM report 92/A/GEA/458/MG, december 1992 (in French).

[5] S.T. McDaniel and A.D. Gorman. An examination of the composite-roughness scattering model. J. Acoust. Soc. Am. 73, pp 1476-1486, 1983.

[6] D.R. Jackson and K.B. Briggs. High-frequency bottom backscattering: roughness versus sediment volume scattering. J. Acoust. Soc. Am. 92, pp 962-977, 1992.

[7] L.A. Chernov. Wave propagation in a random medium. Mc Graw-Hill. 1960.

[8] P.C. Hines. Theoretical model of acoustic backscatter from a smooth sea-bed. J. Acoust. Soc. Am. 88, pp 324-334, 1990.

[9] M. Gensane. Sea bottom reverberation: the role of volume inhomogeneities of the sediment. In Ocean reverberation, Kluwer academic publishers. 1993.

[10]P.C. Hines and P.J. Barry. Measurements of acoustic backscatter from the Sohm Abyssal Plain. J. Acoust. Soc. Am. 92, pp 962-977, 1992.

[11]I.C. Smailes. Bottom reverberation measurements at low grazing angles in the NE Atlantic and Mediterranean sea. J. Acoust. Soc. Am. 64, pp 1482-1486, 1978.

[12]C.M. McKinney and C.D. Anderson. Measurements of backscattering of sound from the ocean bottom. J. Acoust. Soc. Am. 36, pp 158-163, 1964.

[13]M. Gensane. A statistical study of acoustic signals backscattered from the sea bottom. IEEE J. Ocean. Eng. 14, pp 84-93, 1989.

Very-High (Cm scale) Resolution Multichannel Seismology

J. F. Gettrust*, W. T. Wood*, M. M. Rowe*, J. G. Kosalos**, and S. Szender**

*Naval research laboratory
Code 7432
Stennis Space Center, MS 39529
Email: gettrust@nrlssc.navy.mil

**Alliant Techsystems
Marine Systems West
6500 Harbour Heights Pkwy
Mukilteo, WA 98275

Abstract

Seismic imaging techniques together with some non-linear beamforming are used to resolve objects and structures in the shallow subsurface (to ~3 m depth) using 15-35 kHz band signals. The instrument used for this study is proportioned after conventional multichannel seismic systems, but is about 3 orders of magnitude smaller. This geometry and very-high frequency source allows us to image structures on a scale of ~0.1 m, and to detect even smaller-scale objects. While imaging theory is independent of scale, practical application of high-frequency imaging requires continued improvement in our ability to dynamically locate the spatial position of both source and receivers.

Introduction

The theory used for seismic imaging of the earth's subsurface [1] is independent of scale. Therefore, small scale (<1m) acoustic anomalies theoretically may be imaged with the small-scale equivalent of a conventional multichannel seismic system. In shallow-water environments these anomalies may be related to natural geologic activity, (small vents or faults) or to indigenous biologic activity, (mounds, boroughs, or large shells), or even to human activity (shipwrecks, plane wrecks, explosive mines, waste mounds, etc.). Imaging of surface and subsurface impedance mismatches with sub-meter resolution allows detection and more accurate determination of the nature of small anomalies. The multiple offset data obtained with multichannel seismic (MCS) systems makes it possible to measure the compressional and shear velocities within the sediments. These data make it possible to estimates the physical properties of the sediments and, therefore, provide a critical constraint to interpretation of the seismic imagery.

Instrumentation and Data

The data (acoustic targets) used for this study were located in a test range in Puget Sound. The targets were 0.025m diameter armored coaxial cables, some positioned on and some beneath the seafloor. The system used to take these data is scaled directly from the Deep Towed Acoustics/Geophysics System (DTAGS) that was developed at the Naval research laboratory (NRL) several years ago [2]. DTAGS has been used successfully to study subbottom structures on the scale of ~4 m; the new system was designed to resolve features ~0.1 m scale. The 16 receivers used with the very-high frequency system are 0.2 m apart and are attached to the same rigid frame as the source (Figure 1). The nearest offset hydrophone is 3.441 m from the source while the furthest offset sensor is 6.441 m from the source. The source has a 40° beam width and is directed back toward the array at an angle of 30° from vertical. The receiving hydrophones have omni-directional response within the lower halfspace. Each shot trace (i.e., the data recorded by an individual hydrophone for a given source pulse) in this survey consists of 10000 samples with a sample interval of 1.0 x10-5 s. For each survey line, the source was fired 100 times, once every 0.2 s; the shot spacing ranged from 0.06 m to 0.09 m making the lines 6 to 9 m in length. The effective penetration in the soft sediments sampled was up to ~10 m. Data were acquired using both single frequency (25 kHz) tone bursts of 4 cycles with wider frequency-band FM sweeps. Figure 2 shows the amplitude spectra of signals from the two lines discussed in this study. Each spectra computed from an average of 1500 independent "shots".

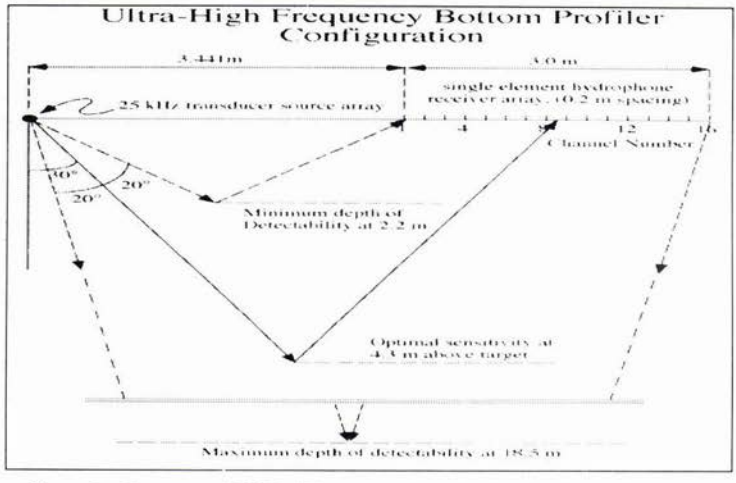

Figure 1. Geometry of UHF-MCS system. Note the directionality of the source.

Note the significant increase in bandwidth for the chirp data (see Figure 2) allowing for significantly enhanced time resolution. The spectral chirp data were deconvolved using an estimate of the wavelet made by stacking, in phase, all water bottom arrivals on channel 2 (the nearest-offset channel) of that line. Note that there was no facility on the MCS system to obtain the source function directly so we used the direct water bottom reflection. Here we assume that the uppermost subbottom structure is laterally uncorrelated and will interfere destructively, whereas the directly reflected source signature will add constructively.

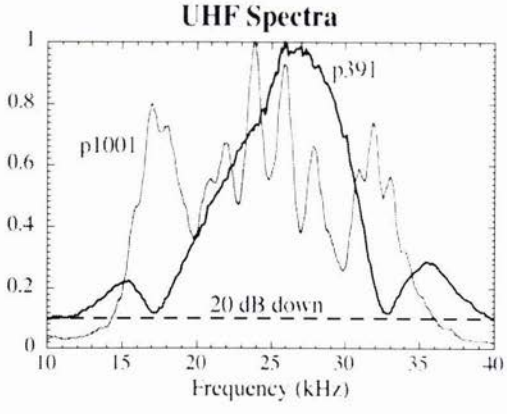

Figure 2. Amplitude spectra of 4-cycle pulse (dark line) and 15-35 kHz chirp (light line) source signals

Practical Aspects of Imaging

The objective of this study was to use seismic imaging theory and methods adapted from conventional hydrocarbon exploration which, usually, makes use of signals in the 10-80 Hz band, to image small scale acoustic anomalies on and just below the sea floor. Previously, we have used these techniques to study features to ~4 m scale to more than 750 m depth using a multichannel seismic system with a 250 Hz - 650 Hz source. Our experience with that system indicated that although the imaging theory is certainly independent of scale, practical aspects of positioning, (towing) the system, and therefore significant portions of the processing are not [3]. These aspects become even more critical when using the very-high frequency (UHF) signals in the 10-40 kHz band where wavelengths are on the order of centimeters.

In particular, uncertainties from GPS positioning of several m are of virtually no consequence for conventional exploration seismic wavelengths of 20 m, but for wavelengths of 0.06 m uncertainties of this magnitude substantially

degrade the ability to correlate events from different survey lines. Fortunately, uncertainties in relative position (shot to shot spacing) can be constrained to be much smaller. Although steady towing at speeds less than 1 kt is extremely difficult, low sea state, careful operation, and the relatively short time over which the experiment is performed allow for a reasonably consistent (~0.005 m) shot spacing over the course of a short, 8 m survey line. To further constrain shot spacing system accelerations in the vertical and the two horizontal planes also were recorded. The integrals of the these accelerations provide significant improvement in determination of relative shot spacing and shot-receiver depths. As we will show, further engineering efforts in terms of system stability will be required to reach the full potential of the resolution available with a 10-40 kHz source frequency.

In contrast to these inter-shot limitations, some aspects of this scale of exploration are significantly simpler than in conventional MCS work. For example, because the source and receivers are mounted on a rigid frame, the uncertainty in the relative positions of the source and receivers is essentially zero. There is no streamer feathering (i.e., curvature of the receive array), and no problems with portions of the streamer sinking or floating, (changes in the orientation, or pitch are small relative to the resolution of the system). Also, because of the frequencies used, one need not be concerned with maintaining a quarter wavelength source depth to reduce ghosting. In fact the system is towed at depth to maintain good angular coverage over the target. Multiples and ghosts from the air water interface tend to be significantly scattered due to the roughness of this interface at the scale of ~0.01 m, and generally arrive too late to interfere with subsurface reflections.

Another fortuitous aspect of processing these UHF data is the relatively small variation in compressional velocity both vertically and laterally in the sediments penetrated. As P-wave velocity increases, penetration is reduced, so the velocity in the penetrated sediments ranges from 1474 m/s in the water column to rarely more than ~1550 m/s, or a change of ~5%. Contrast this with the more than 100% change for conventional seismic work. As shown later these relatively mild velocity changes greatly simplify the velocity analyses and migrations, two important and usually time consuming parts of conventional imaging.

In light of the above observations the first priority in imaging these data was to determine the actual shot spacing for each line. This can be accomplished in several ways, one of which is to iteratively migrate the near trace gather with the known water velocity and trial shot spacings. The water velocity was determined to be 1474 ± 3 m/sec, calculated from the slope of the direct-wave arrival across the array. Preliminary velocity analyses confirmed this value and also confirmed that the receiver array was flying level (with respect to the resolution of the system). Proper shot spacings were determined by varying shot separations used for migration until the diffraction hyperbolae from rough water bottom features or in one case a buoy floating 2 m above the bottom (see Figure 3) were optimally collapsed. In some cases the optimal collapse was not quite complete due to slight changes in shot spacing over the course of the line. The shot spacing corresponding to optimal near-trace migration was determined to be reasonably consistent within a line (± 0.005 m), but varied among lines between 0.06 and 0.1 m. Another way to determine shot spacing is to identify the same small bottom feature on both the near and far channel records. Half of the distance between the two channels divided by the number of shots between the features' appearance on the two records yields another estimate of the shot spacing. These two methods yielded consistent estimates. Because the shot spacing remained reasonably constant over the lines used here, and because irregular shot spacing complicates the processing, the acceleration values were not used and the shot spacing was assumed to be constant.

Imaging the Data Field

The primary goal of imaging is the notion of focusing; this is done by applying operators that concentrate the scattered wave energy back to a reflection "point". Although in some cases a traditional imaging approach of common midpoint gathering followed by move out correction, stacking, migration may produce a satisfactory image with UHF data, we wish to address the problem more comprehensively.

When used as an imaging tool, beamforming is equivalent to prestack migration. Consider an image point $P(x_i,z_i)$ located in the vertical plane defined by our linear array. This point will be ensonified by several shots as the system passes by. When each source pulse arrives we assume based on Huygens' principal that this image point behaves as a secondary point source. The spherical wave (we assume for now a constant velocity medium) emanating from this secondary source strikes each receiver located at (x_r,z_r) in the array at a time given by:

$$t(x_r, z_r) = \frac{\left[(x_s - x_i)^2 + (z_s - z_i)\right]^{1/2}}{v} + \frac{\left[(x_r - x_i)^2 + (z_r - z_i)^2\right]^{1/2}}{v} \qquad (1)$$

where V is the velocity of the medium, and (x_s,z_s) is the source location. The first term is simply the time to the secondary source, and the second term is the time from the secondary source to the receiver. Summing along this trajectory (linearly interpolating as necessary for digitized data) is the mathematical equivalent of physically bending the array in a circular arc whose center is occupied by the point P. This summation is performed for each image point $P(x_i,z_i)$ in the vertical plane to produce the final image. Sample amplitudes are multiplied by their arrival time to compensate for spherical divergence.

Beamforming, or migrating in this ray-based manner also allows for a simple way of incorporating the directivity of the source. Recall that the source transducer used in this study is directed 30° from the vertical, and has a beam width of 40°, (suggested by the asymmetric nature of the large diffraction hyperbola in Figure 3, top, left). For the ray from the source to each image point (first term of Equation 1) the angle with the vertical is easily computed. Gain is applied to the sample amplitudes along the trajectory corresponding to this image point to compensate for the source directivity. When the image point is too far outside the beam (where source levels fall below the noise level) it cannot be imaged so no trajectory is computed and the image value is set to zero.

This operation was applied to every shot of line p1001 (Figure 3 top, left) with the result shown in Figure 3 center, left. As with any prestack migration the diffraction from the buoy is neatly collapsed, while the very flat, somewhat dipping seafloor is not significantly altered. Careful inspection directly below the buoy reveals the cable, which has apparently sunk several cm into the mud.

Note the difference in frequency content between Figures 3 top, left and center left. The beamforming was applied as described above to one shot at a time. The contributions to the image space from neighboring shots will overlap and because of the uncertainties in the shot position the image contributions from these separate shots may interfere destructively, when we would like them to interfere constructively. One way to mitigate this problem is to slightly blur the images by reduce the effective frequency range through computing the instantaneous amplitude and bandpass filtering. This reduces the frequency range from 15-35 kHz to 1-15 kHz, making the uncertainties in shot position smaller relative to the dominant wavelength, and aiding constructive interference. Resolution and polarity information are sacrificed to obtain a clearer image.

Beamforming with Robust Norms

The nature of the beamforming algorithm allows for the easy implementation of a more sophisticated measure of coherency along the trajectory of Equation 1 than a simple summation. Some of the data presented in Figure 3 were computed using a family of norms which are computed using the generalized mean [4] which is defined by:

$$L_j^{\alpha} = \left(\sum_{i=1}^{n} \mathrm{sgn}(x_{j,i}) \left| x_{j,i} \right|^{\alpha} \right)^{1/\alpha} \qquad (2)$$

where the function sgn() (the sign of the variable) is required to maintain the integrity of the polarity information, i.e. on which side of the origin the norm lies. It has been shown [5] that for small signal-to-noise ratios with mixed-Gaussian noise distributions, $0.33 < \alpha < 0.5$ produces a significantly better estimate of the signal than does the conventional summation ($\alpha = 1$). Note that when $\alpha = 0$, the generalized mean is equivalent to "hard limiting", a technique that works well when the noise field is uniformly distributed (reference).

We incorporated the L^{α} norm operator into the beamformer by accumulating at each image point the term under the radical in Equation 2 regardless of which shot the samples came from. After all shots had contributed to the image the a root and rest of Equation 2 was computed. The algorithm was then applied to line p1001 with the results shown in Figure 3, (bottom, left). Note the significant enhancement of the signal compared to Figure 3 (center, left), although the cable near the water bottom is still difficult to distinguish from the water bottom reflection.

Because one important application of this kind of processing is the detection of small objects often we may wish to emphasize point diffractors, and de-emphasize layered geology, essentially the opposite of conventional imaging strategy. One way to accomplish this is to use the apparent dip of diffraction hyperbolas to discriminate against layered horizons. Horizontal events are easily removed from unmigrated common offset gathers by frequency-wavenumber, (F-K) filtering (Yilmaz 1988). Channel 2 of line P1001 before F-K filtering, (Figure 3 top, left) is dominated by the water bottom event. After F-K filtering to remove horizontal events, (Figure 3 top, right) the diffraction hyperbolas from the cable and the attached buoy are quite evident. The F-K filtering is applied to each common offset gather independently.

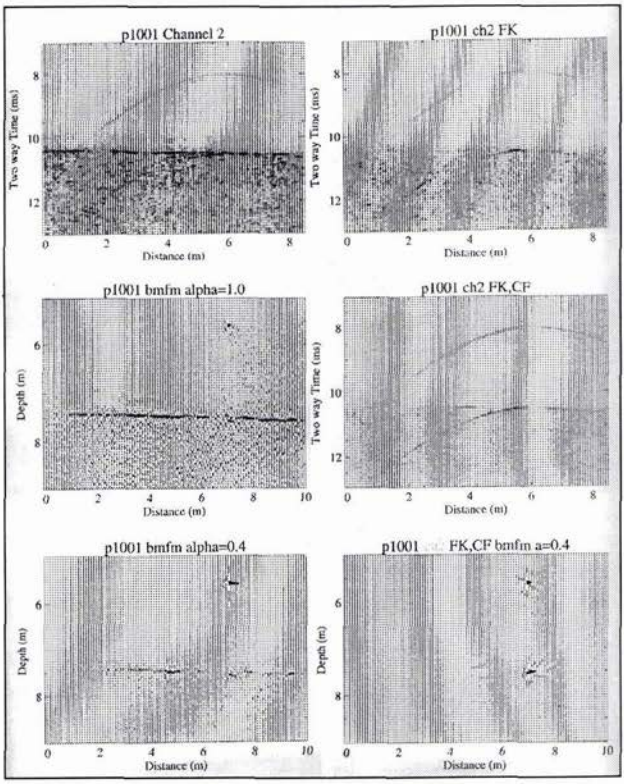

Figure 3.

We incorporated the L^{α} norm operator into the beamformer by accumulating at each image point the term under the radical in Equation 2 regardless of which shot the samples came from. After all shots had contributed to the image the α root and rest of Equation 2 was computed. The algorithm was then applied to line p1001 with the results shown in Figure 3, (bottom, left). Note the significant enhancement of the signal compared to Figure 3 (center, left), although the cable near the water bottom is still difficult to distinguish from the water bottom reflection.

Because one important application of this kind of processing is the detection of these small objects we may wish to emphasize point diffractors, and de-emphasize layered geology, essentially the opposite of conventional imaging strategy. One way to accomplish this is to use the apparent dip of diffraction hyperbolas to discriminate against layered horizons. Horizontal events are easily removed from unmigrated common offset gathers by frequency-wavenumber, (F-K) filtering [6]. Channel 2 of line P1001 before F-K filtering, (Figure 3 top, left) is dominated by the water bottom event. After F-K filtering to remove horizontal events, (Figure 3 top, right) the diffraction hyperbolas from the cable and the attached buoy are quite evident. The F-K filtering is applied to each common offset gather independently.

To further enhance these coherent events a coherency filter can be applied. Much of the noise in these data is incoherent from trace to trace within a shot gather or from shot to shot in a common offset gather. At each sample of each trace in the common offset gather semblance is measured over a suite of trajectories within user specified dips. In these examples this range was -6 to +8 samples per trace and each trajectory extended 3 traces on either side of the current trace. A time window of 10 samples was used for the semblance calculation. Semblance values range from 0 for completely uncorrelated events to 1 for identical events along the specified trajectory. The semblance value from the most coherent direction was multiplied to the original amplitude of the sample. The same procedure is applied to each sample of the common offset gather, resulting in a significant reduction in the incoherent noise (Figure 3 center, right). In this Figure the point diffractors dominate the image.

Once the F-K and coherency filters were applied to each common offset gather the data were reordered into shot gathers and the beamforming algorithm was applied as before, again with a=0.4, (Figure 3 bottom, right). Note the spectacular enhancement of the point diffractors, particularly the cable near the surface which was previously barely detectable. Both the buoy and the cable can be easily located to within ~0.1 m.

Geophysical Parameters

The multiple offset data taken with MCS systems allows one to obtain estimates of the compressional velocities within the sediments. This is done by inverting the reflection hyperbola for a given shot (common shot point or CSP) or at a given point (common mid point of CMP). This technique works very well even though reflection times do not actually hyperbola for multi-layer case [1]. Compressional velocity estimates for data taken with the ultra-high frequency MCS system are presented in Figure 4. These data suggest that there is significant lateral variability in the uppermost sediment column although the absolute change in velocities is ~5%, much smaller than we encounter with deeper probing systems.

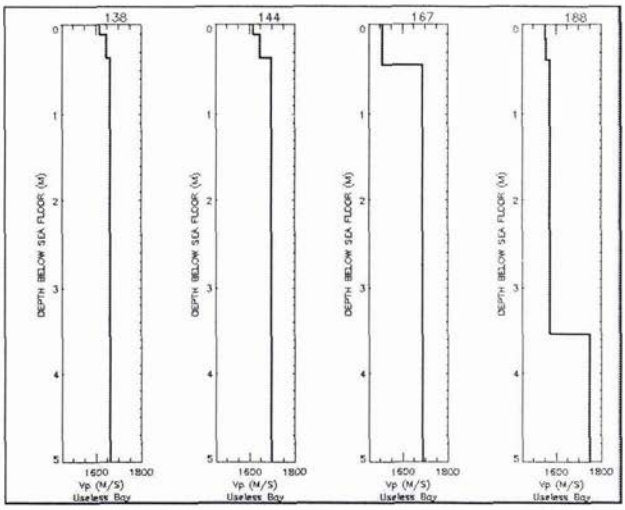

Figure 4.

Another advantage of the multiple-offset data is that it is possible to place constraints on shear velocities in the sediments. This can be done using amplitude versus offset (AVO) analysis [7] or spectrum versus offset (SVO) [8]. Both techniques were tried with these data, but to resolve the low shear velocities associated with these sediments requires a greater range of wavenumbers than is available with these data.

Conclusions

Modern digital seismic data processing techniques can be successfully applied to ultra-high frequency data (10's of kHz) when certain caveats are observed. Objects as small as 2.5 cm dia. were located to within ~0.1 m relative to the system, and bathymetric features on the order of several cm were clearly imaged. This is despite the fact that the data were "blurred" somewhat by uncertainties in shot spacing. The data generally require rather sophisticated prestack imaging (migration or equivalently beamforming) which is capable of incorporating strong source directivity. The use of robust estimators used in concert with the imaging algorithm provide significantly improved results.

Relatively small variations in P-wave velocity, very precise knowledge of the receiver array relative to the source, and lack of surface multiples make these data generally easier to process (image) than conventional (10-80 Hz) data. To fully exploit the potential of ultra-high frequency MCS, improvements in the absolute positioning of the system and the relative shot to shot positioning are required. However, even with current limitations on positioning, our data show that significant improvements in sediment classification (physical properties) and identification of small objects on or beneath the seafloor can be had using MCS technology.

Acknowledgements

The authors thank Alliant Techsystems for permission to publish the data. This work was supported by the Office of Naval Research Program Element/Project Number 0602435N/BE-35-2-02. This paper is NRL Conribution #A/7432--96-0022.

References

[1] J. F. Clearbout, Fundamentals of geophysical data processing with applications to petroleum prospecting. New York, McGraw Hill, 1976

[2] J. F. Gettrust, J. H. Ross, and M. M. Rowe, Development of a low frequency, deep tow geoacoustics System, Sea Technology, 199

[3] M. M. Rowe and J. F. Gettrust, Fine structure of methane hydrate-bearing sediments on the Blake Outer Ridge as determined from deep-tow multichannel seismic data, Journ. Geophys. Res., vol. 98 pp. 463-473, 1993

[4] Abramowitz and Stegun, Handbook of mathematical functions with formulas, graphs, and mathematical tables, Washington D. C., U. S. Dept. of Commerce National Bureau of Standards, 1964.

[5] J. F. Gettrust, Ph.D. dissertation, Univ. of Wisconsin-Madison, 1973

[6] O. Yilmaz, Seismic data processing, Society of Exploration Geophysicists, Investigations in Geophysics Vol. 2, 1988.

[7] J. Castagna and M. Backus, Offset-dependent reflectivity - theory and practice of AVO analysis, Society of Exploration Geophysicists, Investigations in Geophysics Vo:. 8, 1993.

[8] J. F. Gettrust and M. M. Rowe, Constraints on shear velocities in deep-ocean sediments as determined from deep-tow multichannel seismic data, in Shear Waves in Marine Sediments, Kluwer Academic publishers, pp. 369-378, 1991.

Texture Analysis of Sidescan Sonar Imagery Using Statistical Scattering Models

Hugh Griffiths, Jonathan Dunlop and Roger Voles

Department of Electronic and Electrical Engineering
University College London
Torrington Place, London, WC1E 7JE, UNITED KINGDOM
Email: h.griffiths@eleceng.ucl.ac.uk

Abstract

It is shown that the generalised K-distribution provides a good fit to the amplitude statistics of sonar imagery from several different types of seabed sediment. A number of possible explanations for the Ricean nature of the speckle component have been put forward. A method of refining the estimated position of a sediment boundary using maximum likelihood is also presented.

1. Introduction

In the analysis of high-resolution sonar imagery of the seabed, it is important to properly model the image texture in order to be able to detect objects that do not conform to this model. The K-distribution can be used to model the amplitude statistics of a coherent imaging process, and has been applied in the past to high-resolution maritime radar clutter and SAR imagery of land scenes. Oliver [1] demonstrated that a single sonar image of sand ripples followed the K-distribution, but it does not appear to have been applied to a full range of seabed sediment types. Sonar images from several different types of sediment are described in section 2, and the single point statistics of this data is investigated in section 3. A model-based segmentation of a sonar image will be unpredictable where the sample window crosses a sediment boundary, so a method of refining the estimate of the boundary position using maximum likelihood is presented in section 4. The work is summarised in section 5.

2. Sidescan sonar data

Data from two sidescan sonar systems over a wide range of sediments are considered. Both data sets contain amplitude returns quantised to 8-bits, but no phase information was recorded.

Five sonar images from homogeneous regions of stones, gravel, sand, clay and mud from the ground-truthed data set of Pace and Gao [2] are used. These were acquired with a 48kHz centre frequency, 2kHz bandwidth system with a resolution cell of approximately 38cm/2.2m in the across/along track directions. Each of the images was normalised to fill the quantisation range and some contain DC offsets.

The second data set is a 100kHz image from the work in [3] which contains regions of sand, gravel and gravel ripples that were identified from camera footage and grab-sampling. The resolution cell was approximately 20cm in both directions. The change of grazing angle within each image did not appear to alter the local image statistics, so a histogram of the whole sediment region was used for distribution fitting.

3. Statistical scattering models

The physical processes involved in radar backscatter are well understood and statistical models incorporating these processes have been widely used in radar signal processing.

3.1 Rayleigh distribution

The echo of a radar or sonar pulse can be considered to be the sum of contributions from N discrete scattering centres existing within the resolution cell.

$$S = \sum_{n=1}^{N} a_n \exp(j\phi_n) \tag{1}$$

where a_n and ϕ_n represent the amplitude and phase shift of the nth contribution. The randomly phased returns may interfere constructively or destructively, so the amplitude $|S|$ will fluctuate from cell to cell. It is usually assumed that: (i) a_n and ϕ_n are statistically independent random variables; (ii) the positions of the scatterers are sufficiently random to introduce path differences greater than the incident wavelength, so the distribution of ϕ_n can be considered uniform over 2π; (iii) all the contributions are at the same frequency; and (iv) N is large, so the Central Limit Theorem can be applied. Re(S) and Im(S) are then both zero-mean Gaussian, which leads to Rayleigh distributed amplitude $|S|=x$

$$p(x) = \frac{2x}{\overline{a^2}} \exp\left(\frac{-x^2}{\overline{a^2}}\right) \tag{2}$$

where $\overline{a^2}$ is the mean-square of step-lengths a_n.

3.2 K-distribution

At high resolution, spatial structure on the seafloor such as sediment ripples is resolved and N varies from cell to cell. This bunching of scatterers is represented by a spatially varying mean level that modulates the Rayleigh 'speckle' component. The underlying component was found to be an empirical, but good fit to the gamma distribution in maritime radar clutter and SAR images. Combining these two components results in the K-distribution for overall amplitude [4]. This converges to the Rayleigh as $\nu \to \infty$

$$p(x) = \frac{2b}{\Gamma(\nu)}\left(\frac{bx}{2}\right)^{\nu} K_{\nu-1}(bx) \tag{3}$$

$$\text{where } b^2 = \frac{4\nu}{\overline{a^2}} \tag{4}$$

ν is the shape parameter that characterises scatterer bunching, $K_{\nu-1}$ is a modified Bessel function of order ν-1. The particular value of this model is that it can also model all the spatial correlation properties of the texture [1]. A numerical search was used to obtain the least-squares fit of the distribution to the eight sediment histograms and the results are shown in figure 1. A DC offset was included as a search parameter for the 48kHz data.

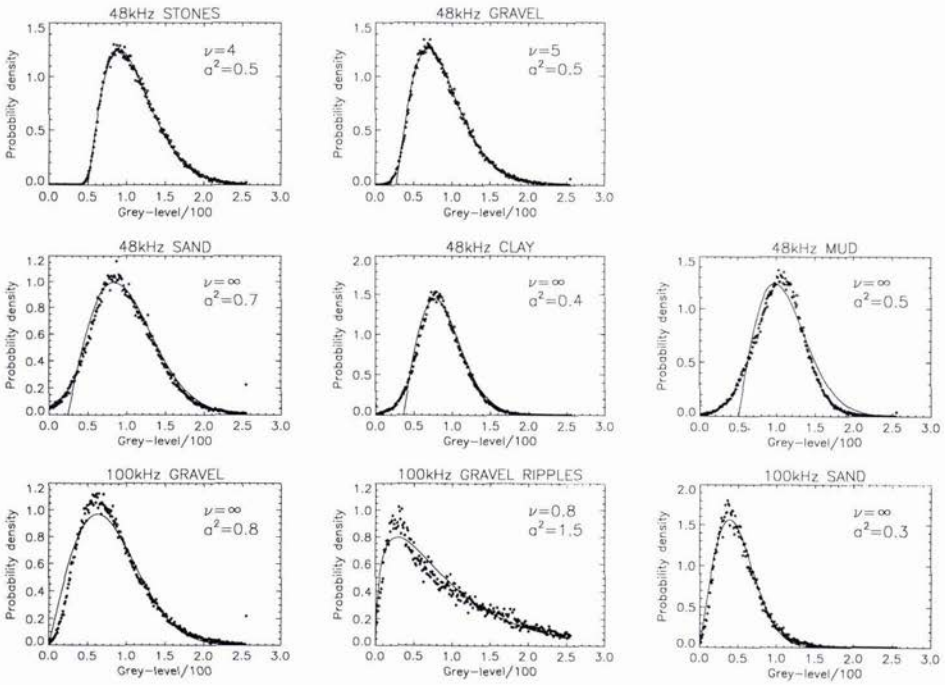

Figure 1: Least-squares fits of K-distribution to data

The K-distribution provided a good fit to sonar data from large particles such as stones and gravel, but the probability density function (PDF) of a very fine sediment like mud resembled a Gaussian distribution with a non-zero mean, and the K-distribution provided a poor fit Other sediments had PDFs between these extremes. The gravel ripples had a very low value of ν indicating large variations in the underlying model.

3.3 Generalised K-distribution

The Ricean distribution [5] results from the envelope detection of a steady sinusoidal signal plus zero-mean Gaussian noise, and reduces to the Rayleigh and non-zero-mean Gaussian distributions in limiting cases. The PDFs of the fine sediments suggest that the Ricean may be a more suitable model for the speckle statistics than the Rayleigh.

If Ricean speckle is modulated by an underlying gamma distribution, the received signal will follow the generalised K-distribution [6].

$$p(x) = \frac{2b}{\Gamma(\nu)}\left(\frac{4\nu x}{b\overline{a^2}}\right)^{\nu} I_0\left(\frac{2\delta x}{\overline{a^2}}\right) K_{\nu-1}(bx) \qquad (5)$$

$$\text{where } b^2 = \frac{4\nu}{\overline{a^2}} + \frac{4\delta^2}{\left(\overline{a^2}\right)^2} \qquad (6)$$

δ is the amplitude of the non-random contribution, and I_0 is a modified Bessel function of zero order. Figure 2 shows the generalised K-distribution fitted to the data.

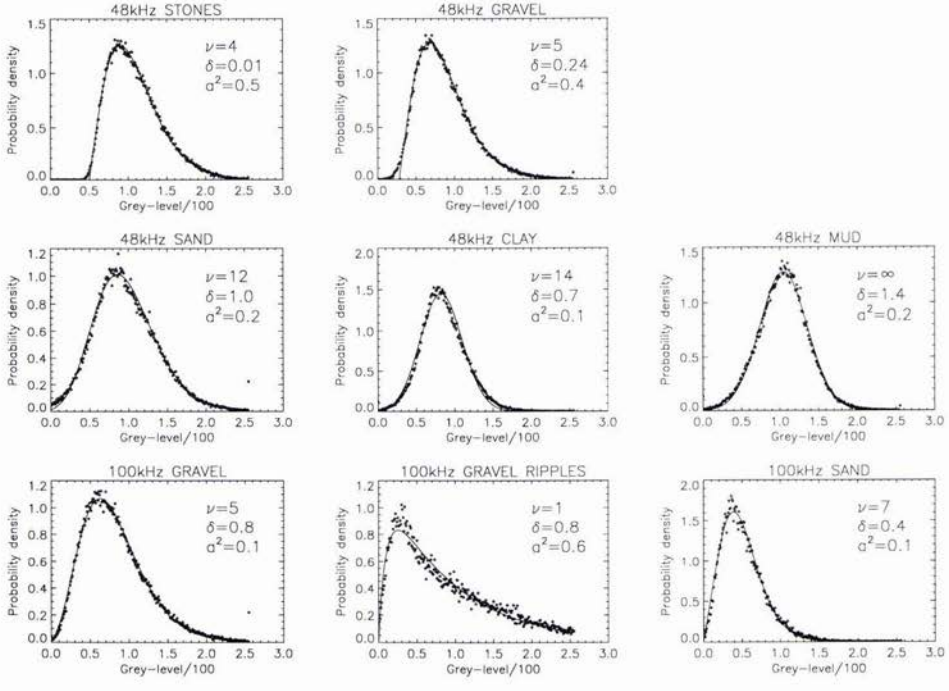

Figure 2: Least-squares fits of generalised K-distribution to data

The generalised K-distribution is an excellent fit to all of the wide range of sediments tested. There is generally more structure visible in the data of sediments with large particle size like stones than fine sediments like mud, subsequently ν tends to decrease with particle size.

A small tail at low amplitudes is visible in the 48kHz data of stones and gravel that is not modelled by the generalised K-distribution. The return signal envelope was recorded in analogue form on magnetic tape [2] which could add zero-mean Gaussian noise to the data. A signal-to-noise ratio of 20dB provides a tail of the magnitude observed in the gravel data and may be a plausible explanation. The tail was ignored in the fitting of distributions, but its existence precluded the use of Kolmogorov-Smirnov or χ^2 statistics, so the mean-square fit was used instead.

There are a number of possible causes of the Ricean speckle:-

(i) Acoustic energy penetrates the sediment and a single specular echo is received from a gas-rich sub-bottom sediment layer [7] or the underlying rock layer.

(ii) The sonar equipment adds a small, constant amplitude signal such as transmitter breakthrough to the received signal before envelope detection. Ricean statistics may be observed from other sidescan sonar systems [8], so this effect is not due to a single piece of faulty equipment. The amplitude of the contribution δ would be constant for all sediments but as the 48kHz data was normalised the parameter δ would tend to zero for strongly backscattering sediments such as stones and gravel, as observed in the data.

(iii) The resolution cell contains a fine sediment with a single stone that gives a strong contribution. Any cells containing 2 or 3 specular reflectors would give non-Ricean returns [9] and an even greater number would produce approximately Rayleigh statistics.

(iv) Small ripples within the resolution cell of equal wavelength to the sonar generate a Bragg resonant effect. This phenomenon is unlikely to occur in all of the images tested

(v) Reverberation from the sonar-bottom-surface-bottom-sonar path with the same delay as the main backscatter. The reverberation would be a random variable and the variance may preclude its simplification to a constant.

(vi) Re(S) and Im(S) were Gaussian with non-zero mean, due to a non-uniform distribution of ϕ_n. The 48kHz sonar had λ ~3cm and range resolution~38cm which gives 12 cycles within the resolution cell at grazing incidence. This should provide sufficient phase run out to ensure a fairly uniform phase distribution.

(vii) The fractional bandwidth of sidescan sonar is much greater than radar, so the assumption of monochromatic speckle in section 3.1 may not hold. The intensity distribution arising from polychromatic laser light or light of finite bandwidth becomes the sum of correlated monochromatic speckle patterns. As the correlation increases there is a transition from Rayleigh distributed amplitude towards a delta function centred at the r.m.s. amplitude [10]. The complexity of the exact PDF makes it computationally unattractive, but the Ricean distribution exhibits very similar behaviour.

3.4 Comparison of distributions

The Weibull and lognormal distributions are empirical distributions that are often used to model radar clutter and have previously been applied to sonar data [11]. These were tested against the Rayleigh, K-distribution, Ricean and generalised K-distributions to determine which modelled the data most accurately. The mean-square difference between the PDFs of the sediment and the candidate distribution are shown in table 1.

	48kHz data					100kHz data			
	Stones	Gravel	Sand	Clay	Mud	Gravel	Ripples	Sand	Overall
Rayleigh	2.29	2.20	2.94	4.60	10.1	4.56	52.3	4.25	10.41
K-dist	0.58	0.89	2.94	4.60	10.1	4.56	4.27	4.22	4.02
Ricean	2.29	2.20	2.36	2.79	1.11	3.83	52.3	4.25	8.89
Weibull	0.82	1.54	2.02	2.81	1.15	2.64	6.28	3.90	2.65
Lognormal	1.08	0.50	0.98	1.18	2.14	2.26	2.89	5.82	2.11
Gen K-dist	0.58	0.89	0.96	1.40	1.11	2.76	2.64	2.76	1.37

Table 1: Mean-square difference between model and sediment PDFs ($\times 10^{-3}$). The best fit in each col. is shaded.

The generalised K-distribution offers the best fit to the data and the lognormal also fits well despite having one less parameter. The advantage of the generalised K-distribution is that it will also model all the spatial correlation properties of the texture.

A statistical model can be used to segment sonar imagery into regions of different sediments. A small sample window is passed across the image and the parameters of the statistical model are estimated. The central pixel of the window is then classified on the basis of these estimated parameters. The even order moments of the generalised K-distribution are given in [6] which could be used for parameter estimation, but with three parameters the 2nd, 4th and 6th moments of the data would be required. The 6th moment would not be a robust estimator unless a very large sample window was used. It is not possible to derive a maximum likelihood estimate analytically for the K-distribution, but Oliver derived a good approximation in [12]. It may be possible to do the same with the generalised K-distribution.

4. Maximum likelihood boundary estimator

As the sample window crosses a sediment boundary the samples will follow a mixture distribution and classification errors will result as shown in figures 3 and 4. The estimate of the boundary position could then be refined if two adjacent sample windows were passed across the boundary.

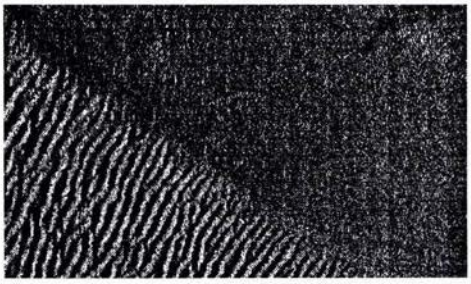

Figure 3: Section of 48kHz image

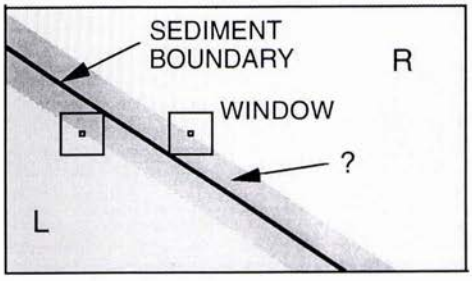

Figure 4: Classification map of figure 3

Suppose that the probability distributions of the amplitude x in the areas L and R are P_L and P_R respectively.

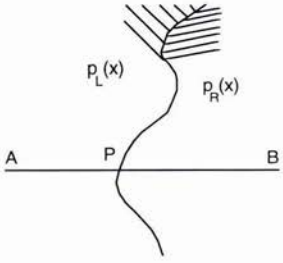

Figure 5: Sediment boundary

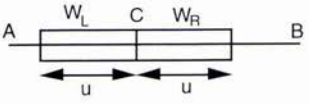

Figure 6: Sample windows

By scanning along the line AB shown in figure 5, it is required to determine the position P of the intersection of the boundary with the line. Consider two contiguous windows W_L and W_R as shown in figure 6, each comprising u adjacent pixels lying along the line AB and abutting at the point C.

The likelihood L that the contents of the u pixels, ω_L, in W_L all coming from the LH distribution is

$$L = \prod_{\omega_L} p_L(x) \tag{7}$$

When W_L is fully immersed in the LH area, the expected value of L will be $\overline{L_L}$, and when fully immersed in the RH area it will be $\overline{L_R}$. Clearly, $\overline{L_L} > \overline{L_R}$. Similarly, for W_R,

$$R = \prod_{\omega_R} p_R(x) \tag{8}$$

with $\overline{R_R} > \overline{R_L}$. Their relationships are shown in figure 7.

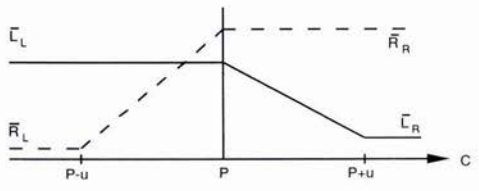

Figure 7: Likelihood as windows cross boundary P

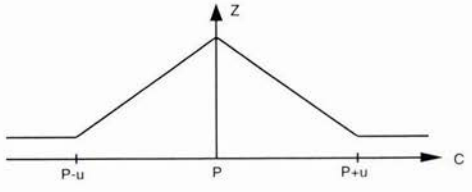

Figure 8: Joint likelihood as windows cross boundary P

It is evident that Z=LR will have an expected maximum when C lies on P as shown in figure 8.

An alternative arrangement would also take into account the degree of 'mismatch' between P_L and P_R, giving

$$L' = \prod_{\omega_L} \frac{p_L(x)}{p_R(x)} \quad (9) \qquad R' = \prod_{\omega_R} \frac{p_R(x)}{p_L(x)} \quad (10)$$

These techniques were applied to the sonar image in figure 3. The K-distribution fits from section 3.2 were used for P_L and P_R, and u was arbitrarily chosen as 40 pixels. The likelihood L' and R' are shown in figures 9 and 10 with high intensity indicating high likelihood. These gave better performance than L and R which are not shown.

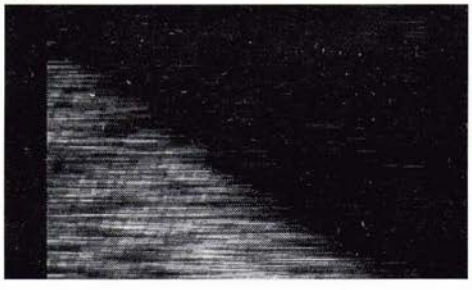

Figure 9: log L'

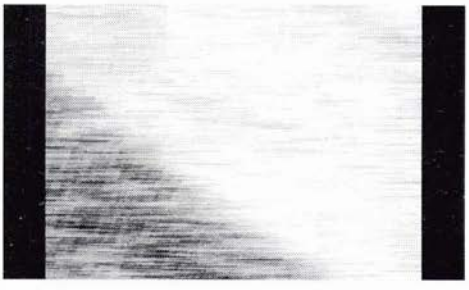

Figure 10: log R'

Figure 11 shows the combined likelihood Z'. A light strip indicating the most likely position of the sediment boundary is visible, but there is a lot of noise within the rippled region that would prevent accurate detection of the boundary.

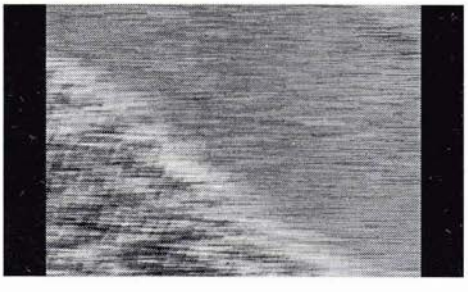

Figure 11: log Z'=log L'+log R'

It is known a priori that a particular row of L' should resemble the profile in figure 7. For every point c, $\overline{L'_L}$ was calculated from the mean of {u<L'<c} and $\overline{L'_R}$ from the mean of {c+u<L'<max(c)-u}. This profile was then tested against L' and the mean-square difference between the two was found. The value of c that minimised this difference should coincide with P. The optimum profile from row 83 of L' is shown in figure 12, and similarly for R' in figure 13. c=200 in both figures, which agrees with the visually estimated boundary in this row..

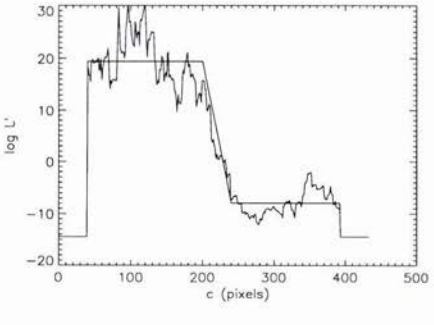

Figure 12: Row 83 of L' with optimum profile

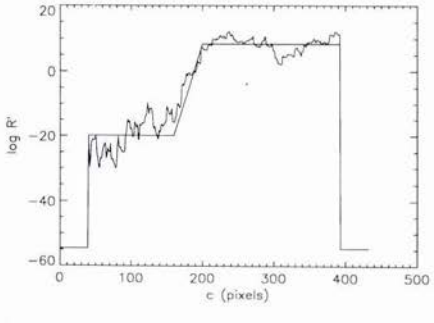

Figure 13: Row 83 of R' with optimum profile

Fitting these profiles on a row-by-row basis has the effect of filtering the likelihoods L' and R'. The filtered likelihoods are shown in figures 14 and 15.

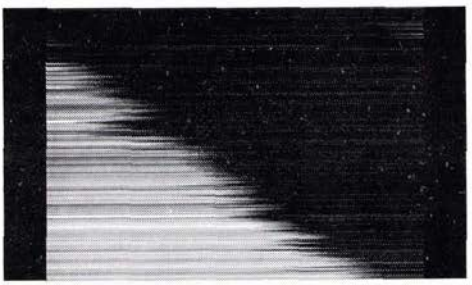

Figure 14: Filtered log L'

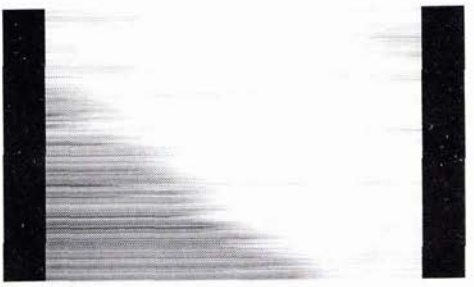

Figure 15: Filtered log R'

Comparison of figures 16 and 11 shows that filtering Z' improves the estimate of the boundary position.

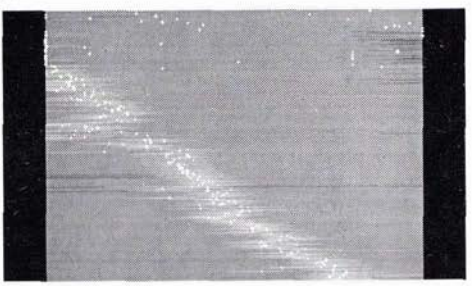

Figure 16: Filtered log L'+Filtered log R' with maxima

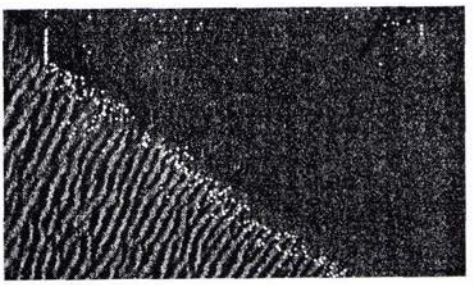

Figure 17: Maxima overlaid onto image

These results were achieved with W_L and W_R having a width of only one pixel. By orienting the search line AB perpendicular to the local boundary, W_L and W_R can have a greater width without sampling both distributions when positioned on the boundary (when C=P). It is proposed that the boundary estimate be represented as a number of linked nodes N. Each node N_i would then search along the normal defined by its neighbours N_{i-1} & N_{i+1} with chevron shaped W_L and W_R as shown in figure 18. These adaptations should allow the boundary estimator to iteratively converge onto a sediment boundary of any shape.

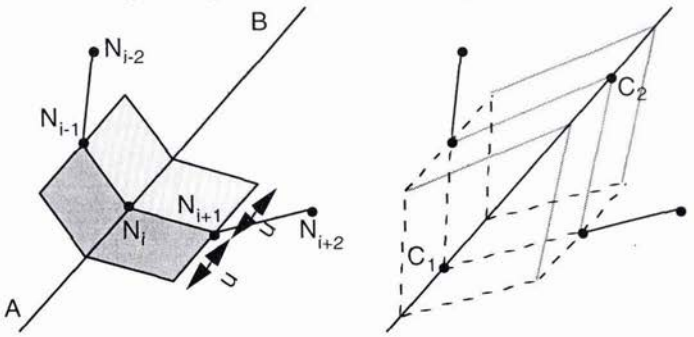

Figure 18: Chevron shaped windows searching perpendicular to local boundary estimate

5. Summary:

The K-distribution has been applied to sidescan sonar data, but poor agreement was found with sand and finer sediments. Modelling the speckle component with a Ricean distribution leads to the generalised K-distribution which provides a good fit to sonar imagery from several different types of seabed sediment. A number of possible explanations for the Ricean nature of the speckle component have been put forward. The lognormal also fits the data well but, unlike the generalised K-distribution, the lognormal will not model the spatial

correlation properties of the data.

A model-based segmentation of a sonar image will be unpredictable where the sample window crosses a sediment boundary. The statistics of the sediment on either side of the boundary are known, so two adjacent windows are passed across the boundary and maximum likelihood used to improve the estimated boundary position.

6. Acknowledgements

This work is supported by the Engineering and Physical Sciences Research Council and by DRA Bincleaves. We would like to thank R. Benjamin and K. Milne (visiting professors at UCL), Dr. D.R. Carmichael and Mr. G.J. Heald (DRA Bincleaves) and Prof. C.J. Oliver (DRA Malvern) for invaluable advice and discussions. We would also like to thank Dr. N.G. Pace for kindly supplying a set of the data from his work in [2].

References

[1] C.J. Oliver, "The interpretation and simulation of clutter textures in coherent images", *Inverse Problems*, vol. 2, pp.481-518, 1986

[2] N.G. Pace and H. Gao, "Swathe seabed classification", *IEEE J. Oceanic Eng.*, vol. OE-13, pp.83-90, 1988

[3] D.R. Carmichael, L. M. Linnet and S.J. Clark, "A multi-resolution directional operator for sidescan sonar image analysis", *J. Defence Science*, vol. 1, pp.453-459, 1996

[4] E. Jakeman and P.N. Pusey, "A model for non-Rayleigh sea echo", *IEEE Trans.* AP-24, pp. 806-814, 1976,

[5] S.O. Rice, "Mathematical analysis of random noise", *Bell Syst. Tech. J.*, vol.23, pp.282-332 & vol.24, pp.46-156

[6] E. Jakeman and R.J.A. Tough "Generalized K distribution: a statistical model for weak scattering", *J. Opt. Soc. Am.*, vol. 4, pp.1764-1772., 1987

[7] D. Tang, G. Jin, D.R. Jackson and K.L.Williams, "Analyses of high-frequency bottom and subbottom backscattering for two distinct shallow water environments", *J. Acoust. Soc. Am.*, vol. 96, pp.2930-2936, 1994,

[8] G. Shippey, A. Bolinder and R. Finndin, "Shade correction of side-scan sonar imagery by histogram transformation", *IEEE Oceans '94 Proceedings*, vol. 2, pp.439-443, 1994

[9] J.K. Jao and M. Elbaum, "First-order statistics of a non-Rayleigh fading signal and its detection", *Proc. IEEE*, vol. 66, pp.781-789, 1978

[10] G. Parry, "Some effects of temporal coherence on the first order statistics of speckle", *Optica Acta*, vol. 21, pp.763-772, 1974

[11] M. Gensane, "A statistical study of acoustic signals backscattered from the sea bottom", *IEEE J. Oceanic Eng.*, vol. 14, pp.84-93 1989

[12] C.J. Oliver, "Optimum texture estimators for SAR clutter", *J. Phy. D: Appl. Phys.*, vol. 26, pp.1824-1835, 1994

Dynamic Attenuation Extraction of Seafloor Sediments from Very High Resolution Acoustic Data

Guigné, J. Y.[1] , Schwinghamer, P.[2], and S. Litvak.[1]

1.Guigné International Ltd.
685 St. Thomas Line
Paradise, Newfoundland, Canada
A1L 1C1
E-mail: guigne@newcomm.net

2.Habitat Ecology Section, Department of Fisheries and Oceans
Bedford Institute of Oceanography,
P.O. Box 1006
Dartmouth, Nova Scotia, Canada
B2Y 4A2

Abstract

An approach to acquire geophysical information of seabed sediments as derived from acoustic attenuation is described. Using the frequencies corresponding to the signal power spectrum maximum and a point 3 dB below, signal loss in the sediment is calculated. These results are compared to reference data for attenuation in sediments published by several authors. Data collected on the Grand Banks of Newfoundland during a controlled trawling experiment was processed using this technique, with results illustrating close agreement with the underpinning theory. Calculations of fractal dimensions were performed to evaluate levels of roughness in the inner structure of the sediments. Since lower levels of the fractal dimensions represent less of a microfaunal presence [1] only the lower fractal valued data were used in the dynamic attenuation extractions. Hence, the correlations were found to be more reliable and reflective of homogeneous sediment structures.

1. Introduction

Quantitative and reliable measurements of acoustic attenuation enable correlations between the acoustic responses and the properties of sediment to be forged. Geotechnical information such as consolidation characteristics and bulk density in marine sediments can be estimated through the acoustic attenuation associated with sound waves propagating into the subseabed sediments [2]. It is recognized in the literature that attenuation is linked to the physical aspects of the sediment such as porosity, particle shape and grain size.

This paper exhibits an approach for rapid and objective computation of attenuation as perturbed by the properties of near surface sediments. The application of the technique was performed on very high resolution acoustic data using a new class of sonar called Benthic-DRUMS™ during a controlled set of trawling experiments conducted on the Grand Banks of Newfoundland [1]. Benthic-DRUMS™ is a very high resolution 40-element non-linear acoustic array developed by Guigné International Ltd. to measure the small scale chaotic changes in a benthic habitat caused by otter trawling.

2. Description of Model and Analysis Approach

2.1 Model

The approach is based on a dynamic (adaptive) model of attenuation first introduced by Guigné [2, 3]. This model assumes non-linear dependence of signal loss on frequency as

$$a = kf^{N} \tag{1}$$

where k is the attenuation coefficient in dB/m/kHz^N at an associated frequency f, and N is the exponent of frequency. Equation (1) expresses the compositive effects of intergranular and viscous losses; N values reflecting the combined effects of both. In the literature, a very wide range of both measured N values and models for the prediction of N have been exhibited and debated, starting from Urick, [4], Biot, [5,6], Shumway, [7, 8], Nolle, [9], Hampton,[10], McCann and McCann, [11, 12], Shirmer, [13], Stoll and Bryan, [14], Hamilton, [15], and Guigné, [2. 3].

Since the Benthic-DRUMS^{TM} sonar is an application of non-linear acoustics, it relies on a matrix of terminated parametric arrays. A useful mode of operation of the parametric array is when the parametric source volume is terminated abruptly by, for example, the water/seabed interface, to give a truncated parametric array. Research performed by Guigné [16], Wingham [17], Pace and Ceen [18], and Muir [19] on this mode of operation of the array has given insight on its characteristics and performance. The equation below represents a base approximation which accounts for the received spectral character of the terminated parametric array in the presence of attenuation losses:

$$P(f) = B_1 f^{2} \exp(-\beta f^{n}) \tag{2}$$

where: B_1 is a constant

f squared is by the parametric generation

β is equal to kR/8.6859; whilst R is the penetration range

The frequency at maximum pressure can be found by:

$$f_{max} = (2/(N\beta))^{1/N} \tag{3}$$

Substituting:

$$x = \beta f^{N} \tag{4}$$

We can express a normalized spectrum by:

$$\frac{P(x)}{P_{max}(x)} = \left[\frac{Nx}{2}\right]^{2/N} \exp(2/N - x) \tag{5}$$

Setting the bandwidth of the received pressure at -3dB we receive:

$$\frac{P(x)}{P_{max}(x)} = 1/\sqrt{2} \quad \text{: i.e. -3dB} \tag{6}$$

and

$$f_3 = \left[\frac{x_1}{\beta}\right]^{1/N} \quad \text{where } x_1 \text{ is left as a root} \tag{7}$$

Combining expressions for the frequencies, we realize:

$$\left[\frac{f_{\max}}{f_3}\right]^N = \frac{2}{Nx_1} \tag{8}$$

2.2 Time Window Selection

The signal processing logic as used to implement the dynamic loss model is introduced in Figure 1. This adaptive attenuation model can be reliably applied to signal portions that compare to an ideal impulse shape. A Butterworth filter of the order of 6 with a cut off frequency of 280 kHz is used to prevent possible interference from residual parametric array carrier frequencies. A Hilbert transform is also applied to acquire an envelope shape. Figure 2 illustrates a typical signal as collected by the sonar with Figure 3 exhibiting the envelope. Figure 4 presents the filtered signal with envelope.

Selected parts of the signal are chosen (using MATLAB) for processing, based on three criteria: i) shape similar to ideal impulse, ii) length of about 50 points, which represents about 1 cm of depth, iii) belonging to one portion of the envelope signal.

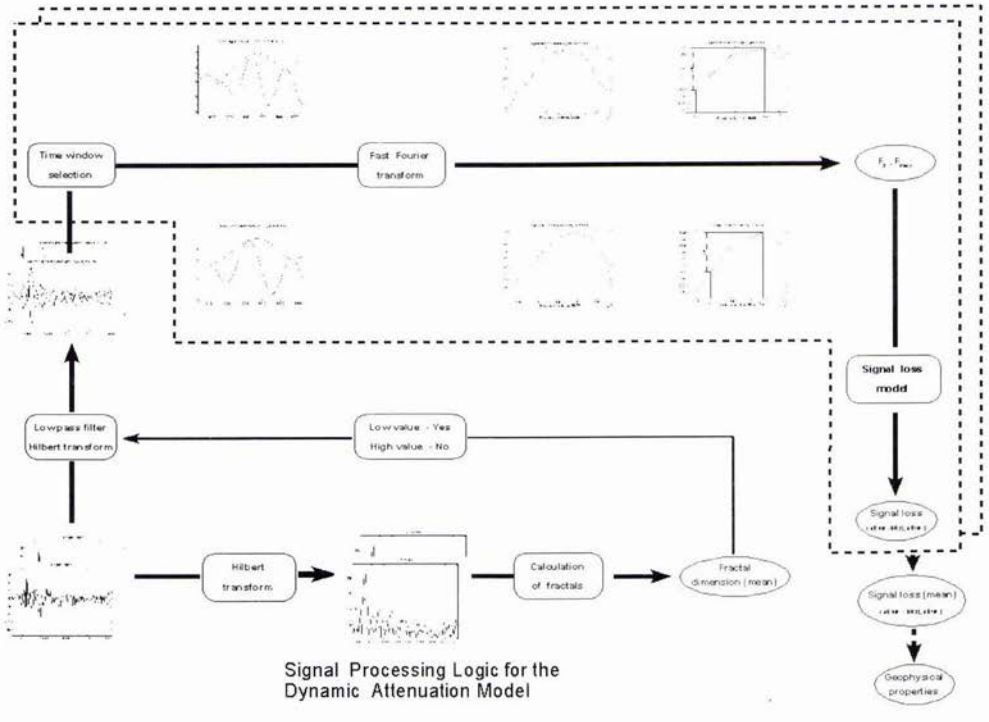

Figure 1: Signal processing flowchart leading to signal loss values

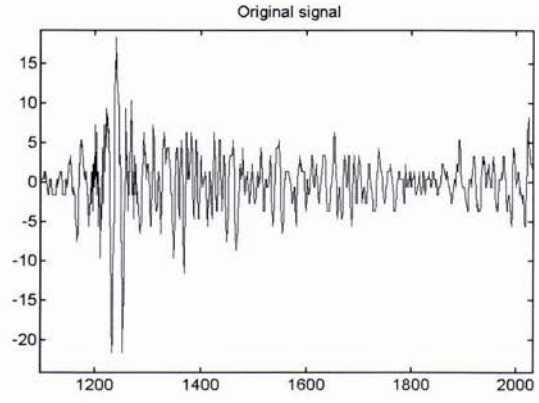

Figure 2: **Signal as used in analysis**
(Vertical axis in dB; horizontal axis represents collected data points)

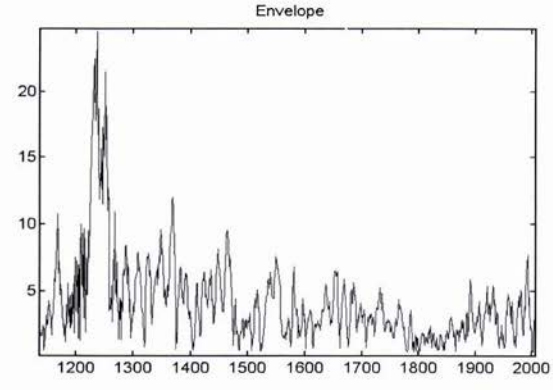

Figure 3: **Hilbert Transform envelope of signal**
(Vertical axis in dB; horizontal axis represents collected data points)

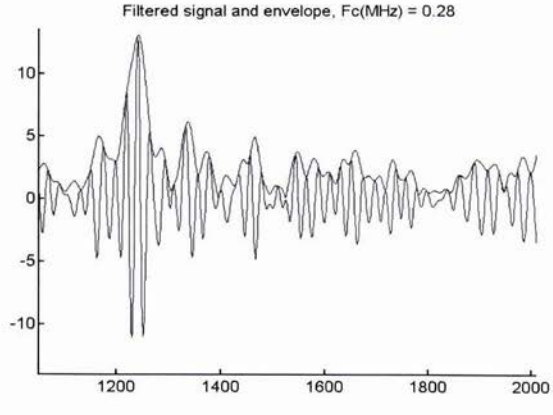

Figure 4: **Filtered signal (cut off frequency 280 kHz) and its envelope**
(Vertical axis in dB; horizontal axis represents collected data points)

Figures 5 and 6 present portions of the signal selected to conform to these criteria which meet the theoretical requirements for inputting into our dynamic signal loss model.

The data collected was held to the first 15 cm of the seabed, with fractal analysis conducted on the initial near surface zones (approx. 4 – 5 cm) conforming to the active zones of a benthic habitat.

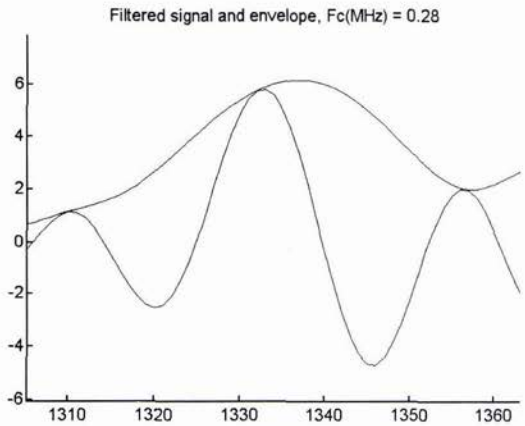

Figure 5: **Upper Curve represents chosen time window of envelope superimposed on lower curve, which represents signal, real part.**
Shape of envelope suitable for inputting into the Signal Loss Model
(Vertical axis in dB; horizontal axis represents collected data points)

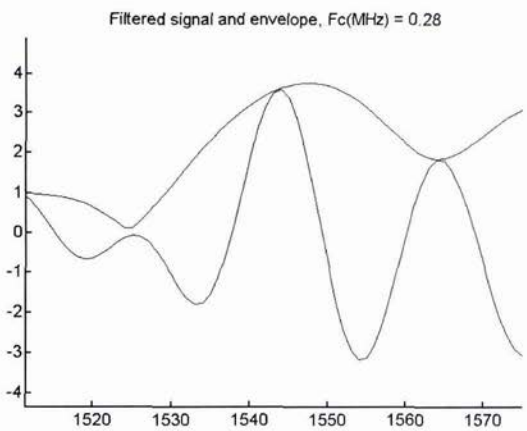

Figure 6: **Upper curve represents chosen time window of envelope superimposed on lower curve which represents signal, real part.**
Shape of envelope suitable for inputting into the Signal Loss Model
(Vertical axis in dB; horizontal axis represents collected data points)

2.3 Fractal Analysis

The Benthic-DRUMS^{TM} data can be analysed in terms of fractal dimensions associated with the signal's "roughness" [1]. From the past research by Schwinghamer and Guigné [1], the Hilbert-transformed acoustic signals occupy 1-dimensional topological space; however, they are more complex than a simple straight line, and they fill 2-dimensional space to a

degree that depends on the frequencies and amplitudes of peaks and undulations which make them complex. The extent to which they fill 2-dimensional space is measured by a non-integer dimension between 1 and 2, called a fractal. By analysing the time series data as fractal curves, the complexity of the acoustic signals in response to structural complexity in the sediment can be quantified.

A modified box counting method by Malinverno [20] was used to determine the fractal dimension for the Hilbert time series from each depth stratum k of each acoustic element M_{ij} of the acoustic array. In this method, the data M_{ijk} were first fully enclosed in a square; thus 1 box contained the whole line. Then the box was divided into quarters and the number of these smaller boxes that contained parts of the line was counted. Each of these smaller boxes was then similarly divided and the number containing parts of the line counted and so on until an arbitrarily small box size was reached.

The number of boxes, M, containing the line is a function, I, of the size, t, of the boxes:

$$M = t^{I} \tag{9}$$

The function, $I_{i,j,k}$ is the fractal dimension for each depth stratum of each element. It can be calculated as:

$$I_{i,j,k} = -\frac{\log_{10}(M)}{\log_{10}(t)} \tag{10}$$

3. Experimental Setting and Application of the Dynamic Loss Model

3.1 Data Collection

An in situ experiment to determine the impacts of otter trawls on the sandy seabed, which covers large areas of the Grand Banks and Scotia Shelf, has been underway since 1993. It was initiated as part of the Northern Cod Science and Atlantic Fisheries Adjustment Programs in response to debate regarding the role of fishing technology in the collapse of the northern cod stock [1]. The experiment allowed for Benthic-DRUMS™ data to be collected in 1994 and 1995. The 40-element array (10 x 4) was reduced to 28 elements (7 x 4) due to structural blockage of the acoustics by the sampling frame. The average water depth in the area was reported to be approximately 135 metres. The bottom sediment was mostly sand with typical grain sizes of approximately 200Φm and registering a water content of 20 ∀ 3%. The overall experimental equipment and field operation / setting are described in detail along with sampling procedures in Schwinghamer and Guigné's work [1].

The data collected was held to the first 15 cm of the seabed, with fractal analysis conducted on the initial near surface zones (approximately 4 – 5 cm) conforming to the active zones of a benthic habitat.

3.2 Calculations

Power spectra of chosen intervals were calculated using a zero-padded Fast Fourier Transform (FFT). Figures 7 and 8 illustrate shapes of the power spectra used, while Figures 9 and 10 depict values for the frequencies associated with peak pressure levels (f_{max}) and with the lower frequencies (3 dB less (f_3)).
Altogether, more than 2500 calculations were performed using the collected data. Distribution of f_{max} is shown in Figure 11.

The calculations of fractal dimensions were used to establish an acceptance level for the data to be considered valid before making the attenuation loss calculations (refer to Figure 1). Signals of low values (below 1.5) were allowed to be analysed for their attenuation; higher values were removed as these indicate strong benthic fauna activity in the sediment.

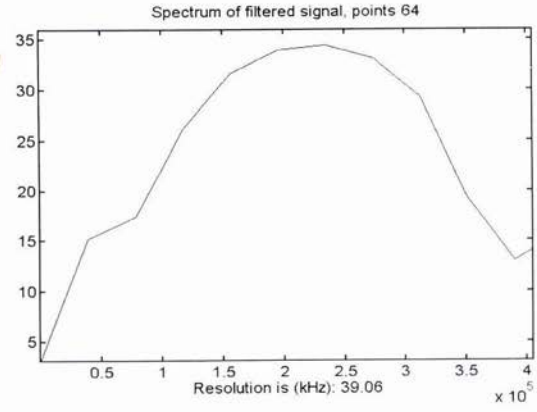

Figure 7: **Response in the Frequency Domain**
(Vertical axis in dB)

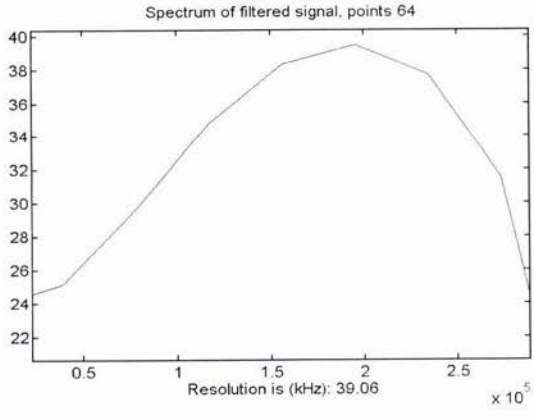

Figure 8: **Spectrum of the Second Impulse**
(Vertical axis in dB)

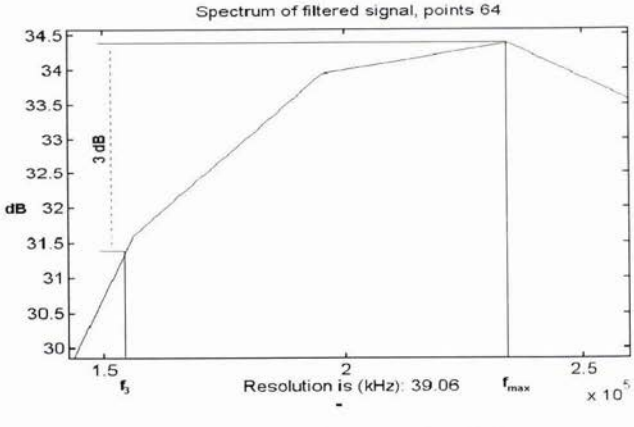

Figure 9: **Frequencies at Maximum and –3 dB Pressure**

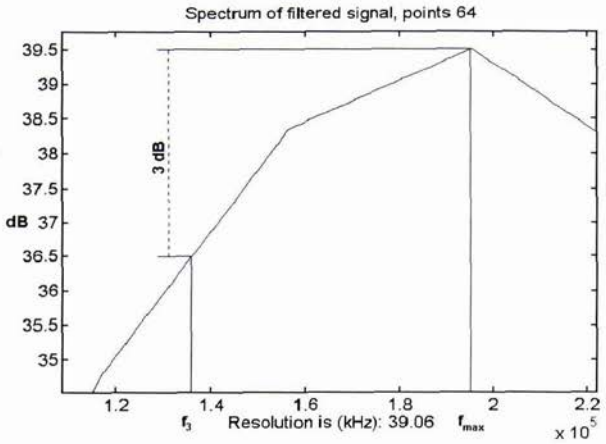

Figure 10: Frequencies at Maximum and - 3dB Pressure

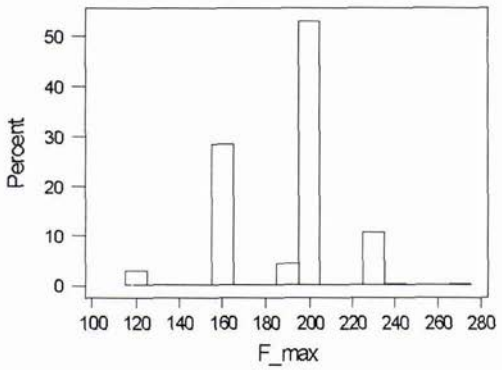

Figure 11: Distribution of Maximum Response Frequency (percentage)

4. Results

The results of the adaptive model's signal loss calculations were assessed by comparing them with published attenuation data. As it is clear from Figure 12, mean values of signal loss for associated frequencies in this research are in agreement with published attenuation data.

Water content data from samples collected on the Grand Banks in 1993 were used and found to be representative of seabed conditions for the Grand Banks (provided by Schwinghamer). Mean values for water content were 21.6% with a standard deviation of 1.8%. Assuming a density of dry soil (mostly sand) as 2.65 g/cm^3, this translates into a porosity of around 43%. Figure 13 represents a relative position of mean value of a calculated signal loss against published data. The results of the dynamic attenuation model losses seem to concur with porosity values.

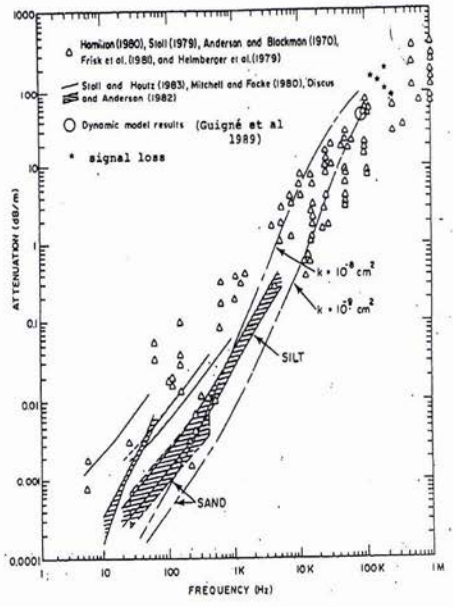

Figure 12: **Signal loss values against frequency using the Dynamic Attenuation Model for the Grand Banks data (signal loss*) and against published data**

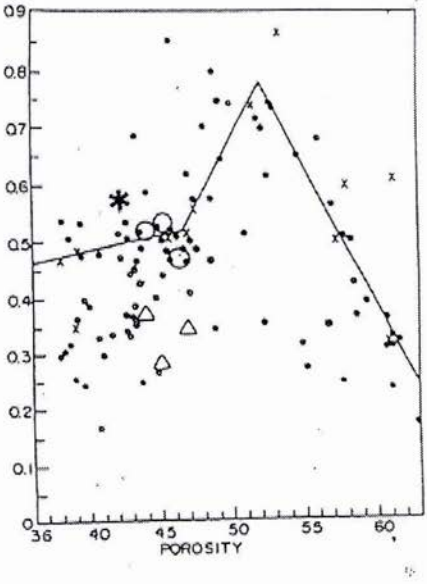

Figure 13: **Signal loss values against porosity using the Dynamic Attenuation Model for the Grand Banks data (signal loss*) and against published data**

5. Conclusions

A dynamic approach to acquire attenuation in sediment was demonstrated with good agreement between the results of the model as used on Grand Banks data with that seen for published data (related to sands). This analysis approach introduces a potentially rapid and reliable technique to extract attenuation from the wave shape of parametric arrays used as subbottom profilers. The introduction of fractal dimensions as a filter cut off, allowed for the chaotic effects of a benthic habitat to be excluded from the computations, thereby removing a potential source of error in the resultant signal loss values.

Acknowledgements

This work was partially supported by the Northern Cod Science Program; our thanks are extended to Dr. J. S. Campbell, Director. The Impact of Trawling on Benthos Project was a collaboration between the Atlantic Fisheries Adjustment Program (AFAP) and the Northern Cod Science Program (NCSP). We acknowledge the infrastructure support shown to the Guigné International Ltd. team by the Department of Fisheries and Oceans (Canada); in particular, the availability of space and time on the CSS Parizeau to allow for the Benthic-DRUMS™ data to be collected. Mr. Quanshun Liu of GIL mobilized and operated DRUMS™ at sea. Mr Liu also assisted in the data reduction processing. Special thanks are also given to Ms. Suzanne Rowsell and Mr. Don Bryant for their attention to this manuscript.

REFERENCES

1 Schwinghamer, P., Guigné, J. Y., and W. C. Siu, Quantifying the impact of trawling on the benthic habitat structure using high resolution acoustics and chaos theory, *Can. J. Fish. Aquatic Sci.*, 53, 288 – 296, 1996.

2 Guigné, J. Y., Chin, V. H., and S. M. Solomon, Acoustic attenuation measurements using parametric arrays, *Ultrasonics*, Vol. 27, 1989.

3 Guigné, J. Y., Pace, N. G., and V. H. Chin, Dynamic extraction of attenuation from sub-bottom acoustic data, *J. Geophys. Res.* 94, 5745 – 5755, 1989.

4 Urick, R. J., Absorption of sound in suspension of irregular particles, *J. Acoust. Soc. Am.*, 20, 283 – 289, 1948.

5 Biot, M.A., Theory of eleastic waves in a fluid saturated porous solid, I. Low frequency range, *Acoust. Soc Am.*, 28, 168 – 178, 1956a.

6 Biot, M.A., Theory of eleastic waves in a fluid saturated porous solid, II. Higher frequency range *J. Acoust. Soc Am.*, 28, 179 – 191, 1956a. Shumway, G., Sound speed and absorption studies of marine sediments by a resonance method, I, *Geophysics, 25*, 451 – 467, 1960a.

7 Shumway, G., Sound speed and absorption studies of marine sediments by a resonance method, II, *Geophysics*, 25, 659 –682, 1960b.

8 Nolle, A. W., W. A. Hoyer, J. F. Misfud, W. R. Runyan, and M. B. Ward. Acoustical properties of water-filled sands, *J. Acoust. Soc Am.*, 35, 1394 – 1408, 1963.

9 Hampton, L. D., Acoustic properties of sediments, , *J. Acoust. Soc Am.*, 42, 882 – 890, 1967.

10 McCann, C., and D. M. McCann. The attenuation of compressional waves in marine sediments, *Geophysics*, 34, 882 – 892, 1969.

11 McCann, C., and D. M. McCann. Compressional wave attenuation in concentrated clay suspensions, *Acoustica*, 22, 352 – 256, 1970.

12 Shirmer, F., Schallausbreitung im Schlick, *Deut. Hydrog. Z.*, 23, 24 – 30, 1970.

13 Stoll, R. D., and G. M. Bryan, Wave attenuation in saturated sediments, *J. Acoust. Soc Am.*, 47, 1440 – 1447, 1970.

14 Hamilton, E.L., Compressional wave attenuation in marine sediments, *Geophysics*, 37, 620 – 646, 1972.

15 Guigné, J. Y., The concept, design and experimental evaluation of an acoustic sub-seabed interrogator, *Ph.D. Thesis*, University of Bath, Bath, UK (1986).

16 Wingham, D. J., The penetration of a water–sediment interface by a parametric array, *Ph.D. Thesis*, University of Bath, School of Physics, UK (1984).

17 Pace, N. G. and R. V. Ceen, Time domain study of the terminated parametric array, *J. Acoust. Soc Am.*, 73 (6), 1972, 1983.

18 Muir, T. G., A survey of several nonlinear acoustic experiments on travelling wave fields, finite-amplitude wave effects in fluids, Proceedings of the 1973 Symposium, Copenhagen. 1973.

19 Malinverno, A., A simple method to estimate the fractal dimension of a self-affine series, *Geophysical Research Letters*, Vol. 17, No. 11, 1953 – 1956.

Effect of waveform on synthetic aperture sonar performances

Stéphane GUYONIC

Groupe d'Etudes Sous-Marines de l'Atlantique
BP 42
29240 BREST NAVAL
Email : guyonic@gesma.fr

Abstract

This paper describes the main properties of the synthetic aperture sidescan sonar and highlights performances and limitations related to sonar features for mine counter measures.

Attention is focused on the theoretical performances : azimuthal resolution, signal-to-noise ratio and mainly shadow-to- reverberation ratio.

This theoretical analysis is finally compared with experimental sonar images. These images have been obtained with transducers moving along a rail and insonifying a sea bottom where some spherical and cylindrical targets are laid. Some of these targets are partly buried. Several signal waveforms, such as monochromatic or Frequency Modulated, have been used within the full 25 - 80 kHz band and different pulse durations have been transmitted as well. These experimental results can be considered as the first in the World under real conditions and with a good shadow-to-reverberation ratio.

1. Introduction

Synthetic aperture techniques in radar is well known [1]. Such technique applied to sonar concept is now within reach. The need of using this technique is obvious. From a military point of view, in the Mine Warfare, threat obliges mine countermeasures specialists to design systems able to achieve high resolution at long range and able to detect and classified buried objects. These objectives can be reached in using synthetic aperture techniques. Today, very few experiments have been realised in the World with such techniques [2], [3]. Thus detection and classification performances that could be achieved by such systems are not well known and not validated. This paper begins by describing the principle and the main characteristics of this technique. Following these well known generalities, concepts of detection and classification are studied and translated into some analytical expressions. Then a real experiment using a 15 meters long rail is described. The goal of this experiment is to study the influence of signal characteristics on sonar performances in terms of detection and classification of objects. Results are then compared with theory.

2. Synthetic Aperture technique : Principle and Characteristics

The synthetic aperture principle consists in generating a virtual antenna from the successive positions of a much smaller physical antenna. Signals received by transducers are stored through the period T during which a considered area of the sea bottom is illuminated and then coherently added. Let us consider the following simplified configuration :

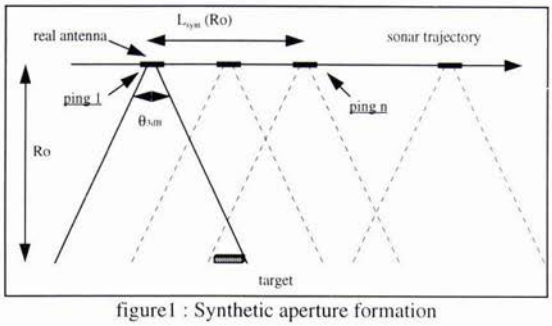

figure1 : Synthetic aperture formation

Let Ro be the minimum distance between the sonar and the target, θ_{3dB} be the 3 dB aperture of the real antenna. The length of the synthetic aperture depends on the range of the current pixel, it is given by

$Lsynt(Ro) = Ro\theta 3dB = Ro\frac{\lambda}{Le}$ (Le is the physical transmission antenna and λ is the signal wavelength)

2.1 Synthetic aperture advantages

By considering the above geometry, the phase of signal received during the displacement of the physical antenna follows an parabolic variation and by the same way the frequency associated with an echo varies linearly. We can notice an analogy with the behavior of a linearly frequency modulated signal with a pulse length of T and a bandwidth of B. These signals are in current use in sonar or radar applications to permit the use of high power. A good range resolution is then achieved by a compressed pulse technique It uses a matched filtering by the cross correlation of the received signal with the inverse replica of the transmit pulse.

By the same way the synthetic aperture technique can be made by a compressed pulse based on the cross correlation of data in the along track direction within the period T and the equivalent law phase history [4]. In this case, T is the target illumination period and B is the doppler frequency bandwidth resulting of the relative sonar-target motion ($T = \frac{R\lambda}{VLe}$, $B = \frac{2V}{Le}$ with R = range, V = sonar speed, Le = transmit antenna length)

Results of this processing generate very fine resolution t, independent of both range and frequency. The azimuthal resolution can indeed be estimated as the value of the 3dB width of the correlation peak that is to say:

$$\delta az = \frac{Le}{2} \qquad (1)$$

This result explains the interest in this technique. In fact, for synthetic aperture sonar, the smaller the size of the transducers is, the better the azimuth resolution is, which is just the opposite behavior of a classical beamforming.

What follows will highlight the other advantages of this technique and especially the improvement reached in the Signal-to-Noise ratio.

2.2 Synthetic aperture limitations

Some particularities of this technique which can involve limitations and need at least more investigations have to be taken into account.

Firstly, the synthetic aperture sonar is characterized by the occurence of ambiguities in the range direction and grating lobes in the azimuth direction. In the range direction, ambiguities are avoided with a condition on the recurrence period Trec. In the along track direction grating lobes resulting from the spatial lacunarity effect of the synthetic aperture technique which generates a synthetic beam repetition. One of the best way to cancel the grating lobes is to adapt the zero of the receiver antenna diagram with the position of the grating lobes. These two conditions are expressed in the following inequalities:

$$\frac{2Rmax}{C} < Trec < \frac{Lr}{2V} \qquad (2)$$

Lr : receiver antenna length

Secondly, the synthetic aperture technique requires a great accuracy in the phase measurements, otherwise imagery defects appear (false echo, contrast degradation,...). Techniques of autofocalisation based on the use of the high signal correlations between successive sonar pings, in the case of a convenient spatial oversampling, authorize us to go beyond the theoretical phase accuracy limits [5].

High computation power needed by synthetic aperture processing should find solutions in the next future with some new studies and algorithms coming from radar [3], [6].

3. Detection and Classification concepts

Synthetic Aperture Sonar performances can be evaluated or approached by computing and analysing theoretical contrasts between Signal and Noise (for detection scenario) and Reverberation and Noise contrasts (for a classification scenario, if shadow analysing is used for target classification). Some differences appear between synthetic aperture sonar ratios and those relative to a classical sonar and are underlined later on.

3.1 Detection concept

Detection is the ability for an operator to isolate a signal from noise. Noises may have different origins (ambiant noise, electric noise, reverberation from sea bottom, sea surface or volume inhomogeneities,...).

- Signal-to-Noise ratio : SNR (or contrast) is given by the following expression :

$$SNR = SL + TS - 2TL - NL + DI + IF \text{ (in dB)} \tag{3}$$

with : - SL : Source Level, NL: Noise Level, DI: Directivity Index, TS : Target strength
- TL : Transmission losses (geometrical spreading and absorption losses)
- IF : Improvement factor = IF_{PC} (pulse compression) + IF_{SAS} (SAS gain)

- Signal-to-Electrical Noise ratio :SER (at the intput of the preamplifier) :

$$SER = SL + TS - 2TL + Sh - 178 + 10\log_{10}B + 20\log_{10}N - 10\log_{10}N + IF \text{ (in dB)} \tag{4}$$

with : Sh : Sensitivity of the receiver, B : Signal bandwidth, N : Number of transducers

In the case of our experiment, the ambiant noise can be regarded as negligible. Thus, the main sources of noise are bottom and sea surface reverberation.
At short ranges, in any case, detection is limited by bottom reverberation. This contrast is given by :

$$SRR = TS - RL - 10\log_{10}S + IF_{SAS} \text{ (in dB)} \tag{5}$$

with : RL: Reverberation Level, S: resolution area cell
If the sonar operates in shallow water conditions, the influence of surface reverberation has also to be taken into account.

3.2 Synthetic aperture and real antenna sonars differences

By comparing classical sonar and synthetic aperture sonar performances in the above expressions, some differences appear. The main one is relative to the improvement factor (IF) which differs by considering a classical processing and a synthetic aperture processing. For a classical sonar, if a pulse compression is made, the theoretical improvement is limited to the gain of $10\log_{10}BT$ (B : signal bandwidth and T : pulse duration)

In the case of a synthetic aperture processing a supplementary gain appears due to the effect of the coherent integration (or azimuthal filtering). This term depends on the number of effective summation or in other terms, is connected to the length of synthetic antenna.

$$IF = 10\log_{10}BT + 10\log_{10}\frac{R\lambda}{2Le\delta az} \tag{6}$$

Another difference can be noted by considering the sonar resolution cells which are given respectively for a classical sonar and a synthetic aperture sonar by :

$$S_{clas.} = C\frac{\tau}{2}xR\frac{\lambda}{Le}\frac{1}{cos\alpha} \tag{7a}$$

$$S_{SAS} = C\frac{\tau}{2}x\frac{Le}{2}\frac{\lambda}{cos\alpha} \tag{7b}$$

A roughly analysis of expressions (5), (6) and (7) as the case of a synthetic aperture technique or a classical beamforming is used, shows that the influence of frequency is exactly inverse in terms of detection ability.

Signal-to-Reverberation ratio increases when frequency becomes higher in the case of a classical beamforming and decreases with a synthetic aperture processing.

3.3 Classification concept

The concept of classification based on a shadow analysis needs to take into account two ratios, first the Reverberation-to-Shadow ratio and secondly the Reverberation-to-Electrical Noise ratio (expression of it can easily found from (4) and (5)). The first ratio expresses the possibility of creating a shadow by the relative geometry of the different sonar beam (transmit sonar beam, receiver beam and synthetic sonar beam) and target geometry (size and orientation). The second ratio expresses the possibility for the shadow to be visible.

Let us consider, Lr as the Reverberation Level and Ls the Shadow Level.

$$Lr = k\int Gt(r,\theta).Gr(r,\theta).Gsynt(r,\theta)d\theta \quad (8)$$

$$Ls = k\int Gt(r,\theta).Gr(r,\theta).Gsynt(r,\theta)F(r,\theta)d\theta \quad (9)$$

$F(r,\theta)$: binary function = 1 if $-arctg(\frac{Ltarg}{2R}.) < \theta < arctg(\frac{Ltarg}{2R}.)$

= 0 elsewhere

$Gt(r,\theta)$, $Gr(r,\theta)$ and $Gsynt(r,\theta)$: transmission, reception and synthetic diagrams.

Let us assume that the other noise components (ambiant noise, electrical noise) and surface reverberation are negligible (not satisfactory in a shallow water environment with wide vertical beam used), shadow depth can be estimated by the following Reverberation-to-Shadow ratio :

$$RShR = 10\log_{10} Lr - 10\log_{10} Ls \quad (10)$$

This above expression has been used for theoretical computation (figure 5)

4. Synthetic Aperture Sonars : experiments

4.1 Facility and equipment set up for experiment

In GESMA, a facility have been designed three years ago and refited last year to test transducers and especially in a synthetic aperture running. This facility consists of a linear rail, 15 meters long that includes a platform moving by a motor. This platform can carry transducers for transmission and reception signals. Moreover, the rail can be displaced along a vertical axis by a chain system and be fixed at seven different positions. By using these possibilities, the effect of surface reverberation on sonar performances can be studied.

This rail is located in a shallow water environment. The maximum water depth is 17 meters and tidal range may be important (7 meters for spring tide). The lowest rail fixation is 6 meters above sea bottom. This is the position used for experiments described in this paper.

The sea bottom in front of the rail is composed with a mixture of sand and fragments of shells caracterized by a high reveberation. Moreover, a little slant of the bottom is perceptible at short ranges and also some ripples.

A target field has been disposed for this experiment and spreads from 15 meters to 50 meters respect to the rail.

Six targets are laid on the sea bottom. Four of them are spherical objects of 1 meter diameter and the others are cylinders (0.55 meter diameter and 2.8 meters long). Spheres located at 15 meters and 39 meters from the rail were laid two years ago and a partial burial is effective. This natural burial is resulting from some important currents which generate a scouring effect. To sum up, these two targets are one third buried and a mound of sand is just against them. The first cylinder (at 22 meters) is laid on a little dune that involves a little slant of the cylinder and a modification of the shape of the shadow in the processed image.

4.2 Objectives

The goal of experiments is to analyse the influence of signal characteristics (frequency, bandwidth, pulse compression,...) on detection and classification operations and to validate, by calibrate trials, the main properties of Synthetic Aperture technique applied to sonar. very few experiments currently exist in a sea context in the purpose of small targets detection and classification. So these objectives and associated results may be considered as the first in the World obtained in a sea environment.

4.3 Transducers and signal characteristics

Transducers used for the experiment had been designed in the 25 to 80 kHz frequency range and have a uniform frequency response. Several transducers were used, one for the transmission and three for the reception.

Several data have been stored for each acquisition, one channel for the transmit signal, one for the motor coding data and six other channels for two superposed antennas (three transducers for each).
Transducers have a rectangular shape of 0.195 m X 0.07 m dimensions. They were fixed at 6.8 meters above the sea bottom with a grazing angle α of 15 degrees. Some acquisitions have been made in CW (Chirp Wave) and others in LFM (Linearly Frequency Modulation).
To sum up :
- CW signals used are : 32, 48, 64, 80 kHz with a pulse length of 150 µs (and someone with pulse lengths of 62 µs and 75 µs)
- LFM signals used are : 32 - 64 kHz, 48 - 80 kHz and 27 - 80 kHz with a pulse length of 10 ms, that is to say a BT product of 320 and 530.

4.4 Data processing and results

Processing had been made in post processing time with two dimensional process, firstly the pulse range compression when a LFM signal is transmitted and secondly the synthetic aperture processing. This focusing is made in the frequency domain, the hyperbolic echo migration is compensated with a dephasing term.

- *Azimuthal resolution results* :
Results show that theoretical along track resolution is achieved in any case and it is really both of range and frequency independent.

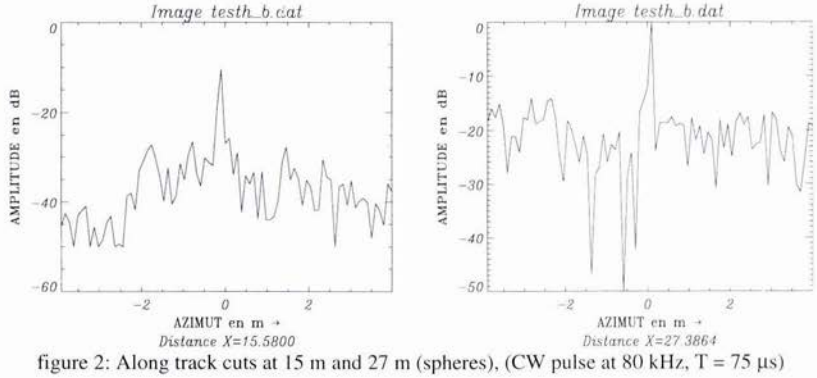

figure 2: Along track cuts at 15 m and 27 m (spheres), (CW pulse at 80 kHz, T = 75 µs)

Figure 2 illustrates the azimuthal echo compression with two examples : two spheres at 15 meters and 26 meters from the sonar. The real along track resolution is really equal to 10 cm (Le/2).

- *Frequency influence* :
Figure 3 shows a cut in range centered on a sphere target echo with two different CW pulses, 80 kHz (left) and 32 kHz (right) with respective pulse lengths of 75 µs and 62 µs. Some remarks may be noted. First the shadow is in both case very convenient for a classification but a sensible degradation appears at the lowest frequency. The wider aperture antenna at low frequency and the effect of surface reverberation may explain it.
No AGC (Automatic Gain Control) is applied on signal so the range propagation effects (losses) are quite visible on data. Moreover, the left side of figure 3 reveals the narrow beam effect at 80 kHz. The first target is outside the main lobe transmission antenna. A last remark on these two signals deals with the Signal-to-Reverberation ratio which is greater at 32 kHz than at 80 kHz, that is in good agreement with theory and equations (5), (6) and (7)

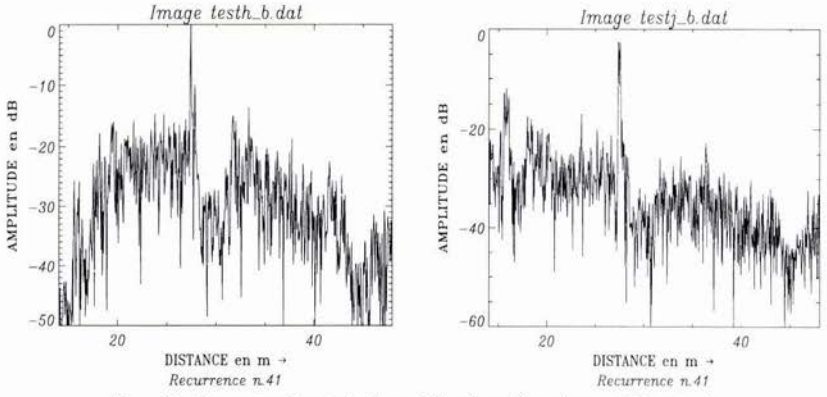

figure 3 : Across track cuts (echo and shadow of a sphere at 26 meters)
(CW pulse - left side f0= 80 kHz, T = 75 µs - right side : f0=32 kHz, T=62 µs)

Signals characteristics have influence on the shadow depth, the computation of equation (10) give the following results (figure 4 : two different target sizes have been used for computation L = 1m equivalent to the spheres laid and L=2.8 m which corresponds to the cylinders).

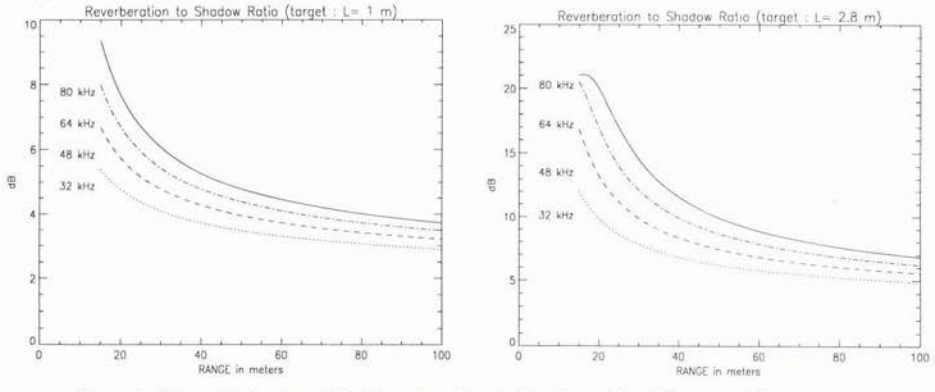

figure 4 : Theoretical value of the Reverberation-to-Shadow ratio : Influence of frequency

These shadow depth values are overestimated in a shallow water environment with wide beam sonar. Nevertheless experimental results show a good agreement with regards to the influence of frequency which figure 4 reveals. Higher frequency is, deeper shadow is and as shown on these diagrams this difference decreases with range to become not sensible on the last targets.

- *Pulse length and bandwidth influence*

One more influent parameter is the pulse length of signal or the effect of wide bandwidth (and pulse compression). That is to say signal parameters used to give a better range or azimuthal resolution lead to the improvement of the shadow depth (reverberation-to-shadow ratio) and especially towards the range limit

Figure 5 illustrates one example of numerous processed data. This sonar image shows a good shadow target quality. Every target laid on the field is strictly classified by its shadow. In the center of this target field, two spheres (ϕ=1m) are laid 0.5 meter from the other. They are discriminated. Their specular echoes are separated by 1.5 meters and shadows are also separated. Data are represented as a projection on the sea bottom and a normalization has been applied on them to compensate the effect of the dynamic variation. This image has a resolution cell of 0.1 m X 0.056 m. (azimuth x range).

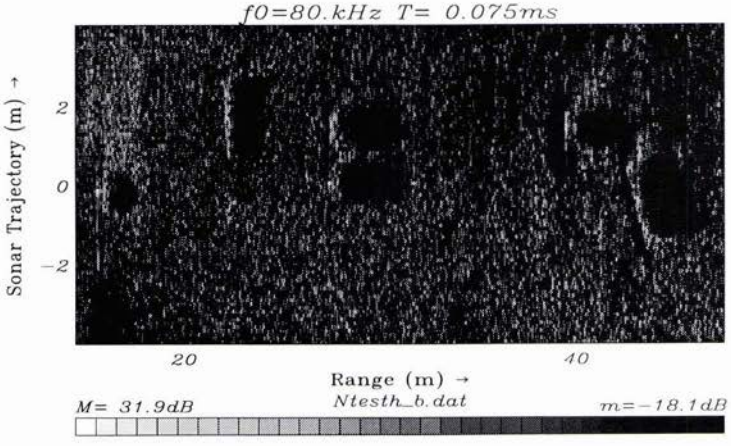

figure 5 :SAS processing results on target field (CW signal f0 = 80 kHz, T = 75µs)

Figure 6 shows the same area insonified with a FM signal of 32 kHz of bandwidth . The azimuth « zero » reference is not the same as the above figure 6.In this case, azimuthal rsolution is also 10 cm and range resolution is equal to 1.4 cm. The shape of shadow are in this last case more outlined. Concerning the two spherical proud targets, located at 26 meters, two echoes are visible, the first one is the direct path from the target and the second one is the first target to bottom path.
These two signal acquisitions have been made within a time interval of two months and the last target have been a little bit displaced.

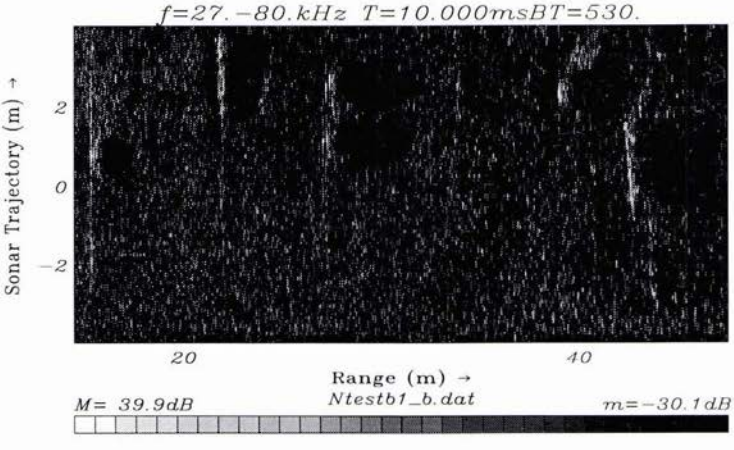

figure 6 :SAS processing results on target field (FM signal f =27 - 80 kHz, T = 10 ms)

- *Window weighting effect* :
Window weighting functions are currently used in classical sonar devoted to classification. In the case of synthetic aperture sonar a weighting function may be applied on each ping of the synthetic antenna.

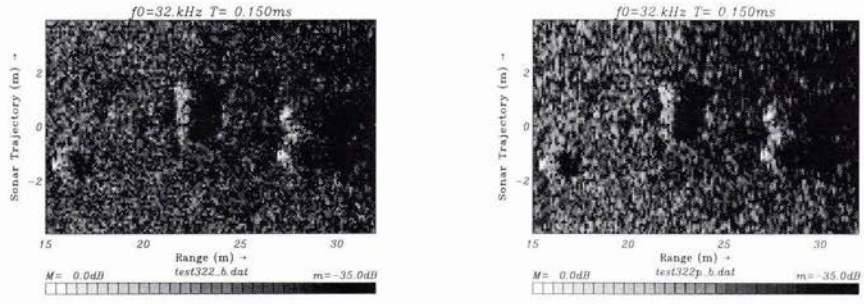

figure 7 : CW signal f0 = 32 kHz, T = 150 µs (on the rigth : HAMMING window)

A Hamming weighting window has been used on data and results compared with those obtained without apodization. A gain of about 3 or 4 dB has been obtained in the case of a CW pulse at 32 kHz and same results in the case of a LFM signals (48 - 80 kHz). Figure 7 and 8 illustrate

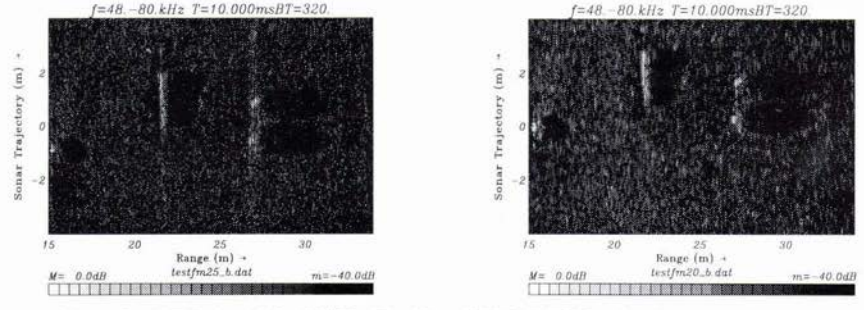

figure 8 a) LFM signal 48 - 80 kHz, T = 10 ms b)HAMMING weighting on synth. antenna

5. Conclusion

This paper provides the main theoretical characteristics of synthetic aperture sonar in terms of detection and classification of objects. The influence of signal characteristics have been studied on synthetic aperture sonar performances and especially on shadow depth.

Many results have been shown such as the interest in using higher frequency for having deeper shadow but this advantage tends to become less sensible when sonar range increases. The use of CW with shorter pulse length or wide bandwidth FM signals also give the best shadows.

A last result shows the reverberation-to-shadow ratio improvement that we can reached by using a weighting function on synthetic antenna (Hamming has been used).

All results obtained with this first experiment have to be confirmed with higher frequency at longer range.

Acknowledgment : *This work has been made within a collaboration with the Coastal Systems Station (Panama-City, Florida, US). I would like to thank Mrs John Lathrop, Jim Christoff and Joël Le Hars (GESMA) for their contribution in the experiment specification and their constant advices and Mr André Salaun et Mrs Corinne Queïnnec for the success of experiments.*

6.References

[1] L.J. CUTRONA « Comparison of sonar system performance achievable using synthetic aperture techniques with the performance achievable by more conventional means ». Journal of the Acoustical Society of America, 58(2),pp 336-348, August 1975

[2] S. GUYONIC « Experiments on a sonar with a synthetic aperture array moving on a rail »,IEEE Oceans'94 Conference Proceedings, pp 571,576

[3] P.T. GOUGH et al « A unified framework for modern synthetic aperture imaging algorithms », University of Canterbury, Christchurch, New Zealand, International Conference on Imagery and Image Processing, Dec. 9-11 1997 (submitted)

[4] G. LEVRINI et al « The sensitivity problem in the synthetic aperture radar (AR) », Alta Frequenza, Vol. LV-N°6 Nov. Dec. 1986, pp 337-348

[5] T. RASTELLO et al « Fourier-Based imaging applied to Synthetic Aperture Sonar »,IEEE Oceans'96 Conference Proceedings, pp1521,1526

[6] R.W. SHERIFF « Synthetic aperture beamforming with automatic phase compensation for high frequency sonars. » Proceedings of the 1992 Symposium on Autonomous Underwater vehicle Technology, pp 236-245, june 1992

Retrodirective Array Performance Case Studies and Implications for Mine Countermeasures

I. M. Hallaj, S. G. Kargl, R. A. Roy†

Applied Physics Laboratory, University of Washington
1013 NE 40^{th} St., Seattle, WA 98105 USA
† Dept. of Aerospace and Mechanical Engineering
Boston University, 110 Cummington St., Boston, MA 02215 USA

Abstract

The use of focused acoustic fields for the mechanical destruction of fluid-borne targets is applied in the medical field for the comminution of kidney stones by lithotripsy. Inhomogeneities in the propagation medium are of practical concern to both the medical and the ocean acoustics communities. The use of phase conjugation to compensate for medium inhomogeneities and multipath effects has been demonstrated for linear acoustics in both medical and underwater contexts. The feasibility of focusing an intense acoustic field onto waterborne targets has implications for mine countermeasures because of the possibility of remotely neutralizing mines. The demonstration of the concept in actual mine countermeasure applications has yet to be realized. We present the results of a numerical study which investigates the performance of linear arrays using time reversal as a means of focusing acoustic fields onto targets in an arbitrary medium modeled after a shallow water channel. The simulation investigates the cases where jitter exists in the initial phase of the time signals. The existence of tight focal widths, narrower than the free-space diffraction limit prediction, sometimes called "super-focusing", was observed for simulations containing small-scale inhomogeneities.

1. Introduction

Time reversal acoustics has a range of medical and underwater applications [1, 2]. The concept of time reversal is an extension of phase conjugation theory, which is known to hold for linear fields in reciprocal media [3, 4]. Remarkable focusing capabilities can be achieved using phase-conjugate arrays in almost arbitrary media by using a time reversal system [5]. However, a number of common phenomena can degrade the performance of a phase conjugate array, including:

- Nonstationary medium
- Limited signal capture resolution or dynamic range
- Nonlinear medium
- Nonlinear acoustical or electrical transfer functions

It is unlikely that perfect time reversal can be practically implemented in a system where the difference between transmitted and received signal levels can exceed 60 dB due to the resolution and dynamic range limitations of current systems. Uncertainties in amplitude, time-domain waveform, and phase will result in a general degradation of the performance of the phased array. The present study shows the results of computer simulations which illustrate the effects of uncertainties introduced into a signal in the receive-transmit operation of an otherwise ideal retrodirective system. The study of the performance and feasibility of an actual retrodirective system can be initially approached using such modeling to get an estimate of the most detrimental factors that might reduce an array's focusing ability.

The problem of building a phase conjugation device capable of operating in the ocean at the intensities required for mine neutralization is far more complex than a simple model problem. Foremost perhaps is the fact that the

modeled system is a linear time-invariant system. An actual usable mine countermeasure (MCM) system will certainly require going to such high intensities that nonlinear properties of the transduction devices and the propagation medium will become important. However, the current model is a good first step towards quantifying some of the permissible uncertainties for effective operation of such systems. The present study presents the results of simulations that compare unfavorable test cases to an idealized reference focusing case. The unfavorable test scenario introduces stochastic jitter into the time-domain signals captured by each of the array transducers. Also, a comparison of focal zone width is done with the free-space diffraction limit, showing the "super-focusing" discussed in [6].

2. Signal Phase Error

Random stochastic jitter is introduced into the time-domain signals that the array elements record during the receive mode. The jitter is meant to model an initial phase error, which can result from limited-resolution data acquisition electronics in the receive and/or transmit modes. The jitter is calculated for each array element individually as a time delay in the *initial* phase of each signal. Because the present study seeks to define a starting point for evaluating the relative effects of the more important parameters described that reduce the effectiveness of the time reversal array, only the simplest cases are studied. For example, one could have introduced jitter into each cycle of the wavetrains, or into each time step. In addition, amplitude jitter could be included. The simulations in this study only introduce jitter into the initial phase information of the pulses because the latter effects should be investigated in the category of pulse shape uncertainties, or nonlinear behavior, which is not addressed here. Ultimately, one would combine several of the above effects together to try and deduce what the performance of such a system might look like in the presence of several debilitating factors, but that would make the analysis of the results more complicated.

The jitter is given in terms of a fraction of the narrow-band signal's period. For a time-domain signal at array element k of the form $p_k(t)$, we introduce a time delay, δt, so that

$$p_k(t) \rightarrow p_k(t + \delta t_k). \tag{1}$$

The base source waveform is a sinusoidal envelope. The uncertainty is introduced for each of the elements independently, padding the leading (jitter) time, δt, with zeros. The jitter's duration is computed randomly for the k^{th} element from the narrow-band period, τ_0, the maximum error, A, as a fraction of 2π of the base wavelength for a run, and a random multiplier, σ_k,

$$\delta t_k = \sigma_k A \tau_0. \tag{2}$$

The random variable, σ_k, can range from zero to unity, and is different for each element, but the maximum possible jitter for any array element is A for a given simulation. Of course, the jitter can be defined in other ways, and could be thought of as being due to two processes: one during to the receive mode, and the other during to the transmit mode of the array.

3. Description of Problem and Solution

A vertical, 64-harmonic-element, equally-spaced linear array with an aperture of $25.6m$ is located in the center of a shallow water channel. A $2kHz$ narrow-band point source is located $51.2m$ away from the array as shown in figure 1.

3.1. The Solution Method

The linear inhomogeneous acoustic wave equation is the governing equation for all simulations presented here,

$$\nabla \cdot \left(\frac{\nabla p}{\rho} \right) - \frac{1}{\rho c^2} \frac{\partial^2 p}{\partial t^2} = 0, \tag{3}$$

with the primary variable being the acoustic pressure, $p(\mathbf{r}, t)$.

The wave equation is solved in the time domain using a two-dimensional second-order accurate (in space and time) finite-difference time-domain (FDTD) code. The calculations are carried out on a rectangular grid space of dimensions 1024 horizontal by 512 vertical mesh points. Absorbing boundary conditions were used at the extreme upper and lower edges of the computational domain to simulate an extended spatial region for visual clarity, although this is not necessary, as the time reversal method is especially useful for situations where multiple paths and scattering exist.

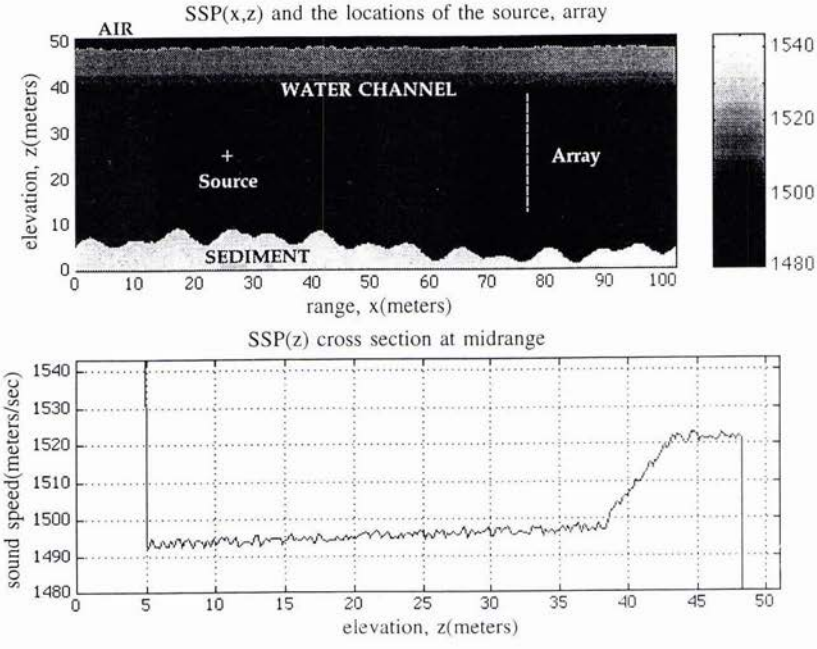

Figure 1: The sound speed profile used in the simulations. The extreme values for sediment and air are truncated to better illustrate the profile in water.

3.2. The Propagation Medium

The wave equation (3) is solved in an inhomogeneous medium modeled as air above a water channel approximately $50m$ deep with a (fast) fluid sediment below it. The sound speed profile (SSP) is fashioned after data given in [7] and [8]. A graphical representation of the SSP is shown in figure 1. Although the basic SSP profile is similar to that used in many studies, it serves to illustrate the physical concepts only, and is not meant to be an accurate oceanographic representation of the SSP of any actual body of water. The properties used for $20°C$ air were a homogeneous sound speed of $343m/sec$ and a density of $1.2kg/m^3$. The sound speed in the water channel was a function of depth below the surface, with inhomogeneities added to that profile. The sediment also had inhomogeneities built on top of a DC sound speed of $1650m/sec$, and a DC density of $1860kg/m^3$. Spectral statistics were not considered for the present study. The density field was obtained in a similar manner to complement the SSP. Inhomogeneities in the water and sediment are in the form of fluctuating regions of excess sound speed and density. Furthermore, a fine random component is added to the sound speed and density to give some fine structure.

The shapes of the air-water and water-sediment interfaces are composed of combinations of sinusoids with small, local, random fluctuations. Again, the intention is to provide simulations in a non-uniform medium with rough interfaces and not to model any oceanographic spectra at this time.

4. Results

The results of the simulations indicate that the time reversal method is in fact a good choice for focusing linear acoustic waves onto a target in an inhomogeneous medium with multipath effects and rough boundaries. Two snapshots are shown for the reference (ideal) case run. Figure 2 shows the pressure field during the receive mode of the array in the top panel, and the instant of maximum focus onto the source during the transmit mode of the array in the lower panel.

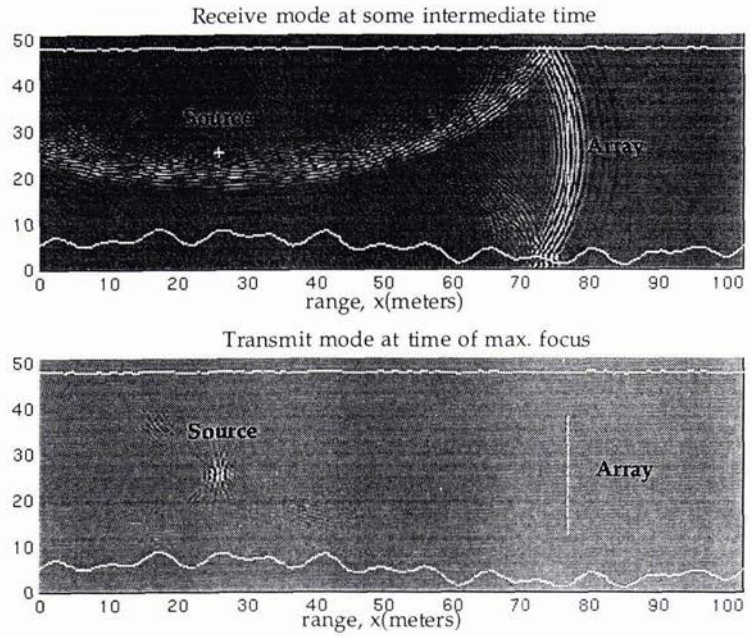

Figure 2: The acoustic pressure field. The top frame shows the pressure after some time from leaving the source during the array's receive mode operation. The lower frame shows the pressure after the array's transmit mode, when the maximum pressure occurs at the source location.

4.1. Phase Jitter

Random time-domain jitter is introduced in the form of zero padding leading the initial phase signal from each array element. Figure 3 shows the pressure field in dB around the location of the source at the instant of maximum focusing. The values are referenced to the maximum pressure (at the source's location usually). It was found that the location of the focus maximum remained near the original location of the source. The reason is that for many-element arrays the focal shift would tend to average out to its original value because the error has a zero mean. On the other hand, significant degradation in focus quality was observed for jitter exceeding about one-tenth of a wave period. As expected, the initial phase of the waveforms was shown to be very important to the focusing ability of the array. Simulations were conducted with jitter than ranged from $0.1(2\pi)$ up to a full 2π of a period. The $-3dB$ points did not show any appreciable spreading from case to case, but the magnitude of the acoustic pressure for the cases with large jitter was far reduced and spread over a large region of the channel, resulting in significant focusing degradation for jitters greater than 0.1 to 0.2 of one period (figure 3).

4.2. Super-focusing

The inhomogeneities in the propagation medium can act to enlarge the effective aperture of the array. This is because the small differences in the index of refraction act as localized sources which are distributed throughout the medium. Since the focal zone's FWHM spot size in free-space is given by the diffraction limit as

$$w = 1.2\ \lambda z/a, \tag{4}$$

the width is inversely proportional to the aperture. In our case the predicted width at $-3dB$ should be approximately $1.8m$ in free-space. In fact we observe that the $-3dB$ points occur at $\pm 0.3m$ from the source location. Simulations in homogeneous media using the same code have shown that the code does follow the predicted focal width in the absence of inhomogeneities [12].

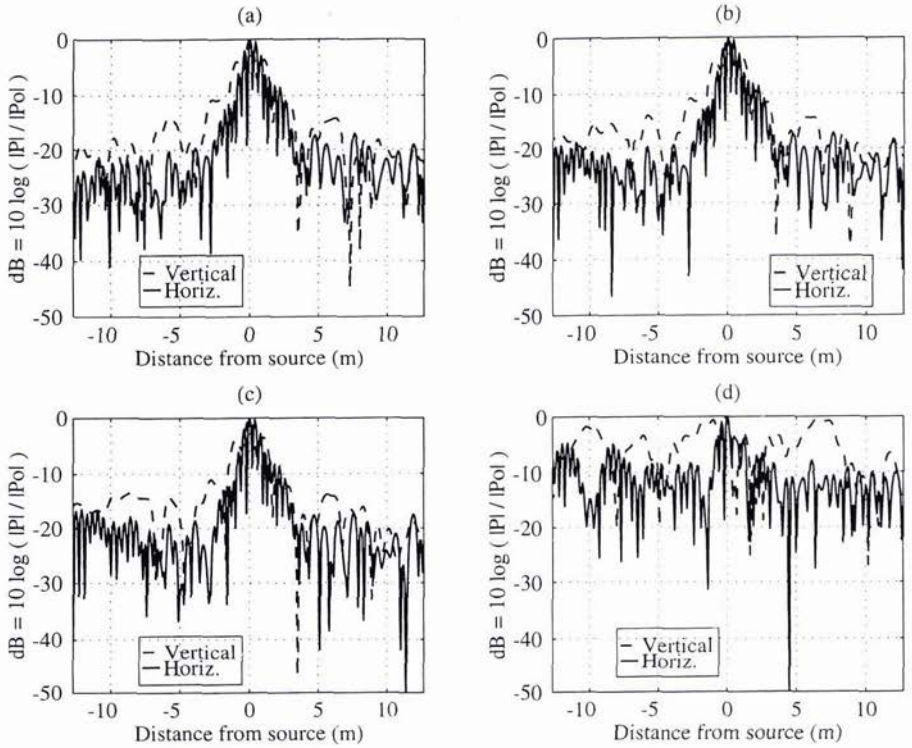

Figure 3: Slices through the source position at the time of maximum focusing for various jitter conditions. The dashed lines denote the vertical slices (parallel to the array), while the solid lines denote the horizontal slices (perpendicular to the array). Panels are for (a) No jitter (reference case), (b) Max. jitter = $0.1(2\pi)$, (c) Max. jitter = $0.2(2\pi)$, (d) Max. jitter = 2π.

Experiments by Derode, *et al.* [5], have also demonstrated this effect in the laboratory for high-order multiple scattering.

5. Conclusions

The premise of using phase conjugate arrays for the focusing of intense acoustic fields onto a remote waterborne target has implications for MCM system design. The possibility of remote neutralization of pressure-sensitive mines would be an asset to the MCM arsenals that exist today [11]. The concept has been demonstrated in theory and in the laboratory for ultrasonic frequencies in medical applications. Ocean field experiments in shallow water have been conducted recently by Kuperman, *et. al.*, (unpublished). These experiments were conducted at $400Hz$, and would not encounter the difficulty with electronic jitter that high frequency arrays would suffer from. However, the results obtained so far from experimental [5] and theoretical [6] groups show a remarkable robustness when using the time reversal technique with multiple scattering and reflection in random media.

In this report we used a linear acoustics model to simulate propagation through a shallow water channel with an inhomogeneous sound speed profile as well as a rough surface and bottom. The results for cases that are expected to degrade the focusing ability of a time reversal array by altering the initial phase information are given. Initial phase timing is corrupted by some jitter introduced to model time-domain electronic system uncertainties affecting the relative phases of the transmitted array element waveforms.

The array's focusing appears to hold up well under these circumstances for jitter up to 0.1 to 0.2 of the narrow-band period. Above a value of 0.2 period results in significant loss of focus. The location of maximum pressure remained at the location of the source because the jitter is a zero-mean random variable. indicating that

initial phase of the returned signals is more important than the details of the waveform phase shape. This is encouraging, since the data aquisition of a *broad-band* time-reversal signal, and the translation of that signal into a corresponding high-intensity array pressure output is unlikely with current technology. This is especially true if the array consists of elements whose bandwidth is significantly greater than PZT transducers.

Other factors not studied here that are detrimental to the focusing of phase conjugate arrays also need to be investigated. Chief among these is the nonlinear behaviour of the medium and the transducer and electronics' transfer functions, which will become important for high intensity or broad-band signals. The nonlinearity of the transduction process under real ocean MCM conditions is certain to play an important role that needs to be studied theoretically and in the laboratory before any definitive conclusions can be made regarding the feasibility of constructing an actual MCM phase-conjugate system.

Acknowledgements: This work was generously supported by the Office of Naval Research (321-TS).

References

[1] Q. Wen, *Spatial Diversity Equalization and Phase Conjugation Applied in Ocean Acoustic Communications* PhD Thesis, University of Washington, 1991.

[2] J.-L. Thomas and F. Wu and M. Fink, "Time reversal focusing applied to lithotripsy", *Ultrasonic Imaging*, vol. 18, no. 1, pp.106-121, 1996.

[3] D. R. Jackson, "Phase conjugation in underwater acoustics", *J. Acoust Soc. Am.*, vol. 89, no. 1, pp.171-181, January, 1991.

[4] M. Fink, "Time reversal of ultrasonic fields - Part I: Basic principles", *IEEE Trans. on Ultrasonics, Ferroelectrics and Freq. Control*, vol. 39, no. 5, pp.555-566, September, 1992.

[5] A. Derode and P. Roux and M. Fink, "Robust acoustic time reversal with high-order multiple scattering", *Phys. Rev. Letters*, vol. 75, no. 23, pp.4206-4209, December, 1995.

[6] D. R. Dowling and D. R. Jackson, "Narrow-band performance of phase-conjugate arrays in dynamic random media", *J. Acoust Soc. Am.*, vol. 91, no. 6, pp.3257-3277, June, 1992.

[7] P. C. Etter, *Underwater Acoustic Modeling* New York, Elsevier Applied Science, ch. 4, pp. 129-130, 1991.

[8] A. L. Anderson and L. D. Hampton, "Acoustics of gas-bearing sediments I: Background", *J. Acoust Soc. Am.*, vol. 67, no. 6, pp.1890-1903, June 1980.

[9] A. B. Coppens, "Simple equations for the speed of sound in Neptunian waters", *J. Acoust Soc. Am.*, vol. 69, no. 3, pp.862-863, March 1981.

[10] D. R. Dowling, "Phase-conjugate array focusing in a moving medium", *J. Acoust Soc. Am.*, vol. 94, no. 3, pp.1716-1718, September, 1993.

[11] Gerken, *Mine Warface Technology* American Scientific Corp., ch. 3, pp. 99-140, 1989.

[12] I. M. Hallaj, "The focusing of ultrasonic fields: A numerical study of the focal width using FDTD simulations," December, 1996, unpublished.

A Noise Directionality Model including Variable Bathymetry

C H Harrison

BAeSEMA
Apex Tower
7 High Street
New Malden
Surrey KT3 4LH
England UK
Email: chris.harrison@baesema.co.uk

Abstract

In this paper we investigate the noise directionality due to distributed surface sources in several environments with a uniformly sloping sea bed. Of particular interest are frequency dependence and the question of the relevance of multipaths to very high frequencies. We look at both uniform source distributions and swathes of sources lying parallel to the coastline. Some closed form solutions are presented, backed up by numerical solutions using the CANARY range and azimuth dependent noise model.

1. Introduction

Noise directionality is an important consideration for the design of high frequency sonar systems as well as low frequency arrays. At low frequencies one tends to convert the noise directionality into a correlation matrix for a given array in the given noise field. This can subsequently be used in beam forming or adaptive beam forming calculations. At very high frequencies it may be more appropriate simply to point the array physically in the desired direction. In both cases noise directionality is probably as important as absolute noise level.

There are several interesting problems in shallow and coastal waters across the frequency range. One is that of noise production mechanisms such as wind, wave and rain [1, 2]. Another is the effect of multipaths, in particular, bottom reflections from a sloping seabed. Yet another is the effect of uniform distributions of noise sources, such as wind, as opposed to discrete shipping sources. And finally there is the effect of more localised, but still distributed, sources such as waves where the water depth approaches zero.

In this paper we present some calculations of the effects of multipaths with uniform and non-uniform source distributions and a sloping sea bed. Since we are interested in directionality only our results are relative (ie relative to a unit source level per unit area of surface). At frequencies of tens or hundreds of kHz one would usually neglect multipaths because of high bottom losses, amongst other things. Here we investigate the validity of this assumption by looking at the frequency dependence of the directionality when sources may not be immediately overhead. At lower frequencies we already know that in deep water (the absence of a sea bed) we obtain Cron & Sherman's [3] result; in a range-independent environment we find a noise notch which is a simple Snell's law refraction phenomenon for surface sources; and in a range and azimuth dependent environment the noise notch is filled in by downslope multipaths [4].

2. Approach

Our calculations are based on a formulation developed by Harrison for range-independent [5] and for range-dependent environments [6] (in press). Analytical results are possible for a wedge-shaped environment with either uniform sources or swathes of sources parallel to the coastline [7]. We will also present some numerical results from the model CANARY (Coherence of Ambient Noise for Arrays) which uses a similar approach.

If we attempt to calculate from first principles, say, the array response A for a receiver with beam pattern $B(\phi,\theta_r)$ we obtain an integral over the entire sea surface whose integrand is the dipole source strength per unit area $q(\phi,r)\sin^2\theta_s$ times a propagation factor $P(\phi,\theta_r,r)$ times $B(\phi,\theta_r)$,

$$A = \iint q(\phi,r)\sin^2\theta_s P(\phi,\theta_r,r)B(\phi,\theta_r)rdrd\phi \tag{1}$$

where ϕ is azimuth, θ_r, θ_s are ray elevation angle at the receiver and surface respectively, and r is range.

Harrison [5] shows that this simplifies as follows. If we imagine the receiver as a source, the ray spreading at the surface because of refraction and distance is what causes the usual weakening of intensity. By reciprocity, sources at the surface provide weakened contributions at the receiver. Simultaneously, however, the number of noise sources in an elementary area goes up (if they are locally uniformly distributed) by the same factor and exactly cancels. Thus the geometric spreading effect disappears even in an arbitrary 3D environment.

For each arrival angle at the receiver θ_r a ray potentially has had many surface hits and we have to add a noise contribution for each one. In a range-independent environment this is relatively simple, and because each ray cycle introduces one extra upper and lower turning point loss and a volume absorption loss we obtain a geometric series which can be solved analytically.

More generally in a range and azimuth dependent environment [6] we find

$$A = \iint q(\phi,r)D(\phi,\theta_r)B(\phi,\theta_r)d\phi\cos\theta_r d\theta_r \tag{2}$$

Here D is the noise directionality that we seek; it is a noise power per unit solid angle. It can be separated into two terms U and S.

$$D(\phi,\theta_r) = U(\theta_r)S(\phi,\theta_r) \tag{3}$$

The function U is the residual attenuation due to bottom reflection (power reflection coefficient R_b) and volume absorption a between the last ray upper turning point and the receiver. For the upward ray the partial path length is s_p, and for the downward path it is (s_c-s_p), where s_c is the complete cycle path length. So for a path steep enough to hit the surface, U is given by

$$\begin{aligned} U(\theta_r) &= e^{-as_p} && ;\theta_r \geq 0 \\ &= R_b(\theta_b)e^{-a(s_c-s_p)} && ;\theta_r < 0 \end{aligned} \tag{4}$$

Central to this paper is the function S which represents the contribution arriving along one ray from multiple dipole sources. It is S that forms a geometric series in a range-independent environment with a uniform source distribution, but elsewhere it is clearly more complicated.

$$S(\phi,\theta_r) = \sum_{n=0}^{N} q(\phi,r)\sin(\theta_s)_n.\exp(-\sum_{j=1}^{n} L_j) \tag{5}$$

with

$$e^{-L_j} = \Re_j = R_s((\theta_s)_j)R_b((\theta_b)_j)\exp(-a\,(s_c)_j) \tag{6}$$

Here the surface and bottom reflection coefficients R_S and R_b (evaluated at appropriate angles) are treated as symmetrical functions of angle.

2.1 **Analytical results**

The position dependence of the source strength q (ϕ,r) can either be assumed to be a constant (uniform distribution) or can be converted to angle dependence given the bathymetry and a ray invariant [8].

In a wedge-shaped ocean the arrival angle θ_r corresponds to a *fixed* ray angle at a given distance from the apex because the water depth at this distance is fixed. Therefore analytical solutions for the noise directionality $D(\phi,\theta_r)$ are also possible with swathes of sources parallel to the coastline because (5) can still be solved [7].

Harrison (in press) [6] derives solutions for uniform sources in a wedge combined with isovelocity or range-independent downward refraction, sound channel or surface duct. The refraction cases explicitly show the classical filling in of the noise notch by upslope sources.

In the isovelocity case we take the bottom to be a tilted plane of (low) gradient ε_o, so that, adopting a N×2D approach the effective slope at a particular azimuth is given by $\varepsilon(\phi) = \varepsilon_o \cos\phi$. After each bottom bounce the ray angle is incremented or decremented by 2ε so that θ and j are linearly related. Joint boundary loss is taken to be $\alpha\sin\theta$ per bounce where α is a constant up to a critical angle θ_c. We can then approximate the sums in (5) as integrals and solve them. Looking downslope from the receiver we have

$$S_{down}(\phi,\theta_r) = \frac{1}{\alpha}\left(1 - e^{-(\alpha/2|\varepsilon|)(1-\cos\theta_r)}\right) \tag{7}$$

whereas going upslope from the receiver we have

$$S_{up}(\phi,\theta_r) = \frac{1}{\alpha}\left(1 - e^{-(\alpha/2|\varepsilon|)(\cos\theta_r - \cos\theta_c)}\right) \tag{8}$$

where θ_c is a critical angle. It is now clear that neither S_{up} nor S_{down} can be greater than the range-independent equivalent which is $1/\alpha$. They can only equal it for low slopes or large losses.

Intensity contours for normalised directionality ($\alpha D=\alpha SU$) are shown in cartesian (ϕ,θ_r) projection in Fig 1. Parameters are: Bottom slope $\varepsilon_o = 0.01$, bottom loss $\alpha = 0.23$ (ie 1 dB per radian), critical angle $\theta_c = 30°$. The intensity for downward angles steeper than θ_c at the receiver is obviously zero as indicated by the black area. The highest intensities (white) are seen slightly up-slope of across-slope. Upslope the weakest returns are for steep ray angles; downslope the weakest returns are in the horizontal. The up/down asymmetry is entirely due to bottom loss $R_b = \exp(-\alpha \sin|\theta_r|)$ in U (see (4)) since absorption has been set to zero. At upward elevation angles greater than critical the formula reverts to Cron and Sherman's [3] leaving $D=\sin\theta_S$. For comparison Fig 2 shows the equivalent plot from [6] for a range - independent surface duct in a wedge.

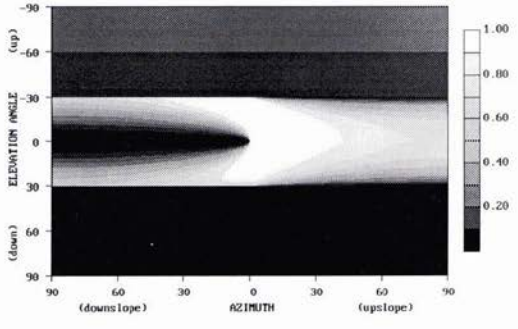

Fig 1 *Analytical noise directionality for an isovelocity wedge using (7) and (8). Intensity is linear.*

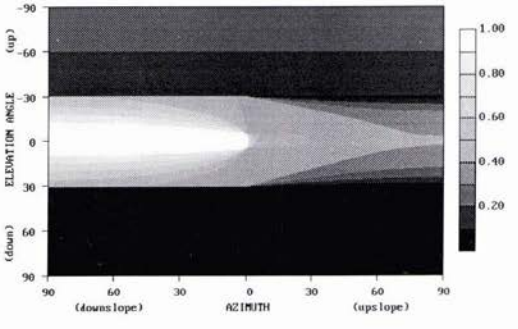

Fig 2 *Analytical noise directionality for a surface duct (formulae in [6]). Intensity is linear.*

2.2 Numerical results

Behaviour of boundary losses and volume loss is clearly crucial. At higher frequencies we need to take better account of the detailed variation of these quantities, so now we turn to numerical methods. In the model CANARY we still have to solve for $S(\phi,\theta_r)$, (5), and again we take a N×2D approach. The gist of this numerical method is given in [9] and [10] (in press).

Because each term in the first sum of (5) represents the contribution from the nth surface hit multiplied by the cumulative losses up to that point it is possible to calculate both sums efficiently in a single loop. We simply trace the ray (at ϕ,θ_r) backwards, simultaneously multiplying the current cumulative loss factor by the RHS of (6) for the latest cycle, and adding q sin θ_s times the current cumulative loss factor as in (5) for each surface hit.

Note that a coarse spread in ray angles will suffice since we do not need to bother with geometric spreading. Some comparisons between CANARY and the analytical cases of [6] are given in [11].

In the following examples we have used Thorp [12] for volume loss a (dB/km)

$$a = f^2\left[3.01\ 10^{-4} + \frac{0.109}{(1+f^2)} + \frac{43.7}{(4100+f^2)}\right] \tag{9}$$

with frequency f in kHz; Marsh, Schulkin and Kneale [13] for surface loss

$$R_s(\theta_s) = exp\left[-5.57\ 10^{-4} f^{3/2} w^4 sin\theta_s\right] \tag{10}$$

with wind speed w in m/s. To represent bottom loss frequency dependence we have invented a formula loosely based on a graph of Marsh's shown in Urick's book [14]. This gives the linear rise to a plateau in angle combined with an increase in frequency.

$$R_b(\theta_b) = exp\left[-1.35(1 + log_{10}f + (log_{10}f)^2)tanh(2.86\theta_b)\right] \tag{11}$$

For frequencies below 1kHz we drop the $(\log_{10}f)^2$ term.

2.2.1 *Frequency dependence in a wedge with uniform source distribution*

Figures 3-5 illustrate the effect of the increasing losses on the directionality at frequencies of 0.25, 1, 4kHz in an isovelocity wedge of slope 0.01 assuming a wind speed of 5m/s. Under these conditions we can safely ignore multipaths above 4kHz.

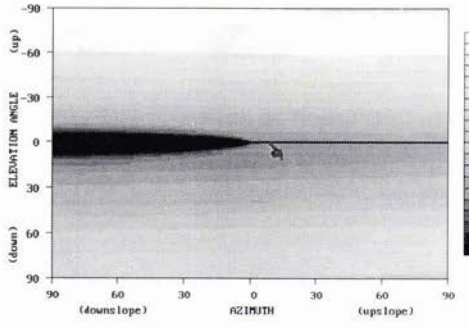

Fig 3 *Numerical noise directionality (dB) for isovelocity with uniform sources at 250Hz*

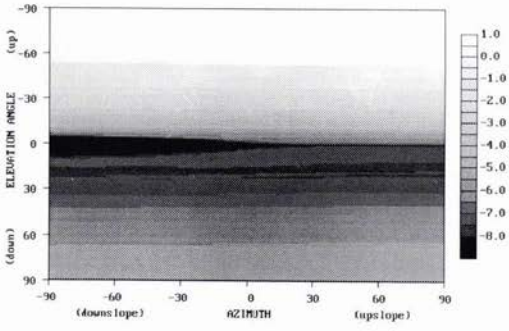

Fig 4 *Numerical noise directionality (dB) for isovelocity with uniform sources at 1kHz*

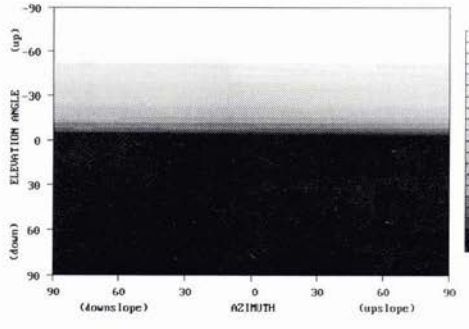

Fig 5 *Numerical noise directionality (dB) for isovelocity with uniform sources at 4kHz*

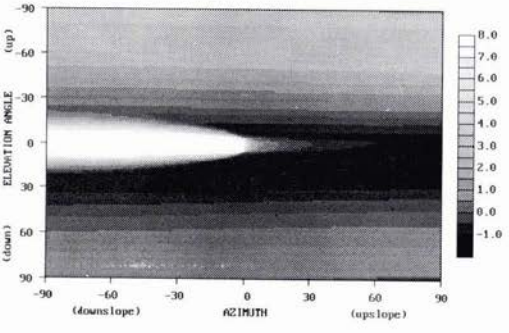

Fig 6 *Numerical noise directionality (dB) for surface duct with uniform sources at 250Hz*

If there is upward refraction with the receiver relatively near the surface then there is a better chance of multipaths without much bottom interaction. In Figs 6-8 (and Figs 3-5) we have the receiver at depth 10m in 100m of water. Here there is potential for strong multipath arrivals at low angles provided wind speeds are low.

Although all figures for uniform source distribution display directionality the direct upward path dominates at high frequencies and there is no azimuth dependence. There is a residual first bottom reflection in the downward direction. As frequency lowers there is a near horizontal contribution from out to sea in the surface duct but a corresponding low in the isovelocity case.

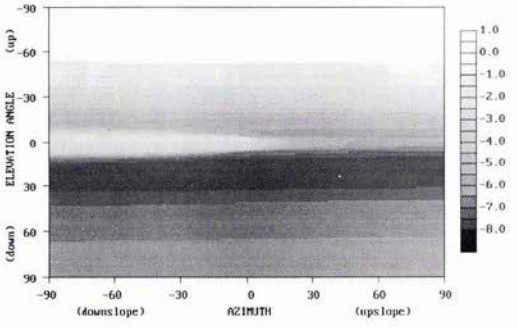

Fig 7 *Numerical noise directionality (dB) for surface duct with uniform sources at 1kHz*

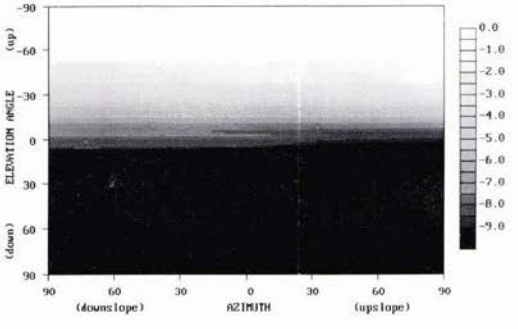

Fig 8 *Numerical noise directionality (dB) for surface duct with uniform sources at 4kHz*

2.2.2 Receiver depth dependence

In an upward or downward refracting duct there is a transition from surface/bottom reflected to waterborne paths some way up the slope depending on final arrival angle and receiver depth. This may have a noticeable effect on the noise directionality.

In a downward refracting duct there would be a 'noise notch' (an angle range of low noise) if the bottom were flat. The slope fills this on the upslope side, and the width of the notch on the downslope side depends on the receiver depth since it affects the velocity contrast for the limiting ray. The right hand side of Fig 9 shows the filled noise notch at 250Hz for a receiver at mid-depth. Doubling the velocity contrast in the sound speed profile or deepening the receiver opens up the noise notch as in Fig 10. Fig 11 shows (by changing the plotting contrast) that the effect is still there at 1kHz and the bottom paths dominate these angles although the noise is weak compared with that for overhead.

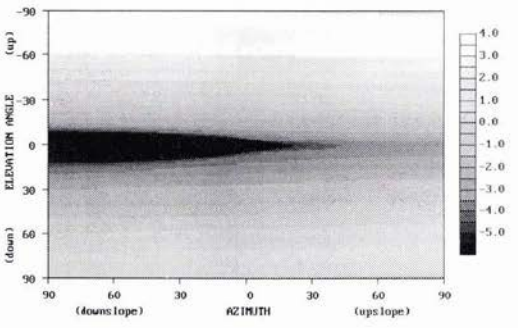

Fig 9 *Weak noise notch for mid-depth receiver at 250Hz for downward refraction with uniform sources*

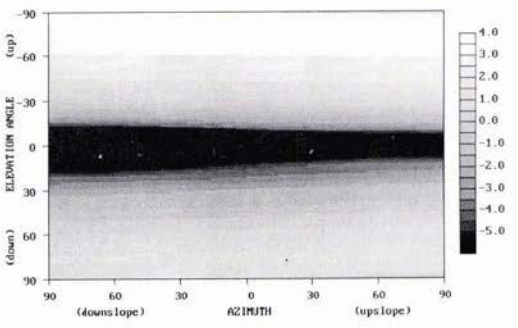

Fig 10 *Strong noise notch for mid-depth receiver at 250Hz for downward refraction with uniform sources*

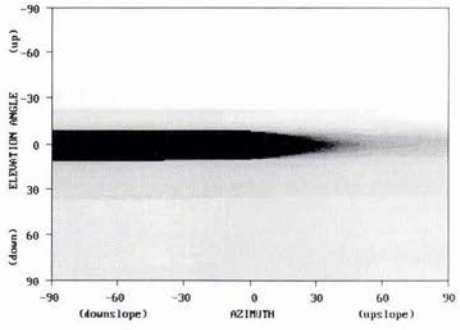

Fig 11 *Strong noise notch for mid-depth receiver at 1kHz for downward refraction with uniform sources (highlighting the lower contour levels)*

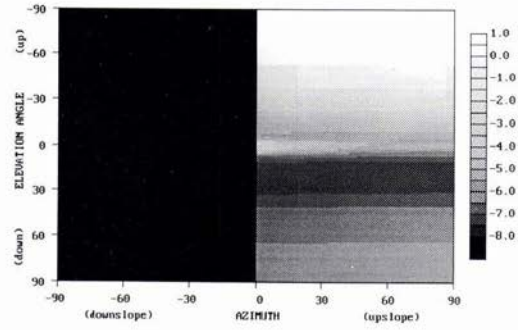

Fig 12 Numerical noise directionality (dB) for surface duct at 1kHz with a swathe of sources; δ=1

2.2.3 Dependence on source distribution

If we are considering wind noise then a uniform distribution seems a reasonable assumption. On the other hand wave noise sources could be assumed to be overhead or to be distributed along a distant beach. We now make the assumption that sources extend in a swathe parallel to the shore out to a fraction δ of the distance from the shore to the receiver. Note that once there are no noise sources (of this type) overhead multipaths to distant sources definitely could be important even at high frequencies because there are no other paths.

Figs 12-14 show the noise directionality at 1kHz for δ=1/3, 2/3, 1 for the upward refracting case. The most obvious effect is that as the swathe becomes narrower the angle range of the noise becomes more and more confined to a narrow range near the horizontal although the transition happens quite near δ=1. Once the swathe edge reaches the receiver position the directionality is close to that of a uniform distribution (see Fig 7) although of course, there is only noise from azimuths between upslope and across slope. Interestingly there is little azimuth dependence in Figs 13 and 14.

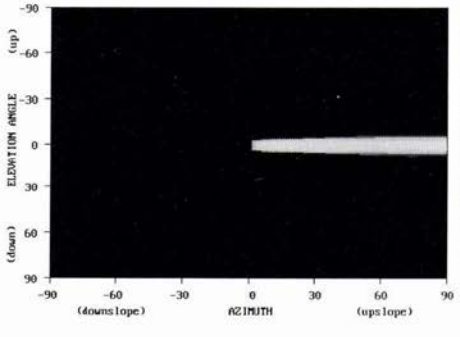

Fig 13 *Numerical noise directionality (dB) for surface duct at 1kHz with a swathe of sources; δ=2/3*

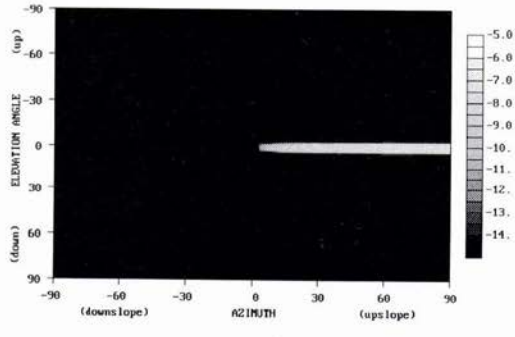

Fig 14 *Numerical noise directionality (dB) for surface duct at 1kHz with a swathe of sources; δ=1/3*

3. Conclusions

By treating surface noise sources as an extended sheet it is possible to derive closed form analytical and numerical results for various conditions in range-dependent environments. Full derivations of the analytical cases are given in [6], and examples are shown here in Figs 1 and 2.

Noise directionality was investigated numerically as a function of frequency, receiver depth and source swathe width for swathes parallel to the coastline. Naturally as frequency rises boundary losses become higher, and multipaths become less significant. If there is a maximum in the sound speed profile above the receiver and with a higher sound speed there will be a vertical noise notch in the downslope direction. Upslope the same angle range will be filled, even at high frequencies, with multipath arrivals. Similarly, if the noise sources only exist near the coastline then even at high frequencies there are significant multipaths, and angles are confined to those near the horizontal.

Acknowledgement

This work was supported by BAeSEMA Ltd. I thank Mr G Horsley and Mrs S Smithers for their assistance with the figures and typing. Related work on the general purpose noise model CANARY and its development have been funded by the UK Defence Research Agency.

References

[1] G B Deane, "Acoustic measurements of breaking waves in the surf zone", in *Proceedings of the Third International Conference on Underwater Acoustics,* ed J S Papadakis, Crete University Press, Crete 1996.

[2] D M Farmer and S Vagle, "Waveguide propagation of ambient sound in the ocean-surface bubble layer", *J Acoust Soc Am,* vol 86, pp 1897-1908, 1989.

[3] B F Cron and C H Sherman, "Spatial correlation functions for various noise models". *J Acoust Soc. Am,* vol 34, pp 1732-1736, 1962.

[4] W M Carey and R A Wagstaff, "Low frequency noise fields", *J Acoust Soc Am,* vol 80, pp 1523-1526, 1986.

[5] C H Harrison, "Formulas for ambient noise level and coherence", *J Acoust Soc Am,* vol 99, pp 2055-2066, 1996.

[6] C H Harrison, "A simple model of noise directionality for range-dependent environments", *J Acoust Soc Am,* in press.

[7] C H Harrison, "Noise directionality in the surf zone: a model", in Proceedings of Sea Surface Sound '97, Southampton, 1997.

[8] D E Weston, "Guided propagation in a slowly varying medium", *Proc Phys Soc, vol* 73, pp 365-384, 1959.

[9] C H Harrison and A Cowley, "CANARY: A model of ambient noise and coherence", in *Proceedings of the Third International Conference on Underwater Acoustics,* ed J S Papadakis, Crete University Press, Crete 1996.

[10] C H Harrison, "CANARY: A simple model of ambient noise and coherence", in *Applied Acoustics,* in press.

[11] C H Harrison, "Tests of range-dependent algorithms in CANARY V6 (CANARD)", BAeSEMA Report CR1007/3/TR-2, January 1997.

[12] W H Thorp, "Analytic description of the low frequency attenuation coefficient", *J Acoust Soc Am,* vol 42, pp 270-271, 1967.

[13] H W Marsh, M Schulkin and S G Kneale, "Scattering of underwater sound by the sea surface", *J Acoust Soc Am,* vol 33, pp 334-340, 1961.

[14] R J Urick, Principles of Underwater Sound, McGraw-Hill, 1983.

High Frequency Matched Field Processing

W.S. Hodgkiss, W.A. Kuperman, J.J. Murray, G.L. D'Spain, and L.P. Berger

Marine Physical Laboratory
Scripps Institution of Oceanography
La Jolla, CA 92093-0701

Abstract

Results are discussed from a high frequency (0.9-5.7 kHz), very shallow water (<10 m) experiment exploring the feasibility of carrying out matched field processing in this frequency and water depth regime. The data was received on a 22-element vertical array with interelement spacing one half-wavelength at 4 kHz. An acoustic source broadcasting a multitone comb was towed along radial tracks with maximum range from the array of several hundred meters. One incoming track was selected for analysis using conventional (nonadaptive) matched field processing. The structure of the range-depth ambiguity surface (incoherently averaged across frequency) is shown as well as the time-evolving range surface (for a fixed source depth). In addition, time series of the range and depth maxima are shown along with their corresponding correlation values. Although a very simple range-independent environmental model was used to generate the matched field replica vectors, the results clearly demonstrate the ability to track the motion of the source and resolve its position to on the order of 0.5 m in depth and 10 m in range.

1. Introduction

As a generalization of conventional (plane wave) beamforming, matched field processing (MFP) measures the similarity between the data observed on an array of sensors and the complex wave field predicted by a full-wave propagation model for a source at a given range, depth, and azimuth [1-2]. MFP has received a great deal of attention recently and impressive broadband detection, localization, and tracking results have been obtained in shallow water (< 200 m) at low-to-mid frequencies (< 600 Hz) [3-4].

Here we discuss the results from a high frequency (0.9-5.7 kHz), very shallow water (<10 m) experiment exploring the feasibility of carrying out matched field processing in this frequency regime. Section 2 will describe the experiment, array geometry, and the bathymetry observed along the source tow track. The results from performing conventional (nonadaptive) matched field processing on the data then are presented in Section 3. Lastly, a summary is provided in Section 4.

2. Experiment Description

The experiment was conducted on 15 October 1996 in San Diego Bay in the vicinity of the Scripps Marine Facilities pier. A chart of the area prepared a few months prior to the experiment indicates that the bathymetry generally is flat in the area north of the pier where two of the three source tow events were conducted.

Figure 1 shows the experiment geometry and a sound speed profile derived from CTD data collected immediately after the source tow event analyzed in Section 3. The vertical array consisted of 22 elements positioned as shown in the upper part of the water column. The array was deployed from the pier with a heavy weight on the bottom keeping it straight. The uppermost array element was 0.67 m below the surface and the interelement spacing was 0.188 m (approximately one half-wavelength at 4 kHz). The time series from each array element was sampled at 48 kHz.

Source tows were carried out with a small boat equiped with differential GPS for accurate positioning. Bathymetry was measured during the source tows with a high frequency echo sounder. Figure 1 also shows the bathymetry measured over the north-to-south source tow track for the data discussed in Section 3. Over the range interval 150-175 m, the track cuts across a small trench with ridges on both sides. This broad east-west feature is evident on the chart of the area north of the pier.

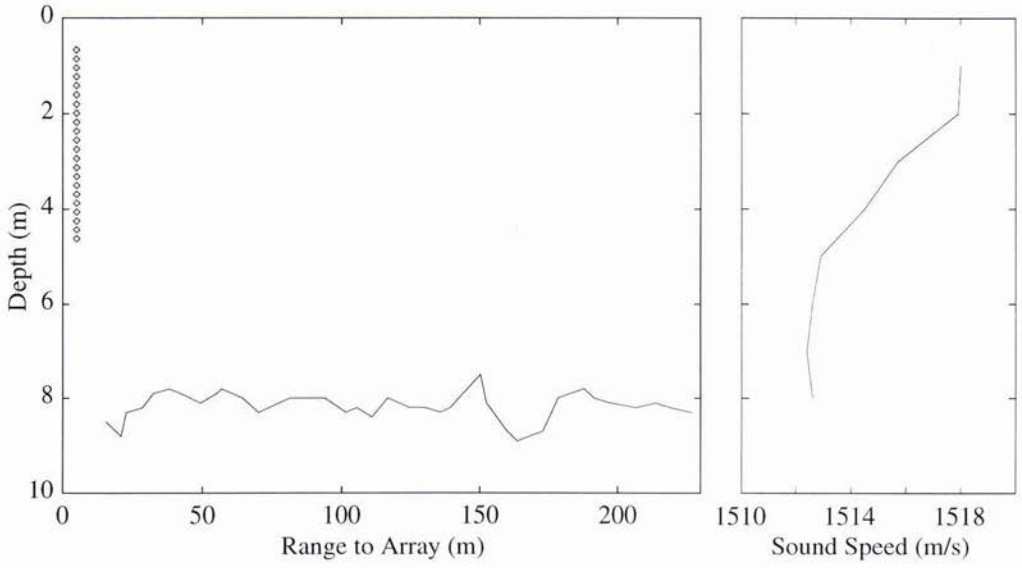

Figure 1. Experiment geometry and sound speed profile. The 22 element vertical array was located in the upper part of the water column. A small trench with slight ridges on both sides was present in the range interval 150-175 m.

During the source tow events, a J-11 was deployed to a depth of approximately 3.8 m and transmitted CW tonals at 0.9, 1.3, 2.4, 3.5, 4.6, and 5.7 kHz.

3. Data Analysis

We selected for analysis the last 3.0 minutes of data from a north-to-south source tow track. The bathymetry for this track is shown in Figure 1. The range of the source to the array was approximately 225 m at the beginning of the track and approximately 15 m at the end of the track.

For simplicity, a range independent environmental model was used to compute replica vectors. The sound speed profile is shown in Figure 1. Due to lack of detailed geoacoustic information on the bottom, representative parameters for a sand-silt-clay half-space were used [5] (compressional sound speed: 1550 m/s, compressional attenuation: 0.35 db/m/kHz, and density: 1.5 g/cm^3). Matched field replica vectors were calculated using the Kraken normal mode code [6]. Since only two modes were predicted to be excited at 0.9 kHz and three modes at 1.3 kHz, these lowest two frequencies of the source tow data were not included in the processed results.

Preprocessing of the array data consisted of computing 50% overlapped, 8192-point (Kaiser-Bessel windowed) FFT's of the hydrophone time series and extracting the (5.86 Hz wide) bins containing the source tow frequencies. At each frequency f_i, a data vector was formed at time t_j from the appropriate complex bin value from each element of the array $\mathbf{X}(f_i,t_j)$. Estimates of the array element covariance matrix were generated by averaging the outer products of successive data vectors:

$$\mathbf{K}(f_i,t) = \frac{1}{N_t} \sum_{j=1}^{N_t} \mathbf{X}(f_i,t_j)\mathbf{X}^H(f_i,t_j) \tag{1}$$

where $N_t = 5$ (0.43 s of data) and H indicates complex conjugate transpose.

Narrow-band, conventional matched field processing was implemented by computing the normalized quadratic form:

$$C(f_i,r,d,t) = \frac{g^H(f_i,r,d)\mathbf{K}(f_i,t)g(f_i,r,d)}{Tr(\mathbf{K}(fi,t))\ |g(f_i,r,d)|^2} \tag{2}$$

where $g(f_i,r,d)$ is the complex wave field (replica vector) predicted by the full-wave propagation model for a source at range r and depth d away from the array and $Tr(\mathbf{K}(f_i,t))$ is the trace of the covariance matrix $\mathbf{K}(f_i,t)$.

Then, the individual frequency matched field processing results were averaged incoherently across frequency:

$$C(r,d,t) = \frac{1}{N_f} \sum_{i=1}^{N_f} C(f_i,r,d,t) \tag{3}$$

As an example of (3), the range-depth ambiguity surface at t = 1.7 min is shown in Figure 2. Although ambiguous sidelobes are present, the source is localized easily at r = 90 m and d = 3.8 m with resolution on the order of 10 m in range and 0.5 m in depth.

In the processing, successive ambiguity surfaces as in Figure 2 are computed. Since the source depth was known to be approximately constant during the source tow, one useful way to visualize the time-evolving structure of the matched field processor output is to display a slice of each ambiguity surface at a given depth. Figure 3 shows the time-evolving range surface for d = 3.8 m. The incoming track of the source clearly is visible.

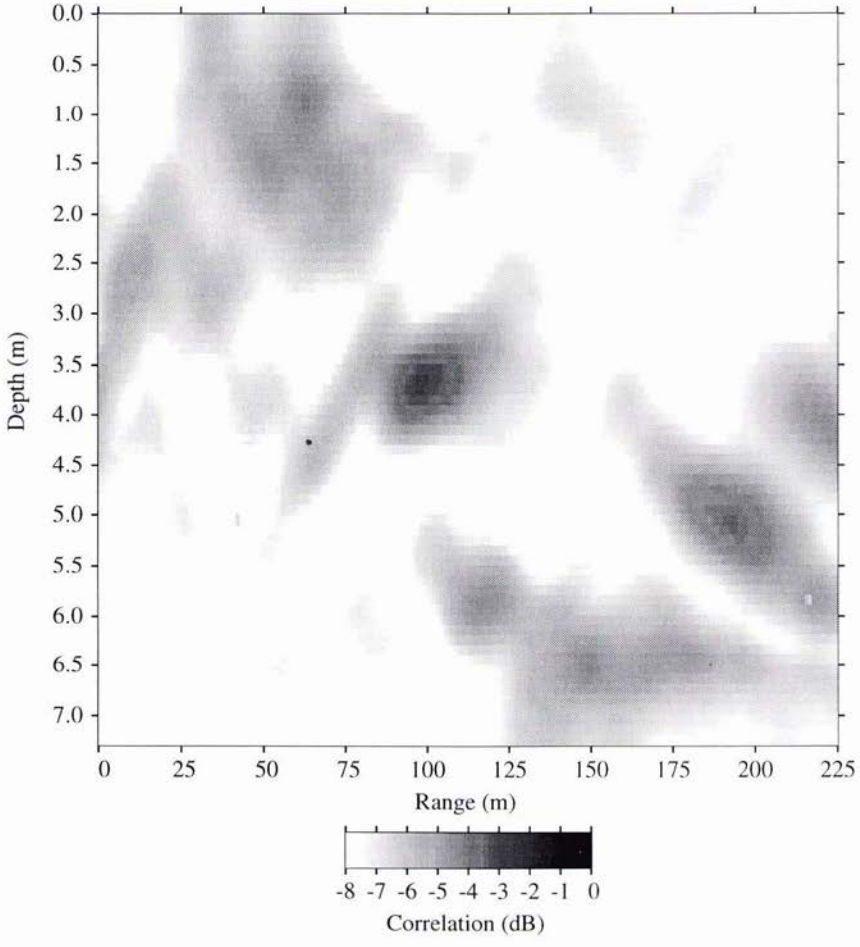

Figure 2. Range-depth ambiguity surface at t = 1.7 min averaged across the source tow tonals at 2.4, 3.5, 4.6, and 5.7 kHz. The source is localized at r = 90 m and d = 3.8 m.

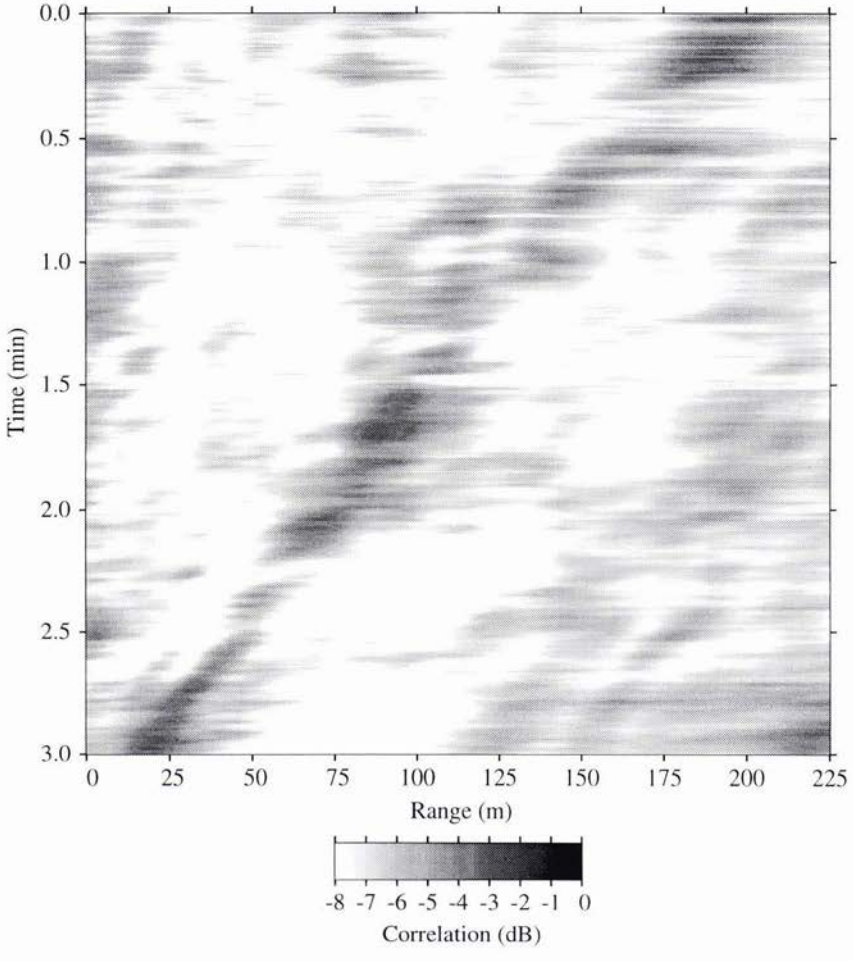

Figure 3. Time-evolving range range surface for d = 3.8 m averaged across the source tow tonals at 2.4, 3.5, 4.6, and 5.7 kHz. The source is closing on the array as time increases.

The time series of range-depth maxima of the successive ambiguity surfaces provides additional information on how well the matched field processor is able to track the source. Figure 4 displays the peak ranges as the source closes on the array along with the true range (based on DGPS measurements of source and array position). Similarly, Figure 5 displays the peak depths along with the bathymetry under the souce as measured by the echo sounder. Although the source track can be discerned in both figures, a substantial number of ambiguous peaks are seen when the source is in the vicinity of the trench (0.4-1.2 min). This is not surprising considering the simple, range-independent environmental model used for computing the matched field replica vectors.

Lastly, the time series of correlation values for the range-depth maxima of the successive ambiguity surfaces is shown in Figure 6. During the last half of the track where the range-independent environmental model is reasonably accurate, the correlation values generally are between -3 and -4 dB. At the high signal-to-noise ratios present in these data, a perfect match between the observed data and predicted replica field would yield a correlation value of 0 dB.

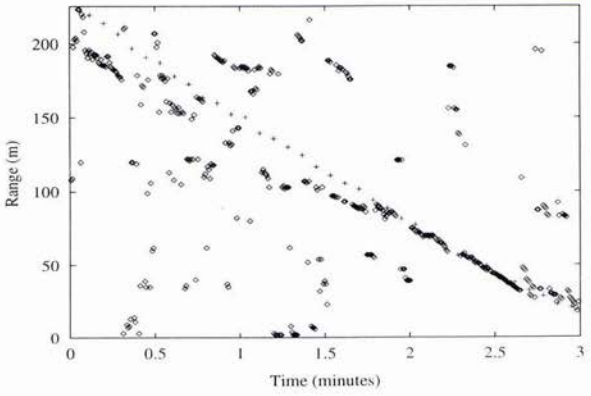

Figure 4. Time series of peak ranges from the individual range-depth ambiguity surfaces. The true source-array range is indicated by +'s.

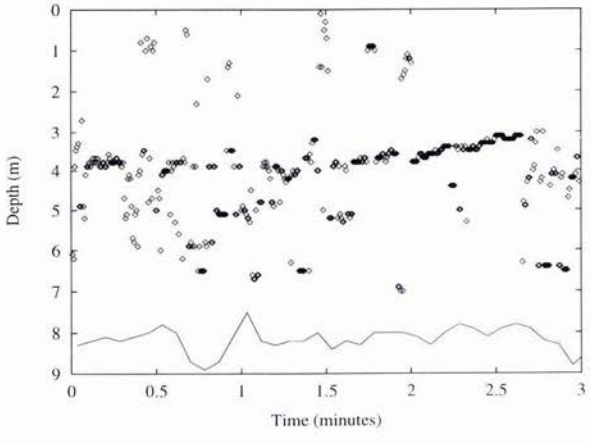

Figure 5. Time series of peak depths from the individual range-depth ambiguity surfaces. The bathymetry under the source also is displayed.

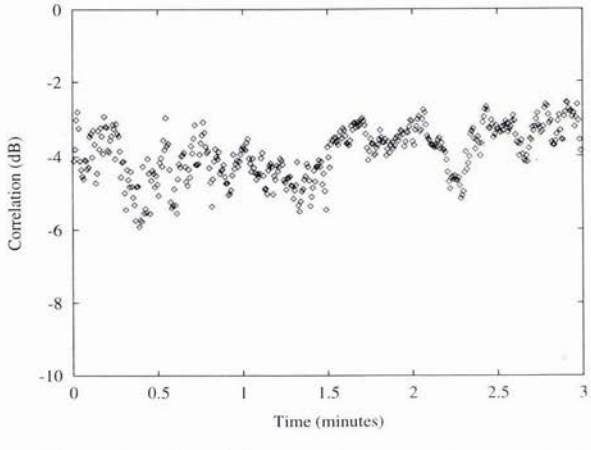

Figure 6. Time series of correlation values for the range-depth maxima from the individual range-depth ambiguity surfaces.

4. Summary

The focus of this paper has been on exploring the feasibility of carrying out broadband matched field processing on high frequency (0.9-5.7 kHz) source tow data in very shallow water (<10 m). A 4.0 m aperture, 22-element vertical array received multitone transmissions from a source towed at approximately 3.8 m depth and ranges of up to several hundred meters. Conventional (nonadaptive) matched field processing was performed on the data from an incoming track where the source range decreased from 225 m to 15 m over 3.0 min. The structure of the range-depth ambiguity surface (incoherently averaged across frequency) was shown as well as the time-evolving range surface (for a fixed source depth of 3.8 m). Time series of the range and depth maxima also were shown along with their corresponding correlation values. Although a very simple range-independent environmental model was used to generate the matched field replica vectors, the results clearly demonstrate the ability to track the motion of the source and resolve its position to on the order of 0.5 m in depth and 10 m in range.

Acknowledgements

This work was sponsored by the Office of Naval Research, Code 321OA.

References

[1] A.B. Baggeroer, W.A. Kuperman, and P.N. Mikhalevsky, "An overview of matched field methods in ocean acoustics," *IEEE J. Oceanic Engr.* vol. 18(4), pp. 401-424 , 1993.

[2] F.B. Jensen, W.A. Kuperman, M.B. Porter, and H. Schmidt. *Computational Ocean Acoustics*. NY: American Institute of Physics , 1994.

[3] N.O. Booth et. al., "Source localization with broadband matched field processing in shallow water," *IEEE J. Oceanic Engr.* vol. 21(4), pp. 402-412, 1996.

[4] Z. Michalopoulou and M.B. Porter, "Matched-field processing for broad-band source localization," *IEEE J. Oceanic Engr.* vol. 21(4), pp. 384-392, 1996.

[5] E.L. Hamilton, "Geoacoustic modeling of the sea floor," *J. Acoust. Soc. Am.* vol. 68(5), pp. 1313-1340, 1980.

[6] M.A. Porter, "The KRAKEN normal mode program," SACLANTCEN SM-254, SACLANT Undersea Research Centre, La Spezia, Italy, 1991.

Source and Receiver Responses in Boreholes

Jens M. Hovem and Oddvar Lotsberg

Norwegian University of Science and Technology
Department of Telecommunications / Acoustics group
O. S. Bragstads plass 2
N-7034 Trondheim, NORWAY
Email: hovem@tele.ntnu.no

Abstract

This report considers the acoustic interaction between the acoustic field in a borehole and the elastic field in the surrounding formation. The problem with acoustic-seismic radiation of energy from a source in a fluid filled borehole with a drillstring surrounded by an elastic formation of infinite extent is first considered. The exact solution is established and simplified expressions are derived for the low frequency case. The source produces a compressional field and a shear wave field. The compressional field has a maximum value at the direction perpendicular to the axis of the borehole, the shear field will in most cases has a maximum approximately at an angle of 45°. *However, in special cases the radiation out into the formation may be completely dominated by shear radiation in a very narrow angle. Secondly, the response of a sensor in the borehole due to an incoming plane wave is considered and the complete solution valid for all frequencies is determined. Numerical examples shows that the receiving response can be very complicated and composed of several modes and each of them may have strong resonances.*

1. Introduction

In many instances borehole measurements are used to determine in situ values for the geo-acoustic properties of marine sediments, either cross-hole measurements or in-hole measurements. Correct interpretation of such results requires an understanding of how acoustic energy in a fluid filled borehole is coupled to the field in the formation in reception and transmission, both in time and frequency domain. This is particularly important with so high frequencies that wavelengths approximately equal the diameter of the hole.

This paper presents theory and examples of transmitting and receiving responses in boreholes. First, we study the field set up in the formation due to a cylindrical source in the borehole. Secondly, we consider the response of a sensor in the borehole due to a plane wave arriving at an arbitrary angle in the formation.

This study is based on previous works reported in the literature. The axisymmetric radiation from a cylindrical source in a homogenous elastic formation has been treated by Heelan [1], Abo-Zena [2], Lee and Balch [3] and Winbow [4]. Lee [5] extended to non axisymmetric excitation. The receiver problem has been thoroughly investigated by Schoenberg [6] and his formulations were later used by Peng et al.[7] to study borehole effects on downhole seismic measurements as function of frequency, angle of incidence and polarization. Borehole coupling and resonances were discussed by Lowell and Hornby [8] in the axisymmetric case with a sensor on the axis of the borehole. We extend the theory to include a hard drillstring in the borehole and nonaxisymmetric sensor locations and we focus the attention to so high frequencies that borehole resonances may play important roles.

2. Mathematical modeling

Consider a cylindrical borehole with a coaxial drillstring with radius respectively a and b, Figure 1. The surrounding formation is assumed to be elastic and homogenous with P-wave and S-wave velocities v_p and v_s and density ρ. Between the drillstring and the formation there is a fluid with sound velocity v_f and density ρ_f. On the drillstring there is mounted a cylindrical source with same radius as the drillstring and with length L. For simplicity we shall in the following assume that the length L is short compared with the wavelength so that transmitter directivity can be neglected.

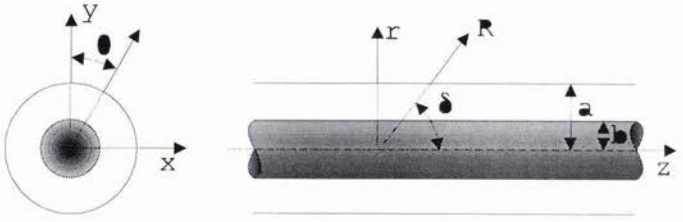

Figure1. Model.

2.1 Transmitter

The radiated waves in the formation are described by a scalar potential for the compressional wave and a vector potential for the shear wave. In this axisymmetric problem the vector potential has only one component and therefore the fields can be described by two scalar functions ϕ and ψ. In cylindrical coordinates the solution to the wave equations for the radiated waves in the formation are

$$\begin{aligned} \phi &= AH_0^{(2)}(\gamma_p r)\exp(i\omega t - ikz) \\ \psi &= BH_1^{(2)}(\gamma_s r)\exp(i\omega t - ikz) \end{aligned} \tag{1}$$

Without the presence of a source the field in the fluid is

$$\phi = \left[A_0 J_0(\gamma_f r) + B_0 N_0(\gamma_f r)\right]\exp(i\omega t - ikz) \tag{2}$$

$H_0^{(2)}(\cdot)$ and $H_1^{(2)}(\cdot)$ are Hankel functions of the second kind, order zero and one, representing outgoing radiated P- and S-waves. $J_\alpha(\cdot)$ and $N_\alpha(\cdot)$ are the Bessel and Neumann functions. The axial wavenumber is k and the radial wavenumbers are γ_p and γ_s, for P and S-waves in the formation, the radial wavenumber in the fluid annulus is γ_f. The time dependency $\exp(i\omega t)$ will hereafter be assumed and omitted.

$$\begin{aligned} \gamma_p^2 &= (\omega/v_p)^2 - k^2 \\ \gamma_s^2 &= (\omega/v_s)^2 - k^2 \\ \gamma_f^2 &= (\omega/v_f)^2 - k^2 \end{aligned} \tag{3}$$

The source function has the form

$$\phi_0 = Q\frac{1}{L}H_0^{(2)}(\gamma_f r) \tag{4}$$

Q is a measure of the source strength and related to the volume displacement of the source V (m^3) by

$$Q = -\frac{V}{2\pi\gamma_f b}\frac{1}{H_1^{(2)}(\gamma_f b)} \tag{5}$$

In the equations above A, B, A_0 and B_0 are unknown coefficients and functions of wavenumber and frequency to be determined by the boundary conditions. These require continuity of normal stress and displacement on the surface of the drillstring and at the borehole wall. We shall assume that the drillstring is infinitely hard so that the displacement at the surface of the drillstring is zero. Having found the coefficients the wave fields are determined by integration over axial wave numbers k.

The pressure in the borehole fluid is

$$p_0(\omega,r,z) = -\frac{\omega^2\rho_f}{2\pi}\int_{-\infty}^{\infty}\left[A_0(\omega,k)J_0(\gamma_f r) + B_0(\omega,k)N_0(\gamma_f r)\right]\exp(-ikz)dk \tag{6}$$

The radial and tangential displacements in the formation are

$$u_r(\omega,r,z)=\frac{1}{2\pi}\int_{-\infty}^{\infty}\left[-\gamma_p A(\omega,k)H_1^{(2)}(\gamma_p r)+ikB(\omega,k)H_1^{(2)}(\gamma_s r)\right]\exp(-ikz)dk \tag{7}$$

$$u_z(\omega,r,z)=\frac{1}{2\pi}\int_{-\infty}^{\infty}\left[-ikAH_0^{(2)}(\gamma_p r)+\gamma_s BH_0^{(2)}(\gamma_s r)\right]\exp(-ikz)dk \tag{8}$$

The expressions above are valid for all frequencies and used for numerical calculation. For low frequencies one can develop approximate results that are more suited to give insight in the physical processes. The low frequency results are valid as long as the first resonance frequency of the fundamental mode is higher and outside the band of excitation of the transmitting element. This will be discussed more later. To arrive at the low frequency approximation it is first assumed that only the farfield solution is of interest and therefore the Hankel functions in (6), (7) and (8) are replaced with their asymptotic values for large arguments [9]. Furthermore, the integrals are approximated with their stationary phase value [10]. New components of the displacements are introduced by

$$\begin{aligned} u_R &= u_r\sin\delta+u_z\cos\delta \\ u_\delta &= u_r\cos\delta-u_z\sin\delta \end{aligned} \tag{9}$$

and the Hankel functions are replaced with their low frequency approximations. The end result of this is that the transmitted field in the formation is decomposed into two parts. A compressional field with a particle displacement in the direction of propagation of

$$u_R=\frac{V}{4\pi R}\frac{i\omega}{v_p}\frac{\rho_0}{\rho_1}\left(\frac{a^2}{a^2-b^2}\right)\frac{v_T^2}{v_s^2}\frac{1-2\frac{v_s^2}{v_p^2}\cos^2\delta}{1-\frac{v_T^2}{v_p^2}\cos^2\delta}\exp(-i\frac{\omega}{v_p}R) \tag{10}$$

and a shear wave with particle displacement normal to the direction of propagation

$$u_\delta=\frac{V}{4\pi R}\frac{i\omega}{v_s}\frac{\rho_0}{\rho_1}\left(\frac{a^2}{a^2-b^2}\right)\frac{v_T^2}{v_s^2}\frac{2\sin\delta\cos\delta}{1-\frac{v_T^2}{v_s^2}\cos^2\delta}\exp(-i\frac{\omega}{v_s}R) \tag{11}$$

R is the distance from the center of the source to the field point (Figure 1).

The pressure in the borehole is by the same approximation

$$p_0(\omega,z)=\frac{i\omega V}{2\pi(a^2-b^2)}\rho_0 v_T\exp(-i\frac{\omega}{v_T}z) \tag{12}$$

This is the so called tube wave propagating in the cylindrical annulus between the drillstring and the formation. The low frequency approximation to tube wave velocity, which also appears in (10) and (11), is

$$v_T=\frac{v_0}{\left(1+\frac{a^2}{a^2-b^2}\frac{\rho_0}{\rho}\frac{v_0^2}{v_s^2}\right)^{1/2}} \tag{13}$$

Normally the tube wave velocity is lower than the shear and compressional wave velocities in the formation and the tube wave sets up an evanescent field in the formation which is not included in (10) and (11).

2.2 Receiver

We will determine the response of a sensor at the surface of the drillstring due to an incoming plane P-wave or SV-wave (vertically polarized shear wave). The calculation of the receiver response is almost the same for the two cases, we outline the derivation for an incoming plane P-wave. The transmitting problem we studied previously is an axisymmetric problem but the receiving problem is not, because of the incoming plane wave and the assumption that the receiving sensor may be in an non-axial position and located on the surface of the drillstring. We consider an incoming plane P-wave with velocity amplitude U, frequency ω, incident angle δ, and azimuth angle θ (Figure 1). The plane incoming wave is expressed as a sum of cylindrical waves [9]

$$\phi_p = -i\frac{v_p U}{\omega}\exp\left(i\gamma_p r\cos\theta\right)\exp(i\omega t - ikz) = \\ -i\frac{v_p U}{\omega}\left[J_0\left(\gamma_p r\right) + 2\sum_{m=1}^{\infty} i^m J_m\left(\gamma_p r\right)\cos m\theta\right]\exp(-ikz) \tag{14}$$

The incoming wave sets up a field in the borehole

$$\phi_f = \left[A_0 J_0(\gamma_f r) + a_0 N_0(\gamma_f r) + 2\sum_{m=1}^{\infty} i^m\left[A_m J_m(\gamma_f r)\cos m\theta + a_m N_m(\gamma_f r)\cos m\theta\right]\right]\exp(-ikz) \tag{15}$$

and two scattered waves in the formation, one SV-wave expressed as

$$\varsigma = \left[B_0 H_0^{(2)}\left(\gamma_S r\right) + 2\sum_{m=1}^{\infty} i^m B_m H_m^{(2)}\left(\gamma_S r\right)\cos m\theta\right]\exp(-ikz) \tag{16}$$

and a scattered P-wave

$$\phi = \left[D_0 H_0^{(2)}(\gamma_p r) + 2\sum_{m=1}^{\infty} i^m D_m H_m^{(2)}(\gamma_p r)\cos m\theta\right]\exp(-ikz) \tag{17}$$

In the expressions above ϕ, ϕ_p and ξ are scalar displacement potentials. There are now four unknown coefficients, A_m, a_m, B_m, and D_m that are determined by the same boundary conditions as before and, in addition, the tangential stress is zero at the borehole wall.

The pressure in the borehole is $p_0 = \rho_f \omega^2 \phi_f$ and examples of numerical solutions for the pressure in the borehole will be presented later. In the same way as for the transmitter problem one can derive simple expressions for the receiver response in the low frequency case. Each mode must be treated separately, for the fundamental mode m=0 the low frequency approximation of the pressure on a sensor at r=b for an incoming P-wave in the formation with a displacement amplitude U_p is

$$p_0 = i\omega U_p(\rho_0 v_p)\frac{a^2}{a^2 - b^2}\frac{v_T^2}{v_s^2}\frac{1 - 2\dfrac{v_s^2}{v_p^2}\cos^2\delta}{1 - \dfrac{v_T^2}{v_p^2}\cos^2\delta} \tag{18}$$

With an incoming plane SV- wave with displacement amplitude U_s the pressure will be

$$p_0 = -i\omega U_s(\rho_0 v_s)\frac{a^2}{a^2 - b^2}\frac{v_T^2}{v_s^2}\frac{2\sin\delta\cos\delta}{1 - \dfrac{v_T^2}{v_s^2}\cos^2\delta} \tag{19}$$

The solutions (18) and (19) are the reciprocal solutions to the transmitting responses of (10) and (11).

3. Numerical results

In this section we will presents numerical results of transmitting and receiving responses in boreholes. The parameters of the examples are given in Table 1.

Parameter	Formation 1	Formation 2
P-wave velocity	3500 m/s	5000 m/s
S-wave velocity	2000 m/s	1000 m/s
Density of formation	2500 kg/m^3	2500 kg/m^3
Fluid velocity	1500 m/s	1500 m/s
Fluid density	1300 kg/m^3	1000 kg/m^3
Borehole radius	0.11 m	0.115 m
Drillstring radius	0.08 m	0.05 m

Table 1. Parameters for the numerical examples

3.1 Transmitting response

Figure 2 shows the transmitted field in a Formation 1 of Table 1 which may be typical for a rather hard and fast formation. Figure 2a shows the directivity patterns for the compressional and the shear components of the particle displacements. The compressional displacement has a maximum perpendicular to the borehole axis, the shear component has a maximum at approximately 45° in this case. The directivity patterns are normalized so that the maximum compressional displacement is set equal to unity, the figure therefore shows that maximum amplitude of the shear displacement may be larger than the maximum amplitude of the compressional displacement. Figure 2b shows an illustration of the evolving radiated field in time and space. The scales are in meters and the field is shown out to a distance of 12 meters from the source. The transmitted signal is a short Ricker pulse and the figure shows a snapshot of the field at a time $T = 3\,ms$ after the transmission. The two components traveling with the compressional and shear speeds respectively are clearly seen.

The direction for maximum shear displacement is given by the value of tube wave velocity of (13). When this velocity is much higher than the shear velocity of the surrounding formation the direction of maximum shear displacement will be close to 45°, as can be seen from (11). In most situations this will be the case and Figure 2 is representative for the normal case with a tube wave velocity of $v_T = 1078\,\mathrm{m/s}$, much smaller than the shear wave velocity of $v_s = 2000\,\mathrm{m/s}$. However, there are cases where (13) gives a value for the tube wave velocity that exceeds the shear wave velocity in the formation. Physically this means that there no longer exist a guided tube wave in the borehole since the tube wave is radiating out in the formation mainly in the direction given by

$$\delta_{max} = \arccos\left(\frac{v_s}{v_T}\right) \tag{20}$$

An example of this is shown in Figure 3 for the parameters of Formation 2 in Table 1. The radiation is totally dominated by shear radiation at a very narrow angle given by (18), in this case $v_T = 1033\,\mathrm{m/s}$, $v_s = 1000\,\mathrm{m/s}$ and $\delta_{max} = 14.5°$. On the scale used in Figure 3b the compressional field would not have been visible.

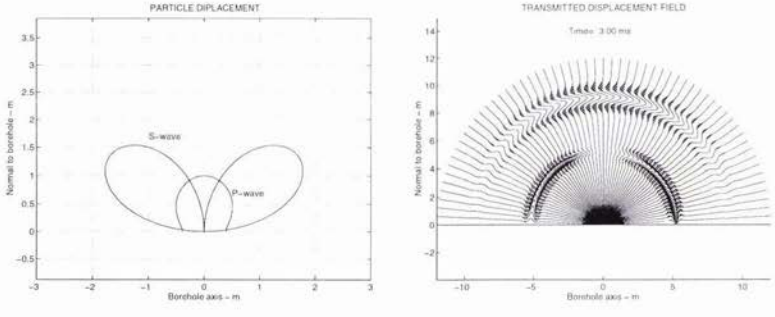

Figure 2 Transmitting response in Formation 1

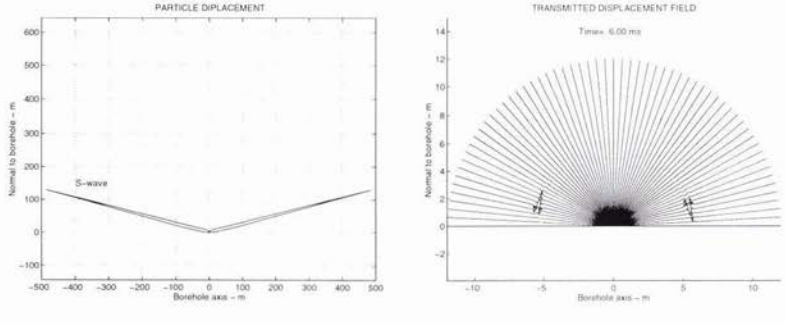

Figure 3 Transmitting responses in Formation 2

3.2 Receiving response

A computer code has been developed that can compute the full waveform field in the borehole by (15), both in time and frequency domain for any type of incoming plane wave. Figure 4 shows an example of the output from this program. The incoming P-wave has the form of a Ricker wavelet and the incidence angle is $\delta = \pi / 2$. The time signal of the incoming wave is shown in the upper right panel and its frequency spectrum is shown in lower right panel. The time response of a sensor located on the drillstring at $r = b$ and $\theta = 0$ is shown in the upper left panel and the frequency response for the borehole signal is shown in the lower left panel. The received signal is quite complicated and spread out in time, the frequency spectra indicates a number of sharp resonances.

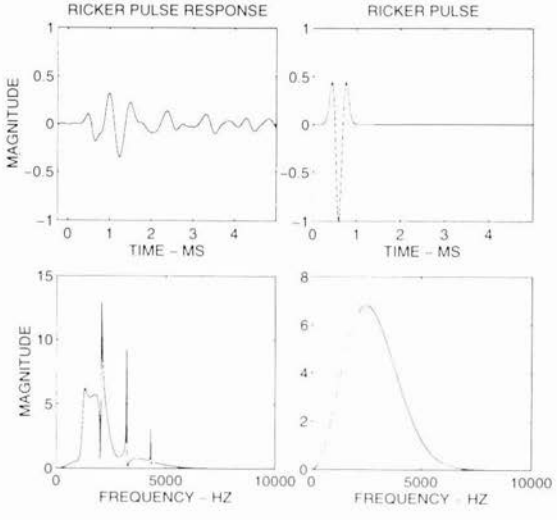

Figure 4. The response of a sensor on the drillstring caused by an incoming plane P-wave arriving from $\theta = 0$ and $\delta = \pi / 2$. Summation of modes $m = \{0, \cdots 5\}$

Equation 15 shows that the response of a sensor located at an angular position θ in respect to the direction of the incoming wave is given by a sum of mode functions $e_m(t)$ weighted by the cosine of the angular separation between the direction of the incoming wave and sensor position. Therefore the received time signal of a sensor can be expressed as

$$s(t) = \sum_{m=0}^{M-1} e_m(t) \cos(m\theta) \tag{21}$$

In principle the number of modes is infinite, in practice only a few modes are significant. The number of significant modes depends on the parameters of the formation, the size of the borehole, the drill string and the frequency spectrum. For realistic parameters, e.g. as given in Table 1, the number of significant modes may be quite small. This is illustrated in Figure 5, showing the time and frequency functions for the first 6 modes, $m = \{0, \cdots 5\}$ for the same example as in Figure 4. The sum of the traces of Figure 5a yields the received signal shown in the upper left panel of Figure 4. In this case only the first 3-4 modes are significant.

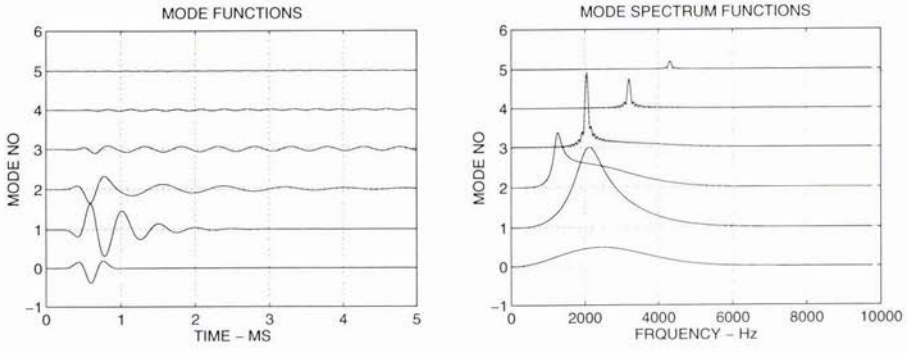

Fig. 5. Mode functions for modes $m = \{0, \cdots 5\}$ Parameter set no.2, Table 1

a) Time functions, b) Frequency spectra functions.

The received signal may have a number of resonances caused by waveguide modes in the fluid annulus between the drillstring and the formation. Borehole resonances were discussed by Lowell and Hornby [8], but only resonances in the received signal of a sensor at the center of a borehole without drillstring. In that case only the fundamental mode m=0 contributes. For a sensor positioned non-symmetrically in the borehole there will be a number of different vibrational modes, each with potentially many resonance frequencies. From Figure 5b it can be observed that the modes m= 5, 4 and 3 have sharp resonances at the approximate frequencies of 4.2 kHz, 3.2 kHz and 2.1 kHz respectively and mode m=2 has a weaker resonance at approximately 1.25 kHz. The resonances are caused by poles in the transfer function and are given by the zeroes of the determinant of the set of linear equations that determines the unknown coefficients. The expression for the determinant is quite complicated and requires numerical analysis. However, an understanding is obtained by considering the simpler case, where both the drillstring and the formation are infinitely hard. With this boundary condition, the radial displacements equal zero at radius $r = a$ and $r = b$. The characteristic equation for borehole modes can easily be obtained from (2) and attains the form

$$\begin{aligned}&\left[mJ_m(\gamma_f a) - \gamma_f a J_{m+1}(\gamma_f a)\right]\left[mN_m(\gamma_f b) - \gamma_f b N_{m+1}(\gamma_f b)\right] \\ &-\left[mN_m(\gamma_f a) - \gamma_f a N_{m+1}(\gamma_f a)\right]\left[mJ_m(\gamma_f b) - \gamma_f b J_{m+1}(\gamma_f b)\right] = 0\end{aligned} \tag{22}$$

Consider first the fundamental mode m=0. The first zero of (22) occurs when $\gamma_f a = 0$ and gives the mode normally referred to as the Stoneley mode or the tube wave mode. The second zero for m=0 is for $\gamma_f a = 11.6$ for the values of a, b and v_f of Formation 1 in Table 1. For normal incidence, $\delta = \pi / 2$, this mode gives a resonance frequency where the thickness of the annulus *(a-b)* is approximately equal to half the wave length in the fluid. This is normally a quite high frequency, in the current case the resonance frequency is 25.2 kHz, which is outside of the frequency range covered by the incoming wave. Therefore the approximate low frequency result derived for the transmission response is valid up to quite high frequencies. The fact that the mode m=0 is only slightly dispersive means that its waveform is nearly an exact replica of the incoming wave. The resonances of the higher modes may occur at rather low frequencies which is important for the shape of the receiving responses. For mode m=1 (22) predicts a resonance at 2.7 kHz which is difficult to recognize in Figure 5. However, in the low frequency approximation the time function of this mode is the negative time derivative of the time signal of mode m=0 (Schoenberg, [6]). The resonance frequencies are also dependent on the angle δ and the dependency is easily determined from (3). When $f_{res}(\delta = \pi / 2)$ is any resonance frequency for normal incident wave, this resonance will for any other incident angle move to the frequency

$$f_{res}(\delta) = \frac{f_{res}(\delta = \frac{\pi}{2})}{\sqrt{1 - \left(\frac{v_f}{v_p}\cos(\delta)\right)^2}} \tag{23}$$

It follows from (21) that the total response will be quite different depending on the angular position of the sensors with respect to the incoming wave. This fact is illustrated by the simulation in Figure 6 which shows the responses of 8 sensors located at equal spacing of 45° on the surface of the drillstring, the incoming plane P-wave arrives at angle of $\theta_{in} = -20°$ with respect to the position of sensor no. 0.

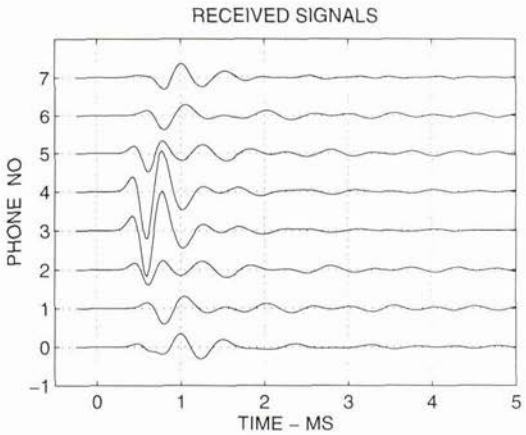

Fig. 6 Simulated received time signals on 8 equally spaced sensors.
Plane wave arriving with $\theta_{in} = -20^0$ and $\delta = 90^0$

4. Conclusions

The radiation and receiving responses for acoustic sources and receivers in fluid-filled boreholes have been studied theoretically and numerically.

Approximate expressions for the radiation from a cylindrical source have been derived. These are valid for frequencies lower than the first resonance frequency of the fundamental mode, which cover most frequencies of interest.

The receiver response of a non axially position sensor on the drillstring due to an incoming plane wave has been established and solved numerically. The results show that the high frequency response is very complicated and composed of many vibrational modes and that the higher modes may have strong resonances at relative low frequencies.

Acknowledgment

This work was sponsored by Statoil Research Center, in Trondheim, Norway. The collaboration and support by Erik Nakken and his POSLOG-team in Statoil is deeply appreciated.

References

[1] P. A. Heelan, "Radiation from a cylindrical source of finite length", *Geophysics*, vol. 47, pp.1308 -1314, 1953.

[2] A. M. Abo-Zena, "Radiation from a finite cylindrical explosive source", *Geophysics*, vol. 42, pp. 1384-1393, 1977

[3] M. W. Lee and A. H. Balch, "Theoretical seismic wave radiation from a fluid-filled borehole", *Geophysics*, vol. 18, pp. 685-696, 1982.

[4] G. A. Winbow, "Seismic source in open and cased boreholes", *Geophysics*, vol. 56, pp. 1040-1050, 1991.

[5] M. W. Lee, "Low frequency radiation from a point source in a fluid-filled borehole", *Geophysics*, vol. 51, pp. 1801-1807, 1986.

[6] M. Schoenberg, "Fluid and solid motion in the neighborhood of a fluid-filled borehole due to the passage of a low-frequency elastic plane wave", *Geophysics*, vol. 51, pp. 1191-1205, 1986.

[7] C. Peng, C. H. Cheng, and M. N. Toksös, "Borehole effects on downhole seismic measurements", *Geophysical Prospecting*, vol. 41, pp. 883-912, 1993.

[8] J. R Lovell, and B. E Hornby, "Borehole coupling at sonic frequencies", *Geophysics*, vol. 55, pp. 806-814, 1990.

[9] M. Abramowitz and I. A. Stegun, Handbook of Mathematical Functions, Dower Publications, Inc., 1965.

[10]A. Papoulis, Systems and transforms with applications in optics, McGraw-Hill Inc., 1968.

Areal Seabed Classification using Backscatter Angular Response at 95kHz

J.E. Hughes Clarke [1], B.W. Danforth [2] and P. Valentine [2]

(1): Ocean Mapping Group,
Geodesy and Geomatics Engineering,
University of New Brunswick,
P.O. Box 4400, Fredericton,
N.B., E3B 5A3, CANADA
jhc@omg.unb.ca

(2): Marine and Coastal Geology Program
U.S. Geological Survey,
384 Woods Hole Road,
Woods Hole,
MA 02543-1590, USA
bwd@boomer.er.usgs.gov, pv@nobska.er.usgs.gov

Abstract

A sediment classification scheme is developed based on the angular response (AR) of the seabed backscatter strength. The AR is characterised based on its mean level and slope over predefined angular sectors, and the presence or absence of abrupt changes in slope. Because the AR is derived from a finite area a test is performed to recognise the presence of sediment boundaries. The AR curves are shown to provide improved discrimination over angle invariant methods.

1. Introduction

Seabed backscattered intensity data is now routinely collected as part of regional swath bathymetry surveying. This data, if properly reduced, provides a measure of the seabed backscatter strength as a function of grazing angle (herein termed the angular response (AR)). For a given frequency, the seabed AR represents an inherent property of the seafloor. Traditional low-aspect ratio sidescan surveys, collect most of their useful data at grazing angles in the range 20 to 10 degrees and thus the variation with grazing angle is generally ignored. For a given narrow range of grazing angles, however, a number of quite different seabed types produce similar mean backscatter strengths. Two approaches have been taken to separate these ambiguities. The first is texture [1][2][3], which relies on recognising characteristics of the spatial variance in the backscattered signal. A second is to look at the same seabed through a range of grazing angles to extract the AR [4][5].

The first method has the advantage that the statistics are generally valid irrespective of absolute calibration of the signal level. In contrast, the second method relies on confidence in the absolute level. Recent developments in swath bathymetric surveying have resulted in increased confidence in the received backscatter intensity [6]. Bathymetric swath surveying relies generally on surface mounted systems with a much higher aspect ratio than towed sidescan and thus backscatter data can be easily extracted over a wider range of grazing angles. For the widest swath systems on the market today, grazing angles from vertical to as small as 15 degree or less are now possible allowing one to view the variation in backscatter strength as one (in some cases) passes through the critical angle.

2. Data Acquisition and Handling

2.1 Instrumentation

The sonar used was a Simrad EM1000 [7] multibeam sonar which transmits a 3.3 degree wide (fore-aft) beam over a 150 degree sector at 95 kHz. Sixty roll-stabilised beams are formed over the same angular sector for reception. Received backscattered intensities are compensated for source power, predicted radiation and receive sensitivities, pulse length, ensonified area, spherical spreading and attenuation [8]. The resulting data is first order estimate of the instantaneous backscatter strength. For shallow water operations, a 0.2ms pulse is used and the data is sampled at 5kHz. The sonar is mounted on the NSC Frederick G. Creed and is operated at speeds of about 16 knots. While a swath of 7.4 x the water depth is covered, due to refraction and motion compensation limitations [9] line spacing is normally limited to about 4.5-5.0 x the water depth.

2.2 Location

The dataset used in this study was collected by the Canadian Hydrographic Service on behalf of the United States Geological Survey (USGS). The survey was designed to cover the Stellwagen Bank U.S. National Marine Sanctuary (SBNMS) which extends for over 2,800 square kilometres in water depths ranging from 20 to 200m (Fig. 1). Approximately 80 days of EM1000 data was collected by the USGS over four distinct field survey periods.

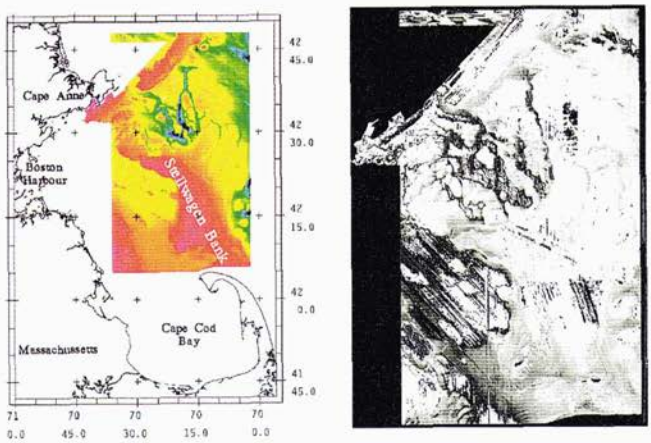

Figure 1:

Left:
Location map showing the relationship of the surveyed area to the region around Boston harbour and Cape Cod. The image is a depth map (blue = 200m, pink = 20m).

The region surveyed extends approximately 70 km N-S and 40 km E-W.

Right:
This is a "normalised" backscatter map for the entire region covered. The grayscale reflects normalised backscatter strength (see text for explanation). Black represents –37.5 dB and white represents –20 dB.

Stellwagen Bank is a shoal ridge extending northward from Cape Cod. It is separated from the cape by an 8 km wide channel herein termed Cape Race Channel. The Bank is exposed to winter storm events from the NE. The sediment on the bank top is known to be actively remobilised during such storm events [11]. The bank terminates abruptly to the west where the bathymetry drops off into the muddy Stellwagen Basin. Seaward of the bank, relict glacial terrains, including glacially scoured boulder and gravel pavements, are common [12]. The bank top and the ramp to seaward are covered with a range of sandy sediments, which are moulded into storm sand ripple fields interspersed with homogenous sand sheets. The Bank has been a rich fishing ground in the past and the modern surface continues to be actively remobilised by a dragger fleet [13]

2.3 Conventional Processing

For the purposes of standard geological mapping a "normalised" backscatter map is generated (Fig. 1). This is an attempt to produce a result comparable to a conventional sidescan mosaic derived from low-aspect ratio towed sidescan sonar (which had previously been the standard mapping instrument for the USGS [10]). Normalisation involves a first attempt at removing the mean variation in backscatter as a function of grazing angle. This is done assuming a lambertian response below 65 degrees grazing and an automatic gain control at higher grazing angles [8]. The aim is to produce a single dimension (normalised backscatter strength) to aid in regional seabed characterisation. This method is sufficient to unambiguously separate the -30 to -40 dB response of the muddy sediments in the basins from the -15 to -25 dB of the coarser sands and gravel from the bank tops (Fig. 1). Such a scheme however, fails when trying to distinguish the wide variety of sand and gravel sediment types that are present on the bank tops and margins. Such materials exhibit little variation in average backscatter strength, yet show obvious physical property differences in cores and bottom photos.

In attempting to distinguish the gravelly sand combinations it was noted that the "normalising" process often failed because the shape of the angular response curve was highly variable. This paper presents a new method, which relies on variations in the shape of the angular response curve as a means of separating lithologies that exhibit similar mean backscatter strengths..

3. Backscatter Data Reduction

3.1 Correcting Radiometric and Geometric Effects.

The EM1000 provides a measure of the instantaneous backscatter strength that has been reduced assuming predicted beam patterns, unrefracted ray paths and a flat seafloor [7][8]. All these assumptions are not strictly correct and additional steps thus have to be taken in order to derive accurate estimates of the true AR.

The EM1000 array has been specifically designed to exhibit uniform radiation and reception sensitivities over the 150 degree angular sector used. In practice, however, there are always +/-2dB variations in the local transmit/receive product

for any particular angular sector. It is thus operationally necessary to estimate these small +/-2dB residuals. The method routinely employed is to find a region of very coarse boulders whose angular response is assumed (from modeling) to be Lambertian, without a strong specular component, and calculate the differences between the observed response and that modeled for all angles. These differences are then subtracted from all other estimates. It is notable that the residuals are observed to be roll insensitive, indicating that the main source of the residuals is not variations in the sensitivity of the physical elements of the array, but variations in the electronics that make up each of the (roll –stabilised) beams.

For the lower grazing angle data the difference in ray path between an ideal straight ray and the refracted ray path may be as much as 3 degrees [9] in strongly downward refracting summer conditions. Fortunately for these surveys all acquisition was performed either in the April or November outside the period when the summer thermocline is developed and thus the effect was not a significant problem.

For regions of strong seabed topography (>2 degrees) it is strictly necessary to estimate the true seabed grazing angles using the local 3D slope of the seafloor derived from the swath bathymetry. Note that the slope is only that exhibited after the bathymetric data cleaning and gridding process and is thus effectively a low-passed filtered version of the true seafloor slope distribution.

3.2 Difficulties at nadir

The near nadir region is in general the hardest place to acquire estimates of the backscatter strength. Conventional sidescan geometries with a broad receive beam merely equate incidence angle with the arccosine of the ratio of time of first arrival and the time of subsequent arrivals. In contrast multibeam sonars extract the backscatter intensity for specific angular sectors from discrete narrow beams. The choice of intensity relies on a good estimate of the slant range to the centre of the beam footprint. Given the amplitude detection methods generally employed (weighted mean time), the estimate may not correspond exactly to the peak in intensity and thus underestimates of the backscatter strength can occur. Another problem that occurs close to normal incidence in the effect of sidelobe interference and subbottom reflections, which both alias the estimate of slant range and contribute to the received intensity, thereby giving false estimates of the backscatter strength.

Prior to 1994 an unrecoverable automatic gain control was applied to all EM1000 backscatter data collected within 25 degrees of vertical incidence [8]. Whilst this was removed in 1994, for the period mid 94 to mid 96, it was clear that the data in this region were being under predicted by about 15dB. A software change in mid 1996 appears to have rectified this problem. As a result the older data (including the first 3 surveys of the SBNMS project) have to be empirically compensated for this. Although seafloor provenance delineation is possible using the near nadir data, the fidelity of the absolute level of the data remain poor. It is presented here, but emphasis is applied to the lower grazing angle data.

3.3 Derivation of mean angular response curves

Because of the stochastic nature of the instantaneously received intensities, it is necessary to average the backscatter strength measurements over a finite time period to come up with a robust estimate of the mean AR. Empirically it was found that 50 ping averages (corresponding to between 100 and 300m forward propagation) were enough to come up with good estimates of the AR curve shape. In addition the data for the full suite of grazing angles has to be acquired from a region extending from nadir to about 3.7 times the water depth to each side (100 to 300m for the range of water depths common on the bank). Thus, as the vessel propagates forward, AR curve estimates are obtained from averaging over two rectangular footprints (of a few 100 metres per side) on either side of the swath (Fig. 2). One therefore runs the risk of averaging over a region of variable seabed character.

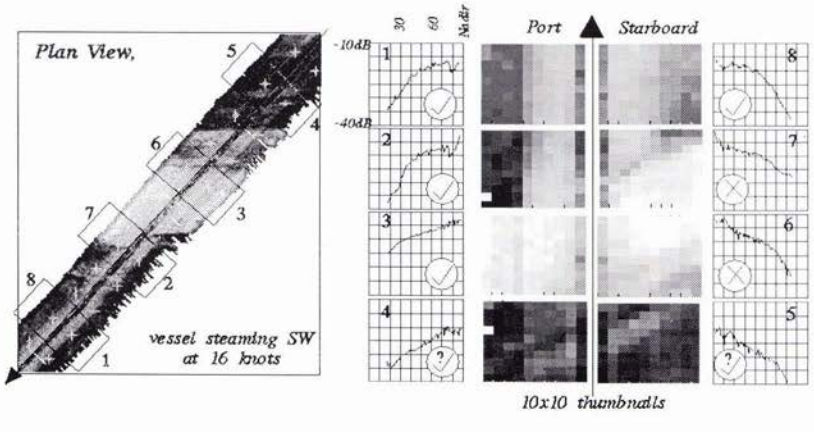

Figure 2: The method of derivation of the 50 ping averages, their corresponding geographic coverage and the method of extracting sidescan "thumbnails" for use in boundary detection (ticks and crosses indicate whether the boundary criteria was met or exceeded).

Whilst for most of the collected data, regions of the scale of the averaging footprint generally appear homogenous in the sidescan imagery, boundaries do occur. Data that is derived over these boundaries is therefore corrupted. In a crude attempt to get around this problem, a 10x10 "thumbnail" image of the seafloor under examination was retained (Fig. 2) for testing purposes. The variance of the averaged intensity distribution in the along track direction only was calculated (in the across track direction, the AR itself will produce a variance). If the variance exceeded a threshold then the angular response curve was rejected.

A result of this approach is that it can only be used to classify homogenous regions on the scale of ½ a swath width or larger. This contrasts markedly with the approach used in deeper water surveys, where commonly the number of survey lines is much lower (as the swaths are much larger), and methods are therefore derived to classify within a single swath [14]. Implicit in the boundary test is a definition of the length scale at which patchy sediment distributions are seen either as a single sediment type or a series of discrete sediment types. For this test, the length scale corresponds to a single pixel, which is 30% of the water depth in size.

4. Parameter Extraction

Early work to invert AR curves for physical properties focussed on the near nadir region to solve for roughness parameters only [15][16][17]. More recent work using EM1000's has focussed on the lower range of grazing angles to attempt full inversion [18]. In all cases the inversion used a single layer seafloor model [19][20]. The inversion assumed that the observed AR curve had no biases due to imperfections in the measurement process (e.g. sections 3.1, 3.2). Because this assumption is invalid for the AR curves herein considered, the focus here has been to extract parameters that adequately describe the salient features of the observed AR curves without being sensitive to small systematic biases.

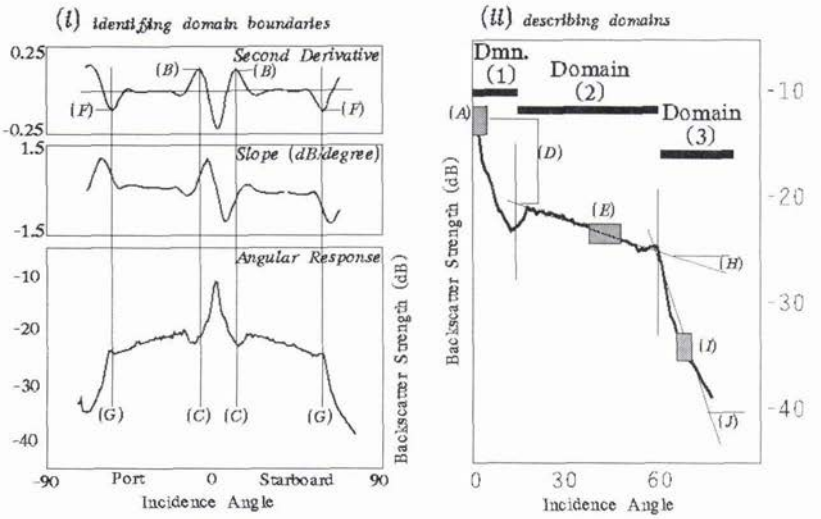

Figure 3: The three main domains of characteristic angular response curves and the parameters extracted to describe the domains

In the application of the model of [19] three main domains within the curve can be easily identified (Fig. 3 zones (1), (2) and (3)). These domains can be clearly seen in the AR curves even with small systematic biases present. Their location and the gross shape of the curve within each domain can be extracted (Fig. 3). The relative importance of the six physical property characteristics used in the single layer fluid model [19] (density and sound speed ratios, spectral strength and exponent, loss tangent and volume scattering) varies as one moves between the three domains. In domains 1 and 2, only the product of the first two terms (which control the impedance contrasts) can be estimated. The boundary between domains 2 and 3 (if visible) in contrast is strongly linked to the sound speed ratio alone (the critical angle effect). The boundary between domains 1 and 2 is most sensitive to the two roughness terms. The volume scattering term is dominant for low impedance sediment in domain 2 but plays little role in domain 3. The roughness terms affect all three domains, but in low impedance sediment they are subordinate to the volume scattering component in domain 2.

The domain boundaries, and the characteristics of the angular response curves within the three domain boundaries can be extracted even in the presence of systematic biases in the data. In this way the important changes in the angular response curves can be reduced to a few parameters that can be used either as a means of empirical classification or even potentially a step toward inversion for seabed physical properties. In addition to parameters describing the shape of the curves, one statistical parameter is used. The coefficient of variance [21] is calculated for narrow angle bins for each 50 ping stack and the average over the range 65-15 degrees grazing is presented.

To illustrate the application of the method, a series of maps are presented (Fig. 4) which show the spatial variation in the parameters over a 30 by 27 km area located on the SE corner of the SBNMS. The different patterns seen in maps A, E

and I illustrate the geographic variation in backscatter strength for three narrow angular subsets of the AR curve. The differences in the 3 maps illustrate that the shape of the AR curves are highly variable. Maps B and F map the confidence with which the domain boundaries are recognised. Maps C and G show the variation in the location of the domain boundaries (note the incoherent pattern in areas where the confidence (expressed in maps B and F) is low). Maps H and J show the spatial variation in the slope of the AR curves for domain 2 and 3 and map D shows the drop in dB in domain 1.

Table 1: description of 12 parameters extracted and the range used in the greyscale spatial maps in Fig. 4.(BS: backscatter strength)

parameter	*description*	*black*	*white*
(A)	Mean BS, 90-85 deg.	-32 dB	-12 dB
(B)	Max. 2nd deriv, (1)-(2) transition	0.02 dB/deg2	0.2 dB/deg2
(C)	Location of (1)-(2) transition	83 deg.	70 deg.
(D)	DB range, domain (1)	-5 dB	10 dB
(E)	Mean BS, 50-40 deg.	-40 dB	-20 dB
(F)	Max. 2nd deriv, (2)-(3) transition	0.0 dB/deg2	0.18 dB/deg2
(G)	Location of (2)-(3) transition	50deg.	15 deg.
(H)	Slope, domain (2)	-0.2 dB/deg	0.0 dB/deg
(I)	Mean BS, 25-20 deg.	-40 dB	-20 dB
(J)	Slope, domain (3)	-1.0 dB/deg	0.0 dB/deg
(K)	Coeff. Variance	0.95	1.0
(L)	Boundary Test Failures	YES	NO

Figure 4: Maps of a 30 by 27 km area (SE section of SBNMS) showing the geographic variation of the 12 parameters described (see table 1, for range used in greyscale).

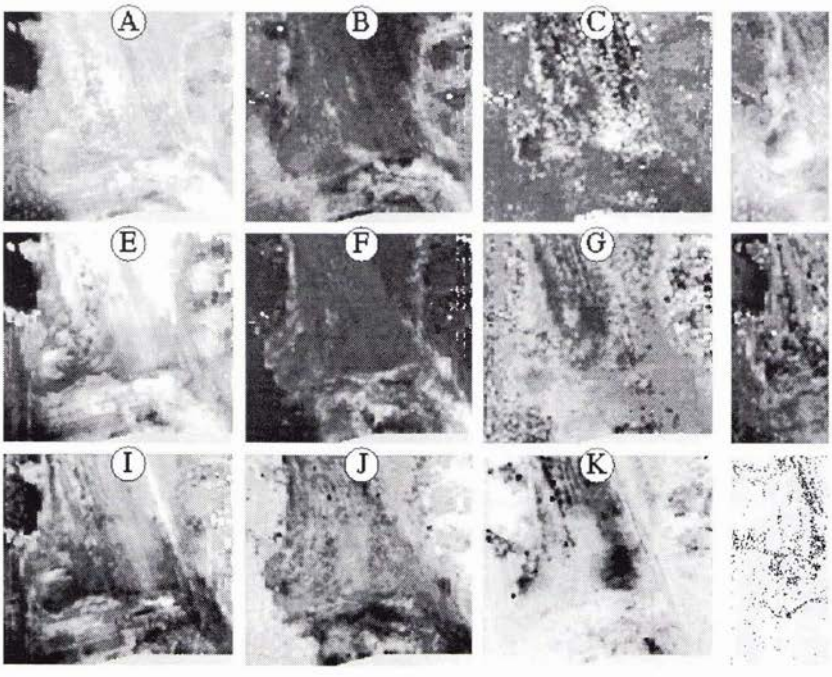

5. GroundTruth Data

While regional historic samples are available [12], the poor positioning confidence of older data and the known temporal variations in the shallow seafloor in this area make their use difficult. More recent, intense sampling programs have been restricted to the southern limit of the bank. This sampling program has consisted of a combination of video imaging, bottom photography and bottom grabs and box cores. Unfortunately for the large fraction the bank which is covered with coarse sediment, sampling limitations (related to the difficulty of recovering statistically significant volumes of coarse sediment in grabs or box cores) have generally resulted in insufficient and unrepresentative samples. Thus descriptions are generally often based on optical imaging only. Grain size is the only commonly available quantitative measurement derived and these data suffer from the aliasing that result when bottom sampling in a spatially heterogeneous area.

6. Characteristic Angular Response Curves

To illustrate the types of AR curves commonly observed within the SBNMS, a representative selection is provided (Fig.'s 5 and 6). All sample curves are derived from acoustic data obtained in the 1994 field season, which was located in the southern area in which the best groundtruth existed. Brief lithologic descriptions are included for all curves, but should be taken as a guide only due to the reasons stated in section 5.

6.1 Stellwagen Bank and Basin

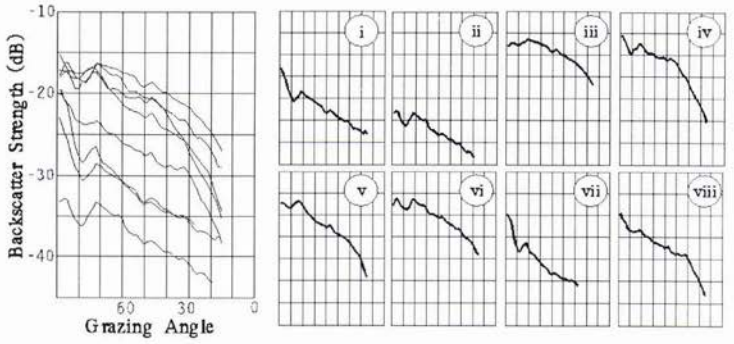

I Silty mud

II Mud

III Cobble pavement

IV Fine sand

V Rippled medium sand, over gravel

VI Boulder fields

VII Sandy mud

VIII Silty sand

Figure 5: Representative AR curves for sediments on Stellwagen Bank and Basin

The AR curves for the sediment on Stellwagen bank and in the basin are similar to those that would be predicted for a single layer model. Lambertian-like AR's are observed for the coarsest sediment (5iii and 5vi) without clear domain boundaries. As expected, for sediments with the lowest sound speed ratios, no domain 3 is observed (5i, 5ii and 5vii). Critical angle effects are seen for sandy sediment (5iv and 5viii).

6.2 Cape Race Channel

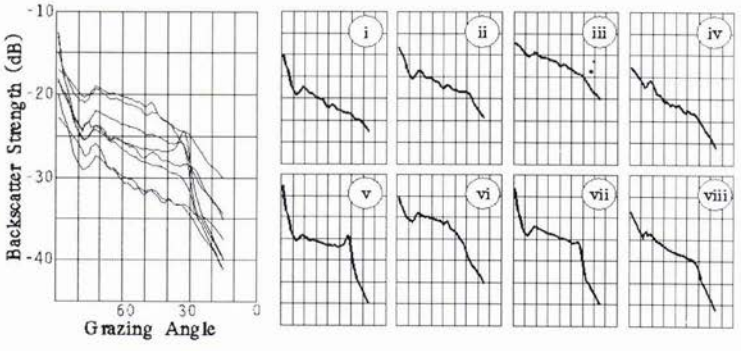

I Silty mud

II Medium sand

III Coarse gravelly sand with cobbles.

IV Clean coarse sand

V Clean medium sand

VI Clean coarse sand overlying gravel

VII Medium sand with pebbles

VIII Medium–coarse sand

Figure 4: Representative AR curves for sediment facies developed in Cape Race channel

In the Cape Race Channel area, critical angle effects are seen throughout (Fig. 6). The location and sharpness of the domain 2-3 boundary is highly variable exhibiting cusps at times (6v and 6vii). In one case (6vi) the location of the critical angle suggests a sound speed ratio of about 1.4 which is far higher than that expected for the surface lithology alone (~1.18) but matches that expected for the underlying layer.. For a number of the sandy sample locations, groundtruth sampling revealed either, interspersed gravel and cobbles, or an underlying layer of gravel.

7 . Discussion on likely physical property controls on observed AR's

Many of the sediments observed in the SBNMS are significantly coarser than those that have been the focus of quantitative acoustic backscatter studies in the past [21][22][23]. Nevertheless they are very representative of the range of coarse facies commonly exhibited on high latitude glaciated continental shelves.

7.1 Explaining the critical angle phenomena observed

While the limitations (outlined in Section 3.2) of the measurement of the AR preclude the confident use of the curves for inversion (note the prevalent depression in all the curves at ~75-80 grazing). The shape, and more particularly the change in shape, of the angular response curves between common lithologies may be compared to predictions for material of similar physical properties. For the case of a single layer seafloor type [19][20], critical angle effects would be expected in sediments in which the sediment/seawater sound speed ratio exceeds ~1.04. For this simple case, the location of the inflection is unique indicator of the sediment sound speed. Two end member cases are recognised: a cusp for cases in which surface roughness is dominant (Fig. 6v), and a step function for the case where volume scattering is terminated (Fig 6viii). A break in slope would not be obvious for the rougher, higher impedance sediment types with no volume contribution (Fig. 5iii and vi) or for softer sediment with a sediment/seawater velocity ratio of less than 1.04 (Figs 5I,,ii and vii, 6i). We find, however, that while models such as [19] can predict the presence of the inflection, they cannot reproduce the rapid drop off below the critical angle sometimes observed(Fig. 6v, 6vii). Also in some cases (Fig. 5iv and Fig. 6vi) the predicted surface sound speed, often in the range ~1900-2000m/s, is too high for typical medium and coarse sands.

Alternate explanations are thus needed. More recent models that include the effect of shallow gradients, layering and shear in the shallow subsurface [24][25] are examined. For the case of a surface sediment layer of less than a wavelength in depth it has been shown [24] that the critical angle often reflects the velocity contrast of the lower (higher velocity layer). With the introduction of shear in the lower layer, the drop off in backscatter beyond the critical angle is notably steeper than that which would be exhibited for the upper layer alone [24]. These two results allow us to better match the observed curves. These, together with field evidence of a discontinuously buried higher backscatter layer (revealed in bottom photos, samples and deep-tow sidescan images) support the idea of a thin surface layer. For this case, the apparent volume scattered phenomena may either be volume scattering from the upper layer or scattering from the partly buried interface.

8. Conclusions

With appropriate data reduction, estimates of the seabed backscatter angular response can be routinely derived from calibrated multibeam echosounders. In the water depths considered (20-200m), to do so requires that there be spatially homogenous regions of the seafloor a few hundred metres wide. Parameters describing the shape of the angular response curve allow improved sediment boundary discrimination in regions where mean backscatter strength is almost constant. The shape of the curve below 40 degrees is especially revealing as the response in the vicinity of the critical angle may be observed. Curve parameterisation allows the potential to invert for seabed physical properties. The success of the inversion, however, is dependent on both the fidelity of the measurements and the appropriateness of the model used.

For a number of the examples presented, comparison of observed angular responses to the results obtained assuming a single layer model suggests that such a simple model is often not valid. An improved fit may be obtained by incorporating more recent models [24][25] that account for shear, gradients and layering in the shallow subsurface (< a few wavelengths ~1-3cm). Limited groundtruth observations support this with evidence of discontinuous surface layers of finer grained sandy sediment over a coarse-grained gravel pavement.

While confident remote sediment classification remains an elusive goal, the routine availability of near-quantitative angular response measurements provides an additional means of seabed discrimination . Used together with other methods such as normal incidence and textural methods, angular response methods can provide an improvement in underway sediment classification.

Acknowledgements

Funding for the SBNMS surveys was provided through the US National Marine Sanctuary Program and the USGS Coastal Marine Geology Program. This research was funded through the NSERC Industrial Research Chair in Ocean Mapping. We are indebted to the officers and crew of the NSC Frederick G. Creed, and greatly appreciate the assistance of Richard Sanfacon (CHS) , Vee-Ann Cross, Jane Denny and Erik Schmuck (USGS).

References

[1] Pace, N.G. and Gao, H., 1988, Swathe seabed classification: IEEE J. Oc. Eng., v.13, p. 83-90.
[2] Reed, T.B. and Hussong, D. , 1989, Digital image processing techniques for enhancement and classiication of SeaMARC II side scan sonar imagery: JGR, v.84, B6, p.7469-7490.
[3] Blondel, P., 1996, Segmentation of the Mid-Atlantic Ridge south of the Azones, based on acoustic classification of TOBI data: in Geol. Soc. Spec. Pub. no. 118, p.17-28.
[4] de Moustier, C. and Alexandrou, D., 1991, Angular dependence of 12 kHz seafloor acoustic backscatter: JASA, v.90, p.522-531.
[5] Hughes Clarke, J.E., 1994, Toward remote seafloor classification using the angular response of acoustic backscattering: a case study from multiple overlapping GLORIA data: IEEE Journal of Oceanic Engineering v.19, no.1, p.364-374.
[6] Hughes Clarke, J.E, 1993, The potential for seabed classification using backscatter from shallow water multibeam sonars, in Pace, N. and Langhorne, D.N., Proc. of the Inst. of Acoustics, v. 15, pt. 2, p. 381- 388.
[7] Simrad, 1992, SIMRAD EM1000, Hydrographic echo sounder, Product Description: Simrad Subsea A/S, #P2415E.
[8] Hammerstad E., 1994, Backscattering and Sonar Image Reflectivity: EM12/950/1000 Technical Note, 10p.
[9] Hughes Clarke, J.E., Mayer, L.A. and Wells, D.E., 1996, Shallow-water imaging multibeam sonars: A new tool for investigating seafloor processes in the coastal zone and on the continental shelf: MGR, v.18, p.607-629.
[10] Danforth,W.C., O'Brien, T.F. and Schwab, W.C., 1991, Near-realtime mosaics from high-resolution sonar: Sea Technology, v.32, no. 1, p.54-59.
[11] Valentine, P.C., and Schmuck, E.A., 1993, Storm-driven sediment transport on Stellwagen Bank, Gulf of Maine region (abs.): Geological Society of America Abstracts with Programs, v. 25, no. 6, p. A379-380.
[12] Schlee,J.D., Folger,D.W. and O'Hara, C.J., 1973, Bottom Sediments on the continental shelf off the Northeastern United States, Cape Cod to Cape Ann, Massachussetts: USGS .Misc. Geologic Investigations, ap I-746.
[13] Auster, P.J., Malatesta, R.J., Langton, R.W., Watling, L., Valentine, P.C., et al., 1996, The impacts of mobile fishing gear on low topography benthic habitats in the Gulf of Maine (northwest Atlantic): implications for conservation of fish populations: Reviews in Fisheries Science, v. 4, no. 2, p. 185-202 .
[14] Dugelay, S., Graffigne, C. and JM. Augustin, 1996, Deep seafloor characterisation with multibeam echosounders by image segmentation using angular acoustic variations: Proceedings SPIE, Denver.
[15] Matsumoto, H., Dziak, R.P. and Fox, C., 1993, Estimation of seafloor microtopographic roughness through modeling of acoustic backscatter data recorded by multibeam systems: JASA v.94, p.2776-2787.
[16] Michalopoulu, Z-H, Alexandrou, D. and deMoustier, C., 1994, Application of a maximum likelihood processor to acoustic backscatter for the estimation of the seafloor roughness parameters: JASA, v.95, p.2467-2477.
[17] Michalopoulu, Z-H and Alexandrou, D., 1996, Bayesian modeling of acoustic signals for seafloor identification: JASA v.99, 223-233.
[18] Gott, R.M., 1995, Seafloor characterization using multibeam sonar amd acoustic backscatter modeling: PhD thesis, Tulane University.
[19] Jackson, D.R., Winebrenner, D.P. and Ishimaru, A., 1986, Application of the composite roughness model to high-frequency bottom backscattering: JASA, v.79, p.1410-1422.
[20] Mourad P.D. and Jackson, D.R., 1989, High frequency sonar equation models for bottom backscatter and forward loss: Proc. OCEANS'89, v.IV, p.1168-1175.
[21] Stanic, S., Briggs, K.B., Fleischer, Sawyer,W.B. and Ray, R.I., 1989, High frequency acoustic backscattering from a coarse shell ocean bottom: JASA, v.85, p.125-136.
[22] Jackson, D.R., Baird, A.M., Crisp, J.J. and Thomson, P.A.G., 1986, High-frequency bottom backscatter measurements in shallow water: JASA, v.80, p.1188-1199.
[23] Jackson, D.R. amd Briggs, K.B., 1992, High frequency bottom backscattering: Roughness versus sediment volume scattering: JASA, v.92, p.962-977.
[24] Essen, H.-H., 1994, Scattering from a rough sedimental seafloor containing shear and layering: JASA, v.95, p.1299-1310.
[25] Moe, J.E. and Jackson, D.R., 1994, First-order perturbation solution for rough surface scattering cross section including the effects of gradients: JASA, v.96, p.1747-1754.

Relating *In Situ* Shear Wave Velocity to Void Ratio and Grain Size for Unconsolidated Marine Sediments

Dei Huws, Angela Davis and James Pyrah

School of Ocean Sciences
University of Wales, Bangor
Menai Bridge, Anglesey
Wales, U.K.
E-mail:oss082@bangor.ac.uk

Abstract

Recent advances in field hardware have meant that it has become possible to measure in situ shear wave velocity in the upper few decimetres of sea floor sediment in a routine manner. It is known that shear wave velocity can be primarily related to overburden depth and void ratio. Field-derived empirical relationships have previously been formulated so that it is now feasible to assess the suitability of shear wave data as a means of predicting in situ void ratio. Field measurements performed on the northern Californian shelf are presented which reveal good agreement between predicted and control data.

1. Introduction

The dynamic rigidity of unconsolidated marine sediments controls a whole range of acoustic transmission and geotechnical behaviour which are of relevance to defence applications in the littoral and near-coast zone. Although it is difficult to directly measure rigidity in the field, it has become possible, over recent years, to measure *in situ* shear wave velocity (Vs) - a property directly related to rigidity via the solution to the general wave equation. Whilst Vs is an important measure in itself, it also has the potential to be related to other, more familiar, sediment properties, most notably void ratio (e) or porosity (n) (where $n = e / (1+e)$).

The hypothesis to be tested herein is that field measurement of *in situ* shear wave velocity can be used as a reliable technique for predicting void ratio, and that it can be demonstrated that grain size dependencies observed in previously acquired laboratory and field data can be related to changes in void ratio.

Given the aim of testing the hypothesis, the objectives of this study are to;

(i) acquire shear wave velocity - depth data along a survey profile,
(ii) acquire and process grab sample data for delineation of grain size changes,
(iii) predict void ratio and/or grain size variation along the profile and assess the predictions by comparison with control data,
(iv) assess previous velocity - grain size - void ratio data in terms of expected velocity changes.

2. Data Acquisition

There are many ways in which to measure shear wave velocity in the field. The approach taken in this study is to directly measure transversely polarised, refracted shear waves using a sea floor -dragged sled system along a survey profile.

2.1. Hardware and Deployment

The hardware and deployment techniques are described in detail in previous publications [1,2] so that only a brief overview is presented here.

The system comprises a sled on which is mounted an electro-magnetic hammer-impact seismic source, the firing being controlled via a direct link to the survey vessel. Transversely polarised shear waves are thus produced and detected by a series of six horizontally gimbaled geophones, towed behind the sled at discrete intervals, to a maximum source-receiver separation of 12.35 m. Received signals are then transferred in real-time via a multi-core cable to a ship-board seismograph for display, quality control and recording. Data are only acquired when the complete sea floor system is made stationary by excessive release of the main towing cable for a short period of time. Having completed a measurement, the cable is taken-up to its original towing point in anticipation of the next repetition of the process. In this way, it has been found that rapid shear wave data acquisition over relatively large survey areas is possible, making the system ideal for delineating subtle variation in shear wave velocity, as well as for general velocity mapping purposes [2,3].

2.2 Location of acquired data

The data were acquired along a profile off the northern Californian coast, running in a North Easterly direction from a starting point c. 5km offshore from Humboldt Bay, Eureka. Figure 1 shows the locations of all shear wave measurement points along the profile. Reference positions 'S40' to 'S70' correspond to bathymetric depth (in metres). Note that deviation away from the intended straight line profile was incurred due to the presence of sea floor obstructions.

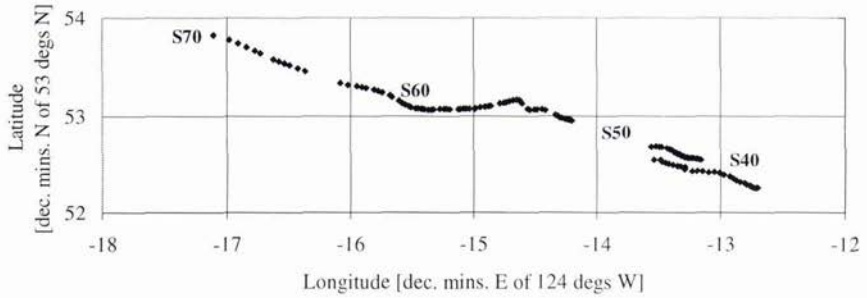

Figure 1. Location of shear wave data acquisition points

Grab samples were collected from a point on the profile at S40 and subsequently at 5m. water depth intervals to S70.

3. Data Processing and interpretation

3.1. Shear wave data

The data are processed in terms of horizontal plane layer refraction events. Thus, interpretations are limited in areas where 'low velocity' layers are present, or on occasions where the subsurface is composed of dipping layers.

Since shear wave velocity is known to be dependent upon, amongst other parameters, effective confining stress [4], it is generally expected that high velocity-depth gradients are present in the near surface. Thus, the idea of a 'direct' wave, traveling along the surface to the nearest receiver may be misplaced during shear wave analysis of unconsolidated marine sediments. The velocity represented by the time delay between firing of the source and arrival at the first geophone is merely an apparent velocity from an unknown and unmeasureable depth. Velocities can only be ascribed a representative depth between subsequent geophones. The interpreted travel-time data are shown in figure 2. Unlike systems which measure time-of-flight between two sub-surface transducers buried at known depth (e.g. the ISSAMS system [5]), the penetration depth of the sled data is determined by the source-receiver spacing on the sea floor and the velocity-depth

structure at the measurement point. The data are presented as they occurred between the bathymetric intervals as shown in the accompanying legend.

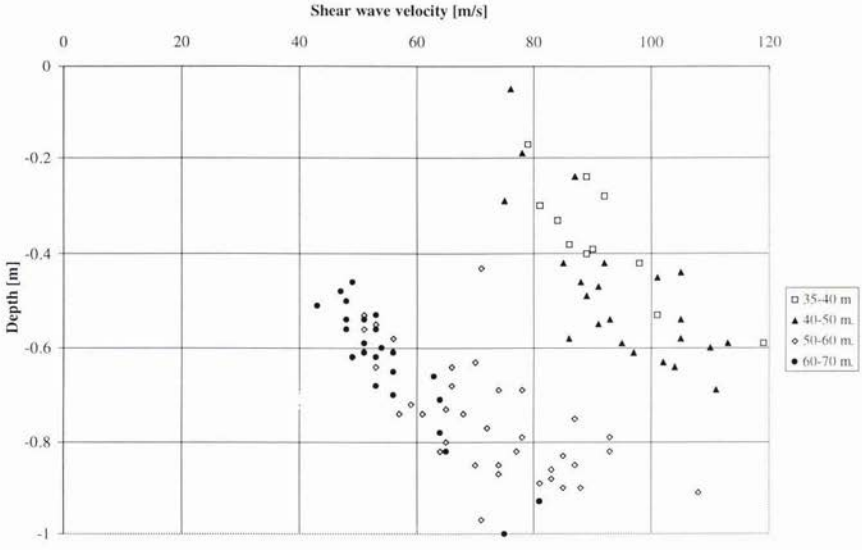

Figure 2. Interpreted shear wave velocity - depth data along the profile

It apparent that shear wave velocity generally decreases with increasing bathymetric depth. In order to clearly delineate the variation of shear wave velocity along the profile, it is necessary to normalise the data to a fixed sediment depth. Previous work has shown that that shear wave velocity is proportional to depth (confining pressure) raised to a power generally in the range 0.28 - 0.32 [5,6,7]. A value of 0.3 is assumed in this study such that the equivalent velocity at a depth of 10 cms below sea floor ($V_{0.1}$) may be calculated from:

$$V_{0.1} = V_z \ (0.1/ z)^{0.3} \qquad (1)$$

where V_z = shear wave velocity at measurement point
z = depth of shear wave measurement [m]

Velocity data normalised in this way are shown in figure 3.

The normalised data reveal a marked variation along the profile - changing from 55-70 m/s in water depths of up to 50 m., to 25-35 m/s at 70 m. Velocity is relatively constant within the water depth ranges 37 m. - 44 m. and 55 m. - 70 m. The greatest change in velocity is observed by inference to occur between the 44 m. and 55 m. isobath. Shear wave velocity data acquired via the ISSAMS probe during the same survey agree very well with the presented data [8].

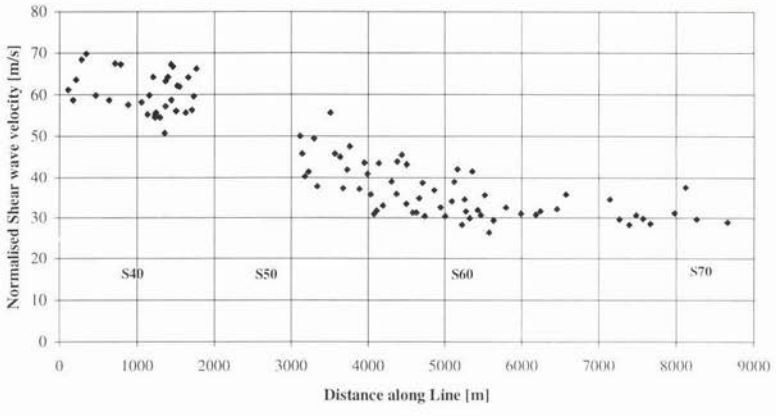

Figure 3. Normalised shear wave velocity along profile

3.2 Grab sample data

Data of sieve and hydrometer particle size analysis are shown in table 1.

Water depth of sample [m]	Mean Diameter [phi units]	Mean Diameter [mm]
40	2.96	0.129
45	2.98	0.127
50	2.79	0.145
55	6.53	0.011
60	7.84	0.004
65	7.27	0.006
70	7.82	0.004

Table 1. Results of particle size analysis (phi dia. = - $\log_2$ [dia. mm.])

It can be seen that mean grain size decreases with increasing water depth and that the largest change is observed between the samples acquired at 50 m. and 55m. (cf. Figure 3)

4. Predictions from shear wave velocity - depth data

4.1 Void ratio (porosity)

It has been established, either quantitatively or qualitatively, that shear wave velocity (or shear modulus) varies with a whole range of physical properties and conditions for sediments (unconsolidated or otherwise) [9, 10]. However, it is generally accepted that the two most important parameters that can be used to simply model the variation in velocity are effective confining pressure and void ratio. The first investigators of this link were Hardin and Richart [4]. They performed a series of resonant column experiments on Ottowa Sand and derived empirical relationships between shear modulus, effective confining pressure and void ratio within a specific range of void ratio and pressure. Subsequently, Bryan and Stoll [6] measured shear wave velocity whilst monitoring void ratio and effective confining pressure for 493 samples in the laboratory, with the intention of deriving as universal a relationship as possible. Whilst the confining pressure range was between 24 to 700 kPa, the data shown in their paper would suggest that the empirical relationship derived should function reasonably at the lower pressures involved in this study.

The relationship of Bryan and Stoll [6] for sands is given as:

$$G/p_a = 2526\ exp^{-1.5e}\ (s_0/\ p_a)^{0.45} \quad (2)$$

where: G = dynamic shear modulus (G = bulk density * $(Vs)^2$)
p_a = atmospheric pressure
e = void ratio
s_0 = overburden pressure

Similarly, Richardson et al. [5] derived an empirical relationship relating shear wave velocity to void ratio and depth:

$$Vs = (85/e)\ z^{0.3} \quad (3)$$

where: z = depth below seafloor

Given the *in situ* velocity-depth data acquired as part of this study, it would appear possible to predict void ratio either indirectly by applying equation (2), or by the direct application of equation (2). Plotted on figure 4 are the data of figure 2, superimposed on which are the velocity-depth trends of the two relationships for a range of void ratio (e) values - here plotted as porosity.

It would appear that there are quite large disparities between the two models, the differences being most accentuated at porosity values of 50% and at shallower depths.

Based upon ISSAMS data acquired over the last five years, equation (3) would appear to be valid for a range of siliclastic sediment types over the depth ranges for which *in situ* data are available in this study [8]. It should be noted that implicit in the application of this formula is the assumption that void ratio does not vary with depth.

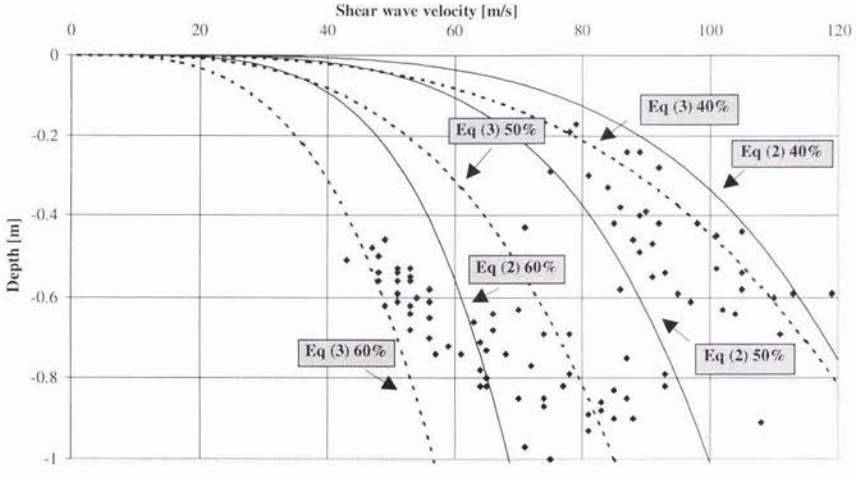

Figure 5. Velocity-depth data along S-line compared to empirical model data for a range of porosities.

The velocity-predicted void ratio data calculated from both (2) and (3) are plotted as porosity against 'distance along survey line' in figure 6. Comparison with porosity data acquired from subsampled box-core data (*pers. comm.* Briggs, 1996) would appear to show very good agreement with the values predicted by (3).

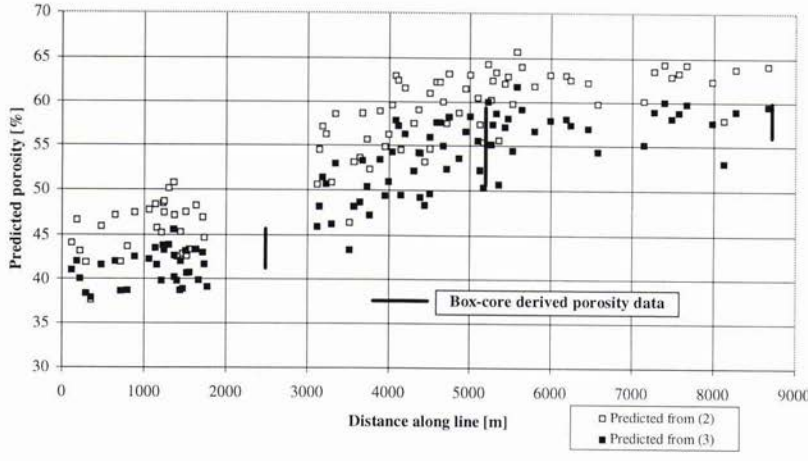

Figure 6 Porosity predicted by empirical relationships

4.2 Mean Grain Size

The causal link between void ratio and shear wave velocity is indirect since it lies in the association between the amount of void space in a sediment and the number (per unit volume) and nature of inter-particle contacts within the fabric. Studies have shown that shear wave velocity would appear to correlate, to some extent, with mean grain size [2,12,13]. However, like void ratio, this link cannot be made directly from velocity. If one considers an ideal case of perfect packing of spherical grains, grain size is a geometrical factor [12] so that there should be no causal link and no correlation between shear wave velocity and mean grain size. Equally, under such artificial circumstances, no correlation should be expected between grain size and void ratio. Empirical studies have shown that there is a link between the latter parameters [14], illustrating that the fabric of natural sediments differ substantially from the perfect case.

Previously published data are presented in figure 7 which reveal how shear wave velocity is observed to decrease with decreasing grain size. Three data sets are given: laboratory derived data [12] show the greatest variation for a given grain size, whereas the field data [2,13] reveal slightly less variability. The data presented have been normalised to a constant overburden depth, but have not been normalised to a constant void ratio. Using the empirical relationship between grain size and void ratio [14], it becomes possible to predict a range of expected void ratios for a given grain size, thus allowing a range of values for shear wave velocity for a given mean grain size to be predicted using (3). These are plotted on figure 7. They reveal that the trends between grain size and shear wave velocity are consistent with the correlation between grain size and void ratio. A logical adaptation of the method of predicting void ratio would be to use velocity as a predictor of mean grain size. Unfortunately, in this study, disparity results from the different effective measurement depth of the seismic and grab sample information (0.2 - 1.0 m and <0.1 m respectively). It should be noted that the laboratory data were acquired over a range from 'loosest packing' by underwater deposition to 'closest packing' achieved by impact invoked settling and are therefore likely to show an artificially high range of shear wave velocities compared with *in situ* data.

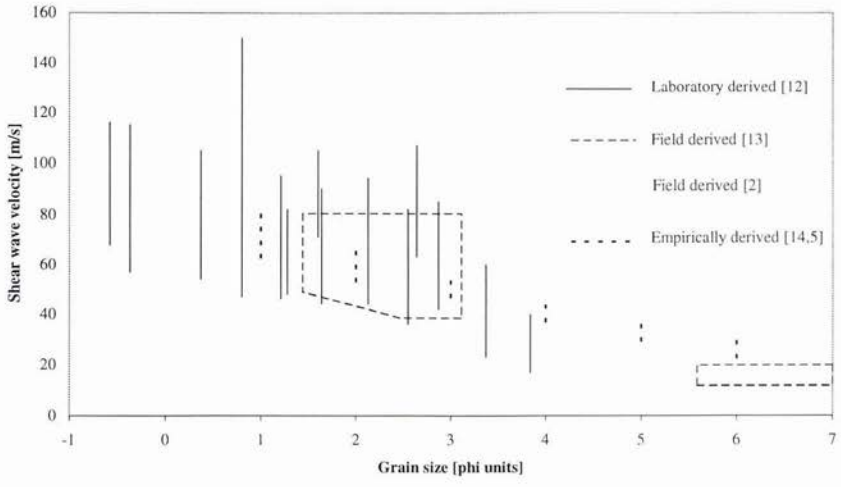

Figure 7. Normalised shear wave velocity versus mean grain size

5. Conclusions

Shear wave velocity - depth data have been successfully acquired and processed along the survey profile. The seismic (figure 3) and grab sample (table 1) data reveal that velocity is sensitive to changes in mean grain size - significant changes in grain size being reflected in the normalised shear wave velocity data. Two empirical relationships have been tested in order to use the velocity-depth data to predict *in situ* void ratio. It has been found that the equation derived by Richardson *et al.* [5] gives excellent agreement with box-core derived control data. Previously published relationships between grain size and void ratio have the potential to adapt the technique to predicting changes in mean grain size although prudence would be required during such procedures since it is known that the nature of the grain size - void ratio relationship varies with sediment type [14]. The implication of this work in the context of sediment classification studies is that the ability to map the shear wave velocity of marine sediments can reliably assist in the truthing of acoustic classification data sets. Other applications arise within the field of mine burial problems.

6. Acknowledgments

The authors wish to thank the crew of the R/V/ Wecoma, the Naval Research Laboratories for funding the study via the Coastal Benthic Boundary Layer Special Research Program, Kevin Briggs (NRL) for providing the box-core derived porosity data and Nigel Toothill (UWB) for analysing the grab sample data.

7. References

[1] A.M. Davis, D.G. Huws, J.D. Bennell and D. Thomas, "Development of a sea floor geophysical sledge," *Marine Geotechnology*, vol. 8, pp. 99-109, 1989.

[2] D.G. Huws, A.M. Davis and J.D. Bennell, "Mapping of the seabed via in situ shear wave (SH) velocities," in *Shear Waves in Marine Sediments*, Hovem J.M, Richardson M.D. and Stoll R.D. (Eds.), Dordrecht, Kluwer Academic Publishers, pp. 337-343, 1991.

[3] A.M. Davis, R. Haynes and D. Huws, "Seabed sediment characteristics assessed geophysically: Results of experiments in the Clyde Sea, Scotland", *this volume*.

[4] B.O. Hardin and F.E. Richart, "Elastic velocities in granular soils," *Journal of the Soil Mechanics and Foundations Division*, ASCE, vol. 89, pp. 33-65, 1963.

[5] M.D. Richardson, E. Muzi., B. Miaschi and F. Turgutcan, "Shear wave velocity gradients in near-surface marine sediments," in *Shear Waves in Marine Sediments*, Hovem J.M, Richardson M.D. and Stoll R.D. (Eds.), Dordrecht, Kluwer Academic Publishers, pp.295-304, 1991.

[6] G.M. Bryan and R.D. Stoll, "The dynamic shear modulus of marine sediments," *Journal of the Acoustic Society of America*, vol. 83, pp. 2159-2164.

[7] B.O. Hardin "The nature of stress-strain behaviour for soils," in *Proceedings of the specialty conference on earthquake engineering and soil dynamics*, ASCE, Pasadena, pp. 30-90, 1978.

[8] M.D. Richardson, *pers. comm.*, 1996.

[9] R.D. Stoll, Sediment acoustics, Lecture notes in earth sciences, no. 26, Springer-Verlag, Berlin, 1989.

[10] R.D. Woods "Soil properties for shear wave propagation," in *Shear Waves in Marine Sediments*, Hovem J.M, Richardson M.D. and Stoll R.D. (Eds.), Dordrecht, Kluwer Academic Publishers, pp.29-39, 1991.

[11] K. Briggs, *pers. comm.*

[12] P.J. Schultheiss P.J. "The influence of packing structure on seismic wave velocities in sediments," Marine Geological Report No. 81/1, University College of North Wales, Bangor, UK., *unpublished*, 1983

[13] S.E. Jones, Geophysical properties of marine sediments: textural and biological controls, Ph.D. Thesis, University of Wales, *unpublished*, 1993.

[14] E.L Hamilton and R.T. Bachman "Sound velocity and related properties of marine sediments," *Journal of the Acoustic Society of America*, vol. 72, pp. 1891-1904.

Wavelet Analysis of Side Scan Sonar Imagery for Classification

John Impagliazzo*, Walter Greene* and Quyen Huynh**

*Naval Undersea Warfare Center, Division Newport
Newport, Rhode Island, USA
**Naval Surface Warfare Center, Dahlgren Division, Coastal System Station
Panama City, Florida, USA

Abstract

Wavelet-based techniques are presented for compressing side scan sonar images communicated from UUV's through band limited communication channels. Testing with an automatic classifier on reconstructed images demonstrates exceptional performance in preserving features required to identify mine-like objects. Wavelet domain automatic target recognition techniques are studied to further improve coefficient selection in compression. These techniques serve to enhance image fidelity in the vicinity of minelike objects while maintaining a high compression ratio.

1. Introduction

Discrete wavelet transform analysis techniques are applied to side scan sonar imagery to develop techniques which efficiently characterize images and features for communication over limited bandwidth channels [1]. A block diagram of the proposed image compression algorithm is shown in figure 1. It combines choosing an optimal wavelet basis to preserve mine-like features as well as a methodology and criteria for reducing the coefficient matrix to a sparse array. Wavelet-based detection and classification methods are incorporated to identify coefficients associated with the local structure of mine-like objects. The surviving coefficient criteria are then weighted to preserve these coefficients when generating the sparse wavelet matrix for compression.

The techniques described here involve two different methods of analyzing wavelet packet coefficients for the presence of mine-like objects. The first method involves the matching pursuit algorithm. A dictionary of functions consisting of the wavelet coefficients corresponding to various object types is created. The method determines which function or combination of functions in the dictionary are most like the object in question. The second method involves a statistical analysis of the coefficients. By calculating the probability density functions (pdf's) of the coefficients, a likelihood ratio test can be performed to indicate the presence of a mine-like object. The advantages of these methods are that they use the wavelet-based time-frequency atoms already computed during the compression process rather than heuristic features, and that they can be used for many different types of image data. All that is required is a set of known objects from the images to create the pdf's or the dictionary functions.

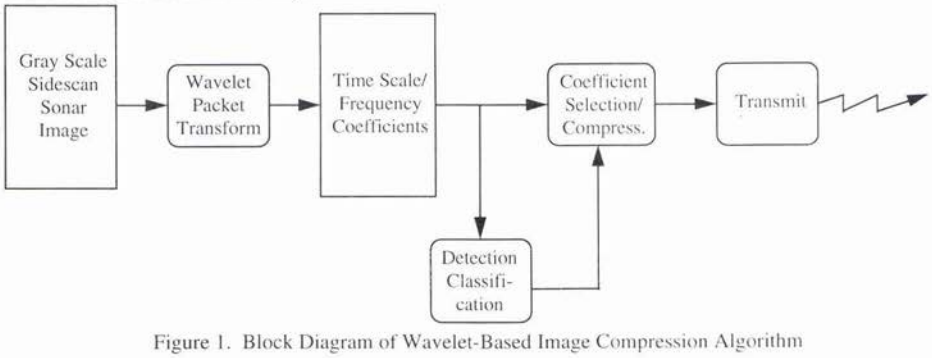

Figure 1. Block Diagram of Wavelet-Based Image Compression Algorithm

1.1 Overall Tactical Picture

Minehunting systems using side scan sonar will require 6 inch resolution in the direction of travel to avoid missing a 21 inch diameter mine-like object. A remotely-deployed minehunting system using an unmanned underwater vehicle (UUV) traveling at six knots could collect 511 sonar pings every 25 seconds. Also, if each sonar ping consists of 1024

samples at a 6 inch resolution, and port and starboard images were collected simultaneously, two 1024 by 511 pixel (picture element) images would be generated every 25 seconds. Without data compression, it could take as long as 45 minutes to transmit 25 seconds of data. To maintain real-time processing requirements, compression ratios of from 25:1 to 100:1 are required for an acoustic communications link or band limited radio frequency (RF) or satellite link.

When a side scan sonar pings, an underwater mine or similar object moored or sitting on the ocean bottom will prevent sound from the sonar system from reaching the sea floor for some distance beyond the object. This produces a characteristic highlight and adjacent shadow highly localized in the side scan sonar image. An automatic target recognition algorithm, therefore, might categorize the dimensions and relative intensity of the highlight and shadow to determine if the object should be classified as mine-like. This algorithm would, however, be susceptible to false alarms if the data compression techniques employed produced artifacts in the compressed image resembling the highlight-shadow characteristic. This is an issue with the conventional Joint Photographic Expert Group (JPEG) technique at high compression ratios.

The Navy Imaging Database at the Naval Surface Warfare Center, Dahlgren Division (NSWCDD), Coastal System Station (CSS), was used in the research described here. The images in this database were produced by a sidescan sonar towed by a helicopter. The database consists of 60 images, 30 of which have been designated as training images and 30 as testing images. Fifteen of the 30 training images contain one mine signature each, 16 of the 30 testing images contain one mine, and one testing image contains two mines, for a total of 33 mine signatures. The mines in this database are cylindrical bottom mines that typically have both a highlight and shadow signature. For this sonar, a typical mine signature has around 36 pixels in the highlight region and about 120 pixels over the shadow zone, but this varies greatly. The data for each image consist of a matrix of 1024 by 511 8-bit unsigned integers. For processing purposes, the last column is duplicated to give 512 columns.

1.2 **Side Scan Sonar Images**

Figure 2, image si000206 (*s*onar *i*mage number 206), is an example from the Navy Imaging Database, which is referred to here as sonar0. Near range is at the top of this figure, with far range at the bottom. Cross-range (the direction of travel) is horizontal across the image. The near range appears to be smooth while the far range is rough; abnormalities appear as striations in the last 5% of range. The apparent smoothness of the near range is due to the higher angle of sound incidence. In reality, the roughness and tracks are distributed uniformly over the image. The dark tracks, in many cases, are caused by fishermen dragging shrimp nets. The orientation of the tracks is also evenly distributed, but more horizontal tracks show up because of their acoustic shadow. The axes shown are in pixels. Resolution in the direction of travel, approximately 15 cm (6 inches), is a function of the speed of the tow vehicle and the round-trip time of the ping to the farthest range. Resolution in range, also approximately 15 cm, is a function of the number of beams and the maximum range. The minimum resolution in range is also determined by the size of objects which need to be detected. Two mines are found at coordinates (427, 370) and (864, 159) and are shown in the blow ups in figure 2. The first mine, at (427, 370), has a modest horizontal highlight and a pronounced shadow. The second mine, at (864, 159), is difficult to see. It has a small strong highlight and a small shadow, which is somewhat disguised because it is located on the edge of a track.

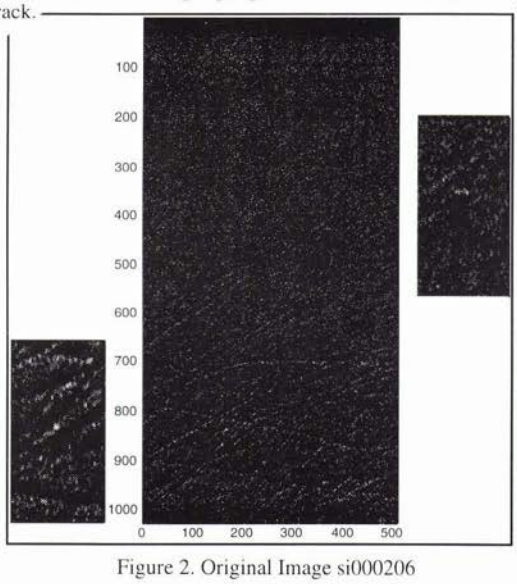

Figure 2. Original Image si000206 with Blowups of Mines

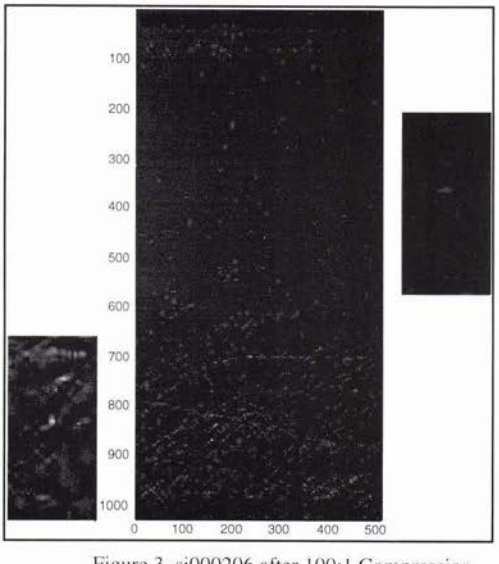

Figure 3. si000206 after 100:1 Compression with Blowups of Mines

2. Orthogonal Wavelets

2.1 Wavelet Transform Analysis

Efficient characterization of images is possible with wavelet time-frequency analysis techniques because of the local support property. Features well-localized in space are well represented by the set of coefficients overlapping the features' location. Other advantages of the discrete fast wavelet transform is that their complexity is of O(n) and they are implemented through finite impulse response filters. All of the discrete fast wavelet transforms provide perfect reconstruction. The primary differences among various types are the length of the filter, the required precision of the filter coefficients, and the relationship between forward and inverse filters. Orthogonal wavelet transform filters implement the same filtering at the forward and inverse transforms.

Evaluation of compression performance is based on the visual fidelity of the image and on comparisons of automatic classifier performance on the original image with performance on a duplicate image reconstructed from the substantially compressed image file. Figure 3 shows image si000206 after 100:1 compression. The automatic classifier used to evaluate the images was developed by Dr. Gerald Dobeck and his colleagues at the Naval Surface Warfare Center, Dahlgren Division, Coastal Systems Station, Panama City, Florida, USA [2].

The impressive success of wavelets is due mainly to the discovery of multiresolution analysis by Mallat [3]. Multiresolution analysis constitutes a useful functional analysis tool in wavelet theory and leads to the development of the very fast pyramid scheme to compute the wavelet coefficients. Although the fleet side scan sonar image is processed in two dimensions with the orthogonal wavelet algorithm, a brief description of the theory is presented here for one dimension. In practice, the one dimensional algorithm is applied twice, first to each row of the input matrix and then to each column of the row processed matrix.

In the continuous wavelet transform, for a given function $x(t)$, the coefficients are defined as follows:

$$C_x(a,b) = \langle x, \psi_{ab} \rangle = \frac{1}{\sqrt{a}} \int_{-\infty}^{+\infty} x(t) \psi_{ab}\left(\frac{t-b}{a}\right) dt, \quad b \in R, \quad a > 0. \tag{1}$$

The parameters a and b have the effects of dilation and translation respectively. To discretize the transform in the time/frequency plane, we let $a = 1/2^j$ and $b = k/2^j$, where $j, k \in Z$. The coefficients thus become

$$C_x\left(\frac{1}{2^j}, \frac{k}{2^j}\right) = 2^{j/2} \int_{-\infty}^{+\infty} x(t) \psi_{jk}(2^j t - k) dt. \tag{2}$$

Finally, discretizing in time gives

$$C_x\left(\frac{1}{2^j}, \frac{k}{2^j}\right) = 2^{j/2} \sum_{n=1}^{N} x[n] \psi_{jk}(2^j n - k), \tag{3}$$

where N is the length of the input vector $x[n]$. The function $\psi \in L^2(R)$ is called an orthogonal wavelet if the family $\{\psi_{jk}\}$ is an orthonormal basis of $L^2(R)$: that is, $\langle \psi_{jk}, \psi_{lm} \rangle = \delta_{jl}\delta_{km}$, where δ is the Kronecker delta function. Note that the wavelet function is in $L^2(R)$ so that it has finite support in time. This differs from the trigonometric functions in Fourier analysis and gives the wavelet its ability to produce time information as well as frequency.

The discrete orthogonal wavelet algorithm is actually implemented as a series of convolution and decimation operations with discrete-time wavelet filter banks, such as those developed by Daubechies [4]. We adopt the compactly-supported wavelet, Daubechies 6. The length of the wavelet was chosen fairly arbitrarily. However, some of our classification work has suggested that longer wavelet filters (e.g., Daubechies 20) tend to miss some mines, while shorter wavelet filters (e.g., Daubechies 2) have many false alarms.

The discrete wavelet transform is implemented by a series of convolution and decimation operations with a pair of filters. Let $x = \{x[k]\}_{k=0}^{K-1}$ be the discrete version of input signal $x(t)$ of length $K = 2^n$. This can be either a row of the image or a column of the coefficients after the rows have been processed. In the fast discrete wavelet transform, the signal x is first decomposed into low and high frequency bands by the convolution-decimation (subsampling by two) operations of x with the pair of a low-pass filter $G = \{g_k\}_{k=0}^{L-1}$ and a high-pass filter $H = \{h_k\}_{k=0}^{L-1}$, where L is the length of the filter. In orthogonal wavelets, the length of the two filters is the same. The filters G and H satisfy the orthogonality conditions:

$$GH^* = HG^* = 0, \quad \text{and} \quad G^*G + H^*H = I. \tag{4}$$

G and H are Quadrature Mirror Filters (QMFs), which allow perfect reconstruction. The decomposition process continues iteratively on the resulting low frequency bands and each time the high frequency bands are left intact. The iteration stops when there is one low frequency coefficient and one high frequency coefficient. As a result, the frequency axis is partitioned *smoothly* and *dyadically* in an octave-band fashion, as shown in figure 4. Figure 4 shows the phase plane produced by the wavelet transform. The wavelet transform converts one-dimensional data into two-dimensional data. The horizontal, or t, axis can be labeled by time or position, depending on the nature of the data, and increases to

the right. The vertical, or f, axis is usually labeled frequency, or scale, and increases upward. Different spatial resolutions are given to different frequency bands. Low frequency with low spatial resolution is at the bottom, while, toward the top of the figure, the frequency resolution is decreased and the spatial resolution is increased. The entire phase plane is covered by disjoint cells of equal area which are called Heisenberg cells [5]. The uncertainty principle can be interpreted as a rectangular cell located around a position in the phase plane, (t,f), that represents an uncertainty region associated with (t,f). The total number of cells is equal to the dimension of the input vector.

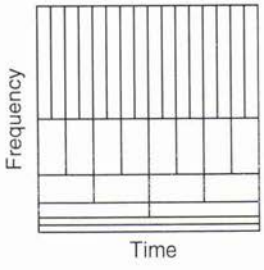

Figure 4. The Time/Frequency Phase Plane for the Standard Wavelet Bases

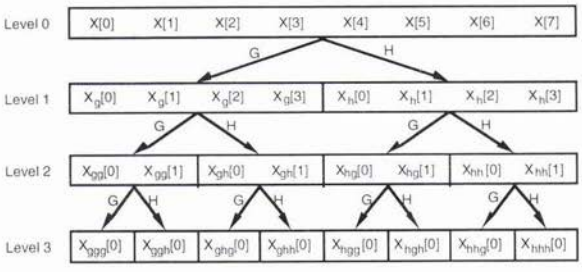

Figure 5. The Complete Wavelet Packet Decomposition Tree

2.2 Wavelet Packet

For the wavelet packet transform [6], the high frequency band, which is left intact during each iteration of the wavelet transform, is also decomposed into finer frequency bands. Figure 5 depicts the entire wavelet packet decomposition tree. Level 0 represents the original signal x. The level 1 decomposition generates Hx, labeled x_h, and Gx, labeled x_g. Gx represents the low frequency band and Hx represents the high frequency band. Applying the low-pass filter G and the high-pass filter H to both low and high frequency bands, we obtain four frequency bands H^2x, GHx, HGx and G^2x ordered in decreasing frequency. This is the level 2 decomposition. The decomposition process continues to the maximum depth of J, where $J = \log_2(n)$, and finer frequency resolutions are obtained toward lower levels. Since each decomposition level generates equal boxes corresponding to a uniform partition of the frequency axis, the time axis is also windowed uniformly. Hence, the extent of the support of each basis function is essentially constant for a decomposition level. Note that each level forms an orthonormal basis on which to project the side scan sonar image.

The full wavelet packet transform produces a wavelet packet tree structure containing many more coefficients than are needed to reconstruct the image. A basis vector of coefficients should be selected. The basis vector of transform coefficients can be constructed by selecting all the coefficients in a level, referred to as a level basis, or by selecting coefficients from different levels to obtain a "best" basis for the input data vector x. Here "best" can be in whatever measure desired. Certain rules apply which constrain the selection of coefficient sets to those having parent-child relationships within the wavelet packet decomposition tree [6]. For the fleet side scan sonar application, a level basis was selected which best characterized the spatial and spectral characteristics of the targets. The transform vector contains the same number of coefficients as the dimension of the input vectors from the original image, so this does not lead to compression. However, the forward transform increases the amount of energy contained in some individual coefficients and decreases others. Increasing the magnitude of individual coefficients increases the data requirements of the transform, but because the energy is conserved in the transform, most of the remaining coefficients are very small, approaching zero. Since deleting small coefficients does not significantly affect the total energy in the image, it will not cause significant distortion in the reconstructed image. The surviving coefficients now comprise the transform vector and can be encoded for compression using a zero run-length encoding technique.

2.3 Orthogonal Transform Algorithm

The algorithm for the orthogonal wavelet case is as follows: the one dimensional wavelet packet algorithm is applied twice, first to each row of the input matrix and then to each column of the row processed matrix. Only the level 3 basis coefficients for the lower half of the frequency spectrum are retained. This provides some filtering of high frequency noise. Next, the coefficients are sorted by magnitude for the spectrum of interest. Processing time is substantially reduced by only processing the pyramid algorithm to level 3 and by limiting the spectrum of interest to the lower half of the image bandwidth. The number of coefficients required to give the desired compression ratio is calculated; only this number of the largest coefficients, along with their locations in the coefficient matrix, are retained in the compressed image file. Zero run length encoding is currently used to encode coefficient locations. For reconstruction, the surviving coefficients are placed into their proper locations in the coefficient matrix while the rest of the coefficients are set to zero. The inverse wavelet packet transform is performed on each column, replacing the data that was there, and then on each row to produce the reconstructed image. This is the reconstructed image which is processed by the classification algorithm.

2.4 **Overall Performance**

The fleet side scan sonar images were compressed 25:1, 50:1, and 100:1 using the orthogonal wavelet technique. The original image si000206 and si000206 after 100:1 compression are shown in figures 2 and 3. The regions containing each of the two mines are shown in enlargements. At a compression ratio of 25:1, the most noticeable difference from the original image is the reduction of high frequency texture information from the background. This effect increases at 50:1 and, as can be seen at 100:1, the texture information has been mostly removed from the near range region. A significant weakening of the highlight or shadow contrast is not observed in either of the mines as the compression ratio is increased to 100:1.

Comparison of the automatic classifier on the original and wavelet compressed data sets demonstrated that only minimal degradation was realized in the compression process. On the original data set, the classifier demonstrated a probability of detection and classification (PdPc) of 91% and 0.28 false alarms per image (FA/image). For the data set compressed by the orthogonal transform algorithm, PdPc = 83% and FA/image = 1.1.

3. Matching Pursuit

3.1 **Description**

Mallat and Zhang [7] introduced a matching pursuit algorithm which allows a signal function to be decomposed into a linear expansion of functions belonging to a redundant dictionary of waveforms. Here, these waveforms are time-frequency atoms computed from sample mine and non-mine images. The assumption is that the time-frequency atoms consist of a pattern of wavelet coefficients related to the local structure of the target. The structure can be difficult to detect from individual coefficients because the forward transform diffuses the information across the basis. The advantage of the wavelet domain is that the signal waveform and dictionary waveform can be compressed using wavelet image compression techniques, preserving information about the local target structure without making assumptions about the nature of the target. This compression, in turn, minimizes the computational requirements on the matching pursuit algorithm.

Mallat and Zhang define a family, $D = \left(g_\gamma\right)_{\gamma \in \Gamma}$, of vectors in H, $H = L^2(R)$, such that $\|g_\gamma\| = 1$. Letting $f \in H$, a linear expansion of f is computed over a set of vectors selected from D to best match the local target structure. This is done by successive approximations of f with orthogonal projections on elements of D. Let $g_{\gamma_0} \in D$. The vector f can be decomposed into

$$f = \langle f, g_{\gamma_0} \rangle g_{\gamma_0} + \mathrm{R}f, \tag{5}$$

where Rf is the residual vector after approximating f in the direction of g_{γ_0}. The vector g_{γ_0} is orthogonal to Rf, hence

$$\|f\|^2 = |\langle f, g_{\gamma_0} \rangle| + \|\mathrm{R}f\|^2. \tag{6}$$

To minimize $\|\mathrm{R}f\|$, $g_{\gamma_0} \in D$, is selected such that $|\langle f, g_{\gamma_0} \rangle|$ is maximized.

Considering the iterative approach, let $\mathrm{R}^0 f = f$. To compute the residue $\mathrm{R}^n f$ at the n^{th} iteration, for $n \geq 0$, a vector $g_{\gamma_n} \in D$ is chosen which best matches the residue $\mathrm{R}^n f$. The residue $\mathrm{R}^n f$ is decomposed into

$$\mathrm{R}^n f = \langle \mathrm{R}^n f, g_{\gamma_n} \rangle g_{\gamma_n} + \mathrm{R}^{n+1} f, \tag{7}$$

which defines the residue at the order $n+1$. Since $\mathrm{R}^{n+1} f$ is orthogonal to g_{γ_n},

$$\|\mathrm{R}^n f\|^2 = |\langle \mathrm{R}^n f, g_{\gamma_n} \rangle|^2 + \|\mathrm{R}^{n+1} f\|^2. \tag{8}$$

Extending this decomposition up to order m, equation (7) yields

$$f = \sum_{n=0}^{m-1} \langle \mathrm{R}^n f, g_{\gamma_n} \rangle g_{\gamma_n} + \mathrm{R}^m f. \tag{9}$$

and equation (8) yields the energy conservation equation

$$\|f\|^2 = \sum_{n=0}^{m-1} |\langle \mathrm{R}^n f, g_{\gamma_n} \rangle|^2 + \|\mathrm{R}^m f\|^2. \tag{10}$$

The original vector f is decomposed into a sum of dictionary elements that are chosen to best match its residues. Although the decomposition is nonlinear, it maintains an energy composition as if it were a linear orthogonal decomposition.

In the matching pursuit algorithm for target classification, the inner product of the signal function with each of the dictionary waveforms is computed. The waveform which best matches the signal function is selected for the iteration and a residue is computed from the signal function. The residue is formed by subtracting the selected waveform, scaled by

the correlation coefficient, from the signal function to produce a new signal function for the next iteration. After the last iteration the signal function is represented as a linear expansion of the scaled dictionary waveforms. Target-like objects are discriminated from non-target signal functions by comparing the energy in the dictionary's target waveforms to that of the non-target waveforms. The class associated with the greater energy is assigned to the signal waveform.

3.2 Neural Network

The classification of the target-like signal functions can be further refined by a back-propagation neural network. In order to implement the matching pursuit/neural network classifier, it was necessary to divide the training set of data into two subsets, A and B. Half of the training set, subset A, was used as target waveforms for the matching pursuit dictionary. Non-target waveforms were also in the dictionary and were selected from areas away from the target from the same target file. The remaining half of the training set, subset B, was processed using the matching pursuit algorithm having subset A in the target dictionary. These results were then scored to form two lists for training the neural network, a list of the functions for correctly classified targets and a list for the false alarms. The list of functions for correctly classified targets was augmented by an additional set generated from targets in training subset B with offset centers. Offsetting the target center in a 3 by 3 pattern increased the number of target waveforms by a factor of nine. Each displaced center was located four pixels horizontally and vertically from its neighbor. The target and false alarm lists were used to train a neural network to discriminate targets from false alarms for the limited set of target-like signal functions classified by the matching pursuit algorithm.

3.3 Libraries

The sonar0 training set consisted of 30 image files, 15 containing bottom targets. In order to decide how to group the targets into subsets A and B, each target in the training set was processed by a matching pursuit algorithm having a dictionary containing the other 14 targets. This test was conducted to identify target images having unique features and those have features redundant with other target images in the dictionary. Two of the targets were found to have unique characteristics based on the results of the matching pursuit processing. A minimum set of 5 targets, including the unique targets, was selected for the matching pursuit dictionary. This approach maximized the number of target samples available to train the neural network stage of the classifier. The dictionary therefore consisted of the 5 target samples and 5 non-target samples randomly selected from the same image file. To scan an image file, a 32 by 32 pixel subimage was selected. Therefore each of the images in the dictionary also corresponded to a 32 by 32 subimage. The number of entries in the dictionary was increased nine fold by duplicating each of the target entries in a 3 by 3 offset pattern, where each displaced center was located four pixels horizontally and vertically from its neighbor. This improved the efficiency of scanning an image file by stepping the subimage processed as the signal function in 8 pixel increments. The sonar0 side scan sonar images contain 512 by 1024 pixels. Scanning a 32 by 32 subimage through a complete side scan sonar image required 8,196 increments.

3.4 Results

The signal functions and dictionary waveforms for the matching pursuit algorithm were compressed wavelet transformed subimages. The Daubechies 6 wavelet packet was used with filtering at levels 1 and 2. This reduced the 32 by 32 coefficient matrix to a 16 by 16 and 8 by 8 which were reformatted to a column vector. This allowed the projection of the signal function onto the dictionary waveforms to be computed as an inner product with the dictionary vectors.

Because of the limited number of target samples in the training set, only modest results were realized after preliminary testing of matching pursuit on the sonar0 test set. With filtering at level 1, PdPc = 89% and at level 2, PdPc = 78%. The neural network further reduced the FA/image by 50%, but dividing the training set into subset A and B degraded the performance of both classifiers. To implement both a matching pursuit dictionary and a neural net training set, unique targets existing in the training set therefore could only be assigned to one or the other subset. The subset that did not have information on the unique feature did not detect targets which would have otherwise been found.

4. Wavelet Coefficient Baysian Classifier

4.1 Generating Probability Density Functions for Coefficients

There are many more coefficients in the wavelet tree structure, shown in figure 5, than are needed for reconstruction of the image or for classification. The question is which coefficients should be used for classification. The matching pursuit algorithm answers this by using a subset of the coefficients in a basis based on compression. The selection of the basis was fairly arbitrary. The statistical classifier described here is an attempt to determine the ability of individual coefficients in the wavelet packet transform to discriminate between two classes of objects. There are a total of $n\log(n)$ coefficients plus the n original data values themselves to choose from. In general, the number of inputs to a classifier will be less than or equal to the number of data points in the original signal. In order to determine which coefficients are best for classification, the probability density function (pdf) for each coefficient can be estimated. By generating the conditional pdf's for each coefficient, one can develop the optimal, or Baysian, classifier. The problem here is to determine the presence or absence of a mine-like object. Thus two conditional pdf's correspond to each coefficient. Transforming the image when there is a mine present, one obtains the values of each coefficient for the mine-present case. By transforming enough images with mines, one can use the distribution of the magnitude of each coefficient as an estimate of its pdf when a mine is present. Transforming an image with no mine produces the values for each coefficient

for the no-mine case. With images where no mine is present, the distribution of the coefficient magnitudes is an estimate of the pdf for the no-mine case.

There are two problems which come up immediately with this procedure. First, the number of images available with and without mines is very limited. To get a good estimate of the pdf's, a large number of examples is needed in each case. Second, not every coefficient is affected by the presence of a mine in the image. Because of the resolution in position of the wavelet transform, the extent of the coefficient may not be on the mine in the image. In fact, if the entire image is transformed, there are very few coefficients which are actually affected by the presence of a mine. The others should all be considered examples of non-mine coefficients.

The first problem is handled by not relying on an accurate pdf for each coefficient. Since there are a large number of coefficients, one can compensate for the inaccuracies of any one pdf by using many of them. There are two methods of handling the second problem. First, one can take the transform of only a small window of the image, approximately the size of a mine. Then, most, if not all, of the coefficients are affected by a mine in the window. The window can be slid through the image and a classification made for each location of the window. This method works well, but is very costly in the number of calculations needed. A second method involves only a single transform of the image. In this method, one transform is done on the entire image producing a large set of coefficients. Instead of scanning through the image in position, the coefficients from a location in the image are determined and only those are fed to the classifier. In effect, the image is scanned by selecting the proper set of coefficients in the right order.

4.2 **Discrimination Threshold**

In the binary classification case there are the following two hypothesis:

1) H_0 - no mine present, and

2) H_1 - at least one mine present.

The Bayesian test can be written as

$$H_0 \text{ if } : \frac{p_{R|H_1}(R|H_1)}{p_{R|H_0}(R|H_0)} < \eta, \quad H_1 \text{ if } : \frac{p_{R|H_1}(R|H_1)}{p_{R|H_0}(R|H_0)} > \eta \tag{11}$$

where $p_{R|H_0}(R|H_0)$ and $p_{R|H_1}(R|H_1)$ are the conditional probability densities and η is the threshold [8]. The ratio on the right is the likelihood ratio and is a random variable. The threshold is a number based on the a priori probabilities and the cost of each course of action. If the likelihood ratio is greater than η, the H_1 hypothesis is chosen and if the likelihood ratio is less than η, the H_0 hypothesis is chosen. Because it is difficult to assign costs and a priori probabilities in this problem, the Neyman-Pearson test is used. In this test, the conditional probabilities, P_F, probability of false alarm, and P_D, probability of detection, are used. A value of P_F is specified and this determines the value of η.

4.3 **Selection of Coefficients for Classifier**

Given a desired probability of false alarm, the pdf's of the coefficients and the threshold determine a probability of detection. This could be done for individual coefficients, although that was not done here. At a particular level in the wavelet packet transform, and at a specific frequency (a frequency bin), there is a set of coefficients which depend only on position. Each coefficient corresponds to the same waveform which only differs by a shift in position. Since the probability of the mine being at any particular location is the same, it doesn't make sense to pick one coefficient out of the set as being better than the others for classification. Instead, all of the coefficients in the set which only differ by a shift are grouped into one pdf. This produces more examples for each pdf and so helps to improve the estimate. The pdf's now provide information about which frequency bins are best for classification.

4.4 **Classification**

Because the pdf's for the mine and non-mine cases overlap and are not perfect, there would be considerable missclassification using any one pdf. To improve the classification, many pdf's are used. To classify an area of the image, the magnitude of all of the coefficients which overlap that area are checked via the Bayesian test. If a majority indicate the presence of a mine, the area is classified as mine-like. To reduce the calculations required, only coefficients with the best pdf's, those with the highest P_D, can be used for the voting. The overall classification procedure is as follows. The entire image is transformed producing a matrix of coefficients the same size as the image. The bases used for this transform should contain the coefficient bins which were determined to be best for classification. Each coefficient in the transform is compared to the threshold as shown in equation (11) for its particular frequency bin, and a classification is made. All the coefficients which detected a mine are compared to see if they fall on the same location in the image. If enough mine classifications are at the same location, that location is classified as mine-like.

4.5 **Results**

Preliminary results produced using the statistical classifier have been encouraging. The method described using the transform of only a small window of the image, approximately the size of a mine, was run on each mine in the training set to generate the pdf's for the coefficients. Because of the small size of the window, the pdf for every coefficient at every level was estimated. The best pdf's were then used to classify the images in the test set. The receiver operating

characteristic (ROC) curve for the results is still being generated. Work has started on the transform coefficients from the whole image. Observations of the mine and non-mine cases show that pdf's for each case appear to be very similar. The best pdf's for classification have yet to be determined.

5. Conclusions

It has been shown that wavelet packet based transforms are an effective compression scheme. A high level of automatic classifier performance on reconstructed side scan sonar images, compressed by as much as 100:1, demonstrates that these schemes effectively preserve the classification features of underwater mines. Promising results have also been presented for detection and classification techniques in the wavelet domain as a guide to the selection of coefficients in the compression process. The matching pursuit algorithm, which attempts to find a best match in a library of coefficient sets, and the statistical analysis, which attempts an optimal discrimination based on individual coefficients, both have shown good results in detecting mine-like areas. Correctly identifying coefficients related to the local structure of mine-like objects provides the ability to enhance the fidelity of the associated areas in the reconstructed image, while maintaining the required compression ratio.

Further analysis will be conducted using a larger side scan sonar data set to resolve problems realized when there are only a small number of mine signatures available, some of which are unique. Redundant dictionaries of time-frequency atoms over multiple bases will also be explored. Even with improvements made, operator intervention will continue to be needed to reconcile false alarms from detected mines. The voluminous amounts of data collected by a 6 knot UUV will still generate a number of false alarms per hour. The enhanced fidelity provided by the methods examined in this paper furnishes operators with a higher quality image with which to reconcile targets and false alarms.

Acknowledgments

The authors would like to thank ONR321TS, Dr. Randy Jacobson, for sponsoring this work, Dr. Gerald Dobeck and his colleagues at the Naval Surface Warfare Center, Dahlgren Division, Coastal Systems Station, for their automatic classifier, and Dr. Börn Jawerth and his colleagues at the University of South Carolina and Summus Ltd. for their work with us using the biorthogonal wavelet transform.

References

[1] J. Impagliazzo, W. Greene, G. Dobeck, Q. Huynh, L. Smedley, B. Jawerth, and L. Mygatt, "Wavelet Based Data Compression for Communication of Side Scan Sonar Images", JUA, July 1997.

[2] G.J. Dobeck and J.C. Hyland, "Automated Detection and Classification of Sea Mines in Sonar Imagery," in *Proceedings of the SPIE 11-th Annual International Symposium on Aerospace/Defense Sensing, Simulation and Control,* 21-24 April 1997, Orlando, Florida, Vol. 3079: Detection and Remediation Technologies for Mines and Minelike Targets.

[3] S. Mallat, "Multiresolution Approximations and Wavelet Orthonormal Bases of $L^2(R)$", Trans. Amer. Math. Soc. **315**, 69-88, 1989.

[4] I. Daubechies, *Ten Lectures on Wavelets*, volume 61 of CBMS-NSF Regional Conference Series in Applied Mathematics, SIAM (1992).

[5] R.R. Coifman and M.V. Wickerhouser, "Entropy-Based Algorithms for Best Basis Selection," IEEE Trans. Inf. Theory, **38** (2), March 1992.

[6] R.R. Coifman, Y. Meyer, and M.V. Wickerhauser, "Wavelet Analysis and Signal Processing," in *Wavelets and their Applications*, eds. Ruskai et al. (Jones and Bartlett, Boston 1992), pp. 153-178.

[7] S G Mallat and Z Zhang, "Matching Pursuit With Time-Frequency Dictionaries," IEEE Trans. on Sig. Proc., Vol 41, no. 12, pp. 3397-3415, December 1993.

[8] H. L. Van Trees, *Detection, Estimation, and Modulation Theory*. New York, John Whiley & Sons, Part I Detection, Estimation, and Linear Modulation Theory, ch. 2, pp. 23-36, 1968.

A Unified Model for Seabed Volume and Roughness Scattering

Anatoliy N. Ivakin

Andreev Acoustics Institute,
Shvernika 4, Moscow 117036, RUSSIA
E-mail: aniva@glasnet.ru

Abstract

Seabed scattering is considered taking into account perturbations of different types : volume inhomogeneities and roughness of the interfaces. A description is given in terms of plane waves. The first-order perturbation solution is presented for the scattering amplitude and scattering cross-section. Cross-correlation matrixes between the roughness of different interfaces and between the volume fluctuations of different parameters are involved. The model is generalized to the case of the fluid sediment placed over an arbitrary basement having its own reflection and scattering properties.

1. Introduction

Sound scattering from the seabed, generally, can be attributed to two major mechanisms, which are due to seabed roughness and volume inhomogeneities. It is known that contributions of these two components of scattering can be comparable for realistic values of seabed parameters [1, 2, 3, 4, 5, 6, 7] or it can be difficult to distinguish and separate them in practice [8, 9, 10, 11, 12]. In such cases it is more justified to consider volume and roughness scattering mechanisms in the frame of a unified model. Each of this two mechanisms in turn can contain different components, which are due to different irregularities of the seabed medium. For unconsolidated (fluid) sediments, volume inhomogeneities are spatial fluctuations of different parameters, the density and compressibility, with respect to their mean values. Roughness component can be attributed as to the seabed surface (water-sediment interface) and to various internal interfaces in the sediment medium as well. Their possible cross-correlations should be taken into account.

Generally, in any model of scattering, a certain mean (averaged) structure of the medium is implied. A related problem is the influence of different parameters of the mean seabed structure on the scattered field. In many cases, inhomogeneous rough seabeds can be considered as stratified (plane-layered on the average), i.e., having mean parameters dependent only upon the depth. Effects of stratification depend on many parameters, such as the frequency, thickness of seabed layers, vertical gradients of the mean parameters and others. Only in the case of sufficiently high frequencies, the seabed medium can be treated as homogeneous on the average because of small sound penetration. At lower frequencies, however, the effects of stratification become essential due to scattering from internal interfaces and volume inhomogeneities of deep layers as well as the influence of regular refraction. For a number of particular seabed models, it has been shown that such layering can have a strong effect on the scattered field [13, 14, 15, 16, 17].

In this paper, a unified model is presented that includes both volume and roughness perturbations of different types in arbitrarily stratified sediment and permits a general consideration of seabed scattering for a wide low-to-high frequency range. The model is based on a unified approach to volume and roughness scattering [18, 19]. The approach considers all the medium irregularities as different kinds of volume perturbations. In this paper, the first-order solution is presented for the scattering amplitude and scattering cross-section. Expressions for the roughness and volume scattering cross-section involve cross-correlation matrixes between the roughness of different interfaces and between the volume fluctuations of different parameters. This model is then generalized to the case where the fluid sediment is placed over an arbitrary basement (e.g., elastic) having its own reflection and scattering properties.

2. Seabed Model

Seabed sediment is considered as a layered fluid medium with volume inhomogeneities and rough interfaces. The interfaces between sediment layers are of the form

$$z = z_j + \zeta_j(\mathbf{R}), \ \mathbf{R} = (x, y), \ j = 1, 2, ..., N, \tag{1}$$

where ζ_j and z_j correspond to roughness and mean plane of the j-th interface. Roughness is assumed to be small comparing to the wavelength.

Volume inhomogeneities are due to spatially varying parameters, the compressibility and density,

$$\tilde{\kappa}(\mathbf{r}) = \kappa(z)(1 + \epsilon_\kappa(\mathbf{r})), \ \tilde{\rho}(\mathbf{r}) = \rho(z)(1 + \epsilon_\rho(\mathbf{r})), \tag{2}$$

where $\kappa(z)$ and $\rho(z)$ are their mean depth-dependences corresponding to an unperturbed plane-layered medium, $\epsilon_\beta(\mathbf{r})$ are relative volume fluctuations defined by random functions of position vector, $\mathbf{r} = (\mathbf{R}, z)$, and assumed to be small, $|\epsilon_\beta| \ll 1$, $\beta = \kappa, \rho$.

Note that the choice of the compressibility and density as bulk parameters is somewhat arbitrary. In particular, considering density and sound speed as a pair of independent parameters, one obtains

$$\epsilon_\kappa = -2\epsilon_c - \epsilon_\rho \tag{3}$$

with ϵ_c as the relative volume fluctuation of sound speed. The mean sound speed is defined as $c(z) = (\kappa\rho)^{-1/2}$. In the case of the one-parameter medium, where all the parameters are controlled by changes of one parameter, e.g., the porosity, s, one obtains

$$\epsilon_\beta(\mathbf{r}) = a_{\beta s}(z)\epsilon(\mathbf{r})_s, \ a_{\beta s} = \frac{s}{\beta}\frac{d\beta}{ds}, \ \beta = \kappa, \rho, c. \tag{4}$$

Relations between different parameters that provide estimates for $a_{\beta s}$ can be taken from compilations of geoacoustic data, for example Hamilton's [20].

All the mean (unperturbed) parameters, compressibility, density and sound speed, are continuous functions $\beta = \beta_j(z)$, $\beta = \kappa, \rho, c$, within the j–th layer, at $z_j < z < z_{j-1}$. They can have discontinuity at the mean interfaces, $z = z_j$,

$$D_j(\beta) = (\beta_{j+1} - \beta_j)_{z=z_j}, \ \beta = \kappa, \rho, c, \tag{5}$$

where D_j denotes the contrast (difference) of the corresponding parameter or function at the j-th interface.

3. Zero-Order Field

The unperturbed (zero-order) field for a plane-layered medium with depth-dependent parameters can be defined in terms of plane waves. Let a plane wave of unit amplitude having wave vector with transverse component $\mathbf{K}_0$ be incident from a homogeneous water half-space, $z > 0$, i.e.,

$$p_{inc}(\mathbf{r}, \mathbf{K}_0) = \exp\left(i\mathbf{K}_0 \cdot \mathbf{R} - i\,\nu_1(K_0)z\right), \tag{6}$$

where $\nu_1(K) = \sqrt{k_1^2 - K^2}$ defines the vertical component of the wave vector with $k_1 = \omega/c_1$ as the wavenumber in the water (first layer). The zero-order solution for the field is of the form

$$p_0(\mathbf{r}, \mathbf{K}_0) = \psi(z, K_0)\exp(i\mathbf{K}_0 \cdot \mathbf{R}), \tag{7}$$

where ψ is its complex amplitude, which obeys Helmholtz equation

$$\left[\rho\partial_z\left(\rho_j^{-1}\partial_z\right) + k^2 - K^2\right]\psi(z, K) = 0, \ k = \omega/c(z), \tag{8}$$

and boundary (continuity) conditions at the mean interfaces, $z = z_j$,

$$D_j(\psi) = 0, \ D_j\left(\rho^{-1}\partial_z\psi\right) = 0. \tag{9}$$

Within j–th continuous fluid layer, at $z_j < z < z_{j-1}$, the function $\psi = \psi_j(z, K)$ can be found by means of well-developed methods [21]. In the vicinity of the mean interfaces, $z = z_j$, the solution for $\psi_j(z, K)$ can be expressed in terms of downward and upward local plane waves with corresponding transmission and reflection

coefficients. The transmission coefficient, $W_j(K)$, is defined as the amplitude of the downward wave incident on the $j-$th interface, $z = z_j$. Corresponding relative amplitude of the upward wave gives the reflection coefficient, $V_j(K)$. Beneath lowest interface in sediment, at the plane $z = z_{N+1}$, an arbitrary basement can be considered characterized by its reflection coefficient, V_{N+1}, which can be taken as an arbitrary function of K, depending on the basement type. The basement reflection coefficient, $V_{N+1}(K)$, is an input parameter for the calculations of the function $\psi(z, K)$ at $z > z_{N+1}$.

4. Scattering Amplitude

The scattered field, $\tilde{p}_s = p - p_{inc}$, above the highest point on the water-seabed interface can be expressed as a superposition of plane waves,

$$\tilde{p}_s(\mathbf{r}, \mathbf{K}_0) = \int d^2K \ \tilde{A}(\mathbf{K}, \mathbf{K}_0) \exp(i\mathbf{K} \cdot \mathbf{R} + i\nu_1(K)z). \tag{10}$$

where $\tilde{A}(\mathbf{K}, \mathbf{K}_0)$ is the so-called scattering amplitude. When it has been found, all the basic characteristics of the scattered field can be determined. In particular, the scattering cross section, σ, is obtained through the equation

$$< A(\mathbf{K}, \mathbf{K}_0) A^*(\mathbf{K}', \mathbf{K}_0) >= \delta(\mathbf{K} - \mathbf{K}')\sigma(\mathbf{K}, \mathbf{K}_0) \ . \tag{11}$$

where $A(\mathbf{K}, \mathbf{K}_0) = \nu_1(\mathbf{K}_0) \left[\tilde{A}(\mathbf{K}, \mathbf{K}_0) - < \tilde{A}(\mathbf{K}, \mathbf{K}_0) > \right]$ is defined by the incoherent component of the scattering amplitude and it is assumed that the statistics of the scattering medium are stationary in the two transverse (horizontal) coordinates. In this paper, $A(\mathbf{K}, \mathbf{K}_0)$ is called also the scattering amplitude for brevity.

4.1. Layered fluid. First-order solution

General expression for the first-order scattering amplitude, or its Born approximation, can be presented in the form

$$A(\mathbf{K}, \mathbf{K}_0) = A^{(r)}(\mathbf{K}, \mathbf{K}_0) + A^{(v)}(\mathbf{K}, \mathbf{K}_0).$$

where $A^{(r)}$ and $A^{(v)}$ are the roughness and volume scattering amplitudes,

$$A^{(v)}(\mathbf{K}, \mathbf{K}_0) = i \int dz \ [\tilde{\epsilon}_\kappa(\mathbf{K} - \mathbf{K}_0, z)\phi_\kappa(z, \mathbf{K}, \mathbf{K}_0) + \tilde{\epsilon}_\rho(\mathbf{K} - \mathbf{K}_0, z)\phi_\rho(z, \mathbf{K}, \mathbf{K}_0)]. \tag{12}$$

$$A^{(r)}(\mathbf{K}, \mathbf{K}_0) = i \sum_j \tilde{\zeta}_j(\mathbf{K} - \mathbf{K}_0)\phi_\zeta(z_j, \mathbf{K}, \mathbf{K}_0). \tag{13}$$

where $\tilde{\epsilon}_\beta(\mathbf{K}, z)$, $\beta = \kappa, \rho$, and $\tilde{\zeta}_j(\mathbf{K})$, are the 2D Fourier transformants of the corresponding perturbation and roughness with respect to horizontal coordinates, ϕ_β are the form-factors dependent only upon the unperturbed structure of the medium and defined for different kinds of the medium perturbation as follows

$$2\phi_\kappa(z, \mathbf{K}, \mathbf{K}_0) = \frac{n^2(z)}{m(z)} \Psi_1(z, K, K_0). \tag{14}$$

$$2\phi_\rho(z, \mathbf{K}, \mathbf{K}_0) = \frac{(\mathbf{K} \cdot \mathbf{K}_0)}{k_1^2 m(z)} \Psi_1(z, K, K_0) + m(z)\Psi_2(z, K, K_0). \tag{15}$$

$$2\phi_\zeta(z_j, \mathbf{K}, \mathbf{K}_0) = \left[D_j(n^2/m) - \frac{(\mathbf{K} \cdot \mathbf{K}_0)}{k_1^2} D_j(1/m) \right] \Psi_1(z_j, K, K_0) + D_j(m)\Psi_2(z_j, K, K_0). \tag{16}$$

where $n(z) = c_1/c(z)$ and $m(z) = \rho(z)/\rho_1$ are the mean refraction index and relative density, c_1 and ρ_1 are the sound speed and density in the water half-space, Ψ_1 and Ψ_2 are continuous functions,

$$\Psi_1(z, K, K_0) = k_1^2 \psi(z, K)\psi(z, K_0). \tag{17}$$

$$\Psi_2(z, K, K_0) = m^{-2}(z)\partial_z \psi(z, K)\partial_z \psi(z, K_0). \tag{18}$$

Equation (12), using (3) and (4), can be easily rewritten for other choice of medium parameters. In the case of the one-parameter medium, the corresponding form-factor, ϕ_s, is defined as follows

$$\phi_s = a_{\kappa s}\phi_\kappa + a_{\rho s}\phi_\rho. \tag{19}$$

Using (14) and (15), it can be presented in the form analogous to (16),

$$2s^{-1}\phi_s(z,\mathbf{K},\mathbf{K}_0) = \left[\frac{d}{ds}(n^2/m) - \frac{(\mathbf{K}\cdot\mathbf{K}_0)}{k_1^2}\frac{d}{ds}(1/m)\right]\Psi_1(z,K,K_0) + \frac{d}{ds}(m)\Psi_2(z,K,K_0). \tag{20}$$

Then the volume scattering amplitude is written in the form close to (13)

$$A(\mathbf{K},\mathbf{K}_0) = i\int dz\,\tilde{\epsilon}(\mathbf{K}-\mathbf{K}_0,z)\phi_s(z,\mathbf{K},\mathbf{K}_0). \tag{21}$$

It is convenient to normalize functions ψ for each layer by the amplitude of incident on this layer wave as follows

$$\psi(z,K) = W_j(K)\psi_{j+1}(z,K),\ z_{j+1} < z \le z_j. \tag{22}$$

Then all the form-factors, ϕ_β, can be presented in the form

$$\phi_\beta(z,\mathbf{K},\mathbf{K}_0) = P_j(K,K_0)F_\beta(z,\mathbf{K},\mathbf{K}_0),\ z_{j+1} < z \le z_j, \tag{23}$$

$$P_j(K,K_0) = W_j(K)W_j(K_0). \tag{24}$$

Defined by (23) normalized form-factors, F_β, are indepenent from the mean structure of the medium at $z > z_j$.

4.2. Fluid over basement

The scattering amplitude of the layered medium can be presented in the form

$$A(\mathbf{K},\mathbf{K}_0) = \sum_j P_j(K,K_0)A_j(\mathbf{K},\mathbf{K}_0), \tag{25}$$

with A_j as the scattering amplitude of the $(j+1)$−th inhomogeneous layer, $z_{j+1} < z \le z_j$, including rough j−th interface,

$$A_j(\mathbf{K},\mathbf{K}_0) = A_j^{(r)}(\mathbf{K},\mathbf{K}_0) + A_{j+1}^{(v)}(\mathbf{K},\mathbf{K}_0). \tag{26}$$

These amplitudes are defined for a plane incident wave of a unit amplitude in an infinite homogeneous half-space with parameters $\rho_j(z_j)$ and $c_j(z_j)$ over j−th interface. Note that the volume component with $j = 0$, $A_1^{(v)}$, can be included in (25) for generality corresponding to scattering from the first layer, $z_1 < z < z_0$, i.e., from inhomogeneities in the water over the seabed. The upper boundary of this layer, $z = z_0$, is totally transparent and has no corresponding roughness scattering component, i.e., $A_0^{(r)} = 0$.

The volume and roughness local scattering amplitudes for the layered fluid (components with $j \le N$) depend upon properties of the basement only through the reflection coefficient of the basement, $V_{N+1}(K)$, as an input parameter. However, the above expression for the total scattering amplitude, (25), can be easily generalized to the case where the basement beneath a layered fluid medium not only reflects but also scatters. In this case, the last term, A_{N+1}, is treated as the scattering amplitude of the basement containing roughness and volume components of the form

$$A_{N+1}^{(r)}(\mathbf{K},\mathbf{K}_0) = i\tilde{\zeta}_{N+1}(\mathbf{K}-\mathbf{K}_0)F_\zeta(z_{N+1},\mathbf{K},\mathbf{K}_0), \tag{27}$$

$$A_{N+2}^{(v)}(\mathbf{K},\mathbf{K}_0) = i\int\limits_{z<z_{N+1}} dz\sum_\beta \tilde{\epsilon}_\beta(\mathbf{K}-\mathbf{K}_0,z)F_\beta(z,\mathbf{K},\mathbf{K}_0), \tag{28}$$

where the roughness and volume scattering form-factors, F_ζ and F_β, depend on the basement type and its mean parameters.

As examples of perfectly scattering basements, hard or soft (impenetrable) rough surfaces can be used with $V_{N+1} = \pm 1$, respectively. Corresponding expressions for the scattering amplitude can be easily obtained from (16) as the limit cases,

$$F_\zeta(z_{N+1}, \mathbf{K}, \mathbf{K}_0) = F^{\pm}(\mathbf{K}, \mathbf{K}_0), \tag{29}$$

$$F^{+}(\mathbf{K}, \mathbf{K}_0) = -\frac{2}{m_{N+1}} \left(k_{N+1}^2 - \mathbf{K} \cdot \mathbf{K}_0\right), \tag{30}$$

$$F^{-}(\mathbf{K}, \mathbf{K}_0) = \frac{2}{m_{N+1}} \nu_{N+1}(K) \nu_{N+1}(K_0). \tag{31}$$

As a realistic example of a penetrable scattering basement, an elastic rough half-space with volume inhomogeneities can be used. In this case, the roughness and volume scattering amplitudes are of the form (27) and (28). Spatially fluctuating parameters are the density, compressional and shear speed, i.e., $\beta = \rho, c_p, c_t$. Expressions for the corresponding volume and roughness form-factors, F_β and F_ζ, can be found in [22] and [23], respectively. Generalized expressions for the scattering amplitude and scattering cross-section of an elastic rough and inhomogeneous half-space and their analysis with a number of numerical examples will be presented in [24, 25].

5. Scattering Cross-Section

If the roughness and volume scattering components are uncorrelated, the total scattering cross-section is of the form

$$\sigma(\mathbf{K}, \mathbf{K}_0) = \sigma^{(r)}(\mathbf{K}, \mathbf{K}_0) + \sigma^{(v)}(\mathbf{K}, \mathbf{K}_0), \tag{32}$$

where indices r and v correspond to the roughness and volume scattering cross-section. The roughness component is defined as follows

$$\sigma^{(r)}(\mathbf{K}, \mathbf{K}_0) = \sum_{j,l} P_j(K, K_0) P_l^*(K, K_0) F_\zeta(z_j, \mathbf{K}, \mathbf{K}_0) F_\zeta^*(z_l, \mathbf{K}, \mathbf{K}_0) \Phi_{jl}(\mathbf{K} - \mathbf{K}_0), \tag{33}$$

$$\Phi_{jl}(\mathbf{K}) = (2\pi)^{-2} \int B_{jl}(\mathbf{R}) \exp(-i\mathbf{K} \cdot \mathbf{R}) d^2R, \tag{34}$$

$$B_{jl}(\mathbf{R}) = < \zeta_j(\mathbf{R}') \zeta_l(\mathbf{R}' + \mathbf{R}) >, \tag{35}$$

where Φ_{jl} and B_{jl} are the cross-spectral and cross-correlation matrixes of the j-th and l-th interfaces roughness, assumed to be statistically uniform. In the case when irregularities of the different interfaces are uncorrelated, i.e., $B_{jl}^{(\zeta)} = \delta_{jl} B_j$, where δ_{jl} is the Kronecker symbol, from (33) we obtain

$$\sigma^{(r)}(\mathbf{K}, \mathbf{K}_0) = \sum_j |P_j(K, K_0)|^2 \sigma_j(\mathbf{K}, \mathbf{K}_0), \tag{36}$$

where σ_j is the $j-$th interface scattering cross-section,

$$\sigma_j(\mathbf{K}, \mathbf{K}_0) = |F_\zeta(z_j, \mathbf{K}, \mathbf{K}_0)|^2 \Phi_j(\mathbf{K} - \mathbf{K}_0), \tag{37}$$

with $\Phi_j = \Phi_{jj}^{(\zeta)}$ as the spatial spectrum of the roughness of the $j-$th interface.

For the volume scattering cross-section, assuming that inhomogeneities of different layers are uncorrelated, one obtains

$$\sigma^{(v)}(\mathbf{K}, \mathbf{K}_0) = \sum_j |P_j(K, K_0)|^2 \sigma_{j+1}^{(v)}(\mathbf{K}, \mathbf{K}_0). \tag{38}$$

Here $\sigma_{j+1}^{(v)}$ is the volume scattering cross-section of the $(j+1)-$th layer defined as follows

$$\sigma_{j+1}^{(v)}(\mathbf{K}, \mathbf{K}_0) = \sum_{\beta,\beta'} \int \int_{z_{j+1}}^{z_j} dz\, dz' F_\beta(z, \mathbf{K}, \mathbf{K}_0) F_{\beta'}^*(z, \mathbf{K}, \mathbf{K}_0) \Phi_{\beta\beta'}(\mathbf{K} - \mathbf{K}_0, z, z'), \tag{39}$$

$$\Phi_{\beta\beta'}(\mathbf{K}, z, z') = (2\pi)^{-2} \int B_{\beta\beta'}(\mathbf{R}, z, z') \exp(-i\mathbf{K} \cdot \mathbf{R}) d^2R, \tag{40}$$

$$B_{\beta\beta'}(\mathbf{R}, z, z') = \left\langle \epsilon_\beta(\mathbf{R}', z) \epsilon_{\beta'}^*(\mathbf{R}' + \mathbf{R}, z') \right\rangle, \tag{41}$$

where $\Phi_{\beta\beta'}$ and $B_{\beta\beta'}$ are the 2D cross-spectral and cross-correlation matrixes of volume inhomogeneities, assumed to be statistically uniform in horizontal directions. In the case of one-parameter medium, using (21), equation for $\sigma^{(v)}_{j+1}$ is of the same form as (39) but contains only one term with $\beta = \beta' = s$.

If inhomogeneities are statistically uniform in all directions, i.e., $B_{\beta\beta'} = B^{(v)}_{\beta\beta'}(\mathbf{r})$, where $\mathbf{r} = (\mathbf{R}, z' - z)$, (39) can be presented in the form

$$\sigma^{(v)}_{j+1}(\mathbf{K}, \mathbf{K}_0) = \sum_{\beta,\beta'} \int d\gamma\, \tilde{F}_\beta(\gamma, \mathbf{K}, \mathbf{K}_0) \tilde{F}^*_{\beta'}(\gamma, \mathbf{K}, \mathbf{K}_0) \Phi^{(v)}_{\beta\beta'}(\mathbf{K} - \mathbf{K}_0, \gamma), \tag{42}$$

where $\tilde{F}_\beta$ is the form-factor defined by the equation

$$\tilde{F}_\beta(\mathbf{K}, \mathbf{K}_0, \gamma) = \int_{z_{j+1}}^{z_j} dz\, F_\beta(z, \mathbf{K}, \mathbf{K}_0) \exp(i\gamma z) \tag{43}$$

and $\Phi^{(v)}_{\beta\beta'}(\mathbf{k})$ is the 3D cross-spectral matrix of volume inhomogeneities,

$$\Phi^{(v)}_{\beta\beta'}(\mathbf{k}) = (2\pi)^{-3} \int B^{(v)}_{\beta\beta'}(\mathbf{r}) \exp(-i\mathbf{k} \cdot \mathbf{r}) d^3 r, \tag{44}$$

with $\mathbf{k} = (\mathbf{K} - \mathbf{K}_0, \gamma)$.

Equations (33), (39) and (42) give first-order solution for the scattering cross-section of a stratified seabed expressed through the cross-spectral and cross-correlation functions of different kinds of volume inhomogeneities and rough interfaces. The mean seabed structure is involved into the model of scattering through of the form-factors, F_ζ and F_β. They are defined once the function $\psi(z, K)$ is determined for the given depth dependence of the unperturbed medium parameters, $\rho(z)$ and $c(z)$, and the basement reflection coefficient, $V_{N+1}(K)$. The basement roughness and volume scattering is involved into these equations through the terms with $j = N + 1$ and corresponding form-factors.

The relationships between the seabed scattering cross-section and roughness spectra are defined in distinct form by (33) and (36). For volume scattering such relationships, generally, are more complicated and expressed through the integrals in (39) and (42). In the general case, for an arbitrary seabed stratification, these integrals can be calculated numerically. But in a number of particular cases, e.g., for the layers homogeneous on the average, they can be simplified and estimated analytically. Details and a number of numerical examples for different seabed types will be given in [26].

References

[1] A. N. Ivakin and Yu. P. Lysanov "Underwater sound scattering by volume inhomogeneities of a bottom medium bounded by a rough surface", *Soviet Physics-Acoustics*, **27**(3), pp.212-215, 1981.

[2] P. A. Crowther, "Some statistics of the sea-bed and acoustic scattering therefrom", in *Acoustics and Sea-Bed*, Edited by N. G. Pace, Bath University Press, England, pp.147-156, 1983.

[3] A. N. Ivakin, "Sound scattering by random volume inhomogeneities and small surface roughness of an underwater ground", *Voprosy sudostroenija, Akustika* (17), pp.20-25, 1983 (in Russian).

[4] D. R. Jackson, D. P. Winebrenner and A. Ishimaru A, "Application of the composite roughness model to high-frequency bottom backscattering", *J. Acoust. Soc. Am.*, **79**(5), pp.1410-1422, 1986.

[5] D. R. Jackson and K. B. Briggs, "High-frequency bottom backscattering: roughness vs. sediment volume scattering," *J. Acoust. Soc. Am.*, **92**(2), pp.962-977, 1992.

[6] N. G. Pace, "Low frequency acoustic backscatter from the sea bed," *Proc. Inst. Acoust.*, **16**, pp.181-188, Dec. 1994.

[7] A. N. Ivakin, "Modelling of sound scattering by the sea floor", *J. de Physique IV*, Colloque C5, vol. 4, pp.1095–1098, May 1994.

[8] A. N. Ivakin, "Backscattering of sound by the ocean bottom. Theory and experiment", in *Acoustics of ocean medium*, Edited by L. M. Brekhovskikh and I. B. Andreeva, Nauka, Moscow, pp.160-169, 1989 (in Russian).

[9] A. N. Ivakin, "Reverberation in a plane randomly inhomogeneous waveguide under narrow-band acoustic probing", *Acoustical Physics,* **40**(3), pp.426-427, 1994.

[10] A. N. Ivakin, "Sound scattering by rough interface and volume inhomogeneities of the sea bottom", *Acoustical Physics,* **40**(3), 427-428, 1994.

[11] E. Y. T. Kuo, "Joint perturbation scattering characterization of a littoral ocean bottom reverberation: Theory, scattering strength predictions, and data comparisons," *IEEE J. Oceanic Engr.*, **20**, 198-210, July 1995.

[12] D. Tang, "A note on scattering by a stack of rough interfaces", *J. Acoust. Soc. Am.*, **99**, pp.1414-1418, 1996.

[13] A. N. Ivakin, "Sound scattering by random inhomogeneities of stratified ocean sediments", *Soviet Physics-Acoustics,* **32**(6), pp.492-496, 1986.

[14] S. T. McDaniel, "Effect of surficial sediment layering on high- frequency seafloor reverberation", *J. Acoust. Soc. Am.*, **91** (3), pp.1353-1356, 1992.

[15] P. D. Mourad, and D. R. Jackson, "A model/data comparison for low-frequency bottom backscatter", *J. Acoust. Soc. Am.*, **94**, pp.344-358, 1993.

[16] J. E. Moe and D. R. Jackson, "First-order perturbation solution for rough surface scattering cross section including the effects of gradients", *J. Acoust. Soc. Am.*, **96**(3), pp.1748-1754, 1994.

[17] A. N. Ivakin, "Sound scattering by rough interfaces of layered media", in *Third International Congress on Air- & Structure- Borne Sound and Vibration*, International Publics, Auburn, AL, vol.3, pp.1563-1570, 1994.

[18] A. N. Ivakin, "A unified perturbation approach to volume and roughness scattering", *J. Acoust. Soc. Am.*, **98**(5), Pt.2, p.2988(A), 1995.

[19] A. N. Ivakin, "A unified approach to volume and roughness scattering", unpublished.

[20] E. L. Hamilton, "Geoacoustic modelling of the seafloor", *J. Acoust. Soc. Am.*, **68**(5), pp.1313-1340, 1980.

[21] L. M. Brekhovskikh and O. A. Godin, *Acoustics of Layered Media I*, Springer-Verlag, Berlin, 1990.

[22] A. N. Ivakin, "Sound scattering by inhomogeneities of an elastic half-space", *Soviet Physics-Acoustics,* **36**(4), pp.377-380, 1990.

[23] H. H. Essen, "Scattering from a rough sedimental seafloor containing shear and layering," *J. Acoust. Soc. Am.*, **95**(3), pp.1299-1310, 1994.

[24] D. R. Jackson and A. N. Ivakin, "Scattering from elastic sea beds: First-order theory", unpublished.

[25] A. N. Ivakin and D. R. Jackson, "Effects of shear elasticity on sea bed scattering: Numerical examples", unpublished.

[26] A. N. Ivakin, "First-order perturbation model for seabed scattering", unpublished.

Temporal Fluctuation of Backscattered Field Due to Bioturbation in Marine Sediments

Christopher D. Jones and Darrell R. Jackson

Applied Physics Laboratory
University of Washington, HN-10
Seattle, WA, 98105, USA
E-mail: cjones@apl.washington.edu, drj@apl.washington.edu

Abstract

Biological activity in marine sediments creates a time-varying, randomly fluctuating medium. A bio-diffusive model is proposed for predicting the temporal and spatial spectrum of sediment density fluctuations. Perturbation theory is used to model sediment volume scattering and the temporal correlation of the scattered field. These models are compared with field data recorded in a biologically active shallow water environment, and sediment bio-diffusion parameters are estimated.

1. Introduction

Biologically active sediments are continually modified by epifauna (organisms that live on the sediment surface) and infauna (organisms living in the sediment). The collective mixing effect of these organisms is termed bioturbation. On micro- and macroscopic scales, bioturbation affects the physical and chemical properties of the sediment. The intensity of bioturbation affects the distribution of marine chemicals which in turn influences the microbial activity in the sediment and the ultimate fate of marine pollutants [1, 2]. Epifaunal activity creates microtopography that may decrease the critical velocity necessary to erode surface layers [3]. Infaunal activity, such as tube building, is responsible for vertical and horizontal redistribution of solid material within the sediment, creating spatial and temporal inhomogeneities in sediment bulk properties (e.g. density and porosity). Often, the traces of these mixing activities provide the only evidence of the existence of fauna in an area [3].

Models of acoustic scattering from the sea floor can be used to invert for sediment properties such as roughness spectra and volume inhomogeneity spectra [5, 6, 7]. In such inversions it is assumed that the sea floor does not change with time, however, on time and distance scales comparable with with scales of bioturbation, acoustic properties of the sea floor will change. Time scales of bioturbation range from diurnal to seasonal, and distances scales range from mesoscale to meter scale patchiness [1].

In this paper, the effects of bioturbation on acoustic backscatter will be discussed. A stochastic model of bioturbation will be introduced, and a review of perturbation theory to model volume backscatter presented. By coupling these models, a model for the decorrelation of an acoustic backscattered field due to bioturbation is obtained. Model predictions will be compared with field data recorded in a biologically active shallow water environment over a two month period.

2. Bio-diffusive Sediment Model

Quantitative analysis of bioturbation requires the use of mathematical models that describe the mixing process. The simplest model of this mixing process is the vertical diffusion equation [1, 2, 4].

$$\frac{\partial}{\partial t}c(z,t) - D_b\nabla^2 c(z,t) = 0 \tag{1}$$

This equation describes the temporal and spatial evolution of a tracer concentration, $c(z,t)$, deposited on the surface of the sediment and being mixed into the sediment by localized diffusion. In this model all the biological

activity is described by a single parameter, the bio-diffusion coefficient D_b. The diffusive nature of the mixing process is not the result of the mixing effects of a single type of organism, but is rather the net effect of a collection of infauna having a wide range of mixing lengths and acting over a long period of time.

While the behavior of a sediment tracer (such as a radio-isotope) may be modeled by the homogeneous and steady-state solution of the one dimensional diffusion equation, in the context of acoustic scattering, the inhomogeneous and transient nature of the process is of primary concern. On the time scales of interest, the movement of sediment is not necessarily restricted to localized mixing between adjacent horizontal layers, rather, larger organism may transfer sediment between non-adjacent layers creating nonlocal (non-diffusive) mixing that give rise to spatial inhomogeneity. Furthermore, over short time periods it cannot be assumed that a large collections of organisms with a broad spectrum of sizes have reworked the sediment. Instead, mixing may be dominated by organisms with discrete length scales.

Given that we are interested in this nonlocal and transient behavior of bioturbation, the simple diffusion model is inadequate. A proposed extension to (1) is the forced diffusion process, generalized in terms of the sediment bulk density ρ_s.

$$\frac{\partial}{\partial t}\rho_s(\mathbf{r},t) - \nabla\cdot[D(\mathbf{r},t)\nabla\rho_s(\mathbf{r},t)] = g(\mathbf{r},t) \tag{2}$$

Here, D is a local diffusion coefficient representing the continuous diffusive activity of smaller organisms (meiofauna) or the collapsing and filling of borrows created by larger organisms. By taking D to be a scalar, we have assumed isotropic diffusion. In general, the horizontal and vertical diffusion rates may differ [1] and a tensor diffusion coefficient must be used. The right-hand side of (2) is an excitation function that represents the nonlocal mixing activities of larger organisms (macrofauna).

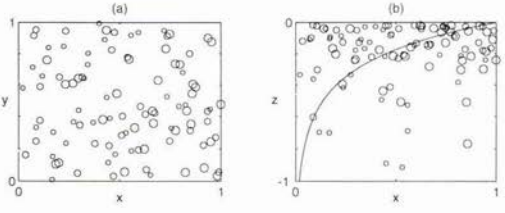

Figure 1: Sediment source and sink functions randomly distributed in the (a) horizontal and (b) vertical directions. The depth-dependent point density, $\lambda(z)$, is plotted as the solid line in (b). The $z = 0$ plane is the sediment-water interface.

If there is a single transport event at time t_n that removes or deposits sediment at a small volume centered at $\mathbf{r}_n$, then the excitation function can be modeled as a series of impulsive source and sink events occurring randomly in space and time.

$$g(\mathbf{r},t) = \sum_n q_n h_n(\mathbf{r}-\mathbf{r}_n)\delta(t-t_n) \tag{3}$$

The function h_n describes the random size and shape of the volume of sediment moved by each event. The coefficient q_n is a zero-mean random variable that represents the amplitude of each event, therefore, mass is conserved within the volume of interest.

In general, the excitation may be anisotropic and inhomogeneous in space. For example, biological activity may decrease with depth into the sediment, as illustrated by Figure 1. This figure shows a hypothetical depth-dependent distribution of spherical shape functions. Activity is concentrated near the sediment-water interface and decreases with depth into the sediment, but is uniform in the horizontal plane. In this paper we will assume spatial homogeneity in the horizontal plane but include the effects of depth dependent mixing activities.

Equation (2) is a deterministic differential equation with a random excitation, g, due to the nonlocal exchange of sediment. The solution, ρ_s, can then be interpreted as the output of a linear system with a stochastic input. Thus the mixing process can be characterized as a linear filtering process where the spectrum, $S_{\rho\rho}$, of the output process is defined completely in terms of the spectrum, S_{gg}, of the input and the frequency response, $H_D(\mathbf{k},\omega)$, of the linear system representing the left hand side of (2).

$$S_{\rho\rho}(\mathbf{k},\omega) = |H_D(\mathbf{k},\omega)|^2 S_{gg}(\mathbf{k},\omega) \tag{4}$$

If t_n and $\mathbf{r}_n$ are Poisson random variables, the spectrum of the input process is found by interpreting the excitation as the output of a filtered Poisson, or shot-noise process [8]. The depth dependence of g will be characterized by the number of events per unit volume and time at each depth, that is, the depth-dependent Poisson point density $\lambda(z)$ (Figure 1). If the point density is a slowly varying function of depth relative to the shape function, it follows that the autocorrelation of g can be expressed in terms of the autocorrelation, R_{hh}, of the shape function,

$$R_{gg}(\mathbf{r}_d,z,\tau) \simeq \sigma_q^2\lambda(z)\langle R_{hh}(\mathbf{r}_d)\rangle\delta(\tau)\ , \tag{5}$$

where σ_q^2 is the variance of q_n. The correlation is expressed in terms of the difference coordinates $\mathbf{r}_d = \mathbf{r}_1 - \mathbf{r}_2$ and $\tau = t_1 - t_2$, therefore, the excitation can be considered a depth-dependent, locally stationary random process.

The shape function is random in general and the expected value of its autocorrelation is used. The spectrum is found by taking the Fourier transform of (5) with respect to $\mathbf{r}_d$ and τ,

$$S_{gg}(\mathbf{k}, z, \omega) \simeq \frac{\sigma_q^2}{2\pi} \lambda(z) S_{hh}(\mathbf{k}) \ , \tag{6}$$

where $S_{hh}(\mathbf{k}) = (2\pi)^3 \langle |H_n(\mathbf{k})|^2 \rangle$ is the expected value of the shape function spectrum, and H_n is the Fourier transform of the shape function h_n. Note that the spectrum is independent of temporal frequency, ω, because of the assumed impulsive nature of the source and sink events.

For the case of a depth-dependent and isotropic diffusion coefficient, the system frequency response can be approximated as

$$H_D(k, \omega) \simeq \frac{1}{D(z)k^2 - i\omega} \ , \tag{7}$$

where $k^2 = k_x^2 + k_y^2 + k_z^2$ and the gradient of $D(z)$ is neglected. Combining (4-7) and performing an inverse Fourier transform in time, the temporal correlation / spatial spectrum of density inhomogeneities in the sediment can be modeled as

$$S_{\rho\rho}(\mathbf{k}, z, \tau) = \sigma_q^2 \frac{\lambda(z)}{D(z)} \frac{S_{hh}(\mathbf{k})}{2k^2} e^{-D(z)k^2|\tau|} \ . \tag{8}$$

The above expression is general in the sense that it attempts to model bioturbation in nonspecific terms (e.g. diffusion and point density) while still accounting for the two-scale nature of the mixing process (meiofauna and macrofauna). The shape function and its expected value should reflect the size and shape of the macrofauna that move sediment nonlocally. Anisotropy can be modeled, for example, by using a shape function that represents directional feeding, such as vertical burrows made by conveyer-belt feeders [1, 4]. The point density should reflect the amount and rate of macrofaunal activity, which in general is depth dependent. The diffusion coefficient should reflect the length and time scales of the meiofaunal activity, which can also be modeled as depth dependent. Assumptions about these parameters will be discussed in the comparison with acoustic data.

3. Seafloor Volume Scattering

The sea floor is modeled as a fluid half-space in which the sediment properties are random functions of space and time. The sediment density and compressibility, ρ_s and κ_s, are defined in terms of their mean and fluctuating components, $\rho_s(\mathbf{r}, t) = \bar{\rho}_s + \delta\rho_s(\mathbf{r}, t)$ and $\kappa_s(\mathbf{r}, t) = \bar{\kappa}_s + \delta\kappa_s(\mathbf{r}, t)$. The water density and compressibility, ρ_w and κ_w, as well as the sediment mean values, $\bar{\rho}_s$ and $\bar{\kappa}_s$, are assumed to be constant in space and time. At the sediment-water interface the density and compressibility are discontinuous, creating an acoustic impedance mismatch. The boundary is in general a rough surface, however, it will be modeled as planar.

A pressure wave, incident upon the sediment, will interact with inhomogeneities in the sediment to create sources of scattered sound, and an integral equation can be obtained by superimposing the induced sources. Thus, for an unbounded region, the resultant scattered field, p', is the sum of the monopole and dipole fields from all the differential sources within the volume of the sediment [9, 10].

$$p'(\mathbf{r}, t) = \int_{V_s} [\bar{k}_s^2(\mathbf{r}')\gamma_\kappa(\mathbf{r}', t)G_0(\mathbf{r}, \mathbf{r}')p(\mathbf{r}', t) - \gamma_\rho(\mathbf{r}', t)\nabla G_0(\mathbf{r}, \mathbf{r}') \cdot \nabla' p(\mathbf{r}', t)] d\mathbf{r}' \tag{9}$$

The average wavenumber in the sediment is defined as $\bar{k}_s^2 = \omega^2 \bar{\rho}_s \bar{\kappa}_s$, where ω is the acoustic frequency. The fluctuating sediment parameters are defined as $\gamma_\kappa = (\kappa_s - \bar{\kappa}_s)/\bar{\kappa}_s$ and $\gamma_\rho = (\rho_s - \bar{\rho}_s)/\rho_s$, and are assumed to vary in time much slower than the acoustic frequency. The Green's function for this system, G_0, is the unperturbed Green's function that satisfies reciprocity and the appropriate boundary conditions along the sediment-water interface. Equation (9) is similar to the well-known integral equation [9] which uses the free-space Green's function. However, in general, G_0 can include gradients in the mean sediment parameters as well as interface effects.

If the field distribution inside the sediment is known, the field outside the sediment can be computed. The total field is the sum of the unperturbed field and the perturbed or scattered field.

$$p(\mathbf{r}, t) = p_0(\mathbf{r}) + p'(\mathbf{r}, t) \tag{10}$$

Equation (9) may be solved by successive approximations using small perturbation theory. Using the known sediment properties and the known Green's function G_0, the total field is expressed as the perturbation series,

$$p(\mathbf{r}, t) = p_0(\mathbf{r}) + p_1(\mathbf{r}, t) + p_2(\mathbf{r}, t) + \cdots \ , \tag{11}$$

where each higher order term is defined in terms of the preceeding order.

$$p_{n+1}(\mathbf{r},t) = \int_{V_s} [\bar{k}_s^2(\mathbf{r}')\gamma_\kappa(\mathbf{r}',t)G_0(\mathbf{r},\mathbf{r}')p_n(\mathbf{r}',t) - \gamma_\rho(\mathbf{r}',t)\nabla G_0(\mathbf{r},\mathbf{r}')\cdot\nabla' p_n(\mathbf{r}',t)]d\mathbf{r}' \tag{12}$$

If the sediment fluctuations are small, the series converges rapidly and a low-order approximation will sufficiently represent the scattered field.

In the far field and over a small patch of sea floor where it is assumed the incident wave is plane, the half-space Green's function near the interface can be approximated as [11]

$$G_0(\mathbf{r},\mathbf{r}') \simeq \frac{T}{4\pi r} e^{-i\mathbf{k}_w\cdot\mathbf{r}+i\bar{\mathbf{k}}_s\cdot\mathbf{r}'} \quad \text{and} \quad G_0(\mathbf{r}',\mathbf{r}) \simeq \frac{1}{a_\rho}\frac{T}{4\pi r} e^{-i\mathbf{k}_w\cdot\mathbf{r}+i\bar{\mathbf{k}}_s\cdot\mathbf{r}'} . \tag{13}$$

T is the pressure transmission coefficient for plane waves incident upon the interface from the water. The position vector $\mathbf{r}$ lies in the water, and $\mathbf{r}'$ lies in the sediment. The origin of the coordinate system is taken on the interface near the center of the region contributing to the integral in (9). The constant a_ρ is necessary to satisfy reciprocity and is defined as the ratio of the average sediment density to water density, $a_\rho = \bar{\rho}_s/\rho_w$. Spherical spreading in the water is included, but neglected in the sediment due to absorption ($r' \ll r$). The wavevector $\mathbf{k}_w$ is in the direction of the incident field, and the wavevector $\bar{\mathbf{k}}_s$ is the corresponding wavevector in the sediment. The transverse components of $\bar{\mathbf{k}}_s$ are the same as those of $\mathbf{k}_w$, and its vertical component is chosen to give the correct sediment wavenumber $\bar{k}_s$. In general the wavenumber in the sediment is complex such that $\bar{k}_s/k_w = (1+i\delta)c_w/\bar{c}_s$, where $\bar{c}_s/c_w$ is the sediment to water sound velocity ratio. The compressional loss factor δ is the ratio of the imaginary to real components of the sediment wavenumber.

Using (12)and (13) the first-order *backscattered* field at position $\mathbf{r}$ in the water is found to be

$$p_1(\mathbf{r},t) = \frac{T^2}{a_\rho(4\pi r)^2}\bar{k}_s^2 e^{-i2\mathbf{k}_w\cdot\mathbf{r}} \int_{V_s} [\gamma_\kappa(\mathbf{r}',t) - \gamma_\rho(\mathbf{r}',t)] e^{i2\bar{\mathbf{k}}_s\cdot\mathbf{r}'} d\mathbf{r}' . \tag{14}$$

The attenuation in the sediment in the z-direction is determined by $Im[\bar{\mathbf{k}}_s] = k_w Im[P(\theta)]z$. The factor $P(\theta)$ is the ratio of the vertical component of the sediment wavenumber to the wavenumber in the water, $P(\theta) = [(\bar{k}_s/k_w)^2 - \cos^2\theta]^{1/2}$, where θ is the grazing angle in water. The pressure transmission coefficient is $T = 2\zeta/(\zeta+1)$, and the z-direction impedance ratio is $\zeta = (a_\rho \sin\theta)/P(\theta)$.

3.1. Temporal Correlation of the Backscattered Field

As the sediment fluctuates randomly in time, the scattered field will fluctuate. Thus, the backscattered field is also a random process, which can be characterized by the cross-correlation of p_1 at two different times, $R_{pp}(\tau) = \langle p_1(\mathbf{r},t)p_1^*(\mathbf{r},t+\tau)\rangle$. In developing the field correlation we will assume that sediment fluctuations are small, stationary in time, and spatially stationary in the horizontal plane only. The latter two assumptions follow from the sediment model of Section 2. Therefore, assuming the sediment can be approximated as a depth-dependent, but otherwise stationary random processes, the correlation of the first-order backscattered field is found to be

$$R_{pp}(\tau) = \frac{1}{a_\rho^2}\frac{|T^2|^2}{(4\pi r)^4}|\bar{k}_s|^4 \int_{V_s} e^{4Im[\bar{\mathbf{k}}_s]\cdot\mathbf{r}_c} d\mathbf{r}_c \int_{V_s} R(\mathbf{r}_d, z_c, \tau) e^{-i2Re[\bar{\mathbf{k}}_s]\cdot\mathbf{r}_d} d\mathbf{r}_d , \tag{15}$$

where the sediment correlation functions appearing in

$$R(\mathbf{r}_d, z_c, \tau) = R_{\kappa\kappa}(\mathbf{r}_d, z_c, \tau) - 2R_{\kappa\rho}(\mathbf{r}_d, z_c, \tau) + R_{\rho\rho}(\mathbf{r}_d, z_c, \tau) \tag{16}$$

are the auto- and cross-correlations of the zero-mean functions γ_κ and γ_ρ. The difference and center coordinates are defined as $\mathbf{r}_d = \mathbf{r}_1 - \mathbf{r}_2$, and $\mathbf{r}_c = (\mathbf{r}_1 + \mathbf{r}_2)/2$, respectively. Following other authors [12], we assume the sediment compressibility fluctuations are proportional to the density fluctuations, $\gamma_\kappa = \mu\gamma_\rho$. The sign of the proportionality constant μ is positive if ρ_s and κ_s are positively correlated and negative if negatively correlated [12, 13].

Applying the above assumptions, the Wiener-Khintchin theorem, and the Fourier windowing theorem, the correlation function (15) can be expressed as

$$R_{pp}(\tau) = \frac{A}{a_\rho^2}\frac{|T^2|^2}{32\pi r^4}|\bar{k}_s|^4(\mu-1)^2 \int_{-\infty}^{0} \tilde{S}_{\rho\rho}(\mathbf{k}_d, z_c, \tau) e^{4\alpha z_c} dz_c , \tag{17}$$

where A is the area of the scattering region and $\mathbf{k}_d = 2Re[\bar{\mathbf{k}}_s]$ is the Bragg wavenumber having magnitude $k_d = 2k_w[\cos^2\theta + (Re[P(\theta)])^2]^{1/2}$. The imaginary component of the vertical wavenumber is $\alpha = Im[\bar{\mathbf{k}}_s] \cdot \hat{z}$, or, using previous notation, $\alpha = k_w Im[P(\theta)]$. The modified density spectrum, $\tilde{S}_{\rho\rho}$, is the convolution of the true density spectrum and the Fourier transform of the half-space window.

$$\tilde{S}_{\rho\rho}(\mathbf{k}_d, z_c, \tau) = \int_{-\infty}^{\infty} S_{\rho\rho}(\mathbf{k}'_d, z_c, \tau) W(k'_z - k_z, z_c) dk'_z \tag{18}$$

The half-space window function, defined in the difference coordinates, is a depth-dependent rectangular window having the Fourier transform

$$W(k_z, z_c) = \frac{\sin(2k_z z_c)}{\pi k_z}. \tag{19}$$

Therefore, the convolution integration of (18) is only over the z-component of the Bragg wavenumber.

3.2. Backscatter Strength

The first-order backscatter strength is defined in terms of the zero-lag correlation of the backscattered field. If the penetration distance into the sediment is small compared to the distance traveled in water ($r' \ll r$), it is typical to describe volume scattering in terms of an equivalent surface scattering strength. From (17) the surface backscatter strength is found to be

$$\sigma_s = \frac{\pi}{2} \frac{|T^2|^2}{a_\rho^2} |\bar{k}_s|^4 (\mu - 1)^2 \int_{-\infty}^{0} \tilde{S}_{\rho\rho}(\mathbf{k}_d, z_c) e^{4\alpha z_c} dz_c \ . \tag{20}$$

This expression for scattering strength is similar to those derived by [11, 12, 13, 14], except half space effects are included. The half-space windowing effect, expressed as the convolution integral in (18), can be interpreted as a smoothing of the density spectrum. Insight into this effect is gained by combining (20) (18) and (19) and assuming the density spectrum is independent of depth. By performing the integration over z_c, a new window is defined.

$$\tilde{W}(k_z) = \frac{1}{2\pi(4\alpha^2 + k_z^2)} \tag{21}$$

If the spectral representation of the half-space window is a narrow function compared to the spectrum of sediment inhomogeneities, the convolution will have little smoothing effect, and the half-space effects are negligible. However, for certain combinations of grazing angle and attenuation, the window is broad and the convolution may significantly alter the density spectrum at the wavenumbers of interest.

4. Model-Data Comparison

Acoustic backscatter data and sediment physical properties were measured in a shallow bay of Orcas Island, Washington State, USA in August 1995. A calibrated 40 kHz monostatic transducer with a fan-shaped beam pattern was used to scan a site approximately 50 meters in radius. The instrument remained at a fixed location for approximately 60 days. Each day, 10 complete circular scans of the site were recorded. The complete acoustic data set provides a series of backscatter images that reveal changes in the sediment occurring over the time and distance scales of the experiment.

The sediment in the area is a silty-clay with moderate biologically activity. No bubbles were observed in the sediment, and an extensive set of sediment physical properties were measured at the site by investigators of the US Naval Research Laboratory. This work included core and in-situ measurement of geoacoustic parameters, X-radiography of sediment inhomogeneity, and stereophotographic measurement of sea floor roughness.

4.1. Backscatter Strength

Backscatter strength per unit area of sea floor was measured as a function of grazing angle for the Orcas site. The scattering mechanism cannot be inferred from the acoustic data only, owing to the similarity of the magnitude and angular dependence of the measured values compared to other sites having a range of different sediment types [7, 12, 15, 16, 17, 18]. By using sediment measurements as inputs to models for acoustic scattering, the model results are compared with observed backscatter data, and the dominant scattering mechanism inferred.

Two scattering models are considered: scattering from volume inhomogeneities and scattering from a rough sediment-water interface. Both models assume a fluid sediment. Surface roughness scattering is treated using a

Density Ratio	a_ρ	1.406	Diffusion Coefficient	D_0	2.4 $(cm^2/year)$
Sound Velocity Ratio	$\bar{c}_s/c_w$	0.977	Macrofauna Rework Depth	L_λ	3.8 (cm)
Proportionality Constant	μ	-0.934	Meiofauna Rework Depth	L	3.8 (cm)
Compressional Loss	δ	0.0019	Mean Radius	η_a	0.4 (cm)
Spectral Strength	w_3	6.443e-05 (cm^{-1})	Radius Standard Deviation	σ_a	0.14 (cm)
Correlation Length	l_c	3.198 (cm)			

Table 1: Sediment parameters estimated from cores and model-data comparison for the Orcas site.

first-order perturbation approximation [12] with roughness characterized by the two-dimensional, isotropic, power-law spectrum estimated from sites with similar sediments [7, 12]. The Orcas roughness data have not yet been analyzed. As Figure 2 shows, the predicted interface scattering was sufficiently below the measured values that interface scattering effects can be safely neglected, even without full knowledge of the actual roughness parameters.

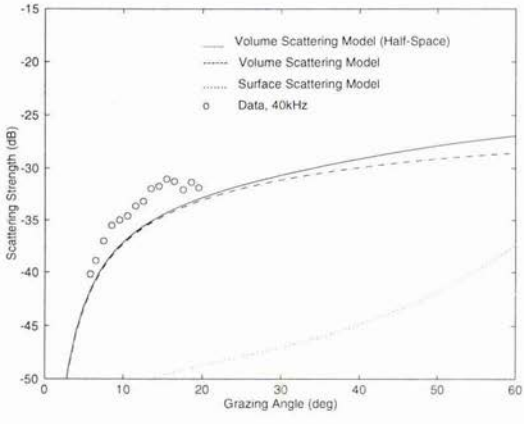

Figure 2: Comparison of measured backscatter with model predictions for the Orcas site.

Volume scattering is treated in a manner similar to Section 3.2 except that the sediment fluctuations are not treated as depth-dependent, owing to lack of resolution in the core data. For the special case of a depth-independent density spectrum and neglecting half-space effects, (20) can be rewritten as

$$\sigma_s = \frac{|T^2|^2}{4\alpha a_\rho^2}\sigma_v \tag{22}$$

where σ_v is the sediment volume backscatter strength.

$$\sigma_v = \frac{\pi}{2}|k_s|^4(\mu-1)^2 S_{\rho\rho}(\mathbf{k}_d) \tag{23}$$

Figure 2 shows the predicted backscatter strengths found using the first-order volume model of (20) and (21) which include half-space effects effects, and using (22) and (23) without half-space effects. In this case, a first-order approximation models the data reasonably well, and half-space effects can be negligible. The difference between model predictions and data is most likely due to errors in the estimated inhomogeneity spectra.

Following [19], the spectra of core density fluctuations were estimated using a first-order auto-regressive (AR) model applied to the Orcas core data. This model assumes that the auto-correlation of the normalized fluctuations (taking density as an example) can be expressed as

$$R_{\rho\rho}(\mathbf{r}_d) = \sigma_\rho^2 e^{-|\mathbf{r}_d|\ln\tilde{a}} , \tag{24}$$

where $\tilde{a}$ is the first order AR coefficient estimated from the core data using the Levinson-Durbin algorithm [20]. Since γ_ρ is a zero-mean process, the zero-lag autocorrelation is its variance σ_ρ^2. The three-dimensional density spectrum is found from (24) to be

$$S_{\rho\rho}(k) = \frac{w_3}{(1/l_c^2 + k^2)^2} , \tag{25}$$

where l_c is the correlation length defined as $l_c = -\delta z/\ln\tilde{a}$, δz is the core sampling interval, and $w_3 = {\sigma_\rho}^2/(\pi^2 l_c)$. Similar expressions are used for the compressibility spectrum and cross-spectrum. The spectral parameters for the Orcas cores are listed in Table 1 along with other geoacoustic parameters supplied by [21]. While these data give reasonable agreement between the acoustic model and data, there are concerns as to the sufficiency of the core inhomogeneity data. The core sampling interval of 2 cm provides marginal resolution compared to the acoustic wavelength. Also, the core data are one-dimensional, which necessitated an assumption of isotropy in the spectral estimates. Both of these concerns could be addressed through use of X-ray data obtained during the Orcas experiment [22, 23].

4.2. Backscatter Correlation

The coherent correlation of the backscattered field is used to observe the changing sediment. First, the complex envelope of the received signal, $s(t)$, is digitized and range-gated to correspond with small patches of sea floor.

Next, the signal from each range bin is cross-correlated with the signal from the same range bin, but from a later scan.

$$R_{ss}(\tau) = \sum_{n=M}^{M+N-1} s_0(t_n) s_\tau^*(t_n) e^{i\frac{\delta c}{c}\omega t_n} \tag{26}$$

The subscript on s denotes the scan time; s_0 is the signal from the scan chosen as a reference, and s_τ is the signal from a scan at time τ later. Sound velocity fluctuations in the water, δc, are compensated by a correction to the phase of the received signal [24]. This phase correction was estimated from sound speed measurements obtained using a conductivity and temperature instrument mounted on the acoustic platform. No significant oceanographic processes or sediment transport events were observed during the experiment. For the Orcas site, sound speed fluctuations were not a significant factor in the observed changes in the backscattered field. Given the nature of the sediment and the expected low level of roughness scattering, it is expected that acoustic penetration into the sediment and the effects of biological mixing are the dominant mechanism for decorrelation.

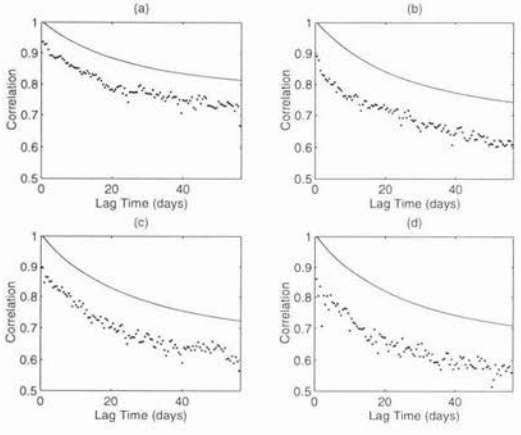

Figure 3: Comparison of measured backscatter correlation and model predictions, (a) $\theta = 14.7°$, (b) $\theta = 9.4°$, (c) $\theta = 7.6°$, (d) $\theta = 6°$

Predictions of the backscatter correlation using the models of Sections 2 and 3.1 are compared with the correlation estimated from the Orcas backscatter data. In this comparison, several simplifying assumptions about the sediment model are made. First, a simple spherical shape function is used, such that

$$H_\eta(k) = \frac{1}{2\pi^2 k^3}(\sin ak - ak\cos ak) \ . \tag{27}$$

The radius a is a Gaussian random variable with normal distribution $N(\eta_a; \sigma_a)$. The depth-dependent point density and diffusion coefficient are modeled as

$$\lambda(z) = \lambda_0 e^{-z^2/L_\lambda^2} \quad \text{and} \quad D(z) = D_0 e^{-z^2/L^2} \tag{28}$$

where the activity decreases with depth at a rate defined by the macrofauna and meiofauna rework depths L_λ and L.

Using (27), (28), and (17- 19), the normalized correlation coefficient is calculated. In general, the convolution and the expected value integral must be performed numerically. Figure 3 shows a comparison of the observed and predicted correlations as functions of lag time. The model was fitted to the data (plotted as points) by trial and error while constraining the parameters of the sediment model to realistic values. The offset is due to uncorrelated noise in the data. Table 1 outlines the parameters estimated from the model-data comparison. These values are presented mainly as an illustration of the model. Further work is required before bioturbation parameters can be estimated with confidence from acoustic backscatter data.

5. Summary

A model for the change in correlation of sea floor backscattering as a function of the time has been presented. We combine a diffusion model having random excitation to describe the time evolution of sediment inhomogeneities and a first-order perturbation treatment of sediment volume backscatter. The first-order volume backscatter model is validated by comparison with acoustic data using sediment inhomogeneity spectra measured from core data. This model includes half-space effects which were found to be negligible in the present case, but which could affect correlation estimates. Higher resolution two- or three-dimensional core analysis (X-ray, CT) is recommended for future work to reduce errors in application of the scattering model. The backscatter correlation model predicts sediment bio-diffusion parameters that are realistic, but further work is needed in which acoustically derived parameters are compared with ground truth.

Acknowledgments

This work was sponsored by the US Office of Naval Research through the Coastal Benthic Boundary Layer Program and through Codes 3210A and 322BC. The authors are indebted to Dr. Kevin Briggs and Dr. Michael Richardson of the US Naval Research Laboratory for supplying some of their unpublished data and to Dr. Peter Jumars who conceived and led the Orcas experiment.

References

[1] P. A. Jumars. *Concepts in Biological Oceanography*, New York, Oxford University Press, 1993.

[2] R. A. Wheatcroft, P. A. Jumars, C. A. Smith, A. R. Nowell, "A Mechanistic view of particulate biodiffusion coefficient: Step lengths, rest periods and transport directions," *J. Mar. Res.*, 48, 177-207, 1990.

[3] R. A. Wheatcroft, C. A. Smith, P. A. Jumars, "Dynamics of surficial trace assemblages in the deep sea" *Deep-Sea Res.*., vol. 36, no. 1, 71-91, 1989.

[4] B. P. Boudreau, "Mathematics of tracer mixing in sediments: III. The theory of nonlocal mixing within the sediment," *Am. J. Sci.*, vol. 287, p. 693-719, September 1987.

[5] C. de Moustier, D. Alexandrou, "Angular dependence of 12 kHz seafloor acoustic backscatter," *J. Acoust. Soc. Am.*, vol. 90, pp. 522-531, July 1991.

[6] H, Matsumoto, R. P. Dziak, C. G. Fox, "Estimation of microtopographic roughness through modeling of acoustic backscatter data recorded by multibeam sonar systems," *J. Acoust. Soc. Am.*, vol 94, pp. 2776-2787, November 1993.

[7] D. R. Jackson, K. B. Briggs, "High-frequency bottom backscattering: Roughness versus sediment volume scattering," *J. Acoust. Soc. Am.*, vol. 92, pp. 962-977, August 1992.

[8] A. Papoulis, *Probability, Random Variables, and Stochastic Processes*, New York, McGraw-Hill Inc., 1991.

[9] P. M. Morse, K. U. Ingard, *Theoretical Acoustics*, Princeton University Press, New Jersy, pp. 410, 1968.

[10] A. N. Ivakin, "A unified approach to volume and roughness scattering," unpublished.

[11] A. N. Ivakin, Yu. P. Lysanov. "Underwater sound scattering by volume inhomogeneities of a bottom medium bounded by a rough surface," *Sov. Phys. Acoust.*, vol. 27, May-June 1981.

[12] D. R. Jackson, K. B. Briggs, K. Williams, M. Richardson, "Tests of models of high-frequency seafloor backscatter," *IEEE Journal of Oceanic Engineering*, vol. 21, no. 4, October 1996.

[13] T. Yamamoto. "Acoustic scattering in the ocean from velocity and density fluctuations in the sediment," *J. Acoust. Soc. Am.*, vol. 99, pp. 866-879, February 1996.

[14] P. C. Hines, "Theoretical model of in-plane scatter from a smooth sediment seabed," *J. Acoust. Soc. Am.*, vol. 88, pp. 325-334, July 1990.

[15] H. Boehme, N. P.. Chotiros, "Acoustic backscattering at low grazing angles from the ocean bottom," *J. Acoust. Soc. Am.*, vol. 84, pp. 1018-1029, Sept. 1988.

[16] A.V. Bunchuk and Y. Y. Zhitkovski, "Sound scattering by the ocean bottom in shallow-water regions (review)," *Sov. Phys. Acoust*, vol. 26, pp. 363-370, 1980.

[17] P. D. Mourad, D. R. Jackson, "High frequency sonar equation models for bottom backscatter and forward loss," in *Proceedings of OCEAN '89*, IEEE, New York, pp. 1168-1175, September 1989.

[18] M. Gensane, "A statistical study of acoustic signals backscattered from the sea bottom," *IEEE J. Oceanic Engr.*, vol. 14, pp.84-93, 1989.

[19] K. B. Briggs, "High-frequency acoustic scattering from sediment interface and volume inhomogeneities," NRL/FR/ 7431–94-9617, December 1994

[20] J. Proakis, D. Manolakis, *Digital Signal Processing*, New York, Macmillan Publishing Company, pp. 116, 262, 1992.

[21] M. D. Richardson, private communication.

[22] K. B. Briggs, private communication.

[23] T. H. Orsi, private communication.

[24] J.G. Dworski and D. R. Jackson, "Spatial and temporal variation of acoustic backscatter in the STRESS experiment," *J. Continental Shelf Res.*, vol. 14, pp. 1221-1237, August 1994.

Numerical modelling of acoustic scattering by smooth inclusions in a layered fluid-solid medium

Ilkka Karasalo

National Defence Research Institute
Hydroac. Environment and Active Sonar
S - 172 90 Stockholm, Sweden
Email: ilkka@sto.foa.se

Johan Mattsson

Royal Institute of Technology
The Marcus Wallenberg Laboratory
S - 100 44 Stockholm, Sweden
Email: johanm@fkt.kth.se

Abstract

A boundary integral equation (BIE) method is described for computing the scattering of a monofrequent acoustic field by a smooth, rigid 3D object in a layered range-independent fluid-solid medium.

The BIE is discretized using B-splines (BSP), point collocation and high-order numerical integration. The discretized equations are solved by an iterative method, enhanced by pre-conditioning with the LU factors of a related linear system for spline interpolation on the scatterer surface.

Numerical examples are given at frequencies of a few kHz, representative e.g. for a parametric transducer. The BSP method is shown to provide order-of-magnitude gains in computation times compared to a standard BEM technique with quadratic elements as frequency increases and/or accuracy requirements are tightened.

1. Introduction

Acoustic scattering from a 3D obstacle inside a range-independent layered fluid-solid medium is an important model problem with numerous applications in underwater acoustics. The fundamental problem - to predict the scattered wavefield for a given source-medium-scatterer-receiver configuration is of interest both in its own right, and, in practice perhaps more frequently, in the inverse problem of detecting and classifying scattering objects by analysis of returned echoes, [1] and references therein. In all but the simplest model cases - notably with a spherical or cylindrical scatterer and a medium composed of very few homogeneous layers - a closed-form analytical solution of the scattered field is not available. The design of methods for numerical modelling of scattering has therefore received much effort in the past few decades and has, together with the rapid development of technology for large-scale numerical computation, brought increasingly complex scattering scenarios within computational reach.

Boundary integral equation (BIE) methods for the modelling of scattering are particularly useful whenever the Green's function of the surrounding medium may be computed efficiently. Among their advantages are (i) the spatial dimension and thus the number of unknowns in the discretized equations is reduced, (ii) the boundary, the interface and the far-field radiation conditions in the surrounding medium are satisfied *a priori*. Examples of BIE modelling of the scattering of underwater sound are [2] where the surface of an acoustically penetrable scatterer is discretized by linear boundary elements, and [3] treating a cylindrically structured scatterer at the interface between two homogeneous fluid halfspaces.

Except for low-frequency fields in simple media and simple scatterer geometries, the BIE approach is computationally demanding, with workload and memory requirements increasing rapidly with frequency: If point collocation with a p'th order method is used for discretisizng the BIE, a crude estimate of the required number of meshpoints on the scatterer surface is $N \approx (ka\ (C/\epsilon)^{1/p})^2$ where k is is the wavenumber, a an average diameter of the scatterer, ϵ is the wanted relative accuracy and C is the error constant of the method of discretization. For example, for the trapezoidal rule $C = 1/12, p = 2$ giving $N \approx 320$ for $ka = 2, \epsilon = 0.001$. For many methods, e.g. FEM with Lagrange-type elements, the discretized BIE has the form of a dense linear system of equations with dimension equal to or close to N. The main computational tasks in a BIE approach are the assembly and solution of this system, and the subsequent computation of the scattered field at say M wanted points in the medium using the surface integral representation. The computational work for these tasks are proportional to at least N^2 (N^3 if a direct method is used) and MN, respectively. It is therefore interesting to note that increasing the order in the above estimate to $p = 4$ reduces the required number of meshpoints to $N = 36$.

In this paper we describe a recently developed BIE method for modelling scattering by smooth 3D bodies immersed in a range-independent fluid-solid medium. The Green's function of the medium is computed by an adaptive, accurate transform integral method [4]. The BIE is discretized by point collocation using high-order B-spline (BSP) basis functions. The collocation integrand is formulated in 'tilted' spherical coordinates θ', ϕ' making it smooth in both variables and periodic in ϕ', and the collocation integrals are computed by high-order schemes.

Sections 2 - 3 review the basic equations of the BIE approach and present the B-spline collocation method. In section 4 numerical examples are presented for super-ellipsoidally shaped rigid scatterers at a few kHz, representative for a parametric bottom-penetrating transducer. A conventional BEM method with second-order elements [5] is used for numerical comparisons. The BSP technique is demonstrated to be highly efficient, providing order-of-magnitude gains in computation time as the frequency increases and/or the accuracy requirements are tightened.

2. The BIE formulation

Consider an acoustically rigid, smooth 3D object submerged in a fluid layer in a range-independent layered fluid-solid medium, cf. fig. 1. A cartesian coordinate system is introduced as shown, with a vertical, downward pointing z axis and origin at water surface. The medium parameters are assumed to be continuous functions of z within each layer, with jump discontinuities allowed at layer boundaries. The materials are modelled as isotropic, with viscous attenuation represented by complex wavespeeds. The wavefield is excited by a vertical array of time harmonic point sources on the z-axis within the water column.

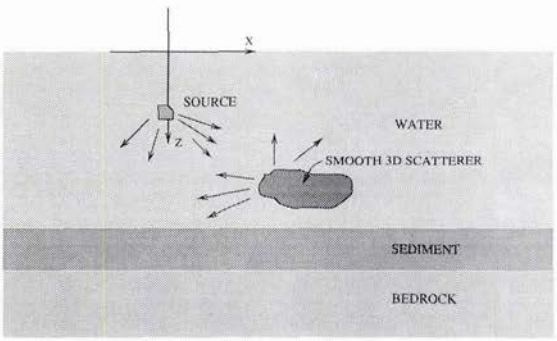

Figure 1: Geometry of model problem.

By the scalar Green's theorem, the 'density scaled' complex pressure $q(\mathbf{r}) = \rho^{-1}(\mathbf{r})p(\mathbf{r})$ at a point $\mathbf{r}_0$ inside a fluid layer is given by

$$q(\mathbf{r}_0) = q^{(in)}(\mathbf{r}_0) - \int_S \nabla_1 g(\mathbf{r}, \mathbf{r}_0) \cdot \hat{\mathbf{n}}(\mathbf{r}) q(\mathbf{r}) dS(\mathbf{r}). \tag{1}$$

S is the surface of the scatterer, $g(\mathbf{r}, \mathbf{r}_0)$ the Green's function of the layered medium, and $q^{(in)} = \rho^{-1}(\mathbf{r})p^{(in)}$ where

$p^{(in)}$ is the incident field, i.e. the field excited by the source in a scatterer-free medium. An integral equation of the second kind for $q(\mathbf{r})$, $\mathbf{r} \in S$, is obtained from (1) in the limit as $\mathbf{r}_0 \to S$.

$$\frac{1}{2}q(\mathbf{r}_s) + \int_S \nabla_1 g(\mathbf{r}, \mathbf{r}_s) \cdot \hat{\mathbf{n}}(\mathbf{r}) q(\mathbf{r}) dS(\mathbf{r}) = q^{(in)}(\mathbf{r}_s). \tag{2}$$

See for example Ström [6, Ch. 2, Sec. 5.4] for a derivation in the free space case. For a smooth surface S, the kernel of the integral in (2) is an equally smooth function of $\mathbf{r}$, except for an integrable $|\mathbf{r} - \mathbf{r}_s|^{-1}$ singularity at $\mathbf{r}_s$. If $g(\mathbf{r}, \mathbf{r}_0)$ and $p^{(in)}$ are (numerically) known, then (2) can be solved numerically, and the pressure field in the medium subsequently computed from (1).

3. A high-order B-spline collocation method

3.1. The B-spline basis

We assume the surface of the scatterer to be defined by a many times differentiable ('smooth') function

$$\mathbf{r} = \mathbf{r}_S(\theta, \phi) \qquad 0 \le \theta \le \pi \qquad 0 \le \phi \le 2\pi \tag{3}$$

where (θ, ϕ) are the spherical angle coordinates of a cartesian coordinate system with origin fixed inside the scatterer. A rectangular, equidistant grid of knotpoints (θ_j, ϕ_i)

$$\theta_j = (j-1)k \quad , \quad \phi_i = (i-1)h \quad , \quad k = \frac{\pi}{M-1} \quad , \quad h = \frac{2\pi}{N}. \tag{4}$$

is introduced, together with associated bases of B-splines [7, Ch. 19] $G_j(\theta)$ and $F_i(\phi)$ with degrees k_G and k_F, and support in $\theta_j \le \theta \le \theta_{j+k_G+1}$ and $\phi_i \le \phi \le \phi_{i+k_F+1}$, respectively. We seek an approximation $\bar{q}(\theta, \phi)$ to the solution of (2) of the form

$$\bar{q}(\theta, \phi) = \sum_{i=1-k_F}^{N} \sum_{j=1-k_G}^{M-1} \gamma_{ij} G_j(\theta) F_i(\phi). \tag{5}$$

At any (θ, ϕ) the number of nonzero terms in this expansion is at most $(k_F+1)(k_G+1)$. Thus the work for computing $\bar{q}(\theta, \phi)$ for given (θ, ϕ) and $\{\gamma_{ij}\}$ does not grow with the total number of terms $(N + k_F)(M - 1 + k_G)$ in the expansion.

To ensure that $\bar{q}(\theta, \phi)$ has spline-like continuity everywhere on the unit sphere, the coefficients γ_{ij} are required to satsify the following *a priori* conditions. First,

$$\gamma_{ij} = \gamma_{(i+N+1)j} \quad , \quad i = 1 - k_F, \ldots, 0 \quad , \quad j = 1 - k_G, \ldots, M-1, \tag{6}$$

to ensure the periodicity in ϕ. Second, the number N of ϕ knot steps is restricted to be even, and

$$\bar{q}(0, \phi_j) = \bar{q}(0, \phi_1) \qquad \bar{q}(\pi, \phi_j) = \bar{q}(\pi, \phi_1) \qquad j = 2, \ldots, N. \tag{7}$$

$$\frac{\partial^l \bar{q}(0, \phi_i)}{\partial \theta^l} = (-1)^l \frac{\partial^l \bar{q}(0, \phi_{i+N})}{\partial \theta^l} \quad , \quad \frac{\partial^l \bar{q}(\pi, \phi_i)}{\partial \theta^l} = (-1)^l \frac{\partial^l \bar{q}(\pi, \phi_{i+N})}{\partial \theta^l} \qquad \begin{matrix} i = 1, \ldots, N/2 \\ l = 1, \ldots, k_G - 1. \end{matrix} \tag{8}$$

Equations (7) and (8) ensure that the smoothness of $\bar{q}$ as function of θ at the 'poles' $\theta = 0$ and $\theta = \pi$ is the same as at other knotpoints. From symmetry properties of the B-spline basis functions follows that (6) - (8) are linearly independent for odd degrees only, and thus k_F and k_G are restricted to be odd for simplicity.

3.2. Computation of the collocation integrals

Equations (6) - (8) impose $k_F(M-1+k_G)$, $2(N-1)$ and $(k_G-1)N$ linear constraints, respectively, on the $(N+k_F)(M-1+k_G)$ coefficients of (5). The remaining $N(M-2)+2$ degrees of freedom are fixed by requiring $\tilde{q}(\theta,\phi)$ to satisfy the BIE, (2), at $(0,\phi_1)$, (π,ϕ_1) (the poles) and at the $N(M-2)$ non-polar knotpoints.

A high-order numerical scheme for the collocation integrals must be chosen with proper care for the (mild) singularity of the kernel of (2) at the collocation point $\mathbf{r}_s$. The following behaviour of the kernel near $\mathbf{r}_s$ is easily verified in a homogeneous space, and is conjectured to hold also for layered media.

For a given $\mathbf{r}_s$, let the surface S be defined by a smooth function $\mathbf{r}(\xi,\eta)$ such that $\mathbf{r}_s=\mathbf{r}(0,0)$ and the tangent vectors $\mathbf{r}_\xi(0,0)$ and $\mathbf{r}_\eta(0,0)$ are linearly independent. Let γ,χ be polar coordinates in the (ξ,η) plane, i.e.

$$\xi=\xi(\gamma,\chi)=\gamma\cos(\chi) \qquad \eta=\eta(\gamma,\chi)=\gamma\sin(\chi) \tag{9}$$

Then, as function of (γ,χ) the integrand in (2) has the form

$$\nabla_1 g(\mathbf{r},\mathbf{r}_s)\cdot\hat{\mathbf{n}}(\mathbf{r})\tilde{q}(\mathbf{r})dS(\mathbf{r}) \quad = \quad k(\gamma,\chi)\tilde{q}(\mathbf{r}(\gamma,\chi))d\gamma d\chi \tag{10}$$

where for some $\gamma_0>0$ the kernel $k(\gamma,\chi)$ is smooth in the closed rectangle $0\le\gamma\le\gamma_0 \quad 0\le\chi\le 2\pi$. Its limit value $k(0,\chi)$ at the collocation point is a smooth function of χ with period π.

Thus, the kernel as function of 'polar-like' coordinates on S with origin at $\mathbf{r}_s$ remains smooth and bounded when $\mathbf{r}_s$ is approached along S from any given direction. Since by (6) - (8) $\tilde{q}(\mathbf{r})$ is smooth everywhere on S, this behaviour holds also for the collocation integrand.

Then, by introducing tilted spherical angle coordinates (θ',ϕ') with the north pole $\theta'=0$ at the collocation point $\mathbf{r}_s=\mathbf{r}_S(\theta_i,\phi_j)$ (cf. (3)) the BIE takes the form

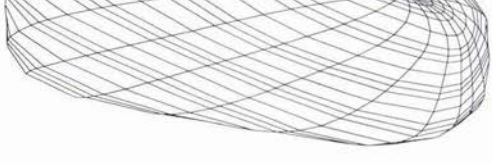

Figure 2: Gridpoints for a collocation integral by use of tilted coordinates (θ',ϕ')

$$\frac{1}{2}\tilde{q}(0,0)+\int_0^{2\pi}\int_0^{\pi} k(\theta',\phi',0,0)\;\tilde{q}(\theta',\phi')\;d\phi'\;d\theta' = q^{(in)}(0,0) \tag{11}$$

cf. fig. 2. The integrand is a smooth function in the closed region of integration, periodic in ϕ' with period 2π. A high-order numerical scheme for this integral is obtained e.g. by combining the trapezoidal rule in ϕ' (the periodicity ensuring super-polynomial order of convergence see e.g. [8, Sec 7.4.4]), and a scheme with the wanted order in θ'. The numerical results presented below were obtained with θ'-schemes of even order, based on linear combination of trapezoidal sums at multiple stepsizes and polynomial extrapolation [9, Sec. 3.3]

By eliminating γ_{ij} with negative i using (6), inserting (5) into (11) and applying the numerical integration scheme, the BIE together with (7) and (8) take the form of a linear system of equations

$$\begin{bmatrix}\mathbf{A}_r\\ \mathbf{A}_c\end{bmatrix}\mathbf{x} \;=\; \begin{bmatrix}\mathbf{0}\\ \mathbf{b}_i\end{bmatrix} \tag{12}$$

$\mathbf{A}_r$ corresponds to (7)-(8) and is $\{N(k_G+1)-2)\}\times\{N(M-1+k_G)\}$ and sparse. $\mathbf{A}_c$ is a dense $\{N(M-2)+2\}\times\{N(M-1+k_G)\}$ matrix of the coefficients of the discretized BIE, and $\mathbf{b}_i$ contains the values of the incident field at the collocation points. The components of $\mathbf{x}$ are the $N(M-1+k_G)$ unknown coefficients γ_{ij} with $i\ge 0$ in (5).

3.3. Solution of the discretized integral equation

Omitting the contribution from the collocation integrals at the assembly of (12) gives a linear system

$$\begin{bmatrix} \mathbf{A}_r \\ \mathbf{A}_i \end{bmatrix} \mathbf{x}^{(in)} = \begin{bmatrix} \mathbf{0} \\ \mathbf{b}_i \end{bmatrix} \tag{13}$$

$\mathbf{A}_i$ represents the term $\frac{1}{2}\hat{q}(0,0)$ of (11), and the components of $\frac{1}{2}\mathbf{x}^{(in)}$ are coefficients $\gamma_{ij}^{(in)}$ of a B-spline expansion interpolating to the incident field at the collocation points.

The coefficient matrix of system (13) is real-valued and sparse, containing at most $(k_F+1)(k_G+1)$ nonzero elements per row. It can be stored compactly and LU-decomposed using sparsity conserving pivoting [10], at a computational cost which is insignificant compared to that of solving (12).

An economical method for solving (12), is then to use an iterative method for nonsymmetric linear systems like the generalized minimum residual method [11], enhanced by preconditioning with the LU factors of system (13). In the numerical examples below, this technique was found to reduce the execution time for solving (12) by a factor of ten or more compared to direct LU decomposition already for systems of moderate size.

4. Numerical examples

In this section we present some numerical examples using a scatterer with superellipsoidal shape, cf. (3),

$$\mathbf{r}_S(\theta,\phi) = \|\hat{\mathbf{r}}\|_p^{-1}\mathbf{D}\hat{\mathbf{r}} \tag{14}$$

where $\hat{\mathbf{r}} = \hat{\mathbf{r}}(\theta,\phi) = (\sin(\theta)\cos(\phi), \sin(\theta)\sin(\phi), \cos(\theta))$, $\|(x,y,z)\|_p = (|x|^p + |y|^p + |z|^p)^{1/p}$ with $p \geq 2$, and $\mathbf{D}$ a diagonal 3×3 matrix with the half-axis lengths a, b, c as diagonal elements.

The incident field is generated by a monofrequent vertical point-source array with length 15 m and center at depth 10 m. The array is steered and weighted to emit a downward-pointing endfire beam with small sidelobes, modelling the beam from a parametric transducer, fig. 3. An adaptive transform-integral method [4] is used to

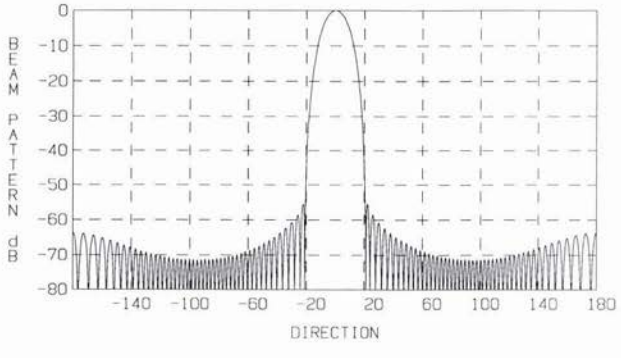

Figure 3: Beam pattern of the source array at 2000 Hz.

compute tables of the incident field and the Green's function of the layered medium on 3D-grids of (source depth, receiver depth, horizontal source-receiver range) values covering the scatterer and the spatial region of interest. The Green's function values for assembling (12) and computing the total field from (1) are obtained by high-order 3D spline interpolation in such tables.

In all examples shown the degree of the B-spline base functions in (5) was $k_F = k_G = 5$. The order of the quadrature scheme for the latitude coordinate (θ' in (11), θ in (1)) was 6, and the trapezoidal rule with a constant stepsize was used for the longitude coordinate. The number of collocation points was adapted in each case to provide visual convergence in plots of the scattered field, i.e. $\approx 1\%$ relative error in complex pressure values. The number of quadrature points was twice the number of collocation points in both coordinates.

Our examples are of two types. First, in sec. 4.1 the performance of the B-spline method is compared to a standard algorithm at selected frequencies for a scatterer in a homogeneous water half-space. The reference algorithm is a boundary element method (BEM), with triangular elements and quadratic basis functions of Lagrange type [5]. Second, in sec. 4.2 the field from a scatterer buried inside a fluid sediment is computed at a dense grid in the upper water column. Greyscale plots are displayed of the interference pattern of the scattered field both for a sediment halfspace, and for a finite sediment layer bounded by a rock halfspace.

4.1. A benchmark case with simple geometry

In our first example the medium is a homogeneous halfspace of water with sound speed 1450 m/s and density 1000 kg/m^3. The scatterer is a rigid superellipsoid defined by (14) with exponent $p = 4$ and half axes $a = 0.5$ m, $b = 0.5$ m and $c = 1.0$ m. The c axis is vertical and the center of the scatterer is on the z-axis at depth $z_c = 40$ m. The scattered field was computed at 181 points along a half-circle with radius $R = 10$ m centered at the scatterer, $x_j = R\sin\theta_j, z_j = z_c + R\cos\theta_j, \theta_j = j\pi/180, j = 0, ..., 180$. The amplitude of the scattered field as function of scattering angle θ at frequency 1000 Hz is shown in fig. 4.

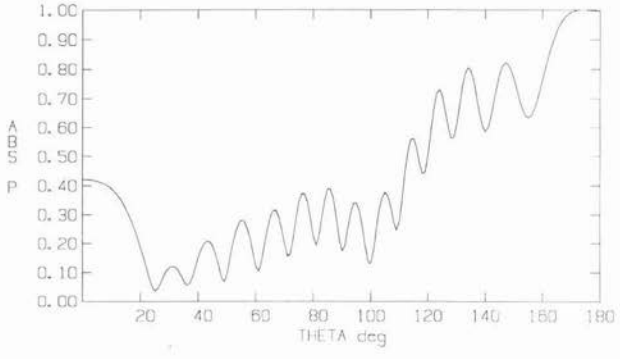

Figure 4: Amplitude of scattered field at range 10 m in the 1 kHz case in Table 1

Table 1 shows the number of unknowns in (12) and the execution times for assembly, solution and field computation at three source frequencies. Execution times refer to real time in (min:sec) on a dedicated HP C160 workstation.

Freq	Nr of unknowns		Assembly and solution		Field computation	
	BEM	BSP	BEM	BSP	BEM	BSP
500	642	192	0:55	0:05	0:04	0:04
750	1024	254	2:03	0:11	0:07	0:08
1000	2050	396	7:53	0:31	0:13	0:13

Table 1: Performance of the BSP and BEM methods

The efficiency of the B-spline method, in terms of execution time and storage space required for (12), is evident. A continuation of the benchmark to higher frequencies was not attempted due to the performance of the BEM algorithm.

The number of iterations required for solving (12) ranged from 7 to 20. No occurrence of a singularity of the kind discussed in [12] was observed in these examples or in the examples below.

4.2. Field from a buried scatterer

As final examples, we consider scattering by a rigid slender superellipsoid buried in a fluid sediment below 35 m of water. The shape of the scatterer is given by (14) with exponent $p = 4$ and half axes $a = 0.5$ m, $b = 0.5$ m

and $c = 2.5$ m. Again, the c axis is vertical and the center of the scatterer is on the z axis, 5 m below the seabed. The acoustic parameters of the sediment are $\rho = 1500\text{kg/m}^3$, $c_p = 1700\text{m/s}$ and attenuation $\beta_p = 0.2\text{dB}/\lambda$. The corresponding normalized half-axis lengths at 1000 Hz are $ka = 1.85$ and $kc = 9.25$.

Two types of seabed are considered, a sediment halfspace, and a 10 thick sediment layer bounded by a rock halfspace with elastic parameters $\rho = 2500$ kg/m^3, $c_p = 2500$ m/s, $c_s = 1800$ m/s, $\beta_p = 0.05\text{dB}/\lambda$ and $\beta_s = 0.2\text{dB}/\lambda$.

Figures 5-6 and 7-8 show greyscale plots of the amplitude of the scattered complex pressure in the region $r \leq 40$ m, $2 \leq z \leq 22$ m for the two media cases at frequencies 500 Hz and 1000 Hz, respectively. The field is normalized by the amplitude of the incident field at the scatterer depth in a water halfspace.

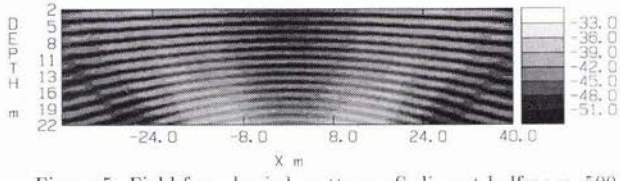

Figure 5: Field from buried scatterer: Sediment halfspace, 500 Hz

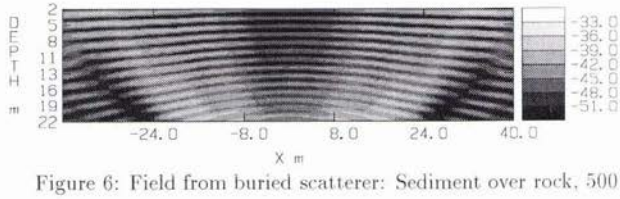

Figure 6: Field from buried scatterer: Sediment over rock, 500 Hz

In figures 5-6 it is interesting to note that the maximal amplitude of the scattered field occurs outside the z axis, thus favouring a bistatic source-receiver configuration. The influence of the bedrock on the strength of the backscattered field is small, however in the bedrock case the maximal amplitude is slightly shifted away from the z axis compared to the halfspace case.

At 1000 Hz, as shown in figures 6-7, the main lobe of the scattered field is on the z axis. The strength of the field is approximatively 10 dB higher than at 500 Hz. Finally, it is also seen here that the influence of the bedrock is very small, giving only a slight outward shift of the sidelobe pattern.

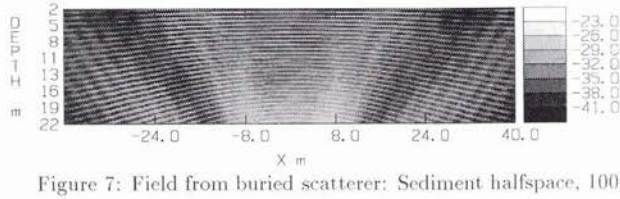

Figure 7: Field from buried scatterer: Sediment halfspace, 1000 Hz

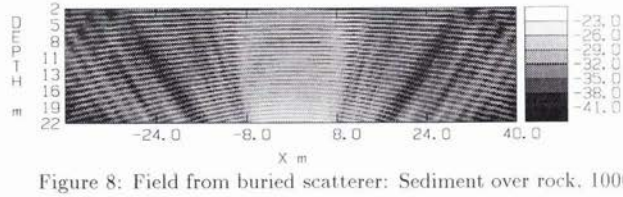

Figure 8: Field from buried scatterer: Sediment over rock, 1000 Hz

Acknowledgment

This work is part of the ISACS project, supported by the EU under contract MAS3-CT95-0046 (DG 12 - DTEE).

References

[1] G.C Gaunard and M.F. Werby, "Acoustic resonance scattering by submerged elastic shells", *Appl. Mech. Rev.*, vol 43, pp. 171-208, 1990.

[2] P. Gerstoft and H.Schmidt, "A boundary element approach to ocean seismoacoustic facet reverberation", *J. Acoust. Soc. Am.* **98**, pp. 1629-1642, 1991.

[3] J.A. Fawcett, "Acoustic scattering from cylindrical objects embedded between two half-spaces", *J. Acoust. Soc. Am.* **100**, pp. 3053-3060, 1996.

[4] I. Karasalo, "Exact finite elements for wave-propagation in range-independent fluid-solid media'. *J. Sound Vib.* **172**, pp. 671-688, 1994.

[5] K.E. Atkinson, "User's Guide to a Boundary Element Package for Solving Integral Equations on Piecewise Smooth Surfaces", Tech. Report 1994, Dept. of Mathematics, University of Iowa.

[6] V.V. Varadan, et.al., *Field representations and introduction to scattering*, Amsterdam, North-Holland, Ch 2, Sec. 5.4, pp. 73-90, 1991.

[7] M.J.D. Powell, *Approximation theory and methods*, Cambridge, Cambridge University Press, Ch 19, pp. 226-240, 1981.

[8] G. Dahlquist, Å. Björck, *Numerical methods*, Englewood Cliffs, Pretice-Hall, Sec. 7.4, pp. 297-301, 1974.

[9] J. Stoer, *Einführung in die Numerische Mathematik I*, Berlin, Springer, Sec. 3.3, pp. 108-117, 1972.

[10] A.R. Curtis and J.K. Reid, "The solution of large sparse unsymmetric systems of linear systems", AERE, Harwell, Report HL71/3280, June 1971.

[11] Y. Saad and M.H. Schultz, "A Generalized Minimal Residual Algorithm for Solving Nonsymmetric Linear Systems" *SIAM J. Sci. Stat. Comput.*, vol. 7, pp. 856-869, 1986.

[12] H.A. Schenk, "Improved integral formulation for acoustic radiation problems", *J. Acoust. Soc. Am.* **44**, pp. 41-58, 1968.

Modeling range-dependent, high-frequency, shallow-water torpedo reverberation data

Ruth Eta Keenan*, Henry Weinberg**, Frank E. Aidala, Jr.***

*Science Applications International Corporation
Box 658
Mashpee, MA 02649

**Integrated Performance Decisions
Waterford, CT 06385

***Naval Undersea Warfare Center Division
Newport, RI 02841-1708

Abstract

The high-frequency, forward bottom losses predicted by a lossy Rayleigh and a Biot poroelastic sediment model are substantially different. These differences will accumulate and become measurable in multiple bottom bounce scenarios. Torpedo reverberation data from a sandy, shallow-water Cape Cod site provides a suitable multipath environment to examine the differences between these sediment models.

1. Introduction

The range-dependent Comprehensive Acoustic System Simulation (CASS) was used with the Gaussian Ray Bundle (GRAB) eigenray propagation model to analyze 110 shallow-water torpedo reverberation time series[1]. The reverberation and geophysical data were collected in shallow water near Cape Cod, Massachusetts. The bottom was modeled in a manner consistent with the geophysical survey, changing sediment composition along the environmental track. The CASS predictions were bottom reverberation dominated and agreed with the data to within 3-5 dB. The analysis used surface, volume and bottom component models recommended by the Applied Physics Laboratory/University of Washington (APL/UW) [2]. The APL/UW bottom forward loss model is based on the idea of a lossy Rayleigh coefficient first published by Mackenzie[3]. The APL/UW bottom backscattering model incorporates a component due to interface roughness and volume scattering [4,5]. Boyle and Chotiros have suggested that sandy sediments might best be modeled structurally via the Biot poroelastic theory [6,7]. The Biot theory differs from other sediment theories in that it treats the sediment as a two-phase medium, consisting of a solid skeletal structure of sediment grains, through which a pore fluid flows. Boyle and Chotiros implemented the Biot theory in their BOGGART model (henceforth referred to as ARL/UT) and provided the authors with curves appropriate for the Cape Cod site [8]. The difference between using the ARL/UT and the APL/UW bottom models in the CASS predictions of several Cape Cod torpedo reverberation time series is examined here.

2. Modeled Environment

Figures 1 and 2 illustrate the bottom forward loss and bottom backscatter curves used in this comparison. Reverberation time series for areas characterized by the geoacoustic sampling sites 44 and 22 were selected for comparison. Grab samples from these stations measured the grain size index. The sandy site 44 had a grain size index between 1 and 2 and the sandy-gravel site 22 had a grain size index between -1 and 3. The different physical assumptions about the behavior of the medium result in very different forward loss and backscattering curves. The APL/UW forward bottom loss is less than -1 dB up to the critical angle at about 35°. The ARL/UT Biot model decays rapidly to the plateau in the 10° to 40° region

at a value about -4 to -6 dB. This plateau is peculiar to Biot's theory due to the slow wave losses in this region. The ARL/UT backscattering strength curves tend to be stronger than the APL/UW curves for the same bottom characteristics.

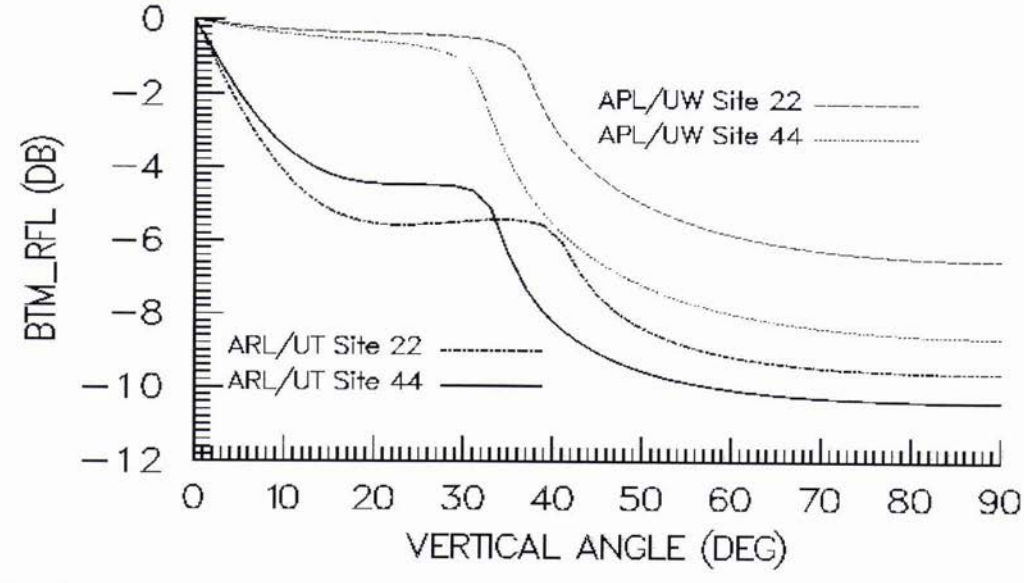

Figure 1. Bottom forward loss models

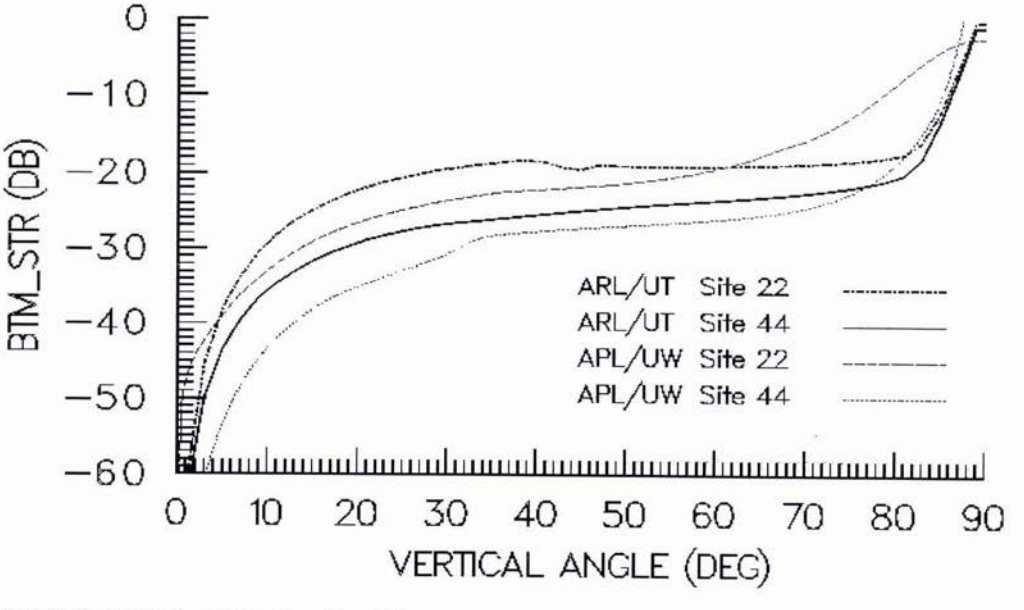

Figure 2. Bottom backscattering strength models

The torpedo data that has been selected for the modeling comparisons is designated torpedo ping 438 collected near sandy site 44 and torpedo ping 160 collected near the sandy-gravel site 22. Figures 3 and 4 illustrate the sound speed and a ray trace appropriate for the modeled environment. The ray trace in figure 3 illustrates a ray fan from -11° (negative angles point toward the surface) to 5° sampled every 0.3° where the ray paths are terminated at the second bottom interaction for the environment representative of torpedo ping 438. Figure 4 illustrates the corresponding sound speed and ray trace (from -6.4° to 2.4° sampled every 0.2°) in the environment representative of torpedo ping 160.

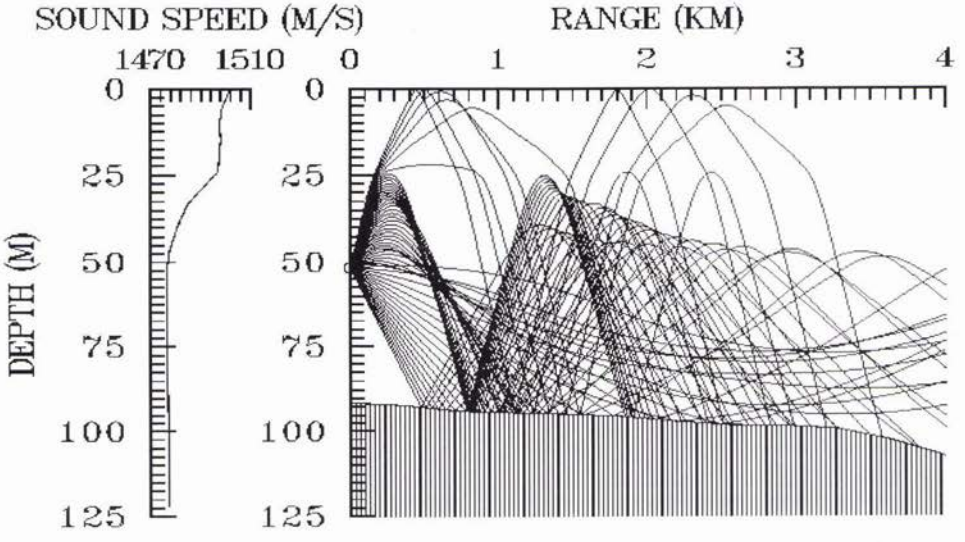

Figure 3. Ray trace for ping 438 environment

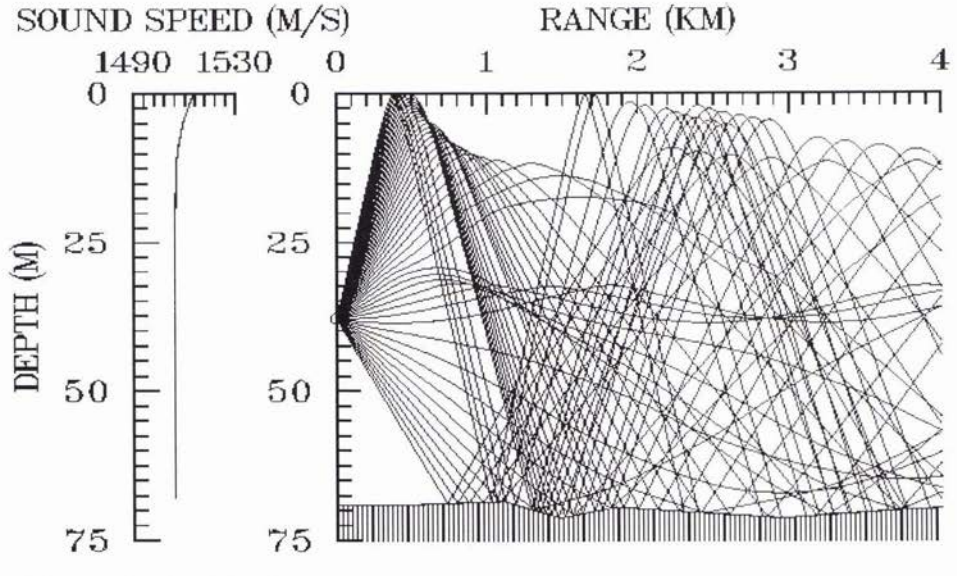

Figure 4. Raytrace for ping 160 environment

3. Model Comparisons

Figure 5 illustrates the CASS model predictions for torpedo ping 438 using the sandy site 44 APL/UW bottom models with data from two other torpedo pings taken close to the same track. The reverberation levels have been adjusted by an arbitrary constant for publication in the open literature. The prediction labeled no bounce indicates that the reverberation is composed of paths that do not propagate beyond the first bottom bounce. Hence no forward bottom loss is applied. The one (two) bounce label indicates that CASS is summing paths up to and including those paths that apply the forward bottom loss once (twice). The default CASS mode sums up to ten bottom bounce paths. The curve labeled Cass_438 indicates the default CASS reverberation prediction. CASS with the APL/UW bottom models predicts the reverberation levels increase another 5 dB (at 4 seconds) due to ray paths that interact with the bottom more than two times. Figure 6 illustrates the same CASS model predictions using the ARL/UT bottom models. CASS with the ARL/UT bottom models predicts little contribution from paths beyond the second bottom bounce. The CASS predictions with the APL/UW bottom models are more consistent with the torpedo reverberation levels and decay rate than are the CASS predictions using the ARL/UT bottom models.

The CASS model predictions using the summation of paths with zero, one, two, five and ten bottom bounce paths for torpedo ping 160 are compared with the torpedo data in figures 7 and 8. In this environment the bottom curves for the sandy-gravel site 22 are used. CASS with the APL/UW bottom models (figure 7) predicts that the net reverberation levels are due to the summation of ray paths with more than 5 bottom bounce interactions. However, ray paths with more than 5 bottom interactions tend to overestimate the measured reverberation levels beyond 3 seconds. CASS predictions using the ARL/UT Biot model show little contribution to the net reverberation levels from ray paths beyond the second bottom bounce (the five bottom bounce curve in figure 8 is hidden by the default Cass_160 ten bottom bounce curve) and significantly underestimates the reverberation levels beyond 1 second.

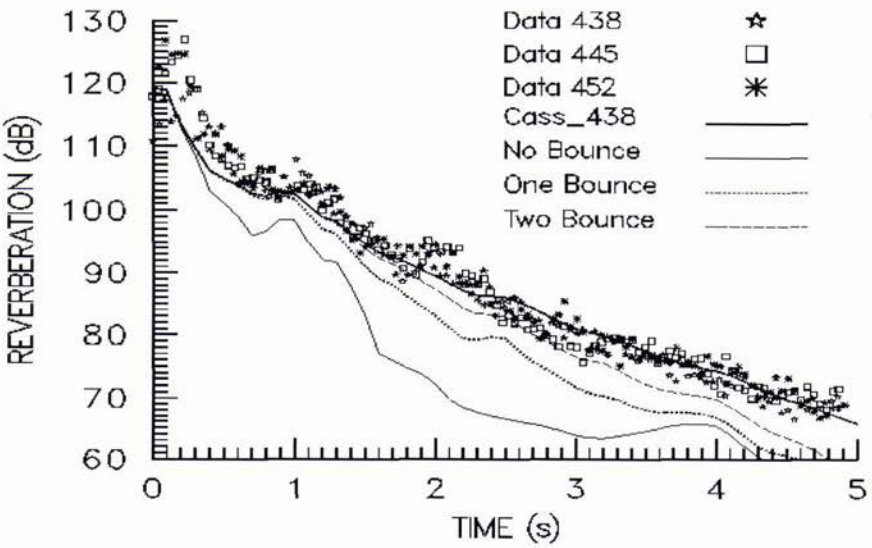

Figure 5. Data 438/Site 44 bottom APL/UW model predictions

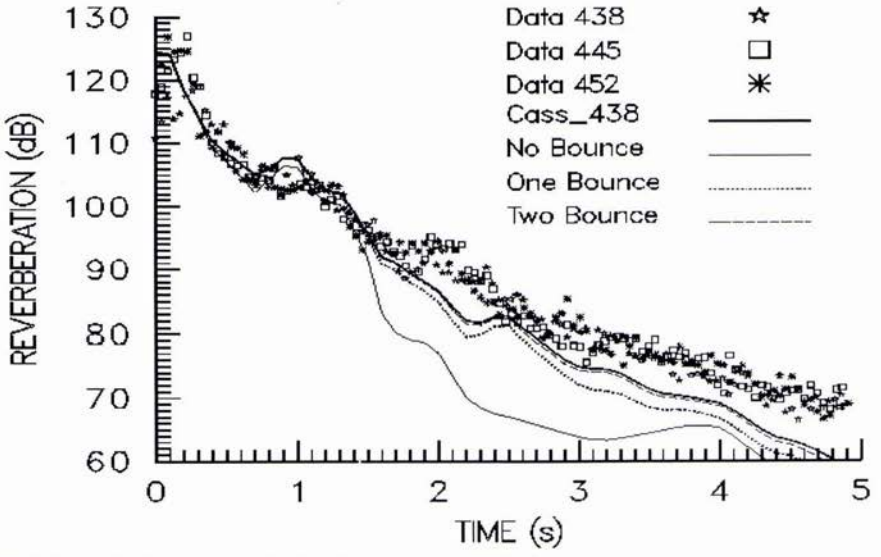

Figure 6. Data 438/Site 44 bottom ARL/UT bottom model predictions

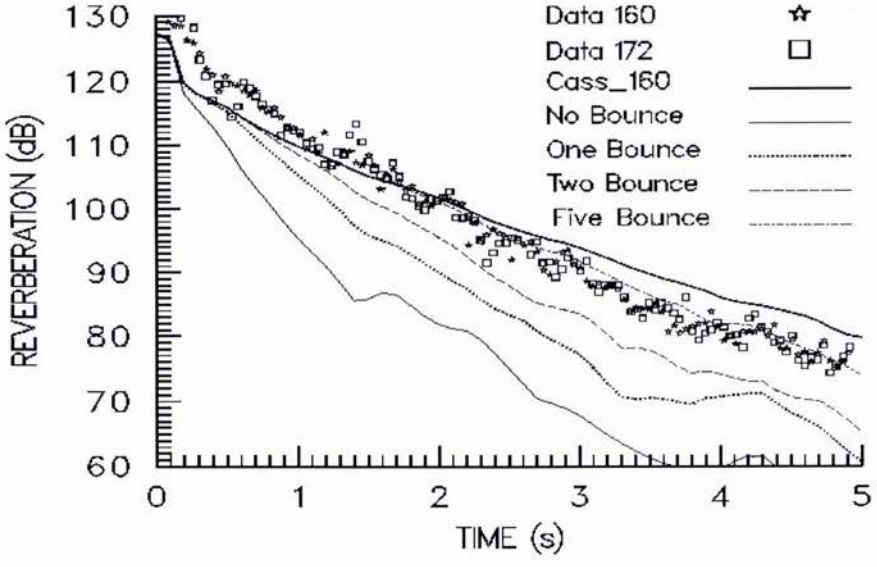

Figure 7. Data 160/Site 22 bottom APL/UW model predictions

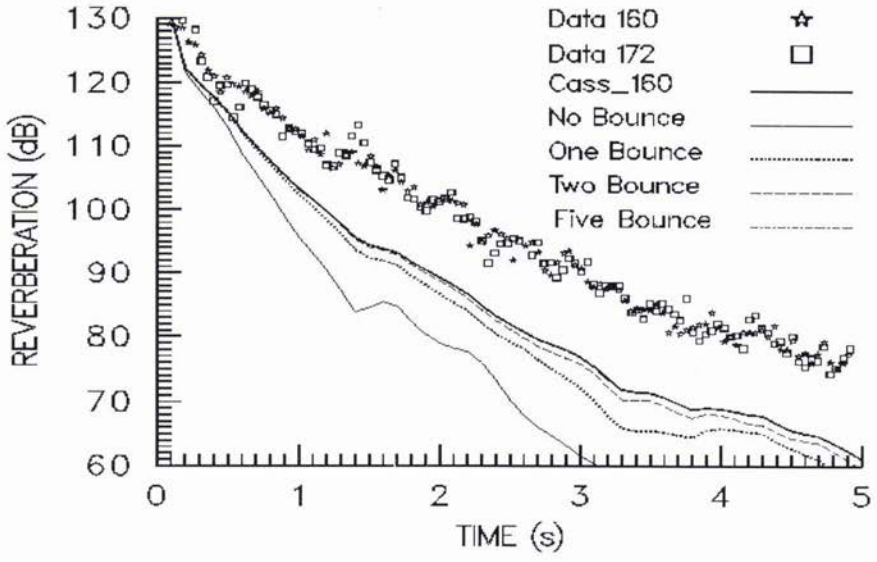

Figure 8. Data 160/Site 22 bottom ARL/UT model predictions

A consequence of the model differences manifests itself in the time spread of the signal on the bottom. The CASS model predicts that the eigenray structure (with levels greater than 95 dB re 1μPa) at a range of 4 km from the source will last 170 msec if the APL/UW Rayleigh model is an appropriate description of the bottom (figure 9) versus 30 msec for a Biot poroelastic model of the bottom (figure 10).

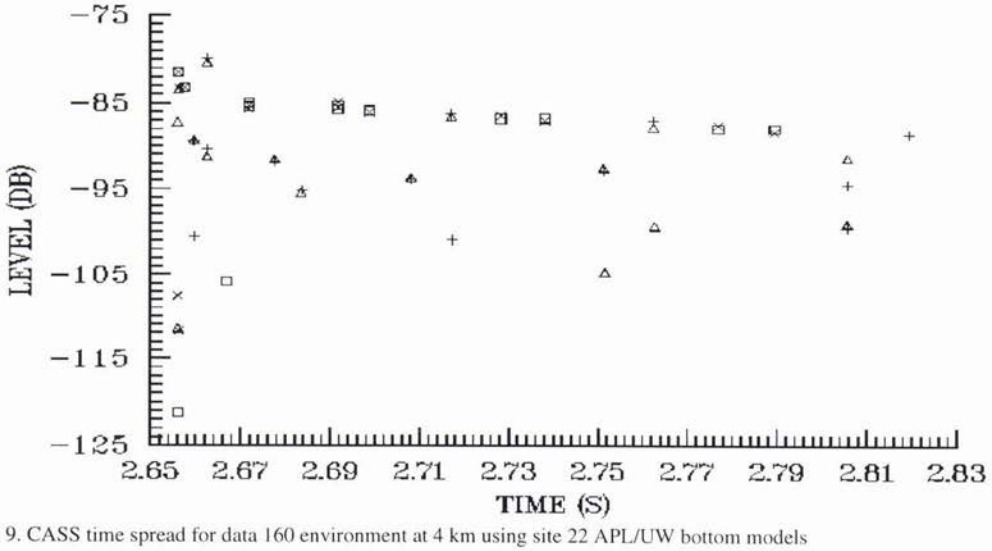

Figure 9. CASS time spread for data 160 environment at 4 km using site 22 APL/UW bottom models

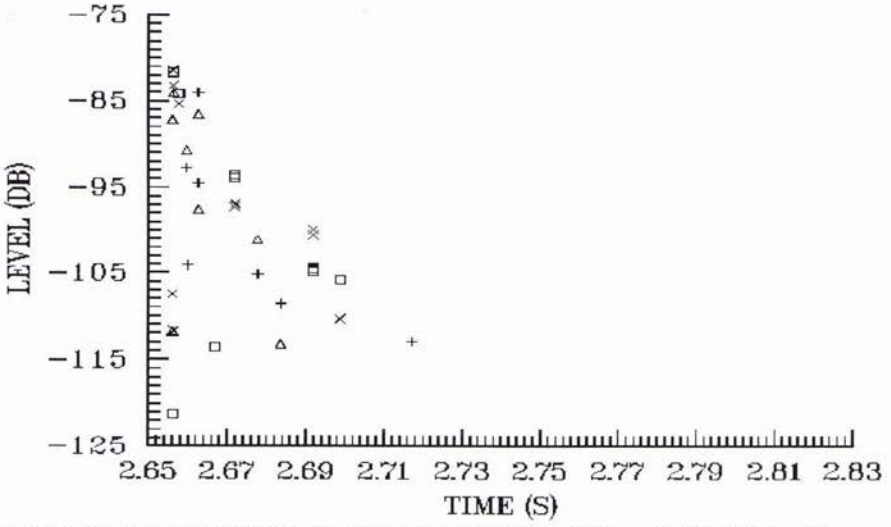

Figure 10. CASS time spread for data 160 environment at 4 km using site 22 ARL/UT bottom models

4. Conclusion

Torpedo reverberation data from a sandy, shallow-water Cape Cod site provides a suitable multipath environment to examine the difference between the forward bottom curves predicted by a lossy Rayleigh (APL/UW) and a Biot poroelastic (ARL/UT) model of the bottom. CASS predicts little contribution beyond the second bottom bounce path when the ARL/UT bottom models are used because the Biot bottom loss quickly extinquishes the higher order paths. CASS predicts contributions from ray paths with as many as five bottom interactions when the APL/UW bottom models are used. In the torpedo reverberation time series this difference manifests itself in the decay rate of the reverberation level and increasingly in the overall reverberation level with time. A measurement of the energy incident on the bottom would show a significantly greater time spread in the arrival structure for a bottom that behaved in accordance with a Rayleigh model versus a Biot model. At this Cape Cod site, the torpedo reverberation data supports modeling the bottom as a lossy Rayleigh model.

REFERENCES

[1] Keenan, R.E., H. Weinberg, F.E. Aidala, "Modeling Cape Cod Site C and Site D Torpedo Reverberation Data with the Comprehensive Acoustic System Simulation", Naval Undersea Warfare Center (NUWC)/Newport Technical Report 10590, 11 July 1996.

[2]____, "APL/UW High-Frequency Ocean Environmental Acoustic Models Handbook," APL/UW Technical Report 9407, Applied Physics Laboratory/University of Washington, Seattle, Washington, October 1994.

[3] Mackenzie, K.V., "Reflection of Sound from Coastal Bottoms", *J. Acoust. Soc. Am.*, **32**, 221-231, 1959.

[4] Mourad, P.D. and D.R. Jackson, "High Frequency Sonar Equation Models for Bottom Backscatter and Forward Loss", in Proceedings of OCEANS'89 (Marine Technology Society and IEEE), 1168-1175, 1989.

[5] Jackson, D.R. and K.B. Briggs, "High-Frequency Bottom Backscattering: Roughness versus Sediment Volume Scattering," *J. Acoust. Soc. Am.*, **92**, 962-977, 1992.

[6] Boyle, F.A. and N.P. Chotiros, "Bottom Grain Gas and Roughness Technique (BOGGART) Version 3.0: Bottom Backscatter Model User's Guide", ARL-TR-96-10, Applied Research Laboratory, University of Texas, June 1996.

[7] Biot, M.A., "Theory of Propagation of Elastic Waves in a Fluid Saturated Porous Solid. II. Higher Frequency Range," *J. Acoust. Soc. Am.*, **28**, 179-191, 1956.

[8] Boyle, F. A., personal communication, February 1997.

ADVANCES IN COTS SIDE SCAN SONAR FOR MCM APPLICATIONS

Garry Kozak

Klein Associates
11 Klein Drive
Salem, N.H. 03079, U.S.A.
Email: sonar@attmail.com
Web Site: www.kleinsonar.com

Abstract

The Persian Gulf War has elevated the awareness to the problems of shallow water mine detection. Today's high technology shallow water anti-invasion mines, such as the Italian made "MANTA" and the Swedish manufactured "ROCKAN", have been designed with stealth shapes and from materials to make detection by sonar systems difficult. Recent trials at NUWC (Naval Underwater Weapons Center), Newport R.I., have demonstrated the advantage of the latest generation of COTS (commercial-off-the-shelf) Side Scan Sonars employing full digital designs in detecting these mine types. This poster session will summarize the design features of these new systems and example results will be presented.

1. Introduction

NUWC (Naval Underwater Weapons Center), Newport R.I., has an on going AUV (autonomous underwater vehicle) development program for MCM applications. The selection process of a COTS side scan sonar for installation on the AUV involved deploying a test mine field and evaluating sonar performance against various mine types. A test mine field consisting of a MANTA, ROCKAN, SSLM (submarine launched mobile mine), and a Russian air dropped conventional ground mine were laid in 20 meters of water depth off Gould Island, NUWC'S test range. Several different sonars were tested including the U.S. Navies older C-MK I Shadowgraph, an ultra high resolution system operating at 1.3 and 1.4 MHz. Klein Associates participated in the trials with their new System 2000, an all new 100% digital side scan sonar system.

A second trial was organized to push the speed envelope for the detection of various mine types. A new mine field was again deployed consisting of a MANTA, a MK 52, a Mk 6 moored mine and a RM-1 moored mine. The Klein System 5000, the first commercially available COTS high speed, dynamically focused multi-beam side scan sonar, was tested against these mines at speeds up to 12.0 knots. This system employs the same design principles for creating continuously range focused receive beams as found in the U.S. Navy's helicopter towed AN/AQS-14 side scan sonar manufactured by Westinghouse.

2. Klein System 2000Description

The System 2000 is an all digital, simultaneous dual frequency, COTS side scan sonar consisting of a small light weight instrumented towfish, a single coaxial towcable and the surface processing unit.

2.1 Towfish

The towfish has port and starboard transducers which contain high performance 100 kHz and 400 kHz arrays. The 100 kHz has a 1.0 degree horizontal by 40 degree vertical beam and the high resolution 400 kHz has a 0.2 degree horizontal by 40 degree vertical beam. Transmitters are of a synthesized tone burst design allowing stable variable transmit pulse

Model 2260NV Instrumented Towfish

lengths to be selected. The pre-amplifier is designed for very low noise with a noise figure of less than 1 db. A TVG (time-variable-gain) amplifier with a digitally synthesized range-gain law ensures a wide backscatter dynamic range compression prior to signal digitisation. The 12 bit digital multiplexed data is transmitted to the surface through a single coaxial conductor towcable. Integrated into the towfish is a sensor package which includes a heading, pitch & roll sensor, a pressure sensor for depth, a temperature sensor and an optional responder for use with a USBL acoustic tracking system. The sensor data is very valuable when used in the target position calcultation since it reduces error in the calculated geographic position of targets on the seafloor.

2.2 Surface Processor

The System 2000 surface unit is a no compromise integration of the sonar processor, a high resolution color video display, a very high resolution 300 dpi, 256 true gray shade thermal printer, and high density digital tape drives for archiving the sonar and navigation data. The hard copy thermal printer can display 2 channel single frequency data or simultaneous dual frequency (100/500 kHz) data. Positioning data is received from the navigation system and on the video display, via the trackball/cursor, real time positioning of mine like targets as well as target mensuration is done This target information is stored on the digital recording tapes and exported to host computers for real time plotting of the target locations, etc. Other standard features included are mapping display (slant range and speed correction), real time target zooming, delay and expand functions. An optional 3.5 kHz sub-bottom profiler can be added onto the system which is a valuable sensor to aid in the classification of bottom hardness, data which is helpful for Q-Route selection.

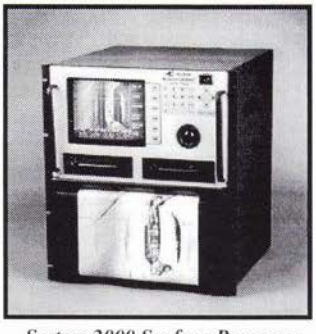

System 2000 Surface Processor

3. Klein System 5000 Mk II Description

The Klein System 5000 Mk II Focused Multi-Beam side scan sonar is designed for high speed (10+ knots), 100% bottom coverage while maintaining very high resolution over the full swath of up to 300 meters. The towfish houses port and starboard transducer arrays that operate a 455 kHz, giving operational ranges of up to 150 meters per side. A complete sensor package containing heading, pitch, roll, pressure, temperature and acoustic responder is included. Phase shift processing techniques are used to develop 5 simultaneous digitally formed receive beams per side. In addition, these beams are dynamically range focused to maintain 20 cm. along-track resolution in standard mode and 10 cm. along-track resolution in high resolution mode. The beam forming, focusing, time variable gain (TVG), and digital multiplexing / de-multiplexing of the sonar (up-link) and control (down-link) data is accomplished in the towfish. The control and sonar / sensor data is bi-directionaly multiplexed on a single coaxial conductor towcable. Data display of sonar imagery and detected MLO's (mine-like-object) is on a PC based image processing system which also handles target position calculations and target mensuration.

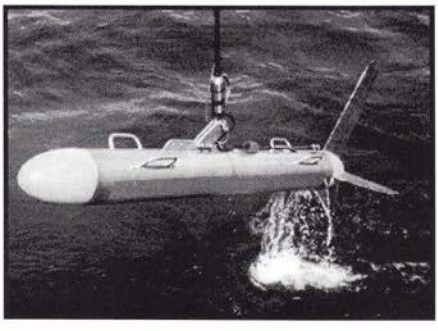

System 5000 Mk II Towfish

4. Mine Target Descriptions

The two trials used mine types which are representative of both traditional steel mines and the newer high technology plastic / stealth types. A summary of the mine types and characteristics follow.

4.1 AMD - 1000 (emulation)

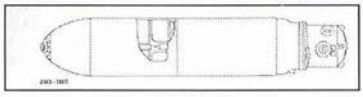

The AMD - 1000 is a conventional steel cased influence ground mine. The dimensions are approximately 2.85 meters long by 0.53 meters in diameter. This target was used for the **System 2000** trial.

4.2 Submarine Launched Mobile Mine (SSLM)

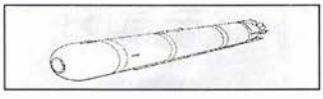

The SSLM mine is essentially a torpedo modified with mine components. The body is metal cased and the dimensions are approximately 4.1 meters in length and 0.50 meters in diameter. This target was used for the **System 2000** trial.

4.3 Manta Mine

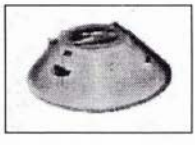

The Italian made Manta mine is one of the newer high technology anti-invasion ground mines. This influence mine is plastic cased and has a low profile conical shape making it one of the more difficult types to detect with a sonar system. The dimensions of the Manta are 0.98 meters in diameter at the base and 0.47 meters high. This mine was used for both the **System 2000** and **System 5000** trials.

4.4 Rockan Mine

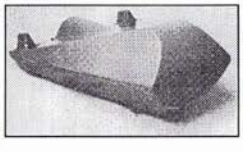

The Swedish made Rockan, which because of it's shape and plastic case, was the most difficult mine to detect during the trials. The sloping angled faces and low profile of this mine make it truly a stealth design. The Rockan is 1.02 meters long, 0.80 meters wide and 0.38 meters high. This mine was used for the **System 2000** trial.

4.5 Mk 52 Mine

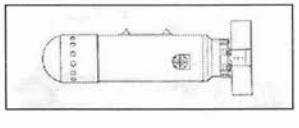

The U.S. Mk 52 mine is a traditional steel cased cylindrical ground mine. Due to it's shape and material it is one of the easier mines to detect. The Mk 52 is 2.25 meters in length and 0.85 meters in diameter. This mine was used for the **System 5000** trials.

4.6 Mk 6 Moored Mine

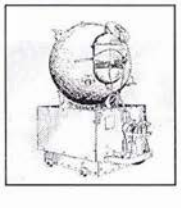

The U.S. Mk 6 mine is an obsolete moored contact mine. This mine was used as a representative mid-water spherical MLO. The mine is approximately 1.0 meters in diameter. The Mk 6 was used for the **System 5000** trials and was moored approximately 2 meters off the bottom.

4.7 RM-1 Rising Mine

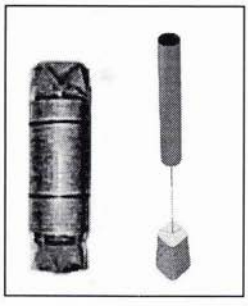

The RM-1 rising mine is a steel cylinder that is moored above the bottom. This mine acoustically senses a target and then is propelled to the target. The cylindrical moored mine case dimensions are 2.76 meters high by 0.64 meters in diameter. This mine was used for the **SYSTEM 5000** trials and was moored 2 meters above the bottom.

5. Trial Results

The trials for both systems were conducted off the NUWC torpedo recovery vessel #841 which is 35 meters in length. Navigation was controlled by an integrated navigation computer using differential GPS input. Both sonar systems were hand deployed on light weight towcables.

5.1 System 2000 Trial Results

The **System 2000** trial was run at towspeeds of 3 to 4 knots and at various sonar ranges up to a maximum of 100 meters. The sample images are from the **System 2000** video display. The upper half of the display shows the un-zoomed sonar image in a reversed gray scale. The lower right sonar image is the zoomed display to full sonar resolution of the mine and in a positive gray scale. The lower left part of the display shows the target data which includes it's geographic position on the seafloor as calculated from the navigation input, and measurements made of it's length, width, and height. All of this data is stored in a target file on the digital tape and exported through an RS 232 port to 3rd party processing systems. Representative sonar images from the **System 2000** of the 4 different mine types used in the trial follow:

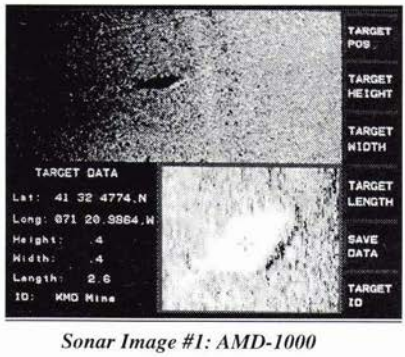

Sonar Image #1: AMD-1000

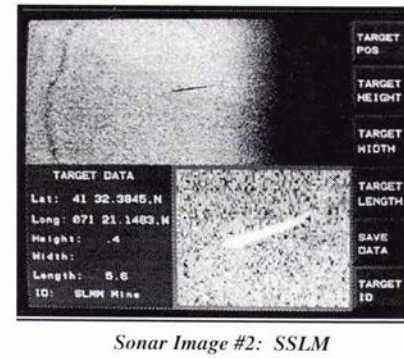

Sonar Image #2: SSLM

The conventional cylindrical steel cased **AMD-1000** and **SSLM** mine were very easy targets to detect and classify using the echo return and characteristic parallelogram shaped acoustic shadow. These two targets were successfully detected on all sonar ranges up to the maximum 100 meter sonar range used during the trial.

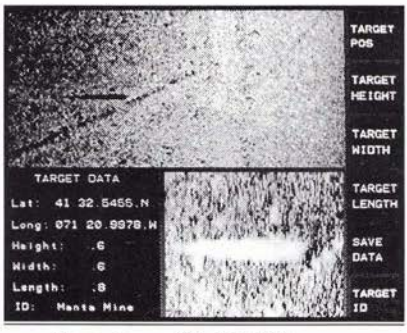

Sonar Image #3: MANTA

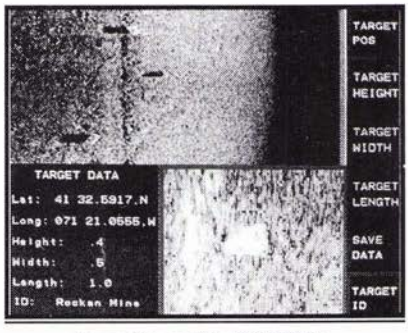

Sonar Image #4: ROCKAN

The **Manta** was a somewhat more difficult mine to detect due to it's plastic case, conical shape and low profile height. In the image the acoustic shadow shape clearly implied a conical shape. The **Manta** was repeatedly detected on all ranges up to a maximum of 75 meters. The linear feature nearby is an old drag scar probably from a fishing trawler.

The **Rockan** was the most difficult mine to detect with it's very low profile, plastic case and unusual shape. Classification was aided by the acoustic shadow which clearly showed a sloping up surface which abruptly drops back down. The **Rockan** was repeatedly detected on all ranges up to a maximum of 75 meters. The two other rectangular objects seen above and below the **Rockan** in the upper part of the video display are New England lobster traps.

5.2 High Speed System 5000 Trial Results

The **System 5000** trial was run at towspeeds of 9 to 12 knots and on various sonar range scales up to a maximum of 100 meters. This trial clearly showed the advantage of modern digitial design against to ambient noise pick-up. The towfish at these high speeds was riding (most of the time) directly in the propeller wash and noise would typically be seen on the sonar imagery. The **System 5000** sonar images were clean with no detectable noise displayed. Representative sonar images of the 4 different mine types used in the trial follow:

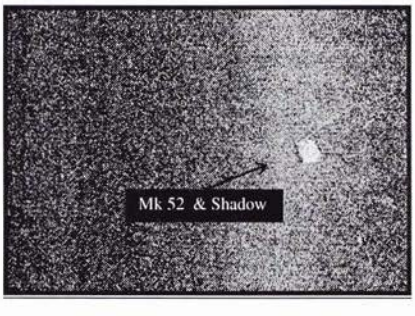

This **System 5000** sonar image of the **Mk 52** was made at a speed of **11.9 knots** and the sonar was set to a 50 meter range scale. The image is comparable to the image produced by the single beam **System 2000** at **4 knots**.

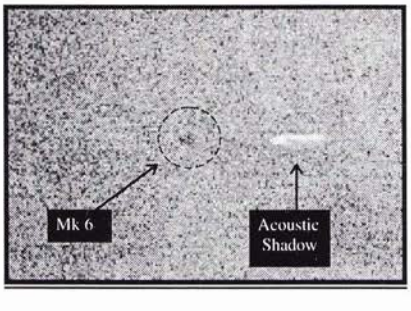

This **System 5000** sonar image of the **Mk 6** moored mine was made at a speed of **9.0 knots** and the sonar was set to a 75 meter range scale. The acoustic shadow is detached from the mine since it is moored above the sea floor.

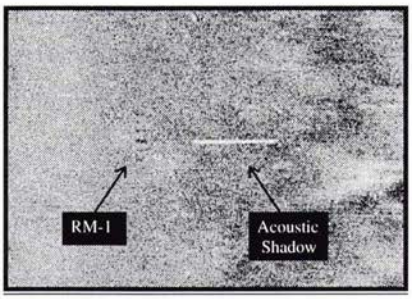

This **System 5000** sonar image of the **RM-1** rising moored mine was made at a speed of **11.8 knots** and the sonar was set to a 75 meter range scale. The sonar successfully detected this mine at very high speed even though, suspended vertically on it's tether, it presented a very small along track dimension to ping on.

+

This **System 5000** sonar image of the **Manta** mine was made at a speed of **11.8 knots** and the sonar was set to a 75 meter range scale.

6. Conclusion

The imaging results from the first trial with the System 2000 showed the advantage of an all digital design compared to the older analog and analog/digital hybrid designs. The image resolution and range performance were clearly superior when compared to older systems and even surpassed the resolution generated by the ultra high frequency C-Mk I Shadowgraph. On this basis a re-packaged System 2000 was selected for installation into the NUWC AUV test platform.

The System 5000 results showed that the large aperature, multi-beam, continuous range focusing techniques provided high speed (10+ knots), full bottom coverage mine detection out to ranges of 100 meters. The sonar image resolution and quality was comparable to that made with the single beam System 2000 at slower tow speeds (less than 5 knots).

Measurement of the bubble population in coastal waters using combination frequencies of MHz order

Timothy G. Leighton, Andy D. Phelps and David G. Ramble

Institute of Sound and Vibration Research,
University of Southampton,
Highfield, Southampton, UK
Email: tgl@isvr.soton.ac.uk

Abstract

This paper describes the use of a combination frequency technique to measure the size distribution of oceanic bubbles. Written between two sea trials, the paper describes how the apparatus can be adapted to design tests for specific environments and data requirements. Parameters which can be changed are the sensing volume, the bubble radii for which data points are taken, and the degree of time resolution in the bubble counts.

1. Introduction

The ability to size and count gas bubbles in liquid has many applications relevant to ocean science, including studies into ambient noise [1,2], the near-surface acoustic waveguide [3,4], the atmosphere/ocean fluxes of mass, momentum and energy [5,6], precipitation [7,8], diver safety [9-11], dynamic loading on structures, sonar occlusion, cavitation inception [12], and passive sensing [13]. Because of the differing compressibilities of the gas and liquid, and the impedance mismatch at the bubble wall, acoustic techniques for bubble detection can be effective. Notably, measurement of the resonance frequency ν_r of a bubble can be used to estimate its equilibrium radius R_0, since ν_r is approximately inversely proportional to the bubble radius [14] (e.g. $\nu_r R_0 \approx 0.01 \sqrt{p_0}$ for air bubbles of $R_0 >\sim 10$ μm in water of static pressure p_0).

A sound field of given angular frequency ω_p (here termed the 'pumping' frequency) can drive a bubble into nonlinear oscillation such that it backscatters a range of frequencies including ω_p, $2\omega_p$, $3\omega_p$ ..., $\omega_p/2$, $3\omega_p/2$ ... etc. The closer ω_p is to the bubble resonance, the stronger in general these emissions. Although bubble sizing has been attempted using these signals, as well as with Doppler techniques and geometrical imaging, all such signals possess limitations [15]: the detector may, for example, mistake a cluster of small bubbles, or a single large bubble, for a resonant bubble. In the method used in this paper the bubble is insonated by the 'pump' frequency ω_p *plus* a higher, fixed, 'imaging' frequency ω_i. Because the latter is much higher than ω_p, the bubble pulsation is effectively 'frozen' during a single imaging cycle. Thus the returned signal is a measure of the geometric scattering from a target whose acoustic cross-section varies periodically. This is shown in figure 1, where the signal returned by the bubble consists of the imaging frequency, amplitude modulated by the pump frequency. Consequently the spectrum of the returned signal contains peaks at $\omega_i \pm \omega_p$, the amplitudes of which increase with the pulsation amplitude of the bubble and therefore, if the amplitude of the pump signal is frequency-independent, with the nearness of ω_p to the bubble resonance. If the off-resonance contributions from bubbles of a size similar to those resonant at ω_p can be incorporated into an analysis of the $\omega_i \pm \omega_p$ signals, then in principle the $\omega_i \pm \omega_p$ signals can be used to estimate the number of bubbles resonant at ω_p in the sensing volume. The two-frequency insonation may also generate signals at $\omega_i \pm \omega_p/2$ with much reduced off-resonance and non-bubble contributions than the $\omega_i \pm \omega_p$ signal [16]. In both techniques the high frequencies allow specific spatial localisation, and low signal-to-noise ratios since bubble-mediated information is transposed from a comparatively noisy frequency window around ω_p up to a frequency window around ω_i. Whilst $\omega_i \pm \omega_p/2$ signals are appropriate for high-accuracy measurements of individual bubbles (as might be useful as a sensor for pressure changes [17]), the parametric nature of the emissions require that the pump signal amplitude at the bubble must be very well controlled. This makes it less suitable for bubble measurement in the oceanic environment than the $\omega_i \pm \omega_p$ signal used here. When the $\omega_i \pm \omega_p$ technique is used at sea,

care must be taken to account correctly for the contributions to the signal of off-resonant, and non-bubble, sources, and the techniques for so doing are now described.

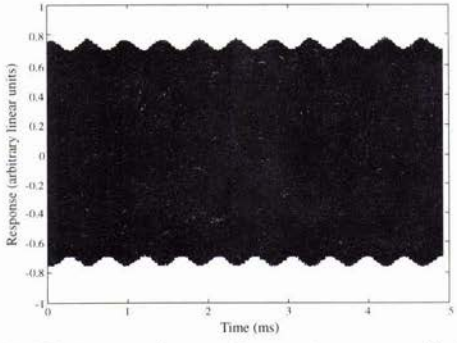

***Figure 1**. Returned signals from a bubble insonated at two frequencies, measured with a high frequency probe - the high frequency imaging signal was set at 1.1 MHz, and the bubble resonance/pump frequency at 2160 Hz. The data was sampled at 10 MHz on a LeCroy 9314L digital oscilloscope. The pump signal amplitude is 25 Pa. The high carrier frequency plots so densely as to appear black in the figure.*

Earlier workers investigated the $\omega_i \pm \omega_p$ signal for measuring an oceanic bubble population [18], using a chirped signal between 2.5 and 6 kHz, with an imaging frequency of 450 kHz. However in those tests no distinction was made between bubble-mediated coupling and that caused by turbulence, and no compensation was made either for the significant off-resonance nature of the $\omega_i \pm \omega_p$ signal, or for the pump transducer frequency response. Later workers documented how turbulent effects can be distinguished from the bubble signals, and compensation made for the off-resonant contribution to the $\omega_i \pm \omega_p$ signal [19]. By employing discrete tones as the pump signal, the variable frequency response of the source transducer could be removed allowing constant and clearly-defined bubble insonation conditions. Interpretation of the energy at the $\omega_i \pm \omega_p$ frequencies in terms of bubble numbers requires modelling of the bubble response. The method used here produces absolute bubble counts, rather than relying on adjustable parameters or fitting models based on historical measurements to the data. Both current and earlier workers [18-21] used simplified forms of the Rayleigh-Plesset equation, which are used to obtain expressions for the pressure amplitudes at the various frequency locations [20,21]. However these earlier procedures [18,20,21] took account only of viscous damping of the bubble motion, which for the bubbles under discussion here and earlier is an order of magnitude smaller than damping through thermal and radiation losses (Newhouse and Shankar [21] made the damping an unknown variable which they optimised to give best fit between their measured data and the bubble counts they expected). Ignoring the thermal and radiation effects produces errors of > 36 dB in relative energies invested at ω_i and $\omega_i \pm \omega_p$. The algorithm for interpreting acoustic data in terms of bubble counts used in this paper incorporates all three damping mechanisms, and reduces such errors to < 1 dB. Full details of the analysis, and of its use in the calibration of the bubble detector (which will be summarised in section 2.1) have been reported elsewhere [19].

2. Materials and methods

2.1 Laboratory calibration

Calibration of the apparatus was performed to ensure that the energy of the $\omega_i \pm \omega_p$ signals could be related to the signal strength associated with one resonant bubble. This was achieved through examination of the acoustic scattering from a steady stream of bubbles of known size. The equipment schematic is shown in figure 2. The pump frequency signal was generated using a Tektronix 2005 arbitrary waveform generator controlled via a GPIB cable connected to a PC, which was passed into a Bruel and Kjaer 2713A power amplifier. The pump transducer comprised a 104 mm inside diameter piezoceramic ring transducer which was set into a polyurethane foam and encased in a nylon housing. The imaging signal was generated by a 1 MHz crystal oscillator amplified with an ENI 240L RF power amplifier, and this was passed to the imaging signal transducer (the head of a Therasonic 1030 ultrasonic therapy unit as manufactured by Electro Medical Supplies) which was potted inside a 45 mm diameter

aluminium cylinder to protect it when used in the open sea. The imaging signal amplitude at the focus of the two transducers was measured as 30 kPa using a calibrated needle hydrophone (active element diameter = 0.5 mm) with a HP1 submersible pre-amplifier, as manufactured by Precision Acoustics Ltd.

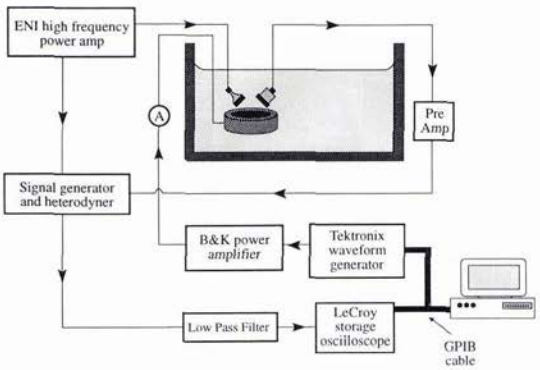

***Figure 2**. Schematic of the equipment used in the lab tests*

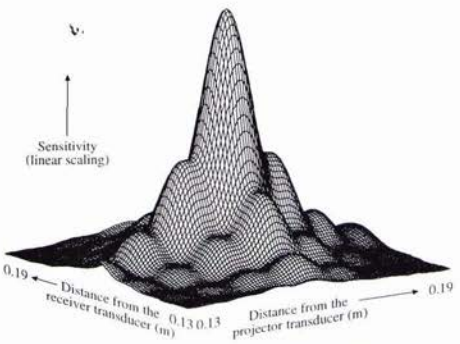

***Figure 3**. The sensitivity within the sampling volume, for the geometry employed in the Channel test.*

The returned signal from the bubble was monitored using a Panametrics V302 piezoceramic transducer, similarly potted in a 45 mm diameter sleeve, and conditioned using a Panametrics 5670 preamplifier. The preamplified signal was then heterodyned with a reference signal from the crystal oscillator: this results in the useful information contained just above and below the imaging frequency being reproduced at just above dc, enabling much lower sampling rates and data storage. The low frequency information was filtered to prevent aliasing using a Barr and Stroud EF5-02 46 dB/octave filter and acquired by a LeCroy 9314L storage oscilloscope. For the laboratory tests the data was sampled at 50 kHz and 10,000 points taken.

Calibration involved, first, verification of the model through comparison of its predictions with the measured energy distribution in the spectra scattered from the bubbles in the stream. Second, the sensitivity of the high frequency receiver transducer was estimated. Third, the behaviour of resonant bubbles at the specific pump frequencies used in the oceanic tests were modelled (using parameters applicable to sea water, rather than those of fresh water as used in modelling the lab tests). With application of the same sensitivity adjustment and the relevant preamplifier / heterodyner corrections, this provided an estimate of the signal levels expected from the different bubbles resonant at the specific pump frequencies chosen.

The calibration was done once in November 1995 in preparation for tests in the surf zone off a beach in the North Sea, and again in March 1997 before tests in deeper water in the English Channel. In each case the transducer geometry employed in the tank tests was unchanged for the subsequent ocean trial, which allowed certain parameters in the pulsation model to be poorly defined without any loss of accuracy [19]. However the two ocean tests used different transducer geometries, so that the sampling volume of the instrument was smaller for the North Sea trial (0.2 cm^3) than in the English Channel trial (1.0 cm^3). This change was made because in the first test a very small test volume was desirable since it was supposed that the bubble number densities would be very high, so that reducing the volume would reduce the chance of acoustic shielding causing under-counting. It was also of interest to investigate how small a test volume could reasonably be generated with this apparatus. However for the English Channel tests, a larger test volume was desirable (to lessen the effect of spatial inhomogeneity in the bubble field by sampling a larger volume) and allowable (since predictions suggested that the bubble densities would be lower out of the surf zone). In each case the sensing volume was calculated by modelling the beam patterns of the two high frequency transducers using a Rayleigh integral over their surfaces. When these patterns were overlapped in the same layout as the transducer arrangement, they allowed the insonation volume to be estimated. This gave an insonation volume, defined by where the sensitivity fell off to 3 dB of its peak value. The result of such a procedure for the English Channel transducer geometry is shown in figure 3, where the distance between both the high frequency transducers and the focus is 16 cm.

2.2 Oceanic data collection

The equipment used in the sea trials was largely similar to that used in the laboratory experiments, and the schematic is shown in figure 4. The most important difference in the layout of the oceanic equipment is the provision of a remote equipment canister, which was set up in the sea and attached to the land based equipment via an underwater bulkhead connector and 200 m of waterproof cable, as manufactured by PDM Group. The canister comprised a 1000 mm long × 355 mm diameter watertight aluminium alloy cylinder, which was painted to minimise corrosion, and clamped to a rigid scaffold structure as shown in figure 5. This canister contained the high frequency power amplifier, the crystal oscillator and heterodyner equipment, the returned signal RF preamplifier, and a temperature sensor to monitor the effects that the enclosed space had on the potential of the equipment to overheat. Additionally, a differential amplifier pair was added to the returned signal circuit to ensure that no signal corruption occurred when passed down the 200 m cable: this additional step was analysed in the laboratory and its frequency response quantified. Because of the higher pump frequencies involved, the data was sampled at 500 kHz, and 50,000 points were taken. To speed up the data collection and storage, the Tektronix output waveform comprised all four frequencies in one signal, and the LeCroy oscilloscope sampling the data was triggered by markers from the signal generator to allow the individual sections to be identified in the returned waveform.

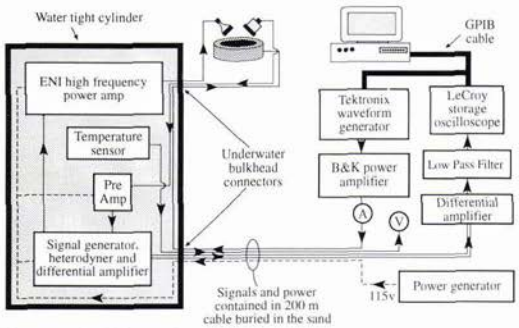

Figure 4. Schematic of the apparatus

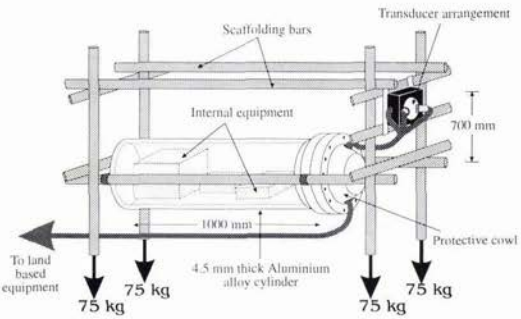

Figure 5. The arrangement of the cylinder for the North Sea test

Preliminary calibration tests were carried out to ensure that the pump signal amplitude was constant for all the pump frequencies employed in a given test. The transducer head was immersed in a test tank to the same depth that it would have whilst activated in the oceanic tests. Then the pump signal amplitude measured with a constant input signal level at each of the pump frequencies using a Bruel and Kjaer 8103 hydrophone conditioned with an 2635 charge amplifier. This allowed the frequency response of the pump transducer to be inverted, and a constant and known pump signal amplitude to be employed.

The specific pump frequencies chosen for the North Sea tests were 28, 50, 60 and 88 kHz, so that three of these would coincide with measurements made in an earlier bubble count using the resonant backscatter from bubbles [4]. This paper is written just prior to the Channel test, for which the rig will employ two different pump signal regimes. In the first, pump frequencies of 17, 28, 50, 60, 88, 10, 145, 165, 180 and 200 kHz will be used, corresponding to bubble radii of 200, 120, 66, 55, 37, 30, 23, 20, 18 and 16 μm. These were chosen since examination of earlier test results [4] indicated that, with bubble radius plotted on a logarithmic scale as is usual, these points would readily identify a possible peak in the spectrum at around $R \sim 20$ μm [4], whilst also indicating key gradients in the curve. The second regime will use fewer pump frequencies, enabling finer time resolution: the interval between consecutive tests using the 10 pump frequencies in the first regime is 3 s, whilst in the second, where only 2 pump frequencies (17 and 145 kHz) are used, it is reduced to 0.85 s. Table 1 summarises the key parameters in the oceanic tests, showing how the same apparatus can be adapted to change the parameters of the investigation, giving the experimenter flexibility to design a given test to meet a specific requirement.

The North Sea tests occurred between 26th and 30th November 1995, on a beach in Tunstall, East Yorkshire, and were carried out in tandem with a group from the Southampton Oceanography Centre. Data was taken over a 3.5 minute period every half hour while the transducers were immersed. As the signals were broadcast consecutively with no gap, each measurement lasted only 0.4 s. The beach was chosen because of its slight gradient, which allowed the equipment to be set up at low tide and anchored to the beach, such that as the tide

came in it would eventually cover the rig to enable measurements to be taken. The rig was weighed down with 75 kg metal weights at each corner which were buried in the sand.

Parameter	North Sea test	Channel test (regime 1)	Channel test (regime 2)
Pump frequencies (kHz)	28, 50, 60, 88	17, 28, 50, 60, 88, 110, 145, 165, 180, 200	17, 145
Pump amplitude at bubble (Pa)	3000	3000	3000
Sensing volume (cm^3)	0.2	1.0	1.0
Depth of sensor (m)	1.5	0.8	0.8
Time per pump frequency (ms)	100	20	20
Interval between repeats (s)	9	3	0.85

Table 1. *The key parameters of the apparatus for the North Sea test, and for the two Channel tests.*

3. Results

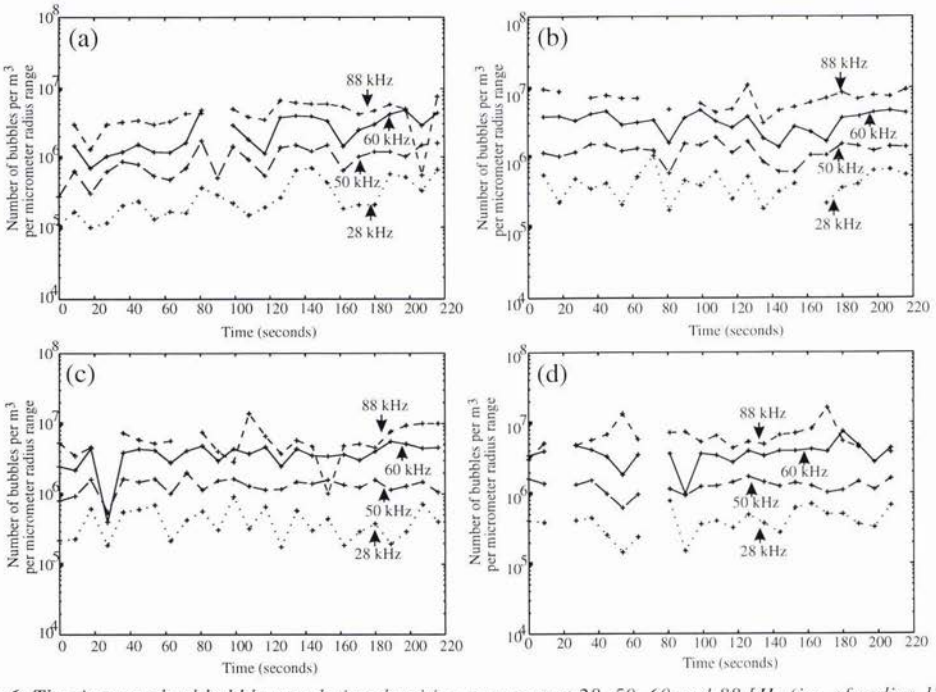

Figure 6. *The time-resolved bubble population densities, resonant at 28, 50, 60 and 88 kHz (i.e. of radius 120, 66, 55 and 37 μm respectively), measured at starting times of (a) 22.00, (b) 22.30, (c) 23.00 and (d) 23.30 GMT on 5 November 1995 in the surf zone at Tunstall. The error associated with each point is +200% and -50%. Some data points in the consecutive tests are missing. The bubble density is expressed in terms of the number of bubbles per cubic metre having a radius within a 1 μm range about the radius given.*

Figure 6 shows the time-resolved bubble counts found in the North Sea test. This degree of time-resolution is possible since the data is collected in a series of 0.4 s 'snap-shots', rather than requiring the time-averaging inherent in earlier studies. It should be noted that on occasions during the analysis the signal height dipped below the noise floor, and in these cases the particular readings have been left as gaps. In general, the smaller bubbles are the most

populous. Certain correlations between the counts of the various bubble sizes do appear at times (e.g. 120 - 180 s in (a); 20 - 40 s in (c)), although in the absence of other measurements there is no way of knowing the time-scales on which the population varies, and therefore whether any aliasing occurs. The time-average bubble counts, made by combining all the data in figure 6, have been reported in an earlier paper [19], in which the +200% and -50% error associated with each data point in figure 6, is described as arising primarily from the uncertainty associated with the sample volume: other sources of error are considered in that paper and found to be much less significant.

4. Discussion

In order to compare the time-resolved surf-zone data presented here with earlier historical measurements of the bubble population, the data must be time-averaged [19], and the results are given in figure 7. The graph suggests that, for a least-squares fit over the four points between 88 and 28 kHz (equivalent to $37 < R_0 < 120$ μm), the bubble distribution is fitted by $n(R_0) = aR_0^b$ where $n(R_0)$ is the number of bubbles per cubic metre having radii between R_0 and R_0+dR_0, and $a = 1.8 \times 10^{10}$ m^{-1} and $b = 2.3$, with associated errors for log (a / m) of ± 1.7 and for b of ± 0.9. This is higher than previous measurements, as would be expected in the surf zone. In deeper waters, the bubble population in the sea tends in the main to increase with wind speed and decrease with depth below the surface.

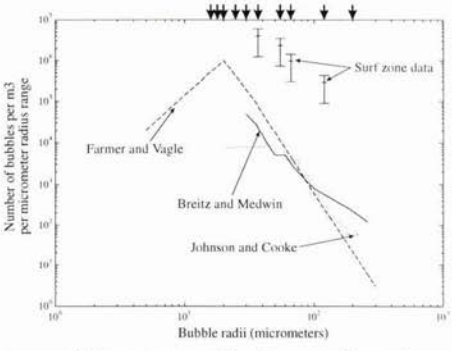

Figure 7: *Comparison of time-averaged data measured in the oceanic surf zone with historical estimates, taken from references [4], [24] and [30]. The error bars on the surf zone measurements mostly reflect an uncertainty in the measurement volume. The bubble population is expressed as the number of bubbles of a specific radius over a 1 μm range, per unit volume. The equilibrium radii corresponding to the frequencies anticipated in the Channel tests, regime 1, are also shown (arrowed).*

Optical investigations have indicated that most of the bubbles in the near-shore zone have equilibrium radii less than 100 μm [22]. Kolovayev [23] photographed and counted bubbles below breaking waves in the open sea at wind speeds of up to 13 m/s, by allowing them to rise onto a transparent plate. Dissolution may have occurred [6]. At depths between 1.5 and 8 m the most common bubbles were those possessing a radius of around 70 μm, and very few bubbles were larger than $R_0 \approx 300$ μm. Johnson and Cooke [24] photographed bubbles *in situ* in the sea, using a camera suspended from a surface float at depths of 0.5 to 4.0 m, and wind speeds of 8 to 13 m/s. They observed that the distribution of bubble size narrowed with increasing depth, the larger bubbles disappearing. The number of bubbles greater than the minimum size they could detect ($R_0 \approx 17$ μm) also decreased with increasing depth, decaying roughly exponentially over depth scales of order 1 m at wind speeds of 11 to 13 m/s, such that at a depth of 1.8 m the density of bubbles of a detectable size was 1.56×10^5 m^{-3}. They obtained a modal bubble radius in the size distribution of 40 - 50 μm. However Walsh and Mulhearn [25] suggest that the photographic observations lack the resolution to accurately count the smallest bubbles. MacIntyre [26] suggests that in addition to the lower limit imposed by resolution, there is an upper size limit on the reliable data resulting from poor statistics, so that only the data for bubbles in the range 60 μm $< R_0 <$ 150 μm is reliable. Medwin [27], making acoustic observations *in situ* through examination of attenuation at various frequencies, suggests that there is higher proportion of much smaller bubbles. Medwin and Breitz [28] confirm that the peak in the size spectrum occurs at a bubble radius less than 30 μm, and Su et al. [29] suggest that the peak is around 20 μm. Farmer and Vagle [4] deployed an upwardly-pointing four-frequency echo sounder (28, 50, 88 and 200 kHz) to investigate the bubble size distribution. Time-of-flight of reflected acoustic pulses gave a measure of distance, with a 10 cm

resolution for vertical samples. The backscattered intensities at the four frequencies for each vertical sample gave point measurements of the bubble population at four specific radii in the range $15 < R_0 < 100$ μm. These were then employed in an iterative calculation to give the size distribution of the whole population. They speculated that an upper bound on the size spectral peak occurs at $R_0 = 22$ μm, the true peak being closer to 20 μm.

Medwin and Breitz [28] have previously made measurements at depths less than 0.5 m, and they have used the variation in Q of several modes of a floating acoustical resonator to determine the bubble spectral size distribution at a depth of 0.25 m below a spilling oceanic breaker. The one-dimensional resonator consisted of a flat transducer facing a reflective plate 126 mm away, so that modes could be set up in the water between these. Bubbly water could flow in readily between the plates from the environment. From resonance broadening measurements for nine specific bubble sizes in the range 30 μm $< R_0 <$ 270 μm, Breitz and Medwin [30] found an average bubble density of $n(R_0) = 7.8 \times 10^8 \, (R_0 / \mu m)^{-2.7}$. In the same radius range the maximum bubble density detected was $n(R_0) = 1.6 \times 10^9 \, (R_0 / \mu m)^{-2.7}$. Both distributions agree with the Tunstall data, with respect to the value for the exponent b (within the ascribed error limits), but as expected the total population densities are higher in the surf zone measurements. Medwin and Breitz [28] however found that only the larger bubbles in the range 60 μm $< R_0 <$ 240 μm followed a $n(R_0) \propto (R_0 / \mu m)^{-2.6}$ distribution: the population of smaller bubbles (30 μm $< R_0 <$ 60 μm) decayed with depth as $n(R_0) \propto (R_0 / \mu m)^{-4}$. The size of the error bars associated with the Tunstall data prevent this kind of fine distinction. A $(R_0 / \mu m)^{-4}$ model distribution fits most of the data obtained by bubble counting reasonably well [5]. It was observations such as these that lead to the choice of frequencies employed in the Channel test. For the first regime, ten frequencies have been chosen (Table 1), corresponding to bubbles in the range 195 μm $> R_0 >$ 16 μm. The spacing of pump frequencies was chosen to allow resolution of the peak in the population density, which is expected to be at $R_0 \sim 20$ μm (figure 7). With ten pump frequencies, the temporal resolution is one sample every 3 s - this resolution is improved to a value of 0.85 s in the second test regime by restricting the number of pump frequencies to two (Table 1).

5. Conclusions

This paper described how a combination-frequency technique can be calibrated to give absolute bubble counts. Written after one trial and just prior to a second, it described how the apparatus could be adapted to allow the test to be designed to suit the environment and data requirements. Sensing volume, bubble radii investigated, and the degree of temporal resolution were all adjustable. For the surf zone measurements in the North Sea, a small sensing volume was required. The uncertainty associated with this volume was the main source of error in the final results. Four specific pump frequencies were investigated to enable comparison with historical data, and such a comparison is reported elsewhere [19]. Time-resolved data from such a test is presented here.

Acknowledgements

The authors wish to acknowledge the Natural Environment Research Council (grant GR3 09992) for support; and for assistance in the Tunstall trial, S.A. Thorpe, D. Baldwin, A. Hall, B. Stansbridge, D. Russell, J. Taylor, J. Hawkes, M. Bartlett and D. Edwards.

References

[1] G.M. Wenz, "Acoustic ambient noise in the ocean: spectra and sources," *J. Acoust. Soc. Am.*, vol. 34, pp. 1936-1956, 1962.

[2] M.S. Longuet-Higgins, "Bubble noise spectra," *J. Acoust. Soc. Am.*, vol. 87, pp. 652-661, 1990.

[3] M.J. Buckingham, "On acoustic transmission in ocean-surface waveguides," *Phil. Trans. R. Soc. Lond.*, vol. 335, pp. 513-555, 1991.

[4] D.M. Farmer and S. Vagle, "Waveguide propagation of ambient sound in the ocean-surface bubble layer," *J. Acoust. Soc. Am.*, vol. 86, pp. 1897-1908, 1989.

[5] D.K. Woolf and S.A. Thorpe, "Bubbles and the air-sea exchange of gases in near-saturation conditions," *J. Marine Res.*, vol. 49, pp. 435-466, 1991.

[6] S. Thorpe. "On the clouds of bubbles formed by breaking wind-waves in deep water, and their role in air-sea gas transfer," *Philos. Trans. R. Soc. London*, vol. A304, pp. 155-210, 1982.

[7] H.C. Pumphrey and P.A. Elmore, "The entrainment of bubbles by drop impacts," *J. Fluid Mech.*, vol. 220, pp. 539-548, 1990.

[8] J.A. Scrimger, D.J. Evans, G.A. McBean, D.M. Farmer and B.R. Kerman, "Underwater noise due to rain, hail and snow," *J. Acoust. Soc. Am.*, vol. 81, pp. 79-85, 1987.

[9] E.O. Belcher, "Quantification of bubbles formed in animals and man during decompression," *IEEE Trans. Biomed. Eng.*, vol. 27, pp. 330-338, 1980.

[10] T.G. Leighton, P.R. White and M.A. Marsden, "Applications of one-dimensional bubbles to lithotripsy, and to diver response to low frequency sound," *Acta Acustica*, vol. 3, pp. 517-529, 1995.

[11] L.A. Crum and Y. Mao, "Acoustically enhanced bubble growth at low frequencies and its implications for human diver and marine mammal safety," *J. Acoust. Soc. Am.*, Vol. 99, pp. 2898-2907, 1996.

[12] V.A. Akulichev, "Cavitation nuclei and thresholds of acoustic cavitation in ocean water," in *Bubble Dynamics and Interface Phenomena, Proceedings of an IUTAM Symposium (Birmingham, 6-9 Sept. 1993)*, edited by J.R. Blake, J.M. Boulton-Stone and N.H. Thomas, Kluwer Academic Publishers, The Netherlands, pp. 171-178, 1994.

[13] M.J. Buckingham and C.L. Epifanio, "Acoustic daylight imaging in the ocean: experimental results," in *3rd European Conference on Underwater Accoustics*, edited by J.S. Papadakis, Forth IACM, Crete, Greece, pp 341-347, 1996.

[14] T.G. Leighton, *The Acoustic Bubble*, Academic Press, London, 1994.

[15] T.G. Leighton, D.G. Ramble and A.D. Phelps, "The detection of tethered and rising bubbles using multiple acoustic techniques", *J. Acoust. Soc. Am.*, (in press).

[16] A.D. Phelps and T.G. Leighton, "High resolution bubble sizing through detection of the subharmonic response with a two frequency excitation technique", *J. Acoust. Soc. Am.*, vol. 99, pp. 1985-1992, 1996.

[17] E.G. Tickner, "Precision microbubbles for right side intercardiac pressure and flow measurements", In: *Contrast Echocardiography*, edited by R.S. Meltzer and J. Roeland, Nijhoff, London, 1982.

[18] D. Koller, Y. Li, P.M. Shankar and V.L. Newhouse, "High speed bubble sizing using the double frequency technique for oceanographic applications", *IEEE J. Oceanic Eng.*, vol. 17, pp. 288-291, 1992.

[19] A.D. Phelps, D.G. Ramble and T.G. Leighton, "The use of a combination frequency technique to measure the surf zone bubble population," *J. Acoust. Soc. Am.*, (in press).

[20] E.A. Zabolotskaya and S.I. Soluyan, "Emission of harmonic and combination-frequency waves by air bubbles", *Soviet Physics - Acoustics*, vol. 18, pp. 396-398, 1973.

[21] V.L. Newhouse and P.M. Shankar, "Bubble sizing using the nonlinear mixing of two frequencies", *J. Acoust. Soc. Am.*, vol. 75, pp. 1473-1477, 1984.

[22] D.C. Blanchard and A.H. Woodcock, "Bubble formation and modification in the sea and its meteorological significance," *Tellus*, vol. 9, pp. 145-158, 1957.

[23] P.A. Kolovayev, "Investigation of the concentration and statistical size distribution of wind produced bubbles in the near-surface ocean layer," *Oceanology*, vol. 15, pp. 659-661, 1976.

[24] B.D. Johnson and R.C. Cooke, "Bubble populations and spectra in coastal waters: a photographic approach," *J. Geophys. Res.*, vol. 84, C7, pp. 2761-3766, 1979.

[25] A.L. Walsh and P.J. Mulhearn, "Photographic measurements of bubble populations from breaking waves at sea," *J. Geophys. Res.*, vol. 92, pp. 14553-14656, 1987.

[26] F. MacIntyre, "On reconciling optical and acoustic bubble spectra in the mixed layer," In: *Oceanic whitecaps and their role in air-sea exchange processes*, edited by E.C. Monahan, I. O'Muircheartaigh and D. Reidel, Dordrecht, Holland, pp. 95-100, 1986.

[27] H. Medwin, "In situ acoustic measurements of microbubbles at sea," *J. Geophys. Res.*, vol. 82, pp. 971-976, 1977.

[28] H. Medwin and N.D. Breitz, "'Ambient and transient bubble spectral densities in quiescent seas and under spilling breakers," *J. Geophys. Res.*, vol. 94, pp. 12751-12759, 1989.

[29] M.Y. Su, S.C. Ling and J. Cartmill, "Optical measurements in the North Sea," In: *Sea surface sound*, edited by B. Kerman, Kluwer, Dordrecht, 1988.

[30] N. Breitz and H. Medwin, "Instrumentation for in situ acoustical measurements of bubble spectra under breaking waves,", *J. Acoust. Soc. Am.*, vol. 86, pp. 739-743, 1989.

Shallow-water seafloor characterization for high-frequency multibeam echosounder: image segmentation using angular backscatter

Xavier Lurton, Jean-Marie Augustin, Samantha Dugelay, Laurent Hellequin, & Michel Voisset

IFREMER Centre de Brest
BP70
29280 Plouzané FRANCE
Email: lurton@ifremer.fr

Abstract

Sonar images from multibeam echosounders are submitted to various degradations, partly due to the sensor itself. Signal artefacts and corresponding corrections are presented, both for signal processing and for array directivity effects. The corrected image is processed using a segmentation method accounting for angular variations of backscattering strength, allowing to compensate effects of specular reflection and bathymetry. These various points are illustrated by experimental data shown at various processing stages.

1. Introduction

A strong analogy exists between works in geology on the continental shelf, and those undertaken onshore; often, main geological structures continue into the sea, in particular on the inner shelf. The main difference between onshore and offshore is sediment dynamics which strongly re-mould the sea floor. For studies of seafloor structures, side-scan sonar imaging has been routinely exploited for years by many scientific teams. More recently, modern multibeam echosounders have appeared allowing deeper investigation thanks to the simultaneous acquisition of bathymetry and reflectivity data by the same sensor.

For the geologist, obtaining a mosaic in which the actual information represents material and interface roughness variations, is an essential tool for a further rigorous interpretation. Typically, information is collected from various distinct sources: geoacoustical sensors (mainly side scan sonar and seismic reflection), or by sampling and photos. At this stage, the geologist analyses the sonar mosaic by making a one-to-one correspondance between a mean grey level and a geological unit. The synthesis document is a map established with methods identical to those used for terrestrial geological maps.

The work presented here deals with two aspects of multibeam echosounder data processing. *Correcting the artefacts* brought by the echosounder itself is an essential requirement, in order to make the image correctly interpretable. *Segmenting the sonar image* relies on an expert geological advice for the training phase; relevant information is used when delimiting the learning zones. The segmentation produces a cartography of different zones whose acoustical characteristics are similar to those estimated in the training stage. This procedure is similar to the one undertaken by the geologist. It produces a mosaic whose parameters are objective because having been rid, as far as possible, of artefacts brought by bathymetry and sensor imperfections. A further stage would consist in *fitting a model* with the backscattered signal characteristics estimated in the learning zones.

The method presented below will be illustrated using experimental data given in Figure 1. These data were obtained on the Atlantic inner shelf in the Bay of Biscay, using a high frequency multibeam echosounder. The extract presented here shows an interesting geological variety, featuring soft sediments alternating with harder deposits and rock areas.

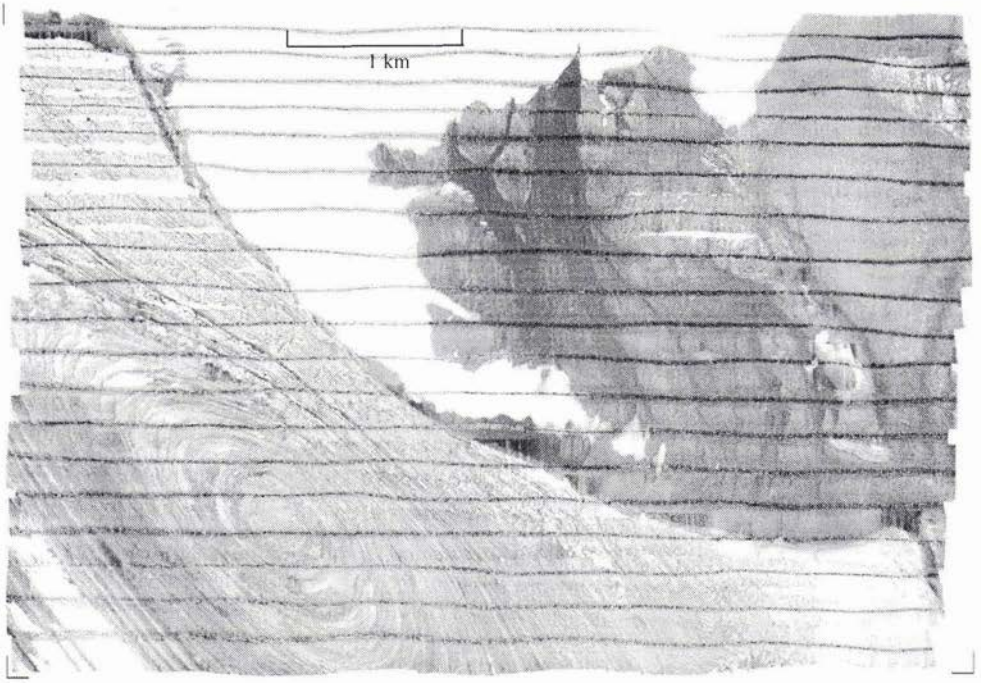

Figure 1. Sonar image from a 95 kHz multibeam echo sounder in shallow water (Bay of Biscay - water depth 15 to 45 m - zone area approx. 5.5 x 4 km)

2. Signal processing and corrections

After a quick presentation of the echosounder, it is shown that its signal processing and array characteristics may lead to undesirable effects in the obtained sonar images. Careful analysis of these effects leads to a correction procedure, indispensable before any image interpretation or processing.

2.1 Basic echo sounder signal processing

We consider in the following signals and data obtained with a Simrad EM950 multibeam echosounder [1]. This system emits pulses of duration 0.2 or 1 ms (according to water depth; the above data correspond to 0.2 ms) in a 150° vertical fan at about 225 dB/μPa/1m level. In reception, beamforming allows to create 120 beams; note that only 60 beams are formed for every other ping. The same array is used for transmission and reception, leading to individual beamwidth of 3.3°x3.3°. The signals inside each formed beam are used for bathymetry measurements: the arrival time is measured directly from the signal envelope for the near-vertical beams; for oblique incidences, every beam is divided into two half-beams for an interferometric precise measurement of the arrival time and angle. The measured time is finally converted into depth using the raypath geometry and the sound speed profile. Individual time signals from each beam are simultaneously exploited to create side-scan sonar images.

The various processing steps inside the echo sounder are as follows. After reception on the listening transducers, a time-varying gain (*TVG*) is applied on raw signals, aimed at compensating the high dynamics between returns from vertical and lateral incidences, both due to transmission losses in water, size of the insonified area, and backscattering strength (at its higher at the vertical, and strongly decreasing at shallow angles). The compensation law in the echo-sounder accounts for the first two effects using simple formulae. The *BS* angular variations are compensated by a Lambert's law in $\cos^2\theta$ for shallow grazing angles, and a gain varying linearly with angle around the vertical; the value of the latter correction adapts from one ping to the next one, and its amplitude is recorded along with other parameters of the ping. These various corrections, concentrated in a single TVG law, are intended to limit the dynamics of the incoming signal to the processing chain, and to homogeneize its level when presenting it as a sonar image.

Beamforming is processed by summing weighted contributions from rows of elementary transducers along the U-shaped array, the active row sliding along the circumference for angle scanning. In extreme sectors on both sides (60° to 75°), beams are formed using conventional beamforming techniques on a fixed row of transducers. Sidelobes are lowered by using a Dolph-Chebyshev shading. Time signals from the various beams are then processed on the one hand for the bathymetry measurement, and on the other hand they are presented in rows for sonar image display, digitized at a 0.2 ms rate; note that the amplitudes are rounded to integer values in half-dBs.

2.2 Beamforming directivity effects

2.2.1 Artefact descriptions

The partial sonar image presented in Figure 1 (left), recorded on a 30 meter depth gravel seabed, allows to identify several echo sounder artefacts, despite image resolution and deceptive grey scale dynamics. This image is presented as corrected by the echosounder, and hence is supposed to reflect only the backscattering strength of the seafloor coupled with bathymetry effects. The corresponding averaged amplitude is presented on the right side, giving a better idea of the order of magnitude of the phenomena.

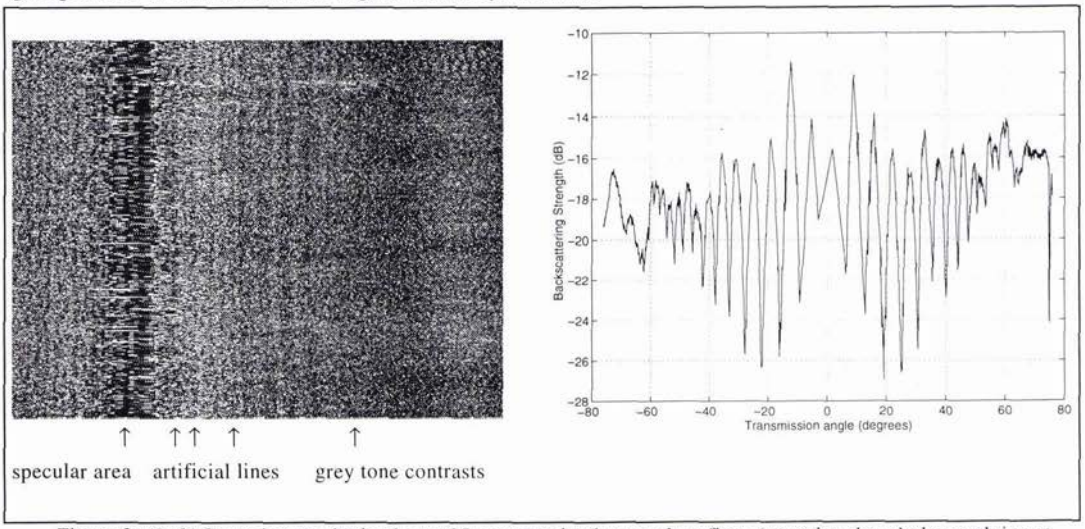

Figure 2: *(Left)* Sonar image obtained on a 30 m water depth, gravel seafloor (note that the whole swath is not presented). *(Right)* Corresponding averaged signal amplitude *vs* angle given by the echosounder

First of all, for emitted angles greater than 50°, slow variations affect the backscattered level: artificial grey tone contrasts appear on the corresponding sonar image. These artefacts are thought to derive from uneven array sensitivity and/or electronic gains applied to the signal emission and reception. Secondly, strong fluctuations (with extinction depths down to -20 dB), whose amplitudes become greater and greater as the angle tends to zero, appear parallel to the vessel track in the sonar image. The stable shape of these artefacts corresponds to the uncompensated directivity diagrams of each one of the 60 reception beams. Finally, the backscattered level is suspicious in the specular region: even after the specular effect compensation has been removed, the backscattered intensity collapses whereas the physics predict an intensity peak. To understand this third phenomenon, we had to detail the TVG law implemented in the sounder, and in particular, the insonified area compensation.

2.2.2 Phenomena analysis.

The estimated backscattering strength $\overline{BS(\theta)}$ is usually obtained from the classical "sonar equation" and basically computed as:

$$\overline{BS(\theta)} = 10\log \iint_{A(\theta)} BS_{nat}(\theta) W^2(\theta) dA \; - \; 10\log \overline{A(\theta)} \qquad (1)$$

where the integral term is the target strength of the actual insonified area $A(\theta)$ at angle θ, featuring $BS_{nat}(\theta)$ the backscattering strength value in natural unit and $W^2(\theta)$ the beam directivity diagram, $\overline{A(\theta)}$ being the estimated insonified area at angle θ. The actual *BS* estimation in our echosounder is based on the following approximations, which are discussed below:

- the integrand in (1) varies slowly enough to be taken out of the integral;
- the insonified area is approximated by

$$\overline{A(\theta)} = \frac{c\tau}{2}\theta_T \frac{H}{\cos\theta \sin\theta} \tag{2}$$

where τ is the pulse duration, and H the water depth.

For shallow grazing angles, the above approximations are acceptable; only the directivity compensation should take into account a slight angle shift corresponding to half a pulse duration. Apart from this minor correction, no deformation of the observed beam diagrams is expected; this justifies to use a method of linear corrections of directivity diagrams for off-specular emission angles.

On the other hand, when the emission angle tends to vertical, the insonified area $A(\theta)$ comes to be limited by beam aperture instead of pulse duration τ; hence its actual value becomes much smaller than its estimation $\overline{A(\theta)}$ based solely on pulse duration limitation. The measured $\overline{BS(\theta)}$ should be increased by an amount of:

$$I = 10\log\left(\frac{\theta_T}{c\tau} H \tan\theta\right) \tag{3}$$

whenever this term is positive. Moreover, in this case, the increase of $A(\theta)$ precludes the simplification of the integral term in (1) and leads to quite intricate effects. These will be detailed in a further paper [10], with signal simulations to evaluate their importance and to determine the validity limits of the correction procedures.

2.3 Artefacts compensation method.

To get rid of the sonar image defects, since no array calibration measurements were available to us, we developed a post-processing correction method using data from a "learning" seabed chosen as flat and homogenous as possible, such as those presented in Figure 2.

1. The various echosounder processing algorithms are compensated as described above. The Lambert's law correction and the specular effect processing provided by the echosounder are removed, and the insonified area is corrected using (3), in order to recover physical *BS* values. At this stage one should have a correct estimation of $BS(\theta)$ mixed with the array directivity effects.

2. Assuming that beam directivity patterns are only slightly deformed by backscattering, an ideal $BS(\theta)$ model is fitted on the beam central samples. We use for this purpose a simple functional form $BS_f(\theta)$, Gauss-like near vertical, and Lambert-like at oblique incidence:

$$BS_f(\theta) = 10\log\left(A\exp(-\alpha\theta^2) + B\cos^\beta\theta\right) \tag{4}$$

This implies that a form such as (4) correctly describes *BS* variations with angle; although this assumption is usually correct, this may be not always the case. The result of such a fitting is given in Figure 3.

3. If one substracts $BS_f(\theta)$ from the measured $BS(\theta)$, the resultant pattern is expected to be the actual array directivity diagrams and should be independent of the seabed nature. In a further step, one may use a realistic directivity model according to the actual array shape and processing, and fit it to the estimated array directivity, beam after beam; this allows to smooth the obtained directivity patterns.

4. The whole image can now be corrected from the directivity effects, using the emission angle and beam number of each pixel. This leads on the one hand to sonar images free of directivity artefacts, on the other hand it allows a correct estimation of $BS(\theta)$ from new homogeneous zones.

Results are presented in Figure 3: the left side shows the "raw" $BS(\theta)$ corrected from Lambert's law, specular effect and insonified area, and fitted with the ideal $BS(\theta)$ given by (4); the right side presents the directivity pattern obtained from three different seafloors (gravel, rock and sand). It is clear from these results that this approach provides remarquably stable directivity patterns, thus justifying *a posteriori* the method validity.

Shortcomings appear nevertheless for beams close to vertical: details of the oscillations are not correctly compensated, and should result in residual fluctuations in the central part of the sonar image; note that this problem is restricted to the [-10°, 10°] sector around the vertical, hence concerning a minor part of the image. Moreover, and more penalising for further identification operations, specular level still remains unexpectedly low after the various compensations have been applied, meaning that correction (3à has not been sufficient to get a correct estimation of the *BS* level. Most presumably, this is due to time undersampling: close to the vertical and in shallow water, signals associated with a given beam may last not more than one time sample. Further analysis of the central beams are presently under study [10], but it seems awkward to get fully informative data inside this angle sector.

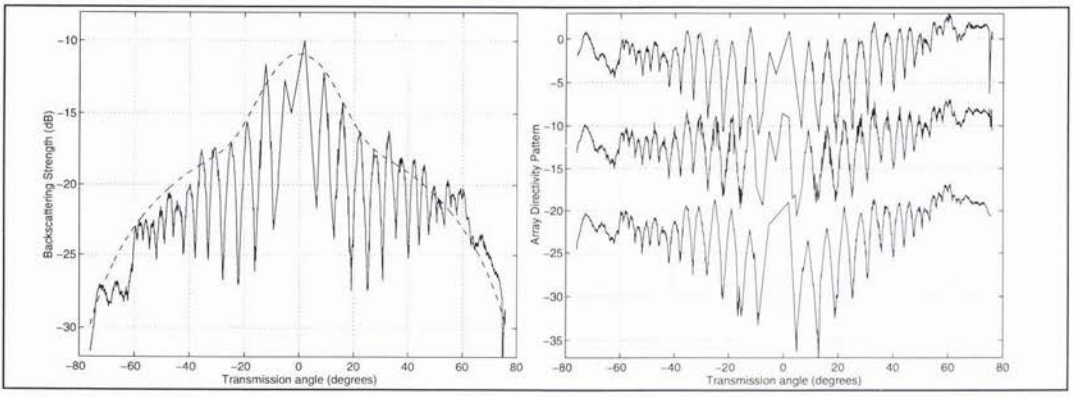

Figure 3. *(Left)* Averaged $BS(\theta)$ after compensation of echosounder processing *(full)* and fitted to an ideal $BS(\theta)$ *(dashed)* - *(Right)* Array directivity pattern obtained from gravel *(upper)*, rock *(middle)* and sand *(lower)* seafloors; the two lower curves have been shifted downwards 10 and 20 dB.

3. Sonar image segmentation

The purpose of image segmentation is to delimit homogeneous zones according to acoustical signal properties, namely backscattering strength level. Due to the fact that *BS* is both strongly dependent on the signal incident angle and on the seafloor properties, and that data are biased by the sounder characteristics, this precludes dealing directly with the raw sonar image; hence removing the sonar artefacts and estimating $BS(\theta)$ on representative zones were the first tasks to be conducted. We propose in the following a sonar image processing method accounting for the physics of the problem.

3.1 Measurement of angular *BS*

The practical measurements of *BS* have been partly described in the previous section. The output signals from the various beams have first to be corrected for propagation losses, and for array directivity effects. The actual incident angle on the seafloor has then to be computed, accounting for two distinct effects:

- refraction inside the water column: raypath angles (related to vertical) at the array and on the seabottom are related by the classical Snell-Descartes' law,
- local topography: data from the local Digital Terrain Model, obtained from bathymetry measurements, is to be used for computing the seafloor slope, both in the acrosstrack and alongtrack directions.

The exact insonified area may then be computed, limited either by the pulse duration or by the beamwidth, and taking into account the local seafloor slope. Finally, for a given signal sample, the obtained *BS* value is affected to the corresponding effective incident angle.

3.2 Image pre-processing

The EM950 signal is sampled at a constant time rate, producing an irregularly spaced sampled signal on the seabed. Mosaicking then consists in projecting this signal onto a regular grid. At shallow grazing angles, all raw sonar samples located in a same mosaic pixel are averaged; alternatively, near vertical, sonar samples are duplicated to compensate for the poor spatial resolution of the echosounder [3]. From this construction process, three levels of representation are produced:

- a chronological mosaic where pings are piled up without taking into account ship navigation, heading or interping distance, but where lateral projection is applied,
- a cartographic representation, where pings are relocated in a cartographic mosaic,
- an interpolated representation obtained from the previous mosaic.

The following segmentation method has been developed for chronological mosaics; on the one hand, neighbourhood computation is easier with this representation than with the cartographic representation, on the other hand, interpolation introduces pixel correlation therefore rending the model of the interpolated image complex [6].

3.3 Image segmentation

3.3.1 Segmentation using Markov Field theory

Segmenting means associating a label to each pixel in order to partition the image into homogeneous regions conditionally to the observed image. Mathematically, this involves maximising the *a posteriori* probability $P(X = \omega / Y = y)$, where X is the estimated label image, and Y is the observed mosaic.

Analysis of the backscattered signal shows that data is noisy, that the signal contains angular acoustic variations and at the same time contains bathymetric effects [3]. Since images are produced from a projection of the signal onto a regular grid, mosaics are in fact, a degraded view of the seabottom. Hence, the deformation that leads from X to Y is known and is expressed by the conditional probability $P(Y = y / X = \omega)$. We also have before hand knowledge of pixel interactions or existing correlations. This is described by the *a priori* probability $P(X = \omega)$. Using Baye's rule, the *a posteriori* probability is then expressed by:

$$P(X = \omega / Y = y) = \frac{P(Y = y / X = \omega) P(X = \omega)}{P(Y = y)} \tag{5}$$

where $P(Y = y)$ is a constant.

The Markov Random Field theory (MRF) [4] is particularly interesting in the sense that only a local model is sufficient, which means that there is no need to take into account the whole image when analysing a specific pixel, a set of local neighbouring pixels will suffice. It is then clear that defining an adapted neighbourhood system is an important step in the Markov modelling. In addition, the Hammersley-Clifford theorem states that the probability law of a Markov Random Field is a Gibbs distribution:

$$P(\omega) = \frac{1}{Z} \exp\left(-U(\omega)\right) \tag{6}$$

where $U(\omega)$ is the energy function defined over the neighbourhood θ and Z the partition function, a normalizing constant. X, X/Y and Y/X are all MRF's and therefore

$$P(X = \omega / Y = y) = \frac{1}{Z} \exp\left(-U_1(y / \omega) - U_2(\omega)\right) \tag{7}$$

where $U_1(y / \omega)$ is the energy function translating the deformation from X to Y, and $U_2(\omega)$ the component due to the spatial interaction of the labels. So, the maximization problem has now become the minimization of the energy functions. An extensive computation of all configurations is impossible due to the large number of possibilities. Therefore, in order to find the optimum configuration, we use a standard optimization algorithm (Iterated Conditional Mode) which computes the marginal probabilities for each pixel of the image and iterates over the image until satibilization of the process. The advantage of the algorithm is its speed, which is an important feature when dealing with images as large as we do. But, on the other hand, this process needs a correct initialisation in order to converge to a suitable solution. Finally, we work in a supervised framework; training zones delimited before the segmentation are essential to determine the number of classes in the image, and characteristic features of each label. These learning zones must be carefully chosen and sufficiently distinguishable so that the process may achieve a satisfactory segmentation.

3.3.2 Characteristic features of the labels

Because of angular variations and bathymetric effects, a homogeneous seafloor will not present a uniform grey level image. In this paper, we have considered the characteristic feature of a homogeneous zone is the estimated angular reverberation [2]. In this manner, we are substracting bathymetric effects from the signal and we are looking to segment according to seafloor nature.

3.3.3 Modelling the interaction energy

The segmentation process is applied to the chronological mosaic. The interaction energy is described by a classical function, which counts the number of similar labels in the pixel neighbourhood. In order to compensate for the interping distance and geometry which have been dropped in the representation, information is re-injected into the interaction energy .

- a rectangular neighbourhood in the mosaic is taken so that in reality a square neighbourhood is considered on the seabed,
- the influence of a pixel is weighted by the inverse of its relative distance on the seabed.

Interaction energy is then described by the following equation:

$$U_2(x) = \alpha \sum_{(s,t)} c_{st} \delta(x_s, x_t) \tag{8}$$

where c_{st} is the weighting coefficient and $\delta(a,b)=1$ if $a=b$, and $\delta(a,b)=0$ if $a \neq b$.

3.3.4 Modelling the deformation energy

Analysis of pixel distributions show that we do not have a homogeneous noise over the entire image. Probability distributions vary with the position of the pixel according to vertical incidence. Previous works with a 13 kHz multibeam system have proven that raw amplitude data follow a truncated Rayleigh law [5], [6]. Equivalently, intensities follow a truncated $\chi^2(2)$ probability distribution while averaged observations are modelled by a weighted χ^2 law where degrees of freedom depend on the number of averaged observations. Consequently, the deformation model is described by:

$$U_1(y/\omega) = \sum_{s\in S} -\ln(\exp(-y_s/x_s) - \exp(-10^{1/20} y_s/x_s))\,\delta(n_s = 1)$$
$$+\left[-(n_s-1)\ln y_s + n_s y_s/x_s - n_s \ln(n_s/x_s) + \ln\Gamma(n_s)\right]\delta(n_s > 1) \tag{9}$$

where y_s is the pixel intensity, x_s is the label intensity, and n_s the number of averaged observations.

We have considered that this is still a reasonable assumption in the case of our high frequency echosounder. Obviously, the model can be improved by taking into account specific aspects linked to the EM950, such as probability laws including textural diffraction (K distributions), texture features, or spectral parameters.

4. Real case application results

The leg we are presenting here (Figure 1 and 4) is an extract from the survey PLABAS where a EM950 echosounder was employed aboard the IFREMER *R/V Thalia* off the Basque coast (France). We have also acquired supplementary data on the same zone: side scan sonar, VHR seismics, samples, photos. The substratum is is a layer cake of calcareous layers and marl; each layer is less than 1 meter thick. These ancient rocks were folded, faulted and then eroded. The fold fault forms a cliff approximately 10 meters high visible in F, the full line AB is very close to its axis. Recent sedimentary deposits partially recover the substratum. These sediments are mainly constituted of fine to coarse sands and gravels. The spatial organization of these sediments is controlled by storm currents and tides which are very strong in this area (dunes, macrowaves). In the yellow region (S), fine sands have been deposited in a relatively shallow depression. The ocher zone corresponds to to coarse sands, and the green zone includes cobbles and gravels.

The segmented image was considered to be quite satisfactory by the geologists, and correctly reflecting their interpretation of the physical reality. Some particular points are to be highlighted:

- Most of the specular effect present on Figure 1 has been removed on Figure 4. Some reliquates are found on the upper part of the fine sediment area; note that they correspond to very strong and wide specular stripes on the original image.
- The various local features present on Figure 1 have been respected by segmentation, e.g. small sediment areas on the extreme left of the image; although the lighter area on the upper right corner may have been insufficiently identified by segmentation (it might have been interesting to introduce one more seafloor class).
- The distinction between fine and coarser sediments has been clearly established, although it was not at all evident on the original image.
- The stratified texture of the lower left corner of the image was the most challenging part of the process; it is comforting to see that it was most correctly segmented, globally respecting the concentric textural features of the geological structure.

Together with the segmented image, the $BS(\theta)$ curves obtained from the various test zones are presented in Figure 5. Their general shapes and levels are in good accordance with other observations found in the litterature. However the pattern shapes for the two soft sediments are remarkable, featuring an unusually slow decay in the [10-30°] sector. Obviously this is in contradiction with the general shape proposed in (4); note that our directivity pattern estimation was not affected by this effect since it proved to be the same for three different seafloors described using (4). Further studies are under progress for identifying characteristic features of the $BS(\theta)$ curves, and fitting them with physical models.

5. Conclusions

We showed in this paper that, provided that a correct compensation of echosounder artefacts is applied, sonar images can be efficiently segmented using the physical phenomena knowledge. Results obtained in a complex shallow water configuration appear quite satisfactory, leading to a segmented image in excellent accordance with the geologist perception, although it is clear that validation of information revealed with this method can only be fully achieved selectively with sample analyses and photos. This was obtained despite somehow penalising performances of the echosounder, especially around the vertical.

The emphasis should be stressed on a careful and relevant selection of the test zones as a preliminary to segmentation processing. All the above was presented with backscattering strength as the only characteristic physical feature to be used for segmentation; other signal characteristics are known to be potentially usable for high frequency echosounders used in shallow water (amplitude statistics, spectral and textural features...), and this should be checked in the future. Another important direction to explore, and also presently under study, is the identification of the measured $BS(\theta)$ with a theoretical model, and the possibility of extracting objective seafloor parameters from such a fit.

References

[1] SIMRAD, EM950 Product description.

[2] R.M. Gott, Remote seafloor classification using multibeam sonar, Doctoral Thesis 1995.

[3] J.M. Augustin et al., Contribution of the multibeam acoustic imagery to the exploration of the sea-bottom, Marine Geophysical Researches, 18, pp 459-486, 1996.

[4] S. Geman, D. Geman, Stochastic relaxation, Gibbs Distribution and the Bayesian Restoration of Images, IEEE transactions on pattern analysis and machine intelligence, vol. PAMI-6, NO. 6, 1984

[5] S. Dugelay, X. Lurton, J.M. Augustin, A new method for seafloor characterization with multibeam echosounders: image segmentation using angular backscattering, Proc. 3rd European Conference on Underwater Acoustics, vol. I, pp 439-444, 1996.

[6] S. Dugelay, Caractérisation des fonds marins à partir de données sondeur EM12, Mémoire de thèse, Université Paris-Sud-Orsay, 1997.

[7] L.Hellequin, Postprocessing and signal corrections for multibeam echosounders, unpublished

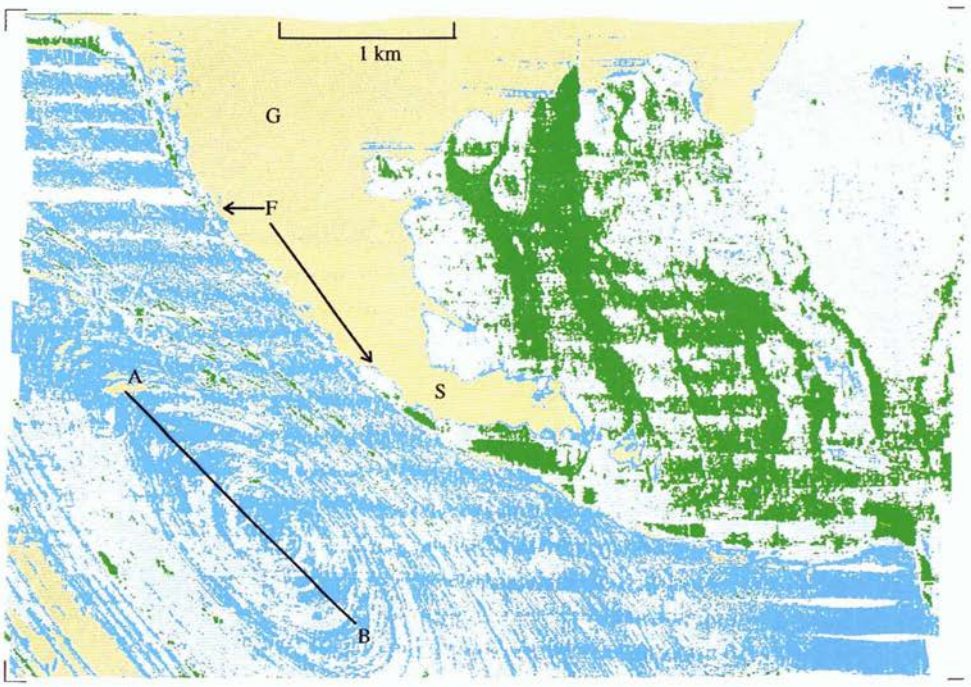

Figure 4. Segmented image corresponding to the sonar image of Figure 1.

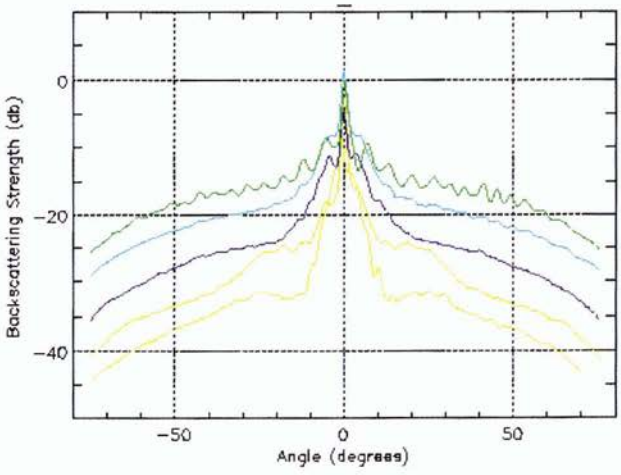

Figure 5. Backscattering Strength *vs* incident angle, for the five test zones used in segmentation

Statistical Evaluation of 80 kHz Shallow-Water Seafloor Reverberation

Anthony P. Lyons, Douglas A. Abraham, Tuncay Akal and Piero Guerrini

SACLANT Undersea Research Centre
Viale San Bartolomeo 400
19138 La Spezia, ITALY
E-mail: lyons@saclantc.nato.int

Abstract

In this work a comparison is presented between 80 kHz reverberation statistics obtained at shallow water sites around Sardinia and Sicily. The data include measurements from several distinct bottom provinces, including sites with Posidonia Oceanica sea grass and sites covered with live shellfish. The reverberation statistics did not always exhibit a Rayleigh probability distribution function (PDF), but exhibited statistical distrubutions with longer tails. Several more appropriate models of reverberation PDF were examined in order to better describe the measured amplitude distributions. The Rayleigh mixture and the K models were found to be the most robust in describing the observed data.

1. Introduction

The detection and identification of objects on the seafloor is made more difficult by seafloor reverberation. While the problem of understanding and predicting high-frequency background reverberation level or mean energy scattered per unit area of the sea bed has received considerable attention, studies of high frequency reverberation statistics are relatively scarce. Of these studies, many have dealt with scattering from more or less homogenous seafloors in terms of bottom type [1, 2, 3]. Most shallow water areas, however, will not be homogeneous but will have patchiness in space and time, which is often a result of biology. An example of spatial inhomogeneity are shellfish which often do not exist uniformly on the seabed but are distributed in clumps of varying density. The motion of seagrass due to swell or currents causes a constantly changing number of scattering sites which can be thought of as time varying patchiness. Clutter is the acoustic expression of the non-uniformity of these types of seafloor environment.

When the effective numbers of scatters in the resolution cell of a sonar is large enough, the amplitude distribution is expected to be Rayleigh as the central limit theorem holds resulting in gaussian in-phase and quadrature components of the received signal. The changes in density of scatterers commonly found in shallow water suggests that this model might not always be appropriate especially when the area ensonified by the transmit and receive beam patterns is not large enough to encompass enough of the patches of differing scatter density. More general distributions for addressing amplitude statistics of scattering from heterogeneous seafloors are the Weibull, K, and Rayleigh mixture distributions each of which has the Rayleigh distribution as a submember. The K distribution, used to succesfully describe the statistics of radar sea surface clutter [4, 5], can be described as being the product of two components; a rapidly fluctuating Rayleigh (or 'speckle') distributed component and a chi distributed component. The physical interpretation is that the Rayleigh distributed component is from many scatterers that are modulated by large scale (time varying) structure. The Rayleigh mixture model [6] is a combination of Rayleigh random variables with each component having its own power. This distribution can be thought of as describing scattering from two (or more) different types of materials in a manner similar to that put forward by Crowther [7].

This paper presents acoustic data collected at 80 kHz at shallow water sites around Sardinia and Sicily. Fifteen sites were examined and results from seven of the sites are presented in terms of system independent site characterization. The sites studied included a variety of bottom types, including sites with *Posidonia Oceanica*

sea grass and sites covered with live shellfish. Examples of three of the types of seafloor studied are shown in the video stills seen in Figure 1. The diversity of sites studied allowed an excellent opportunity to examine the

(a) Posidonia covered sand bottom - station RR06

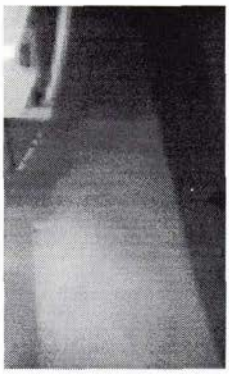

(b) Sand bottom - station RR12

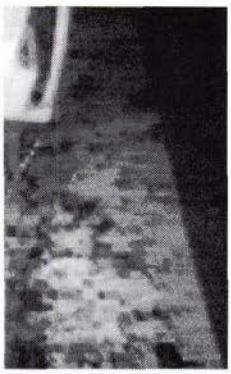

(c) Shell covered sand bottom - station RR13

Figure 1: Examples of the nonhomogeneous nature of sand seafloors.

statistics of reverberation from a wide variety of seafloor environments. Results of statistical analysis are cast in terms of mean power value or backscattering coefficient as well as analysis of the amplitude statistics. Rayleigh, Weibull, K, and 3-component Rayleigh mixture PDFs are compared to measured data and a non-parametric test is used to describe the goodness of fit between modeled and measured amplitude distributions.

2. Data Analysis

The 80 kHz acoustic system used in this study has been fully characterized against reference hydrophones at the SACLANT Undersea Research Centre to quantify source level and beam pattern. System gains were measured while at sea. Using the transducer calibration value (pressure to voltage transfer function), processing gain and system gains, the absolute received levels at the hydrophone were recovered from the recorded data. In order to get quantitative seafloor information out of the received level, three effects that may modify the sound pressure level as the pulse travels from the source to seafloor and back to the receiver have been taken into account. These three factors are the effects of the beam pattern, transmisssion loss, including both spherical spreading and absorption, and equivalent ensonified area. With the above described components, seafloor backscattering strength as a function of time can easily be calculated using an inverted form of the sonar equation with a knowledge of the source level, transducer calibration and logging calibration. The backscattering strength as a function of grazing angle can then be obtained from knowledge of the transducer height and the sound speed of the sea water. In data processing only grazing angles within the $3dB$ down points of the one-way beam pattern were considered.

From each experimental site, returns from 200 $1ms$ pulses at each of four tilt angles (measured relative to the main beam axis) were analyzed. The 20 degree beamwidth of the transducer allowed scattering strength measurements versus grazing angle to be taken with these four tilt angles (for most sites the range of grazing angles from which data were obtained was from 10° to 80°. Every 15th data point of scattering curve was used for the amplitude statistics study as correlation analysis determined these to be independent. Data at each grazing angle were normalized by the mean power of 200 pings in order to remove grazing angle dependence. Data was grouped in 20 degree grazing angle bins, to increase the number of data points for statistical analysis. Amplitude data was tested for stationarity using the Mann-Whitney test as in [2, 3]. For a two tailed test at 95% confidence, values less than 1.96 and greater than -1.96 are considered to be from the same distribution. Data that fell out of this range was excluded from the analysis. The top graph of Figure 2 shows an example of the normalized amplitude for 200 pings in a 20 degree grazing angle bin, while the bottom two graphs illustrate the Mann-Whitney results for comparisons of groups of 20 pings and comparisons between grazing angle respectively. Rayleigh, Weibull, K, and Rayleigh mixture distributions were compared to the experimental PDFs. Fitting the model distributions to the experimental results entailed estimating the parameters of each of the candidate CDFs. Maximum likelihood estimates obtained using an iterative algorithm [8] were used for the parameters of the Weibull

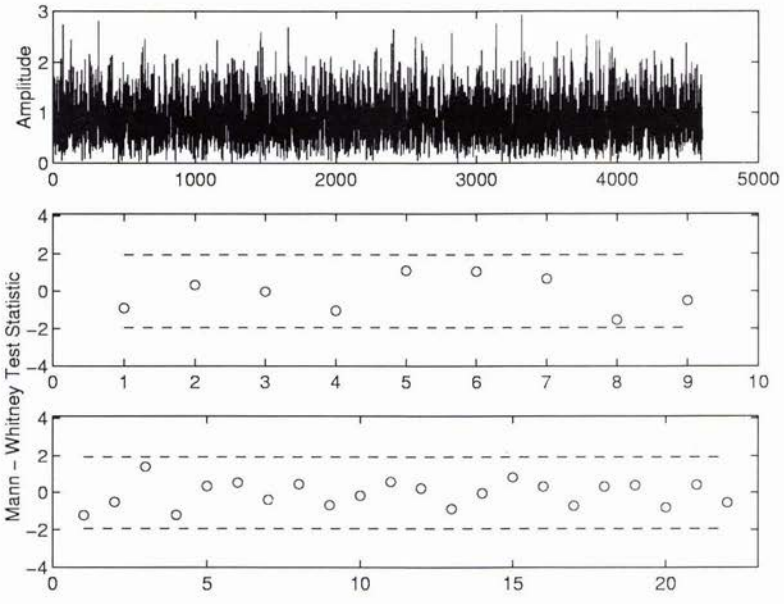

Figure 2: Sample results from the Mann - Whitney stationarity test

distribution, method of moments estimates were used for the parameters of the K distribution, matching the mean and variance, and for the Rayleigh mixture model the maximum likelihood parameter estimates were obtained using the expectation-maximization (EM) algorithm [9].

Backscattering strength resulting from the inversion described above from four sites is shown in the top graphs of Figures 3 - 6. Because all system dependent factors, as well as measurement geometry effects (including spreading loss and absorption) and the ensonified area contribution have been removed from the original raw data, the resulting inverted values represent the true quantitative acoustic response of the seafloor (backscattering strength.) Thus, in the graphs, quantitatively correct values indicate the different scattering properties of the three sites. The general patterns of the curves for the measurement sites are consistent with values reported near this frequency in that they approach a maximum as they near normal incidence, fall off to a nearly constant level over a wide range of grazing angles, then decrease at low grazing angles. In some of our sites the signal to noise ratio is too low to give reliable scattering strength estimates at the smallest grazing angles as seen by figure 3. The shellfish covered site had extremely high levels of backscatter at 80 kHz as did the posidonia covered site. Surprisingly the sand and mud sites shown in these examples had similar levels of backscattering, suggesting that absolute level is not sufficient to separate different bottom types.

Also shown in Figures 3 - 6 are visual examples of the the experimentally observed reverberation PDFs along with the fitted models. The non-Rayleigh nature of the distribution is easily seen in the high grazing angle shellfish, posidonia, and sand data. The distributions tend to Rayleigh at lower grazing angles. A simple explanation for this effect is that as a consequence of the height of the transducer remaining constant the resolution cell of the sonar will increase at the smaller grazing angles. More patches of seafloor are included in the beam at low grazing angle which drives the amplitude distribution toward Rayleigh as the central limit becomes valid. Chotiros [1] has discussed similar effects of the resolution cell (receive beamwidth). A quantitative table of goodness of fit of the observed data to each of the model distributions will be shown in the next section.

3. Results

To evaluate the flexibility and accuracy of the models in representing the reverberation from the different seafloor types, the Kolmogorov-Smirnoff (K-S) test statistic p-values were used to compare real data to model distributions [10]. These values provide a measure of the goodness of fit between the model distributions and the observed distributions. Results are presented for each of seven sites and are grouped in terms of grazing angle. Table 1 shows bottom type, average scattering level, and K-S p-values for the 60° to 80° grazing angle, Table 2 for 40° to

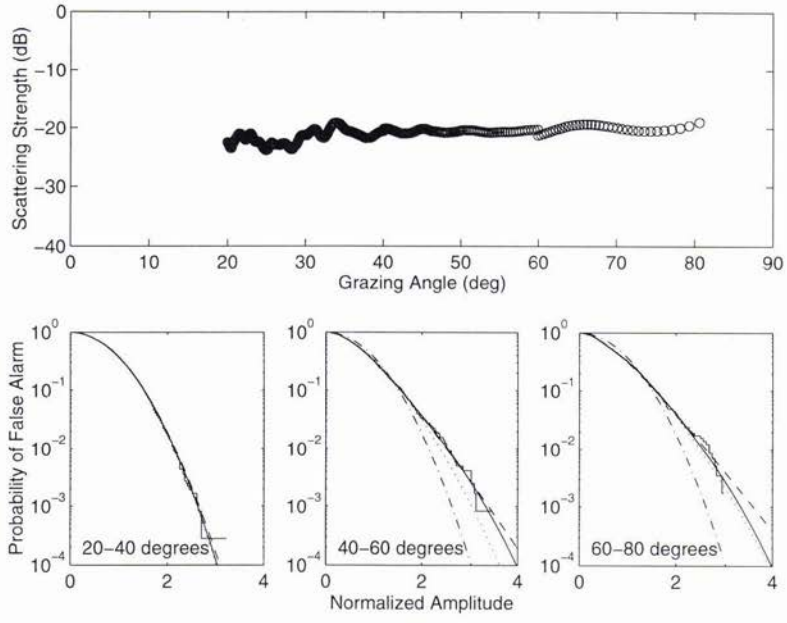

Figure 3: Posidonia statistics - station RR06. The dashed-dotted line is the Rayleigh distibution, the dotted is the Weibull, the dashed is the K, and the solid is the Rayleigh mixture

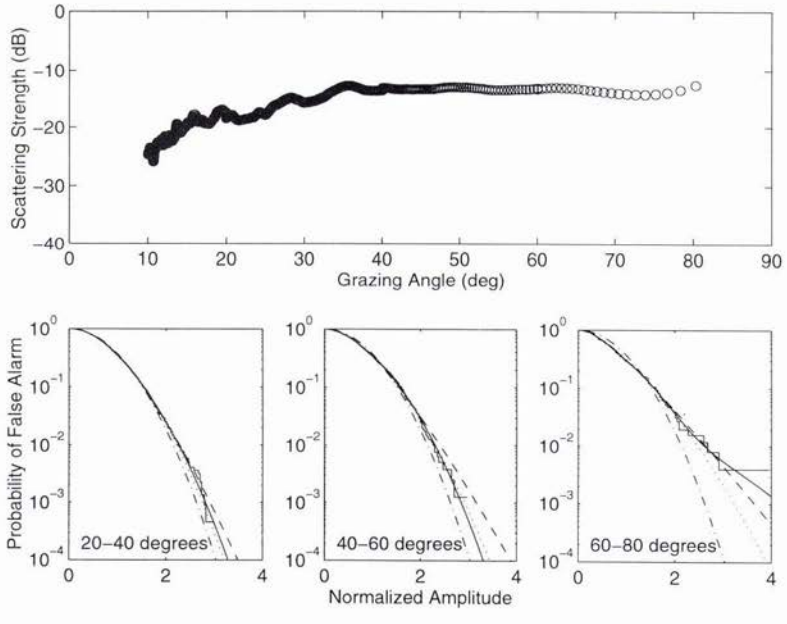

Figure 4: Shellfish statistics - station RR13. Line types as in Figure 3

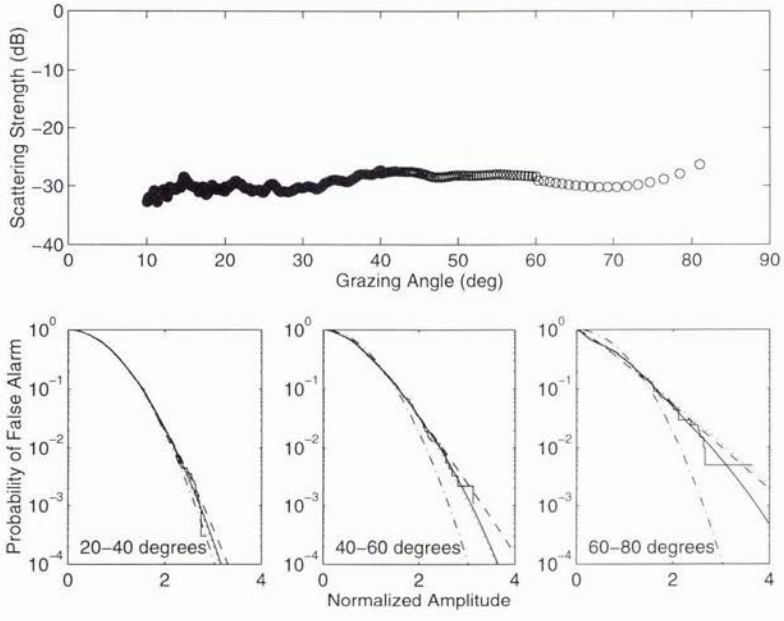

Figure 5: Sand statistics - Station RR12. Line types as in Figure 3

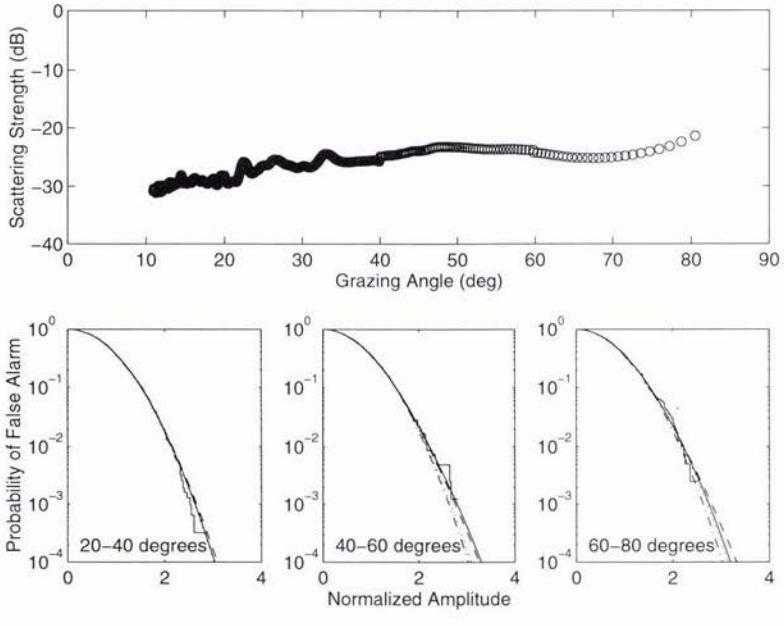

Figure 6: Mud statistics - station RR09. Line types as in Figure 3

60° grazing angle, Table 3 for 20° to 40° grazing angle, and Table 4 for 10° to 20° grazing angle. Any p-values above 0.7 are shown in bold to highlight the best fits to observed data. Quantitative agreement is seen with the qualitative assesment of the last section. The highest grazing angles are usually not well described by the Rayleigh distribution. The Weibull, Rayleigh mixture, and K distributions all do a better job of matching the observed distribution than a standard Rayleigh. The fact that this is true is obvious as each of the other distributions has more parameters to tweak to fit the data. The Rayleigh mixture and K distributional models are more robust in fitting the observed data and work over the entire range of grazing angles (resolution cell size). The scattering levels are not generally separable by bottom type. In general the muds give the lowest scattering level, the sands give medium scattering level, and the shellfish and posidonia covered bottoms give the highest levels.

4. Conclusions

Rayleigh PDFs were often found to not be accurate descriptors of the shallow water 80 kHz reverberation analyzed, especially at high grazing angles. This more than likely is due to the number of patches of differing scatter density or strength included in the sonar resolution cell at a given grazing angle. Rayleigh Mixture or K distributions are the best in fitting the observed distributions over all bottom types at high grazing angles and, as these contain the Rayleigh distribution as a submember, also work very well at low angles. A 3-component Rayleigh mixture model was used in this analysis but could be expanded easily to more to include more components which would allow it to fit almost any distribution.

References

[1] N. P. Chotiros, H. Boehme, T. G. Goldsberry, S. P. Pitt, A.L. Garcia and R. A. Altenburg, "Acoustic backscattering at low grazing angles from the ocean bottom. Part II. Statistical characteristics of bottom backscatter at a shallow water site," *J. Acoust. Soc. Am.* , vol. 77, pp. 975-982, March 1985.

[2] S. Stanic and E. G. Kennedy, "Reverberation fluctuations from a smooth seafloor," *IEEE J. Ocean. Eng.* , vol. 18, pp. 95-99, April 1993.

[3] S. Stanic and E. G. Kennedy, "Fluctuations of high-frequency shallow-water seafloor reverberation," *J. Acoust. Soc. Am.* , vol. 91, pp. 1967-1973, April 1992.

[4] E. Jakeman and P. N. Pusey, "A model for non-Rayleigh sea echo," *IEEE Trans. Ant. Prop.* , vol. 24, pp. 806-814, 1976.

[5] K. D. Ward, "Compound representation of high resolution sea clutter," *Electronics Letters*, vol. 17, pp. 561-563, August 1981.

[6] W. K. Stewart, D. Chu, S. Malik, S. Lerner and H. Singh, "Quantitative seafloor characterization using a bathymetric sidescan sonar," *IEEE J. Ocean. Eng.* , vol. 19, pp. 599-610, October 1994.

[7] P. A. Crowther, "Fluctuation statistics of sea-bed acoustic backscatter," in *Bottom Interacting Ocean Acoustics*, edited by W. A. Kuperman and F. B. Jensen, pp. 609-622, Plenum, New York, 1980.

[8] N. L. Johnson, S. Kotz, N. Balakrishnan, *Continuous Univariate Distributions*, vol. 1, second edition, John Wiley and Sons, Inc., New York, 1994.

[9] D. A. Abraham, "Modeling non-Rayleigh reverberation", SACLANT Undersea Research Centre report SR-266, June 1997.

[10] M. Fisz, *Probability Theory and Mathematical Statistics*, fourth edition, Macmillan Pub. Co., New York, 1978.

Table 1: Results for selected sites and for 60°-80° grazing angle. Values over 0.7 are given in bold.

Station	*Bottom Type*	*Scattering Level*	*Rayleigh*	*Weibull*	*Rayleigh Mixture*	*K*
RR06	posidonia covered sand	-20.0 dB	1.04×10^{-9}	0.667	**0.983**	**0.933**
RR09	mud	-23.5 dB	**0.902**	**0.986**	**0.998**	**0.999**
RR10	coarse sand/shell hash	-20.4 dB	**0.818**	**0.843**	**0.818**	**0.747**
RR11	coarse sand/shell hash	-23.0 dB	**0.992**	**0.999**	**0.997**	**0.999**
RR12	medium sand	-28.9 dB	3.42×10^{-12}	0.543	**0.977**	0.123
RR13	shell covered sand	-13.8 dB	1.57×10^{-4}	0.440	**0.850**	**0.802**
RR16	mud	-25.7 dB	0.026	0.473	**0.999**	**0.875**

Table 2: Results for selected sites and for 40°-60° grazing angle.

Station	*Bottom Type*	*Scattering Level*	*Rayleigh*	*Weibull*	*Rayleigh Mixture*	*K*
RR06	posidonia covered sand	-21.0 dB	1.28×10^{-7}	0.367	**0.989**	**0.996**
RR09	mud	-23.8 dB	**0.827**	**0.979**	**0.999**	**0.999**
RR10	coarse sand/shell hash	-21.2 dB	**0.978**	**0.853**	**0.978**	**0.984**
RR11	coarse sand/shell hash	-24.4 dB	**0.953**	**0.941**	**0.953**	**0.969**
RR12	medium sand	-28.2 dB	4.25×10^{-4}	**0.716**	**0.881**	0.615
RR13	shell covered sand	-13.5 dB	0.002	0.508	**0.963**	**0.866**
RR16	mud	-25.4 dB	0.246	**0.785**	**0.951**	**0.965**

Table 3: Results for selected sites and for 20°-40° grazing angle.

Station	*Bottom Type*	*Scattering Level*	*Rayleigh*	*Weibull*	*Rayleigh Mixture*	*K*
RR06	posidonia covered sand	-21.8 dB	**0.955**	**0.982**	**0.955**	**0.794**
RR09	mud	-27.0 dB	**0.941**	**0.886**	**0.941**	**0.974**
RR10	coarse sand/shell hash	-23.7 dB	**0.803**	**0.983**	**0.952**	**0.980**
RR11	coarse sand/shell hash	-26.1 dB	**0.812**	**0.871**	**0.986**	**0.885**
RR12	medium sand	-29.5 dB	0.070	**0.927**	0.616	**0.749**
RR13	shell covered sand	-16.2 dB	0.014	0.328	**0.888**	**0.863**
RR16	mud	-26.2 dB	**0.888**	**0.924**	**0.888**	**0.877**

Table 4: Results for selected sites and for 10°-20° grazing angle.

Station	*Bottom Type*	*Scattering Level*	*Rayleigh*	*Weibull*	*Rayleigh Mixture*	*K*
RR09	mud	-30.1 dB	**0.995**	**0.999**	**0.995**	**0.875**
RR10	coarse sand/shell hash	-24.7 dB	**0.970**	**0.997**	**0.999**	**0998.**
RR12	medium sand	-29.0 dB	0.204	**0.915**	**0.902**	**0.912**
RR13	shell covered sand	-21.1 dB	**0.939**	**0.999**	**0.968**	**0.992**

High Resolution Feature Extraction from Reverberation Data

Robert B. MacLeod*, Donald W. Tufts**

*Naval Undersea Warfare Center
Newport R.I. 02841 USA
macleod@fs811.npt.nuwc.navy.mil

**University of Rhode Island
Kingston R.I. 02881 USA
tufts@ele.uri.edu

Abstract

A new method of signal approximation is presented which has the capability to model complex active returns due to reverberation. The method explored herein is data adaptive in the sense that high resolution processing is attempted where necessary, while fast algorithms are used to estimate the remaining components. The basic goal is to achieve accurate and unbiased estimation of the delays and time scalings of a group of closely spaced signal returns. A secondary goal is to achieve this estimation performance without sacrificing the computational efficiency of the fast algorithms available.

1. Introduction

We will be treating the problem of feature extraction from high frequency sonar data, generated by an active transmission. Our viewpoint will be that the portion of returning signal due to backscattering in the environment can be adequately approximated as the sum of frequency shifted (time scaled) and delayed replicas of the transmit. This is to be contrasted with the statistical approach taken in references [1, 2]. We will present means to make signal approximations with these assumptions, motivating alternative post-processing algorithms which use these features vice the original data sequence.

This type of approximation becomes more valid for the higher acoustic frequencies of the problem considered here. In particular, for the frequency range of interest, 15 kHz to 25 kHz, propagation can be approximated by ray models, and propagation through the bottom is of diminished importance. Interaction of a ray with the surface or bottom can be approximated as an attenuation of the path, along with the direction change and possible signal inversion. Target returns, under these conditions, will arrive at the receiver with the same temporal relationships within the return as were generated at the target. This will also hold true for returns due to prominent features in the scattering environment, due to structured discontinuities on the bottom or surface. Wavelengths are on the order of magnitude of 1/4 foot, which in combination with the wider-bandwidth signals being transmitted, result in resolution of target features down to 5 feet with traditional processing methods.

1.1. Signal Model

With these considerations in mind, the returned signal will be assumed to be a sampled, vectorized representation of the signal

$$\begin{aligned} x &= \sum_{i=1}^{K_S} \tilde{A}_i s(a_i t - \tau_i) + \sum_{i=K_S+1}^{K_S+K_I} \tilde{A}_i s(a_i t - \tau_i) + n \\ &= x_S + x_I + n \,. \end{aligned} \tag{1}$$

The signal x_S, and the interference x_I, are both modeled as linear combinations of time delayed (τ_i) and time scaled (a_i) replicas of the transmit, s. The signals modeled will be taken as a complex valued (in general), as is typical for sonar systems processing in a single sideband. The signal and interference amplitudes, delays, and time

scaling factors will be considered to be deterministic but unknown parameters, the amplitudes $\tilde{A}_i$ complex valued. The noise will be assumed to be complex Gaussian, i.e.

$$n \sim \mathcal{N}\left(0,(\sigma^2/2)I\right) + j\mathcal{N}\left(0,(\sigma^2/2)I\right) \ . \tag{2}$$

1.2. Parameter Estimation

For the case of the measurement noise of equation 2, the maximum likelihood estimate of the signal parameters can be made by maximizing the compressed likelihood function (CLF)

$$\begin{aligned} \mathsf{L}_{\text{clf}} &= x^t * \mathbf{H}(\mathbf{H}^t\mathbf{H})^{-1}\mathbf{H}^t * x \\ &= \|\mathbf{P}_{\mathbf{H}}x\|^2 \ , \end{aligned} \tag{3}$$

searching over the dimension $2(K_S+K_I)$ space of the vector model parameters a and τ. The compressed likelihood is a compact notation describing the likelihood that given the data sequence x, parameters $[a_i,\tau_i]$ generated the sequence. Maximizing the compressed likelihood function results in the maximum likelihood estimates for the time scale and delay of the components. The amplitudes are functionally related to the time scale and delay estimates, in fact, given the maximum likelihood estimates of $[a_i,\tau_i]$, the maximum likelihood est imates of the amplitudes (vector notation) are

$$\left[\ \tilde{A}_1 \quad \tilde{A}_2 \quad \ldots \quad \tilde{A}_{K_S+K_I}\ \right]' = (\mathbf{H}^t\mathbf{H})^{-1}\mathbf{H}^t * x \ . \tag{4}$$

A complete treatment of the topic is offered in reference [3]. Here, $\mathbf{H}$ is the combined signal and interference model matrix, formed by stacking together in columns time delayed and scaled transmit replicas.

$$\mathbf{H} = [s(a_1t-\tau_1)\ldots s(a_{K_S}t-\tau_{K_S})\ldots s(a_{K_S+K_I}t-\tau_{K_S+K_I})] \tag{5}$$

Since both the signal and the interference are modeled in exactly the same way, it will not be necessary to distinguish the components, and we will refer to the model matrix as simply $\mathbf{H}$.

1.3. Parameter Estimation as Feature Extraction

We will make the somewhat unorthodox assumption that all signal components in $\mathbf{H}$, due either to target returns or environmental scattering, are high signal to noise components. A more typical approach would be to focus on the strength of target components with respect to some measure of the strength of the reverberant field. In our work, we seek to estimate all components due either to reverberation or target scattering, and as such, they compete only against the measurement noise (and each other). The noise will be simple measurement noise, such as is generated by analog preamplification and 16 bit sampling. With this viewpoint, we refer to components due to the reverberant field as 'features' of the field, in the sense that any post processing desired can use the extracted features in lieu of the data itself.

2. Cramer-Rao Lower Bound on Variance of Model Parameters

Given the high signal to noise ratio of the model components, very accurate estimation of 'single' components is possible, that is components that are orthogonal to all other components. For more complicated portions of the signal, for example a target with several closely spaced highlights, estimation becomes more difficult. To illuminate this, the Cramer-Rao lower bound on variance of estimated model parameters for a pair of linear frequency modulated signals has been calculated. The signals modeled are similar to that transmitted in sea trials here in Narragansett Bay, presented later in this paper. Each signal component is of the form

$$s(A_i,\phi_i,a_i,\tau_i) = w(a_in-\tau_i)A_ie^{j\phi_i}e^{j2\pi(c+d(a_in-\tau_i))(a_in-\tau_i)} \ . \tag{6}$$

The function $w(a_in-\tau_i)$ is a real valued windowing function, a_i and τ_i time scale and delay the i^{th} signal component. The parameters c and d are selected to sweep the fm signal by a rate of $k = 2d = (\Omega_2-\Omega_1)/(N-1)$, from digital frequency Ω_1 to Ω_2. The bound can be calculated by evaluating Fisher's Information Matrix for complex processes [4],

$$[\mathbf{I}(\xi)]_{ij} = \text{tr}\left[\mathbf{C}_x^{-1}(\xi)\frac{\partial\mathbf{C}_x(\xi)}{\partial\xi_i}\mathbf{C}_x^{-1}(\xi)\frac{\partial\mathbf{C}_x(\xi)}{\partial\xi_j}\right] + 2\text{Re}\left[\frac{\partial\mu^H(\xi)}{\partial\xi_i}\mathbf{C}_x^{-1}(\xi)\frac{\partial\mu(\xi)}{\partial\xi_j}\right] \tag{7}$$

For our example, the covariance matrix $\mathbf{C}_x(\xi)$ does not depend on the modeling parameters ξ, in fact $\mathbf{C}_x(\xi) = \sigma^2\mathbf{I}$, which simplifies the evaluation of 7. The remaining parameters are

$$\mu(\xi) = s(A_1,\phi_1,a_1,\tau_1) + s(A_2,\phi_2,a_2,\tau_2) \tag{8}$$

$$\xi = \left[\ A_1 \quad \phi_1 \quad a_1 \quad \tau_1 \quad A_2 \quad \phi_2 \quad a_2 \quad \tau_2\ \right]^t \ . \tag{9}$$

The partial derivatives, neglecting minor perturbations due to the windowing, will be

$$\begin{aligned}
\frac{\partial \mu(\xi)}{\partial A_i} &= \frac{1}{A_i} s(A_i, \phi_i, a_i, \ tau_i) \\
\frac{\partial \mu(\xi)}{\partial \phi_i} &= j s(A_i, \phi_i, a_i, \tau_i) \\
\frac{\partial \mu(\xi)}{\partial a_i} &= j 2\pi \left(cn + 2da_i n^2 - 2dn\tau_i\right) s(A_i, \phi_i, a_i, \tau_i) \\
\frac{\partial \mu(\xi)}{\partial \tau_i} &= j 2\pi \left(-c - 2da_i n + 2d\tau_i\right) s(A_i, \phi_i, a_i, \tau_i) \ .
\end{aligned} \tag{10}$$

The variance bounds are found by inverting 7,

$$\sigma_{\xi_i}^2 \geq \left[\mathbf{I}^{-1}(\xi)\right]_{ii} \tag{11}$$

An example has been prepared, using a 50 sample fm signal, sweeping from digital frequencies $\Omega = -0.2$ to $\Omega = +0.2$. Two components are placed close together, and the variance bound of the first component's parameters calculated as the second component is moved closer. The first component has a time scale of $a_1 = 1$, and a delay of $\tau_1 = 0$. Both components have real amplitude $A = 1$, and the signal to noise ratio is 0 dB. These figures

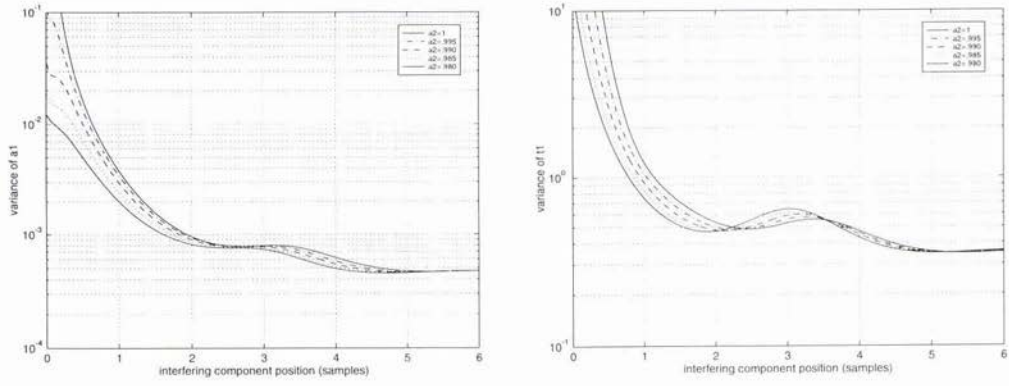

Figure 1: Variance of time scale parameter (left) and time delay parameter (right) of a component placed at $(a = 1, \tau = 0)$,with a second component in the vicinity. Abscissa is the separation of the components, a family of curves are shown for differing values of the second component's time scale, a2. Signal to noise ratio is 0dB

are shown on an expanded scale for the separation of the two components, to show some of the structure on the variance bounds. Basically, as the second component moves closer to the component of interest, the variance of the estimated parameters increases. If the two components have differing time scale parameters, the degradation of the estimation is less severe, since the two signals will not become congruent even as the separation goes to zero. A second case was run, to calculate usable bounds on estimation for the data presented later in this paper. Two components were again placed close together, this time each with a signal to noise ratio of 90dB, each component at a time scale of $a_i = 1$. The results are summarized in table 1, where component separations resulting in the Cramer-Rao bound exceeding a given error tolerance (standard deviation) are shown.

3. Estimation Biasing When the Number of Components is Unknown

In the previous section, estimation variance bounds were calculated for the situation where all the components in the model were accounted for. If an unknown component is present, the problem becomes more difficult, since the error bounds are functionally related to the position and parameters of the unknown component. One approach to calculating the Cramer-Rao bounds on the known component would be to treat the parameters of the unknown component as random variables, and calculate expected values for the bounds. We will not pursue this result

parameter	typical value	tolerance	separation limit
A	1	$\sigma_A = 0.1$	.0011
ϕ	0	$\sigma_\phi = 1$ deg	.0011
a	1	$\sigma_a = .001$	.0021
τ	0	$\sigma_\tau = .0076$	.0076

Table 1: Typical resolution performance for a 40% band 50 sample LFM Signal, 90 dB above measurement noise. Units for separations and τ are in samples.

here, that is we are more interested in detecting situations where an unknown component may be present, and concentrating the effort of the estimation algorithms in these areas.

With this in mind, we have calculated the estimation biasing which occurs when an unknown component nears the location of a component whose parameters we are estimating. This biasing occurs because (in general)

$$\underset{a_1,\tau_1}{\arg\max} \left\{x^t * \mathbf{H}_1(\mathbf{H}_1^t\mathbf{H}_1)^{-1}\mathbf{H}_1^t * x\right\} \neq \underset{a_1,\tau_1}{\arg\max} \left\{x^t * \mathbf{H}_{1,2}(\mathbf{H}_{1,2}^t\mathbf{H}_{1,2})^{-1}\mathbf{H}_{1,2}^t * x\right\} , \tag{12}$$

where $\mathbf{H}_{1,2}$ is the model matrix with a second component added. Continuing the analysis of the 50 sample LFM signal we are interested in, we have run Fast Maximum Likelihood Estimation on a series of simulated returns, when a second unknown component is present. The measurement noise for this example is zero, as we are interested in the biasing of the estimation on the first component. This is equivalent to evaluating the right side of equation 12. Figure 2 shows why it is dangerous to take literally the time scale estimates of a Maximum Likelihood Estimation

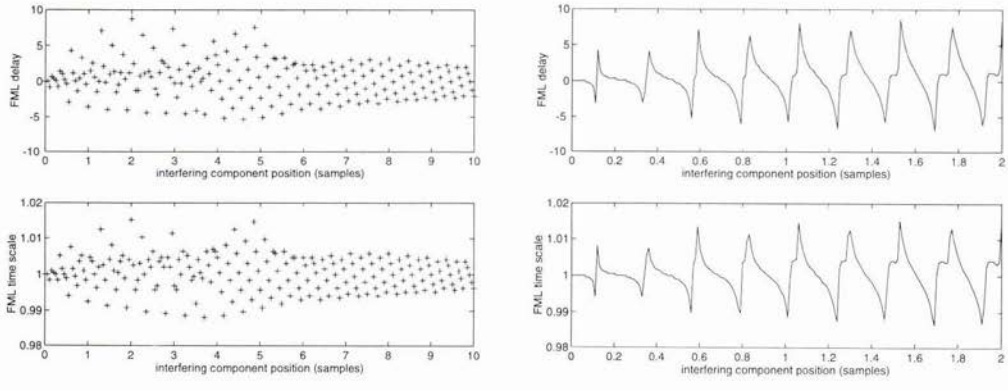

Figure 2: 50 Sample FM Pulse, -0.2 to +0.2 freq. Top left are the delay estimates and bottom left are the time scale estimates for the first FML component. A second unknown is placed near the estimated component, at the indicated delay separation. The correct estimates of the first component are $(a = 1, \tau = 0)$ in all cases. On the right are close-ups of the biasing.

procedure. If target or channel features are present with closely spaced time delays, and the estimation is forced to model these features with fewer components than required, the time scale estimates can be significantly biased. In this example, two zero Doppler components can generate an estimate with a time scale approaching $a_i = 1.02$, wh ich, for the sonar system we are modeling, corresponds to a feature moving at approximately 50 feet per second.

4. High Resolution Parameter Estimation

With the fundamental limits on parameter variance and bias in mind, the basic problem to be solved is to decide if any single component of an approximated signal may actually be due to two underlying components. We have shown that two very closely spaced components can generate an estimate of a single component with a radically biased time scale estimate, even though the Cramer-Rao bounds on variance (for the two underlying components) are quite low. We will attempt to exploit this situation, by detecting unusual time scale estimates, and making appropriate substitutions.

One simple approach would be to let the Fast Maximum Likelihood method continue to add components to the estimation, until the signal is resolved. This may result, however, in excessive components being added to the model, before the features we are interested in are resolved. We propose an alternative method, based on maximum posterior probability, a test

$$\max_{\xi} \{\mathsf{L}_{\mathrm{lf}}(x|p(a_1,a_2))\} \stackrel{?}{>} k \max_{\xi_0} \{\mathsf{L}_{\mathrm{lf}}(x|p(a_0))\} \ . \tag{13}$$

We will apply this test to components generated from a Fast Maximum Likelihood analysis, focusing on estimates which have unlikely time scale parameters. This situation, of course, drives the right hand side of equation 13 down. This test checks, component by component (s_0), whether it is more likely that two components ($s_1 + s_2$), generated the data sequence x. The notation $\mathsf{L}_{\mathrm{lf}}(x|p(a_0))$ means the likelihood function, modified for a probabilistic prior on the estimated parameter a_0. We are now treating the time scale parameters a_i as random variables, with a multidimensional probability density function with the following properties,

- probability is concentrated near $a_i = 1$
- unlikely that two very closely spaced components have dissimilar time scales, i.e. $a_1 \approx a_2$.

This situation would apply when data were collected with a relatively static platform, in calm seas. Reverberation highlights could have some Doppler (time scale), but since nearby highlights would be moving in unison, the time scale parameters for each highlight would be identical. Let $\mathbf{H}_0 = [s_0]$, $\mathbf{H}_1 = [\ s_1 \quad s_2\ ]$, and the parameter ve ctor ξ be broken up into the linearly entering parameters $\theta_0 = [A_0 e^{j\phi_0}]$, $\theta_1 = [\ A_1 e^{j\phi_1} \quad A_2 e^{j\phi_2}\ ]^t$, and the non-linearly entering parameters $\xi_0 = [\ a_0 \quad \tau_0\ ]^t$, and $\xi_1 = [\ a_1 \quad \tau_1 \quad a_2 \quad \tau_2\ ]^t$. Then,

$$\mathsf{L}_{\mathrm{lf}}(x|p(a_1,a_2)) = \frac{1}{(2\pi)^N |\mathbf{C}|} e^{-(x-\mathbf{H}_1\theta_1)^h \mathbf{C}(x-\mathbf{H}_1\theta_1)} p(a_1,a_2) \ , \tag{14}$$

$$\mathsf{L}_{\mathrm{lf}}(x|p(a_0)) = \frac{1}{(2\pi)^N |\mathbf{C}|} e^{-(x-\mathbf{H}_0\theta_0)^h \mathbf{C}(x-\mathbf{H}_0\theta_0)} p(a_0) \ , \tag{15}$$

and

$$\begin{aligned} p(a_1,a_2) &= \delta(a_1 - a_2) p_a(a_1) \\ p(a_0) &= p_a(a_0) \ . \end{aligned} \tag{16}$$

Then, the test 13 would be equivalent to, letting $\mathbf{C} = \sigma^2 \mathbf{I}$,

$$\max_{\xi_1'} \left\{ \ln p_a(a_1) + \frac{1}{\sigma^2} \|\mathbf{P}_{\mathbf{H}_1} x\|^2 \right\} \stackrel{?}{>} k' + \max_{\xi_0} \left\{ \ln p_a(a_0) + \frac{1}{\sigma^2} \|\mathbf{P}_{\mathbf{H}_0} x\|^2 \right\} \ , \tag{17}$$

where $\xi_1' = [\ a_1 \quad \tau_1 \quad a_1 \quad \tau_2\ ]^t$. This test has been re-written by noting that the maximization of $\ln p_a(a_i)$ does not depend on θ_i, and substituting the maximum likelihood estimate (MLE) for θ_i into each side of the equation. It is well known that substitution of the MLE will maximize this form, see for example [5]. This likelihood test, equation 17, will be the test we are primarily concerned with. The simplest case would be a uniform prior on the time scale parameter, $p_a(a) = (a_U - a_L)^{-1} \mathrm{U}(a_L, a_U)$. For this case, time scale estimates outside the limits of $p_a(a)$ drive either side of equation 17 to $-\infty$, and the likelihood test is reduced to, dropping the record keeping on the different likelihood thresholds 'k',

$$\max_{a_1,\tau_1,\tau_2} \|\mathbf{P}_{\mathbf{H}_1} x\|^2 \stackrel{?}{>} k + \max_{a_0,\tau_0} \|\mathbf{P}_{\mathbf{H}_0} x\|^2 \ . \tag{18}$$

5. Data Analysis

We have applied our algorithm to a data set collected in Narragansett Bay, in November of 1994. In this test, a series of linear frequency modulated signals were transmitted against a field of targets situated in about 120 feet of water. This was a static test, that is neither the transmitter, receiver, or the targets were moving. We have chosen a transmit which, in the decimated signal domain, lasts about fifty samples, and sweeps from digital frequencies of approximately $\Omega = -0.2$ to $\Omega = +0.2$. Records of reverberation data were extracted from the raw data by beamforming the data away from the targets, and selecting data segments of manageable record size. We have implemented the equation 17 test as follows.

- Perform Fast Maximum Likelihood estimation on a data record.
- Identify 'singleton' components with unreasonable time scale.
- Perform the likelihood test, equation 17, searching over 2-d space of $(\Delta\tau, a)$, where $\tau_1 = \tau_0(a) - 1/2\Delta\tau$, and $\tau_2 = \tau_0(a) + 1/2\Delta\tau$. Replace the single component with two components, if the test 17 is satisfied. τ_0 is a function of a, and follows the likelihood ridge passing through the single component's location.

Figures 3 and 4 show a typical result of the analysis. In figure 3, the reverberation signal has been approximated using Fast Maximum Likelihood. The analysis has been purposely stopped short, that is only the most significant components of the signal were approximated to avoid over-resolving the signal. A prior probability on the time scale parameter was not invoked, the algorithm was free to fit using any time scale between $a_i = .98$ and $a_i = 1.02$. Figure 4 shows the result of implementing the likelihood test of equation 17. We chose the time scale threshold to be $|a_i - 1| = .005$, and the noise parameter σ to be equivalent to the residual of the Fast Maximum Likelihood analysis. The left hand side of figure 4 shows the wide band cross ambiguity function of the reconstructed signal,

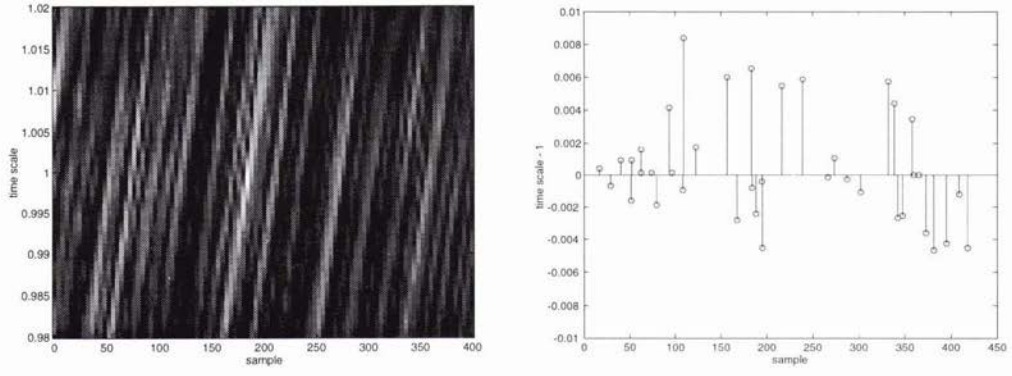

Figure 3: Fast Maximum Likelihood Analysis Result of High Frequency Reverberation Data. Left is wide-band cross ambiguity function of a section of return with the transmit. Right are the delays and time scalings which represent this signal.

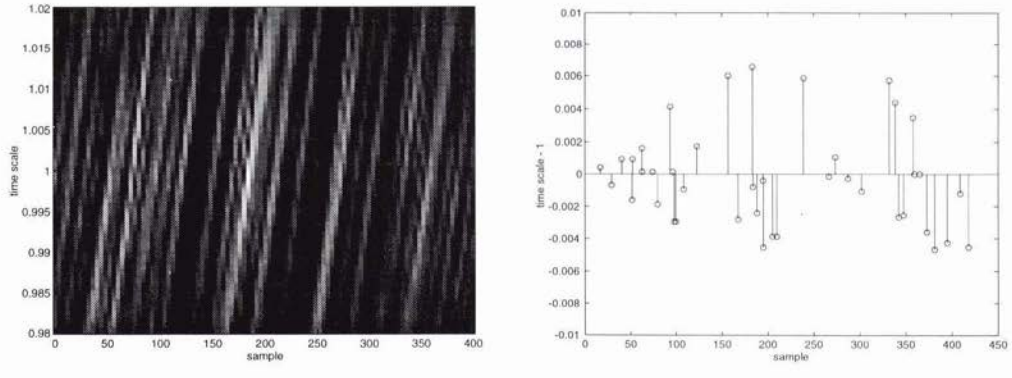

Figure 4: High Resolution Analysis Result of High Frequency Reverberation Data. Left is wide-band cross ambiguity function of reconstructed signal with the transmit. Right are the delays and time scalings which represent this signal.

to be contrasted with the left hand side of figure 3. The high resolution test has replaced two of the Fast Maximum Likelihood components with closely spaced components at more likely time scales. The reconstructed signal retains the important features of the original signal, especially the highly structured nature of the wide band ambiguity function.

6. Conclusion

We have shown a method to extend the performance of Fast Maximum Likelihood estimation, by performing localized likelihood searches on individual signal components. This method can be used to introduce prior probability information to the estimation procedure, particularly information related to propagation and the environment. We hope to extend this work to address probabilistic scattering models for structured targets present in the reverberation.

References

[1] D. Middleton, "A statistical theory of reverberation and similar first-order scattered fields, part 1: Waveforms and the general process," *IEEE Transactions on Information Theory*, vol. IT-13, no. 3, pp. 372–392, July 1967.

[2] D. Middleton, "A statistical theory of reverberation and similar first-order scattered fields, part 2: Moments, spectra, and special distributions," *IEEE Transactions on Information Theory*, vol. IT-13, no. 3, pp. 393–414, July 1967.

[3] D. W. Tufts, H. Ge, and S. Umesh, "Fast maximum likelihood estimation of signal parameters using the shape of the compressed likelihood function," *IEEE Journal of Oceanic Engineering*, vol. 18, no. 4, pp. 388–399, October 1993.

[4] S. M. Kay, *Fundamentals of Statistical Signal Processing, Estimation Theory*, Prentice-Hall, Inc., Englewood Cliffs, NJ, 1993.

[5] L. L. Scharf and B. Friedlander, "Matched subspace detectors," *IEEE Transactions on Signal Processing*, vol. 42, pp. 2146–2157, August 1994.

Estimating Surface Orientation from Sonar Images

Nicholas C Makris

Naval Research Laboratory
Washington, DC 20375
USA
Email: makris@abyss.nrl.navy.mil

Abstract

A maximum likelihood method for estimating remote surface orientation from multi-static sonar images is presented. It is assumed that the sonar images are corrupted by signal-dependent noise, known as speckle, arising from complex Gaussian field fluctuations, and that the surface reflectance properties are effectively Lambertian. The minimum number of independent samples necessary for maximum likelihood estimates to be asymptotically unbiased and attain classical estimation theory's lower bound on resolution are also derived.

1. Introduction

Sonar images of remote surfaces are typically corrupted by signal-dependent noise known as speckle. This noise arises when wavelength scale roughness on the surface causes a random interference pattern in the sound field scattered from it by an active system. Relative motion between source, surface and receiver causes the received field to fluctuate over time with circular complex Gaussian random (CCGR) statistics [1]. Underlying these fluctuations, however, is the expected radiant intensity from the surface, from which its orientation may be inferred. In many cases of practical importance, Lambert's Law is appropriate for such inference because variations in the projected area of a surface patch, as a function of source and receiver orientation, often cause the predominant variations in its radiance. Maximum likelihood estimators for Lambertian surface orientation are derived. These are asymptotically optimal when a sufficiently large number of independent samples is available, even though the relationship between surface orientation and measured radiance is generally nonlinear. Here the term optimal means that the estimate is unbiased and its mean-square error attains classical estimation theory's lower bound, the inverse Fisher information matrix, which is also derived by analytic means. By evaluating this bound, it is found that optimal resolution varies significantly with illumination direction and measurement diversity. In a particularly compelling example, it is shown that the minimum error in estimating the angle of incidence with respect to a Lambertian surface is at best proportional to the *cotangent* of this angle, so that surface orientation varies from irresolvable at normal incidence to perfectly resolvable at shallowest grazing. General expressions for the requisite number of independent samples necessary for asymptotic optimality of the maximum likelihood estimate are derived. When evaluated, this number is also found to vary significantly with illumination direction and measurement diversity, as may be expected from the inherently nonlinear nature of the surface estimation problem. A far more detailed account of this material will appear in Reference 2.

2. Radiometry

The flux $d\Phi$, received in a sonar beam of solid angle $d\beta$, is related to the area of the resolved surface patch dA_β, the local surface radiance L_β, and the solid angle subtended by the sonar aperture $d\Omega$, by the linear equation

$$d\Phi = dA_\beta L_\beta d\Omega \tag{1}$$

The solid angle subtended by the sonar aperture, from the surface patch dA_β, is $d\Omega = \cos\psi_r \, dA/r^2$. where dA is the area of the aperture, $\cos\psi_r$ is the foreshortening of the surface patch with respect to the receiver, ψ_r is the scattering angle, and r is the range to the aperture. The intensity of the received beam is then

$$I_\beta = \frac{d\Phi}{dA} = dA_\beta L_\beta \frac{\cos\psi_r}{r^2}. \tag{2}$$

Assuming that the sonar is of sufficiently high resolution that it resolves an elemental surface patch dA_β that is locally planar and small enough so that

$$d\beta = dA_\beta \frac{\cos\psi_r}{r^2}, \tag{3}$$

surface radiance can be directly measured by the sonar as

$$\frac{dI_\beta}{d\beta} = L_\beta. \tag{4}$$

For a Lambertian surface,

$$L_\beta = \rho E \cos\psi_i, \tag{5}$$

so that the radiance measured in a sonar image of the scene L_β is independent of the viewing direction ψ_r. It follows a linear relationship with the foreshortening $\cos\psi_i$ of the surface patch, the surface irradiance E, and the surface bidirectional reflectance distribution function ρ which is $1/\pi$ for a perfectly reflecting Lambertian surface. Here ψ_i is the angle of incident insonification and E is defined as the incident flux per unit area on the surface of albedo $\pi\rho$.

3. Measurement Statistics

Let the stochastic measurement vector $\boldsymbol{R}$ contain the independent statistics R_k whose expected values $\sigma_k(\boldsymbol{a})=\langle R_k\rangle$ are linearly related to measured surface radiance for k=1,2,3 ...N, where the vector $\boldsymbol{a}$ contains the surface orientation parameters a_j to be estimated from the measurements $\boldsymbol{R}$ for j=1,2,3 ... N_a. More succinctly, let $\boldsymbol{\sigma}(\boldsymbol{a}) = \langle \boldsymbol{R} \rangle$.

Assuming the R_k are corrupted by CCGR field fluctuations, the conditional probability distribution for the measurements $\boldsymbol{R}$ given parameter vector $\boldsymbol{a}$ is the product of gamma distributions [1][3]

$$P_R(\boldsymbol{R}|\boldsymbol{a}) = \prod_{k=1}^{N} \frac{\left(\frac{\mu_k}{\sigma_k(\boldsymbol{a})}\right)^{\mu_k} (R_k)^{\mu_k - 1} \exp\left\{-\mu_k \frac{R_k}{\sigma_k(\boldsymbol{a})}\right\}}{\Gamma(\mu_k)}. \tag{6}$$

The quantity μ_k is the number of coherence cells in the measurement average used to obtain R_k [1][3]. This number is equal to the signal-to-noise ratio (SNR) $\langle R_k \rangle^2 \Big/ \left(\langle R_k^2 \rangle - \langle R_k \rangle^2\right)$. For example, μ_k equals the time-bandwidth product of the received field if each R_k is obtained from a continuous but finite-time average. Additionally, μ_k can be interpreted as the number of stationary speckles averaged over a finite spatial aperture in the image plane or the number of stationary multi-look images averaged for a particular scene [3].

4. Classical Estimation Theory

The maximum likelihood estimator $\hat{\boldsymbol{a}}$, for the parameter set $\boldsymbol{a}$, maximizes the likelihood function for $\boldsymbol{a}$. The likelihood function for $\boldsymbol{a}$ is the conditional probability $P_{\boldsymbol{R}}(\boldsymbol{R}|\boldsymbol{a})$ evaluated at the measured values $\boldsymbol{R}$. If $\ln P_{\boldsymbol{R}}(\boldsymbol{R}|\boldsymbol{a})$ is differentiable, the maximum likelihood estimate $\hat{\boldsymbol{a}}$ can be found by solving the equation

$$\left.\frac{\partial \ln P_R(\boldsymbol{R}|\boldsymbol{a})}{\partial \boldsymbol{a}}\right|_{a=\hat{a}} = 0. \tag{7}$$

For sufficiently large μ_k, the maximum likelihood estimate asymptotically obeys the Gaussian distribution

$$P_{\hat{a}}(\hat{\boldsymbol{a}}|\boldsymbol{a}) \approx \sqrt{\frac{|\boldsymbol{J}|}{(2\pi)^{N_a}}} \exp\left\{-\frac{1}{2}(\hat{\boldsymbol{a}}-\boldsymbol{a})^{\mathrm{T}}\boldsymbol{J}(\hat{\boldsymbol{a}}-\boldsymbol{a})\right\}, \tag{8}$$

where $\boldsymbol{J}$ is the Fisher information matrix, with elements

$$J_{ij}(\boldsymbol{a}) = \sum_{k=1}^{N}\left(\mu_k \frac{\partial \ln \sigma_k(\boldsymbol{a})}{\partial a_i}\frac{\partial \ln \sigma_k(\boldsymbol{a})}{\partial a_j}\right). \tag{9}$$

following References [1][3]. In this limit, the estimate $\hat{\boldsymbol{a}}$ is unbiased and attains classical estimations theory's lower bound $\boldsymbol{J}^{-1}$ on the mean square error of any unbiased estimate of $\boldsymbol{a}$. In the deterministic limit $\mu_k \to \infty$, where the R_k are obtained from exhaustive sample averages, $\boldsymbol{P}_{\hat{a}}(\hat{\boldsymbol{a}}|\boldsymbol{a})$ becomes the delta function $\delta(\hat{\boldsymbol{a}}-\boldsymbol{a})$.

5. A Higher Order Asymptotic Approach to Inference

I have recently developed higher order asymptotic methods for determining the sample size μ_k necessary for the maximum likelihood estimate to be effectively unbiased and attain the classical bound on mean-square error. These are derived in detail in Reference 2. Assuming uniform sampling, $\mu=\mu_k$, and letting $\boldsymbol{g}(\sigma)=\hat{\boldsymbol{a}}(\langle \boldsymbol{R}\rangle)$, the bias of $\hat{a}_i$ will be negligible when

$$\mu >> \left|\frac{\sum_{k=1}^{N}\sigma_k^2\frac{\partial^2 g_i}{\partial \sigma_k^2}}{2g_i}\right|, \tag{10}$$

and the mean-square error covariance $\left\langle(\hat{a}_i-a_i)^2\right\rangle$ will attain the lower bound $\left[\boldsymbol{J}^{-1}\right]_{ii}$ when

$$\mu >> \left|\frac{\sum_{k=1}^{N}2\sigma_k^3\frac{\partial g_i}{\partial \sigma_k}\frac{\partial^2 g_i}{\partial \sigma_k^2}+\frac{1}{4}\sum_{l=1}^{N}\sum_{m=1}^{N}(1-\delta_{lm})\sigma_l^2\sigma_m^2\left\{\frac{\partial^2 g_i}{\partial \sigma_l^2}\frac{\partial^2 g_i}{\partial \sigma_m^2}+2\left(\frac{\partial^2 g_i}{\partial \sigma_l \partial \sigma_m}\right)^2\right\}}{\sum_{k=1}^{N}\sigma_k^2\left(\frac{\partial g_i}{\partial \sigma_k}\right)^2}\right|, \tag{11}$$

where the denominator of this expression merely equals $\left[\boldsymbol{J}^{-1}\right]_{ii}$.

6. INFERRING LAMBERTIAN SURFACE ORIENTATION

6.1 PROBLEM STATEMENT

For measurement k, a collimated source with known unit incident direction $\boldsymbol{s}_k$ irradiates a planar Lambertian surface with unknown unit normal vector $\boldsymbol{n}$. For each measurement, the receiver measures Lambertian surface radiance from any hemispherical observation position within view of the surface. For convenience, a Cartesian coordinate system (x,y,z) is adopted where the ultimate viewing direction is aligned with the positive z axis. Because surface irradiance E_k is presumed known, given knowledge of source power, directionality, and transmission characteristics to the surface, it is deterministically scaled out of the measured surface radiance leaving $\sigma_{L_k}=\langle L_k\rangle/E_k$. When signal-independent additive CCGR noise of intensity $\sigma_{N_k} d\beta_k E_k$ is also measured with the radiant field from the surface, the expected measurement vector $\langle \boldsymbol{R}\rangle$ becomes $\boldsymbol{\sigma}(\boldsymbol{a}) = \boldsymbol{\sigma}_L(\boldsymbol{a}) + \boldsymbol{\sigma}_N(\boldsymbol{a})$.

Lambert's Law for the expected radiometric component of the data is then

$$\boldsymbol{\sigma}_L = \mathbf{S}\boldsymbol{x}, \tag{12}$$

where the matrix $\mathbf{S}$ is defined by

$$\mathbf{S}^{\mathrm{T}} = \left[\boldsymbol{s}_1\ \boldsymbol{s}_2\ \boldsymbol{s}_3\ \ldots \boldsymbol{s}_N\right], \tag{13}$$

and the vector $\boldsymbol{x}$ equals $\rho\boldsymbol{n}$.

The general problem is to determine both the Labertian surface normal vector $\boldsymbol{n}$ and the albedo $\pi\rho$ from the fluctuating measurements $\boldsymbol{R}$. The surface normal is typically expressed in terms of the surface gradient components,

$$\boldsymbol{n}^{\mathrm{T}} = \left[-p_n\ -q_n\ 1\right] / \left(1 + p_n^2 + q_n^2\right)^{1/2}, \tag{14}$$

where

$$p_n = \frac{\partial z}{\partial x},\ q_n = \frac{\partial z}{\partial y}, \tag{15}$$

or in terms of spherical coordinates

$$\boldsymbol{n}^{\mathrm{T}} = \left[\cos\phi_n \sin\theta_n\ \ \sin\phi_n \sin\theta_n\ \ \cos\theta_n\right]. \tag{16}$$

6.2 THE ANGLE OF INCIDENCE

Suppose that the angle of incidence ψ is to be estimated from a single measurement R, with variance σ^2/μ, given that the albedo $\rho\pi$ is known. From (9), the resulting mean-square error bound is

$$E\left[(\tilde{\psi} - \psi)^2\right] \geq J^{-1} = \frac{(\cos\psi + \sigma_N)^2}{\mu \sin^2\psi}, \tag{17}$$

for any unbiased estimate $\tilde{\psi}$, which becomes

$$E\left[(\tilde{\psi} - \psi)^2\right] \geq J^{-1} = \frac{\cot^2\psi}{\mu}, \tag{18}$$

when the signal-independent noise is negligible. These expressions show resolution of the incident angle to be highest when the Lambertian surface is illuminated at shallow grazing and lowest when the surface is illuminated near normal incidence. This can be motivated physically by noting that for shallow grazing angle illumination Lambert's Law has a first order dependence that is proportional to the incident angle. Conversely, for illumination near normal incidence Lambert's Law is independent of the incident angle to first order. It is also significant that when the rms-error bound is finite, it can be reduced in proportion to the square-root of the number of independent samples μ averaged to obtain the radiometric statistic R.

The maximum likelihood estimate for the the angle of incidence is

$$\hat{\psi} = \cos^{-1}\left(\frac{R-\sigma_N}{\rho}\right) \tag{19}$$

Many of the potential benefits and difficulties associated with maximum likelihood estimation can be illustrated by examining the statistical properties of $\hat{\psi}$.

For the remainder of this section, let σ_N be negligible, as may be expected in practical imaging systems except at shallow grazing where ψ is very near $\pi/2$. First of all, because R is a gamma variate and can take on any positive definite value, the estimate $\hat{\psi}$ is real for $0 \le R/\rho \le 1$ and imaginary for $R/\rho > 1$. The probability that $\hat{\psi}$ is real is found to be $\chi(\mu, \mu/\cos\psi)/\Gamma(\mu)$ by appropriately integrating $P_R(R|\psi)$. But this leaves finite probability $\Gamma(\mu, \mu/\cos\psi)/\Gamma(\mu)$ that $\hat{\psi}$ is imaginary. More specifically, the statistic $\hat{\psi}$ is distributed according to

$$P_{\hat{\psi}}(\hat{\psi}|\psi) = \rho \sin\hat{\psi} P_R(\rho\cos\hat{\psi}|\psi) \qquad \text{over } 0 \le \hat{\psi} \le \pi/2, \tag{20}$$

for $\hat{\psi}$ real, and

$$P_{\hat{\psi}}(\hat{\psi}|\psi) = \rho \sinh\hat{\psi} P_R(\rho\cosh\hat{\psi}|\psi) \qquad \text{over } 0 \le \hat{\psi} \le \infty, \tag{21}$$

for $\hat{\psi}$ imaginary. The probability $\Gamma(\mu, \mu/\cos\psi)/\Gamma(\mu)$ that $\hat{\psi}$ is imaginary decreases as the angle of incidence ψ and the sample size μ increase, as does the bias of $\hat{\psi}$.

Apparently, CCGR fluctuations in the radiant field can lead to unphysical maximum likelihood estimates of the incident angle ψ. This can be remedied by reconditioning the maximum likelihood estimate, given ancillary information [4] that is $\hat{\psi}$ real, so that

$$P_{\hat{\psi}}\left(\hat{\psi}|\psi, \hat{\psi} = \mathrm{Re}\{\hat{\psi}\}\right) = \rho \sin\hat{\psi} P_R\left(\rho\cos\hat{\psi}|\psi\right)\Gamma(\mu)/\gamma(\mu, \mu/\cos\psi) \qquad \text{over } 0 \le \hat{\psi} \le \pi/2. \tag{22}$$

For sufficiently large samples μ, the relationship between maximum likelihood estimate $\hat{\psi}$ and data R approaches linearity, so that $\hat{\psi}$ obeys the Gaussian distribution

$$P(\hat{\psi}|\psi) \approx \sqrt{\frac{\mu}{2\pi\cot^2\psi}} \exp\left(-\frac{1}{2}\mu\frac{\{\hat{\psi}-\psi\}^2}{\cot^2\psi}\right), \tag{23}$$

with bias vanishing and variance equaling the inverse Fisher information.

Following Section 5, $\hat{\psi}$ is effectively unbiased when

$$\mu >> \left| \frac{\cot^3 \psi}{2\psi} \right|, \tag{24}$$

and effectively attains the bound J^{-1} when

$$\mu >> 2\cot^2 \psi . \tag{25}$$

As these expressions show, the number of samples necessary for $\hat{\psi}$ to behave as a minimum variance unbiased estimate varies nonlinearly from unity at shallow grazing angles to an arbitrarily large number near normal incidence.

Even if the location of the surface is known with respect to the source of illumination, knowledge of the angle of incidence only places the surface within a cone about the incident vector s. At minimum, a second measurement is necessary to determine the orientation of the surface in this cone, and a third is needed to determine the albedo.

6.3 SURFACE ORIENTATION AND ALBEDO

The 3-D parameter vector $\boldsymbol{x}$ is to be estimated from the potentially over-determined N-D measurement vector $\boldsymbol{R}$. From (9) and (12), the mean-square error bound on any unbiased estimate $\tilde{\boldsymbol{x}}$ is

$$E\left[\left(\tilde{\boldsymbol{x}}-\boldsymbol{x}\right)\left(\tilde{\boldsymbol{x}}-\boldsymbol{x}\right)^{\mathrm{T}}\right] \geq \boldsymbol{J}_x^{-1} = \left[\mathbf{S}^{\mathrm{T}}\boldsymbol{J}_\sigma \mathbf{S}\right]^{-1}, \tag{26}$$

where $\left[\boldsymbol{J}_\sigma\right]_{ij} = \delta_{ij}\mu_{ij}/\sigma_i^2$ is infinite when all incident vectors s_k are tangent to $\boldsymbol{n}$ in the absence of signal-independent noise.

More generally, such as for surface gradient $\boldsymbol{a}^{\mathrm{T}}=[p\ q\ r]$, or polar coordinate $\boldsymbol{a}^{\mathrm{T}}=[\theta\ \phi\ \rho]$ parametrizations, the bound

$$E\left[(\tilde{\boldsymbol{a}}-\boldsymbol{a})(\tilde{\boldsymbol{a}}-\boldsymbol{a})^{\mathrm{T}}\right] \geq \boldsymbol{J}_a^{-1} = \frac{\partial \boldsymbol{a}}{\partial \boldsymbol{x}} \boldsymbol{J}_x^{-1} \frac{\partial \boldsymbol{a}}{\partial \boldsymbol{x}}^{\mathrm{T}} \tag{27}$$

becomes singular when all the s_k are coplanar but not tangent to the surface for non-zero σ_N, or when the Jacobian $\left|\frac{\partial \boldsymbol{a}}{\partial \boldsymbol{x}}\right|$ is singular. When σ_N vanishes, $|\boldsymbol{J}_x|^{1/2}|\boldsymbol{J}_\sigma|^{-1/2}$ can be interpreted as the effective weighted volume of incident vectors s_k. For example, when $\boldsymbol{R}$ is a 3-D vector, the bound is

$$\left[\boldsymbol{J}_x^{-1}\right]_{ij} = \frac{\sigma_1^2\left[s_2 \times s_3\right]_i\left[s_2 \times s_3\right]_j + \sigma_2^2\left[s_3 \times s_1\right]_i\left[s_3 \times s_1\right]_j + \sigma_3^2\left[s_1 \times s_2\right]_i\left[s_1 \times s_2\right]_j}{\left(s_1 \cdot s_2 \times s_3\right)^2}, \tag{28}$$

so that $|\boldsymbol{J}_x|^{1/2}|\boldsymbol{J}_\sigma|^{-1/2}$ simply is the volume $(s_1 \cdot s_2 \times s_3)$ of the parellelepiped of incident vectors. Behavior of the Jacobian $\left|\frac{\partial \boldsymbol{a}}{\partial \boldsymbol{x}}\right|$ depends upon the final coordinates $\boldsymbol{a}$, as can be seen from the respective forms $\left(p^2+q^2+1\right)^{3/2}/\rho^2$ and $1/\left(\rho^2 \sin^2\theta\right)$ for the surface gradient and polar systems.

The maximum likelihood estimate, given linearity between $\boldsymbol{x}$ and σ,

$$\hat{\boldsymbol{x}} = \left[\mathbf{S}^{\mathrm{T}}\boldsymbol{J}_\sigma \mathbf{S}\right]^{-1}\mathbf{S}^{\mathrm{T}}\boldsymbol{J}_\sigma\left(\boldsymbol{R}-\sigma_N\right), \tag{29}$$

is unbiased and attains the error bound $J_{\hat{\boldsymbol{x}}}^{-1}$.

Given this information, the maximum likelihood estimates for albedo $\pi\hat{\rho} = \pi\left|\hat{\boldsymbol{x}}\right|$, surface normal $\boldsymbol{n} = \hat{\boldsymbol{x}}/\hat{\rho}$, cone and polar angles $\hat{\theta} = \cos^{-1}\hat{n}_3, \hat{\varphi}_n = \tan^{-1}\dfrac{\hat{n}_2}{\hat{n}_1}$, and surface gradient components $\hat{p}_n = -\dfrac{\hat{n}_1}{\hat{n}_3}, \hat{q}_n = -\dfrac{\hat{n}_2}{\hat{n}_3}$, however, are not generally unbiased and do not generally have minimum variance except for sufficiently large sample sizes.

Taking the case where $\boldsymbol{R}$ is a 3-D vector and σ_N is negligible, for example, the joint distribution for $\hat{\boldsymbol{x}}$ is

$$P_{\hat{\boldsymbol{x}}}\left(\hat{\boldsymbol{x}}|\boldsymbol{x}\right) = \left|s_1 \cdot s_2 \times s_3\right| P_{\boldsymbol{R}}\left(\mathbf{S}\hat{\boldsymbol{x}}|\sigma\right), \tag{30}$$

which leads to the respective joint distributions

$$P_{grad}(\hat{p}_n, \hat{q}_n, \hat{\rho}|p_n, q_n, \rho) = \frac{P_{\hat{\boldsymbol{x}}}(-\hat{\rho}\hat{p}_n(1+\hat{p}_n^2+\hat{q}_n^2)^{-1/2}, -\hat{\rho}\hat{q}_n(1+\hat{p}_n^2+\hat{q}_n^2)^{-1/2}, \hat{\rho}(1+\hat{p}_n^2+\hat{q}_n^2)^{-1/2}|\boldsymbol{x})}{\left|\hat{\rho}^2(1+\hat{p}_n^2+\hat{q}_n^2)^{-3/2}\right|}, \tag{31}$$

and

$$P_{polar}(\hat{\theta}_n, \hat{\phi}_n, \hat{\rho}|\theta_n, \phi_n, \rho) = \frac{P_{\hat{\boldsymbol{x}}}(\hat{\rho}\cos\hat{\phi}_n \sin\hat{\theta}_n, \hat{\rho}\sin\hat{\phi}_n \sin\hat{\theta}_n, \hat{\rho}\cos\hat{\theta}_n|\boldsymbol{x})}{\left|\hat{\rho}^2 \sin^2\hat{\theta}_n\right|}, \tag{32}$$

for the gradient and polar coordinate maximum likelihood estimates.

Returning to the general case when $\boldsymbol{R}$ is an N-D vector, the asymptotic maximum likelihood distributions for surface orientation and albedo follow (8) when (10) and (11) are satisfied.

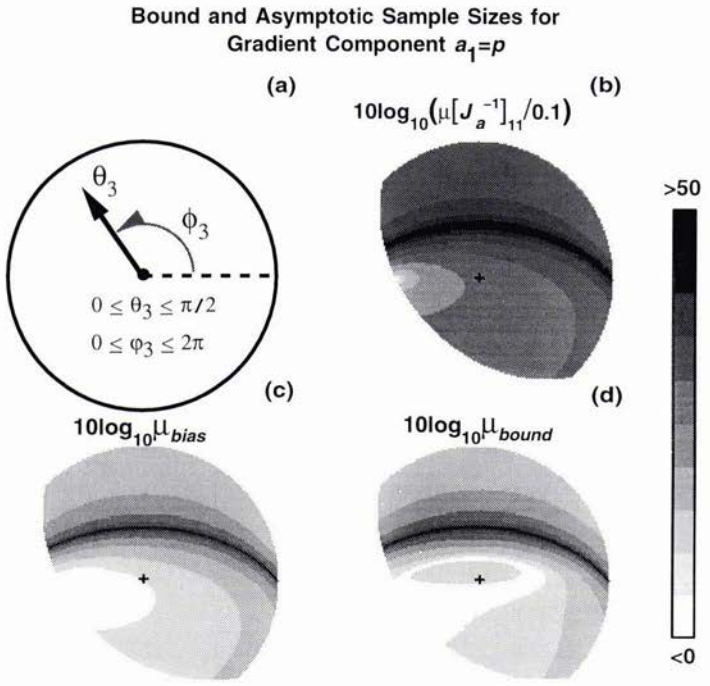

Figure 1. A visualization for $\boldsymbol{a}$ corresponding to the surface gradient parametrization for a 3-D measurement vector $\boldsymbol{R}$ with $\boldsymbol{\sigma}_N$ negligible and Lambertian surface defined by the polar coordinate parameterization ($\theta_n=\pi/4$, $\phi_n=\pi/4$, $\rho=1$). Incident vectors $\boldsymbol{s}_1$ and $\boldsymbol{s}_2$ are fixed by cone and polar angles ($\theta_1=\pi/2$, $\phi_1=0$), ($\theta_2=\pi/4$, $\phi_2=\pi/4$) but $\boldsymbol{s}_3$ is allowed to vary as in (a) where the positive z-axis is central and points out of the page. (b) The bound $\left[J_a^{-1}\right]_1$ on the x-gradient $a_1=p$, including full 3-D coupling. Only values where $\boldsymbol{s}_3 \cdot \boldsymbol{n}$ is positive and the Lambertian surface is in view from the positive z-axis are shown. Optimal resolution occurs when $\boldsymbol{s}_3$ is tangent to the Lambertian surface along the x axis (horizontal), for the p-bound, and the y axis (vertical), for the q-bound (not shown), with sign so as to maximize the volume of incident vectors. Poorest resolution occurs when the volume of incident vectors approaches zero, as realized along the dark arc. (c) The number of samples necessary for the maximum likelihood estimate $\hat{a}_1 = \hat{p}$ to be effectively unbiased, from (10). (d) The number of samples necessary, from (11), for $\hat{p}$ to effectively attain the bound given in (b).

These computations exhibit the dramatic nonlinear variations in sample size necessary to first obtain an unbiased estimate and then a minimum variance estimate of Lambertian surface orientation and albedo from multi-static sonar images corrupted by signal-dependent speckle noise.

References

[1] N. C. Makris, "The effect of saturated transmission scintillation on ocean-acoustic intensity measurements," J. Acoust. Soc. Am. 100, 769-783, 1996.

[2] N. C. Makris, "Resolving Lambertian surface orientation from fluctuating radiance," J. Optical Soc. Am. (unpublished).

[3] N. C. Makris, "A foundation for logarithmic measures of fluctuating intensity in pattern recognition," Optics Letters 20, 2012-2014, 1995.

[4] R. A. Fisher, *Statistical Methods and Scientific Inference*, Hafner Publishing Co., New York, 1956.

Estimation of Chirp Sonar Signal Attenuation for Classification of Marine Sediments : Improved Spectral Ratio Method

C. S. Maroni, A. Quinquis

ENSIETA
Dpt EIA
2, rue François Verny
29806 Brest Cedex 9, France
E-mail: maronicl@ensieta.fr

Abstract

Remote sediment classification through acoustic methods is of great interest for a few years . The attenuation coefficient of the transmitted wave is an important feature to characterize physical sediment layers properties. Hence, an improved spectral ratio method for the estimation of the chirp sonar signal attenuation is proposed in the paper. A new time-frequency based on technique to compute the least square line is outlined. Finally, the method is tested on synthetic data and some results are discussed.

1. Introduction

Remote sediment classification through acoustic methods has the potential to reduce the cost and effort that current methods require using coring for seafloor classification. But over the past two decades of marine subbottom exploration, the reflection profiling technique has been used primarily to delineate geological and stratification structures. To date, seafloor properties have been determined by sampling the sediment followed by laboratory analyses. This process not only fails to obtain undisturbed samples but also is extremely slow, very expensive, and provides information only at discrete sites. A remote acoustic sediment classification system would eliminate most of the present needs for sediment sampling, while generating continuous profiles of sediment properties. A quantitative analysis of the reflected signal to characterize subsurface sediments is proposed for a few years, but it is still far from being effective in practice.

The attenuation coefficient can be used to classify sediments and to estimate physical sediments properties. Several attenuation measurement techniques have been proposed both in the time and frequency domains : rise-time, spectral ratio, spectral shift, and matched filtering [1] [2]. For the spectral ratio method, overlapping reflections produce errors in the spectral estimates of the different echos. That's why we propose in this paper a new approach to improve results yielded by this classical method.

The subbottom profiler used, transmits a FM pulse, that is linearly swept from 4.5 kHz to 2.5 kHz during 25 ms. This pulse is compressed using a matched filter which correlates the return signal with a replica of the outgoing FM pulse. Owing to a 2 kHz frequency bandwidth, the compressed chirp width is 0.5 ms, which provides a forty centimeters vertical resolution. It's a monostatic configuration in normal incidence.

2. Classical Spectral Ratio Method

2.1. Sea bottom model

The sea bottom is modeled as a layered medium. Unlike the Goupillaud model [3], the one way travel-time in each layer need not be equal. The assumption involved are:

1. The layers are parallel and laterally homogeneous. Normally, this can be quantified in terms of the roughness scale, which should not be greater than the $\frac{1}{4}$ wavelength measured at the central frequency of the FM pulse.
2. The interface reflection coefficients are frequency independent.
3. Phase dispersion and pulse spreading due to attenuation can be neglected. However, the loss of signal energy due to attenuation is accounted for in the model.
4. The acoustic wave travels through the layers as a plane wave at normal incidence. The reflected signal can be written as the convolution of the source signal with the impulse response of the medium.

2.2. Attenuation model

When the sonar pulse travels through an absorbent sea bottom, its energy is reduced in several ways. All the mechanisms lead to the attenuation coefficient α. Attenuation will cause the amplitude of a plane wave to fall off exponentially with the distance traveled. The pulse amplitude losses are evaluated by $\exp(-\alpha\tau)$, where τ is the traveling time.
Hamilton [4] has compiled an important part of the available data published on sea bottom effective attenuation. This author concludes that α varies linearly with frequency. If this assumption was sometimes debated, it is usually allowed in this frequency range. Hence, α can be written as follows :

$$\alpha(f) = \frac{1}{8,686} \times \beta \times \tau \times f \tag{1}$$

Note that β is the attenuation coefficient of the compressional wave in dB/wavelength ($8.686 = 20\log_{10}(e)$). Typical values of β range from 0.1 to 1.0 dB/wavelength. Let us consider a medium with two sediments layers, and assume that the second one is semi-infinite. In other words, the lower bound interface of the second layer, is not caught by the sonar, because of sediment attenuation and layer thickness. Reflected signal in the frequency domain, can be written :

$$\begin{aligned} Y(f) &= R_{12} \times S(f) + T_{12}R_{23}T_{21}\exp(j\tau\omega)\exp\left(-\frac{\beta\ \tau\ f}{8,686}\right) \times S(f) \\ &= A_1(f) + A_2(f)\exp(j\tau\omega) \end{aligned}$$

where $A_1(f)$ and $A_2(f)$ are the amplitude spectra of the seabed echo(reflected by the water-sediment interface) and the first reflector (reflected by the interface between the first and the second subbottom layer). Hence we infer the equation (2) that links together the spectral contributions of the two echos.

$$A_2(f) = G \times A_1(f) \times \exp\left(-\frac{\beta \times f \times (t_2 - t_1)}{8.686}\right) \tag{2}$$

where f stands for frequency, $t1$ and $t2$ are respectively the locations of the seabed and the first reflector echoes, and $\tau = t_2 - t_1$. G is a frequency independent factor that allows for change in pulse magnitude due to reflection and transmission coefficients (R_{12}, R_{23}, T_{12} and T_{21}).

2.3. Estimation technique

Equation (2) can be rewritten as (3), taking the logarithm of the Spectral Ratio$A_2(f)/A_1(f)$

$$\ln\frac{A_2(f)}{A_1(f)} = \ln(G) - \beta \times \frac{(t_1 - t_0)}{8.686} \times f \tag{3}$$

The linear dependence of $\ln A_2(f)/A_1(f)$ versus frequency makes possible the attenuation coefficient (β) estimation, by simply plotting the left side of equation (3) versus frequency. The least squares line fitted through the plotted data yields an estimation of the attenuation coefficient β, because $t1$ and $t2$ can be estimated from the peaks of

the reflected signal envelope, after the matched filtering.
This method provides good results if pulse reflections produced by sediment layers are well separated, allowing good spectral estimation for $A_1(f)$ and $A_2(f)$. With a 25 ms pulse width, the first layer thickness should be larger than 19 m $(25.10^{-3} * 1500/2)$ to avoid overlapping of the two echoes. Fortunately the reflected signals are processed by matched filtering so that the compressed chirp width is 1 ms. Good estimation of β can then be expected, for a delay between the two echoes larger than 1 ms. But, as we will see in the simulation results section, the spectral information of the first reflector is corrupted by the presence of the reflection on the seabed a few ms before. In fact, although the side lobes are very small with respect to the correlated signal main lobe, their influence disturbs the spectrum estimation. Also bad estimations of $A_2(f)$ can provide for β a value which is really different from the real one. That's why an improved spectral ratio method is proposed.

3. Improved Spectral Ratio method

In order to improve the previously presented method, we develop a time-frequency analysis of the compressed chirp, and prove that overlapping reflections produce disturbance only in a limited frequency band.

3.1. Time-frequency analysis of the correlated signal

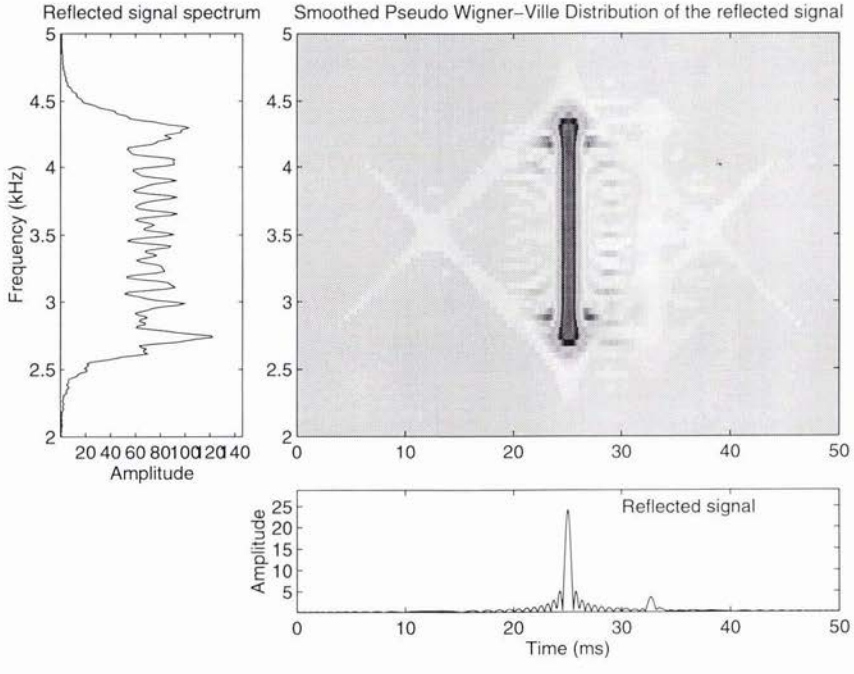

Figure 1: Reflected signal representations in time, frequency and time-frequency domains

Different properties of a signal are revealed if it is represented in the time or in the frequency domain. But the most complete manner for the visualization of its behaviour is the time-frequency analysis. For instance, this is particularly adapted to subbottom echoes, because it can display the evolution of the frequency content versus time, i.e., versus propagation distance, which does not appear when classical spectral analysis is used.
A lot of time-frequency analysis tools was developed in the last few decades. Among them, the Wigner-Ville distribution is a quite powerful instrument with excellent properties concerning the temporal and frequency support preservation and the compatibility with the filtering and modulation operators. It is defined [5] by:

$$WD_s(t,\nu) = \int_{-\infty}^{+\infty} s(t+\frac{\tau}{2})\ s^*(t-\frac{\tau}{2})\ e^{-j2\pi\nu\tau} d\tau \tag{4}$$

where s(t) is the original signal. Its popularity among the Cohen's class distributions is due to the fact that it achieve the best trade-off between the temporal and frequency resolution for a given signal and it allows an exact pursuit of the CHIRP instantaneous frequency.
Its main disadvantage concerns the existence of the cross components which can lead to difficulties of interpretation. Hence, a modified version, named Smoothed Pseudo Wigner-Ville distribution (SPWD) given by:

$$SPWD_s(t,\nu) = \int_{-\infty}^{+\infty} h(\tau) \int_{-\infty}^{+\infty} g(t-u)\ s(u+\frac{\tau}{2})\ s^*(u-\frac{\tau}{2})\ du\ e^{-j2\pi\nu\tau} d\tau \tag{5}$$

has been used in the paper. The introduction of the two windows, h and g, leads to a smoothing of the cross components in the time-frequency domain. In order to improve the legibility of the time-frequency image, the following parameter s have been used: FFT length: 128 points, window type: Hamming, h window length: 128 points, g window length: 33 points, with a 12 kHz sampling frequency.
The figure 1 shows the SPWD of the CHIRP correlated signal reflected by two layers subbottom. Note that the two CHIRP components corresponding to the two reflections are well pursuited and the two correlation maxima are well localized. This image will be used in the section 3.3. to describe the improved spectral ratio method principle.

3.2. Analytical expression of the correlated signal

The autocorrelation function of the signal s(t) is given by:

$$\Gamma_s(\tau) = \int_0^{T-\tau} s(t)\ s(t+\tau)\ dt, \qquad 0 \le \tau \le T \tag{6}$$

with

$$\Gamma_s(\tau) = \Gamma_s(-\tau)$$

where the CHIRP signal expression is:

$$s(t) = \cos\left(\omega_0 t + \frac{\mu t^2}{2}\right), \qquad 0 \le t \le T \tag{7}$$

Consequently:

$$\begin{aligned}
\Gamma_s(\tau) &= \int_0^{T-\tau} cos\left(\omega_0 t + \frac{\mu t^2}{2}\right) cos\left(\omega_0 (t+\tau) + \frac{\mu\ (t+\tau)^2}{2}\right)\ dt \\
\Gamma_s(\tau) &= I_1 + I_2 \\
&\quad where\ : \\
I_1 &= \frac{1}{2}\int_0^{T-\tau} cos\left(\omega_0\tau + \mu\ \tau\ t + \frac{\mu\tau^2}{2}\right)\ dt \\
I_2 &= \frac{1}{2}\int_0^{T-\tau} cos\left(2\omega_0 t + \omega_0\tau + \mu\ t^2 + \mu\ \tau\ t + \frac{\mu\tau^2}{2}\right)\ dt
\end{aligned}$$

It was found that for compression ratios larger than 30, that is the case of this work, I_2 can be neglected. Therefore:

$$\Gamma_s(\tau) = cos\left(\left[\omega_0 + \frac{\mu\ T}{2}\right]\tau\right)\left[\frac{sin\left(\frac{\mu\ \tau\ (T-\tau)}{2}\right)}{\frac{\mu\ \tau\ (T-\tau)}{2}} \times \frac{T-\tau}{2}\right] \tag{8}$$

which can be expressed also as:

$$\begin{aligned}
\Gamma_s(\tau) &= \frac{1}{2}\frac{sin\left(\omega_0\tau + \mu\ \tau\ (T-\tau) + \frac{\mu\tau^2}{2}\right) - sin\left(\omega_0\tau + \frac{\mu\tau^2}{2}\right)}{\mu\tau} \\
&= \frac{1}{2}\frac{sin\left(\omega_0\tau + \mu\ \tau\ T - \frac{\mu\tau^2}{2}\right) - sin\left(\omega_0\tau + \frac{\mu\tau^2}{2}\right)}{\mu\tau}
\end{aligned} \tag{9}$$

The former equation (8) is the well known expression of the correlated signal and it highlights the 'sinc' envelope and the oscillating component at the central frequency :

$$\nu_c = \frac{\omega_0 + (\mu\ T)/2}{2\pi} = 3.5\ kHz$$

This is the most commonly considered expression of the correlated signal when the CHIRP signal is used. However, for the time-frequency analysis, it is more interesting to consider the second expression (9), which shows that the correlated signal can be viewed as the superposition of the two CHIRP having opposed frequency variation slopes. The interpretation of the figure 1 can be now readily done.

3.3. Attenuation coefficient estimation

A simplified representation of the Smoothed Pseudo Wigner Ville Distribution of the reflected signal 1, is displayed on figure 2.

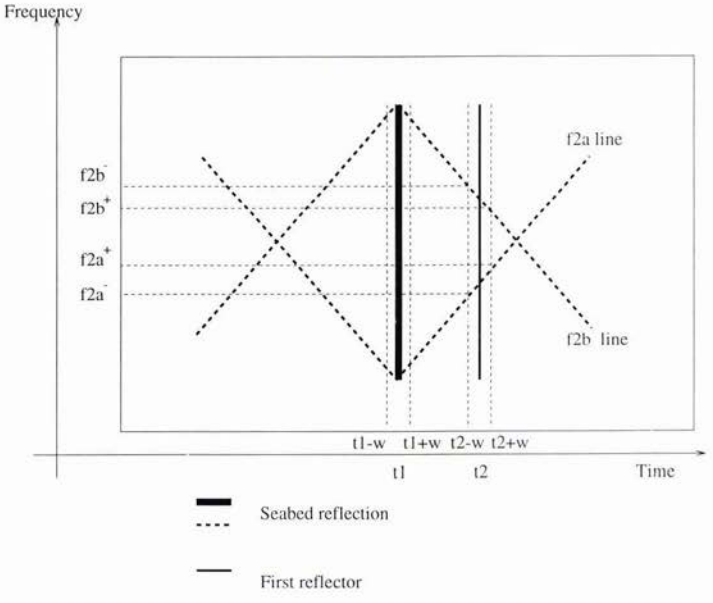

Figure 2: Simplified representation of the reflected signal SPWD

Note that, around $t2$, the spectrum of the signal will be composed of two contributions : the former (the vertical one) provided by the reflector, and the second one due to the presence of two oblique lines. These latter correspond to the two chirps, that were highlighted in previous section, and whose equations are given by

$$f2_a(\tau) = \frac{1}{2\pi}\frac{d}{dt}(\omega_0\tau + \mu\ \tau\ T - \frac{\mu\tau^2}{2}) \quad (10)$$

$$f2_b(\tau) = \frac{1}{2\pi}\frac{d}{dt}(\omega_0\tau + \frac{\mu\tau^2}{2}) \quad (11)$$

where $\tau = t - t1$, or in others words, $t1$ time arrival of the seabed reflection, is the time origin. Equations (10) and (11) become :

$$f2_a(\tau) = 2.5 + 80 \times \tau\ in\ kHz \quad (12)$$

$$f2_b(\tau) = 4.5 - 80 \times \tau\ in\ kHz \quad (13)$$

by substituting parameters with their numerical values, corresponding to the EPSHOM subbottom profiler used, i.e $T = 25\ ms$, $f_0 = 4500\ Hz$, and $\Delta f = -2\ kHz$ $\mu = 2\pi\frac{\Delta f}{T} = -2\pi \times 80000$ Note that for the subbottom profiler used, $\mu =< 0$. We are dealing therefore with a decreasing frequency modulation. Hence, the frequencies affected by the previous reflection, can be estimated after τ estimation. More precisely, not only two frequencies are disturbed, but two little frequency bands. Actually, in order to estimate $A1(f)$ and $A_2(f)$, a Nw-point rectangular window centered on the envelope peaks, is used (Nw=2*w+1, see figure 2). So we have to compute :

$$f2_a^- = f2_a((t2 - w) - t1) \quad (14)$$
$$f2_a^- = f2_a((t2 + w) - t1) \quad (15)$$
$$f2_b^- = f2_b((t2 - w) - t1) \quad (16)$$
$$f2_b^+ = f2_b((t2 + w) - t1) \quad (17)$$

Afterwards, $\ln A_2(f)/A_1(f)$ is computed, but the least squares line calculation takes now into account in a different manner the part of the frequency band which is affected by perturbation and the valid part. That means that we not longer consider $\ln A_2(f)/A_1(f)$ values for $f\epsilon[f2_a^-, f2_a^-] \cup [f2_b^-, f2_b^+]$, when the least squares line is computed.

4. Simulation results

We test our method on synthetic data generated with the model proposed in section 2.. Four sediment types are considered, for the first layer : silt, fine sand, sand and gravel. For the second layer, rock is also proposed. Sediment and rock acoustical parameters used [6] are presented in table 1. More precisely, parameters presented in this table, are central parameters of each type of sediment, and we usually consider an interval around this central value. For each class the first layer is fixed, until the second layer fluctuates as shown in table 2.

	Silt	Fine Sand	Sand	Gravel	Rock
Density (g/cm^3)	1.5	1.75	1.95	2	2.6
Celerity (m/s)	1520	1650	1750	2200	4000
Attenuation (dB/lambda)	0.15	0.20	0.8	0.5	

Table 1: Sediment acoustical parameters used for generating reflected signals

	First layer	**Second layer**
Classe1	Silt	Fine sand Sand Gravel Rock
Classe2	Fine sand	Sand Gravel Rock
Classe3	Sand	Gravel Rock
Classe4	Gravel	Rock

Table 2: Different subbotom types considered when testing estimation methods

Both classical and improved Spectral Ratio Method are tested on these different subbottom. Firstly, the subbottom composition is fixed, and only the time interval τ between the two reflections is varied. That means that attenuation coefficient is estimated for various first sediment layer thickness. Figure 3 displays an example of these graphs for each class. The display has been limited to a 0.2 error, because we considered that extra error values were too large. It's readily seen that estimation error provided by the second method is smaller than that provided by the former one. In order to take into consideration the random fluctuation of layer thickness between successive shots, these graphs have been moving average filtered.
Secondly, for fixed τ value, the attenuation coefficient is computed for different subbottoms. Results are presented on figure 4. The dotted curve stands for theoretical attenuation value, until the solid and the dashed plots represent the first and respectively the second attenuation estimation method. The four regions of these graphs correspond to four different theoretical attenuation values of the first subbottom layer. For each of them, second layer features

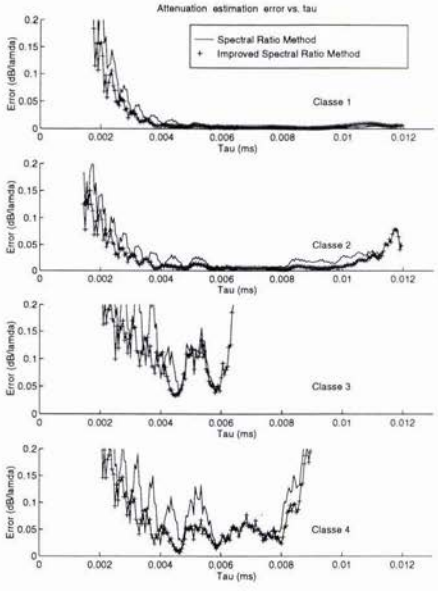

Figure 3: Estimation error ($|\beta_{estimated} - \beta_{theoritical}|$), with the spectral ratio method (solid line) and with the proposed method(++). Each subplot stands for a class of subbottom type.

have been varied to better match practical situations. In any case the proposed method leads an improvement of the attenuation estimation. In addition, the estimation is less sensitive to the second layer type, because in each region, the solid line decreases progressively with the second layer variation, until the dashed line is nearly horizontal.

5. Conclusions

In the case of overlapping reflections, bad attenuation coefficient estimations are provided by the classical Spectral Ratio Method. To overcome this difficulty,a time-frequency analysis of the compressed chirp is developed , and it is proven that overlapping reflections produce disturbances only in limited frequency bands, whose positions depend on the traveled time between echoes. Hence, we have proposed to modify the estimation method, taking into account in a different manner the frequency bands that are affected by perturbation, and the valid ones. This approach was tested on synthetic data, and results were compared with those of the classical one. The estimation is not yet valid in any case, nevertheless the error is appreciably reduced. We plan to extend this improvement on real data. Other time-frequency methods are also being considered in order to relieve the spectral estimations of the other echoes influence, by separating the two echoes before the matched filter processing.

Acknowledgment

We would like to thank SHOM (Brest, France), which supported this work, for supplying real subbottom profile. We are also greatful to Emmanuel Radoi for his support and technical discussions.

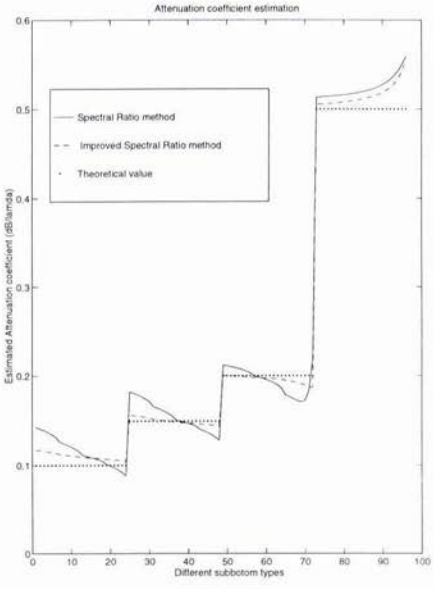

Figure 4: β estimation with both classical and proposed spectral ratio method.

References

[1] D. Jannsen, J. Voss, and F. Theilen, "Comparaison of method to determine q in shallow marine sediments from vertical reflection seismograms," *Geophysical Prosepecting*, vol. 33, pp. 479–497, 1985.

[2] R. Kuc, "Estimating acoustic attenuation from reflected ultrasound signals: Comparaison of spectral-shift and spectral difference approaches," *IEEE Transactions on Acoustics Speech and Signal Processing*, vol. ASSP-2(1), pp. 1–6, 19984.

[3] P. L. Goupillaud, "An approach to inverse filtering of near surface layer effects from seismic records," *Geophysics*, vol. 26, pp. 754–760, 1961.

[4] E. Hamilton, "Geoacoustic modeling of the sea floor," *J. Acoust. Soc. Am*, vol. 68, pp. 1313–1340, 1980.

[5] P. Flandrin, *Temps-Fréquence*. Traité des Nouvelles Technologies, Série Traitement du signal, 14, rue Lantiez, 75017 Paris: Hermes, 1993.

[6] E. Pouliquen, *Identification des fonds marins superficiels à l'aide de signaux d'écho-sondeurs*. Thèse de doctorat, Université Denis Diderot (Paris 7), 1992.

Interactive tools for the Exploration and Analysis of Multibeam and other Seafloor Acoustic Data

Larry A. Mayer, Semme Dijkstra, John Hughes Clarke, Mark Paton and Colin Ware

Ocean Mapping Group
Dept. of Geodesy and Geomatics Engineering
University of New Brunswick
Fredericton, N.B. E3B 5A3 CANADA
Email: larry@omg.unb.ca

Abstract

The Ocean Mapping Group has developed a full suite of software tools for the real-time or near real-time display, editing, quality control, interpretation and visualization of multibeam sonar data. The combination of detailed bathymetry and sonar imagery provides quantitative depth information and a qualitative description of the spatial distribution of seafloor materials and textures. While the qualitative picture of the distribution of seafloor types is a very useful tool for a number of applications, our research efforts are currently aimed at attempts to extract more quantitative seafloor property information from the sonar record. These efforts include the analysis of the characteristics of the vertically incident acoustic waveform as well as evaluation of the angular dependence of backscatter. To facilitate this research, several interactive 2-D and 3-D software tools have been developed that allow for the simultaneous exploration of sonar data in both geographic and multivariate space. The ultimate objective of this work is to provide a robust approach to the remote classification of seafloor type as well as the tools necessary to easily implement and utilize this approach.

1. Introduction

Over the past few decades, revolutionary changes have taken place in our ability to map and visualize the ocean floor. These changes, brought about by the concurrent, rapid advancement of sonar technology, positioning and vessel orientation technology, computer hardware, data bases, signal processing and visualization techniques, are beginning to result in detailed depictions of large pieces of the seafloor that are, in many ways, analogous to airborne or satellite derived images of the earth's surface. Just as the first airborne and satellite images of the earth resulted in a quantum leap in our understanding of earth processes, the newly produced seafloor images have the potential to radically change our knowledge and understanding of submarine morphology and processes. Just as satellite remote sensing studies progressed from an emphasis on the accurate depiction of a scene to the quantitative extraction of thematic data from the scene, so too are sonar studies progressing from the presentation of bathymetry and imagery to the extraction of more quantitative seafloor property information.

At the core of these new technologies is the development of multibeam sonar systems which insonify large swaths of the seafloor while producing high resolution (both lateral and vertical) bathymetry and seafloor imagery (from acoustic backscatter). When collected in slightly overlapping swaths, multibeam sonars can produce a sonar data set that represents near 100 percent acoustic coverage of the seafloor. The Ocean Mapping Group of the University of New Brunswick has been pursuing research and developing tools related to multibeam sonar mapping for the past five years, with much of our early work focused on the development of real-time and near-real-time processing tools designed to ensure that high-quality bathymetric and imagery data was being collected.

The detailed bathymetry and imagery produced by multibeam sonars allow the experienced observer to derive a tremendous amount of information about the seafloor, but while the bathymetric data extracted from the multibeam system provides a quantitative depiction of geomorphological relationships (slopes, roughness scales, etc.), the sonar imagery (even if derived from the quantitative measurement of backscatter that some systems provide) has historically been interpreted in a qualitative sense. In an effort to turn these qualitative interpretations into quantitative data, the Ocean Mapping Group is also pursuing research and developing tools for the remote classification of seafloor material type. These efforts include the analysis of the characteristics of the vertically incident acoustic waveforms as well as

evaluation of the angular dependence of backscatter. To facilitate this research, several interactive 2-D and 3-D software tools have been developed that allow for the simultaneous exploration of sonar data in both geographic and multivariate space. The ultimate objective of this work is to incorporate robust approaches to remote seafloor classification into easy-to-use toolkits that will greatly facilitate the application of sophisticated classification techniques and the interpretation of the resulting data.

2. O. M. G. Multibeam Sonar Processing Tools:

As with all acoustic systems operating in the ocean, multibeam sonar systems are plagued by serious problems caused by the environment (noise, motion, refraction, etc.). The initial efforts of the Ocean Mapping Group focused on the development of a series of software tools that would allow the hydrographer to edit and verify the massive amounts of data collected by multibeam systems in order to produce a "clean" data set suitable for incorporation into hydrographic charts. While hydrographers have tended to process their data on shore well after the data was collected, our goal in developing new tools was to be able to process and display the cleaned data on board the vessel collecting it, in as close to real-time as possible. What has evolved is a suite of software tools that work in real-time, near-real time and for post-survey analyses.

2.1 Real-time tool:

In order to derive a complete solution for the relative position of each sounding produced by a swath sonar, a multibeam sonar system must also include ancillary sensors for the precise determination of ship's position, ship's heading, vessel motion (heave, pitch and roll) and the sound speed profile in the water column. Most multibeam sonar manufacturers provide some means of integrating the data from these various sensors and then produce a "data telegram" with the information necessary to determine the position of each sounding (or imagery pixel). Our real-time tool strips out the essential features of these telegrams to produce a computer display that shows, in real-time, a color-coded bathymetric map (or imagery mosaic, if selected) of the survey as it progresses. The advantages of real-time display are manifest. Shipboard scientists are instantly provided feedback on data quality and coverage; decisions can be made in real-time as to changes in the survey and sampling programs. Any area on the real-time geographic display can be expanded and, with the click of a mouse button, targets or features on the display selected and interrogated for geographic position. In addition, if historical data exists (e.g. previous swathmap or other digital data or even raster scans of existing charts), these can be loaded into the tool and used as a backdrop upon which real-time navigation and plots can be overlain. Using these tools, a vessel can be instantly and unambiguously directed to a seafloor target for sampling, photography or instrument deployment.

2.2 SWATHED: Gridding and Mosaicing:

Upon completion of a survey line, the data from that line is loaded into our SWATHED toolkit which facilitates the interactive editing of the data on a swath by swath basis. User selectable, automatic filters remove obvious outliers from the data and then the operator interactively selects further points for editing. While this process is subjective (and thus done with great care and scrutiny by hydrographers who have legal obligations about the data included in [or excluded from] their charts), for the purposes of geologic research, it can be done with great speed, typically in much less than the time it took to collect the data. Additional tools can be applied at this point that can help resolve problems with sound speed corrections and provide detailed insight into the quality of the sonar data. The final result of this process is a cleaned, tide and refraction corrected data set that is now suitable for gridding and mosaicing.

One of the greatest advantages of multibeam sonar data is that, if used properly, multibeam systems can provide near 100 percent coverage of the seafloor (at a data density that depends on the system, water depth, vessel speed, ping rate, etc.) and thus obviate the need to extrapolate beyond, or interpolate between, sparse soundings. The price we pay for this coverage is massive data rates -- an EM1000 in 100 m of water produces about 28 Mbytes of data per hour, an EM3000 at the same depth about 80 Mbytes of data/hour and EM3000 in 5 m of water produces about 450 Mbytes/hour (including sidescan imagery). The advantage of this dense database is that it can be used to create accurate digital terrain models (DTM's) and imagery mosaics of the seafloor. With our software this process is done on board the ship and is completed not long after each line is edited. Thus by the end of a survey day, an up-to-date, edited DTM and imagery mosaic can be produced and displayed in a variety of forms.

3. SEAFLOOR CLASSIFICATION TOOLS:

3.1 Vertical Incidence Tools:

In recent years a number of investigators have looked at various characteristics of normally incident echoes returned from the seafloor in an attempt to derive information on seafloor type [1]- [5]. Each of these studies uses particular aspects of the returned waveform or its multiple to derive information about the composition and/or texture of the

seafloor. In an attempt to evaluate the relative merits of these techniques as well as provide a means to implement classification algorithms that we have developed, we have built a modular software toolkit that easily accommodates multiple approaches to seafloor classification. This package (TracEd) is built around a series of very robust event pickers that can track and display the seafloor return (as well as other horizons above or below the seafloor) and then analyze a number of characteristics of the returned acoustic waveform (e.g., amplitude, rise-time, spectral characteristics, returned pulse length, length of reverberation, separation between layers, etc.) that may be indicative of various seafloor characteristics. Once a useful classifier is selected, the tool will then plot the distribution of this feature (and a second feature if desired) in geographic space providing a derivative map that may well represent an enhanced and quantitative display of the distribution of a particular seafloor property or properties.

3.1.1 Event Picking:

As with any analysis of acoustic data, one of the key elements is the ability to robustly track events. For a given digitized vertical incident waveform, TracEd uses a combination of both edge and threshold detection to determine the location of up to 10 events in a given waveform. For each event, the position of the leading edge, the peak amplitude, and the trailing edge (tail length) are determined and stored (Fig. 1). Once selected, the shape of the event is compared to the shape of all other events in the previous trace (through a correlation process) and the relative correlation coefficients are stored.

In order to determine which of the events represents the seafloor, all events are compared to a user-selected acceptance window. Once an initial bottom pick is made, this window is maintained automatically by using the mean depth of a number of previous seafloor picks and the incorporation of a "prediction window" that takes into account local slopes. Once the acceptance window is established, the algorithm checks the correlation coefficients of all events in the acceptance window with the previous seafloor pick and chooses that event with the highest correlation coefficient as the candidate bottom pick. It also checks whether a multiple exists at the depth predicted by this bottom pick and, if all criteria are met, selects this event as the current bottom pick. If no events meet these criteria, the predicted value is used and the acceptance window criteria are re-evaluated. This approach has proven extremely robust with a bottom-detect failure rate of less than 2% in practice.

A similar ping-to-ping correlation process is done on the multiple return and for up to 8 other "horizons" either preceding or following the bottom return; for each of these horizons, the leading edge, peak amplitude, tail length and correlation coefficients (with other events) are stored. A scrolling, graphical display shows a grayscale acoustic profile with the horizon picks superimposed and color-coded; a window can also be set up to show the individual waveforms and the position of the picks made on them (Fig. 2).

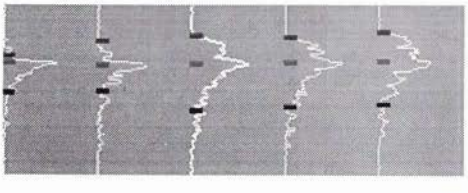

Fig. 1. Picks of leading edge, peak amplitude and trailing edge on an individual "event" in a return. TracEd will make similar picks on the ten largest events in each return.

The separation of the acoustic returns into a series of discrete events and the storage of a dataset that serves to describe each event presents us with the opportunity to evaluate a number of approaches to seafloor classification through waveform characterization. For example, given the described digital characterization of waveforms we can easily implement modules that use previous established criteria (e.g., area under multiple vs. area under tail of primary [2] or time envelope approaches [4]). It also presents the opportunity to explore alternative approaches to classification and to design specific algorithms for specific tasks. An example of this is presented in Fig. 2 where we were seeking to identify the distribution of seaweed known to occur in patches within a well-studied intertidal survey area [6]. Several waveform criteria were identified to be characteristic of returns from seaweed: 1- the sudden appearance of a strong return preceding the identified bottom; 2- a rapid rise of the leading edge of this return and 3- a multiple return that is displaced in peak amplitude from its predicted location. We can select any one (or combination) of these parameters and plot their geographic distribution as the survey progresses. The resulting display (Fig. 2) looks like a standard sidescan sonar mosaic but is, in reality, a derivative product that produces an enhanced view of the geographic distribution of a particular parameter (in this case representing the distribution of seaweed).

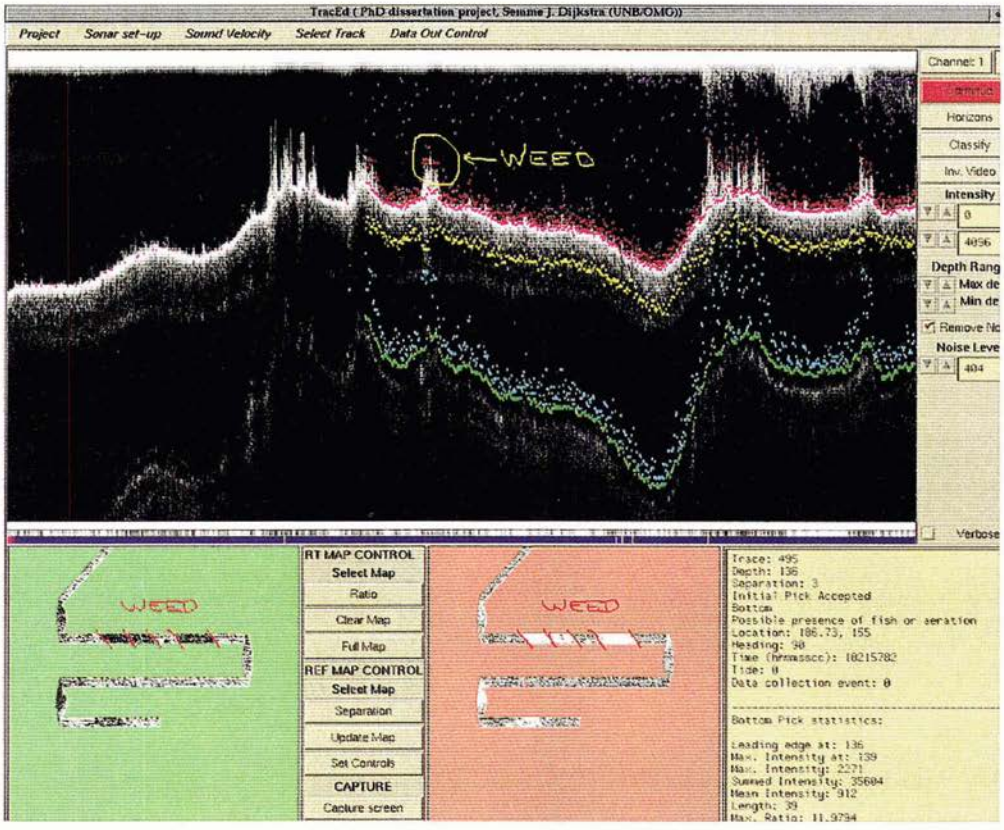

Fig. 2. Screen dump from TracEd. Upper window is continuous scrolling display of profiler data (in this case from a 210 kHz Navitronics sweep system collecting data in an intertidal area of St. John Harbor, New Brunswick). Horizon picks are displayed as color-coded dots beginning about one-third along the window. The two lower graphics windows can be set to display a range of parameters including individual waveforms with picks (as in Fig 1), or various characteristics or statistics of the waveforms in a geographic context. The text window in the lower right reports the statistics and details of the currently processed trace. In this example, the separation between the leading edge of the trace and the peak amplitude is displayed as a gray-scale intensity plot in geographic space. The resulting plots (plotted here with large separation as dark in left window and light in right window) produce a clear and accurate portrayal of the distribution of seaweed in the area.

3.2 Lassoo

In many of the classification methods mentioned above classification "rules" are established either theoretically or from empirically derived relationships between waveform characteristics and observed seafloor properties. To facilitate this relational process we have developed another interactive graphical tool (LASSOO!) that allows us to interactively explore the relationships between variables in both multivariate and geographic space [7]. For example, if we have performed an analysis on our acoustic dataset to derive waveform characteristics (e.g. E1 and E2 as in [2]) or we have a series of physical property measurements made on ground truth samples in a survey area, we can plot these data in multivariate space (as a scatter plot) and graphically establish natural groupings (Fig. 3). These groupings are then instantly displayed in geographic space (e.g. select all points with high sand content and/or high organic carbon content -- Fig. 4). Inversely we can select regions in geographic space and see how the samples from these regions group in multivariate space.

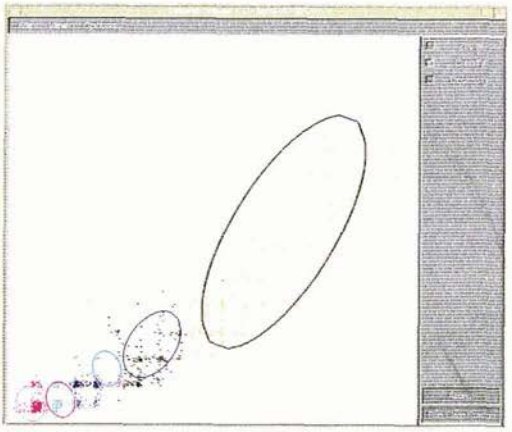

Fig. 3. Acoustic or physical properties of survey displayed in multivariate space. In this example parameters are E1 (area under tail of primary return) and E2 (area under seafloor multiple) derived from RoxAnn survey system used over area of dredge spoil dump sites off Quebec. TracEd allows the interactive redefinition of classes in multivariate space.

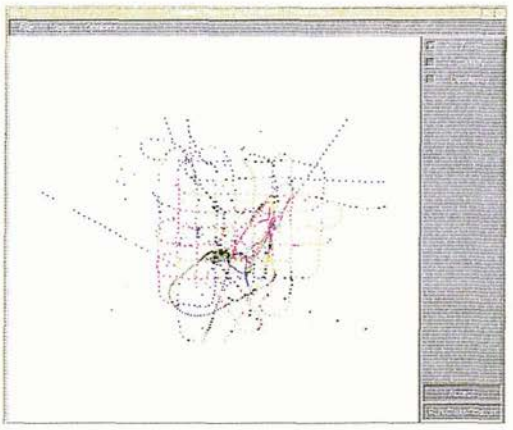

Fig 4. Redisplay of E1/E2 values in geographic space. The redefined definitions of E1/E2 classes resulted in a much clearer indication of dumpsite deposits.

Most importantly, LASSOO allows us to view any of these data sets superimposed on an image (e.g. backscatter data - Fig. 5). We can outline these targets with a mouse-driven cursor (i.e., "lassoo" the data), extract all data points within this area, analyze the statistical properties of the extracted data points and assign them to a "class". These classes can then be assigned to all other data showing these same characteristics in either geographic or multivariate space.

3.2.1 Application of LASSOO to assessment of dredge-spoil dumpsites

As part of a long-term study on the impact of ocean dumping on fisheries habitat, a series of dredge-spoil dumpsites off L'Anse-a-Beaufils, Quebec were surveyed with both a RoxAnn system and an EM-1000 multibeam sonar. We evaluated the ability of each system to: 1- identify individual dump sites and; 2- "date" the sites, i.e., discriminate between sites deposited in different years. Our initial data analysis revealed that while the EM-1000 imagery data clearly identified the dumpsites (Fig. 5) the shipboard classification produced by the RoxAnn system was not able to identify the dumps and neither the EM1000 imagery nor the RoxAnn system could discriminate between two generations of dump sites (1992 and 1994). We were able to use LASSOO however to interactively redefine the RoxAnn E1/E2 classes and establish a classification scheme that could distinguish the dumpsites from the surrounding seafloor but still could not separate the different generations of dumpsites (Fig. 4). We further used LASSOO in a training mode by "lassooing" the different dumpsites and extracting the backscatter data from these regions (after correction for a range of instrumental and geometric artifacts [8]). A simple histogram of backscatter (expressed as pixel value) revealed that the 1992 and 1994 dumpsites showed discernible differences and most importantly, the sequential surveys of these sites (1994 and 1995) revealed a consistent shift in the backscatter histograms indicating a decrease with backscatter with time (Fig. 6).

While a simple examination of the distribution of the mean backscatter values proved a viable mechanism to distinguish seafloor characteristics in this survey, it is important to note that the targets in this region were quite distinctive from the surrounding seafloor and that we needed *a priori* knowledge of the location of the different dumps to train the classification technique. Additionally, the "aging" issue lends itself to a general shift in mean backscatter as the dumped material is winnowed and smoothed by bottom currents (a conclusion supported by grain size analyses) [9]. The development of an absolute classification scheme, if at all attainable, will depend not only on the approaches described above but also on the development of more quantitative techniques to extract as much additional information as possible from the acoustic record.

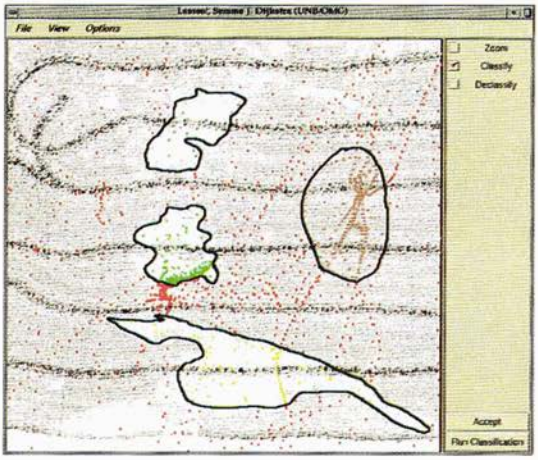

Fig. 5. LASSOO in the training mode. Superposition of physical or acoustic property data on top of sidescan sonar imagery. Here RoxAnn data (E1/E2) is superimposed on 95 kHz backscatter data from EM-1000 multibeam sonar. The EM-1000 imagery clearly defines the dredge-dump sites (two areas in the central region) as well as regions of gravel, bedrock and background substrate. LASSOO allows these regions to be selected and assigned classes.

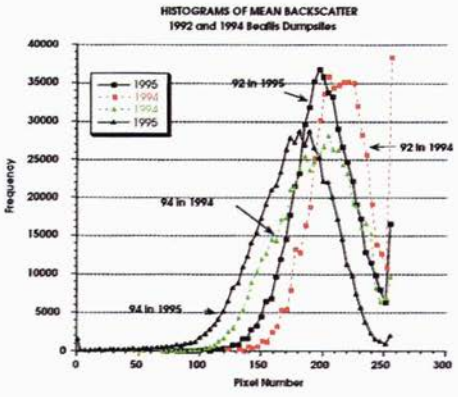

Fig. 6 -- Comparison of histograms of mean backscatter values (expressed as pixel value) derived from EM-1000 backscatter data and extracted with the LASSOO tool from the two areas outlined on left. The two regions represent two generations of dumps (1992 and 1994) and were surveyed in two sequential years (1994 and 1995). Both the differences between the sites and a consistent shift (to lower backscatter) is clearly discernible.

4. Multibeam Classification:

Along with our development of tools for using vertical incidence acoustic data for seafloor classification, we are also taking advantage of the additional information provided by the wide swath over which multibeam sonars insonify the seafloor. Both theoretical and field studies have established that acoustic backscatter from the seafloor should vary in a predictable (Lambertian) fashion as a function of the angle of incidence of sound on the seafloor [10]. If all other factors were held constant, the shape of the backscatter versus angle of angle of incidence curve should vary as a function of seafloor type. Using this approach, we are developing techniques to minimize the instrumental and environmental artifacts in multibeam backscatter data and then to extract and display (either in real-time or in post-processing) backscatter as a function of angle of incidence across the swath. This approach is discussed in detail in [11]. Future studies will hopefully combine both our vertical incidence and multibeam approaches.

5. Interactive 3-D Visualization:

The tools described above provide the shipboard scientist with an accurate depiction of the 2-D bathymetry, an areal distribution of backscatter, and an ability to extract the geographic distribution of potentially more quantitative parameterizations of seafloor characteristics. The capabilities that lead to the production of these data represent tremendous advances in our ability to acquire and process seafloor acoustic data but the volume and complexity of the information represented by these data sets present fundamental challenges to us in terms of interaction, integration and interpretation. To help meet these challenges, we have chosen to take advantage of the ultimate signal processor (the human brain) and the rapidly advancing capabilities in computer hardware and have developed a 3-D visualization software package ("Fledermaus") that allows for the interactive exploration of very large data sets in a natural, intuitive yet quantitative fashion. Through artificial sun-illumination, shading, and 3-D rendering, Fledermaus presents digital bathymetric data (DTM) in the form of a natural looking and easily interpretable landscape. Color can be used to represent depth or other parameters (like backscatter) which can be draped over the DTM. The user can "fly" around the data and view it from all angles through the use of a 6-degree of freedom mouse ("bat") that transforms simple hand motions into a data exploration tool; with special LCD glasses, the scene can be seen in true stereo. Data entry is very simple and 3-D interaction can take place within a few minutes of the production of a DTM or sonar mosaic. Thus if these products are produced on board the vessel, 3-D interaction can be used for quality control and mission planning. This mode of exploration allows complex interrelationships between bathymetry, morphology , backscatter and other parameters to be easily discerned.

While interactive 3-D data exploration greatly aids in interpreting complex spatial data sets, Fledermaus also preserves all the quantitative aspects of digital data in that the displayed datasets are fully georeferenced and interrogatable in 3-D for position, depth, and other attributes (Fig. 7 imagery draped over 3-D bathymetry, has proven to be extremely useful to those interested in planning submarine cable or pipeline routes (Fig. 8). Multiple, georeferenced layers can easily be added to a scene as well as other objects like subsurface seismic lines, borehole data or high-resolution sidescan data. When applied to sediment classification studies, 3-D visualization allows one to gain an instant understanding of the complex relationships between seafloor morphology and a range of parameters that can be extracted from the acoustic data (e.g., components of the angular response of backscatter as discussed in [11], Fig. 9).

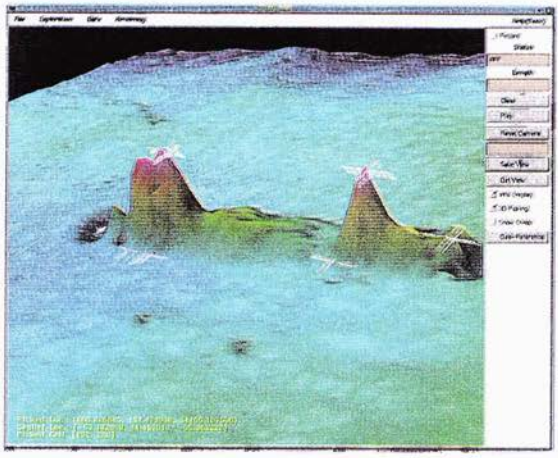

Fig 7. Single frame from interactive flight through EM-1000 multibeam bathymetry collected over 150 m long wreck of freighter *British Freedom* outside of Halifax Harbor demonstrating ability to pick, make measurements, and interrogate points in 3-D -- picked points are marked with cross-hairs. Attributes of latest point are displayed in lower left of screen and can be saved to file for later reference.

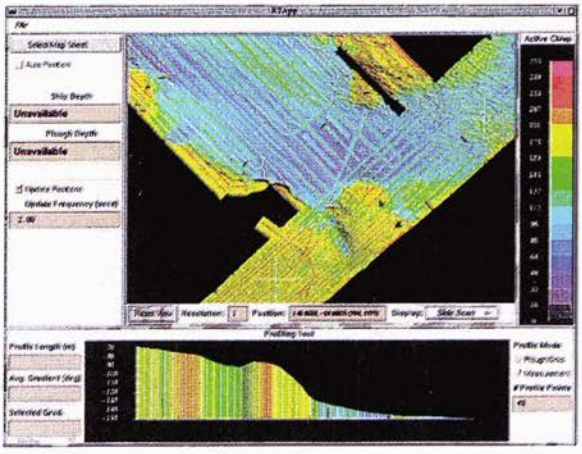

Fig. 8. 2-D component of pipeline and cable-route planning tool. Multibeam sonar imagery is draped over bathymetry providing simultaneous depth and seafloor property information for route planner -- prospective routes can be interactively explored with cross-sections, gradients and segment lengths displayed. The example above is from an application where real-time navigational information allowed the progress of the cable laying vessel and the plow (cross hairs) to be monitored within the context of previously collected multibeam sonar data.

Fig. 9. 3-D visualization of two of the twelve parameters extracted by Hughes Clarke [11] from the angular response of backscatter data from a 30 x 27 km area of Stellwagen Bank National Marine Sanctuary. Each is draped over bathymetry and displayed (in original) with color coding. Lower figure (A) represents slope of segment of backscatter curve between 75 and 30 degrees grazing ; upper figure (B) represents mean backscatter between 50 and 40 deg grazing. Parameterization of the backscatter curve may provide important insight into the distribution of seafloor properties; visualization in this mode shows the direct relationship between these parameters and the seafloor morphology. See [11] for details of analysis.

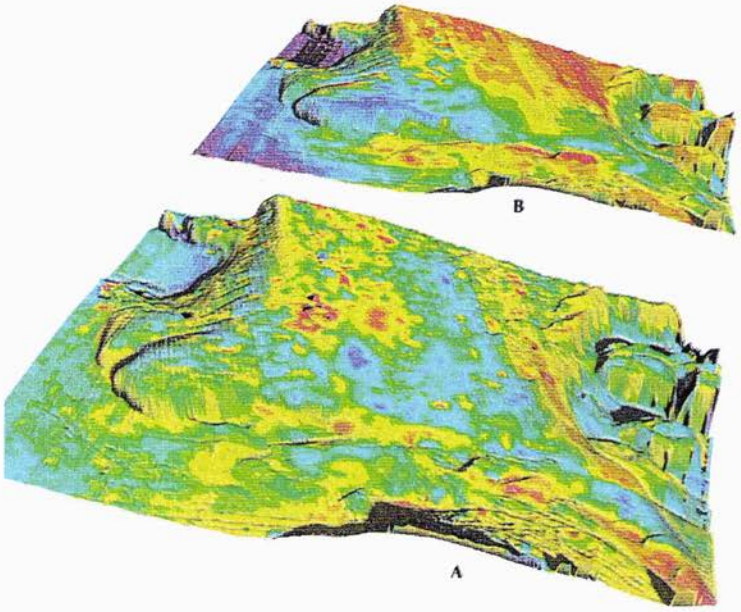

6. Conclusions

Concomitant advances in sonar technology and theory are providing us with the raw information necessary to address the critical questions of acoustic seafloor classification. With a knowledge that the most likely path to successful seafloor classification will involve the simultaneous application of multiple techniques, the UNB Ocean Mapping Group has developed a series of interactive software tools that are designed to assure the quality of the collected data and allow the user to integrate a range of approaches utilizing both vertically incident and angularly varying sonars. Our tools permit the exploration of acoustic datasets in both multivariate and geographic space and, most importantly, allow complex derivative datasets to be interactively explored in a 3-D environment. The ability to view the spatial relationships of various parameters with respect to seafloor topography, while taking advantage of our innate ability to see and understand complex data relationships in 3-D, is proving to be a very powerful interpretation and analysis tool whose limits have just begun to be explored.

Acknowledgements:

Funding by the sponsors of the NSERC Chair in Ocean Mapping, The Office of Naval Research (Contract No. N00014-95-1-0064) and Dept. of Fisheries and Oceans (Contract No. F3707-5-2209/01) is gratefully acknowledged as is the always professional service provided by the officers and the crew of the Canadian Hydrographic Service's vessel NSC Frederick G. CREED.

References

[1] A.O. Orlowski, "Application of multiple echoes energy measurements for evaluation of sea bottom type" *Oceanologia* v. 19, pp. 61-78, 1984.

[2] R.C. Chivers, N. Emerson, D.R. Burns, "New acoustic processing for underway surveying:, *Hydrographic Journal*, no 56, ppl. 9-17, April, 1990.

[3] L.R. LeBlanc, L.A. Mayer,M. Rufino S. Schock, and J. King, "Marine sediment classification using the chirp sonar, *Jour. Acous. Soc. America*, v. 91, 1, p.107-115, 1992

[4] E. Pouliquen and X. Lurton, "Sea-bed identification using echo-sounder signals" *Proceedings of the European Conference on Underwater Acoustics*, pp. 535 - 539, Sept. 1992

[5] D. N. Lambert, J.C. Cranford, and D. J. Walter, "Development of a high resolution acoustic seafloor classification survey system, *Proc. Inst of Acoustics*, v. 15, pt 2., pp. 149 - 156, April, 1993.

[6] L.A. Mayer and the Hygro-92 Team, "A multi-faceted acoustic ground-truthing experiment in the Bay of Fundy, in *Proceedings of the Inst. of Acoustics*, v. 15, pt. 2, pp. 203-210, April, 1993.

[7] S. Dijkstra and L.A. Mayer, "Lassoo!: An interactive graphical tool for seafloor classification", *Proc. IEEE-MTS Oceans '96*, pp. 1064-1070, 1996.

[8] J.E. Hughes Clarke, L.A. Mayer and D.E. Wells, "Shallow-water imaging multibeam sonars: A new tool for investigating seafloor processes in the coastal zone and on the continental shelf", *Marine Geophysical Researches*, v. 18, n. 6, p. 607-629, 1996.

[9] L.A. Mayer, D. Pothier, and S. Dijkstra, "Analysis of two hydroacoustic datasets -- EM100 and RoxAnn -- collected at the ocean dumping site of L'Anse-A-Beaufils, Baie des Chaleurs in 1995, Dept. of Fisheries and Oceans Rept. No. F3707-5-2209/01, 80 pp., March, 1996.

[10] D.R. Jackson and K.B. Briggs, " High-frequency bottom backscattering: Roughness versus sediment volume scattering" *Jour. Acoust. Soc. America*, v. 92, pp. 962 - 977, 1992.

[11] J.E. Hughes Clarke, B.W. Danforth, and P. Valentine, "Acoustic seabed classification using backscatter angular response at 95kHz, in *Proc. Inst. of Acoustics*, this volume.

Acoustic Characterization of Submerged Aquatic Vegetation

Elena McCarthy

Naval Undersea Warfare Center
Newport, RI 02841 USA

Abstract

The acoustic characteristics of submerged aquatic vegetation (SAV) were investigated in order to enhance the performance of mine-hunting and weapon sonars in littoral regions. The species of seagrass initially studied was Zostera marina. Laboratory measurements of target strength and backscatter were made under controlled conditions in an acoustic tank. Experimental target strength measurements compared well to the theoretical value. Target strength for an individual blade of Zostera was measured to be approximately -21 dB from 300-700 kHz. No frequency dependence was found in this range. Beam patterns for individual specimens were also generated and displayed a strong dependence on blade orientation. In-situ measurements were carried out in the shallow water eelgrass beds of Narragansett Bay with both side-scan and single beam sonars. These experiments clearly illustrated the backscatter and potential masking effects of submerged aquatic vegetation in the 100-400 kHz frequency range. This experimental data will aid in the verification of theoretical models and in the development of methods to enhance the performance of mine-hunting and weapons sonars. The data will also supply environmental input to range-dependent sonar models and enhance tactical and environmental databases. Another application of this research includes remote sensing of seagrass beds to monitor pollution and aid in species distribution and density studies.

1. Introduction

The US Navy's emphasis on shallow water research dictates the need for improved range dependent sonar models and a better understanding of bottom interactions. This project was initiated after naval operations in littoral regions indicated that acoustics were often ineffective in finding mines in part due to extensive seagrass beds [1]. Seagrass is known to adversely affect the Navy's ability to detect mines, thus compromising shallow water mine countermeasures. Backscatter from seaweeds and seagrasses creates interference with sonars and could mask the presence of a mine during mine-hunting. Some foreign mines are designed specifically to exploit this backscatter effect.

In Tarut Bay, in the Arabian Sea, a survey of fifty locations yielded an estimate of 66% grass cover for the entire bay; i.e. 175 sq. km of seagrass coverage [2]. In the Gulf of Oman, *Sargassum aquifolium* , a seaweed, may grow to a length of about 1.50 meters and produce dense masses of plants. The leaves contain hundreds of tiny air sacs (radii from 0.02 to 0.17 cm.) and act as effective sound scatterers; their air sacs are resonant at frequencies of 5 to 20 kHz at pressures of 2 to 5 atmospheres [3]. This may have a significant effect on many mine-hunting systems. In addition to physically creating interference with mine burial during placement, algal fouling can create problems for mines which have been deployed for some time (weeks to months) as it can plug and interfere with the acoustic detonator. This can damp out signals and make the mines ineffective against targets [4].

1.1 Previous Work

There is no published literature on the physics of wave scattering by submersed vegetation. Overwhelmingly the literature consists of papers which investigate acoustics of marine mammals, plankton or fishes. An informal study was carried out by the Army Corps of Engineers which used acoustics to determine the presence of "nuisance species" in estuaries [5]. More recently a Russian effort attempted to develop physical models for estimation of scattering [6].

1.2 Approach

The Naval Undersea Warfare Center Division, Newport, RI (NAVUNSEAWARCENDIV NEWPORT) received funding in Fiscal Year 1996 from the Deputy Assistant Secretary of the Navy (Environment and Safety) to initiate a preliminary investigation of the acoustic characteristics of submerged aquatic vegetation for environmental monitoring applications. The vegetation initially investigated was *Zostera marina*, a well-documented seagrass which was chosen because it is widely studied and abundant in the local waters of Narragansett Bay. Commonly called eelgrass, it is broadly distributed in both the northern Pacific and Atlantic Oceans. It extends from the intertidal zone to the subtidal, often in extensive meadows. In clear waters it can be found in water depths as great as 30 m. [7].

The shallow water eelgrass beds of Narragansett Bay, Rhode Island created an ideal testbed to gather experimental data. This allowed for the development of a methodology which could later be applied to other areas of strategic importance such as the Persian Gulf and the Adriatic Sea. The experience gained from studying eelgrass can be carried over to other types of submerged aquatic vegetation such as kelp and Sargassum which will likely have even more pronounced acoustic signatures.

1.3 Physiology of *Zostera marina*

The plant is composed of a rhizome 2-5 mm wide with numerous roots and a leaf at each node. The leaf blade is up to 2 m. long and 1.5-12 mm wide [7]. Gas pockets or tubes called lacunae run the length of the plant. These lacunae are shown in Fig. 1. Any backscatter created by the plant is primarily a volume-scattering phenomena likely caused by these gas-filled lacunae.

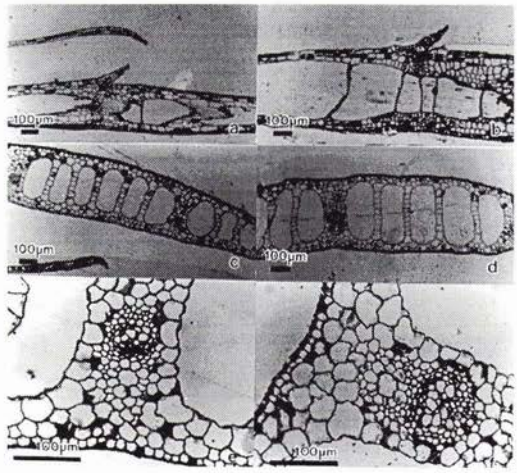

Fig. 1. Lateral cross-section of *Zostera* lacunae. The lacunae run the entire length of each blade.

2. Experimental Approach

It was proposed to carry out acoustic measurements in controlled conditions in the laboratory to determine the fundamental acoustic characteristics of eelgrass. These experiments were carried out on a single specimen of grass in order to investigate frequency response and determine resonance. Aggregate testing was then carried out in large tanks of eelgrass (mesocosms) which provided testing of the grass as it is found in-situ but still under controlled conditions. The final component of experimentation involved field testing in Narragansett Bay using various sonars in existing eelgrass beds and ground-truth referencing by a dive team.

2.1 Tank Testing

Monostatic target strength measurements were made in controlled conditions in the acoustic tank at the Naval Undersea Warfare Center in Newport. An individual blade of healthy *Zostera* approximately 30 cm in length was suspended in the acoustic tank which measures 20 meters long by 13 meters wide by 12 meters deep. The location of the grass within the tank was accurately measured. Due to the specimen size and the high frequencies being used, the

majority of the experiments were carried out in the near field. The reflected sound from the grass was measured and recorded at a range of frequencies from 300-750 kHz. The grass was then removed and a 20 cm. radius, solid aluminum sphere of known target strength was then positioned in the tank in the same location and its backscatter was measured. The target strength of the eelgrass could then be determined. This was carried out at a range of frequencies in an attempt to determine frequency dependence. Little frequency dependence was found in the range of 300-750 kHz. The average target strength over this range was measured to be -21 dB. This figure compares well with fish of the same size; the size of the eelgrass lacunae can be compared with the similarly-sized swim bladders of these fish. The ensemble of cylindrical-shaped gas-filled lacunae are the dominant scatterer and the overall target strength level in the 300-750 kHz frequency range is consistent with scattering by a similar number of air-filled cylinders of the same dimensions. Fig. 2 shows the target strength of the eelgrass as a function of frequency.

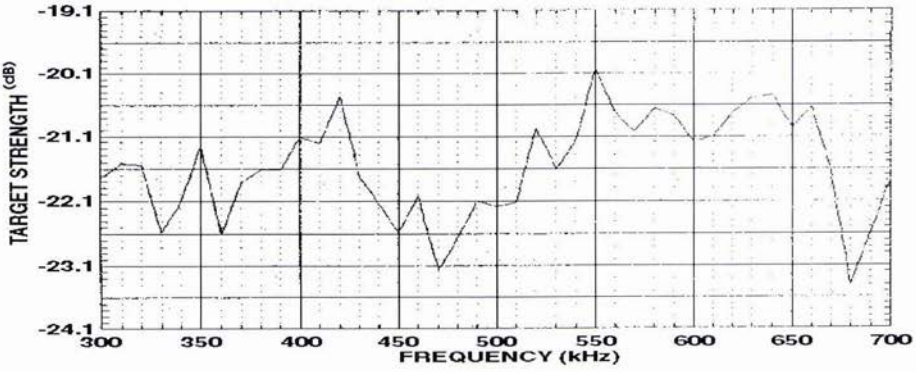

Fig. 2. Target strength of eelgrass blade as a function of frequency. These values are calculated from a 2 cycle sample FFT for rms value.

Beam pattern at a fixed frequency was also plotted during these tank tests to investigate the backscatter intensity from various angles of incidence. The blade of grass was rotated in 0.5 degree increments over a 12 hour period to cover 200 degrees. There was a strong return when the blade was insonified on its main axis (broadside) and a sharp drop-off beyond this angle. The results are shown in Fig. 3

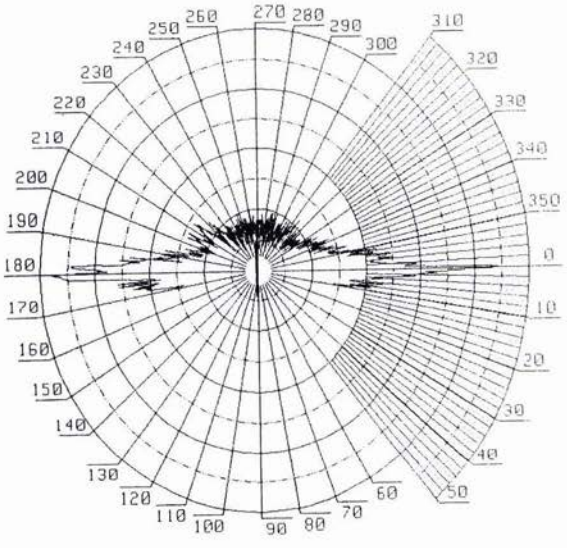

Fig. 3. Beam pattern of eelgrass blade at 400 kHz. Each division on the polar plot represents 5 dB.

2.2 Mesocosm Testing

Mesocosm testing allowed for examination of grass behavior in beds as it is found in-situ. The experiments were carried out in the University of Rhode Island mesocosm tanks which are designed to grow communities of eelgrass for biological and ecological experiments. These tanks measure approximately 1.5m square by 1.2 meters deep and contain approximately 15 cm of sediment. The bottom of each tank is densely covered in *Zostera* (Fig. 4). Monostatic measurements were made in increments of 50 kHz from 200-750 kHz. The backscatter measured was significant. As demonstrated earlier in the acoustic tank tests, backscatter was again pronounced throughout the frequency range but no clear frequency dependence was found.

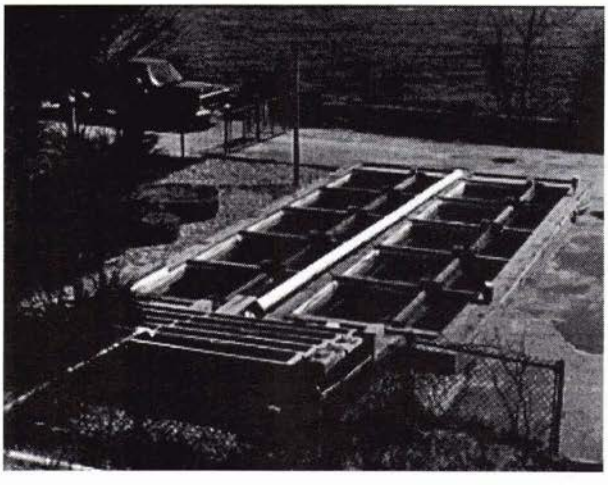

Fig. 4. Mesocosm tanks at the University of Rhode Island.

2.3 In-situ Testing

During August 1996 a brief field study was conducted in the East Passage of Narragansett Bay in an area with well-established beds of eelgrass. Several types of hydroacoustic measurement equipment and sampling procedures were deployed from a shallow-draft, coastal vessel. A team of Navy divers made visual inspections, took underwater video imagery, and collected eelgrass samples at ground truth locations.

2.3.1 Ground truth sampling

Four locations of varying densities of eelgrass were selected based on a preliminary survey with the single beam sonar. The vessel was anchored above the selected location and stationary depth sounder measurements were collected. An anchor and buoy marked the insonified area and a dive team then placed a 0.25 square meter quadrat on the bottom in the marked area and measured the in-situ height of eelgrass and then removed all vegetation within the quadrate at the base of the plants. The area and sampling operation were filmed by a diver with an underwater video camera and sediment samples were also taken. Eelgrass samples were iced and stored in darkness until laboratory measurements were performed the next day. Laboratory measurements included blade count, blade length, width and thickness, and wet and dry weights. Sample means for blade density ranged from 500-1200 blades per square meter with the average blade length ranging from 30 to 70 cm. Sediment samples indicated a sand bottom composed primarily of fine sand (54.3 %) in this area.

2.3.2 Single beam sonar

A single beam 420 kHz, 6 degree beam width sonar (Biosonics, Inc., Seattle, Washington) was integrated with a differential GPS to yield a digitized file of amplitudes as a function of latitude and longitude. Figure 5 illustrates the return from the eelgrass in a bed at a depth of approximately four meters. The eelgrass can be clearly seen growing up from the steep slope in the 2-4 meter water depth.

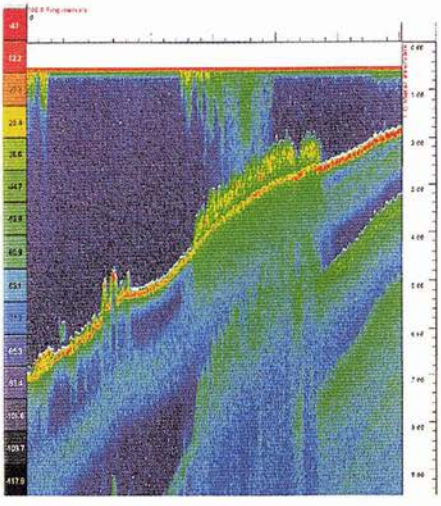

Fig. 5. Bottom return and eelgrass bed off Rose Island, Narragansett Bay, Rhode Island.

2.3.3 Side-scan sonar

An EG&G 272TD dual frequency side scan sonar was used to map known eelgrass beds in Narragansett Bay. The tow fish was deployed from a small shallow draft coastal vessel and operated at 100 kHz. Figure 6 illustrates an image from the starboard channel of the sonar. The bottom appears quite hard and well defined in the deeper water. Rocks and distinct features can be seen here. The grass bed begins to show in the 4 meter water depth. At this point, the sonar image is quite fuzzy and the grass can be seen growing up from the bottom. If a mine were located in this area, it would be acoustically masked and likely not detected by sonar. In addition to diver observations, underwater video confirmed the presence and boundary of the eelgrass bed just as shown in the sonar images.

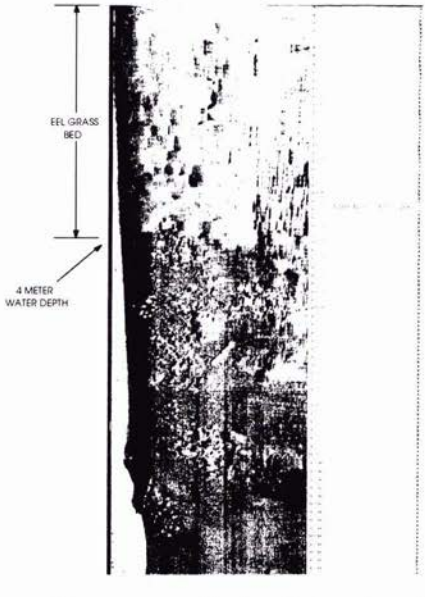

Fig. 6. The starboard trace from a side-scan sonar showing the boundary of an eelgrass bed and the backscatter it creates.

3. Model development

Presently no model exists which explains the acoustic behavior of submerged aquatic vegetation. This is the first effort to gather experimental data in support of model development. Based on the data from these experimental measurements and the fundamental physical acoustics, a model is under development for a single blade of *Zostera marina*. Due to the large volume of gas in the grass, the blade can be modeled as a small air-backed structure. The model will be parameterized by frequency, water depth, blade size, and orientation. An aggregate model which combines the effects of the many blades which are found in a bed of eelgrass can then be develop

4. Future Work

Future research would support model development and allow for field testing with mine-like objects. Additional efforts are also required to measure target strength and backscatter from seagrasses at lower frequencies (20 - 200 kHz). The development of new signal processing techniques and waveforms may be required to specifically exploit the unique characteristics of seagrasses which in turn would help distinguish mine returns from seagrass acoustic effects. Finally, in-situ experiments should be carried out with operational mine-hunting sonars to further quantify the effect of the seagrass on actual fleet hardware.

5. Dual Use Applications

Eelgrass meadows are critical to the health of their ecosystem; they provide sanctuaries for many fish, reduce shoreline erosion by slowing currents, clean the water by filtering nutrients and particles, and provide food for crabs, ducks, and other marine life. Eelgrass beds are six times more productive than any other bottom cover. Other applications of this research include tracking seagrasses acoustically to monitor pollution and help biologists carry out distribution and density studies. Discussions with the Environmental Protection Agency (EPA), National Oceanic and Atmospheric Administration (NOAA), National Marine Fisheries (NMFS), and Army Corps of Engineers (among others) indicate that a reliable, cost-effective method for monitoring and locating eelgrass beds in regions of turbid water (i.e. Boston Harbor) is required. Conventional methods involving aerial photography can be difficult and expensive if water clarity is not sufficient. Physical techniques for detection and characterization are labor and cost intensive and provide little insight into spatial distribution.

This eelgrass acoustics study has been identified as a Coastal America Program which integrates the capabilities of existing resources with those of federal, state and local agencies and non-governmental concerns. It is expected that the same technology that the Navy develops to eliminate the "noise" from seagrass during mine-hunting operations will be used to locate and track seagrass for environmental projects such as the National Estuary Project.

6. Conclusions

Results from initial laboratory and in-situ testing have indicated that seagrass may adversely affect the Navy's ability to detect mines by creating backscatter or acoustic interference with mine-hunting sonars. A more thorough understanding of the acoustic properties of seaweeds and seagrasses is therefore essential for optimal performance of mine-hunting sonars in littoral regions.

Research to date has provided for experiments with side-scan sonar and conventional single beam sonars which have clearly shown the backscatter effects of submerged aquatic vegetation in the 100 - 700 kHz frequency range. No frequency dependence was found from 200-700 kHz although backscatter is significant in this region. The target strength measured approximately -21 dB. The acoustic response of a single specimen of grass was found to be largely dependent on orientation.

It is hoped that these measurements will aid in the development of methods to enhance the performance of mine-hunting and weapon sonars. The data should also supply important environmental input to range-dependent sonar models and enhance tactical and environmental databases.

Acknowledgments

The author would like to thank Robert Tompkins, Dr. Bruce Sandman, Dr. Tom Wettergren, Jason Gomez and Walt Boober from the Naval Undersea Warfare Center in Newport, Rhode Island. She would also like to thank Steve Granger, Sue Sherwood Dr. James Miller and Blaine Kopp from the University of Rhode Island, Ken Rocha from the Environmental Protection Agency in Narragansett, RI and Bruce Sabol from the Army Corps of Engineers, Waterways Experimental Station, Vicksburg, MS.

References

[1] R. Alberte, Office of Naval Research, e-mail from R. Alberte to E. McCarthy, 6 June 1995.

[2] Basson et al, Biotopes of the Western Arabian Gulf., Dhahran, Saudi Arabia, Aramco Dept. of Loss Prevention and Environmental Affairs, 1977.

[3] Naval Research Laboratory, Report NRL/AE/7170-93-0001, May 1994.

[4] R. Alberte, Office of Naval Research, e-mail from R. Alberte to E. McCarthy, 11 Oct. 1995.

[5] B. Sabol. and R.E. Melton, "Development of an automated system for detection and mapping of submersed aquatic vegetation with hydroacoustic and global positioning system technologies, Report I: The submersed aquatic vegetation early warning system (SAVEWS)-System description and user's guide (Version 1.0)," Joint Agency Guntersville Project Aquatic Plant Management, 1995.

[6] E. Shenderov., Research and Development Institute, "Morfizpribor", St. Petersburg, Russia, unpublished.

[7] R. Phillips and E. Menez, Seagrasses, Washington, D.C., Smithsonian Institution Press, pp. 30-33 1988.

Terrain Mapping With Forward Looking Sonar on Unmanned Underwater Vehicles

Michael R. Medeiros and Robert N. Carpenter

Naval Undersea Warfare Center
1176 Howell Street
Newport, Rhode Island 02841-1708, USA
medeirosmr@tech.npt.nuwc.navy.mil carpenterrn@tech.npt.nuwc.navy.mil

Abstract

In the future, successful reconnaissance operations conducted in shallow water with Autonomous Underwater Vehicles will rely heavily on a high performance, high resolution, forward look sonar coupled with terrain mapping algorithms for object detection, localization and classification, sea bottom mapping and feature extraction. This paper describes in detail a terrain mapping algorithm based on an advanced forward look sonar design. The development is illustrated with in-water results.

1. Introduction

In the future, successful reconnaissance operations conducted in shallow water with Autonomous Underwater Vehicles (AUVs) will rely heavily on a high performance, high resolution, forward looking sonar (FLS). These mission functions include object detection, localization and classification (DLC), sea bottom mapping and feature extraction for navigation guidance and control (NG&C) and obstacle avoidance. For several years, the U.S. Navy's Advanced Systems & Technology Office (ASTO) and Office of Naval Research (ONR) have sponsored the development of NUWC's high resolution array (HRA). The HRA is a planar array designed for operation in a 21-inch diameter vehicle. Its current design consists of half-wavelength elements of 1-3 composite material configured in a 20 wavelength circular aperture. Recently, NUWC has embarked on the development of algorithms that rely on the wide transmit coverage and narrow receive beams of the HRA to provide images of seabed topography, objects on the bottom and objects in the volume. This paper focuses on two aspects of this effort: a terrain mapping algorithm and the small object localization performance of the HRA. The paper is organized as follows. First, a brief system description of the HRA will be given. Next, the terrain mapping algorithm will be discussed in detail and will include processed results from in-water data collected with the HRA. Finally, theoretical bounds on the variance of target angle estimates made with the HRA will be reviewed and compared with in-water results.

2. HRA Overview

The HRA is a forward looking planar array designed for operation in a 21-inch diameter vehicle. It has evolved from a prototype 40x40 receive-only array constructed from polyvinylidene fluoride (PVDF) [1] to its current design consisting of 1272 half-wavelength elements of 1-3 composite material (PZT-5H) configured in a 20 wavelength circular aperture (design frequency of 87 kHz) [2]. A subset of the elements consisting of two rows of 32 elements each are chosen to provide single ping transmit coverage of approximately 80 degrees in azimuth by 40 degrees in elevation with a source level of 210 dB. Wide angle azimuthal transmit coverage is achieved by means of element phase shading. Receive beams are formed from a subset of 511 of the remaining 1208 elements. These elements were chosen and fixed during the design process to yield the lowest peak sidelobe level (Å 20 dB down from the peak mainlobe level) while constraining the mainlobe to be approximately three degrees wide for beams steered over the transmit coverage region [3].

3. Terrain mapping algorithm

The terrain mapping algorithm is designed to provide single ping, wide swath seabed topographic data from FLS's. In this section, a detailed description of the functional flow of the algorithm is presented. In order to best illustrate the various steps of the algorithm, a series of intermediate results based on a set of in-water test data collected with the HRA will be presented.

3.1 Test data description

The HRA was deployed at a 9 meter depth in 21 meters of water (nominally). The array was mounted on a panning mechanism at the end of an elevator of the Gould Island Test Facility, located in Narragansett Bay, Rhode Island. A sidescan sonar map of the area is shown in Figure 1. The test area is characterized as a nearly flat, silt bottom bowl, with a seven meter high, curved rim to the south and east of the facility. The rim is clearly evident along the bottom and right-hand sides of the sidescan image. The elevator with the panning mechanism and the array are located at the northeast corner of the pier complex seen near the lower left-hand corner of the figure. The origin of the coordinate system is centered on the array. The array was mechanically panned so that its ±40° transmit beam was directed towards the rim and a 10 mS, 3000 Hz linear stepped FM waveform was transmitted. The mapping coverage is depicted as the solid white lines emanating from the elevator. To better illustrate the terrain mapping algorithm, detailed results will be presented along a single scan line, indicated by the dashed line in Figure 1, as well as the entire single-ping map subtended by the solid lines.

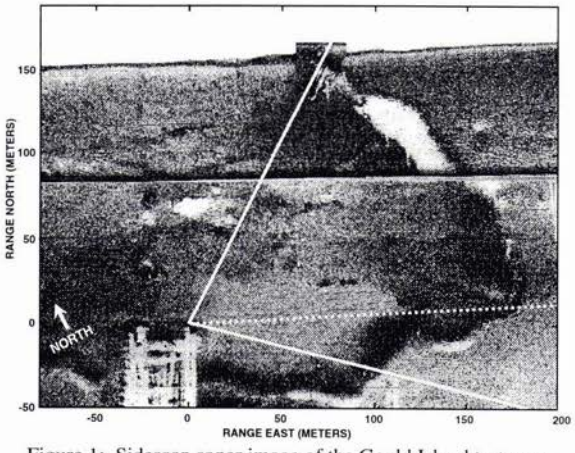

Figure 1: Sidescan sonar image of the Gould Island test area.

3.2 Algorithm functional description

The functional flow diagram is shown in Figure 2. Each numbered functional block will be detailed separately and example results presented where appropriate.

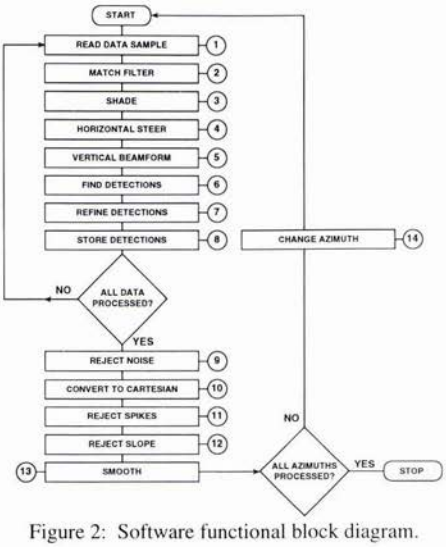

Figure 2: Software functional block diagram.

1. Read Data Sample: A single, complex-valued data sample is retrieved from each receive element. All system gains are removed so that incoming data values represent pressure at the face of the array (re 1 μPa).

2. Matched Filter: A complex-valued, unity norm, basebanded digital replica of the transmit waveform is used.

3. Shade: Two-dimensional Chebyshev weights are applied to the data.

4. Horizontal Steer: Complex phase delays are applied to each element (511 elements) to steer the array to a given azimuth. The elements in each row are then summed to form horizontal staves.

5. Vertical Beamform: 256 vertical beams are formed via FFT and beam powers are computed. Figure 3 depicts an example vertical beamscan, steered horizontally to the dashed line in Figure 1. The sonar array is located at 0 meters range and 0° vertical angle. Positive valued vertical angles are down. The echo from the bottom is clearly seen starting roughly 45° below the sonar. A small bump is evident in this bottom echo trace at a range of 120 meters from the sonar. This bump is due to a portion of the rim at the test site. Note that Figure 3 shows the vertical beam powers for an entire ping receive cycle (many consecutive time samples), and that the method presented here operates systolically (one sample at a time), the entire beamscan is presented for clarity. This convention will be used in other illustrations.

6. Find Detections: For each time slice, the average beam power across the 256 vertical beams is computed. Detections are defined as those beams with power exceeding the average by 6 dB. Figure 4 shows those beams from the vertical scan that exceed the threshold. Next, in order to determine target directions, detection peaks are found from beams whose power is larger than that of their immediate neighbors. Figure 5 illustrates detection peak localization at a range of 120 meters from the sonar. The rim (at +5°) and a reflection of the bottom off of the surface (at -10°) are the sources of the two detection peaks shown in the figure.

7. Refine Detections: The raw detection peak powers are refined by fitting, via least squares, a parabola to the peak and the two values on either side of the peak.

8. Store Detections: The refined angles are accumulated into 512 equal angular vertical bins (spanning ±90°). Only the maximum power response is maintained in each angular bin, together with its corresponding refined angle and sample number. Steps 1 through 8 are repeated until all received data samples from a sonar transmit cycle have been stored into the 512 equal angular vertical bins, this concludes systolic operation. Figure 6 depicts the stored refined bottom detection angles versus range, overlaid on top of the set of detections from Figure 4. The bottom profile is cluttered with outliers caused by noise (volume reverberation and sidelobe returns). The post-systolic filtering performed in steps 9 through 13 reject clutter from the raw bottom profile.

9. Reject Noise: A nine sample moving average filter is run along the stored power estimates, starting from the maximum stored downward angle and proceeding to the minimum stored angle. If the power of the point under inspection is more than 10 dB lower than the mean power, the point is considered noise and rejected from the profile. Figure 7 illustrates the bottom profile after noise rejection.

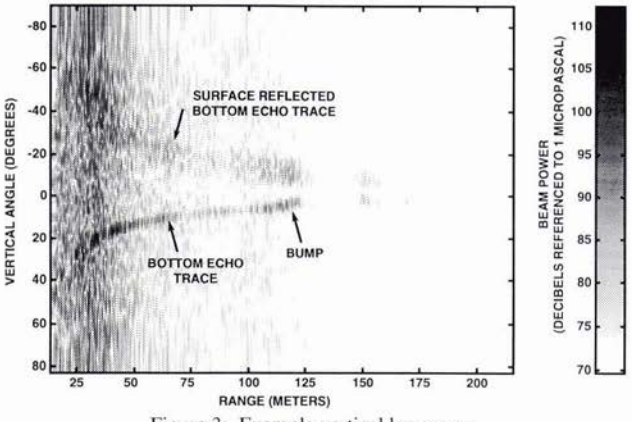

Figure 3: Example vertical beamscan.

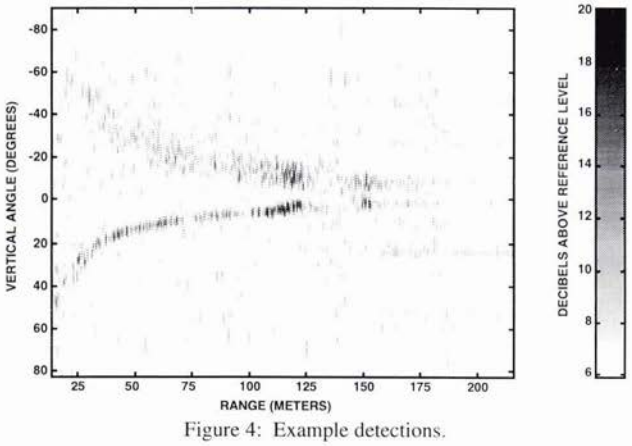

Figure 4: Example detections.

10. Convert to Cartesian: The stored, noise rejected, bottom profile is converted from vertical angle versus sample number to depth versus horizontal range, and the overall slope of the bottom profile is determined (via a linear fit) for later use in slope rejection. Two methods have been employed to perform this conversion. One is based on straight-line propagation and one is based on ray theory. The sound speed profile at the test site was nearly isovelocity; therefore, the straight-line propagation conversion method was used. Figure 9 displays the bottom profile after conversion to depth below the sonar versus horizontal range.

11. Reject Spikes: The converted bottom profile presented in Figure 9 shows a nearly flat bottom 12 meters below the sonar. Clearly seen is a portion of the rim 120 meters away from the sonar. This profile is contaminated by single sample spikes due to volume reverberation (spikes point toward the sonar) and sidelobe noise (spikes point away from the sonar). Noise spikes are especially prevalent in the area close to, and almost directly under, the sonar, where the transmit beam is weak. Spike removal is accomplished by running a six sample comparative filter (three samples before and after the point under inspection) along the profile displayed in Figure 9. If the horizontal range to the point under inspection is greater than, or less than that of its six immediate neighbors, the point is rejected as a spike. Figure 10 shows the example bottom profile after spike removal.

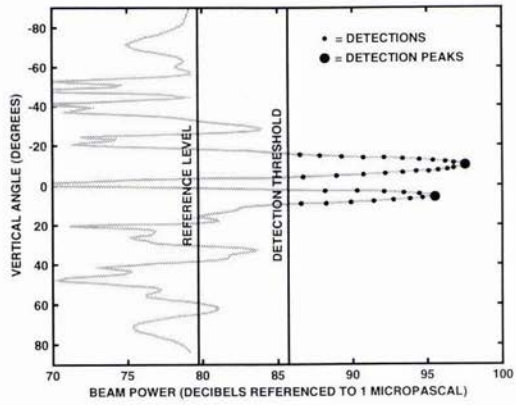

Figure 5: Example determination of detection peaks.

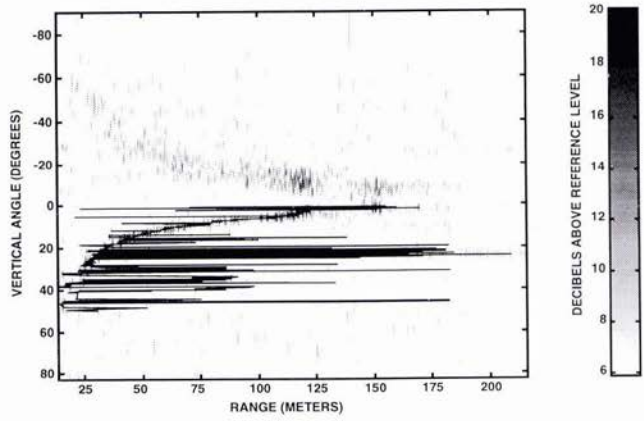

Figure 6: Example stored bottom profile at the conclusion of systolic operation.

12. Reject Slope: The point-to-point slope is computed between each pair of points in the bottom profile. If the slope differs from the overall slope (step 10) by more than 60°, the rejection flag is set. If the slope differs from the overall slope by more than 30°, the profile is examined for an upward or downward trend. If a directional trend exists, points are allowed to pass (up to the 60° point-to-point slope limit), otherwise, the rejection flag is set. If the rejection flag has been set, the current depth point and the previous 9 depth points are averaged, and the point furthest from the mean is rejected from the profile. The example bottom profile after slope rejection is presented in Figure 11.

13. Smooth: A three sample moving average filter smoothes the bottom profile (Figure 12). This concludes the processing of one azimuth.

14. Change Azimuth: The azimuthal steering angle is incremented, and steps 1 through 13 are repeated until all desired azimuth angles are processed. The HRA has a ±40° horizontal transmit beam, and a 3° wide receive beam. Processing azimuth angles from -40° to +40° in 2° increments covers the transmit angular swath with adequate spacing to minimize scalloping loss. An entire single ping, forward-looking terrain map is presented in Figure 13 in which a large section of the test area rim is clearly seen. The corresponding echo level (previously referred to as beam power) map is shown in Figure 14. Note the rise in backscatter levels due to the face of the rim, and the fall in backscatter levels as the range from the sonar increases. This drop in echo level versus range is expected and is caused by transmission loss and decreasing grazing angle versus range from the sonar (assuming a flat bottom). Details on multiple ping map construction can be found in [4].

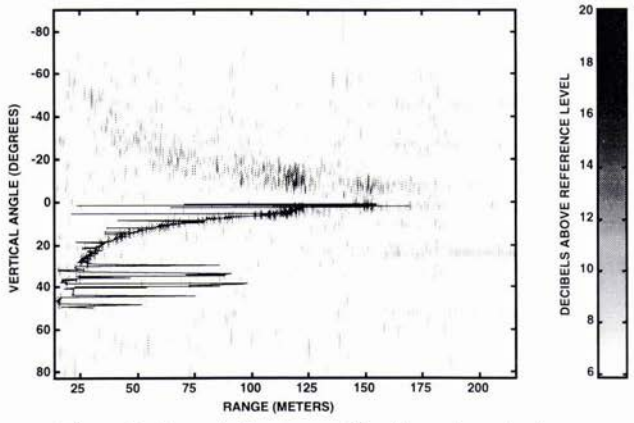

Figure 7: Example bottom profile after noise rejection.

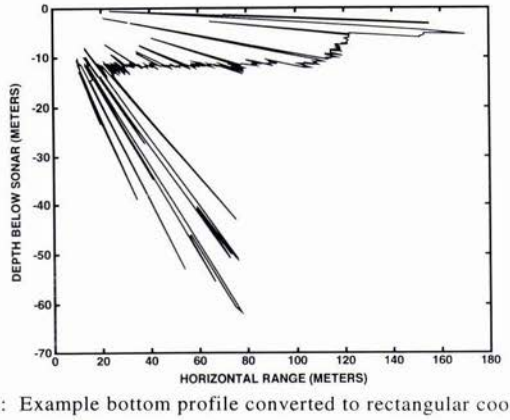

Figure 9: Example bottom profile converted to rectangular coordinates.

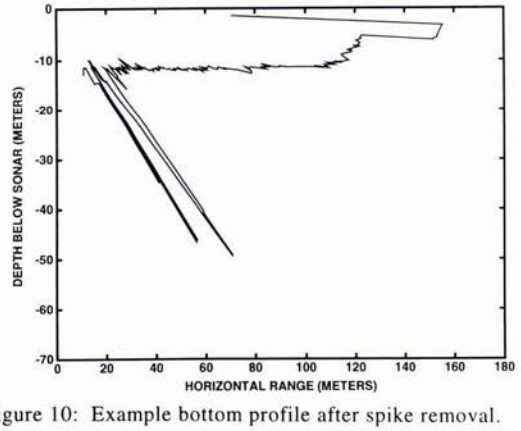

Figure 10: Example bottom profile after spike removal.

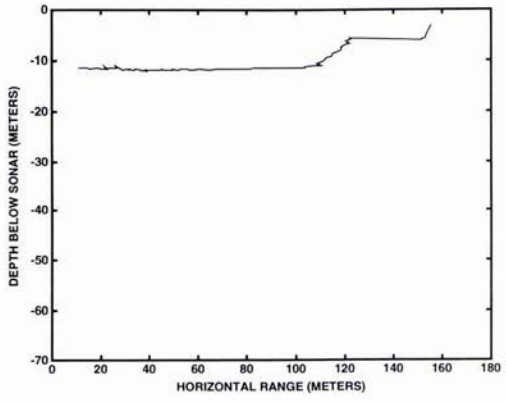

Figure 11: Example bottom profile after slope rejection.

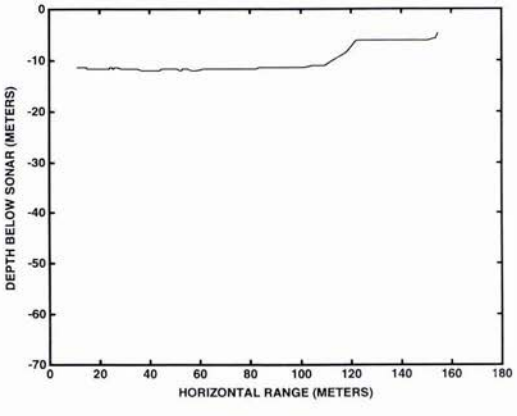

Figure 12: Example bottom profile after smoothing.

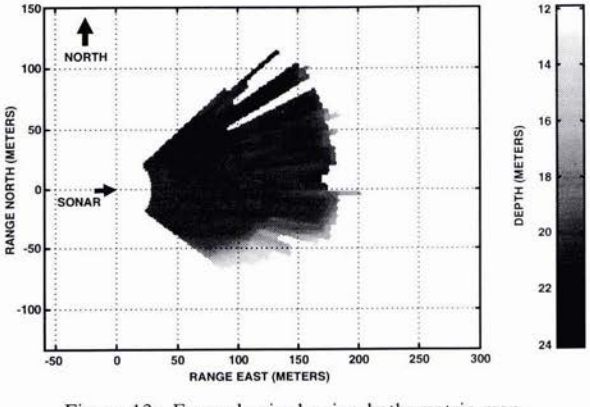

Figure 13: Example single ping bathymetric map.

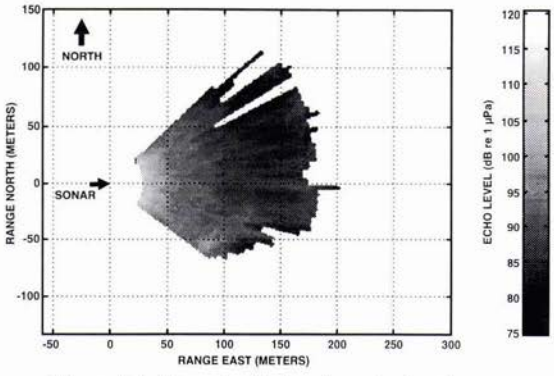

Figure 14. Example single ping echo level map.

4. HRA angle estimation accuracy

In addition to terrain mapping, the HRA is ideally suited for detecting and localizing small objects. The theoretical detection performance of the HRA can be found in [5] and a detailed development of the theoretical bounds on target position can be found in [6]. In this section, a brief review of those bounds will be given and compared with in-water results taken against small spherical targets. The geometry of interest is shown in Figure 15 where the array is located in the x-y plane and the point target of interest is located at x_t, y_t, z_t (r, θ, ψ). Given the return from an arbitrary transmit signal $s(n), n = 0,1,\cdots,N-1$ (baseband samples), the Cramer-Rao bound on the variance of any unbiased estimator of θ can be calculated as follows (note that for values of $\psi = 0$ or π, θ represents azimuth angle). Let SNR_A denote the array output signal-to-noise-ratio due to the point target. Define the mean square bandwidth of the signal as

$$MSB = \frac{\sum_{k=0}^{N-1} \omega_k^2 \left|\tilde{S}(k)\right|^2}{\sum_{k=0}^{N-1} \left|\tilde{S}(k)\right|^2}, \tag{1}$$

where $\tilde{S}(k)$ is the k^{th} DFT coefficient of basebanded signal and $\omega_k = \frac{2\pi k B}{N}$, with B the bandwidth of the waveform. Also, define the mean square aperture function of the array as

$$MSA = \frac{\sum_{m=1}^{M} \left(\frac{x_m}{c}\right)^2 \left|A(m)\right|^2}{\sum_{m=1}^{M} \left|A(m)\right|^2}, \tag{2}$$

where x_m is the x value of the m^{th} element in the array (the array is assumed to have mirror symmetry about the x and y axes), $A(m)$ is the amplitude of the m^{th} element and c is the speed of sound. The Cramer-Rao bound for any unbiased estimator $\hat{\theta}$ of θ is

$$\mathrm{var}\left(\hat{\theta}\right) \geq \left(2 SNR_A MSA\left(\omega_0^2 + MSB\right)\cos^2\theta\right)^{-1}, \tag{3}$$

where ω_0 is a measure of the center frequency of the signal.

A set of 48 measurements were taken with the HRA using a 10 mS, 6000 Hz linear stepped FM waveform in the Gould Island test area against an air-filled steel sphere target located at approximately r = 110 m, θ = 5° and $\psi = 0°$. The data were processed as follows to estimate the value of θ. A set of vertical staves were formed from the unweighted element level data and phase-shift beamforming was implemented via an FFT to form 128 beam outputs steered in azimuth. The peak beam output from the target was compared to the data immediately before and after the target to determine SNR_A. The average value over the 48 data sets was 22 dB. The peak beam output of the target return also provides a coarse estimate of θ. A refined estimate is derived by least squares fitting a parabola to the peak and three values on either side of the peak. The mean and standard deviation of the refined angle estimates were calculated to be 5.12 ° and 0.14° respectively. Figure 16 shows a comparison of the standard deviation of the estimates with the bound derived in (3). The in-water result matches fairly well with the theoretical result.

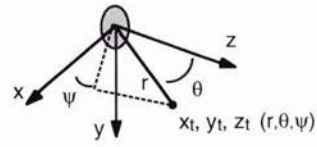

Figure 15: Geometry

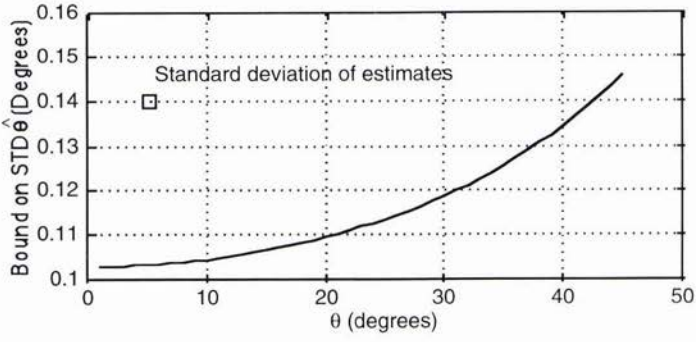

Figure 16: Comparison of theoretical angle estimate bound and in-water result

References

[1] J. Kelly, et. al., "A wideband sonar for high resolution imaging," in *Proc. Undersea Defense Technology Conf.*, Cannes, France, Jun. 1995.

[2] F. Nussbaum, et. al., "Sensors for a forward-looking high resolution AUV sonar," in *Proc. 1996 Symp. on Autonomous Underwater Vehicle Technology,* Monterey, California, Jun. 1996.

[3] D. O'Neill, "Design of the receive element placement pattern for the second high resolution array (HRA-2)," NUWC-NPT Technical Memorandum 962024, Naval Undersea Warfare Center Division, Newport, RI., Mar. 1996.

[4] M. R. Medeiros and R. N. Carpenter, "High resolution array signal processing for AUV's," in *Proc. 1996 Symp. on Autonomous Underwater Vehicle Technology,* Monterey, California, Jun. 1996.

[5] D. Nagle, "Mine reconnaissance forward look sonars GSM performance prediction," Naval Undersea Warfare Center Division, Newport, RI, 1995.

[6] R. Altes, "Target position estimation in radar and sonar," *Proc. of IEEE*, vol. 67, no. 6, June 1979.

[7] R. N. Carpenter and D. Cousins, "Positional resolution of a high resolution array," unpublished.

Historical Measurements of Bubbles in Coastal Environments: Effects of Biogenic Bubbles on Propagation of High Frequencies

H. Medwin

OCEANAC, 4021 Sunridge Road, Suite A
Pebble Beach, CA 93953
and
Physics Department, Naval Postgraduate School
Monterey, CA 93943, USA
E-mail: pouliq@saclantc.nato.int

Abstract

The presence of microbubbles can have a significant effect on sound attenuation, refraction, dispersion, and phase fluctuations during high frequency propagation in coastal waters. Early research by students at the U.S. Naval Postgraduate School measured large populations of coastal bubbles, apparently generated by biological activity in nearly calm conditions, that appeared to be omnipresent within many meters of the sea surface. These biogenic bubbles supplement the bubbles due to rain and breaking waves, which have received much attention recently.

1. Introduction

In the 1960's a program of student experimental research was initiated at the U.S. Naval Postgraduate School to answer the question asked by a U.S. Navy Oceanographer "Do Invisible Bubbles Exist in the Sea?" The answer turned out to be an emphatic "yes". The research was conducted between 1964 and 1974 by a succession of ten students, each with a different experimental project which served to fulfill his thesis requirement for the M.S. degree. The methods used were standard physical acoustics techniques, common to laboratory studies of structural and molecular characteristics of gases, liquids, and solids; the same type of measurements in the ocean were inverted to yield bubble densities, sound speed dispersion, and phase fluctuations.

These first measurements of bubbles at sea were summarized in [1–4]. The publications dealt with the interpretation (as due to *in-situ* bubbles) of excess sound attenuation, dispersion, and phase fluctuations on experiment depth, frequency, time-of-day, season, presence of sea slicks, instantaneous wave height, and wind speed. The early research, most of which was conducted for convenience in shallow coastal waters during nearly calm seas, revealed very large numbers of bubbles. The experimental evidence of these omnipresent populations of coastal bubbles of resonance frequencies from 20 to 200 kHz, strongly suggests that they are due to biological activity in the volume and at the bottom. Some bubbles may also be caused by continental aerosols when they fall into the sea.

To our knowledge no one has gone beyond these coastal bubble measurements which were published over two decades ago.

2. Bubble Theory

A bubble of gas ratio of specific heats γ, and radius a in water of ambient density ρ_A at ambient pressure p_A, can resonate to an incident acoustic wave of frequency f_b because of its oscillating mass (the water in the skin surrounding the bubble) and its stiffness (due to the compressibility of the gas). The result is a natural pulsation frequency given by

$$f_b = \frac{1}{2\pi}\sqrt{\frac{s}{m}} = \frac{1}{2\pi a}\sqrt{\frac{3\gamma p_A}{\rho_A}}\ , \tag{1}$$

which allows one to specify the radius of the bubble resonating to the incident frequency f. Linear theory shows that there will be a frequency-dependent bubble damping constant at resonance δ_R of order 0.1 due to thermal conductivity, shear viscosity, and reradiation of the sound. At resonance, this will cause a scattering cross section, absorption cross section, and extinction cross section, of order 10^2 times the geometrical cross section. (The backscattering cross section is the ratio of the backscattered power to the incident intensity. The scattering is omnidirectional at resonance.) The result is backscatter and excess attenuation compared to bubble-free water.

Linear theory also shows that the compressibility of a bubbly medium leads to a complex propagation constant with velocity dispersion as well as attenuation, see Fig. 1. The deviation of the sound speed from that measured by a sound velocimeter (which operates in the megahertz range) depends on the bubble density and the ratio of the incident frequency to the bubble resonance frequency. At frequencies much greater than the resonance frequencies of the predominant bubbles, the speed is equal to the value obtained from a sound velocimeter. At frequencies much less than the resonance frequency of the largest bubbles, the speed depends on the void fraction of the medium and can deviate by tens of meters per second from the bubble-free medium. There will be a fluctuation in the phase of transmitted sound that depends on the variation of the number of bubbles per unit volume $c(u)$ as well as the change of resonance frequency [i.e., due to a change of ambient pressure $c(z)$ in (1)] and the damping constant δ_R. See bottom of Fig. 1, which is based on theory in reference [13].

3. Measurement Techniques

The first measurements of bubble densities at sea consisted of photographing and then counting and sizing the bubbles in a volume of about one cubic centimeter [5]. We then proceeded to the more promising acoustical tests.

The linear acoustical techniques for measuring ocean bubble densities depend on the appropriate inversion of the distinctive effects of insonified bubbles [6] and consist of employing many frequencies to determine bubble densities for many radii in the range 20 μm to 200 μm. In the period from 1964 to 1974 they included:

a) excess attenuation in a pulse-echo system in which a low Q, 30 cm diameter, mylar transducer faced a 30 cm diameter rigid reflector at a separation of about 100 cm; the transducer radiates a tone burst and then is switched to receive the series of echoes which follow;

b) measurement of the relative backscatter compared to reflection in the pulse-echo system;

c) travel time between echoes, for different frequencies in the pulse-echo system;

d) ratio of amplitudes at two point receivers at separation of the order of meters in the field of a frequency-variable source;

e) difference of phase at two point receivers separated by one to five meters in the field of a frequency-variable source.

Much later an effective one-dimensional multi-frequency acoustical resonator technique was pioneered by Breitz and Medwin [7, 8] for measurements close to the surface of breaking waves. The device has recently been improved by others and used to obtain much data under a variety of breaking wave conditions at sea. It could also be used in coastal waters, of course.

In the early 1970's, measurements were also made of the spectral density of sound phase modulation during propagation in bubbly water [2, 3]. Prominent bubble populations cause phase shifts that mimic the spectral density of ocean surface wave displacements, which are the source of ambient pressure changes that create shifts in the bubble resonance frequencies described by (1); see the 95.6 kHz data in Fig. 2. On the other hand, randomly variable void fractions cause a Gaussian spectrum of phase fluctuations as demonstrated by 24.4 kHz in Fig. 2.

4. Empirical Bubble Densities in Quiescent Coastal Waters

Based on measurements by Medwin [1, 4], and separate analysis by P. J. Mulhearn [9], and J. C. Novarini and G. V. Norton [10], it is possible to describe the form and speculate about the causes of bubble densities as a function of bubble radius and depth in quiescent coastal waters. Figures 3 and 4 tell a complex story. Figure 3, from [4], is a summary of results, measured in mid or late afternoon, at approximately the same depths, during different months of the year, under similar meteorological and oceanographic conditions, in Monterey Bay, CA and San Diego Bay, Ca, approximately 700 km to the south. The slope of bubble density vs. radius changes at approximately 40 to 60 microns bubble radius. Figure 4 shows that there is a depth dependence that is different for high frequencies

(small bubbles) and low frequecies (larger bubbles). Using both figures, the density can be described by

$$n(a)da = K_1 \left(\frac{a}{60}\right)^{-2} (z)^{-1/2} \quad \text{for} \quad 200\,\mu\text{m} > a > 60\,\mu\text{m} \tag{2}$$

$$n(a)da = K_2 \left(\frac{a}{60}\right)^{-4} e^{-z/L} \quad \text{for} \quad 10\,\mu\text{m} < a < 60\,\mu\text{m} \tag{3}$$

where

$$\begin{aligned} a &= \text{bubble radius in microns;} \\ n(a)da &= \text{number of bubbles in a 1 micron increment, per meter}^3\text{;} \\ L &= \text{small bubble folding depth} \cong 7 \text{ m;} \\ z \geq 1.5 \text{ m} &= \text{depth in meters,} \end{aligned}$$

and K_1 and K_2 are constants that depend on the time of day and season.

Figures 3 and 4 show rough averages based on many measurements. There appears to be a definite dependence on season, as would be expected for biological sources of bubbles. The fact that small bubbles are more prominent in the daytime than at night is ascribable to photosynthesis. The evidence that larger bubbles are more dense at night than in the daytime may be due to continental aerosols carried off-shore by night "sea breeze" or may be due to increased biological activity at the sea floor. To add to the complexity of the coastal situation, there is evidence that bubble densities will be greater under sea slicks and windrows, and are even affected by the presence of fog [4]. Bubble densities in other locations with different flora and fauna will be very different. There will also be a wind dependence and a dependence on distance from the surf zone due to breaking waves.

5. Conclusions

Historical measurements of bubble densities and bubble-derived phase modulations of high frequency sound strongly suggest that the effects of biogenic bubbles should be included in propagation models even in nearly calm coastal waters. Once they are known, values of coastal ocean bubble densities may be used to obtain estimates of the acoustical parameters, sound attenuation, backscatter, and dispersion, by application of formulas in books such as references [11, 12].

References

[1] H. Medwin, "*In-situ* acoustic measurements of bubble populations in coastal waters," *J. Geophys. Res.*, vol. 75, pp. 599–611, 1970.

[2] H. Medwin, "Acoustic fluctuations due to microbubbles in the near-surface ocean," *J. Acoust. Soc. Am.*, vol. 56, pp. 1100–1104, 1974.

[3] H. Medwin, J. Fitzgerald, and G. Rautmann, "Acoustic miniprobing for ocean microstructure and bubbles," *J. Geophys. Res.*, vol. 80, pp. 405–413, 1975.

[4] H. Medwin, "*In-situ* measurements of microbubbles at sea," *J. Geophys. Res.*, vol. 82, pp. 971–976, 1977.

[5] P.D.C. Barnhouse, M.J. Stoffel, and R.E. Zimdar, "Instrumentation to determine the presence and acoustic effect of microbubbles near the sea surface," M.S. Thesis, U.S. Naval Postgraduate School, 1964.

[6] H. Medwin, "Acoustical determinations of bubble-size spectra," *J. Acoust. Soc. Am.*, vol. 62, pp. 1041–1044, 1977.

[7] N.D. Breitz and H. Medwin, "Instrumentation for *in-situ* acoustical measurements of bubble spectra under breaking waves," *J. Acoust. Soc. Am*, vol. 86, pp. 739–743, 1989.

[8] H. Medwin and N.D. Breitz, "Ambient and transient bubble spectral densities in quiescent seas and under spilling breakers," *J. Geophys. Res.*, vol. 94, pp. 12,751–12,759, Sept. 15, 1989.

[9] P.J. Mulhearn, "Distribution of microbubbles in coastal waters," *J. Geophys. Res.*, vol. 86, pp. 6429–6434, July 1981.

[10] J.C. Novarini and G.V. Norton, "Acoustic index of refraction in the background bubble layer of the ocean; an updated bubble spectrum and the computer program CBUBBLY," Naval Research Lab report, NRL/FR/7181-93-9432, March 10, 1994.

[11] C.S. Clay and H. Medwin, *Acoustical Oceanography*, John Wiley, New York, 1977.

[12] H. Medwin and C.S. Clay, *Applied Ocean Acoustics*, in preparation 1997.

[13] P.C.C. Wang and H. Medwin, "Stochastic models of the scattering of sound by bubbles in the upper ocean," *Quart. J. of Appl. Math*, pp. 411–425, Jan. 1975.

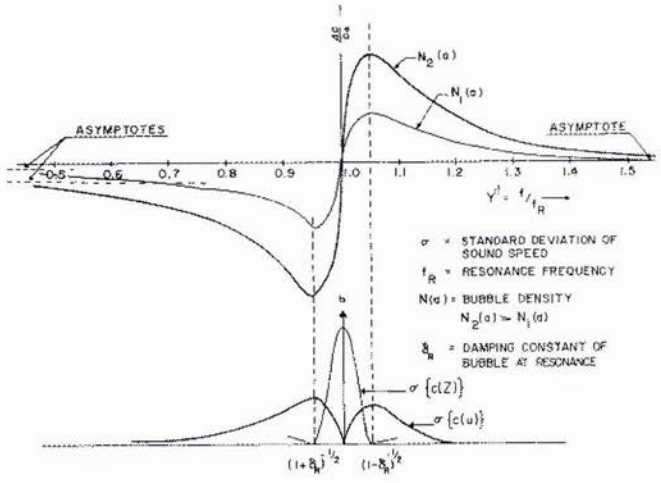

Fig. 1. Sound speed dispersion as a function of ratio of insonifying frequency f to bubble resonance frequency f_R for a mono-radius bubbly region. The bubble density $N_2 > N_1$. The standard deviation of the sound speed depends on whether the speed change is due to change of the number of bubbles, $c(u)$, or due to change of pressure $c(z)$. See Reference [13] for details.

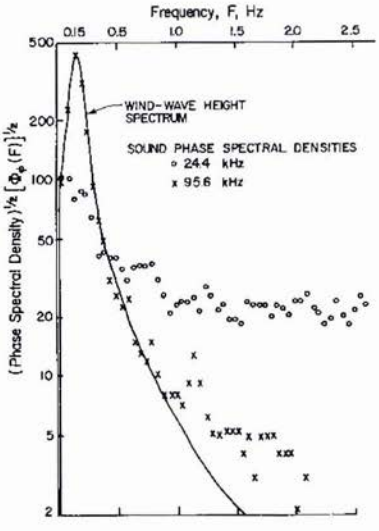

Fig. 2. Spectral density of the phase change due to a mixed population of bubbles. The theoretical wind-wave height spectrum for a Pierson-Moskovitz sea is the solid line. The phase spectral density is nearly Gaussian when the source of change is the random change of void fraction (at 24.4 kHz). It is closely correlated to the wind-wave height spectrum when the phase shifts are due to pressure changes (at 95.6 kHz). See Reference[3] for details.

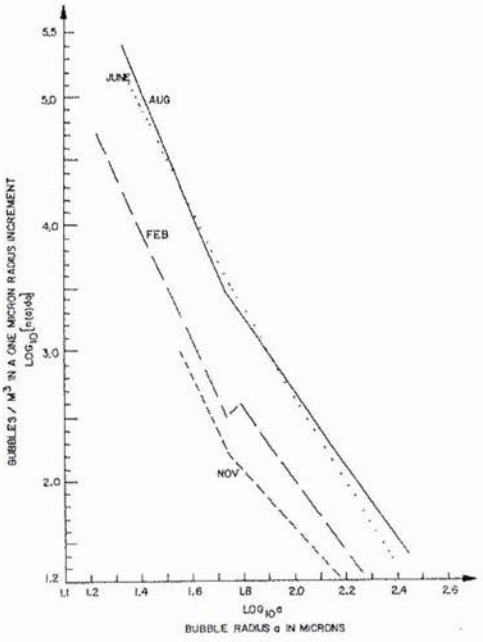

Fig. 3. Seasonal change of bubble density at low wind speeds and 3 to 8 meter depths in late or mid- afternoon. See Reference[4] for details.

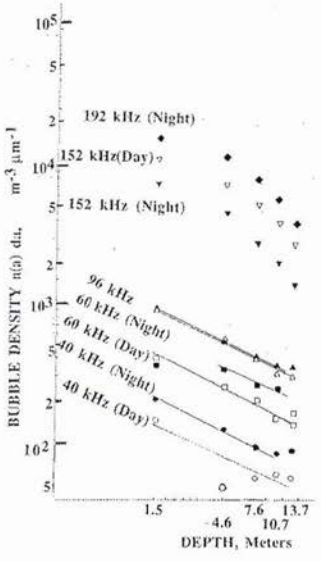

Fig. 4. Bubble densities in coastal waters as observed by high frequency acoustical measurements, as a function of *in-situ* depths from 1.5 to 13.7 m during day and night experiments in February 1965. See Reference[1] for details.

Seabed Survey by VHR Multichannel Seismics: GEOSIS Project

J. Meunier*, J.C. Dubois**, H. Kuhn***, Th. Desvallières****, A. Puech *****

*IFREMER, Centre de Brest, BP 70, 29280 PLOUZANE, FRANCE
**IFP, 1 et 4 avenue de Bois Préau, 92500 RUEIL MALMAISON, FRANCE
***Elf Aquitaine Production, CSTJF, 64018 PAU, FRANCE
****TOTAL, Tour Total, 92069 PARIS LA DEFENSE, FRANCE
*****Géodia, 205 avenue Georges Clémenceau, 92000 NANTERRE, FRANCE

Abstract

Site surveys prior to the installation of offshore facilities are required to obtain shallow soil structural and geotechnical information. The French project GEOSIS was aimed at improving both geophysical and geotechnical investigation methods and at providing a valuable methodology for the intercorrelation of the results. The GEOSIS methodology for integrated soil investigation includes the following items: VHR multichannel seismic survey, fine grained geotechnical boreholes (coring and in-situ tests) and vertical seismic profiling (P and S waves). This paper describes the acquisition and processing strategies and their application to a site survey in the western Mediterranean Sea (Monaco). Correlations established within the project between geophysical and geotechnical properties are discussed.

1. Introduction

Offshore site surveys are mainly carried out in the domain of oil industry prior to the installation of platforms or sealines, but also in coastal and harbour domain, as well as in mineral resources evaluation and in sedimentary studies. The GEOSIS project was aimed at improving site survey methodology in the view point of the integration of the geotechnical and the geophysical data. The GEOSIS methodology includes the following steps:

- Very High Resolution multichannel seismic survey (in lieu of conventional single channel seismic survey) which will provide a metric accuracy whereas P wave velocity information will be recovered using multichannel technology,
- Geotechnical fine grained boreholes including coring and in-situ tests,
- Vertical seismic profiling in order to link borehole information to the processed seismic lines.

The purpose of a GEOSIS survey is to establish correlations between the geotechnical parameters obtained in boreholes and the geophysical properties within the first 100 m.

The ultimate step in data processing is to adapt the techniques of stratigraphic deconvolution routinely used in reservoir studies to quantitative extrapolation of some geotechnical properties around a borehole along seismic profiles. The paper describes the tasks to get both sets of data ready for the stratigraphic deconvolution (which is not presented here).

2. Acquisition System at Sea

2.1. Multichannel survey

We are referring to the term "Very High Resolution" (VHR) seismics as the ability to obtain a one meter accuracy both horizontal and vertical. Therefore the entire acquisition system and the layout must be tailored in order to meet our specifications.

2.1.1. Seismic source

The source must be able to provide a seismic signal with a frequency bandwidth adapted to the expected metric definition. The P-wave velocity law, within the upper sediments, typically ranges from 1500m/s (water) to about 3000 m/s (consolidated sediments). Therefore the frequency content of the signal should range between 0.5 and 3 kHz. This implies that the source must be towed within 20 to 40 cm below the sea surface in order to avoid destructive summation (ghost). The source must be able to provide a repetitive signal.

During the Monaco experiment described later in this paper, both a 15 cubic inch airgun and a 1500 Joules sparker were used.

2.1.2. Dedicated multichannel seismic streamer

The GEOSIS streamer has to be designed regarding two different constraints. First, it should allow the computation of the P-wave velocities within the sediments, therefore both its length and the number of traces must be adapted to the target. Second, the trace spacing within the streamer must be carefully adapted to the frequency content of the signal in order to avoid destructive summation in the stacking process due to spatial aliasing. Again the immersion of the streamer should be kept very close to the sea surface in order to avoid interference with the reflected ghost.

The speed of the vessel towing the streamer ranges from 2 to 4 knots. The shot rate ranges from 1 and 4 shots per second depending on the speed of the vessel and the water depth.

During the Monaco experiment, a 48 metre long streamer including 24 traces (2 metres apart) was used, the trace itself consisting in 6 hydrophones.

2.1.3. Acquisition system

The high sampling rate (up to 8000 kHz) has needed to cope with the signal frequency content and the great number of channels. When the project was launched no such high performance recorder was available on the market. Therefore a recording and quality control system (Delph24) was developed by IFREMER together with ELICS, a French company already involved in single to dual channel VHR seismic acquisition. The main characteristics of the Delph24 are the following ones:

number of channels:	24
maximum sampling frequency:	12 kHz
recording length:	312 ms at 8 kHz or 208 ms at 12 kHz.
maximum shot rate:	4 shots per second

16 bit A/D converter
internal or external trigger
display of signals in control or profile modes
recording of data under compressed Delph format or SEG-Y

2.1.4. Positioning strategy

In order to correlate seismic data to geotechnical borehole information, accurate positioning is needed. This can be easily achieved using either high performance D-GPS, land based beacons or laser theodolites.

2.1.5. Weather condition requirements

Sea state conditions are of uppermost importance for such high accuracy seismic surveys. Whereas detrimental effects caused by large swell can be easily removed during the processing of the seismic data, choppy seas will dramatically deteriorate the quality of the data in terms of seismic Signal to Noise ratio as well as positioning accuracy.

2.2. Geotechnical survey

The geotechnical survey will include at least two boreholes at the same location: one for sampling purposes and one for in-situ measurements. Information extracted from the latter as well as properties calculated on the recovered samples will be used to extrapolate geotechnical characteristics over the seismic lines.

2.2.1. Laboratory analyses

Conventional laboratory tests are carried out on the soil samples. The tests typically include sediment characterisation (density, water content, void ratio, grain size,...) as well as the determination of mechanical properties (cohesion, internal shaft friction angle, consolidation stress,...) Depending on the size of the samples, P-wave and S-wave velocities can be measured.

2.2.2. In-situ measurements

The Cone Penetrometer Test consists in measuring the point and shaft resistances and the excess pore pressure generated by sharing during the penetration of the tool into the sediment. The CPT is operated through a wire-line tool which allows 3 metres of continuous measurement. The standard penetration velocity is 2 cm/s.

2.3. Seismic measurements in geotechnical borings

The VSP experiment includes P-wave and S-wave measurements, acquisitions being carried out one after another for a given receiver depth within the borehole.

2.3.1. Seismic sources

In order to make the processing easier, the same P-wave high frequency seismic source must be deployed for the VHR multichannel seismic survey and the VSP.

The S-wave signals are generated by applying a horizontal force on the sea bottom. The device is placed on the sea bottom.

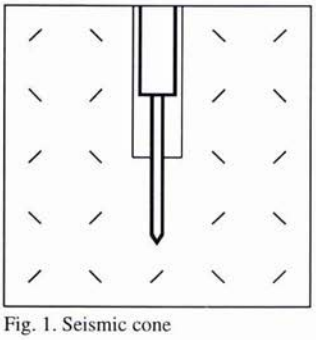

Fig. 1. Seismic cone

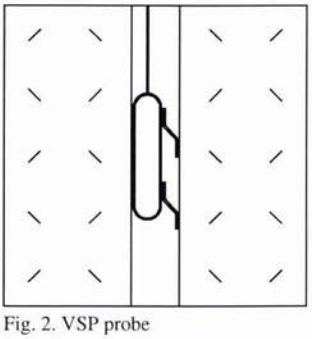

Fig. 2. VSP probe

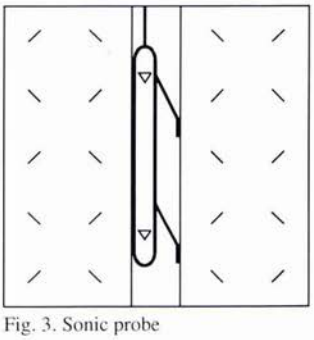

Fig. 3. Sonic probe

2.3.2. Seismic receivers

The use of a Seismic Cone Penetrometer Test is preferred because it ensures a very good coupling with the soil as it houses 3 pre-amplified geophones (X, Y, Z) in the cone (Fig. 1.). In-situ measurements and VSP can be carried out in the same sounding. Nevertheless, seismic acquisition should be recorded while the tool is at rest in order to decrease the noise level.

If a SCPT cannot be performed, a conventional VSP probe can be operated (Fig. 2.). The profiler is lowered inside the borehole and the measurements are performed continuously when rising the probe. The coupling with the soil is obtained using "arms" which strongly press the probe against the wall of the borehole. This technique requires the self stability of the borehole.

In addition a sonic probe can also be used in a borehole. The velocity of the surrounding soil is measured between a transmitter and a receiver 1 metre apart, while rising the probe (Fig. 3.).

2.3.3. Recording

The same acquisition system (Delph24) can be used. X, Y, Z components are recorded separately as well as a Time Break signal in order to synchronize the different recordings. During the Monaco experiment, a 10 kHz sampling frequency and a 500 millisecond recording length were used.

3. Data Processing

The data processing was mainly carried out using conventional seismic software. Nevertheless, special attention was paid to the broad frequency content of the seismic signal as well as to the source and receiver motions.

3.1. Multichannel seismic data processing

Apart from the imaging process (Signal/Noise improvement, time imaging artefacts,...), the multichannel seismic data will be used for two different purposes:

- Determination of the P-wave velocity field,

- Extrapolation of the geotechnical attributes determined from the borehole.

The seismic processing includes the following steps:

- Data edition (band pass filtering, correction of spherical divergence,...),
- Corrections of the vertical motions of the source and the receivers. These corrections were evaluated by picking the seismic arrivals from the reflection on the sea-bottom,
- Sort in Common Mid Points gathers,
- Velocity analysis,
- Stack,
- Migration.

From this processing sequence, we gain access to a depth section corrected for the travel time artefacts. Furthermore, using the average velocity field extracted through the NMO analysis, slice velocities for each of the encountered sediment layer can be computed.

3.2. VSP data processing

The P-wave VSP will be used as the pilot trace to extrapolate geotechnical attribute along the seismic lines. The S-wave VSP will allow the recovery of the S-wave velocity field and will serve for determination of the mechanical properties of the sediment.

The VSP seismic processing includes the following steps:

- Data edition (band pass filtering, Time Break corrections, shot summation,...)
- Separation of the down going waves and up-going waves using FK filtering,
- Deconvolution of the up-going waves,
- Corridor stacking,
- Migration.

4. Application

The above methodologies have been applied offshore Monaco (Mediterranean sea) in water depths ranging from 40 to 80 m. This application was carried out in the framework of geotechnical studies for the design of an embankment facing the harbour of 'La Condamine'.

4.1. Tests at sea

Multichannel lines were run over previously drilled boreholes. Fig. 4. and Fig. 5. display a scheme of two profiles (the first one parallel, the second one perpendicular to the coast). The vertical scale corresponds to a two way time of 250 ms and the length of the profiles is about 800 metres.

The site is characterised by thick sedimentary layers built up by several successive stages of deposition and erosion:

layer 1: soft to very soft clay with organic material,
layer 2: cemented silt with strong reflectors,
layer 3: homogeneous silt with local layers of sand or gravel (partially eroded),
layer 4: silt with layers of gravels and pebbles (strong reflectors),
layer 5: Cretaceous limestone.

The location of boreholes P5 (SCPT), P'5 (coring and VSP) and P7 (SCPT) are shown on Fig. 4 and Fig. 5.

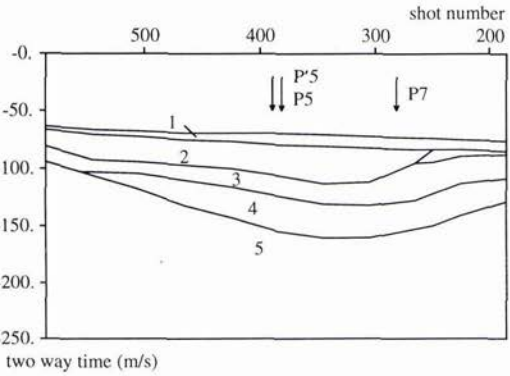

Fig. 4. Profile parallel to the coast

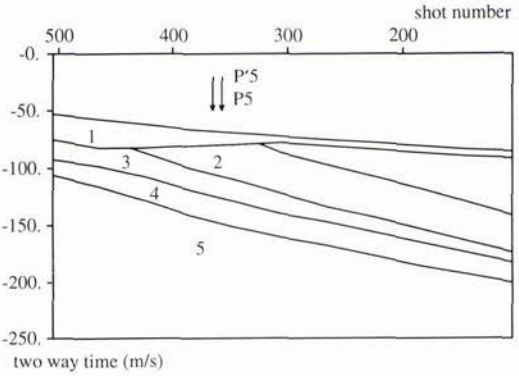

Fig. 5. Profile perpendicular to the coast

Fig. 6. presents the main results obtained in boreholes P5 and P'5: the penetrometric point resistance (a), P-wave (b - solid line) and S-wave (c) velocities measured using the seismic cone in borehole P5, P-wave velocity (b - doted line) measured using the VSP profiler, and the P-wave velocity measured by sonic probe in the open borehole P'5.

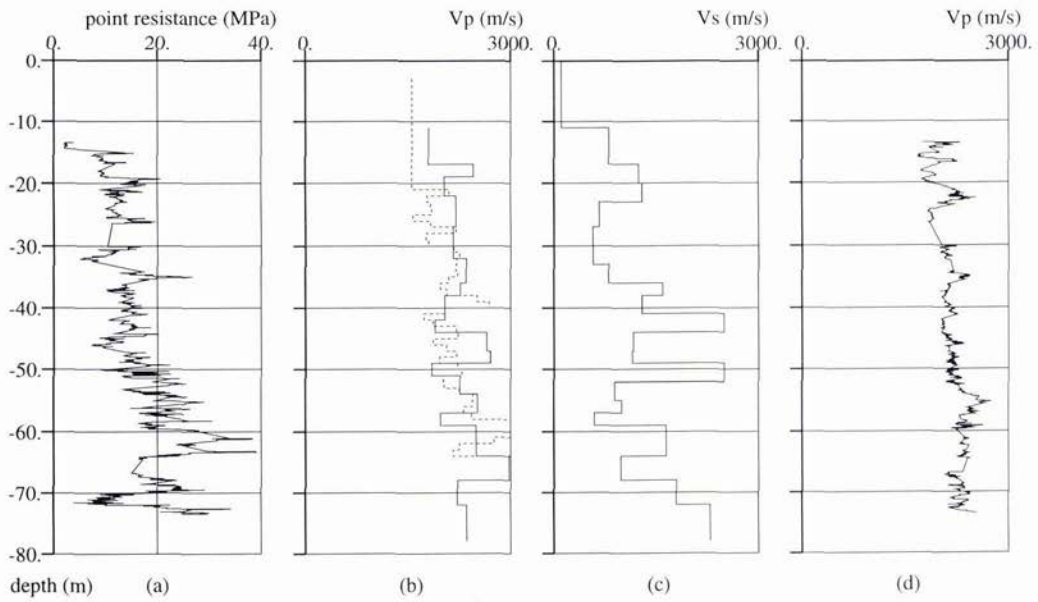

Fig. 6. Point resistance and velocities in borehole P5

4.2. Seismic and geotechnical correlations

Three types of correlations within the data obtained on Monaco site are discussed below:

correlations: seismics velocities (V_P or V_S) $\leftrightarrow$ penetrometric point resistance (q_c)

correlations: seismics velocities (V_P or V_S) $\leftrightarrow$ porosity (n)

correlations: point resistance (q_c) $\leftrightarrow$ acoustic impedance

4.2.1. Correlations between velocities and point resistance

This type of correlation seems to be promising because of the visual similarity between the profiles of the seismic velocities versus depth and the penetrometric profile of point resistance q_c. However, the establishment of a quantitative correlation is difficult because of the scattering of the values, their mode of acquisition (local values, mean values on a long range, artefacts,..) and the difficulties of the site due to the cementation of some layers.

Correlations have been established using mean values of velocities and point resistances in each soil layer and in gathering the results of several neighbouring boreholes.

Linear correlations between V_P and q_c and between V_S and q_c can be proposed (Fig. 7. and Fig. 8.):

$$V_P = 42.5\ q_c + 1500$$
$$V_S = 70\ q_c$$

where V_P and V_S are in m/s and q_c in MPa.

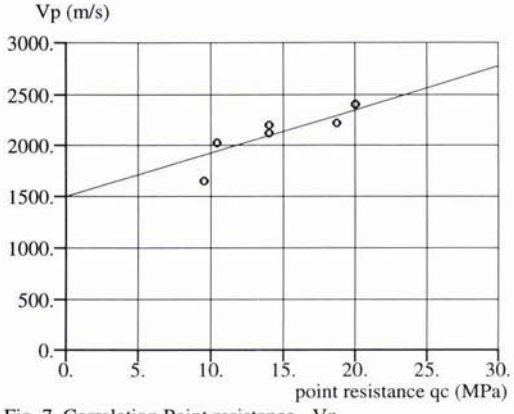

Fig. 7. Correlation Point resistance - Vp

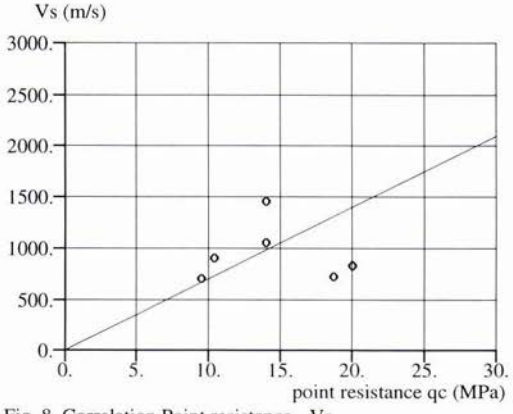

Fig. 8. Correlation Point resistance - Vs

4.2.2. Correlations between velocities and porosity

The values of porosity measured on samples are displayed Fig. 9. and Fig. 10. A trend to the decrease of V_P with the increase of porosity n seems to exist, but it would be audacious to propose a correlation because of the scattering of the data, and the low range of variation of the porosity in the encountered sediments.

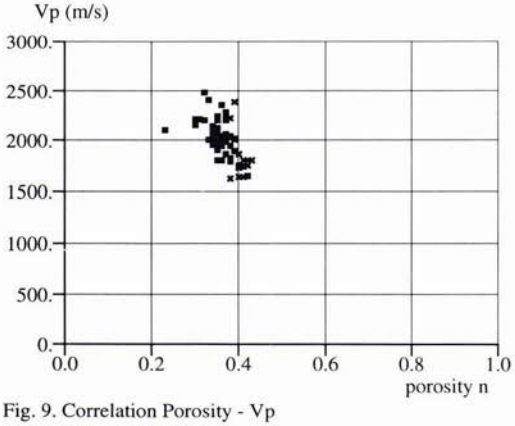

Fig. 9. Correlation Porosity - Vp

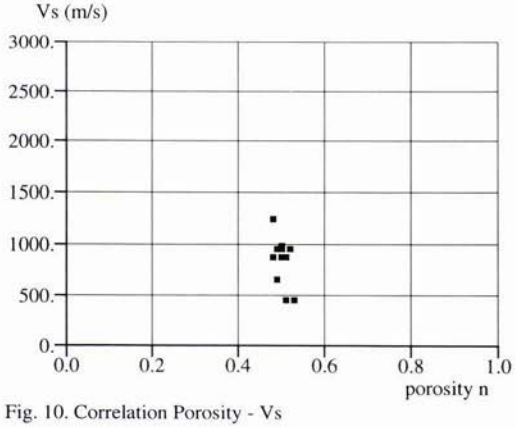

Fig. 10. Correlation Porosity - Vs

4.2.3. Correlations between point resistance and acoustic impedance

As the values of point resistance display unrealistic high values, they must be processed (interpolation in zones containing no values and filtering) in order to obtain a smooth curve (Fig. 11.)

The impedance profile is obtained using the sonic profile and assuming that the density is constant. This is acceptable because of the low range of variation of the density. This method is more accurate than the inversion of the VSP profile. The values of the two vertical profiles must be shifted of 1.7 m in depth in order to adjust the correlation as the data come from two neighbouring boreholes. Fig. 12. displays the correlation between the point resistance and the impedance.

A linear relationship is found :

$$q_c = 8.9.10^{-3} * impedance - 24.0$$

or

$$impedance = 112\ q_c + 2689$$

where q_c is in MPa and *impedance* in kPa/(m/s).

In comparing this formula with formula $V_P = 42.5\ q_c + 1500$ (section *4.2.1*) and in considering a constant unit mass of 2000 kg/m^3 it gives:

$$impedance = 85\ q_c + 3000$$

These two relationships differ because, in the first one, q_c was assumed to be equal to 0 in water in the upper part of the soil column.

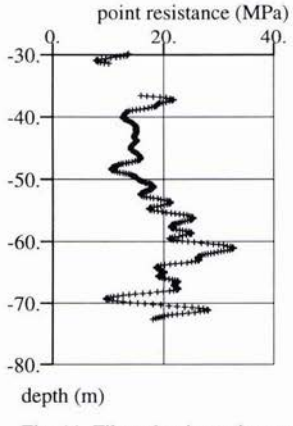

Fig. 11. Filtered point resistance

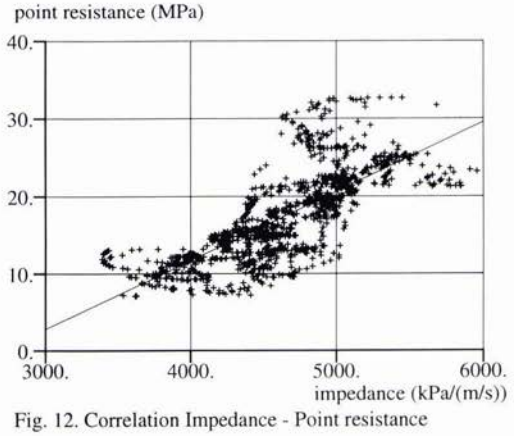

Fig. 12. Correlation Impedance - Point resistance

4.3. Point resistance as a function of two way time

In order to assimilate the values of q_c versus depth to the values of impedance versus two way time, to be used as input data into a stratigraphic inversion software, we tried to express q_c as a function of the same time scale as the time scale of seismic data.

This involves to define a fictive velocity law in order to find a relationship $t = f(z)$ applicable to the values of q_c. So, the extreme values of q_c are forced to be equal to the values of impedance (at the top and at the bottom of the sounding) to begin and to end on the same two way time.

The law of variation was interpolated between the extreme values. The difference of time regarding the law of the sonic profile shows two zones with different slopes for the point resistance. The limit is located at a depth of about 13 m, where a significative change in consolidation is observed on cored samples. (Fig. 13. and Fig. 14.)

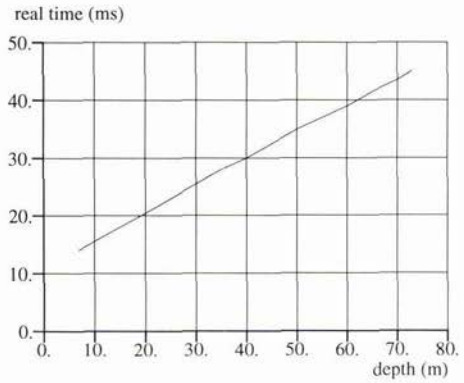

Fig. 13. Cumulated time from sonic mesurements

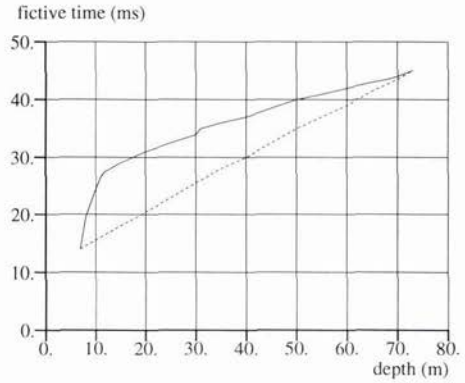

Fig. 14. Fictive time and sonic cumulated time

The real $t = f(z)$curve is plotted on Fig. 13. This curve is repeated (doted line) on Fig. 14. to show the time difference with the fictive q_c-time curve (solid line). This highlights the fact that the equivalence between q_c and impedance cannot be expressed by only one relationship for all the depths, but needs to be split into several laws (two in this case). In a later stratigraphic inversion, the changes of the signal properties have required the use of two windows having the same boundary. So, the above procedure can appear as a quick approach to define several domains of q_c-impedance relationship.

5. Conclusion

A survey following the specifications of GEOSIS, by integrating the geophysical and the geotechnical data can provide extended mechanical parameters around boreholes and give a quantitative interpretation of seismic profiles. The definition is about 1 or 2 metres vertically and horizontally with a penetration of about 100 metres, by water depths ranging from 20 to 80 metres. The next step would be the stratigraphic deconvolution which allows the quantitative extrapolation of geotechnical data along VHR seismic profiles around boreholes.

6. Acknowledgement

This work was performed in the framework of CLAROM, a French research association on offshore structures. The partners of the "GEOSIS" and "Stratigraphie Geotechnique" projects are thanked for their authorization to publish.

7. References

NAUROY J.F., DUBOIS J.C., PUECH A., POULET D., COLLIAT J.L., MARSSET B. "Vertical Seismic Profiling in offshore Geotechnical Boreholes" 47th Canadian Geotechnical Conference, Halifax, Nova Scotia, Sep. 1993

NAUROY J.F., DUBOIS J.C., MEUNIER J., MARSSET B., PUECH A., LAPIERRE F., KERVADEC J.P., KUHN H. "Tests in offshore Monaco of new Techniques for a Better Integration of Geotechnical and Seismic Data" Offshore Technology Conference, Houston, Texas, May 1994

NAUROY J.F., DUBOIS J.C., MEUNIER J., MARSSET B., PUECH A., COLLIAT J.L., POULET D., LAPIERRE F. "The Use of VSP Techniques in Geotechnical Boreholes: First Tests in offshore Monaco" Boss '94

NAUROY J.F., COLLIAT J.L., PUECH A., POULET D., MEUNIER J., LAPIERRE F. "Better Correlation between Geophysical and Geotechnical Data from improved offshore Site Investigations" Advances in site investigation practice, London, ICE, 30-31 Mar. 1995

MEUNIER J., MARSSET B., NAUROY J.F., DUBOIS J.C., KUHN H., KERVADEC J.P. ,LAPIERRE F., PUECH A. "Integration of Geotechnical and Geophysical Data: GEOSIS Project" Ocean 94 Osatès, Brest, 13-16 Sep. 1994

Riverine Environmental Acoustics at an Ocean Estuary

T. G. Muir[1], J. E. Blue[2], and A. L. Anderson[3]

Applied Research Laboratories
The University of Texas at Austin
Austin, Texas, U.S.A.

Present Affiliations:
1) Department of Physics and Undersea Warfare Academic Group U.S. Naval Postgraduate School Monterey, California, U.S.A.

2) Leviathan Legacy Corp. Orlando, Florida U.S.A.

3) Department of Oceanography Texas A&M University College Station ,Texas, U.S.A.

Abstract

The purpose of these studies was to investigate some of the more important geoacoustic parameters that might govern the use of high frequency sonar in muddy rivers, where they flow into the sea. Both environmental and acoustic measurements were made in an effort to identify which parameters were significant. The environmental measurements included water level, current, temperature, salinity, suspended sediment concentration and grain size distribution, bottom topography, sediment composition, including gas content, and sub-bottom layering. The acoustic measurements included absorption vs range, at a frequency of 200 kHz, and bottom backscattering vs grazing angle, at a frequency of 85 kHz.

1. Introduction

Several unique environmental factors should be considered at the confluence of a river with the sea. Depending on the riverine discharge rate, there may be high currents, a suspended sediment load, a layered salt water intrusion, and a bottom containing sufficient anaerobic baterial action to produce gas. These effects may effect the attenuation and reverberation experienced by high frequency sonars. Some years ago we conducted a series of environmental and acoustical studies of the lower reaches of the Brazos River near its estuarine with the Gulf of Mexico. It was our first such study and it was done without any prior experience with the art. Existing riverine and ocean research tools were simply adapted.

2. Riverine Environment

The Brazos is a muddy river with a high discharge rate, draining approximately 44,000 square miles of southeast, central, and northwest Texas and New Mexico. Our study was made at the little town of Brazoria, approximately 20 miles upstream from the Gulf of Mexico, where the maximum water depth was 10 m., and the tidal fluctuations varied from 15 cm to 1 m. The river meanders extensively in this area, with many cuts and shoots. A generic cross section of the river is shown in Fig 1. A typical water current cross section of the river is displayed in the contour plot of Fig 2, which shows the currents to be in the 0.4 to 0.55 knot range. Fig 2 also shows a contour plot of the suspended sediment concentration in the river, which is typically 0.024% by weight of the water samples acquired. The sediment particles were determined to be quartz with a specific gravity of 2.65. An electron microscope photograph of the particulate matter carried by the stream showed that the particulates were quite rough and angular. The grain size distribution of the suspended sediment is shown in Fig 3, and shows a peak at 2.8 microns. These data were obtained from an analysis of water samples by the settling technique; that is, the amount of solids in suspension was weighed as a function of their settling time after agitation. The procedure is based on Stokes' settling velocity for spherical particles, and yields an "equivalent spherical probability density" when the particulates are rough and not spherical. Over the period of the measurements, intrusion of a salt water "wedge" frequently occurred at high tide, sending salt water of up to 15 parts per thousand salinity up the river to mid depth. When this happened, the temperature of the saline wedge was typically 3 deg C higher than that of the fresh water flowing down the river, a consequence of the thermal makeup of the river and the gulf in the month of June, during which the measurements were made.

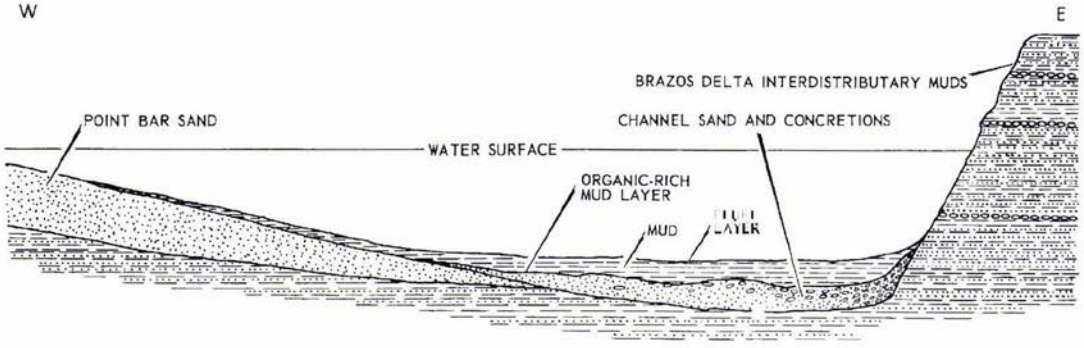

Figure 1. Schematic cross section of the Brazos river near its confluence with the Gulf of Mexico

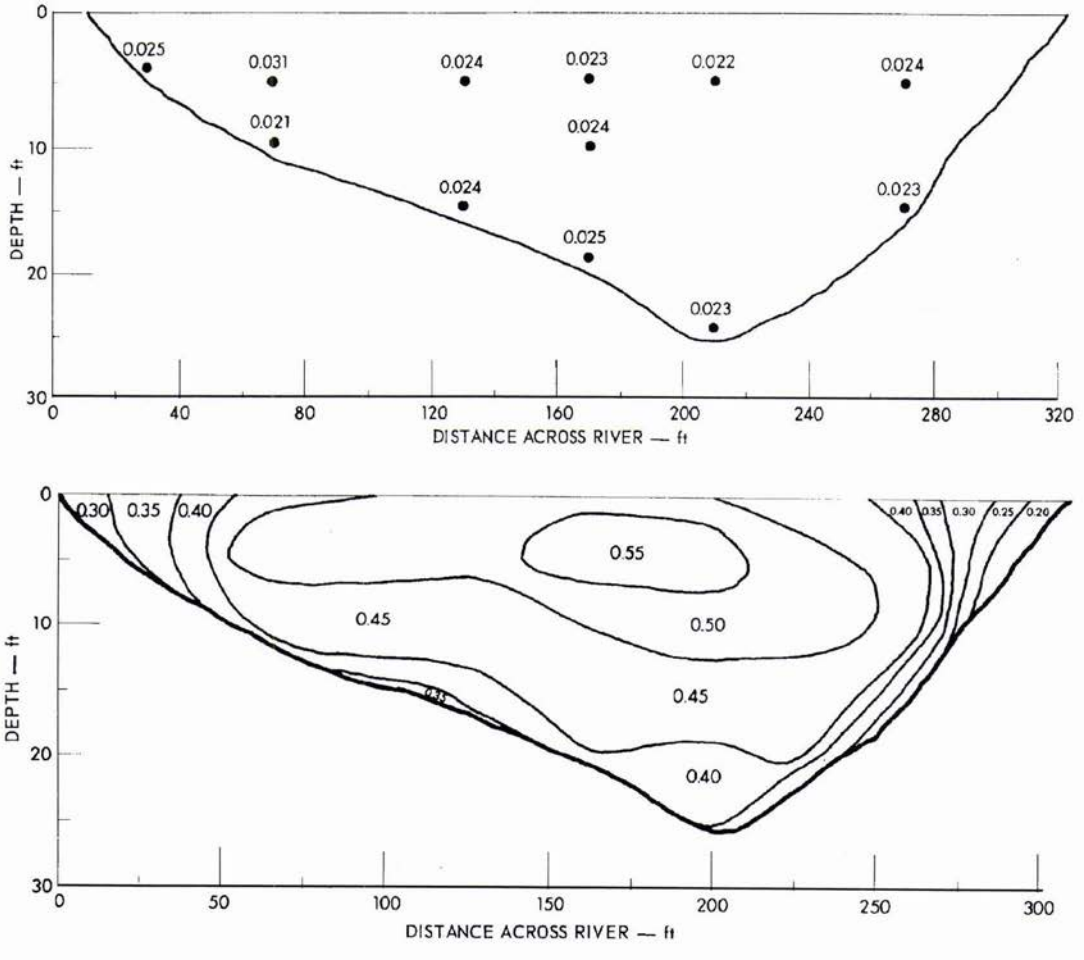

Figure 2. Current and suspended sediment cross sections

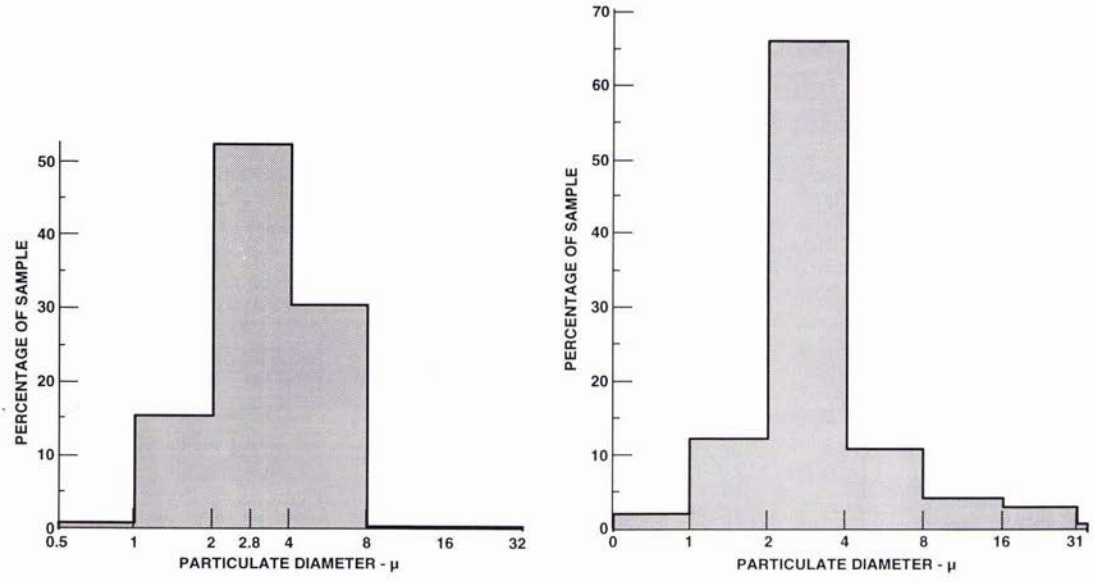

Figure 3. Particulate grain size distributions, left - suspended sediments, right de-flocculated "fluff" layer sediments

The river bottom was essentially featureless, with a maximum bottom relief of 2 - 5 cm. The river bed was cut in sediments of the Brazos River delta that was formed in the late Pleistocene era. These sediments consist of distributary channel sand bodies that are lenticular in cross section, and vary in width from a few hundred feet to half a mile along the reach of a meandering loop. Recent point bar sand and channel sand overly the eroded bottom. This sand is fine to medium graned, well sorted, with predominantly rounded subarkose grains (5 to 25% feldspar, 75 to 95% quartz), and its grainsize distribution peaked at 400 microns. Soft, homogeneous, brownish grey mud overlies the sand, varying in thickness from several cm at the river boundaries to 1 m, in the center of the river channel. At the base of this mud layer is an organic rich and very black sub-layer of mud, 2 to 5 cm thick, containing fragments of decaying teresestial plants. At the top of the mud layer, there is a 5 to 8 cm layer of very fine, highly dispersible material that formed a "fluffy" interface to the water column. It's density was 1.13 g/cm^3, very near that of water, and its .de-flocculated grain size distribution, shown in Fig 3, peaked at 3.0 microns. Gas bubbles of various sized were observed in all cores containing the mud layers. Analysis showed it to consist of methane - 50%, nitrogen - 45%, carbon dioxide - 2%, oxygen - 1.5%, argon - 1.2%, and probably a significant amount of hydrogen sulfide, which could not be measured with the apparatus used. The abundance of gas pockets in every core taken left the distinct impression that the bottom was essentially a "gas bottom," raising the question of the acoustical significance of the sand and other sedimentary layers. Abundant concretions, cemented by calcite, were also found in all of the bottom layers, and these could be acoustically significant due to their density and size (1 - 10 cm).

3. Acoustical Attenuation

The first acoustical measurement was on attenuation, thought due to the presence of the suspended sediment carried by the river. Projectors and receivers were attached to tiltable and trainable soundheads on mid-depth columns affixed to anchored, floating platforms. The transmission loss between projector and hydrophone was measured as a function of range, at a frequency of 200 kHz. The measurements were made in a body of water 6 m deep and 200 m long so that for a transmitted pulse length of 75 μsec we had enough path length difference to be immune from image interference out to a range of 170 m.

We focused on the attenuation due to the suspended sediment load, and we were fortunate that during the time of the attenuation measurements, the river was essentially isothermal (at about 29 deg C) and isohaline (at less than 0.2 of a part per thousand) with uniform sound velocity over the acoustic propagation path. The presence of fresh, muddy water during the time of these measurements was due primarily to the fact that large quantities of water had been released from a dam several hundred miles upstream a few days before, and this influx flushed out the usual salt wedge intrusion with a large volume of high energy water.

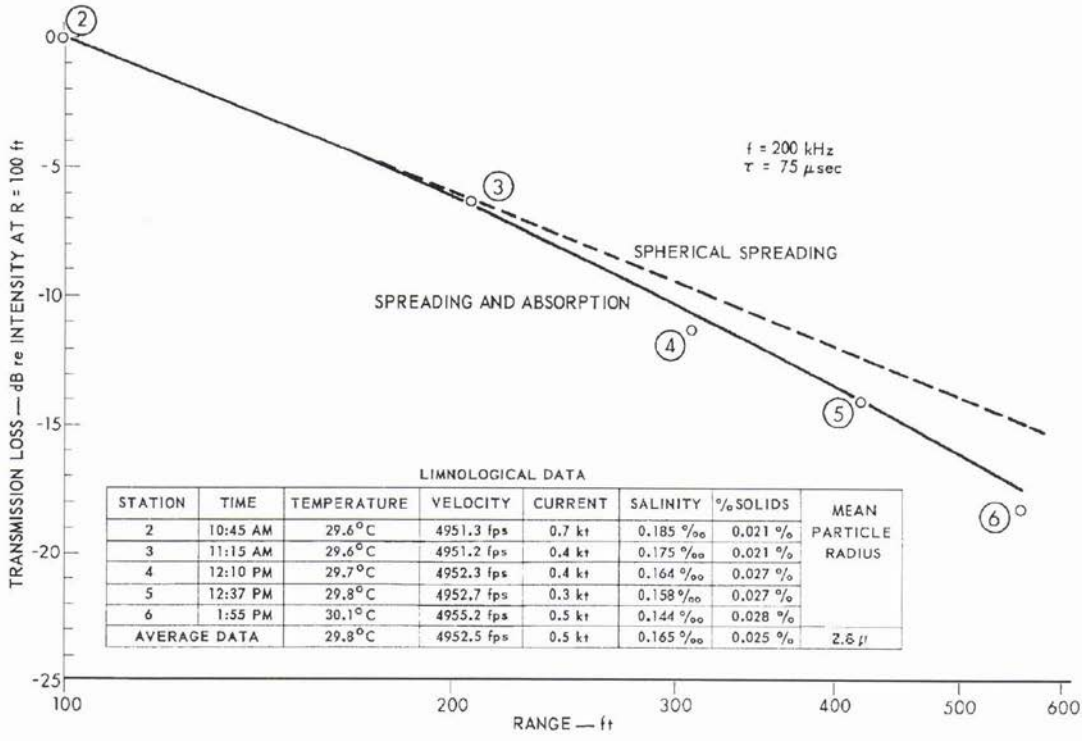

LIMNOLOGICAL DATA

STATION	TIME	TEMPERATURE	VELOCITY	CURRENT	SALINITY	%SOLIDS	MEAN PARTICLE RADIUS
2	10:45 AM	29.6°C	4951.3 fps	0.7 kt	0.185 ‰	0.021 %	
3	11:15 AM	29.6°C	4951.2 fps	0.4 kt	0.175 ‰	0.021 %	
4	12:10 PM	29.7°C	4952.3 fps	0.4 kt	0.164 ‰	0.027 %	
5	12:37 PM	29.8°C	4952.7 fps	0.3 kt	0.158 ‰	0.027 %	
6	1:55 PM	30.1°C	4955.2 fps	0.5 kt	0.144 ‰	0.028 %	
AVERAGE DATA		29.8°C	4952.5 fps	0.5 kt	0.165 ‰	0.025 %	2.6 μ

Figure 4. Transmission loss vs range at a frequency of 200 kHz

Fig 4 shows the measured propagation curve and environmental data. Each propagation data point shown has been referenced to the first measurement which was made at a range of 30 m. The spherical spreading curve is also shown. It can be seen that a surprisingly small amount of attenuation was present. When the spherical spreading term is removed from the data, the resulting attenuation curve shows a slope of 1.5 dB per 100 m. This amount of attenuation compares to a value of about 7 dB per 100 m for sea water, so that the dB value of attenuation measured in this river is only about 20% of what one should expect from sea water. The attenuation in clear fresh water is about 0.6 dB per 100 m so that we measured a dB value that was roughly 2.5 times greater in this river than one would expect from a clear, freshwater lake.

4. Backscattering

When suspended particulates meet a salt wedge intrusion normally present in the lower reaches of riverine estuaries, they are flocculated onto the river bottom in an upper layer of recent deposition. It was this uppermost layer of predominately fine, recently flocculated particulate matter that the reverberation or acoustic backscatter had to traverse. This fluff layer had a density of 1.13 g/cc, a velocity of 1506 m/sec, a temperature of 32.4 deg C (4 degrees higher than the water column). It also had a very high attenuation of 0.27 dB per wavelength at a frequency of 300 kHz. As mentioned above, the mud beneath this layer was saturated with gas that was visible as cm size voids in cores brought to the surface. This gas undoubtedly bubbled through the fluff layer as well.

The reverberation experiment was done in the center of the channel. A piston transducer with a 10 deg half power beamwidth at 85 kHz was used in conjunction with a transmit-receive switch to study the backscattering coefficient for 500 μsec cw pulses as a function of the grazing angle the acoustic axis makes with the bottom. The transducer was positioned near the bottom on a column mounted on an anchored boat, and rotated in azimuth during data acquisition. The data were reduced according to a simple sonar equation, making the scattering coefficient referenced to the calculated area of insonification on the bottom.

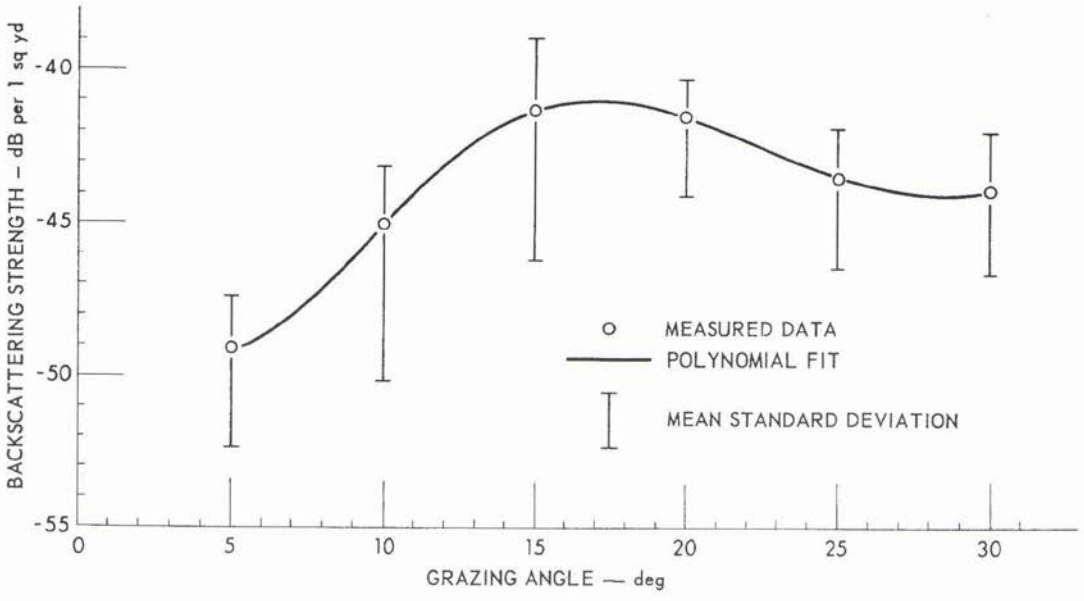

Figure 5. Backscattering from the river bottom

The backscattering results are shown in Fig 5. Each of the six experimental data points shown is representative of 36 measurements taken over a 360 deg azimuth angle in adjacent 10 deg sectors. A rough measure of the deviations is shown in the figure. The backscattering levels for these sediments fall in the very low range of scattering coefficients expected for fine mud and reported by others, notably McKinney and Anderson [1], for similar sediments in coastal areas. The data at the high grazing angles suggest a secondary "dip" in the scattering strength, which could represent an angle of intromission. It could also be due to increased bottom penetration at angles of incidence greater than the critical, or to a decrease in velocity with depth in the sediment. It was not possible to measure the velocity gradient in the mud layer beneath the fluff layer because the attenuation was in excess of 120 dB/m at 300 kHz, presumably due to the presence of gas. However, there was a negative temperature gradient of 4.5 deg C per meter of depth, and this could have easily provided for an overall velocity decrease.

5. Summary, Discussion, and Conclusions

In summary, our study of the Brazos River delineated a number of significant environmental parameters pertinent to high resolution sonar operating in a riverine estuary. The acoustic measurements showed a relatively small amount of attenuation at a frequency of 200 kHz and a rather low level of bottom reverberation at a frequency of 85 kHz.

We expect the small amount of attenuation to be due to the suspended particulate matter carried by the river. One would like to have a theoretical understanding of the mechanisms contributing to this attenuation. The viscous drag resulting from the motion of the particulates induced by the sound field is thought to be the predominant mechanism, although scattering could be expected from the very large particles. Some early researchers making laboratory measurements of particulate absorption at high concentrations, and at very high frequencies, have used a model for spherical particles developed by Lamb [2]. Urick [3] reported some measurements that showed agreement between high concentration, very high frequency measurements, and Lamb's model for irregular particles. The variables in our Brazos River study were at the other end of the spectrum from Urick's laboratory measurements in that the concentration of particulates was very low, on the order of several hundredths of a percent instead of several percent, and our frequency was in the kilohertz rather than the megahertz frequency range. The results of our Brazos River field measurements did not compare to the predictions of the Lamb-Urick math model. That model predicts an attenuation of 6 dB per 100 m while our experiment showed only 1.5 dB per 100 m. Recent theoretical and experimental work by Thorne [4] is more extensive and includes a computer based model of much greater accuracy, and it will be interesting to compare the results presented here to Thorne's model.

The low level of backscattering we observed may be due to the highly absorptive, uppermost layer of fine, gas infiltrated mud, which may also be a poor backcatterer, making this type of river bottom less reverberant at low grazing angles, despite the presence of a large gas concentration in the underlying mud. It appears that backscattering from estuarine river bottoms

like this one may be predictable from measurements reported in the literature for similar bottoms in coastal areas. The variation of backscattering strength as a function of discharge rate, and consequently of the degree of bottom scouring should, however, make an interesting subject of future study, as would the effect of the entrapped gas in the intermediate mud layers.

The supporting environmental measurements in this study on the sediment load and bottom material content may be useful to those modelling high resolution sonar performance, specifically on issues relating to attenuation and backscattering. Unfortunately, it is very difficult to acquire meaningful in situ measurements on gas content in mud. The question remains as to what environmental measurements are really necessary to characterize the medium in a way that will advance the science of high frequency sonar. A concurrent question remains as to what techniques should be exploited for rapid assesment for operational requirements involving mine countermeasures sonar.

There are undoubtedly newer measurement tools available today that facilitate the acquisition of riverine acoustical and environmental data, reducing time on station, and allowing for the making of more extensive measurements. However, some things do not change, and these apply to the basics. We derived much information from cores, which we acquired ourselves, by pressing clear plastic tubes into the river bottom. We also learned a great deal by by diving to the pitch black bottom of the river and feeling by hand the locations of interfaces between the layers as well as their their lateral extent. This was actually quite easy to do. It was amazing how much could be learned by "braille". The sedimentary layers were readily identifiable by their relative shear strengths. The interfaces between layers were typically quite level and smooth - except for the channel sand and concretions which had a rougher "feel", due to some large and small stones plus clay balls and twigs at the interface. One of us (Anderson) distinctly remembers lying on the bottom in darkness, partially buried in the upper muddy layers, and while developing information by "feel" for the representative geological cross section of the river, experienced some frequent 'nips' at his bare sides where his body emerged from the mud into the water. The first few times that happened, he fervently hoped that it was small fish or crabs at the worst, and not something like sharks or piranha like predators tasting a potential meal.

Acknowledgements

The authors would like to thank W.H. Tolbert, R.S. Adair, R.L. Batey, and J.G. Willette (deceased) for their assistance in data acquisition. This work was sponsored by the U.S. Navy Office of Naval Research.

References

[1] C.M. McKinney and C.D. Anderson, "Measurements of Backscattering of Sound from the Ocean Bottom," J. Acoust Soc. Am., vol. 36(1), pp. 158-163, 1964.

[2] H. Lamb, Hydrodynamics, Articles 361-363, 6th Ed., Dover Pubs., New York, 1945.

[3] R.J. Urick, "Absorption of Sound in Suspensions of Irregular Particles," J. Acoust. Soc. Am., vol. 20(3), pp. 283-289, 1948.

[4] P. Thorne, private communication.

Shallow Water Propagation Incorporating Both Bubble Plumes and Sea-Surface Roughness

Guy V. Norton

Naval Research Laboratory - Stennis Space Center
Stennis Space Center, MS 39529-5004
Email: norton@vixen.nrlssc.navy.mil

Jorge C. Novarini

Planning Systems Incorporated
21294 Johnson Rd. Long Beach, MS 39560-9702
Email: nova@felix.nrlssc.navy.mil

Abstract

The effect of including a range dependent bubble layer and a suitable sea surface spectrum in modeling shallow water propagation is analyzed. Propagation is simulated through a highly accurate model based on a modified PE algorithm which handles surface roughness via conformal mapping. The bubble layer is modeled as a collage of bubble plumes and is included through a complex index of refraction. Propagation at 5 kHz in a 30 m isovelocity waveguide is analyzed in detail.

1. Introduction

Among the many factors affecting the propagation of sound in shallow water, the presence of surface-generated microbubbles has received little attention. The collection of microbubbles which is normally assumed to form a uniform layer, actually presents a very complex structure that varies not only in depth but also in range, and can be characterized as a collage of bubble clouds. This collage creates a strong range-dependent perturbation in the index of refraction and introduces additional attenuation. A numerical procedure is adopted in which a type of bubble cloud (the plume) is modeled following a classification scheme proposed by Monahan [1,2]. The resulting complex index of refraction is then calculated. Since in waveguide propagation the surface roughness mainly causes a re-distribution of energy, the use of a high fidelity model to handle roughness in the presence of strong gradients is essential to obtaining accurate results. An acoustic propagation model, which couples a conformal mapping algorithm to a PE model which properly handles sea surface roughness is used to generate the numerical results [3]. To properly model the sea-surface roughness characteristic of shallow waters, the parametric spectrum GONO has been implemented [4]. The combined effect that the sea surface roughness along with the refractive and lossy bubbly environment have on transmission loss and coherence is examined. The case of a point source, operating at 5 kHz in a 30 m depth isovelociy shallow water waveguide is analyzed in detail.

2. Methodology

2.1 Modeling the Bubble Assemblages

The presence of microbubbles is included through a range-dependent bubble layer made up of different bubble assemblages, namely, bubble plumes and a weak background layer. Due to the lack of information on bubble plumes in shallow water we have adopted and modified a scheme proposed by Monahan for classifying plumes in deep water. Monahan [1,2] postulated the existence of three types of plumes (α, β, γ). He associated two of

them with two stages of whitecap development (stage A and stage B). The α-plume is the subsurface extension of the stage A whitecap which is attached to the crest of the spilling breaker. Although they present the highest void fraction, O (10^{-1} to 10^{-2}), they are very small in size and have a very short lifetime (< 1 sec.). The α-plume quickly decays into a β-plume once the momentum of the downward moving jet associated with the breaking wave is dissipated. Accordingly, the stage A whitecap evolves into a foam patch (stage B whitecap). The β-plumes have a much smaller void fraction, O (10^{-3} to 10^{-4}), and are attached to the foam patch. That is, the stage B whitecap is the top of the β-plume. They are spatially much bigger than the α-plume and have longer lifetimes (about 4 sec). The β-plume then evolves into a γ-plume and eventually detaches from the originating whitecap. The γ-plumes have an even smaller void fraction, O (10^{-6} to 10^{-7}), much larger dimensions, and longer lifetimes (10 to 100 times longer) than the β-plume. They drift and may be affected by circulation processes (such as Langmuir cells). Although Monahan identifies the γ-plume with Thorpe's clouds [5], which allows for both billowy and columnar types, his description of the geometrical aspect (exponentially decreasing cross-section) better fits the columnar type. The γ-plume decays into a weak, stratified background layer with a void fraction, O (10^{-8}). Both the β and γ-plumes are modeled as conical intrusions with cross-sections that decrease exponentially with depth, as prescribed by Monahan and consistent with the v-shape described by Crawford and Farmer [6]. Monahan also provided typical values (void fraction, bubble density at 100 μm, size, penetration scale) for the different bubble assemblages.

In the original Monahan's scheme, the spectral shape for the different stages are essentially identical to each other (spectral slope for large bubbles close to -4). However the bubble concentration and hence the void fraction is different for each plume. However, short time sampling of bubble data gathered close to the surface under breaking waves [7,8,9] show spectral slopes for large bubbles shallower (about -2.5) than those coming from long term averages at deeper depths (-4 and steeper) [10]. Wu suggested that both types of slopes can coexist, the shallower slope close to the breaker and the steeper slope away from the breaker [11]. This can be re-interpreted in terms of Monahan's classification as inside a β-plume for the steeper slope or inside either the γ-plume or the background layer for the shallower slope. Therefore, we have adopted the scheme proposed by Monahan as the basic framework for classifying the different assemblages of microbubbles, with the spectra proposed by Monahan for the different stages having been modified based on more recent findings and Wu's interpretation relating measured spectral slopes for large bubbles with the proximity of the bubble assemblage to the breaker. The α-plumes are not included in the modeling, because of their small size and physical connection to the breaking crests, which are not modeled in the numerical surfaces (the α-plume can be thought of being contained within the crest of the breaking wave).

To parameterize the plumes we have adopted a parameterization scheme similar to that commonly used for the "average, uniform bubble layer," i.e., writing the bubble density per unit volume (bubbles per cubic meter in a 1 μm radius increment) within a given assemblage as

$$n(a,z,u) = N_0\, G(a,z)\, Z(z)\, U(u) \qquad (1)$$

where a is the bubble radius, z is depth, and u is the wind speed. The function G describes the spectral shape, Z the depth dependence, U controls the wind dependence, and N_0 is a constant with controls the bubble density so as to fit Monahan's reference points for the different assemblages (plumes and background layer). Following Monahan, the β-plumes are assumed to have uniform density in depth, while the γ-plume and the background layer decay exponentially. Since, in the present scheme the maximum penetration of the β-plume is assumed to be equal to one-half the significant waveheigth (h_s) of the surface roughness, it is adjusted to the shallow water case by adopting h_s coming from the GONO spectrum which is described in the next section. The cross sectional area of the β and γ-plumes are also exponential in depth. For a full description of the adopted spectra, see Novarini, *et. al.* [12]. Figure 1a shows the bubble density spectra for a 15 m/s wind speed, at 0.25 m below the surface. The collection of plumes are randomized by imposing stochastic fluctuations to: the separation between plumes, the e-folding depth, the area cross-section and the constant N_0 within each realization of the environment.

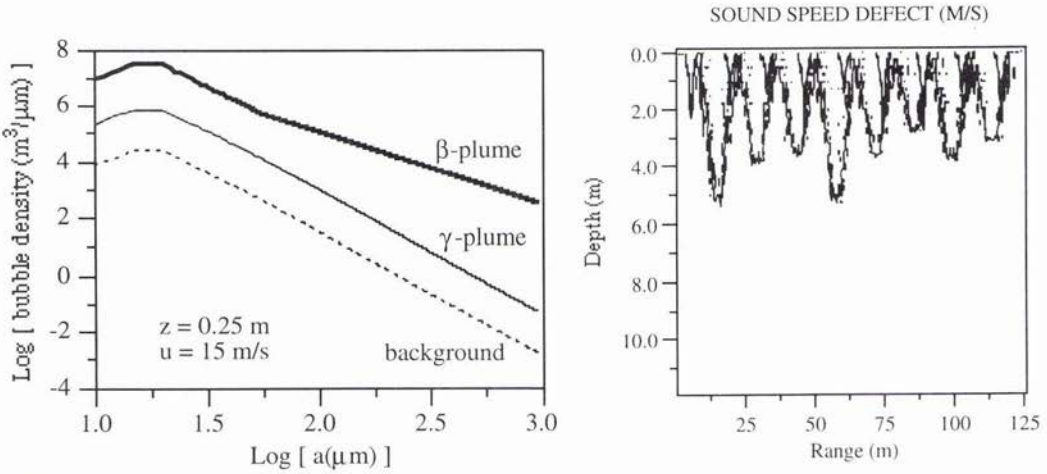

Figure 1 Bubble plume spectra and sound speed defect. a) Bubble spectra for the β and γ-plume, along with the background bubble layer. b) Sound speed defect in m/s, verse depth and range for a 15 m/s wind speed. Contours are 1000 m/s and 1 m/s.

The sound speed perturbation and the additional attenuation are calculated from the change of compressibility introduced by the bubbles. The calculation is carried out following Clay and Medwin [13], integrating over all bubbles, with due regard to viscous and thermal effects. The limits of numerical integration over the bubble radii are 10 and 1000 μm. The effect of the bubbles at a frequency of 5 kHz is to reduce the sound speed and introduce an additional attenuation. Close to the surface (0.25m), for a wind speed of 15 m/s a sound speed defect on the order of 1,210 m/s occurs within the β-plumes (void fraction $8x10^{-4}$). For the γ-plumes the corresponding defect is on the order of 22 m/s (void fraction $1.5x10^{-6}$), while the background layer reduction is about 0.7 m/s (void fraction $5x10^{-8}$). The corresponding attenuation values are 4.4, $6.3x10^{-3}$, and $2x10^{-4}$ dB/cm, respectively. Figure 1b shows a contour plot of the resulting sound speed defect over a short segment of the environment, for a 15 m/s wind. The smaller and sharper intrusions are the 1000 m/s sound speed defect contour which outlines the shape of the β-plumes. The other contour line corresponds to 1 m/s sound speed defect, which essentially delimits the region of significant influence of the γ-plumes. For this example the sound speed defect within the γ-plumes ranges from about 26 m/s very close to the surface to about 0.1 m/s 13m below the surface.

2.2 Modeling the Sea Surface

GONO [4] is a parametric spectrum for wind-driven seas in shallow water. The main parameter is the stage of development ζ of the depth-limited wave growth, defined as

$$\zeta = \sqrt{\frac{h_s}{h_s^{dw}}} \tag{2}$$

where h_s is the significant waveheight for the shallow water site and h_s^{dw} is the corresponding value for a fully developed deep water case at the same wind speed. The spectrum has the form,

$$S(f) = \begin{cases} 0 & 0 \le f \le f_{min} \\ \dfrac{\hat{\alpha} g^2 (f - f_{min})}{(2\pi)^4 f_p^5 (f_p - f_{min})} & f_{min} < f \le f_p \\ \dfrac{\hat{\alpha} g^2}{(2\pi)^4 f^5} & f > f_p \end{cases}$$

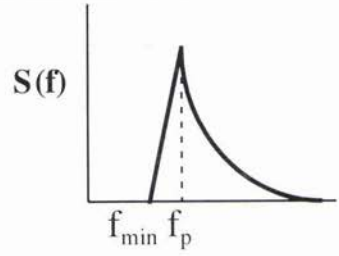

Figure 2. Numerical and graphical representation of the GONO spectrum.

where the spectral parameters are given by the following empirical equations:

$$\hat{\alpha} = \text{modified Phillips "constant"} = 4.93\text{x}10^{-3}\ \zeta^{-1.944} \tag{3}$$

$$\nu = \text{normalized peak freq} = uf_p/g = 6.89\text{x}10^{-2}\ \zeta^{-1.376}/\beta \tag{4}$$

and

$$f_{min} = \mu f_p;\ \mu = \tfrac{1}{2}\left[3 - \frac{4(2\pi)^4 f_p^4 E}{\hat{\alpha} g^2}\right];\ E = \frac{h_s^2}{16};\ \beta = 0.21 \tag{5}$$

The basic assumptions are that dissipation at the bottom is limited to the forward face of the spectrum, and that during the building-up of a wind-driven sea, the bottom dissipation manifests itself rather sharply. The high frequency side of the spectrum has the same decay that the Pierson-Moskowitz spectrum has for deep water (i.e., proportional to f^{-5}). The spectrum requires the knowledge of the significant waveheight for the shallow water site, which can be obtained from satellite observation; visual estimation, etc.. For practical applications in acoustics it is desirable to have the wind speed as the main parameter. A procedure to accomplish this has been developed by Sanders and Bruinsma [4]. It starts with the total energy in the wave system of a deep water case for the given wind speed and assumes all dissipation of the long wave components is due to friction at the bottom. The energy of the wave system is then obtained at the specified water depth by solving an ordinary differential equation with a term describing non-linear dissipation. Once the total energy (E) for the shallow water case is known, the corresponding significant waveheight is given by $h_s = 4\ E^{1/2}$. This value is then used to obtain the spectral shape as outlined above.

Surface realizations of the sea surface (1D) were generated by linear filtering of an array of uncorrelated random numbers whose transfer function is proportional to the square root of the desired power density spectrum. Both GONO and Pierson-Moskowitz spectra are non-directional, originally expressed in terms of the frequency of the waves. They were converted to the wavenumber domain via the dispersion relation connecting frequency with wavenumber for 1-D surfaces, which implicitly assumes all the energy goes in the windward direction.

2.3 Inclusion of Rough Surface

When the effect of the surface roughness is included, it is normally done so by introducing an additional loss mechanism. However, since the surface roughness causes a redistribution of energy, the method of including a loss mechanism to account for the rough surface will not be adequate. Hybrid approaches have been developed to account for the re-distribution of energy induced by the surface roughness. They utilize statistical kernels from sea surface scattering theories in connection with deterministic propagation models [14,15]. Although this type of methodology may improve the calculation of transmission loss, coherence effects are not properly included. Operating in coastal areas where the wave amplitude may become a significant fraction of the water column, strong mode coupling results and perturbative approaches are no longer appropriate. Note that inclusion of a rough surface transforms a range independent problem into a range dependent one.

The approach used to generate the numerical results in this work combines an acoustic propagation model with a conformal mapping algorithm to handle surface roughness in a mathematically consistent manner. The model EFEPE-CM [3] combines the energy-conserving finite element PE propagation model [16] with Dozier's conformal mapping formalism [17] to obtain the acoustic field from a single realization of the environment. The quantities of interest (transmission loss, modal amplitudes, etc.) are then calculated through ensemble averages. The model has been shown to achieve results of benchmark quality for the problem of scattering from randomly rough surfaces [3].

3. Numerical Experiment

The environment for this numerical experiment, is as follows. The water depth is 30 m and constant over a range of 3000 m. An isovelocity, homogeneous water mass was assumed for the bubble-free environment (sound speed = 1500 m/s). The sediment was modeled as a semi-infinite half space of constant sound speed (1541 m/s) and density (1.5 gm/cm^3). Both GONO and Pierson-Moskowitz sea-surface spectra were used to generate the necessary deterministic surfaces. The different surfaces and bubble fields were each characterize by varying the local wind speed (15 and 20 m/s). The acoustic frequency is 5 kHz. The source depth is 5 m.

It is instructive to observe the effect that combining a single β and γ-plume with the background bubble layer has on the propagating field. It is insightful, because we see that even though the individual plumes are small

and spatially do not account for a large area, the effect that they have on the acoustic field is significant. Therefore, utilizing a wind speed of 15 m/s and keeping the sea-surface flat, a single β-plume was placed at a range of 500 m, followed by a γ-plume at a range of 550 m. The β and γ-plume had a width at the surface of approximately 4.5 and 13.5 m respectively. For this example, the plumes did not overlap. The weak background bubble layer spanned the range of 500 to 600 m. The complex acoustic field was determined for this environment. This bubble field was then removed and the complex acoustic field once again determined. The two fields were differenced and the resulting field was converted into an intensity and expressed in dB. Figure 3a depicts this result. Note that before 500 m there is no difference between the two fields since the environments were the same up to this range. However, this rather simple and small bubble field results in multiple beams, one being quite significant. The refractive effects of the two types of bubble plumes can be seen. The process is repeated, except now where the bubbles are present, a rough surface is included (between the ranges of 500 and 600 m). Figure 3b depicts this result. The effect of the rough surface is to redirect the acoustic field at all angles in the forward direction. The beams which were present when the surface is flat have been destroyed. Also note that the strength of the difference for this case (bubble plumes with rough surface and isovelocity with flat surface) is greater than that observed for the previous case.

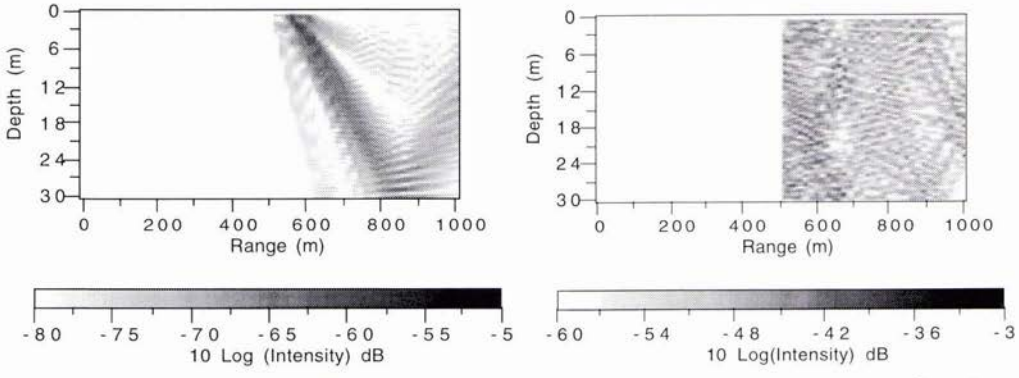

Figure 3. Depth vs. range difference plots. a) Difference in the acoustic fields when a single β, γ-plume and background bubble layer are located between 500 and 600 m and when they are removed. Flat surface used in each case. A wind speed of 15 m/s is assumed. b) Difference in the acoustic fields when a single β, γ-plume and background bubble layer and a rough surface are located between 500 and 600 m and when they are removed. A wind speed of 15 m/s is assumed.

The remaining comparisons will be between environments consisting of rough surfaces using the GONO spectrum with bubble plumes and background bubble layer (bubbles) and rough surfaces using the Pierson-Moskowitz spectrum in the bubble free environment (no bubbles). Two local wind speeds were used, 15 and 20 m/s. These combinations were selected because for the most part bubbles are ignored and when the effect of a rough sea-surface is included, it is often based on a deep water spectrum.

Transmission loss vs. range is now compared for both environments at the two different wind speeds for a single realization of each rough surface. The receiver depth is 15 m, or mid-waveguide depth. Figure 4 depicts the results. Figure 4a compares the results for a wind speed of 15 m/s. Note the GONO with bubbles result (solid line) shows more loss than the Pierson-Moskowitz without bubbles result (dashed line), even though the rms surface height based on the GONO spectrum (1.0 m) is smaller than that from the Pierson-Moskowitz spectrum (1.4 m). This difference in transmission loss is due in large part to the additional attenuation that the plumes introduce. The difference can be as large as 10 dB. Figure 4b is the same comparison except for a wind speed of 20 m/s. Again note that the GONO with bubbles result (solid line) shows more loss than the Pierson-Moskowitz without bubbles result (dashed line), even though the rms surface height based on the GONO spectrum (1.2 m) is smaller than that from the Pierson-Moskowitz spectrum (2.5 m).

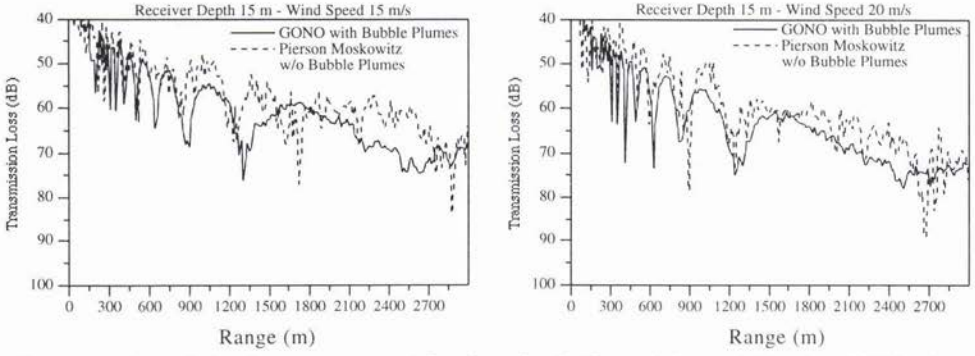

Figure 4. Transmission loss vs. range. a) Receiver depth 15 m, wind speed 15 m/s. GONO with bubbles (solid line) and Pierson-Moskowitz without bubbles (dashed line). b) Receiver depth 15 m, wind speed 20 m/s. GONO with bubbles (solid line) and Pierson-Moskowitz without bubbles (dashed line).

The dependence of transmission loss vs. depth will now be examined using an ensemble of surfaces. Figure 5a shows the results for an ensemble of ten surfaces each from the GONO and Pierson-Moskowitz spectrum. The bubble plumes were used only with the GONO surfaces. The quantity <PP*>, which is proportional to the total intensity, is plotted vs. depth at a range of 3 km. The GONO with bubbles result is the solid line while the Pierson-Moskowitz without bubbles is the dashed line. Note that the result based on the GONO spectrum with bubbles shows more loss throughout the depth of the waveguide and has a maximum difference at the surface. The large difference at the surface is due to the additional attenuation introduced by the bubbles. Overall the two results have the same general shape, showing a notch at approximately 12 m. In addition the Pierson-Moskowitz result has more oscillations in depth. It is of interest to compare the results coming from the present model with those obtained from a standard propagation code under the assumption of a range independent, isovelocity environment (i.e. ignoring bubble plumes and including the rough surface in an approximate manner). To that end we ran SNAP [18], assuming isovelocity water sound speed and with the surface roughness routine activated. The rms surface heights corresponding to the two different spectra for a wind speed of 20 m/s were used. The results are shown in Fig. 5b. The result using 1.2 m rms surface height, corresponding to the GONO surface, is shown with the solid line. The result using 2.5 m rms surface height, corresponding to the Pierson-Moskowitz surface, is shown with the dashed line. The result using the smaller rms surface height shows less loss than when using the larger rms surface height, opposite to what was observed when using EFEPE-CM with an ensemble of rough surfaces. The location of the notch is at 15 m as opposed to 12 m for the EFEPE-CM result.

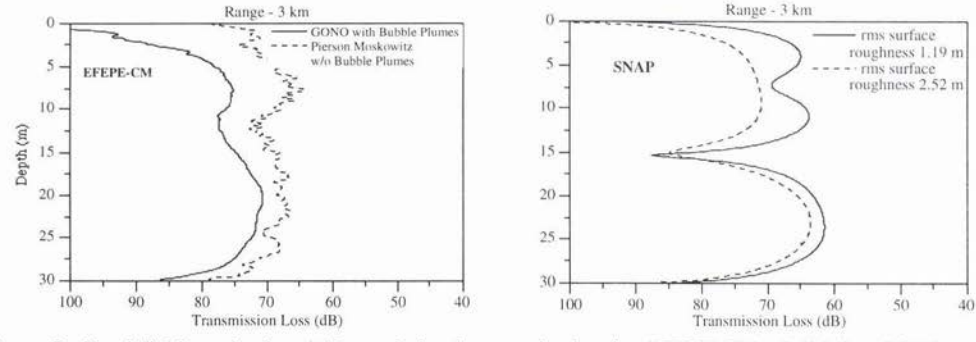

Figure 5. Total field vs. depth. a) Transmission loss vs. depth using EFEPE-CM. Solid line GONO spectrum with bubbles, dashed line Pierson-Moskowitz without bubbles. Ten surfaces in the ensemble. b) Transmission loss vs. depth using SNAP. Solid line, rms surface height 1.19 m (corresponding to GONO spectrum). Dashed line, rms surface height 2.52 m (corresponding to Pierson-Moskowitz spectrum).

Finally the degree of coherence is compared for the two environments (GONO with bubbles and Pierson-Moskowitz without bubbles) at three ranges 1, 2, and 3 km. The degree of coherence is determined by

$$\Gamma = \frac{\left| < PP_0^* > \right|}{\left[< PP^* >< P_0 P_0^* > \right]^{1/2}} \tag{6}$$

where P and P_0 are the complex acoustic pressures for the environment with bubbles and rough surface, and no bubbles and flat surface respectively, while the asterisk (*) denotes the complex conjugate of the corresponding complex acoustic pressure.

Figure 6 depicts the results for the three ranges. Note in each case, the GONO spectrum with bubbles result shows a higher degree of coherence. In addition, the variability in depth decreases with range for both cases but more for the case of the GONO spectrum with bubbles. It is interesting that for both cases the degree of coherence at 1 km has the largest variation which indicates that these fields are most different from the flat surface, isovelocity case at short ranges. This is due to the fact that, initially as the field propagates, the steeper angle (higher-order) modes are stripped-off leaving the interaction with the surface to shallower angle (lower-order) modes. Therefore, the perturbative effect of the surface roughness on the phase of the propagating field diminishes with range. For the case of the GONO spectrum with bubbles, a uniform distribution of Γ with depth is quickly achieved. This is because the high attenuation induced by the bubbles close to the surface prevents the scrambling effect that the rough surface causes on the phase of the propagating field.

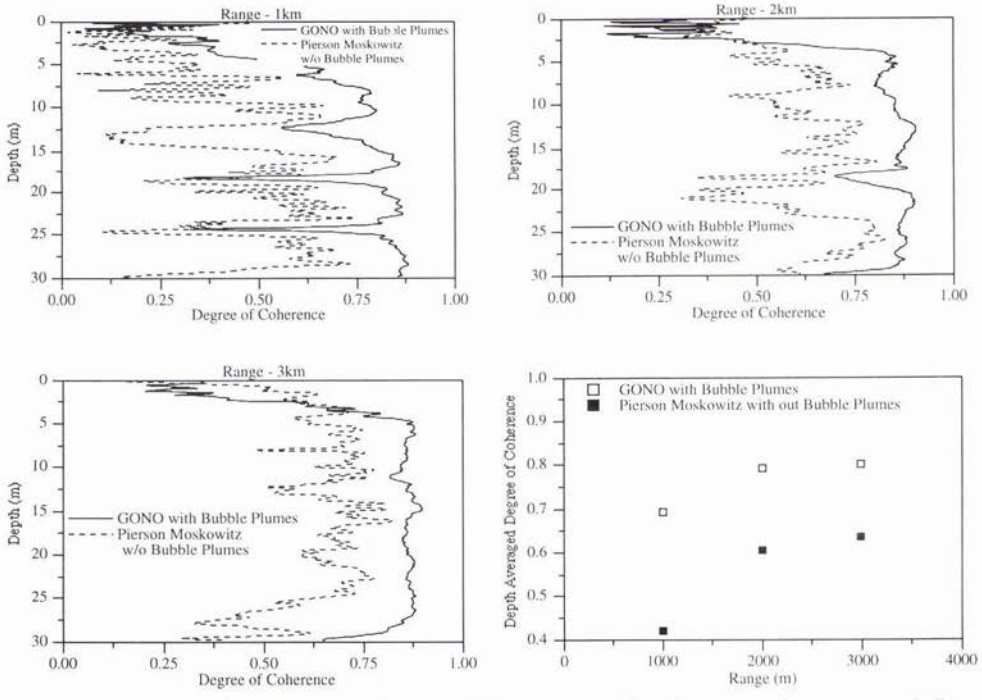

Figure 6. Degree of coherence vs. depth for 3 different ranges for the two environments. a) Degree of coherence vs. depth at 1 km. GONO with bubbles, solid line. Pierson-Moskowitz without bubbles, dashed line. b) Degree of coherence vs. depth at 2 km. GONO with bubbles, solid line. Pierson-Moskowitz without bubbles, dashed line. c) Degree of coherence vs. depth at 3 km. GONO with bubbles, solid line. Pierson-Moskowitz without bubbles, dashed line. d) The depth averaged degree of coherence vs. range for the two environments. GONO with bubbles un-shaded square, Pierson-Moskowitz without bubbles shaded square.

Finally, a depth averaged degree of coherence is obtained by averaging the values obtained at each range over depth. The results are shown in Fig. 6d. At each range, values for the GONO with bubble result are larger than those for the Pierson-Moskowitz without bubbles result. However the trend is the same for each case, that is, the average degree of coherence increases with range. With the limited data shown, it appears that for each case, the average degree of coherence is converging to a different value for each environment.

4. Concluding Remarks

The standard procedure of ignoring the presence of bubble clouds and resorting to a deep water sea-surface spectrum when modeling shallow water propagation at high frequencies leads to significant errors in both, transmission loss and coherence calculations. For the numerical experiment discussed in this work, transmission losses are underestimated by about 5 to 10 dB, and a lower degree of coherence of the propagating field is predicted. Large discrepancies are observed when results from the present model are compared to an acoustic model which treats the waveguide as range independent, ignores bubbles, adopts a deep water sea-surface spectrum and handles surface roughness in an approximate manner.

5. Acknowledgments

This work has been supported by the Office of Naval Research and a grant of HPC time from the DoD HPC Shared Resource Center, CEWES Cray YMP and NAVO Cray C90.

References

[1] Monahan E. C., Proc. 7th Conference on Ocean-Atmosphere Interaction, Anaheim, CA, Amer. Meter. Soc. 188 (1988).

[2] Monahan, E. C. Natural Physical Sources of Underwater Sound, Ed. by B .v R. Kerman, 503, (1993).

[3] Norton, G. V., Novarini, J. C. and R. S. Keiffer, "Coupling scattering from the sea surface to a one-way marching propagation model via conformal mapping: Validation," J. Acoust. Soc. Am. **97**, 2173-2180, (1995).

[4] Sanders J. W. and J. Bruinsma, in Wave dynamics and radio probing of the ocean surface, pp. 615- 637. Edited by O. M. Phillips and K. Hasselmann, Plenum Press, N. Y. (1986).

[5] Thorpe, S. A., "On the clouds of bubbles formed by breaking waves in deep water and their role in the air-sea gas transfer, " Philos. Trans. R. Soc. London Soc. A **304**, 155-210 (1982).

[6] Crawford G. B. and D. M. Farmer, "On the spatial distribution of ocean bubbles," J. Geophys. Res. **92**, C8, 8231-8243 (1987).

[7] Medwin, H. and N. Breitz, "Ambient and transient bubble spectral densities in quiescent seas and under spilling breakers, " J. Geophys. Res. **94**, 12751-12759 (1989).

[8] Su, M. Y., R. Burge and J. Cartmill, "Measurements of near-surface microbubble density during SWADE," (Unpublished).

[9] S. Baldy, "Bubbles in the close vicinity of breaking waves: Statistical characteristics of their generation and dispersion mechanisms," J. Geophys. Res. **93**, 8239-8248 (1988).

[10]Johnson R. C., and B. D. Cooke, " Bubble population and spectra in coastal waters: a photographic approach," J. Geophys. Res. **84,** 3761-3766 (1979).

[11]Wu, J., "Bubbles in the near-surface Ocean: Their various structures," J. Phys. Oceanog. **24**, 1955-1965 (1994).

[12]Novarini, J. C., R. S. Keiffer and G. V. Norton , "A model for variations in the range and depth dependence of the sound speed and attenuation induced by bubble clouds under wind-driven sea surfaces," (Unpublished).

[13]Clay C. S. and H. Medwin, Acoustical Oceanography, John Wiley, New York , pg. 471 (1977).

[14]Dozier, L. B., J. S. Hanna, and C. R. Pearson , in Ocean Variability and Acoustic Propagation, edited by J. Potter and A. Warn-Varnas (Kluwer Academic, Dordrecht), 265-281, (1991).

[15]Schneider, H. G., "Surface loss, scattering and reverberation with the split-step parabolic wave equation model," J. Acoust. Soc. Am. **93**, 770-781 (1993).

[16]Collins, M. D., "A split-step Pade solution for the parabolic equation method," J. Acoust. Soc. Am. **93**, 1736-1742 (1993).

[17]Dozier, L. B., "PERUSE: A numerical treatment of rough surface scattering for the parabolic wave equation," J. Acoust. Soc. Am. **75**, 1415-14432 (1984).

[18]Jensen, F. B. and M. C. Ferla, "SNAP: The SACLANTCEN Normal-mode Acoustic Propagation model," SACLANTCEN Memorandum SM-121, 15 January 1979.

High-Resolution Characterization of Seafloor Sediments for Modeling Acoustic Backscatter

Thomas H. Orsi[†], Michael E. Duncan[†], Anthony P. Lyons[‡], Kevin B. Briggs[§], Michael D. Richardson[§] and Aubrey L. Anderson[*]

[†]Planning Systems Incorporated
115 Christian Lane
Slidell, LA, U.S.A.
Email: torsi@psislidell.com; mduncan@psislidell.com

[‡]SACLANT Undersea Research Centre
Viale San Bartolomeo 400
19138 La Spezia, ITALY
Email: lyons@saclantc.nato.int

[§]Naval Research Laboratory
Stennis Space Center, MS, U.S.A.
Email: kbriggs@zephyr.nrlssc.navy.mil; miker@zephyr.nrlssc.navy.mil

[*]Department of Oceanography
Texas A&M University
College Station, TX, U.S.A.
Email: aanderson@ocean.tamu.edu

Abstract

Quantitative information on fine-scale sediment inhomogeneity is extremely scarce and sorely needed for developing realistic volume scattering models. To address this deficiency, we present a novel approach for sediment core characterization, X-ray computed tomography (CT). By providing a means to construct extremely fine-scale density profiles and to quantify volume inhomogeneities in two- and three-dimensions, CT analyses can assist efforts in characterizing benthic processes and result in more accurate inputs for modeling acoustic backscatter.

1. Introduction

At the high frequencies used by many sonar systems, the spatial structure of the sediment's physical properties plays a key role in determining the scattering characteristics of the seafloor. This spatial heterogeneity, however, is exceedingly complex with three-dimensional characteristics that have largely defied measurement by traditional methods. Aside from the fact that rather coarse laboratory sample intervals are necessary to obtain statistically reliable values (on the order of a few centimeters), the physical property measurement is usually an integrated value in which some spatial information is lost. As a result, quantitative information on near-surface fine-scale sediment inhomogeneity is lacking, particularly at spatial scales used in the development of realistic volume scattering models. To address this lack of information, we present a novel approach to sediment core characterization, X-ray computed tomography (CT). We have found CT to be a powerful analytical technique for characterizing sediment cores: it is non-destructive and quantitative, has sub-millimeter resolution, and permits two- and three-dimensional visualization of sediment structure [1, 2]. We begin by briefly discussing the physics and mechanics of CT and CT scanners. We then describe several CT applications useful for high-frequency acoustic modeling.

2. CT Principles and Approach

Non-destructive testing techniques have been used for decades in geotechnical engineering, geology, and soil science to examine the internal structure of rock and sediment samples. X-radiography, one of the more common of these techniques, is based on the differential transmission loss of radiation through a substance. The technique remains popular because it is rapid, non-destructive, and provides information concerning density variations within a sample. Despite its popularity,

several problems arise when using X-ray transmission images for quantitative purposes: (1) a large proportion of available information is lost when three-dimensional structures are superimposed on two-dimensional photographic film; (2) the ability to record and/or display small differences (1-2%) in radiation transmission is limited because of film non-uniformities; and (3) much of the detected radiation is scattered "out-of-plane" from within the specimen [3, 4]. Thus, X-radiography is of limited value for our purposes.

X-ray computed tomography (CT) is a medical technique developed during the early 1970's to generate cross-sectional X-ray images of the brain [5]. Also called computer-assisted tomography or CAT scanning, CT is a method of reconstructing detailed cross-sectional images of a sample from a series of projections taken at angular increments about the object. Although CT is similar to conventional radiography, it differs in several key ways [3]: (1) there is no superimposing of structures due to the geometry of the apparatus and characteristics of the radiation beam; (2) contribution of scatter to the detected signal is minimized through the use of a finely collimated X-ray beam; (3) high signal-to-noise detectors used in CT scanners permit the recording of attenuation differences as small as 0.1%; and (4) sophisticated image reconstruction algorithms solve for X-ray attenuation of a local volume element independent of the surrounding media.

The medical community quickly demonstrated the diagnostic power of CT in their analysis of body tissues and in the detection of tumors. Industrial and scientific applications that soon followed have studied an amazing diversity of materials, ranging from tomatoes and trees, mummies and fossils, concrete and meteorites, to rock and ice. Applications more relevant to marine geoacoustics include those of soil scientists and agricultural engineers who have used CT to examine soil bulk density, water content, macroporosity, and water-plant root interactions [6]. Vinegar and others [7] pioneered its use in the characterization of oil reservoir rock cores and flow processes. As a result CT studies are common in the petroleum industry. In contrast, CT applications to technical problems in marine geology and geotechnical engineering have thus far been more limited in scope [see Ref. 1], although each has demonstrated convincingly the utility of CT. Interestingly, the geoacoustic modeling community is only beginning to appreciate the power of CT data and its potential benefit for model development in high-frequency acoustics.

For CT analysis, a sample is centered within a circular gantry which supports the X-ray source and a bank of detectors. Depending on the generation (i.e., style) of the scanner, either the source and detectors rotate together around the sample in a circular path, or the source rotates about a stationary detector bank, measuring X-ray attenuation along multiple ray paths through the sample. Each source-detector location provides a line integral measurement of X-ray attenuation, called a ray sum. Ray sums are generally made over a span of locations >180° and then combined and transformed via a computer interface into a two-dimensional "map" of attenuation coefficients using a filtered back-projection reconstruction algorithm. The data, in the form of a numerical matrix generally 256 x 256 or 512 x 512 elements in size, can be viewed on a dedicated video monitor where pixel brightness (or color) is proportional to the associated X-ray attenuation value for that element. Alternatively, as we have done, the stored digital data can be output for further analysis on a workstation using standard image processing techniques.

3. CT Applications

We have used CT techniques to characterize cores from various environments and sediment types, including: (1) gassy lacustrine muds from central Texas [8]; (2) high-porosity (and commonly gassy) muds of Eckernförde Bay, western Baltic Sea [9]; (3) sandy shell hash of the Louisiana continental shelf [10]; (4) fine to medium quartz sands off Panama City, FL [11, 12]; and (5) sandy calcareous muds off Marquesas Keys and Dry Tortugas, FL [13, 14]. Currently, we are using CT to examine bioturbated muds off Orcas Island, WA, and heterogeneous sediments at the California STRATAFORM site. In the following, we discuss two CT applications relevant to the development of realistic acoustic backscatter models: (1) the transformation of CT numbers to equivalent sediment bulk density for deriving high-resolution density profiles of the seafloor; and (2) characterization of sediment volume inhomogeneities, such as those found in gassy, shell-bearing, and/or bioturbated seafloor sediments.

3.1 Construction of High-Resolution Density Profiles

Among geoacoustic parameters, bulk density often exhibits strong gradients in the upper 30 cm of the seafloor [11]. While these high-gradient layers are relatively thin compared to low-frequency wavelengths, they can be very important at higher frequencies (10-100 kHz). This is due to the fact that at shorter wavelengths the interaction of these layers with a sonar signal may lead to a frequency-dependent acoustic impedance profile. The effects of the density profile on high-frequency reflection and transmission of acoustic energy, as well as, on surface and volume scattering strengths have a direct impact on the detection of buried objects, classification of bottom/subbottom types, and determination of propagation loss.

With respect to geoacoustics, one of the more advantageous characteristics of CT is its strong linear dependency on sediment density (Figure 1A). Historically, the most common way of determining the seafloor density structure has been through laboratory analysis of "undisturbed" sediments obtained either by divers or by subsampling box cores. To determine its density structure, a sediment core is transported to the laboratory (or any processing area) where the material is either extruded or collected after splitting the core liner. This material is weighed wet, dried, then reweighed to determine its bulk density (assuming an average grain density). However, much information regarding the variability of the sediment is lost due to the integrated nature of the measurement. In contrast, Figure 1B shows a high-resolution density profile constructed using

CT images. Construction of these logs is made by incrementing the sample through the scan plane using a positioning table. Quantitative analysis is then conducted on an image-by-image basis using a "fixed" region-of-interest (ROI). These high-resolution profiles can be used for a variety of geoacoustic purposes, such as constraining the maximum scattering response correlation length as a function of frequency. For example, Lyons [12] examined the finely layered sediments of Eckernförde Bay, western Baltic Sea, and concluded that for frequencies greater than about 10 kHz, sampling intervals should be less than 1 cm. (This interval is smaller than the measurement interval normally used when making seafloor core measurements.) Instead, Lyons used the CT profiles (2-mm vertical scale) to estimate correlation lengths of 0.5 cm and 0.7 cm and variances ranging from ~10^{-4} to 10^{-5} for Eckernförde sediments. We emphasize that to detect correlation lengths this small requires sampling resolutions of at least 2.5 mm, a value that cannot be obtained with traditional sampling methods.

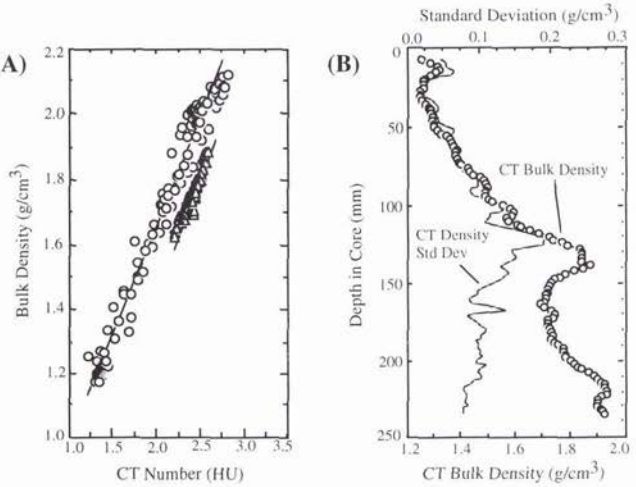

Figure 1. Transformation of CT numbers to sediment bulk density. (A) Empirical correlation. Circles—terrigenous marine sediments (i.e., those with low calcium carbonate content) taken in Eckernförde Bay, Germany; Panama City, FL; and the Louisiana continental shelf ($R^2 = 0.979$). Triangles—carbonate sediments from Marquesas Key, south Florida. (B) Typical high-resolution CT profile (Core 250-BS-BC; Eckernförde Bay, Germany) derived image-by-image.

In another study, we examined the impact of a thin layer of varying density on high-frequency reflection, forward loss, and backscattering of acoustic plane waves from the seafloor [11]. A functional form for density stratification was determined by examining a number of high-resolution CT density profiles, and a solution based on these general profiles was used to estimate the reflection coefficient. The influence of the density profile on reflection loss and backscatter was then calculated using the estimated reflection coefficient. Parameter values used in simulations were also obtained from the CT scans of the cores, as well as from the literature. We found that inclusion of a density profile adds a strong frequency dependence to estimates of the reflection coefficient and forward loss, and the largest effect on total scattering strength is near normal incidence where returns are dominated by interface scattering. The effect of the density profile on the strength of acoustic returns suggests that care should be exercised when using high-frequency systems for measuring sediment properties, especially near-normal incidence.

3.2 Characterization of Volume Inhomogeneities

A complete description of backscattering from the seafloor must include three components: (1) scattering from random discrete scatterers; (2) scattering from random continua; and (3) scattering from rough surfaces. Of the three components, discrete scatterers, such as bubbles, buried shells, and marine organisms (and/or their burrows) are the least understood in terms of their effect on acoustic propagation. This is due in large part to the lack of an appropriate analytical technique for quantifying these features. As we show next, X-ray CT is uniquely suited for quantitative volume descriptions at spatial scales directly relevant for modeling high-frequency acoustic backscatter (i.e., much smaller than 1 cm^3).

3.2.1 Gassy Sediments

It was our interest in characterizing gas bubbles in seafloor sediments that lead to our initial use of CT. In one of our first investigations, Orsi and Anderson [8] obtained a sediment core from Camp Creek Lake, a naturally gassy, man-made lake near College Station, TX (Figure 2). The primary accomplishment of this study was a conclusive demonstration that CT

could indeed image, and be used to quantify, bubble characteristics in sediments because of the great density contrast between free gas and the sediment matrix. Bubbles in the studied lake sediment were large, in agreement with the macrobubble model proposed by Wheeler [15] and with earlier visual observations made by Anderson and Hampton [16]. Interestingly, the bubbles deform the sediment matrix to create cavities as they grow, changing shape in a sequence from spheres to ellipses to amorphous "blobs" with increasing size. The increasing departure from sphericity with increasing size results as the bubble overcomes the restraining strength of the sediment and develops in a manner generally dictated by larger scale sedimentary structures. Most important, however, is that the results stressed caution when developing models of gassy sediments, emphasizing that the traditional assumption of tiny spherical bubbles within pores distributed uniformly throughout a volume of sediment may not always be accurate. In fact, our CT analysis revealed that individual sedimentary gas bubbles can grow quite large and possess a multitude of shapes.

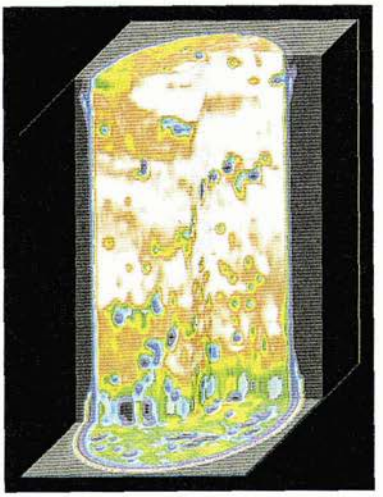

Figure 2. Volume rendering of a gassy Camp Creek core. The core is 1-ft long (30.5 cm) and is oriented properly, i.e., the top of the core and top of image is the lake bottom. This composite image is consists of 147 horizontal CT slices (2-mm thick). Note the gas bubbles (dark) and the general increase (lighter shades) in density with depth in the core.

Since our initial study, CT research into the nature and geometry of gas bubbles has advanced considerably [e.g., 17, 18], and has furthered the development of acoustic backscattering models for gassy sediments. The high downcore resolution of CT data has provided detailed descriptions of depth-dependent bubble fields within the sediment. CT information has enabled computation of discrete bubble scattering cross sections *versus* frequency which has formed the basis of a "thick layer" bubble scattering model described by Lyons et al. [19]. This model accounts for two-way propagation loss through a depth-dependent bubble distribution. Model results have shown that bottom loss predictions produced by "thin layer" or integrated bubble profiles may underestimate actual values by as much as 10 dB depending on frequency and bubble size distribution.

3.2.2 Shelly and Coarse-Grained Sediments

Of the common sediment types in shallow-water environments, sands and shell-bearing material are two of the more difficult types to characterize geotechnically. The main problem with studying these sediments is obtaining representative "undisturbed" samples for testing, due to their lack of cohesion and/or to the presence of shells. Besides identifying regions of disturbance, CT analysis of these sediments can also be used to investigate seemingly anomalous physical property values or to pin-point regions where laboratory measurements may be unknowingly in error. Figure 3 is one such example, which shows the occurrence of considerable intratest porosity in sediments collected off Marquesas Keys, Florida [13, 14]. Intratest porosity is common in shelly sediments where it serves to increase sediment porosity and decrease sediment density, due to the addition of water and/or slurry trapped within the interior of the buried shells. Another difficult-to-detect artifact, common in density profiles of sands, is shown in Figure 4. The high laboratory densities in the upper centimeters of Core CBBL 490-PC-DC are inaccurate and attributable to sediment dewatering that occurred unknowingly during laboratory sampling. They are easily corrected, however, using CT information since the approach is non-destructive and conducted before taking physical samples.

Figure 3. Identification of intratest porosity in shelly sediments using X-ray CT (CBBL 89-2-KW-DC, Marquesas Keys [13]). Note the intratest porosity as indicated by the dark regions contained within the interior of the two gastrapod shells. Also note the considerable hetereogeneity resulting from the shell fragments and calcified burrow (circular feature located in the center of the image). For scale, this image is 10 cm per side.

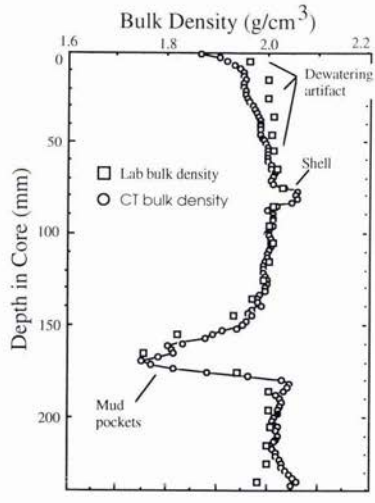

Figure 4. Detection and correction of a dewatering artifact in a density profile of sandy Panama City sediments (Core CBBL 490-PC-DC). Note the dewatering zone in the lab density profile, influence of a shell on the CT density profile, and interval of mud pockets detected by both methods.

3.2.3 Bioturbated Sediments

As attenuation of short wavelengths in sediments is high, properties in the region very close to the water-sediment interface will have a dominant effect on acoustic wave propagation. In this near-surface region, seafloor sediments are frequently highly bioturbated [20] and often display a tiering with depth. This tiering has been thought to explain vertical variations in sediment structure [21, 22]. We have extended this type of analysis to CT density profiles of sediment cores obtained in a variety of shallow-water areas [23]. Our model consists of the following tiers listed in order of increasing subbottom depth (Figure 5):

1. **Mixed layer**—characterized by low bulk densities and high variability due to intense small-scale (meiofaunal, juvenile, and/or small adult macrofaunal) burrowing.
2. **Transitional layer**—characterized by gradually increasing bulk density and high property variability associated with large-scale, but less frequent, mixing by head-down feeding organisms.
3. **Historical layer**—associated with increasing density with a simultaneous decrease in variability resulting from an increase in mechanical compaction and the closing of open burrows and other voids.

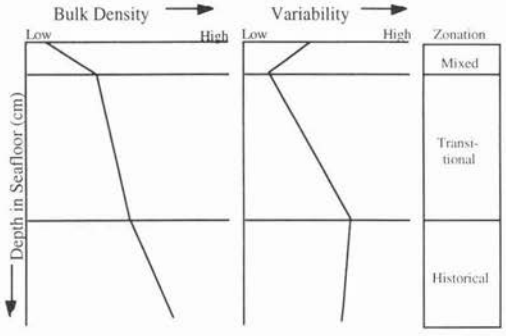

Figure 5. Conceptual CT model of physical property (density) variability in seafloor sediments. "Bulk density" refers to average CT bulk density and "variability" to its standard deviation.

By providing a conceptual framework, the characterization in Figure 5 should assist in modeling physical property variations within the upper decimeters of the seafloor, an important consideration for a variety of scientific and engineering investigations. Figure 6 shows a recently developed representation of the density profile shape for the upper few decimeters of the seafloor based on a smoothed version of the tiered near-surface seafloor structure [11]. Density approaches ρ_s with depth according to the function, $f_\rho = 1 + az$. (We refer to the parameter, a, in this equation as the density profile parameter which is a measure of the thickness of the high density gradients in the combined mixed and transitional layers in Figure 5.) This functional form matches a variety of CT density profiles from Eckernfšrde Bay, the Florida Keys, and Panama City. In these examples, the region of the core profiles which exhibits strong density gradients is the upper 1-5 cm. It is important to note that density data from this region is lacking as it is often disturbed by the coring/sampling process or skipped entirely in a coarse sampling scheme.

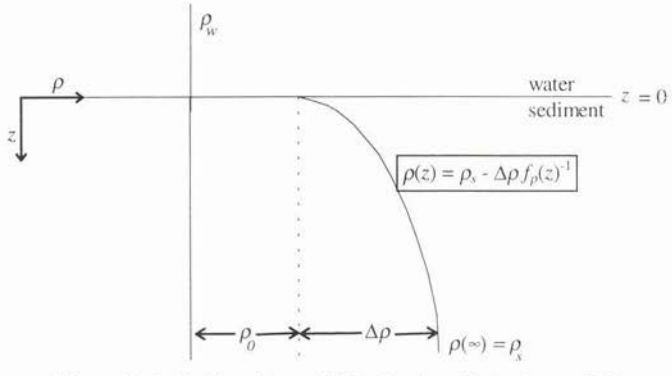

Figure 6. Seabed layering model for density with $f_\rho = 1 + az$ [11].

4. Summary

High frequency sonar systems such as those used in MCM are greatly affected by the small scale density structure of near surface marine sediments. Bioturbation, gas accumulation, and shell material all contribute to the highly variable nature of surficial density profiles. The need to quantify such variability is acute as accurate models of acoustic scattering cannot be developed without a thorough knowledge of relevant environmental factors. Traditional methods of core analysis are typically averages which are insufficient to fully quantify the nature of seafloor inhomogeneities. We have found X-ray CT to be a powerful technique for nondestructive characterization of intact sediment cores. CT methods are capable of obtaining high-resolution, three-dimensional information from which ground truth or model input parameters may be extracted. Methods of analysis have been refined by the medical community and the petroleum industry where CT has been used for several years. The geoacoustic modeling community, however, has yet begun to exploit the richness of CT data. Researchers involved in modeling efforts can, through the use of CT, verify results and gain significant new insight concerning the nature of high-frequency acoustic interaction with the seafloor. Such insight will advance the design of sonar systems and interpretation of sonar data for a variety of applications.

5. Acknowledgments

The bulk of our work has been conducted as a part of the Coastal Benthic Boundary Layer (CBBL) program, which has been funded by the Office of Naval Research (ONR) and managed by the Naval Research Laboratory (NRL). Initiation of our CT research was sponsored by ONR's G&G program; we thank Dr. Joseph Kravitz for his interest and support.

6. References

[1] T.H. Orsi, "*Computed tomography of macrostructure and physical property variability of seafloor sediments*," Ph.D. Thesis, Texas A&M Univ., College Station, TX, 184 p., 1994.

[2] T.H. Orsi, C.M. Edwards, and A.L. Anderson, "X-ray computed tomography: A nondestructive method for quantitative analysis of sediment cores," *Jour. Sed. Res.*, vol. A64, pp. 690-693, 1994.

[3] E.C. McCullough and J.T. Payne, "X-ray transmission computed tomography," *Med. Phys.*, vol. 4, pp. 85-98, 1977.

[4] E.C. McCullough, "Photon attenuation in computed tomography," *Med. Phys.*, vol. 2, pp. 307-320, 1975.

[5] G.N. Hounsfield, "Computerized transverse axial scanning (tomography): Part I. Description of system," *Brit. Jour. Radiology*, vol. 46, pp. 1016-1022, 1973.

[6] G.S. Warner, J.L. Nieber, I.D. Moore, and R.A. Geise, "Characterizing macropores in soil by computed tomography," *Soil Sci. Soc. Am. Jour.*, vol. 53, pp. 653-660, 1990.

[7] H.J. Vinegar and S.L. Wellington, 'Tomographic imaging of three-phase flow experiments," *Rev. Sci. Instr.*, vol. 58, pp. 96-107, 1987.

[8] T.H. Orsi and A.L. Anderson, "Bubble characteristics in gassy sediments,Ó *Trans. Gulf Coast Assoc. Geol. Soc.*, vol. 44, pp. 533-540, 1994.

[9] T.H. Orsi, A.L. Anderson, and A.P. Lyons, "X-ray tomographic analysis of sediment macrostructure in Eckernförde Bay, western Baltic Sea," *Geo-Mar. Lett.*, vol. 16, pp. 232-239, 1996.

[10] T.H. Orsi and A.L. Anderson, "X-ray computed tomography of macroscale variability in sediment physical properties, Offshore Louisiana," *Trans. Gulf Coast Assoc. Geol. Soc.*, vol. 45, pp. 475-480, 1995.

[11] A.P. Lyons and T.H. Orsi, "The effect of a layer of varying density on high-frequency reflection, forward loss and backscatter," SACLANTCEN Report, La Spezia, Italy, in press.

[12] A.P. Lyons, "*Acoustic volume scattering from the seafloor and small scale structure of heterogeneous sediments*," Ph.D. Thesis, Texas A&M Univ., College Station, TX, 184 p., 1995.

[13] T.H. Orsi, A.L. Anderson, W.R. Bryant, K.S. Davis, and A.K. Rutledge, "Computed tomography of carbonate macrostructure: Marquesas Keys and Dry Tortugas (south Florida),Ó *Geo-Mar. Lett.*, in press.

[14] T.H. Orsi, K.B. Briggs, M.D. Richardson, and A.L. Anderson, "CT analysis of physical property variability in carbonate sediments," Lavoie, D. (ed.), *Proc, Key West Workshop*, Naval Res. Lab., Stennis Space Center, MS, in press.

[15] S.J. Wheeler, "A conceptual model for soils containing large gas bubbles," *Geotechnique*, vol. 38, pp. 389-397, 1988.

[16] A.L. Anderson and L.D. Hampton, "Acoustics of gas-bearing sediments," *JASA*, vol. 67, pp. 1865-1903, 1980.

[17] F. Abegg and A.L. Anderson, "The acoustic turbid layer in muddy sediments of Eckernförde Bay, western Baltic Sea: Methane concentration, saturation, and bubble characteristics," *Mar. Geol.*, vol. 137, in press.

[18] A.L. Anderson, F. Abegg, and R.A. Weitz, "Gas concentration and bubble distribution in the floor of Eckernförde Bay: Ground truth from core sample measurements," Wever, T.F. (ed.), *Proc., Modeling Methane-Rich Sediments of Eckernförde Bay, 26-30 June, 1995*, Forschungsanstalt der Bundeswehr fÝr Wasserschall- und Geophysik, Kiel, Germany, FWG Report 22, pp. 70-72, 1995.

[19] A.P. Lyons, M.E. Duncan, A.L. Anderson, and J.A. Hawkins, "Predictions of the acoustic scattering response of free-methane bubbles in muddy sediments,"*JASA*, vol. 99, pp. 163-172, 1996.

[20] M.D. Richardson and D.K. Young, "Geoacoustic models and bioturbation," *Mar. Geol.*, vol. 38, pp. 205-218, 1980.

[21] W.H. Berger, "The benthic interface of deep-sea carbonates: a three-tiered sequence controlled by depth of deposition,Ó in Fanning, K.A., and F.T. Manheim (eds.), *The Dynamic Environment of the Ocean Floor*, Lexington Books, Lexington, MA, pp. 95-114. 1982.

[22] M.D. Richardson, K.B. Briggs, and D.K. Young, "Effects of biological activity by abyssal benthic macroinvertebrates on sedimentary structure in the Venezuela Basin," *Mar. Geol.*, vol. 68, pp. 243-267, 1985.

[23] T.H. Orsi and A.L. Anderson, "Vertical tiering of sediment bulk density in Eckernförde Bay: A conceptual geotecnical model using X-ray CT,Ó *Cont. Shelf Res.*, in review.

Autofocusing a synthetic aperture sonar using the temporal and spatial coherence of seafloor reverberation

M.A. Pinto[1], F. Fohanno[1], O. Trémois[1], S. Guyonic[2]

[1]Thomson Marconi Sonar SAS
Route de Ste Anne du Portzic
29600 BREST Cedex

[2]STSN/GESMA
BP42
29240 - BREST NAVAL

Abstract

An autofocusing algorithm for the compensation of translational motion errors of a sea floor imaging synthetic aperture side scan sonar is presented. The algorithm does not depend on the presence or absence of dominant scatterers in the field of view and is based on the displaced phase center antenna concept. The theoretical performances are studied and the algorithm is shown to perform satisfactorily on simulated data. Preliminary results obtained for a sonar moving on an underwater rail are presented. Sea trials are planned to validate an extension of the algorithm, termed " multibeam interferometry ", to arbitrary motion errors.

1. Introduction

The ideal synthetic aperture is perfectly linear, and the time delays required to form a beam in a given direction can be computed a priori. Synthetic aperture processing then reduces to a straightforward extension of conventional beamforming to multiple pings. In reality, there are deviations of the platform from the specified track, which distort the synthetic aperture. Focusing the synthetic aperture, despite these distortions, is a major difficulty which has up to now prevented operational deployment of such systems in the ocean.

Autofocusing is an adaptive array processing technique which aims at using the sonar signals to focus the distorted array. Similar techniques are been studied for the same purpose in real and synthetic aperture radar [1,2], and for correcting wavefront distortions in radio-astronomy and optics [3]. If proved feasible in sonar, it is obviously a very interesting and cost-effective technique.

It is highly desirable that autofocusing be performed without imposing any condition on the distribution of power in the source field. This independence is seldom achieved by the existing algorithms. Those used in radar often assume the presence of point scatterers in the field of view, which play the part of beacons. They are not suited to sea floor imaging sonar where reverberation is dominant. Others [4] exploit instead the spatial coherence properties of statistically homogeneous reverberation. These suffer then in the presence of features of any kind on the sea floor (highlights, shadows...). This paper discusses a class of algorithms, suited for side scan sea floor imaging with a linear physical array, which achieve the required independence by appropriate sonar design.

The paper is organized as follows. In part 2 the problem to be solved is posed. In part 3, the waveform invariance principle, which forms the basis of correlation navigation sonar, is introduced. In part 4, this principle is used to focus a synthetic array in the presence of arbitrary translational motion errors, using improved correlation navigation sonar techniques to extend previous work by Sheriff [5]. In part 5, results of simulations and preliminary experiments obtained for a sonar moving on an underwater rail are presented.

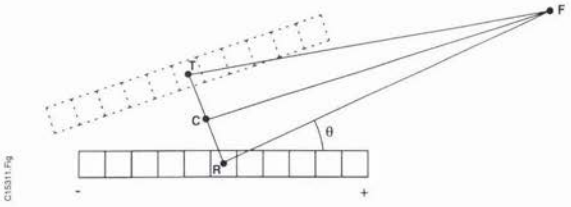

Figure 1 : Array positions at transmission and reception of echo from F

2. Problem description

Focusing a linear array at a point F of the sea floor requires knowledge of the round-trip travel times to the phase center of each hydrophone of the array. For the physical array, assuming far field conditions (or suitable focusing), the travel time to the hydrophone located at abscissa x along the array can be written as τ-xu, where τ is the travel time to the phase center of the array located at x=0, and u is proportional to cosθ, where θ is the bearing (see figure 1). Point F is therefore determined by the two sonar coordinates u and τ in the physical image formed at each ping. Due to the sonar displacement, these coordinates change from ping to ping, and the problem is that of tracking the displacements of F in a sequence of consecutive images with the precision required to coherently register the corresponding physical pixels. For any given pair of adjacent pings 1 and 2, the sonar coordinates of F at ping 2 can be expressed as :

$$u + \Delta u\,(u,\ \tau),\ \tau + \Delta\tau\,(u,\ \tau) \qquad (1)$$

where u and τ are the sonar coordinates at ping 1. The displacements Δu and $\Delta\tau$ are the necessary and sufficient information required to focus the synthetic array since, by iterating (1), an arbitrary number of pings can be registered.

It is important to note that the corrections to the coordinate displacements derived from ideal-track assumptions will not be the same, in general, for points at different coordinates in the sonar image. Indeed the corrections for F depend on the projection of the motion errors in the radial direction of F, which depends also on the local bottom topography. For example, sway (horizontal across-track displacement) leads to a change in travel time which depends also on the grazing angle at F. Furthermore the shape of the distorted array changes with time and is therefore not the same at the arrival times of echoes at short range or far range. Nevertheless, for the purpose of the estimation, these corrections will be assumed constant or slowly varying in portions of the sonar image, termed "isoplanatic regions". The dimensions of these regions, ideally as small as possible, determine the resolutions in u and τ of the estimation. This concept of isoplanatism comes from astronomy, where it is known that the phase shifts required to correct wavefront distortions are anisotropic, ie, depend on the angle of arrival of the wave. For example, a guide star (beacon) can be used to measure the distortions which affect the source of interest only provided it is sufficiently close for the light rays coming from the guide star to undergo the same propagation disturbances. This condition defines the isoplanatic angle.

In what follows, we consider only the simpler case of purely translational motion errors. The problem then reduces to the estimation of $\Delta\tau$ (u,τ). The medium is also assumed ideal.

3. Waveform invariance

The use of the correlation properties of signals returned by a diffuse scattering medium, like the sea floor, to measure displacements between two successive transmissions forms the basis of existing navigation sonars termed correlation logs [6]. The main features of such logs may be summarized as follows :

After transmission at a specific location T, and backscatter by the sea floor, the echo received at a specific receiving point R, at a given delay τ after transmission, can be viewed as a realization of a given random variable. The echo results from the interference between an arbitrarily large number of scatterers in the sonar resolution cell. In far field conditions, transmission at T_1 and reception at R_1 after a delay τ is equivalent to transmission and reception from a single spatial location $C_1=(T_1+R_1)/2$, known as the sonar phase center (see figure 1). If the same waveform is transmitted twice from the same phase center, and if the propagation medium and the scatterer geometry has not changed between the transmissions, the same random realization will be received (except for noise) for the same propagation delay, irrespective of the distribution of the scatterers in the sonar resolution cell. This is known as the "waveform invariance" principle.

In the case of interest where transmitter and receiver are on board a moving platform, the second transmission and reception occur at displaced spatial locations T_2 and R_2. As a result the second phase center C_2 is displaced with respect to C_1 by a vector quantity $\Delta C=C_1C_2$. Then first and second echoes received at delay τ are no longer identical. Due to the displacement, each scatterer undergoes a change in round-trip travel time $\Delta\tau$ determined by the projection of ΔC onto the radial direction to the scatterer. If these changes are identical for all scatterers in a sonar resolution cell, their interference is not affected by the displacement and "waveform invariance" is restored for first and second echoes received at τ and $\tau+\Delta\tau$. If, however, these changes vary, as it will be if the radial direction varies too much within the sonar resolution cell, these first and second echoes will partially decorrelate. Additive noise in the sea or in the receiver will also contribute to this decorrelation.

We will refer to this effect as "baseline decorrelation", by analogy to a similar situation which occurs in interferometric bathymetry [7]. One seeks there to estimate the depression angle of the rays arriving from the sea floor, using phase comparison between the echoes received by two displaced transducers. These form an interferometer whose angular resolution is given by the receiver separation (or baseline) in wavelengths. In the present application, the baseline is synthetic rather than real but, apart from issues relative to temporal coherence, this difference is unimportant. Baseline decorrelation occurs when the spread in bearing (relative to the baseline) within the sonar resolution cell is no longer small compared to the angular resolution of the interferometer, which can then resolve different scatterers F_1 and F_2 in the resolution cell. An example of such a situation is pictured on figure 2, for a vertical displacement of amplitude P and a non planar sea floor.

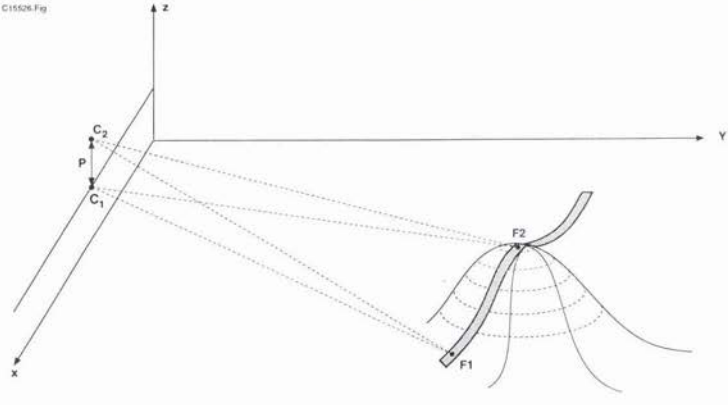

Figure 2 : Influence of bottom topography on baseline decorrelation. Are shown an interferometric baseline C_1C_2, and two points F_1 and F_2 in a sonar resolution cell (shaded).

The most important decorrelation occurs when the displacement is colinear to the array. In the case of statistically homogeneous reverberation, and for an along-track displacement of D, the resolution of the interferometer is $\lambda/2D$ (where the factor two is because the baseline is synthetic) and the spread in bearing is λ/L, where L is the length of the physical array, since the baseline is colinear to the array. It can be then be shown that the field correlation is $1-(\lambda/L)/(\lambda/2D)=1-2D/L$. Independence of two looks of the same scene (which is the effect sought for in incoherent synthetic aperture) is achieved for D=L/2. Even for D<L/2, which appears as a basic condition for autofocusing on reverberation, the speckle in the pixels which correspond to F remains weakly correlated. This makes the estimation of (1) from direct cross-correlation of the physical images difficult.

A correlation log attempts to restore waveform invariance despite platform motion by displacing the receiver between the first and second receptions. Such a displacement can be achieved very simply by using at least two identical receivers R and R'. Use of R' instead of R at the second reception displaces the second phase center from $C_2=(T_2+R_2)/2$ to $C'_2=(T_2+R'_2)/2$. The condition to restore waveform invariance is $C'_2=C_1$, which occurs when $R_2R'_2=-2C_1C_2$ as in figure 3.

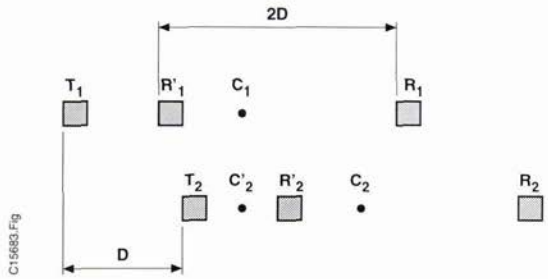

Figure 3 : Achieving waveform invariance by displacing the phase center
At ping 1, (2) transmission occurs at T_1 (T_2) and reception at R_1, (R_2). Motion between pings is D.

In pratice, one uses an array of hydrophones and computes the cross-correlation at all the possible discrete values of the hydrophone separation vector. One then uses appropriate interpolation to estimate the best separation vector, ie, the one at which the cross-correlation is maximum. This vector provides an estimate of the displacement projected along the array, whereas the correlation delay provides an estimate of the displacement in the look direction. It is desirable to have as many hydrophone pairs with distinct separation vectors as possible in the array and correlation logs often use planar rather than linear arrays. In many cases of application with a linear array, it is not possible to achieve strict waveform invariance. Then the correlation log limits baseline decorrelation as much as possible by shortening the baseline, so as to coarsen the resolution of the interferometer. It will also orient the baseline in space so as to minimize the angular spread in bearing (relatively to the baseline) within the sonar resolution cell.

It must be cautioned that, although correlation logs have been around for a long time now, few systems exist (compared to the number of Doppler logs). With few exceptions, the theory has focused on the measurements of translations alone, ignoring possible errors introduced by rotations or the possibility of measuring both translations and rotations by suitable extensions.

4. Application to autofocusing

Sheriff proposed to use the physical linear array as a simplified correlation log to measure translational motion errors. His algorithm can be described as follows :

Choose a hydrophone pair of the physical array with vector separation 2D, where D is the ping-to-ping displacement derived from ideal-track assumptions, to play the part of R and R' of part III (the existence of such a pair requires D<L/2, where L the length of the array). Measure next the phase shift between the echoes received by R at ping 1 and R' at ping 2 in the same range bin, ie, at the same delay τ after first and second transmissions. Finally, apply the opposite phase shift, range bin by range bin, to all the hydrophones of ping 2 and then register ping 2 with ping 1 using ideal track assumptions.

Sheriff recognized that further (unspecified) processing may be necessary to correct possible residual phase errors. Nevertheless the method is reported to have performed successfully in tank experiments with rods used at point targets. However it does make some simplifications with respect to existing correlation log techniques. First correlation is reduced to phase comparisons on the basis of a single pair of measurements. Next the hydrophone separation vector is fixed a priori. Finally it is also seen that the phase shift corrections are assumed isotropic (not to depend on u). These assumptions limit rather severely the precision and the angular resolution of the autofocusing, as shown below.

4.1 Precision of the estimation

It is well-known in bathymetry that, due to the baseline decorrelation, the estimation of interferometric phase shifts on the basis a single pair of measurements is noisy. This measurement is a random variable which is by no means constrained to remain some kind of average of the phase shifts of the unresolved scatterers within the resolution cell. This is true for the ensemble average but, for individual realizations, large deviations may occur, in particular in the range bins where the reverberation fades. This effect is known in tracking sonar as the "glint" of an extended target. Maximal glint occurs when the target highlights interfere destructively. Glint is reduced by averaging over K range bins, after which the standard deviation of the phase estimate is given by :

$$\frac{1}{\sqrt{K}}\sqrt{\frac{1-\mu^2}{\mu^2}} \tag{3}$$

where μ is the field correlation coefficient. This formula is established by Goodman in [8].

Furthermore the estimation of time delays, rather than only phase shifts, is necessary when $\Delta\tau$ is no longer small compared with 1/B, where B is the sonar bandwidth. This time delay estimation can be carried out using standard interferometric techniques, which may be summarized briefly as follows. One first estimates the correlation phase at the position of the maximum of the correlation envelope. This provides an ambiguous estimation of the time delay because phase measurements are modulo 2π. Amongst all the ambiguous time delays, which correspond to time delays which differ from the true time delay by an integer number of carrier periods, the one which is closest to the maximum of the correlation envelope is chosen.

It must be emphasized that precision is an important issue since the price to pay for processing only adjacent pings, as in the class of algorithms studied here, is a build up of errors, analogous to a random walk. The precision required on the ping-to-ping correlation delay increases with the total number N of pings to be coherently registered. For a given value of μ, determined by the physics of the backscatter and the level of additive noise, the precision can be increased by increasing K. The required values of K to limit the loss in synthetic aperture array gain to 1dB is plotted on figure 4 as a function of μ for different values of N. This follows from (3) and a calculation similar to the one presented in [1].

It is also preferable to choose the hydrophone separation vector adaptively, as in a correlation log, rather than to base this choice on ideal-track assumptions. In particular along-track motion errors introduce time delay errors for all image points off boresight. It is then elementary to show that, on the time window for which the correlation is performed, $\Delta\tau$ is given by :

$$\Delta\tau = \alpha u + \beta \tag{4}$$

where α is the best separation vector and β the correlation delay.

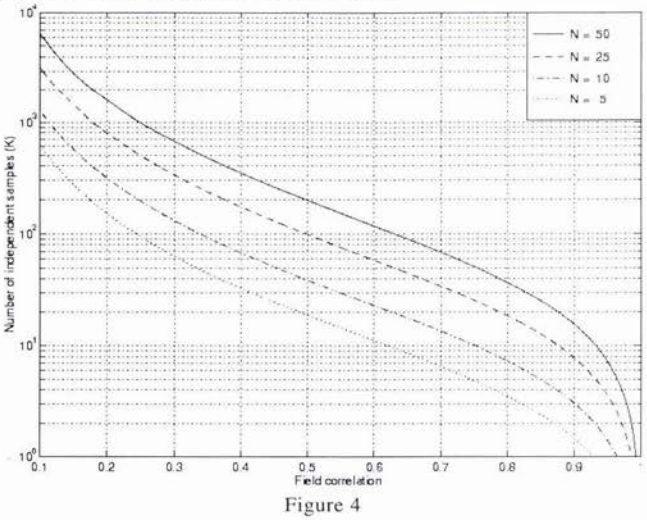

Figure 4

4.2 Resolution of the estimation

The length of the time window upon which the correlation is performed determines the temporal resolution of the estimation of (1). The maximal value of K is determined by the condition that the variations with τ of $\Delta\tau$ remain a small fraction of the carrier period (isoplanatic condition). For instance, K=100 allows coherent registration of 25 pings for μ >0.5. With a 20kHz sonar bandwidth, this corresponds to a time window of 5ms. Platform dynamics on this time scale can be neglected but it is necessary to assume that variations of the line of sight over slant range intervals of 3m to 4m are small enough. This condition is easier to satisfy at small grazing angles.

It is seen from (4) that the time delay correction now varies linearly with u in the field of view. Thus both the precision, and to some extent the angular resolution, of the estimation have been improved. Further increase in precision and resolution is possible by using $M \geq 2$ hydrophone pairs with redundant separation vectors. M can be increased by reducing the ping-to-ping displacement D to a smaller fraction of L/2 (see figure 5). The redundancy can be used to increase the temporal and angular resolutions. Since spatial redundancy increases by M the number of points in the correlation, K can be reduced by M which leads, if required, to an improvement in temporal resolution by a factor of M. The improvement in the angular resolution, which is more critical, can be obtained by processing the M hydrophone pairs as a displaced sub-array. One can take benefit of the angular resolution of the sub-array in the autofocusing. In the example of the 400kHz sonar considered above, distinct piece-wise linear corrections (4) could be estimated in subsectors of 0.1°, by choosing D=L/4, assuming L=3m.

The isoplanatic angle is then reduced from 5° to 0.1° which should significantly relax constraints, in particular on the bottom topography.

The use of $M \geq 2$ redundant hydrophone pairs is not new. It was proposed by Raven [9] for the purpose of estimating the phase corrections in the presence of both angular and translational motion errors. He used the M pairs to estimate separately M phase shifts by the algorithm discussed by Sheriff. He then adjusted a linear law to these M phase shifts. The autofocusing consisted in applying the opposite phase shift law, range bin by range bin, to all the hydrophones of ping 2 prior to registration with ping 1 using ideal track assumptions. This extension is interesting, because it shows that autofocusing in the presence of arbitrary motion errors is possible, in principle. However Raven's method suffers from the same limitations in precision and angular resolution as Sheriffs'.

5. Results

Simulated synthetic aperture images (3mx5m) autofocused using both Sheriff's method and the method presented here are shown on figure 6. The scene consists of a spherical target on a flat uniformly reverberating sea floor. The reverberation is generated using a standard point scatterer model. The target is a sphere of 1m diameter at 150m range for a sonar at 30m above the sea floor. The central frequency is 400Khz with a bandwidth of B=30kHz. The physical array length is L=1m 20, and the ping-to-ping displacement D =L/4. The motion error was a bias in sway velocity of 3mm from ping to ping. The total number of integrated pings was 11. It is seen that Sheriff's autofocusing fails by far to achieve the required precision. The improvements proposed here solve the problem.

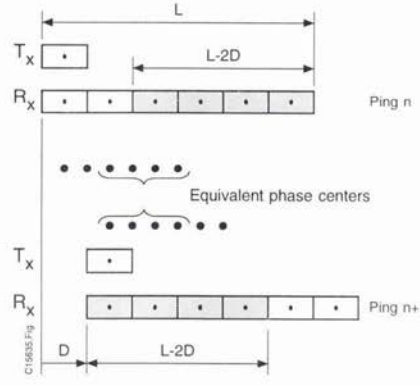

Figure 5 : Hydrophone pairs with redundant separation vectors

Images were formed (cf figure 7) for a sonar constrained to move on a rail which guarantees an ideal track. The physical array length is L=3x19.5cm and the ping-to-ping displacement is D=L/3. The sonar operates at 53kHz with a 15° tilt and the rail is at 6m80 above the sea floor. In this case the phase errors where not due to motion errors but to electronic jitter. This situation is, however, only partially representative of the one which will be encountered at sea. This is first because the time delay corrections due to jitter are isotropic (so that autofocusing does not require angular resolution) and second because the causes of baseline decorrelation in the case of jitter differ significantly from those in the case of motion errors. Nevertheless this example illustrates that the autofocusing algorithm is not limited by its principle to the compensation of motion errors alone. By analogy with astronomy, it can be anticipated that the compensation of medium induced wavefront distortions require an autofocusing algorithm which accounts for anisoplanatism. The method presented here should therefore be capable, in principle, to correct both array and wavefront distortions. However the effect of medium inhomogeneities on baseline decorrelation requires more attention.

6. Conclusion

An autofocusing algorithm for the compensation of translational motion errors has been presented. The algorithm is based on a local isoplanatic assumption, that is, the redundancy of the time delay corrections in small portions in range and bearing of the physical sonar image. The estimation makes use of correlation sonar techniques : the decorrelation of speckle in pixels of adjacent looks, termed "baseline decorrelation", is reduced by phase center displacement. Improvements which allow order of magnitude gains of precision and resolution on the previous work by Sheriff, such as the use of range averaging to combat "glint", or sub-array processing with multiple redundant hydrophone pairs, have been proposed. The theoretical performances of the algorithm have been studied, in particular the build up of errors due to the processing of only adjacent pings, and

promising results have been obtained on simulated data and on experimental data obtained for a sonar moving on a rail. An extension of the algorithm to arbitrary translational and angular motion errors, termed " multibeam interferometry ", has been defined by Thomson Marconi Sonar. The extended algorithm, which exploits two-dimensional correlations of sonar images formed with a displaced sub-array, estimates both displacements in (1), with order of magnitude improvements in precision and resolution over the method proposed by Raven. GESMA and Thomson Marconi Sonar are planning sea trials in June using the PVDS (Propelled Variable Depth Sonar) of Thomson Marconi Sonar.

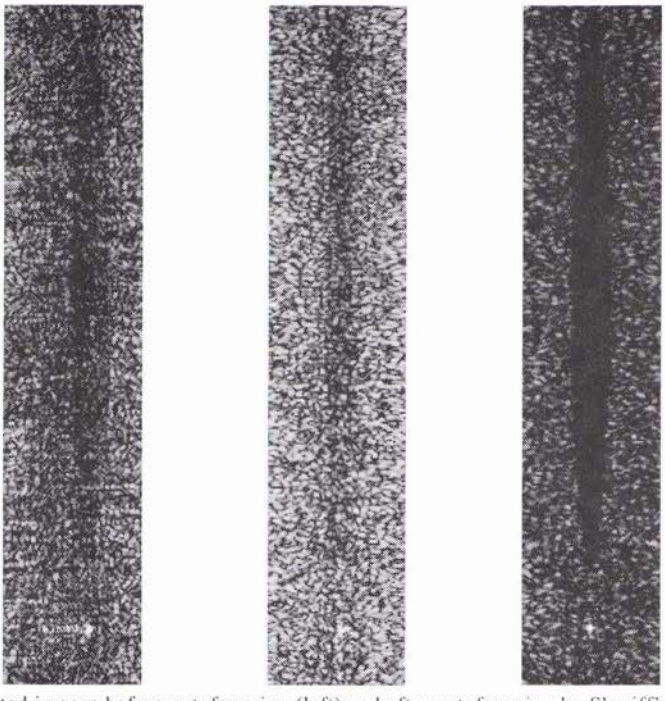

Figure 6 :Simulated images before autofocusing (left) and after autofocusing by Sheriff's method (middle) and the method presented here(right).

References

[1] B.D. Steinberg, H.M. Subbaram, Microwave imaging techniques, Wiley and Sons, Inc. New York 1991.

[2] W.G. Carrora, R.S. Goodman, R.M. Majewski , Spotlight synthetic aperture radar, Signal Processing Algorithms, Artech House, London, 1995.

[3] C.A. Primmerman et al, Compensation of atmospheric optical distortion using a synthetic beacon, Nature Vol 353 12 Sept. 1991 pp 141-143.

[4] K.A. Johnson, M.P. Hayes, P.T. Gough, A method for estimating the sub-wavelength sway of a sonar towfish, IEEE J. Ocean. Eng. Vol 20. No 4, Oct 1995 pp 258-267.

[5] R.W. Sheriff, Synthetic aperture beamforming with automatic phase compensation for high frequency sonars, Proc. IEEE Symp. On AUV Technology, Wash. DC, June 1992 pp 236-245.

[6] P.N. Denbigh, A design study for a correlation log to measure speed at sea, J. Navigation 1982, Vol 35 pp 160-184.

[7] G. Jin, D. Tang Uncertainties of Differential Phase Estimation associated with interferometric sonars, IEEE J. Ocean. Eng. Vol 21, No 1 Jan 1996.

[8] J. W. Goodman, Statistical Optics, 1985, J. Wiley and Sons, New York.

[9] R.S. Raven, Electronic Stabilization for displaced phase center systems, U.S. Patent 4244036, Jan 1981.

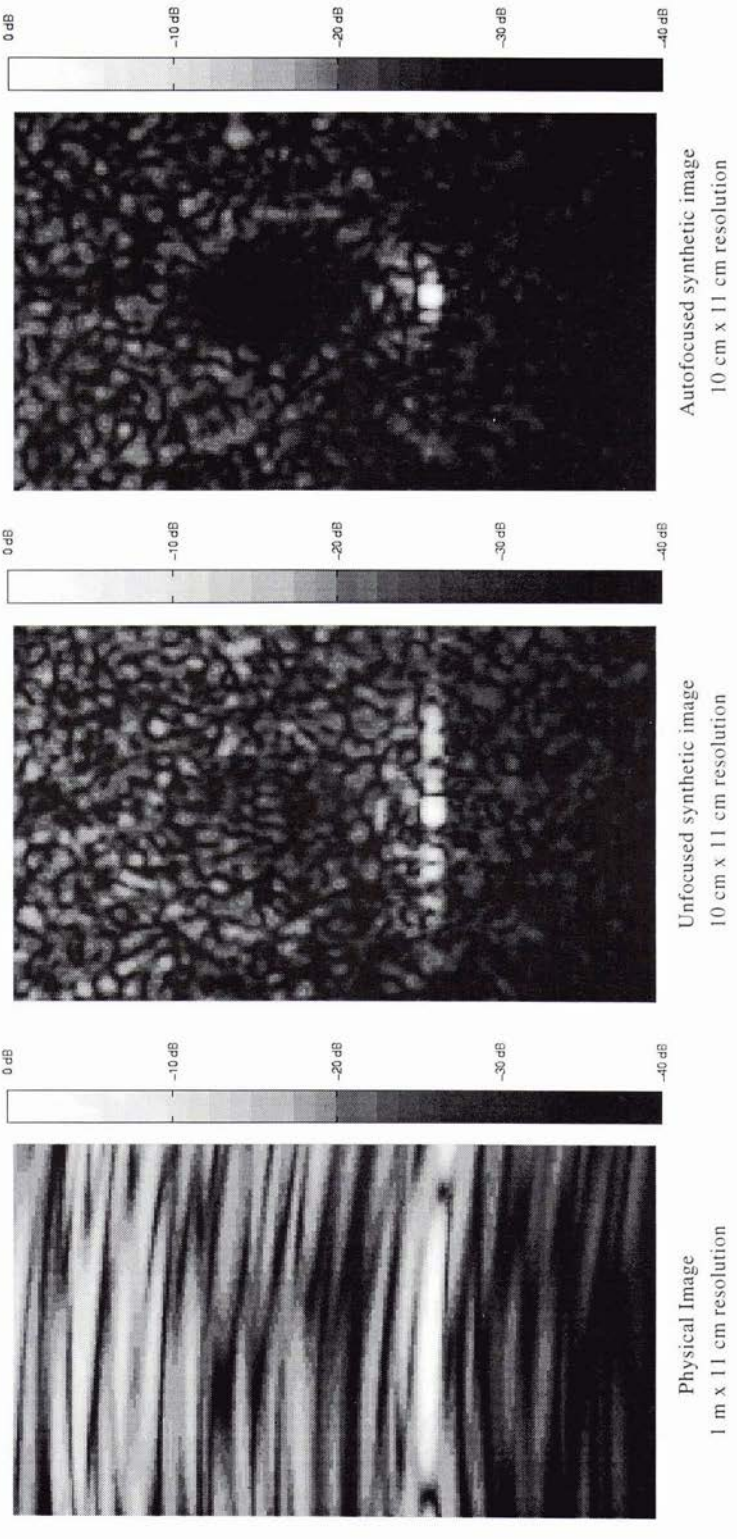

Figure 7 : Target sphere at 53 kHz. Image sizes 3 m x 6 m

A new Ambient Noise Imaging system for ANI, passive and bistatic active acoustic imaging in shallow water.

John R. Potter

Acoustic Research Laboratory
c/o Physics Dept., NUS,
10 Kent Ridge Crescent
Singapore 119260
email: phyjp@nus.sg
www.arl.nus.edu.sg

Abstract

Shallow water active and passive sonars can be usefully complimented by broadband Ambient Noise Imaging (ANI) systems. The first ANI system was largely analogue, produced good images at 38 m range, but was bulky and permitted only a limited range of signal processing options. A 24 Gflop 20-120 kHz second-generation phased-array system, ROMANIS, is being built in Singapore. The ROMANIS design is described, detailing the substantial performance improvements and novel processing that it exploits.

1. Introduction

The concept of a third sonar operating principle, using ambient noise in the ocean as the sole source of illumination to form images of submerged objects, is now a demonstrated fact [1].

While the potential benefits of such systems could be wide-ranging, the possibility of achieving practical and useful performance has sometimes been viewed with considerable skepticism [2]. The overriding advantage of an Ambient Noise Imaging (ANI) system would be, obviously, its completely covert nature. Images can be formed of entirely quiet objects without the need to make any transmission. Against this exciting potential, it must be admitted that the signal-to-noise ratio will usually be inherently low and the sources on which the system relies for its illumination are statistically complicated. Propagation analysis and scattering simulations, both ray-like and full-wave, have indicated that useful images could be formed at ranges considerably exceeding optical (even laser scanning) devices [3,4]. Following a successful proof-of-concept experiment carried out in 1991 [5], an SIO team designed a more ambitious device with 126 pixels which would produce moving coloured images, the Acoustic Daylight Ocean Noise Imaging system (ADONIS). ADONIS was completed and first deployed adjacent to the Marine Facilities Pier in San Diego Bay, CA in August 1994.

Some of the results from this deployment have now been published [6,7], with several papers in press or in the review process. Other research groups are also experimenting with ANI and confirming that useful images can be obtained [8]. The overwhelming outcome of the first ADONIS deployment is that ANI works, and does so better than anticipated. The excellence of the results stem in part from the presence of snapping shrimp at the deployment site, which provide more useful high-frequency energy than anticipated. Other, more fundamental, features of this ambient noise have become apparent in subsequent detailed studies of ADONIS data. These developments, together with newly-available Commercial Off-The-Shelf (COTS) products, have led to the design of a second-generation system described here.

2. Design considerations from existing experience

A second-generation system should exceed the performance envelope of ADONIS, learning from our experiences with that system and capitalising on our improved understanding of the ANI principle as a more general concept which encompasses Acoustic Daylight. To place the new design in perspective, an outline of

ADONIS is presented. The lessons that have been learnt from ADONIS will then be summarised, and the provisional design solution for the next-generation system will be described.

2.1 The ADONIS system

The Acoustic Daylight Ocean Noise Imaging System (ADONIS) produces real-time, moving, colour pictures of silent objects in the ocean. In brief, the positive capabilities of ADONIS can be listed as follows:

- Real-time imaging
- 126 separate beams
- Acoustic colour information at 16 frequencies from 8-80 kHz
- 24 Hz frame rate, providing near-video rate moving acoustic pictures

One basic limitation on such a system is angular resolution, which is essentially bounded by the Rayleigh criterion that the beamwidth cannot be substantially less than λ/D where λ is the wavelength of the propagating wave and D is the aperture of the antenna. There is an upper limit on frequencies that can be employed due to thermal noise [9] and volume absorption, and hence how small we can make λ. To gain maximal resolution, we therefore seek to maximise D, the aperture of the antenna. This also has its practical limitations. ADONIS used a reflecting lens of 3m diameter. The advantage of such a lens is that active receiving elements are not required to 'tile' the massive surface that a 3m fully-populated 2-D array would normally demand. The beamforming and focusing of energy is achieved by geometric means, rather than electronic. This avoided the computational obstacle of dealing with a very large number of elements and processing the data. The disadvantages included the analogue reflecting lens performing only as well as a fully-populated phased array half the size, and that the beam configurations were fixed. Some photographs of ADONIS and a sketch of its engineering construction are shown in Fig. 1.

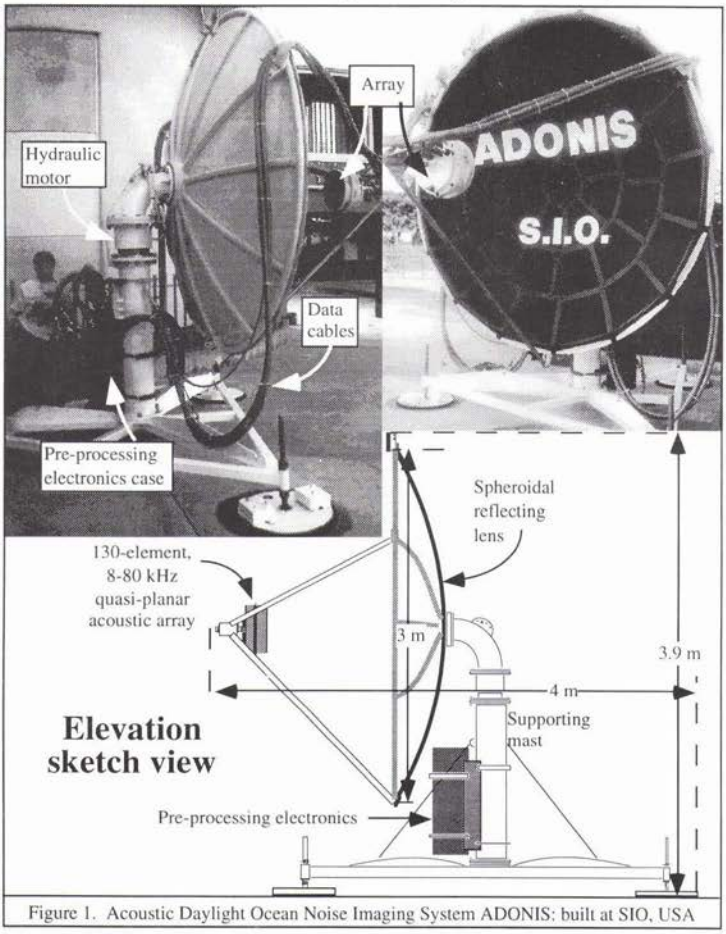

Figure 1. Acoustic Daylight Ocean Noise Imaging System ADONIS: built at SIO, USA

Even using the analogue lens to circumvent the beamforming computation, it was still not possible to FFT the data from all 126 beams in real time and acquire the large amount of data that would be produced. The frequency spectrum for each beam was therefore estimated by an analogue filter, which was switched to each of 16 frequencies in turn. Allowing for settling time and an extra period at the end of each frame cycle (to clear the sample-and-hold circuits), some 95% of the data was effectively being discarded.

Finally, the 3m lens took the form of a concave dish, which would have been very difficult to move through the water. ADONIS was therefore constructed as a fixed system, to be placed on the sea floor at one location.

2.2 Data experiences with ADONIS

Data from the first deployment have now been extensively examined at the ARL in Singapore. This work was carried out on a contract which provided for the acquisition of a dedicated fast computer, with which the ARL has been able to implement a suite of rapid visualisation tools and carry out a wide range of lines of inquiry. The results have been most interesting, and sometimes rather surprising. Meanwhile the SIO group have concentrated on upgrading ADONIS and re-deploying it to obtain new data. The major points that have been established by the ARL concerning ADONIS data are:

- The image information is contained not only in the mean illumination, as anticipated, but in other measures of the intensity distribution, such as variance [7].
- Images can also be obtained using only the normalised cross-correlation of received intensity between beams, without regard to mean brightness or variance [10]. These two aspects generalise the concept of Acoustic Daylight to Ambient Noise Imaging, which includes processes for which there is no visual analogue.
- The loss of 95% of the data (by the analogue spectral filters in ADONIS pre-processing) places a very restrictive and damaging bound on our ability to extract statistical information, which is now understood to be of central importance [10]
- Snapping shrimp are the overriding sources of acoustic energy above a few kHz, permitting imaging at far higher frequencies than the thermal limit was expected to allow [9]. It had previously been thought that surface wave action would provide most of the useful energy, even in warm coastal regions.

With regard to snapping shrimp noise, the episodic nature and frequency spread of this biological source mechanism demands improved data sampling densities at the same time as permitting much higher frequencies to be employed, with a corresponding improvement in resolution. The presence of snapping shrimp greatly enhances ANI operation. Since snapping shrimp are encountered in all shallow waters where the temperature never drops below 11 °C, there exists a continuous band between about 30 degrees North and South of the equator where these animals dominate the ambient noise above a few kHz in shallow water.

A recent investigation of the nature of snapping shrimp noise and distribution was carried out by an Australian research centre [11]. Quoting directly from the Abstract of their report,

"sustained ambient noise at frequencies up to 200 kHz in temperate and tropical waters of depths less than about 60 m is characterised by the numerous sharp transient sounds of snapping shrimps"

In the light of these discoveries, there are certain shortfalls in the ADONIS design which now appear a top priority to rectify in a next-generation system:

- 95% of data discarded, severely hampering statistical analysis
- Only crude image processing possible in real time
- Frame rate too slow for smooth transitions or to track the temporal statistics
- Frequency range too low for snapping shrimp environments
- Too bulky and heavy for resolution performance obtained

Despite these limitations, ADONIS has already been extraordinarily successful, easily imaging targets and holes only $1m^2$ in area at a range of 38m [7]. We therefore anticipate that a second-generation system will be able to provide significant image products for operation in shallow warm waters.

3. The ROMANIS design concept

The Remotely Operated Mobile Ambient Noise Imaging System (ROMANIS) is a next generation system design which provides a cost-effective solution to the ADONIS limitations, while improving performance in every respect. Some of the most damaging limitations in ADONIS arise from not using a phased array. A fully-populated phased array is still a prohibitively expensive option. ROMANIS avoids this difficulty by using a sparse array, with a unique primary beamforming technique which nullifies many of the disadvantages known to trouble sparse array systems. Additionally, the massive computational demands of real-time FFT's and beamforming have been reduced by an order of magnitude by an innovative technique which allows a nine-fold decrease in the number of beams formed, while retaining virtually all of the useful information that would be provided by a full set of beams.

These techniques permit us, for the first time, to design a system which significantly raises the maximum

frequency of operation to include more snapping shrimp illumination and improve resolution, while simultaneously overcoming the other shortfalls of ADONIS. Commercial Off-The-Shelf (COTS) products have been sourced which provide a solution to the data collection and analysis demands of the ROMANIS concept at moderate cost.

3.1 ROMANIS overview

The ROMANIS concept is to produce real-time acoustic colour video images of underwater environments with an unprecedented resolution, accuracy, data density and flexibility. To provide a much greater freedom in deployment scenarios and environments, ROMANIS is to be mounted on a Remotely Operated Vehicle (ROV) as a host platform. Each major component of ROMANIS has been designed to be a stand-alone asset, so that investment in the modular components can benefit related programs. The elements of the system are shown in Fig. 2, and the more innovative components will be described individually in the subsections that follow.

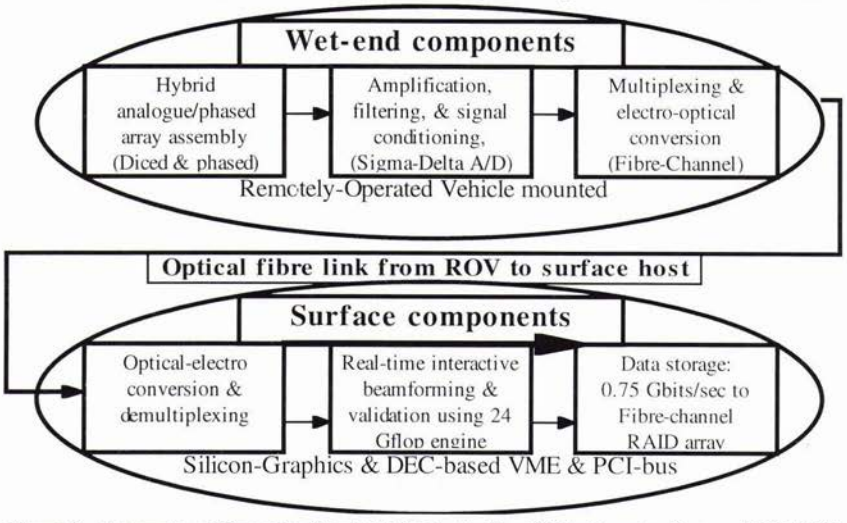

Figure 2. Schematic of Remotely Operated Mobile Ambient Noise Imaging System ROMANIS

3.2 Remotely-operated vehicle

We wish to provide ROMANIS with the capability to be deployed in a variety of environments and scenarios, and to make it mobile and navigable. Rather than consider building some form of mobile platform, with all the associated engineering problems, it has been decided to use a COTS Remotely Operated Vehicle (ROV). A deep-diving hydraulic ROV with 50 kg load capacity would weigh perhaps 250 kg, and require a dedicated surface handling system. For our purposes, we prefer an electrically-powered ROV, since we do not require powerful manipulators, and would additionally benefit from removing the high-frequency acoustic noise associated with high-pressure hydraulic flows. Furthermore, we do not anticipate requiring a depth capability in excess of 100m.

In addition to the basic ROV, some specific additional equipment is required to mount ROMANIS. This equipment falls into two groups. The first group consists of commercially-available items, particularly a dynamic position-sensing package which is necessary to correct the ROMANIS acoustic beams for tilt, yaw and roll of the ROV while imaging. The second group consists of unique mechanical fittings to mount the ROMANIS wet-end hardware, permitting mechanical tilt etc., which will be developed at the National University of Singapore in collaboration with other engineering centres.

3.3 Acoustic Sensor Array

This component is the most crucial and custom-designed part of ROMANIS. To realise the advantages of phased-array acoustic beamforming, a solution to the massive cost and computational difficulties associated with a fully-populated 2-D array of sufficient aperture must be found. The oft-applied solution is a sparse array, defined as an array with fewer elements at larger spacings than the $\lambda/2$ value required by a fully-populated array. There is a considerable body of research on sparse array theory, but there are basically two central disadvantages.

The first is that a sparse array suffers from spatial aliasing of its beams. This means that (for example) while aimed at broadside, equally sensitive beams are formed at angles corresponding to asin(λ/d), where d is the element spacing (d>λ). This drawback can be partially overcome by using a variable spacing and shading, so that the grating lobes become diffuse and are suppressed, compared to the central beam which remains fully coherent.

The second disadvantage is that sensitivity is sacrificed, due to the reduced number of elements which receive acoustic energy. This is not so crucial a loss to an active system, where the transmitted signal can be made strong and, in any case, should normally be louder than the background ambient noise in order to be heard with good signal quality. For an ANI system, the background noise **is** the signal, and so the system needs to be very sensitive. Analogue beamforming lenses overcome these problems by focusing energy geometrically, as ADONIS does, but suffer from other disadvantages. For ROMANIS, a unique solution is proposed, which we shall term a hybrid analogue-phased array.

3.3.1 Hybrid analogue-phased array principle

A fully-populated circular array of some 1.5m diameter (the projected size for ROMANIS) would require some 4 x 10^4 elements. We do not believe that we can accommodate more than 256 at reasonable cost, over two orders of magnitude fewer. The conventional answer is to place the (reduced number of) elements in a sparse pattern, pseudo-random being popular for large numbers, as it converges to an optimal suppression of side lobes.

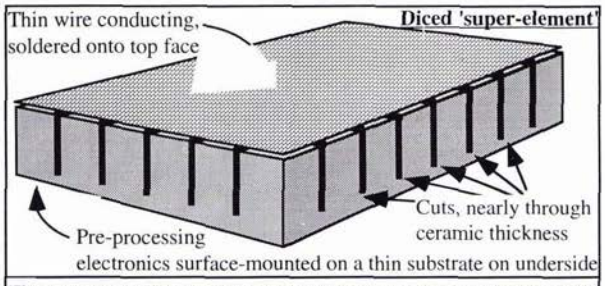

Figure 3. 'Super-element' design, using sub-elements from one block

In our case, we wish also to collect the energy incident on the entire surface, so that a normal sparse array will not suffice. We have therefore designed an array which is *fully populated*, but where groups of elements are hard-wired for broadside beamforming, that is, with their outputs simply connected in parallel without phase or amplitude modulation. These 'super-elements' are in fact never cut into truly separate elements, but partially-diced from larger blocks to create ceramic sub-elements with appropriate mechanical properties (resonances etc.,) while maintaining the alignment with neighbouring sub-elements by retaining a thin substrate of ceramic connecting their bases. A sketch diagram of such a super-element is shown in Fig. 3, though the cuts would probably be arranged to form hexagonal sub-elements, rather than rectilinear as shown. The collection of sub-elements into super-elements allows us to fully populate the array surface for incident energy, while keeping the number of independent outputs two or more orders of magnitude fewer. The analogue hardwiring of sub-elements combined with the phased beamforming of the super-elements constitutes a hybrid array system.

But what is the impact on the beams that one can form in this hybrid fashion? How large should one make the super-elements? Consider a super-element of characteristic diameter d, where d>>λ. It is simple to show that the grating lobes associated with a sparse array of uniform element spacing d steered to an angle θ from broadside occur at ϕ, given by

$$\sin(\phi) = \pm\frac{nc}{fd} + \sin(\theta) \qquad (1)$$

where n is a positive integer small enough so that sin(ϕ) is real, c is the speed of sound and f is the frequency. For d>>λ, and for small θ we can use the Taylor expansion for the sin functions and, collecting terms, we find that

$$\phi_+ \geq \lambda/d + \theta, \qquad \phi_- \leq -\lambda/d + \theta \qquad (2)$$

so that the first side lobe on either side of the desired steering angle occurs further away than λ/d radians. From Rayleigh's results, we

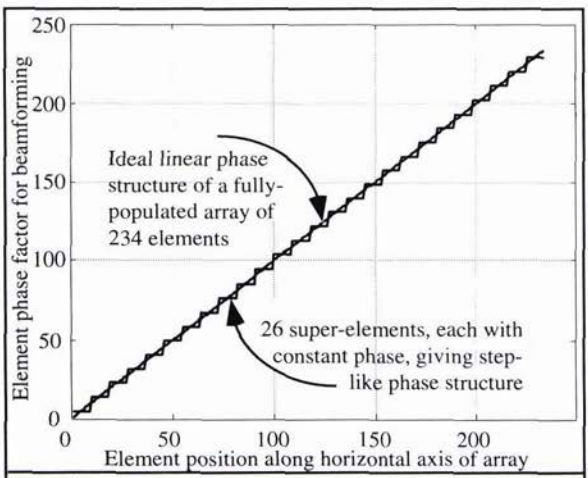

Figure 4. Ideal phase vs. sparse hybrid beam phasing

know that the beamwidth of an aperture of diameter d is characterised by the same factor, λ/d. This tells us that such a sparse array, if formed from sub-elements which fully-populate the antenna surface, will have side lobes which are significantly attenuated by the beampattern of the analogue-phased super-element grouping. The size, d, of these super-elements is then determined only by the range of angles which we require to form beams. For ROMANIS, we anticipate the luxury of full 3-D maneuverability with the host ROV, so a narrow 'letterbox' shaped forward-viewing region is appropriate. We have therefore designed the ROMANIS array for an approx. 10-degree viewing angle in the horizontal, and 5 degrees in the vertical. Taking the horizontal dimension as an example, we show the effective phase shading of the elements as a function of position along the array compared to an ideal fully-populated array in Fig. 4. The super-element grouping used in Fig. 4 equates to a decimation factor of 9, so that the beamforming problem would be reduced by some two orders of magnitude using this decimation over a 2-D array.

The last issue concerning the hybrid array design is the impact on beamforming quality. For the decimation factor 9 used in Fig. 4, we have calculated the beampattern of a 1.5m array at 120 kHz, the most demanding (upper) frequency of interest, for an equally-spaced sparse array. Lower frequencies correspond to lesser decimation factors, and hence more closely ideal fully-populated performance. For broadside beam-forming, there is no degradation of performance, since the analogue beam-forming is equivalent to broadside phasing. The worst performance occurs at maximum θ. We show the worst case scenario in Fig. 5, where we have computed the beam sensitivity vs. angle at 120 kHz steered 5 degrees off broadside for incoming angles of 0-19 degrees. The beampattern of a perfect fully-populated array is shown as a dashed line for comparison. It can be seen that the primary beam and side-lobes are very similar, apart from a 2 dB drop in peak sensitivity for the sparse hybrid array. The fully-populated array has no grating lobes, of course, but the sparse array has a set in the predicted positions, the first occurring at about 18 degrees in almost precise agreement with the equality in (2). The grating lobes are successively attenuated as anticipated by the super-element beampattern, the first being 13 dB below the primary beam with subsequent lobes lower still. An added bonus is that there is an improvement in sidelobe performance at intermediate angles.

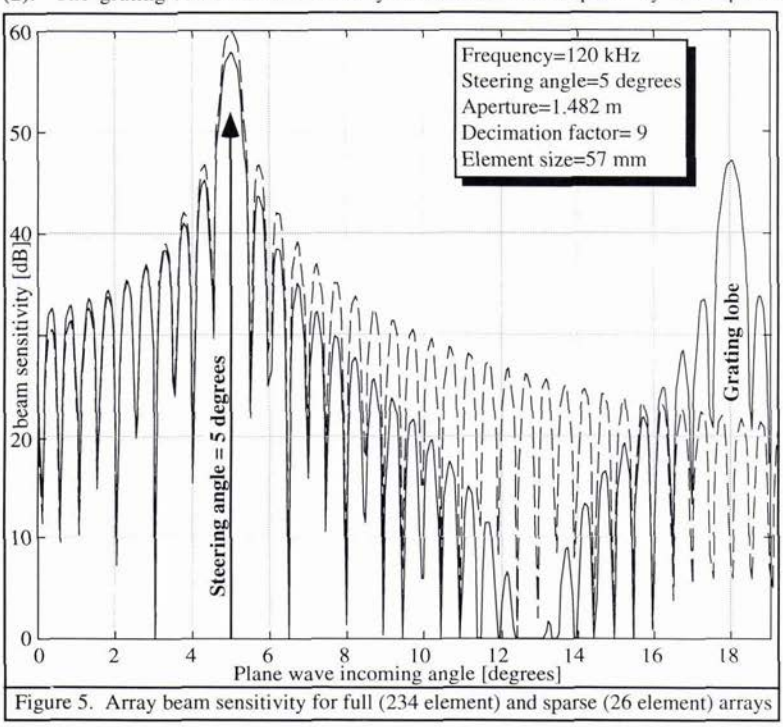

Figure 5. Array beam sensitivity for full (234 element) and sparse (26 element) arrays

3.3.2 Array configuration

ROMANIS is of course designed with conventional variable super-element size and spacing, so that the traditional methods of grating lobe suppression in sparse array designs are simply aided by the additional tech-nique of hybrid beam-forming which simult-aneously reinstates the full sensitivity of a fully-populated array. We are also concerned with the hydrodynamic performance of the array. ROMANIS must be maneuverable, and so the array area should ideally be no larger than the frontal aspect of the ROV that carries it. Indeed, one would norm-ally construct the array on a convex surface, a nose-cone, for an operational system. To keep ROMANIS as simple as possible, we have initially limited ourselves to a planar array, but with slots cut into the array plate to facilitate hydrodynamic flow. These slots are made possible by the variable spacing of the sparse array, which has element separations which increase logarithmically from the array centre. The differing required angles of view in the horizontal and vertical proscribe different element dimensions in the vertical and horizontal, and thence spacings. A sketch of

the overall design, combining the best of sparse array variable spacing, hybrid beamforming and hydrodynamic performance, is shown in Fig. 6. A total of 256 super-elements are used, arranged with a fully-populated 'core' area consisting of 188 super-elements, surrounded by a further 68 elements in a variable-spacing arrangement.

3.4 Amplification, filtering and signal conditioning

The output from ceramic elements is of the order 10^{-10} V at 1 μPa. To reduce EM contamination, the signals need to be amplified as close as possible to the elements themselves. This is normally carried out within the array assembly, with shielded twisted pair conductors being used to carry the signal to the first amplification stage. This traditional approach requires considerable space and careful assembly to accommodate the shields and twisted pairs, mount the several hundred amplifier chips etc., particularly when the elements are so closely spaced as for ROMANIS.

The solution developed for ROMANIS is to deposit the complete signal-conditioning stage directly onto the silvered back face of each super-element group, including a Sigma-Delta A/D device such as an Analogue Devices model AD776 or Motorola DSP56ADC16 in surface-mount configuration. Developments in micro-electronics, for which Singapore now has a new research institute, permits this cost-effective technique to be developed. The successful commercial development of this idea could be of substantial value.

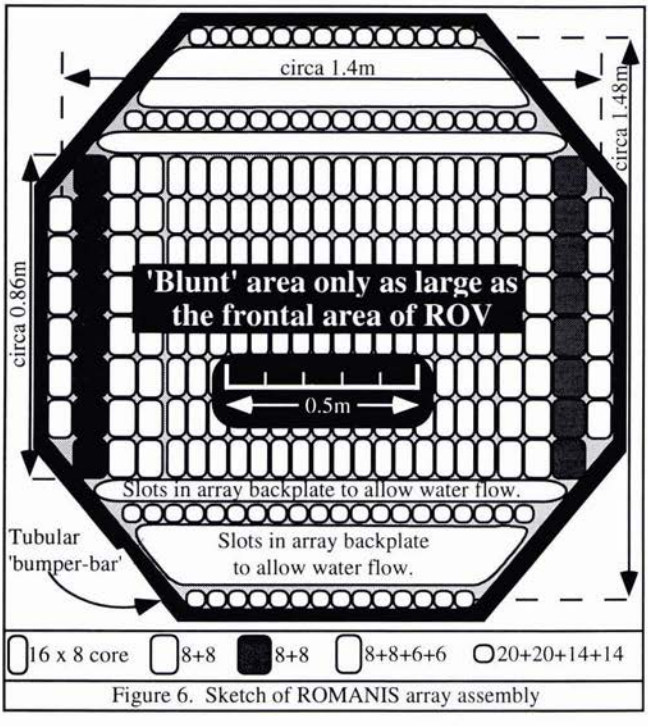

Figure 6. Sketch of ROMANIS array assembly

3.5 Multiplexing and electro-optical conversion

To keep the weight and size of the wet-end electronics to a minimum, we plan to convert the signals to Fibre-Channel protocol on the element itself. The Fibre-Channel communications protocol includes a loop topology which allows data to be collected from a large number of nodes and assembled in a 'train' of data. This can be configured to achieve multiplexing from our elements, so that the control node simply takes the assembled data train and transmits it via optical fibre to the surface. Each channel will be sampled at 250 kHz. The total bandwidth of the signal (from all 256 elements) will be some 25.6 MHz, and will require a 64 MHz sampling rate, easily accommodated by Fibre-Channel and inexpensive multi-mode optical fibre technologies.

3.6 Opto-electrical con-version and demultiplexing

This stage will be accomplished by the same family of Fibre-Channel card products as is selected for the wet-end data management tasks. The conversion will not be required for data storage, as a Fibre-Channel RAID array (very recently available on the open market) can accept the data directly. The demultiplexed signals are for data validation by our Silicon Graphics machine, and real-time beamforming by a multi-processor DEC alpha engine.

3.7 Time domain interactive beamforming

The 24 Gflop DEC computational engine will be fully configurable on the fly, permitting the selection of arbitrary weights and delays for the elements, update of roll, pitch and yaw of the ROV and beam steering. This permits interactive beamforming which includes ROV motion compensation and a digital zoom facility for a fully-variable field of view. Nevertheless, the computational load still greatly exceeds the 24 Gflop available. The load can be reduced by 50% if we use 2 rather than the normal 4 taps for the sample interpolation necessary in the beamforming process. This degrades the sidelobe rejection from -40 dB to only -20 dB, but given the nature of our application (where neighbouring beam energies usually differ by only a few dB), this is still acceptable. Still, a further order of magnitude reduction in computational load is required. To achieve this we

have developed an idea which uses the redundancy in the spatially-aliased beams at lower frequencies and the excess frequency resolution inherently available in the rapid sample rate compared to the desired frame rate to reduce the number of beams that need to be formed simultaneously. We term this technique beam-dithering.

3.7.1 Beam dithering

One way to reduce the number of beamforming boards is to form only some beams simultaneously, and to steer the beams on the fly through a succession of look directions to obtain the full number of required pixels. The disadvantage of this technique is that, if only 1/n of the total number of beams are formed simultaneously, then we are discarding (n-1)/n of the data. This was precisely the most damaging limitation of ADONIS, which discarded 95% of the data. It is in the recovery of this discarded data that the innovation lies.

We know that there must be a redundancy in the information. We can demonstrate this by considering the case where beams are formed in the frequency rather than in the time domain. Since the effective λ/D of the aperture increases at lower frequencies, the beamwidth must increase. We therefore require fewer beams to cover the same viewing region. There is a further redundancy. We require a frame rate of no more than 100 Hz to provide smooth transitions to track even the fastest targets. Nevertheless, we must sample at 250 kHz or more to estimate energies at 120 kHz, even with Sigma-Delta systems. This allows us a 2,500 point FFT length for each frame, which will yield some 1,250 frequency estimates. Since all the conceivable sources for ANI illumination are broad-band, and we seek only to characterise the spectra for acoustic colour purposes, it is difficult to imagine that we shall require more than perhaps 64 independent frequency estimates (ADONIS used 16). There is therefore an inherent redundancy of a factor of 20 in the information from this point of view alone.

The question remains, how do we utilise this redundancy to permit lossless time-domain beam dithering? Imagine the pixels divided into blocks of 3 x 3. We propose to assign only one beam to each block of nine pixels, steering it to each in turn for just over 1/2 msec to collect 128 samples. In 5 msec, all the pixels will have been sampled. We propose that the received energy is separable into a rapidly-fluctuating level (responsive to individual snapping shrimp events) and a slowly-varying spectral shape (since all shrimp sound alike). So, the spectral shape changes slowly (as targets and ROMANIS move about), while the energy may change rapidly (as the statistics of the sources fluctuate).

We know that the lower frequencies will have overlapping beams, so that each pixel will cover an angle of vision some 3 x 3 times as large at 33 kHz as at 100 kHz, providing complete coverage at the lower frequencies, even when dithered. We can thus use the lower frequencies to track the (rapidly-varying) intensity over the entire image region. The discarded data at higher frequencies can then be recovered by interpolating the spectral shape changes between successive ground-truth samples of each pixel, constraining the spectral energy to follow the intensity, tracked at the lower frequencies. We obtain some 200 'ground-truth' frames per second for each pixel, allowing us to average for increased stability before displaying at 60-100 Hz frame rate. The validity of the beam-dithering technique can be verified by comparing the spectral shapes of successive samples for each pixel and confirming that the shape correlation remains high over the 5 msec required. If an environment is encountered where the dithering is undesirable, we can eliminate it by reassigning the beam steering on the fly. Similarly, we could choose to zoom out with increased dithering to view larger areas (within the constraints of the beam patterns provided by the hybrid lens system).

4. Conclusions

COTS products and a 10^3 reduction in computational load achieved through novel signal processing put a high-performance second-generation ANI system within reach. A hybrid analogue/phased array has been designed for ROV mounting, married to a 24 Gflop computational engine via fibre-optic cable. The Remotely Operated Mobile Ambient Noise Imaging System (ROMANIS) will be a valuable tool for high-frequency ambient noise studies (such as for breaking wave processes) and imaging, with a spatial and temporal resolution greatly exceeding any current instrument. Furthermore, full data stream recording on Fibre-Channel RAID arrays will permit arbitrary post-processing and permits the exploration and development of new image-processing algorithms.

References

[1] Buckingham, M.J., J.R. Potter and C.L. Epifanio. "Seeing underwater with background noise", *Scientific American*, **274**(2), 40-44. 1996.

[2] Makris, N.C., W.A. Kuperman & F. Ingenito. "Bounds on the detection of a submerged object insonified by surface noise in a shallow water waveguide", *Sea Surface Sound* '94, M.J. Buckingham & J.R. Potter, eds., 45-64. 1995.

[3] Potter, J.R. "Acoustic imaging using ambient noise: Some theory and simulation results", *Jnl. Acoust. Soc. Am.*, **95** (1), 21-33. 1994.

[4] Buckingham, M.J. "Theory of acoustic imaging in the ocean with ambient noise", *Jnl. Comp. Acoust.* **1**, 117-140. 1993.

[5] Buckingham, M.J., B.V. Berkhout & S.A.L. Glegg. "Imaging the ocean with ambient noise", *Nature* **356**, 327-329. 1992.

[6] Potter, J.R., M.J. Buckingham, G.B. Deane, C.L. Epifanio and N.M. Carbone. "Acoustic Daylight: Preliminary results from an ambient noise imaging system", *Jnl. Acoust. Soc. Am.*, **96** (5 Pt.2), 3235. 1994.

[7] Potter, J.R. & M. Chitre. "ADONIS imaging with a Kalman filter and higher-order statistics", *Proceedings of the Third European Conference on Underwater Acoustics*, Heraklion, Greece, 349-354. 1996.

[8] Olivieri, M.P. and S.A.L. Glegg. "Imaging of passive targets in shallow water using an ambient noise imaging system", *Jnl. Acoust. Soc. Am.*, **99** (4 Pt.2), 2453. 1995.

[9] Mellen, R.H. "The thermal noise limit in the detection of underwater acoustic signals", *Jnl. Acoust. Soc. Am.*, **24**, 478-480. 1952.

[10]Potter, J.R. & M. Chitre. "Statistical models for ambient noise imaging in temperate and tropical waters", *132 meeting of the Acoustical Society of America*, Honolulu, HI. Dec. 1996, **100** (4) Pt. 2, 2738. 1996.

[11]Cato, D.H. and M.J. Bell. "Ultrasonic ambient noise in Australian shallow waters at frequencies up to 200 kHz", DSTO Materials Research Laboratory report # MRL-TR-91-23. 1992.

Acoustic Signal Dispersion and Distortion by Shallow Undersea Transmission Channels

Joseph A. Rice

Naval Command, Control & Ocean Surveillance Center, RDT&E Division (NRaD)
Acoustic (Undersea Propagation) Branch (Code D881)
San Diego, CA 92152 USA
Email: rice@nosc.mil

Abstract

The undersea littoral is an adverse medium for acoustic signal transmission to horizontal ranges of many water depths. Reflections and scattering in the bounded, nonhomogeneous channel disperse the arrival of received signal energy with a prolonging effect called multipath spread. Motion of the reflectors and scatterers disperses the frequencies of the received signal with a bandwidth broadening effect called Doppler spread. This paper examines the oceanographic causes and acoustic effects of the doubly-spread channel. Dispersion and distortion phenomena are evaluated according to relationships between the spread parameters and the signal parameters. This categorization, along with considerations of received signal-to-noise ratio, provides a context for identifying digital communications strategies for the shallow-water undersea acoustic channel.

1. Introduction

In littoral seas 10 to 200 meters deep, wireless signaling technology is needed to link underwater stations separated by horizontal ranges greater than five kilometers. For many applications, accessing atmospheric transmission channels by way of surface buoys is impractical or unacceptable. Most forms of undersea signal radiation are inadequate. Electromagnetic waves suffer high transmission loss because of the high conductivity of seawater. Extremely-low-frequency lateral electromagnetic waves show promise for low data rates, but require large transmitter apertures and power sources. Optical waves, including those produced by blue-green lasers, are rapidly attenuated. Seismic waves are overly dependent on local geology.

Sonic pressure waves provide the best impedance match to the environmental channel. Nature affirms the use of sound energy as evidenced by the many marine biosonar and bioacoustic systems selectively evolved for feeding and reproduction. To advance digital acoustic telemetry and ranging capabilities for autonomous undersea systems, the U.S. Navy has initiated exploratory development of "telesonar" signaling [1].

The difficulties with communicating acoustically in shallow water arise primarily from dynamic interference effects induced by inhomogeneities and nonstationarities of the bounded, multipath medium. Spatiotemporal variability and complex boundaries distort the propagating wavefront, disperse the received energy in time and frequency, and cause signal fluctuations in both amplitude (*i.e.* fading) and phase. Even for unreflected propagation, kinetic channel inhomogeneities produce scintillations similar to the atmosphere's effect on starlight. With horizontal channel geometries, dispersion and distortion are compounded by severe refraction and multiple boundary interactions. Also hindering signal demodulation are the dynamic noise background and transmission loss by spatial spreading and absorption. These impediments historically have limited acoustic telemetry in littoral water to vertical, ducted or short-range horizontal channels.

Advent of the low-power, low-cost, digital signal processor (DSP) has fostered application of modern communication theory to ocean acoustic signaling [2]. Now it is practical to overcome impairments of the long-range horizontal medium with methods developed in the 1960s for telephony, space communications, and Rayleigh fading channels [3,4]. Indeed, rates exceeding 10 kbit/s have been achieved in certain horizontal undersea channels [5].

This paper examines the shallow undersea transmission channel and categorizes dispersion and distortion

phenomena according to the relative time and frequency parameters defining the signal waveform and the channel spread.

2. Transmission channel

The essence of the physical transmission channel includes propagation mechanisms, boundary interactions, and noise phenomena. These time-variant and space-variant processes determine received signal dispersion, signal distortion, and signal-to-noise ratio (SNR).

2.1 Propagation

Communication systems are commonly based on electromagnetic-wave propagation through media such as the atmosphere (radio), wire (electricity), and fiber (light). By contrast, underwater sound is a mechanical transmission of energy in the form of pressure waves propagating through an elastic medium. The transmitter converts electric energy to acoustic energy, thereby projecting sound into the compressible undersea environment. Transducer radiation is described in spherical coordinates by a beam pattern representing the mean-square pressure at a reference distance $r_0 = 1$ m from the theoretical point-source origin. An omnidirectional projector radiates uniformly at all angles with a vector intensity I_{omni}. A directional projector radiating the same total acoustic power and aligned with the axis of maximum intensity I_0 toward the receiver provides gain (in decibel units) according to the transmitting directivity index $DI_T = 10 \log I_0/I_{omni}$.

As the acoustic wavefront expands into the undersea environment to range r, geometric spreading reduces the signal intensity I_r. A commonly applied estimate of spatial transmission loss for shallow-water channels is $TL_{spa} = 10 \log I_r/I_0 \approx 15 \log r$. This rule provides a realistic compromise between spherical spreading by r^2 in an unbounded free field and cylindrical spreading by r in an ideal planar waveguide. Further attenuation by volume scattering occurs upon incidence with suspended particulates, entrained bubbles, and biomass abundantly present in nearshore waters. Section 2.2 describes additional transmission losses at the sea surface and seafloor.

As early as World War I, narrowband submarine communication was performed by on-off keying rudimentary moving-coil transducers. Quantitative evidence for the coherence of a broad bandwidth appeared in the 1940s, when a series of experiments involving small underwater explosions showed that a shock-induced pressure wave retained a rise time of $T = 20$ μs at the propagation range $r = 1{,}000$ m [6]. Preservation of this sharp leading edge implies that the useful sonic bandwidth of the observed channel, viewed as a filter, is $W = 1/T = 50$ kHz. The flat response to a broad acoustic spectrum indicates the potentially large communications capacity of seawater channels. At the very short range $r = 60$ m, a 1-MHz acoustic band provided a record-setting digital throughput of 500-kbit/s [7]. But the useful spectrum diminishes with increasing range because seawater cumulatively absorbs sound roughly in proportion to the square of the frequency. The dominant absorption mechanism at frequencies between 5 and 100 kHz is acoustic energy conversion to heat by ionic relaxation of $MgSO_4$ salt molecules. Absorption therefore causes additional transmission loss, $TL_{abs} = \alpha r \times 10^{-3}$. The 10^{-3} factor allows range r to be in units of meters while the frequency-dependent and mildly temperature-dependent absorption coefficient α is conventionally expressed in units of dB/km. Empirical formulae yield absorption coefficients at 20°C of $\alpha = 0.5$ dB/km at $f = 10$ kHz and $\alpha = 2$ dB/km at $f = 20$ kHz, for example. Even within the useful propagating band, absorption will differentially attenuate the frequency components of a spread-spectrum or other wideband signal.

Traveling orders of magnitude slower than familiar electromagnetic signals, ocean acoustic waves propagate at the nominal speed $c = 1500$ m/s, and require nearly seven seconds to reach a notional range of $r = 10{,}000$ m. Sound speed in seawater increases with temperature, salinity, and pressure. In littoral waters, these variables are governed by large-scale circulation and seasonal forcing, and influenced by wind, upwelling, daily temperature cycles, mixing, tides, surface waves, internal waves, evaporation, precipitation, and runoff. The ensuing medium is inhomogeneous and stratified, producing sound-speed variations that distort the acoustic wavefront. The net result is time-dependent, range-dependent, and strongly depth-dependent acoustic refraction.

The expanding wavefront is often illustrated as a set of emanating rays depicting discrete propagation paths governed by Snell's law of refraction. A ray intersecting the receiver location is an eigenray. If several eigenrays exist for the transmitter-receiver geometry, the transmission medium is a multipath channel, with asynchronous convergence and interference of geometrically distinct arrivals at the receiver. Some eigenrays comprise many slightly divergent and reconvergent micropaths created by nonuniform refraction at small-scale inhomogeneities. Since shallow water is a bounded medium, most of the multipath structure results from specular boundary reflections.

Signaling range is ultimately limited by the propagation pattern. Knowledge of the oceanography in the intended operating environment is essential for anticipating the availability of a reliable acoustic path. Oceans

are predominantly characterized by a warm, wind-mixed, surface layer overlying a thermocline of increasingly colder water with depth. Such temperature gradients produce sound-speed profiles that refract sound rays downward. In the deep ocean, isothermal conditions prevail at depths exceeding z = 1,000 m where sound is refracted upward by the influence of pressure. Refraction toward the depth of sound-speed minima results in a duct known as the deep sound channel. In littoral seas, however, the shallow seafloor generally rules out long-range, ducted propagation. Bottom-limited downward refraction produces bottom-to-bottom paths favoring acoustic modems placed near the seafloor. Here modems are more likely to be connected by waterborne signal energy propagating along refracted direct paths, long-range refracted bottom-bounced paths, and surface-reflected paths. Furthermore, the shadow zones existing beyond the convergence of downward reflected and refracted energy do not occur near the bottom.

2.2 Boundaries

Transmission is strongly dependent on the acoustic characteristics of the sea surface and seafloor. Incident propagating energy is reflected, scattered, and absorbed in varying proportions, producing a weakened specular reflection and a spatially distributed redirection of scattered sound. Sensitivity to boundary roughness is proportional to signal frequency because scattering features increasingly distort the signal wavefront as the signal wavelength is shortened. A criterion for the acoustical roughness or smoothness of a boundary is the Rayleigh parameter, $\rho = k\Gamma \sin\theta$, where k is the acoustic wave number $2\pi f/c$, Γ is the boundary trough-to-crest height variation at the localized region of eigenray incidence, and θ is the grazing angle [8]. If $\rho << 1$, the surface is primarily a reflector and yields a coherent wavefront reflection at the specular angle equal to the angle of incidence. When $\rho >> 1$, the scattering is incoherently distributed in space.

The sea surface is a high-impedance interface between the liquid acoustic channel and the pressure-releasing air above. Absorption does not occur at this boundary, but reflection and scattering patterns can exhibit rapid time variability. If the surface is roughened by wind waves such that $\rho \geq 1$, the "specular" reflection actually comprises many component micropaths scattered forward from evolving sets of momentarily aligned facets or corrugations on some large elliptic region of the boundary. Motion of a finite sea-surface scattering element imposes a Doppler shift $\Delta f = 2f(v/c)\sin\theta$, where f is the signal frequency and v is the vertical component of the surface velocity. The instantaneous reflectors have assorted vertical motions, so that each forward-scattered waveform is subject to a distribution of Doppler shifts related to the power spectral density of the sea surface. Hence the reflected waveform experiences a phase reversal, loses energy to out-of-beam scattering, and acquires a Doppler-smeared frequency band. In summary, forward scattering from the sea surface is time-variant and sensitive to the acoustic frequency, grazing angle, and sea state.

The redistribution of bottom-scattered energy depends on the acoustic frequency, grazing angle, bottom composition, and bottom slope. Geoacoustic properties differ dramatically within littoral seabeds, depending on the varying composition of seawater, clay, silt, sand, gravel, moraine, chalk, limestone, and basalt (here listed in increasing order of sound speed). Irregular bathymetry and sediment deposition are attributable to faults and fractures created by continental-margin geophysics, and from now-submerged terraces and canyons formed during the last ice age by reduced sea levels. Above some critical grazing angle sound penetrates the bottom and is converted to bottom-borne energy or is reradiated as waterborne energy. Penetration into the bottom is generally greater in the summer than in the winter because sea-surface warming increases the temperature gradient and strengthens downward refraction. Bottom absorption is a significant cause of transmission loss, irretrievably reducing the net signal energy reaching the receiver. For frequencies above 5 kHz, bottom-borne energy is absorbed within an effective acoustic penetration depth of about ten meters. An advantage of absorption is the alleviation of complexities from bottom-borne propagation. Above 5 kHz, therefore, bottom relief is the significant influence on received signal energy. In shallow water, irregular or sloping bathymetry produces three-dimensional eigenrays. Forward scattered sound is spatially distributed amongst the many boundary-induced micropaths, including reradiated energy from sound that has penetrated the bottom.

For transmitter and receiver near the sea surface or at intermediate depths, the multipath structure is usually stable and successfully modeled by ray theory. The bottom interaction occurs at discrete, localized sites and the relatively steep grazing angles allow sound waves to reflect coherently, despite partial absorption by the bottom. Near-surface modems can suffer image interference between the nearly synchronous arrival of parallel eigenrays having approximately the same intensity, one reflected at the nearby surface and the other not reflected.

For transmitter and receiver at or near the seafloor, the wavefront includes small bottom-grazing angles where the reflected waves are perturbed by an angle-dependent phase shift [9]. These phase shifts affect the many three-dimensional micropaths joining near-bottom stations, and the net boundary effect is diffuse, noncoherent smearing of received signals. For frequencies above a few kilohertz, the seafloor is often assumed to be a solid half-space supporting only shear waves and forming a rigid boundary where the pressure field is maximum and acoustic particle velocity is small. Under this assumption, a receiver near the bottom would sense all

compressional propagating modes of the fluid waveguide, and be influenced by evanescent bottom-boundary interface waves and reradiated energy from bottom-borne shear waves. If the seafloor is fluid or elastic, however, sound wave interference could result from the nearly coincident image reflection from the bottom [10]. With downward refraction, a pair of modems at some height above the bottom would have clustered multipath arrivals, with each cluster comprising four parallel eigenrays formed by image reflections from the seafloor in the vicinity of neither, both, or either modem.

Horizontal propagation in shallow water involves repeated interaction of the wavefront with rough boundaries. Propagation is further complicated by the time-varying nature of the sea surface and the range-varying nature of the seafloor. Thus the bounded shallow-water channel is an imperfect waveguide. For a wide range of propagation angles and frequencies, acoustic energy is trapped as discrete, frequency-dependent modes. The channel impulse response is normally dominated by a sparse pattern of discrete multipath arrivals. Complications arise from nonstationarities and nonhomogeneities of the boundaries. Within the shallow waveguide, propagation modes may also oscillate because of hydrodynamic sea-surface waves and internal waves, further disrupting channel stationarity. These time-variant and space-variant influences smear the impulse response and make it time-dependent.

2.3 Noise

Littoral acoustic channels are impacted by dynamic noise mechanisms both natural (biologics, waves, wind, rain) and man-made (distant shipping, local traffic, industry). These produce fluctuating background levels with a dynamic range of 60 dB over seasonal time scales. A contributor to in-band noise is incoherent signal reverberation. Likewise, co-channel multiple-access interference can elevate the noise level. Distortion can result from these interference sources to the extent that they correlate with the desired signal. Otherwise, ambient noise is an additive effect rather than a distortive effect, but its presence prevents signal demodulation if the SNR is inadequate. Demodulators that adaptively remove signal distortion are particularly inhibited by low SNR. Directional transmitters and receivers improve SNR by increasing the correlated received signal power relative to the uncorrelated omnidirectional noise.

Sonic frequencies below 1 kHz are known to offer optimal propagation in shallow-water environments [11], but the decreased signal attenuation does not offset the elevated ambient noise arriving from many distant sources. Telemetry signals must have sufficient energy to overcome range-dependent and frequency-dependent transmission loss, $TL(r,f)$, and frequency-dependent ambient noise level, $NL(f)$. The sonar equation permits analysis of these phenomena to identify optimal signaling frequencies for the intended horizontal range, r [8]:

$$SNR(r,f) = SL(f) - TL(r,f) - NL(f) \tag{1}$$

For flat transmitter source-level spectra with $SL(f) = constant$, the frequency band with highest $SNR(r,f)$ emerges as the minima of the summed spectra of $TL(r,f)$ and $NL(f)$ phenomena for the littoral waters. Equation (1) favors increasingly higher frequencies with decreasing range, r. For transmission to ten-kilometer ranges, $SNR(r)$ is maximum for the spectral region around $f = 8$ kHz.

3. Spreading

The transmitter digitally encodes the data message using block codes or convolutional codes. The encoding provides redundant binary information enabling the receiver to more reliably decode the data message despite noise and interference introduced by the channel. Next the transmitter modulates the digitally encoded information by mapping it into analog waveforms compatible with the physical channel. A transmitted waveform has time duration, T, and frequency bandwidth, W. The product TW is a measure of processing gain available to an energy detector. Define R as the transmission rate of a waveform sequence. Direct-sequence spread-spectrum modulation utilizes the entire available channel bandwidth with each waveform and transmits consecutively with time interval $T = 1/W = 1/R$. Thus $TW = 1$ for direct-sequence modulation. Frequency-hopped spread-spectrum modulation is less bandwidth efficient but allows greater design flexibility in choosing transmitted signal duration T, transmitted signal bandwidth W, and transmission rate R.

3.1 Multipath spread and Doppler spread

The receiver responds to energy from a given waveform over an interval of duration $T+L_{max}$ and at frequencies of bandwidth $W+B_{max}$. L_{max} and B_{max} are the maximum extent of channel-induced multipath spread and Doppler spread, respectively, of the received waveform. In practice, $T+L_{max}$ and $W+B_{max}$ are the interval and band over which the received signal exceeds some power threshold relative to received noise levels. Because the undersea channel often produces multipaths resolvable in the time domain, multipath spread L_{eff} and Doppler spread B_{eff} associated with the resolvable multipath may be measured and used as the effective spread parameters associated

with that multipath subchannel.

Multipath spread is the added duration of the received waveform by the arrival of transmitted energy in the form of specular multipath reflections and forward scattering. Therefore L is a measure of channel time dispersion. The channel coherence bandwidth W_{coh} is the bandwidth over which the channel or subchannel is "flat" and passes all spectral components with approximately equal gain and linear phase. For totally scattered channels with no resolvable multipath, an estimate of the channel coherence bandwidth is $W_{coh} \approx 1/L_{max}$. For resolvable multipaths, the estimate is $W_{coh} \approx 1/L_{eff}$. Multipath spread and coherence bandwidth describe the time-dispersive nature of the channel but offer no direct information about temporal variability.

Time-dependent variations in the channel are impressed upon the signal as Doppler shifting of spectral components and an overall broadening of the signal band. Time-variant channel phenomena include motion of the source or receiver themselves, motion of the sea surface, motion of volume scatterers, and motion of refracting nonhomogeneites such as internal waves. The largest range of positive and negative frequency deviations observed at the receiver for a given spectral line of the original signal is the Doppler spread, a measure of channel frequency dispersion. The channel coherence time, during which the channel is stable and the impulse response is essentially invariant, is estimated by $T_{coh} \approx 1/B$. For example, if channel Doppler spread is B = 20 Hz, then impulse-response measurements of the channel separated by $1/B > 0.05$ s are uncorrelated.

The channel may be represented as a time-variant linear filter $h(\tau,t)$ describing the response of the channel at time t to an impulse applied at time t-τ. Instantaneous multipath spread is the duration of $h(\tau,t)$ at fixed t. Instantaneous Doppler spread is the time variation of the channel at fixed t, and can be measured by the rate of variations of $h(\tau,t)$. Because τ and f are Fourier conjugate variables, the measurement is conveniently obtained in the frequency domain as the bandwidth of $H(f,t)$ at fixed t.

The maximum observed spread is useful for generally characterizing the channel. L_{max} and B_{max} are, respectively, the maximum duration over all t of $h(\tau,t)$ and the maximum bandwidth over all t of $H(f,t)$.

3.2 Spread factor

Channels spread in both time and frequency are called doubly spread. In general, such channels exhibit both time-selective and frequency-selective fading. Stated alternatively, the fading is neither time-invariant nor frequency flat. The ionosphere and troposphere are doubly spread electromagnetic channels where multipath and Doppler spread are caused principally by scatterers moving randomly within the medium. The undersea acoustic channel, on the other hand, introduces random spread principally at boundary scatterers. Multipath propagation is otherwise slowly varying and largely deterministic. Insofar as the deterministic component of the spread can be tracked or adapted to, receivers must contend only with random scattering by the boundaries. Moving from deep ocean to shallow ductless waters, the channel begins to resemble the random scattering model as the eigenray structure degenerates to purely reverberant transmission.

For conservative, distortionless signaling without tracking or adaptation, the doubly spread channel constrains the signal design:

$$\left.\begin{array}{l} T >> L_{max} \text{ prevents } h(\tau,t) \text{ distortion} \\ 1/T >> B_{max} \text{ prevents } H(f,t) \text{ distortion} \end{array}\right\} \Rightarrow \quad L_{max} << T << 1/B_{max} \tag{2}$$

$$\left.\begin{array}{l} W >> B_{max} \text{ prevents } H(f,t) \text{ distortion} \\ 1/W >> L_{max} \text{ prevents } h(\tau,t) \text{ distortion} \end{array}\right\} \Rightarrow \quad B_{max} << W << 1/L_{max} \tag{3}$$

Conditions (2) cannot be jointly satisfied unless $B_{max}L_{max} < 1$. Conditions (3) represent a dual requirement that $B_{max}L_{max} < 1$ in order to choose the bandwidth of a distortion-resistant signal. If tracking and adaptation are employed with coherent demodulation when $B_{max}L_{max} < 1$, then $T \approx 1/W$ may be specified to achieve a bandwidth-efficient single-carrier serial transmission with direct-sequence modulation.

Therefore an appropriate measure of channel adversity is the spread factor, identified as the product of multipath and Doppler spread, $B_{max}L_{max}$. For a noise-free channel, condition $B_{max}L_{max} < 1$ implies the channel is underspread and instantaneous measurements of the channel impulse response are meaningful. Otherwise, for $B_{max}L_{max} > 1$, the channel is overspread and measurement of the channel impulse response is ambiguous [12].

A tracking or adapting demodulator with knowledge of a sparse multipath structure or knowledge of constant Doppler shifts can use that information to function in nominally overspread channels. In that case, deterministic slowly-varying dispersion of a resolvable multipath or induced by relative modem motion may be measured or predicted. The effective multipath spread L_{eff} and effective Doppler spread B_{eff} may be used to obtain the effective spread factor, $L_{eff}B_{eff}$. For such a demodulator, the effective spread factor is confined to the area covered in the time- and frequency-spreading plane rather than the gross rectangular spreading area defined by

$L_{max}B_{max}$ [13]. For example, if the channel impulse response contains discrete resolvable multipath arrivals with intervening periods of negligible response, L_{eff} would exclude time periods with negligible response. However, adaptation to time-variant channels requires high SNR to reduce the detrimental effects of intersymbol interference (ISI) without being impeded by residual estimation errors.

3.3 A doubly-spread undersea acoustic channel

As a hypothetical illustration of spreading estimation for ocean channels, consider acoustic transmission between a pair of submerged modems at depths $z_1 = z_2 = 200$ m, separated by range $r = 1.0$ km. For simplicity, a constant sound speed $c = 1500$ m/s renders an isovelocity, nonrefractive medium. Signal transmission begins at time t_0. A direct path arrives at $t_d = t_0 + [(z_1-z_2)^2+r^2]^{1/2} / c$, and a reflected path strikes the surface with grazing angle $\theta = \arctan[(z_1+z_2)/r] = 22°$ and arrives at $t_s = t_0 + [(z_1+z_2)^2+r^2]^{1/2} / c$. Neglecting additional multipaths and reverberation, the multipath spread is $L_{max} = t_s-t_d = 0.051$ s.

Now estimate Doppler spread by examining the interaction of the reflected path with the dynamic sea surface. A surface wave with period p and trough-to-crest height Γ has vertical velocity $v = d[(\Gamma/2)\sin(2\pi t/p)] / dt = \pi\Gamma/p \cos(2\pi t/p)$. For waves with average period $p = 8.6$ s and average height $\Gamma_{avg} = 4.1$ m (empirically corresponding to waves driven by 30-knot winds), the sea surface would experience vertical surface velocities $-1.5 < v < 1.5$ m/s. For a hypothetical carrier frequency $f = 20$ kHz, the Doppler spread is $B_{max} = 2\ \Delta f = 30$ Hz. This conservative estimate neglects additional spread from larger-than-average waves (*e.g.*, the average height of the highest 10% of waves developed by 30-knot winds is $\Gamma = 8.5$ m) and from the compound surface reflections of longer multipaths (*e.g.*, the surface-bottom-surface path).

The spread factor of the hypothetical channel is $L_{max}B_{max} = 1.5$. Because highly processed, high-SNR tracking or adaptive demodulators recognize deterministic spreading features such as the two stable modeled eigenrays, an estimate of the effective spread factor is based solely on the area occupancy of the delay-Doppler surface during a finite observation time. For these more complex receivers, however, the degrading spread from refracted micropaths and boundary scattering must be modeled to avoid overly optimistic spreading assumptions and to account for SNR degradation. Statistically distributed beams are a possible way of extending ray theory to account for these phenomena. Eigenrays are first modeled in the usual way, and are then augmented with a probability density function describing the spatial distribution of acoustic energy about the ray. Interactions with complex scattering surfaces may then be mathematically modeled according to theoretical redistribution functions. The net received energy is summed as a time-dependent response of the recombined "eigenbeams."

4. Distortion

Multipath spread and Doppler spread are each responsible for a different type of signal distortion. Fourier transforms can be used to examine dispersion and distortion, but the use of spread estimates provides a convenient way of categorizing these effects and identifying signaling methods to overcome them.

4.1 Time-dispersive channels

A channel nondispersive in frequency (B=0) is a linear time-invariant system. Such is a noncirculating, mirror-flat ocean with no transmitter-receiver motion and no moving scatterers. A slowly time-varying channel (BT<0.01) may also be so modeled if demodulation is adaptive. The response of a frequency-nondispersive channel to a sinusoid is the summation over all eigenrays of the input sinusoid scaled by a constant attenuation and delayed by a constant phase. The received signal is the superposition of contributions from all the reflectors and scatterers forming the channel. Wideband signals in such a channel suffer frequency-dependent gains and phase shift across the signal band. If $W > 1/L$, the constructive and destructive combinations of reflected returns enhance certain frequency components and attenuate others. Hence, the signal frequencies are affected differently by the channel, and the distortion effect is frequency-selective. Frequency selectivity caused by $W > 1/L$ occurs even if $T > L$; here the received waveform has negligible time spreading but may have an altered structure compared to that of the transmitted signal. If $W < 1/L$, the time-dispersive channel behaves as though it is nondispersive and is frequency-nonselective. Lastly, a time-dispersive, frequency-nondispersive channel with $WL << 1$ is frequency nonselective. .

4.2 Frequency-dispersive channels

Doppler spread accounts for temporal variations in the channel, and the associated distortions are time-selective variations in signal strength. Pure Doppler shifts produced solely by a constant transmitter-receiver range rate do not necessarily result in distortion. Channels dispersive only in frequency (L=0) are the duals of channels dispersive only in time. For a frequency-flat fading channel, if the signal bandwidth is much less than the Doppler spread, $W << B$, then the channel appreciably spreads the transform of the signal. But if $B << 1/T$, the

channel is slowly fading and alters the received signal by only a scale factor and a carrier phase shift. Hence, a channel dispersive only in frequency behaves nondispersively and without distortion if $BT << 1$. When $BT >> 1$, the signal is always distorted by the channel, and is dispersed when $B/W >> 1$.

4.3 Doubly-dispersive channels

For doubly spread channels, dispersion-induced fading is both time-selective and frequency-selective. The effect of the channel on the transmitted signal therefore depends on the signal structure, bandwidth, and duration. Table 1 categorizes the gross occurrence of distortion and dispersion on the received signal according to the relative values of T, W, L, and B.

BT	WL	B/W	L/T	Distorted	Time Dispersed	Frequency Dispersed	Remarks
<<1	<<1	<<1	<<1	No	No	No	Implies BL<<1
<<1	>>1	<<1	<<1	Yes	No	No	Implies BL<<1 and TW>>1
<<1	>>1	<<1	>>1	Yes	Yes	No	
>>1	<<1	<<1	<<1	Yes	No	No	Implies BL<<1 and TW>>1
>>1	>>1	<<1	<<1	Yes	No	No	Implies TW>>1
>>1	>>1	<<1	>>1	Yes	Yes	No	Implies BL>>1 and TW>>1
>>1	<<1	>>1	>>1	Yes	No	Yes	
>>1	>>1	>>1	<<1	Yes	No	Yes	Implies BL>>1 and TW>>1
>>1	>>1	>>1	>>1	Yes	Yes	Yes	Implies BL>>1

Table 1: Received signal characteristics [14].

4.4 Intersymbol interference

ISI results when consecutive symbols arrive simultaneously at the receiver via a time-dispersive channel. ISI is negligible if $T >> L$. ISI is avoided if the waveform interval includes a guard time larger than the multipath spread, $1/R > T+L$, thus clearing the channel. Furthermore, since signal waveforms separated in time by at least 1/B are statistically independent, the waveform rate can be increased without incurring ISI if $1/R > T+L+1/B$.

A means of increasing R is by introducing additional transmission bands. Statistical independence is obtained by choosing a guard band $\Omega > W+B+1/L$. The frequency separation between the spectra of adjacent waveforms thereby exceeds the coherence bandwidth of the channel. When a high rate with limited bandwidth is required, resolving interfering symbols is possible only by tracking or adapting to channel dispersion at the demodulator. Tracking or adaptation can only occur with an effectively underspread channel.

If the channel is overspread ($BL > 1$), it is not possible to assign waveform parameters simultaneously satisfying $W << 1/L$ and $T << 1/B$ and $TW \approx 1$. Thus adaptive coherent demodulation cannot be achieved. On the other hand, if $TW \approx 1$ and the signal has long duration $T >> L$, then the signal bandwidth is much smaller than the coherence bandwidth $W << 1/L$ even in an overspread channel. Alternatively a signal with $W >> 1/L$ will resolve the multipath components and provide LW resolvable signal components. Overspread channels may therefore be overcome by transmitting encoded data with waveforms occupying different time-frequency cells separated by at least T_{coh} and W_{coh}. The waveforms will fade independently and diversity coding will allow the receiver to retrieve the encoded information.

5. Conclusions

A signaling philosophy for doubly-spread undersea channels should include appropriate strategies for tolerating or removing dispersive and distortive effects.

Coherent demodulation of a serial stream of phase-encoded symbols has recently been shown to yield surprisingly high bit rates in certain ocean environments by probing, sampling, tracking and adapting to channel fluctuations. To compensate for signal perturbations, the demodulator relies on high SNR, high symbol rates, adaptive equalization, and phase-locked tracking. This reliance imposes the need for high transmit power and sophisticated signal processing. Signal demodulation fails when the channel is effectively overspread unless

augmented with vertical beamforming to directionally resolve effectively underspread subchannels. Therefore, this approach has limited applicability for channels severely impaired by dispersion and noise.

If lower bit rates are acceptable, orthogonal signal waveform sets may be implemented with intersymbol guard times and guard bands sufficient to resist intersymbol interference. Such signals tolerate overspread channels and may be noncoherently demodulated without tracking and adaptation. Other benefits include reduced signal power, reduced processing, and reduced reliance on spatial beamforming. Transmission security and networking are accommodated by the associated low SNR, block or convolutional encoding, and frequency-hopped spread-spectrum modulation.

Environmental adaptation and improved channel efficiency are achieved by tracking deterministic and slowly varying channel parameters, such as stable multipaths and Doppler shifts. This use of channel memory supports refined signal parameters and optimized demodulation. Likewise, bidirectional links allow transmission power control to produce sufficient but not excessive received SNR. Lastly, redundant transmission in time, frequency and space statistically improves signaling performance by providing channel diversity.

Acknowledgments

This work is supported by the U.S. Office of Naval Research Sensors, Sources and Arrays Program (ONR-321SS) as a task of the NRaD Deployable Surveillance Technology Project and a component of the NRaD Code D881 Telesonar Program.

References

[1] J.A. Rice and K.E. Rogers, "Directions in littoral undersea wireless telemetry," *Proc. TTCP Symp. Shallow-Water Undersea Warfare*, October 1996.

[2] M. Stojanovic, "Recent advances in high-speed underwater acoustic communications," *IEEE J. Oceanic Eng.*, vol. 21, no. 2, pp. 125-136, April 1996.

[3] J.M. Wozencraft and I.M. Jacobs, Principles of Communications Engineering, John Wiley & Sons, 1965.

[4] J.G. Proakis, Digital Communications, 3rd ed., McGraw-Hill, 1995.

[5] M. Stojanovic, J.A. Catipovic and J.G. Proakis, "Phase-coherent digital communications for underwater acoustic channels," *IEEE J. Oceanic Eng.*, vol. 19, no. 1, pp. 100-111, Jan. 1994.

[6] A.B. Arons, "Underwater explosion shock-wave parameters at large distances from the charge," *J. Acoust. Soc. Am.*, vol. 26, pp. 343-346, 1954.

[7] A. Kaya and S. Yauchi, "An acoustic communication system for subsea robot," *Proc. Oceans'89*, pp. 765-770, October 1989.

[8] R.J. Urick, Principles of Underwater Sound, 3rd ed., McGraw-Hill, 1983.

[9] K.V. Mackenzie, "Reflection of sound from coastal bottoms," *J. Acoust. Soc. Am.*, vol. 32, no. 2, pp. 221-231, February 1960.

[10] L.M. Brekhovskikh and Y.P. Lysanov, Fundamentals of Ocean Acoustics, 2nd ed., Springer-Verlag, 1991.

[11] F.B. Jensen and W.A. Kuperman, "Optimum frequency of propagation in shallow-water environments," *J. Acoust. Soc. Am.*, vol. 73, no. 3, pp. 813-819, March 1983.

[12] T. Kailith, Measurements on time-variant communication channels," *IRE Trans. Inform. Theory*, vol. IT-8, pp. S229-S236, Sept. 1962.

[13] P.A. Bello, "Measurement of random time-variant linear channels," *IEEE Trans. Inform. Theory*, vol. IT-15, no. 4, pp. 469-475, July 1969.

[14] R.S. Kennedy, Fading Dispersive Communication Channels, Wiley-Interscience, 1969.

The Effect of Suspended Particulate Matter on the Performance of High Frequency Sonars in Turbid Coastal Waters

S.D. Richards [1], A.D. Heathershaw [1], N.R. Brown [2] & T.G. Leighton [2]

(1) Defence Evaluation & Research Agency,
DERA Winfrith,
Winfrith Technology Centre, Dorset DT2 8XJ, United Kingdom
E-mail: sdrichards@dra.hmg.gb

(2) Institute of Sound & Vibration Research,
University of Southampton,
Highfield, Southampton S017 1BJ, United Kingdom

Abstract

Shallow coastal environments are characterised by high levels of suspended mineral particles relative to the open ocean and such suspensions can have a significant effect on the performance of high frequency sonars operating in these environments through thermo-viscous absorption and scattering. This paper shows how the increased attenuation due to these processes can be calculated and results presented demonstrate that such calculations should be included in future high frequency, shallow water, sonar performance models.

1. Introduction

Classically, efforts in sonar performance prediction modelling have concentrated on the low frequency, long range, anti-submarine warfare (ASW) scenarios in the deep ocean (so-called 'blue-water'), well away from coastal influences. Sonar applications in shallow, coastal waters employ relatively high frequencies, in the range 50 - 300 kHz, and operate over shorter ranges, of the order several hundred metres. Shallow coastal environments are characterised by high concentrations of suspended mineral particles relative to the open ocean, resulting from the action of rivers discharging into the sea or from the actions of waves and tidal currents stirring up bottom sediments. Previous calculations [1, 2] have shown that such suspensions can lead to significant additional acoustic attenuation at high frequencies for quite moderate concentrations of order 0.1 kg m^{-3}. Concentrations of this level have been detected several tens of kilometres offshore in sediment plumes (e.g. South Atlantic offshore of the Amazon river [3], the Yellow Sea and the East China Sea offshore of the Yellow and Yangtze rivers [4]), and may easily be an order of magnitude greater in some river estuaries and in the beach surf zone.

2. Attenuation theory

Sound attenuation in seawater containing suspended particulate matter may be considered to be the sum of attenuation due to the clear seawater and the additional attenuation due to the suspended particles. Existing sonar performance models consider only the attenuation in clear seawater, neglecting the effects of the particles.

The sound intensity attenuation coefficient α is defined by the expression

$$I = I_0 e^{-2\alpha r} \tag{1}$$

where I_0 is the initial sound intensity and I is the intensity after propagation over range r. In this equation α is in units of Nepers m^{-1}, but units of dB m^{-1} have been used in the rest of this paper to be consistent with units used in sonar work.

The attenuation coefficient in seawater containing suspended solid particles may be written

$$\alpha = \alpha_w + \alpha_v + \alpha_s \tag{2}$$

where α_w, α_v and α_s are the attenuation coefficients due to clear seawater, viscous absorption by suspended particles and scattering by suspended particles respectively. Simple expressions for the attenuation coefficients due to viscous absorption and scattering have been used in this work, and these are discussed below. These simple models have been validated by comparison with a more complete numerical model of the physical processes involved [5].

2.1. Attenuation in clear seawater

The absorption in clear seawater may be considered as the sum of absorption due to pure water, through volume and shear viscosity, and absorption due to two ionic relaxation mechanisms involving magnesium sulphate and boric acid. Absorption due to ionic relaxations involving other salts is negligible.

Several empirically derived expressions exist in the literature for calculating the acoustic attenuation coefficient of seawater (e.g. [6, 7, 8, 9, 10]). The one that appears to be the most complete for use at high frequencies is that of Francois & Garrison [9, 10], and it is their expression that has been used in this work.

2.2. Viscous absorption

Viscous absorption arises as a result of the density difference between the fluid and the solid particles. Since the particles are generally more dense than the fluid they have more inertia than an equivalent volume of fluid. This causes the oscillatory motion of the particles resulting from the incident sound field to lag behind that of the fluid, and there will therefore be a boundary layer in the fluid at the surface of each particle in which there is a velocity gradient. Since the fluid has a finite viscosity, this velocity gradient leads to frictional heat generation and hence loss of energy from the sound field.

Urick [11] derived an expression for the viscous absorption attenuation coefficient for spherical particles based on consideration of the expression for viscous drag developed by Stokes [12]. Urick's expression can be written

$$\alpha_v = (10 \log e^2) \left(\frac{\epsilon k (\sigma - 1)^2}{2} \left[\frac{s}{s^2 + (\sigma + \delta)^2} \right] \right) \quad \text{dB m}^{-1} \tag{3}$$

with

$$\delta = \frac{1}{2} \left[1 + \frac{9}{2\beta a} \right] \quad , \quad s = \frac{9}{4\beta a} \left[1 + \frac{1}{\beta a} \right] \tag{4}$$

where ϵ is the volume fraction of suspended material, $k = \omega/c$ is the wavenumber of the incident compression waves with c the compression wave speed, $\sigma = \rho'/\rho$ is the ratio of the solid density to the fluid density, a is the particle radius and $\beta = \sqrt{\omega/2\nu}$ is the reciprocal of the skin depth for viscous shear waves, with ω the angular frequency and ν the kinematic viscosity of the fluid.

2.3. Scattering

Many workers have investigated sound scattering from suspended spheres, and expressions may easily be found in the literature (e.g. [13]) for the far-field scattering form function, f_∞. Such approaches generally treat the particle as a homogeneous sphere which may be: rigid and movable; rigid and immovable; or elastic. The elastic models in particular lead to complicated scattering form functions owing to resonant excitation. However, when dealing with naturally occurring sediment populations, the particles will be irregular in shape and size, and each particle will have differences in the detailed structure of the scattering form functions. Therefore, when considering the combined effect of a large number of such irregular particles, such details become smeared out, and it is appropriate to use a simpler form for the scattering form function. Such an approach was used by Johnson [14] in developing

the so called high-pass model for backscattered intensity from a fluid sphere. Here, a simple polynomial in $x = ka$ is used to represent the scattering form function approximately by requiring that it fits the form of f_∞ exactly in the Rayleigh (small x) and geometric (large x) regimes. The exact amplitude scattering form function for a sphere varies as x^2 in the Rayleigh regime and becomes constant in the geometric regime, so a polynomial fit to this resembles the response curve of a high-pass filter, hence the nomenclature.

Sheng and Hay [15] constructed a high-pass model for the attenuation coefficient for scattering by a suspension of spheres, and their expression may be written

$$\alpha_s = (10 \log e^2) \frac{\epsilon K_\alpha x^4}{a\left(1 + \xi x^2 + \frac{4}{3} K_\alpha x^4\right)} \quad \text{dB m}^{-1} \tag{5}$$

where

$$K_\alpha = \frac{1}{6}\left(\gamma_\kappa^2 + \frac{\gamma_\rho^2}{3}\right) \tag{6}$$

and ξ is an adjustable constant ≥ 1. The ξ term allows the form of the polynomial to be adjusted to improve the fit to experimental data for intermediate x values. The terms γ_κ and γ_ρ are the compressibility and density contrasts given by

$$\gamma_\kappa = \frac{\kappa' - \kappa}{\kappa} \tag{7}$$

$$\gamma_\rho = \frac{3(\rho' - \rho)}{2\rho' + \rho} \tag{8}$$

where κ and κ' are the bulk compressibilities of the fluid and solid respectively.

3. Sonar performance calculations

In this paper simple sonar equation calculations have been used to investigate the effect of suspended particulate matter on sonar performance. These calculations, which are based on References [16, 17], assume isovelocity conditions and uniform bathymetry, and multiple propagation paths have been neglected.

The active sonar equation for signal excess (SE) may be written

$$SE = EL - BG + PG \tag{9}$$

where EL is the target echo level, BG is the combined noise and reverberation background and PG is the processor gain.

The target echo level may be written

$$EL = SL + TS - 2TL + V_{pt} \tag{10}$$

where SL is the source level, TS is the target strength, TL is the one-way transmission-loss and V_{pt} is a vertical beam pattern correction factor to allow for target echoes which arrive off the main beam axis.

The transmission loss is assumed to be identical for both the forward and reflected pulse, and is approximated here by the sum of spherical spreading and volume attenuation

$$TL = 20 \log(r) + \alpha r \tag{11}$$

where r is the one-way distance to the target and α is the total attenuation coefficient for seawater containing suspended particles, given by Equation 2.

The combined background level, BG is given by

$$BG = 10\log\left[10^{RL_s/10} + 10^{RL_b/10} + 10^{RL_v/10} + 10^{NL/10}\right] \tag{12}$$

where RL_s, RL_b, RL_v are the surface, bottom and reverberation levels and NL is the noise level.

The surface and bottom reverberation levels are given by

$$RL_s = SL - 2TL + \Phi + 10\log\left(\frac{rc\tau}{2}\right) + S_s + V_s \tag{13}$$

$$RL_s = SL - 2TL + \Phi + 10\log\left(\frac{rc\tau}{2}\right) + S_b + V_b \tag{14}$$

where Φ is the equivalent beamwidth for sea surface and seabed reverberation, c is the sound speed, τ is the pulse length, S_s and S_b are the surface and bottom scattering strengths and V_s and V_b are vertical beam pattern corrections for surface and bottom scattering.

Calculation of the equivalent beamwidth Φ uses an approximation employed in the Searay model [18]. Similarly, the surface scattering strength and bottom scattering strength use the same methods as the Searay model. The quantity S_s is expressed as a function of grazing angle, frequency and wind speed, and S_b is expressed as a function of grazing angle, frequency and bottom type, m, where m can take any value between 1 (mud) and 4 (rock).

The volume reverberation level is given by

$$RL_v = SL - 2TL + \Psi + 20\log(r) + 10\log\left(\frac{c\tau}{2}\right) + S_v \tag{15}$$

where Ψ is the equivalent beamwidth for volume reverberation and S_v is the volume scattering strength. In this paper the volume scattering strength is simply taken to be [16]

$$S_v = -88.6 + 7\log(f(\text{kHz})) \tag{16}$$

It is realised that the presence of suspended particulate matter that is being considered in this paper will influence the volume scattering strength. The model for volume scattering strength should therefore be modified to take this into account, and this will be done in future investigations.

The ambient noise level at the receiver is given by

$$NL = Ns + 10\log(B) - DI \tag{17}$$

where Ns is the noise spectrum level, B is the bandwidth of the receiver system and DI is the directivity index of the receive array.

In this paper we have used the Searay approximation for the directivity index of a rectangular array, together with the expression for the noise spectrum used in the Searay model.

The processor gain, PG, is given by

$$PG = 10\log(B\tau) \tag{18}$$

4. Laboratory measurements

A series of laboratory experiments to investigate viscous absorption by aqueous suspensions of mineral particles is being undertaken by Brown & Leighton at the Institute of Sound and Vibration Research, University of Southampton, United Kingdom [19, 20]. These experiments are described in a separate paper at this conference [21]. Preliminary experimental data presented in that paper shows a general increase in attenuation with increasing frequency in agreement with theoretical predictions. The measured attenuation is, however, greater than predicted. The reasons for this are not yet clear but it is possible that the additional attenuation results from effects not included in the theory, such as turbulence. This will be investigated further.

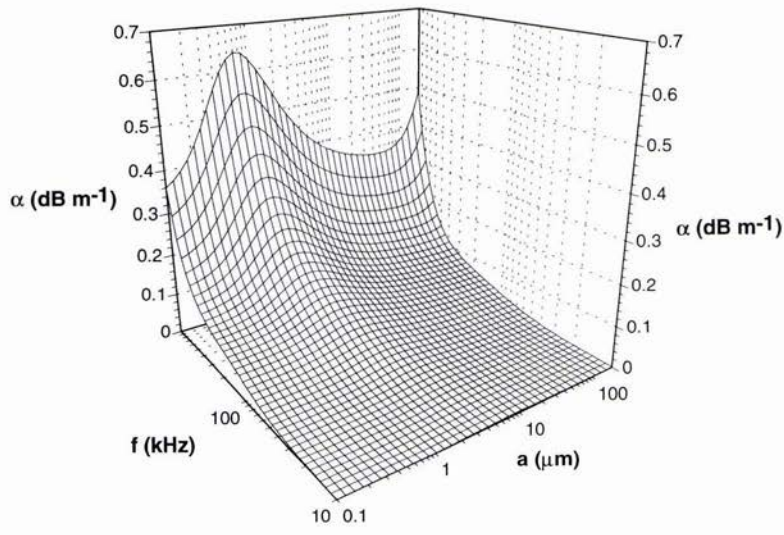

Figure 1: Absorption coefficient for seawater containing 0.2 kg m^{-3} suspended quartz particles as a function of frequency and particle radius

5. Results

Figure 1 shows the total attenuation coefficient due to absorption by clear seawater and viscous absorption and scattering by a suspension of quartz particles of concentration 0.2 kg m^{-3}, as a function of frequency and particle radius, calculated using Equations (3) and (5). This figure clearly demonstrates how the viscous absorption peaks at a particular particle size for a given frequency. The attenuation also increases as the frequency and particle size become large (i.e. increasing ka) due to scattering. The attenuation due to the particles is added to the background attenuation due to the clear seawater in this figure, calculated using the Francois & Garrison expression for a temperature of 15°C and a salinity of 35 on the Practical Salinity Scale.

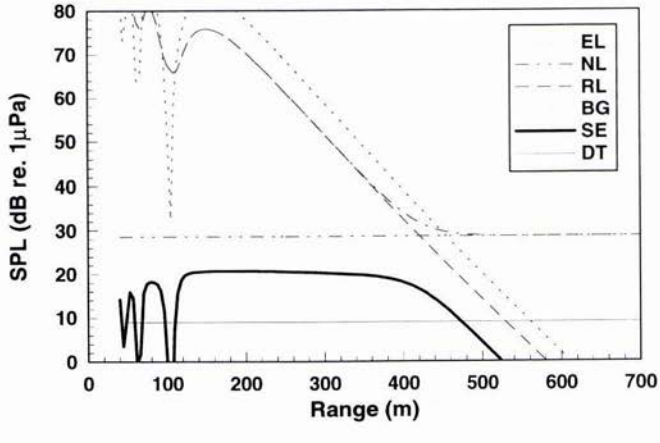

Figure 2: Sound Pressure Level as a function of range for various terms in the sonar equation model (see text)

Figure 2 shows the results of the sonar equation model, using some typical sonar parameters for a sonar operating at 120 kHz in shallow water. In this calculation a suspension of quartz particles of radius 1 μm with a concentration of 0.2 kg m^{-3} was used in the calculation of the absorption coefficient, together with the attenuation due to clear seawater using the Francois & Garrison expression for a temperature of 15°C, a salinity of 35 on the Practical Salinity Scale and a pressure corresponding that at half the water depth of 40 m. The target strength was taken to be -25 dB, the target depth was 40 m (i.e. at the seabed), the array depth was 20 m, and the detection threshold was 9 dB re. 1 μPa. The reverberation level (RL) shown in the figure is the total reverberation level due to seabed, surface and volume reverberation, using a wind speed of 15 knots and a bottom type of 2 (sand).

The detection range may be defined as the range within which the signal excess exceeds the detection threshold, giving a detection range of around 473 m in Figure 2. This may be compared with a detection range of about 660 m in the absence of the particles, as shown in Figure 3, which shows the signal excess with and without the 0.2 kg m^{-3} suspension of 1 μm quartz particles

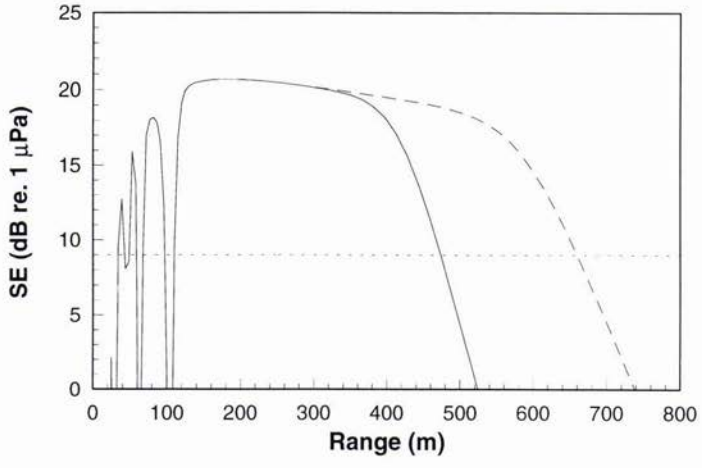

Figure 3: Signal excess with (solid) and without (dashed) 0.2 kg m^{-3} suspension of 1 μm quartz particles. The dotted line shows the detection threshold, DT

Figure 4 shows the variation in detection range with concentration of suspended particles for three different particle sizes, at a frequency of 120 kHz. This shows that there is a significant reduction in detection range for all particle sizes at even quite moderate concentrations of suspended particles. The greatest reduction in detection range at this frequency occurs for $a = 3$ μm, with smaller, but still significant, reduction for the other particle sizes. This is to be expected, as Figure 1 shows that the viscous absorption peak occurs for particle sizes of around 3 μm for a frequency of 120 kHz.

6. Conclusions

This paper has shown how the additional acoustic attenuation at high frequencies due to viscous absorption and scattering by suspended mineral particles in turbid seawater may be taken into account in sonar performance models by using a modified absorption coefficient. This approach has been used to incorporate the effects into a simple, isovelocity, single path, sonar equation model with uniform bathymetry and the results presented demonstrate that concentrations in the range commonly found in shallow coastal waters can have a significant impact on the detection range of high frequency sonar systems. It is therefore recommended that future predictive models of the performance of high frequency sonars in turbid coastal waters should take the additional attenuation due to the suspended particles into account. This would require accurate knowledge of the suspended particle populations, which might come from *in-situ* measurements or remote sensing and assimilation into hydrodynamic models. The latter would be important for Rapid Environmental Assessment (REA).

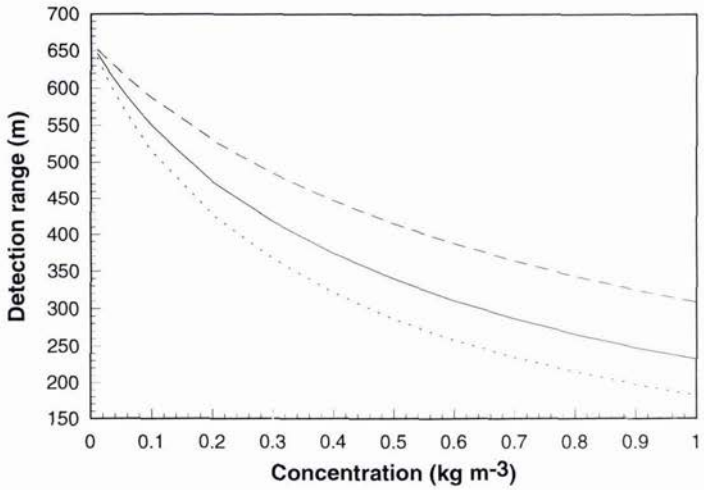

Figure 4: Detection range as a function of concentration for $a = 1$ μm (solid), $a = 3$ μm (dotted), $a = 10$ μm (dashed)

7. Acknowledgements

The assistance of P. Thomson of DERA Bincleaves on the subject of sonar performance calculations is gratefully acknowledged.

References

[1] A D Heathershaw, S D Richards & P D Thorne, (1996), 'Acoustic absorption and scattering by suspended sediments in turbid coastal waters', (unpublished)

[2] S D Richards, A D Heathershaw & P D Thorne, (1996), 'The effect of suspended particulate matter on sound attenuation in seawater', *J. Acoust. Soc. Am.*, **100**, 1447-1450

[3] C A Nittrouer & D J DeMaster (Ed.), (1986), 'Sedimentary processes on the Amazon continental shelf', *Cont. Shelf Res.*, **6**, 1–357

[4] J D Milliman & J Qingming (Ed.), (1985), 'Sediment dynamics of the Changjiang Estuary and the adjacent East China Sea', *Cont. Shelf Res.*, **4**, 1–251

[5] S D Richards & A D Heathershaw, (1996), 'An investigation of viscous absorption of sound energy in turbid seawater at mine-hunting frequencies', DRA Report (unpublished), March 1996

[6] W H Thorpe, (1965), 'Deep ocean sound attenuation in the sub and low kilocyle per second range', *J. Acoust. Soc. Am.*, **42**, 648–654

[7] M Schulkin & H W Marsh, (1962), 'Sound absorption in seawater', *J. Acoust. Soc. Am.*, **34**, 864–865

[8] F H Fisher & V P Simmons, (1977), 'Sound absorption in sea water', *J. Acoust. Soc. Am.*, **92**, 558–564

[9] R E Francois & G R Garrison, (1982), 'Sound absorption based on ocean measurements: Part I: Pure water and magnesium sulfate contributions', *J. Acoust. Soc. Am.*, **72**, 896–907

[10] R E Francois & G R Garrison, (1982), 'Sound absorption based on ocean measurements: Part II: Boric acid contribution and equation for total absorption', *J. Acoust. Soc. Am.*, **72**, 1879–1890

[11] R J Urick, (1948), 'The absorption of sound in suspensions of irregular particles', *J. Acoust. Soc. Am.*, **20**, 283–289

[12] G G Stokes, (1922), 'On the effect of internal friction of fluids on the motion of pendulums', *Math. and Phys. Papers*, **3**, 1–122

[13] Faran, Jr., J J, (1951), 'Sound scattering by solid cylinders and spheres', *J. Acoust. Soc. Am.*, **23**, 405–418

[14] R K Johnson, (1977), 'Sound scattering from a fluid sphere revisited', *J. Acoust. Soc. Am.*, **61**, 375–377

[15] J Sheng & A E Hay, (1988), 'An examination of the spherical scatterer approximation in aqueous suspensions of sand', *J. Acoust. Soc. Am.*, **83**, 598–610

[16] P A G Thomson & I Foster, (1994), 'Sensitivity study and review of current minehunting sonar performance prediction modelling', DRA Report (unpublished), October 1994

[17] P A G Thomson, (1997), Private communication

[18] S M Tuovila, (1989), 'Searay Sonar Simulation Model', NCSC TN 946-88

[19] N R Brown & T G Leighton, (1996), 'Sound Absorption by Suspended Particulate Matter,' ISVR Contract Report No. 96/22

[20] N R Brown & T G Leighton, (1997), 'Sound Absorption by Suspended Particulate Matter,' ISVR Contract Report No. 97/04

[21] N R Brown, T G Leighton, S D Richards & A D Heathershaw, (1997), 'Sound absorption by suspended particulate matter', this conference.

Attenuation of Shear Waves in Near-Surface Sediments

Michael D. Richardson

Naval Research Laboratory
Marine Geosciences Division
Stennis Space Center, MS 39529-5004 USA
e-mail: Mike.Richardson@nrlssc.navy.mil

Abstract

In situ measurement of compressional and shear speed and compressional attenuation in near-surface marine sediments is a well-developed technology but techniques required to measure shear attenuation have lagged behind. In this paper, a pulse technique based on transposition is used to measure wave attenuation. Compressional attenuation determined by transposition compared favorably with standard techniques, confirming use of this approach for shear waves. Shear attenuation was much higher than compressional attenuation but within the range of previously reported measurements.

1. Introduction

Knowledge of sediment geoacoustic properties is of fundamental importance to marine environmental, military, and engineering applications. For instance, geoacoustic properties are used to predict the stability of marine slopes, sediment consolidation behavior, strength of marine foundations, liquefaction potential, mine burial, and high-frequency bottom acoustic scattering. In situ measurement of compressional wave speed and attenuation in marine sediments is a well-developed technology [1,2]. Recent developments in instrumentation allow in situ measurement of shear wave speeds but techniques required for measurement of shear wave attenuation have lagged behind [3]. In most unconsolidated sediments, near surface values of shear wave attenuation are estimated to be 1-2 orders of magnitude greater than for compressional waves [4,5,6,7]. Most of the few higher frequency (>100 Hz) shear attenuation measurements were made under laboratory conditions; whereas, most in situ measurements were made at lower (<10 Hz) frequency. This lack of comparable data has hampered the development of frequency-dependent and depth-dependent predictive relationships [7]. No attempt has been made to develop a predictive relationship between shear wave attenuation and easily measured sediment physical properties such as mean grain size, porosity, or bulk density. Simultaneous measurement of in situ compressional and shear wave speed and attenuation in unconsolidated sediment is rare. In this paper, a pulse technique is developed to measure in situ shear wave attenuation in surficial sediments. The validity of this new approach is demonstrated for compressional waves of known attenuation. Simultaneous measurements of compressional and shear wave speed and attenuation are presented for muddy and sandy sediments on the northern California continental shelf.

2. Attenuation Measurement Techniques

Measurement of compressional wave attenuation in sediments is facilitated by the presence of a convenient standard (seawater). Attenuation can be calculated as 20 $\log_{10}$ of the ratio of received voltage amplitude between probes in seawater and in sediment. No such convenient standard exist to measure shear wave attenuation. The transposition technique described below allows both compressional and shear wave attenuation to be measured without standards. The need to know transducer sensitivity or variable insertion loss when measuring shear wave attenuation is therefore eliminated.

The technique requires two transmitters (T_a and T_b) and two receivers (R_1 and R_2). Transducers are inserted into sediment at fixed distances with the two receivers located between transmitters (Fig. 1). As will be shown,

only the three distances between transducers (d_1, d_2 and d_3) and the four received voltages (e_{1a}, e_{1b}, e_{2a}, and e_{2b}) are needed to calculate shear or compressional wave attenuation.

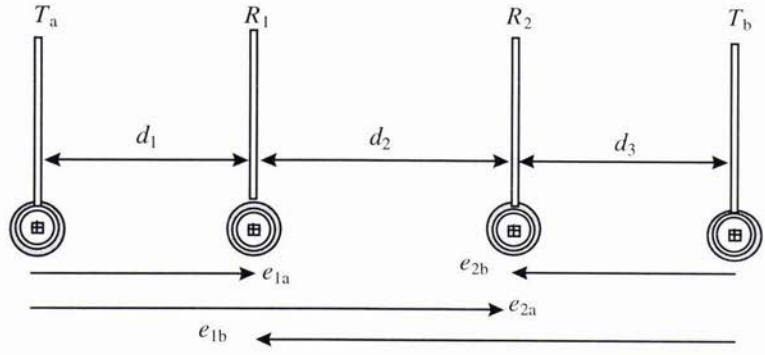

Figure 1. A schematic depiction of the transducer configuration for measuring shear and compressional wave attenuation by transposition of transmit direction. See text for definition of symbols.

The voltage received at R_1 and R_2 when transmitter T_a is driven can be expressed as

$$e_{1a} = M_1 p_{1a} \tag{1a}$$

$$e_{2a} = M_2 p_{2a}\,, \tag{1b}$$

where p_{1a} and p_{2a} are the acoustic pressures or wave amplitudes at receivers R_1 and R_2 and M_1 and M_2 include receiver sensitivity and insertion loss for R_1 and R_2. Sensitivity includes mechanical to electronic conversions and insertion loss accounts for the variable coupling of receivers to the sediment. The transfer function of the transmitters is included in the pressures (p) and are later canceled out. If we assume symmetry in the sensitivities of R_1 and R_2, it follows that the receive voltage at R_1 and R_2 when transmitter T_b is driven is

$$e_{1b} = M_1 p_{1b} \tag{2a}$$

$$e_{2b} = M_2 p_{2b}\,. \tag{2b}$$

Solving (2a) and (2b) for M_1 and M_2, substituting M_1 and M_2 into (1a) and (1b), and dividing the results yields

$$\frac{p_{1a}}{p_{2a}} = \frac{p_{1b}}{p_{2b}}\left(\frac{e_{1a}}{e_{2a}}\right)\left(\frac{e_{2b}}{e_{1b}}\right) \tag{3}$$

Assuming measurements are made in a homogeneous free-field and receivers are in the far-field, the ratio of the pressures in (3) is only dependent on spreading loss and sediment attenuation. If spherical spreading is assumed (far-field), the ratio of pressures can be expressed as

$$\frac{p_{1a}}{p_{2a}} = \frac{d_1 + d_2}{d_1}\exp(\alpha_a d_2) \tag{4a}$$

$$\frac{p_{1b}}{p_{2b}} = \frac{d_3}{d_2 + d_3} \exp(-\alpha_e d_2) \tag{4b}$$

Inserting (4a) and (4b) into (3) and solving for the attenuation (α) yields

$$\alpha_e = \frac{1}{2d_2} \ln\left[\left(\frac{d_1}{d_1 + d_2}\right)\left(\frac{d_3}{d_2 + d_3}\right)\left(\frac{e_{1a}}{e_{2a}}\frac{e_{2b}}{e_{1b}}\right)\right], \tag{5}$$

where attenuation α_e is measured in nepers per meter. Attenuation (α in dBm^{-1}) can be calculated from the following expression

$$\alpha = \frac{4.343}{d_2} \ln\left[\left(\frac{d_1}{d_1 + d_2}\right)\left(\frac{d_3}{d_2 + d_3}\right)\left(\frac{e_{1a}}{e_{2a}}\frac{e_{2b}}{e_{1b}}\right)\right]. \tag{6}$$

3. Measurements with ISSAMS

Compressional and shear wave transducers were deployed with the latest version of the In Situ Sediment geoAcoustic Measurement System (ISSAMS) [2]. ISSAMS is a remotely-operated, hydraulic platform that allows fixed mounted geoacoustic probes to be driven into the sediment at precise depths (Fig. 2). Live video is used to monitor probe deployment and to provide visual information on seafloor type. Water conductivity, pressure, and temperature are used to calculate bottom water sound speed. Compressional and shear wave speed and attenuation are measured over pathlengths ranging from 30 to 100 cm and at depths up to 50 cm below the sediment-water interface. For compressional wave measurements, transmit pulses were driven utilizing 38-kHz pulsed sine waves and time delays and voltages were used to determine values of speed and attenuation between identical radial-poled ceramic cylinders. Speed (V_p) is calculated by comparison of received signals transmitted through the sediment with those transmitted through seawater overlying the sediments, where C_w is the bottom water speed, d is the distance between transmitter and receiver, and Δt the water travel time minus the sediment travel time.

$$V_p = \frac{C_w}{1 - (\Delta t C_w / d)}. \tag{7}$$

Compressional wave attenuation (α_p in dBm^{-1}) is calculated as

$$\alpha_p = \frac{20}{d} \log_{10}\left(\frac{e_w}{e_s}\right) \tag{8}$$

where e_w / e_s is the ratio of received voltage between probes in seawater and sediment. For these measurements, the maximum amplitude of the first sine wave (e.g., the second peak) was used as the received voltage. Distances between transmitters and receivers are calculated from the known water speed (C_w) and measured time delays. Shear wave speed is calculated from time-of-flight between bimorph bender elements mounted in flexible silicone rubber mounts and driven at 0.25 to 2.0 kHz. Distances between shear wave transducers are measured from center-to-center of the bender elements before and after deployment [8].

For measurement of attenuation, as described in section 2, distances d_1 and d_3 are calculated from known water speed (C_w) and measured time delays between compressional transducers and measured directly between shear wave transducers. The distance between receivers (d_2) is calculated as one-half the sum of the distance difference between transmitters (T_a, T_b) and their respective near and far receivers (R_1, R_2). Received voltages (e_{1a}, e_{1b}, e_{2a}, and e_{2b}) were measured as described in the preceding paragraph for both compressional and shear waves.

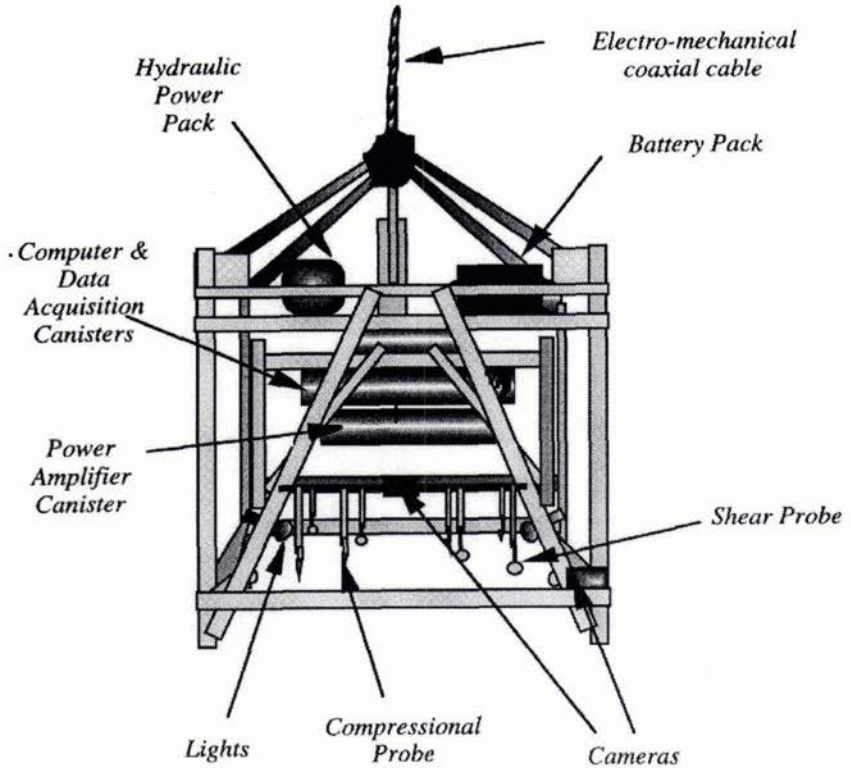

Figure 2. In Situ Sediment geoAcoustic Measurement System (ISSAMS): the aluminum and stainless steel platform weighs approximately 1 metric ton in air, is just under 3 meters in height and has a 2.5-meter square footprint.

4. Results

Sediment geoacoustic measurements were made along the northern California continental shelf as part of the Office of Naval Research STRATAFORM program [9]. The overall objective of our study is to quantify the effects of biological (bioturbation) and hydrodynamic (storms and floods) processes on sediment physical and geoacoustic properties. In order to achieve this goal, techniques needed to be developed to measure shear wave attenuation which complements existing techniques used to measure other sediment geoacoustic properties. Measurements reported here were made at two sites (S-40 and S-80, where number gives approximate water depth) chosen to represent contrasting sediment types. Three deployments of the ISSAMS system were made at both the shallower sandy (S-40) and the deeper muddy (S-80) sites. Compressional and shear wave speed and attenuation were measured at sediment depths of 10, 20 and 30 cm. The results of 36 measurements of compressional and shear wave speed and compressional wave attenuation (V_p, V_s, α_p) and the 9 measurements of compressional and shear wave attenuation (α_p , α_s) using the new transposition technique are presented in Table 1. Attenuation is expressed as dBm^{-1}, $dB\lambda^{-1}$ and dBm^{-1} kHz^{-1} in order to facilitate comparision with shear wave attenuation reported from other studies. Compressional velocity ratio (V_p-ratio = ratio of in situ sediment compressional speed to the sound speed of the overlying pore water) is used for inter-site comparisions to eliminate the effect of temperature, salinity and pressure on compressional speeds. Compressional and shear wave speed and compressional wave attenuation were significantly higher at the shallower sandy site. Wave speeds and attenuation are in agreement with past studies for the given sediment types (Fig 3).

Table 1. A comparison of sediment physical and geoacoustic properties for two sites on the northern California continental shelf. Most values of sediment geoacoustic properties are complement with standard deviations in parentheses.

Site	S-40	S-80
Depth (m)	43	80
Sediment type	Sand	Clayey-silt
Mean Grain Size (ϕ)	2.97	7.82
V_p (ms^{-1})	1623 (10.3)	1479 (4.3)
V_p -ratio	1.097	0.999
V_s (ms^{-1})	80 (5.1)	42 (3.8)
α_p (dBm^{-1}@38kHz)	20.8 (4.4)	5.6 (1.6)
k_p (dB m^{-1} kHz^{-1})	0.55	0.15
Transposition		
α_p (dBm^{-1}@38 kHz)	26.7 (5.5)	4.9 (2.5)
α_s (dBm^{-1}@1.0 kHz)	59.7 (11.3)	
α_s (dBm^{-1}@0.3 kHz)		25.6 (5.7)
Shear log decrement ($dB\lambda^{-1}$)	4.7 (1.0)	3.8 (0.9)
Compressional log decrement ($dB\lambda^{-1}$)	1.14	0.19
k_p (dBm^{-1} kHz^{-1})	0.70 (0.14)	0.13 (0.06)

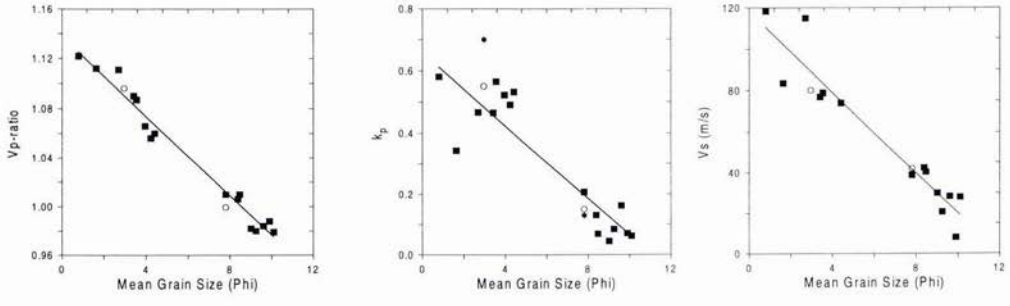

Figure 3. Predictive relationships between sediment mean grain size and compressional wave velocity ratio (V_p-ratio), compressional wave attenuation (k in dBm^{-1} kHz^{-1}) and shear wave speed (V_s in ms^{-1}) for near surface silicilastic sediments. Data were compiled from geoacoustic studies, using ISSAMS, in a variety of sediment types near the Bay of La Spezia, Italy, hard-packed sand near Panama City, Florida, and soft mud in Eckernförde Bay, Baltic Sea [8,10]. Sediment geoacoustic measurements from the northern California continental shelf include standard methods (o) and by measurement of attenuation using transposition (*).

Compressional wave attenuation determined by transposition (6) was not significantly different (t-test) than attenuation measured using standard techniques (8) which are based on the ratio of received amplitudes in water and in sediment. These data confirm the use of transposition to measure wave attenuation and techniques of (6) were therefore used to calculate shear wave attenuation. Shear wave attenuation was very high; 2-3 orders of magnitude higher than compressional wave attenuation when compared as dBm^{-1} per kHz (Hamilton's k) and 5-20 times higher when expressed as $dB\lambda^{-1}$ (log decrement in decibels per wavelength).

5. Discussion and Conclusions

Based on reviews of both laboratory geotechnical testing and in situ geophysical studies, Hamilton [4,5,11] concluded that in near-surface sediments most values of shear attenuation or log decrement range between 0.86 to 5.21 $dB\lambda^{-1}$ (0.1 to 0.6 nepers per wavelength) with slightly higher log decrements in sandy (mean = 2.6 $dB\lambda^{-1}$) compared to muddy (mean = 1.7 $dB\lambda^{-1}$) sediment. High-frequency laboratory shear wave measurements summarized by Kibblewhite [6] show shear attenuation in sand, measured at 1.0-kHz, range between 20-70 dBm^{-1}. Bowles [7] summarized values of shear wave attenuation based recent direct borehole measurements and from inversion of Scholte waves. He found near surface (upper 5 meters) attenuation ranged from 0.1 to 6.7 $dB\lambda^{-1}$. All values of log decrement, in his summary, greater than 1.8 $dB\lambda^{-1}$ were measured at higher frequency (80-100 Hz). In summary, shear wave attenuation reported here (Table 1) is higher than the average of previously reported measurements, but well within the range of those measurements.

Comparison of values of near-surface shear wave attenuation is complicated by differences in the variety of laboratory and field measurement techniques used to measure shear wave attenuation, very steep shear wave attenuation gradients, poorly understood frequency dependence, and because measured shear attenuation often includes not only intrinsic attenuation but losses due to scattering and conversion of shear energy to compressional energy (i.e., the effect of sediment heterogeneity and layering). Based on theory and confirmed by laboratory measurements, Stoll [12,13,14] has shown that the power law relationship between shear wave attenuation and frequency is not constant over the entire frequency range and that steep gradients of shear wave attenuation are to be expected in the upper few meters of sediment. Steep gradients reflect the effects of increased overburden pressure (effective stress) on frame moduli. These steep gradients in shear wave attenuation are supported by laboratory and field measurements [7] and may account for part of the wide variation in reported surficial shear wave attenuation. The nonlinear dependence of shear wave attenuation with frequency results when different forms of energy dissipation (intergranular friction, relative motion between fluid and solid, and local fluid motion) dominate at different frequencies. Recent field [15] and laboratory [16] measurements support the nonlinearity of this frequency-attenuation relationship. Based on an admitted scarcity of comparable data, Hamilton (5) presents a case for a power law (with frequency scaled to the first power) relationship between shear wave attenuation and frequency. Buckingham (17) provides a theory of wave propagation in which shear wave attenuation is scaled to the first power of frequency. ISSAMS is ideally suited to contrast these competing theories by providing shear attenuation measurements in the frequency band (0.1 to 2.5 kHz) where changes in dissipation mechanisms are predicted to occur. These data may help reconcile differences in shear attenuation measured by low frequency geophysical techniques and higher frequency laboratory methods and bring order to predictive relationships between shear wave attenuation and sediment physical properties.

6. Acknowledgments

ISSAMS benefited from the electro-mechanical expertise of Enrico Muzi and Bruno Miaschi (SACLANTCEN) during early development and from engineering expertise of Sean Griffin and Frances Grosz (Omni Technologies) for its current remotely-operated, hydraulic configuration. Bob Stoll (Lamont-Doherty) provided the original suggestion to measure shear wave attenuation using transposition techniques and David Trivett (NUWC) provided the mathematical framework. The paper was strengthened by reviews of Darrell Jackson and Warren Wood. This work was supported by the Office of Naval Research (ONR), Program Element 0601153N, and by the ONR Coastal Benthic Boundary Layer Program. This is NRL contribution NRL/JA/7431-97-008.

7. References

[1] A. Barbagelata, M.D. Richardson, B. Miaschi, E. Muzi, P. Guerrini, L. Troiano, and T. Akal, ISSAMS: an in situ sediment geoacoustic measurement system, pps. 305-312. In, *Shear Waves in Marine Sediments* (J.M. Hovem, M.D. Richardson and R.D. Stoll, Editors), Kluwer Academic Publishers, Dordrecht, The Netherlands, 1991.

[2] S.F. Griffin, F.B. Grosz and M.D. Richardson, ISSAMS: a remote in situ sediment acoustic measurement system. *Sea Technology 37*: 19-22, 1996.

[3] M.D. Richardson., E. Muzi, B. Miaschi and F. Turgutcan, Shear wave gradients in near-surface marine sediment, pps. 295-304. In, *Shear Waves in Marine Sediments* (J.M. Hovem, M.D. Richardson and R.D. Stoll, Editors), Kluwer Academic Publishers, Dordrecht, The Netherlands, 1991.

[4] E.L. Hamilton, Attenuation of shear waves in marine sediments. *J. Acoust. Soc. Am., 60*:985-996, 1976.

[5] E.L. Hamilton, Acoustic properties of sediments, pps. 3-58. In, *Acoustic and Ocean Bottom* (A. Lara-Sáenz, C. Ranz-Guerra and C. Carbó-Fité, Editors), *Instituto de Acústica,* Madrid, Spain, 1987.

[6] A.C. Kibblewhite, Attenuation of sound in marine sediments: a review with emphasis on mew low frequency data. *J. Acoust. Soc. Am., 86*:716-738, 1989.

[7] F.A. Bowles, Observations on attenuation and shear-wave velocity in fine-grained, marine sediments. *J. Acoust, Soc. Am., 101*:in press.

[8] M.D. Richardson, E. Muzi, L. Troiano and B. Miaschi, Sediment shear waves: A comparison of in situ and laboratory measurements, pps. 403-415. In, *Microstructure of Fine Grained Sediments* (R.H. Bennett, W.R. Bryant and M.H. Hurlbert, Editors), Springer-Verlaag, New York, NY, 1990.

[9] C.A. Nittrouer and J.H. Kravitz, STRATAFORM: a program to study the creation and interpretation of sedimentary strata on continental margins. *Oceanography 9*:146-152, 1996.

[10] M.D. Richardson, and K.B. Briggs, In-situ and laboratory geoacoustic measurements in soft mud and hard-packed sand sediments: implications for high-frequency acoustic propagation and scattering. *Geo-Marine Letters* 196-203, 1996.

[11] E.L. Hamilton, Geoacoustic modeling of the seafloor. *J. Acoust. Soc. Am., 68:*1313-1340, 1980.

[12] R.D. Stoll, Marine sediment acoustics. *J. Acoust. Soc. Am.*, 77:1789-1799, 1985.

[13] R.D. Stoll, Sediment Acoustics. Springer-Verlag, New York, 153 pps., 1989.

[14] R.D. Stoll, Shear waves in marine sediments - bridging the gap from theory to field applications, pps. 3-12. In *Shear Waves in Marine Sediments* (J.M. Hovem, M.D. Richardson, R.D. Stoll, Editors), Kluwer Academic Publishers, Dordrecht, The Netherlands, 1991.

[15] T.G. Muir, T. Akal, M.D. Richardson, R.D. Stoll, A. Caiti and J.M. Hovem, Comparison of techniques for shear wave velocity and attenuation measurements, pps. 283-294. In, *Shear Waves in Marine Sediments* (J.M. Hovem, M.D. Richardson, R.D. Stoll, Editors), Kluwer Academic Publishers, Dordrecht, The Netherlands, 1991.

[16] B.A. Brunson, Shear wave attenuation in unconsolidated laboratory sediments. In *Shear Waves in Marine Sediments*, (J.M. Hovem, M.D. Richardson, R.D. Stoll, Editors), Kluwer Academic Publishers, Dordrecht, The Netherlands, 1991.

[17] M.J. Buckingham, Theory of compressional and shear wave in fluid-like marine sediments. *J Acoust. Soc. Am.*, submitted.

An experimental investigation of the contribution of sediment volume scattering to acoustic backscatter measured in the shallow waters of the Florida Strait

Andrew K. Rogers*

Planning Systems Incorporated
7923 Jones Branch Drive
McLean, Virginia 22102
Email: arogers@plansys.com

*work for this paper was performed while at the University of Miami

Abstract

Experiments were conducted in the Florida Strait region of the United States in July 1995 for the purpose of investigating the contribution of sediment volume scattering to measured backscatter levels at frequencies between 3.5 and 30 kHz. Each of five sites were analyzed for bottom backscattering level in both the radial and azimuthal directions. A relatively new volume scattering model was employed and the results compared with predictions made using a composite rough interface scattering model. Environmental parameters were established by a cross well tomographic measurement and used as input values for the modeling. Comparison of model predictions with the measured data showed that for grazing angles from the critical angle to approximately 60° volume scattering dominated, while for angles greater than approximately 60° surface roughness scattering consistently dominated. In geographic areas where the interface sound speed ratio exceeded one, roughness scattering controlled the backscattered level for grazing angles less than the critical angle.

Inversion of the measured backscatter data was performed using a genetic optimization algorithm developed around the volume scattering model. Inversion results were found to agree well with measured data and measured environmental parameters which describe the scattering volume. A second similar inversion was made to determine spectral properties of a two dimensional transform of the compressional velocity tomograms. This inversion was based upon a power law representation of the spectral structure.

1. Introduction

Ocean bottom scattering can have a beneficial or detrimental effect, depending on the objectives of the acoustic study. For many sonars, sea bottom scattering has a detrimental and limiting effect; for others, the scattered noise may be used as a tool for examining the physical properties of the scatterers. In either case, a thorough knowledge of the effect of the sea bottom on acoustic propagation is needed.

A great deal of seafloor acoustic reverberation data has been taken in the past, much of which has been processed for bottom scattering strength. In general, the results have been characterized by the empirical value $10\log(\mu)$ taken from Lambert's rule [1]. Lambert's rule works well for the water - sediment interface, but neglects the contribution from the sub-bottom volume and sub-bottom interfaces. It also does little to relate the measured backscatter to the physical properties of the scatterers. This limitation is profound when the interface roughness is very small or as the impedance ratio between the water and sediment approaches unity. Under these conditions the volume and/or sub water - sediment interface horizons become significant or even dominant scattering mechanisms and cannot be neglected.[2] The desirability of a physically based model of the complete scattering phenomenon has become a topic of recent interest to many and is the reason for this study.

Two models, one developed for rough interface scattering and the other for volume scattering were chosen for their physics based approach to scattering and are utilized in the data analysis. Jackson's composite roughness model [3] and Yamamoto's volume scattering model [4] combine to help yield insight into the physics of the scattering mechanisms. The composite roughness model describes the rough interface via the Kirchhoff approximation for angles near the Snell's law

direction and via perturbation theory for all other directions. Interpolation combines the pair. Although Jackson's model provides a formulation for volume scattering, it is disregarded in this work because of its empirical nature. Yamamoto's volume scattering model also follows perturbation theory and represents the scattering kernel with a power law formulation when describing the fluctuations of compressional velocity within the volume. The general form of the volume scattering model is

$$VBS = 10\log(\sigma_v) \tag{1}$$

$$\sigma_v = k_o^4 \Gamma^2 \beta \Lambda^2 B\left(\Lambda^2 k_1^2 + \Lambda^2 k_2^2 + k_3^2\right)^{-\frac{(\beta+2)}{2}} \tag{2}$$

where *VBS* is volume backscatter, σ_v is the differential backscattering cross section per unit volume, k is the wavenumber incident (subscript o) and axial (subscripts 1, 2, 3), Γ is a magnification factor due to the relationship of density and compressional velocity fluctuations in the sediment, β is the spectral exponent factor, B the spectral intensity factor and Λ the aspect ratio describing the anisotropy of the inhomogeneities in the sediment. A provision for dipped layering may be included in the definitions of the axial components of wavenumber and is outlined by Yamamoto [5]. Propagation effects are accounted for as direct path spreading loss, attenuation and transmissivity.

$$\sigma_a = \sigma_v \left(\frac{\sin\theta_s}{4\alpha}\right) T_{12}^2 T_{21}^2 \left(\frac{\cos^2\theta_s}{\cos^2\theta_w}\frac{\sin^2\theta_w}{\sin^2\theta_s}\right) \tag{3}$$

This result is expressed as an equivalent interface scattering strength and may be combined directly with the result from the composite roughness model. θ_w and θ_s are the incident and refracted grazing angles at the water sediment interface, $T_{12}^2 T_{21}^2$ is the transmissivity across the interface and $\left(\frac{\cos^2\theta_s}{\cos^2\theta_w}\frac{\sin^2\theta_w}{\sin^2\theta_s}\right)$ accounts for the spreading of incident wave energy at the interface. Total bottom backscatter is computed as

$$BBS = 10\log\left(\sigma_r + \sigma_a\right) \tag{4}$$

σ_r is rough interface scattering.

This volume scattering model was the motivation for much of the work done in the Florida Strait. Beyond its' direct or forward application, the volume scattering model is inverted to find the sediment properties from the collected backscatter data. To do this one of the first applications of genetic algorithm optimization techniques to underwater acoustics is implemented. This type of inversion was chosen for its' robust nature and computational efficiency and provided a useful and unique tool for sediment classification.

Collocated acoustic backscatter and sediment property data were taken on the Florida continental shelf at site 1 of 5 experimental sites and is emphasized in this short paper. The measurements were made using newly developed instrumentation and techniques; a sparse volumetric array to measure seafloor scatter generated by a central omnidirectional sound source and cross well acoustic tomography for determining the sediment character. The sparse array expedited data collection where information in both grazing angle and azimuthal angle was desired. The technique of high frequency marine cross well acoustic tomography provided an advantage over traditional coring methods for sediment measurement by providing largely undisturbed measurement. Sediment coring tends to disturb the sediment structure and lacks two or three dimensional information which is necessary to describe the scattering mechanism sufficiently. Two or three dimensional information is also required for implementation of the volume scattering model and inversion comparison.

2. Experiment

The Florida Strait experiment included five acoustic backscatter sites and one cross well tomographic experiment at site 1. The concentration of this paper will be upon the 38 foot deep site 1. For both types of experiment, center frequencies of

7.5kHz and 15kHz were used. Cross well tomography was used to measure the sediment properties to be used as input parameters to scattering models and for inversion comparison. During burial of equipment for cross well tomography divers noticed strong layering as wells were driven into the seafloor. This is confirmed by the cross well tomography result. Based upon these and samples taken during the diving operation it is proposed that the site has sediment structure consisting of sand and shell fragments intermixed with layers of mud and silty clay.

2.1 Equipment

Traditional approaches to measuring acoustic backscatter from the seafloor use either a single fathometer device which yields a reflection result (near grazing angle = 90^{o}), a line array which has ambiguity about its axis when beamformed, or a seafloor mounted tower with a directional source and receiver. The last of these three approaches is the most accurate and repeatable but in its' most common configuration it requires that the directional source receiver pair be steered to all angles of interest and this can make data collection a time consuming endeavor. In an effort to reduce experimental duration and still provide a system which could examine all points on the bottom within the region about the measurement device, an array of receivers were chosen which would be recorded simultaneously and later beamformed. Recognition that the use of a broadband source signal with a sparse array can yield a high resolution result for a minimal number of hydrophones further defined the array [6]. The orientation of the sensors was therefore very important and after much simulation and evaluation were arranged in a manner to give excellent broadband beamformed response throughout all grazing and azimuthal angles for the frequencies of interest. The design is similar to a vertically extended Mill's cross as seen below (figure 1a).

An omnidirectional sound source located at the geometric center of the array was activated repeatedly using Hanning weighted linear frequency modulated signals and the reverberation recorded at each hydrophone for some period of time. Averaging of repeated traces removed much of the incoherent noise. With this source and receiver array pair the seafloor backscattered response was quickly and accurately imaged.

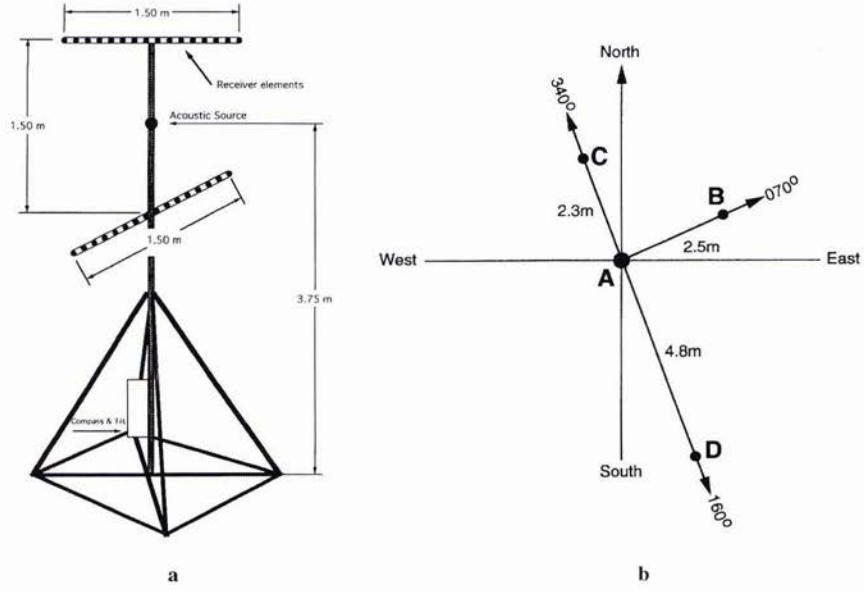

Figure 1a and 1b: a - A schematic diagram of the sparse volumetric acoustic array; b - A diagram of the cross well tomographic plan on the seafloor, wells are located at positions A, B, C and D.

2.1.1 Three dimensional broadband array design

The standard approach to array design for signals which contain more than one octave of bandwidth has been to nest several sub-arrays each cut for a different octave. Data from each is band passed for its corresponding octave and beamformed conventionally. This method requires a significant number of sensor elements. An alternative is to process the data over the entire frequency band using only the array cut for the lowest octave. Using this method, with sufficient

bandwidth, the many grating lobes which occur for frequencies greater than the frequency for which the array was cut (spatially aliased frequencies) tend to smear one another out leaving the beam along the maximum response axis intact or even narrowed. Integration over the full bandwidth reveals a comparable directivity index while sharply reducing the number of sensors. During processing the backscattered data were examined every 2.5^{0} in azimuth and every 2^{0} of grazing angle.

The physical design of the 3-D broadband array, called the acoustic backscatter antenna (ABA), consisted of two 16 channel linear arrays of hydrophones spaced 0.10m and placed horizontally in orthogonal directions. A preamplifier providing 50 times gain accompanied each hydrophone. Vertical separation between the linear arrays was equivalent to a single segment's aperture of 1.5m. Onboard compass and tilt sensors provided the array's relationship to with the earth; angles if inclination or declination were accounted for as a step of data processing. The array is illustrated in figure 1a with the acoustic source located at the geometric center of the receive array.

2.2 Acquisition of backscattering data

Source signals were Hanning windowed linear frequency modulated (LFM) upsweeps of bandwidths 15 and 30 kHz centered at 7.5 and 15 kHz respectfully. These signals were chosen for their fairly low sidelobe level upon correlation and good correlation gain, i.e. high signal to noise. The signal also provided sufficient bandwidth for the broadband beamforming techniques employed in the processor.

Data acquisition took place via a cable connection to the research vessel. Traces were amplified one hundred times and high pass filtered using a -3dB cutoff at 1kHz. This ensured maximum amplitude would be recorded without clipping the A/D converter and that 60Hz electronic noise would be suppressed without harming the data integrity. Data then passed through a 200kHz throughput, 12 bit, 16 channel A/D converter and was recorded to the hard disk of a 486/66 personal computer. Experiment backup was made on Exabyte 8mm magnetic tape. The control software recorded three channels at a time at 66666 Hz for 0.2 s per shot. 200 signals were recorded per station . This yielded 85.33 Mb per experimental location and the duration of an experiment was just under 20 minutes. Data were later averaged, correlated with the source function and beamformed.

2.3 Cross well tomography experiment

The tomography measurement was collocated with the scattering experiment at site 1. Four wells were bored into the seafloor approximately 2m in depth. The orientation of these well is shown in figure 1b. Into the well

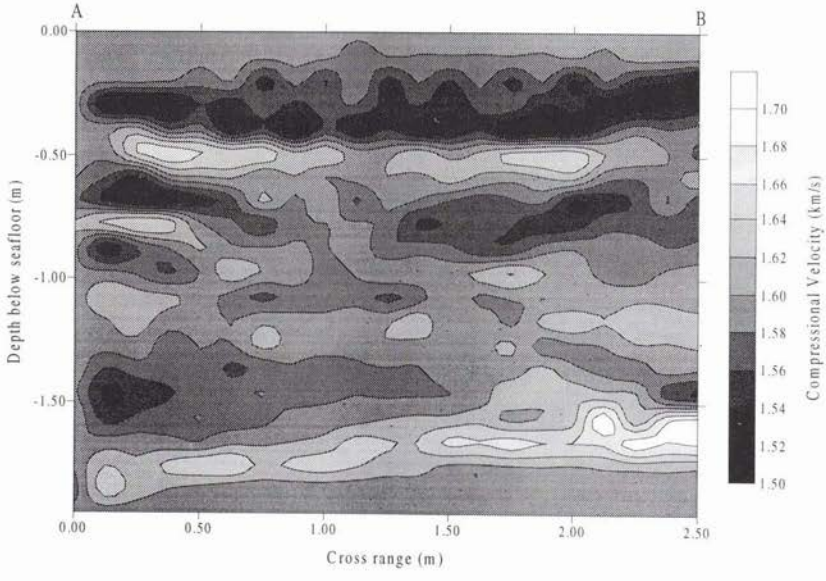

Figure 2: Compressional velocity cross well tomogram of section A-B at site 1 Florida Strait continental shelf acoustic experiments 1995.

'A' an array of 16 acoustic sources spaced 0.10m was deployed and into wells 'B,C & D' arrays of 16 receivers were deployed also separated at 0.10m. Multiple source shots were transmitted for each source channel which were averaged and recorded after being received. A shipboard display of the incoming traces successively averaged was observed until it was determined that a sufficient signal to noise ratio was achieved and the first arrival of the signal could be determined. These data were archived and later used in the tomographic inversion which determined the compressional velocity structure of the sections between well 'A' and the others. Information on the tomographic inversion may be found in the paper by Bregman *et al.* [7]. The compressional velocity cross well tomogram cross section A-B is shown in figure 2.

3. Data analysis and modeling

3.1 Cross well tomograms

To determine the properties needed for input to the acoustic models the tomograms were analyzed using one and two dimensional Fourier analysis. Using a virtual sediment core taken as a one dimensional section in depth and analyzing the power spectral density of the compressional velocity fluctuations along that section the power law behavior expected from equation 2 was revealed. A first order polynomial fit to the spectrum provided the spectral exponent and spectral intensity factors, β and B respectfully. One dimensional data such as this or from sediment cores cannot provide information needed such as the aspect ratio or dipped structure. From a two dimensional power spectrum of the tomographic section the aspect ratio of the horizontal to vertical inhomogeneities and any dipped structure can be determined. A useful tool for finding all four of these parameters from the two dimensional power spectrum was an inversion of the volume scattering model to fit the spectral data. A genetic algorithm similar to the one used in the inversion of the measured backscatter data was applied. An example of the two dimensional power spectra of the compressional velocity cross section is shown in figure 3a and the result of the inversion in figure 3b.

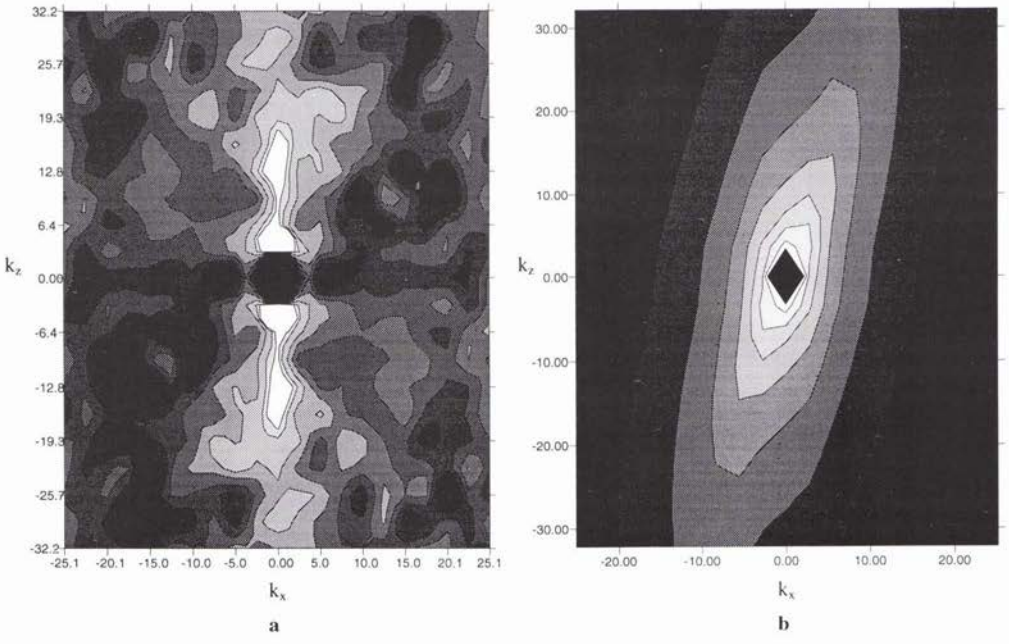

Figures 3a and b: a- Power spectral density of compressional velocity cross well tomogram A-B from site 1. b- Result of inversion using the volume scattering model to fit the power spectral density computed directly from the cross well tomogram A-B. Axis are wavenumber (1/m).

Note the off axis nature of the elliptical shape in figure 3b. This indicated the existence of a preferential dipped structure at the site. Aspect ratio is determined as the ratio of the major ($k_z/\cos\delta$) axis to minor ($k_x/\sin\delta$) axis of the

ellipse, where δ is the dip angle from the k_z axis. Table 1 lists the sediment parameters computed from both one and two dimensional techniques and inversion along with several estimates made for use with the scattering models where data was not available. No interface properties were measured at the site, therefore these were estimated based upon diver observations and sediment samples referenced to previous work by Jackson and Briggs [8].

	Volume Values						Sediment			Surface	Values
LINE	Spectral B	Model β	Aspect Ratio Λ	Dip from A δ	Vertical B	Cores β	Sound Speed C_p/C_w	Attenuation α_a (dB/m/kHz)	Density Ratio ρ	Spectral Strength ω2	Spect. Exp. γ
A-B	4.98e-5	0.312	4.556	-14.1°	1.16e-5	0.500	1.039	0.15	1.79	0.0042	3.25
A-C	1.27e-5	0.214	4.442	1.36°	1.04e-5	0.341	1.047	0.15	1.81	0.0042	3.25
A-D	2.29e-5	0.778	6.77	-1.39°	4.68e-5	0.744	1.043	0.15	1.76	0.0042	3.35

Table 1: Sediment parameters computed from one and two dimensional spectral techniques and inversion. Underlined values are estimated values for modeling purposes only.

3.2 Backscatter

The beamformed acoustic scattering data were evaluated azimuthally and found to have only minor azimuthal variation at these sites. Emphasis was placed on the azimuthal data whose radials coincided with the directions of the measured cross well tomograms. From figure 1b it is seen that these lie along 70^0-250^0 and 160^0-340^0 magnetic. Along these azimuths the measured and inverted sediment properties from table 1 were input into the composite roughness and volume scattering models.

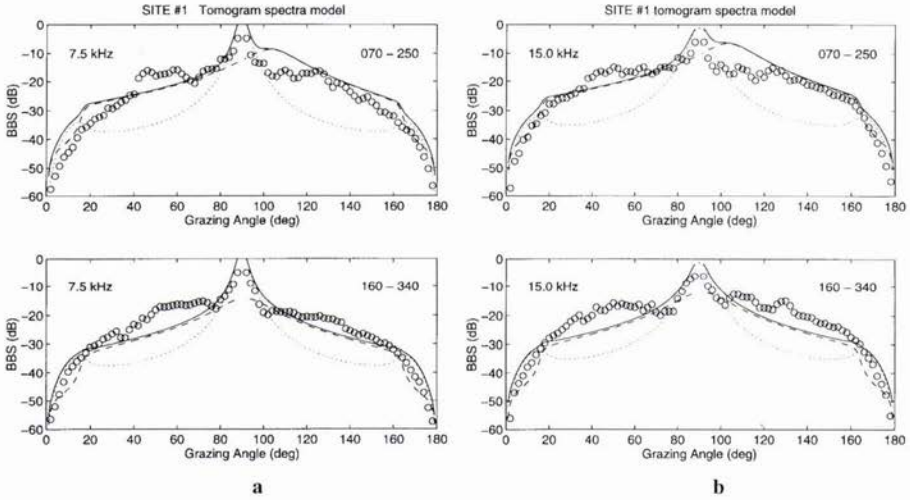

Figure 4a - b: Acoustic backscatter data and modeling results for the composite roughness model estimate (dotted line), the volume scattering model (dashed line) and their combination (solid line). a- 7.5 kHz 070°-250° and 7.5 kHz 160° -340° b- 15.0 kHz 070°-250° and 15.0 kHz 160°-340°

Figures 4a and 4b show the measured data verses grazing angle at 7.5 kHz and 15.0 kHz along with the forward model predictions based on the values from table 1. Note the effect of the dipped structure in the 070^0-250^0 result as the peak is offset to roughly 14^0. The volume scattering model shows a particularly good fit for this bearing. The choice of the interface scattering parameters is constant throughout these examples due to the

lack of measured data but facilitates some indication, under the assumption of a similar sediment, of the roughness scattering effect. It shows that at very high grazing angles and angles beyond the critical angle, in this case approximately 16^0 grazing, rough interface scattering dominates. Through the mid angle sections volume scattering largely controlled scattering behavior.

Inversion of the volume scattering model was made for data at each of the azimuthal directions 70°, 160°, 250° and 340°. This inversion predicted seven parameters: a dip azimuth, dip grazing angle, spectral exponent, spectral intensity, aspect ratio, attenuation and sound speed ratio at the water-sediment interface. Table 2 shows the results for 7.5 kHz and 15.0 kHz.

Freq. (Hz)	Heading (deg.)	Dip Azimuth (deg.)	Dip Angle (deg.)	Spectral Exponent	Spectral Intensity	Aspect Ratio	Atten. (dB/m/ kHz)	Sound Speed (km/s)
7.5	070	12	-5.03	0.222	5.02e-5	6.53	0.35	1.061
7.5	160	263	19.8	0.379	4.53e-5	5.44	0.35	1.045
7.5	250	276	18.9	0.695	5.77e-5	2.85	0.29	1.040
7.5	340	193	3.4	0.746	5.94e-5	3.11	0.24	1.037
15.0	070	24	-15.7	0.318	4.58E-5	5.85	0.37	1.045
15.0	160	121	-12.6	0.382	8.15E-5	1.95	0.39	1.055
15.0	250	213	14.2	0.760	1.0E-4	1.97	0.20	1.041
15.0	340	2	2.54	0.633	5.07E-5	2.60	0.185	1.037

Table 2: Inversion results for experiments conducted in the Florida Strait at site 1.

The best fit results for site 1 are shown in figure 5 using the previous estimates for inputs into the composite roughness model. It can be seen that at both frequencies there is excellent model data agreement. The model to data error was less than 0.17 for all cases when measured as a ratio of the sum of the errors to the sum of the data, better than 83% agreement.

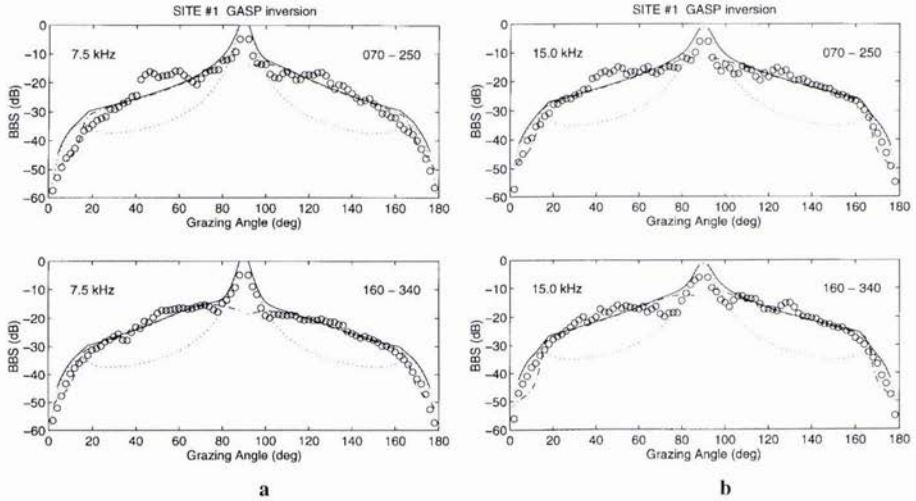

a b

Figures 5a - b: Results of the volume scattering model inversion and composite roughness model estimates. The dash-dot, dotted and solid lines indicate the inversion, roughness model estimate and combined inversion and roughness model estimate results respectively. a- 7.5 kHz 070°-250° and 7.5 kHz 160°-340° b- 15.0 kHz 070°-250° and 15.0 kHz 160°-340°

The inversion is limited in describing the scattering due to the exception of the rough interface scattering model. In the future it is hoped that this will be included and the data reevaluated. The estimate made for this data evaluation of the rough interface backscatter level combined with the inversion result shows very good agreement to the data. A collocated interface and volume physical property measurement is needed and should be pursued. The volume/rough interface inverse model at that point could be evaluated and should prove a very useful tool for estimating the physical properties of the sediment via a single remote measurement.

4. Acknowledgments

This work was supported by the United States Office of Naval Research and conducted by the author while at the University of Miami Rosenstiel School of Marine and Atmospheric Science. Much appreciation is given to Tokuo Yamamoto, Murat Kuru, Brian Rapids and Tom Nye from the University of Miami Geoacoustics Laboratory for their efforts. The experiments were conducted from the R/V Seward Johnson operated by the Harbor Branch Oceanographic Institute (HBOI).

5. References

[1] R.J. Urick, Principles of Underwater Sound. New York, McGraw-Hill, ch. 8, pp. 277-279, 1983.

[2] P.C. Hines, "Theoretical model of acoustic backscatter from a smooth seabed," *J. Acoust. Soc. Am.*, vol. 88, p.324, 1990.

[3] D.R. Jackson, D.P. Weinbrenner and A. Ishimaru, "Application of the composite roughness model to high frequency bottom scattering," *J. Acoust. Soc. Am.*, vol. 79, 1986.

[4] T. Yamamoto, "Acoustic scattering in the ocean from velocity and density fluctuation in the sediment," *J. Acoust. Soc. Am.*, vol. 99 (2), pp. 866-879, 1996.

[5] T. Yamamoto, "Velocity fluctuations and other physical properties of marine sediments measured by cross well acoustic tomography and cores," *J. Acoust. Soc. Am.*, vol. 98 (4), pp. 2235-2248, 1995.

[6] M.E. Huster, D.W. Miklovik and S.L. Schmidt, "Broadband sparse array image processing for localization and classification in shallow water environments," Arete Associated Report AS-93-0012.0, 1993.

[7] N.D. Bregman, R.C. Bailey and C.H. Chapman, "Crosshole seismic tomography," *Geophysics.*, vol. 54, pp. 200-215, 1989.

[8] D.R. Jackson and K.B. Briggs, "High-frequency bottom backscattering: Roughness verses volume scattering," *J. Acoust. Soc. Am.*, vol. 92 (2), pp. 962-977, 1992.

Obtaining the Ocean Index of Refraction Spectrum from the Acoustic Amplitude Fluctuations

Daniel Rouseff, Terry E. Ewart and Stephen A Reynolds

Applied Physics Laboratory
University of Washington
1013 NE 40th Street
Seattle, WA 98115 U.S.A.
Email: rouseff@apl.washington.edu

Abstract

The feasibility of using acoustic measurements to determine the properties of a shallow water internal wave field is investigated through numerical simulations. The random internal wave field is modeled by a generalized Garrett-Munk spectrum. The goal of the inversion is to recover the characteristic mode number, energy level and power-laws associated with the model. A hierarchy of inversion strategies is considered. Results from numerical simulations are presented together with a discussion of the remaining theoretical challenges.

1. Introduction

Based on a large number of experimental observations, Garrett and Munk developed a universal spectral model for deep water internal waves [1]. The Garrett-Munk (GM) model features appropriate power-law behavior for both the temporal and vertical wavenumber spectra and a scaling of the wave amplitude with depth. Prompted by the increased operational interest in the littoral zone, the quest has begun for an analogous shallow water internal wave model. Shallow water internal wave behavior is complicated by the presence of discrete internal solitary waves that can be generated at sills or the continental shelf break. In addition to these event-like waves, it is hypothesized that there is an underlying background internal wave field that remains to be characterized. It is the development of acoustical techniques for parameterizing this background internal wave field that is the subject of the present study.

An acoustic wave propagating through an internal wave field will acquire random fluctuations in both its magnitude and phase. The statistical properties of these fluctuations can be calculated using wave propagation in random media theory. The theory has reached a level of maturity and there is good agreement between calculations and experimental observations. The Mid-Atlantic Transmission Experiment (MATE) is an example of a deep water experiment where acoustic and oceanographic measurements are in accord [2,3]. Success in solving the forward problem suggests that acoustics might be used in an inverse sense: from measurements of the statistical properties of the acoustic field, is it possible to infer the statistical properties of shallow water internal waves? Acoustics offers the flexibility to probe the medium over a range of spatial/temporal scales not easily accessible by other towed, dropped or moored instrumentation. It also offers spatially integrated results difficult to achieve with traditional ocean sensors.

It is our working hypothesis that background shallow water internal waves satisfy a GM-like spectrum, but with energy levels, power-laws, and modal structures that may differ markedly from those observed in deep water. We take it as the goal of an acoustic inverse to estimate the numerical values for these parameters.

In the present work, we use numerical simulations to study the feasibility of recovering shallow water internal wave properties from acoustical measurements. We begin by simulating numerical realizations of a time-evolving, three-dimensional internal wave field. Internal wave parameters are defined for the simulation based on observations near the site of the 1996 Coastal Mixing and Optics (CM&O) Experiment. Acoustic propagation through the internal wave field is then simulated using the parabolic equation method. The results are time series of the acoustic log amplitude and phase at discrete receivers. The synthesized data are then compared to theoretical predictions. Using a modified least-squares procedure, the free parameters in the theory are adjusted to fit the experimental observations. The predicted values for the internal wave parameters are then compared to what was originally input into the oceanographic simulations. Implications for future shallow water experiments are discussed.

2. Shallow Water Internal Wave Model

The spatial and temporal properties in the internal wave field are not independent; they are related via a dispersion relationship. Flatté et al. [4] give alternative forms for the deep water Garrett-Munk spectrum in terms of different combinations of the spatial and temporal transform variables. As a shallow water model, we assume a similar representation but with additional free parameters. It will further prove useful to use a mixed representation for the spectrum Φ of the index of refraction as a function of both the wavenumber $\mathbf{k} = (k_x, k_y, k_z)$ and the time separation τ:

$$\Phi(\mathbf{k};\tau) = F(\mathbf{k})\cos(\omega_0 \tau), \tag{1}$$

$$F(\mathbf{k}) = \frac{\phi_g \kappa |k_z|}{\left(\kappa^2 + (\omega_i / N)^2 k_z^2\right)^{q} \left(k_z^2 + k_g^2\right)^{p/2}}, \tag{2}$$

where $\kappa^2 = k_x^2 + k_y^2$. The inertial frequency ω_i is known from the latitude of the experiment. In general, the buoyancy frequency N is a function of depth. Within a WKB approximation, the break wavenumber is given by $k_g = j_*(\pi / b)(N / N_0)$, where j_* is the internal wave modal bandwidth, N_0 is the reference buoyancy frequency, and b is the reference depth . The cosine in (1) ensures that the internal waves have no preferential direction. Finally, the value for ω_0 is set by the dispersion relationship

$$\omega_0(\mathbf{k}) = \left(\frac{\kappa^2 N^2 + k_z^2 \omega_i^2}{\kappa^2 + k_z^2} \right)^{1/2}. \tag{3}$$

It remains to fix the spectral level ϕ_g. In general, the index of refraction variance for internal waves is a function of depth. In deep water, the variance scales with N^3. For simplicity, we assume that this also applies in shallow water. Accordingly, the reference variance $<\mu_0^2>$ is defined by

$$<\mu_0^2> (N / N_0)^3 = \int d\mathbf{k} F(\mathbf{k}). \tag{4}$$

Substituting (2) into (4), the integrals can be evaluated exactly. Solving for the spectral level yields

$$\phi_g = \frac{2}{\pi^{3/2}} <\mu_0^2> \beta \left(\frac{N}{N_0} \right)^{1+p} \left(\frac{\omega_i}{N_0} \right)^{2q-3} \left(\frac{\pi j_*}{b} \right)^{p+2q-5}, \tag{5}$$

$$\beta = \sin(\pi(q - 3/2)) \frac{\Gamma(p/2)\Gamma(q)}{\Gamma((p+2q-5)/2)}, \tag{6}$$

and Γ is the gamma function.

Assuming the buoyancy frequency is known from direct measurement, there are up to four free parameters in the model: the variance $<\mu_0^2>$, the mode bandwidth, j_*, and the power law exponents p and q. Values for the exponents, within the standard Garrett-Munk model, are p=q=2. In the deep water MATE experiment, however, a value of $2q$=3.7 was observed. A typical deep water value is $j_* = 3$, although there is reason to believe a smaller value is more appropriate in shallow water; see Henyey et al. for a discussion and a review of the literature [5]. In solving the inverse problem, the goal is to determine some combination of the free parameters of the internal wave model from the acoustic measurements.

3. Rytov Theory and Implications for the Inverse Problem

The Rytov approximation yields useful expressions for the statistics of a wave propagating through a weakly fluctuating random medium. The general theory is well established. When there is no background sound speed profile, two point statistics for both the log amplitude and phase of the acoustic field can be calculated. Munk and Zachariasen [6] extended the theory to include a profile, but considered only the variance of the field and not the vertical autocorrelation.

For this initial analysis, we neglect ray curvature and assume a constant background sound speed. We justify this choice based on an analysis of the August 1996 Synthetic Aperture Sonar (SAS) Experiment. The experiment, conducted near the CM&O site, was 100 km south of Woods Hole, MA in waters 72 m deep. Assuming a source 60 m deep, a pre-experiment ray trace showed an isolated path traveling nearly horizontally out to ranges greater than 600 m [5]. This approximation further allows the buoyancy frequency along the propagation path to be approximated by the constant reference value N_0.

To formulate the problem, consider a point source generating an acoustic field that is measured at range $x=L$ at discrete depths as a function of time. Within the Rytov approximation, the autocorrelation of the log amplitude, χ, and phase, ϕ, of the field is

$$B_{\chi/\phi}(\tau, z_d) = 2\pi k^2 \int_0^L dx \int_{-\infty}^{\infty} dk_y \int_{-\infty}^{\infty} dk_z \, \Phi(0, k_y, k_z; \tau)\, g_{\chi/\phi}(k_y, k_z) e^{ik_z z_d x/L} , \tag{7}$$

where τ and z_d are the separations in time and depth, respectively, of the two observation points [7]. The integrations are over range and the spectral components transverse to the direction of propagation. The Fresnel filter functions $g_{\chi/\phi}(k_y, k_z)$ are

$$g_{\chi/\phi}(k_y, k_z) = \frac{1}{2}\left[1 \mp \cos\left(\frac{x(L-x)}{kL} (k_y^2 + k_z^2) \right) \right] , \tag{8}$$

with + corresponding to ϕ and - to χ.

The Fresnel filters for the phase and log amplitude emphasize different portions of the internal wave spectrum. Because g_ϕ is at a maximum at $k_y = k_z = 0$, the acoustic phase is sensitive to the large scale (low spatial frequency) fluctuations in the medium. The filter g_χ is zero at $k_y = k_z = 0$ and the log amplitude is most sensitive to fluctuations in the medium at the Fresnel scale or smaller. This has implications for solving the stochastic inverse problem; certain features of the medium may be more easily extracted from measurements of the acoustic log amplitude, for example, rather than from the phase.

In principle, the inverse problem is solved by substituting the spectral representation for internal waves (1) into (7). The free parameters in the internal wave model are then found by matching the calculated acoustic quantities with the experimental observations.

In practice, the way in which Rytov theory would be applied to solve the inverse problem is highly dependent on the specific experimental geometry. At one extreme, consider a rigid vertical receiving array. If the positions of the receiving elements were known precisely, it would be possible to use both the acoustic log amplitude and the phase in the inversion. If the array were fully populated, it would be possible to estimate the vertical wave number spectra for both the log amplitude and the phase from the measurements. The corresponding theoretical expressions for these quantities can be derived by taking the Fourier transform of (7) with respect to depth. At the other extreme, consider a moored array. Here, the positions of the receiving elements may not be known with great accuracy; it likely would prove difficult to separate sensor motion from acoustic phase fluctuations. Consequently, it may not be reliable to use the acoustic phase in the inverse. The log amplitude, however, is relatively insensitive to sensor motion. An inversion algorithm that used only the acoustic log amplitude fluctuations would be relatively simple to implement in the ocean.

Our emphasis is on a geometry loosely based on the configuration of the SAS experiment. The measurements were made on a rigid platform. The vertical aperture, however, was limited. We consider an inverse that uses time series of the log amplitude phase measured at a limited number of discrete positions in the vertical. From this configuration, the temporal spectra as a function of vertical receiver separation can be observed. The corresponding theoretical expressions can be derived. Define the two-sided temporal acoustic spectra by

$$S_{\chi/\phi}(\omega; z_d) = \frac{1}{2\pi} \int_{-\infty}^{\infty} B_{\chi/\phi}(\tau; z_d) e^{i\omega\tau} . \tag{9}$$

It follows from (7)

$$S(\omega; z_d) = \pi k^2 \int_0^L dx \int_{-\infty}^{\infty} dk_y \int_{-\infty}^{\infty} dk_z F(0, k_y, k_z) \left[\delta(\omega - \omega_0) + \delta(\omega + \omega_0) \right] g(k_y, k_z) e^{ik_z z_d x/L} . \tag{10}$$

where we have suppressed the subscripts. The delta functions in (10) can be used to evaluate the k_y integral. Since S is an even function of ω, it suffices to evaluate the integral for positive values; negative frequencies are recovered by symmetry. Use the property [8]:

$$\delta[\omega-\omega_0]=\sum_n \frac{\delta(k_y-k_{y0}^{(n)})}{\left|\omega_0'(k_{y0}^{(n)})\right|}, \tag{11}$$

where $k_{y0}^{(n)}$ are the values of k_y that are zeros of ω_0. From (3), there are zeros at $\pm k_{y0}$ where

$$k_{y0}^2=\frac{\omega^2-\omega_i^2}{N^2-\omega^2}k_z^2. \tag{12}$$

Note that k_{y0} is real only when $\omega_i<\omega<N$. Outside of this interval, the delta functions are not captured by the integration and the acoustic spectra are exactly zero. Inside this interval,

$$S(\omega;z_d)=2\pi k^2\int_0^L ds\int_{-\infty}^{\infty} dk_z F(0,k_{y0},k_z)\left|\omega_0'(k_{y0})\right|^{-1} g(k_y,k_z)e^{ik_z z_d x/L}, \tag{13}$$

where the derivative of ω_0 gives

$$\omega_0'(k_{y0})=\frac{N^2-\omega^2}{\omega^2-\omega_i^2}\frac{1}{\omega}\frac{k_{y0}}{k_z^2}. \tag{14}$$

Finally, combining (2), (13) and (14), and exploiting the even nature of the integrand

$$\begin{aligned} S_{\chi/\phi}(\omega;z_d)&=4\pi k^2\omega^{1-2q}N^{2q-2}\phi_g \\ &\int_0^L dx\int_0^\infty dk_z k_z^{3-2q}\left(k_z^2+k_g^2\right)^{p/2} g_{\chi/\phi}(k_{y0},k_z)\cos(k_z z_d x/L) \end{aligned}, \tag{15}$$

where we have approximated $N^2-\omega^2$ by N^2 except in the Fresnel filter.

Before presenting specific results, it is instructive to examine the qualitative behavior of (15) in the context of solving the inverse problem. Particular parameters of the internal wave model are most easily recovered from particular acoustical measurements.

The integrand in (15) is only weakly dependent on ω through the Fresnel filter; to a good approximation, both S_χ and S_ϕ go like ω^{-2q+1}. As a result, by observing the asymptotic behavior of the measured acoustic spectra it should be possible to infer the internal wave parameter q. Recovering the other internal wave parameters is not as straight forward.

For the log amplitude spectra S_χ the dominant contribution to the inner integral in (15) comes from $k_z^2>>k_g^2$. To a good approximation, $k_z^2+k_g^2\approx k_z^2$ within the integrand. Consequently, S_χ is dependent on the characteristic internal wave mode number j_* only through the spectral strength ϕ_g. As a result,

$$S_\chi\propto\left\langle\mu_0^2\right\rangle j_*^{p+2q-5}. \tag{16}$$

For the standard values $p=q=2$, the result is proportional to j_*. The primary point is that the strength of the acoustic log amplitude spectrum depends on a complicated combination of ϕ_g and j_*. Even if q was inferred from the asymptotic behavior and p set to the traditional value, the inversion is likely to be underdetermined; it may not be possible to separate the contributions from ϕ_g and j_* from measurements of the log amplitude spectrum alone.

A similar analysis is possible for the phase spectrum S_ϕ. The primary contribution comes from small k_z. To examine the approximate behavior, replace the Fresnel filter by the constant two; this is effectively a geometric acoustics approximation. The integrand is singular as k_z approaches zero. Physically, this is because the phase is sensitive to the large scale fluctuations in the medium. The largest allowable vertical fluctuations is set by the water depth D, so the lower limit of integration is truncated at π / D. The integrals can then be evaluated analytically. For the standard values $p = q = 2$, the result is

$$S_\phi \propto \ln(j_*^2 + 1) / j_* . \tag{17}$$

Again, the individual contributions from ϕ_g and j_* cannot be separated. If both the log amplitude and the phase are measured, however, there is the prospect of making the separation by combining (16) and (17). Note, however, that for values near unity as expected to prevail in shallow water, (17) is relatively insensitive to the precise numerical value of j_*.

4. Numerical Results

The viability of an inversion for the parameters of a shallow internal wave model is tested using numerical simulation. The simulation involves a two-step procedure. Internal wave fluctuations are generated within a three-dimensional numerical box. These fluctuations are converted to sound speed changes and the box is subdivided into eight depth-range slices. A PE-propagator is then used to obtain the acoustic field transmitted through each slice. The analog for the geometry of this numerical experiment derives from the SAS transmission experiment that took place during CM&O [see [5] and http://cofdl.whoi.edu/cmohome.html]. The result of the simulation are time series of acoustic amplitude and phase at several vertical receivers. Both the forward and inverse problem are considered below. A nonlinear least squares optimizer is used to invert the model discussed in Section 2 for the parameter values.

4.1 Internal Wave Simulations

The internal wave simulation is not discussed in detail here. We refer the reader to Winters and D'Asaro [9]. A form of the GM-spectral model is used to set the strength and modal bandwidth j_* of the internal wave field. The principle difference between the model discussed in Section 2 and the GM-model used in simulating the internal wave fluctuations is that a modal decomposition is used rather than taking a WKB-approximation. An internal wave displacement fields is generated in the computational volume (Lx,Ly,Lz). This defines the horizontal and vertical scales produced in the simulation. Once a spatial realization is obtained, the internal wave dispersion relationship is used to evolve the field in time.

For the simulations, a water depth of 128 m is used. We specify a constant buoyancy frequency, N = 4 cph, and a constant sound speed of c_0=1480 m/s. These numbers were observed near 60 m depth over a direct, near bottom path at the CM&O site. The length and width of the computational box is 32 km by 8 km. This domain is a reasonable trade-off between a desire to sample high wave numbers as well as resolve much of the low-wave number, energy containing internal waves. A total of 128 vertical modes were used. Internal wave displacement was converted to sound speed using the formula

$$\frac{1}{c_0}\frac{\partial c_p}{\partial z} = GN^2 \tag{18}$$

with G=0.7 [4] for the CM&O site. This results in a $<\mu_0^2>$ of $3 \cdot 10^{-8}$. The modal bandwidth is $j_* = 1$ (a value commonly associated with the shallow water case). We use here a time series of 128 hours sampled every 225 seconds.

4.2 PE-Simulations

A narrow-angle PE-propagator is used to obtain the acoustic energy at a vertical aperture of receivers. The transmission range is 1 km with the transmitter depth and receiver aperture centered at 64 m depth. The point source is a 2_ Gaussian with a frequency of 6 kHz. Eight separate realizations are obtained for each time step by sub-sampling the 3-D internal wave computational box into nearly independent one-km range/depth slices. The internal wave output is spectrally interpolated in depth and range to assure accuracy in the PE. Energy at the surface and bottom is absorbed. Because the acoustic fluctuations are the quantities of interest, each received field is normalized by the "deterministic" field resulting from the range independent, constant sound speed case. We take the phase and log-amplitude data from the center 20 m receiving aperture over the 128 hour internal wave simulation. Both forward and inverse modeling, require the statistics of log-amplitude. From the time/depth series of acoustic data, depth-lagged covariance and temporal spectral

estimates are calculated. For all estimates, a mean is removed from the data and a 10% cosine data taper is applied to the ends of the time series for calculating spectra.

4.3 Forward model comparison

An obvious test of our procedure is to treat the forward problem: using the theory of Section 3 with the medium spectra of Section 2, how well are the log-amplitude fluctuations described by theory? Using data from receivers separated by 4 m over the vertical aperture, the depth lagged frequency co-spectra are estimated for several separations and displayed in Fig. 1 along with theory. The values of the co-spectra at each frequency decrease as separation increases, going negative for depth separations greater than 8 m. We note that the data generally have less energy near the inertial frequency, ω_i, than predicted by theory (note that the frequency is scaled by ω_i). This is a result of two things. First, resolution of the inertial frequency depends upon the length of the time series. We chose to end the simulation at 128 hours for practical reasons. Second, there is a deficit of low wave numbers in the internal wave simulation, a problem needing further investigation. Overall, however, the data/theory comparison is quite good.

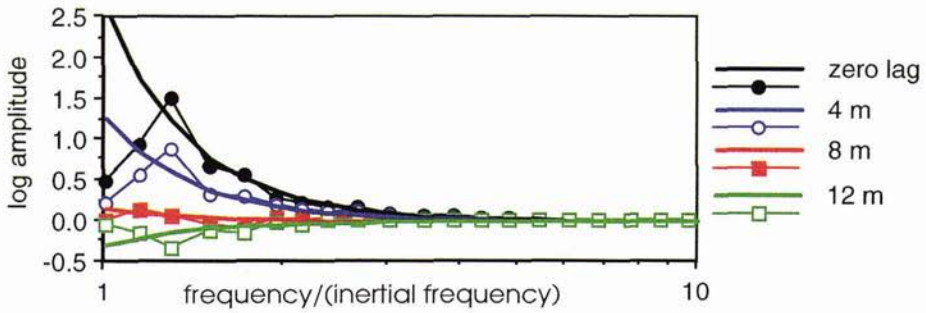

Figure 1 The depth lagged frequency co-spectrum of log-amplitude at 6 kHz. For this forward comparison, theory parameters are $<\mu_0^2>=3.5\cdot10^{-8}$, $j_*=1$, and $p=q=2$. The frequency is scaled by the inertial frequency, $\omega_i=0.0541$ cph.

Integrating the curves in Figure 1 over frequency gives the depth covariance function of log-amplitude. This is compared with theory in Figure 2. The data have a slightly lower variance at zero lag probably indicating a need to carry our simulation farther in time and to lower wave numbers as mentioned above. Data and theory compare well for almost all lags away from zero.

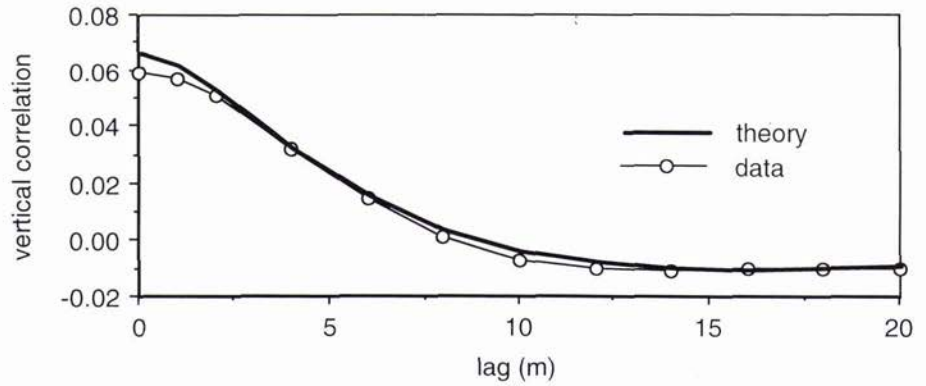

Figure 2. The covariance of log-amplitude with lag in depth. Theory is shown solid, simulated data as dashed with circles. Theory parameters are as in Fig. 1.

4.4 Inverse model comparisons

A nonlinear least-squares optimizer [10] is used to invert theory and obtain the model parameters. It should be emphasized that while a discrete mode representation is used to generate the internal wave field, the inversion seeks the parameters of a continuous spectral representation; we thus avoid the "inverse crime" of using exactly the same model to both synthesize data and do the inversion [11]. Because of the relatively short lags used here, along with the fact that shallow water internal waves appear to be low-mode, it is difficult to solve for all parameters. An inverse using only the log amplitude frequency auto-spectrum is shown in Fig. 3. It was shown in (16) that the contributions from $<\mu_0^2>$ and j_* are not easily separated for this measurement. By assuming p=2, a two parameter estimation is done for ϕ_g and q. The estimate for the product $<\mu_0^2> j_*$ is then inferred from the two estimated parameters using (5). Parameter values obtained are $<\mu_0^2> j_* = (3 \pm 2) \cdot 10^{-8}$ and $q = 2.04 \pm 0.07$. The values are quite close to those input to the simulations and the theory/data comparison in Figure 3 is excellent. The error in $<\mu_0^2> j_*$ is a reflection of the fact that the parameters are not independent. Further work is needed on developing an inversion scheme that decreases this dependence. For this case, and those in Figs. 1 and 2, data averaged over all eight range slices are used. The same inverse as that shown in Figure 3 was repeated using a single receiver's output. Parameter values near those of Figure 3 were obtained indicating that a single receiver inversion is possible with measurements made over six inertial periods. The errors, however, were large.

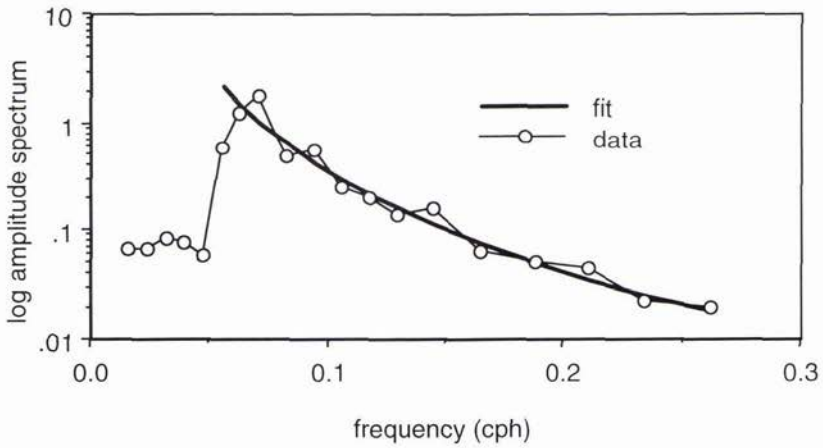

Figure 3. 6 kHz log-amplitude spectrum obtained from a 128 h simulated time series and an average of eight separate depth/range slices. A data fit from an inversion of theory is shown as solid-bold.

5. Discussion

There are important implications for oceanographic research in these results. When conventional Rytov theory is valid, we have shown that one can obtain integral scale measurements of subsets of the four internal wave parameters using stochastic inverse methodology. In time varying internal wave fields, this gives a mechanism to obtain model parameters for the weakly non-stationary, and possibly intermittent shallow water internal wave processes.

We have considered a very simple inversion using only the log amplitude of the field. A single transmitter mooring located an appropriate distance from a single receiver mooring will provide estimates of $<\mu_0^2> j_*$ and the fundamental power law parameter q. Such an experiment would be simple to implement and relatively inexpensive. Adding more receivers in the vertical adds redundancy and also potentially allows one to obtain the other power law parameter, p. It is a simple matter to add a few temperature sensors to the moorings, and obtain $<\mu_0^2>$ directly, thus providing the oceanographer with the four (possibly time varying) parameters of the internal wave field. Clearly, if phase or phase difference measurements are added to the moorings, then further redundancy in the parameter estimates is obtained. It is extremely important to note that the method provides these parameters from a horizontal scale equal to the transmission range, thus, an integral or averaged measurement of the stochastic parameters.

There is a possible caveat. We have assumed, in order to apply the conventional Rytov approximation, that the acoustic transmission range is large compared to the integral scale of the medium. In shallow water we find that j_* is very

small, so the internal waves are thin in depth and large in the horizontal. Thus, the theory may have to be modified if the conditions for Rytov are not met. This is a research issue. A second research issue is the extension of the formalism to include ray curvature. This curvature could invalidate conventional Rytov theory due to thin nature of shallow water internal waves.

References

[1] W. H. Munk, "Internal waves and small-scale processes," in *Evolution of Physical Oceanography*, B. A. Warren and C. Wunsch, eds., MIT Press, pp. 264-291, 1981.

[2] T. E. Ewart and S. A. Reynolds, "Ocean acoustic propagation measurements and wave propagation in random media" in *Wave Propagation in Random Media (Scintillation)*, V. I. Tatarski, A. Ishimaru, and V. U. Zavorotny, eds., SPIE, 1993

[3] C. Macaskill and T. E. Ewart, "Numerical solution of the fourth moment equation for acoustic intensity correlations and comparison with the mid-ocean acoustic transmission experiment.," *J. Acoust. Soc. Am.*, vol. 99, pp.1419-1429, 1996.

[4] S. M. Flatté, ed., Sound Transmission through a Fluctuating Ocean, Cambridge, 1979.

[5] F. S. Henyey, D. Rouseff, J. M. Grochocinski, S. A. Reynolds, K. W. Williams, and T. E. Ewart, "Effects of internal waves and turbulence on horizontal aperture sonar," *IEEE J. Oceanic Eng.*, in press.

[6] W. H. Munk and F. Zachariasen "Sound propagation through a fluctuating, stratified ocean: Theory and observation," *J. Acoust. Soc. Am.* vol. 59, pp. 818-838, 1976.

[7] A. Ishimaru, Wave Propagation and Scattering in Random Media, Vol. 2, Ch. 18, Academic Press, 1978.

[8] A. Papoulis, The Fourier Integral and its Applications, McGraw-Hill, 1962.

[9] K. B. Winters and E. D'Asaro, unpublished manuscript.

[10] B. Bell, unpublished manuscript.

[11] P. M. van den Berg, M. G. Coté and R. E. Kleinman, "'Blind' shape reconstruction from experimental data,' *IEEE Trans. Antennas Propagat. v* vol. 43, pp. 1389-1396, 1995.

Multistatic bottom reverberation in shallow water

Henrik Schmidt, Jaiyong Lee, Huaiyu Fan, and Kevin LePage*

Department of Ocean Engineering
Massachusetts Institute of Technology
Cambridge, MA 02139
E-mail: henrik@keel.mit.edu

Abstract

A wavenumber integration approach to modeling of the full multistatic reverberant field produced by small-scale bottom roughness in stratified shallow water waveguides has been developed. A perturbation approach to rough elastic interface scattering has been combined with the OASES seismo-acoustic propagation model for stratified waveguides, yielding the capability of producing realizations and spatial statistics of bottom reverberation for multistatic sonar configurations in shallow water with a rough, stratified, elastic bottom. The formulation handles roughness with arbitrary anisotropic power spectra, and incorporates scattering into both the water column and the various seismic waves in the bottom.

1. Introduction

A numerically efficient wave-theory model of the full multistatic reverberant field produced by small-scale roughness patches in stratified shallow water waveguides has been developed. A perturbation approach to rough elastic interface scattering [1, 2] has been combined with the OASES seismo-acoustic propagation model for stratified waveguides. The original perturbation theory was based on a 2-D Fourier transform formulation, allowing only short range reverberation modeling for computational reasons. However, coordinate transformations have been developed, translating the representation for the scattered field into an azimuthal Fourier series expansion of wavenumber integrals. This representation is directly compatible with the 3-D version of the OASES/SAFARI code [3], which has consequently been modified to provide extremely efficient numerical simulation of high-frequency seismo-acoustic reverberation in shallow water waveguides. The model's efficiency allows for Monte-Carlo estimation of the statistical properties of the reverberation from patches with anisotropic roughness statistics, including mean reverberation intensity and spatial correlation.

2. Rough Interface Reverberation Theory

2.1. Perturbation Theory

The perturbation theory for scattering from rough elastic interfaces decomposes the wavefield into coherent and scattered components of the field potentials in layer number ℓ,

$$\chi_\ell = \langle \chi_\ell \rangle + s_\ell = \begin{cases} \phi_\ell &= \langle \phi_\ell \rangle + p_\ell \\ \psi_\ell &= \langle \psi_\ell \rangle + q_\ell \\ \Lambda_\ell &= \langle \Lambda_\ell \rangle + r_\ell \end{cases} \tag{1}$$

where χ_ℓ is a generic potential representing the compressional potential ϕ_ℓ and the two scalar shear potentials ψ_ℓ and Λ_ℓ, representing SH and SV waves, respectively [3].

Away from physical sources and the rough interfaces, both the coherent and scattered potentials satisfy homogeneous Helmholtz equations

$$\left[\nabla^2 + k_\ell^2\right] \langle \chi_\ell(\vec{\mathbf{x}}) \rangle = 0 , \tag{2}$$

$$\left[\nabla^2 + k_\ell^2\right] s_\ell(\vec{\mathbf{x}}) = 0 , \tag{3}$$

*Presently with BBN Systems and Technologies, Cambridge, MA 02138.

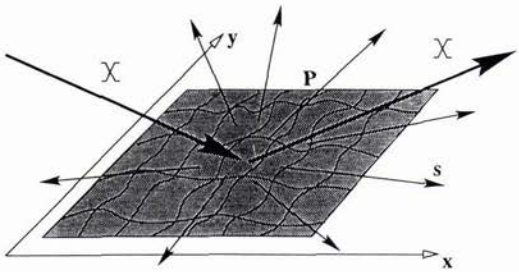

Figure 1: Rough interface patch in stratified waveguide, insonified by a seismo-acoustic field.

where k represents the appropriate medium wavenumbers.

In addition, the fields must satisfy the boundary conditions at all interfaces z_ℓ in the stratification, as well as the source conditions. Assuming the *physical sources* are limited to a single depth, z_s, a dummy interface is added at this depth, and the interface conditions may be written in the operator form

$$B_\ell(\vec{\mathbf{x}})\langle\chi_{\ell;\ell+1}(\vec{\mathbf{x}})\rangle = -f_s(\vec{\mathbf{x}})\delta(z_\ell - z_s)\ , \ell = 1, 2\cdots N\ . \tag{4}$$

where N is the total number of physical and dummy interfaces in the stratification. The differential matrix operator B_ℓ represents the derivatives relating the physical parameters involved in the boundary conditions to the potentials [1]. Thus, Eq. 4 represents continuity conditions at all physical interfaces and discontinuity conditions imposed by the physical source distribution $f_s(\vec{\mathbf{x}})$.

Similarly, the perturbation theory leads to a set of boundary conditions to be satisfied by the scattered field $s(\vec{\mathbf{x}})$ at all interfaces in the stratification [2], including a rough interface at depth z_v,

$$B_\ell(\vec{\mathbf{x}})s_{\ell;\ell+1}(\vec{\mathbf{x}}) = -f_v(\vec{\mathbf{x}})\delta(z_\ell - z_v)\ , \ell = 1, 2\cdots N \tag{5}$$

where the distribution function $f_v(\vec{\mathbf{x}})$ is given by [1, 4, 5]

$$f_v(\vec{\mathbf{x}}) = \left[\overbrace{\gamma(\vec{\mathbf{x}})\frac{\partial B_\ell(\vec{\mathbf{x}})}{\partial z}}^{\text{elevation}} + \overbrace{\nabla\gamma(\vec{\mathbf{x}})\circ b_\ell(\vec{\mathbf{x}})}^{\text{rotation}}\right]\langle\chi_{\ell;\ell+1}(\vec{\mathbf{x}})\rangle\ . \tag{6}$$

Here, $\gamma(\vec{\mathbf{x}})$ is the interface roughness elevation. B_ℓ is the same boundary operator as above, while b_ℓ represents the rotation of the boundary conditions due to the roughness slope.

Obviously, Eq. 5 is totally equivalent to Eq. 4, with the physical source distribution $f_s(\vec{\mathbf{x}})$ replaced by the distribution function $f_v(\vec{\mathbf{x}})$ at the depth of of the rough interface. Thus, $f_v(\vec{\mathbf{x}})$ represents a *virtual source distribution*, the amplitude and phase distributions of which are determined by the coherent field and the roughness through Eq. 6.

2.2. Wavenumber Representation

For interfaces corresponding to separable cartesian geometry, the boundary equations 4 and 5 are conveniently transformed into the wavenumber domain, yielding for the scattered field [2]

$$\widetilde{s}^{\mp}_{\ell;\ell+1}(\vec{\mathbf{q}}) = -\widetilde{B}^{-1}_\ell(\vec{\mathbf{q}})\frac{1}{2\pi}\int d^2\vec{\mathbf{k}}\widetilde{\gamma}(\vec{\mathbf{q}}-\vec{\mathbf{k}})\left[\frac{\partial\widetilde{B}_\ell(\vec{\mathbf{k}})}{\partial z} - j(\vec{\mathbf{q}}-\vec{\mathbf{k}})\widetilde{b}_\ell(\vec{\mathbf{k}})\right]\langle\widetilde{\chi}^{\mp}_{\ell;\ell+1}(\vec{\mathbf{k}})\rangle \tag{7}$$

For random, spatially homogeneous interface roughness, the roughness statistics is given by the spatial correlation function $N_\ell(\Delta\vec{\mathbf{r}})$ or its Fourier transform, the normalized roughness power spectrum $P_\ell(\vec{\mathbf{p}})$, and the roughness variance $\langle\gamma^2_\ell\rangle$

$$N_\ell(\Delta\vec{\mathbf{r}}) = \langle\gamma_\ell(\vec{\mathbf{r}})\gamma_\ell(\vec{\mathbf{r}}+\Delta\vec{\mathbf{r}})\rangle \tag{8}$$

$$\langle\gamma^2_\ell\rangle P_\ell(\vec{\mathbf{p}}) = \frac{1}{2\pi}\int d^2\Delta\vec{\mathbf{r}}N_\ell(\Delta\vec{\mathbf{r}})e^{-j\vec{\mathbf{p}}\cdot\Delta\vec{\mathbf{r}}} \tag{9}$$

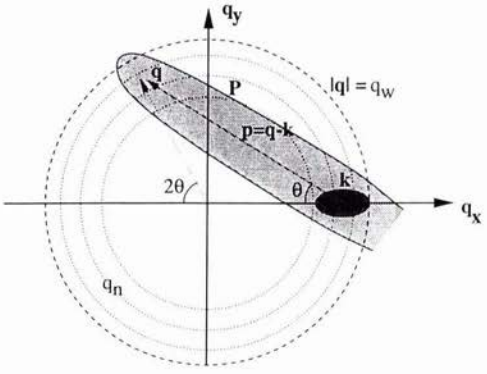

Figure 2: Graphical representation of the scattering wavenumber kernel. The scattered field is a convolution in the wavenumber plane of the incident field by the anisotropic roughness wavenumber spectrum.

Then, the following expression is achieved for the spatial correlation function for the scattered field [2]

$$C_S(\vec{\mathbf{r}}_1, z_1, \vec{\mathbf{r}}_2, z_2) = \frac{\langle \gamma_\ell^2 \rangle}{(2\pi)^3} \int d^2\vec{\mathbf{p}} P_\ell(\vec{\mathbf{p}}) \left[\int d^2\vec{\mathbf{q}} A_m(z_1, \vec{\mathbf{q}}, \vec{\mathbf{q}} + \vec{\mathbf{p}}) e^{-j\vec{\mathbf{q}}\cdot\vec{\mathbf{r}}_1} \right] \left[\int d^2\vec{\mathbf{q}} A_n(z_2, \vec{\mathbf{q}}, \vec{\mathbf{q}} + \vec{\mathbf{p}}) e^{-j\vec{\mathbf{q}}\cdot\vec{\mathbf{r}}_2} \right]^\dagger \tag{10}$$

where $A_m(z, \vec{\mathbf{q}}, \vec{\mathbf{k}})$ is the scattering kernel

$$A_m(z, \vec{\mathbf{q}}, \vec{\mathbf{k}}) = e_m(z, \vec{\mathbf{q}}) \widetilde{T}^*_{\ell;m}(\vec{\mathbf{q}}, \vec{\mathbf{k}}) \langle \widetilde{\chi}^{\mp}_{\ell;\ell+1}(\vec{\mathbf{k}}) \rangle$$

Here $e_\ell(z, \vec{\mathbf{q}})$ contains the exponentials representing the up- and downgoing scattered wavefield in layer ℓ, and $\widetilde{T}_{\ell;m}$ is a generalized *T-matrix* for the field in layer m produced by scattering from rough interface number ℓ,

$$\widetilde{T}_{\ell;m}(\vec{\mathbf{q}}, \vec{\mathbf{k}}) = -\widetilde{B}^{-1}_\ell(\vec{\mathbf{q}}) \frac{1}{2\pi} \left[\frac{\partial \widetilde{B}_\ell(\vec{\mathbf{k}})}{\partial z} - j(\vec{\mathbf{q}} - \vec{\mathbf{k}}) \widetilde{b}_\ell(\vec{\mathbf{k}}) \right] \tag{11}$$

The scattering integrals of both Eq. (7) and (10) are of a form convolving a medium dependent boundary operator term by the roughness spectrum at the difference wavenumber. This *Bragg scattering* condition is illustrated graphically in Fig. 2. An incident field with a wavenumber spectrum centered around the wave vector $\vec{\mathbf{k}}$ is convolved with an anisotropic roughness spectrum with skewness θ, creating a scattered field composed of wave vectors $\vec{\mathbf{q}}$ within the lightly shaded envelope in Fig. 2, representing the roughness spectrum. The medium dependent part of the kernel represents the modal structure of the waveguide, as indicated by the circles in Fig. 2. Thus, the resulting scattered field will have a modal structure in all directions, but shaded by the roughness spectrum centered at the incident wavenumber. As will be evident from the examples following below, the reverberation from finite size patches will qualitatively exhibit the same spectral behavior.

3. Finite Roughness Patch

Unfortunately, for realistic two-dimensionally rough interfaces, the convolution integrals in the correlation function, Eq. 10, become four-dimensional. Even though a normal-mode expansion of Eq. 10 has recently been developed, yielding orders of magnitude in computational savings [5], the full numerical evaluation of the three-dimensional field statistics through Eq. 10 has sofar been impossible. Consequently, numerical implementations have been limited to plane or axisymmetric problems with one-dimensional roughness [2, 5].

To allow modeling of the fully three-dimensional reverberant field important to multistatic sonar concepts, an alternative approach has therefore been developed. Instead of directly evaluating the spatial statistics through Eq. 10, a deterministic form of the perturbation theory has been developed, based on spatial integration over finite roughness patches. As described in the following, this formulation leads to field expressions which are evaluated using modified versions of existing seismo-acoustic propagation models. It yields extremely efficient computation of specific realizations of the reverberant field from rough interface patches, such that estimates of the 3-D spatial

field statistics can be readily achieved through Monte-Carlo simulation with random realizations of the roughness statistics.

For a finite size roughness patch or sonar footprint, the scattered field is more efficiently represented by spatial integral over the patch P,

$$s(\vec{\mathbf{x}}) = \int_P G_v(\vec{\mathbf{x}}, \vec{\mathbf{x}}_v) d^2\vec{\mathbf{x}}_v \tag{12}$$

where $G_v(\vec{\mathbf{x}}, \vec{\mathbf{x}}_v)$ is a *Generalized Green's Function* satisfying the standard Helmholtz equation, and the boundary conditions,

$$B_\ell(\vec{\mathbf{x}}) G_v(\vec{\mathbf{x}}, \vec{\mathbf{x}}_v) = -\delta(\vec{\mathbf{x}} - \vec{\mathbf{x}}_v) f_v(\vec{\mathbf{x}}) \delta(z_\ell - z_v) \; . \tag{13}$$

where the virtual source distribution $f_v(\vec{\mathbf{x}})$ is given by Eq. 6. In a horizontal stratification, Eq. 13 is most conveniently solved in the wavenumber domain,

$$\widetilde{B}_\ell(\vec{\mathbf{q}}) \widetilde{G}_v(\vec{\mathbf{q}}, \vec{\mathbf{x}}_v) = -\widetilde{f}_v(\vec{\mathbf{q}}, \vec{\mathbf{x}}_v) \delta(z_\ell - z_v) \; , \tag{14}$$

where the spectrum $\widetilde{f}_v(\vec{\mathbf{q}}, \vec{\mathbf{x}}_v)$ is the Fourier transform of the virtual 'point source' term $\delta(\vec{\mathbf{x}} - \vec{\mathbf{x}}_v) f_v(\vec{\mathbf{x}})$. It is a vector containing coherent displacement and stress discontinuities on the patch,

$$\widetilde{f}_v(\vec{\mathbf{q}}, \vec{\mathbf{x}}_v)^T \simeq \Delta \, [\widetilde{u}, \widetilde{v}, \widetilde{w}, \widetilde{\sigma}_{zz}, \widetilde{\sigma}_{zx}, \widetilde{\sigma}_{zy}] \tag{15}$$

The wavenumber spectrum of the total scattered field is then obtained by integrating the solutions to Eq. 14 over the patch,

$$\widetilde{s}(\vec{\mathbf{q}}) = \int_P \widetilde{G}_v(\vec{\mathbf{q}}, \vec{\mathbf{x}}_v) d^2\vec{\mathbf{x}}_v \; , \tag{16}$$

with the spatial distribution following by a two-dimensional Fourier synthesis,

$$s(\vec{\mathbf{x}}) = \frac{1}{2\pi} \int d^2\vec{\mathbf{q}} e^{-j\vec{\mathbf{q}}\cdot\vec{\mathbf{x}}} \left[\int_P \widetilde{G}_v(\vec{\mathbf{q}}, \vec{\mathbf{x}}_v) d^2\vec{\mathbf{x}}_v \right] \tag{17}$$

When numerically evaluating the inverse Fourier transform, the wavenumber increments must satisfy the Nyquist criteria, $\Delta q_{x,y} \leq \pi / R_{\max}$ [6]. Unfortunately, this condition severely limits the maximum range $R_{\max}$ that is numerically feasible, to a few times the horizontal extent of the roughness patch [4].

However, it is possible to transform Eq. 14 to cylindrical coordinates, [7]. The associated spatial distribution of the field is then given by a Fourier series of Hankel transforms,

$$s(r, \theta) = \Sigma_m \left\{ \begin{array}{c} \cos m\theta \\ \sin m\theta \end{array} \right\} \int dq \, q J_m(rq) \left[\int_P \widetilde{G}_v^m(q, r_v, \theta_v) r_v dr_v d\theta_v \right] \tag{18}$$

Here, the generalized Green's function $\widetilde{G}_v^m(q, r_v, \theta_v)$ can be directly computed using the three-dimensional version of OASES [3] with the virtual source distribution being the discontinuities of the displacement and stress components of m-th Fourier order on the patch,

$$\widetilde{f}_v^m(q, r_v, \theta_v)^T \simeq \Delta \, [\widetilde{u}^m + \widetilde{v}^m, \widetilde{u}^m - \widetilde{v}^m, \widetilde{w}^m, \widetilde{\sigma}_{zz}^m, \widetilde{\sigma}_{zr}^m + \widetilde{\sigma}_{z\theta}^m, \widetilde{\sigma}_{zr}^m - \widetilde{\sigma}_{z\theta}^m] \tag{19}$$

The details of the coordinate transformation relating the components of the cylindrical source terms f_v^m in Eq. 19 with the cartesian components $f_v(\vec{\mathbf{q}}, \vec{\mathbf{x}}_v)$ in Eq. 15 involves a significant amount of algebra, the details of which are described in Ref.[7].

The Fourier series in Eq. 18 converges very fast for orders larger than the dimensionless size ka of the patch, due to the asymptotic behavior of the virtual source terms

$$f_v^m(q, r_v, \theta_v) \sim J_m(qr_v) \to 0, \text{ for } m > qr_v \; , \tag{20}$$

and the truncation is therefore easily determined *a priori*. Thus, the number of significant terms in the series depends only on the patch size with the typical number being equal to a few times the *patch size* in wavelengths. In contrast the number of terms in the numerical evaluation of each of the two dimensions of the Fourier transform in Eq. 17 is determined by the *receiver range*. This difference is the key to the numerical superiority of the cylindrical form.

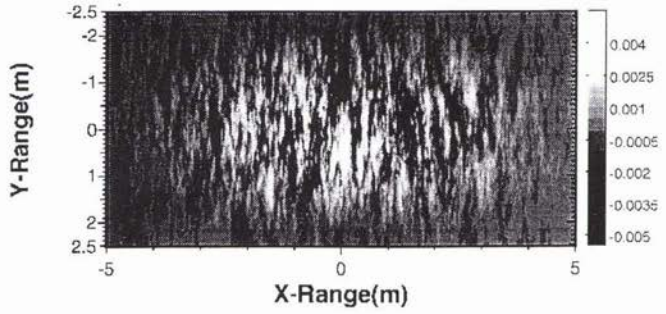

Figure 3: Bottom patch with anisotropic roughness, insonified from the left at 40 kHz. The roughness has a Goff-Jordan power spectrum with correlation lengths $l_x = 1.04$ m and $l_y = 0.13$ m, and RMS elevation of 4.7 mm.

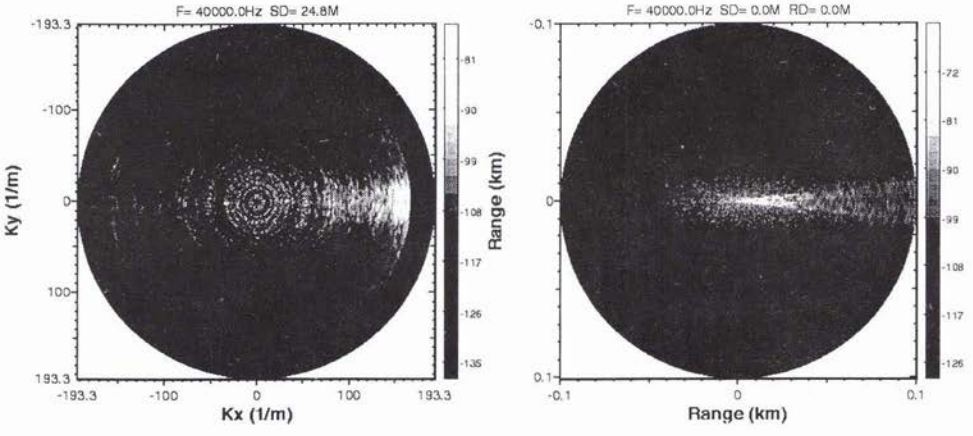

Figure 4: Multistatic reverberation from the roughness patch in Fig. 3. Left frame shows contours of the two-dimensional wavenumber spectrum of the scattered field 5.2 m above the seabed. The wavenumber of the incident field is $(k_x, k_y) = (168, 0)$ corresponding to incidence onto the patch from the left. The right frame shows contours of the scattered field in a horizontal plane at the same depth. Directions to the right represent forward scattering, while directions to the left represent backscattering.

4. Numerical Results

To illustrate the performance of the theoretical formulation in predicting the full multistatic reverberant field at high frequency, the Panama City bottom scattering experiment performed by Tang *et al.* is applied [8].

The experiment was carried out in a water depth of 30 m. An isovelocity water sound speed of 1495 m/s is assumed, and the bottom is assumed to be a homogeneous, elastic halfspace with compressional speed 1711 m/s, shear speed 118 m/s, and density 2.01 g/cm^3. The compression and shear attenuations were estimated to 0.09 dB/λ and 0.2 dB/λ, respectively.

The bottom was insonified at low grazing angles by a 40 kHz projector mounted on a tower, 5.2 m above the bottom. The insonifying beam had a vertical and horizontal beamwidths of 6° and 14°, respectively. With a nominal grazing angle of 12.6° the sonar footprint was centered at a distance of 23 m from the tower, and had a size of approximately 10×5 m.

Figure 3 shows the sonar footprint with seabed roughness, for a case where the large main axis of the roughness power spectrum is aligned with the incident beam, i.e. the insonificition is 'broadside' to the roughness striation. The roughness has a Goff-Jordan [9] power spectrum with correlation lengths $l_x = 1.04$ m and $l_y = 0.13$ m, and RMS elevation of 4.7 mm.

Figure 4 shows the computed multistatic reverberation from the roughness patch in Fig. 3. Left frame shows

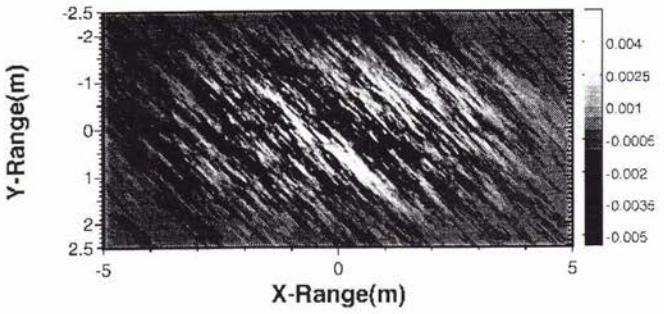

Figure 5: Bottom patch with anisotropic roughness, insonified from the left at 40 kHz. The roughness has a Goff-Jordan power spectrum with correlation lengths 1.04 m and 0.13 m, and RMS elevation of 4.7 mm. The skew angle of the roughness anisotropy is 45°

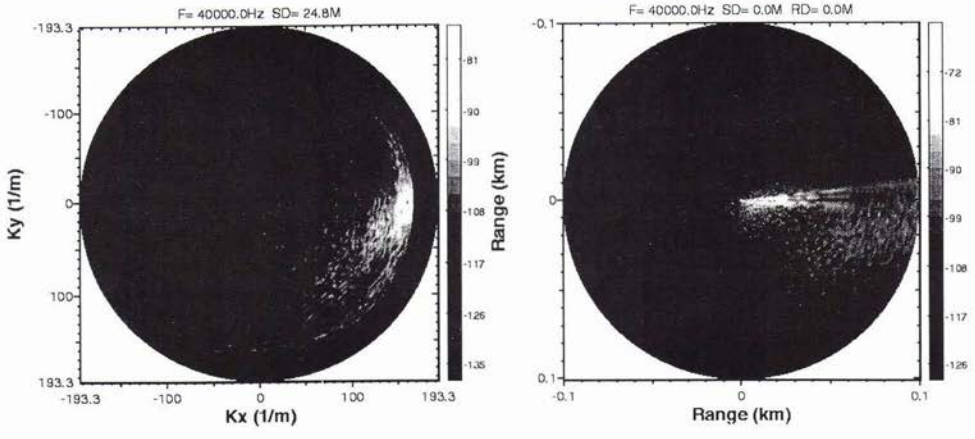

Figure 6: Multistatic reverberation from the roughness patch in Fig. 5. Left frame shows contours of the two-dimensional wavenumber spectrum of the scattered field 5.2 m above the seabed. The wavenumber of the incident field is $(k_x, k_y) = (168, 0)$ corresponding to incidence onto the patch from the left. The right frame shows contours of the scattered field in a horizontal plane at the same depth. Directions to the right represent forward scattering, while directions to the left represent backscattering.

contours of the two-dimensional wavenumber spectrum of the scattered field 5.2 m above the seabed. The wavenumber of the incident field is $(k_x, k_y) = (168, 0)$ corresponding to incidence onto the patch from the left. The right frame shows contours of the scattered field in the same horizontal plane, i.e. the same level as the projector. The square area shown is 200 × 200 m, centered over the sonar footprint. Directions to the right represent forward scattering, while directions to the left represent backscattering. In this 'broadside' configuration, even though the forward scattering is dominant, the backscattering is significant. On the other hand, the out-of-plane, i.e. ±90°, bistatic angles show very low reverberation levels.

Figure 5 shows the same sonar footprint, but with the main axes of the roughness anisotropy rotated counterclockwise by 45° . The roughness statistics is the same as in the previous case, i.e. the power spectrum corresponds to correlation lengths 1.04 m and 0.13 m, and RMS elevation of 4.7 mm.

Figure 6 shows the computed multistatic reverberation from the roughness patch in Fig. 5. The left frame shows contours of the two-dimensional wavenumber spectrum of the scattered field 5.2 m above the seabed. Again the wavenumber of the incident field is $(k_x, k_y) = (168, 0)$ corresponding to incidence onto the patch from the left. The shading controlled by the Bragg scattering condition illustrated in Fig. 2 is evident, with the dominant scattering being into wave vectors in the lower right quadrant. This translates to out-of-plane-scattering towards the right relative to the incident direction, as is also evident in the right frame in Fig. 6 showing contours of the scattered field in the same horizontal plane. The square area shown is 200 × 200 m, centered over the sonar footprint. Again,

directions to the right represent forward scattering, while directions to the left represent backscattering. In this configuration the forward scattering is still dominant, but the monostatic backscatter is reduced substantially, replaced by a significant out-of-plane component. Consistent with Fig. 2, the dominant scattering spans angles up to 90° from the forward direction, corresponding to bistatic angles up to twice the roughness skew angle (45°) from the direction of the incident field.

5. Conclusion

A numerically efficient formulation for wave theory modeling of the full multistatic, reverberant field in stratified waveguides has been developed. A previously developed perturbation approach to scattering from rough interface patches has been transformed into a cylindrical coordinate formulation and implemented in the three-dimensional version of OASES/SAFARI. The new modeling capability has been applied to investigate the high-frequency reverberation from anisotropic roughness in a shallow water environment with a stratified, elastic bottom.

Acknowledgements

This work was supported by the Office of Naval Research.

References

[1] W.A. Kuperman and H. Schmidt. Self-consistent perturbation approach to rough surface scattering in stratified elastic media. *J. Acoust. Soc. Am.*, 86:1511–1522, 1989.

[2] H. Schmidt and W.A. Kuperman. Spectral representations of rough interface reverberation in stratified ocean waveguides. *J. Acoust. Soc. Am.*, 97(4):2199–2209, 1995.

[3] H. Schmidt and J. Glattetre. A fast field model for three-dimensional wave propagation in stratified environments based on the global matrix method. *J. Acoust. Soc. Am.*, 78:2105–2114, 1985.

[4] K. LePage. *Elastic scattering in oceanic waveguides.* PhD thesis, Massachusetts Institute of Technology, June 1992.

[5] B. Tracey and H. Schmidt. Seismo-acoustic field statistics in shallow water. *IEEE Journal of Oceanic Engineering*, Submitted, 1996.

[6] F. Jensen, W.A. Kuperman, M.B. Porter, and H. Schmidt. *Computational Ocean Acoustics.* AIP Press, New York, 1994.

[7] H. Fan. *Wave theory modeling of three-dimensional seismo-acoustic reverberation in ocean waveguides.* PhD thesis, Massachusetts Institute of Technology, September 1995.

[8] D.J. Tang, G. Jin, D.R. Jackson, and K.L. Williams. Analyses of high-frequency bottom and subbottom backscattering for two distinct shallow water environments. *J. Acoust. Soc. Am.*, 96:2930–2936, 1994.

[9] J. Goff and T. Jordan. Stochastic modeling of seafloor morphology: Inversion of sea beam data for second order statistics. *J. Geophys. Res.*, 93:13589–13608, 1988.

Swath Bathymetry and SAS Autofocus using a Chirp Source

Geoffrey Shippey[1] and Olle Kröling[2]

[1]Dept of Applied Electronics
Chalmers University of Technology
S-412 96 Gothenburg, Sweden
Email: gsh@ae.chalmers.se

[2]SubVision AB
Bredgatan 18
S-222 21 Lund, Sweden
Email: subvisab@algonet

Abstract

Swath bathymetry and SAS autofocus can both be treated as problems in correlating echoes from a scatterer distribution on the seabed. Using a chirp source, the phase derived from quadrature match-filtering can replace the narrowband phase in complex correlation operations. Pulse compression then enables bathymetry to be estimated more easily and accurately than with the corresponding narrowband processing. Using similar processing, the SAS auto-focus method gives direct estimates of unknown cross-track platform displacement. Field experimental equipment for the Swedish project is briefly described.

1. Introduction

The research presented here has been carried out under the Swedish DAIM (Digital Acoustic IMaging) Project. Emphasis is on high-frequency wideband insonification to maximise resolution at short range. Earlier papers [1,2] described the application of quadrature match-filtering to sidescan imaging and synthetic-aperture processing. The present paper concentrates on the inverse problem of swath bathymetry. SAS autofocus will also be addressed rather briefly since the two problems are more closely related than may appear at first sight. Swath bathymetry can be regarded as a problem in correlating echoes from a random distribution of reflectors on the seabed received at apertures separated in elevation. For synthetic-aperture auto-focus, the apertures are separated in the along-track direction.

2. State-of-the-Art

2.1 Sonar Imaging

Consider a linear array of receiver transducers with a plane echo wavefront arriving at azimuth angle θ from a reflector in the far field (Fig 1). Time-delay beamforming aligns the echoes from reflectors at angle θ by compensating for differential time-delays between the arrival of the wavefront at each transducer in turn. Because of its essential simplicity, there have been many attempts to find a digital implementation of time-delay beamforming. Superficially this appears easy, because echoes can be aligned in store by sample shifting. Unfortunately angular resolution is coarse unless the sampling frequency is high compared with the acoustic frequency, and this has led to a number of interpolation schemes over the years, eg [3,4].

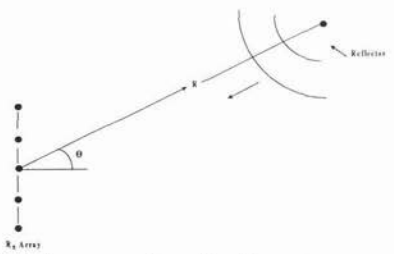

Fig 1. Sonar reception with a linear array

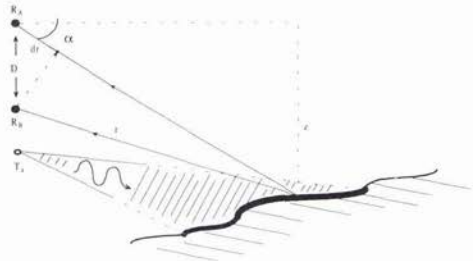

Fig 2. Bathymetric estimation : $z \approx r.dr / D$

2.2 Swath Bathymetry

Swath bathymetry is the operation of determining a depth map, or digital terrain model, from the elevation angle of echoes arriving from different slant ranges. For each output pulse or "ping", a profile of the seabed each side of the survey vessel can be computed, enabling the surface model to be built up as the sonar moves through the water. For shallow angles of incidence, an interferometric technique can be used [5]. Here elevation angle is inferred from the differential time-delay between the arrival of echoes at receivers spaced in elevation (Fig.2). This time difference is itself inferred from the differential phase of the echoes. [5] describes an elegant method in which analog echoes received at R_A and R_B are I and Q sampled to give complex echo sequences $\{a(n)\},\{b(n)\}$. The differential phase $\Delta\phi(r)$ in the neighbourhood of $n=r$ is given by the phase angle of the local ccf with zero displacement:

$$\gamma(r,r) = \sum_{k=-½L}^{L} w(l)\, a(r+k)\, b^*(r+k) \qquad (1)$$

where $w(l)$ is some taper function of length L, eg a Hanning window function. With narrowband echoes this local differential phase is still extremely noisy, even when L is large, so considerable smoothing is required. The consequent depth error depends on the baseline D. If this exceeds ½λ, the phase angle given by (1) is ambiguous. This ambiguity must be resolved by phase unwrapping, although problems can arise where there are step discontinuities in the scattering surface. To avoid such problems, "multibeam" systems such as the SIMRAD EM1000 [6] have been developed. Here a number of physical split-apertures are mounted around the hull of the survey vessel, and a large number of distinct elevation beams are constructed by a combination of aperture selection and beam-steering. Phase is now only used to determine the cross-over point of the beams from each split aperture.

2.3 "Auto-Focus" with Synthetic Aperture Sonar

Synthetic aperture sonar (SAS) is the acoustic analogue of SAR (synthetic-aperture-radar), routinely used to generate radar maps of the earth's surface. SAS would seem to be simpler to implement than SAR because of the lower frequencies involved. Unfortunately there are special problems with the water medium. Firstly the propagation time to the target and back varies from ping to ping unless the water is very calm. Movement of the sonar platform through the water is also subject to perturbation, leading to uncertainty in the relative positions of the sonar platform along the aperture. In side-looking mode, the lateral position of the sonar platform should be known within a fraction of the acoustic wavelength, ie to 1mm at cm acoustic wavelengths. Such accuracy is impossible to achieve by dead reckoning unless an expensive inertial platform is used, so reported experiments have been carried out at relatively low acoustic frequencies [7,8]. For airborne SAR, deviations of the platform track from a straight line have led to the development of auto-focus techniques where platform position is corrected from the image itself. The term "auto-focus" arises from methods where the platform track is perturbed until the best focus is obtained in the resulting SAR image [9]. For sonar, more direct methods have recently been proposed. Johnson, Hayes and Gough [10] describe a method of inferring lateral platform movement by cross-correlation of side-scan echoes. The final correlation operation uses a similar expression to (1).

3. Quadrature Match-filtering and Precise Range Estimation

3.1 Quadrature Phase and Time Delays

If the seabed echo is treated as the convolution of the source pulse with a random distribution of surface reflectors, many properties of an algorithm can be derived by considering the idealised echo from an isolated reflector. Consider range estimation using a chirp pulse such as $f(u)$, (Fig.3) with a symmetrical envelope function. Time zero at $u=0$ lies in the centre of the envelope. For digital processing, the received echo is sampled at regular time intervals τ_s. For match-filtering, the transmitted pulse is sampled to give $f_n = f(n\tau_s)$. The illustrated pulse has 129 samples, and a normalised frequency (with respect to sampling frequency) rising from 0.2 to 0.4 during the pulse length. Apart from a scale factor, the echo of $f(u)$ is $f(u\text{-}t)$ where t is the echo time. (pulse length = 2R+1 samples) for the required values of n. The analytic signal corresponding to the sampled pulse The sampled, delayed, echo $f(n\tau_s - t)$ will be denoted $f_n(t)$. Then the in-phase match-filtered echo is given by

$$p_n(t) = \sum_{|r|<R} f_r f_{n+r}(t) \qquad (2)$$

is given by

$$h_n = f_n + ig_n \qquad (3)$$

where $\{g_n\}$ is the Hilbert Transform of $\{f_n\}$. The quadrature match-filtered echo $z_n(t)$ is then expressed as

$$z_n(t) = p_n(t) + iq_n(t) = \sum_r h_r f_{n+r}(t) \tag{4}$$

The sequence of complex samples $\{z_n(t)\}$ has amplitude

$$e_n(t) = |z_n(t)| \tag{5}$$

and phase (which will be termed "quadrature phase"):

$$\phi_n(t) = arctan\text{-}((q_n(t)/p_n(t)). \tag{6}$$

Write t in the form $$t = N\tau_s + \tau, \quad |\tau| < \tfrac{1}{2}\tau_s \tag{7}$$

If t is an integral multiple of τ_s, e_n peaks at $n=N$ with $\phi_N = 0$. Otherwise e_n peaks at $n=N$ with non-zero phase. Appendix A shows that, subject to certain condition on the source signature, quadrature phase is the same linear function of t as analog phase for a carrier at the mid-frequency f_{mid}. The restrictions on the chirp pulse are

(i) carrier frequency should be a linear function of time (linear swept frequency chirp)

(ii) the pulse envelope should be symmetric about f_{mid}

(iii) this envelope should change slowly compared with the lowest chirp frequency present in the pulse.

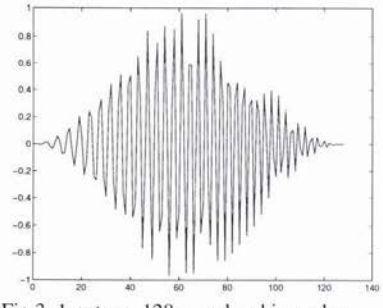

Fig 3. 1-octave, 128 sample, chirp pulse 0.2-0.4 normalised frequency

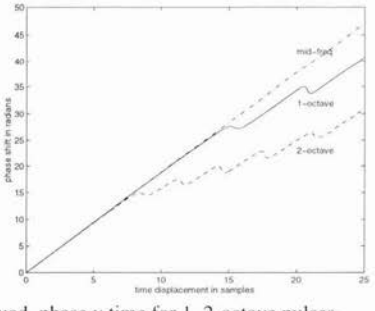

Fig 4. Quad. phase v time for 1, 2-octave pulses, analog phase for mid-frequency signal

Fig. 4 shows quadrature phase versus time displacement τ for a 1-octave and 2-octave chirp pulse. Phase-unwrapping is used to extend the phase-shift beyond $\pm\pi$. $\psi(x) = 2\pi f\tau$ is plotted for comparison, where f is the mid-frequency of the chirp pulses. The linear approximation remains good until the compressed envelope becomes small.

3.2 Polar Beamsteering

This digression on imaging will be helpful later on. Suppose we have a linear array of receiver elements R_k. It is required to point the receiver beam in a direction α with respect to the array normal. Then using the far-field approximation, time-delay beamsteering requires echoes from receiver transducer R_k at distance d_k from the array centre to be delayed with respect to echoes from the centre element by

$$t_k = (d_k/V)\ sin\ \alpha \tag{8}$$

For simplicity, the time delay t_k could be approximated by the nearest integer number of samples, m_k, and the k'th echo shifted by m_k samples in store. The receiver beam is then generated by taking the weighted sum over all transducers to generate the receiver beam. What is the angular resolution obtainable in this way? If $\frac{1}{2}\lambda$ spacing is used, the required time delay between adjacent echoes is given by

$$\Delta t \approx \alpha/2f \tag{9}$$

At a sampling frequency of f_s, the smallest time delay increment is $1/f_s$, so angular resolution is of order f/f_s. Beamsteering to 1° requires a minimum sampling frequency of $60\ f_{mid}$ unless some form of interpolation is used. By far the simplest interpolation method is to reverse the usual order of beamforming and rectification, and begin by quadrature match

filtering all transducer echoes. Each required time delay t_k is broken down into an integer number of sample intervals τ_s and a residue:

$$t_k = m_k \tau_s + \tau_k , \quad |\tau_k| < \tfrac{1}{2} \tau_s \tag{10}$$

All the match-filtered samples from R_k are now shifted by m_k samples and phase-shifted by $\theta_k = 2\pi f_{mid} \tau_k$. The weighted sum of such shifted sequences over all the transducers gives a quadrature match-filtered receiver beam pointing in the direction α, and with the same sample spacing as the original transducer echoes.

3.3 Differential Range Estimation for Bathymetry using a Chirp Source.

Using a chirp source it is not possible to use expression (1) directly, since there is no longer a unique phase obtainable from I,Q filtering. One solution is to correlate the in-phase match filtered sampled echoes [12], but angular resolution is poor unless the sampling frequency is much higher than the acoustic frequencies. Instead it is to better to correlate the quadrature match-filtered echoes, which are complex valued so can be inserted directly into (1). After pulse compression, $|(m,n)|$ now has a well-defined peak for each m at $n = peak(m)$. Then

$$tdiff_m = [m - peak(m)]t_s \tag{11}$$

gives the best estimate of time displacement between echoes to the nearest integer number of sample intervals. The subsample time displacement is obtained from the phase, ϕ_m ,of

$$\gamma(m, peak(m)) = \sum_{k=-\frac{1}{2}L}^{\frac{1}{2}L} w(l)\, a(m+k)\, b^*(peak(m)+k) \tag{12}$$

The total time displacement is then given by

$$\Delta t = tdiff_m + \phi_m / 2\pi f_{mid} \tag{13}$$

For swath bathymetry, time difference is converted to differential range, and thence to elevation angle in the usual way. Since pulse compression enables a well-defined peak to be found in the ccf, there is no need to limit D to $\frac{1}{2}\lambda$ to avoid phase ambiguity. Much longer baselines can be used for elevation angle conversion.

4. Bathymetry Simulation

4.1 Simulation Model

The seabed was be modelled as a random distribution of surface scatterers. This is a plausible model for bathymetry at higher acoustic frequencies. Most properties of the bathymetric algorithm can be investigated using a simple one-dimensional model. The seabed profile was modelled as a random distribution of N scatterers/m with random reflectivity. N was varied from 100 up to 10000 reflectors/m. The scatterer distribution was also distributed randomly across the mean line of the slope in order to represent surface roughness. This distribution also accounts for the finite azimuth beamwidth, since variation between different profiles within the beamwidth contribute to the width of the vertical distribution. Two simple geometrical profiles were tested – HILL and STEPS (Figs.5a, b) – at horizontal ranges of 50 m. Sonar shadow was not modelled, so the back slope of HILL is not occluded by the front slope. Tests with STEPS established that the algorithm could cope with rapid changes in depth.

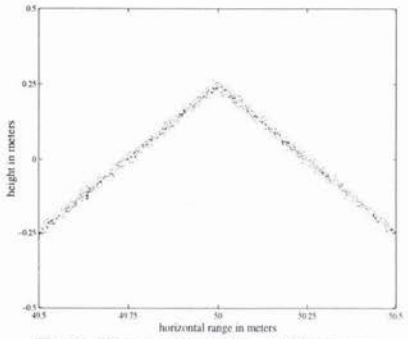

Fig 5a. Test profile HILL at 50 m range
500 reflectors/m, 1 cm lateral noise

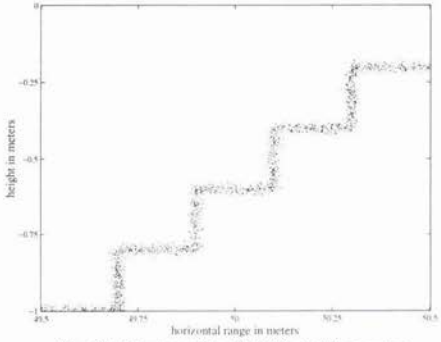

Fig 5b. Test profile STEPS at 50 m range
500 reflectors/m, 1 cm lateral noise

The acoustic mid-frequency was set at 150 kHz, giving a mid-wavelength λ_{mid} = 1 cm at a sound speed of 1500 m/sec. Sampling frequency was 500 kHz, giving a normalised mid-frequency f_{mid} = 0.3. With these parameters the 1-way differential distance corresponding to 1 sample interval is 3 mm. The 1 ms chirp pulse consisted of 512 samples with a Hanning envelope and a selectable bandwidth f_b. The value f_b=0.2 gives a 1 octave chirp pulse between 100 kHz and 200 kHz. Range resolution = $V/2f_b$ = 7.5 mm or 5 samples at the 100 kHz bandwidth. The vertical separation of the two receiver transducers was varied between $0.1\lambda_{mid}$ and 500 λ_{mid} , ie 1mm and 5m, with the transmitter located midway between them. White Gaussian noise could be added to the echoes. The length L of the correlation window was varied between 3 and 257, the latter corresponding to spatial smoothing of nominally 257 x 1.5 mm = 38 cm.

4.2 Simulation Results

Preliminary simulation runs were carried out in order to establish the qualitative effects of different parameters. Figs.6a,b show bathymetric estimates of HILL with N = 500 reflectors/m and 1 cm rms vertical noise. The processing parameters were 30 dB signal/noise ratio, 20 cm receiver separation, and a 17 sample window. These results demonstrate degraded profile tracking at lower bandwidths (strictly it is the absolute bandwidth which matters). Fig.7 shows a bathymetric estimate of STEPS with the same parameters, and a normalised bandwidth of 0.3.

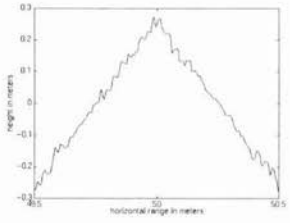

Fig 6a. Estimation of HILL,
normalised bandwidth = 0.4

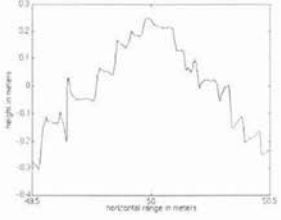

Fig 6b. Estimation of HILL,
normalised bandwidth = 0.05

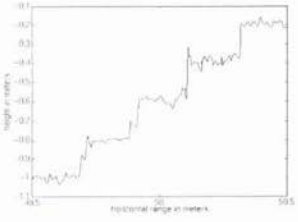

Fig 7. Estimation of STEPS,
normalised bandwidth = 0.3

Bathymetric accuracy was estimated by carrying out sets of 10 bathymetric runs, with different random reflector distributions and additive noise in each run. The error measure was the rms vertical difference in cms. between the bathymetric estimate and the profile centreline. Most results simply confirmed intuitive expectations, for example that performance deteriorates when a low reflector density, N, is combined with high profile noise, particularly if the window length is very short.. Rms errors of a few cms were obtained under most conditions, fairly independent of N.

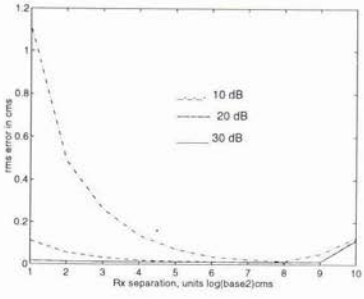

Fig 8a. Rms error versus receiver separation for SNR = 10, 20, 30 dB and bw = 0.3

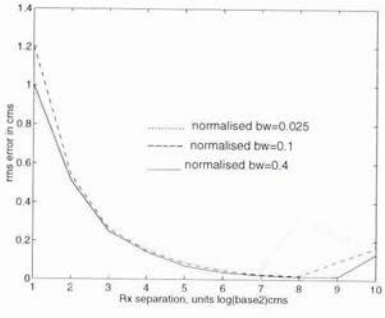

Fig 8b. Rms error versus receiver separation for bw = 0.025, 0.1, 0.4 and SNR = 10 dB

The more interesting results concern parameters which are under the system designer's control - correlation length, transducer separation, bandwidth. One question of particular interest concerns the choice of receiver separation. Fig.8a shows the effect of increasing receiver separation from 1 cm to 512 cm ($1\lambda_{mid}$ to 512 λ_{mid}) in the presence of noise. Around 50 cm separation gives best performance. When signal/noise ratio is high, the increase in receiver separation has a negligible effect on accuracy, implying no significant error other than that due to spatial resolution. For lower signal/noise ratios, accuracy improves with transducer separation, kappa, up to a certain limit. Fig.8b shows the effect of varying both separation and bandwidth, while keeping SNR fixed at 10 dB. This confirms that the useful region of kappa increases with bandwidth. For very large separations, accuracy falls off again due to misalignment between correlation windows for the upper and lower receiver apertures (Fig 9). When these are too far apart, the sample intervals resolved along the slope differ significantly in length, so samples can never be aligned along the whole length of the window.

4.3 Bathymetry Combined with Beam Steering

The proposed method of bathymetric processing can readily be combined with polar beamsteering (Fig.10). The simplest configuration is one where the transmitter beam provides the required azimuth resolution, while a split aperture with long axis in elevation is used for reception. Polar beamsteering is used to generate "multibeams" spanning the elevation angles of interest. The quadrature match-filtered sampled echo for each aperture generated by the polar beamsteering algorithm can be substituted directly into the bathymetric computation.

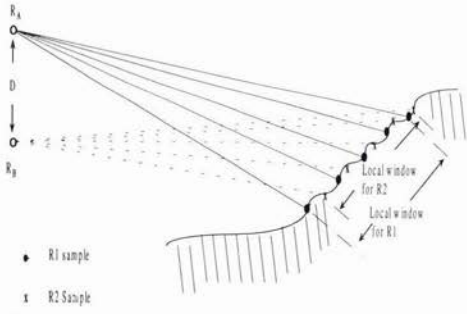

Fig 9. Misalignment of correlation windows

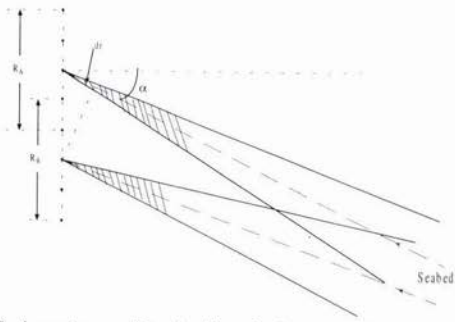

Fig 10. Bathymetry combined with polar beamsteering

5. Synthetic Aperture Auto-Focus

Fig 11. Compare echo from leading Rx, trailing array with trailing Rx, leading array

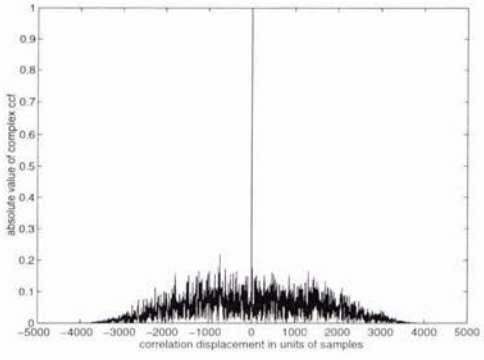

Fig 12. Echo ccf, 15 dB signal/noise ratio 500 random reflectors/m^2

5.1 Methodology

Johnson, Hayes and Gough [10] proposed the estimation of lateral platform movement by cross-correlation of sampled side-scan echoes. The author has investigated a similar method with the differences that quadrature match-filtered echoes are correlated, and that displacement is estimated both from the ccf peak position and the quadrature phase at the peak. Simulation studies show that lateral platform displacement can be estimated with high accuracy for small along-track displacements of the platform. However correlation fails completely when the along-track movement between pings approaches half the length of the receiver array – precisely the movement required for SAS processing [13]. A simple heuristic argument explains this phenomenon. Consider the point-spread functions for a particular echo sample in adjacent platform positions. For synthetic-aperture operation, the point spread function for the combined aperture, with platform positions half the receiver array length apart, is half the area of the separate psf's. Now suppose that the random reflectors in this combined footprint make a contribution to the echo of $\{z_i\}$. Then contributions for the individual footprints must be of the form $\{z_i\} \pm \{z_j\}$, where $\{z_j\}$ represents the contribution from random reflectors which are not in the combined footprint. The expected correlation between corresponding samples from adjacent positions is given by

$$\gamma = E\left[\sum_i \sum_j (z_i + z_j)(z_i^* - z_j^*)\right] = E\left[\sum_i \sum_j (z_i z_i^* + z_j z_i^* - z_i z_j^* - z_j z_j^*)\right] \qquad (14)$$

The expected contribution from the middle terms is zero, because of the random phases of the z_i and the z_j. The expected contribution from $z_j z_j^*$ cancels the contribution from $z_i z_i^*$, since the areas containing the two sets of reflectors are equal. Hence the expectation of γ reduces to zero as platform separation approaches half the length of the receiver array, and cross-correlation provides no information. Because of this problem, the alternative geometry of Fig.11 is proposed in order to align the point-spread functions for adjacent platform positions. The transmitter is located in the centre of the receiver array, and only the receivers at each end of the array are used for auto-focus. The platform moves precisely half this receiver array length between pings (pulses). For cross-correlation, the point-spread functions are aligned by comparing echo received by the leading transducer from the trailing array position with the echo received by the trailing transducer in the leading array position.

5.2 Simulation Studies

Simulation studies have been carried out with similar pulse parameters to Section 5, and a receiver array length of 1 m. The scatterers were distributed randomly over a 10 m x 10 m region. For simulation runs with 500 points/m^2 and 10 dB signal/noise ratio, the average error in estimating platform displacement was 60 μ. A typical ccf is shown in Fig.12. Correlation failed when SNR was reduced to 0 dB, though it succeeded again for sparser scatterer distributions. Using the

above method, it would be possible to align all platform positions in the synthetic aperture by successively aligning adjacent platform positions. However this is almost certainly not the optimum method of aligning a sequence of platform positions, since information available from other transducers on the platform is ignored. This optimization is planned as a main area for investigation, possibly as suggested in [11]. The sensitivity of correlation to scatterer density in the presence of noise is a matter for concern. The maximum density of 500 points/m^2 used in the simulation runs is not particularly high for sediment, since it corresponds to a scatterer spacing of several centimetres. On the other hand, a uniform random scatterer distribution is not representative of higher frequency sonar data, where some feature can usually be detected by eye, so there should be more information in real sonar echoes.

6. Experiments and Experimental Equipment

An experimental 32-channel sonar recorder has been designed by the Dept. of Technical Geology at Lund Technical University, in collaboration with SubVision AB who constructed the equipment. The recorder is designed for operation over a very wide bandwidth, 50-500 kHz, with sampling rates up to 2 MHz for each channel. Each channel includes a DSP chip to control sampling and other channel operations, as well as an individual hard disc. In future this DSP chip could be used for quadrature match filtering of all input echoes, required for both imaging and bathymetry. The large number of parallel channels allows a reasonably long array length for physical aperture imaging. It is also valuable for SAS processing, since the movement of the receiver array between pings is set by the length of the receiver aperture [1]. The technical objective is to combine good quality physical aperture images obtained at medium frequency into SAS images. This requires auto-focus techniques which perform well at centimetre wavelengths. The 32-channels can be split into separate apertures for bathymetry. Tank experiments have now begun, and the first experimental images obtained. The next stage is to move out to Malmö harbour for bathymetric and auto-focus experiments using real sea-bed. It is then planned to carry out lake experiments from a moving vessel in conjunction with Bofors Underwater Systems.

7. Conclusions

The paper has presented theoretical and simulation studies which imply radically superior performance for bathymetric sonar using a chirp source. If these studies are validated by field experiment, it could provoke a revival of interest in the simpler interferometric geometries, and further increase interest in chirp sonar developments. Interesting simulation results have also been obtained for SAS auto-focus, although here there is much theoretical work still to be done. However a powerful tool should be available for estimating cross-track positioning errors over "featureless" terrain. It is urgent to obtain experimental support for these claims, but also to obtain a more realistic seabed simulation model suitable for echo correlation investigations

8. Acknowledgments

The research presented was carried out with the support of the Swedish State Research Board, NUTEK, under the Autonomous Robotic Systems Programme. Technical support and advice from other partners in the Project – Peter Ulriksen at Lund Technical University, Klas Themner at Bofors Underwater Systems - is gratefully acknowledged.

9. References

[1] G.A. Shippey and T. Nordqvist, "Phase-array acoustic imaging in ground coordinates, with extension to synthetic aperture processing", *IEE Proc. Radar, Sonar, and Navigation*, vol. 143, pp. 131-139, June 1996.

[2] G.A. Shippey, "Simple Algorithms for sonar imaging and swath bathymetry using a linear-swept-frequency (chirp) source", *Proc. Int Conf. on Imaging and Image Interpretation*, Santa Barbara, Dec. 1996 (in press)

[3] R.G. Pridham and R.A. Mucci, "Digital interpolation beamforming for low-pass and band-pass signals", *Proc. IEEE*, vol. 67, pp 904-919, 1979.

[4] S. Ries, "Digital time-delay beamforming with interpolated signals", *Proc. European Conf. on Underwater Acoustics* (ECUA Luxembourg 1992), ed. M.Weydert , Elsevier, ECUA (Luxembourg) , pp.594-689

[5] M.A. Masnadi-Shirazi, C. de Moustier, P. Cervenka and S.H. Zisk: "Differential phase estimation with the SEAMARC II bathymetric sidescan sonar system", *IEEE J.Oceanic Eng.*, vol. 16, pp 239-250, July 1992.

[6] E. Hammerstad and F. Pohner, "Ultra wide swath deep sea interferometric multibeam echo sounder with sea bottom imaging system", *Proc.IEEE Oceans 90 Conf.* ,Washington, pp.63-68, 1990
[7] D.W. Hawkins and P.T. Gough, "Recent sea trials of a synthetic aperture sonar", *Proc. Inst. Acoustics* , vol. 17, Pt 8, pp. 1-10, 1995.
[8] M.A. Lawlor, V.S. Rayait, A.E. Adams, O.R. Hinton, and B.S. Sharif, "Results from sea-trals of a real-time synthetic processing system", *Proc. 3rd European Conference on Underwater Acoustics*, Ed J.S.Papadakis, Pub. FORTH-IACM, Heraklion, Crete, pp. 889-894, June 1996.
[9] D. Blacknell and S. Quegan, "SAR motion compensation using auto-focus", *Int. J. Remote Sensing*, vol. 12, no. 2, pp. 253-275, 1991.
[10] K.A. Johnson, M.P. Hayes, and P.T. Gough, "A method of estimating the sub-wavelength sway of a sonar towfish", *IEEE J. Oceanic Eng.*, vol. 20, no. 4, pp. 258-267, 1995.
[11] J. Chatillon and M.E. Zakharia, "Self-focusing of a synthetic aperture sonar in the case of bottom reverberation", *Proc. 3rd European Conference on Underwater Acoustic*, Ed J.S.Papadakis, Pub. FORTH-IACM, Heraklion, Crete, pp. 433-438, June 1996.
[12] J. Chatillon and M.E. Zakharia, "Validation of bathymetry algorithms using wideband synthetic aperture techniques by means of tank experiments", *Proc. 3rd European Conference on Underwater Acoustics*, Ed J.S.Papadakis, Pub. FORTH-IACM, Heraklion, Crete, pp. 427-43, June 1996.
[13] K.D. Rolt and H. Schmidt, "Azimuthal ambiguities in synthetic aperture sonar and synthetic aperture radar imagery", *IEEE J. Oceanic Eng.*, vol. OE-17, pp 73-79, Jan.1992.

10. Appendix A: Instantaneous Phase Measurement by Quadrature Match Filtering

Consider the chirp source signal $p(t) = A(t) \cos(ft + gt^2)$ (A1)

where A(t) is a symmetrical envelope function centred on t=0. If $A(t)$ varies slowly in comparison with the lowest period of the chirp, then the Hilbert Transform of $p(t)$,

$$q(t) \quad A(t) \sin(ft + gt^2) \tag{A2}$$

The in-phase match filtered signal is given by

$$P(\tau) = \int A(t-\tfrac{1}{2}\tau)A(t+\tfrac{1}{2}\tau) \cos[f(t-\tfrac{1}{2}\tau)+g(t-\tfrac{1}{2}\tau)^2] \cos[f(t+\tfrac{1}{2}\tau)+g(t+\tfrac{1}{2}\tau)^2]dt \tag{A3}$$

using symmetrical displacements for convenience. Then by standard trigonometry,

$$P(\tau) = P_1(\tau)+ P_2(\tau) (\tau) = \tfrac{1}{2} \int A(t-\tfrac{1}{2}\tau)A(t+\tfrac{1}{2}\tau) \cos(f\tau +2gt\tau)dt \tag{A4}$$

where $P_2(t) = \tfrac{1}{2} \int A(t-\tfrac{1}{2}\tau)A(t+\tfrac{1}{2}\tau) \cos[2ft+g(2t^2 +\tfrac{1}{2}\tau^2)]dt$ (A5)

Now $P_1(\tau) = \cos(f\tau) \int A(t-\tfrac{1}{2}\tau)A(t+\tfrac{1}{2}\tau) \cos(2gt\tau)dt$ (A6)

plus the integral of a sin term which vanishes because of the symmetry of $A(t-\tfrac{1}{2}\tau)A(t+\tfrac{1}{2}\tau)$ about zero. $P_2(\tau)$ is small because of the high frequency of the modulation under the integral sign, provided $A(t)$ varies slowly as stipulated. Hence

$$P(\tau) \approx \cos(f\tau) \int A(t-\tfrac{1}{2}\tau)A(t+\tfrac{1}{2}\tau) \cos(2gt\tau)dt \tag{A7}$$

Similarly the quadrature match-filtered signal

$$Q(\tau) \approx - \sin(f\tau) \int A(t-\tfrac{1}{2}\tau)A(t+\tfrac{1}{2}\tau) \cos(2gt\tau)dt \tag{A8}$$

Consider the complex quadrature match-filtered signal $X(\tau) = P(\tau) + iQ(\tau)$. The envelope

$$E(\tau) = |X(\tau)| \approx \int A(t-\tfrac{1}{2}\tau)A(t+\tfrac{1}{2}\tau) \cos(2gt\tau)dt \tag{A9}$$

is a function of bandwidth, while the phase, $f\tau$, is a function only of the mid-frequency f.

Results from the use of broad-band, sub-bottom seismic data with statistically based sediment classification techniques.

Peter G. Simpkin

INRS-Océanologie
310, Allées des Ursulines
Rimouski, Québec,
Canada, G5L 3A1
E. Mail: Peter_Simpkin@uqar.uquebec.ca

William T. Collins

Quester Tangent Corporation
9865,West Saanich Road
Sidney, British Columbia ,
Canada, V8L 5Y8
E-Mail: bill@questercorp.com

Abstract

The QTC VIEW sediment classification system has been applied to shallow, high resolution seismic data recorded with the IKB-SEISTEC™ profiler from the navigable channel of the St. Lawrence estuary in Canada. A number of 10 minute sections of seismic data in water depths from 10-15 m were selected from profiles covering a the wide variety of bottom sediment types found in the channel. These data sets were used in n unsupervized classification scheme to differentiate the various sediments and seafloor morphologies. Five distinct classes (of sediments) were identified ranging from fine silt/clay to medium sand. However, it was found that shallow gas, in various forms has a controlling influence in some areas.

On a appliqué la methode QTC VIEW de classification des sédiments à des données sismiques de haute résolution recueillies avec un profileur IKB-SEISTEC dans le chenal navigable de l'estuaire du Saint Laurent (Canada). Parmi la grande variété de types de sediments qu'on trouve dans le chenal, on a choisi des sections de 10 minutes provenant de profondeurs situées entre 10 et 15 metres. On a utilisé ces données dans un plan declassification dirigé pour identifier les différents sédiments et les différentes morphologies du fond. On a identifié cinq classes de sediments, allant de vase/argile fine à sable moyen. Toutefois on a trouvé que des gas de différentes formes dans les sediments peu profonds ont une influence déterminante à certains endroits.

1. Introduction

Marine surveyors have been using echo sounders to classify the seabed for many years. Normally the echogram displays the time of arrival of the echo from the seafloor and presents depth as a mark placed on scaled paper. Inferences on the nature of the seabed can be made by observing the intensity of the seabed return as well as the changes in arrival time. This qualitative evaluation is possible because more information is present in the returning signal than that solely utilized by the echo sounder to indicate water depth. The echo received from the seafloor by an echo sounder is a measure of the acoustic properties combined with the acoustic backscatter characteristics of the sediment. Acoustic backscatter is controlled, in part, by the roughness of the seabed. If the surface of the seafloor is rough, then reflected energy will be return to the sounder transducer from wide angles. Since the distance travelled by off-axis energy is longer than the normal case, the received echo from a rough surface is longer in duration than for echoes reflected from a smooth surface. By

applying signal processing techniques to sea floor echoes, accurate and repeatable acoustic classification of the seabed can be accomplished.

In the early 1970's, certain attributes such as echo amplitude and energy content were extracted from the bottom echo to provide real-time indications of acoustic reflectivity. In the 1980's, dedicated seabed classification was introduced which processed the seafloor echo envelope thereby generating values representing the acoustic response from specific seabed types.

The present generation of committed instruments uses high speed digital signal processors to extract many dominant features from the echo envelope in real-time providing greater accuracy and reliability in the discrimination of seabed types. One such commercially available instrument is the QTC VIEW which has recently been introduced for digital seafloor classification [1],[2].

In parallel with these improvements in processing sonar data, there has been advances in the techniques for sub-bottom profiling in shallow water. In 1987 a novel bi-static, broadband, seismic system was tested in the Mackenzie Delta area of the Canadian arctic where water depths less that 10 metres predominate [3]. Subsequent development of this technique lead to the introduction of the IKB SEISTEC™ in 1992 which has enabled high resolution profiling to be extended into water as shallow as 2 metres [4],[5]. In 1995, such a seismic system was used in a pre-dredging survey in the navigable channel, of the St. Lawrence between Montréal and Québec City in Canada. The raw seismic data was recorded in digital format on a DAT recorder so that various types of post-processing could be undertaken. The fact that good weather prevailed for the duration of this survey meant that the quality of the recorded data was very high and therefore ideal for further analysis.

With the recent introduction of the QTC VIEW classification system, an opportunity existed to replay the seismic data from the St. Lawrence through this advanced system to evaluate its performance with broad-band seismic rather than higher frequency sonar echoes for which it was originally designed. In a recent experiment, the seismic data was replayed to simulate, as accurately as possible, actual survey conditions. The recovered analog seismic signal was applied to the normal input terminals of the QTC VIEW system and processed in data collection mode also in real time. The results of the application of the normal sonar seafloor classification routines to this seismic data set are discussed briefly in this paper. Initial results indicate that river floor sediments can be classified in real time by their seismic response using this technique.

2. Equipment

2.1 The high resolution profiling system

The sound source used in the IKB SEISTEC™ high resolution profiler is an electrodynamic "Boomer" with produces a single positive pressure pulse with a peak amplitude of 216 dB//1μPa@1m and a pulse duration ranging from 100 - 140 μs (Figure 1). Spectral analysis of the far field pulse reveals that useful energy is available from this source from 1 kHz - 12 kHz. Although Boomers have been used in geophysical surveying for many years, shallow water performance was limited by the traditional "eel" receiving array since target echoes and signals often coincided. The receiver used in this system comprises a short 25 cm line hydrophone mounted axially in a fixed reflecting cone with a 62 cm circular aperture. This *line-in-cone* receiver is supported in a surface towed catamaran along with the Boomer source. The advantage of this configuration over traditional methods for shallow water surveying is that the geometry of the source and receiver is fixed and the combined acoustic response of the source and receiver is consistant over a wide range of operational conditions.

The directional characteristics of the Boomer coupled with a near matching response of the receiver means that very consistent echoes can be received in target water depths ranging from 1 to 200 m. Figure 2 is an example of an echo response obtained from a relatively flat area of the seafloor in shallow water. The system impulse response consists of a small amplitude precursor (+ve pressure), followed by a negative excursion, a single positive and a second negative excursion. This characteristic shape is useful for determining the phase characteristics of reflecting horizons. The overall bandwidth of the system allows for a vertical resolution between reflecting layers of 25 cm; a feature has that has recently been exploited in discriminating shallow faults in San Francisco Bay [6].

The normal arrangement for data recording is shown in Figure 3. The signal from the *line-in-cone* receiver is amplified before transmission to the surface where it is made available for recording and analog processing prior to imaging on a grey scale recorder or direct digital recording. On playback, either the raw or processed analog signal together with a synchronizing pulse corresponding to "time zero", the Boomer firing instant, are recovered from the DAT recorder and made available for further conditioning, processing and analysis. In this experiment, the unprocessed (Raw) signal was recovered from the DAT and applied to the QTC VIEW input terminals without any additional analog signal conditioning. A synchronizing pulse was also recovered from the DAT recorder to simulate the transmitter excitation pulse.

2.2 The QTC VIEW

The QTC VIEW is a seabed classification system designed for use with echo sounders with operating frequencies up to 220 kHz. The system consists of hardware package whose input is normally connected directly to the sounder transducer terminals. An accompanying software package running on a Personal Computer analyzes, displays and stores the acoustic

parameters. In operation, the system automatically tracks the bottom echo, digitizes the echo and analyzes the resulting waveforms using multiple trace statistics and multivariate analysis.

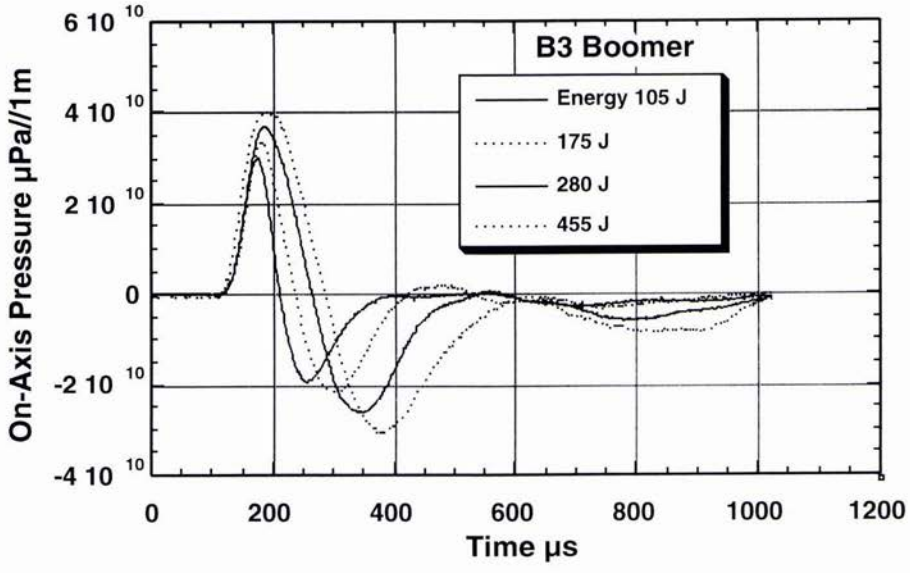

Figure 1. Output pressure signatures from B3 Boomer at different energy levels

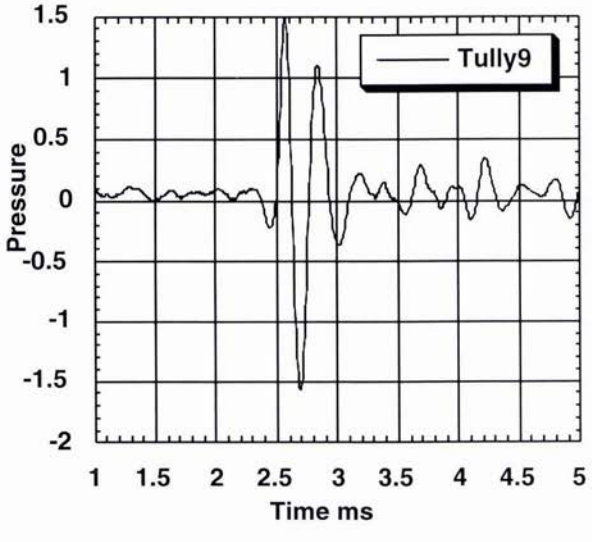

Figure 2. Typical seafloor echo from smooth surface (Inverted - positive pressure down)

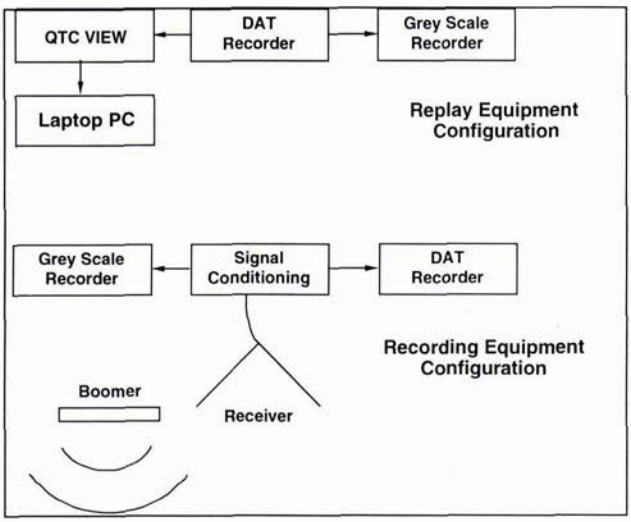

Figure 3. Schematic of recording and replay equipment configurations.

A sonar pulse impinging on a seabed is reflected and scattered at the seabed/water interface and the immediate sub-surface structure. The returned echo pulse contains components of the transmitted pulse (direct reflection) with the off-axis backscatter and volume reverberation superimposed. The shape of the returning signal is therefore influenced by the seabed roughness, the impedance contrast between the water and sediment and the volume reverberation of sound in the upper sediment layers. Thus, the combined response contains contributions from the physical properties of the water and seafloor material, the geometry of the sediment surface and the internal structure of the sediment all of which change considerable even over short distances in any dynamic environment. The bottom response, therefore, is highly variable and complex suggesting that a statistical analysis, applied to extracted parameters from multiple echoes, may be an appropriate method for differentiating and ultimately classifying sediments.

The seabed classification technique is comprised of the following processes: First a number of waveform shape descriptors are generated from each bottom echo. These are then reduced in number using a statistical analysis to determine those parameters which most usefully describe the echoes. These parameters are then used to classify logical groups of similar echoes into a dynamic, real time, 3 dimensional (colour) display.

The system can be applied in a supervised or unsupervised manner. Using a supervised classification technique, a series of sample echoes are collected from known seabed types. The information is compiled into a catalogue and used during subsequent real-time sea floor mapping. The system analyzes incoming echoes, chooses an acoustic class from the catalogue which most closely resembles the new echo, and provides an estimate of the confidence in the choice of class. It is the responsibility of the operator to relate the acoustic class to the physical nature of the seabed. An unsupervised approach utilizes a suite of tools which have been developed to analyze individual echo traces, extract the most useful information and logically group the total number of traces into a set of acoustic classes. The classification scheme is applied to the echoes with their associated geographic reference to classify sea floor sediments.

3. Geological Setting

The Gulf of St. Lawrence is the main drainage system for eastern Canada and the Great Lakes and an important shipping route for ocean going vessels. Between Montréal and Québec city, normal river flow conditions exist with the river flowing in a north-east direction. Although the river can be up to 5 km wide in places (Lac Saint-Pierre), for most of this region its width is normally less than 2 km. However, a relatively narrow navigable channel with a minimum depth of 12 m is maintained by dredging.

The 1995 seismic survey commenced at the port of Montréal where the river bed is composed mainly of glacial material or rock outcrop covered by a thin, mobile layer of silts and fine sand. From an acoustic viewpoint, the riverbed is "hard" and penetration using high resolution seismic profilers is limited to the surface mobile layer. However, further east the river sediments increase in thickness and are finer in composition. As one approaches Lac Saint-Pierre 80 km, north east of Montréal, the sediments are finer still with interbedded clays and silts being common. At the eastern part of Lac Saint-Pierre, less internal structure is seen in the upper sediment column indicating that fine to medium sands are present.

4. Data Reduction Methodology - Unsupervised Classification

The seismic data set replayed through the QTC VIEW consisted of 17 ten minute profiles selected from the original survey records. Each 10 minute section of data represents about 2.5 nautical miles and is composed from approximately 2000 individual echoes. The data were analyzed using unsupervised classification. Echo shape descriptors were generated from the entire data set. Each data record was reduced to three values representing the first three principal components of variance from the total data set.. All data were plotted and five distinctive acoustic classes associated with individual line sections were identified (Fig. 4).

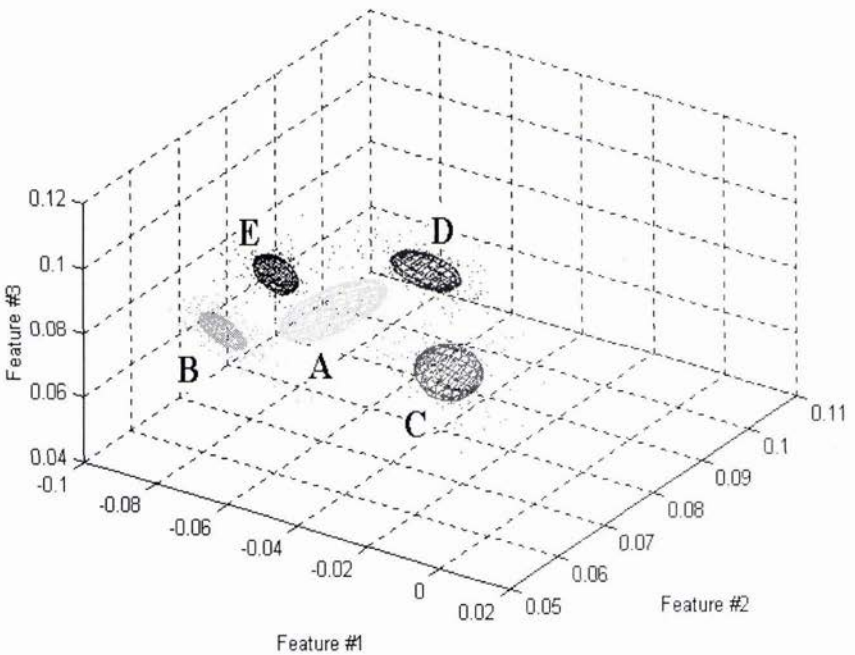

Figure 4. Plot of the three principal components from each data record. Clusters of points represent the five acoustic classes. Each ellipse is centered on the mean of each cluster and the wire mesh surface represents 1 standard deviation.

The original, unprocessed, hardcopy from the five profiles identified above were analyzed (Fig. 5). Five broad seismic facies were interpreted (Table 1). These data were compiled into a catalogue and used as the reference by which classify the seventeen original profiles of which two are discussed below.

Class	Description
A	Acoustically hard surface with much reverberant energy.
B	Rough surface topography - distributed gas curtain
C	Moderately rough surface with horizontal structure visibly all the way to surface
D	Very consistent section of softer sediments
E	Soft sediment with rippled surface

Table 1. Classification scheme used to describe the seismic data set.

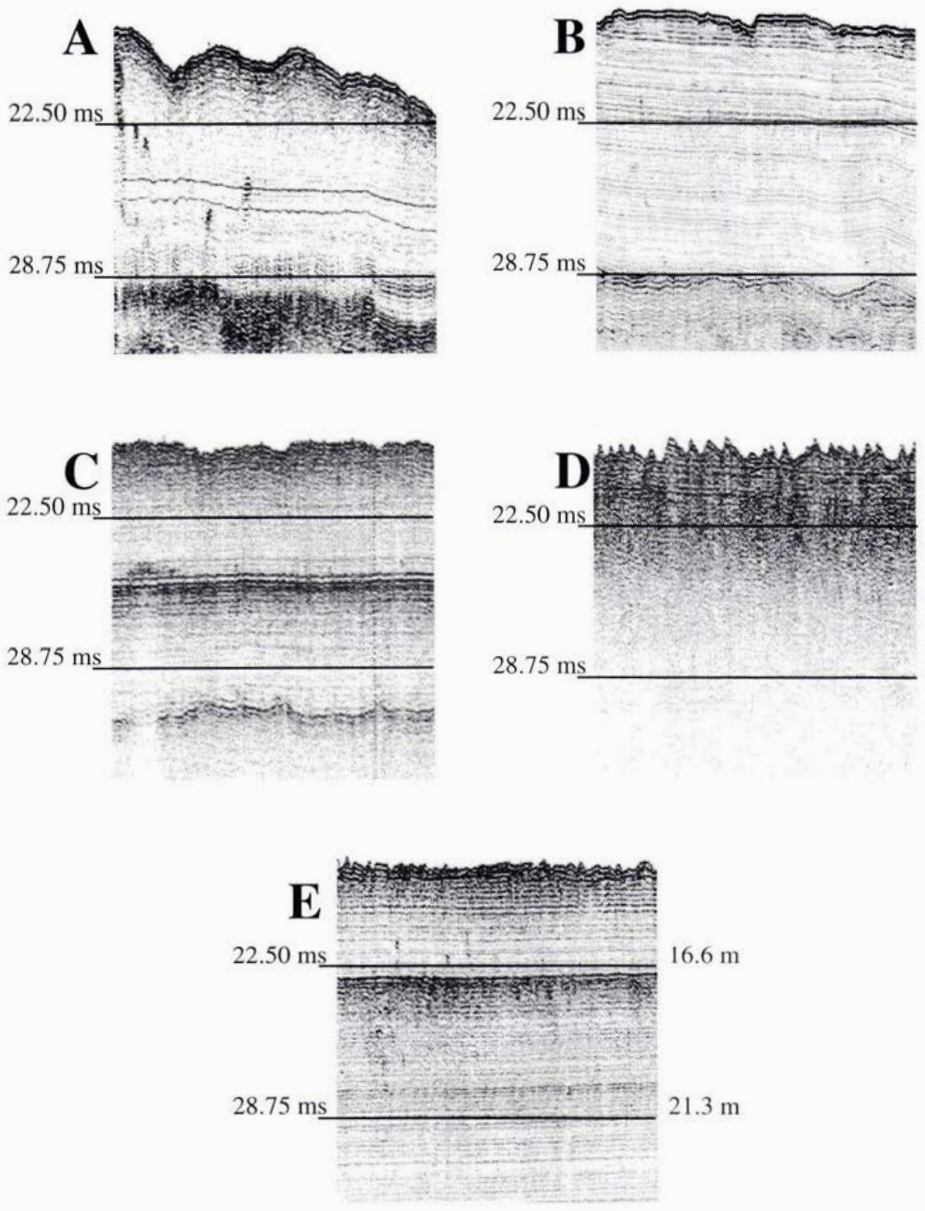

Figure 5. Seismic profiles from the five reference sections. The left hand scale is two-way travel time from the sea surface in milliseconds. The right scale on section E is distance in meters calculated with a sound speed of 1460 m.sec-1. Note the gas enhanced reflectors at 18.5 m in Panel C and at 17m in Panel B

5. Results

Initially, each of the five reference profiles were processed using the catalogue developed from the five reference profiles. As expected each of the sections were classified as having an acoustic signature similar to that class in the catalogue. One exception occurs where profile "A" contains a small number of echoes similar to that of Class "B". This is explained by recognising that each cluster of points from the reference profile has a relatively tight scatter but outliers may overlap with other classes.

When the reference catalogue processed profiles other than those used to generate the catalogue, the results are variable. Figure 6 is a ten minute section of data with the classification shown as a bar of various shades of grey representing the classification.

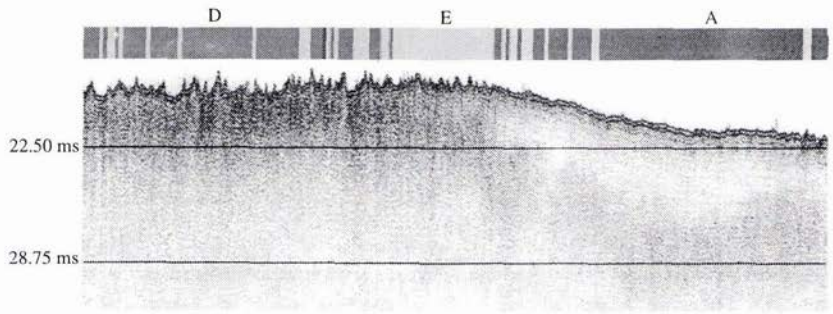

Figure 6. Seismic profile representing a ten minute section of data processed by the reference catalogue. The scale on the left is the two-way travel time to the sea surface. The bar at the top shows a shade of grey representing a class for the seabed directly below. Letters at the top of the bar indicate the class associated with the shade of grey below it.

The profile shows two distinct surface reflectors. To the left the section exhibits a high relief surface that is virtually free from reverberation. A gas curtain with associated 'gas brightening' has masked most subsurface structure and appears to be more defuse at the center of the section [7]. There is a distinct difference in the acoustic character of the bottom echo over the latter part of this section where the seabed has less relief and more immediate reverberation possibly indicating a coarse surficial sediment. This portion of the profile shows less gas near the surface and weak parallel reflectors are visible to approximately 3 ms of the seabed. The lack of a gas curtain to the right of the section also suggests coarser sediments.

The section was identified as having an acoustic response similar to class D initially followed by class E near the center and class A towards the end. The correlation between the first part of this profile and class D as seen in Figure 5 appears weak. There is a stronger correlation between the center portion of this profile and class E which shows slight relief on the surface of the seabed with little reverberation possibly indicating less dense material and gas brightening at depth. There is a high correlation with the latter portion of the section and class A which exhibits some reverberation at the sea bed surface and weak parallel reflectors. The class A reference section exhibits gas enhanced reflectors at depth.

Figure 7 is ten minute section of data exhibiting a more varied acoustic response. The section can be characterized in terms of surface scatter effects and a gas curtain at specific depths below surface.

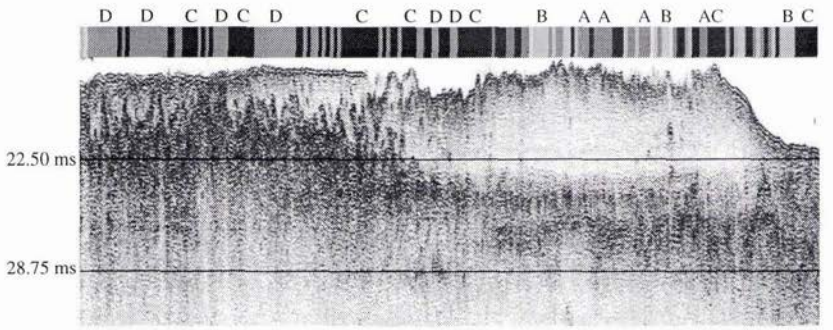

Figure 7. Seismic profile representing a ten minute section of data processed by the reference catalogue. The scale on the left is the two-way travel time to the sea surface. The bar at the top shows a shade of grey representing a class for the seabed directly below. Letters at the top of the bar indicate the class associated with the shade of grey below it.

The left side of the profile in Figure 7 has a relatively flat seabed with little surface reverberation suggesting a soft material. There is little shot to shot coherency except towards the end of the initial portion where surface reverberation may indicate a coarsening of the sea bed material. Gas appears to be diffuse in the near surface and increases at 2-3 ms below the sea floor. The highly undulating appearance of the deeper gas reflector, may represent off-axis response from gas charged sediments. The character of the sea floor changes just before the center of the section by exhibiting higher bathymetric relief and increased surface scatter. Weak parallel reflectors are observed in the sub-surface and gas near the base of the section masks any deeper structure.

The classification along this section consists of acoustic responses similar to classes A through D. In a broad sense the initial portion of the section contains class D and the latter portion contains classes A and B. Class C is represented

throughout the section but is predominant near the center. There is a reasonable correlation between class D and the first portion of the section. Both exhibit weak surface reflectors and defuse gas. The correlation with class C is less clear and may be related to increased surface scatter effects. Classes A and B occur in the latter portion of the section with Class A exhibiting mixed correlation with very similar surface reverberation and weak parallel reflectors at depth, yet poor shot to shot coherency. At the very end of the section, class B correlated well with the reference section showing high reverberation at the surface and good shot to shot coherency of the immediate bottom echo.

6. Summary and Conclusions

The purpose of the experiment was to evaluate the application of statistical based seabed classification techniques to sub-bottom profile data. The *line-in-cone* receiver and fixed geometry of the SEISTEC profiler provides certain advantages in consistency of data to allow detailed statistical treatment of sub-bottom seismic data to proceed. The results indicate a certain level of repeatability with the data set in that the five original reference sections were identified and classified properly when reprocessed independently of the reference catalogue.

The success in the classification of other processed sections independant of the reference profiles was variable. For seabeds with minimal shot to shot echo coherency at the seabed, the success was limited whereas other seabeds exhibiting strong coherent surface reflectors were classified correctly. The success rate could probably have been improved by more closely constraining the time window being used for processing and analysis. In addition, the selection of a ten minute section as a data window may have contributed to added biases and uncertainties. In some cases, there was a degree of variability along these reference sections which would have influenced the choice of useful acoustic parameters and limit accurate classification.

Since the analysed seismic signal is influenced by sub-seabed structure as well as the physical properties and surface geometry of the seafloor, we must conclude that where the sub-bottom characteristics change significantly, we can expect errors in classification. Shallow gas, which appears in the seismic sections in various forms:- as defuse reflectors, brightened reflectors or coherent layers at various depths, demands special consideration. Not only are the gas charged sediments highly variable in terms of their acoustic reflection characteristics but gas enhanced reflectors produce echoes with very high amplitudes relative to normal sub-bottom reflectors. These high amplitude yet delayed reflectors could dominate the classification process particularly in the softer sediments where gas often accumulates. We must therefore consider using shorter windows at various depths when future seismic data is being processed in this manner.

7. References

[1] W. T. Collins, R. Gregory and J. Anderson, "A digital approach to seabed classification," Sea Technology, August 1996

[2] W. T. Collins and P. Lacroix, "Operational philosophy of acoustic waveform data processing for seabed classification", *in Proceedings of Oceanlology International '97*, in press

[3] P. R Hill, "Late Quaternary sequence stratigraphy of the Mackenzie Delta," *Canadian Journal of Earth Sciences,* vol. 33, No. 7, pp.1064-1074, 1996.

[4] P.G. Simpkin,. "Seismic profiling in shallow water". In: *Proc. International Conference - Acoustic Classification and Mapping of the Seabed. Inst. of Acoustics*, Volume 15 Part 2, pp. 279-286. University of Bath, UK 14 - 16 April 1993.

[5] P.G. Simpkin, and A. Davis. "For Seismic Profiling in very shallow water, a Novel Receiver," Sea Technology, September, 1993.

[6] M.S. Marlow,, P.E. Hart,, P.R. Carlson,, J.R. Childs, and D.M. Mann,., "Misinterpretation of lateral acoustic variations on high-resolution reflection profiles as fault offsets on Holocene bay mud beneath the southern part of San Francisco Bay, California." Marine and Petroleum Geology, Vol. 13, No. 3, 1996.

[7] Angela Davis, Ed. "Methane in Marine Sediments" in *Continental Shelf Research*, Vol. 12, No. 10. Pergamon Press, 1992.

Time Domain Finite Difference Methods for Range Dependent Biot Media

Ralph Stephen

Woods Hole Oceanographic Institution (MS#24)
360 Woods Hole Road
Woods Hole, MA 02543-1542, USA
Email: rstephen@whoi.edu

Abstract

The physics of sound propagation in saturated, porous (Biot) media differs from propagation in fluids and elastic/anelastic solids because of the existence of a second compressional wave, the "slow" wave. Many environments in bottom interacting ocean acoustics consist of mud and sands which can be modeled as saturated, porous solids with low shear moduli. In order to understand the physical mechanisms responsible for acoustic propagation, attenuation, and scattering in these processes, we have extended our Numerical Scattering Chamber code to solve Biot's equations in two dimensional Cartesian coordinates. The NSC formulation is based on the method of time domain finite differences and is applicable to the rough and laterally heterogeneous structures that are found on the seafloor. Within the same code we can compare acoustic, elastic, anelastic and Biot models for realistic environments with subbottom heterogeneities and seafloor roughness with scale lengths comparable to acoustic wavelengths. All multiple interactions and mode conversions are included in the solution.

1. Introduction

Chotiros [1] outlined three cases where Biot's theory for wave propagation in porous media could be applied to the interpretation of bottom interacting acoustic data. He postulated that the existence of the Biot slow wave was necessary to interpret the energy partitioning of an acoustic beam on a water to water-saturated sand interface. If slow waves play an important role at flat interfaces between homogeneous media, what role do they play in forward and back scattering from rough interfaces or from sub-bottom heterogeneities? Time domain finite differences have proven to be a useful tool in identifying the physical processes responsible for scattering from elastic and anelastic seafloors [2-4]. We are developing a time domain finite difference code to study the additional mechanisms that may be introduced in saturated porous media.

Time domain finite difference methods have a number of advantages over other methods for simulating bottom scattering. Time domain solutions to the two-way wave equations contain all multiple interactions between scatterers, including all mode conversions between compressional (fast and slow), shear and interface waves. Interface roughness and sub-bottom heterogeneities, with length scales on the order of acoustic wavelengths, can be studied with the same methodology. Models can consist of arbitrary combinations of acoustic, elastic, anelastic and poro-elastic media. Wavefront snapshots, in addition to time series at arbitrary locations within the model, provide useful insights into the propagation and scattering of sound in complex media.

2. The Method

2.1 Biot's Equations for Heterogeneous Media with Non-Uniform Porosity

Biot [5] (Equation 8.24) gives the wave equation for a heterogeneous, non-uniform porosity, poro-elastic medium:

$$
\begin{aligned}
&2\sum_j \frac{\partial}{\partial x_j}\left(\mu e_{ij}\right)+\frac{\partial}{\partial x_i}\left(\lambda_c e-\alpha M\zeta\right)=\frac{\partial^2}{\partial t^2}\left(\rho u_i+\rho_f w_i\right)\\
&\frac{\partial}{\partial x_i}\left(\alpha M e-M\zeta\right)=\frac{\partial^2}{\partial t^2}\left(\rho_f u_i+m w_i\right)+\frac{\eta}{k}\frac{\partial w_i}{\partial t}
\end{aligned}
\tag{1}
$$

where μ, λ_c, α and M are poro-elastic parameters, u_i and U_i are displacement vectors for the solid and fluid components respectively, f is porosity, η is the fluid viscosity, k is the permeability, ρ_f is the fluid density, ρ is the total mass of bulk material per unit volume, and m is a third mass parameter. Also:

$$
\begin{aligned}
&\mathbf{w}=f(\mathbf{U}-\mathbf{u})\\
&\zeta=-div[\mathbf{w}]\\
&e=div[\mathbf{u}]\\
&e_{ij}=\begin{Bmatrix}
\dfrac{\partial u_x}{\partial x} & \dfrac{1}{2}\left(\dfrac{\partial u_y}{\partial x}+\dfrac{\partial u_x}{\partial y}\right) & \dfrac{1}{2}\left(\dfrac{\partial u_z}{\partial x}+\dfrac{\partial u_x}{\partial z}\right)\\
\dfrac{1}{2}\left(\dfrac{\partial u_y}{\partial x}+\dfrac{\partial u_x}{\partial y}\right) & \dfrac{\partial u_y}{\partial y} & \dfrac{1}{2}\left(\dfrac{\partial u_y}{\partial z}+\dfrac{\partial u_z}{\partial y}\right)\\
\dfrac{1}{2}\left(\dfrac{\partial u_z}{\partial x}+\dfrac{\partial u_x}{\partial z}\right) & \dfrac{1}{2}\left(\dfrac{\partial u_y}{\partial z}+\dfrac{\partial u_z}{\partial y}\right) & \dfrac{\partial u_z}{\partial z}
\end{Bmatrix}
\end{aligned}
\tag{2}
$$

Note that just about all other equations in Biot's porous media papers, including all of the familiar equations, assume uniform porosity and homogeneous material. In our finite difference approach we rely on gradients of elastic parameters (and porosity) to compute the effects of interfaces. We do not introduce boundary conditions explicitly. So it is important to have the correct equations for heterogeneous, non-uniform porosity material. A finite difference solution to Biot's equation 8.25 for a homogeneous, uniform porosity, medium was treated by Zhu and McMechan [6]. Hassanzadeh [7] presented solutions to Biot's equations for dilatational waves in a homogeneous, uniform porosity medium ([8], equation 7.1). Neither of these approaches is satisfactory for our applications.

Following Biot [5] (1) can be rewritten in a form similar to Biot's equation 8.25 but valid for heterogeneous, non-uniform porosity material:

$$
\begin{aligned}
&\mu\nabla^2\mathbf{u}+(\mu+\lambda_c)\nabla e-\alpha M\nabla\zeta+\nabla\mu\cdot\left[\nabla\mathbf{u}+(\nabla\mathbf{u})^T\right]+\nabla\lambda_c e-\nabla(\alpha M)\zeta\\
&\qquad=\frac{\partial^2}{\partial t^2}\left(\rho\mathbf{u}+\rho_f\mathbf{w}\right)\\
&\nabla\left(\alpha M e-M\zeta\right)=\frac{\partial^2}{\partial t^2}\left(\rho_f\mathbf{u}+m\mathbf{w}\right)+\frac{\eta}{k}\frac{\partial\mathbf{w}}{\partial t}
\end{aligned}
\tag{3}
$$

Also, the more familiar form of Biot's equation 8.1 becomes for a heterogeneous, non-uniform porosity material:

$$
\begin{aligned}
&N\nabla^2\mathbf{u} + (N+A)\nabla e + Q\nabla\varepsilon \\
&+\frac{Q}{f}\left\{\nabla\left[\nabla f\cdot(\mathbf{u}-\mathbf{U})\right]+\nabla f(e-\varepsilon)\right\}+\nabla\mu\cdot\left[\nabla\mathbf{u}+(\nabla\mathbf{u})^T\right] \\
&+\left[\nabla\lambda_c - f\nabla(\alpha M)\right]e-\left[\nabla(\alpha M)-f\nabla M\right]\left[\nabla f\cdot(\mathbf{u}-\mathbf{U})+f(e-\varepsilon)\right] \\
&\qquad = \frac{\partial^2}{\partial t^2}(\rho_{11}\mathbf{u}+\rho_{12}\mathbf{U})+b\frac{\partial}{\partial t}(\mathbf{u}-\mathbf{U}) \\
&f\left[\nabla\left(\frac{Q}{f}e+\frac{R}{f}\varepsilon\right)+\nabla\left\{\frac{R}{f^2}\left[\nabla f\cdot(\mathbf{U}-\mathbf{u})\right]\right\}\right] \\
&= \frac{\partial^2}{\partial t^2}(\rho_{12}\mathbf{u}+\rho_{22}\mathbf{U})-b\frac{\partial}{\partial t}(\mathbf{u}-\mathbf{U})
\end{aligned}
\tag{4}
$$

where from Biot's equations 8.19, 8.2 and 3.31 (low frequency approximation):

$$
\begin{aligned}
\rho_{11} &= \rho - 2\rho_f f + mf^2 \\
\rho_{22} &= mf^2 \\
\rho_{12} &= \rho_f f - mf^2 \\
b &= \frac{\eta}{k}f^2 \\
Q &= f(\alpha - f)M \\
R &= f^2 M \\
N &= \mu \\
A &= \lambda_c - 2\alpha f M + Mf^2
\end{aligned}
\tag{5}
$$

Alternatively, in terms of the porosity weighted pressure in the fluid, s=-fp, and the volume averaged stress tensor for the solid, Σ, (1) can be expressed as a coupled system of the equations of motion [9]:

$$
\begin{aligned}
\rho_{11}\frac{\partial^2\mathbf{u}}{\partial t^2}+\rho_{12}\frac{\partial^2\mathbf{U}}{\partial t^2} &= \nabla\cdot\Sigma + b\frac{\partial}{\partial t}(\mathbf{U}-\mathbf{u}) \\
\rho_{12}\frac{\partial^2\mathbf{u}}{\partial t^2}+\rho_{22}\frac{\partial^2\mathbf{U}}{\partial t^2} &= \nabla s - b\frac{\partial}{\partial t}(\mathbf{U}-\mathbf{u})
\end{aligned}
\tag{6}
$$

and the stress-strain relations in terms of displacement:

$$s = Q\nabla\cdot\mathbf{u} + R\nabla\cdot\mathbf{U} + \frac{R}{f}\nabla f\cdot(\mathbf{U}-\mathbf{u})$$
$$\Sigma = N\left[\nabla\mathbf{u} + (\nabla\mathbf{u})^T\right] + \left[A\nabla\cdot\mathbf{u} + Q\nabla\cdot\mathbf{U} + \frac{Q}{f}\nabla f\cdot(\mathbf{U}-\mathbf{u})\right]\mathbf{I} \tag{7}$$

where **I** is the identity matrix. Note that contrary to elasticity, in poro-elasticity the infinitesimal cube over which the stresses and strains are defined is not homogeneous. It is necessary to consider the gradients in porosity in the stress-strain relation. On comparing (6) to (4) it would appear that the first and second equations in (4) should correspond to ·Σ and s respectively but they do not. The discrepancy has not been resolved. Equations(6) and (7) are equivalent to equation (4), however, when porosity is uniform (f=0). The equations in this case which are valid for heterogeneous, uniform-porosity material are:

$$\begin{aligned}&(A+N)\nabla(\nabla\cdot\mathbf{u}) + N\nabla^2\mathbf{u} + Q\nabla(\nabla\cdot\mathbf{U}) + \nabla A(\nabla\cdot\mathbf{u})\\ &+\nabla N\times(\nabla\times\mathbf{u}) + 2(\nabla N\cdot\nabla)\mathbf{u} + \nabla Q(\nabla\cdot\mathbf{U})\\ &= \frac{\partial^2}{\partial t^2}(\rho_{11}\mathbf{u} + \rho_{12}\mathbf{U}) + b\frac{\partial}{\partial t}(\mathbf{u}-\mathbf{U})\end{aligned} \tag{8}$$

$$\begin{aligned}&Q\nabla(\nabla\cdot\mathbf{u}) + R\nabla(\nabla\cdot\mathbf{U}) + \nabla Q(\nabla\cdot\mathbf{u}) + \nabla R(\nabla\cdot\mathbf{U})\\ &= \frac{\partial^2}{\partial t^2}(\rho_{12}\mathbf{u} + \rho_{22}\mathbf{U}) - b\frac{\partial}{\partial t}(\mathbf{u}-\mathbf{U})\end{aligned}$$

A finite difference solution to these equations was presented by Stephen [10]. A solution to these equations, valid for uniform porosity media, is discussed below.

2.2 Approximations and Assumptions

In establishing the wave equations for poro-elastic media Biot made the following assumptions [9]. Disconnected pores are treated as part of the solid matrix. The porous medium is macroscopically isotropic. The pore size is much less than all geoacoustic wavelengths. Deformations are small so that the differential equations will be linear. The force of gravity and temperature variations are neglected. A low frequency approximation is made so that the flow between the pores can be considered Poïseuille type.

In applying our finite difference approach to these equations we make further assumptions. All of the parameters are assumed to be frequency independent over the bandwidth of the source, which is an octave in pressure in our examples. We do not include intrinsic anelasticity for the solid frame. We solve the poro-elastic equations for a point source in a two dimensional, Cartesian geometry. We neglect porosity gradients in the stress-strain relation so the code is appropriate for only slowly varying porosity.

3. An Example

For testing purposes we consider as an example a point source in a poro-elastic layer between an acoustic half-space and an elastic half-space (Figure 1). The parameters for the poro-elastic medium represent a water saturated sand [11] without intrinsic attenuation (Table 1). Our values differ slightly from [11]. Our bulk modulus of the fluid corresponds to a water velocity of 1500m/s. Also we chose a very small permeability to initially test the code without the viscous coupling term.

Table 1: Parameters for the poro-elastic layer in Figure 1.

Porosity	f	0.47	
Viscosity	η	10^{-6}	kg/(m-s)
Permeability	k	10^{-10}	m^2
Fluid Density	ρ_f	10^3	kg/m^3
Solid Grain Density	ρ_s	2650	kg/m^3
Grain Bulk Modulus	K_s	$3.6x10^{10}$	Pa
Fluid Bulk Modulus	K_f	$2.25x10^9$	Pa
Dry Skeleton Bulk Modulus	K_B	$4.36x10^7$	Pa
Dry Skeleton Shear Modulus	N	$2.61x10^7$	Pa

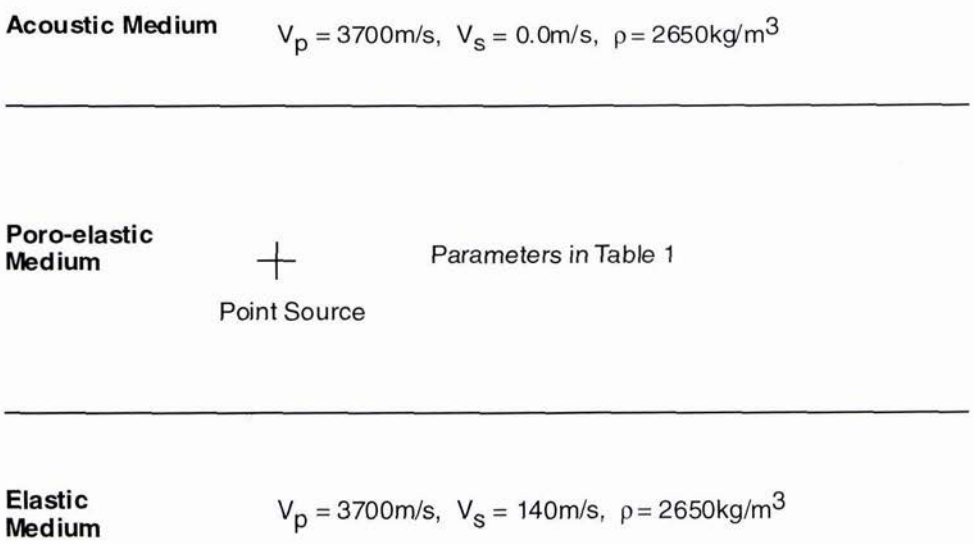

Figure 1: For testing purposes we consider a poro-elastic layer between an acoustic half-space and an elastic half-space.

The parameters required in (8) can be expressed in terms of the parameters in Table 1:

$$A = \frac{(1-f)\left(1-f-\frac{K_b}{K_s}\right)K_s + f\frac{K_s}{K_f}K_b}{1-f-\frac{K_b}{K_s}+f\frac{K_s}{K_f}} - \frac{2}{3}N$$

$$Q = \frac{\left(1-f-\frac{K_b}{K_s}\right)fK_s}{1-f-\frac{K_b}{K_s}+f\frac{K_s}{K_f}} \qquad (9)$$

$$R = \frac{f^2 K_s}{1-f-\frac{K_b}{K_s}+f\frac{K_s}{K_f}}$$

$$\rho_{11} = (1-f)\rho_s + \tfrac{1}{3}f\rho_f$$

$$\rho_{12} = -\tfrac{1}{3}f\rho_f$$

$$\rho_{22} = \tfrac{4}{3}f\rho_f$$

The source time series in pressure is the third derivative of a Gaussian curve with a peak frequency of 400Hz. The time increment is 1/400th of a period at the peak frequency. The spatial sampling is 1/280th of a compressional wavelength at the peak frequency in pressure in the acoustic medium. This corresponds to sampling the shear waves in the lower medium at 10 points/wavelength. For testing we chose the compressional velocity and density of the upper acoustic medium and the lower elastic medium to match the compressional velocity and density of the poro-elastic layer when the porosity is zero. Obviously more realistic values for the compressional velocity and density of the upper acoustic medium would be 1500m/s and 1000kg/m^3, corresponding to water. For this case the spatial sampling would be about 114 points per wavelength. Since all times and distances in the calculation scale proportional to inverse frequency the output can be specified in periods and compressional wavelengths in the acoustic medium.

Figure 2 shows a snapshot at 7.5Periods after the initiation of the source pulse for a layer thickness of 1.82 wavelengths with the source at a depth of about 0.9wavelengths. The top frame labeled 'compressional' corresponds to a scaled version of the divergence of the solid displacement vector. The lower frame corresponds to the curl of the solid displacement vector. At this stage we have not confirmed the validity of the amplitudes. Kinematically however we can see the wavefronts corresponding to the direct, surface reflected and bottom reflected fast compressional waves to the right of the upper figure. The slow wave generated at the source is the circular wavefront on the left of the upper figure. The short wavelength bottom reflection corresponds kinematically to a converted slow wave but the amplitudes have not been tested. Since the formulation assumed uniform porosity it is unlikely that the converted slow wave is correct.

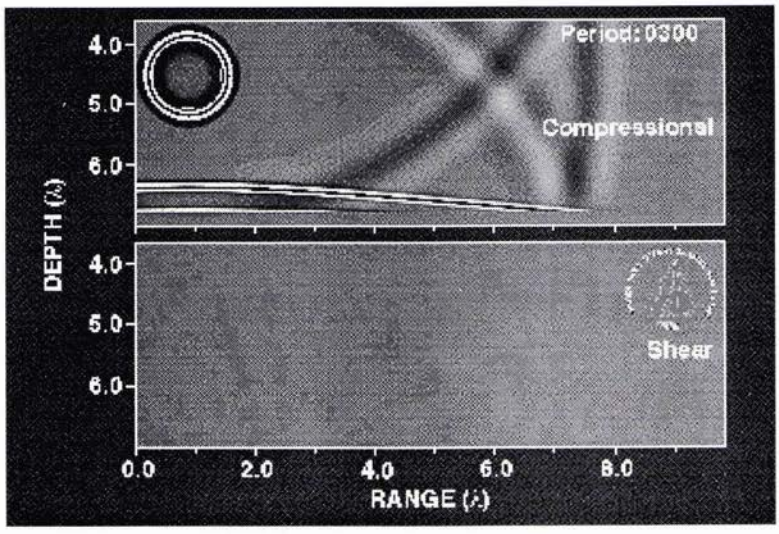

Figure 2: Snapshots of the divergence (top) and curl (bottom) of the solid displacement vector 7.5 periods after the source pulse was initiated in the test model.

4. Conclusions

This paper is a progress report of on-going research. Further validity testing for homogeneous, porous media is clearly required. We recommend that benchmarks be established for porous media problems. Using a Gaussian pulse-beam rather than a point source will limit the wave number content of the incident field while restricting the computational domain. Ultimately the code should be applied to analysis of actual field data.

The time domain finite difference method is a promising technique for addressing the physical mechanisms of forward and back scattering from range dependent porous media with interface roughness and/or volume (sub-bottom) heterogeneities. Wavefront snapshots provide insight into the conversion between fast, slow and shear waves at interfaces between homogeneous poro-elastic and elastic layers. Within the Numerical Scattering Chamber methodology one can address a broad range of scattering problems for acoustic, elastic, anelastic and poro-elastic media.

5. Acknowledgements

The work described in this paper was supported by the Office of Naval Research under Contract Number N00014-96-1-0460.

References

[1] N. P. Chotiros, "Biot model of sound propagation in water-saturated sand," *J. acoust. Soc. Am.*, vol. 97, pp. 199-214, 1995.

[2] R. A. Stephen and S. A. Swift, "Finite difference modeling of geoacoustic interaction at anelastic seafloors," *J. acoust. Soc. Am.*, vol. 95, pp. 60-70, 1994.

[3] R. A. Stephen and S. A. Swift, "Modeling seafloor geoacoustic interaction with a numerical scattering chamber," *J. acoust. Soc. Am.*, vol. 96, pp. 973-990, 1994.

[4] S. A. Swift and R. A. Stephen, "The scattering of a low-angle pulse beam by seafloor volume heterogeneities," *J. acoust. Soc. Am.*, vol. 96, pp. 991-1001, 1994.

[5] M. A. Biot, "Mechanics of deformation and acoustic propagation in porous media," *J. appl. phys.*, vol. 33, pp. 1482-1488, 1962.

[6] X. Zhu and G. A. McMechan, "Numerical simulation of seismic responses of poroelastic reservoirs using Biot theory," *Geophysics*, vol. 56, pp. 328-339, 1991.

[7] S. Hassanzadeh, "Acoustic modeling in fluid-saturated porous media," *Geophysics*, vol. 56, pp. 424-435, 1991.

[8] M. A. Biot, "Theory of propagation of elastic waves in a fluid saturated porous solid. I. Low-frequency range," *J. acoust. Soc. Am.*, vol. 28, pp. 168-178, 1956.

[9] N. Dai, A. Vafidis, and E. R. Kanasewich, "Wave propagation in heterogeneous, porous media: A velocity-stress, finite-difference method," *Geophysics*, vol. 60, pp. 327-340, 1995.

[10] R. A. Stephen, "A finite difference formulation of Biot's equations for vertically heterogeneous full waveform acoustic logging problems," in *Full Waveform Acoustic Logging Consortium Annual Report*, M. N. Toksöz and C. H. Cheng, Eds. Boston: Massachusetts Institute of Technology Earth Resources Laboratory, 1987, pp. 115-123.

[11] R. D. Stoll and T. K. Kan, "Reflection of acoustic waves at a water-sediment interface," *J. acoust. Soc. Am.*, vol. 70, pp. 149-156, 1981.

Temporal Modeling of High Frequency (30 - 100 kHz) Acoustic Seafloor Backscatter: Shallow Water Results.

D. D. Sternlicht and C. de Moustier

Marine Physical Laboratory
Scripps Institution of Oceanography
9500 Gilman Drive
La Jolla, CA 92093-0205, USA
E-mail: dan@mpl.ucsd.edu

Abstract

A temporal model of high frequency seafloor acoustic backscatter is presented and compared to recorded echoes from terrigenous sediments. Using acoustic properties correlated with mean grain size, the echo shapes and amplitudes of the model are compared to data collected in San Diego Harbor with fully calibrated 33 kHz and 93 kHz narrow beam piston transducers. While there is considerable variation for small horizontal translations of the transducer, the mean echo envelopes compare well with the shapes and amplitudes predicted by model simulations.

1. Introduction

In recent years a number of acoustic techniques have been developed for characterizing the upper layer of seafloor sediment: [1, 2, 3, 4, 5, 6]. While empirical techniques have demonstrated market value, we are investigating a physical approach with a temporal model of high frequency acoustic seafloor backscatter. Using geo-acoustic parameters correlated with the grain-size distribution of ocean sediments, this model simulates the shape and magnitude of echo-envelopes received by a monostatic transducer aimed at the bottom. The primary goal in working with a temporal representation is to facilitate a greater understanding of acoustic scattering at the bottom/sub-bottom interface. However, the ability to match simulations with measured echo envelopes, where the only unknowns are the bottom characteristics, is the foundation of a sediment classification tool currently under development.

The *temporal model* predicts average echo shapes and energy levels for realistic scenarios defined by acoustic frequency, sediment type, system configuration, and deployment geometry. The software representation of the model was developed by iterative comparisons to data recorded with a fully characterized system. In this paper we first describe the mathematical formulation of the model. Specifications and calibration of a dual frequency system are then presented along with the signal processing steps necessary after echo digitization. Deployment of the system and data collection are described, followed by comparisons of the model with recorded echoes from fine-grade, shallow water sediments, where the transducers were inclined 0 to 16 degrees from nadir. Finally, we discuss the prospects of using the temporal model as a tool for sediment classification.

2. Model

The *temporal model* simulates the expected intensity envelope of echo-sounding monostatic piston transducers operating between 10 and 100 kHz. It incorporates the transducer's geometry and beam pattern, ocean volume spreading and absorption losses, and the geoacoustic parameters which describe the water/bottom interface and the sediment volume. The model component representing interface backscatter incorporates the roughness spectrum of the interface, the local bottom slope, and a coherent reflection coefficient. Sediment volume backscatter is derived from the spectrum of subbottom refraction index fluctuations, and the roughness characteristics of the interface governing sound transmission to the sediment.

Figure 1 illustrates the process described by the model. A short acoustic pulse represented by the arc, insonifies

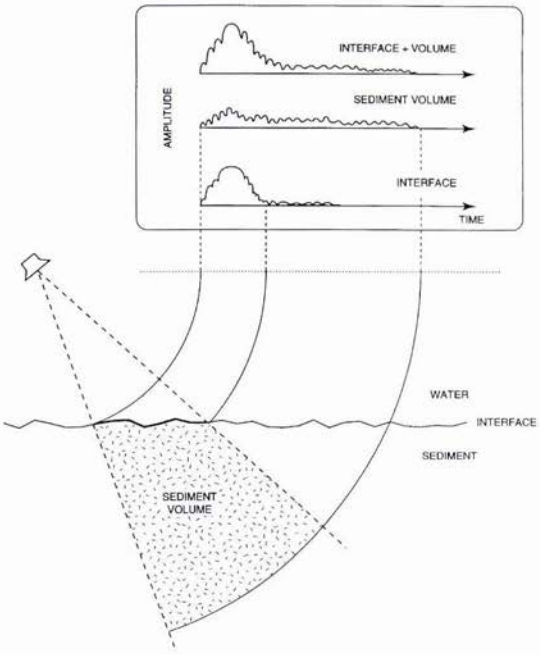

Figure 1: Graphic representation: Temporal Model of High Frequency Acoustic Seafloor Backscatter

the sediment which scatters energy back to the transducer. The graphs in the upper right corner depict the measured backscatter from the insonified areas and volumes as a function of time. The bottom graph represents the backscatter from the sediment/water interface as the projection of the pulse onto the seafloor traverses the main lobe of the transducer. The middle graph represents energy penetrating the sediment volume and scattering from subbottom inhomogeneities. The model computes these components separately and combines them to estimate the measured signal represented by the top graph.

Consider a transducer which insonifies the bottom with a short, non-uniform pulse, and subsequently measures the echo. $I(t)$ is the integral over the bottom area and represents the backscattered energy coincident upon the transducer face at time t:

$$I(t) = \int_A \frac{(I_i + I_v)\, b(\phi, \psi)}{r^2\, 10^{\alpha_w(\frac{r}{10})}} dA$$

In this formulation, A is the area of seafloor which has come into contact with the transmitted pulse; b represent the directivity, where ϕ and ψ are angles referencing the transducer axes and elemental area, dA; r is the distance between the transducer and dA; and α_w is the seawater absorption coefficient. I_i and I_v represent the interface and sediment volume backscatter intensities referenced 1 meter from dA. I_i is the product of transmitted intensity incident at dA and interface backscatter function $\sigma_i(\rho, \nu, \gamma, \omega_2, f_a, \theta)$. σ_i is based on the Kirchhoff approximation as described in Jackson et al [7] and Mourad and Jackson [8], where; ρ and ν are the relative density and the relative sound-speed; γ and ω_2 are the exponent and strength of the roughness spectrum, f_a is the acoustic frequency of the pulse, and θ is the incidence angle of the wave-front upon the interface. With slight modification to Jackson et al, I_v is calculated by integrating the subbottom component of the signal, the sediment attenuation α_v, and the sediment volume backscatter function σ_v through the sediment, and properly modulating by the interface roughness statistics governing transmission through the interface.

For most natural seafloor surfaces, the variance of heights between two points on the seafloor increases as the distance between the points, l, becomes larger. In our measurements l represents the horizontal distance traveled by the pulse within the transducer's footprint - where the footprint, $l_f = 2\, alt\, \tan(\theta_{bw}/2)$, is defined at normal incidence by the transducer's half power beam width θ_{bw}, and altitude over the bottom, alt. For situations where the variance of sea-floor heights is large compared to the transmitted pulse length, the output of the temporal model may be convolved with the corresponding altitude distribution as described in Pouliquen [4]. When applying

this method, we assume that the altitude is normally distributed with variance equal to the structure function described in [7] and evaluated with l: $\sigma_h^2 = D_h(l)$.

3. System

For testing the *temporal model* we built a dual-frequency echosounder system which was calibrated in a shallow water tank. A Hewlett Packard Arbitrary Wave Form Generator creates a gated sinusoid which is amplified by an ENI 2100 power amplifier. The TR (Transmit-Receive) switch constructed for this system has 2 input channels (power amplifier and A/D) and one output to the transducer. Its active circuit allows the high-voltage output signal to excite the piezoelectric ceramic transducer, while protecting the receive circuitry. The small transducer voltages generated by the echo, pass undistorted through the TR switch and are subsequently amplified, band pass filtered, and digitized by a Gagescope CS125 oscilloscope card, sampling slightly faster than the outgoing signal's Nyquist frequency. An Applied Geomechanics clinometer, measuring pitch and roll at 0.1 degree resolution, is installed parallel with the transducer face and sampled every ping repetition. Envelope detection is performed by inverse system filtering (described in section 3.2), base-banding, and low pass filtering.

3.1. Transducer Specifications

For each transducer, the following table summarizes the acoustic transmit frequency (f_a), half power beam width (θ_{bw}), transmit pulse length (τ_p), transmit voltage response (TVR in dB re: 1 μPa/Volt @ 1 m), and the open circuit voltage response (OCV in dB re: 1 Volt/μPa).

Transducer	f_a (kHz)	θ_{bw} (deg)	τ_p (msec)	TVR (dB)	OCV (dB)
Reson TC2084	33	21	0.450	164.5	-179.0
AirMar M192	93	10	0.160	157.5	-176.5

The measured beam patterns of these transducers are conical, approximated by the first order Bessel function, with sidelobes lower than -15 dB.

3.2. Extracting Pressure Signal from Voltage Time Series

To exploit the angular dependence of seafloor acoustic backscatter, short acoustic pulses are used to insonify a series of small sectors within the footprint. This ideal scenario is illustrated by the arcs of figure 1. The footprint becomes smaller with decreasing altitude, therefore the pulse must be made commensurately smaller. However, the shortest pulse length achievable is roughly $1/\Delta f$, where Δf is the transducer bandwidth. In this work we operate with pulse lengths close to this limit and correct for the rise/fall times introduced by the device's transfer function.

In its raw form, the *temporal model* assumes a uniform frequency response for the transducer, but few transducers have such ideal characteristics - especially when operated near resonance. Thus we must convert the measured voltage waveforms into the correct pressure waveforms before comparison with the model. The transducer's mechanical-electrical transfer function is determined by deconvolving a direct path measurement, made with an independent broadband hydrophone, from the signal received by the transducer after reflection from a flat aluminum plate. Figures 2.a and 2.b show the digitized direct path and reflection measurements, $x(t)$ and $y(t)$, while figure 2.c shows the corresponding spectra. Figure 2.d presents the mechanical-electrical transfer function, $H(f)$, calculated as $H(f) = Y(f)/X(f)$.

The input to the temporal model of seafloor acoustic backscatter is thus, the echo envelope of the direct path measurement, appropriately scaled using the TVR. The output of the temporal model is compared to measured echoes which have been inverse filtered ($H^{-1}(f)$) and appropriately scaled using the OCV.

4. Measurements

The difficulty of reproducing representative seafloor substrates and appropriately scaled survey geometries in the lab, makes field testing of the model mandatory. Development of the model was therefore coordinated with echoes measured pier-side and underway from a small launch.

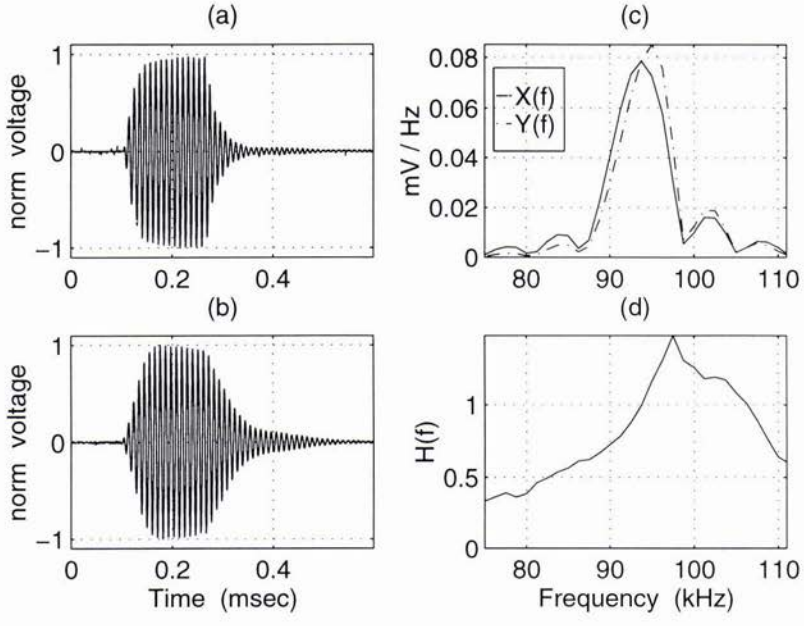

Figure 2: AirMar M192 signal characteristics @ 93 kHz: (a) $x(t)$, transmit signal; (b) $y(t)$, reflected signal; (c) $X(f)$ and $Y(f)$, spectra; (d) $H(f)$, transfer function

4.1. Pier-side Measurements

Preliminary versions of the model were compared to measurements from a transducer attached firmly to a pier insonifying a flat section of seafloor. These tests confirmed the accuracy of the time-base and relative sound intensity levels predicted by the model, and demonstrated the necessity of incorporating the transducer's transfer function in shallow water applications. In sequences of pings recorded over 5 minute intervals, echo shapes were nearly identical. Thus, the acoustic character of the bottom below the pier varies slowly over time, yielding stable echo statistics. In addition similar bottom stability is expected during the 20 minutes of a short survey in the bay, such that variability in the echo structure should be mostly due to changes in substrate roughness or composition.

4.2. Shallow Water Survey

In January of 1997, the echo sounder described in section 3 was installed in the instrument well of the 40 foot launch ECOS, operated by NRaD. We surveyed a N-S trackline of the San Diego Harbor trough - the deepest part of the bay with depths of 15-20 meters. With survey speeds of 1-2 knots and ping repetition rate of 5 Hz, the bottom was typically sampled 30 to 60 times over the length of a footprint. Bottom echoes were recorded with the 33 kHz and 93 kHz transducers inclined 0 to 16 degrees from nadir in the roll plane. Angles of pitch and roll were digitized for each ping repetition. Sea conditions were mild, with pitch and roll standard deviations typically less than 0.5 degrees.

4.3. Survey Site Bottom ID

Bottom characterization was based on video coverage recorded during the survey, consulting a sediment data base for the surrounding area, and the analysis of particle size distribution for several sediment grabs taken during the survey. The *Mean Grain Size*, M_ϕ, of the samples is calculated via Inman [9]. This standard method for characterizing sediments assumes that the variable $\phi = -log_2(D_g)$, where D_g is the measured grain size in mm, is normally distributed. Analysis of the samples implies that the substrate ranges between *Clayey Sand* and *Sandy Mud* per the labeling scheme set forth in the *High-Frequency Ocean Environmental Acoustic Models Handbook* [10]. Associated with these sediments are empirically derived values of the geoacoustic parameters used in the sediment interface and volume backscatter functions and summarized in the following table:

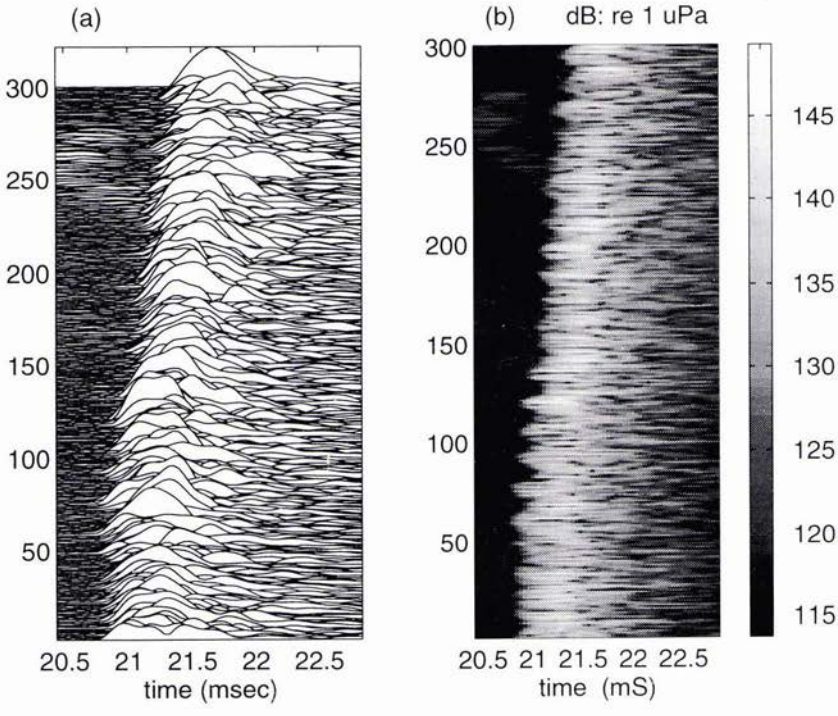

Figure 3: Survey Data - 33 kHz

Site	Sed Name	M_ϕ	ρ	ν	σ_2	γ	ω_2 (cm^4)
North	Clayey Sand	4.093	1.224	1.0364	0.002	3.25	0.001119
South	Sandy Mud	5.876	1.149	0.9873	0.001	3.25	0.000518

These values are defined in section 2, where σ_2 is known as the *volume parameter* and defined by $\sigma_2 = \sigma_v/\alpha_v$.

The video image reveals an uncomplicated bottom, appearing as long stretches of homogeneous substrate. This, combined with $> 98\%$ spatial overlap of echoes and the generally level bathymetry, were conditions we felt ideal for testing the accuracy of the temporal model.

4.4. Data

The *waterfall plot* of figure 3.a displays 300 consecutive bottom echoes received with the 33 kHz transducer. These measurements were made underway, with the transducer inclined 2 degrees with respect to nadir in the roll plane. Figure 3.b displays the same data in raster grayscale format expressed in dB re: 1 μPa. The abscissa represents time after pulse transmission. Using the standard approximation of sound speed in seawater (1500 m/sec), the transducer's altitude over the bottom is $\sim$16 meters, the footprint diameter is $\sim$6 meters and, at 5 Hz ping repetition, spatial overlap amounts to $\sim$60 pings per footprint diameter. The raster image for this 40 second (20 meter) track segment shows the gradual downward slope of the bottom modulated by the vessel heave. The early returns evident in pings 230-280 are, most likely, caused by a school of fish swimming over the bottom.

4.5. Ping Alignment and Averaging

The waterfall plot demonstrates the high variability of echo amplitude and shape for horizontal translations which are small compared to the diameter of a footprint. The scattering theory employed is stochastic, and upon averaging echo envelopes, the form and amplitude predicted by the temporal model takes shape. Before averaging, pings

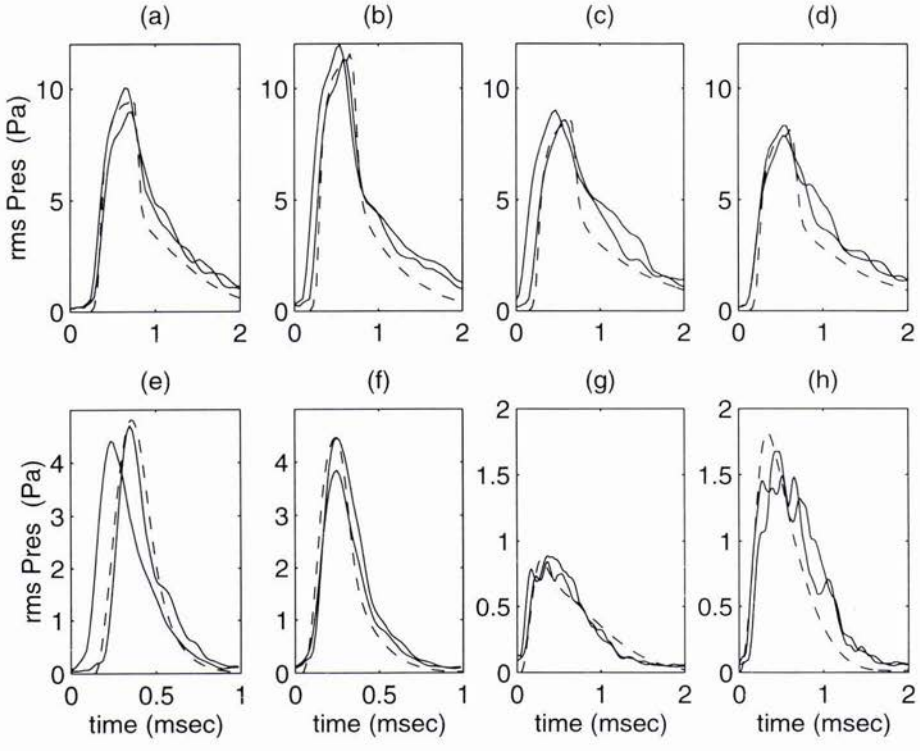

Figure 4: Model vs Data

are aligned along a minimum amplitude threshold, filtering out vessel heave and small fluctuations in altitude. Pressure envelopes are averaged using a kernel of 20 pings, discounting sections of data in which fish or vegetation are obviously present.

4.6. Analysis

Figure 4 compares the *temporal model* with data for scenarios where the main lobe of the transducer intersects the bottom near-normal and slightly off-normal, as summarized in the following table:

	$f_a(kHz)$	θ_T (deg)	alt (m)	M_ϕ	d_s (cm)	σ_h (cm)	*macro*
(a)	33	2.0	15.63	5.0	64	2.9	
(b)			15.80	4.5	38	3.6	
(c)		8.0	16.35	4.3	39	5.2	
(d)			16.40	4.5	38	4.8	
(e)	93	2.0	19.35	4.2	14	3.1	√
(f)			19.27	5.0	23	2.2	√
(g)		8.5	18.97	6.0	74	2.7	√
(h)			18.82	4.0	15	4.0	√

where the acoustic frequency (f_a), transducer tilt angle (θ_T), and altitude (alt) are preset, or directly measured quantities; and the mean grain size (M_ϕ) represents the descriptive parameter used to generate the model. The quantity (d_s) represents the calculated 10 dB skin depth of the inferred substrate - taking into account the sediment

absorption and the interface transmission coefficients, and σ_h represents the standard deviation of the altitude due to macro-roughness. Note that due to the gentle slope of the bottom in this area, θ_T approximates the main lobe's incidence angle with the seafloor.

For these graphs, the theoretical pressure envelope, $P(t)$, is derived from the square root of the modeled intensity envelope, $I(t)$: $P(t) = [I(t) \cdot \rho_w \cdot c_w]^{1/2}$, where c_w and ρ_w denote respectively the sound speed and the density of seawater. Dashed lines represent the model output for mean grain size (M_ϕ) values between 4 and 6. Solid lines represent aligned/averaged data. The graphs are arranged such that pairs (a,b), (c,d), (e,f), (g,h) represent data from the same track - where each graph shows two averaged envelopes displayed approximately 50 pings apart. While data and model are displayed with the time-base shifted to zero, their relative temporal positions remain intact.

From inspection of the graphs, the *temporal model* does a reasonable job predicting the mean amplitude of the data, where measured amplitudes appear to obey Gaussian or Rayleigh statistics, and amplitudes near-normal are larger than off-normal - due to the angular dependence of the backscatter functions. Also evident from the graphs is the agreement in echo shape between model and data. The echoes for the off-normal measurements are longer than those measured near normal incidence as the tilted transducer insonifies a longer swath of the bottom. We expect that matches in amplitude and shape, as functions of M_ϕ and θ_T, will be useful tools in identifying seafloor substrates.

For most natural sediments, the variance of heights (σ_h^2) over a given footprint (l_f) increases as the mean grain size increases. Sediments dominated by large grains are considered to be *rougher* than sediments dominated by small grains. This relationship can be seen in (σ_h) for the data pairs of figure 4. The most dramatic example is the 1.3 cm increase in (σ_h) between data pair g and h, as the inferred substrate changes from *sandy mud* to *clayey sand*. The 33 kHz and 93 kHz transmit signals have physical round-trip lengths in water of 34 cm and 12 cm respectively. On comparing these lengths with σ_h, we applied the macro-roughness convolution described at the end of section 2, to model calculations for the 93 kHz transducer. As a result, the modeled returns appear smoother, thus simulating the effect of averaging echoes from a substrate with relatively large σ_h.

While the data shown here are well-behaved, there are segments of data which exhibit energy spurs, ocurring after the expected interface return, and not predicted by the volume component. This may be due to large scale roughness or to the presence of a subbottom layer. Inspection of skin depth (d_s) implies that for appreciable backscatter to occur, this layer would have to exist within a meter of the sediment/water interface for the finer sediments, and within 50 cm for the substrates with M_ϕ nearly equal to 4 - as dictated by the difference in sediment absorption coefficient between *sandy mud* and *clayey sand*. From these observations we infer that small changes in the large scale interface roughness are responsible for the variation in shape and amplitude observed in the data.

5. Conclusions

In this paper we have described a temporal model of high frequency acoustic seafloor backscatter, demonstrating ability to estimate the shape and amplitude of stacked/averaged echoes collected under survey conditions. In shallow water applications, the accurate representation of signal and data are important for making meaningful comparisons. Therefore in this procedure, the transducer's directivity, transmit/receive response, and mechanical-electrical transfer function are used for expressing model and data in physical units, and to insure fidelity in signal shape.

The appropriate choice of variables for calculating large scale interface roughness (macro-roughness) and sediment volume backscatter is not entirely clear, and better understanding of these issues should increase the model's accuracy. Furthermore, we need to investigate a more robust method of calculating representative echo envelopes from the raw data - as in better methods of stacking, averaging, and filtering. With echo shape and backscatter strengths derived from model and data, we are currently working on algorithms which compare these features and deduce sediment type.

Acknowledgements

We thank NRaD, ENI Inc., Reson Inc., and MPL's DeepTow staff for their technical support, and we thank ONR for supporting this work under Contract # N00014-94-1-0121.

References

[1] T. K. Stanton and C. S. Clay, "Sonar echo statistics as a remote sensing tool: Volume and Seafloor", *IEEE Transactions of Ocean Engineering*, vol. OE-11, No. 1, pp. 79-96, 1986.

[2] S. G. Schock and L. R. Le Blanc and L. A. Mayer, "Chirp Subbottom Profiler for quantitative sediment analysis", *Geophysics*, vol. 54, pp. 445-450, 1989.

[3] R. Chivers and N. Emerson and D. R. Burns, "New acoustic processing for underway surveying", *The Hydrographic Journal*, No. 56, pp. 9-17, 1990.

[4] E. Pouliquen, "Identification des fonds marins superficiels a l'aide de signaux d'echo-sounders", Doctoral Thesis, Univ. Paris VII, 1992.

[5] D. R. Jackson and K. B. Briggs and K. L. Williams and M. D. Richardson, "Test of models for high-frequency seafloor backscatter", *IEEE Journal of Oceanic Engineering*, vol. 21, No. 4, pp. 458-470, 1996.

[6] S. J. Dijkstra and L. A. Mayer, "Lassoo!: An interactive graphical tool for seafloor classification", *Proceedings of OCEANS 89*, pp. 1064-1070, 1996.

[7] D. R. Jackson and D. P. Winebrenner and A. Ishimaru, "Application of the composite roughness model to high-frequency bottom backscattering", *Journal of the Acoustical Society of America*, vol. 79, pp. 1410-1422, 1986.

[8] P. D. Mourad and D. R. Jackson, "High frequency sonar equation models for bottom backscattering and forward loss", *Proceedings of OCEANS 89*, pp. 1168-1175, 1989.

[9] D. L. Inman, "Measure for describing the size distribution of sediments", *Journal of Sedimentary Petrology*, vol. 22, pp. 125-145, 1952.

[10] Applied Physics Laboratory - University of Washington, "High-Frequency Ocean Environmental Acoustic Models Handbook", Technical Report APL-UW TR 9407 AEAS 9501, October 1994.

Geoacoustic Modeling of the Seabed at Higher Frequencies

Robert D. Stoll and Edgar O. Bautista

Lamont-Doherty Earth Observatory of Columbia University
Palisades, New York 10964
Email: stoll@ldeo.columbia.edu

Abstract

In propagation at higher frequencies, local fluid motion in "hidden coordinate" systems and local discontinuities due to gas bubbles and bioturbation have a perturbing effect on the wave field. To model these effects, a baseline model that reflects the influence of basic primitive variables such as porosity and mean effective stress is first derived on the basis of the Biot theory and then effects of various discontinuities are introduced as perturbations to the baseline model.

1. Introduction

Since the Biot theory was first applied to the geoacoustic modeling of the seafloor by Stoll and Bryan [1], it has proved to be a powerful tool in studying the response of a wide variety of sediments that make up the ocean bottom. The initial motivation for modeling these particulate materials with a two-component, phenomenological formulation, such as the Biot theory, was to allow more flexibility in incorporating various physical mechanisms that control energy loss, compressibility and shear stiffness in a realistic manner, attributing each to the component (individual grains, fluid or skeletal frame) that is appropriate. The resulting model is much better able to replicate the complex behavior that is observed over a wide frequency range than a straight viscoelastic formulation. However, one pays a price for this flexibility in that the user is required to evaluate over thirteen input parameters, many of which are interrelated in a very specific manner by the mechanics of particulate material.

Much of the early experimental work by geophysicists studying the geoacoustic properties of seafloor sediments was carried out at relatively high frequencies in the range of several kHz to a MHz. On the other hand geotechnical engineers, interested in earthquakes and building vibrations, carried out experimental studies at low frequencies ranging from less than one Hertz to about 100 Hz. If the attenuation measurements made by these two groups are compared and it is assumed that the sediments respond essentially as constant Q materials (i.e., attenuation in dB/m linearly proportional to frequency) there is a major inconsistency particularly when considering the coarse sediments such as sand. It was this inconsistency that motivated the search for a more realistic mechanical model that could account for energy losses of various kinds that would be expected in water-saturated, particulate sediments. In the ensuing application of the Biot theory it was found that for the coarser sediments, motion of the interstitial fluid relative to the skeletal frame produced viscous losses which, when added to frictional losses occurring at the intergranular contacts, resulted in an overall attenuation that matches experimental results at both high and low frequencies.

In finer grained sediments, overall relative motion of the pore fluid in the direction of propagation is much smaller because of low permeability, however viscous dissipation still plays a role in determining overall attenuation because of local fluid motion in a "hidden coordinate system" near the intergranular contacts. Using the principle of viscoelastic correspondence, this kind of viscous loss is incorporated into the model by casting the moduli of the skeletal frame as viscoelastic operators. Biot discusses a number of different kinds of operators in two of his later papers [2,3]. This kind of viscoelastic operator was recently used by Stoll and Bautista to model the soft sediment of Eckernfoerde Bay in the Baltic [4]. Biot also discussed an operator that is appropriate to model the behavior of sediments containing free gas bubbles in [2] and [3]; we will use this kind of operator in a later example.

2. Constructing a Baseline Model

In studying various acoustical phenomena such as scattering, bubble resonance and bottom interaction, it is necessary to supply various geoacoustic parameters that describe sediment compressibility, shearing stiffness and attenuation, usually in the form of complex, frequency dependent moduli. In many cases reference to historical data collections such as those given by Hamilton (e.g., [5]) can provide useful input provided the data base includes entries for a similar sediment type obtained in the appropriate frequency range. However, this is not always possible because of the limited scope of the historical data available and the wide range of frequencies and sediment types that are currently of interest. Furthermore, attempts to extrapolate these data over several decades of frequency or to use a regression curve based on a single independent variable such as grain size have lead to some misleading generalizations . A good example is the persistent and erroneous notion that attenuation can always be assumed to vary as the first power of frequency. Hence a properly formulated baseline model, derived on the basis of the Biot theory and able to predict the correct response over a wide frequency range, becomes an important tool in determining the starting point for studies of the perturbing effects we wish to study.

The first step in establishing a baseline model is to determine complex bulk moduli for the individual grains, K_r, the skeletal frame in a water environment, K_b, and the interstitial fluid, K_f, and the complex shear modulus of the frame, μ, all potentially frequency dependent. These familiar moduli can then be related to the parameters used in the Biot coupled equations of motion using the following equations provided the assumption of homogeneous strain is made (i.e., volumetric strain of pore volume is the same as volumetric strain of frame so that the porosity of the sediment, β, remains unchanged - see [6], pp. 9-10).

$$\begin{aligned} \tilde{H} &= (K_r - \tilde{K}_b)^2 / D + \tilde{K}_b + 4\tilde{\mu}/3 \\ \tilde{C} &= K_r(K_r - \tilde{K}_b) / D \\ \tilde{M} &= K_r^2 / D \end{aligned} \qquad (1)$$

where

$$D = K_r(1 + \beta(K_r/\tilde{K}_f - 1) - \tilde{K}_b$$

Since each of the moduli in (1) is associated with a specific attribute of the model, it is possible to selectively incorporate realistic mechanisms for energy loss depending on the type of sediment being modeled. For example, in a granular sediment composed of hard, polycrystalline grains of fairly uniform size and shape, the sum of two kinds of energy dissipation result in the overall attenuation that is observed; one is the result of overall relative motion between the fluid and the skeletal frame which is controlled by the permeability of the frame and the other is friction at the intergranular contacts between particles. Since friction is an inherently nonlinear phenomenon, we are forced to use a linear approximation or a truncated constant complex modulus in order to keep the resulting equations of motion linear. Many viscoelastic models that result in an approximately constant value for the quality factor ,Q,have been proposed for this purpose (e.g., see [1] and [3]).

When there is no fluid in this kind of sediment, the attenuation of a propagating plane wave is a linear function of frequency since the energy loss per cycle is constant irrespective of frequency. When fluid is introduced into the voids, additional viscous damping occurs due to relative motion between the fluid and frame and since fluid mobility depends on the permeability, the frequency at which the effects of viscous damping become dominant depends on the intergranular pore size and geometry. In clean sands the effects of viscous damping begin to dominate at frequencies as low as 100 Hz whereas in sediments that contain significant amounts of much finer material, the effects may not be obvious until one reaches the high kHz region. The Biot parameters that control the fluid mobility are the permeability , the viscosity of the pore fluid, a pore-size parameter and a so-called structure factor (also sometimes referred to as an inertial coupling factor).

In addition to the global fluid motion, or "sloshing" as it is sometimes called, there is local fluid motion near the intergranular contacts and between adjacent cells in finer sediments composed of plate-like particles in a "cardhouse structure. This local flow, which occurs in a "hidden coordinate system" as Biot puts it, is generated by relative approach of particles causing squeeze-film motion or by the nonuniform volumetric strain of adjacent cells in the finer sediment. Hence, it is essentially in phase with the volumetric strain of the skeletal frame and its effect can be incorporated into the

model by the use of viscoelastic operators which operate on the bulk and shear moduli of the frame. This approach was used by Stoll and Bautista [4] to establish a baseline model for the soft sediments of Eckernfoerde Bay in the Baltic. They used a generalized viscoelastic model based on an adjustable distribution of relaxation times as proposed by Cole and Cole [7]. This formulation is one of many that have been used in the physical sciences to describe rate-dependent processes (e.g., see Gross [8]) and is particularly adaptable to the present problem because of the wide distribution of cell sizes and geometries that exist in real sediment which necessitates a correspondingly wide distribution of relaxation times.

The distribution function used in the Cole-Cole model is of the form

$$F(s)ds = \frac{1}{2\pi} \cdot \frac{\sin \alpha \pi \, ds}{\cosh(1-\alpha)s - \cos \alpha \pi} \tag{2}$$

where $s = \ln \tau/\tau_0$ and α controls the sharpness of the peak in a bell-shaped symmetrical distribution. (e. g., see Stoll [6], pg. 97). The distribution of relaxation times given by (2) results in a complex modulus with real part N_r and imaginary part N_i given by

$$\begin{aligned} N_r &= N_\infty - \frac{N_\infty [1 + (\omega \tau_0)^{1-\alpha} \sin(\alpha \pi/2)]}{1 + 2(\omega \tau_0)^{1-\alpha} \sin(\alpha \pi/2) + (\omega \tau_0)^{2(1-\alpha)}} \\ N_i &= \frac{N_\infty (\omega \tau_0)^{1-\alpha} \cos(\alpha \pi/2)}{1 + 2(\omega \tau_0)^{1-\alpha} \sin(\alpha \pi/2) + (\omega \tau_0)^{2(1-\alpha)}} \end{aligned} \tag{3}$$

N_∞ is an amplitude factor and τ_0^{-1} is the frequency at which N_i is maximum. The overall complex moduli of the skeletal frame are determined by adding the above modulus to a constant complex modulus that is determined on the basis of the sediment response at low frequency.

In modeling the soft, gassy sediments of Eckernfoerde Bay, parameters input to the Biot model were determined mainly on the basis of field experiments performed during the Coastal Benthic Boundary Layer Special Research Program sponsored by the Naval Research Laboratory. This sediment has an average porosity of 86% and a low permeability of the order of 5×10^{-11} cm ^{2} so that global relative fluid motion has a negligible effect on the response at frequencies less than about .5 MHz. Hence simplification to the Gassmann approximation is warranted and only the first of equations (1) is significant. Since the Biot equations reduce to the Gassmann equation when the fluid mobility is very low, no special treatment is necessary in using the full set of Biot equations except to choose the parameters controlling fluid motion (i.e., permeability, pore-size parameter and density coupling factor) to be of the right order of magnitude. The complex shear modulus, μ, was evaluated on the basis of measurements of shear wave velocity and attenuation at low frequency using Love wave measurements [9]. The three parameters for the Cole-Cole modification of the frame bulk modulus were chosen in order to match p-wave attenuation measurements at 58 and 400 kHz by Richardson and Briggs [10]. The attenuation predicted by the model is shown in Fig. 1 along with some historical data for ocean bottom silts and clays from Hamilton [5] and other sources (see [11] for a general review of attenuation measurements in marine sediments). The model predicts an increase of p-wave velocity from 1421 m/s at 1 Hz to 1434 to 1440 m/s at 400 kHz which is in agreement with the range of observed velocities in the Eckernfoerde experiments.

3. Effects of Free Gas as a Perturbation of the Baseline Model

When gas bubbles form in the pore water of a sediment, significant changes in the geoacoustic response occur. Much of the research on this topic through 1980 was summarized in two papers by Anderson and Hampton [12]. From their discussion and several more recent papers [13,14], it is clear that the size and distribution of the gas bubbles can be quite variable, ranging from a uniform distribution of small bubbles in the normal interstices of the sediment to large disruptive bubbles that create their own cavities to distributed regions of free gas that encompass volumes of sediment containing many grains. Hence the problem of modeling the effects of gas in a comprehensive way is quite challenging. In general,

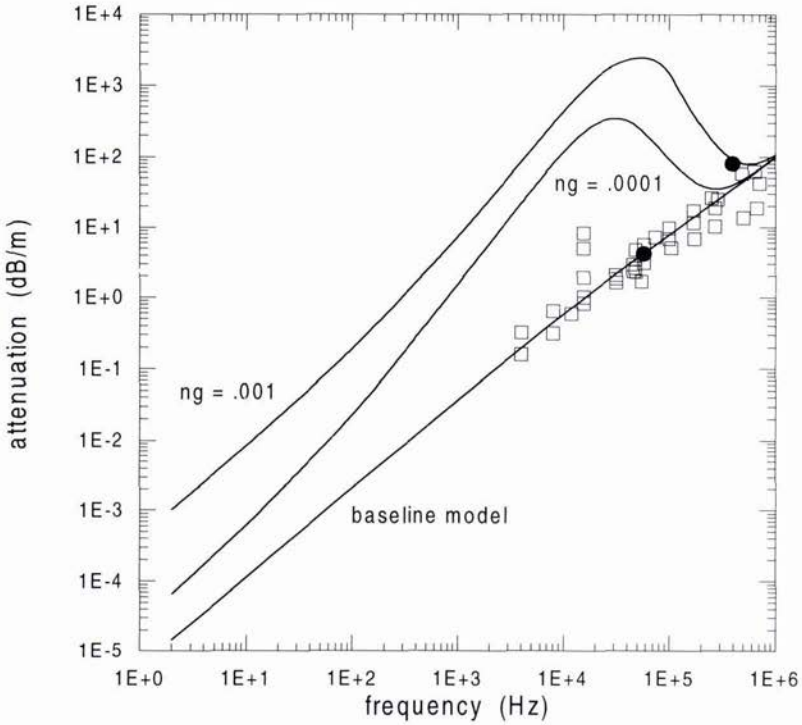

Fig. 1. Attenuation for baseline model and two cases of partial gas saturation. The historical data points are for clays and other fine-grained materials with the two solid symbols corresponding to the soft sediments of Eckernfoerde Bay.

significant changes in compressional wave speed and attenuation are to be expected and a pulsation of the bubbles in the frequency range near their resonance frequency can be expected to produce a marked effect on the geoacoustic response.

In order to incorporate the effects of bubbles into his model, Biot [3] suggested that the fluid compressibility be modified by invoking an operator that produced a phenomenological response similar to a simple harmonic oscillator such as the one shown in Fig. 2. By incorporating mass and damping elements, this model takes into account an inertia effect in the hidden coordinates and viscous dissipation arising from the concentrated radial velocity of the fluid in the vicinity of a bubble. In this model the compressibility of the fluid at frequencies well below resonance is essentially controlled by the elastic elements k_1 and k_2 acting in series so they are related to the quasistatic compressibility of the gassy sediment, $1/K'_w$, by

$$1/k_1 + 1/k_2 = [n_g K_w + (1 - n_g) K_g]/K_w K_g = 1/K'_w \tag{4}$$

where n_g is the fraction of sediment pore space occupied by gas and K_w and K_g are the bulk moduli of the water and gas respectively. At frequencies well above resonance the bubbles have insufficient time to compress and the apparent compressibility of the gassy fluid is essentially $1/k_2$ so that $k_2 = K_w$ and $k_1 = K_w K'_w / (K_w - K'_w)$. With these assumptions the model shown in Fig. 2 leads to a complex compressibility of the form

$$1/\bar{K}_f = 1/K_w + 1/[(k_1 - m\omega^2) + i c \omega] \tag{5}$$

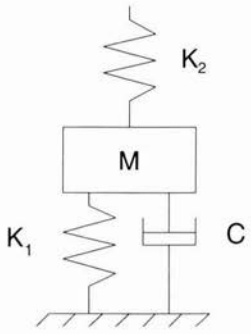

Fig. 2. Schematic of model for compressibility of gassy fluid suggested by Biot.

Since the viscosity, c, and mass, m, are parameters in a phenomenological model, which are not easily quantified in terms of physical variables such as bubble size and resonance frequency, it is useful to recast this equation in the form

$$1 / \bar{K}_f = 1 / K_w + 1 / k_1[1 - (\omega / \omega_n)^2 + i(2D\ \omega / \omega_n)] \tag{6}$$

wherein the damping ratio, D, may be written in terms of the inverse quality factor, 1/Q

$$D = (1/Q)/\sqrt{4 + (1/Q)^2} \tag{7}$$

and the undamped natural frequency, ω_n, related to the resonance frequency using

$$\omega_n = \omega_{resonance}/\sqrt{1 - 2D^2} \tag{8}$$

Hence the complex bulk modulus of the fluid, $\bar{K}_f$, can be introduced into the equations (1) once the resonance frequency and damping for the bubbles in a specific micro-model of the gassy sediment are determined. However, for the reasons mentioned above, this is a formidable task because of the wide variety of different configurations the gas may assume and a number of different approaches to this problem have been attempted . As examples, Anderson and Hampton [12] calculated resonance frequency using a hybrid equation based on historical equations derived for resonance of bubbles in water and in elastic solids whereas Dutta and Ode [15] studied the problem of radially oscillating gas pockets using the Biot theory applied to repeating cells containing a gas pocket in a porous matrix.

As an example of how the above equations modify the predictions of the baseline model, p-wave velocity and attenuation have been calculated for a hypothetical case where bubble resonance occurs at 20 kHz and overall damping of the pulsating bubbles results in a quality factor of approximately 1. While resonance frequencies are found to vary over a wide range depending on bubble size and water depth (i.e., from 2 kHz to over 600 kHz) these values were chosen as typical for soft, fine-grained sediment with bubble radius of the order of 0.5 mm on the basis of calculations given in [12]. Calculations were made for two different gas concentrations, n_g = .001 and .0001 (i.e., voids containing .1% and .01% gas by volume). The effect on attenuation by gas in these concentrations is shown by two curves in Fig. 1 and the

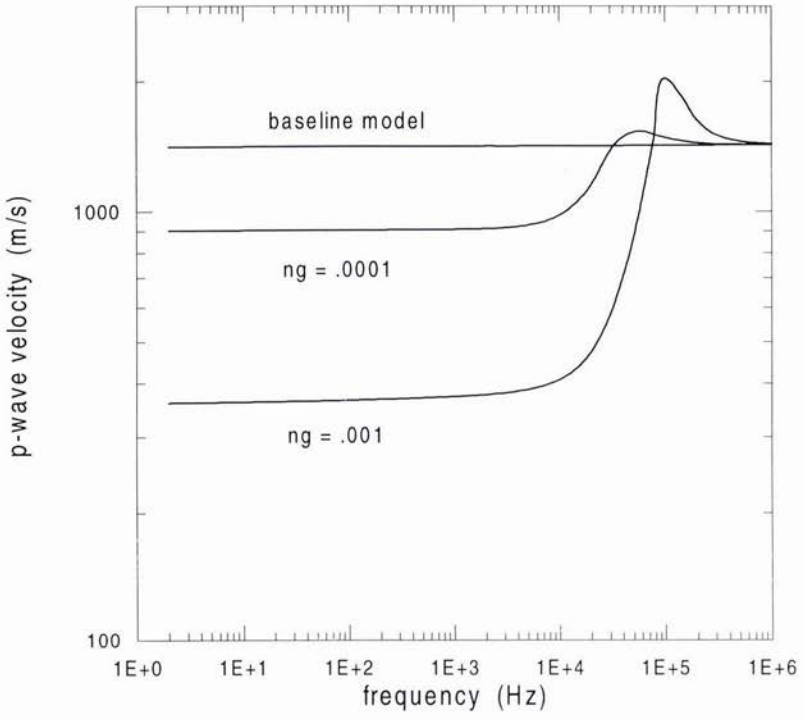

Fig. 3. P-wave velocity for baseline model and for two cases with partial gas saturation. Resonance frequency is 20 kHz and gas fraction of pore space is shown next to curves.

effect on p-wave velocity is depicted in Fig. 3. As can be seen from these figures, even the addition of a small amount of gas results in significant changes in velocity and attenuation. While the cases shown here are hypothetical, they illustrate how the effects of gas can be introduced as a perturbation on a carefully fitted baseline Biot model thus allowing comparative studies of the predictions of various micro-models for evaluation and comparison with experimental results. Moreover the simple model shown in Fig. 2 may be generalized to include the effects of a distribution of bubble sizes by casting the mass, viscous and elastic parameters as distribution functions in a manner similar to that used in Section 2 where a distribution of relaxation times based on the Cole-Cole model was used to modify the complex modulus of the skeletal frame.

4. Use of the Baseline Model in Scattering Studies and Other Cases of Interest

The usefulness of a baseline model in studies of scattering can be seen by considering the parameters used in a recent paper by Lyons et al [13]. The scattering model used in this paper depends on the resonance frequency of the bubbles in the sediment and on the attenuation of waves propagating in the sediment between the pulsating bubbles. These authors considered a scattering model because microscopic and radiographic studies of the pore structure revealed rather large, irregular gas pockets that suggested that scattering would become important at frequencies much lower than in cases where small gas bubbles were contained within the natural interstices of the sediment. Hence the dynamic shearing modulus of the sediment surrounding the bubbles becomes important in determining the resonance frequency, and the propagation characteristics of the sediment (p-wave velocity and attenuation) between larger bubbles, play a key role in constraining the scattering model. Unfortunately the proportion of gas present in bubbles smaller than about 1 mm was unknown, so that it is not clear what would be the most appropriate choice for these propagation characteristics given the important effects of very small amount of gas demonstrated in Section 3 above. In any event, it is felt that use of a baseline model and systematic parametric studies such as those demonstrated in Section 3 would be useful in defining the basic parameters necessary to constrain this kind of study since it forces the user to consider all pertinent input

parameters in an integrated way rather than choosing bits and pieces of experimental and historical data in an *ad hoc* manner.

Another perturbation of the basic Biot theory was recently proposed by Leurer [16] who incorporated more damping into the response of montmorillonite-rich fine-grained sediments by modelling the individual composite grains as viscoelastic to account for "squirt flow" from the interlayers of the montmorillonite. In this case the bulk modulus of the grains, K_r becomes complex with a frequency dependence that is determined by the form of viscoelastic operator that is chosen.

5. Summary and Conclusions

Several examples have been described wherein the basic Biot theory can be used as a baseline model in order to study the effects of different kinds of perturbing effects. These include the effects of local fluid motion in "hidden coordinate systems " caused by inter-cell flow or squeeze-film motion, the influence of free gas in the form of bubbles and the effects of anelastic particle response. In each case operator equations of the kind suggested by Biot have been used to modify the moduli of various components in the baseline model which serves as a reference for assessing the relative influence of the perturbing effect. In the case of scattering studies, the baseline model constrains the choice of input parameters which have often been chosen in an *ad hoc* and sometimes unrealistic manner.

Thus the Biot theory allows more realistic modelling of the physical mechanisms that control energy loss, compressibility and shear stiffness, allowing each to be assigned to the most appropriate component of the sediment. Moreover it forces the user to consider the response of the sediment over a wide range of frequencies, taking into account all of the interacting physical mechanisms rather than concentrating on a single mechanism over a narrow bandwidth wherein predominant trends in overall behavior may be overlooked.

6. Acknowledgment

The work described in this paper was supported by the Office of Naval Research, Code 321 (Ocean Acoustics)

References

[1] R. D. Stoll and G. M. Bryan, "Wave Attenuation in saturated sediments," *J. Acoust. Soc. Am.*, vol. 47, pp. 1440-1447, 1970.
[2] M. A. Biot, "Mechanics of deformation and acoustic propagation in porous dissipative media," *J. Appl. Phys.*, vol. 33, pp. 1482-1498, 1962.
[3] M. A. Biot, "Generalized theory of acoustic propagation in porous dissipative media," *J. Acoust. Soc. Am.*, vol. 34, pp. 1254-1264, 1962.
[4] R. D. Stoll and E. O. Bautista, "Using the Biot theory to establish a baseline geoacoustic model for seafloor sediments," *Continental Shelf Res.*, submitted - unpublished.
[5] E. L. Hamilton, "Compressional-wave attenuation in marine sediments," *Geophysics*, vol. 37, pp. 620-646, 1972.
[6] R. D. Stoll, Sediment Acoustics, New York, Springer-Verlag, 1989.
[7] K. S. Cole and R. H. Cole, "Dispersion and adsorption in dielectrics," *J. Chem. Physics*, vol. 9, pp. 341-351, 1941.
[8] B. Gross, Mathematical Structure of the Theories of Viscoelasticity, Paris, Hermann, 1953.
[9] E. O. Bautista and R. D. Stoll, "Remote determination of *insitu* sediment parameters using Love waves," *J. Acoust. Soc. Am.*, vol. 98, pp. 1090-1098, 1995.
10] M. D. Richardson and K. B. Briggs, "The effects of methane gas bubbles on the sediment geoacoustic properties in Eckernfoerde Bay," *Proc. Workshop Modelling Methane-Rich Sediments of Eckernfoerde Bay*, Editor T. Wever, pp.199-206, 1995.
[11] A. Kibblewhite, "Attenuation of sound in marine sediments: A review with emphasis on new low-frequency data," *J. Acoust. Soc. Am.*, vol 86, pp. 716-738, 1989.
[12] A. L. Anderson and L. D. Hampton, "Acoustic of gas-bearing sediment I. Background and II. Measurements and models,"*J. Acoust. Soc. Am.*, vol. 67, pp. 1865-1903, 1980.
[13] A. P. Lyons, M. E. Duncan, A. L. Anderson and J. A. Hawkins, "Predictions of acoustic scattering response of free-methane bubbles in muddy sediment," *J. Acoust. Soc. Am., vol. 99, pp. 163-172, 1996.*
[14] G. C. Sills, S. J. Wheeler, S. D. Thomas and T. N. Gardner, "Behavior of offshore soils containing gas bubbles," *Geotechnique,* vol. 41, pp. 227-241, 1991.
[15] N. C. Dutta and H. Ode, "Attenuation and dispersion of compressional waves in fluid-filled porous rocks with partial gas saturation (White model)-Part 1: Biot theory," *Geophysics,* vol. 44, pp. 1777-1788, 1979.

[16] K. C. Leurer, "Velocity and absorption of acoustic waves in fine-grained marine sediments - extension of Biot-Stoll model by the effective grain model," Excerpt from Doctoral Dissertation, Institut fur Geophisik, Univ. Keil, Germany, 1995.

Intensity moments of underwater sound scattered by a Gaussian spectrum corrugated surface: Measurements and comparison with a catastrophe theory approximation

John S. Stroud* and Philip L. Marston

Department of Physics
Washington State University
Pullman, WA 99164-2814

Kevin L. Williams

Applied Physics Laboratory
University of Washington
Seattle, WA 98105

* Current Address: University of Cincinnati, Department of Radiology, Cincinnati, OH 45267-0579

Abstract

An underwater forward-scattering investigation was undertaken with a random rough corrugated pressure release surface manufactured out of Styrofoam. Measured wavefields associated with the reflection caustics agree with predictions. The frequency dependence of the m*th higher-order intensity moments* I_m *was measured and compared to theoretical predictions. The dependence of* I_2 *on distance from the surface was also investigated.*

[This work was partially supported by the Office of Naval Research.]

1. Introduction

The interaction of an incident wavefield with a non-planar surface can introduce regions of focusing in the scattered (reflected or transmitted) portion of the wavefield. The solution to the scattered pressure is simply the Helmholtz-Kirchoff integral. In general, this integral can not be solved analytically, so one uses numerical techniques that involve approximations (e.g. stationary phase approximation). However, in the regions of focusing, (the caustics) the stationary phase approximation breaks down. Therefore an extension to that approximation that can handle the focusing effects of caustics is in order. Once the extension has been made, then information regarding the caustic structure itself can be used to extract physical insight to the underlying processes.

An extension to the stationary phase approximation for corrugated surfaces has been derived [1]. The extension is

$$P(\mathbf{x}_s,\mathbf{x}_r,t) \cong e^{-i\omega t}\left[k^0\sum_{j=0}^{J} a_j e^{ik(\underline{R}_{r,j}+\underline{R}_{s,j})} + k^{\frac{1}{6}}\sum_{l=0}^{L} b_l \,\mathrm{Ai}\left(k^{\frac{2}{3}}w_l\right)e^{ik(\underline{R}_{r,l}+\underline{R}_{s,l})} + k^{\frac{1}{4}}\sum_{q=0}^{Q} d_q \,\mathrm{P}_{\pm}\left(k^{\frac{1}{2}}w_{2,q},k^{\frac{3}{4}}w_{1,q}\right)e^{ik(\underline{R}_{r,q}+\underline{R}_{s,q})}\right] \tag{1}$$

where P is the pressure amplitude at time t measured at receiver location $\mathbf{x}_r$ due to a source located at $\mathbf{x}_s$, k is the wave number, ω is the angular frequency, Ai is the Airy function, $\mathrm{P}_{\pm}$ is the Pearcey function, $\underline{R}_{r,n}$ ($\underline{R}_{s,n}$) represent the distance from the receiver (source) to the nth scattering point on the surface. The other terms (a_j, b_l, d_q, and the w) are all geometric terms depending upon the locations of the source and receiver as well as the particular scattering surface. The three summations in (1) represent the three different types of contributions one can obtain for the particular class of problem at hand. The j sum represents the standard ray approximation (no echoes having merged), the l sum represents the merging of two rays (referred to as fold terms), and the q sum represents the merging of three rays (called cusp terms). Some regions have only rays, some only folds, some only cusps, and some have mixtures of the three.

1.1 Surface Generation

The formulation of (1) explicitly assumes a one-dimensional corrugated surface. A one-dimensional surface is a surface whose height function depends only upon one of its coordinates, $z(x,y) = z(x)$. A computer program capable of generating realizations of a population of Gaussian spectrum random rough corrugated surfaces with root-mean-square (rms) roughness 1.5 cm, and correlation length 10 cm was used to generate a number of such surfaces. From this number, a particular surface realization was selected for manufacture out of Styrofoam. The physical dimensions of the surface were about 1 m wide by 1.5 m long. The variations were in the long dimension. This surface then served as a pressure release surface in the underwater investigation. Since the surface profile was specified numerically, the same surface was used in the computer implementation of (1) as well as the underwater experiments. The caustics of this surface are those for the reflected wavefield. (For a picture of the caustics for this surface, see Figure 3 of [1].)

1.2 Source/Receiver

A broad-band omnidirectional source was operated in the frequency range of 95-400 kHz. The source was located approximately 1.1 m from the surface, and the receiver was scanned from 5 cm to 60 cm from the surface. Two types of pulses were of interest, the first were "short" pulses (similar to single cycle pulses used for B-Mode imaging in clinical diagnostic ultrasound) and the second were "long" pulses or tone-bursts (similar to Doppler ultrasound pulses). The short pulses allowed us to isolate the effect of individual contributions to the reflected signal (this corresponds to knowing the values for J, L, and Q in (1) and tracking them individually). The long pulses allow the various contributions to interfere and thus approximate the steady state field scattered from the surface.

Since the pulse would be used in the underwater experiments and in the computer simulation of (1), the frequency content needed to be minimize. In order to minimize the bandwidth of the output signal, a sine wave modulated by a cosine-squared envelope pulse was used. This pulse was synthesized by a computer and drove the signal generator. The equation that gives the pulse shape is the real part of

$$\begin{array}{ccc} 0 & , & t < t_0 \\ i\exp(-i2\pi ft)\cos^2 2\pi F(t-t_1) & , & t_0 < t < t_1 \\ i\exp(-i2\pi ft) & , & t_1 < t < t_2 \\ i\exp(-i2\pi ft)\cos^2 2\pi F(t-t_2) & , & t_2 < t < t_3 \\ 0 & , & t > t_3 \end{array} \qquad (2)$$

where f is the center frequency of the tone burst, F is the envelope parameter given below, and t_j (with j=0,1,2,3) are times related to the number of cycles in the burst. The relations of the t_j to t_s (the time for the center of the burst) are as follows:

$$\begin{array}{ll} t_0 = t_s - \dfrac{1}{f}\left(\dfrac{n_{cw}+n_{env}}{2}\right) & t_1 = t_s - \dfrac{1}{f}\dfrac{n_{cw}}{2} \\ t_2 = t_s + \dfrac{1}{f}\dfrac{n_{cw}}{2} & t_3 = t_s + \dfrac{1}{f}\left(\dfrac{n_{cw}+n_{env}}{2}\right) \end{array} \qquad (3)$$

where n_{env} (n_{cw}) is the number of cycles in the envelope (steady state) region of the burst. To calculate the envelope parameter F, use

$$F = \frac{f}{2n_{env}}. \tag{4}$$

The cosine squared envelope was chosen to start at a time such that the zero of the envelope corresponded to the first zero in the first cycle. The maximum of the envelope would occur when the oscillations under the envelope crossed through a center zero (antisymmetric about the center of the pulse). This resulted in pulses with integral number of cycles. The number of cycles chosen depended on the center frequency of the pulse and were set to maintain quasi-constant bandwidth over the signals of interest. For example one frequency cycle number combination is 125 kHz 4 cycle: This choice gives a bandwidth for the envelope of approximately 15 kHz. By keeping this bandwidth constant, the following combinations were utilized: 95 kHz 3 cycle, 200 kHz 6 cycle, 250 kHz 8 cycle, 275 kHz 8 cycle, and 400 kHz 12 cycle. Figure 1 shows a representative synthesized pulse for a case without and with steady state cycles.

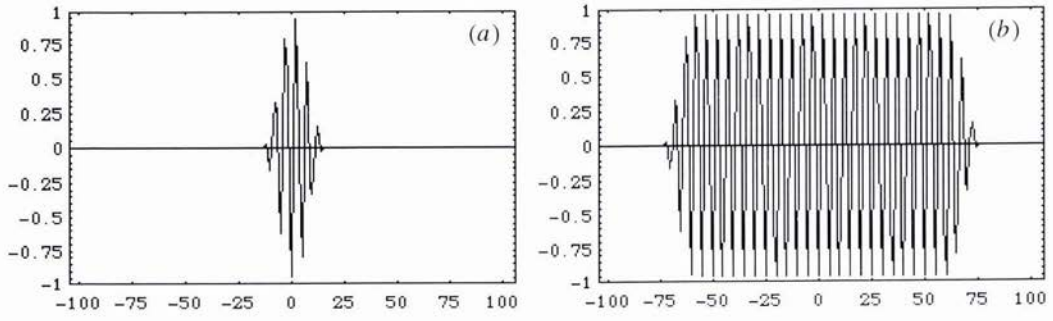

Figure 1. Representative types of pulses used. Panel (a) shows a 200 kHz center frequency with a cosine squared envelope, a total of 6 cycles are present. This sort was used in both types of experiments. Panel (b) shows the same 200 kHz center frequency and the ends are 6 cycles with the cosine squared envelope, the middle portion contains 24 cycles with unit amplitude envelope. This sort was used only in the Gaussian recovery experiments.

2. Experiments

Though two distinct types of experiments were performed, the methods and procedures were nearly identical. In both cases, the measurement of the reflected wavefield was the goal. In the first type of experiment (which will be called twinkling exponent type) the incident frequency was the primary variable changed. In the second type (called Gaussian recovery) the pulse duration (number of cycles) was the primary variable changed. The frequency was held constant for this type.

The experiments were conducted in a 7'6" deep by 8' diameter yellow-pine tank, filled with filtered tap-water. A corrugated Styrofoam surface was mounted at one "end" of the tank. The source was located 1.1 m away from the surface, at the same depth in the water tank as the top of the surface, and in the midplane of the surface. The top of the surface was designated as the origin for the scattered wavefield geometry. In the geometry of the surface (no y dependence) the source was located at $(x_s, z_s) = (1.1, 0)$ where the distances are in meters.

A broadband omnidirectional receiver was used to sample the scattered wavefield for a variety of receiver locations (x_r, z_r). A computer-controlled two-dimensional positioning system was used to move the receiver to scan the reflected wavefield. The total effective range of scanning is 1.4 m by 0.75 m. A schematic of the experimental setup is shown in Figure 2. The pressure amplitudes were measured at each receiver location for each frequency of interest. The computer simulation using (1) would be ran over the same receiver locations. The results could then be compared.

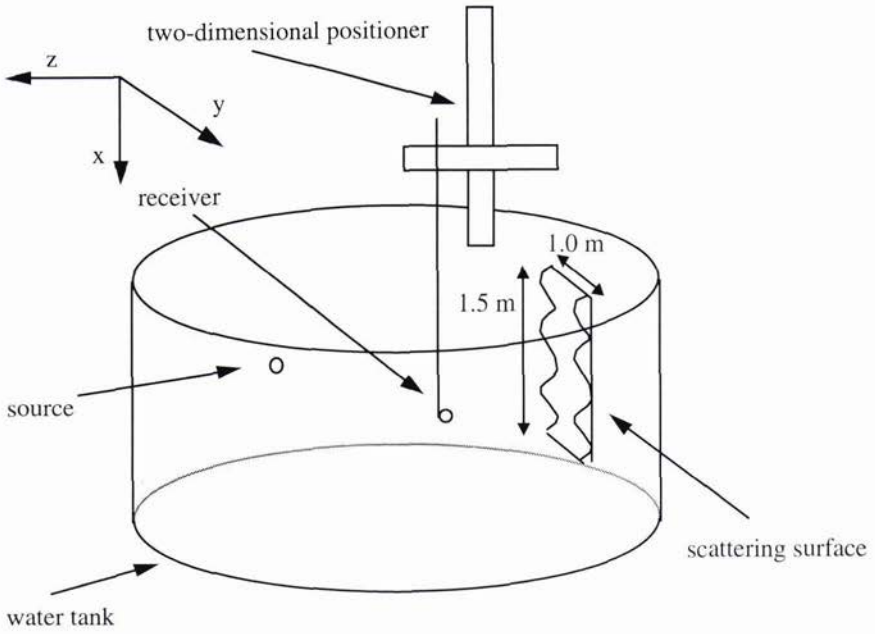

Figure 2 Schematic of experimental setup.

3. Extraction of frequency dependence

In a harmonic acoustical wave field, the intensity I is taken to be proportional to $|P(x,y,z)|^2$ where P is the pressure amplitude at a receiver location (x,y,z). Thus for this setup the mth normalized moment of the intensity becomes

$$I_m = \frac{\langle I^m \rangle}{\langle I \rangle^m} = \frac{\langle |P(x,y,z)|^{2m} \rangle}{\langle |P(x,y,z)|^2 \rangle^m} \tag{5}$$

where $\langle\ \rangle$ denotes a spatial average over the scattered wavefield from the surface. From (5) it is obvious that $I_1 = 1$ which is clearly independent of k. This is simply the statement that the energy flux (proportional to I_1) is not altered by phase perturbations. For the remaining moments, the behavior depends upon the number of contributors, (pulse echoes) interacting at a given site. The number of contributors determine the values of J, L, and Q for (1).

3.1 Theoretical predictions

3.1.1 Small number of contributors

When the number of contributors is small and caustics are dominating the wave field, then the higher moments ($m > 1$) diverge with increasing k. Berry [2] showed that this divergence scales with k according to

$$\langle I^m \rangle = C_m \langle I \rangle^m k^{\nu_m} \quad , \quad \nu_m > 0 \quad , \quad m > 2 \tag{6}$$

where ν_m is the twinkling exponent for the mth moment and C_m is a coefficient related to the random medium (in this case the surface). Note that by using the formalism of (5) the normalized moments I_m will retain only the k^{ν_m} dependence. In addition the requirement in (6) that $m > 2$ follows because the leading dependence on k is different for $m = 2$. The form of (5) gives,[2]

$$\nu_m \equiv \lim_{k\to\infty} \frac{d}{d\ln k}(\ln I_m) \tag{7}$$

which is insensitive to factors of $\ln k$ in I_m. Thus the second moment *which is proportional to* $\ln k$ is predicted to have $\nu_2 = 0$ and (7) does not capture the dependence on $\ln k$. (For a discussion of the $\ln k$ dependence, see section 1 of [3] and the references cited therein.)

The results of catastrophe theory predict that the contribution to I_m from the jth class of catastrophe is [2-6]

$$I_{m,j} \propto k^{\nu_{m,j}} \quad , \quad \nu_{m,j} = 2m\beta_j - \gamma_j \tag{8}$$

where β_j describes the increase of the amplitude for increasing k at the caustic while γ_j describes the decreasing focal volume. Thus the $\nu_{m,j}$ exponent is a competition between these two effects.

For any corrugated surface only cuspoids need to be considered. For the geometry of the surface used in this investigation, however, the full list is not required; only the fold (or A_2) and cusp (or A_3) are necessary. For the fold ($j = 1$)

$$\beta_1 = \tfrac{1}{6} \quad , \quad \gamma_1 = \tfrac{2}{3} \tag{9}$$

and for the cusp ($j = 2$),

$$\beta_2 = \tfrac{1}{4} \quad , \quad \gamma_2 = \tfrac{5}{4} \tag{10}$$

So combining (8) and (9) yields the twinkling exponents associated with the fold as

$$\nu_{m,1} = \tfrac{m-2}{3} \tag{11}$$

and combining (8) and (10) yields the twinkling exponents for the cusp as

$$\nu_{m,2} = \tfrac{2m-5}{4} \tag{12}$$

Since the I_m are defined as ensemble averages, as $k \to \infty$ the largest of the available $\nu_{m,j}$ will determine how I_m diverges. For the two cuspoids available, the possible ν_m are (for the fold)

$$\nu_{3,1} = \tfrac{1}{3} \quad , \quad \nu_{4,1} = \tfrac{2}{3} \quad , \quad \nu_{5,1} = 1 \tag{13}$$

and (for the cusp)

$$\nu_{3,2} = \tfrac{1}{4} \quad , \quad \nu_{4,2} = \tfrac{3}{4} \quad , \quad \nu_{5,2} = \tfrac{5}{4} \tag{14}$$

thus the largest of each of these gives

$$\nu_3 = \tfrac{1}{3} \quad , \quad \nu_4 = \tfrac{3}{4} \quad , \quad \nu_5 = \tfrac{5}{4} \tag{15}$$

However, the experimental setup is such that almost all of the data are taken from regions that exclude the cusp points. This means that although (15) represents the twinkling exponents one should expect *if the entire wavefield were measured in the* $k \to \infty$ *limit*, for an experiment with only a few cusps and a limited range of k, the exponents are expected to be close to those of fold caustics alone [given by (14)]. Therefore for this experimental work, the predicted approximate functional dependence for the second through the fifth moments are:

$$I_2 \propto \ln k \quad , \quad I_3 \propto k^{1/3} \quad , \quad I_4 \propto k^{2/3} \quad , \quad \text{and} \quad I_5 \propto k \quad . \tag{16}$$

The hypothesis tested in the experiments is that these catastrophe theory predictions are correct.

3.1.2 Large number of contributors

When the number of contributors is large, which corresponds to receiver locations far from the rough surface, the real and imaginary components of the complex amplitude pressure become Gaussian distributed. Gaussian quadrature fields imply an amplitude, $|P|$, that obeys a Rayleigh probability density function [7]. The resulting intensity distribution will obey a negative exponential probability density function (PDF). The probability density function of intensity becomes the exponential distribution:

$$p_I(I) = \frac{1}{\langle I \rangle} \exp\left(-\frac{I}{\langle I \rangle}\right) \quad , \quad I \geq 0 \quad . \tag{17}$$

By knowing that a random process whose quadrature fields obey Gaussian statistics yields an exponential intensity PDF, a means of checking if a random process is Gaussian is evident: If the measured intensity PDF is not consistent with the predicted exponential PDF then this suggests that the process is not Gaussian. This is important because the focusing discussed previously is highly non-Gaussian. As such if the wave field is being dominated by caustics then the measured intensity PDF should not be in agreement with (17).

In addition, the moments for the exponential distribution are known to be [8]

$$\langle I^m \rangle = m! \langle I \rangle^m , \tag{18}$$

thus giving normalized moments of

$$I_m = m! . \tag{19}$$

Clearly (19) has no frequency dependence in it and thus does not diverge as $k \to \infty$. This is in direct contradiction of the predictions using (6) so the interaction of the number of contributors is clearly important.

3.2 Measurements

The results for four data runs are shown in Figure 3. The specifics for each of the data sets are in Table 1.

Set	X_r range (m)	Z_r range (m)	Number of sampled points	Frequencies used (kHz)			
1	0.1 -> 1.35	0.20 -> 0.21	2505	95	125	275	
2	0.1 -> 0.6	0.20 -> 0.26	5025	95	125	275	
3	0.1 -> 0.65	0.04 -> 0.44	5082	95	125	200	250
4	0.1 -> 0.5	0.18 -> 0.22	2737	95	125	200	

Table 1: Experimental conditions for twinkling exponent measurements

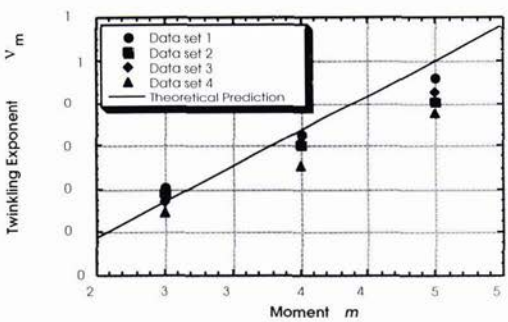

Figure 3 The results for the twinkling exponents vs. moment number for the four data sets. The line shows the theoretical prediction (13) for the fold case.

Since part of the work involved an improved numerical technique based on(1), the resulting computer simulation code was also tested for similar regions of interest as the experimental regions. The two experimental sets labeled 3 & 4 in Figure 3 were used as the basis for simulation runs 1 & 2. The results for the simulation runs are shown in Figure 4. The region scanned in data set 3 (4) is labeled as simulation 1 (2). The frequencies in simulation 2 are the same as for those used in data set 4. Due to computer time constraints, simulation 1, used only the lowest three frequencies from the experiment and the simulated region was reduced slightly.

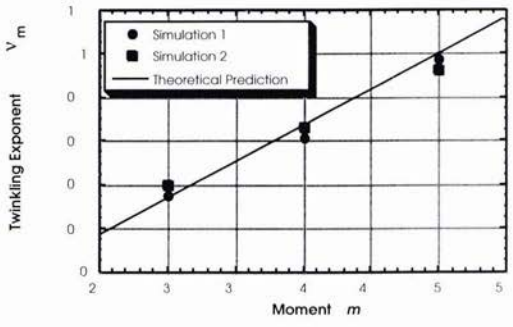

Figure 4 The results for the twinkling exponents vs. moment number for the two computer simulation sets. The simulation was an implementation of (1). The line shows the theoretical prediction for the fold case based on (13).

4. Extraction of distance dependence for I2

A separate set of experiments was performed to test the prediction that the second moment behavior depended upon distance from the surface as well as number of echoes. For these experiments, the pulses used were those with the long unit amplitude envelope shown earlier. These pulses were long enough that the various echoes could interfere with each other and allow the recovery of the Gaussian wavefield moments.

For both the experimental data and the simulation data (shown in Figure 5), the second moments started out below the Gaussian limit of 2! and grew as the region of the cusps was encountered. After reaching a maximum, the value would begin to decrease with distance. For the short pulses, the value would decrease below the 2! limit. For the long pulses, the value would settle near 2! at approximately 30 cm from the surface.

The experimental conditions are show in Table 2.

X_r range (m)	Z_r values (m)			Short Pulse	Long Pulse
0.1 -> 1.4	0.035	0.06	0.2	200 kHz	200 kHz
	0.04	0.07	0.25	6 cycles	30 cycles
	0.045	0.08	0.3		
	0.05	0.1	0.4		
	0.055	0.15	0.5		

Table 2: Experimental conditions for Gaussian recovery measurements.

5. Conclusions

In a caustic dominated wavefield, the higher order moments of the intensity ($m > 2$) were found to increase as the wave number to an exponent as predicted by theory. High-frequency approximations based on catastrophe theory were demonstrated to give physical insight into the non-Gaussian behavior of the intensity statistics in the caustic dominated portion of the wavefield. It also explains the transition to the classical Gaussian result for regions where the number of ray contributors is large.

The effort documented here was carried out after a forward scattering experiment off of the arctic ice canopy [9] revealed merging of echoes. The results are relevant to other rough surfaces or volume propagation through inhomogeneities if these problems are dominated by large scale (relative to the acoustic wavelength) features. For surfaces with both large and small scale features further research is needed to understand how the small scale features effect the wavefield and thus the higher order moments of the scattered intensity.

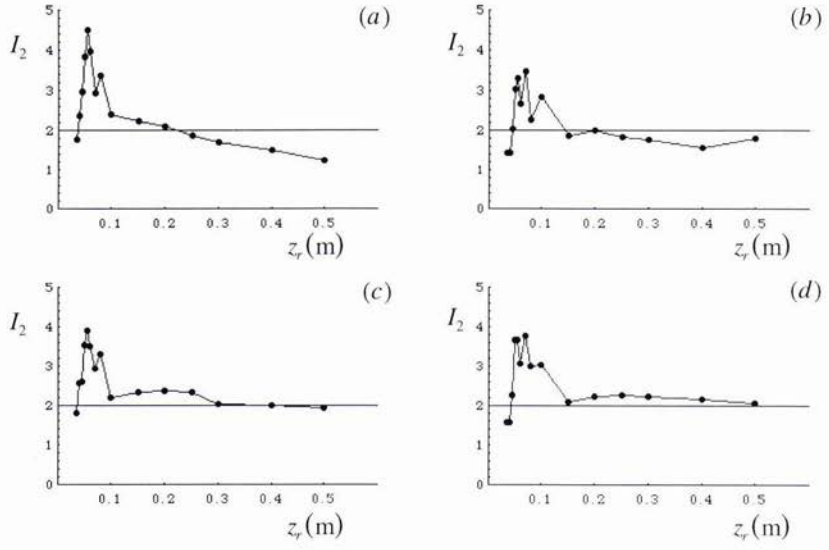

Figure 5 The normalized second moment as a function of distance from the surface. The Gaussian limit of 2! is shown for reference. Panels (a) data and (b) simulation are for the short pulse. Panels (c) data and (d) simulation are for the long pulse.

References

[1] K. L. Williams, J. S. Stroud, and P. L. Marston, "High-frequency forward scattering from Gaussian spectrum, pressure release, corrugated surfaces. I. Catastrophe theory modeling," *J. Acoust. Soc. Am.* **96**, 1687-1702 (1994). Throughout, the abnormal convention has been adopted that for a pressure release surface, the reflection coefficient $\Re = +1$.

[2] M. V. Berry, "Focusing and twinkling: critical exponents from catastrophes in non-Gaussian random short waves," *J. Phys. A. Math. Gen.* **10**, 2061-2081 (1977).

[3] J. G. Walker, M. V. Berry, and C. Upstill, "Measurements of twinkling exponents of light focused by randomly rippling water," *Optica Acta* **30**, 1001-1010 (1983).

[4] M. V. Berry and C. Upstill, "Catastrophe optics: morphologies of caustics and their diffraction patterns," in Progress in Optics XVIII, edited by E. Wolf (North-Holland, Amsterdam, 1980) pp. 257-346.

[5] M. V. Berry, "Twinkling exponents in the catastrophe theory of random short waves," in Wave Propagation and Scattering, edited by B. J. Uscinski (Clarendon, Oxford, 1986) pp. 11-35.

[6] J. H. Hannay, "Intensity fluctuations beyond a one-dimensional random refracting screen in the short-wavelength limit," *Optica Acta* **29**, 1631-1649 (1982).

[7] J. W. Goodman, Statistical Optics, (Wiley, New York, 1984), see especially Sec 4.2

[8] S. M. Flatté, "Wave propagation through random media: contributions from ocean acoustics," *Proc. IEEE* **71**, 1267-1294 (1983).

[9] K. L. Williams and D. E. Funk, "High frequency forward scattering from the arctic canopy: Experiment and high frequency modeling," *J. Acoust. Soc. Am.*, **96** 2956 - 2964 (1994)

Wavefront Curvature Ranging as a Passive Synthetic Aperture Problem

E. J. Sullivan

Code 82101
Naval Undersea Warfare Center
1176 Howell St.
Newport RI, 02841, USA
E-mail: sullivanej@tech.npt.nuwc.navy.mil

Abstract

A new method of wavefront curvature passive ranging is introduced that is based on a model-based approach. The signal and measurement systems are placed into state-space form, thereby allowing the unknown parameters of the model, such as the signal bearing, range, and source frequency to be estimated by an extended Kalman filter. Since the processor treats the parameters of interest as unknown parameters to be estimated, there is no explicit beamformer structure. After a theoretical exposition of the underlying theory. The performance of the processor is evaluated with synthesized data sets. The results indicate that the method is a highly effective approach.

1. Introduction

Recent studies in ocean acoustic model based processing (MBP) have shown it to be a very effective technique, since it allows the introduction of the signal and propagation models directly into the signal processing structure in a self-consistent manner. The approach is based on casting the problem into state-space form. There are basically two sets of equations in the MBP representation: the state equations themselves, and the measurement equations, which relate the states to the actual measured quantities. In the stochastic case, a Gauss-Markov representation evolves, which allows the inclusion of both the measurement noise and the state or "process" noise as second-order statistical models. Once this framework is established, it is possible to investigate ocean acoustic signal processing problems in a very general way, since full advantage can be taken of existing systems theory (e.g., observability, identifiability) and techniques (Kalman state estimators) to characterize a recursive processor which constitutes a minimum-variance, adaptive estimator [1-4]. That is, the so-called innovation sequence, which is automatically generated by the Kalman filter, allows the performance of the model to be monitored, while at the same time Kalman estimators can be utilized on-line to continuously update model parameters, such as the sound speed profile, thus making great inroads into the so-called *mismatch problem* [5]

In this study we shall consider the problem of estimating the range, bearing, and source frequency of a narrow band source with a towed array. In the next section we shall formulate the problem under the assumption that the signal at the array can be modeled as a circular wavefront [6] This permits the time delay between a given hydrophone and the circular wavefront to be expressed as a function of the hydrophone's position as a function of time. This formulation is then put into state space form. This leads to approximate minimum variance estimates of the parameters. These estimators take the form of an extended Kalman filter.

The formulation of the model is given in the next section. This is followed by the state space form of the processor in Section 3. Section 4 evaluates the performance of the processor using synthetic data and the last section contains a discussion of the results.

2. Circular Wavefront Model

The geometry and kinematics are depicted in Figure 1 where a single hydrophone is considered. The initial bearing θ_0, and initial range, r_0 are related to the instantaneous range $r(t)$ by the law of cosines. That is

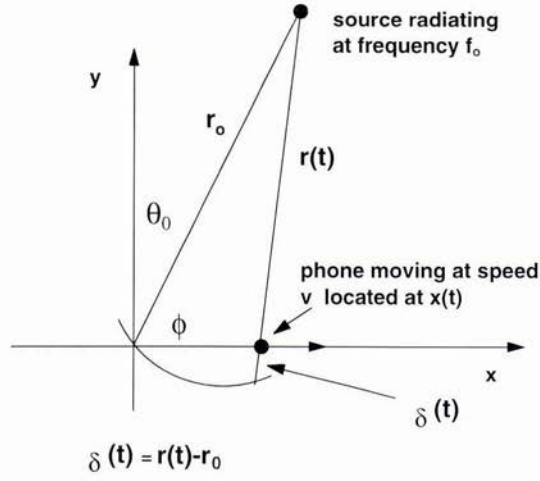

Figure 1: Geometry of example scenario

$$r^2(t) = r_0^2 + x^2(t) - 2r_0x(t)cos\phi. \tag{1}$$

Since $\cos\phi = sin\theta_0$, (1) becomes

$$r^2(t) = r_0^2 + x^2(t) - 2r_0x(t)sin\theta_0. \tag{2}$$

The difference between r_0 and the range at time t, denoted by δ, is

$$\delta = r_0 - r(t) = r_0 - r_0\left[1 + (x(t)/r_0)^2 - 2(x(t)/r_0)sin\theta_0\right]^{1/2}. \tag{3}$$

Thus, the travel time from the hydrophone position and the wavefront is

$$\tau = \delta/c \tag{4}$$

where c is the speed of sound.

Now consider an N element array where the first hydrophone is located at the origin ($x(0) = 0$). We denote the value of the travel time for the nth hydrophone as τ_n where $\tau_n = \delta_n/c$ and

$$\delta_n = r_0[1 - S_n(t)] \tag{5}$$

with the definitions

$$S_n(t) = \left[1 + (x(t)_n/r_0)^2 - 2(x(t)_n/r_0)sin\theta_0\right]^{1/2} \tag{6}$$

and

$$x_n(t) = x_n(0) + vt. \tag{7}$$

Here, v is the speed of motion of the nth hydrophone along the x axis, and $x_n(0)$ is the position of the nth hydrophone at $t = 0$. Although it is not necessary, for simplicity we shall assume the values of r_0 and θ_0 to be the same for all hydrophones. This is equivalent to assuming that the aperture of the array is small compared to the range of the source.

3. State-Space Form

In order to cast our problem into state space form, we define the state vector as $[r_0\ f_0\ \phi_0]'$. The corresponding system equation is given by

$$\frac{d}{dt}\begin{bmatrix} r_0 \\ f_0 \\ \phi_0 \end{bmatrix} = \begin{bmatrix} 0 & 0 & 0 \\ 0 & 0 & 0 \\ 0 & 0 & 0 \end{bmatrix}\begin{bmatrix} r_0 \\ f_0 \\ \phi_0 \end{bmatrix}. \tag{8}$$

Assuming a narrow band source, the resulting measurement equation, which models the hydrophone outputs, is

$$\begin{bmatrix} p_1 \\ \vdots \\ p_N \end{bmatrix} = \begin{bmatrix} e^{i\omega_0(t+\tau_1)} \\ \vdots \\ e^{i\omega_0(t+\tau_N)} \end{bmatrix}. \tag{9}$$

The fact that the propagator matrix in (8) is zero means that the parameter vector is being treated as a constant, i.e., there are no dynamics to the system. Since the measurement equation is nonlinear in the parameters of interest, it will be necessary to implement the so-called extended Kalman filter (EKF). The EKF represents the nonlinearities with a first order Taylor series approximation. The necessary derivatives for this approximation are contained in the Jacobian matrix, which we denote as CJ, where

$$CJ = \begin{bmatrix} \frac{\partial p_1}{\partial r_0} & \frac{\partial p_1}{\partial f_0} & \frac{\partial p_1}{\partial \theta_0} \\ \vdots & \vdots & \vdots \\ \frac{\partial p_N}{\partial r_0} & \frac{\partial p_N}{\partial f_0} & \frac{\partial p_N}{\partial \theta_0} \end{bmatrix}. \tag{10}$$

Equations 8, 9, and 10 c ompletely define the necessary equations to implement the EKF. We use the discrete form of the equations and carry out the caluclations on SSPACK [7]. Those readers who interested in the details of the implementation of the EKF are directed to [1].

4. Performance Analysis

The synthetic time series generated to test our algorithm is based on the source - receiver configuration depicted in Figure 1. Here, a stationary point source is radiating at a frequency $f_0 = 51.0\ Hz$. Although the technique is clearly not limited to high frequencies alone, we use a low frequency in our example for the purpose of computational expediency. If the source were moving, the Kalman filter would track the slowly changing bearing The receiving array is assumed to be moving at speed v in the x direction. r_0 and θ_0 are, respectively, the initial ($t = 0$) range and bearing of the source. In the following examples, the true values of r_0 and θ_0 are 2000 meters and 25°. $r(t)$ is the instantaneous value of the range to the single hydrophone shown in the Figure. The towed array is assumed to have four hydrophones spaced at 15 meters moving at a speed of 5 meters/sec. This constitutes a physical aperture of 45 meters. Since the aperture is much shorter than the range r_0, we shall assume that $r(t)$, r_0, and θ_0 are the same for all four hydrophones. Although this assumption is not necessary, it simplifies the kinematics of the example.

In Figure 2, the estimates of r_0 and θ_0 for the case of 0 dB SNR are shown. Here, it is assumed that the bearing θ_0 is known *a priori*. It could be obtained, for example, from an initial array bearing measurement. The Kalman filter was initialized with a range of 3000 meters and a source frequency of 51.1 Hz. As can be seen, the source frequency converged quite rapidly, whereas the range required a full minute. In Figure 3, everything is the same as in Figure 2 except that SNR has been increased to 10 dB. Not surprisingly, the range estimate is not only less "noisy" but converges more rapidly. In Figure 4, the source bearing h as been included as an unknown. Thus the state vector is as shown in Equation 8. whereas for the previous examples the state vector contained only r_0 and f_0. The source frequency was initialized at 27° and, as can be seen, the convergence is quite rapid.

5. Discussion

This study has shown that by assuming a circular model for the wave front for the signal model, a Kalman estimation scheme can provide a simultaneous estimate of the range, bearing and frequency of an acoustic source. This approach has already been developed for a plane wave model [8], where it was shown that the bearing and source frequency can be jointly estimated. The major advantage of this approach is that it *explicitly* includes the array motion in the signal model, thereby improving the detection and estimation behavior.

An analysis of the performance bounds on a moving array has been treated in the works of Stergiopoulos [9] and Edelson [10] in which it is concluded that the CRLB on the bearing variance is lower when the source

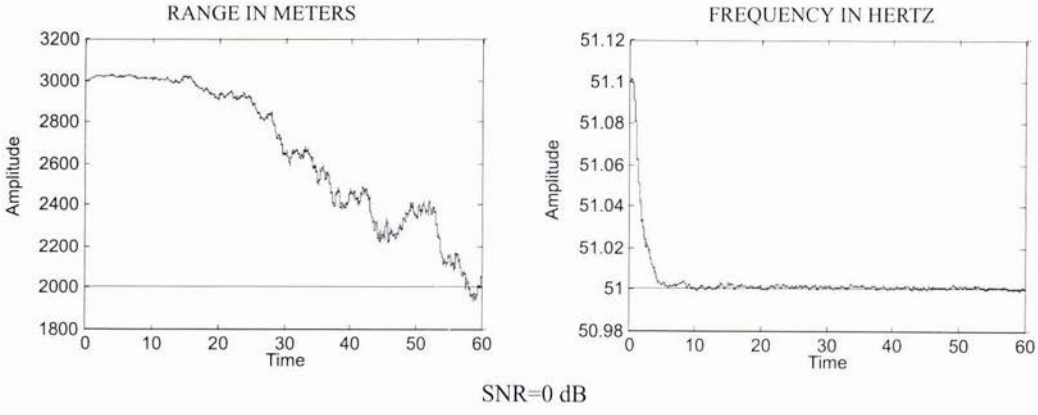

Figure 2: Range and source frequency estimates at 0 dB SNR

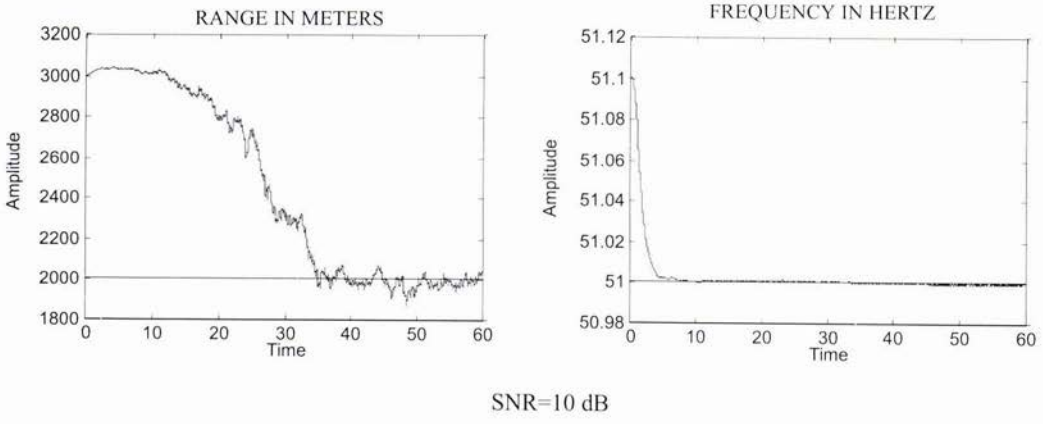

Figure 3: Range and source frequency estimates at 10 dB SNR

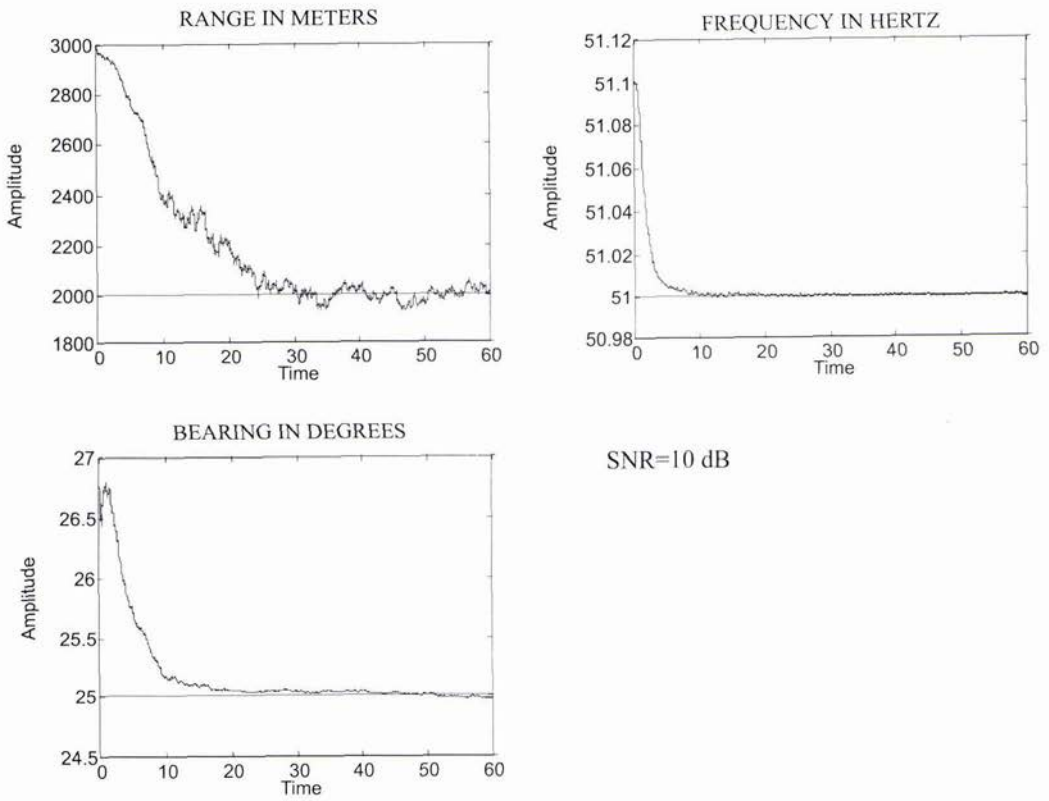

Figure 4: Range, source frequency and bearing estimates at 10 dB SNR

frequency is known *a priori*. In particular, it can be shown that the *ratio* of the CRLB of the moving array to that of the same array when it is fixed is given by

$$CRLB_{moving}/CRLB_{fixed} = 1/[1 + (3/2)(D/L) + (D/L)^2]. \tag{11}$$

Here, D is the "dynamic aperture," i.e., the speed of motion of the array times the total time, and L is the length of the physical aperture. As can be seen, there is the potential for a highly significant improvement in performance since this ratio dramatically decreases as D increases.

Heuristically, this improvement in performance arises from the fact that there is bearing information contained in the Doppler. Consider a single hydrophone moving at speed v. Assuming that the source frequency ω_0 is known, the observed (doppler shifted) frequency is given by

$$\omega = \omega_0[1 + (v/c)sin\theta]. \tag{12}$$

Thus, the bearing angle θ can be estimated from the doppler *shift* if the speed of motion is known. What is important here is that this estimator of bearing uses information that is *independent* of any bearing information that would be obtained from an array beamformer, which does not explicitly include the motion of the array in its algorithm. A fully populated array, then, has the potential to (1) estimate the source frequency, (2) obtain bearing information from the doppler on each hydrophone and (3) obtain bearing information from the finite aperture. In our example, this property of moving arrays has provided the ability to estimate the range of an acoustic source at a distance of 2000 meters with an array whose physical aperture is only 45 meters, but whose synthetic aperture is several hundred feet for times on the order of a minute by introducing a circular wavefront model in place of the plane wave model.

References

[1] J. V. Candy, *Signal Processing: The Model-Based Approach*. New York, McGraw-Hill, 1986.

[2] J. V. Candy and E. J. Sullivan, "Ocean acoustic signal processing: a model-based approach," *J. Acoust. Soc. Am.*, vol. 10, 3185-3201, 1992.

[3] J. V. Candy and E. J. Sullivan, "Model-based inversion for a shallow ocean application," *Proc. Full-Field Inversion Confr.*, SACLANT, La Spezia, Italy, also LLNL Report, UCRL-JC-112345, 1994.

[4] J. V. Candy, and E.J. Sullivan, "Passive localization in ocean acoustics: a model-based approach" *J. Acoust. Soc. Am.*, vol 98, 1995.

[5] A. Tolstoy, "*Matched field processing for Ocean Acoustics*," World Scientific Publishing Co., River Edge, NJ, 1993.

[6] G. C. Carter, "Time - delay estimation for passive sonar processing," *IEEE Trans. Acoust., Speech, Signal Processing*, vol. ASSP-29, pp 463-470, June 1981.

[7] J. V. Candy and P. M. Candy, "SSPACK_PC, A model-based signal processing package on personal computers," *DSP Applic.*, vol. 2, pp 33-42, 1993.

[8] E. J. Sullivan and J. V. Candy, "Space-time array processing: a model-based approach," unpublished

[9] S. Stergiopoulos, "Optimum bearing resolution for a moving towed array and extention of its physical aperture," *J. Acoust Soc. Am.*, vol. 87, pp 2128-214 0, 1990.

[10] G. S. Edelson, "On the Estimation of Source Location Using a Passive Towed Array," PhD Dissertation, University of Rhode Island, 1993.

Small Scale Volumetric Inhomogeneities of Shallow Water Sediments: Measurements and Discussion

Dajun Tang

Applied Physics Laboratory
University of Washington
1013 NE 40th Street
Seattle, WA 98105, USA
E-mail: djtang@apl.washington.edu

Abstract

There is a consensus that high-frequency acoustic scattering by the ocean bottom is partly due to sediment volumetric inhomogeneities, i.e., random fluctuations in sediment sound speed and density. Understanding the spatial distribution and temporal variability of such inhomogeneities at the centimeter scale is of great importance to modeling and predicting sound interaction with shallow water sediments. Core data provide only sediment variability in depth, which is not sufficient for determining sound scattering, since fluctuations of sediment parameters versus horizontal dimensions are also needed. Efforts were made to measure sound speed and porosity variabilities of sediments using techniques based on acoustic tomography and microelectric conductivity. While the results are still preliminary, it is clear from the available data that sediment inhomogeneity is a general phenomenon, and measurements such as those reported here will make it possible to conduct unambiguous model-data comparisons in future high-frequency bottom-scattering experiments.

1. Introduction

Natural sedimentation processes make sediment parameters, such as the compressional and shear speeds, density, and attenuation coefficients, deviate from stratification in a random fashion, and such deviations will cause sound to scatter. Conventionally, these deviations are divided into two categories: water-bottom interface roughness and sediment volume inhomogeneities, which include all variabilities other than the roughness. While the roughness issue has been extensively studied both theoretically and experimentally, it is only relatively recently that scattering by volume inhomogeneities has started to receive serious attention. This paper is devoted to the issues concerning the measurement of volume inhomogeneities in sediments. While rocks, shell pieces, and gas bubbles in sediments can be significant contributors to scattering, they should be studied as separate subjects. We confine the discussion in this paper to scattering due to the fluctuating medium parameters of the bottom.

Since it is impractical to measure the details of the sediment volume inhomogeneities deterministically, to study sediment volume scattering, a statistical approach is often used to study the average intensity of the scattered sound. References on modeling sediment volume scattering can be found in [1]–[7]. These models are based on a first-order perturbation approximation of the wave equation, and the sediment is assumed to be a fluid medium. Recently, Ivakin and Jackson [8] showed that for a sedimented bottom, a fluid model is an excellent approximation in treating scattering problems. When the sediment is modeled as a fluid medium, there are three acoustic parameters that determine the scattering process. They are the sediment sound speed, density, and attenuation coefficient. While it is not certain that the attenuation coefficient is a constant over space for a given frequency, it is potentially a scatterer. However, since attenuation manifests itself in the wave equation as the imaginary part of the wavenumber for a given frequency, and it is known that the imaginary part of the wavenumber is much smaller than the real part for almost all sediments concerned, scattering due to the random fluctuation of the attenuation coefficient is a second-order effect at best compared with that due to the fluctuations of sound speed and density. Thus, the sound speed and density are the only parameters left to be determined. If we assume that the sound speed and density fluctuate randomly in three-dimensional space around their mean profiles, the

first-order scattering cross section is completely determined if the auto- and cross-correlation functions of the two random quantities are known [1, 4]. In order to compare measured high-frequency scattering strengths to model predications, it is essential to have measurements of these correlation functions that are accurate to sub-wavelength scales. These correlation functions could be estimated from core data. But cores provide only depth information; estimation of correlation functions from such cores can result in error because (1) variabilities in depth can be due to fine, flat layering, which does not cause scattering, and (2) the statistical characteristics of variability in the horizontal direction can be quite different from those in depth. In the following, two efforts aimed at providing horizontal, as well as depth, data for estimating the correlation functions of sound speed and density in sediments are presented. The section on sediment microconductivity presents a method to measure porosity fluctuations, and therefrom, density fluctuations. The section on acoustic tomography presents a method for measuring sediment sound speed variability.

2. Sediment Microconductivity

Seawater is a conducting medium whereas the sediment solids themselves usually are made of poorly conducting materials. Thus, sediment electric conductivity, or equivalently its reciprocal, resistivity, is a measure of sediment porosity. When sediment porosity is known, sediment density can be obtained from the densities of the seawater and the sediment grains, quantities that are relatively easy to measure. Archie [9] proposed the following empirical relationship between conductivity and porosity:

$$F = \frac{c_w}{c_s} = \phi^{-n}, \tag{1}$$

where ϕ is porosity, F is a "formation" factor which is the ratio of the conductivity of the interstitial water, c_w, to that of the sediment, c_s, and the parameter n is a constant depending on the type of the sediment being measured. Later, in order to better fit data, Archie's formula was modified to include an additional parameter, a, which depends on the distribution of sediment particle sizes [10]:

$$F = \frac{c_w}{c_s} = a \cdot \phi^{-n}. \tag{2}$$

It can be understood that the conductivity of sediments depends on the shape and packing structure of the sediment grains because they will decide the passageways for charges to go through. For sediments made of identical spherical particles, there is a theoretical predication of the relation between porosity and conductivity [11]. However, theoretical relations are not available for real sediments owing to the complexity of the grain size composition and packing. In practice, the constants n and a are determined using an independent method for each sediment.

Conventional conductivity probes consist of a single sensor which can measure conductivity versus depth [12]. In order to measure density variability in the horizontal as well as in depth, we are developing a multi-sensor conductivity probe. Figure 1 is a schematic of the probe system. It consists of 16 equally spaced (1 cm), identical probe tips made of platinum spheres with a diameter of 0.6 mm, which ensures that the spatial resolution of each tip will be better than 1 m^3. By mechanically controlling the penetration depth of the probe into the sediments, we will be able to obtain a two-dimensional data set of sediment conductivity, and from that an estimation of the two-dimensional variability of the sediment porosity using (2). The system has been tested and calibrated in the laboratory using shallow-water sediment samples obtained from cores. First, the conductivity of sediment samples and that of the overlaying water were measured using the probe, and the porosity of the samples was estimated using (2). The porosity of the samples was also measured independently by weighing the samples while wet and after drying. Owing to space limitations, we will not give the details of the calibration process in this paper.

We have used this probe to measure the conductivity of a few sediment cores obtained off the Northern California coast in the summer of 1996. Figure 2a is one example of the measured data. The figure shows the reciprocal of the formation factor, or the ratio of sediment conductivity to that of overlaying water, plotted against depth for the 16 channels. The result is unity during the first few millimeters, indicating the probe was measuring the seawater just above the sediment. The sediment conductivity decreases quickly over depth in the next few millimeters and then stabilizes. Since there are 16 channels on the probe, the horizontal variability is obtained over a width of 15 cm. Figure 2b shows the mean profile of the conductivity averaged over the 16 channels and the mean porosity profile estimated from the mean conductivity profile. The parameters used to convert conductivity to porosity were taken from [13] based on empirical data. One of the advantages of having two-dimensional data is that we can estimate the depth-dependent mean profiles as shown here. Let the two dimensional porosity data be $p(x, z)$ and the mean porosity profile be $P(z) = \langle p(x, z) \rangle$; we define the normalized fluctuation ϵ_p as

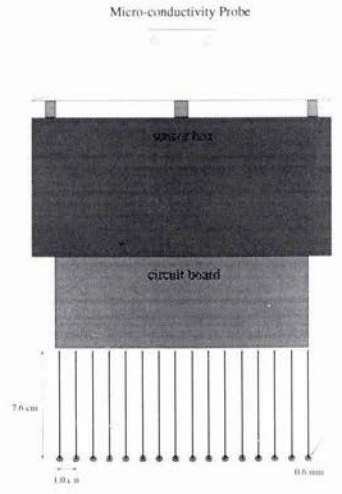

Figure 1: Configuration of the Conductivity Probe

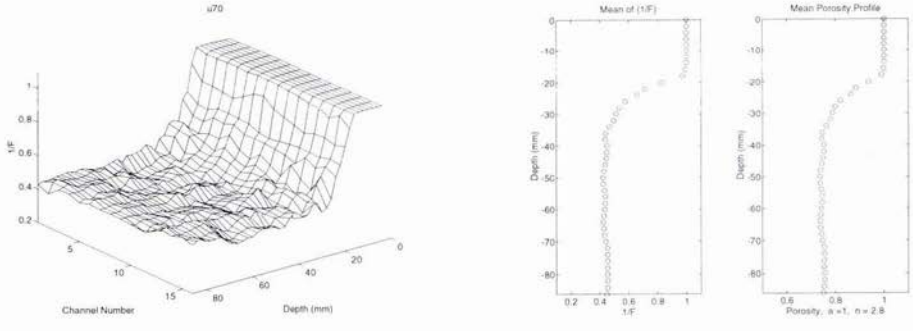

(a) Two-dimensional data

(b) Mean profiles

Figure 2: Example of 2-D conductivity data and mean profiles averaged across all 16 channels; core u70.

$$\epsilon_p = \frac{p(x,z) - P(z)}{P(z)}. \tag{3}$$

As stated in the Introduction, this is one of the two quantities for which we want to estimate the spectra.

One of the interesting questions is whether ϵ_p is spatially stationary. Since the mean profile is depth dependent, the stationarity of ϵ_p over depth is of special concern. Figure 3 shows three different sets of porosity variability data. There is no apparent depth or horizontal dependence in any of the three. Therefore we conclude that in these particular sets of data the porosity variability is spatially stationary. When a random process is stationary, its correlation function depends only on the difference coordinates, and its power spectrum is the quantity that is the input to first-order scattering models [1]. Next, we estimate the two-dimensional power spectrum of ϵ_p. The power spectrum is obtained by averaging the square of the absolute value of the Fourier transform from all data sets. Figure 4 is the estimated power spectrum. In this particular case, the two-dimensional power spectrum is isotropic. Hence, assuming that the three-dimensional power spectrum is isotropic in the horizontal dimensions as well, we can estimate it through its one-dimensional power spectrum [14]. Figure 5 shows an averaged one-dimensional power spectrum and a fit to a power-law spectrum of the form:

$$W_1(k) = \frac{w_1}{k^{m_1}}, \tag{4}$$

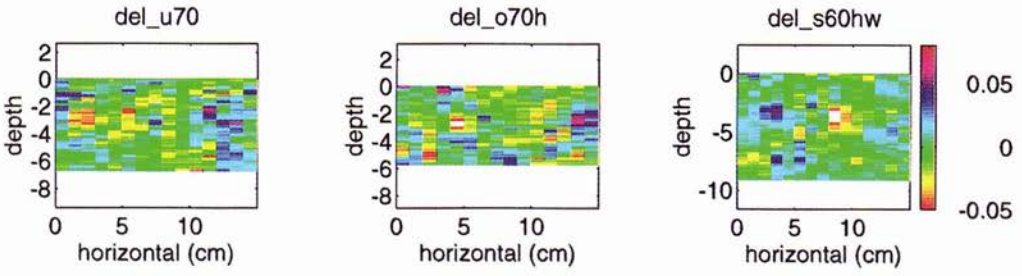

Figure 3: Porosity variability, ϵ_p, data of three cores, u70, o70h, and s60hw.

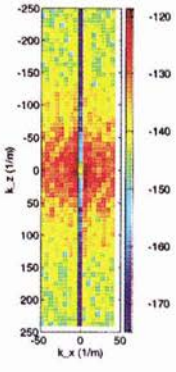

Figure 4: Two-dimensional power spectrum obtained from averaging multiple core data.

where $w_1 = 1.1 \times 10^{-6}$ and $m_1 = 1.7$. Based on this result, the isotropic three-dimensional power spectrum is

$$W(k) = \frac{w_3}{k^{m_3}}, \tag{5}$$

with $w_3 = 2.9 \times 10^{-7}$ and $m_3 = 3.7$. Here we have demonstrated the capabilities of the sediment microconductivity probe in providing data for estimating the sediment porosity power spectrum. While encouraging, we emphasize that these results are preliminary and a field version of the probe is yet to be built that will be able to provide *in situ* data.

3. Acoustic Tomography

Now we shift our attention to sound speed measurement. In order to measure *in situ* sediment sound speed variability in both horizontal and depth dimensions, acoustic tomography is a natural choice. Yamamoto [14] has conducted a series of tomographic measurements. Here we present an acoustic tomographic system specifically designed to measure *in situ* sediment sound-speed variabilities to support modeling of high-frequency bottom-scattering work.

The *in situ* sediment acoustic imaging system consists of an array of needle-like probes that can be pressed into the sediment, where each probe is a vertical line array of acoustic transducers. The current system consists of three identical probes attached to a sturdy frame and connected to a subsea electronics pressure housing. Two probes are oriented vertically and pressed into the sediment about 1 m apart; the third is oriented horizontally, just above the seafloor, between the two vertical probes (see Figure 6). Since these probes are all aligned on a common plane, the current system is capable of only two-dimensional imaging. Eventually, more probes may be added to obtain three dimensional data. Each probe contains 20 acoustic transducers, arranged as a line array with 5-cm spacing. Thus the active area is approximately 1 m long on each side. Each transducer in every probe is capable of both transmit and receive. An internal multiplexer in the probe is used to select a single transducer so that the number of wires in the cabling is minimized. The probes are connected to the subsea electronics module which

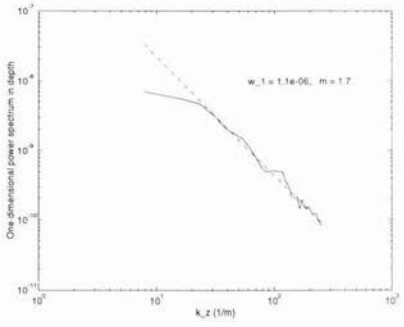

Figure 5: One-dimensional power spectrum in depth and a fit to a power-law spectrum.

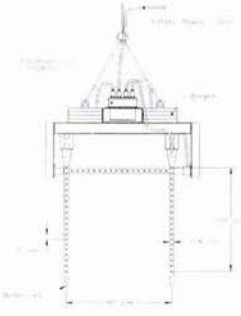

Figure 6: Configuration of the sediment tomography probe system.

contains a transmitter, a receiver, and a microcontroller for multiplexer and gain control. A multi-conductor cable extends to the surface. This cable connects to a PC via an analog input for data acquisition and to a serial port for multiplexer control. A small power supply is the only other surface equipment required to operate the subsea electronics. Individual transducers are selected by the PC software for transmit and receive, and a ping is initiated. This design allows 1200 direct raypaths between pairs of transducers and receivers. Figure 7 demonstrates some of the ray paths crisscross the 1 m^2 area.

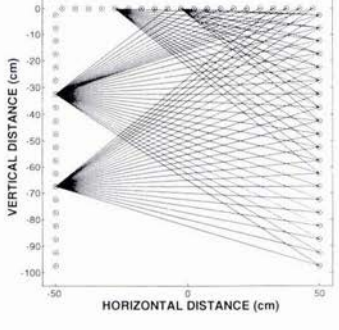

Figure 7: Sample ray paths of the sediment tomographic system.

All possible raypath combinations between the probes are sequentially interrogated. The objective is to accurately estimate the travel time from transmit to receive on each ray path. Data are acquired by an analog-to-digital data acquisition board plugged into the PC. A Windows based application program has been written to control the multiplexer for transducer selection and to acquire and store the raw sonar data. The resulting set of average sound velocities forms the input to the tomography processing algorithm.

The transducers used are free-flooded cylinders, with a resonant frequency of 100 kHz and a bandwidth of approximately 40 kHz. These cylinders have a torroidal beam pattern, and therefore are oriented with their longitudinal axes perpendicular to that of the probe itself, so that their beam patterns are aligned with the imaging plane. The elements are potted in polyurethane and suspended between two high-strength steel stiffening bars. The diameter of the probe is 1.5 in., expanded slightly at the top to accommodate the interface circuitry and connector pigtail. A long, thin printed circuit board extends along the entire length of the probe, outside of one of the steel bars. Also encapsulated in the polyurethane is a stainless steel tube connected to the probe tip to allow use of a water jet for assistance in penetrating difficult sediment.

One experiment was conducted at the Hadley Harbor near Woods Hole, Massachusetts, on November 15, 1996, on the vessel *Asterias* belonging to the Woods Hole Oceanographic Institution. First, a set of calibration data were obtained when the entire system was in the water column. Then two divers guided the system into sediments. There were two deployments about a mile apart, both in soft clay sediments. The probe system worked flawlessly and easily penetrated into the sediment at these muddy sites without use of the water jet. Although we could not tell the difference between the two sites by visually examining the sediment samples, the first location allowed little sound transmission, whereas the second provided clear data with better quality than expected. It is hypothesized that large amount of gas might have been present at the first location so sound waves were prevented from going through the 1 m course. However, further measurement is needed to verify this hypothesis.

Figure 8 shows some selected channels of time-series data. In this figure, the transmitter is the tenth element from the bottom on the left vertical probe, and the receivers are all the 20 hydrophones on the other vertical probe. On the left is a set of calibration data recorded when the system was suspended in the water column. On the right are actual time series on the hydrophones corresponding to those as on the left. The signal gain was 8 and the signal level in the figure was normalized, with the highest channel having a value of 100. Signal levels in other channels relative to the highest one are given in the figure on the right. The normalization factor is 2.13. The arrival-time changes relative to the calibration data were picked up and used in a back-projection algorithm to invert for the sound speed in the sediment. Figure 9 is the inverted sound-speed image.

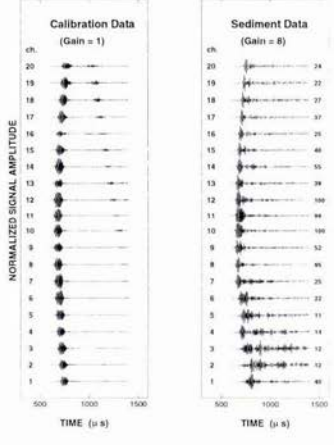

Figure 8: Field experiment time series. (left) calibration data; (right) data measured in the sediment.

The pixel size of the image is 5 cm by 5 cm. The mean sound speed is 1480 m/s. The variability is moderate in the upper half meter, whereas the lower half shows large variabilities. An examination of time series such as those shown in Figure 8 reveals that, in addition to the direct arrivals, there are multiple later arrivals with considerable amplitude. Clearly they are the result of forward scattering due to the presence of yet unknown scatterers. Further, note that the amplitudes of the direct arrivals on the lower hydrophones are considerably smaller than those on the upper ones, indicating a strong attenuating mechanism at work. It is known that when gas is present, the

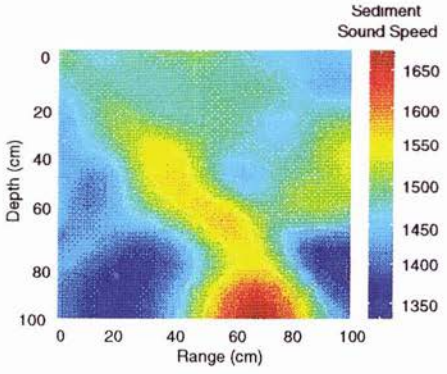

Figure 9: Inverted two-dimensional sound speed variation from field data.

effective sound speed will be markedly reduced. Indeed, in the lower half of the image, the inverted sediment sound speed is much lower than that in the water column. Therefore, we hypothesize that there was gas present in the sediment. From the arrival amplitudes, we estimated the attenuation coefficient as a function of depth. The result is given in Figure 10. Since in the estimation we used the amplitudes of the first arriving peak, and the transmitted signal is an up-chirp starting at 80 kHz, the attenuation coefficient is that at 80 kHz only. While the attenuation coefficient is about 25 dB/m in the upper half, a common value for this type of clay sediment, it jumps to 65 dB/m in the lower half. At two of the hydrophones, the first arrivals were so small that we could not reliably estimate the amplitude at all. Such a high attenuation coefficient is rare except when gas is present. To verify the presence of gas, a new experiment will be conducted at the same site in the next phase along with coring and gas-catching measurements.

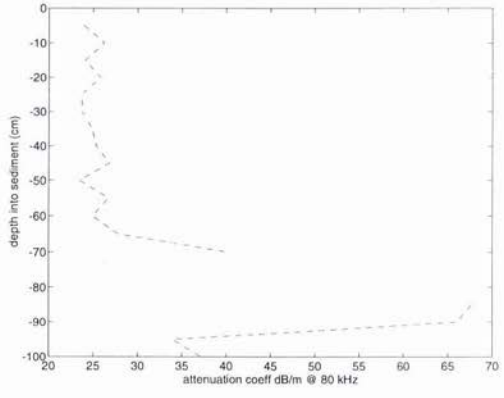

Figure 10: Estimated attenuation coefficient versus depth from field data.

4. Discussion

Two major issues need to be worked on concerning the conductivity probe. The first is the frailty of the tips of the probe. While the resolution requirement forces the tips to be small, it is mechanically difficult to make its structure sturdy enough to withstand repeated field deployment. The second issue is on converting conductivity to porosity. Although empirical relations such as (2) have been used extensively, a systematic verification of their applicability is yet to be done. Finding the relation between the conductivity and the tortuosity of the sediments in addition to porosity would also be potentially fruitful.

While the tomographic instrument works as designed, an increase in its spatial resolution would be desirable. Currently, its resolution is about 5 cm, too coarse compared with that of the conductivity probe, which is 1 cm.

As a result, we cannot resolve the issue of the cross correlation between sound speed and density. In addition, deployment of this system in sandy sediments remains to be tested.

In summary, we have developed two systems for the purpose of supporting modeling of high-frequency bottom scattering by sediment volume inhomogeneities. With such instruments, two-dimensional data on sediment variabilities can be obtained, and a model-data comparison with no free parameters is possible. Conducting a comprehensive high-frequency bottom-scattering experiment along with measurements of the environmental parameters using such instruments as described here, a clear understanding of the bottom scattering process can be expected.

Acknowledgments

The following people made major contributions to the conductivity probe: Neil L. Brown, Jia-Qin Zhang of the Woods Hole Oceanographic Institution, and Daniel G. Frisk of MIT who was working under a summer research program at WHOI. Dr. Robert A. Wheatcroft provided the core data for measuring conductivity.

Dr. Dezhang Chu, Thomas A. Austin, and Alan A. Hinton of WHOI are the principle co-workers on the tomographic system.

This work has been supported by the Office of Naval Research.

References

[1] Jackson, D. R., K. B. Briggs, K. L. Williams, and M. D. Richardson, "Tests of models for high-frequency seafloor backscatter," *IEEE J. Oceanic Engineering*, vol. 21, No. 4, pp. 458-470, October 1996.

[2] A. P. Lyons, A. L. Anderson, and F. S. Dwan, "Acoustic scattering from the seafloor: Modeling and data comparison," *J. Acoust. Soc. Am.*, vol. 95, pp. 2441-2451, May 1994.

[3] Jackson, D. R. and K. B. Briggs, "High-frequency bottom backscattering: Roughness versus sediment volume scattering," *J. Acoust. Soc. Am.*, vol. 92, pp. 962-977, August 1992.

[4] P. D. Mourad and D. R. Jackson, "High frequency sonar equation models for bottom backscatter and forward loss," *Proc. OCEANS '89*, IEEE vol. 4, pp. 1168-1175, September 1989.

[5] D. R. Jackson, D. P. Winebrenner, A. Ishimaru, "Application of the composite roughness model to high-frequency bottom scattering," *J. Acoust. Soc. Am.*, vol. 79, pp. 1410-1422, May 1986.

[6] An. N. Ivakin and Yu. P. Lysanov, "Theory of underwater sound scattering by random inhomogeneities of the bottom," *Sov, Phy. Acoust.*, vol. 27, pp. 61-64, 1981.

[7] P. C. Hines, "Theoretical model of acoustic backscattering from a smooth seabed," *J. Acoust. Soc. Am.*, vol. 88, pp. 325-334, July 1990.

[8] A. N. Ivakin and D. R. Jackson, unpublished (submitted to *J. Acoust. Soc. Am.*).

[9] G. E. Archie, "The electrical resistivity log as an aid in determining some reservoir characteristics," *Trans. AIME*, vol. 146, pp. 54-62, 1942.

[10] V. N. Dakhnov, "Geophysical well logging," *Quarterly of the Colorado School of Mines*, pp. 57, 1962.

[11] P. N. Sen, C. Scala, and M. H. Cohen, "A self-similar model for sedimentary rocks with application to the dielectric constant of fused glass beads," *Geophysics*, vol. 46, pp. 781-795, May 1981.

[12] D. Andrews and A. Bennett, "Measurements of diffusivity near the sediment-water interface with a fine-scale resistivity probe," *Geochimica et Cosmochimica ACTA*, vol. 45, pp. 2169-2175, 1981.

[13] R. H. Bennett *et al.*, "Geoacoustic and geological characterization of surfacial marine sediments by in situ probe and remote sensing techniques," in *CRC handbook of Geophysical Exploration at Sea*, 2nd Ed., R. A. Geyer, Editor, CRC Press, Boca Raton, FL, pp. 295-350, 1992.

[14] T. Yamamoto, "Velocity variabilities and other physical properties of marine sediments measured by crosswell acoustic tomography," *J. Acoust. Soc. Am.*, vol. 98, pp. 2235-2248, October 1995.

Effects of Sea Bed Structure on High Frequency Acoustic Reverberation in Shallow Water

Heidi A. Terrill-Stolper, Roger W. Meredith

Naval Research Laboratory
Bldg. 1005, Code 7174
Stennis Space Center, MS 39529
Email: terrill@zoe.nrlssc.navy.mil, meredith@vixen.nrlssc.navy.mil

and

Melvin D. Wagstaff

Planning Systems, Inc.
115 Christian Lane
Slidell, LA 70458
Email: mel_wagstaff@psislidell.com

Abstract

Although undoubtedly sea bed structures, patterns, and composition affect the reverberation of high-frequency acoustic energy, the extent of their influence is not well known. The effects of varying selected bedform parameters for sandy sea floors in shallow water at two depths are modeled. Visible changes are observed for different bedform patterns and sandwavelength changes of ~0.5 m. Changes of 0.05 in the sand wave height-to-length ratio are statistically detectable.

1. Introduction

One of the challenges in sonar operation is identifying the signature of a real "target" in the clutter produced by the environment. The sea floor, including material, structure and pattern, is one source of environmental clutter. Furthermore, in addition to background interference, variability of the sea floor structure and parameters can produce constructive interference, or "false" targets, that mimic real targets.

The purpose of this research is to help characterize the effects of bathymetry on general sonar operations and, specifically, in mine hunting tasks. This includes investigating the types of sea bed parameters that lead to the production of false targets, assessing the role of bathymetry in target fading of mine hunting sonars, and determining if range dependent bathymetry is relevant to mine hunting sonars. A full understanding also requires a general assessment of how bathymetry affects the statistical variability of bottom reverberation.

2. Method

2.1. Bathymetry Model

Observations have shown that sand covered regions of the sea floor are relatively dynamic with wave- or current-generated bedforms occurring from depths of a few centimeters near a beach to as much as 200 m on the continental shelf [1]. Wave generated sand waves are generally symmetric, having patterns classified as long-, intermediate-, and short-crested, brick, and random. Current or wave-current generated sand wave patterns include long crested, wavy (sinuous), cuspate, linguoid, as well as asymmetric versions of the wave generated sand waves.

The bathymetry-generation model developed for this study allows for choice of symmetric or asymmetric sand waves, maximum sand wave height, h, and length, λ, sand wave pattern (currently, choices are long-crested, short-crested, and random), and orientation of the sand wave pattern with respect to the primary observation direction. Although it is possible to combine several overlying sand bedforms (i.e., sand ripples formed on larger sand waves or dunes, and/or a sloping bed), these features have not been implemented in the present study.

The sand wave height equations used to generate the symmetric (wave-generated) and asymmetric (primarily current-generated) bedforms are modified from the equation given in Sleath [2] for symmetric sand ripples. For symmetric sand waves, the equation was modified to have the sand wave height run from zero to a maximum desired sand wave height, and the equation for ξ was abbreviated to first order. In the symmetric sand wave case the equation for sand wave height, y, is

$$y = \frac{h}{2}(1 + \cos k\xi) \tag{1}$$

$$\xi \equiv x + \frac{h}{2}\sin kx \tag{2}$$

where h is the maximum sand wave height, k is the wave number, and x is the range along the beam path.

In the asymmetric case, the equation was modified by the addition of a phase angle, ϕ; all other parameters are unchanged. The value of ϕ determines the extent of the asymmetry. Calibration of the phase factor to the symmetry parameter is not yet complete, therefore no determination as to the affect of the symmetry parameter on the reverberation has been attempted. Furthermore, some of the sand waves that have been classified as asymmetric may be either essentially symmetric or unrealistic since selection of the phase factor in the present study was random. The asymmetric sand wave equation is

$$y = \frac{h}{2}(1 + \cos[k\xi + \phi]). \tag{3}$$

Each bathymetry generated has a built-in random factor. For the long-crested sand waves, this is a randomly selected phase shift. In the symmetric case, the phase shift is implicitly included in value of x, altering the starting point on but not the shape of the sand wave profile. It is separated explicitly as the phase factor, ϕ, for the asymmetric case. Figure 1 (a.-b.) shows the effect of the phase shift on the shape of the sand wave profile. Figure 1a. is a 10 m wavelength, symmetric sand wave, as defined by (1), with a phase shift of 90°, or 2.5 m, implicitly included in the value of x. Figure 1b. shows the same sand wave with the phase shift now explicitly included as the factor ϕ in (3). Defining the direction of increasing range towards the shore, this sand wave has a symmetry parameter of .325, as defined by Inman [3].

Short-crested sand waves, defined by Inman [3] as sand waves having crest lengths between 1 and 3 λ, are all started in the trough, with the crest length and position along the crest determined randomly for each successive sand wave. If the randomly selected position on the sand wave is within 0.25λ of either end of the crest, then the sand wave amplitude, h, is linearly interpolated from between 0 and the selected wave height coordinated with the distance from the end of the crest. Figure 1c. demonstrates the effect of this random variation in sand wave amplitude along a single radial.

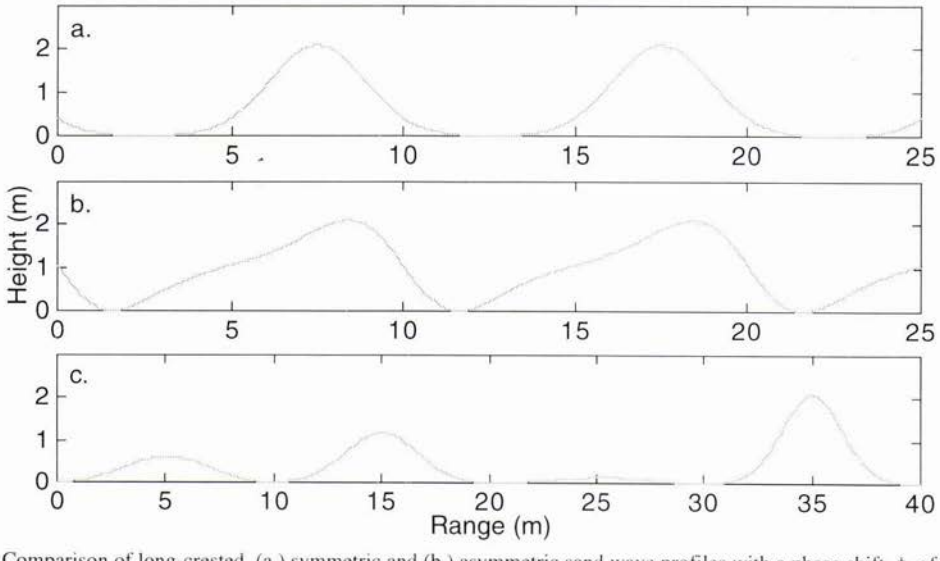

Figure 1: Comparison of long-crested, (a.) symmetric and (b.) asymmetric sand wave profiles with a phase shift, ϕ, of 90° and (c.) short-crested, symmetric sand wave profile. Sand wavelength is 10 m, height-to-length ratio is .21.

2.2. **The Reverberation Imaging Program (RIP)**

The Reverberation Imaging Program (RIP) [4] uses a modified ray trace model from the Naval Research Laboratory (NRL) range-dependent active system prediction (RASP) model [5]. Input for the model includes sound speed profiles for each beam path, sonar data, bathymetry files, and sea floor material, with choices ranging from mud to rock. Other environmental data, such as the surface, bottom, and volume loss and scatter may be user supplied or based on standardized models. The model calculates a one dimensional directional derivative along each beam pathway by linearly interpolating between

successive bathymetry points for use in determining the backscatter from a ray impact point. Model output consists of reverberation level versus time step.

2.3. **Modeled Sonar and Environment**

The sonar parameters including pulse length, frequency, and source level (dB re 1 microPa/Hz) are based on the SQQ-14 sonar. The sonar is placed at a depth of 20 m, with a 5° down tilt. The vertical profile is "standardized," with rays traced out to ±88 degrees from the sonar center with an interval of one ray every 1° for angles greater (less) than +21° (-21°), from +14° (-14°) to +21° (-21°) with an interval of one ray every 0.2°, and from +14° to -14° with an interval of one ray every 0.1°. The pulse length is 0.001 seconds, the center frequency is 80 kHz, and the source level is 224.0 dB re 1 microPa/Hz. Although the RIP program takes as input specific sonar parameters, the output is the reverberation off the sea floor, not the traditional sonar screen output.

The modeled environment consists of a typical shallow water summer sound speed profile (ssp), modified from a real summer ssp measured near Panama City, Florida. The ocean surface is assumed to be flat. Surface, bottom, and volume loss are based on standard models. The sea floor sand is taken to be medium grained sand over the total range for all beams. The same sound speed profile was used in RIP for each beam path. This ssp was measured at intervals of approximately 1 meter to a depth of 30 m. RIP runs are made at depths of 35 and 100 m. Consequently, the measured sound speed profile was modified by changing the depth of the last measured value to 100 m, making it appropriate for use at both the model depths. This modification is reasonable for the 35 m depth, since the water temperature, salinity, and pressure are unlikely to have changed significantly over 5 m. However, this is not necessarily the case for the 100 m depth. It is estimated, using the sound speed equation from Clay and Medwin [6], that between the actual measured depth of 30 m and the model depth of 100 m, there would be a change in the sound speed on the order of 5 m/s, assuming an average water temperature of about 15.6° C, and a temperature change on the order of 2° C, and constant salinity. Colder water would result in a greater difference in the sound speed, as would greater temperature changes. However the worst case sound speed change is estimated to be ~15 m/s, assuming a temperature change of 4° C (measured from Arctic data [7]) and water temperatures from 11.6° C to 15.6° C. Since the primary focus of this research is changes in the reverberation with bathymetry changes, this discrepancy in the sound speed at the maximum depth has been neglected, but further investigation of the influence ssp has on the reverberation is planned.

The pulse length determined the minimum sand wavelength allowed. The minimum allowed step size (in meters) was determined from the pulse length, T (in seconds), using the relation

$$(c/2) \times T \tag{4}$$

where c is the sound speed, taken in this case to be 1500 m/sec. For the SQQ-14 sonar, this translates to a 0.75 m minimum step size. The minimum sand wavelength allowed is then no less than 5 times the minimum step size. Each bathymetry file consists of 800 range/height pairs, calculated from the bathymetry model described above. The range of interest was 1000 m, with the actual step size used being the smaller of one fifth of the sand wavelength or 1.25156 m, the step size required to give 800 data points ranging from 0 to 1000 m.

This research concentrates on symmetric and asymmetric sand waves having long- and short-crested patterns. Sand wavelengths range from 7.5 m to 15 m, with height-to-length ratios from .05 to .21. The sand waves grow out of a flat bed at the selected depth; each depth choice (35 m and 100 m) is the maximum depth of the sea bed at that level. Figure 2 shows pseudocolor plots of the long- and short-crested sand wave bathymetries. The selected wavelength is 10 m, the height-to-length ratio (htlr) is .21.

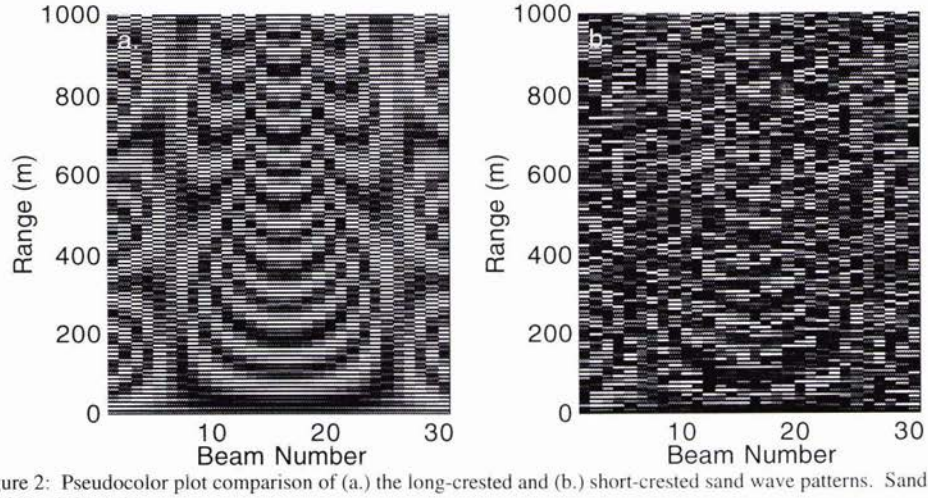

Figure 2: Pseudocolor plot comparison of (a.) the long-crested and (b.) short-crested sand wave patterns. Sand wavelength is 10 m., htlr = .21.

Thirty-one beams are used to construct the reverberation plots. These beams are numbered 1 to 31, with the center beam, beam number 16, defined as the primary observation direction. The horizontal beam width is 2°, so the 31 beams span an angular width of 60°, or ±30° on either side of the primary observation direction. RIP employs scattering angles measured in the vertical plane containing the sonar and the scattering point. No horizontal scattering component is currently included when computing reverberation. Evaluation of sea beds having orientations other than perpendicular to the primary observation direction is deferred until a horizontal component is included in the scattering. Beams 12 to 16 are used to obtain statistical results.

3. Results

The output of RIP was studied both directly through graphical examination of the model output and indirectly through a variety of statistical methods. Each of these methods has different strengths, and reveals different features of the simulated reverberation. The two depths have been treated separately, but comparisons between the results for other input parameters for a given depth have been made.

3.1. 100 meter depth

At the 100m depth, at least three RIP runs were completed for each of the selected symmetric case parameter sets, and one RIP run for each of the asymmetric parameter sets. The additional RIP runs completed for the symmetric case at this depth have greatly improved the reliability of the statistical results.

The reverberation at this depth has much more variability than that at the shallower depth. Reverberation returns start at about .1 seconds after the start of the time series. In the region between .1 and .4 seconds the reverberation has minimal variation, except for the presence of two "dark" bands. After about .4 sec, return from the main "beam" of the sonar starts. This region is characterized by relatively high variation in the reverberation. Although the magnitude of the variability of the reverberation reduces with time through this region, the average reverberation level does not change substantially. Eventually, the overall variation in the reverberation drops to negligible levels, but, unlike the reverberation for the 35 m depth which tends to smooth out completely, there are still "bright" spots or peaks in the reverberation all the way to the end of the time series, at about 1.3 sec. Figure 3 shows a comparison of the pseudocolor plots of the reverberation from the 10 m wavelength, htlr = .21 long- and short-crested bedforms at 100 m. The shading is scaled from darkest, reverberation level 30 dB, to lightest, reverberation level of 110 dB.

The reverberation histograms show a consistent pattern of narrowing the total reverberation range as the htlr is lowered. This shift in the shape of the reverberation histogram is most obvious in the short-crested symmetric sand wave case. Figure 4, shows the changes in the reverberation histograms with the height-to-length changes for the 100 m depth.

3.1.1. *Symmetric Sand Waves*

Symmetric sand waves were modeled in both the long- and short-crested wave patterns for wavelengths of 7.5, 8.0, 10.0, 12.5 and 15.0 m, and wave height-to-length ratios of .05, .10, .15, and .21.

A sand wavelength change of 0.5 m (7.5 m to 8.0 m) is detectable for the long-crested symmetric sand waves at this depth, but cannot be consistently identified for short-crested sand waves. Changes of 2 and 2.5 m, however, are readily detected for both sand wave types. Changes in the sand wavelength may be easier to detect for smaller height-to-length ratios, since the reverberation from the lower height to length ratios generally have fewer areas in the reverberation plot where the return from the sand wave is unusually high.

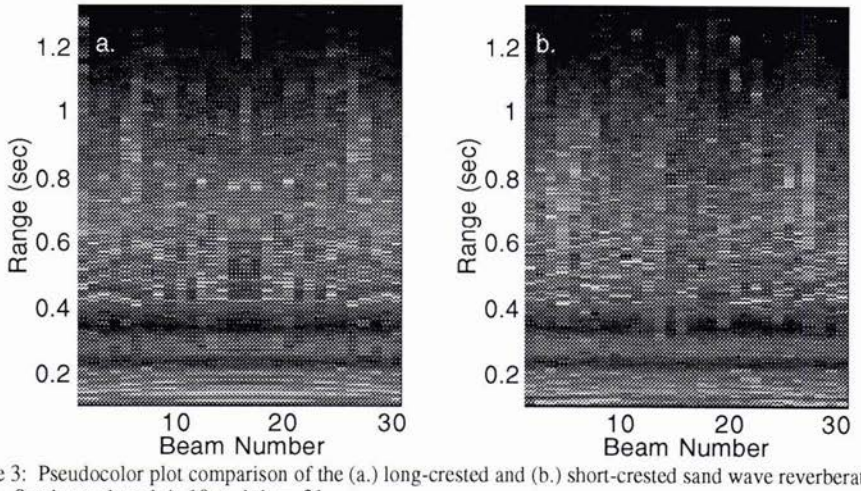

Figure 3: Pseudocolor plot comparison of the (a.) long-crested and (b.) short-crested sand wave reverberation at the 100 m depth. Sand wavelength is 10 m, htlr = .21.

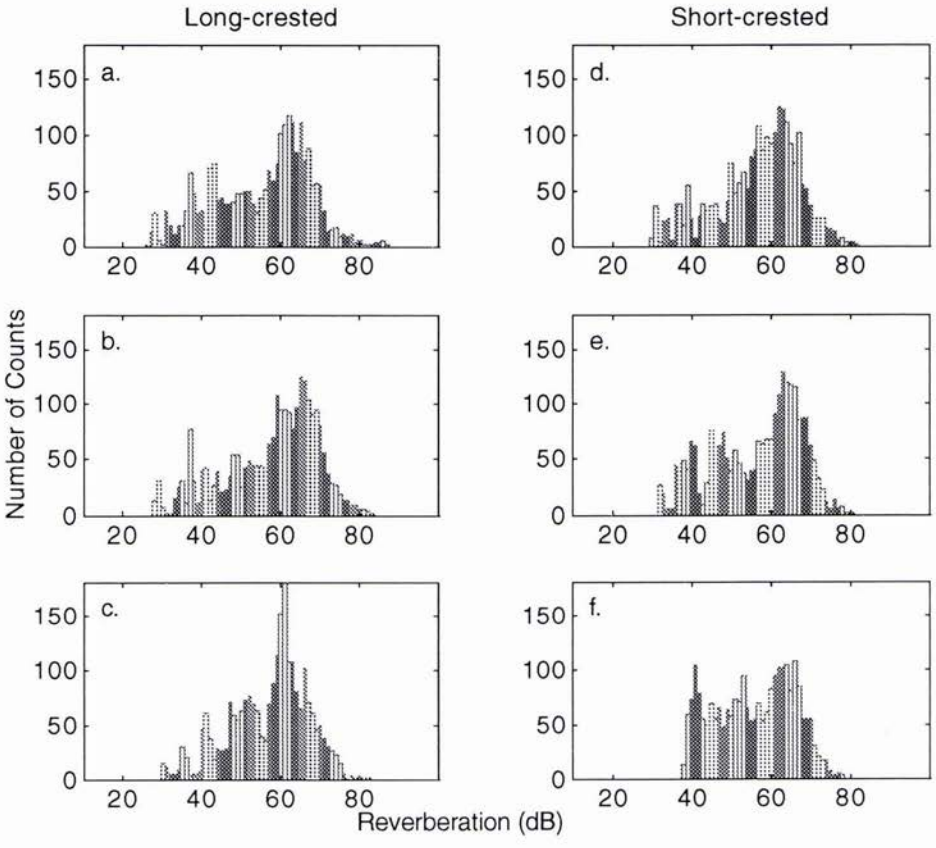

Figure 4: Comparison of the reverberation histograms of symmetric sand waves. For long-crested sand waves, a.) htlr = .21, b.) htlr = .15, c.) htlr = .10. and for short-crested sand waves, d.) htlr = .21, e.) htlr = .15, f.) htlr = .10.

Interestingly, although the reverberation histograms of the long- and short-crested sand waves show a similar pattern, the patterns of the mean reverberations are not consistent. The long-crested sand waves have the lowest mean reverberation for the htlr .05 at around 54 dB, the next lowest mean reverberation is at htlr .21, at about 55.5 dB, the highest mean reverberation is for htlr .15, averaging around 57.5 dB, with htlr .10 averaging about 57.0 dB. Short-crested sand waves with htlr .05 have the lowest mean reverberation, again around 54 dB, but the next lowest mean reverberation is for htlr .10, averaging around 56 dB, htlr .15 mean reverberation averages around 56.5 dB, and htlr .21 slightly higher.

Not only do short-crested sand waves have smaller variability in the centroid and mean reverberation levels between the various height-to-length ratios, but greater variability between the mean reverberation values for sand waves having the same parameters than do the long-crested sand waves. This is attributed to the variability in the maximum sand wave height when the beam path intersects the ends of a sand wave crest.

3.1.2. *Asymmetric Sand Waves*

Asymmetric sand waves were modeled in the long-crested wave pattern for wavelengths of 7.5 and 10.0 m, with wave height-to-length ratios of .10, .12, .15, .193, and .21, wavelength 7.75 m with height-to-length ratio .21, and wavelength 8.0 m, height-to-length ratios of .10, .15, and .21. Wavelengths 7.5, 8.0, 10.0, and 15.0 m with height-to-length ratios .10, .12, .15, .193, and .21 were modeled in the short-crested wave pattern.

Although the shape of the reverberation peaks and troughs in the long-crested case varies between the different sand wave parameter choices, the variation cannot be coordinated to the change in the shape of the sand wave with changes in starting phase. Modeled short-crested asymmetric sand waves had the same shape, since the starting phase was the same for all. Further study into the effect on the reverberation of the shape of the asymmetric sand wave is planned.

Differentiating between reverberation plots having sand wavelength differences of 2.0 m or more is easily done for both sand wave patterns. For the long-crested sand wave pattern, differentiating between the reverberation plots with sand

wavelength differences of 0.5 m (7.5 to 8.0 m) can be done consistently, but requires much more careful examination of the reverberation plots. It is not always possible to differentiate between the 7.5 m and 8.0 m sand wavelength reverberation plots in the short-crested sand wave case.

3.1.3. *Comparison of Symmetric and Asymmetric Sand Waves at 100 m*

No differences in the reverberation plots can be detected between symmetric and asymmetric sand waves of similar sand wavelengths. In general, the larger the height-to-length ratio, the wider the reverberation range and the greater the frequency of high reverberation levels. This pattern is in accord with the idea that the greater height-to-length ratios increase the back scatter by providing a larger component of the gradient perpendicular to the acoustic ray path over larger areas of the sand wave.

3.2. **35 meter depth**

At the 35 m depth, one RIP run was done for each set of parameters selected. Statistical evaluation gave very little useful information; often there were no clear differences between the results for different parameters. As yet it is not clear if this lack of differentiation in the reverberation statistics is due to the low grazing angle of the main beam acoustic rays, the large distance (≥15 m) between points of impact of successive rays, or, since this problem is most obvious in the asymmetric case, inconsistency in sand wave shape.

The reverberation for this depth reaches its peak values in a short (time scale) region of high variability. This is followed by a more moderate region, starting between .2 and .3 sec., where the reverberation output follows the design of the sand wave, with the average reverberation level steadily decreasing. The highest times (from around 1.0 to 1.33 sec.) correspond to reverberation from the region beyond the sand wave field. This reverberation zone is generally flat, with the total return continuing to decrease. Often the last few time steps are accompanied by a sharp drop in the reverberation level. Figure 5 shows a comparison of the pseudocolor plots of the reverberation from the symmetric 10 m wavelength, htlr = .21, long- and short-crested bedforms at 35 m. The shading is scaled from darkest, reverberation level 10 dB, to lightest, reverberation level of 155 dB.

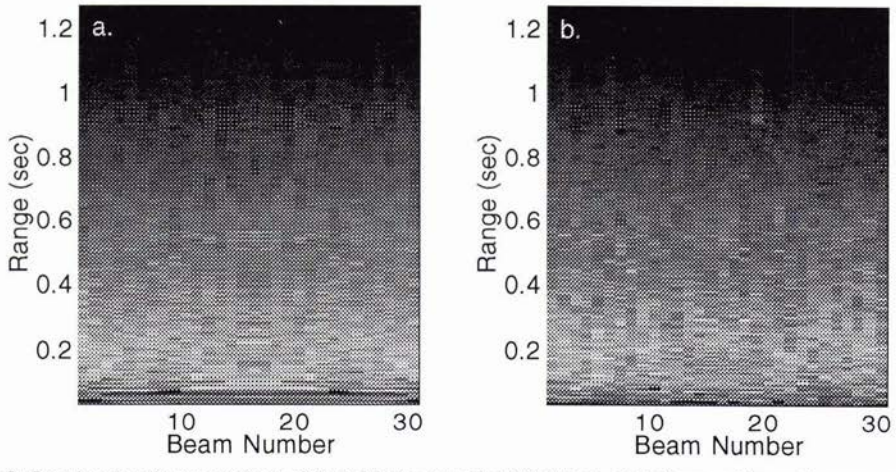

Figure 5: Pseudocolor plot comparison of the (a.) long-crested and (b.) short-crested symmetric sand wave reverberation at the 35 m depth. Sand wavelength is 10 m, htlr = .21.

3.2.1. *Symmetric Sand Waves*

Reverberation results were modeled for long-crested sand waves with the following parameters: wavelengths 7.5 m and 10.0 m, height-to-length ratios .10, .15, and .21; wavelength 8.0 m at height-to-length ratios of .05, .10, .15, and .21; wavelength 12.5 m, height-to-length ratios .05 and .10; and for wavelength 15.0 m, height-to-length ratios of .15 and .21. For short-crested sand waves, reverberation results were modeled for sea floors characterized by the following parameters: for wavelength 7.5 m; height-to-length ratios .10, .15, and .21, for wavelength 8.0 m, height-to-length ratio .05; for wavelength 10.0 m, height-to-length ratios .05, .10, .15, and .21; for wavelength 12.5 m, height-to-length ratio .15; and for wavelength 15.0 m, height-to-length ratios .10 and .21.

As with the sand waves at 100 m, differences in the sand wavelength were apparent in the reverberation. Long-crested sand waves having wavelengths of 7.5 m and 8.0 m could generally be differentiated. Variations in the sand wavelength of approximately 2 m were easily seen in both the short-crested and long-crested sand wave cases. A minimum change in the sand wavelength producing an observable change in the reverberation is currently under investigation. Changes in the height-to-length ratio were not obvious in the reverberation plots.

Although there is no clear differentiation between the reverberation histograms for most height-to-length ratios at the 35 m depth, in the symmetric, long-crested case, there is an indication of a trend towards a pattern that is consistent with the statistical results for long-crested sand waves at the 100 m depth in the mean values of the reverberation. This is continued in the centroids of the reverberation histograms of symmetric sand waves.

The most notable exception to the rule that reverberation plots for bathymetries are indistinguishable with respect to changes in height-to-length ratio (htlr) is htlr .05. Bathymetries having this htlr are easily identified in both the reverberation, and through statistical tools including the reverberation histograms, mean reverberation values, and the centroids of the reverberation histograms. They have significantly lower maximum levels of reverberation, and narrower total reverberation ranges, as seen in the reverberation histogram.

3.2.2. *Asymmetric Sand Waves*

Asymmetric sand waves were observed for long- and short crested sand waves having wavelengths of 7.5 m, 7.75 m, 8.0 m, and 10.0 m and height-to-length ratios of .10, .12, .15, .193, and .21. Asymmetric short-crested sand waves were also modeled at wavelength 15.0 m. A very limited number of "random" sand waves, consisting of 4-7 overlying, randomly oriented long-crested sand waves were also studied. These had sand wavelength ranges of 6.0--10.0 m, 7.5--12.5 m and 10.0--15.0 m, with sand wave heights based on a height-to-length ratio of .21 for the shortest wavelength of the selected range.

Direct observation of the reverberation showed that distinguishing between the different sand waves patterns is relatively easy, although the reverberation of the short-crested and long-crested sand waves have many features in common. Distinguishing between the different wavelengths and wave height-to-length ratios was not as straight forward. In a side by side comparison of the reverberation plots of the 7.5 m, 7.75 m, and 8.0 m sand waves, it was possible to distinguish between the 7.5 m wavelength and the 8.0 m wavelength, but the 7.75 m wavelength sand wave was not distinguishable from either of the other wavelengths. As the wavelength difference is increased, it becomes easier to distinguish between the reverberation results, with sand wavelength differences of 2 m easily detected. No significant, consistent differences were detected between the reverberation results with changes in the height-to-length ratio of the sand wave.

Statistical results were inconclusive for this data set. The reverberation histograms were essentially indistinguishable when comparing the various height-to-length ratios or the sand wave type. The centroids of the reverberation histograms, with the exception of the centroid of the short-crested sand waves for height-to-length ratio of .10 with a centroid reverberation level of 59 dB, were all confined within a range of approximately 0.5 dB located between 60 and 61 dB.

3.2.3. *Comparison of Symmetric and Asymmetric Sand Waves at 35 m*

There is very little noticeable difference between the reverberation plots for the symmetric and asymmetric sand waves at this depth. Furthermore, the reverberation histograms of the symmetric and asymmetric, and long- and short-crested sand waves are virtually indistinguishable for most height-to-length ratios (the exception is for height-to-length ratio .05, which has not been observed in the asymmetric case). However, other statistical methods reveal some differences. The means of the reverberation histograms of the asymmetric sand waves are randomly distributed, while those of the symmetric sand waves suggest a pattern, although there is not yet enough data to confirm this. The centroids of the reverberation histograms also support the suggestion of a trend in the mean for the symmetric case. Another difference is in the cumulative distribution functions (cdf) of the reverberation. Surprisingly, the symmetric sand waves show greater variation in cdf than do the asymmetric sand waves, even though the asymmetric sand waves have great variability in the sand wave shape, in addition to the random shifts previously discussed.

4. Discussion

The reverberation is generally consistent with the bathymetry producing it. The long crested sand waves, which were very symmetric, produces reverberation plots that show the symmetry of the bedform. Short crested sand waves that have a higher degree of randomness due to the variations in amplitude produce reverberation that demonstrates a higher degree of randomness than do the reverberation from long crested sand waves. However, reverberation plots often demonstrate substantial variability between nearby beam radials that is not seen in the bathymetry that produces them, and along a single radial they generally show less trough-to-peak variability. This is attributed to the effects of other environmental conditions to which the reverberation is subject.

Sand wavelength changes as small as 0.5 m could be detected in many circumstances, particularly for long-crested sand waves. Sand wavelength changes of 2 m could be detected for all sea bed patterns examined. Study to further narrow the threshold level for detectable wavelength change for each combination of sea bed parameters is in progress.

The reverberation from the 100 m depth is much more likely to have multiple occurrences of "false" targets, regions in the simulated reverberation where the return is much higher than the typical return of the beam path. This is true of all height-to-length ratios examined, except .05, which does not show a tendency towards "false" targets at 100 m. However, the overall peak reverberation levels and total reverberation range are lower at 100 m than at 35 m. Comparison of Figures 2, 3, and 5 gives an overview of the effects of bathymetry type and depth on the reverberation. Figure 2 shows a pseudocolor plot comparison of the long- and short-crested symmetric bathymetries and the corresponding reverberation plots are shown in Figure 5 for the 35 m depth and Figure 3 for the 100 m depth. The bedform parameters are sand wavelength, 10.0 m, and height-to-length ratio = .21. Although the plots shown are of the symmetric sand waves, there are no substantial differences in the results for the asymmetric sand waves.

5. Conclusion

It is clear that the sea bed structure can have a significant impact on high frequency acoustic reverberation in shallow water. As yet it is not possible to quantify the effects of the sea bed parameters, however, qualitative conclusions can be drawn. Although it was expected that higher sand wave height-to-length ratios would result in increased incidence of high reverberation levels, the effect is not obvious in the pseudocolor reverberation plots. It was not until the statistical results were examined that it became clear that as the sand wave height-to-length ratio is reduced, the number of high reverberation regions is reduced and the overall consistency of the reverberation is increased. Various sand wave types produce different reverberation patterns consistent with the bathymetry. Smaller changes in sand wavelength are evident for the more symmetric sea bed patterns.

6. Acknowledgments

This work was funded by the Office of Naval Research, with technical management by Naval Research Laboratory, Code 7170.

References

[1] D. A. Cacchione and D. E. Drake, "Shelf Sediment Transport: An Overview with Applications to the Northern California Continental Shelf," in *The Sea: Ocean Engineering Science*, New York, Wiley, ch. 21, pp. 729-773, 1990.

[2] J. F. A. Sleath, Sea Bed Mechanics. New York, Wiley, ch. 2, p. 70, 1984.

[3] D. L. Inman, "Wave-Generated Ripples in Nearshore Sands", Department of the Army Corps of Engineers, Technical Memorandum #100, Oct. 1957.

[4] M. D. Wagstaff, unpublished.

[5] L. B. Palmer and D. M. Fromm, "The Range-Dependent Active System Performance Prediction Model (RASP)," Naval Research Laboratory Technical Report # NRL/FR/5160-92-9383, 1992.

[6] C. S. Clay and H. Medwin, Acoustical Oceanography: Principles and Applications. New York, Wiley, ch. 1, p. 3, 1977.

[7] M. A. Wilson, "Volume Reverberation in the Fram Strait Marginal Ice Zone: May 1988," Naval Research Laboratory, Technical Report # NRL/FR/7174-93-9420, 1993.

Analysis and Problems of HF Acoustic Coherent and Incoherent Simulations in Shallow Water

Pat Thomson

DRA Bincleaves,
Newtons Road, Weymouth,
Dorset, DT4 8UR

Judith Bell

Dept. of Computing and Electrical Eng.,
Heriot Watt University,
Riccarton, Edinburgh, EH14 4AS
Email: jmb@cee.hw.ac.uk

Abstract

Shallow water environments create complex scattering conditions due to the sea surface and bottom scattering mechanisms. An analysis of the effects of the scattering mechanisms on sonar images of simple targets in shallow water scenarios will be presented and will include a examination of both incoherent and coherent scattering. The analysis will use an incoherent model for the simulation of sidescan sonar images, as well as two dimensional coherent ray propagation and isovelocity models.

1. Introduction

This paper aims to discuss the effects of incoherent and coherent scattering and the inclusion of such effects in sonar simulation models in shallow water environments. In shallow water environments, high resolution sonar images include contributions from many complex scattering mechanisms including the seabed, sea surface and target scattering and associated multi paths. Modelling of such scenarios often simplifies the calculations by assuming only incoherent scattering, or by limiting the number of paths calculated.

A model for the simulation of sidescan sonar and the images generated by such systems has been developed [1], and will be discussed in Section 2. This model attempts to replicate the underlying physical processes and create realistic synthetic sonar images. The processes incorporated include the transducer motion and directivity characteristics and the propagational effects and losses in a horizontally stratified media. In addition the model includes the scattering from complex, realistic seabeds and can include targets on the seabed or in the water column. The scattering from the seabed and sea surface includes the multi-path returns which can influence sonar images of targets and their associated shadows. These effects of the sea bottom and sea surface scattering with various target scenarios will be illustrated. This model however, is at present limited to the simulation of sidescan sonar as a result of the simplifying assumptions of a point source and the neglection of the phase. The implications of these assumptions will be examined in this paper, as well as introducing the concepts and complexity which arises from the inclusion of coherent effects.

The coherent effects will be illustrated using a simple two dimensional ray propagation model and an isovelocity model which can examine the various scattering paths. The coherent received signal is generated using versions of the same underlying seabed and sea surface scattering models as are used in the incoherent case, and summing many pulse replicas with relative phases and amplitudes as calculated from the ray trace and these models. The effects of small perturbations to both amplitude and phase of some of these replicas will be demonstrated for an idealistic environment (i.e. flat seabed and sea surface and very simple target) with the object of showing the possible effects of in-water inhomogenieties on high resolution sonar images. The consequences of the limitation of the current sonar image synthesis model will then be examined as result of the analysis of the coherent effects along with some of the problems envisaged in further developments.

The analysis will therefore consider three different models, viz. the sidescan simulation model, a 2D coherent ray propagation model and a coherent isovelocity model. Each of these models will be presented, along with details of their implementations and the results obtained from the application of the model. To permit comparison of the models and the effects of in-water inhomogeneities in high resolution models, the same scenario will be

used in all three cases. This utilises the sound velocity profile of Figure 1, with the transducer positioned at a depth of 11m, and assumes a target with dimensions of 2m by 1m positioned on the seabed at a range of 150m from the transducer.

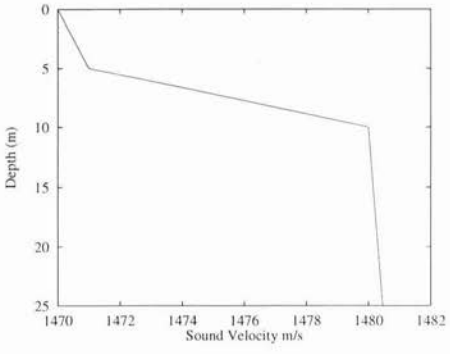

Figure 1

An analysis and comparison of the results obtained from the three models will also be presented. This will highlight the problems which are envisaged in extending a model, such as the model for the sidescan simulation, to a general coherent sonar simulation model capable of producing realistic high resolution sonar images.

2. Sidescan Simulation Model

A model for the simulation of sidescan sonar images which permits the direct visualisation of synthetic sonar images, generated by consideration of the underlying physical processes has been developed [1]. This model is based on ray theory and generates each line of the image by tracing a set of rays to represent each emitted pulse of acoustical energy. For each ray traced two values are calculated: the time for the ray to propagate through the water and be scattered back to the transducer and the intensity of sound received back at the transducer. These values are then processed to form one line of the image. The processing to form the image considers only the magnitude of the signals and neglects the phase [2].

The ray path is calculated assuming a horizontally stratified media, but can include any sound velocity profile. The intensity calculations include the effects of the spreading and absorption losses incurred during propagation, the three dimensional beam pattern for both the transmit and receive and the scattering from the seabed. The scattering can be calculated using the simple approximation of Lamberts Law or from the bistatic model of Jackson [3], which includes terms for both the scattering from the surface roughness and volume inhomogeneities in the sediment. The seabed is modelled as a realistic rough surface using fractals, which have been illustrated to provide a good representation of the seabed on a range of scales from centimeter to kilometer resolution [4] [5]. In addition targets can also be included in the scene using procedurally defined objects.

2.1 Simulation using backscatter only

In its simplest form the model calculates only the direct backscatter from the seabed and assumes the returning ray follows an identical trajectory to the outgoing ray. Part of a line of the image generated by calculating only the backscatter is displayed in Figure 2, for the scenario described previously, showing only the region in the vicinity of the target. A rough seabed surface has been used and the scattering model assumes a sandy sediment. The initial peak of the target in this signal is due to scattering from the face of the target orientated towards the transducer. The resulting shadow is clearly defined. This figure also shows the simulated signal if a totally flat seabed had been utilised in the modelling. This signal is unrealistic, and the advantage of the utilisation of complex fractals to model the topography and sediment roughness can be visualised. The fractal seabed was also used to generate the synthetic sidescan sonar image of Figure 3 which shows the target lying on the rough seafloor and the resulting pattern of highlights and shadows.

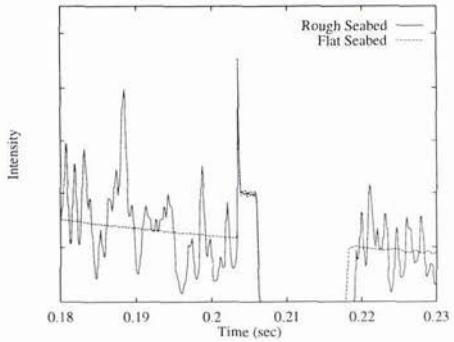

Figure 2

Figure 3

2.2 Seabed Multi-paths

The model can then be extended to include the multiple reflections from the seabed to account for the fact that the sound is scattered in all directions upon interaction with the seabed. The principle direction of the reflected energy tends to be in the specular direction, and the rays are traced in this direction upon intersection with the seabed or the target. The process of tracing the specular ray from each intersection can be repeated iteratively until the relative magnitude of the energy received at the transducer is no longer significant. With the use of Jackson's bistatic scattering model the magnitude of the signal can be easily calculated in both the specular and backscatter directions.

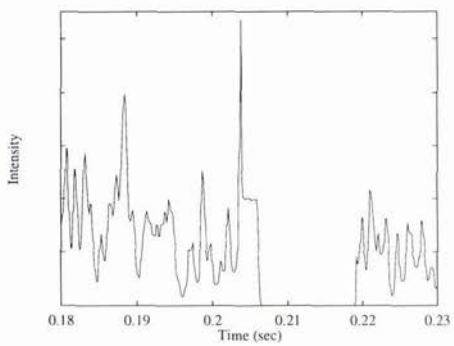

Figure 4

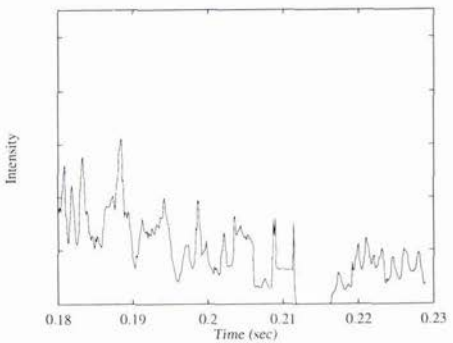

Figure 5

The effect of the multiple reflections is most pronounced in the area directly in front of the target, as the signal is reflected repeated between the seabed and the target. This produces a larger peak in the signal and subsequent smaller peaks where the target is detected, as can be seen in Figure 4. The bottom bounce only paths, have little other effect on the signal as the energy is reflected away from the scene without being reflected from any other objects.

2.3 Sea Surface Reflections

As has been illustrated in Section 2.2, the bottom only multi-paths have only a small effect on the signal in the vicinity of the target. In shallow water, the addition of the sea surface multi-paths has a greater effect on the signal. This is illustrated in Figure 5, which includes the influence of the sea surface reflections as well as the bottom reflections. The direct backscatter path produces the first image of the target and the first surface reflected path creates a clear multiple view of the target and a subsequent reduction in the shadow zone, due to the multiple images of the target. This effect can also be visualised in the simulated image of the target, shown in

Figure 6, where the visual detection of the object in the image becomes more difficult.

The simulated signal of Figure 5 assumed that the sea surface was a perfectly flat reflecting plane. The effect of the moving sea surface can be included by manipulating the surface normal of this plane to simulate the orientation of the sea surface waves at the point where the rays intersect the plane. This incorporated a more random effect into the simulated image as is illustrated in Figure 7.

Figure 6

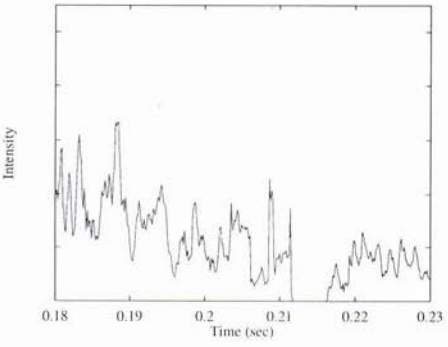

Figure 7

The model to produce the signals and images shown in the above figures has neglected the phase of the signals in the calculations and has assumed a point source and receiver. However, already the complexity of the model, to permit it to model realistic seabed topographies and roughness, ray refraction and 3D beam patterns, means that it can take several hours to generate the synthetic images shown. To extend the model to include the coherent scattering and beam forming at a realistic transducer could prove to be too computationally expensive. The effect of modelling the coherence is discussed in the following sections.

3. 2D Coherent Ray Propagation Model

To extend the investigation of the modelling to include the coherent effects, the study will use a very simple two dimensional raytrace model, which assumes a flat seabed and sea surface. The model has been modified to generate a spike array containing information about ray paths and arrival times at the target, seabed and sea surface. A time series is then generated by coherently adding pulse replicas modified by the time delays and information contained in the spike array. The amplitudes of the pulses summed are adjusted according to the source of the return, and the amplitude can also be given a small random perturbation to account for less than perfect surfaces. As no attempt is made to identify eigenrays, this approach for an active sonar simulation is only valid for direct path calculations and the assumption that the outward and return trajectory are identical.

Figure 8 shows the raytrace for the sound velocity profile shown in figure 1, and the resultant spike array and time series representing the calculated acoustic return for direct paths. On comparison with the flat seabed incoherent a-scan shown in Figure 2, the additional complexity and randomness introduced from the coherent addition is clearly visible.

3.1 Effect of velocity profile

As shown in the previous section it is desirable to include additional ray paths involving reflections from the seabed and sea surface in this study. The ray trace and resulting time series and spike array of Figure 8 was calculated for the profile previously discussed, this can be compared to Figure 9 which was calculated for the same target scenario but with isovelocity conditions. This shows that the effect of the profile on the spike array, as compared with that for isovelocity conditions, will only affect the sea surface returns and will not make a great deal of difference to the outcome, apart from in certain infrequently occurring conditions when the array beampattern and tilt should happen to be critical for the angle and range concerned.

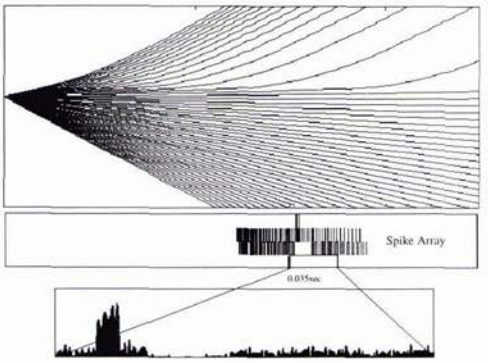

Figure 8

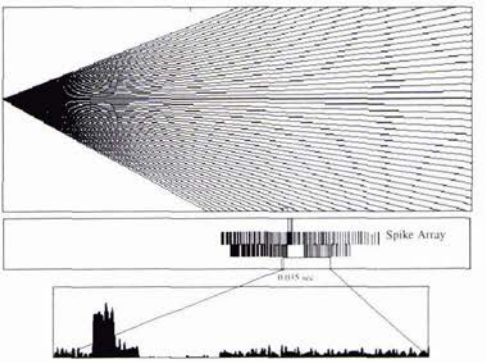

Figure 9

4. Coherent Isovelocity Model

As a result of the small effect of the sound velocity profile, as discussed in Section 3.1, a coherent isovelocity model has also been developed to simplify the calculations without distorting their accuracy. Limiting the environment to isovelocity conditions reduces the identification of eigenrays to simple geometry, making the study of the effects of the multiple paths considerably easier.

A two dimensional scenario is again considered initially for a single receive beam, as is illustrated in Figure 10, for a scene with a flat seabed and sea surface with the target positioned at a range of 150m and the transducer at a depth of 11m. The number of reflections can be limited to 0 or 1, thereby including direct paths only (e.g. Figure 10 path a) or those involving only one reflection from either the seabed or the sea surface (combinations of paths a, b and c). The model also has the ability to include up to two reflections, therefore calculating paths involving both a seabed and a sea surface reflection (paths d and e).

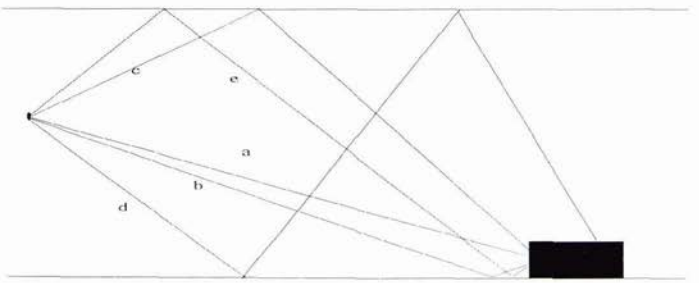

Figure 10

4.1 Comparison with Incoherent Modelling

The model is an extension of an isovelocity sonar equation model and uses the same underlying acoustic models to describe the level of the scattering from both seabed and sea-surface as the Sidescan Simulation Model, which was described in Section 2. It also includes the effects of the array beam patterns, beam steer and target size and position.

Once again a spike array is generated for all two way paths containing arrival time, cumulative path loss, and path type. Reflections at the sea surface undergo a phase reversal but those at the seabed do not [6]. Figure 11

compares (for a small time window in the target vicinity) seabed and sea surface reverberation levels and received signal level including target echo from the energy model (Figure 11a), with a plot of the information held in the spike array (Figure 11b). In addition, the time series data generated using that spike array is also illustrated in Figure 11c.

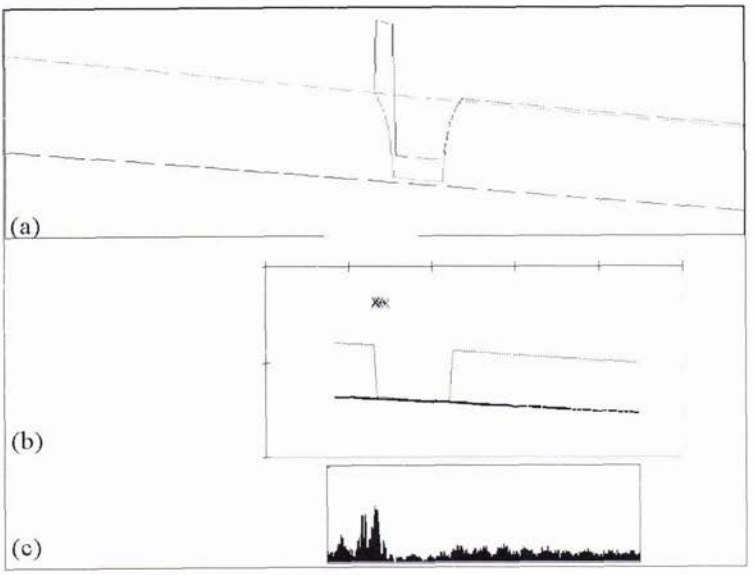

Figure 11

4.2 Time series simulation

This information is then used to coherently sum pulse replicas to give a simulated a-scan return. Provision has been made to allow the addition of a random phase shift or jitter to each pulse replica summed, but no alteration to the amplitude except as calculated from the cumulative path loss. This phase shift was included to allow a little variation between consecutive calculations using identical information and attempt to include the effects of sea surface movement, less than ideal surfaces, array movement, and through water inhomogenieties. The maximum size of this random shift can be chosen in terms of the wavelength from 0 upwards.

The summation is carried out in the time domain, as convolving the spike array timings with the transmit waveform would have involved a large number of dummy points in the spike array to retain the time structure, thus removing any speed advantage this method might have had. For simplicity a limit has been set on the size of the window that can be considered which in practice for a 100kHz simulation gives a window of 35msec.

4.3 Simulation Results

Figure 12 shows the effect on the simulated time series of including direct paths and reflected paths in the calculations. Figure 12a allowed only the direct paths in the calculations, whereas Figure 12b included the paths with one reflection and Figure 12c included paths with two reflections. As might be expected the obvious shadow in Figure 12a is filled in to the point of being obliterated as more reflection paths are included in this example. Figure 13 shows the sort of effect that might be expected by including different levels of phase jitter in the calculation of the time series using the same spike array.

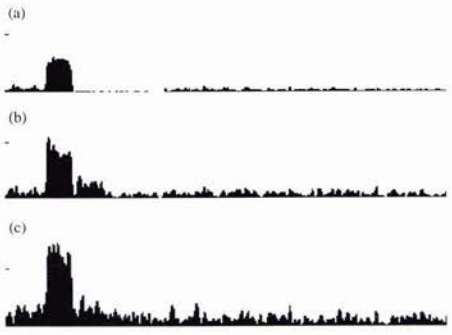

Figure 12

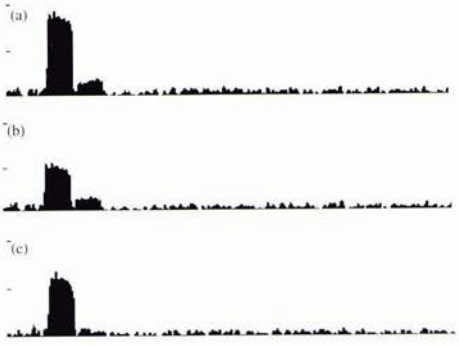

Figure 13

Figure 14 is an example of an image that can be built up by combining the time series for beams with different steer angles. Figure 14a shows examples of the coherent time series for different beams which were used to generate the image of Figure 14b, including examples in which the target was within and outwith the beam.

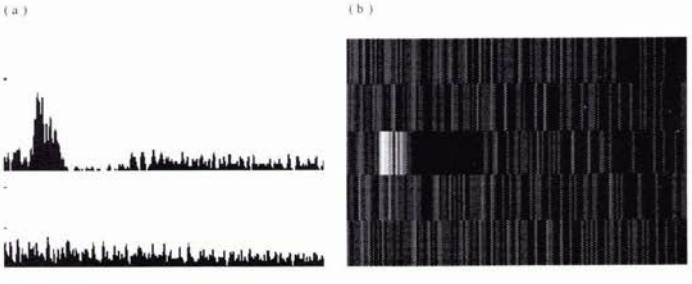

Figure 14

5. Analysis and Conclusions

It has been shown that inclusion of more realistic seabed descriptions to an incoherent model adds a great deal of confusion to the predicted time series data, and that the inclusion of bottom and surface reflected paths has a significant effect on these results. These results indicate that detailed bathymetry and sea surface description are important components in a realistic HF sonar simulation.

The simple coherent models add further degree of confusion even for assumed flat surfaces. Using these models the effect of including the forward reflected paths on the predicted time series data can be shown. Applying small perturbations to the amplitude or the phase of the components added into the time series might be a reasonable way of including effects of in-water inhomogenieties and less than perfect surfaces, and can have a noticeable effect on the predictions.

There has been a considerable amount of study of the effects and methods of including bottom topography and reflectivity [7], and in modelling 3D environments. Many of these studies have concentrated on rather longer ranges and wavelengths, and deeper water scenarios than are being considered here. It is apparent from the results presented here that the inclusion of seabed bathymetry and sea surface topography is essential in a realistic shallow water HF acoustic simulation, but as yet it is unclear whether it is realistic to model the complete scenario in a coherent manner.

Further work is currently being undertaken to investigate possible model architectures which are able to handle the additional complexity and permit the extension of the Sidescan Simulation Model to a coherent HF sonar model, since the original ray tracing approach may be too computationally expensive, as has been illustrated in this paper. This work will also require experimental data gathering for representative scenarios for

comparison with the simulated data, and the development of methods for the comparison of real and simulated data.

References

[1] J.M. Bell, " A Model for the Simulation of Sidescan Sonar", Ph.D Thesis, Heriot-Watt University, November 1995

[2] J.M. Bell," Application of Optical Ray Tracing Techniques to the Simulation of Sonar Images ",in Optical Engineering, in press.

[3] D.R. Jackson, "Models for scattering from the seabed", Proc. Inst. Acoustics, 16(6), Dec 1994

[4] K.B. Briggs, "Microtopographical Roughness of Shallow-Water Continental Shelves", IEEE J. Oceanic Eng., 14(4), pp. 360-367 (1989).

[5] C.G. Fox and D.E. Hayes, "Quantitative Methods for Analyzing the Roughness of the Seafloor", Rev. Geophysics, 23(1), pp. 1-48, 1985

[6] J.B. Keller and J.S. Papadakis, "Wave Propagation and Underwater Acoustics", Lecture Notes in Physics 70, Springer-Verlag Press.

[7] A.R. Robinson and D. Lee, "Oceanography and Acoustics Prediction and Propagation Models", (Chapter 9. J.F. Lynch, AE Newhall, CS Chiu and JH Miller) AIP Press

Modeling of Subcritical Penetration into Sediments Due to Interface Roughness

Eric I. Thorsos, Darrell R. Jackson, John E. Moe,[1] and Kevin L. Williams

Applied Physics Laboratory, University of Washington
1013 NE 40th Street
Seattle, Washington 98105
E-mail: eit@apl.washington.edu, drj@apl.washington.edu, jemoe@aol.com, williams@apl.washington.edu

Abstract

Recent experimental results reveal acoustic penetration into sandy sediments at grazing angles below the critical angle. We have been investigating a mechanism for subcritical penetration based on scattering at a rough water–sediment interface. Using perturbation theory, a numerically tractable three-dimensional model has been developed for simulating experiments. Data–model comparisons show that interface roughness is a viable hypothesis for the observed subcritical penetration.

1. Introduction

High-frequency acoustic penetration into seafloor sediment at low grazing angles is of interest for buried mine detection. For sandy sediments the critical angle can be in the 25° to 30° range, which suggests that penetration at lower grazing angles might be quite limited. However, recent experimental results reported by Chotiros [1] reveal acoustic penetration into sandy sediments at grazing angles below the critical angle over a broad frequency range (5–80 kHz). In addition, the propagation speed in the sediment was inferred to be near 1200 m/s, significantly lower than the compressional sound speed of about 1700 m/s in unconsolidated 28. March 1997sands. Chotiros interprets these results to indicate the excitation of a Biot slow wave in the sediment. Subcritical acoustic penetration into sediments has also been reported by Lopes [2].

We have investigated an additional mechanism for subcritical penetration based on scattering at a rough water–sediment interface. Examples of data–model comparisons will be given that show interface roughness is a viable hypothesis for the observed subcritical penetration. For this mechanism, the propagation speed of the sound penetrating the sediment is the standard compressional wave speed of about 1700 m/s, but the apparent speed found through a processing technique similar to that used in the experiments can be significantly less and ranges from about 1200 m/s to about 1500 m/s depending on the roughness conditions assumed. A simple explanation for this lower apparent speed will be given. We believe that further field experiments are necessary to clarify whether the observed subcritical penetration is due to the Biot slow wave mechanism, to the interface roughness mechanism, or to possibly some other mechanism.

Before considering simulations of experiments, we present results in Section 2 for the penetrating field in two dimensions obtained with an exact integral equation method. These results show the potential for a rough interface to couple sound into the sediment at subcritical grazing angles. In order to simulate experiments a tractable three-dimensional (3-D) model is required that accounts for the finite pulse lengths used, and such a model has been developed using perturbation theory. In Section 3 exact results are used to demonstrate that perturbation theory is valid in a 2-D geometry for roughness conditions of interest and thus should be valid for the 3-D geometry as well. In Section 4 perturbation theory is used in a 3-D model for data–model comparisons of apparent sound speed, propagation direction, and attenuation in the sediment. A concluding discussion is given in Section 5.

[1]Presently at Acuson, 1220 Charleston Rd., P.O. Box 7393, Mountain View, CA 94039.

2. Exact simulations of acoustic penetration into sediment

In our work to date, we have modeled the sediment as a fluid supporting only compressional waves, since for sand sediments it can be shown that coupling into shear waves is negligible. The problem of scattering from and transmission through a rough two-fluid interface can be solved exactly in the cw case for particular rough interface realizations using an integral equation method. Because of high computational requirements, this method is essentially limited to a 2-D geometry with a 1-D rough interface. Nevertheless, such results illustrate that surface roughness can couple acoustic energy into sediments when the incident grazing angle is below the critical angle. Space does not permit a detailed exposition of the integral equation method here. A formulation for electromagnetic scattering at a rough surface separating two media (closely analogous to the two-fluid case) is given in [3], and the simpler case of a single fluid with rough surface subject to a Dirichlet boundary condition is treated in [4].

With a specified incident pressure field on the rough surface, solution of the integral equation (actually two coupled integral equations) gives the field and the normal derivative of the field on the surface. With these quantities known, it is possible to compute, via the Helmholtz-Kirchhoff integral formula, the field at any point on either side of the interface and thus construct maps of the field structure. Absorption in the sediment is incorporated by using a complex wavenumber in the fluid below the interface.

To illustrate the effects of roughness on acoustic penetration into sediment, we consider parameters similar to those for the Acoustic Testbed Experiment (ATBE) near Panama City [1] to be discussed further in Section 4. Denoting the sound speed and density by c_1 and ρ_1 in the water and c_2 and ρ_2 in the sediment, respectively, we use $c_2/c_1 = 1.13$ (which gives a critical angle of 27.8°), $\rho_2/\rho_1 = 2.0$, and a sediment absorption of 0.5 dB/m/kHz. The 2-D spectrum of sediment roughness was not measured during ATBE. For numerical simulations in two dimensions, we require a 1-D roughness spectrum $W(K)$, which we model in the following modified power-law form:

$$W(K) = w_1 / \left(K^2 + K_L^2\right); \tag{1}$$

$W(K)$ is defined such that $W(-K) = W(K)$, where K is the spatial wavenumber, and the mean square surface height, h^2, is obtained by integrating $W(K)$ over all K. In (1) a "lower cutoff," K_L, has been introduced to yield a finite mean square surface height. A similar cutoff will be used in Section 4 with the 2-D roughness spectrum and discussed further there. An upper cutoff, $K_U = 2k_1$, where k_1 is the acoustic wavenumber in the water, is also imposed on (1) such that $W(K) = 0$ if $|K| > K_U$. For the example in this section, $w_1 = 0.02$ cm and $K_L = 0.1$ cm^{-1}, which yield a roughness parameter $k_1 h = 0.66$ at a frequency of 20 kHz. The results shown are not changed qualitatively if K_L is made smaller or if K_U is made larger.

Examples of pressure fields obtained with the integral equation method for both a flat and a rough surface are shown in Fig. 1. In these figures the mean water–sediment interface is at 0.0 cm on the vertical scale, and the color display is linear in pressure. A 20-kHz plane wave of unit magnitude is incident from the left at a grazing angle of 20°, which is below the critical angle of 27.8°; this incident wave has been omitted to simplify the field structure. In Fig. 1(a) the surface is flat, and the phase fronts of the reflected wave can be seen moving up and to the right above the interface. For this flat surface case, the field in the sediment is evanescent; it decreases exponentially with depth and has a significant magnitude for only about a wavelength into the sediment. In Fig. 1(b) the rough surface realization is consistent with the spectrum given by (1). Energy can be seen to radiate down into the sediment at relatively steep angles, in part because absorption will tend to remove energy propagating closer to the horizontal.

One might expect acoustic penetration into the sediment to occur at regions along the surface where the local grazing angle (accounting for the local surface slope) exceeds the critical angle. However, acoustic penetration due to roughness occurs even if this condition is not met anywhere on the surface. It is evident from Fig. 1 that the field scattered down into the sediment is spatially incoherent, while for the Biot slow wave hypothesis, the penetrating field would be a spatially coherent wave (assuming that interface and volume scattering effects are negligible.)

In order to see if the rough surface scattering mechanism could explain the acoustic penetration results reported by Chotiros, it is necessary to model the full 3-D experiment geometry, which is not practical using the integral equation approach. Thus, we have employed perturbation theory to account for the effects of scattering. In doing this, we sometimes consider levels of surface roughness, as indicated by the parameter $k_1 h$, which are uncomfortably large for the normal application of lowest-order perturbation theory. Therefore, we first turn to the question of the applicability of perturbation theory for our regime of interest. This is done in two dimensions, where integral equations results can serve as ground truth.

3. Validity of perturbation theory for acoustic scattering into sediment

Formally, we require $k_1 h << 1$ for lowest-order perturbation theory to be accurate in predicting bistatic scattering back into the water from a rough bottom that can be modeled as a homogeneous fluid. Numerical studies using the integral equation method show that, as $k_1 h$ increases, the inaccuracy of perturbation theory first becomes noticeable at a $k_1 h$ of about 0.3–0.4. For scattering into the sediment, however, numerical results show that perturbation theory accuracy extends to much

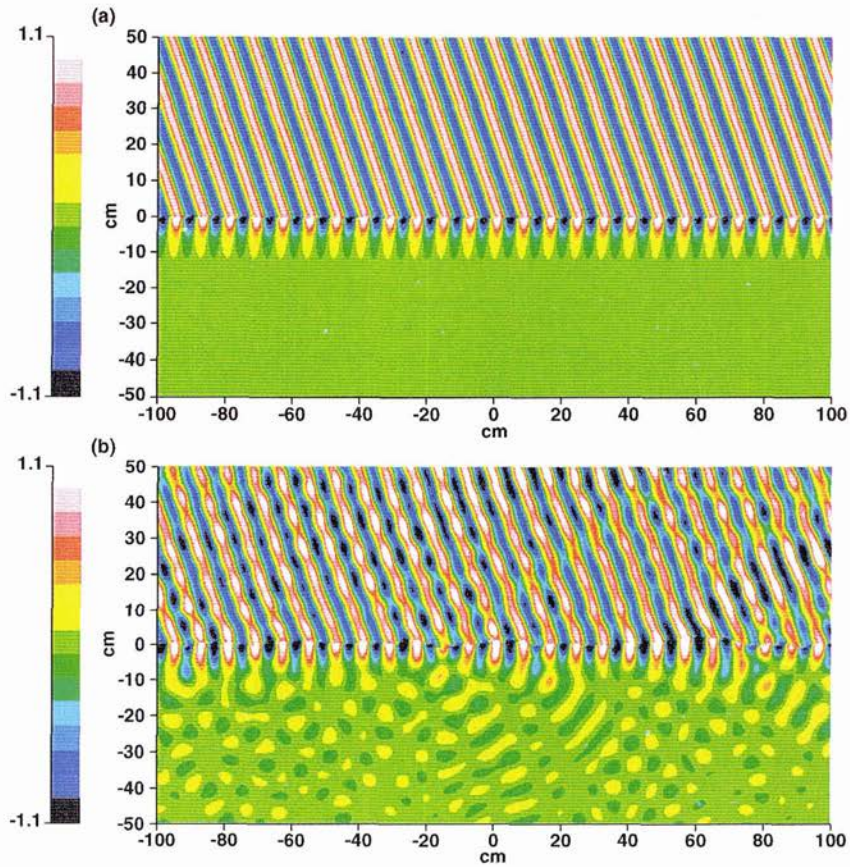

Figure 1. Pressure fields above (in water) and below (in sediment) a flat surface (a) and a rough surface (b) obtained for a 2-D geometry using the exact integral equation method. The incident field (not shown) is from the left at a grazing angle of 20°, which is below the critical angle of 27.8°.

higher roughness levels. Essentially, the smallness of the sound speed contrast between the water and sediment reduces the effective roughness of the interface for the transmission scattering problem. As a result, perturbation theory remains accurate for much larger k_1h than might be expected.

Here we simply illustrate this improved accuracy with an example without pursuing a fundamental explanation. Figure 2 shows a comparison between perturbation theory and exact integral equation bistatic scattering results for an example with $k_1h = 1.0$. The sound speed and density ratios are the same as in Fig. 1, and the roughness spectrum is again given by (1) with $w_1 = 0.02$, but K_L has been reduced to 0.044 cm^{-1} to obtain $k_1h = 1.0$. Again as in Fig. 1, the incident grazing angle of 20° is below the critical angle of 27.8°. For simplicity, absorption in the sediment has been suppressed in this example. For this two-dimensional scattering problem, the scattering strength is 10 $\log_{10}$ (σ), where σ is the bistatic scattering cross section given by $< I_s > r/I_iL$. Here I_i is the incident intensity on the surface of length L, and $< I_s >$ is the average intensity at far-field range r. With the integral equation method, the average scattered intensity was obtained using 50 surface realizations, and a tapered plane wave incident field was employed as described in [4]. Finally, for scatter back into the water, the coherent intensity (over the ensemble of surface realizations) was removed, leaving only the incoherent intensity, which is the appropriate quantity to compare with perturbation theory. For scatter into the sediment, there is no coherent field in the far zone since the incident angle is below the critical angle.

Figure 2 shows that for scattering back into the water lowest-order perturbation theory overpredicts the scattering level by about 1 dB near the specular direction (a scattering angle of 160°), which is not surprising since $k_1h = 1.0$. Nevertheless, accuracy for scattering into the sediment is excellent, and this agreement extends to even higher values of k_1h, well beyond

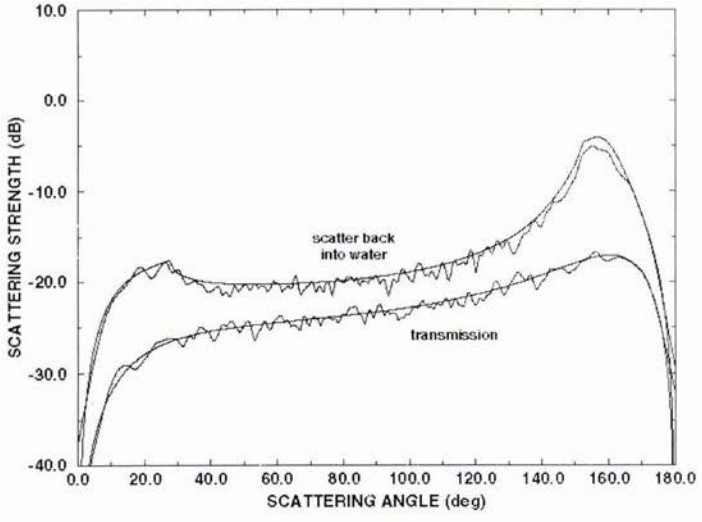

Figure 2. Bistatic scattering strengths for scattering from a rough sediment surface for a 2-D geometry. The smooth curves are obtained using lowest-order perturbation theory, and the fluctuating curves with the integral equation method. The incident grazing angle is 20°, the critical angle is 27.8°, and $k_1 h = 1.0$.

what is need for experiment simulations. In this comparison absorption in the sediment has been neglected. When absorption is included, the comparison is again excellent, except within about 10° of grazing where the situation becomes much more complicated. Low grazing angle paths will be unimportant in our experiment modeling, however, since these paths will be highly attenuated. Thus, we believe perturbation theory is highly accurate for simulating the effects of sediment roughness on acoustic penetration into sediment.

4. Simulation of measured acoustic penetration into sediment

In this section we use full 3-D simulations to examine whether the rough surface scattering mechanism for penetration into sediment can explain results reported by Chotiros [1]. In the experiment an acoustic projector on a movable tower transmitted short sound pulses to an array of buried hydrophones (Fig. 3). Because the projector was movable, the incident grazing angle could be varied, and (after processing) the temporal resolution was about 0.1 ms. The received signals from the buried array were used to deduce the propagation speed and direction in the sediment. Because the hydrophone locations were not known to the precision of a fraction of a wavelength, these deductions were made with an incoherent processing technique as described in [1]. When the incident grazing angle was well above the critical angle, the propagation speed deduced is consistent with the measured sediment sound speed of 1729 m/s, and the direction is consistent with Snell's law.

We consider 20-kHz ATBE results at an incident grazing angle of 12.7°, well below the critical angle of about 28°. Figure 4(a) (adapted from [1]) shows an ambiguity plot in sound speed and depression angle obtained from the experimental data indicating a propagation speed for this case of about 1300 m/s. For the region between the solid and dotted lines, the propagation direction and speed were considered consistent with Snell's law, given the experimental uncertainties [1].

A detailed description of the experiment simulation is given by Moe [5] and is only briefly summarized here. The intensity time series at each hydrophone is obtained as a sum of incoherent and coherent intensities, the latter being important only in the evanescent region near the interface. A Gaussian pulse with pressure envelope given by $\exp(-t^2/t_s^2)$ with t_s = 0.1 ms is used. The incoherent intensity is found by dividing the surface area into a large number of subareas and summing the time delayed contributions from each using the bistatic scattering cross section (lowest-order perturbation theory) appropriate for each subarea. The signal level is reduced by spherical spreading from the source to each area element and by spherical spreading and attenuation from each area element to each hydrophone. The coherent intensity is found ignoring interface roughness. This contribution can be expressed in terms of a Fourier transform of a quantity which itself is given by an integration over wave vector. Analytical approximations are often used for the latter integral based on a steepest descent solution [6], but here a full numerical evaluation is used.

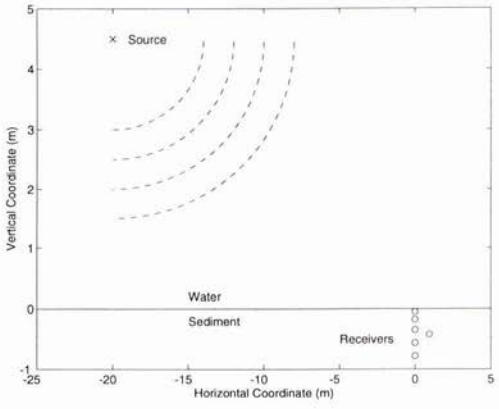

Figure 3. Simulation geometry for acoustic penetration measurements. Note exaggeration of vertical scale.

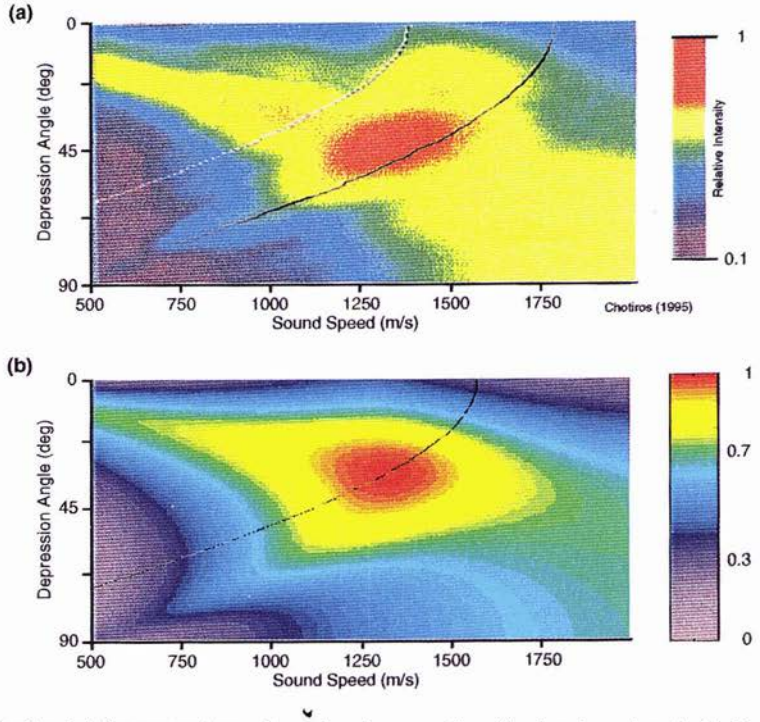

Figure 4. Ambiguity plot for apparent sound speed and propagation direction in sediment. (a) Experimental results reported by Chotiros [1] and (b) simulation results based on scattering from a rough sediment interface. The frequency is 20 kHz and the incident grazing angle is 12.7°. In (a) the region between the lines is considered consistent with Snell's law; in (b) points on the line are consistent with Snell's law.

A 2-D spectrum of surface roughness is needed to evaluate the perturbation theory cross section, and, as mentioned previously, the roughness spectrum was not measured during ATBE. Some guidance is provided by a spectrum obtained in the same region with similar water depths and sediment properties in 1984 [7], about 2 years before ATBE. These data can be represented in the isotropic form [8]

$$W(\mathbf{K}) = w_2 / K^3 \tag{2}$$

valid over a length scale range from about 50 cm down to 0.8 cm (for $2\pi/K$), where $w_2 = 6.2 \times 10^{-3}$ cm and $K = |\mathbf{K}|$. Unfortunately, owing to the spatial separation and the time lapse between the spectrum and penetration measurements, we cannot have confidence that (2) applies to the sediment surface near ATBE. In addition it is likely that the sediment was disturbed in the process of burying hydrophones. For simulations we have modified (2) with two different forms of low-wavenumber cutoffs: a "Gaussian" cutoff form

$$W(\mathbf{K}) = \frac{w_2}{K^3}\left[1 - \exp\left(-\frac{1}{2}K^2 a^2\right)\right]^2 \tag{3}$$

and an "algebraic" cutoff form

$$W(\mathbf{K}) = \frac{w_2}{\left(K^2 + K_L^2\right)^{3/2}}. \tag{4}$$

Using (3) with w_2 from (2) and with $a = 4$ cm yields a spectrum relatively rich in high-wavenumber structure. Doing the simulation with these parameters and using an incoherent processing technique similar to that used for the experimental data yields the ambiguity plot shown in Fig. 4(b), which agrees closely with Fig. 4(a). It must be emphasized that in this simulation the actual propagation speed in the sediment is 1729 m/s, but the apparent speed as measured by this processing method is close to 1300 m/s in this example. Snell's law is satisfied for points on the black line in Fig. 4(b), which passes through the maximum in the simulation ambiguity plot.

By using different choices for the form of the spectrum and for the low-wavenumber cutoff, we obtain apparent propagation speeds in roughly the 1200–1500 m/s range. As the low-wavenumber cutoff is reduced, the apparent speed increases and finally stabilizes at about 1500 m/s, becoming insensitive to further reductions. For example, using (4) with $K_L < 0.2$ cm^{-1} gives about 1500 m/s. Thus, if the spectrum were of the form of (2) down to length scales of about 30 cm or beyond, we would predict an apparent speed of about 1500 m/s. (The example in Fig. 1 should be consistent with this case.) With roughness spectra relatively richer in high-wavenumber components, apparent speeds in the 1100–1300 m/s range can be obtained.

In addition to propagation speed and direction in the sediment, attenuation in the sediment is also of interest. For ATBE Chotiros reports slow-wave attenuations of 30–40 dB/m at 20 kHz [1]. A fit to the signal levels for all six hydrophones used in the simulation of Fig. 4b yields an attenuation of 19 dB/m. However, if only the top three hydrophones are used in the fit, an attenuation of 36 dB/m is obtained. This difference occurs because the top hydrophone is strongly affected by the evanescent wave and by scattered waves propagating close to horizontally, whereas the signal at the deeper hydrophones is made up of scattered waves propagating more steeply.

5. Discussion

The way in which scattered waves traveling at the normal sediment compressional speed (c_2) can appear to be traveling at a much slower speed is illustrated in Fig. 5. Consider a short-pulse plane wave whose leading edge at some time is aligned with the arrows on the water side of the interface. Assume the pulse scatters at the surface and for simplicity propagates

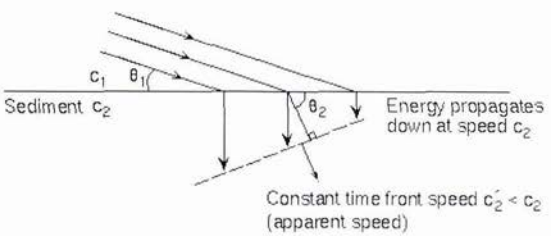

Figure 5. Schematic showing how scattering at the sediment interface can mimic a slow wave in the sediment. For simplicity energy is assumed to scatter straight down.

straight down. The leading edge will propagate down at speed c_2 and at some later time be aligned with the arrows shown in the sediment. If one assumes the propagation direction is normal to this leading edge (as done for these experiments and

in our simulations), the apparent speed will be $c_2' < c_2$. For c_2 of about 1700 m/s, for low-incident grazing angles, and for vertical propagation in the sediment, it is easy to show that c_2' is about 1100 m/s. As the mean propagation direction moves forward from vertical, c_2' increases so that a range of apparent speeds can be obtained depending on the mean propagation direction, which in turn depends on the properties of the sediment roughness spectrum. It is also easy to show that the apparent speed and direction will always be consistent with Snell's law in this simple model of a single propagation direction in the sediment, whether vertical or not.

In summary, we have shown that scattering from a rough water–sediment interface is a viable hypothesis for subcritical penetration into sediments. With a suitable choice of roughness spectrum, this mechanism can explain the observation of apparent slow wave speeds in sediments. Simulated attenuations are less than reported experimentally, but if the analysis is restricted to a subset of hydrophones closest to the surface, simulation results are consistent with the reported values. Acoustic penetration experiments with the roughness spectrum measured in the precise experimental area should be able to determine if scattering from sediment roughness is the actual mechanism.

Acknowledgment

This work was supported by the U.S. Office of Naval Research, Code 321OA.

References

[1] N. P. Chotiros, "Biot model of sound propagation in water-saturated sand," *J. Acoust. Soc. Am.*, vol. 97, pp. 199–214, January 1995.

[2] J. L. Lopes, "Observations of anomalous acoustic penetration into sediment at shallow grazing angles," *J. Acoust. Soc. Am.*, vol. 99, pp. 2473–2474, April 1996.

[3] A. A. Maradudin, T. Michel, A. R. McGurn, and E. R. Mendez, "Enhanced backscattering of light from a random grating," *Annals of Physics*, vol. 203, pp. 255–307, November 1990.

[4] E. I. Thorsos, "The validity of the Kirchhoff approximation for rough surface scattering using a Gaussian roughness spectrum," *J. Acoust. Soc. Am.*, vol. 83, pp. 78–92, January 1988.

[5] J. E. Moe, "Near and far-field acoustic scattering through and from two dimensional fluid-fluid rough interfaces," Technical Report APL-UW TR 9606, Applied Physics Laboratory, University of Washington, October 1996.

[6] L. M. Brekhovskikh, *Waves in Layered Media*, San Diego, Academic Press, 1980.

[7] S. Stanic, K. B Briggs, P. Fleischer, R. I. Ray, and W. B. Sawyer, "Shallow-water high-frequency bottom scattering off Panama City, Florida," *J. Acoust. Soc. Am.*, vol. 83, pp. 2134–2144, June 1988.

[8] P. D. Mourad and D. R. Jackson, "High frequency sonar equation models for bottom backscatter and forward loss," in *Proceedings of OCEAN '89*, IEEE Press, vol. 4, pp. 1168–1175, 1989.

A Novel Method to Enlarge the Scanning Region of a Focused Beamformer

Andrea Trucco

Dpt. of Biophysical and Electronic Engineering (DIBE), University of Genoa
Via all'Opera Pia, 11A
16145 Genova, ITALY
Email: fragola@dibe.unige.it

Abstract

Often focused beamforming systems use the Fresnel approximation to compute the required delays. Unfortunately, such an approximation has a validity region that is very narrow around the broadside direction. To investigate wider areas, in this paper, a novel approximation composed of the weighted terms of the conventional Fresnel approximation is presented. The attractive results (in terms of mean square error and enlargement of the validity region) obtained by applying the proposed approximation to a planar array are presented.

1. Introduction

Beamforming is a linear technique aimed at processing array signals in order to enhance incoming signals from a selected steering direction and to abate incoming signals from any other direction [1]. Thanks to its flexibility, beamforming can be successfully employed in many application fields (e.g., sonar, radar, medical imaging, non-destructive testing, etc.) with different objectives. In any case, if the array works under far-field conditions, the delays required by the beamforming operation can be easily computed in an exact way, whereas, if the array works under near-field conditions, the focalization of beamforming is required to take into account the curvature of waves [1]. In the latter case, due to the presence of a square root operation, a fast computation of the exact delays is often prohibitive and an approximate version is preferred: generally, the Fresnel approximation (obtained by the expansion of the time-independent free-space Green's function [2][3]) is adopted [1]. Moreover, the Fresnel approximation makes it possible to apply the Fast Fourier Transform (FFT) in the implementation of beamforming even when focalization is necessary [4], thus resulting in a great computational profit.

These issues are particularly important in three-dimensional (3D) sonar imaging systems, where: the focalization is required, the enormous number of different delays to be used disallows an off-line computation of them, and the FFT implementation of the beamforming is highly demanded. In this case, the Fresnel approximation allows one to compute on-line the delays and to apply the FFT implementation, thus achieving a 3D real-time imaging [4]. Despite its simplicity and advantages, the Fresnel approximation has a well defined region of validity [2] that forces potential steering directions to be contained inside a narrow scanning region around the broadside direction. This constraint is heavy in applications like acoustic imaging that require a wide region of view, for both medical and underwater investigations. To avoid this drawback, some imaging techniques that do not need the Fresnel approximation have been devised [5][6] but, unfortunately, they increase the computational load and/or the system complexity.

This paper presents a novel approximation (not too different from the Fresnel one) based on the minimization of the mean square error, so resulting in an acceptable precision inside wide scanning regions. In more detail, the same terms as used for the Fresnel expansion are weighted by coefficients whose values are fixed, given the array geometry, by a least-squares procedure on the basis of the desired scanning region. Thus, the new approximation keeps the low computational load and the low system complexity that characterize the Fresnel expansion and maintains the opportunity to be implemented in an FFT focused beamformer, too.

This paper is organized as follows. Section 2 presents a background concerning the delay approximation and the related validity region. In Section 3, the weighting of the Fresnel approximation is presented and its application to a planar array is described in Section 4. Finally, results are discussed and some conclusions are drawn in Section 5.

2. Background on Delay Approximation

A beam signal (generated by a conventional delay and sum beamformer [1]) steered in the direction of the unit vector (versor) $\mathbf{u}$ is defined as:

$$b(\mathbf{u},t)=\sum_{i=1}^{M} w(i)\cdot x_i\left(t-\tau(\mathbf{u},i)\right) \tag{1}$$

where $x_i(t)$ is the temporal signal received by the i-th sensor, $\tau(\mathbf{u}, i)$ and $w(i)$ are the delay and the weight applied to such a signal, respectively, and M is the number of array elements.

Under the far-field hypothesis, the exact delay $\tau(\mathbf{u}, i)$ can be written as:

$$\tau_{ff}(\mathbf{u},i)=\frac{\left(\mathbf{u}\,\mathbf{v}_i^{+}\right)}{c} \tag{2}$$

where $\mathbf{v}_i = [x_i, y_i, z_i]$ is the position vector of the i-th sensor, $^+$ indicates the transposition operator (both $\mathbf{u}$ and $\mathbf{v}_i$ are row vectors), and c is the carrier speed. This delay formulation is compatible with the FFT implementation of beamforming.

If focalization is necessary, as the far-field hypothesis does not hold any more, then the exact delay is:

$$\tau_{ex}(\mathbf{u},i)=\frac{R-\sqrt{R^2+\|\mathbf{v}_i\|^2-2R\mathbf{u}\,\mathbf{v}_i^{+}}}{c} \tag{3}$$

where R is the focalization distance in the steering direction $\mathbf{u}$ and $\|\cdot\|^2$ is the Euclidean norm. These delays are heavy to compute on line (mainly due to the presence of a square root) and inhibit the implementation of focused beamforming by the FFT.

For these reasons, one tries to approximate the exact delay by a formulation that allows an easy on line computation and the FFT implementation. This target is generally achieved thanks to the Fresnel expansion, which results in the following approximation [1] to the exact delay:

$$\tau_{Fr}(\mathbf{u},i)=\frac{\left(\mathbf{u}\,\mathbf{v}_i^{+}\right)}{c}-\frac{\|\mathbf{v}_i\|^2}{2Rc}\approx\tau_{ex}(\mathbf{u},i) \tag{4}$$

The first term of the addition depends on both $\mathbf{v}_i$ and $\mathbf{u}$, and represents the distance-independent delay equal to that defined in (2). The second term takes into account the wave curvature, depends on $\mathbf{v}_i$ and does not depend on $\mathbf{u}$. Thanks to the latter fact, one can show that the FFT implementation of focused beamforming is feasible [4].

According to Ziomek [2], there are three necessary conditions that define the validity region of the Fresnel approximation. The first imposes a small steering sector, the second condition stipulates the minimum focalization distance, and the third establishes the boundary between near-field and far-field regions:

$$72^\circ\le\phi\le108^\circ \tag{5}$$

$$R>1.356V \tag{6}$$

$$R<\pi V^2/\lambda \tag{7}$$

where ϕ is the angle between $\mathbf{u}$ and $\mathbf{v}_i$, V is the maximum value of $\|\mathbf{v}_i\|$, and λ is the wavelength of the carrier. These restrictive conditions (in particular, the one that limits the angular extension) are often not satisfied in imaging systems, with potential low performances in the lateral regions of images.

3. Weighting the Fresnel Approximation

In order to relax the constraint of (5), a possible solution is to weight the terms of the Fresnel approximation by two constants, k_1 and k_2, computed on the basis of the desired steering region and of a fixed focalization distance. The importance of keeping unchanged the two terms of the Fresnel approximation lies in their computational simplicity and in the possibility of implementing focused beamforming by the FFT. One can write the novel delay approximation as follows:

$$\tau_{ls}(\mathbf{u},i)=k_1\frac{\left(\mathbf{u}\,\mathbf{v}_i^{+}\right)}{c}+k_2\frac{\|\mathbf{v}_i\|^2}{Rc} \tag{8}$$

and try to fix the values of the two constants by minimizing the sum of the square differences between the delays provided by the approximation and the exact delays. Square errors can be measured over a two-dimensional grid containing all the possible pairs (**u**, *i*). Denoting by $e(\mathbf{u}, i)$ the error between the approximate and exact delays, and by $\mathbf{u}_1$, $\mathbf{u}_2$, ..., $\mathbf{u}_N$ the steering directions of interest, one can write an overdetermined system of equations by using a matrix formulation:

$$\begin{bmatrix} \tau_{ex}(\mathbf{u}_1,1) \\ \mathrm{M} \\ \tau_{ex}(\mathbf{u}_1,M) \\ \tau_{ex}(\mathbf{u}_2,1) \\ \mathrm{M} \\ \tau_{ex}(\mathbf{u}_2,M) \\ \mathrm{M} \\ \mathrm{M} \\ \mathrm{M} \\ \tau_{ex}(\mathbf{u}_N,M) \end{bmatrix} = \begin{bmatrix} \left(\mathbf{u}_1\,\mathbf{v}_1^+\right)/c & \|\mathbf{v}_1\|^2/(Rc) \\ \mathrm{M} & \mathrm{M} \\ \left(\mathbf{u}_1\,\mathbf{v}_M^+\right)/c & \|\mathbf{v}_M\|^2/(Rc) \\ \left(\mathbf{u}_2\,\mathbf{v}_1^+\right)/c & \|\mathbf{v}_1\|^2/(Rc) \\ \mathrm{M} & \mathrm{M} \\ \left(\mathbf{u}_2\,\mathbf{v}_M^+\right)/c & \|\mathbf{v}_M\|^2/(Rc) \\ \mathrm{M} & \mathrm{M} \\ \mathrm{M} & \mathrm{M} \\ \mathrm{M} & \mathrm{M} \\ \left(\mathbf{u}_N\,\mathbf{v}_M^+\right)/c & \|\mathbf{v}_M\|^2/(Rc) \end{bmatrix} \begin{bmatrix} k_1 \\ k_2 \end{bmatrix} + \begin{bmatrix} e(\mathbf{u}_1,1) \\ \mathrm{M} \\ e(\mathbf{u}_1,M) \\ e(\mathbf{u}_2,1) \\ \mathrm{M} \\ e(\mathbf{u}_2,M) \\ \mathrm{M} \\ \mathrm{M} \\ \mathrm{M} \\ e(\mathbf{u}_N,M) \end{bmatrix} \tag{9}$$

The system in (9) can be written in a shortened form as:

$$\mathbf{d} = \mathbf{A}\mathbf{k} + \mathbf{e} \tag{10}$$

where **d** is the column vector (*MN* by 1) of the exact delays, **k** is the column vector (2 by 1) of the unknowns, **e** is the column vector (*MN* by 1) of the errors, and **A** is the matrix (*MN* by 2) containing the two terms of the approximation.

By using a least-squares inverse [7], $\mathbf{A}^{ls}$ (2 by *MN*), of the matrix **A**, one can compute a system solution $\mathbf{k}^*$ that minimizes the mean square error:

$$\min_{\mathbf{k}} \left\{ \|\mathbf{e}\|^2 \right\} \tag{11}$$

as follows:

$$\mathbf{k}^* = \left(\mathbf{A}^{ls}\right)\mathbf{d} = \left[\left(\mathbf{A}^+\mathbf{A}\right)^{-1}\mathbf{A}^+\right]\mathbf{d} \tag{12}$$

Once the solution, $\mathbf{k}^*$, has been computed off-line, one can begin the focused beamforming operation under the guarantee that the approximate delays τ_{ls} are optimum in the least-squares sense. One can verify that, if one fixes a steering region perfectly overlapped with the validity region of the Fresnel approximation, the differences between the least-squares and Fresnel approximations are negligible, i.e., $k_1 \approx 1$ and $k_2 \approx -0.5$.

4. Results for a Planar Array

The effectiveness of the proposed method has been assessed in the following cases: equispaced linear array (as described in [8]) and equispaced square array. In the latter case, the steering faculty is extended to the 3D space, as shown in Fig. 1. Therefore, supposing the array to be placed on the plane $z = 0$ and according to Fig. 1, the steering versor $\mathbf{u}_{\alpha\beta}$ can be defined as a function of the angles α and β; the vector $\mathbf{v}_i$ and the least-squares delay τ_{ls} can be written as follows:

$$\mathbf{u}_{\alpha\beta} = \left[\sin\alpha, \sin\beta, \cos\alpha\cos\beta\right] \tag{13}$$

$$\mathbf{v}_i = \left[x_i, y_i, 0\right] \tag{14}$$

$$\tau_{ls}\left(\mathbf{u}_{\alpha\beta}, i\right) = k_1 \frac{\left(x_i \sin\alpha + y_i \sin\beta\right)}{c} + k_2 \frac{x_i^2 + y_i^2}{Rc} \tag{15}$$

where *i* is an integer included between 1 and *M*. One can define an angle θ as the angle between the steering versor and the *z* axis (see Fig. 1), as a consequence, the relation with α and β is: $\theta = \arccos[\cos(\alpha)\cos(\beta)]$.

To test the accuracy of the delay approximation, one can use the total mean square error (i.e., $MSE = \|\mathbf{e}\|^2/MN$) plotted versus the focalization distance, the *MSE* as a function of the steering direction (computed at a fixed focalization distance):

$$MSE(\alpha,\beta)=\frac{1}{M}\sum_{i=1}^{M}e(\mathbf{u}_{\alpha\beta},i)^2 \quad , \tag{16}$$

and the *MSE* as a function of the array element position (computed at a fixed focalization distance):

$$MSE(x_i,y_i)=\frac{1}{N}\sum_{l=1}^{N}e(\mathbf{u}_l,i)^2 \tag{17}$$

where $\mathbf{u}_l$ is one of the N steering directions.

As an example, one can consider an array composed of 11×11 3λ-spaced elements, working at 500 kHz, with a sound speed c = 1500 m/s (i.e., M = 121 and λ = 3 mm). Such an array can be employed in a 3D imaging systems working under wide-band conditions to avoid grating lobes [9]. A collection of 25×25 steering directions with an angular spacing of 2.8° for both α and β has been considered for the computation of (k_1, k_2). From these 625 steering directions, the pairs (α, β) for which the related θ is higher than 30° has been disregarded; as a consequence, the final number of considered steering directions is N = 357. Finally, a range domain 0.25 m ≤ R ≤ 5 m has been required. The angular extension of this scanning region is larger than that of the validity region of the Fresnel approximation (i.e., from (5) one can derive the constraint: |θ| < 18°), whereas the range extension is similar (i.e., the Fresnel approximation is valid for 0.09 m < R < 4.24 m). Figure 2 shows the computed values of k_1 (panel a) and k_2 (panel b) versus the focalization distance R, and the total *MSE* (panel c), measured in μs^2, for both the least-squares approximation τ_{ls}, the Fresnel approximation τ_{Fr}, and the far-field delay τ_{ff}. Moreover, Fig. 3 compares the $MSE(\alpha,\beta)$ of the least-squares approximation with that of the Fresnel approximation, after fixing β = 0°; Fig. 4 shows the same comparison for the $MSE(x_i, y_i)$, after fixing y_i = 0.045 m. Both errors were computed after fixing R = 0.5 m and were measured in μs^2.

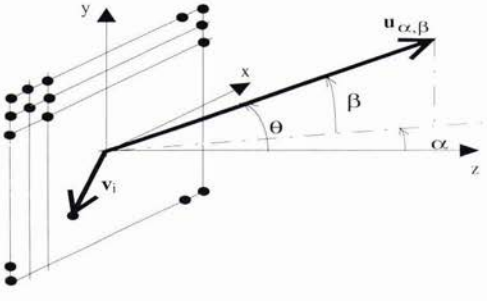

Figure 1: Geometry of a square array and related notation.

5. Discussion and Conclusions

One can notice that, for every delay approximation, the total *MSE* decreases as the focalization distance increases. Within the near-field region, the proposed approximation has a total *MSE* lower than that of the Fresnel approximation. Moreover, the weights k_1 and k_2 tend to assume constant values for a focalization distance larger than few meters, so excluding the strict necessity for computing them for each R (in particular, k_1 tends to be equal to 1, as in the Fresnel approximation).

Concerning the *MSE* versus the steering direction and the array element, one can notice that the proposed approximation has the lowest error for whatever array element, whereas the situation is more complex for the error as a function of the steering angles. In the latter case (see Fig. 3), as β was fixed equal to 0° one can notice that θ = α and that the error of the Fresnel approximation increases with |α| and its value at the border of the validity region (i.e., $MSE(18°, 0°)$) is about 0.006 μs^2 (at R = 0.5 m). Despite the error of the least-squares approximation is not null for α = 0°, its value does not exceed 0.006 μs^2 over the domain |α| < 26°. Therefore, as within the validity region of the Fresnel approximation the loss of image quality is negligible, one can deduce that, generally, moving from the Fresnel approximation to the least-squares approximation, the safe scanning region can be enlarged from |θ| < 18° to |θ| < 26°, with a gain factor of about 1.45.

By repeating the same reasoning on the errors computed for R ≠ 0.5 m, the same conclusion (about the potential enlargement of the scanning region) will be reached. Moreover, if a change of the desired scanning sector is performed, one can verify that the least-squares approximation provides a sort of compromise between the approximation precision and the extension of the desired scanning region.

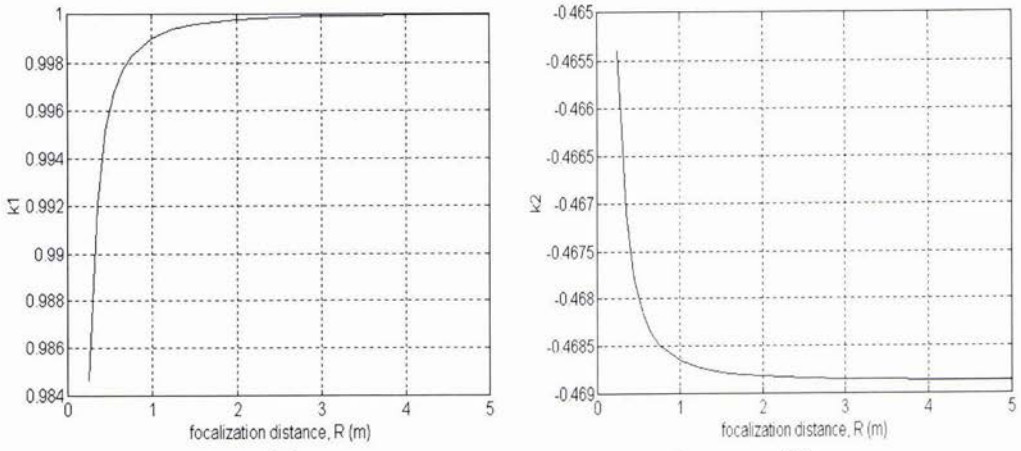

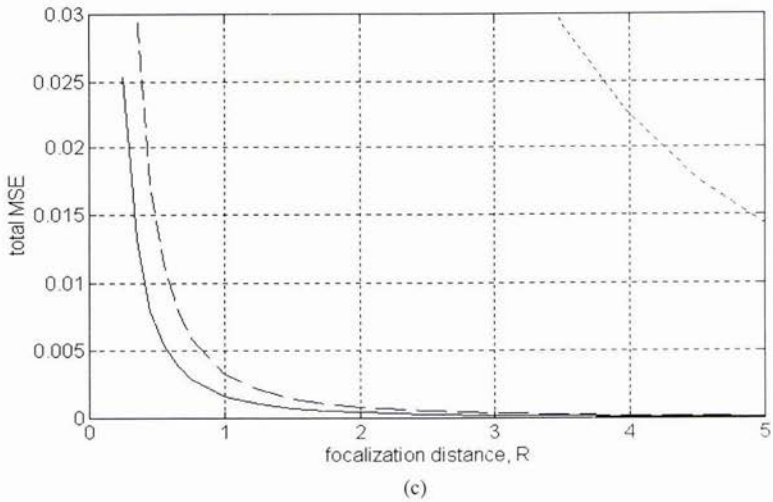

Figure 2: Behaviours of the weights k_1 (a) and k_2 (b) of the least-squares approximation versus the focalization distance R in m. (c) Total MSE in μs^2 versus R for the least-squares approximation (solid line), the Fresnel approximation (dashed line), and the far-field hypothesis (dotted line).

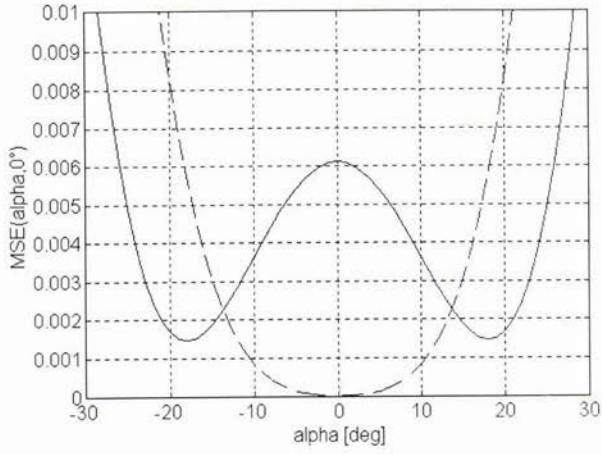

Figure 3: Behaviours of $MSE(\alpha, \beta)$ versus α, after fixing $\beta = 0°$, computed at $R = 0.5$ m and measured in μs^2, for the least-squares approximation (solid line) and the Fresnel approximation (dashed line).

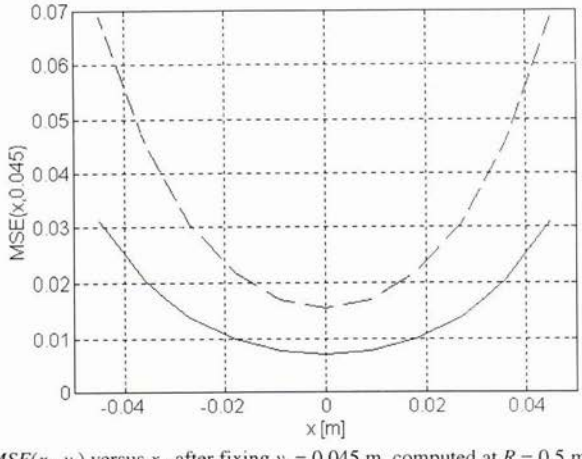

Figure 4: Behaviours of $MSE(x_i, y_i)$ versus x_i, after fixing $y_i = 0.045$ m, computed at $R = 0.5$ m and measured in μs^2, for the least-squares approximation (solid line) and the Fresnel approximation (dashed line).

Finally, concerning the FFT implementation of focused beamforming, one can verify that for a large set of focalization distances, the value of k_1 can be set equal to 1, without a notable loss of precision. Then, the equations that link the spatial frequencies of the FFT to the steering angles can hold their conventional form [4][10]. Instead, if $k_1 \neq 1$, such equations should be slightly updated by an adequate scaling factor.

In conclusion, an approximation for the delays required by focused beamforming has been proposed that minimizes the *MSE* computed over the scanning region of interest. The minimization has been obtained by weighting the terms of the conventional Fresnel approximation through a least-squares solution of an overdetermined equation system. In general, one can observe that, if the desired scanning region is not too extended, the least-squares approximation yields an acceptable precision for many practical operations. At the same time, thanks to the similarity of the proposed approximation to the Fresnel one, the computational load and the system complexity do not notably increase, and the opportunity of implementing focused beamforming via the FFT can be easily kept. The application of such an approximation to a planar array has been analysed and the advantages have been described.

References

[1] R.O. Nielsen, *Sonar Signal Processing*, Artech House, Boston, 1991.

[2] L.J. Ziomek, "Three Necessary Conditions for the Validity of the Fresnel Phase Approximation for the Near-Field Beam Pattern of an Aperture," *IEEE Journal of Oceanic Engineering*, vol. 18, pp. 73-75, January 1993.

[3] J.W. Goodman, *Introduction to Fourier Optic*, McGraw-Hill, New York, 1968.

[4] V. Murino, A. Trucco, "Dynamic Focusing by FFT Beamforming for Underwater 3D Imaging," *Acoustics Letters*, vol. 17, no. 9, pp. 169-172, March 1994.

[5] M. Soumekh, "Array Imaging with Beam-Steered Data," *IEEE Transactions on Image Processing*, vol. 1, pp. 379-390, July 1992.

[6] R.K. Hansen, P.A. Andersen, "3D Acoustic Camera for Underwater Imaging," *Acoustical Imaging*, vol. 20, pp. 723-727, 1993.

[7] C.R. Rao, S.K. Mitra, *Generalized Inverse of Matrices and its Applications,* Wiley, New York, 1971.

[8] A. Trucco, V. Murino, "A Weighted Fresnel Approximation for the Delays Used in Focused Beamforming," in *Acoustical Imaging, Volume 23*, S. Lees, Ed. New York: Plenum Press, 1997 (in press).

[9] V. Murino, A. Trucco, A. Tesei, "Beam Pattern Formulation and Analysis for Wide-Band Beamforming Systems Using Sparse Arrays," *Signal Processing*, vol. 56, no. 2, January 1997 (in press).

[10] V. Murino, A. Trucco, "Underwater 3D Imaging by FFT Dynamic Focused Beamforming," *1st IEEE International Conference on Image Processing*, Austin, Texas (USA), vol. I, pp. 890-894, November 1994.

A PC/Linux Software Toolkit for Coastal Swath Mapping

Robert C. Tyce(1), Stephen M. Dzurenko(1), Paul A. Cohen(2), David W. Caress(2,3)

(1)Dept. of Ocean Engineering
University of Rhode Island
Narragansett, RI 02882 USA

(2)SeaBeam Instruments Corp.
141 Washington St.
E.Walpole, MA 02032 USA

(3)Lamont-Doherty Earth Observatory
Palisades, NY 10964
USA

Abstract

Assembly of a PC/Linux based data acquisition and processing software toolkit for coastal (shallow water) multibeam and sidescan swath mapping sonar systems has been undertaken by the URI Ocean Mapping Development center (OMDC) in collaboration with government agencies and industry. This toolkit integrates existing software developments with a powerful menu driven Real Time Geographic Information System (RTGIS). This paper represents a progress report on this effort along with examples of some of the software tools.

1. Introduction

The OMDC (directed by Dr. Tyce) is part of the NSF/Industry sponsored Ocean Technology Center of the University of Rhode Island (URI). Members include NOAA, NAVOCEANO, USGS, SAIC, Raytheon, Datasonics and Sea Beam Instruments. This software effort is supported by NOAA, NSF and industry members (particularly SeaBeam Instruments). With the software originally intended for workstations running UNIX, more recently we have moved to PCs running Linux, a public licensed UNIX operating system. The intent is not really to develop completely new tools but to integrate compatible software tools for multibeam and sidescan sonar surveying with a powerful Real Time Geographical Information System (RTGIS), utilizing the diverse set of software packages already developed for related applications.

The toolkit is built around the following public software tools:

- Linux public licensed UNIX for PC's
- Xfree86 Xwindows display software for Linux from The Xfree86 Project
- Tcl/Tk graphical user interface software
- Ghostscript and Ghostview public domain Postscript software from The GNU Project at MIT
- GRASS 4.1 GIS and data base software developed by the USACE CERL
- Xsonar and Mini Image Processing System (MIPS) Sidescan Sonar processing packages from the USGS
- Multi-Beam System (MB-System) and Generic Mapping Tools (GMT) from LDEO and NOAA researchers
- netCDF data management software from UNIDATA
- Data Transfer Mechanism (DTM) IPC messaging software from National Center for Supercomputing Applications

The toolkit also makes use of the following proprietary software tools for those with licenses:

- Motif graphical user interface software
- OpenGL graphical display language for Linux
- Maptech Professional PC Helm guidance software from Resolution Mapping
- SeaView/ SeaSurvey multibeam processing enhancements to MB-System from SeaBeam Instruments
- Swathmap Realtime multibeam tools from the University of New Brunswick
- RTGIS Real Time extensions to GRASS GIS software from URI OMDC

During the past 15 years, personnel from URI's OMDC have developed and installed hardware and software to support multibeam and sidescan sonar operations aboard more than 15 ships from the National Oceanic and Atmospheric Administration (NOAA), the U.S. Naval Oceanographic Office (NAVOCEANO), Woods Hole Oceanographic Institution (WHOI), Lamont–Doherty Earth Observatory (LDEO), URI and private industry. From 1990 to 1992 the OMDC worked with the USGS and the British IOS to integrate shipboard data collection and processing of combined sidescan sonar

imagery and bathymetry from the GLORIA sidescan sonar aboard the research Vessel Farnella. As part of this effort we introduced the GRASS GIS to the shipboard environment for monitoring survey progress in real time with such success that we concluded that the next generation of hydrographic / oceanographic survey data acquisition and processing system should be built around a Real Time GIS (RTGIS) [1] [2].
In 1994 we began the development of an RTGIS software package as a project under URI's newly formed NSF/Industry sponsored Ocean Technology Center. The GIS software chosen for our RTGIS effort was the Geographic Resource Analysis Support System (GRASS) written primarily by the United States Army Corps of Engineers [3]. The GRASS GIS package was chosen for this work because of its low cost, because the source code is included with the distribution, and because its raster based origins make it particularly good at dealing with swath sonar data.

The GRASS system is written in C and runs under UNIX operating systems. GRASS has been ported to a variety of computer systems ranging from 386 PC's to high-end workstations and the only specific system requirement is that GRASS must be run under UNIX. Our original multibeam processing software development was VAX/VMS based in Fortran. With the conversion to UNIX as the operating system of choice for swath sonar data processing in recent years, new tools needed to be developed. A number of government, university and industry organizations have undertaken to develop UNIX based tools for multibeam and sidescan (swath) sonars, with impressive results.

In 1995 the OMDC undertook a project for NOAA to develop a UNIX-based software toolkit for hydrographic data collection and processing from coastal (shallow water) multibeam and sidescan sonar systems. The intent was to build a set of compatible software tools specific to U.S. multibeam and sidescan sonar hydrography out of the diverse set of software packages already developed for related applications rather than developing a new set of tools. Central to this effort were our prior efforts to develop RTGIS tools. This paper represents a progress report on this project.

Our software toolkit effort began first aboard Silicon Graphics UNIX workstations, the platform of choice for most multibeam software developers, and it has proven to be a forgiving host. Our intention was to eventually migrate the code to workstations from other vendors. However, from the beginning we hoped that we would be able to migrate the toolkit to a PC platform running some form of UNIX. Since the GRASS GIS had already been ported to the PC-based public licensed Linux operating system, this became our platform of choice early in 1997. This choice was made primarily for cost (low cost computer and zero cost operating system) with performance improving with time. Porting to Linux has been surprisingly straightforward for most of our tools, in part due to the wealth of support code available for standard user interfaces and graphical environments. The work described here was done on a Gateway 133 MHz Pentium with 32 Mbytes of memory. One 1.6 Gbyte disk was used for Windows 95 operations and one 4 Gbyte disk for Linux operations. Graphics were provided by an ATI Mach 64 PCI bus card. Peripherals included an 8 port RS-232 serial port card from Cyclades with Linux drivers, a PMI PCI bus ethernet card, an Adaptec SCSI adapter, an Exabyte 8200 tape drive, and an HP 650C large format color plotter.

2. Software Toolkit Contents

Software components of our toolbox include both cost free public software and proprietary code with licenses available either commercially or through special arrangements with the developers or their clients. The first type of public code includes the operating system (Linux) with TCP/IP ethernet support, supporting graphics software (Xfree86), Graphical User Interface (GUI) widget software (Tcl/Tk), and public Postscript compatible printing software (Ghostscript and Ghostview). The second type of public code includes powerful general purpose GIS software (GRASS 4.1), special purpose sidescan sonar processing software (Xsonar), and multibeam processing software (MB-System) together with supporting display graphics (GMT) and data management (netCDF) tools.

The first type of proprietary software in the toolkit is low cost support software including the Motif GUI widget software and an OpenGL graphic library for Linux to provide maximum compatibility with different packages. The second type of proprietary code is commercial mapping products, which includes 1) the electronic nautical chart program Maptech Professional run on a second DOS/Windows PC for helm guidance and autopilot control (based upon routes and standard NMEA data messages provided by the RTGIS Linux system), and 2) a sophisticated commercial set of multibeam mapping tools (SeaView / SeaSurvey from SeaBeam Instruments Corp.) which build upon the MB-System tool set. The last type of proprietary software includes software developed at universities in consort with commercial and government clients who have the right to use and license the software. This last type includes components of the Swathmap multibeam mapping software developed by the Ocean Mapping Group at the University of New Brunswick, and RTGIS enhancements to GRASS and other tools developed by the University of Rhode Island. NOAA and SeaBeam Instruments are supporters of both these university groups. A summary list of software components is provided in Table 1.

3. Software Functions

The software packages above are part of either toolkit system software or toolkit user software. Each user software package has been selected for this toolkit because it satisfies a particular need, though overlap does occur in user functions with some tools. The RTGIS operator directly interacts with the user software to perform a specific task (i.e., data acquisition, processing, or display). The system software generally does not directly interact with the user. It is provided as necessary support for the user software. Table 2 presents a list of toolkit modules along with a brief summary of the functions performed by each software module.

Table 1. Toolkit Software Components

Package	Description	Source	Information	Restrictions
Linux	Public UNIX for PCs	ftp://ftp.cdrom.com/pub /linux/slackware	http://www.linux.org	Free public licensing with terms included
Xfree86	X windows for UNIX	ftp://ftp.xfree86.org	http://www.xfree86.org	Free public licensing with terms included
Tcl/Tk	X Windows GUI development system	ftp://ftp.smli.com/pub/tcl/	http://www.smli.com/research/tcl	Free public licensing with terms included
Ghostscript	Postscript interpreter	ftp://ftp.cs.wisc.edu/ghost/aladdin/	http://www.cs.wisc.edu/~ghost /index.html	Free public licensing with terms included
Ghostview	Postscript viewer	ftp://ftp.cs.wisc.edu/pub /X/	http://www.cs.wisc.edu/~ghost /index.html	Free public licensing with terms included
GRASS4.1	Geographic Information System	ftp://moon.cecer.army .mil/pub/grass/grass4.1 /release/	http://www.cecer.army.mil/grass /GRASS.main.html	Public domain No license required
XSonar	Side scan sonar processing system	ftp://boomer.er.usgs.gov /pub/sonar/	ftp://boomer.er.usgs.gov/pub/sonar/xsonar.ps.Z	Public domain No license required
MB-System	Multibeam sonar processing system	ftp://lamont.ldeo.columbia.edu/pub/swath_data/	http://www.ldeo.columbia.edu/MB-System/MB-System.intro.html	Public domain No license required
GMT	Generic Mapping Tools	ftp://kiawe.soest.hawaii.edu/pub/gmt/	http://www.soest.hawaii.edu/wessel/gmt.html	Free public licensing with terms included
netCDF	Common data exchange utility	ftp://ftp.unidata.ucar.edu /pub/netcdf/	http://www.unidata.ucar.edu /packages/netcdf/	Free public licensing with terms included
DTM	Data Transfer Mechanism for Interprocess Communication	ftp://ftp.ncsa.uiuc.edu /DTM/	http://xtc.ncsa.uiuc.edu/DTM/Documentation/DTM2.4/dtm.tp.html	Public domain No license required
Motif 2.0	X Windows GUI programming system	Metrolink, Inc.	http://www.metrolink.com holly@metrolink.com	Proprietary $199 license per installation
OpenGL	Graphics programming system	Metrolink, Inc.	http://www.metrolink.com holly@metrolink.com	Proprietary $199 license per installation
Maptech Professional	Helm Guidance Electronic Nautical Chart program	Resolution Mapping	1-617-860-0430	Proprietary $500-1000 license per installation
SeaView / SeaSurvey	Multibean collection and processing software	SeaBeam Instruments Corp.	mkt@seabeam.com 1-800-732-2326	Proprietary commercial licensing
Swathmap	Multibeam collection and processing software	Univ. of New Brunswick Ocean Mapping Group	jhc@atlantic.cs.unb.ca	Distribution limited to supporting members who can license
RTGIS	Real Time Extensions to GRASS	URI Ocean Mapping Development Center	tyce@oce.uri.edu	Distribution limited to supporting members who can license

4. Real Time Geographic Information System (RTGIS) for Swath Mapping

Real time in the context of mapping generally means aboard ship. Figure 1 represents our RTGIS shipboard mapping configuration with sensor data being concentrated and time stamped, then passed on for collection, processing, and display. Both before and during surveying, line planning and trackline selection generally occurs, based upon previous operations. The tracklines are then supplied to a track-following system which provides helm guidance (preferably on an electronic nautical chart or ENC) and autopilot control if so equipped. Our present PC toolkit configuration uses two PC's to accomplish the tasks in figure 1. The first PC runs the Linux toolkit with RTGIS capability and performs all functions except helm guidance. The second runs an ENC based helm guidance system (e.g. Maptech Professional) in DOS or Windows. The helm guidance system is provided a single RS-232 interface with multiple NMEA 0183 format messages containing time, position, depth, heading, course and speed. Track lines to follow are provided via ethernet file transfer. The RTGIS system allows for line, track and coverage displays on top of any number of GIS data layers from previous surveys, including nautical charts. GIS data layers are one of the end products of all the processing tools. An example of GIS data layers which might be used by the RTGIS is shown in figure 2, which includes NOAA chart, coastline, sidescan mosaic, sample sites and sidescan imagery draped over bathymetry [4].

Table 2. Toolkit Software Functions

Module	Software	Functions
System Software		
Computer Environment	Linux 2.0.0	UNIX operating system- host for all other system and user software
	Xfree86 3.2	Xwindows implementation- host for all Xwindows-based user applications
	TCP/TP	Complete TCP/IP implementation- host for networking applications, ftp, telnet and ethernet data acquistion.
	Motif 2.0	Port of OSF/Motif for Linux, includes Motif window manager and all Motif libraries and headers for support of Motif-based application GUIs
	OpenGL	Fully SGI-compliant port OpenGL for Linux, includes software double buffering, depth buffering, accumulation buffering, anti-aliasing, texture mapping, fog, lighting, etc. Supports OpenGL-based graphics applications
	Tcl/Tk	System for developing and using GUI applications. Provides the top level RTGIS interface, or "Toolkit"; menus provide consistent interface to all other Toolkit user software
	netCDF	Data structure to support GMT and MB-System user software
	DTM	Interprocess Communication to supports RTGIS real time extensions
	Ghostview	Postscript map viewing
	Ghostscript	Postscript hard copy map output to user-selectable printer or plotter
	GMT	High quality map creation of user defined data overlays and multibeam data / MB-System support
User Software		
Survey Planning	RTGIS	Historic data browsing, Sidescan sonar coverage display, Survey line layout, Survey line export to Helm Guidance Digital Terrain Model creation from raster NOAA chart data layers
Data Acquisition	RTGIS	Serial data acquisition and logging of multiple navigation sources, gyro heading, magnetic heading, and single beam bathymetry via 8-port serial port extenders Sidescan sonar data acquisition and logging of digital output from EG&G 960 Deck Unit via PC parallel port Multibeam data acquisition and logging via PC Ethernet port
Survey Monitoring	RTGIS	Real time text and graphical monitoring of data logging, Real time ship track display Real time swath coverage display
RTGIS	RTGIS	Real time output of reconstructed NMEA messages to Helm Guidance for line steering and autopilot control
	Maptech Pro	Laptop display of NOAA chart with ship navigation overlay Display of current survey line, Output to autopilot
Data Management	GRASS4.1	Provides geographical data base structure and interface to an RDBMS
	RTGIS	Post-survey data reporting, CD-ROM writing of raw and processed swath data for storage and on-line reference
Sidescan sonar	RTGIS	Data acquisition and logging, Import of Xsonar raster output to GRASS raster coverage
	Xsonar	Complete sidescan sonar processing and gridding
	GRASS4.1	Swath mosaicing, translation, and rubbersheeting
Multibeam sonar	RTGIS	Real time data acquisition and logging Import of MB-System raster output to GRASS raster coverage
	MB-System	Complete multibeam sonar processing, gridding, and mosaicing
	SeaSurvey	Produce realistic geological views of multibeam data in real time
	SeaSwath	Produce waterfall, profile views of multibeam data in real time
	SeaMapper	Interactive, graphical processing and mapping of multibeam data
	Swathmap	High performance multibeam sonar monitoring and editing software

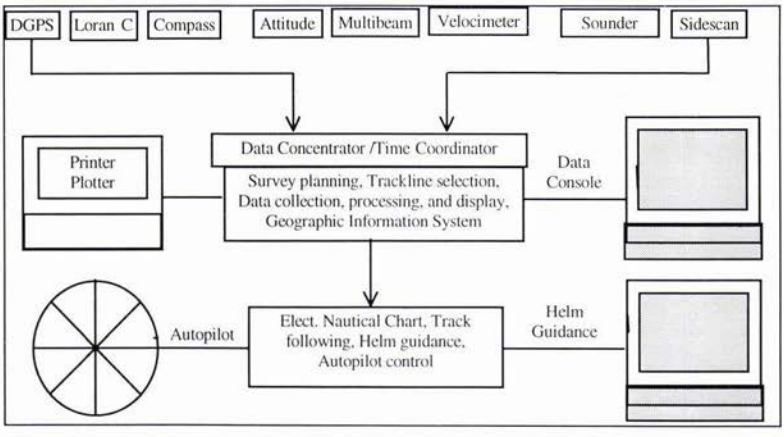

Figure 1. RTGIS shipboard swath mapping configuration

5. RTGIS Real Time Extensions to GRASS

GRASS 4.1 is a fully functional GIS consisting of over 300 programs for displaying and analyzing geographic data. There are more than 46 display programs, 18 general management programs, 72 raster manipulation programs, 68 vector manipulation programs, 20 site manipulation programs, 32 imagery processing programs, 5 photo processing programs, 8 printing/painting programs, 3 postscript interface programs, 32 miscellaneous programs, and 18 shell scripts. There are also numerous related programs included with the GRASS4.1 distribution, such as PROJ4 from USGS for coordinate transformations and PBMPlus for image file translation. However, GRASS has historically been used for land-based applications where the databases are well

populated and real time data acquisition has not been a necessity. Thus, GRASS4.1 by itself is not well suited for real time operations.

In order to give GRASS Real Time capabilities, a 3 component system was created. The first component consists of a modification to certain GRASS library routines. GRASS4.1 uses a resource file which defines a set of variables to define the GIS environment, similar to UNIX environment variables. GRASS uses the state of these variables as a form of Inter-process Communication (IPC). However, the library routines provide no mechanism for controlling access to the resource file. This is highly inadequate for real time operations, when many background processes write and read the resource file asynchronously. To control access to the resource file in real time mode, the standard GRASS4.1 library was modified to use semaphore file locking which guarantees that only one single process will have access to the resource file at any one time.

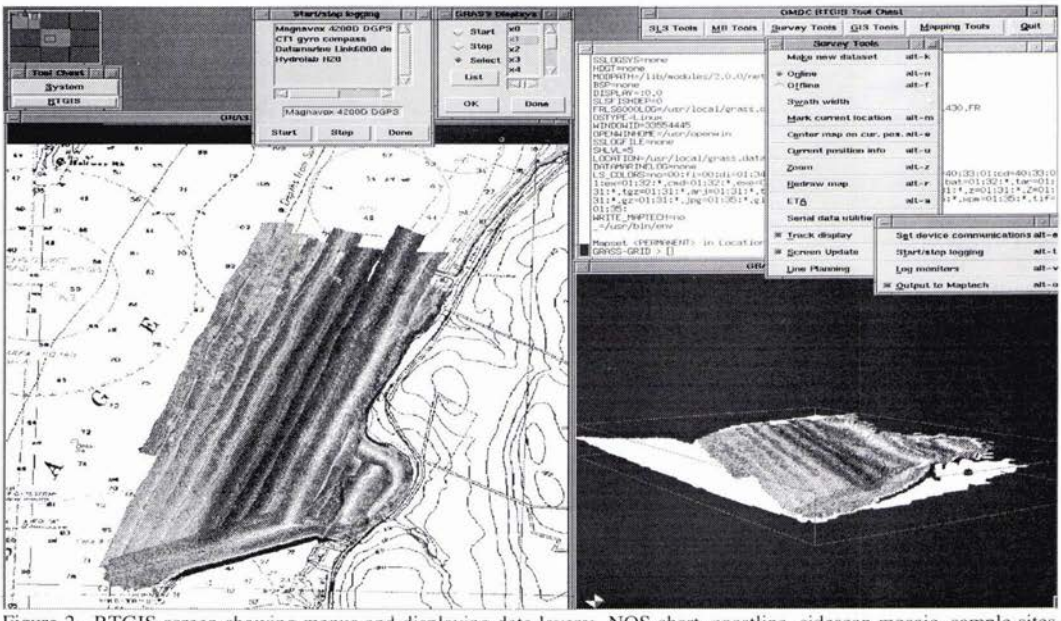

Figure 2. RTGIS screen showing menus and displaying data layers: NOS chart, coastline, sidescan mosaic, sample sites, and 3-D bathymetry draped with sidescan mosaic.

The second component for providing real time capabilities consists of a message passing facility to simplify the IPC. The Data Transfer Mechanism (DTM) from the NCSA fulfills this task. DTM provides a highly simplified interface to Berkeley sockets for IPC. The third component goes hand-in-hand with the DTM implementation. It is simply a C header file which coordinates the DTM port addresses for all real time modules. By including this centrally located header file, each real time module is provided with coordinated access to all other real time modules via message passing to the predefined ports. Using this 3 component real time extension to GRASS4.1, any module may request data from the loggers and respond accordingly in real time. While the toolkit is aimed at support for swath sonar operations (sidescan and multibeam), the comprehensive nature of the GIS allows support for single beam hydrography, sampling programs, bottom photography, survey data management, etc.

6. Sidescan Sonar Processing with Xsonar

The Xsonar software package was developed by Bill Danforth at the Woods Hole office of the U.S. Geological Survey for shipboard processing of sidescan sonar data [5]. This software has been integrated with our RTGIS environment and provides standard sidescan data processing including automatic and manual bottom tracking and water column removal, geometric and radiometric corrections and filtering, track integration and geo-referencing, and multi-swath mosaicing via cut and paste of hardcopy output to a thermal printer.

Figure 3 shows some of the menus and beginning screen displays for Xsonar. In the upper left hand corner is the main setup window. This window is used to select a sidescan sonar file for processing, configure its input parameters, and select the processing function. Here we have selected the input file 13-14.dat. We have selected latitude/longitude navigation input, a navigation filtering interval of 0.41 minutes (time), 100 meter swath width, and 16 bit input with only the lower 12

bits being significant. The process frame shows that we have selected slant range correction, destriping, and beam pattern removal processing. In addition, Xsonar provides file translation from several common sidescan sonar file formats to the Xsonar internal format, interactive navigation editing and smoothing, linear stretch and equalization image processing, histogram generation, and gridding of sonar imagery.

The Showimage window at the lower right hand corner of figure 3 is used to view the sidescan sonar imagery, either raw or at any one of the intermediate processing steps. Showimage may also be used to obtain per ping information from the sonar file. The Showimage Telemetry window at the upper middle of Figure 3 contains pertinent information for the ping currently selected with the middle mouse button. A significant and powerful feature of Showimage is the ability to interactively correct bottom tracking using the Showimage Zoom Window shown at the lower middle of figure 3.

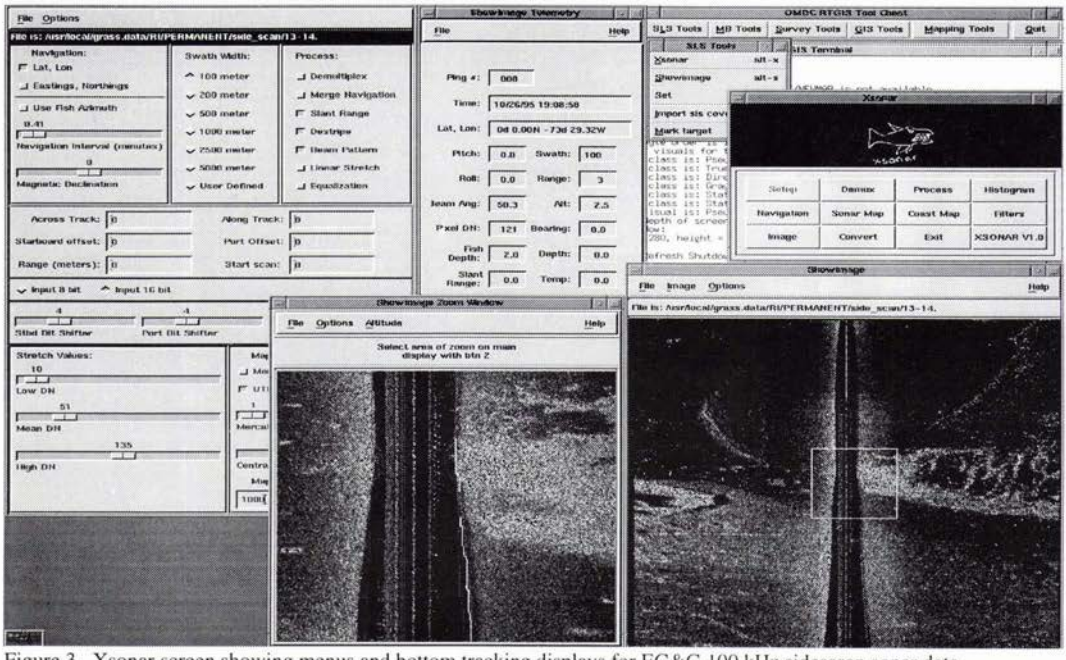

Figure 3. Xsonar screen showing menus and bottom tracking displays for EG&G 100 kHz sidescsan sonar data.

When all sidescan sonar processing is complete, the Sonar Map function is used to grid the sonar imagery for a user-defined region and resolution. The geo-referenced raster imagery file is then provided to the RTGIS using the Import sls coverage function. GRASS is then used for mosaicing the swath imagery. Included is the ability to translate and rubbersheet the swath imagery for full control of the final mosaic. The sidescan sonar mosaic in figure 2 above was created with XSonar and its interface to GRASS.

7. Multibeam Sonar Data Processing

Multibeam sonar processing is accomplished with the public licensed MB-System [6] and a subset of SeaBeam's proprietary SeaView package which includes SeaSurvey, SeaSwath, SeaMapper, and SeaVisualize [7][8]. Figure 4 shows multibeam sonar data processing sessions using MB-System and its interface to the RTGIS. The MB Project window at the upper left of figure 4A is used to define a set of multibeam sonar data files to include in the current Project. Each multibeam Project is uniquely named and has an associated Project File which stores the complete processing history of all sonar data files in the Project. Included in the Project history is information about all sonar processors who have worked with the Project.

At the left middle of Figure 4A is the MB Process window which provides interactive control of MB-System processing routines. Processing may be applied to all files in the project or any subset thereof. MB-System contains a large set of programs for various processing tasks. The RTGIS interfaces to the subset of processing routines suggested by the MB-System documentation. The RTGIS interfaces to multibeam sonar processing include generating and viewing file statistics, beam editing (fig. 4A), navigation editing, sidescan destriping, beam angle and grazing angle sidescan corrections, bathymetry and sidescan gridding, user-selectable 2D and 3D plot generation to user-selectable printers and plotters (fig. 4B), and import of geo-referenced grids to GRASS.

SeaSurvey is a new SeaView software package from SeaBeam Instruments. A subset of this package has been adapted to the toolkit. This product provides screen-based tools for viewing and analyzing swath sonar data in real-time. A variety of map and 3D perspective views of bathymetry and sidescan data are generated as the sonar data are collected. The underlying data i/o is modular and supports many sonar data formats. The displays can be interactively queried to show data values at particular locations, the sizes of targets of interest, or the distance and heading between two points. Survey or cable routes can be entered and adjusted interactively. Sections of data can be selected and loaded into several analysis tools. If one or more sections of ship tracks have been selected, users may launch various data analysis tools which work with the selected data.

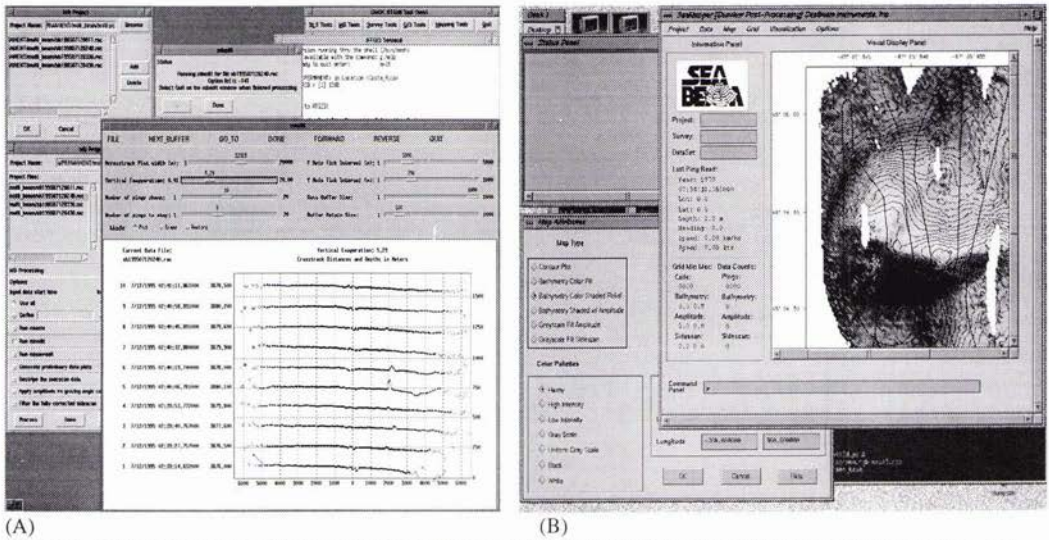

(A) (B)

Figure 4. (A) MB-System multibeam sonar processing showing the RTGIS interface and the mbedit beam editor. (B) SeaMapper multibeam trackline and coverage display.

The bathymetry browser allows the user to inspect the swath bathymetry across track profiles several pings at a time, stepping forward and backward through the selected data as needed. This utility is valuable for verifying the quality of bathymetry data and identifying the nature of artifacts when problems occur.

The navigation browser shows the longitude, latitude, speed, heading, roll, pitch, and heave data as time series. The user may compare speed and course made good with the recorded values, helping to identify problems with the navigation. This tool also allows the user to correlate bathymetry errors with problems in the motion sensor or VRU.

The sound velocity analysis tool displays the current water sound velocity profile (SVP) used by the sonar, an SVP derived from a global database, and "bathymetry residuals" calculated using the current SVP. The "bathymetry residuals" derive from the average residuals of the across-track bathymetry relative to linear fits to each of the across-track profiles. If the seafloor is reasonably planar, the residuals are dominated by the "curl up" or "curl down" of the outer swath when the SVP is incorrect. Users can interactively modify the SVP and recalculate the residuals to arrive at an SVP which "flattens" the bathymetry swath.

The patch test tool (fig. 5A) displays the selected data in a fashion quite similar to SeaSurvey's 2D map mode. Users can drag the mouse to select a slice of bathymetry data, which is then displayed as individual soundings in a depth-distance section. If there are problems with the roll bias, pitch bias, heading bias, or navigation time lag parameters used by the sonar, mismatches between the data from different swaths will be obvious. The bias parameters can be interactively adjusted so that the data become consistent. If a proper patch test survey is done, the tool allows users to isolate and determine the errors in the bias parameters. For survey monitoring, SeaSurvey provides tools for real time viewing of data in 3-D from different perspectives (fig. 5B).

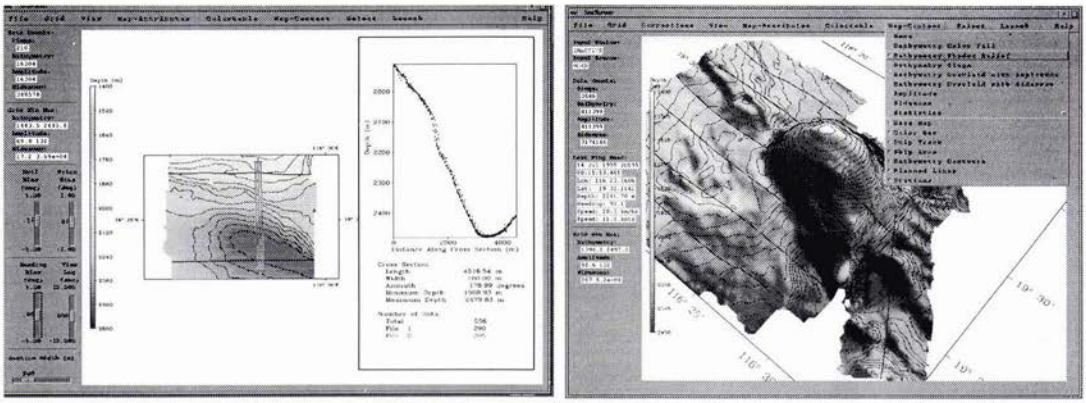

(A) (B)

Figure 5. (A) SeaPatch tool for roll, pitch, heading, time correcting (B) SeaSurvey 3-D real time bathymetry display

For NOAA multibeam hydrographic operations, a subset of the Swathmap processing tools developed by the University of New Brunswick, Canada, has been adapted to the toolkit for shipboard operations. Swathmap is a developmental set of tools particularly well adapted for processing data from very high data rate multibeams like the Reson Seabat.

8. Conclusions

Our toolkit effort has had considerable success migrating powerful UNIX workstation software tools for swath sonar mapping to the PC under the Linux operating system, in major part due to the depth and breadth of the operating system and supporting software. While some of the tools which support intense OpenGL graphics run slowly under our present software emulation, faster processors and dedicated graphics hardware are expected to be available soon. In the future we hope to be able to add NOAA sounding selection software tools to the toolkit along with much of the Hydrographic Multibeam Processing System software (HMPS) developed by the U. S. Naval Oceanographic Office.

References

[1] R. Tyce and G. Hatcher, "Real Time Geographic Information Systems For Survey Data Management." Proceedings, 21st Joint Meeting of the UJNR Sea-Bottom Surveys Panel. Pp. 161-182, Rockville MD, 16-20 Nov. 1992.

[2 G. A. Hatcher Jr., "A Geographic Information System as a Data Management Tool for Seafloor Mapping", M. S. Thesis. The University of Rhode Island, Kingston, Rhode Island, 1992.

[3] J. Westervelt, "Introduction to GRASS4.0" Central Washington University, Extended University Programs, Ellensburg, Washington. 1991.

[4] S. M. Dzurenko, "Development of a Real Time Geographic Information System Toolbox for Oceanographic Survey Data Acquisition, Monitoring, and Processing", M. S. Thesis. The University of Rhode Island, Kingston, Rhode Island, 1997.

[5] W. W. Danforth, "Xsonar/Showimage: A complete Processing and Display System for Rapid Sidescan Sonar Processing", U.S. Geological Survey, Open-File Report 96-XXX (in press).

[6] D. W. Caress and D. N. Chayes, "Improved processing of Hydrosweep DS multibeam data on the R/V Maurice Ewing", Mar. Geophys. Res., 18, pp. 631-650, 1996.

[7] P. A. Cohen, S. E. Spitzak and S. P. Miller, "A Graphical User Interface for Multibeam Map Production and Survey Management", in Oceans 96 MTS/IEEE Conference Proceedings, pp. 980-983, 23-26 Sept. 1996.

[8] S. E. Spitzak, D. W. Caress, and S. P. Miller, " Advances in Realtime Multibeam Survey Visualization and Quality Control", in Oceans 96 MTS/IEEE Conference Proceedings, pp. 975-979, 23-26 Sept. 1996.

Uniqueness Problems in Extracting Environmental Parameters from High-frequency Shallow-water Reverberation Measurements

Henry Weinberg*, Ruth Eta Keenan**, Frank E. Aidala Jr.***

(*)Integrated Performance Predictions
23 Colonial Drive, Waterford CT 06385
Email: hweinberg@ipdinc.com

(**)Science Applications International Corp.
Box 658, Mashpee, Massachusetts 02649
Email: keenan@RS3.npt.nuwc.navy.mil

(***)Naval Undersea Warfare Center Division
Newport Rhode Island, 02841-1708
Email: aidala@C80.npt.nuwc.navy.mil

Abstract

Inversion techniques that extract environmental parameters from measured reverberation often lead to mathematical problems that are not well-posed. Two examples illustrate this possibility. The first shows how a model can produce accurate forward predictions though based on erroneous physical assumptions. The second example involves measured torpedo data, and offers some guidance to resolving ambiguities that are due to abrupt changes in the bottom sediment.

1. Introduction

Inversion techniques are now used to extract environmental parameters, such as bottom-backscattering strengths, from measured reverberation. The simplest scheme requires a forward model to compute reverberation levels at some initial state, and adjusts the unknown quantities using trial and error until the computed and measured levels agree. More sophisticated techniques estimate rates of change of reverberation with respect to the unknown quantities at some initial state, and iterate until convergence occurs.

Typical inversion problems lead to mathematical models that are not well-posed in the sense of Hadamard. In other words, the solution may not exist, may not be stable under data perturbations, or may not be unique. Numerical methods that are concerned with stability are called regularization methods. The recently published book by Engl, Hanke, and Neubauer [1] is devoted to this subject. The material below, on the other hand, is concerned with uniqueness, but not in the mathematical sense. The problems stem from a misrepresentation of the underlying physics.

For example, consider the following simulation for extracting 30-kHz surface-backscattering strength. The inputs are generated by a *primary* model that includes refraction and multipath effects. In contrast, the *inverse* model assumes that the ocean sound speed is constant and neglects multiple boundary interactions. Both models use an Applied Physics Laboratory, University of Washington (APL-UW) surface-backscattering strength algorithm [2] as described below. The results support the conclusion that refraction and multipath effects are insignificant. However, closer scrutiny reveals that this is fortuitous. Refracted, bottom interacting paths often dominate backscattered energy. Since conflicting physical assumptions produce the same reverberation level, the inverse problem is not well-posed.

Reverberation anomalies frequently lead to incorrect conclusions regarding the ocean environment. For example, 20-kHz reverberation measured in shallow waters off the coast of southern California show an unexpected rise in reverberation followed by a gradual decay into the noise background. Similar anomalies have been attributed to caustics created by

sound-speed profiles having strong, negative gradients. But in this case, photographs and grab samples of the ocean bottom provide overwhelming evidence that the rise in reverberation was due to the bottom sediment changing from mud to rock along the track. The measurement was eventually simulated using an APL-UW bottom-backscattering strength algorithm [3] and the Gaussian ray bundle eigenray model [4].

2. A Wonsan site in the Fall

The three sets of data in figure 1 are computer generated predictions of monostatic reverberation versus elapsed time for a 100-ms pulse. The predictions are based on APL-UW surface and bottom back-scattering models [2] and [3], the APL-UW surface and bottom forward reflection loss models [5] and [6], and Francois-Garrison volume attenuation [7]. In these predictions, surface reverberation dominated bottom reverberation by about 10 dB, and volume reverberation was neglected. A complete list of environmental and system parameters and the sound speed profile are provided in Table 1 and figure 2, respectively

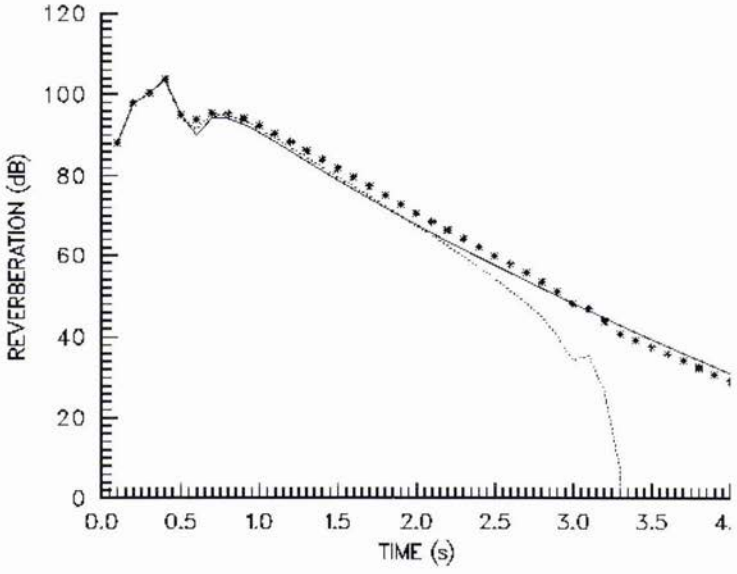

Figure 1: Computer generated predictions of monostatic reverberation versus elapsed time for the Wonson site in the fall. The (*) are assumed to be correct, the (-) is an initial attempt by the inverse model to match the (*), and the (...) denotes the contribution of simple surface backscatter to the (*).

Parameter	Value
site	Wonsan
season	Fall
bottom depth	65 m
bottom sediment type	coarse silt
wind speed	15 knots
surface scattering strength	APL-UW [2]
bottom scattering strength	APL-UW [3]
surface reflection coefficient	APL-UW [5]
bottom reflection coefficient	APL-UW [6]
volume attenuation	Francois-Garrison [7]
source level	220 dB
pulse length	100 ms
transmitter depth	26 m
transmitter beam pattern	sin(x)/x
transmitter vertical beamwidth	3°
receiver depth	26 m
receiver beam pattern	sin(x)/x
receiver vertical beamwidth	10°
horizontal beamwidth	3.2°

Table 1: Environmental and system parameters for reverberation models.

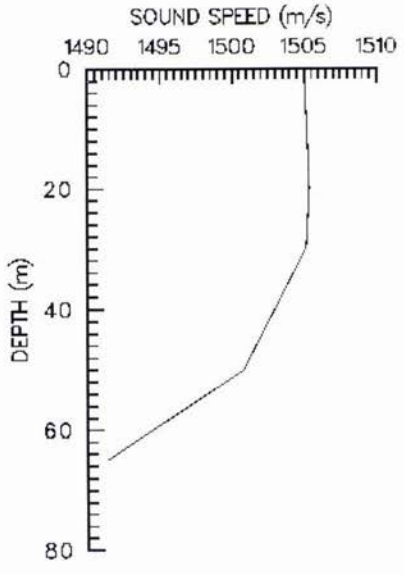

Figure 2: Sound speed profile for the Wonsan site in the Fall.

The (*) in figure 1 were produced by a primary model, which, for the sake of this discussion, are assumed to be correct. This data will be used as inputs for extracting surface-backscattering parameters. The (-) is an initial attempt to match the primary data using an inverse model. Finally, the (...) denote the contribution of direct path surface reverberation to the primary result. In practice, one extracts the surface-backscattering strength by adding the differences between the (*) and (-) in decibels to the initial ARL-UT values. The resulting reverberation levels would match the primary data exactly. Since the primary and initial inverse data agree to within a couple of decibels over the entire time axis, one can argue that the inverse predictions including the estimate of surface-backscattering parameters are accurate.

As noted in the introduction, the primary and inverse models differ by two major assumptions. Because the high value of volume attenuation at 35 kHz limits the ranges of interest to a few kilometers, the inverse model neglects ray diffraction and multipath; The primary model includes both effects. An obvious conclusion is that ray diffraction and multipath are not significant in this example. Many analysts agree that the computer resources required to gain a couple of decibels in accuracy is not warranted in most practical applications.

A more thorough analysis has shown that the conclusions stated above are quite erroneous. It was just fortuitous that the primary and initial inverse results agreed, and the primary contribution to surface reverberation is not the simple surface-backscattered path as claimed by the inverse model. According to the (...) curve in figure 1, the actual contribution to surface reverberation falls off quite rapidly at times beyond 2.5 sec as the direct path enters the shadow zone. The transmitter-surface backscatter-bottom reflection-receiver path (not shown alone) is the dominant source of reverberation. The analysis at shorter times is more complicated. Here the direct path has less propagation loss and shallower surface grazing angles than the bottom interacting paths. Since shallower surface grazing angles are associated with less surface backscattering, the direct path reverberation may be weaker at the shorter times as well. In contrast, the transmitter-bottom reflection-surface backscatter-receiver path is not a significant contributor because the narrow transmitter beam pattern rejects steep downward directed energy.

3. SOCAL Torpedo data

The reverberation data to be examined next consists of 38 torpedo pings along 14 tracks. The data was measured at the NUWC SOCAL site near southern California. An extensive environmental survey of SOCAL was conducted in two phases by NUWC [8]. The first phase, November 17-23, 1993 measured bottom bathymetry and acoustic backscatter characteristics. The second phase, December 7-15, 1993, collected high-fidelity forward propagation acoustic data and in-situ measurements of water column conductivity, temperature, and depth. The research vessel R/V Glorita performed a bottom survey with precision navigation, precision bathymetry, side-scan sonar, bottom acoustic reverberation characterization and sediment profile and plan-view imagery. Bathymetric data were collected every second from an ODOM Echo Trac dual-frequency precision survey fathometer with a 3° beam and a 208-kHz transducer. Attached to the hull of the R/V Glorita was a bottom acoustic data acquisition system (BADAS) which acquired and digitized signals from a 24-kHz transducer. A towfish with an EG&G Model 260 side-scan sonar system acquired data at 100 kHz, but malfunctioned during the last part of the survey. A small camera attached to the REMOTS frame, a device that can penetrate and image the upper 20 cm of the sediment, took plan-view photographs above the bottom. In addition, a Van Veep grab sampler collected sediment samples.

In spite of the excellent data, the observed reverberation would not be successfully modeled for several years. The main reason was that our experience in explaining blue-ocean acoustics failed when the bottom depth was under 200 m. The first mistake was to try and extract one bottom-backscattering strength for the entire reverberation data set. The data measured from all 38 torpedo pings appears in figure 3. This shows a 20- to 30-dB variability at individual received times. No single bottom-backscattering strength can produce this phenomena. The explanation was literally in front of our eyes. The REMOTS camera and grab samples showed that the SOCAL bottom sediment varied from mud to rock. Some of the torpedo pings were confined to all mud or all rock tracks, while other pings received reverberation from both types of sediments. Once this obvious observation was brought to light, it became clear that any successful inversion technique must allow for range-dependent variations in the ocean environment, and in particular, in the bottom sediment. Although the variation in SOCAL bathymetry was relatively large, the variation in bottom-sediment properties played a much greater acoustic role.

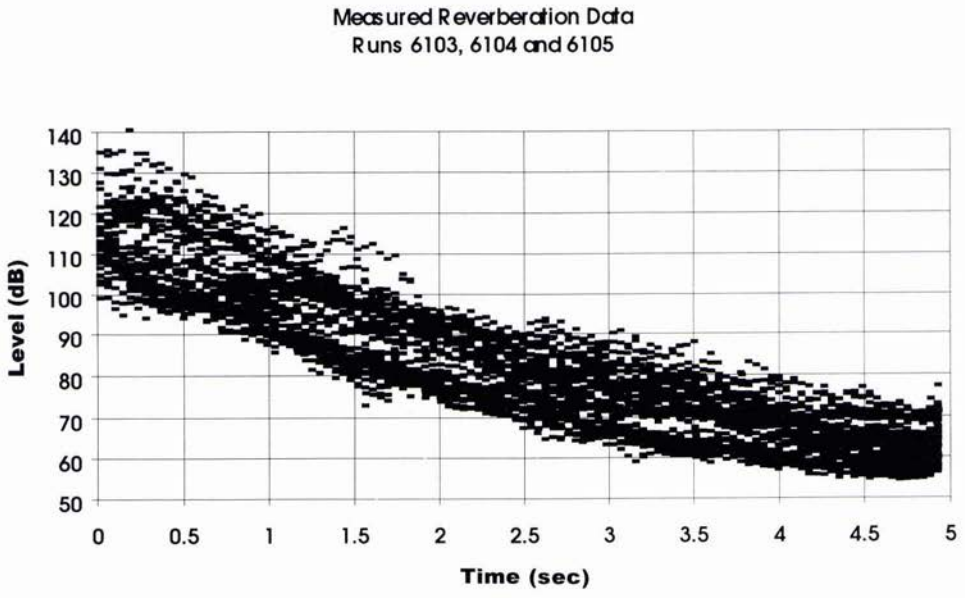

Figure 3: All 38 torpedo pings measured at the NUWC SOCAL site.

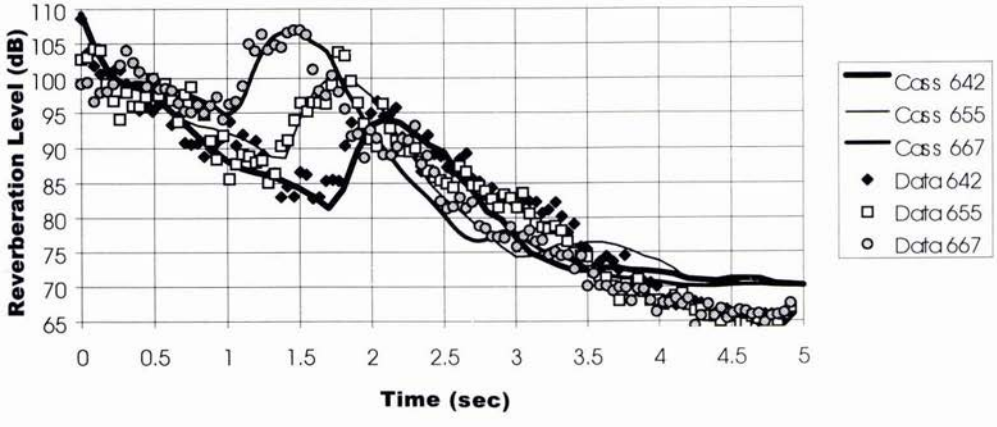

Figure 4: Measured torpedo pings 642, 655, and 667 compared to CASS model predictions.

The numbers 642, 655, and 667 in figure 4 refer to consecutive pings on a mud to rock track. The symbols refer to measured torpedo reverberation, while the lines refer to Comprehensive Acoustic System Simulation (CASS) model predictions [9]. The measured data is a subset of figure 3. Note that the variability in the data is considerably more between one and two seconds than at the earlier and later times. For all three pings, the increase in reverberation levels is due to the increase in bottom backscattering from mud to rock. Ping 667 is furthest away from the transition range, and so its increased reverberation level occurs at a later time. By including the transition range in the environment, CASS was able to extract the bottom-scattering strengths in terms of sediment type.

There was a major difficulty due to an oversight in applying the APL-UW bottom forward reflection loss. This model, basically a plane wave reflection coefficient, showed almost no loss over rock until a critical angle of 60°. The inverse analysis required the loss to be 6 dB per bounce. The APL-UW documentation stated that their model did not include scattering or shear losses. REMOTS camera photographs of the rock areas showed that the rocks were about the size of one's fist, or about a wavelength at 20 kHz, so that scattering due to roughness could not be ignored.

4. Conclusions

Environmental parameters that are extracted from measured reverberation data may not be unique unless sufficient constraints are imposed. Fluctuating reverberation levels are particularly difficult to invert. If the fluctuations occur over time periods that are consistent with internal waves, the source is clear. For shorter time periods, the fluctuations may be due to phenomena as diverse as multipath interference and sand ripples. The ambiguity may be resolved by changing system parameters whenever feasible. Fluctuations due to sand ripples should change dramatically with bearing, but not frequency. The opposite should hold for near-surface multipath interference.

In the analysis presented here, the environmental models that were used to perform the inversions were acceptable with one exception. There is currently no generally excepted model for bottom forward reflection loss over rough rock-like sediments. Another shortfall is out ability to model coherent reverberation effects. The examples shown above were all modeled by power summing the various contributions to reverberation at specific times. This approach cannot explain near-surface multipath interference.

References

[1] H.W. Engl, M. Hanke, and A. Neubauer, Regularization of Inverse Problems, Kluwer, Dordrecht, 1996.

[2] "APL-UW High-Frequency Ocean Environment Acoustic Models Handbook," Technical Report APL-UW TR9407, II-5, October 1994.

[3] "APL-UW High-Frequency Ocean Environment Acoustic Models Handbook," Technical Report APL-UW TR9407, IV-21, October 1994.

[4] H. Weinberg and R.E. Keenan, "Gaussian ray bundles for modeling high-frequency propagation loss under shallow-water conditions," Journal of the Acoustical Society of America, vol. 100 (3), pp. 1421-1431, September 1996.

[5] "APL-UW High-Frequency Ocean Environment Acoustic Models Handbook," Technical Report APL-UW TR9407, II-19, October 1994.

[6] "APL-UW High-Frequency Ocean Environment Acoustic Models Handbook," Technical Report APL-UW TR9407, IV-18, October 1994.

[7] R.E. Francois and G.R. Garrison, "Sound Absorption Based on Ocean Measurements. Part II. Boric Acid Contribution and Equation for Total Absorption," Journal of the Acoustical Society of America, vol. 72 (6), pp. 1879-1890, December 1982.

[8] M. Buffman, "Results of Shallow-Water High-Frequency Acoustic Testing and Environmental Characterization SOCAL 93" (U), NUWC-NPT Technical Memorandum (unpublished), Naval Undersea Warfare Center Division, Newport, RI, April 1994 (CONFIDENTIAL).

[9] R. Keenan and H. Weinberg, "Torpedo Reverberation Data Modeling with the Comprehensive Acoustic System Simulation (CASS)," NUWC-NPT Technical Report 10,480, June 1995.

Determination of Velocity Profile and Sea Bed Characteristics from High Frequency Pulse Propagation in a Shallow Water Mediterranean Environment

M.F. Werby*, M.K. Broadhead*, R. Field* and Natalia A. Sidorovskaia**

*Naval Research Laboratory, Code 7181 and 7173,
Stennis Space Center, MS 39529, USA

**Physics Department,
University of New Orleans,
New Orleans, LA 70148, USA
E-mail: nasph@uno.edu

Abstract

Time-domain features of shallow water Mediterranean and Yellow Sea data are simulated for frequency band widths of 0.8 kHz with a central frequency of 3.2 kHz. Contour plots of pulse arrivals in time and depth are analyzed for several source locations and receiver off-sets. Calculations have been carried out using a new Shallow Water Acoustical Modal Propagation model - SWAMP. Results indicate the ability to extract the adumbration of velocity profiles, critical angles of the ocean bottoms and source localization.

1. Introduction

The examination of the transmission loss in a wave guide over range and depth may reveal limited information about ducting and even less about ocean bottom properties. Researchers have become accustomed to examining transmission data and may be skilled with interpreting data to form reasonable guesses of desired properties. Data for the less studied pulse problem, particularly, for contour plots over depth either in range for fixed time or in time for fixed range appears more likely to reveal information of both the velocity profile and bottom properties. Indeed, a single array over depth for pulse signals would yield far more information than a sequence of arrays over depth distributed over a broad range in uniform steps required to produce single frequency contours. A single horizontal array for fixed frequency over range would likely yield ambiguous information, while in time-domain calculations it would yield relative arrival times of modes and thus possibly give a measure of ocean bottom properties. In the presence of ducting and poor placement, it could miss some modal arrivals and would unlikely give the information about ducting. Shallow water measurements yield less information about profiles, because they require larger frequency band widths to achieve comparable resolution in contrast with the deeper water cases and because mode stripping is more pronounced in range for the shallow water case and may lead to vague results in range as more and more modes are stripped particularly when the number of modes are small. What we wish to show here is how to exploit information from transmission loss or pressure fields from pulse signals in time steps for fixed range or in range steps for fixed time. The particular information we determine is at the very least an adumbration of the velocity profile as well as the critical angle of the bottom. We use the velocity profiles obtained from a shallow water Mediterranean region (80m) to explore strong features of pulse arrivals that are characterized by the velocity profile and bottom properties. The profiles typically have broad bottom ducts in about 80 meters of water commencing at about 30 meters. The gradient is not strong and varies over most of the bottom 50 meters of depth. There is surface ducting in some of the profiles which can be seasonally observed in the experimental measurements . We calculate arrivals at uniform depths over the entire range of the water column and plot outputs of arrivals in terms of group front intensity contours over time windows that encompass the entire pulse widths. The sources are alternatively placed in two locations, namely close to the surface and close to the bottom of the water column. The off-set distances are 2.5 km, 5 km and 7.5 km. The pulses vary from 2.8 kHz to 3.6 kHz, with a band width of 800 Hz and a central frequency of 3.2 kHz. The effect of surface

ducting is of particular interest and is seen to have the effect of capturing energy from high angle modes that traverse from the bottom ducted region and are manifested as uniform discrete arrivals that have earlier arrival times than the predominate bottom ducted low mode group arrivals. The results indicate that some systematics are obtained that are useful in extraction of overall features of both the sound speed profile and the spectrum of angular modes governed by bottom properties. Further we show that source localization can be obtained by examining crossing patterns of the group intensity contours. A comparison of this result is made with Yellow Sea data which have much stronger gradients and lead to rather different group intensity arrival features. An interesting feature of strong bottom ducted profiles with some surface ducting was observed in an analysis of data from the Florida Straits by Harry DeFerrari and Charles L. Monjo. [1,2] For a 550 m water column and pronounced bottom ducting with weak surface ducting over the first 70 m of the water column, pulse signals are observed to get trapped periodically as high angle modes initiated at the bottom of the wave guide traversed to the top and returned to the bottom in a typically cyclical manner. However, at each contact of the higher order modes made with the upper surface duct some energy was trapped in that duct and traveled at the some what higher characteristic group velocity, thus leading to discrete localized arrivals that preceded the major and typical duct arrivals. This rather remarkable and unexpected results which may be initiated above some frequency threshold can give a powerful sensitive tomographycal tool that enables one to determine additional refined structures of a wave guide. In addition to giving evidence of surface ducting, it allows one to determine source distance and ocean depth. This observation is presently referred to as the DeFerrari-Monjo effect and we investigate it for the shallow water cases presented here.

2. Method of Calculation

The pulse propagation problem in oceanic waveguides can be solved via the frequency domain by Fourier synthesis of CW (continuous wave) results:

$$p(\mathbf{r},t)=\frac{1}{2\pi}\int_{freq\ band} S(w)p(\mathbf{r},w)e^{-iwt}dw, \tag{1}$$

where $p(\mathbf{r},w)$ is a spatial transfer function, $S(w)$ is a source spectrum. Thus, the first computational step is associated with solving the Helmholtz equation with the source spectral function $f(\mathbf{r},w)$:

$$\left[\nabla^2+\frac{w^2}{c^2(\mathbf{r})}\right]p(\mathbf{r},w)=f(\mathbf{r},w) \tag{2}$$

and generating the transfer function at a number of discrete frequencies within the frequency band of interest. The evaluation of the integral in (1) can then be done by, for instance, the Fast Fourier Transform at each spatial position ($\mathbf{r}$). Despite the relative simplicity of (1), there is no universal solution technique avalaible for arbitrary sound speed profiles $c(\mathbf{r})$.

The numerical results presented below were obtained by using a new normal mode model SWAMP. The variable velocity normal mode solution given by SWAMP is based on obtaining the solution of a related reference isovelocity problem. [3,4] Ocean bottom layering is assumed to be composed of fluid layers, but large numbers of layers are feasable so that it is possible to account for gradient effects. As in any normal mode model, it is not difficult to generalize to include layers with elastic properties. Once the depth dependent iso-velocity eigenfunctions are obtained, they are used as spanning functions that transform the isovelocity space solution by means of a rotational or unitary transformation into solutions of a space with a variable velocity profile. The transformation may be viewed as a worping operation that deforms the iso-velocity space into a variable velocity space. However, the spanning functions which are readily transformed into a spherical representation are retained, so that solutions of the distorted space may easily be expressed in a spherical representation, albeit a linear combination of such functions. This is an important development, because a spherical representation is required in the development of a unified approach that couples free three dimentional scattering solutions with a wave guide solution. The new modal eigenvalues are obtained by transforming the worping super matrix - which is real and symmetric - to tri-diagonal form from which the eigenvalues of the transformed space are readily obtained. Once the eigenvalues are obtained, sets of linear equations that form independent sub-systems are obtained. Each system of equations is in a linear solver form, represents independent systems and generates the required eigenfunctions in terms of expansion coefficients of the spanning space. Because the system of equations are independent, only one or any desired set of eigenfunctions may be obtained. Since the set of expansion matrices forms a super-matrix that is rotational by design, the new eigenfunctions are guaranteeded to be orthogonal as required by the

nature of the problem. Since each of the solver equations are independent and are not based on iterative calculations which for example occurs in Gram-Schmidt construction, errors are not accumulated that often result in violation of the orthogonality conditions. The detailed consideration of the method is presented in the referenced literature. Here we would like to discuss what can be learned from the numeraical studies of the pulse propagation obtained by using SWAMP. It is important to notice that the model works reasonably fast for high-frequency calculations and successfully competes with the Parabolic Equation approach models with respect to computational time.

3. Numerical Simulation and Interpretation of the Results of Mediterranean Data

The first environment which was tested represents the typical shallow water Mediterranean waveguide with wide single bottom duct, described in the introduction. Figure 1 shows the intensity picture of the received pulse vs. depth vs. time for ranges (a) - 2.5, (b) - 5, (c) - 7.5 km. The source was placed in the duct, at depth 65 m.

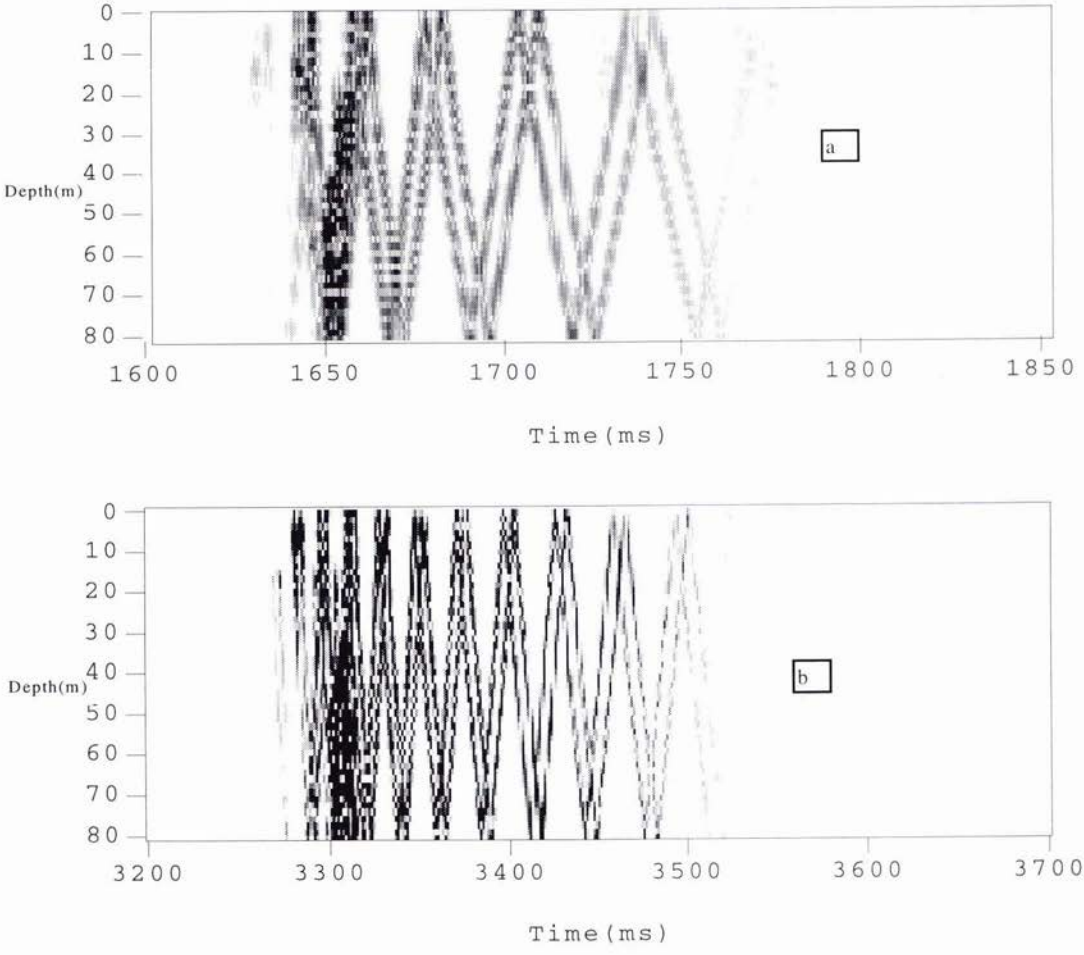

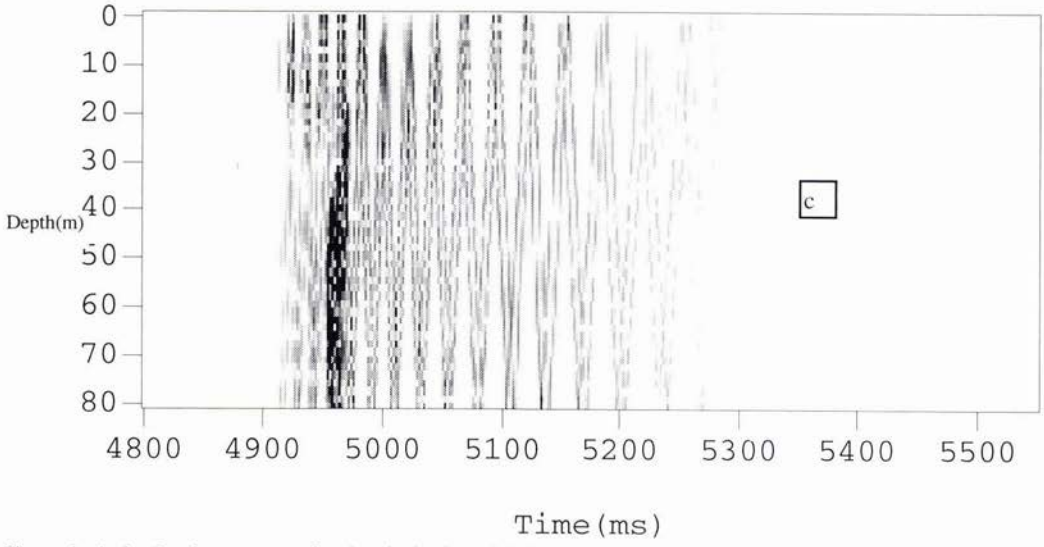

Figure 1. Arrived pulse structure for the single duct Mediterranean environment with the source at depth 65 m for distances: a - 2.5 km, b - 5 km, c - 7.5 km.

We can see that the low order modes are trapped in the duct and are the major first arrivals. The high order modes correspond to Surface-Reflected-Bottom-Reflected (SRBR) paths are well observed at the tail of the pulse. SRBR arrivals can be modeled as clustered groups of modes with different group velocities and with different modal angles with respect to horizontal or vertical axis. Thus, the travel time separation between these arrivals for fixed depth expands with increasing time. The intensity group fronts change as a function of mode angle with the vertical axes from 0 degree for the earliest major arrivals to the critical angle for the later "coda" waves determined by the total bottom impedance. The higher order modes can be approximated by the sum of up-going and down-going plane waves with the same inclination angle. The simple geometrical consideration shows that the intersection of intensity lines forms the source image at its real and imaged depths. It gives a simple geometrical algorithm to determine the source localization. If the source is located out of duct, the excitation coefficients for the low-order modes are small and we cannot effectively excite these modes. Thus, for this source geometry we may not obtain reliable information about the presence of the duct from any receiver geometry. This effect is manifested in Figure 2.

By introducing weak surface duct, we can observe that results does allow for some energy to arrive ahead of the main arrivals (precursors) due to approximate maxima values of the group velocity in the upper duct region. At that point the returns are not susceptible to arrivals interpreted in terms of the mathematical definition of "group" velocity since the second order asymptotics from the method of stationary phase fails and group velocity concepts are rendered meaningless. In that case the pulse amplitudes are frequency-modulated and lead to precursor waves. For some surface duct trapping the precursor effect is particularly pronounced and is particularly well discussed in the seminal work of Monjo and DeFerrari. [2] The DeFerrari-Monjo effect is present for the same Mediterranean duct with a slight surface duct added to it. This is evident in Figure 3 for the Mediterranean profile with a slight surface duct for which we are able to identify additional and more pronounced precursors. These precursors correspond to energy that is trapped in the upper duct region from the higher modes that traverse the wave guide from the bottom. It is conditional upon non-leaky trapped modes at the upper duct surface and accordingly there is a frequency cut-off below which no trapping will take place. Thus, it may be viewed as a high frequency feature.

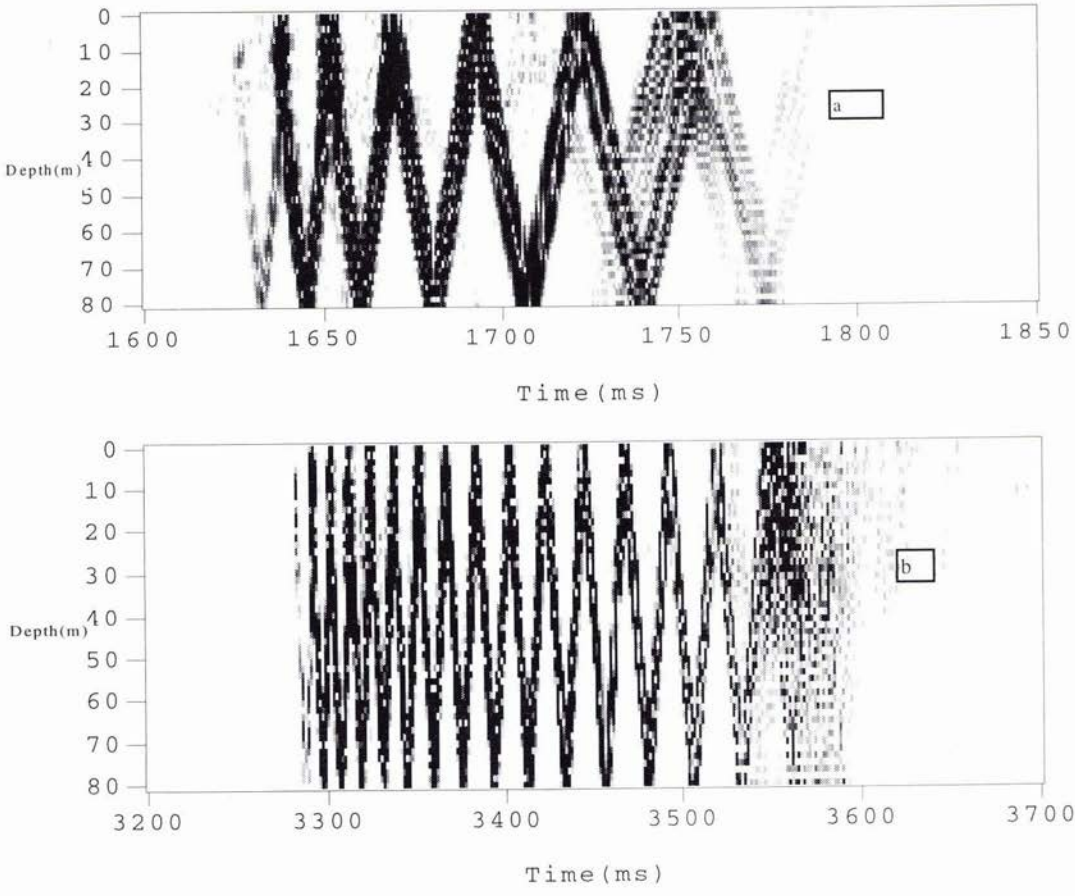

Figure 2. Arrived pulse structure for the single duct Mediterranean environment with the source at depth 10 m for distances: a - 2.5 km, b - 5 km.

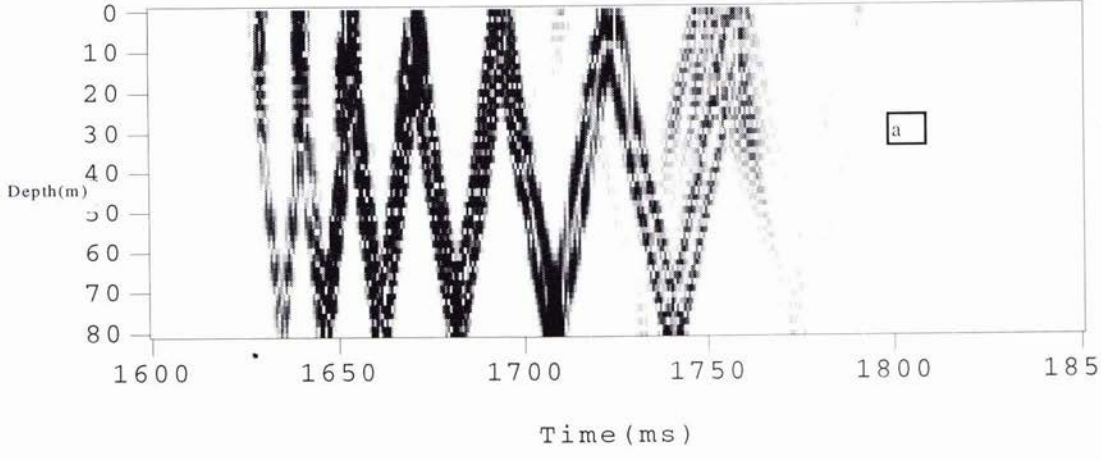

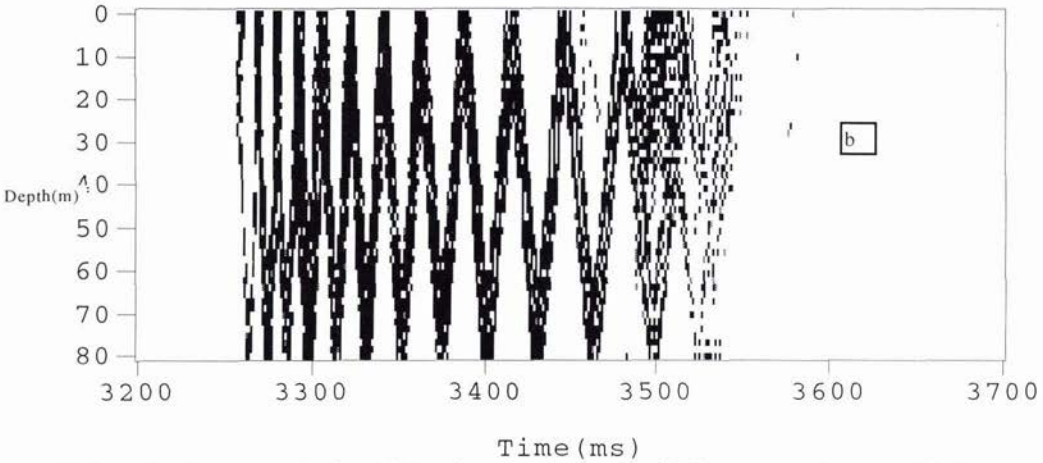

Figure 3. Arrived pulse structure for the added weak surface ducting duct Mediterranean environment with the source at depth 10 m for distances: a - 2.5 km, b - 5 km.

Since the Mediterranean profile is rather broad extending from 30-80 meters in a gradual fashion the outline or adumbration of the velocity profile though present is not strong. The next example of a similar region but with a narrower and stronger and more precipitous duct yields a "profile adumbration" that is much more pronounces.

4. Numerical Simulation and Interpretation of the Results of Yellow Sea Data

The Yellow Sea profile has a very much stronger gradient and progresses rapidly to the bottom of the water column. Thus, the effect of the profiles are more evident and one may observe a reasonable suggestion - adumbration of the velocity profile. In these calculations we have allowed for some small surface ducting for calculations represented by Figures 4-6, so that the arrivals of strong precursors leading the main bulk of arrivals is always present for these examples. However, in Figures 5 and 6, when the source is at the mid-point of the water column or in the main bottom duct we see a rather pronounced outline of the ducted region, so that for strong ducting in this case and other examples the outline of the ducting is to a reasonable degree associated with the actual velocity profile. Once again the critical angle of the bottom is determined by the "coda" arrivals which presents one with a means to extract the critical angle of the fluid-bottom interface and the relative sound speeds of the bottom.

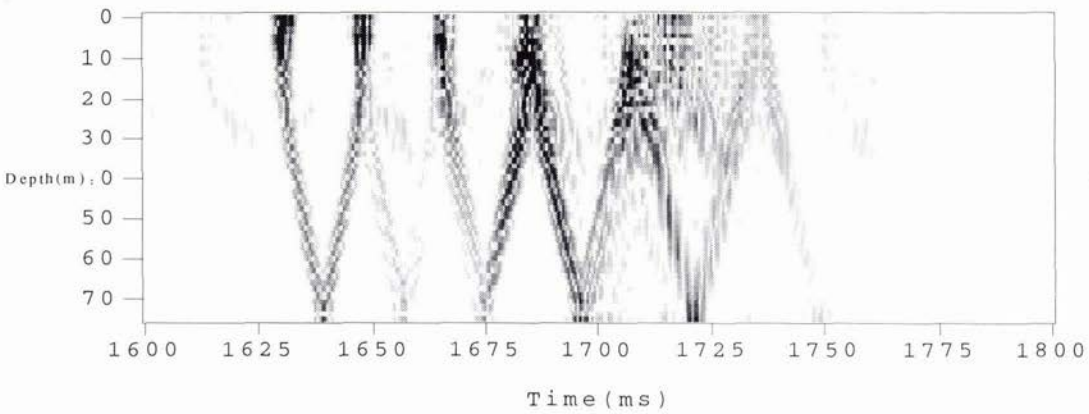

Figure 4. Arrived pulse structure for the Yellow Sea environment with the source at depth 7 m for distance 2.5 km.

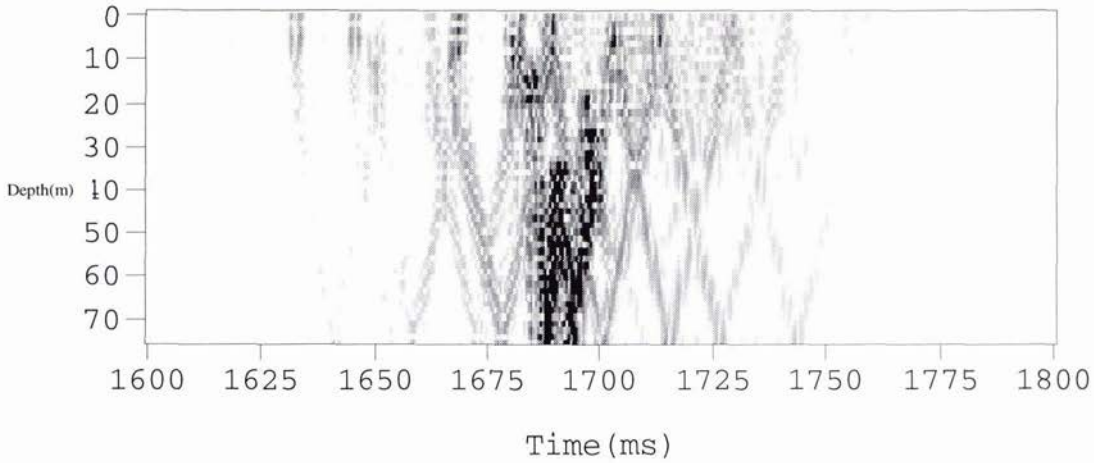

Figure 5. Arrived pulse structure for the double duct Yellow Sea environment with the source at depth 38 m for distance 2.5 km.

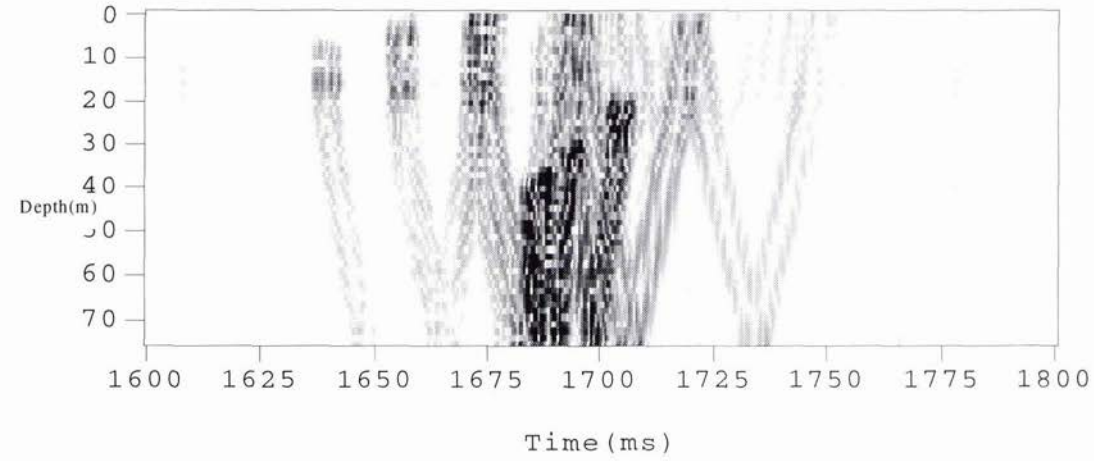

Figure 6. Arrived pulse structure for the double duct Yellow Sea environment with the source at depth 65 m for distance 2.5 km.

Figure 5 which has the source mid-way from the top to the bottom of the water column also illustrates the effect that the conjugate pair of energy fronts crosses at the source depth, here at 38 m. In the other two examples which have the sources close to the top and the bottom, we can observe crossings close to the top and bottom but appear as doublets which are in fact group energy fronts corresponding to the initiation of traveling directly to the bottom and traveling the short distance to the top and then reflecting to the bottom. Had the source been very close to the top or bottom, the doublet effect disappears but is most pronounced at the mid-point. Needless to say conjugate pair group energy effect is much more dramatic for deeper oceans. Strong diffraction will cause the group fronts to appear to bend due to more pronounced diffraction and the crossing effect will obviously be more pronounced in weakly varying velocity profiles. The effect of the group front bending is reasonably pronounced for the Yellow Sea environment having the stronger gradient of the changes of the sound speed profile.

5. Summary

Pulse signals at suitable frequencies and band widths allows one to extract moderately accurate information of the ocean properties. Although the results are not as impressive as for the intermediate depths it nevertheless gives one a tomographycal tool to extract environmental parameters using "vertical acoustical profile" methods akin to the analogous seismic case. The precursors due to even weak surface duct appear to be very sensitive indicators of the shallow water environment and could prove to be powerful oceanographic tools. Range-independent modeling of such environments will make the understanding of surface duct propagation more complete. Further investigation and comparison with data may prove fruitful in studying these kinds of environments.

Acknowledgments

We wish to thank NRL management and both 6.1 and 6.2 ONR funding. N.A. Sidorovskaia is particularly grateful to the graduate school of the University of New Orleans for financial support.

References

[1] H.A. DeFerrari and H.B. Nguyen, "Acoustic reciprocal transmission experiments, Florida Straits," *J. Acoust. Soc. Am.*, vol. 79, pp. 299-315, 1986.

[2] C.L. Monjo and H.A. DeFerrari, "Analysis of pulse propagation in a bottom-limited sound channel with a surface duct," *J. Acoust. Soc. Am.*, vol. 95(6), pp. 3129-3148, 1994.

[3] N.A. Sidorovskaia and M.F. Werby, "Broad-band pulse signals and the characterization of shallow water oceanic properties," in *Proceedings of the SPIE Conference*, pp. 97-108, April 1995.

[4] M.F. Werby and N.A. Sidorovskaia, "A range-dependent one-way coupled normal mode model with ocean bottom layering and a fast algorithm for reproduction of transmission loss to high frequency," *Mathematical Modeling and Scientific Computing*, vol. 6, 1996, in press.

Bottom Bistatic Scattering: Experimental Results and Model Comparison for a Carbonate Sediment

Kevin L. Williams and Darrell R. Jackson

Applied Physics Laboratory, University of Washington
1013 NE 40th Street
Seattle, Washington 98105
Email: williams@apl.washington.edu, drj@apl.washington.edu

Abstract

Bistatic scattering measurements were carried out under the Coastal Benthic Boundary Layer (CBBL) program. The results presented here are for a carbonate sand-silt-clay, and the data were collected in February 1995 near Key West, Florida. The experiments used a directional source operating at 40 kHz in conjunction with a mobile, steerable, directional receiver. The data set obtained is much larger than previous sets collected via the same general procedure. The experiment is briefly outlined, and the improvements resulting in the larger data set are highlighted. A model that accounts for scattering due to interface roughness and volume inhomogeneities is then summarized. Finally, the bistatic scattering results are compared with this model. The parameters needed in the model were measured by other CBBL researchers during the same time period and in the same area as the acoustic experiments. [This work was supported by ONR through the CBBL program.]

1. Introduction

Recently there has been increased interest in acoustic scattering geometries where the transmitter and receiver are not co-located. This interest led to the development of a bistatic scattering model [1] that includes contributions to scattering from both the rough sediment interface and inhomogeneities within the sediment. Tests of this bistatic model require both acoustic experiments where specified geometries can be accurately realized and concurrent determination of the environmental parameters required by the model. Such was the case in the experiments described in [2–4]. Those experiments are the predecessors of the work described here.

Section 2 outlines an experiment carried out in February 1995 as part of the Coastal Benthic Boundary Layer Special Research Program (CBBL, managed by the US Naval Research Laboratory) near Key West, Florida. Further details of the experimental procedure can be found in [2–4]. Improvements relative to those previous experiments are highlighted.

The fundamental quantity predicted in the model [1] is the bistatic cross section. Section 3 presents the form of the bistatic cross section as well as the environmental inputs and gives an equation for the scattered intensity as a function of time which incorporates the bistatic cross section. This scattered intensity is the quantity that most directly relates the model to the experimental data, and the use of this expression in facilitating data/model comparisons for the bistatic scattering cross section is summarized.

A comparison of model predictions and experimental results is given in Section 4. A fundamental part of this comparison is knowledge of the environmental parameters needed for the model. All the environmental parameters used here were determined either *in situ* or via diver cores taken by Naval Research Laboratory, Stennis Space Center, personnel as part of the CBBL program. It is important that the measured parameter set is complete, that is, there are no free parameters in the model/data comparison.

2. Experiment

Figure 1 shows a simplified diagram of the experimental arrangement. The two essential acoustic components were the sonar housed on the bottom-mounted tripod (this sonar/tripod system is referred to as the Benthic Acoustic Measurement System (BAMS)) that operates at 40 kHz and the ship-deployed receiving arrays. The BAMS sonar was a planar trans-

mitter array mounted on a rotator mechanism at the top of the 5-m-high tripod. All BAMS operations were under control of an onboard computer. A BAMS "scan" involved a series of 5° steps, with each step followed by a pulse transmission. Each scan covered a full 360° in 72 steps. The horizontal directivity pattern (full width at 1/2 maximum power) was 6.5°. The vertical directivity pattern had a full width of 14° at 1/2 maximum power. The level of the first sidelobes relative to the main lobe was down 13–15 dB for the various directivity patterns. The maximum response axis of the array was pointed downward at a depression angle of approximately 12.5° below the horizontal. The time interval between rotational steps was 5 s, of which about 2 s were required to achieve the change in direction. The remaining time allowed the transmitter array to come to complete rest before each transmission. The transmitted signal was an FM waveform having a constant amplitude over its 2-ms duration. During this 2-ms interval, the frequency was swept from 39 kHz to 41 kHz with a source level of 217 dB re 1 μPa.

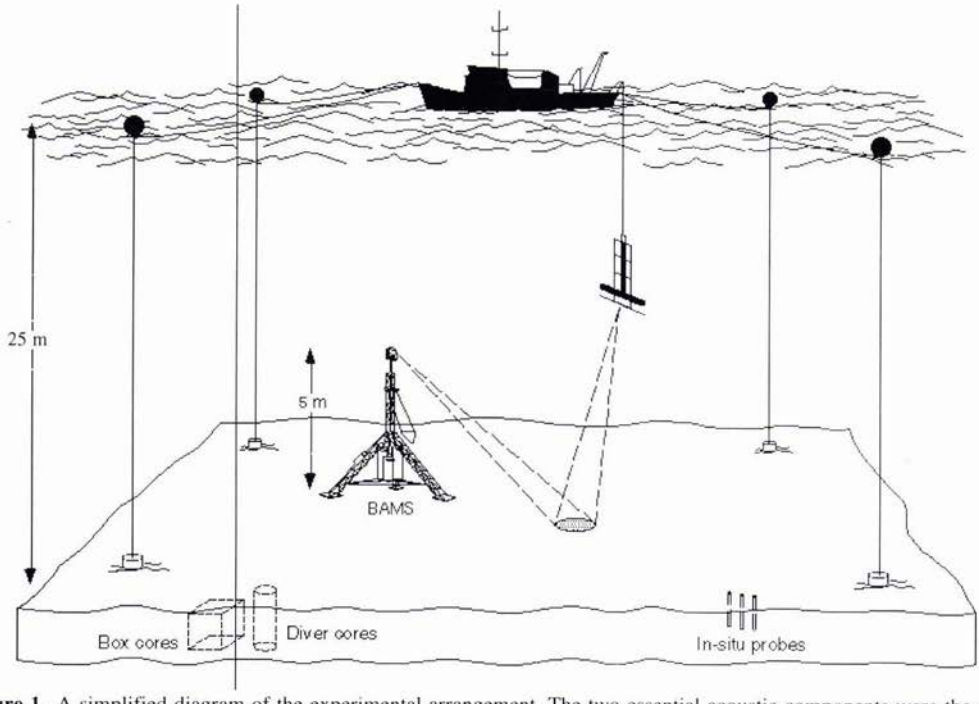

Figure 1. A simplified diagram of the experimental arrangement. The two essential acoustic components were the sonar housed on the bottom-mounted tripod and the ship-deployed receiving arrays.

The ship-deployed linear receiving array was divided into four sections, or "quads," each about 32 cm long. The horizontal and vertical beamwidths of each quad were 8° and 37°, respectively. The bistatic results shown here were acquired using one quad at two different gains to increase the dynamic range. It was necessary to have a ship-deployed receiving array in order to obtain scattering from different regions of the bottom as required to develop the ensembles implicit in the model. The array was deployed over the side of the ship after it was put in a four-point moor near the bottom-mounted tripod. In the data to be presented, the horizontal distance between BAMS and the receiving array was always less than 70 m. A data set in the experiment consisted of data taken by the mobile array during a 360° rotation of the tripod array. The receiving array was steered so that the centers of the transmit and receive beams intersected each other on the bottom such as to realize different bistatic scattering angles (defined in the following section).

Measuring all the geometrical parameters needed to determine the bistatic angles obtained during each data run requires several supplemental devices, including compasses, ranging transducers, and inclinometers. One primary data analysis effort concerned the determination of these angles from the data set. The bistatic scattering strength results given in Section 4 were derived from comparisons of the pressures received at the face of the mobile arrays with the results of simulations of the experiment that incorporated the bistatic model described below, the experimental geometry, the transmitted pulse length, and the beampatterns of the receiving and transmitting arrays.

There were three major improvements relative to the previous bistatic experiments [2–4]. All three were aimed at better control and determination of the geometries obtained. The first improvement was mentioned above: The ship was placed in a four-point moor. Previously, a single-point moor was used which worked adequately during periods of light, steady weather but caused problems under variable conditions. The four-point moor allowed the ship's position to be altered with a minimum of effort. The second improvement was the development and use of a heave-compensation system that decoupled motion of the ship's aft deck from the ship-deployed array. This pneumatic system's efficiency was examined at one point in the experiment; aft deck vertical variations of over 1 m resulted in array vertical motions of less than 15 cm as measured by a pressure sensor and an altimeter housed on the array. Lastly, a transponder was placed on BAMS, and a separate excitation signal was sent by an omnidirectional transducer (co-located with the receiving array) 100 ms before each BAMS transmission. This allowed the transponder signal from BAMS to be recorded within the data-acquisition time window but isolated in time from the bottom-scattered signal. This transponder signal thus gave an accurate measure of range separation at the time of each transmission. Previous experiments also used a transponder onboard BAMS, but it was exercised independently of the transmission cycle and measurement of range was carried out approximately every 10th transmission.

3. Model

Using the bistatic angles defined in Figure 2, the model developed in [1] gives the bistatic scattering strength

$$S_b = (10)\log\left(\sigma_{br}(\theta_s, \phi_s, \theta_i) + \sigma_{bv}(\theta_s, \phi_s, \theta_i)\right). \tag{1}$$

The scattering cross section is decomposed into a interface roughness component, σ_{br}, and a volume component, σ_{bv}. The interface cross section, σ_{br}, appearing in (1) is formed by smooth interpolation between the Kirchhoff cross section near the specular direction and the surface-perturbation-theory cross section elsewhere. The volume-scattering cross section, σ_{bv}, is based entirely on perturbation theory. The volume perturbations are variations in density and compressibility produced by biological and hydrodynamic reworking. The environmental parameters needed to drive this model are shown in Table 1. Several are carried over from the backscattering model [5] that forms the precursor to the bistatic model. The parameter values used in the model results shown in Section 4 are given in the right-hand column of the table and were derived from NRL environmental measurements.

The scattering cross sections in (1) were used in an expression derived to determine the scattered intensity as a function of time for the arrays, geometries, and incident pulses of the experiment. That expression is the time convolution of the pulse emitted from the transmitter with the bistatic scattering "impulse" response. This impulse response is

$$I(t) = I_0 \iint \left(\frac{(\sigma b_x b_r)}{(R_1 R_2)^2} 10^{-\frac{\alpha(R_1+R_2)}{10}} \right) dxdy\,. \tag{2}$$

In (2) σ is the summation of the surface- and volume-scattering cross sections, α is the attenuation of sound for the frequency of interest in decibels per unit length, b_x and b_r are the beampatterns of the transmitter and receiver, respectively, and R_1 and R_2 are the distances from the source to the scattering point on the bottom and from the receiver to the scattering point on the bottom, respectively. The integrals are over the elliptical area of the bottom that is scattering energy to the receiver between time t and time $(t + dt)$. Equation 2 and its convolution with the transmitted signal were implemented numerically and used, as described in the next section, in obtaining experimental values for the bistatic cross section.

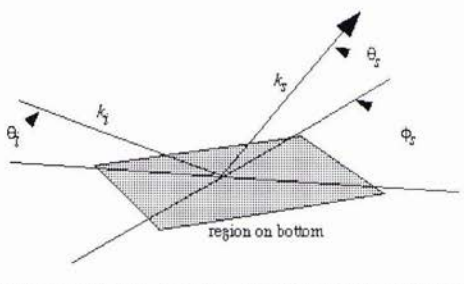

Figure 2. The incident and scattered wavevectors, k_i and k_s, are shown and the bistatic angles defined; θ_i is the incident grazing angle, θ_s is the scattered grazing angle, and ϕ_s is the bistatic angle.

Symbol	Definition	Short Name	Values for Sec. 4
ρ	Ratio of sediment mass density to water mass density	Density ratio	1.475
v	Ratio of sediment sound speed to water sound speed	Sound speed ratio	1.0
δ	Ratio of imaginary wavenumber to real wavenumber for the sediment	Loss parameter	0.0915
γ_3	Exponent of sediment inhomogeneity spectrum	Inhomogeneity exponent	4
w_3	Strength of sediment inhomogeneity spectrum (cm^3) at wavenumber $(2\pi) / \lambda = 1$ cm^{-1}	Inhomogeneity strength	0.0000241
μ	Ratio of compressibility to density fluctuations in the sediment	Fluctuation ratio	−1.31
γ_2	Exponent of the bottom relief spectrum	Spectral exponent	3.29
w_2	Strength of bottom relief spectrum (cm^4) at wavenumber $(2\pi) / \lambda = 1$ cm^{-1}	Spectral strength	0.0122

Table 1: Bottom parameters used as model inputs.

4. Model /Data Comparisons

The objective is to obtain experimental values for the bistatic scattering strength and compare them with model predictions. For each transmission, the geometry information recorded at the time of transmission, the attenuation in water, the beampatterns of the source and receiver, and the values for the bistatic cross section predicted using Table 1 were used in (2) to obtain an impulse response by numerical integration. This result was convolved with the transmitted waveform to obtain a prediction of the magnitude and temporal structure of the intensity scattered from the bottom into the receiver. This prediction was compared with its experimental counterpart. The region of the bottom that contributed significantly to the integral was also examined. If the scattering was localized on the bottom enough that a definite set of bistatic angles could be associated with the bottom-scattered intensity near the time of its peak amplitude, the bistatic angles were determined and the difference between the theoretical prediction and the data was used to arrive at an experimental value for the bistatic scattering strength [2].

The resulting data set is in the form of scattering strength values (1) associated with the triplet of angles in Figure 2. Data/model comparisons for other sites [2,3] have been previously displayed via three-dimensional plots. However, a simpler view [2–4] of data/model comparison will be used here. All data for incident and scattering angles within specified ranges were grouped and plotted as a function of ϕ_s. Model predictions were then calculated using $\theta_i = \theta_s$ for the lower and upper ends of each range. In the top left panel of Figure 3, for example, the upper curve is for $\theta_i = \theta_s = 15°$ and the lower curve is for $\theta_i = \theta_s = 5°$. This technique eliminates data where the incident and scattering angles are not similar but suffices to discuss data/model comparisons.

An initial examination of the data/model comparisons in Figure 3 indicates very good overall agreement throughout the entire ϕ_s range for all the grazing-angle ranges examined (5° to 30°). It is worthwhile to remember that the model has no free parameters. There are several points of detail that are significant in this data/model comparison.

Two significant points come from the extra control and expanded data set possible with the new experimental procedure. First, the data points shown are actually averages of individual data points. These averages were performed by binning the data into ϕ_s bins of 5°. A mean value was determined for all the data in each bin, and a 90% confidence interval was established assuming that the intensity and thus the scattering strength were independent samples from a chi-squared distribution [6]. The vertical lines associated with each data point in the figure indicate the 90% confidence level for each ϕ_s bin. Second, the data in the vicinity of $\phi_s = 0$ (near forward scattering) were not obtainable in previous experiments. It is easy to see the need for these near-forward-scattering data in testing the overall viability of the model, since the model predictions vary significantly in this region.

The other points concern the details of the data/model comparisons and the values of the environmental parameters given in Table 1. First, the data points in the top right panel seem to have an overall oscillation in the region of $70 \leq \phi_s \leq 180$ not seen in the model. Furthermore, in the same panel, the model seems to overpredict the scattering cross section in the region of $30 \leq \phi_s \leq 70$. Second, there is some indication in the bottom two panels that the model underpredicts the scattering in the region of $130 \leq \phi_s \leq 180$ for the higher grazing angles of those panels. This second behavior has also been seen in backscattering data from this region [7] (this reference also discusses in more detail the sediment-property meas-

urements leading to the values given in Table 1). The reason for these differences between the model and data is unknown at present; however, one possibility is that the environmental processes and resulting gradients in sediment parameters need to be modeled in more detail. In particular, the values for density and sound speed given in Table 1 are actually the "surficial" values, i.e., the values within 1–2 cm of the water/sediment interface. The sedimentation process is known to result in a gradient of these parameters over the first 5 cm [7]. The next level of sophistication for the model could be a two-layer view of the sediment with rough interfaces both at the water/sediment interface and at an interface 5 cm deep in the sediment. Regardless of whether this two-layer model would improve the data/model agreement, the fact that arguments about detailed comparisons between the model and the data can be carried out implies that understanding of bistatic scattering has progressed considerably both experimentally and theoretically.

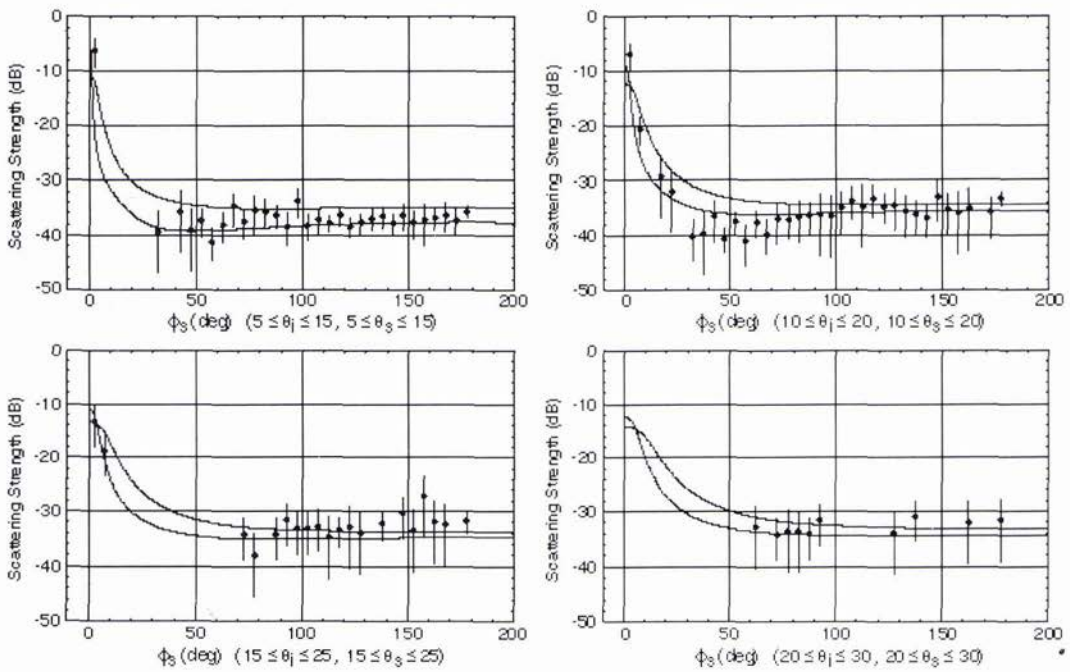

Figure 3. Model predictions of bistatic bottom-scattering strength compared with experimental data points from the Key West carbonate sand-silt-clay bottom. Model predictions, shown as curves, are for the upper and lower values of the grazing angles given at the bottom of each panel of the figure. (See Table 1 for site parameter values.)

References

[1] D. R Jackson, "A Model for Bistatic Bottom Scattering in the Frequency Range 10–100 kHz," Technical Report APL-UW TR 9305, Applied Physics Laboratory, University of Washington, August 1993.

[2] K. L. Williams and D. R Jackson, "Monostatic and bistatic bottom scattering: Recent experiments and modeling," *Proceedings of Oceans 94*, IEEE Press, vol. 2, pp. 225–260, 1994.

[3] K. L. Williams and D. R. Jackson, "Bistatic Bottom Scattering: Model, Experiments, and Model/Data Comparison," Technical Report APL-UW 9602, Applied Physics Laboratory, University of Washington, 1996.

[4] K. L. Williams and D. R. Jackson, "Bistatic bottom scattering: Model, experiments, and model/data comparison," unpublished manuscript (submitted to *J. Acoust. Soc. Am.*).

[5] D. R. Jackson, D. P. Winebrenner, and A. Ishimaru, "Application of the composite roughness model to high-frequency bottom backscattering," *J. Acoust. Soc. Am.*, vol. 79, pp. 1410–1422, 1986.

[6] F. T. Ulaby, R. K. Moore, and A. K. Fung, *Microwave Remote Sensing: Active and Passive*, Reading, Massachusetts , Addison-Wesley Publishing Company, pp. 486–488, 1982.

[7] D. R. Jackson, K. B. Briggs, K. L. Williams, and M. D. Richardson, "Tests of models for high-frequency seafloor backscatter," *J. Oceanic Eng.*, vol. 21, pp. 458–470, 1996.

Bottom/Subbottom Surveying Using a New, Parametric, Sidescan Sonar

Warren T. Wood*, Joseph F. Gettrust*, Mrinal K. Sen**, and James G. Kosalas***

*Naval Research Laboratory
Code 7432
Stennis Space Center, MS, 39529
Email: warren.wood@nrlssc.navy.mil

**University of Texas Institute for Geophysics
8701 MoPac Blvd N.
Austin, TX, 78759
Email: mrinal@utig.ig.utexas.edu

***Aliant Techsystems
Marine Systems West
6500 Harbour Heights Pkwy
Mukilteo, WA, 98275

Abstract

The Naval Research Laboratory (NRL) has developed a dual-frequency, towed, interferometric, sidescan sonar system known as the Subbottom Swath System, which is capable of detecting objects and structures buried below the sea floor. The transducer geometry is that of a conventional interferometer side scan sonar system but with a more powerful (241 dB re 1 μPa @ 1m) source. As a result of this power, S^3 is capable of generating low frequency (500 Hz - 2 kHz) parametric signals (~203 dB re 1 μPa @ 1m for 1600 Hz) that can easily penetrate several meters to tens of meters into the bottom. Data from a test in Puget Sound, WA show evidence of bottom penetration of parametrically generated sound.

1. Introduction

The Subbottom Swath System (S^3), conceived at the Naval Research Laboratory [1] and developed in cooperation with Aliant Techsystems, represents a breakthrough over conventional side scan sonars in that the earth structure and reflectivity within a vertical plane may be measured with a single ping, (Figure 1). This advance to a 2-D image for each ping is analogous to the advance of side scan (1-D per ping) over single transducer depth finders (a single depth estimate per ping). With the S^3 technology, not just the sea floor but the structures hidden beneath it can be mapped many times more efficiently than was previously possible. High resolution single-channel 3-D surveys could be done in a matter of days instead of weeks. Many of the technical problems encountered in this new technology have been overcome and we are able to demonstrate the bottom penetrating capabilities of S^3 in a test area in Puget Sound, WA.

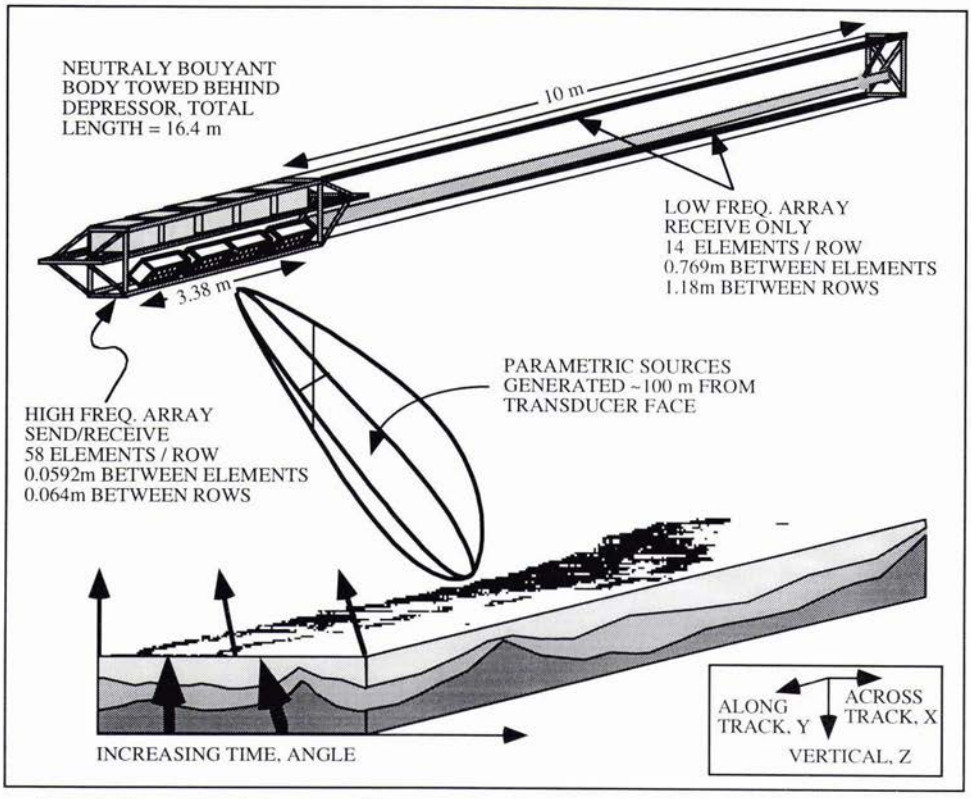

Figure 1. The Subbottom Swath System or S^3 operates using the same geometry as a conventional side scan sonar but with parametrically generated frequencies low enough to penetrate many meters into the seafloor.

2. Theory

In order to maintain high-resolution in the along-track direction with frequencies low enough to penetrate 10's of m, S^3 uses the nonlinear characteristics of high power sound generation, or parametrically generated sound. Through this phenomenon, energy can be transferred from high frequencies with their characteristic beam pattern to much lower frequencies within the same beam. The phenomenon of parametric sound generation was first described mathematically in detail by Westervelt [2,3,4] and is reviewed more succinctly by Clay and Medwin [5], so only a brief overview is given here.

Consider the pressure, (p) at a point, (x_o) on the x axis due to a single frequency, (w_1) plane wave traveling along the x axis with peak amplitude P_o. Assuming, without loss of generality, that we choose time, t=0 to coincide with x_o lying on a wave crest,

$$p(x_o,t) = P_o \cos \omega_1 t \tag{1}$$

The pressure due to a second wave with the same phase and amplitude but different frequency (w_2) can be represented by;

$$p(x_o,t) = P_o \cos \omega_2 t \tag{2}$$

If P_o is large enough that the medium of propagation, (water) behaves anelastically then the total pressure from the two waves at x_o is given not simply by the sum but by;

$$p(x_o,t) = P_o[\cos \omega_1 t + \cos \omega_2 t + m \cos \omega_1 t \cos \omega_2 t] \tag{3}$$

where $m = m(P_o)$ which is a measure of the non-linearity of the system and is quite small (~-40 dB) even at the rather high powers used by S^3. Because

$$2 \cos a \cos b = \cos(a+b) + \cos(a-b) \tag{4}$$

we get

$$p(x_o,t) = P_o[\ \cos \omega_1 t + \cos \omega_2 t + (m/2)\cos \omega_s t + (m/2)\cos \omega_d t\ ] \tag{5}$$

where $\omega_s = \omega_1 + \omega_2$ and $\omega_d = \omega_1 - \omega_2$. This interaction results in 4 waves, of frequencies ω_1, ω_2, ω_s, and ω_d. Thus a source of 11 and 12 kHz would result in parametric conversions to 1 and 23 kHz.

In practice, however, the parametric sound from S^3 is generated by a modulated single frequency rather than interfering dual frequencies. For the field data shown here the two rows of 11.5 kHz transducers are fired simultaneously, but in bursts of 4 cycles on and 3 cycles off for a total of 231 cycles or 20.09 ms resulting in a ω_d of 1.6 kHz. This modulation can be altered to yield a lower ω_d at a cost of decreasing m and signal level, or to yield a higher ω_d at a cost of decreased sediment penetration. The modulation could also be swept resulting in a larger bandwidth for ω_d and therefore increased spatial resolution.

As mentioned above, the parametric sound generation occurs only in the presence of the source frequency and therefore has the same beam pattern, (Figure 2). We are thus able to generate the 1.6 kHz signal with a much narrower along-track beam width and corresponding higher resolution than could be achieved by generating the low frequency signal directly. This is discussed further in the next section.

3. Instrumentation and Operation

Figure 1 is a drawing of the system, (not to scale with the beam or seafloor), built for NRL by Aliant Techsystems [6]. The neutraly buoyant 16.4 m long system is towed at the desired depth behind a depressor. The high frequency (HF) source array is made up of two rows of 11.5 kHz nominal resonance ceramic transducers, 3.38 m long. The electronics for the 58 transducer elements in each row are connected in parallel resulting in a two channel system. The physical separation between elements in each row is 0.0592 m, and the separation between rows, (channels) is 0.064 m. When fired simultaneously the two rows form a very intense beam (20 kW, corresponding to a sound intensity level of 241 dB re 1 µPa @ 1 m), which is relatively wide across-track and relatively narrow along-track, (~60° and 2.5° respectively, down to the -6 dB point, see Figure 2). This allows for high along-track resolution, yet broad across-track coverage maximizing the range ensonified.

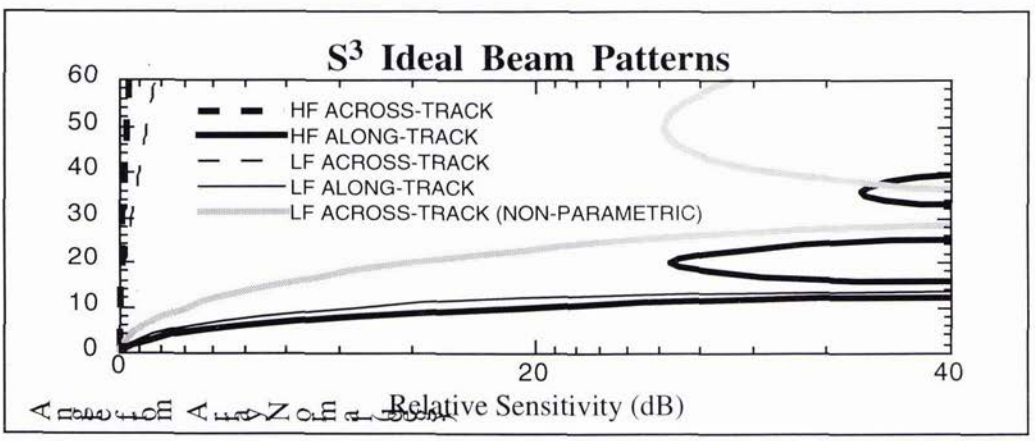

Figure 2. Like a conventional side scan system, the beam pattern is very wide across-track and very narrow along-track. The combined transmit-receive pattern for the along-track LF signal is much narrower (fine curve) than would be possible for the same array under non-parametric conditions, (gray curve), due to the virtual sources lying only within the narrowest part of the HF beam, (heavy black curve). The beams shown here were computed for point sources and receivers and do not include effects of the transducer housing.

The HF source array also acts as a receive array, further narrowing the beam width of the recorded signal and generating a conventional, although very high power, side scan image. As with conventional side scan there is a trade off between the area investigated (maximized with the shallowest towing) and the resolution achieved, (maximized with the deepest towing). Because of the high power used, the system must be towed deeper than ~10 m to prevent transducer cavitation. Also, the parametric sound generation occurs about 100 m from the face of the HF array [5].

As operated during the Puget Sound test, the high-power HF array produced a parametric source at a frequency of 1.6429 kHz with an estimated power level of 204.5 dB (re 1 μPa @ 1 m). The backscattered sound is received by a low frequency, (LF) array located along a "stinger" or "tail" boom, (Figure 1). The 14 hydrophones per row, (element separation 0.769 m and row separation 1.18 m) which make up the two row, 10 m long, LF array are spaced proportionately to give approximately the same beam pattern and direction as the HF array. Figure 2 shows the beam patterns of both arrays. These are combined transmit and receive beams. For the HF array the transmit is the same as the receive beam so the result is just the square of the transmit beam, (heavy and heavy dashed lines). For the low frequency array we assume the LF transmit beam is the same as the HF transmit beam without the side lobes [5]. This is multiplied by the receive beam pattern of the LF array itself to give the LF result shown in Figure 2, (fine and fine dashed lines). The heavy gray line shows what the along-track beam width would be for a 1.6 kHz source generated non-parametrically with an array configured like the LF array. The parametric approach allows for a narrower beam and therefore greater resolution for an array of a given size, making practical a 1.6 kHz system with the along-track resolution comparable to that of a 11.5 kHz system.

4. The Data

The data presented here are from a test cruise in Puget Sound, near Seattle, WA, (water depth <200 m), in which the first clearly identifiable low-frequency returns from the system were recorded, (Figure 3). The data are recorded as four complex time series of 5000 samples each corresponding to each of the two rows of high and low frequency elements. Each time series is digitized after a base band shift, also called heterodyning, or in phase and quadrature down conversion, a process which shifts the band to a lower frequency which then allows the data to be adequately sampled at a rate of 5 kHz. The high frequency data were shifted to DC as is the usual practice, but because the lower frequency is variable they were shifted by 1.3068 kHz. The S^3 was fired once per second and the towing speed was 1.4 kts resulting in 0.72 m/ping. Each ping shown in Figure 3 is simply the sum of the complex absolute values of the two complex samples at each time, after appropriate bandpass filtering.

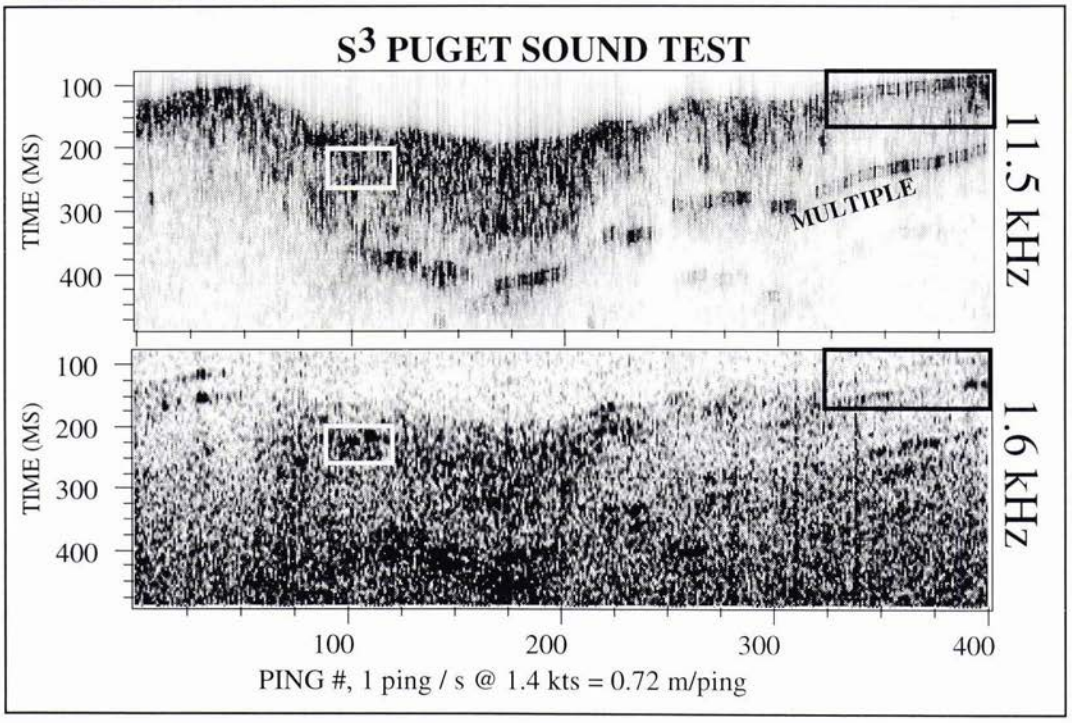

Figure 3. The HF (upper) and LF (lower) scattered returns are largely similar as would be expected but differ significantly in certain locations (boxes) due to bottom penetration. Note the significantly lower signal to noise ratio of the LF data.

5. Data Imaging and Inversion

Processing of the S^3 HF data is virtually identical to the processing of side scan data, but the steps involved with mapping the parametric energy to its proper spatial location involve somewhat different steps. The 4 complex time series are first band pass filtered and also cepstral filtered according to their respective bands to remove events which are known to be noise. At this stage the data are mapped from time and amplitude into the spatial cylindrical coordinates y,R,θ, where R is the range from the ship track, y is measured along the towing track, and θ is the angle from vertical. The complex data at each time are first converted from Cartesian (r,i), to polar (A,ϕ), via

$$A = \text{sqrt}(z_r^2 + z_i^2) \quad \text{and} \quad \phi = \text{atan}\,(z_r\, z_i^* / A) \qquad (6)$$

Where * denotes complex conjugate and f is the relative phase angle (electrical angle) between the signals from the upper and lower components of each array. Knowing the distance between the array elements, the angle the array makes with the vertical, and the speed of sound in water allow us to convert this phase angle into a physical angle (θ) measured from the vertical. The range, R is also easily computed giving us the point in image space (R,θ) to which the amplitude at that sample should be mapped. This is different than conventional processing in that the LF data are not forced to lie along a surface but may be mapped to any depth along the circular trajectory given by R.

A more sophisticated imaging (positioning, migration) scheme has been developed which includes a variable velocity function in the sediments and therefore a non circular trajectory [7]. The algorithm is a modification of Kirchoff migration algorithm commonly used in the oil exploration industry [8]. The S^3 data can be viewed as stacked (or coincident source-receiver) data, and a slightly modified Kirchoff post stack migration algorithm is well suited for imaging these data. Our approach involves tracing rays from the source/receiver location to each point in a 2-D velocity model. The travel time and arrival angle for the ray at each grid point in the subsurface are stored in a table, for use as the imaging condition for the S^3 data. The measured amplitude at a given time is mapped via the phase and stored table information to the subsurface location where it originated, assuming that the velocity function is known. This migration algorithm can be modified to include iterative velocity refinement and inclusion of shear wave paths through the sediments in the ray calculation.

A synthetic experiment was conducted to test the inversion algorithm with the results displayed in Figure 4. The model earth was composed of two, semi-parallel rough layers. In the ideal case of no noise (Figure 4, left), the inversion is robust, clearly positioning the backscattered energy on the two rough surfaces. Note, however, that the performance suffers in the presence of noise, (Figure 4, right). This is not so much a characteristic of the inversion algorithm as it is a characteristic of the wavelength, array size, and range. Like conventional side scan systems this one is much more sensitive to errors in phase than errors in amplitude. A signal to noise ratio of 20 dB, which is suitable for most imaging, degrades the migrated image such that the two layers can be seen but little interpretation can be done.

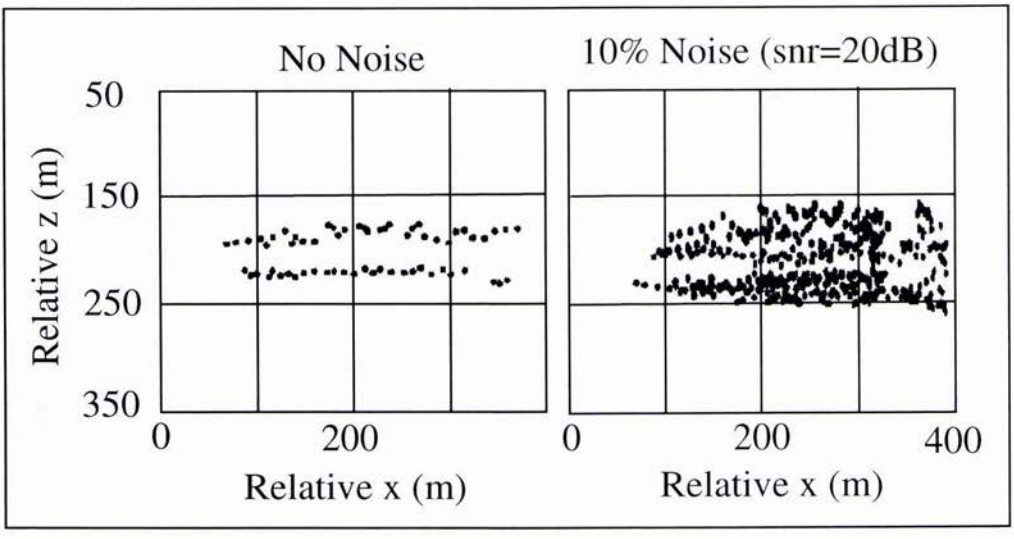

Figure 4. The Kirchoff inversion was applied to a synthetic using an earth model composed of two flat, but rough layers. A signal to noise ratio of better than 20 dB is required for robust performance of the algorithm, [7].

This sensitivity of the inversion due to the presence of noise in phase measurements was seen in the field data as well. While the amplitudes of the events seen in the boxes in Figure 3, (lower) can be seen through the noise, even small amounts of noise in the phase produce large distortions, preventing these data from yielding a satisfactory sub-bottom image. Compounding the problem for this particular data set is the fact that the LF data are aliased, the array elements are > 0.5 wavelengths apart. This is not an insurmountable problem since the less noisy HF data can be used to determine the bathymetry which can then be used to guide the LF inversion. We assume that arrivals at similar times come from similar angles, a reasonable assumption if penetration is not too deep. This divides the LF data into time zones or lanes within which the LF electrical angle varies from $-\pi$ to π. However, it is the noise contamination in the phase measurement which is the main obstacle to creating a subbottom imagewith these particular data.

6. Conclusions

The data image in Figure 3 show strong returns from both high and low frequency signals. Although the signal to noise ratio of the low-frequency data is disappointing, the data clearly show features which are not visible in the corresponding conventional 11.5 kHz image. We interpret these signals as evidence of subbottom penetration. Additional tests have confirmed that the self-noise of the low-frequency array is the limiting factor in the performance of this system [9]. That array is currently being modified to improve its noise characteristics, and additional tests are scheduled for summer 1997.

This work was supported by ONR program element 0601153N31.

References

[1] J. F. Gettrust and M. M. Rowe, "High-resolution geoacoustic studies in deep ocean environments",in *Proceedings of Oceans '91, IEEE* , pp.442-445, 1991.

[2] P. J. Westervelt "Scattering of Sound by Sound" *The Journal of the Acoustical Society of America,* vol. 29, pp.199-203, February 1957.

[3] P. J. Westervelt "Scattering of Sound by Sound" *The Journal of the Acoustical Society of America,* vol. 29, pp.934-935, August 1957.

[4] P. J. Westervelt "Parametric Accoustic Array" *The Journal of the Acoustical Society of America,* vol. 35, pp.535-537, April 1963.

[5] C. S. Clay and H. Medwin, Acoustical Oceanography, New York, John Wiley and Sons, pp. 162-175, 1977.

[6] Aliant Techsystems Marine Systems *SeaMARC 12/1.5 3-D Imager Field Service Manual*, 1992.

[7] M. K. Sen, F. A. Akbar, P.L. Stoffa, and J. F. Gettrust, Imaging of Ocean Subbottom Structure using Swath Mapping Data: Feasability Studies, abstract., *The Journal of the Acoustical Society of America*, vol. 93, p. 2341, 1993.

[8] O. Yilmaz, Seismic data processing, Society of Exploration Geophysicists, Investigations in Geophysics Vol. 2, 1988.

[9] M. T. Kalcic and A. B. Martinez, Subbottom Swath Sonar: SNR Analysis, Naval Research Laboratory Report, NRL/MR/7441--96-8035, December 1996.

SACLANTCEN CONFERENCE PROCEEDINGS SERIES CP-45

High Frequency Acoustics in Shallow Water

Proceedings of a conference held in
Lerici, Italy, 30 June to 4 July, 1997,
organized and sponsored by the
NATO SACLANT Undersea Research Centre

edited by

Pace N.G.
SACLANT Undersea Research Centre, La Spezia, Italy

Pouliquen E.
SACLANT Undersea Research Centre, La Spezia, Italy

Bergem O.
SACLANT Undersea Research Centre, La Spezia, Italy

and

Lyons A.P.
SACLANT Undersea Research Centre, La Spezia, Italy

Increased awareness of the importance of littoral processes in environmental and defence research, has given impetus to new approaches to the application of high frequency acoustics to the sensing of water column, seabed and surface parameters.

ISBN 88-900194-1-7

NATO SACLANT Undersea Research Centre